2023 BERLIN MNE
MICRO AND NANO ENGINERING CONFERENCE

ABSTRACT BOOK

Berlin, September 25th – 28th, 2023

49. International Conference on Micro- and Nano Engineering

Table of Contents

Abstracts

Track1 - Novel Developments in Nano/Micro Fabrication Methods and Processes

Track2 - Fabrication and Integration of Micro/Nano Structures, Devices and Systems

Track3 - Micro/Nano Engineering for Life Sciences

Track4 - Micro/Nano Engineering for Physical and Chemical Applications

Focus Track - Next Generation Quantum Computing and related Materials / Track2 - Fabrication and Integration of Micro/Nano Structures, Devices and Systems

Poster Session1.1: Focus Track/Track1/Track3

Poster Session 1.2: Track3, Track4

Track3 - Micro/Nano Engineering for Life Sciences / Track4 - Micro/Nano Engineering for Physical and Chemical Applications

Poster Session2.1: Track 2

Poster Session2.2: Track 4

Track1 - Novel Developments in Nano/Micro Fabrication Methods and Processes / Track3 - Micro/Nano Engineering for Life Sciences

Papers

Novel Developments in Nano/Micro Fabrication Methods and Processes - Papers

Fabrication and Integration of Micro/Nano Structures, Devices and Systems - Papers

Micro/Nano Engineering for the Life Sciences - Papers

Micro/Nano Engineering for Physical and Chemical Applications - Papers

Focus Track - Next Generation Quantum Computing and related Materials - Papers

Poster Session1.1: Focus Track/Track1/Track3 - Papers

Poster Session 1.2: Track3, Track4 - Papers

Micro/Nano Engineering for Life Sciences / Track4 - Micro/Nano Engineering for Physical and Chemical Applications - Papers

Poster Session2.1: Track 2 - Papers

Poster Session2.2: Track 4 - Papers

Novel Developments in Nano/Micro Fabrication Methods and Processes / Track3 - Micro/Nano Engineering for Life Sciences - Papers

Abstracts

Track1 - Novel Developments in Nano/Micro Fabrication Methods and Processes

O-S11-T1-1 Scalable, Full-Wafer Fabrication of High Performance, All-Inorganic Metalenses, Waveguides and Diffractive Optics via Nanoimprint Lithography

Dr. Dae Eon Jung [1], ***Dr. Vincent Einck*** [1], ***Mr. Lucas Verrastro*** [1], ***Prof. Amir Arbabi*** [1], ***Prof. James Watkins*** [1]

1. *University of Massachusetts Amherst*

All-inorganic visible wavelength metalenses with absolute efficiencies of 75% (>90% design efficiency) and waveguide gratings for AR/VR were fabricated using nanoimprint lithography (NIL) with cycle times of 2 minutes on full wafer imprint tools. 1000s of metalenses were fabricated on a single wafer. Atomic layer deposition (ALD) was used as a post-imprint treatment to precisely tune the refractive index of the optical structures from 1.9 to 2.2 using a small number of cycles, which enables higher efficiencies for metalenses, expanded fields of view for AR/VR, and substrate/imprint RI matching for improved process efficiencies and performance. The all-inorganic nature of the imprinted optical components offers superior optical and materials stabilities while the additive NIL approach offers compelling cost advantages relative to subtractive processing.

O-S11-T1-2 Investigation of different focused ion beam systems and milling strategies for structuring crystalline semiconductors and polycrystalline metal layers

Dr. Thomas Loeber [1], ***Dr. Bert Laegel*** [1], ***Prof. Georg von Freymann*** [1]

1. *RPTU Kasierslautern - Landau*

We report on different milling strategies for structuring crystalline semiconductors and sputtered polycrystalline metal layers on Silicon. Besides a standard Gallium FIB a novel Caesium FIB with a low temperature ion source is used. The Cs FIB can operate at lower acceleration voltages (V = 2 to 16 kV) with beam spot sizes down to 2 nm. Structures are milled in sputtered gold and silver layers on silicon at different beam parameters to optimize the result.

O-S11-T1-3 Research and Development Activities of EUVL at NewSUBARU Synchrotron Light Facility

Prof. Takeo Watanabe [1], ***Dr. Tetsuo Harada*** [2], ***Dr. Shinji Yamakawa*** [2]

1. *University of Hyogo,* ***2.*** *Center for EUVL, Laboratory of Advanced Science and Technology for Industry, University of Hyogo*

Since 1996, R&D of the fundamental study of EUV lithography has been done at NewSUBARU synchrotron light facility. This facility is the largest synchrotron light facility which is operated by the university in Japan. EUVL technology started to use for the fabrication of 7 nm+ logic device from 2019. EUVL are expected to use for the fabrication of 0.5 nm node logic device. In this situation, the technical issues are EUV resist, EUV mask and pellicle, and EUV light source development.

O-S11-T1-4 Nano-antennas with decoupled transparent leads for opto-electronic studies

Ms. Melanie Sommer [1], ***Dr. Florian Laible*** [1], ***Dr. Kai Braun*** [1], ***Prof. Alfred Meixner*** [1], ***Prof. Monika Fleischer*** [1]

1. *University of Tübingen*

Plasmonic nanoantennas find a wide range of applications in optoelectronic devices, like photodetectors and solar cells. But to integrate single nanostructures into circuits some challenges have to be faced. To use the nanoantennas' surface plasmon polaritons (LSPPs) to their full potential the placement of the electrical leads has to be carefully chosen. By using transparent indium tin oxide (ITO) instead of gold or other metals as leads, this difficulty can be overcome. ITO is electrically conducting but insulating at optical frequencies. This way the LSPPs do not propagate away along the leads, but the antennas are still electrically connected.
The connected dimer bow tie antennas are fabricated with electron beam lithography (EBL), shadow lithography and focused helium ion beam milling. The leads are made from sputtered ITO that is etched into the shape of the EBL pattern by reactive ion etching. A small gap, that exhibits a high near field is located in the middle of the dimer structure. The spectral properties show the typical characteristics of non contacted bow tie antennas.

O-S21-T1-2 An effective and promising process for manufacturing nanofluidic channels in large scale

Mr. Wentao Yuan [1], ***Mr. Shuoqiu Tian*** [1], ***Prof. Yifang Chen*** [1]

1. *Fudan university*

Nanofluidic channels can find extensive applications in enzyme analysis [1], sensor [2], and nanofluidic chips [3]. Unfortunately, the manufacturing of nanofluidic channels still remains a challenge. So far, it has been reported that nanofluidic channels can be fabricated by nanoimprint, near-field electrospinning, imprinting-induced cracks, etc. However, at the stage for prototype, electron beam lithography (EBL) based processes are still needed in the areas of nanochannels owing to its advantages of high accuracy and mask less. In this work, a novel sealing method based on isotropic growth of silica on hydrogen silsesquioxan (HSQ) gratings prepared by EBL was used to fabricate inorganic nanofluidic channels with the channel-width of 60 nm.

O-S21-T1-3 3D laser direct lithography for maskless patterning on large-format complex surfaces

Mr. Julian Hürtgen [1]

1. *Fraunhofer ILT*

A 5-axis 3D direct laser lithography system is currently under construction at the Fraunhofer ILT. This system allows lithography to be performed on curved substrates, such as mirror surfaces or lenses, where classical mask-based lithography is no longer possible. Direct laser lithography is used to create a resist mask, allowing electrodes and conductive tracks to be applied in a subsequent metallization step. The 5 axes of the system are moved in a highly coordinated manner so that a perpendicular incidence of the laser beam relative to the surface of the substrate is guaranteed throughout the entire exposure process. This guarantees a high edge quality of the resist mask and consequently also for subsequent metallized structures. Also integrated into the system is a spray coating unit, which can be used to produce a homogeneous coating layer on complex surfaces of a wide variety of materials. In addition, the system has a camera detection system that enables precise substrate-mask alignment for the creation of multilayer systems.
Overall, this 5-axis 3D direct laser lithography system can write structures with 5 µm resolution on curved substrates up to 150 mm in diameter, representing an important step towards the industrial production of three-dimensional optoelectronic devices.

O-S21-T1-4 Rapid Tooling for Injection Moulding with DLP 3D Printing

Mr. Duarte Menezes [1], ***Ms. Alysha Hunter*** [1], ***Prof. Nikolaj Gadegaard*** [1]

1. *University of Glasgow*

The field of microfluidics is repeatedly addressed as having great potential to influence and revolutionize modern biology. However, the predominant use of poly(dimethylsiloxane) (PDMS) is seen as a limiting factor constraining the transition of the technology from academic research to industry, partly due to its associated low scalability and material properties. The present work addresses this gap by suggesting an alternative manufacturing procedure based on Digital Light Processing (DLP) 3D Printing, as an affordable solution to rapid prototyping moulds, followed by injection moulding, to mass produce polystyrene replicas of the moulds at industrial rate, and finally, ultrasonic welding and hot bonding, to seal the microfluidic channels together into a complete device. The present manufacturing procedure is capable of producing, from scratch, hundreds of devices within the time frame of a single working day. The side wall of features in the mould is designed to present a waviness of Wa = 0.97 [µm], as a critical factor to ensure easy demoulding during injection moulding. Furthermore, surface properties of moulds can be controlled to sub-micron roughness, Ra = 0.95 [µm], subsequently conferring high optical properties to injection moulded PS chips, rivalling those presented by a glass slide.

O-S31-T1-1 A Unique New Correlative Microscopy Platform for Combined Nanoscale Microscopy by Combination of AFM and SEM

Dr. Christian Schwalb [1]

1. *Quantum Design Microscopy GmbH*

The combination of different analytical methods into one instrument is a powerful technique for the contemporaneous acquisition of complementary information. In this work, we introduce a highly integrated new corelative microscopy platform, the FusionScope, that seamlessly combines AFM and SEM within a unified coordinate system.

We will present a variety of novel case studies to highlight the advantages of this new tool for interactive, correlative, in-situ nanoscale characterization for different materials and nanostructures. First results will focus on hard-to-reach samples. FusionScope allows for fast and easy identification of the area of interest and precise navigation of the cantilever tip for correlative SEM and AFM measurements.

In addition, we will present first results for the in-situ characterization of individual nanowires that will be used for energy harvesting applications. The SEM enables the easy location of individual or multiple nanowires, whereas the in-situ AFM allows the characterization of topography, surface roughness, mechanical, and electrical properties of the nanowire.

Based on the broad variety of applications regarding the inspection and process control of different materials and devices, we anticipate that this new inspection tool to be one of the driving characterization tools for correlative SEM and AFM analysis in the future.

O-S31-T1-2 Millimeter-Scale Van Der Waals Graphene-MoS2 Heterostructures Verified by Raman Spectroscopy

Mr. Nico Rademacher [1], ***Mr. Eros Reato*** [1], ***Ms. Annika Grundmann*** [2], ***Prof. Prof. Dr. Michael Heuken*** [3], ***Dr. Holger Kalisch*** [2], ***Prof. Andrei Vescan*** [2], ***Dr. Alwin Daus*** [1], ***Prof. Max C. Lemme*** [4]

1. *Chair of Electronic Devices, RWTH Aachen University,* ***2.*** *Compound Semiconductor Technology, RWTH Aachen University,* ***3.*** *AIXRT,* ***4.*** *Chair of Electronic Devices, RWTH Aachen University and AMO GmbH, Advanced Microelectronic Center Aachen*

Verifying the interaction between 2D materials is crucial for the fabrication of van der Waals heterostructures (hereafter referred to as heterostructures), as loosely stacked materials lack the properties of true heterostructures. Raman spectroscopy proves to be an effective non-destructive method for this purpose. As an example heterostructure, we focus on a graphene and MoS2 heterostructure.

This study successfully fabricates mm²-scale heterostructures and provides a guideline and methodology for quantitatively examining the interlayer coupling between graphene and MoS_2. Raman area measurements conducted before and after annealing demonstrate a change in the interaction between MoS_2 and graphene, indicated by the increased Raman shift of the 2D peak.

To identify heterostructure regions, a statistical analysis is employed, comparing the difference between the graphene G and 2D peak positions across all measured points. By defining a threshold at Δ Pos(2D)-Pos(G) of approximately 1100 cm-1, heterostructure regions can be distinguished. Additionally, considering the full width at half maximum (FWHM) of the graphene 2D peak helps differentiate between bilayer graphene (BLG) and a heterostructure.

To validate the preparation principle on a larger scale, a heterostructure of approximately 40 mm² is fabricated, demonstrating the scalability of the evaluation methodology.

O-S31-T1-3 Wafer-Level Zone Casting of Additive-Free Graphene Dispersion

Mr. Marc Stevens [1], ***Dr. Sascha Hermann*** [1]

1. *Fraunhofer ENAS*

Duo to its exceptional properties, Graphene has inspired its integration in functional applications via ink based printing techniques. In this work we present a liquid phase printing technique for highly conductive Graphene Films based on zone casting. Zone casting consists in the deposition of dispersion on a moving substrate, with a continuous supply to the evaporation zone by a flat nozzle. The solvent evaporates from the meniscus zone and the Graphene is deposited on the moving substrate. This leads to a high orientation of the Graphene Sheets and the use of little dispersion. A pure, additive free Graphene-Water Dispersion with an average flake size of 1-2µm and a 2%wt was used for printing onto a 200mm Si-Wafer with an HfO surface. Film thicknesses between 20nm and 100nm were achieved. All Films were measured via 4-point-measurments through sputtered Cr-Pt contact pads. With an average electrical conductivity of 130 kS m^{-1} and a sheet resistance under 200Ω/q, the reported Films show a high conductivity, exceeding the results of prior reported conductivities of established printing technologies and various Dispersions. The presented printing technique shows a improvement of electrical conductivity without complex post-processing processes, as well as without the usage of toxic solvents.

O-S31-T1-4 Damage-free Plasma-assisted Atomic Layer Deposition of High-quality Dielectrics on 2D Materials

Dr. Sarah Riazimehr [1], ***Dr. Harm Knoops*** [1], ***Mrs. Ardeshir Esteki*** [2], ***Dr. Gordon Rinke*** [3], ***Mr. Martin Otto*** [3], ***Dr. Zhenxing Wang*** [3], ***Prof. Max Lemme*** [3], ***Dr. Katie Hore*** [1]

1. *Oxford Instruments,* ***2.*** *RWTH Aachen,* ***3.*** *AMO GmbH*

A novel method has been established to grow dielectric on two-dimensional (2D) materials through an in-situ-prepared protective seed layer without apparent damage to the 2D materials. In the shown example, low-damage plasma atomic layer deposition (ALD) of aluminum nitride (AlN) is used as a seed layer to protect the graphene layer against plasma ALD of aluminum oxide (Al_2O_3). The low-damage plasma ALD AlN conditions prevent damage to the graphene and simultaneously provide sufficient protection for graphene against plasma ALD Al_2O_3.

O-S31-T1-5 Synthesis of super-flat graphene on substrates selected by molecular dynamics calculation

Dr. Satoru Kaneko [1], ***Prof. Takashi Tokumasu*** [2], ***Dr. Satomi Tanaka*** [1], ***Dr. Chihiro Kato*** [1], ***Dr. Manabu Yasui*** [1], ***Dr. Masahito Kurouchi*** [1], ***Dr. Daishi Shiojiri*** [3], ***Mr. Masahiko Mitsuhashi*** [1], ***Prof. Ruei-Sung Yu*** [4], ***Dr. Shihgeo Yasuhara*** [5], ***Prof. Musa Can*** [6], ***Dr. Kripasindhu Sardar*** [7], ***Dr. Sumanta Sahoo*** [8], ***Prof. Masahiro Yoshimura*** [7], ***Dr. Akifumi Matsuda*** [9], ***Prof. Mamoru Yoshimoto*** [10]

1. *KISTEC,* ***2.*** *Tohoku University,* ***3.*** *aaa,* ***4.*** *Asia University,* ***5.*** *Japan Advanced Chemicals,* ***6.*** *Istanbul University,* ***7.*** *National Cheng Kung University,* ***8.*** *Radhakrishna Institute of Technology and Engineering,* ***9.*** *Tokyo Institute of Technology,* ***10.*** *T*

Super-flat graphene grew on a target substrate selected by using molecular dynamics (MD) calculation. In order to select optimal substrates for graphed growth, an absorption energy between carbon clusters and candidate substrates was estimated by using molecular a dynamics calculation. The candidate substrates were silicon, magnesium oxide, sapphire and strontium titanate. Supercell was constructed by carbon cluster, (1) six-ring membered carbon and (2) 6 six-ring carbon (nano-graphene) placed on the candidate substrates, and absorption energy was estimated by MD calculation with optimizing the supercells.

Absorption energies were relatively stable on STO, MgO and Si substrates compared to Al_2O_3. After the structural optimization of supercells, 6-ring vertically stood up on Al_2O_3, Si(100) and MgO(001) substrates, and nano-graphene was distorted on Si(111) substrate. Both six-ring and nano-graphene flatly covered only the surface of STO substrate among the candidate substrates. Experimentally carbon films were deposited on the candidate substrates by pulsed laser deposition, and super-flat graphene was experimentally grown on the STO substrate.

O-S41-T1-1 Junctionless Nanowire Transistor: From Devices to Sensing Applications

Mr. Sayantan Ghosh [1], ***Dr. Muhammad Bilal Khan*** [1], ***Mr. Ahmad Echresh*** [1], ***Mr. Ulrich Kentsch*** [1], ***Dr. Slawomir Prucnal*** [1], ***Ms. Vaishali Vardhan*** [2], ***Dr. Subhajit Biswas*** [2], ***Dr. John Wenger*** [2], ***Dr. Stig Hellebust*** [2], ***Prof. Justin Holmes*** [2], ***Prof. Artur Erbe*** [1], ***Dr. Yordan Georgiev*** [1]

1. *Institute of Ion Beam Physics and Materials Research, Helmholtz-Zentrum Dresden-Rossendorf (HZDR),* ***2.*** *University College Cork*

Silicon junctionless nanowire transistors (JNTs) have shown excellent sensitivity to record-low concentrations of the protein streptavidin in the liquid phase. However, JNTs have not yet been tested for sensing in the gas phase.

The aim of this work is to develop small, low-cost JNT-based nanosensors for radical detection. Silicon-on-insulator wafers were doped by ion implantation and flash-lamp annealing. Device patterning was based on electron beam lithography, inductively-coupled reactive ion etching, metal deposition, and lift-off.

The sensor tests exhibited characteristic shifts in the transfer curve and a systematic increase and decrease of p- and n-type current, respectively, under the influence of NO_2. These tests confirmed the potential suitability of the ambipolar JNT as sensors in a gaseous environment. Additionally, these devices will be functionalized and tested for the electrical detection of atmospheric free radicals.

O-S41-T1-2 Two-photon laser 3D printing enhancement by quantum dots and in-situ exchange

Dr. Ye Yu [1], Dr. Anatol Prudnikau [2], Dr. Vladimir Lesnyak [3], Mr. Man Ho Wong [1], Ms. Madhuri Chennur [1], Ms. Tanya Saxena [1], Mr. Josua Zscheile [1], Dr. Robert Kirchner [4]

1. *HETEROMERGE GmbH, Gostritzer Str. 61, 01217 Dresden, Germany,* ***2.*** *Center for Advancing Electronics Dresden (cfaed), Technische Universität Dresden, Helmholtzstr. 18, 01069 Dresden, Germany,* ***3.*** *Physical Chemistry, Technische Universität Dresden, Zellescher Weg 19, 01069 Dresden, Germany,* ***4.*** *TU Dresden*

2PP direct laser writing has been significantly improved in the last decades. One remaining challenge is the availability of functional print materials and efficient processing of them. We present a novel quantum dot enhanced material enabling superior feature size reduction and a novel in-situ material exchange for 2PP systems enabling functional micro additive fabrication.

O-S41-T1-3 Combining thermal scanning probe lithography and dry etching for grayscale nanopatterns amplification in SiO2

Mr. Berke Erbas [1], ***Dr. Ana Conde Rubio*** [2], ***Dr. Xia Liu*** [3], ***Prof. Giovanni Boero*** [1], ***Prof. Jürgen Brugger*** [1]

1. *Ecole Polytechnique Federale de Lausanne (EPFL),* ***2.*** *ICMAB-CSIC,* ***3.*** *Beijing Institute of Technology*

While nanolithography has historically focused on downscaling, there is now a growing interest in grayscale nanolithography for introducing or enhancing functionality in micro- and nanodevices. Thermal scanning probe lithography (t-SPL) achieves single-digit nanometer spatial resolution and sub-nanometer depth control for grayscale nanofabrication, but it is limited to shallow depths typically below 100 nm. Here, we combine t-SPL with dry etching to overcome the limitation in grayscale nanopatterning depth. The aspect ratios of the “shallow” polymer patterns are amplified up to 10 times in a dry etch process when transferred from thermally-sensitive polyphthalaldehyde (PPA) resist into the underlying SiO_2 layer using CHF_3/SF_6 plasma. Our newly developed dry etch recipe enables the transfer without introducing additional surface roughness, and the aspect ratio amplification is achieved without any distortion of the original shapes in etching with up to 5 times depth amplification. This technique for the fabrication of the high aspect ratio and smooth grayscale dielectric nanostructures presented in this work has the potential to enable new photonic and nanoelectronics applications.

O-S41-T1-4 Multi-process compatibility of hybrid polymers allowing advanced micro- and nano-patterning

Mr. Johannes Wolf [1], ***Dr. Arne Schleunitz*** [1], ***Dr. Maria RUssew*** [1], ***Mrs. Gabi Grützner*** [1]

1. *micro resist technology GmbH*

The material class of hybrid polymers is established for many years in industrial manufacturing processes as UV-curable polymer mostly used in replication technologies to manufacture permanent micro- and nano-optical pattern. Among other benefits such as optical performance and physical stability, hybrid polymers e.g. endure reliability tests such as temperature cycling and temperature-humidity aging. With its proven qualification as a production material, any novel technologies employing the hybrid polymers can be transferred to industry even more quickly. This is important as market requirements change and hence alternative patterning technologies continue to develop. In this perspective, an exceptional advantage of the material class of the hybrid polymers is its multifunctionality resulting in a compatibility to various micro- and nano-fabrication processes using the very same material, e.g. OrmoComp®. Consequently, diversified process compatibility enables faster innovation cycles for example for micro-optics manufacture to go from rapid prototyping over small scale production to large scale mass fabrication using different schemes of micro- and nano-fabrication. We verified the hybrid polymer processing diversity beyond generic replication processes using the following material and process innovations: 1) Inkjet printing as alternative coating technique, 2) 3D printing for mastering and prototyping, 3) Micro-Macro-Integration, 4) i-line stepper lithography for alternative micro-patterning

O-S51-T1-1 New high-resolution SiO2-based positive-tone resist for electron beam lithography

Prof. Andrea Cattoni [1], ***Dr. Dominique Mailly*** [2], ***Prof. Ivan Maximov*** [3]

1. *Politecnico di Milano,* ***2.*** *Centre de Nanosciences et de Nanotechnologies (C2N) CNRS, Université Paris-Saclay,* ***3.*** *Lund University*

We developed a new hybrid organic-inorganic SiO_2-based positive-tone resist for high-resolution Electron Beam Lithography at 100 KeV. When developed in HF 1%, the remaining resist is a hydrophobic SiO2 ceramic due to the presence of the Methyl group in its structure. We demonstrated the patterning of isolated features down to 38 nm (period 100 nm) in 100 nm-thick films. We expect to improve resolution and sensitivity of such Electron Beam Lithography resist by optimizing the process parameters as well as by using Focused Helium Ion Beam Lithography. Preliminary results indicate that the resist can be also used for Deep UV lithography and Talbot lithography when the chemistry of the resist is modified by substituting the Methyl group with the Phenyl group.

O-S51-T1-2 Greyscale lithography beyond 100 µm pattern depth facilitated by a novel photoresist and optimized processing

Dr. Christine Schuster [1], ***Ms. Marina Heinrich*** [1], ***Ms. Gerda Ekindorf*** [2], ***Dr. Anja Voigt*** [1], ***Dr. Arne Schleunitz*** [1], ***Mrs. Gabi Grützner*** [1]

1. *micro resist technology GmbH,* ***2.*** *Heidelberg Instruments Mikrotechnik GmbH*

Greyscale lithography is applied to manufacture complex 2.5D and freeform microstructures in photoresists which serve as master for the pattern transfer into materials for permanent applications, often used in micro-optics.
We present a novel photoresist enabling greyscale lithography of very deep patterns. Issues limiting the pattern depth caused by the photoresist chemistry were addressed. Greyscale pattern depths of 120µm were possible with this prototype, with a well-considered choice of photoresist ingredients, and lithography process adjustments, with the prospect of even deeper patterns up to 150-160µm.

O-S61-T1-1 Additive micro-structuring of non-planar optical waveguides for multifunctional neural interfaces

Dr. Marco Bianco [1], ***Dr. Antonio Balena*** [1], ***Dr. Marco Pisanello*** [2], ***Dr. Elisa Scarpa*** [1], ***Dr. Filippo Pisano*** [1], ***Dr. Barbara Spagnolo*** [1], ***Ms. Maria Samuela Andriani*** [1], ***Mr. Miroslav Stiburek*** [3], ***Dr. Petra Kolbabkova*** [3], ***Dr. Hana Uhlirova*** [3], ***Prof. Tomas Cizmar*** [4], ***Dr. Ferruccio Pisanello*** [1], ***Prof. Massimo De Vittorio*** [1]

1. *Istituto Italiano di Tecnologia,* ***2.*** *OptogeniX s.r.l.,* ***3.*** *Institute of scientific instruments of Czech Republic, Complex photonics,* ***4.*** *Leibniz institute of photonic technology*

Microstructured implantable neural interfaces are vital for mapping neural circuits, controlling brain activity, and developing treatments for neurological disorders. However, the increasing complexity of neuroscience experiments requires multifunctional devices capable of detecting diverse neural signals with cell specificity and delivering precise therapies. Creating such tools presents challenges for micro- and nano-fabrication, including integrating multiple functionalities on different substrate geometries, ensuring biocompatibility, and minimizing invasiveness to avoid tissue damage.

In this study, we propose a method using Two-Photon Polymerization (TPP) to fabricate micro-patterns on non-planar optical fibers of various geometries. Our aim is to integrate microelectrodes, optical channels, and microelectronic components directly onto the surface of a low-invasiveness probe. We employ TPP to pattern the optical waveguide on the entire surface, followed by conformal or masked deposition of metallic and dielectric layers, wet etching, and wire-bonding to an external circuit board.

We describe (i) the fabrication of a probe based on a tapered optical fiber (TF) equipped with micro-electrodes and optical channels for optogenetic neuron activation, (ii) a multifunctional probe based on a 45°-polished sideview optical fiber for combined electrophysiology and holographic endoscopy, (iii) the integration of a thermistor on a TF for temperature monitoring in deep-brain.

O-S61-T1-2 Guided Domino Lithography for Uniform Ultra-Sharp Nanoantenna Arrays

Mr. Dong Kyo Oh [1], ***Mr. Jaekyung Kim*** [1], ***Ms. Jihae Lee*** [1], ***Prof. Junsuk Rho*** [1]

1. *pohang university of science and technology*

Plasmonic nanoantennas are essential components in optical sensors and quantum plasmonics, but achieving uniform fabrication at the single-digit-nanometer scale remains challenging. We propose guided domino lithography as a method for producing uniform ultra-sharp nanoantenna arrays. By exploiting the collapsing behavior of unstable photoresist nanostructures, we achieve uniform fabrication of ultra-sharp bowtie photoresist masks. We compare the yields of conventional and guided domino lithography techniques under optimized electron beam exposure and development conditions. Additionally, we rigorously analyze the electric field enhancement effect of different geometries of ultra-sharp bowtie nanoantennas. Our results demonstrate the potential of guided domino lithography as a practical manufacturing method for single-digit-nanometer plasmonic nanoantennas.

O-S61-T1-3 Intra-level Mix and Match Approach of the Photoresist mr-EBL 6000.5 using E-Beam and i-line Stepper Lithography for PICs

Mr. Sebastian Schermer [1], ***Mr. Markus Reinhardt*** [1], ***Dr. Christian Helke*** [1], ***Ms. Susanne Hartmann*** [2], ***Dr. Georg Heldt*** [1], ***Mr. Franz Tank*** [2], ***Dr. Anja Voigt*** [3], ***Dr. Danny Reuter*** [4]

1. *Fraunhofer ENAS, Technologie Campus 3, 09126 Chemnitz,* ***2.*** *Technische Universität Chemnitz, Center for Microtechnologies, Reichenhainer Str. 70, 09126 Chemnitz, Germany,* ***3.*** *micro resist technology GmbH,* ***4.*** *Fraunhofer ENAS*

In recent years, the miniaturization of modern integrated circuits (IC´s) and micro-electro-mechanical systems (MEMS) became more and more demanding. Complex structures with different sizes down to nanometer scale requires precision and high writing speeds at the same time. In order to achieve sub 100 nm structures, maskless writing tools such as electron beam (e-beam) lithography is used. The downside of these sequential writing techniques are low writing speeds. To overcome those problems, one of the methods for complex pattern transfer is Mix and Match (M&M) lithography, which in general means the combination of exposures from two different lithographical devices on one wafer. In contrast, we make use the intra-level mix and max approach (ILM&M). This approach combines at least two lithography techniques on just one resist layer. In this paper we describe the lithographic technique of exposing photonic integrated circuit (PIC) related structures such as waveguides, ring resonators and coupling structures within this ILM&M approach.

O-S61-T1-4 Novel Fabrication of Arbitrary Optical Probe Array by 4D Printing

Dr. Dominique Decanini [1], ***Mr. Abdelmounaim Harouri*** [1], ***Ms. Ayako Mizushima*** [2], ***Dr. Jongho Park*** [2], ***Prof. Beomjoon Kim*** [2], ***Prof. Yoshio Mita*** [2], ***Dr. Gilgueng Hwang*** [3]

1. *C2N/CNRS-University Paris-Saclay,* ***2.*** *The University of Tokyo,* ***3.*** *LIMMS/CNRS-The University of Tokyo*

Probes are essential elements for electrical, mechanical or optical characterizations of biological or chemical samples. Particularly the optical probes are promising for near field sub-wavelength imaging technologies various fabrication methods either on the optical fiber or on the cantilever have been proposed. However, their fabrications usually require sophisticated micro/nanofabrication technologies therefore batch production of optical probe array is challenging. In this work, we propose a novel fabrication of arbitrary optical probe array with 4D printing driven by surface tension assisted closing and consequent bonding of the closed structures by sputtering of metallic layers which serve as a mirror to reflects and guide the light through the aperture of microprobe.

O-S61-T1-5 Penrose Patterns for Error Measurement in Electron Beam Lithography

Dr. Paul Reynolds [1], ***Dr. Stephen Thoms*** [1]

1. *University of Glasgow*

Penrose patterns have been shown to have a number of advantages for correlation-based marker search in electron beam lithography. We show that by writing the Penrose pattern in two halves it is possible to accurately measure small displacement errors, leading to a convenient method to measure stitch, overlay and drift errors which arise from the electron beam writing process. We demonstrate the use of split penrose patterns to measure offsets with sub nanometer precision in an automated fashion which can be implemented on the majority of commercial electron beam lithography systems. A key benefit of using an interleaved penrose is reducing the area required for accurate measurement of errors to a few square microns.

O-S71-T1-1 Fast Hybrid-ALE to etch amorphous carbon.

Ms. Atefeh Fathzadeh [1], ***Dr. Philippe BEZARD*** [2], ***Prof. Stefan De Gendt*** [3]

1. *KU Leuven University/ IMEC,* ***2.*** *IMEC,* ***3.*** *Ku Leuven / IMEC*

Hybrid-Atomic Layer Etching (H-ALE) is a novel cyclic etch process that co-integrates a Reactive Ion Etching component (etch rate improvement) with quasi-ALE (profile correction). ALE-like profiles in amorphous carbon are demonstrated with reasonable process times. The purge-less process consists of gas adsorption (injecting O_2/ Ar) and plasma desorption steps (injecting Ar only). Most of the etching happens in the early stage of the plasma step (RIE phase), when the neutral to ion ratio () is still high (injection of reactants just stopped, and those are being pumped away). Excess in neutral flux causes RIE-like profile deterioration (footing, undercut, etc.) – which is why the adsorption step is gas-, not plasma-based. The ALE phase starts when most of the neutrals have been pumped away (minimal) so that the majority of neutrals reacting with the surface are the ones previously adsorbed but not yet desorbed: an optimal profile can then be reached by increasing the ion fluence and each cycle exhibits an excellent profile. Understanding the etching mechanisms allows for bringing neutrals and ions of adequate energy only when needed during the desorption step. This Hybrid-ALE is an economically viable process with ALE-like performance.

O-S71-T1-2 Multi-layer nanoimprint lithography material system for nanopattering of functional substrates

Dr. Mirko Lohse [1], ***Dr. Martin Messerschmidt*** [1], ***Mrs. Nadja Heidensohn*** [1], ***Mrs. Susanne Grützner*** [1], ***Dr. Arne Schleunitz*** [1], ***Mrs. Gabi Grützner*** [1]

1. *micro resist technology GmbH*

Nanofabrication technologies have moved from purely academic interest to industrial relevance for the last decades and enabled the miniaturization of devices in fields of application of non-semiconductor domains such as optics, photonics and life science applications. In our presentation, we will show how nanoimprint lithography (NIL) is one of the key enablers in the fabrication of precise nano patterns for emerging application fields, such as meta lenses, where deviations from the design lead to an unacceptable loss in performance. We will present our view on industry driven imprint materials, their advantages and limitations and how a multilayer approach can overcome certain challenges in particular for non-classic substrates as used for high RI glasses in AR/VR. While our described approach with this material system is particularly targeting NIL manufacturing industry, we strongly believe that it will enable academics to further push the technology and explore a multitude of options in terms of patterns and substrates, developing the novel processes beyond current industrial usage.

O-S71-T1-3 Plasma Parameters Impact on Carbon Microlens Shape and Surface Roughness

Dr. Delia Ristoiu [1], ***Mr. Pierre Ducluzaux*** [1], ***Mr. Guillaume Claveau*** [1], ***Ms. Ece Aybeke*** [1], ***Mr. Etienne Mortini*** [1]

1. *STMicroelectronics, 850 rue Jean Monnet, 38926 Crolles Cedex, France*

CMOS image sensor technologies are now extensively used in various fields such as machine vision, computational photography, augmented reality, digital healthcare, biomedical imaging. One of the main components of the image sensor are microlenses which allow light focalization onto the photodiode. Etched microlens are one of the most powerful techniques to achieve high surface fill factor and therefore maximize the quantum efficiency of the image sensor.

Spherical microlenses are obtained by photoresist reflow and then they are transferred into a subjacent carbon-based layer by plasma etching. The purpose of this transfer process is to use shrink the lateral gap between microlenses, while maintaining the spherical shape. This study is focused on the plasma conditions impact on microlens shape and surface roughness.

Microlenses are etched in a CF_4 plasma, generated in a commercial CCP (capacitively coupled plasma) reactor using 2 plasma generators: a high frequency generator (HF power), and a low frequency generator (LF power) and a continuous negative high voltage generator (HVDC). In this study, a screening on CF4 flow, HF power, LF power, HVDC bias and pressure was performed and resulting microlens height, diagonal gap and roughness were analyzed

O-S71-T1-4 Blurred Electron Beam Induced Deposition for Direct Fabrication of Plasmonic Nanoantennas onto Tapered Optical Nanofibers towards Enhanced Single Photon Emission

Dr. Antonio Balena [1], ***Dr. Chengjie Ding*** [2], ***Mrs. Marianna D'Amato*** [2], ***Dr. Muhammad Fayyaz Kashif*** [3], ***Dr. Filippo Pisano*** [3], ***Dr. Marco Pisanello*** [4], ***Dr. Gaia de Marzo*** [3], ***Prof. Massimo De Vittorio*** [3], ***Prof. Alberto Bramati*** [2], ***Dr. Ferruccio Pisanello*** [3]

1. *Istituto Italiano di Tecnologia; Laboratoire Kastler Brossel,* ***2.*** *Laboratoire Kastler Brossel,* ***3.*** *Istituto Italiano di Tecnologia,* ***4.*** *OptogeniX s.r.l.*

Solid-state emitters, which have simple fabrication and can operate at room temperature, coupled with plasmonic structures and integrated directly onto optical nanofibers (ONFs) are of great interest for various applications in quantum photonics. Nevertheless, deterministic methods to fabricate single nanostructures or complex geometries directly on ONFs are not currently available, nor have been proposed. In this work, we introduce a bottom-up fabrication approach based on Electron Beam Induced Deposition to directly fabricate plasmonic nanoantennas onto the ONFs' surface. The deposited material is thoroughly characterized by Energy Dispersive X-Ray Spectroscopy, Scanning Electron Microscopy, and Atomic Force Microscopy. The structures directly fabricated on suspended, dielectric, and nanometric ONFs are optically characterized by measuring the dependence of the scattering intensity from the polarization of a propagating NIR laser, as well as how, by fixing the input polarization of the beam, the scattered light is polarized. Furthermore, we characterized the broadband spectral response using a supercontinuum laser and measured the spectral differences in the scattering from the two geometries, highlighting a redshift of the scattered signal for the nanoantenna configuration. The results and numerical predictions suggest that the fabricated structures can enhance the single photon emission properties of room-temperature solid-state emitters.

O-S81-T1-1 Advancements in Fabricating Polymer based Microring Resonators by Nanoimprint Lithography

Dr. Santhosh Pandian [1], ***Dr. Petri Karvinen*** [2], ***Dr. Heikki Rekola*** [2], ***Dr. Subhajit Bej*** [1], ***Dr. Paul Müllner*** [3], ***Dr. Eggeling Moritz*** [3], ***Dr. Rainer Hainberger*** [3], ***Prof. Tapio Niemi*** [1]

1. *Nanophotonics Research Group, Tampere University, Tampere,* ***2.*** *University of Eastern Finland, Joensuu,* ***3.*** *AIT Austrian Institute of Technology GmbH*

Polymeric materials for photonic integrated circuits (PIC) have attracted much interest over the past decades due to their unique properties, including low absorption, wide wavelength range, and simple and low-cost fabrication process. When compared to its counterparts (semiconductor materials), the polymer-based materials have the capability to fine tune their refractive index more easily. Polymeric materials also can incorporate active dopants, such as dyes providing optical gain, to realize devices with enhanced functionality. Advanced 3D structures are required to allow a high integration density of the photonic systems. Some of the classic examples of these systems are very large-scale integrated (VLSI) photonics and microring resonators (MRRs). Polymer based MRRs have been widely used in many applications ranging from optical communication and signal processing to sensing. One important field of application of polymer waveguide MRRs is biosensing, which is highly relevant for medical diagnostics, food analysis, and environmental monitoring due to its high sensitivity and real-time monitoring capabilities. Another interesting area for polymer waveguide MRRs is the realization of miniaturized ultrasonic detectors, which are key elements for photoacoustic imaging. These MRRs have been prepared using the established Nanoimprint Lithography (NIL) technique.

O-S81-T1-2 3D Ice Lithography

Dr. Bingdong Chang [1], ***Mr. Affan Kaysa Waafi*** [1], ***Mr. Joachim Lyngholm-Kjærby*** [1], ***Dr. Rubaiyet Haque*** [1], ***Prof. Anpan Han*** [1]

1. *Technical University of Denmark*

We report a novel 3D lithography strategy using condensed organic vapour thin films and electron beam exposure layer by layer. The process uses a focused electron beam to chemically cross-link the organic ice into a solid and shares software and CAD databases with industrial 3D printing. Guided by electron-matter-interaction simulations, we control the cross-linking thickness between 250 nm and 2 μm. The 3D prints contained up to 500 layers, and the smallest structures are 550-nm-wide. Our digital process complements two-photon lithography in three areas; (i) it is compatible with chemistry beyond photopolymers, (ii) we can print delicate suspended structures and tubes because our structures are not immersed in liquid resins that reside in cavities and destroy structures by interfacial forces, (iii) hanging structures are printed without sacrificial supports. Nanophotonics and microfluidics applications are demonstrated.

O-S81-T1-3 Manipulating droplet motion on superhydrophobic glass by contact electrification

Mr. Kuan-Ting Chen [1], ***Prof. Jiann Shieh*** [1]

1. *National United University*

The manipulation of water droplet movement has garnered significant attention due to its wide range of applications in various fields, such as self-cleaning, heat transfer, and energy harvesting. Various strategies involving both active methods and passive methods have been employed to drive droplet movement. However, a major challenge that remains is overcoming surface resistance to achieve fast movement over long distances. Recently, the generation of static charge through contact electrification has emerged as a promising approach for effective droplet manipulation. While the charging phenomenon has been shown to affect droplet sliding on surfaces and motion in air, the spontaneous repulsion between droplets on surfaces has not been identified, despite being observed in vapor-mediated systems or under external field conditions. Here, we present a spontaneous charging method for water droplets to repel each other on surfaces. We grew silica nanowires on a quartz plate to create a superhydrophobic glass. After contact electrification by injecting water, the generated static charge allows pure water droplets to repel each other, preventing them from merging and enabling droplets to become stuck on the surface and even move uphill. Remarkably, these charged droplets can travel at speeds exceeding a few centimeters per second over centimeter-scale distances.

O-S91-T1-1 Avoiding Sidewall Redeposition when Dry Etching Nonvolatile Materials: A Reverse Liftoff Process

Dr. David Lishan [1], ***Mr. Vincent Genova*** [2], ***Dr. Samantha Norris*** [3], ***Dr. Kyle Dorsey*** [4]

1. *Plasma-Therm, LLC,* ***2.*** *Cornell University (Ret.),* ***3.*** *Axoft,* ***4.*** *Physical Sciences, Inc.*

This work demonstrates a subtractive approach intended for use with materials that do not readily form volatile and desorbing byproducts under common plasma etching operating conditions. Our approach is derived from the well-known additive method of patterning thin metal layers using liftoff. Like the additive liftoff approach, our “reverse” liftoff technique also uses a structure with sacrificial layer that is laterally undercut beneath the upper pattern defining layer. After etching, the material that was physically sputtered etched and deposited on the mask sidewalls is removed along with the sacrificial layer. The typical undesirable artifacts of sputter redeposition, often called “dog or rabbit ears, veils, or fences” are avoided. Using Pt as a representative test film for materials challenged by traditional dry etching, results are shown for etching up to 200 nm films without unwanted resputtered features. Modeling efforts considered feature spacing, resputter distribution (cosine power function), and incident ion angles. Both IBE (ion beam etching) and ICP (inductively coupled plasma) configurations were used with similar results. This is relevant as ICP etching equipment is significantly more common in wafer processing facilities than IBE and provides a route for plasma etching low or nonvolatile materials without sidewall redeposition.

O-S91-T1-2 Realization of fully independent complete field-effect devices grown all-in-situ with the innovative Shadow Wall Epitaxy technique

Dr. Yurii Kutovyi [1], ***Dr. Nils von den Driesch*** [1], ***Ms. Christine Falter*** [1], ***Mr. Felix Khamphasithivong*** [2], ***Mr. Denny Dütz*** [2], ***Dr. Lars R. Schreiber*** [2], ***Prof. Detlev Grützmacher*** [1], ***Dr. Alexander Pawlis*** [1]

1. *Forschungszentrum Jülich GmbH,* ***2.*** *RWTH Aachen University*

Innovative forward-looking solutions in chip manufacturing technology are vital nowadays to meet the global growing demands for consumer products and services. In this regard, the leveraging and integration of new material systems such as compound semiconductors into state-of-the-art semiconductor technology, which is experiencing now a technologically challenging time, promises a revolutionary impact on the global chip production and development systems. However, for this to happen, cost-efficient, fast, and sustainable fabrication concepts have yet to be matured. With this perspective, we developed an innovative shadow-wall-assisted growth concept for the molecular beam epitaxy technique. The concept involves the use of prefabricated shadow walls to confine molecular beams to specific device regions, enabling selective and in-situ growth of superior-quality semiconductor platforms under ultrahigh-vacuum conditions. The technique allows for the in-situ fabrication of electrical contacts and gate terminals through the deposition of metals and oxides, eliminating the need for post-processing steps. The proposed shadow-wall epitaxy technique has been demonstrated by accomplishing low-ohmic electrical contacts to buried ZnSe films. The results confirm the excellent quality contacts with low sheet resistance and contact resistivity and, therefore, pave the way for the realization of fully-in-situ-processed compound semiconductor devices with superior electrical performance such as electrostatic spin qubits.

O-S91-T1-3 FEBID field emitters for vacuum nanoelectronics

Prof. Teodor Gotszalk [1], ***Ms. Ewelina Gacka*** [1], ***Mr. Bartosz Pruchnik*** [1], ***Mr. Piotr Kunicki*** [1], ***Mr. Krzysztof Kwoka*** [2], ***Dr. Tomasz Piasecki*** [1], ***Prof. Ivo W. Rangelow*** [3], ***Dr. Andrzej Sierakowski*** [4], ***Dr. Isaac Stricklin*** [5], ***Dr. Tito Busani*** [5]

1. *Wroclaw University of Science and Technology,* ***2.*** *Department of Nanometrology, Wrocław University of Science and Technology, Wroclaw, 50-370, Poland,* ***3.*** *Technische Universität Ilmenau,* ***4.*** *Institute of Microelectronics and Photonics,* ***5.*** *University of New Mexico*

e report FE conducted with use of the FEBID nanowires deposited on the operational microelectromechanical system (opMEMS) microbridge (fig. 1). The opMEMS was microbridge – 600 μm long, 40 nm thick structure suspended above an opening in the [110] silicon. The structure integrates three independent metal paths – two for displacement actuation, one to be cut for deposition of the FEBID electrodes[4]. Before the electrode deposition the device conductivity was tested. The conductivity tests were also performed after the electrodes were removed with FIB and measured in the same way. Gap for the FE electrodes was milled in the gallium focused ion beam (FIB) process. FEBID pedestal was fabricated to increase the structure stiffness, the FIB fiducial marks were used to observe the distance between cathode and electrode. We performed FE measurements in the tip-tip (fig. 2) and point-plane setup (fig. 3). The cathode and anode were fabricated out of Pt(C) material, which were also implanted with gallium ions. The electrodes were imaged between the measurements in order to analyze electrode structural changes[5]. We recorded FE in the range of up to 40 nA at the voltages ranging up to 60 V (fig. 4,5). Calculated Fowler-Nordheim curves confirmed FE process.

O-S91-T1-4 Diffuse Reflection of Neutrals as a Mechanism for Inverse Reactive Ion Etching Lag in Semiconductor Manufacturing

Dr. Patrick Vanraes [1], ***Dr. Syam Parayil Venugopalan*** [2], ***Dr. Matthieu Besemer*** [2], ***Prof. Annemie Bogaerts*** [1]

1. *University of Antwerp,* ***2.*** *ASML*

The control of process non-idealities in semiconductor manufacturing due to aspect ratio dependent etching (ARDE) remains a crucial challenge. The etch rate or depth usually decreases with aspect ratio in ARDE, known as regular reactive ion etching (RIE) lag. The less common opposite effect, where the etch rate or depth increases with aspect ratio, is referred to as inverse RIE lag. It is often attributed to a shift towards a more polymerizing chemistry at a higher incident neutral-to-ion flux ratio, or to ion scattering at the sidewalls. We propose an alternative explanation based on the diffuse reflection of neutrals. Through multiscale modeling and experiments, we demonstrate how microtrenches can be formed at low aspect ratios due to the Knudsen transport of neutrals towards the etch front, instead of ion funneling as frequently assumed. At a higher aspect ratio around unity, these microtrenches merge, resulting in the inverse RIE lag. We further used the model to investigate how ARDE may be regulated with several strategies, where the hardmask shape was found to have the strongest effect. These findings provide a deeper insight in etch non-uniformity in semiconductor manufacturing.

Track2 - Fabrication and Integration of Micro/Nano Structures, Devices and Systems

O-S12-T2-1 Plasmonic black coatings with broadband absorption

Dr. Mario Ziegler [1], ***Dr. David Zanders*** [2], ***Mr. Valentin Ripka*** [1], ***Mr. Hanjörg Wagner*** [1], ***Ms. Vilborg Vala Sigurjónsdóttir*** [1], ***Prof. Anjana Devi*** [2], ***Dr. Uwe Hübner*** [1]

1. *Leibniz Institute for Photonic Technology e.V.,* ***2.*** *Ruhr University Bochum*

For most light-driven catalytic applications, large 3D surface areas are favourable. Typically, atomic layer deposition (ALD) nor chemical vapor deposition (CVD) processes are the methods of choice as these techniques are dedicated to 2D layer depositions and are in need for a 3D scaffold to generate 3D structures. Here, we report on an approach for the generation of broadband absorbing three-dimensional structures, so-called metastable atomic layer deposition (MS-ALD). MS-ALD enables the mixture of different scaffold materials such as silica, zinc oxide or titania and incorporate silver nanoparticles into the scaffold. Optically optimized structures consisting of silica scaffolds and silver nanoparticles (AgNP@SiO_2) revealed high performance absorption characteristics above 99.5 % over a broad wavelength range from 220 nm up to 4000 nm at a film thickness of only 9 µm. The structures are able to withstand long humidity exposures at elevated temperatures as well as thermal cycling or exposure to atomic oxygen without any remarkable loss of the optical properties resulting in long-term stable plasmonic absorber. The substitution of the non-conductive scaffold SiO_2 by conductive carriers such as titania (TiO_2) or zinc oxide (ZnO) revealed promising absorption efficiencies in visible spectra of 94 % and 80 % in near infrared.

O-S12-T2-2 A spin-on-carbon/thin-metal based metasurface for broadband light modulation

Mr. Shuoqiu Tian [1], ***Prof. Yifang Chen*** [1]

1. *Fudan university*

Metasurface is of great interest in nanophotonics for the ability to abrupt manipulate light in a subwavelength dimension. However, typical design strategy based on metal or dielectric nano optical antennas suffers from ohmic loss or challenging to fabricate. In this work, we introduce spin on carbon (SOC) to the design and fabrication of metasurface which greatly alleviates the above difficulties. As a proof of concept, a SOC/thin-metal based chessboard metasurface is proposed and fabricated. High aspect ratio nanopillars with width under 50 nm in a large scale are acquired through a simple electron beam lithography (EBL) process. A plasmon hybridization mechanism is revealed through finite difference and time domain (FDTD) simulations and experiments. This hybridization results in a tunable structure color and wavelength-selective antireflection ability in visible and near infrared band. In this work, we successfully introduced SOC is applied in design and fabrication of metasurface, which is of great importance of next generation nanophotonic device.

O-S12-T2-3 Durable Icephobic Superhydrophobic Silicon Nanowires Surfaces

Mr. Miika Heikkilä [1], ***Ms. Laura Fieber*** [1], ***Mr. Seyed Mehran Mirmohammadi*** [1], ***Dr. Ville Jokinen*** [1], ***Prof. Sami Franssila*** [1]

1. *Aalto University*

Adhesion of ice on surfaces can be detrimental to windmill blades, power lines, airplanes, and sensors, motivating a search for icephobic surfaces. Superhydrophobic surfaces can repel water droplets, where an air pocket prevents the majority of the water from making contact with a solid. In many cases, superhydrophobicity can lead to time-delayed freezing or reduced ice adhesion strength on the surface. A key challenge is the durability of icephobicity: the ability to repel ice over multiple icing cycles. This has been achieved by several of the previous studies with superhydrophobic surfaces made from polymeric materials utilizing interfacial slippage, but it remains a challenge, especially for hard materials. Here, we present durable superhydrophobic icephobic silicon surfaces utilizing microscale protective microstructures, monolithic nanowires, and protective hard coatings.

O-S12-T2-4 Photoinduced reconfigurable hydrophilic pattern generation in thin film metal oxides

Mr. Jesper Navne [1], ***Ms. Rucha A. Deshpande*** [1], ***Mr. Mathias Adelmark*** [1], ***Mr. Evgeniy Shkondin*** [2], ***Prof. Julien Bachmann*** [3], ***Prof. Rafael Taboryski*** [1]

1. *Technical University of Denmark,* ***2.*** *DTU Nanolab,* ***3.*** *Friedrich-Alexander-Universität Erlangen-Nürnberg*

Metal oxides like TiO2 and ZnO become hydrophilic when irradiated with UV light. Here, we exploit the effect to demonstrate reversible patterning of biphilic surfaces. The induced hydrophilicity can be reversed to pre-exposure levels either by leaving the samples in a dark room, by controlled annealing or exposure to higher wavelength photons. The mechanism behind the phenomenon is the light induced excitation of electron-hole pairs that diffuse to the surface and engage in surface reactions such as a reduction of oxygen.
We have investigated: 1) The difference between TiO2 and ZnO 2) The sub-wavelength thin film thicknesses and roughness influencing the effect. 3) Variation in UV intensities and wavelengths.
4) The electronic bandgap was measured with reflective electron energy loss (REELS), and the effect on wettability by surface adsorbed carbon from the environment was characterized with X-ray photoelectron spectroscopy (XPS).
The resulting contact angles were measured both statically while exposed to UV light, and dynamically with a pre-exposed dose and compared with a theoretical model, constructed from Cassie Baxter model wetting model, the absorbance in the metal oxide layers, and the probability for the electron-hole pair to reach the surface by diffusion.

O-S13-T2-1 3D Printing of Molecularly Imprinted Polymers by Digital Light Processing for antibiotics recovery

Ms. Elena Camilli [1], ***Mr. Wei Tang*** [2], ***Dr. Ignazio Roppolo*** [1], ***Dr. Francesca Frascella*** [1], ***Mrs. Valentina Bertana*** [1], ***Prof. Matteo Cocuzza*** [1], ***Prof. Tsuyoshi Minami*** [2], ***Dr. Simone Luigi Marasso*** [3]

1. *Politecnico di Torino,* ***2.*** *The University of Tokyo,* ***3.*** *CNR*

Molecularly Imprinted Polymers (MIPs) as artificial receptors are nowadays employed in a large number of applications and fabricated in a variety of techniques, including photopolymerization methods, even though fabrication through additive manufacturing (AM) appears mostly as an unexplored field. The challenge of this work is in the employment of AM technology to realize 3D-printed MIP-based objects. A composite photocurable resin was developed and optimized to be suitable for a Digital Light Projector printer. The resin consists of Oxytetracycline (OTC) as the template molecule, methacrylic acid (MAA) as the functional monomer, Dipropylene Glycol Diacrylate (DPGDA) as the photopolymerizable crosslinker and DMSO as the solvent. The interaction mechanism between MAA and OTC was computationally investigated through density functional theory (DFT) calculations, including the presence of the solvent. At first, multi-material disks were printed, consisting of a MIP 50 µm thick layer on a 500 µm thick support base of DPGDA. Then, complex 3D filters were printed, entirely made of MIP resin. The samples were tested for Oxytetracycline recovery from aqueous media and the target absorption was characterized by UV-Vis spectrophotometry.

O-S13-T2-2 Fully inkjet printed and metallized waveguide antenna for RADAR application

Mr. Peter Bauer [1], ***Mr. Gerald Stubauer*** [1], ***Dr. Pavel Kulha*** [1], ***Dr. Michael Haslinger*** [1], ***Mr. Christian Debatin*** [2], ***Mr. Jochen Seeser*** [2], ***Dr. Alexander Fischer*** [3], ***Dr. Istvan Denes*** [3], ***Dr. Dieter Holzinger*** [4], ***Dr. Doron Gurovich*** [5], ***Mr. Semyon Melamed*** [5]

1. *PROFACTOR GmbH,* ***2.*** *Notion Systems GmbH,* ***3.*** *Robert Bosch GmbH,* ***4.*** *TIGER Coatings GmbH & Co KG,* ***5.*** *PV Nano Cell Ltd*

In this work a fabrication process for metallized 3D waveguide antenna structures via inkjet printing is presented. Various 3D antenna structures were printed with non-transparent UV-curable dielectric Ink on printed circuit boards (PCBs) and afterwards metallized by a precise overprinting with conductive nanoparticle silver ink. The printing was performed with the TINKER-Pilot Printer, a multi-material printer which can be equipped with up to 4 printheads. The developed inkjet materials (UV-curable dielectric Ink and nanoparticle silver ink) as well as the TINKER-Pilot-Printer are presented in more detail. In addition, RADAR functionality testing of the inkjet printed 3D waveguide antenna structures, will be presented.

O-S13-T2-3 Focused Ion Beam sample preparation for Reverse Tip Sample SPM applications

Mr. Pieter Lagrain [1], ***Mr. Lennaert Wouters*** [1], ***Mr. Kris Paulussen*** [1], ***Dr. Eva Grieten*** [1], ***Dr. Geert Van den Bosch*** [1], ***Dr. Sana Rachidi*** [1], ***Dr. Didit Yudistira*** [1], ***Dr. Thomas Hantschel*** [1]

1. *IMEC*

Scanning probe microscopy (SPM) measurements often require very frequent switching of tips, which can lead to inefficient and time-consuming work. One of the most promising methods to tackle this problem, is by making use of the reverse tip sample (RTS) concept, which switches position of the sample and the tip. To achieve this, the sample itself must be mounted on a tipless cantilever. However, to our knowledge no practical information on how to prepare these samples is available. This work describes a practical way of mounting samples on tipless cantilevers using a dual-beam FIB/SEM system. Using this system, we extracted pieces of material, containing functional semiconductor devices, from standard silicon wafers. With a standard built-in Pt deposition module we could anchor the samples to the cantilevers. The same module could also be used to make an electrical contact between the surface of the samples and the cantilever, which is a requirement to perform electrical SPM measurements. Both cross-section and top view samples were successfully prepared this way. The method was also extended to make samples from an inline waferflow. The stability and functionality of all samples was tested afterwards using high force electrical measurements (C-AFM and SSRM).

O-S13-T2-4 Block copolymer nanostructured Si thin films for thermoelectric enhancement

Mr. Alex Rodriguez-Iglesias [1], ***Dr. Iñigo Martín-Fernández*** [1], ***Dr. Francesc Perez-Murano*** [1], ***Dr. Joaquín Santander*** [1], ***Dr. F. Xavier Álvarez*** [2], ***Dr. Aitor F. Lopeandia*** [2], ***Dr. Luis Fonseca*** [3], ***Dr. Libertad Abad*** [3], ***Dr. Marc Salleras*** [3], ***Dr. Marta Fernández-Regúlez*** [3]

1. *Institute of Microelectronics of Barcelona (IMB-CNM-CSIC),* ***2.*** *Universitat Autònoma de Barcelona (UAB),* ***3.*** *Instituto de Microelectrónica de Barcelona (IMB-CNM, CSIC)*

In this contribution, we present the study of suspended silicon ultra-thin films with surface nanostructuration as thermoelectric material, with the aim to reach thermoelectric figures of merit similar to the best reported values in the literature for Si structures. These structures are based on rough surface Si nanowires (NWs), whose large-scale fabrication remains unsolved because the synthesis of high density and uniform Si NW arrays with homogeneous nanoscopic surface morphology is a challenging process. Here, we present a cost-effective and scalable approach for the fabrication of the membranes by block copolymer (BCP) nanopatterning. Nanostructurated Si membranes are fabricated on the device layer of a Silicon on Insulator wafer with ultrathin device layer (30 – 50 nm). A thin film BCP is self-assembled perpendicularly oriented to the Si surface. The BCP used for surface nanostructuration is polystyrene-block-polymethylmethacrylate (PS-b-PMMA) with cylindrical or lamellar morphology and a period between 28 and 80 nm. After self-assembly, the PMMA block is selectively removed, and PS features are transferred into the Si underneath by reactive ion etching. With this work we will study the effect of surface nanostructuration on thermoelectric performance.

O-S23-T2-1 Integrating top-down nanopatterning with bottom-up self-assembly to fabricate photonic cavities with atomic-scale dimensions

Mr. Ali Nawaz Babar [1], ***Mr. Thor August Schimmell Weis*** [1], ***Mr. Konstantinos Tsoukalas*** [1], ***Dr. Shima Kadkhodazadeh*** [2], ***Dr. Guillermo Arregui*** [1], ***Dr. Babak Vosoughi Lahijani*** [1], ***Dr. Søren Stobbe*** [1]

1. *DTU Electro, Department of Electrical and Photonics Engineering, Technical University of Denmark, Kgs. Lyngby, Denmark.,*

2. *DTU Nanolab, Technical University of Denmark, Kgs. Lyngby, Denmark.*

Nanostructure fabrication techniques encompass two main methods: top-down nanopatterning and bottom-up self-assembly. While top-down approaches offer control and scalability, they have limitations in achieving small feature sizes. On the other hand, bottom-up self-assembly provides atomic-scale resolution but lacks geometric freedom and production yield. Combining the strengths of both methods is highly desirable, particularly in nanophotonics, where the feature size limits light confinement, yet large-scale circuit fabrication is crucial.
Our work presents a novel approach to integrating top-down nanopatterning with bottom-up self-assembly for fabricating photonic cavities with atomic-scale dimensions. Our method utilizes surface forces like van der Waals, Casimir, and capillary forces to self-assemble structures patterned only through lithography and etching. We demonstrate a self-assembled nanobeam cavity with a 2 nm air bowtie width and an aspect ratio of 100, a mode volume more than 100 times below the diffraction limit, and an experimental quality factor of Q = 4.2 × 10^4.

O-S23-T2-2 Evaluation of the van der Waals force on the CNT Slipping Process in Transmission Electron Microscope

Mr. Keisuke Higashitani [1], ***Prof. Samel Jeong*** [1], ***Prof. Keishi Akada*** [1], ***Dr. Toshihiko Fujimori*** [2], ***Prof. Fujita Jun-ichi*** [1]

1. *University of Tsukuba,* ***2.*** *Sumitomo Electric Industries, Ltd.*

The breaking strength of carbon nanotubes (CNTs) is reported to have over 100 GPa in a single CNT molecule. However, the breaking strength of CNT fiber reached only ~4 GPa due to the van der Waals force decreasing between CNTs molecules in the fiber. The slipping force between the CNTs depends on the contact length, the longer contact length gives the larger breaking strength against the CNT's slipping motion. Here, we report the direct measurement and evaluation of the slipping force under the high-resolution TEM using a homemade piezo-driven TEM holder. From the relationship between bundle contact length and sliding force obtained by stress-strain curves, the slipping force of CNT bundles will be approximately 0.26 N/m. The defects that caused the bending and/or diameter mismatch, as well as the impurities attached on the CNT body would weaken the van der Waals force and decrease the breaking strength of the CNT's fiber. Our experiment suggests only 2 micrometers of perfect contact length enables the production of ultra-high strength of CNT fiber.

O-S23-T2-3 Harvesting and optical manipulation of 4D printed hydrogel microrobots

Mr. Stefan Sützl [1], ***Mr. Daniel Maher*** [1], ***Mr. Marcin Piekarczyk*** [1], ***Dr. Colm Delaney*** [2], ***Dr. Larisa Florea*** [2], ***Dr. Ada-Ioana Bunea*** [1]

1. *Technical University of Denmark,* ***2.*** *Trinity College Dublin*

Microrobots are gaining momentum as tools for biomedical applications due to their small size and ability to perform microscale tasks. Here, we present the harvesting and optical manipulation of microrobots fabricated by two-photon polymerization 4D printing of a pH-responsive hydrogel. The use of a smart material enables the microrobots to perform a task on the microscale, which in this case is localized pH sensing. However, the intrinsic softness of the material makes it challenging to harvest and transfer microrobots into the measurement cell, which means that the microrobots are easily damaged during these steps. On the other hand, the strength of optical trapping depends on the refractive index contrast between the trapped object and its environment, so using a hydrogel in an aqueous environment is not ideal for this purpose. Nevertheless, our study shows that it is possible to harvest, trap and manipulate hydrogel microrobots using our optical trapping setup. To bypass the challenges posed by the hydrogel material, our group is looking into alternatives, such as combining the use of a hard polyacrylic scaffold and a pH-responsive hydrogel component for sensing. However, this approach requires a multi-step fabrication procedure, including careful alignment.

O-S23-T2-4 Conventional fabrication techniques with high yield for a tuneable room temperature single-electron transistor and field-effect transistor

Mr. Kai-Lin Chu [1], ***Dr. Faris Abualnaja*** [1], ***Mr. Wenkun He*** [1], ***Dr. Mervyn Jones*** [1], ***Dr. Zahid Durrani*** [1]

1. *Imperial College London*

Conventional nanofabrication techniques for complementary metal-oxide-semiconductor (CMOS) devices have been used to produce room-temperature (RT) field-effect transistors (FETs) that may be tuned via gate bias to operate as single-electron transistor (SET) quantum devices. A total of 180 devices across 4, 15 mm × 15 mm chips have been fabricated using a silicon-on-insulator (SOI) material. Electron-beam lithography (EBL) followed by a reactive-ion etching process defines the device pattern, which includes a 20 nm × 20 nm point-contact region, in the top-Si layer. A geometric oxidation process then partially oxidises the point-contact region, leaving behind a Si-channel core, with phosphorous (P) donor atoms embedded into the surrounding SiO_2, which forms the tunnel barriers. A high yield of ~ 37 % (66 out of 180 devices) have shown FET behaviour with Coulomb diamond, single electron charging characteristics, near gate threshold. These results show that standard fabrication techniques can be implemented to produce functioning quantum devices. Furthermore, RT FET-SETs may be regarded as the bridge of applications between conventional FET and quantum devices.

O-S23-T2-5 Structural and morphological study on a-Ge based nanostructures: dewetting from flat to patterned films

Dr. Sonia Freddi [1], ***Mr. Michele Gherardi*** [2], ***Dr. Dominique Chatain*** [3], ***Prof. Gianfranco Sfuncia*** [4], ***Prof. Giuseppe Nicotra*** [4], ***Dr. Mohammed Bouabdellaoui*** [5], ***Ms. Chiara Barri*** [2], ***Mr. Luca Fagiani*** [6], ***Dr. Alexey Fedorov*** [2], ***Dr. Marco Abbarchi*** [7], ***Dr. Monica Bollani*** [8]

1. *Institute of Photonics and Nanotechnology (IFN) – CNR,* ***2.*** *Department of Physics, Politecnico di Milano,* ***3.*** *Aix-Marseille Univ, CNRS, CINaM,* ***4.*** *Istituto per la microelettronica e microsistemi (IMM) -CNR,* ***5.*** *Aix-Marseille Univ, CNRS, CINaM and Solnil,* ***6.*** *Politecnico di Milano,* ***7.*** *Aix Marseille Univ, Université de Toulon and Solnil,* ***8.*** *CNR*

Germanium is of particular interest for photonic devices working at near and mid-infrared frequency. Thus, the study and validation of a low-cost processing of Ge film, such as solid state dewetting (SSD), is of considerable interest. Despite the relevance of this material for photonics, investigation of its dewetting features is not yet complete and a deep understanding of the process is still missing.
This work aims to study the morphological evolution of an amorphous-Ge thin film (a-Ge) and investigate the structural properties of the dewetted islands. In detail, a-Ge is deposited by MBE on thick thermal silicon oxide, whereas dewetting of a-Ge is obtained by an annealing in the range between 600-700°C in UHV conditions. By in-situ RHEED and electron back scatter diffraction during high-temperature annealing, we clarify the initial crystallization dynamics of the Ge film. Structural characterization of the dewetted islands involves HR-TEM, AFM and SEM, while chemical composition is assessed by EELS. Different initial film thickness and annealing treatments are investigated. A full control over the final outcomes of the dewetting is obtained guiding the dewetting fronts toward precise and reproducible shapes. So SDD is also performed on a previously patterned a-Ge film achieved by EBL and RIE.

O-S32-T2-2 Scalable, Flame-resistant, Superhydrophobic Ceramic Metafibers for Sustainable All-day Radiative Cooling

Ms. Ching Wen Hwang [1], ***Ms. Meng-Ting Tsai*** [1], ***Ms. Pin-Hui Lan*** [1], ***Ms. Tai-Chi Chen*** [1], ***Prof. Dehui Wan*** [1]

1. *National Tsing Hua University*

Passive daytime radiative cooling, as a strategy to dissipate heat through an atmospheric transparency window (ATW) to outer space without energy consumption, has been recently considered as a novel approach for global net-zero emissions. However, limited to poor thermal/chemical stability, or insufficient weather-resistance, the development of a PDRC building material for long-term outdoor usages still remains a challenge. Here, a scalable superhydrophobic silica metafibers (sh-SMF) was fabricated via an electrospinning process combined with the fluorosilane-modification on fiber surface. The optically engineered sh-SMF could attain an extremely high reflectivity (~97%) in the solar spectrum. In addition, the sh-SMF possessed a high emissivity (~90 %) in ATW. Thus, the optimal sh-SMF realized a sub-ambient cooling performance of 6 °C and the maximum cooling power of 112 W/m^2 under a solar irradiance of ~790 W/m^2. Besides, the temperature decline for the sh-SMF-covered house and vehicle models could also achieve 9.4°C and 22°C under sunlight, respectively. Noteworthily, the sh-SMF could withstand temperatures over 1200°C, which might prolong the time for resident to evacuate from firegrounds. Moreover, the superhydrophobic surface of sh-SMF demonstrated attractive self-cleaning and anti-mildew properties. Finally, the sh-SMF with above mentioned properties opens a path for future energy-efficient and sustainable architectural applications.

O-S33-T2-1 Dry release of MEMS Al2O3 origami for facet-based device integration with assistance of SU-8 reinforcement and folding stopping bars

Mr. Jianran Zhang [1], ***Dr. Carsten Strobel*** [2], ***Prof. Thomas Mikolajick*** [1], ***Dr. Robert Kirchner*** [1]

1. *Dresden University of Technology Center for Advancing Electronics Dresden,* ***2.*** *TU Dresden*

Micro-scale origami structures have shown significant potential for various device functionalities, including microscale antennas, sensors, and actuators. However, previous works have primarily focused on single-device applications, limiting the overall integration density. In an earlier paper, we presented a wafer-scale production method for Al_2O_3-based origami cubes, enabling the integration of logic transistors and circuits on all six facets. We successfully addressed challenges related to folding behaviour control, such as blocking folding routes and facet twisting, by incorporating SiO_2 bars and careful origami shape designing. This work represents an update on our progress toward achieving precise control of folding behaviours in Al_2O_3 origami structures. We specifically focus on the implementation of stopping bars for enhanced control. To overcome the patterning challenges of thick bars, we explored in this study different approaches using SU-8. What is shown in this abstract is the current result and process problems mostly regarding SU-8 thick bars patterning. While adhesion issues were encountered during patterning, we devised a solution involving a protective SiO_2 cap and optimized etching steps. The experiments of this improved process are currently on going but should be able to catch up with the conference.

O-S33-T2-2 Near-infrared photodetectors based on single germanium nanowires

Mr. Ahmad Echresh [1], ***Mr. Mohd Saif Shaikh*** [1], ***Prof. Manfred Helm*** [1], ***Prof. Artur Erbe*** [1], ***Dr. Yonder Berencén*** [1], ***Dr. Lars Rebohle*** [1], ***Dr. Yordan Georgiev*** [1]

1. *Institute of Ion Beam Physics and Materials Research, Helmholtz-Zentrum Dresden-Rossendorf (HZDR)*

Photodetectors based on Ge material have been fabricated with different structures such as metal-semiconductor-metal (MSM) and p–n junctions. On the other hand, the observation of high responsivity in semiconductor nanowires with a high surface-to-volume ratio has attracted growing interest in using nanowires in photodetectors. So far, significant efforts have been made to fabricate single nanowire-based photodetectors with different materials such as Si, Ge, and GaN to achieve miniaturized devices with high responsivity and short response time [3-5]. Hence, Ge nanowires are an excellent candidate to fabricate single nanowire-based near-infrared photodetectors. In this work, we report on the fabrication and characterization of an axial p–n junction along Ge nanowires. First, through a resist mask created by electron beam lithography (EBL), the top Ge layers of germanium-on-insulator (GeOI) substrates were locally doped with phosphorus ions using ion beam implantation followed by rear-side flash lamp annealing. Then, the single Ge nanowire-based photodetectors containing an axial p–n junction were fabricated using EBL and inductively coupled plasma reactive ion etching. The fabricated single Ge nanowire devices demonstrate the rectifying current–voltage characteristic of a p–n diode in dark conditions. Moreover, the photoresponse of the fabricated photodetectors was investigated under light illumination with three different wavelengths.

O-S33-T2-3 The coexistence of volatile and non-volatile resistive switching in WTe2 conductive bridge random access memory devices for neuromorphic computing

Dr. Haider Abbas [1], ***Dr. Asif Ali*** [1], ***Mr. Jiayi Li*** [1], ***Prof. Diing Shenp Ang*** [1]

1. *Nanyang Technological University*

The computing efficiency in von Neumann architecture-based conventional computing systems is limited by the physical separation of memory and computing units. Neuromorphic computing offers a promising solution to overcome this so-called memory wall problem owing to its brain-inspired computing functionalities. Emulating the synaptic plasticity of biological synapses is a crucial step for the practical realization of a neuromorphic computing system. Conductive bridge random access memory (CBRAM) is a promising electronic synaptic device because it can emulate both short- and long-term synaptic plasticity functions of biological synapses. In this work, we fabricated WTe_2 chalcogenide-based CBRAM devices that present the coexistence of volatile switching (VS) and non-volatile switching (NVS) with high uniformity. This coexistence of VS and NVS is exploited to mimic the short-term and long-term plasticity (STP/LTP) behaviors of the biological synapses. The device also presents LTP and LTD characteristics with a better linearity in synaptic weight modulation which is highly desirable for neuromorphic computing.

O-S33-T2-4 Development of thermal rectification on asymmetric defect engineered graphene device

Dr. Mohammad Razzakul Islam [1], ***Dr. Afsal Kareekunnam*** [1], ***Prof. Hiroshi Mizuta*** [1]

1. *Japan Advanced Institute of Science and Technolgy*

Graphene has become a subject of great interest in the field of thermal rectification due to its unique properties and previous studies have demonstrated its potential for such applications through simulation. This study aimed to experimentally develop a graphene-based thermal rectifier by employing asymmetric defect-engineered suspended graphene nanostructures. The resulting fabricated devices exhibited an impressive thermal rectification ratio of 80%. The fabrication process involved advanced graphene nanoelectromechanical systems technology, along with introducing a periodic pattern on half of the graphene ribbon. To accurately assess the thermal transport properties, a high precision 'differential thermal leakage' method was developed and confirmed the dependence of temperature and defect structure on phonon scattering and localization in thermal rectification. The outcomes substantiated the crucial role played by temperature gradients and defect structures in dictating the phonon behavior and overall thermal rectification in asymmetric defect-engineered suspended graphene devices. The experimental realization of high thermal rectification ratios in the fabricated defect-engineered graphene-based devices not only validated the theoretical simulation but also paves the way for practical implementation in various energy-efficient applications.

O-S33-T2-5 2D BDiode – A Switchable Bidirectional Diode for Analog Electronic Circuits Fabricated Entirely from 2D Materials

Dr. Christian Matthus [1], ***Mr. Phanish Chava*** [2], ***Dr. Kenji Watanabe*** [3], ***Dr. Takashi Taniguchi*** [4], ***Prof. Thomas Mikolajick*** [5], ***Prof. Artur Erbe*** [2]

1. *Chair for Circuit Design and Network Theory, Technische Universität Dresden,* ***2.*** *Institute of Ion Beam Physics and Materials Research, Helmholtz-Zentrum Dresden-Rossendorf (HZDR),* ***3.*** *Research Center for Functional Materials, National Institute for Materials Science, 1-1 Namiki, Tsukuba 305-0044, Japan,* ***4.*** *Internat. Center for Materials Nanoarchitectonics, National Institute for Materials Science, 1-1 Namiki,,* ***5.*** *Dresden University of Technology Center for Advancing Electronics Dresden*

In this work, we demonstrate new opportunities of a 2D material-based device, we call 2D BDiode (switchable fully-**2D b**idirectional **diode**). In detail, the gate-induced switchability of the diode behavior due to the different current transport mechanisms (band-to-band tunneling and drift-diffusion) offers versatile possibilities for analog circuit design. Our device is based on a MoS2/WSe2 heterojunction encapsulated with insulating hBN layers along with semi-metallic few-layered graphene as contact and backgate electrodes. We measured the I-V characteristics in forward and reverse direction with different voltages applied to the backgate. The diode works like a conventional pn-diode in case of a negative backgate voltage while it changes to a reversely conducting, rectifying diode in case of positive backgate voltage. It was modeled for both scenarios by the conventional semi-empirical diode model. From this, we developed a SPICE building block (subcircuit) consisting of two 2D BDiodes in parallel: one for forward and one for reverse direction; the gate was modeled in a first order approximation by switches. We applied this model for the design and (transient) simulation of circuit concepts with bidirectional working scenarios like AC/DC, DC/AC converters, and charge pumps with the capability of handling positive and negative voltages.

O-S42-T2-1 Fabrication of electron transparent membranes and nanostructures in fluidic devices by nanoimprint lithography and “Flow-Through”-gas phase deposition

Mr. Jeremy Teuber [1], ***Mr. Manuel Müller*** [1], ***Mr. Rukan Nasri*** [1], ***Dr. Arwen Pearson*** [1], ***Ms. Judith Estengre-Perez*** [1], ***Dr. Irene Fernandez-Cuesta*** [1]

1. *Universität Hamburg*

Scanning and transmission electron microscopy (SEM and TEM) have revolutionized nanometer-resolution imaging. Integrating flow cells into these techniques enables dynamic imaging under controlled flow conditions. However, current flow cells have limitations like high costs, limited geometries, and reliance on slit-like chambers.

This work presents a fabrication method for producing polymeric foils with selectively coated micro and nanofluidic structures from the inside by using atomic layer deposition (ALD). UV nanoimprint lithography is used to create a pattern on a silicon stamp, which is transferred to a PDMS stamp. The stamp is aligned onto a polycarbonate plate covered with a UV-curable polymer, and a polymer coverslip seals the channels to produce the liquid cell.

A specialized ALD reactor with a “Flow-Through” mode ensures conformal coating of the channels with Al2O3. The structured and coated polymer foil is detached, and the nanochannels are suspended by etching the surrounding polymer for electron transparency.

The electron transparency is demonstrated by imaging polystyrene beads using SEM and TEM. This fabrication method allows for easy structuring, diverse geometries, and eliminates the need for slit-like chambers. The fabricated samples, with sub-100 nm Al2O3 walls, show promise as flow cells in TEM.

O-S42-T2-2 The performance improvement of multi-layered ZnO/SnO2 thin-film transistors by varying growth temperatures

Mr. Chan-Yeong Park [1], ***Mr. Se-Hyeong Lee*** [1], ***Ms. So-Young Bak*** [1], ***Mr. Dongki Baek*** [1], ***Mr. Hyeongrok Jang*** [1], ***Mr. Jinwoo Lee*** [1], ***Prof. Moonsuk Yi*** [1]

1. *Department of Electrical and Electronics Engineering, Pusan National University*

Conventional ZTO thin film transistors(TFTs) using atomic layer deposition(ALD) have shown optimum performance at high annealing temperatures above 500□. To overcome high annealing temperature, we deposited a channel layer with a multilayer structure and obtained optimal values by adjusting the growth temperature of multilayered ZnO/SnO_2 film and annealing conditions. In conclusion, we fabricated multilayered ZnO/SnO_2 TFTs with similar performance to ZTO TFTs at a low process temperature. The optimized performance was achieved at a growth temperature of 180□ with 350□ annealing for 1 hour and exhibited as a carrier mobility of 8.09 cm^2/V·s, a threshold voltage of 1.6V, an on/off current ratio of 2.63 x 10^7, and a subthreshold swing of 0.58V/dec. To analyze why the device is optimized at 180□, X-ray photoelectron spectroscopy (XPS) was measured and O 1s peak deconvolution was conducted. Afterward, we intend to perform the optimization of the multilayered TFTs based on the cycle variation of Zn and Sn to improve the carrier mobility and overall performance, and the trend with respect to film thickness is also going to be examined.

O-S44-T2-1 Integration of hard magnetic materials in MEMS devices

Dr. Federico Maspero [1], ***Mr. Simone Cuccurullo*** [1], ***Dr. Alejandro Plaza*** [1], ***Ms. Francesca Marson*** [1], ***Ms. Oksana Koplak*** [1], ***Mr. Andrea Del Giacco*** [1], ***Ms. Maria Cocconcelli*** [1], ***Ms. Giulia Pavese*** [1], ***Prof. Andrea Cattoni*** [1], ***Prof. Riccardo Bertacco*** [1]

1. *Politecnico di Milano*

The integration of piezoelectric and magnetic materials in micro-electro-mechanical systems (MEMS) enables several existing applications, ranging from energy harvesting to magnetic field sensors. In this work we present the integration of hard magnetic materials (SmCo, NdFeB) in MEMS devices. To demonstrate our fabrication flow, we have realized a proof-of-concept device composed of a MEMS resonator equipped with micro-magnets of hard magnetic material.

O-S44-T2-2 Simultaneous Estimation of dI/dV and dI/dZ with Ultrafast feedback loop for Scanning Tunnelling Microscopy

Ms. richa mishra mishra [1], Prof. Reza Moheimni [1], Dr. Ehud Fuchs [2], Dr. James Owen [2], Dr. John Randall [2]

1. *The University of Texas at Dallas,* ***2.*** *Zyvex Labs*

We present a control technique to simultaneously measure the topography of the surface, the local tunnel barrier height (dI/dZ), and the differential conductivity (dI/dV). We obtain the above-mentioned terms by closing the feedback loop on the natural logarithm of differential conductance, *ln(dI/dV). In this approach, the tip-sample distance is regulated even when the applied sample DC bias voltage is zero, allowing for information about the engagement of electronic states for the full range of sample bias voltage. The I−V curve can be obtained orders of magnitude faster than the conventional spectroscopy method.*

We modulate the voltage with sinusoidal signals s.t. the frequency of the modulating signal should be above the closed-loop bandwidth of the system since the topography information lies in the low-frequency region and then apply the lock-in-amplifiers are tuned at ω and 2ω to the tunneling current, and controller output to obtain dI/dV and dI/dZ respectively. In conventional methods, two modulation signals are required to obtain dI/dV and dI/dZ but we have proposed and implemented the idea using one modulation and three lock-in amplifiers. This reduces implementation complexity that may affect the feedback control if parameters are not designed properly for two modulation signals.

O-S44-T2-3 Through Silicon MEMS inspection with a near infrared laser scanning setup

Dr. Diogo E. Aguiam [1], ***Ms. Inês S. Garcia*** [1], ***Ms. Joana D. Santos*** [1], ***Dr. Filipe S. Alves*** [1]

1. *International Iberian Nanotechnology Laboratory*

Silicon is opaque in the visible spectrum but is mostly transparent in the near infrared region (λ>1100 nm). The high refractive index of this semiconductor material makes it somewhat reflective, resulting in high Fresnel losses at the interfaces. In addition, the absorption coefficient within the material increases with doping in conductive silicon substrates. Taking this optical behavior into consideration, a light beam in the near infrared is able to propagate through the material, with transmitted signal attenuations observed at the interfaces between materials and through thick doped silicon materials.

In this work, we present the concept and preliminary experimental validation of a near-infrared laser scanning setup to inspect silicon-encapsulated microstructures such as MEMS by measuring small variations of transmitted intensity. The high sensitivity of this system suggests it could be used for the non-destructive inspection of processed samples and even in between process steps to confirm alignments between front-side and back-side masks.

O-S44-T2-4 Advanced defect detection procedure in immersion lithography for minimizing yield-killing defect classes through high sensitivity optical inspection, guided e-beam inspection, and AI technology by track parameters optimization

Dr. Jorge Pablo Nacenta Mendivil [1], ***Mr. Alexis ROYER*** [1], ***Mrs. Karine JULLIAN*** [1], ***Dr. Michael MAY*** [1], ***Mr. Fabrice KOUEMENI-TCHOUAKE*** [1], ***Prof. Raluca TIRON*** [1], ***Mr. Laurent Couturier*** [2], ***Mr. Yuji Tanaka*** [3], ***Mr. Christophe Couderc*** [1], ***Dr. Masahiko Harumoto*** [3], ***Mr. Masanes Masanes*** [1]

1. *Univ. Grenoble Alpes, CEA, Leti, F-38000 Grenoble, France,* ***2.*** *Applied Materials France, 864 Chem. des Fontaines, 38190 Bernin, France,* ***3.*** *SCREEN Semiconductor Solutions Co., Ltd. 480-1 Takamiya-cho, Hikone, Shiga, Japan*

We present the results of a new defect inspection, review, and classification procedure that combines an extremely sensitive multi-attribute optical defect inspection with the use of ExtractAI™ technology (combining AI and guided e-beam inspection) to rapidly search, map and classify yield-killing defects, regardless of their contribution to the total defectivity. Its relevance has been demonstrated in the simultaneous reduction of minority (embedded, watermarks and microbridges) and majority defects (residues) in an immersion lithography gate process targeting 28nm dense lines post-etch. The optimization of these killer defects has been tackled, by tuning track process parameters resulting in a 95% reduction in total post-lithography defectivity. In addition, crucial information about the root cause of microbridging, which arises from residue redeposition in specific areas, has been obtained without increasing the total machine time.

O-S52-T2-1 3D Printed Microscale Static Geometry Check Valve

Prof. (Edwin) En-Te Hwu [1], ***Mr. Dali Reda*** [1], ***Dr. Tien-Jen Chang*** [2], ***Prof. Nikolaj Gadegaard*** [3], ***Prof. Anja Boisen*** [1]

1. *Technical University of Denmark,* ***2.*** *Technical university of Denmark,* ***3.*** *University of Glasgow*

We report a microscale check valve utilizing nozzle and diffuser actions to enforce unidirectional liquid flow. The valve is manufactured via microscale 3D printing and possesses a compact footprint of 3x2.5x1.5 mm. When coupled with an oscillation source, the valve exhibits a flow rate of 9.18 µL/s at a frequency of 185 Hz.

The static geometry of the valve is responsible for the unidirectional flow. During the expansion stroke of actuation, the inlet region acts as a diffuser and the outlet region acts as a nozzle. As a result, more fluid enters an oscillation chamber from the inlet side than from the outlet side. Conversely, during the compression stroke, the inlet region acts as a nozzle, and the outlet region acts as a diffuser, expelling more fluid from the outlet.

Simulation studies demonstrate the valve's efficacy in rectifying flow for laminar flows. This attribute makes it ideal for microfluidic systems that require precision and accuracy in flow control. Microscale precision 3D printing facilitates the valve's design customization.

This valve has implications in numerous fields, including microscale biomedical devices and lab-on-a-chip technology. The small footprint of the valve makes it an addition to the toolbox of microfluidic systems.

O-S52-T2-2 Design and All-In-One Etch of Silicon Metalens for Near-Infrared Focusing

Dr. Bingrui Lu [1], ***Mr. Søren Engelberth Hansen*** [1], ***Mr. Thor August Schimmell Weis*** [1], ***Dr. Guillermo Arregui*** [1], ***Dr. Søren Stobbe*** [1]

1. *Technical University of Denmark*

Metalenses play an essential role in the new generation of micro- and nano-optical systems because of their small footprint, planar geometry, and excellent optical performance. All-dielectric metalenses demonstrate an advantage of better material efficiency than their metallic counterparts. In our work, we design a silicon metalens consisting of nanopillars of various diameters placed in a hexagonal lattice for near-infrared (NIR) focusing. Through iterative design space exploration, a fixed height and a range of diameters of the silicon nanopillars can be determined to produce a relative phase difference over 2π. Aside from benefitting from the mature fabrication processes in the silicon industry, we also apply a unique All-In-One etch of the silicon nanopillars in the metalens to avoid wet procedures such as lift-off and metal mask removal. The high-precision silicon slow-etching process named CORE (Clear, Oxidize, Remove, and Etch) developed in our cleanroom ensures precise control of the nanostructure geometries.

The silicon metalens can be placed directly on top of other photonic circuits or components to form a 3D integrated system. The fabrication process developed in this work is fully compatible with the current silicon industry but with a greener execution. Further measurements and applications of the metalens will be presented.

O-S62-T2-1 Development of surface acoustic wave phase modulators for physical reservoir computing

Mr. Taiki Ijima [1], ***Dr. Claude Meffan*** [1], ***Prof. Amit Banerjee*** [1], ***Dr. Jun Hirotani*** [1], ***Prof. Toshiyuki Tsuchiya*** [1]

1. *Kyoto University*

This paper proposes to utilize a surface acoustic wave (SAW) phase modulator for physical reservoir computing. SAW phase modulators with various designs with respect to a waveguide are fabricated, and their frequency responses are investigated. We confirmed the peak at their center frequency decayed exponentially with the waveguide length while we observed mild relationship between the amplitude and the waveguide width. Furthermore, the modulation effect was detected by applying a RF voltage to the modulators. The measured results gave us beneficial information for optimization of the structural parameters. These can be regarded as hyperparameters in the SAW reservoir system. In the future, we intend to use these modulators as a physical reservoir system through a time-delayed feedback loop.

O-S62-T2-2 A silicon carbide (SiC) carbon nanotube (CNT) composite for high aspect ratio harsh environment MEMS

Mr. Jiarui Mo [1], ***Mr. Shreyas Shankar*** [1], ***Dr. Sten Vollebregt*** [1]

1. *Delft University of Technology*

Silicon carbide (SiC) is a promising material for MEMS devices, especially for those aiming at harsh-environment applications. However, the lack of a proper bulk fabrication process is a factor that impedes the development of SiC MEMS. Here, we propose to use an array of vertically aligned carbon nanotubes (CNT) reinforced by amorphous SiC as an alternative for high aspect ratio (HAR) SiC-based MEMS fabrication. We found that the CNT dominates the electrical properties of the composite. In contrast, the mechanical properties can be tuned over 3 orders of magnitude by varying the thickness of the a-SiC filler. Two different working devices were successfully fabricated and tested at elevated temperatures using this approach: a chevron-shaped thermal actuator and a capacitive accelerometer.

O-S62-T2-3 Parallel In-Plane Electrothermal Actuators

Ms. Yen Nee Ho [1], ***Dr. Aron Michael*** [1], ***Prof. Chee Yee Kwok*** [1], ***Dr. Cibby Pulikkaseril*** [2]

1. *UNSW Sydney,* ***2.*** *Baraja*

This paper reports a novel electrothermal actuator with large in-plane displacement designed for MEMS-based pitch-tunable diffraction grating for beam steering applications such as in microlidar systems. The device consists of two sets of parallel electrothermal beams that pull and push a lever to produce large in-plane displacement. The actuator has been simulated, fabricated and tested. The results show that the actuator generates a large displacement of 177μm at a driving voltage of 6V. By increasing the number of parallel electrothermal beams, the actuator uniquely reduces power consumption while generating large displacement in comparison to the existing in-plane electrothermal actuators.

O-S62-T2-4 Fabrication of On-Chip Carbon Microelectrodes by Catalytic Graphitization of 3D Printed Polymers

Mrs. Zoi Maria Papadopoulou [1], ***Ms. Swetha Vasudevan Kanakkottu*** [2], ***Prof. Babak Rezaei*** [2], ***Prof. Stephan Sylvest Keller*** [2]

1. *National Centre for Nano Fabrication and Characterization, DTU Nanolab, Technical University of Denmark, 2800 Lyngby, Denmark,* ***2.*** *Technical University of Denmark*

We present a novel approach for fabricating carbon-based microelectromechanical systems (CMEMS) using additive manufacturing. CMEMS find applications in medical devices, sensors, and energy storage. Traditional fabrication methods have limitations, which we overcome by employing layer-by-layer 3D printing. This technique allows the formation of on-chip 3D carbon microstructures with a high aspect ratio reducing cost, time and complexity of the process.

To improve the electrochemical properties of the microelectrodes, we introduced an iron catalyst into the 3D print resin. The printed structures were then pyrolyzed at 900°C to convert them into carbon. The addition of the catalyst resulted in improved electrochemical performance caused by the graphitization improvement. During cyclic voltammetry (CV), we observed decreased internal resistance and increased peak current for the modified precursors. Electrochemical impedance spectroscopy (EIS) showed a significant reduction in charge transfer resistance, indicating enhanced electrochemical properties.

Overall, our additive manufacturing approach enables the fabrication of on-chip carbon microelectrodes. The use of an iron catalyst during precursor preparation enhances graphitization and improves electrochemical performance. This research opens up possibilities for developing CMEMS with enhanced functionality and performance.

O-S62-T2-5 Flexible photonic integrated circuit technology and characterization platform

Mr. Franz Tank [1], ***Mrs. Julia Wecker*** [2], ***Dr. Chris Stöckel*** [3], ***Dr. Christian Helke*** [3], ***Mrs. Alexey Shaporin*** [2], ***Dr. Joerg Martin*** [2], ***Mr. Sebastian Schermer*** [2], ***Mr. Toni Großmann*** [2], ***Dr. Karla Hiller*** [3], ***Dr. Danny Reuter*** [3], ***Mr. Micha Haase*** [3], ***Dr. Alexander Weiss*** [2]

1. *Technische Universität Chemnitz, Center for Microtechnologies, Reichenhainer Str. 70, 09126 Chemnitz, Germany,* ***2.*** *Fraunhofer ENAS, Technologie Campus 3, 09126 Chemnitz,* ***3.*** *Fraunhofer ENAS; Technische Universität Chemnitz, Center for Microtechnologies, Germany*

The authors present a flexible photonic integrated circuit technology and characterization platform (PIC-TCP) with silicon nitride Si_3N_4 as an optical transparent material with a spectral range from 400 nm to 2350 nm. The PIC-TCP is able to vary a large number of chip designs and characterize the photometric and spectral parameters automatically on wafer level scale with a minimum impact on time and resources. The flexible PIC-TCP is realized by using an automatic wafer prober with fibers and grating couplers based optical characterization setup. An efficient optical coupling of optimized grating structures is needed for this PIC-TCP, which includes a precise fabrication of subwavelength structures.

The authors present a technology flow for a low tolerance fabrication of grating couplers with a deviation of $½\cdot(m_t - t_t) = 3$ nm and a slope of 3.2° (figure 1). The functionality of the PIC-TCP is shown at a PIC device, optimized for 1550 nm wavelength, including the coupling elements, waveguides and a ring resonator structure (figure 2). The optical bench is placed on a wafer prober for automatic wafer level mapping (figure 3). The functionality of the PIC-TCP is shown exemplary at ring resonators with a high Q-factor of > 10000 (figure 4).

O-S73-T2-1 Plasmonic Metamaterial Absorber for MWIR and LWIR Bispectral Microbolometers

Mr. Alexander Litke [1], ***Dr. Elahe Zakizade*** [1], ***Dr. Marvin Michel*** [1], ***Dr. Sascha Weyers*** [1], ***Prof. Anna Lena Schall-Giesecke*** [1]

1. *Fraunhofer IMS, 47057 Duisburg*

Plasmonic metamaterial absorbers (PMAs) designed for multispectral imaging in the infrared (IR) with uncooled microbolometers are investigated. The study presents Fourier transform infrared spectroscopy (FTIR) measurements of fabricated PMAs consisting of metal-insulator-metal-stacks (MIM) with square-shaped micropatches as top metal layers. The measurements reveal high absorptances of more than 90 % for distinct wavelengths within a range from 2 µm to 9.5 µm. The spectra are evaluated with respect to the lateral dimensions of the patches and to the refractive indexes of the used dielectrics SiO_2, Al_2O_3 and Ta_2O_5. Numerical simulations and analytical calculations of the TM_{010}-mode using the Transmission Line Model (TLM) for microstrip antennas show good qualitative agreement with the measurement results. Additionally, bispectral PMAs were fabricated consisting of fields of PMAs with two different patch sizes arranged in a chessboard pattern. The individual fields of this pattern correspond to microbolometers with 12 µm pitch in shape and size. Two distinct absorption maxima can be seen in the spectra measured by FTIR. The choice of materials, deposition methods and patterning processes is suitable for the integration into the existing Fraunhofer IMS's nanotube microbolometer technology. The fabrication process is CMOS-compatible and carried out on 8-inch wafers.

O-S73-T2-2 Liquid crystal integrated multifunctional metasurfaces for photonic security platform

Mr. Gyeongtae Kim [1], ***Dr. Inki Kim*** [1], ***Dr. Jaehyuck Jang*** [1], ***Prof. Junsuk Rho*** [1]

1. *pohang university of science and technology*

Metasurfaces with the recent development of nanofabrication have gained attention for enhanced optical security. However, conventional metasurfaces were limited in actual applications because they are passive after fabricated. Reported active metasurface in the visible light were operated based on temperature, but practical applications are challenging due to the high price of active materials and difficulties in the process. On the other hand, liquid crystal is inexpensive, and can be operated at high speed through voltage.

Here, we proposed liquid crystal integrated multifunctional metasurfaces exhibiting up to four reflective structural color, and nine-channel polarized hologram. To encode multiple polarization channels, we adopt superpixels consist of designed combination of phase gradient meta-atomic groups that rotate clockwise or counterclockwise. The meta-atoms are calculated to impart both spatially-varying phase distribution and reflection spectrum. Then, liquid crystal is integrated to actively manipulate holographic images. As proof-of-concept, we devise an electrically tunable double encrypted optical security platform: a color print image decipherable by camera scan provides the first key and that information is used to fully unlock the double encrypted information via the projected vectorial holographic image. These electrically tunable optical security platforms will provide a new path toward IoT sensors for security and anti-counterfeiting applications.

O-S73-T2-3 The state of the art and first glimpse of wood based printed electronics

Dr. Václav Procházka [1], ***Dr. Thomas Geiger*** [2], ***Dr. Pavel Kulha*** [1], ***Dr. André van Zomeren*** [3]

1. *PROFACTOR GmbH, Im Stadtgut D1, Steyr, Austria,* ***2.*** *EMPA, Dübendorf, 8600, Switzerland,* ***3.*** *TNO, 1755 LE Petten, Nederlands*

Electronics manufacturing currently poses significant environmental pressures, such as resource scarcity, energy-intensive processes, and electronic waste accumulation. To address these concerns, the concept of green electronics has emerged, encompassing low-impact materials, energy optimization, and additive manufacturing. The HyPELignum project aims to demonstrate net-zero carbon emissions in electronics manufacturing through a holistic approach. By utilizing wood and wood-derived materials, which offer technical versatility and a low environmental footprint, the project aims to unlock the potential of additive manufacturing. HyPELignum will develop greener inks, adhesives, and coatings, and introduce circularity through sustainable product design and a novel separation concept for improved recyclability.

O-S73-T2-4 UV-Nanoimprint and Bosch Deep Reactive Ion Etching of metasurfaces and integration into thin-film piezoelectric MEMS

Dr. Christopher Dirdal [1], ***Dr. Karolina Milenko*** [1], ***Dr. Anand Summanwar*** [1], ***Dr. Firehun Dullo*** [1], ***Mr. Paul Thrane*** [1]

1. *SINTEF*

As metasurfaces begin to find industrial applications there is a need to develop scalable and cost-effective fabrication techniques which offer sub-100nm resolution while providing high throughput and large area patterning. Here we demonstrate the use of UV-Nanoimprint Lithography and Deep Reactive Ion Etching (Bosch and Cryogenic) towards this goal. Robust processes are described for the fabrication of silicon rectangular pillars of high pattern fidelity. To demonstrate the quality of the structures, metasurface lenses, which demonstrate diffraction limited focusing and close to theoretical efficiency for NIR wavelengths λ (1.3 μm, 1.6 μm), are fabricated. These are also integrated into active MEMS architectures for active light modulation, and we present the demonstration of a tunable lens for NIR.

We demonstrate a process which removes the characteristic sidewall surface roughness of the Bosch process, allowing for smooth 90-degree vertical sidewalls. We also demonstrate that the optical performance of the metasurface lenses is not affected adversely in the case of Bosch sidewall surface roughness with 45 nm indentations (or scallops).

Track3 - Micro/Nano Engineering for Life Sciences

O-S83-T3-1 Growth of Vertically Aligned MoS2 with Diffused SiOx Film for Ag-Migration-Based Resistive Switching Devices

Ms. Jimin Lee [1], ***Ms. Sofía Cruces*** [1], ***Mr. Benny Ku*** [2], ***Dr. Satender Kataria*** [1], ***Dr. Ke Ran*** [3], ***Prof. Joachim Mayer*** [4], ***Dr. Alwin Daus*** [1], ***Prof. Max C. Lemme*** [5]

1. *Chair of Electronic Devices, RWTH Aachen University,* ***2.*** *AMO GmbH, Advanced Microelectronic Center Aachen,* ***3.*** *Central Facility for Electron Microscopy (GFE), RWTH Aachen University,* ***4.*** *Central Facility for Electron Microscopy (GFE), RWTH Aachen University and Ruska-Centre for Microscopy and Spectroscopy with Electrons (ER-C 2), Forschungszentrum Jülich,* ***5.*** *Chair of Electronic Devices, RWTH Aachen University and AMO GmbH, Advanced Microelectronic Center Aachen*

MoS_2 is promising for resistive switching (RS) due to ion movement along its van der Waals gaps. We grow vertically-aligned MoS_2 (VA-MoS_2) layers by sulfurization. We observed differences in orientation after growth on SiO_2 and Au surfaces. In both cases, an additional amorphous SiO_x layer is formed on top of VA-MoS_2 because of Si and O diffusion from the substrate. We analyzed volatile RS in cross-point devices with Ag top electrodes and confirmed Ag migration by transmission electron microscopy. This study reveals that the growth of VA-MoS_2 is non-trivial for integration into RS devices.

O-S83-T3-2 A method for measuring the d33 piezoelectric coefficient of soft thin films under weak loads

Dr. Gaia de Marzo [1], ***Ms. Valentina Antonaci*** [2], ***Dr. Luca Fachechi*** [1], ***Dr. Vincenzo Mastronardi*** [2], ***Dr. Maria Teresa Todaro*** [3], ***Mr. Luigi Portaluri*** [2], ***Dr. Antonio Qualtieri*** [1], ***Dr. Francesco Rizzi*** [1], ***Prof. Michele Scaraggi*** [2], ***Prof. Massimo De Vittorio*** [2]

1. *Istituto Italiano di Tecnologia,* ***2.*** *Istituto Italiano di Tecnologia; Department of Innovation Engineering, Unisalento,* ***3.*** *Istituto Italiano di Tecnologia; Institute of Nanotechnology, CNR Lecce*

Novelties in wearable technologies often rely on thin piezoelectric soft materials that combine self-powering, stability, and flexibility and whose optimization of their piezoelectric performances is crucial. Approaches proposed until now for measuring the piezoelectric coefficient d_{33} of thin films suffer from long measurement time, environmental contributions, and strong mechanical impacts that risk damaging the soft materials. Here we propose an approach based on weak loads to extrapolate d_{33} in a fast and reliable way. The measurement setup was first validated with commercial samples having known piezoelectric properties, and then it was employed to analyze the d_{33} of innovative biomaterials.

O-S83-T3-3 Automatic markerless overlay with the NanoFrazor: towards batch-fabricated nanodevices

Dr. Jana Chaaban [1], ***Dr. Antoaneta Damyanova*** [1], ***Mr. Jonas Vergés*** [1], ***Mr. Robin Erne*** [1], ***Dr. Emine Çağin*** [1]

1. *Heidelberg Instruments Nano AG*

The NanoFrazor uses thermal scanning probe lithography for the simultaneous patterning and inspection of nanoscale structures as well as direct laser sublimation for mix & match lithography to create nanodevices. Automation of the lithography steps carried out by the NanoFrazor is a natural next step in the expanding application space where the tool is used. Here we present successfully implemented use cases of automated, markerless overlay with the NanoFrazor, including nanopillars centered on pre-patterned matrices of microstructures. The overlay is shown to work even when the underlying structures are buried under resist layers, thanks to the highly sensitive in-situ reading capability of the tool. Using multiple reference points to calibrate for rotation and scaling errors on the substrate, the NanoFrazor software remains independent of the substrate placement and accuracy of the previous lithography steps. In one example, we combine the NanoFrazor's grayscale patterning capability with the automatic overlay process to integrate 47 grating couplers onto silicon waveguides to create unique nanophotonic devices.

Track4 - Micro/Nano Engineering for Physical and Chemical Applications

O-S14-T4-2 Group IV nanowires for nano-/optoelectronic and sensing applications

Dr. Muhammad Bilal Khan [1], Mr. Ahmad Echresh [1], Mr. Sayantan Ghosh [1], Mr. Oliver Steuer [1], Mr. Muhammad Moazzam Khan [1], Dr. Slawomir Prucnal [1], Dr. Lars Rebohle [1], Dr. Shengqiang Zhou [1], Prof. Manfred Helm [1], Prof. Artur Erbe [1], Dr. Yordan Georgiev [1]

1. *Institute of Ion Beam Physics and Materials Research, Helmholtz-Zentrum Dresden-Rossendorf (HZDR)*

Group IV nanowires are excellent building blocks of various nanoelectronic, optoelectronic, photovoltaic, sensing, etc. devices. Beside the well-known advantages of the single-element Si and Ge nanowires, the Si-Ge-Sn alloys (SiGe, GeSn and SiGeSn) offer additional unique properties. With suitable Sn concentrations it is possible to achieve effective bandgap engineering and very high charge carrier mobilities for high-performance nanoelectronic devices as well as direct-bandgap Group IV semiconductors for optoelectronic applications. Therefore, the SiGeSn alloy systems would allow successful on-chip integration of nano- and optoelectronic devices, which makes them ideal candidates for post-Si applications.

We will discuss the top-down fabrication as well as the challenging structural and electrical characterisation of various group IV nanowires: Si, Ge, SiGe, GeSn and SiGeSn. Special attention will be paid to the Hall Effect measurements using a novel six-contact Hall-bar configuration, which permits to evaluate the electrical properties of even very small nanowires and reliably quantify their carrier concentration, Hall mobility, and resistivity.

The innovative nanoelectronic devices that we are targeting will also be discussed. These include junctionless nanowire transistors and reconfigurable field effect transistors for nanoelectronic and sensing applications as well as nanowire phototransistors and photodetectors for optoelectronics.

O-S14-T4-3 Gas sensing properties of thin Carbyne-enriched coatings on micro- InterDigitated Electrodes

Dr. Ioannis Raptis [1], ***Dr. Petros Oikonomou*** [2], ***Mr. Athanasios Botsialas*** [2], ***Prof. Mariya Aleksandrova*** [3], ***Dr. Angeliki Tserepi*** [2], ***Dr. Evangelos Gogolides*** [1]

1. *NCSR Demokritos,* ***2.*** *Institute of Nanoscience and Nanotechnology, NCSR Demokritos, Aghia Paraskevi 15341, Attiki, Greece,* ***3.*** *TU Sofia*

Carbyne has unique properties that make it useful in nanoelectronics, sensors and other fields. Here, novel carbyne films are characterized and explored as potential sensing layers on micro-IDEs for the detection of analytes in air.

The absorption potential of carbyne was assessed through spectroscopic reflectance thickness measurements in the presence of various analytes (humidity, ethanol, ethyl acetate, toluene). The selectivity of the response in VOCs against humidity is high; a promising indication for use of carbyne in various sensing platforms.

Arrays of IDEs with CD of 1 and 2 μm are fabricated on glass by mainstream microelectronic processes. The carbyne layer is deposited though stencil mask to protect the contact pads and facilitate wire bonding. The performance of the sensors was evaluated at different levels of humidity and VOCs. The capacitance decreases with increase of the concentration; opposite behavior for polymer-based IDEs. The capacitance change is high and presents good selectivity between humidity and VOCs making carbyne a potential sensing material in IDE arrays. The performance of carbyne-coated IDEs will be further improved through carbyne thickness optimization, carbyne layer annealing, and deposition method optimization. Finally, the sensing performance of IDE array with polymer and carbyne-coated areas will be assessed.

O-S24-T4-1 Micro-scaled chemical oscillator networks - towards chemical computing

Ms. Jacqueline Figueiredo da Silva [1], ***Dr. Robert Lovchik*** [1], ***Dr. Vesna Bacheva*** [1], ***Ms. Ute Drechsler*** [1], ***Mr. Steffen Reidt*** [1], ***Prof. Juan Perez-Mercader*** [2], ***Dr. Armin Knoll*** [1], ***Dr. Heiko Wolf*** [1]

1. *IBM Research Zurich,* ***2.*** *Harvard University*

The need for diversification and optimization of information processing systems is increasing. We explore 'chemical computers' (CCs) based on information processing by an oscillatory reaction in micrometer scale compartments. Some benefits of CCs are that the processing unit and memory share the same space and minimal power is needed for their operation.

To harvest the energy efficiency and nanoscale dimensions of molecules, chemical computing units, we will have to be scaled to dimensions in the micrometer range or below. We designed and fabricated a diffusion driven network comprising a set of sub-100 µm silicon-based micro-chemical reactors (MCRs) connected by nanofluidic channels. The advantages of silicon-based fabrication of MCRs are the use of a chemically inert material and the scalability and freedom of design inherent with silicon based micro-fabrication. We use the Belousov–Zhabotinsky (BZ) reaction as oscillatory chemistry in the MCRs. The catalyst of the BZ reaction enables visualizing oscillations by fluorescence microscopy.
As first step towards computing, we demonstrate diffusion-related coupling and synchronization of MCRs. Connecting channels mediate a coupling between compartments which leads to synchronization, an important ingredient for data processing. These steps are important first results towards scalable chemical computing architectures based on simple molecules.

O-S24-T4-2 Laser production of clean energy by laser micro and nano-bubbling in liquids

Prof. G.W. Yang [1]

1. *School of Materials Science & Engineering, Sun Yat-sen University, Guangzhou 510275, P. R. China*

Laser ablation in liquids (LAL) has stimulated wide attention over the last decade and is gradually becoming an irreplaceable technique to synthesize nanocrystals and fabricate functional nanostructures, because LAL can offer effective solutions to some challenging puzzles in the field of nanotechnology [1]. We have witnessed the exciting developments in understanding and applying LAL to fabricate unique nanostructures [2]. Following LAL, we have developed a simple, clean, and efficient laser micro and nano-bubbling in liquids (LBL) to produce clean energy [3]. Our preliminary research has shown that LBL, as a new concept of laser chemistry, will have great potential applications in clean energy manufacturing such as laser overall water splitting to produce hydrogen without any catalysts, and nitrogen activation and solidification including synthetic ammonia and nitric acid.

[1] G. W. Yang, Laser ablation in liquids: applications in synthesis of nanocrystals, Progress in Materials Science, 52 (4), pp. 648-698, (2007).

[2] J. Xiao et al. External field-assisted laser ablation in liquids: an efficient strategy toward nanocrystals synthesis and nanostructures assembly, Progress in Materials Science, 87, pp. 140-220, (2017)

[3] B. Yan et al. Highly efficient and highly selective CO_2 reduction to CO driven by laser, Joule, 6, pp. 2735-2744, (2022).

O-S24-T4-3 Fabrication of self-powered wearable pressure sensing system based on PVDF-TrFE and ionic liquid

Prof. Je Hoon Oh [1], ***Ms. Chaeeun Lee*** [1], ***Mr. Changwoo Cho*** [1]

1. *Hanyang University*

With the increasing demand for flexible sensors in various fields, numerous sensor types have been developed. Among them, ionic capacitive pressure sensors exhibit higher sensitivity and faster response time by introducing an electrochemical double layer into conventional capacitive pressure sensors. The most of devices for processing signals from sensors rely on battery. However, the inconvenience periodically recharging or replacing batteries has led to the demand for alternative energy sources. As a result, triboelectric nanogenerator (TENG) has garnered considerable attention as one of the sustainable energy sources.

Here in, we fabricated a self-powered wearable pressure sensing system composed of TENG and ionic capacitive pressure sensor using poly(vinylidene fluoride co-trifluoroethylene) and ionic liquid. The electrical energy harvested from TENG utilized to charge the batteries, which subsequently provide power to an Arduino kit for signal processing. The ionic capacitive pressure sensor, whose sensitivity was improved by the ionic liquid, was able to respond to various pressures and was integrated with TENG and Arduino kits to realize a self-powered wearable sensing system. We employed this sensing system to measure the pulse of the radial artery, indicating its potential application as a self-powered healthcare monitoring system.

O-S24-T4-4 Resonance tuning in plasmonic nanorings

Mr. Wei Tao [1], Dr. Florian Laible [2], Dr. Abdelhamid Hmima [1], Ms. Oceane Guillot [2], Prof. Thomas Maurer [1], Prof. Monika Fleischer [2]

1. *University of Technology of Troyes,* ***2.*** *University of Tübingen*

The spectral properties of plasmonic nanostructures acting as optical antennas can be noticeably modified via mode coupling. This effect can be used as a sensitive measure of the interparticle gap size in so-called plasmon rulers. Likewise, in larger arrays of nano-antennas, the antenna dipoles can collectively couple in the far-field, leading to surface lattice resonances with a much narrower bandwidth than the individual particle plasmon resonances. The present work aims at preparing plasmonic nano-rings on polymer substrates using electron beam lithography and a transfer process. Gold nano-rings with different thicknesses and diameters are prepared on silicon substrates with a chromium sacrificial layer and subsequently transferred to an elastic polydimethylsiloxane (PDMS) film. These flexible samples serve as an environment in which the coupling conditions between the antennas can be continuously and reversibly tuned by applying external strain. The evolution of the mode spectrum is tracked by reflection spectroscopy, and the evolution of the shape is monitored by scanning electron microscopy. This way, conclusions on the influence of the nanoring geometries on their deformation under strain can be drawn.

O-S24-T4-5 Fabrication of silicon gratings for an X-ray free electron laser spectrometer

Dr. Joan Vila-Comamala [1], ***Dr. Elisabeth Marie Skoropata*** [1], ***Dr. Cristian Svetina*** [2], ***Prof. Luc Patthey*** [1], ***Dr. Konstantins Jefimovs*** [1], ***Dr. Elia Razzoli*** [1], ***Dr. Christian David*** [1]

1. *Paul Scherrer Institute,* ***2.*** *IMDEA Nanociencia*

X-ray free electron lasers (FEL) deliver coherent, highly intense femtosecond X-ray pulse that enable unprecedented investigations of dynamics processes in matter. To date, X-ray FEL pulses are mostly generated via self-amplified spontaneous emission (SASE), in which a high-energy electron beam passes through a chain of undulator magnets to produce the intense coherent X-ray pulses. The SASE process relies on the inherent fluctuations of the electron beam, resulting in a coherent emission that is further amplified in the last sections of the undulator. The inherent stochastic nature of SASE emission leads to a substantial shot-to-shot variation of the energy spectrum of the X-ray FEL pulses. At the SwissFEL facility, located at the Paul Scherrer Institut in Switzerland, we are currently developing a high-resolution X-ray SASE FEL spectrometer that will be capable of providing online shot-to-shot energy spectra. Here, we present the fabrication of the required X-ray diffraction gratings with 120 nm pitch combining high-resolution e-beam lithography and silicon reactive ion etching, in which a 100 nm thin layer of PMMA resist is directly used as etching mask to transfer the pattern into the required thickness of silicon up to 300 nm.

O-S34-T4-1 3D printed diffractive optical elements for rapid prototyping.

Dr. Daniel Fan [1], ***Dr. Sejeong Kim*** [1]

1. *University of Melbourne*

Diffractive optical elements (DOE) allow control over the phase of a propagating wavefront. Fabrication of these elements can be tedious, requiring precision and possible post-processing. We introduce a simple and robust method for DOE fabrication by structuring and curing two separate resins with a small refractive index difference. This allows the fabrication tolerance such as DOE height and surface roughness to be relaxed. We fabricated a m = 1 vortex phase plate using two-photon lithography in IP-Dip, followed by encapsulation in IP-S which was then cured using one-photon UV flood illumination. Because the difference in refractive index of the two materials is ~0.04, the height of the vortex plate could be relaxed from ~600 nm to ~15 μm. Measurement of the image produced by such a vortex DOE using a simple lens and camera arrangement showed an intensity doughnut with central dark region size matching that of scalar approximation simulations. Using this simple fabrication method will allow rapid prototyping of DOEs for a variety of applications ranging from point-spread-function engineering in microscopy to telecommunications encoding schemes using orbital angular momentum.

O-S34-T4-2 Bowtie photonic-crystal waveguides as strong light-matter interfaces

Dr. Guillermo Arregui [1], ***Mr. Ali Nawaz Babar*** [1], ***Ms. Anastasiia Vladimirova*** [1], ***Mr. Christian Anker Rosiek*** [1], ***Dr. Babak Vosoughi Lahijani*** [1], ***Dr. Søren Stobbe*** [1]

1. *Technical University of Denmark*

Strong light-matter interaction in waveguide quantum electrodynamics experiments and applications has often been pursued by operating the waveguide-emitter system at frequency regions where the photonic waveguide exhibits slow light. This is because the interaction strength is proportional to the group index. Nevertheless, slow light is extremely sensitive to fabrication imperfections, e.g. sidewall roughness, which has impeded their use at large group indices, even in state-of-the-art low-loss waveguides. We numerically and experimentally investigate a different approach to enhance the interaction by using two-dimensional photonic-crystal waveguides that include bowtie-shaped dielectric bridges along the line defect (W1-BTs). The tight spatial field confinement at the periodic material bridges allows a 15-fold enhancement of the Purcell factor in the fast light regime compared to conventional W1 waveguides, although propagation losses increase due to the intense fields close to the sidewalls. Nevertheless, short waveguide segments in near-unity transmission terminations, which we design, may still enable the operation of W1-BTs coupled to quantum dots or to atomically thin materials as broadband light-matter interfaces for the efficient generation of single photons with a large degree of quantum coherence.

O-S34-T4-3 qBIC-based metasurfaces on SOI for light polarization control

Mr. Luca Fagiani [1], Dr. Luca Bolzonello [2], Dr. Johann Osmond [2], Prof. Domenico de Ceglia [3], Prof. Niek Van Hulst [2], Dr. Monica Bollani [4], Dr. Maria Antonietta Vincenti [3]

1. *Politecnico di Milano,* ***2.*** *ICFO - Institut de Ciencies Fotoniques,* ***3.*** *University of Brescia,* ***4.*** *Institute of Photonics and Nanotechnologies - Consiglio Nazionale delle Ricerche (IFN-CNR)*

An ultra-compact integrated polarizer is presented, using quasi-bound states in continuum (q-BIC), which has been rarely demonstrated experimentally. The control is independent of the polarization state of the incoming light.

O-S34-T4-4 UV-NIL based High-Throughput, Reproducible, and Cost-Effective SERS Platforms

Dr. Firehun Dullo [1], ***Dr. Karolina Milenko*** [1], ***Dr. Christopher Dirdal*** [1], ***Mr. Paul Thrane*** [1], ***Mr. Zeljko Skokic*** [1]

1. *SINTEF*

We present a novel SERS platform that addresses the need for a controlled and reproducible nanostructure . To achieve this, we utilized ultra-violet nanoimprint lithography (UV-NIL) to create large-area, well-ordered nanostructured arrays. By employing, UV-NIL imprinted patterns in resist, we successfully overcame the prevalent limitations associated with most conventional SERS platforms, including irregularity, lack of reproducibility, low throughput, and high cost, our approach involved simulating and fabricating C-shaped plasmonic nanostructures that exhibited signal enhancement when excited at wavelength of 785 nm. Instead of etching patterns in silicon, we directly coated the imprinted resist with a thin layer of gold, significantly reduced fabrication time, cost, enhancing reproducibility. We validated the functionality of the SERS substrates experimentally and achieved enhancement factor (EF) between 2.8×10^3 and 2.4×10^4.

O-S72-T4-1 MEMS Vibrometer for Structural Health Monitoring: Modeling and Characterization

Mr. Jan Niklas Haus [1], ***Mr. Zhengchun Zhu*** [1], ***Prof. Andreas Dietzel*** [2]

1. *Technische Universität Braunschweig / Institut für Mikrotechnik,* ***2.*** *Institute of Microtechnology, Braunschweig, 38124, Germany*

This study demonstrates the potentials and the limitations of designing the inertial core system of a MEMS (micro-electro-mechanical system) vibrometer based on FEM (finite element method) modeling. The in-depth comparison of results by simulation and experimental characterization reveal that the suggested double-cantilever oscillator yields a reasonable design for expanding the operating frequency of the MEMS vibrometer by electrically suppressing the signal component of the oscillator's first torsional mode. Moreover, the study illustrates that the presented MEMS vibrometer is capable of precisely resolving its high frequent displacements and thereby fulfilling the requirements for the operation as a pickup for guided ultrasonic waves in a structural health monitoring system.

O-S72-T4-2 Surface Lattice Resonances in Plasmonic Gold Nanocone Arrays

Mr. Lukas Lang [1], ***Prof. Monika Fleischer*** [1]

1. *University of Tübingen*

The excitation of surface lattice resonances (SLRs) in regular arrays of plasmonic noble metal particles is strongly dependent on the dielectric properties of the surrounding medium. Homogeneity of the refractive index as a necessary condition for SLRs might however be difficult to realize in experimental applications designed for e.g. molecular sensing, which is often conducted in flow cells. The utilization of three-dimensional nanoparticles, such as gold nanocones, provides the possibility to excite out-of-plane localized surface plasmon resonance modes. When arranged in regular arrays with lattice periods in the order of the particle resonances, out-of-plane SLRs may be excited respectively. It is proposed that the stronger coupling between the out-of-plane dipole moments results in higher stability of the respective SLR in terms of a refractive index mismatch.
To investigate the feasibility of in-plane versus out-of-plane plasmonic resonances, regular lattices of gold nanocones are fabricated on glass substrates by using an etch-mask-based argon ion milling procedure.
By optical investigation using collimated white light, it could be shown that out-of-plane SLRs indeed show stronger coupling of individual dipole moments as compared to their in-plane counterpart. This is further exploited for the enhanced adjustability of the plasmonic properties to emerging application needs.

O-S72-T4-3 Highly sensitive pseudo-capacitive iontronic pressure sensor with MXene electrode to enhance ion intercalation

Mr. Changwoo Cho [1], ***Ms. Chaeeun Lee*** [1], ***Prof. Je Hoon Oh*** [1]

1. *Hanyang University*

The demand for wearable pressure sensors has increased due to the growth of electronic technologies. Among various types, capacitive pressure sensors are preferred due to their tremendous advantages. However, these sensors still struggle with low sensitivity, resulting from small capacitance changes under pressure. Recently, capacitive sensors based on ionic liquid (IL)/polymer composites have used a nanometer-sized electrical double layer (EDL) between the composite and the electrode to achieve high capacitance variation and sensitivity. However, this type of pressure sensor relies on the structural shape of the composite, which limits its sensitivity improvement and cost. MXene, a two-dimensional sheet material, has emerged as a potentially excellent electrode material for capacitors due to its ability to intercalate ions of IL/polymer composites at high rates. In this study, we propose an iontronic capacitive pressure sensor incorporating a microstructured IL/polymer composite dielectric layer and a top electrode derived from $Ti_3C_2T_x$, a type of MXene. The purposed sensor accelerates the formation of the EDL in the composite, creating a pseudo-capacitive effect, a larger volumetric capacitance, and higher sensitivity compared to the conventional sensor. In addition, the sensor exhibited excellent performances in various sensing evaluations, demonstrating its potential as a wearable pressure sensor.

O-S72-T4-4 Evaluation of highly sensitive vibration states of nanomechanical resonators in liquid using a convolutional neural network

Mr. Kazuki Bessho [1], ***Prof. Shin'ichi Warisawa*** [1], ***Prof. Reo Kometani*** [1]

1. *The University of Tokyo*

Nanomechanical resonators can detect various small physical quantities with high sensitivity using changes in resonant characteristics. However, the measurement sensitivity is significantly reduced due to viscous damping in liquids. In this study, Convolutional Neural Network (CNN)-based vibration spectrum analysis was used to evaluate highly sensitive vibration states of nanomechanical resonators, which are useful for in-liquid measurements. This research was carried out through the measurement of acetone concentration. First, by comparing the concentration classification ability, it was indicated that the method of analyzing vibration spectral changes using the CNN model provides higher measurement sensitivity than the conventional measurement method of observing resonance characteristic changes. Next, Gradient-weighted Class Activation Mapping (Grad-CAM) was applied to confirm which frequency bands are important for concentration classification in CNN model decision-making. By examining the vibrational shape of the nanomechanical resonator in the frequency bands important for the measurements identified by Grad-CAM, a highly sensitive vibrational state in the liquid was identified. The measurements revealed that the resonant state and the vibration state with very small amplitude were important. This result indicates that in addition to the resonance state used in conventional methods, vibration states with very small amplitudes may be useful for in-liquid measurements.

O-S82-T4-1 Scalable Si-based architectures obtained by templated solid state dewetting

Dr. Sonia Freddi [1], Dr. Michele Gherardi [2], Dr. Nicoletta Granchi [3], Dr. Angelo Gatta Zini [2], Dr. Alexey Fedorov [1], Dr. Marco Abbarchi [4], Dr. Andrea Chiappini [1], Dr. Maria Antonietta Vincenti [5], Dr. Francesca Intonti [3], Dr. Monica Bollani [1]

1. *Institute of Photonics and Nanotechnologies - Consiglio Nazionale delle Ricerche (IFN-CNR),* ***2.*** *Politecnico di Milano,* ***3.*** *University of Florence,* ***4.*** *Aix Marseille Univ, Université de Toulon and Solnil,* ***5.*** *University of Brescia*

Here we demonstrate simple, low cost and efficient protocols for fabricating $Si_{1-x}Ge_x$-based, sub-micrometric dielectric antennas working as Mie resonators. The dielectric antennas are realized exploiting the natural instability of thin solid films to form regular patterns of monocrystalline atomically smooth silicon and germanium nanostructures. This is obtained by a proper combiantion of e-beam lithography, reactive ion etching and annealing treatments. Efficient protocols for encapsulating them also into flexible and transparent, organic supports are investigated and validated. We benchmark the optical quality of the antennas with light scattering measurements, demonstrating the control of the islands structural colour and the onset of sharp Mie modes after nanofabrication process.

O-S82-T4-2 Integration of Plasmonic Structures and Controlled Multimode Optical Fibers for Advanced Endoscopic Systems: Fabrication, Characterization, and Spatially Resolved SERS Enhancement

Ms. Linda Piscopo [1], ***Dr. Liam Collard*** [2], ***Dr. Di Zheng*** [2], ***Dr. Filippo Pisano*** [2], ***Dr. Antonio Balena*** [3], ***Dr. Marco Pisanello*** [4], ***Prof. Massimo De Vittorio*** [3], ***Dr. Ferruccio Pisanello*** [3]

1. *Istituto Italiano di Tecnologia, Center for Biomolecular Nanotechnologies, Arnesano,73010,* ***2.*** *Istituto Italiano di Tecnologia, Center for Biomolecular Nanotechnologies, Arnesano,73010, Italy,* ***3.*** *Istituto Italiano di Tecnologia,* ***4.*** *OptogeniX s.r.l.*

Plasmonic structures offer exciting possibilities for advanced biosensors in various applications, such as neuroendoscopy. However, the interaction of plasmonic structures with brain cells in an endoscopic manner requires precise control of the excitation light achievable only through a microscopy-based sensing scheme, where is possible to finely tune of wavevector and wavelength of the excitation field. In this abstract, we introduce a wavefront shaping system that, by implementing a phase modulation algorithm with a custom-made supercontinuum source, can tailor key parameters of the excitation field including spatial confinement, angular properties and excitation wavelength. We applied this system to two plasmonic configurations: propagating surface plasmon resonances (SPRs) and localized SPRs. For propagating SPRs, elliptical nano-holes are fabricated in a gold layer, and the propagation of plasmonic resonances is recorded through the fiber. For localized SPRs, nano-islands are nucleated on the fiber facet, and the surface-enhanced Raman scattering (SERS) response is tested in a solution. We optimize a multispectral photonic system to study the dispersion curves of plasmonic structures and demonstrate the ability to excite precise working points of the coupled system. The proposed platform shows potential for spatially-resolved endoscopic SERS and holds promise for future applications in the field of plasmonic neuroendoscopy.

O-S82-T4-3 Towards photon-noise limited room temperature IR detection using optomechanical resonators

Mr. Paolo Martini [1], ***Mr. Kostas Kannelopulos*** [1], ***Prof. Silvan Schmid*** [1]

1. *Institute of Sensor and Actuator Systems TU Wien*

The infrared (IR) portion of the electromagnetic spectrum holds many and important information about the interaction between radiation and matter. This information is of high value in many fields. The low energy carried by the photons in the IR range makes their detection challenging for room temperature detectors, and often in order to achieve the necessary sensitivity, thermal IR detectors make use of cryogenic cooling. A figure of merit for thermal detectors is the noise-equivalent power (NEP), which for an optomechanical resonator is proportional to the ratio between the Allan deviation of the fractional frequency signal and the relative responsivity to the impinging power. In this work, we propose a square drum resonator made of 50 nm thick silicon nitride (SiN) with a 5 nm thin film of platinum (Pt) deposited as a broadband IR absorber (~50% absorptance). The novelty of our work consists of the presence of a circular area where the Pt is not deposited. By using this particular design, we are able to significantly increase the responsivity of the structure, while keeping the photothermally induced noise coming from the readout laser low, thus reaching a NEP of hundreds of pW/sqrt(Hz), two o.f.m higher than the theoretical limit.

O-S82-T4-4 Electrochemical analysis on the SERS structure using boehmite

Mr. Shunya Saegusa [1], ***Dr. Masayuki Naya*** [2], ***Mr. Takao Fukuoka*** [1], ***Dr. Yuichi Utsumi*** [1], ***Dr. Akinobu Yamaguchi*** [1]

1. *University of Hyogo,* ***2.*** *Keio University*

SERS sensor using boehmite is highly sensitive molecular sensors that are easy to fabricate. However, if the adsorption of molecules is strong, we cannot reuse the sensor. Therefore, from the viewpoint of sensor reuse, it is important to realize desorbable labeling. Therefore, we are investigating a desorption method using an electrochemical redox reaction of thiol bonds. In this presentation, we evaluated the desorption of thiol bond by electrochemical reaction using cyclic voltammetry and Raman measurement of cysteine attached to the surface of SERS sensor.

Focus Track - Next Generation Quantum Computing and related Materials / Track2 - Fabrication and Integration of Micro/Nano Structures, Devices and Systems

O-S22-FT-1 Optimizing Josephson Junction manufacturing to increase yield and throughput in Qubit fabrication

Dr. Marcus Rommel [1]

1. *Chalmers University of Technology*

Superconductor based transmon qubits are one of the most promising platforms for building quantum computers. Fortunately many concepts from Silicon industry can be adapted to qubit fabrication and raise therefore hopes for a very fast scale up ones the technology grew up sufficiently. To reach our goals of 100 qubit and 1000 qubit devices in the coming years our fabrication process needs to be improved to increase throughput and yield. In this work we would like to present current improvements in the manufacturing process of the Josephson junctions (JJs), which reduces the qubit resonance frequency deviation and the wafer to wafer reproduciblity. Our process is based on Aluminium and uses shadow evaporation to manufacture JJs. Investigating the position dependency of the junction resistance and size with the help of automated electrical probing and SEM measurements, we identified a systematic correlation between them. Based on the throw distance and the distance to the tilt axis we developed a model explaining this position depending effect. In order to correct for it, we bias the junctions using a look-up table based on earlier fabrication runs. Finally, we could remove the position dependency both increase our yield and throughput.

O-S22-FT-2 Nanofabrication methodology and optimization for photon extraction on diamonds' NV center

Dr. Mohammad Soltani [1], ***Dr. Behrooz Semnani*** [1], ***Mr. AbdolReza Pasharavesh*** [1], ***Mr. Vinodh Raj Rajagopal Muthu*** [1], ***Prof. Christopher Wilson*** [1], ***Prof. Michal Bajcsy*** [1]

1. *Institute for quantum computing (IQC), University of Waterloo*

We report on our contributions to design and fabrication of various nanostructures for enhancing photon extraction from NV centers in diamonds. We investigate structures built with and on the diamond, including plasmonic structures on top of bulk diamond and structures made in the diamond itself, such as pillars, bullseye gratings, and inverse metastructures. Fabrication methods and materials selection were characterized to reach each desired structure. The effect of mask material on the morphology of etched diamond pillars and the micromasking effect was also investigated. These fabrication mechanisms are also suitable for applications beyond quantum communication or computing.

O-S22-FT-3 Integrated superconducting single photon detectors for trapped ion quantum computers

Mr. Philipp Hoffmann [1], ***Dr. Alexander Fernandez Scarioni*** [1], ***Dr. Sebastian Raupach*** [1], ***Mr. Peter Hinze*** [1], ***Dr. Thomas Weimann*** [1], ***Dr. Mark Bieler*** [1]

1. *Physikalisch-Technische Bundesanstalt (PTB)*

The readout of a qubit state in an ion trap architecture can be achieved by observing the presence or absence of ion fluorescence, which is typically analyzed by collecting the individual fluorescence photons and directing them out of the vacuum system using free-space optics to commercially available photon detectors. This method is incompatible with the miniaturization of ion trap chips required to increase the number of qubits in a trapped-ion quantum processor. One solution to this problem is to integrate the photon detectors directly into the read-out region of the ion trap, which can be achieved by using a Superconducting Nanowire Single Photon Detector (SNSPD).

In this work, we pursue the use of niobium as a superconducting detector material for the SNSPD. Niobium has a bulk critical temperature of ~9K, which is actually lower compared to other commonly used superconducting materials used in SNSPDs. For this purpose, we have fabricated two main types of SNSPDs from sputtered 15nm thick niobium films. The first type of these detectors consists of a 120nm wide meander structure. The second type of detector is a “cheese” detector in which we etched 80nm holes in a square area of 30µm.

O-S22-FT-4 Design, fabrication and characterization of diamond nanophotonic structures for quantum networks applications

Mrs. Nina Codreanu [1], ***Dr. Lorenzo De Santis*** [1], ***Mr. Matteo Pasini*** [1], ***Mrs. Julia Brevoord*** [1], ***Mr. Christian Primavera*** [1], ***Mr. Adria Riera-Moral*** [1], ***Prof. Ronald Hanson*** [1], ***Prof. Simon Groeblacher*** [2]

1. *QuTech and Kavli Institute of Nanoscience, Delft University of Technology,* ***2.*** *Department of Quantum Nanoscience and Kavli Institute of Nanoscience, Delft University of Technology*

Future quantum networks require end nodes that combine excellent qubit control and coherence with efficient spin-photon interfaces. Optically active spin qubits in diamond represent an auspicious building block. Among these, the group-IV-vacancy qubits are emerging as promising candidates: thanks to inversion symmetry these systems are first-order insensitive to charge noise, rendering them compatible with the monolithic nanophotonic integration in photonic crystal waveguides and cavities. This would potentially increase the collection efficiency and together with the extended coherence shown at low temperature, such systems could provide entanglement generation rates beyond current state of the art.

Nanofabrication of free-hanging diamond devices is itself challenging, as there is no known wet-processing technique that allows to fabricate suspended structures starting from bulk diamond material. Moreover, the employed conventional nanofabrication methods are extensively challenged when adapted to the fabrication aforementioned devices' designed dimensions.

Here we present our optimized fabrication process flow and demonstrate that such structures can be fabricated employing a quasi-isotropic crystal plane dependent reactive-ion-etch. We report as well on our latest experimental results and the related optical properties on the all-diamond photonic waveguides and photonic crystal cavities.

O-S22-FT-5 MOCVD of 2D Materials and Heterostructures

Mr. Jan Mischke [1], Dr. Simonas Krotkus [1], Dr. Sergej Pasko [1], Mr. Haonan Tang [1], Dr. Xiaochen Wang [2], Mr. Ben Conran [2], Dr. Clifford McAleese [2], Dr. Richard John Walker [2], Dr. Alexander Henning [1], Prof. Prof. Dr. Michael Heuken [1]

1. *AIXTRON SE,* ***2.*** *AIXTRON Ltd.*

Owing to their unique properties, two-dimensional (2D) van der Waals (vdW) materials are considered promising for future optical and electronic devices. One of the key challenges for the commercial realization of 2D materials for application in (opto)electronic devices is the controlled wafer scale synthesis of 2D materials at conditions that are compatible with established processes (e.g., CMOS). In this work growth of 2D material such as MoS_2 and WS_2 on up to 200 mm silicon/SiO_2 and sapphire substrates served as demonstrator to evaluate the abilities of the MOCVD technology. In this contribution we present our recent progress on the uniform deposition of transition-metal dichalcogenides by MOCVD on up to 200 mm wafer scale with commercial AIXTRON Close-Coupled Showerhead (CCS®) systems. The nucleation and growth of TMDC domains is monitored using in-situ reflectometry. The influence of growth parameters such as nucleation/deposition temperature, reactor pressure, carrier gas composition and precursor molar flows on the growth of TMDC crystallites has been investigated. Based on these metrology capabilities integrated with an AIXTRON close-coupled showerhead (CCS) system, we were able to synthesize 2D layers of transition-metal dichalcogenides (TMDs), graphene, hexagonal boron nitride (hBN) and their heterostructures with wafer-scale uniformity and excellent crystal quality.

Poster Session1.1: Focus Track/Track1/Track3

P-S11-01-T1 Design and preparation of one-dimensional LiFePO4 cathode by electrophoretic deposition method for flexible knitted batteries

Ms. Nuray Zhalgas [1], ***Dr. Almagul Mentbayeva*** [1], ***Dr. Batukhan Tatukayev*** [1]

1. *Department of Chemical and Materials Engineering, School of Engineering and Digital Sciences, Nazarbayev University*

Flexible batteries have gained significant attention in recent years due to their possible applications in wearable electronics and have several advantages such as mechanical flexibility, good energy storage capabilities, affordability, and environmentally safety. The proposed methodology involves the electrophoretic deposition of lithium iron phosphate on conductive nickel wire, providing a one-dimensional cathode structure. The EPD method allows greater precision and control over the deposition of active material on the current collector, and also has possible applications on different structures such as 1D and 3D. Also, the electrolyte was obtained by layer-by-layer method, by dipping them in polymers to coat the cathode material as a electrolyte-separator film. Overall, the research discusses the implementation of EPD method to obtain one-dimensional cathode material as it approaches an effective energy storage system and electrochemical performances for its future applications in next generation batteries.

P-S11-02-T1 Recent Developments in Processing Large Area 2D Materials, Dielectrics, and Metals via CVD and ALD for Functional Applications

Dr. Nils Boysen [1], ***Ms. Rahel-Manuela Neubieser*** [1], ***Mr. Jan-Lucas Wree*** [2], ***Dr. David Zanders*** [2], ***Mr. Florian Zimmermann*** [3], ***Dr. Kai Oliver Brinkmann*** [3], ***Dr. Marvin Michel*** [1], ***Prof. Thomas Riedl*** [3], ***Prof. Anjana Devi*** [2]

1. *Fraunhofer IMS, 47057 Duisburg, Germany,* ***2.*** *Ruhr University Bochum,* ***3.*** *University of Wuppertal*

Metal-organic chemical vapor deposition (MOCVD) and atomic layer deposition (ALD) are established in semiconductor manufacturing. Especially ALD, with its layer-by-layer fabrication capability reaching an unmatched conformality on intricate and high aspect-ratio structures, is gaining significant importance for the continuous downscaling of device dimensions. This not only requires advanced manufacturing tools and methods but also new and promising materials for semiconductor manufacturing. Among the different materials, high-k dielectrics, 2D materials or precious metals are in great demand to realize next-generation devices with complicated structures like gate all-around field effect transistors (GAA-FET). As both of the deposition methods are driven by chemical reactions of a precursor on the surface of the substrate in the vapor phase, a precise control of the precursor chemistry has to be ensured. This paper gives an overview of our joint research activities at Ruhr University Bochum (RUB) and Fraunhofer Institute for Microelectronic Circuits and Systems (IMS) in collaboration with the University of Wuppertal (BUW). Over the last years, our collaboration focussed on the rational development of precursors and CVD/ALD processes for the realization of materials such as MoS_2, WS_2, Y_2O_3, Ag, Cu, Co among others, which are highly relevant for different micro- and optoelectronic applications.

P-S11-03-T1 A new tool for single ion implantation and nanoscale materials engineering: System design and source development

Dr. Gianfranco Aresta [1]

1. *Ionopotika Ltd*

Single impurity atoms in semiconductors are receiving attention as potential quantum technologies, and proof-of-concept devices have shown promise. However, such devices are incredibly challenging to manufacture, as single atoms must be placed within ~ 20 nm of each other within a pure ^{28}Si matrix.

Real-world devices will require arrays of hundreds or thousands of impurity atoms, highlighting the requirement for a scalable method of positioning single atoms with nanometer precision.
We report on a new commercial instrument for the fabrication of quantum materials and devices via single ion implantation.
The instrument features a high-resolution mass-filtered focused ion beam (FIB), a deterministic single ion implantation system, and a high-precision stage. The deterministic implantation system allows single ion implantation with confidence levels as high as 98%.
The delivered ion dose can be adjusted across a wide range, providing many nanoscale materials engineering capabilities in a single tool, from single ion implantation to direct-write capabilities such as isotopic enrichment and targeted ion-implantation of nanomaterials.
The liquid metal alloy ion sources, coupled with a mass filtered column will enable the implantation of many different elements with isotopic resolution. LMIG source development carried out at Ionoptika in collaboration with our partners will discussed.

P-S11-04-T1 Challenges in adapting an established lift-off process based on e-beam lithography (EBL) for use with less harmful developers and removers

Dr. Silvia Diewald [1], ***Prof. Gernot Goll*** [1]

1. *KIT*

Recently, modifications of well-established fabrication processes have often been necessitated by disrupted supply chains, delivery problems, and sudden price hikes in addition to new regulations. Such challenges have motivated the search for adequate (or even superior) alternatives for resists, developers, etchants, removers, and other process chemicals which are not only reliably obtainable and still affordable, but also less hazardous and – in the best case – more sustainable as well. Having to adapt a fabrication process seems much less daunting if a knowledge base already filled with basic empirical information about the involved materials, substances, tools and their (not always easy to precisely predict) interactions is available.

As example, the gradual transformation of a standard lift-off process for EBL based on a PMMA 950K/600K double-layer resist system is used to illustrate the worth of having such data available. While evaluating empirical metal/remover compatibility charts made it easy to find less hazardous drop-in replacements for the NEP used as remover, finding an alternative to the IPA-MIBK based developer turns out more challenging. As contrast curves show, switching to an IPA-water based developer will entail some adjustments to either the lithography or the developing step. Different solutions (and workarounds) are investigated.

P-S11-05-T1 Patterning of Ormostamp films at the nanometer scale for large scale surface functionalization

Ms. Olga Muntada-Lopez [1], ***Mr. Alex Rodriguez-Iglesias*** [2], ***Dr. Francesc Perez-Murano*** [1], ***Dr. Marta Fernández-Regúlez*** [1]

1. *Instituto de Microelectrónica de Barcelona (IMB-CNM, CSIC),* ***2.*** *Institute of Microelectronics of Barcelona (IMB-CNM-CSIC)*

By means of texturing at the nanoscale, it is possible to create functional surfaces of interest in multiple fields such as the automotive industry, food, security or packaging. Although various methods have been demonstrated at the laboratory level, achieving functional surfaces on a large scale, affordably and with robust procedures is a challenge that is not yet fully established. We present a process that it is scalable. It is based on block copolymer lithography (BCPL) to define nanometer scale features in silicon stamps, and transferring of these features to Ormstamp films. The advantage of using BCPL is its simplicity, high throughput and high resolution. Ormostamp films can be used in roll-to-roll nanoimprint or injection plastic molding to further transferring the patterns to large-scale surfaces. We will present a systematic study of the fidelity of the replicated patterns on the Ormostamp film, and the optimization of the replication conditions. Achieving and accurate replication of the patterns will allow to address exciting surface functionalization with deterministically defined structures in virtually any material and any surface area.

P-S11-06-T1 Positioning accuracy of the direct laser lithography for a large-scale Fresnel Zone Plate

Mr. Viacheslav Vlasenko [1], ***Dr. Kahraman Keskinbora*** [1], ***Dr. Leonid Litvin*** [1], ***Dr. Michael Kahl*** [1], ***Mr. Jacco Houter*** [2]

1. *Raith GmbH,* ***2.*** *Raith Laser Systems B.V.*

Large scale Fresnel Zone Plates (FZP) can be used to interferometrically measure the aspherical lens or mirror aberrations. In such measurements, it is crucial to manufacture the FZP which produces a precise spherical wavefront. Therefore, the positioning accuracy of the direct laser writer should satisfy a very strict tolerance. In this work a 100-mm-diameter FZP was fabricated on a glass substrate with maskless laser lithography technique and measured with a dedicated SEM based metrology tool. The production was carried out on a temperature-stabilized Raith PICOMASTER 200 direct laser writer tool. Extensive metrology results have proven that aspherical deviation of the FZP prepared with the laser beam writer was in the range of 100 nm across 100 mm distance.

P-S11-07-T1 Resistless lithography on Si surfaces by EUV-induced surface modification

Dr. Prajith Karadan [1], ***Dr. Yasin Ekinci*** [1], ***Dr. Dimitrios Kazazis*** [1]

1. *Paul Scherrer Institute*

Extreme ultraviolet lithography (EUVL) is the most advanced lithographic technique for mass production of integrated circuits with the ability to achieve ultimate resolution and high throughput. The EUV interference lithography (EUV-IL) endstation at the XIL-II beamline of the Swiss light source (SLS) has extensively been used in the research and development of EUV materials with half-pitch resolutions down to the sub-10 nm regime. However, the use of photoresists leads to several issues such as line edge roughness and pattern collapse, which arise from the finite thickness of the photoresist films. Recently, our group has demonstrated resistless EUV patterning on HF-treated Si surfaces by exposing with EUV light followed by TMAH etching. It was observed that the EUV exposure promotes the growth of a dense oxide layer at the exposed region, which provides the etching selectivity in TMAH etching. Here, we extend our studies on, resistless EUV lithography on differently modified surfaces such as OH terminated and Si with SiO_2 are studied in detail. These Si surfaces show better sensitivity compared to HF-treated Si and the mechanism behind the pattern formation is extensively studied using synchrotron X-ray photoemission spectroscopy (XPS).

P-S11-08-T1 Study reactive ion etching- transformer coupled plasma (RIE-TCP) mode for patterning of MgZnO alloys, used for computing and memory applications

Ms. Leila Ghorbani [1], ***Dr. Shreya kundu*** [2], ***Dr. Frederic Lazzarino*** [2], ***Prof. Stefan De Gendt*** [1]

1. *Ku Leuven, Celestijnenlaan 200f, Leuven, 3001, Belgium, IMEC, Kapeldreef 75, Leuven, 3001, Belgium,* ***2.*** *IMEC, Kapeldreef 75, Leuven, 3001, Belgium*

Magnesium Zinc Oxide (MgZnO) is a novel metal alloy considered a dielectricum in transistors in dynamic random-access memory (DRAM) or core elements in resistive random-access memory (RRAM). Therefore, minimal damage-inducing patterning of the alloy for use in electrical nanoscale devices is needed.
During the etching process, MgZnO film may be chemically and physically damaged, impacting its electrical performance. The etch process developed should preserve the chemical composition and roughness in MgZnO when patterning other layers of the stack and hard mask (HM). Reactive ion etching (RIE) generates an etching mechanism that can provide an optimal combination of chemical and physical etching.
In this work, we carried out etch investigation of 10 nm MgZnO film using an RIE-transformer coupled plasma (TCP) system. The etching of MgZnO thin films is carried out using Cl2/CH4/Ar mixture. Cl2 increases chemical reactivity by creating MgCl2 and ZnCl2 by-products and CH4 produces organometallic volatile etch by-product – Zn (CH3)2. Based on the results Zn gets etched faster than Mg in MgZnO and the etching of Mg is more physical, and Zn is more chemical. This study can enable a more systematic patterning study of MgZnO-based features at different scaled dimensions and densities.

P-S11-09-T1 Realization of Highly Uniform Surface Functionalization and Applications to Organic Transistors

Dr. Ming Chen [1], ***Prof. Xing Cheng*** [1]

1. *Southern University of Science and Technology*

The employment of surface functionalization by self-assembled monolayers (SAMs) covers a wide range of areas owing to the fine control over the essential physical properties of the surface/interface. The high-quality surface functionalization is tremendously preferred; however, the SAM deposition is easily suffered from defects due to the complexity of the growth process. The current work aims to develop an effective and practical method for the elimination of morphological defects and realize the defect-free SAM deposition. Particularly, the conventional vapor phase approach for SAM deposition is ameliorated, which drastically reduces the contamination from the reaction vessel. After the parameter optimization, wafer-scale and highly unform surface functionalization is obtained. The successful deposition of SAM is verified by the element analysis and the surface energy measurement. It is fascinated that this approach is applicable to frequently used SAM materials. Finally, the high-quality surface treatment is utilized into the fabrication flow of the bottom-gate top-contact organic thin-film transistors and improves the hole mobility significantly. The current work offers a general strategy for the preparation of high-quality surface functionalization, and meanwhile, paces up the fabrication of large-area and high-performance organic electronics.

P-S11-10-T1 Wafer scale fabrication of pyrolytic carbon sub-100 nm nanogap electrodes for electrochemistry by etching of insulating oxides

Mr. Nicolai Støvring [1], ***Prof. Stephan Sylvest Keller*** [1], ***Prof. Jenny Emnéus*** [1], ***Dr. Arto Heiskanen*** [1]

1. *Technical University of Denmark*

Electrically separated electrodes with submicron/nanometer sized gaps are attractive in electrochemical sensing applications. Here, small gaps can induce redox cycling, a mechanism in which the same molecule of target analyte is reduced/oxidized multiple times amplifying the electrochemical signal many-fold. Pyrolytic carbon presents itself as a desirable material in electrochemistry offering beneficial properties, such as being mechanically stable, chemically inert, and highly tailorable in terms of surface chemistry

So far, nanometer gaps with pyrolytic carbon have only been achieved on single devices with processes that are not compatible with wafer scale cleanroom fabrication [4]. In this work, we show the current development of a process for wafer scale fabrication of sub-100 nm nanogap electrodes using a stacked layer approach with two pyrolytic carbon layers separated by insulating materials. Here, major challenges present themselves in terms of layer compatibility and stability during pyrolysis and etching.
We are currently finalizing the process to optimize the yield by reducing delamination and will perform electrochemical redox cycling experiments in the near future.

P-S11-11-T1 Patterning of Novolac-based negative resist using EBL and its performance as etch mask for DRIE of silicon

Mr. Rahul Singh [1], ***Mr. Christian Vinther Bertelsen*** [1], ***Dr. Maria Dimaki*** [1], ***Prof. Winnie Edith Svendsen*** [1]

1. *Technical University of Denmark*

Electron-beam lithography (EBL) is a pivotal tool in fabrication of nanoscale patterns which are widely used in the field of semiconductor devices and photonics. Although both positive and negative tone resists are available for EBL, in certain cases, negative resists provide critical advantages over positive resists, for instance, reduction in writing time and high selectivity etch mask.

Therefore, in this work, firstly, an e-beam dose test is performed on AR-N 7520.17 (new) which is Novolac-based negative e-beam resist, using 100 kV EBL exposure system (JEOL JBX-9500FSZ). Secondly, DRIE of silicon is done using different AR-N 7520.17 patterns to study its performance as etch mask.
The results show that, for both 160 nm and 90 nm diameter features, resist pattern as well as silicon nanopillars have vertical side walls. Furthermore, no significant damage to the resist layer is observed after the DRIE step.

P-S11-12-T1 Ion incidence angle-dependent pattern formation on AZ® 4562 photoresist by (reactive) ion beam etching

Mr. Tom Rüdiger [1], ***Mr. Martin Mitzschke*** [1], ***Dr. Carsten Bundesmann*** [1], ***Ms. Andrea Prager*** [1], ***Dr. Ying Liu*** [2], ***Prof. Bernd Abel*** [3], ***Dr. Agnes Schulze*** [1], ***Dr. Frank Frost*** [1]

1. *Leibniz Institute of Surface Engineering e.V. (IOM),* ***2.*** *University of Science and Technology of China,* ***3.*** *University Leipzig*

Reactive ion beam etching is a versatile method to alter the surface morphology and the chemical composition of the surface/near-surface area of various materials. It is applied in the production of high-end optics by utilizing a pattern transfer from a photoresist to a surface. The formation of roughness, e.g. through nanopatterns, lowers the quality of the products. There are models that explain nanopatterning at inorganic surfaces, but it's questionable if they are transferable to more complex issues like the combination of non-monoatomic targets and reactive ion beam.

In this study, nanopatterning on a photoresist with different ion incidence angles (0° - 75°), variation of fluence and etch gas is investigated. The utilization of AFM and SEM reveals the emergence of nanopatterns (nanoholes, ripples, triangular features, protrusions, facets). The formed nanopatterns resembles those known from inorganic materials and leads to the assumption that local redeposition, surface viscous flow and dispersion plays an important role for the pattern formation on polymer surfaces. Spectroscopic ellipsometry shows that the thickness of the surface layer depends on the ion incidence angle but not on the fluence. XPS reveals trends in the chemical composition of the surface in dependence of the ion incidence angle and fluence.

P-S11-13-T1 Selective ion-assisted nanostructuring process of silicon devices

Mr. Alessandro Cian [1], ***Dr. Elia Scattolo*** [1], ***Dr. Michele Crivellari*** [1], ***Dr. Jordi Llobet*** [2], ***Dr. Francesc Perez-Murano*** [3], ***Dr. Lorenza Ferrario*** [1], ***Mr. Damiano Giubertoni*** [1]

1. *FBK, Fondazione Bruno Kessler,* ***2.*** *Alba CELLS Synchrotron,* ***3.*** *Instituto de Microelectrónica de Barcelona (IMB-CNM, CSIC)*

This study was focused on the effectiveness of using Au+ ion implantation as a mask-less patterning method.
The results demonstrated that Au+ ion implantation could replicate the etching rate variation of silicon in tetramethylammonium hydroxide solution. By doping the silicon substrate with Au+ ions at fluences ranging from 1e15 to 1e17 ions/cm2, the irradiated areas acted as masks for pattern transfer without significant sputtering effects.
Simulation results indicated the depth profiles of Au in Si and the affected region within the substrate due to ion implantation. The experimental observations showed that fluences below the saturation value (8.0e16 ions/cm2) were sufficient to enable the masking effect and create suspended structures. By adjusting beam parameters such as energy, fluence, and writing strategy, it was possible to achive suspended features with critical dimensions and various layout possibilities.
In comparison to Ga+ implantation, the Au+ implanted structures showed potential for improved electrical conductivity after annealing. Ongoing experiments are investigating the effects of high-temperature treatments on gold concentration and changes in electrical properties within the implanted regions.
This study highlighted the versatility of the technological platform, paving the way for potential applications in gas and bio-sensing with specific geometries and functionalization of the suspended structures.

P-S11-14-T1 Plasma conversion of polydimethylsiloxane and perhydropolysilazane precursor layers by a pulsed atmospheric pressure plasma jet to a silicon oxide thin film

Dr. Patrick With [1], ***Dr. Martin Rudolph*** [1], ***Mr. Peter Birtel*** [1], ***Prof. Thomas Arnold*** [1], ***Ms. Andrea Prager*** [1], ***Dr. Sergej Naumov*** [1], ***Dr. Ulrike Helmstedt*** [1], ***Prof. Andre Anders*** [1]

1. *Leibniz Institute of Surface Engineering e.V. (IOM)*

The economical deposition of a barrier thin film material like silicon oxide onto flexible and thermally sensitive polymer substrates such as polyester foils is of great relevance to many applications, e.g., encapsulation of flexible photovoltaics, OLEDs and other flexible electronics. Common approaches to deposit metal or metalloid oxide thin films require either high processing temperatures >350 °C, e.g. in sol-gel methods and atmospheric pressure CVD which are not compatible with polyesters, or costly low pressure processes, e.g. CVD, ALD and PVD methods. Atmospheric pressure plasma treatment of materials is a flexible and efficient technology for the modification of surfaces. In some cases, such as in the activation of polymer surfaces, atmospheric pressure plasmas have become the tool of choice. For other purposes, such as the fabrication of thin films, the potential of atmospheric pressure plasmas is yet to be fully leveraged. We discuss the conversion of perhydropolysilazane (PHPS) and polydimethylsiloxane (PDMS) layers to silicon oxide thin films using a pulsed atmospheric pressure plasma jet. Varying the scan velocity and the number of treatments resulted in various film compositions and morphologies. An insight into the conversion of the precursors and the processes involved will be given.

P-S11-15-T1 Comparative Study of NbN Deposition via Magnetron Sputtering and Atomic Layer Deposition (ALD)

Dr. Rodolfo Previdi [1]

1. *ISTA*

Comparative Study of NbN Deposition via Magnetron Sputtering and Atomic Layer Deposition (ALD)

The deposition of superconducting thin films is of paramount importance for various applications in fields such as electronics, sensing, quantum computing, and energy storage. In this study, we present a comparative investigation of niobium nitride (NbN) thin film deposition using two prominent techniques: magnetron sputtering and atomic layer deposition (ALD). The aim of this research is to evaluate and compare the structural, electrical, and morphological properties of NbN films deposited via these two methods.

To investigate material quality differences, we plan to compare SEM images, AFM scans and 4 point-probe electrical resistivity measurements, both at room temperature and at superconductive transition temperature(±16K).

P-S11-16-T1 Optical waveguides made of inkjet-able high refractive index materials using Nanoimprint Lithography

Dr. Michael Haslinger [1], ***Mr. Gerald Stubauer*** [1], ***Mr. Peter Bauer*** [1], ***Mr. Sebastian Kauscheder*** [1], ***Ms. Viktorija Jonaityte*** [1], ***Ms. Katerina Masopustova*** [1], ***Ms. Sonja Kopp*** [1], ***Dr. Michael Muehlberger*** [1]

1. *PROFACTOR GmbH*

An Optical Phased Array (OPA) LiDAR is a system which enables the beam steering without need for moving parts. On such a system light is guided in optical waveguides made of high refractive index material. By the use of high refractive index materials and a Nanoimprint Lithography (NIL) process, optical components like waveguides and photonic integrated circuits can be directly fabricated in a single production step. In this work we present the direct imprint of waveguide structures in various high refractive index materials. The one step manufacturing process of waveguides by using NIL and the combination of inkjet and NIL allows for a very sustainable manufacturing process.

P-S11-17-T1 No more macros: Open-source method for layout cell parameterization through feature recognition for procedural generation of lithography files

Mr. Tom Maslin [1], ***Dr. Stefanie Gutschmidt*** [1]

1. *University of Canterbury*

This work presents a Python-based architecture packaged as a standalone tool to enable feature recognition and parameterization of GDSII geometries, without the need for scripting. By feeding a GDSII file obtained from an existing layout editor into the tool, a 'scaffold' shape is created and recognized. The tool allows for the parameterization of created geometries and the establishment of parameterized rules between geometry features, which can be conveniently modified in a CSV file generated by the tool. This work facilitates no-code procedural generation of geometrically distinct instances, significantly reducing the time required for complex lithography PCell development compared to traditional scripting-based methods.

P-S11-18-T1 Lithographic Patterning of Electrochemical Sensors on Flexible Substrates

Mr. Faraz Kaiser Malik [1], ***Dr. Florent Seichepine*** [1], ***Prof. Kristel Fobelets*** [1]

1. *Imperial College London*

Electrochemical transduction is promising for the development of portable diagnostic technology due to its high sensitivity within a compact form factor. Two separate fabrication protocols based on conventional optical lithography techniques are presented here, enabling the development of micrometer-scale tri-electrode transduction elements made of gold and graphene, respectively, on flexible substrates. The devices are suitable for mass production and integration with microfluidic sample collection and signal processing systems. They may therefore be incorporated as an array of miniaturized sensors in a wearable system capable of detecting multiple analytes in biofluidic samples collected without conscious user effort. The sensor performance is characterized through resistivity, wettability and electrochemical measurements. The bilayer substrate used for the gold-based electrodes significantly improves yield and reduces performance degradation upon deformation. The graphene electrodes, meanwhile, exhibit no clear deterioration with bending stress, but exhibit higher resistivity due to material properties. Further work is being carried out to decrease the resistivity of MLG and optimize its electrochemical response, with a view to developing low-cost, flexible sensors for integration in wearable health monitoring systems.

P-S11-19-T1 Extracting extra information from STM images using machine learning

Dr. Ehud Fuchs [1], ***Dr. John Randall*** [1], ***Dr. James Owen*** [1]

1. *Zyvex Labs*

Scanning Tunneling Microscope (STM) can image a silicon surface at the atomic scale. The STM image is closely related to the topography of the surface, but it actually represents the electronic state of the surface. Collecting additional electronic information about the surface, such as the Local Barrier Height (LBH), requires an extra lock-in amplifier. We demonstrate that the LBH data is already contained in the original image and can be extracted with the use of Machine Learning (ML).

The input to the ML algorithm is the pseudo-Topography image and the tunneling current. The output of the algorithm is the LBH image and an enhanced topography image that more closely represent the actual topography of the surface.

P-S11-20-T1 Degradable PVAc-graphene nanofibrous membrane for flexible piezocapacitive sensors

Dr. Debarun Sengupta [1], ***Prof. Ajay Kottapalli*** [1]

1. *University of Groningen*

With growing life expectancy and a rise in population with sedentary lifestyles, the load on existing healthcare infrastructure is expected to increase manifolds in the next two decades. As per National Institute for Public Health and the Environment (RIVM) the number of centenarians will quadruple by 2040 [1]. The need of the hour is robust, reliable, sensitive, and inexpensive wearable sensors capable of providing intimate and detailed information regarding a person's physiological parameters. However, it is also critical that such sensors are environmentally friendly and that production is sustainable. In this work, we present graphene-polyvinyl acetate (PVAc) electrospun nanofibrous membrane-based degradable piezocapacitive sensors for applications in wearables. The sensor featured in this work comprises of 0.25 wt.% graphene-loaded electrospun nanofiber membrane sandwiched between two layers of fabric-based flexible electrodes. The degradability of the sensors has been demonstrated previously [2]. It is expected that sensors similar to the one presented here will gain widespread acceptance for future applications in flexible electronics and wearable devices.

[1] "Life expectancy | Volksgezondheid Toekomst Verkenning." [Online]. Available: https://www.vtv2018.nl/en/life-expectancy.

[2] D. Sengupta et al., ACS Appl. Mater. Interfaces, vol. 15, (2023) 22351–22366.

P-S11-21-T1 SiO2 & SiNx Thin Film Deposition by Plasma Enhanced Spatial Atomic Layer Deposition Processes

Mr. Jaehee Kim [1], ***Mr. Hyeonjin Choi*** [2], ***Mr. Jinmyeong Kim*** [2], ***Prof. Heeyeop Chae*** [2]

1. *Department of Semiconductor and Display Engineering, Sungkyunkwan University,* ***2.*** *School of Chemical Engineering, Sungkyunkwan University*

In this study, thin film deposition processes for dielectric SiO_2 and Si_3N_4 were developed by a spatially divided plasma enhanced atomic layer deposition (spatial PEALD) process. Trisilylamine (TSA, $N(SiH_3)_3$), Bis(tertiary-butylamino)silane (BTBAS, $[(CH_3)_3CNH]_2SiH_2$ were selected as silicon precursors, and NH_3 plasma was used as a reactant material. The ALD window of SiO_2 was observed in the temperature range of 125-150□ and the chemical composition ratio in ALD window determined to be O/Si~1.92. Carbon components were identified as major impurities in the films. The impurities were reduced through high temperature, high plasma power. The growth per cycle (GPC) of the SiO2 and SiNx films were 1.33Å/cycle and 0.27Å/cycle at temperatures 150□ respectively. The film characteristics of various process parameters were investigated according to the growth temperature, plasma power, and scanning speed of substrate. Finally the optimal deposition conditions with low impurities was found and the characteristics of SiO2 & SiNx thin films were confirmed. These results demonstrate the potential of spatial ALD combined with the intrinsic advantages of atomic layer deposition in the semiconductor industry.

P-S11-22-T1 Plasma Atomic Layer Etching of SiO2 with Low-Global Warming Perfluoroisopropyl Vinyl Ether (PIPVE)

Ms. Jihye Kim [1], ***Mr. Hojin Kang*** [1], ***Mr. Minsuk Choi*** [1], ***Ms. Daeun Hong*** [1], ***Ms. Yongsun Cho*** [2], ***Mr. Junsik Hong*** [2], ***Prof. Heeyeop Chae*** [1]

1. *School of Chemical Engineering, Sungkyunkwan University,* ***2.*** *Samsung Electronics*

In this work, plasma atomic layer etching (ALE) was developed for SiO_2 with perfluoroisopropyl vinyl ether (PIPVE, $C_5F_{10}O$) and compared with conventional global warming C_4F_8 gas. PIPVE has a lower lifetime and global warming potential of 3 which is significantly lower than that of C_4F_8, 9,540.[1],[2] ALE is a cyclic process that removes layers with atomic-scale precision and consists of a surface modification step and an etching step.[3],[4] In the surface modification step, SiO_2 surfaces were fluorinated with fluorocarbons generated from C_4F_8 or PIPVE plasmas. In the etching step, the fluorinated surface was etched by ions generated from Ar plasma.[5] The ALE window was observed in the bias voltage range of 20-27.5V for both C_4F_8 and PIPVE. The etch per cycle of SiO_2 in the ALE window was determined to be 5.3 Å/cycle for C_4F_8 and 3.3 Å/cycle for PIPVE. The composition of the fluorocarbon layers on the SiO_2 surface was analyzed by X-ray photoelectron spectroscopy, and the F1s/C1s ratio was calculated using the F1s and C1s spectrum.[6,7] The PIPVE produces the lower than C_4F_8 the F1s/C1s ratio. This work demonstrates that PIPVE can reduce global warming effects as compared to C_4F_8 and be used as potential etchants for ALE.

P-S11-23-T1 Fabrication of Flexible Transparent Silver Electrodes via Maskless Evaporation

Mr. Sihai Luo [1], ***Mr. Enkui Lian*** [1], ***Prof. John De Mello*** [1]

1. *Norwegian University of Science and Technology*

We report template-patterned, flexible Transparent Electrodes (TEs) formed from an ultrathin silver film on top of a commercial optical adhesive, which is shown to be an effective base-layer for ultrathin silver films that advantageously prevents coalescence of vapour-deposited silver atoms into large, isolated islands (Volmer-Weber growth), and so aids the formation of ultrasmooth continuous films. 12-nm silver films on top of free-standing NOA63 combine high, haze-free visible-light transparency (» 60 % at 550 nm) with low sheet-resistance (ca. 16 Ohm/sq.), and exhibit excellent resilience to bending, making them attractive candidates for flexible TEs. Etching the NOA63 base-layer with an oxygen plasma before silver deposition causes the silver to laterally segregate into isolated pillars, resulting in a much higher sheet resistance than silver grown on pristine NOA63 (> 8^10^6 Ohm/sq.). Hence, by selectively etching NOA63 before metal deposition, insulating regions may be defined within an otherwise conducting silver film, resulting in a differentially conductive film that can serve as a patterned TE for flexible devices. The described procedure has several advantages over conventional methods for micropatterning metals such as shadow-mask evaporation (blurring and shadowing artefacts) and photolithography (easier to implement with a correspondingly lower environmental impact).

P-S11-24-T1 A comparison of granular aluminum deposited via electron beam evaporator and sputtering

Dr. Bruno Martins Magalhaes [1], ***Dr. Salvatore Bagiante*** [1], ***Dr. Rodolfo Previdi*** [2], ***Dr. Lubuna Shafeek*** [1], ***Mr. Abdulhamid Baghdadi*** [1]

1. *Institute of Science and Technology Austria (ISTA),* ***2.*** *ISTA*

The deposition of granular aluminum thin films is critical for various technical applications. This study compares two commonly used deposition techniques, electron beam evaporator, and sputtering, and evaluates their impact on film properties. The influence of oxygen during deposition was specifically examined. Oxygen-free deposition resulted in pure aluminum films with low oxidation susceptibility, while controlled oxygen presence led to the formation of a protective oxide layer. SEM and AFM analyses provided insights into the morphological features, including grain boundaries, film thickness, particle size distribution, and surface roughness. Four-point probe measurements characterized the electrical properties, such as conductivity and resistivity. The choice of deposition technique depends on the desired film properties and specific application requirements. Overall, understanding the influence of oxygen and its comparative characteristics aids in optimizing granular aluminum films for diverse applications.

P-S11-25-T1 Measurement of short range PSF in EBL

Dr. Leonid Litvin [1], ***Dr. Michael Kahl*** [2], ***Ms. Julia Shapiro*** [1]

1. *Raith GmbH, Dortmund, 44263, Germany,* ***2.*** *Raith GmbH*

Nowadays the simulated PSFs are often used for proximity effect correction and deliver rather acceptable results. Nevertheless, the experimental verification of these PSFs would contribute to better performance of proximity effect correction and understanding of problems for high resolution lithography. We measured short-range part (SR) of PSFs by method of line exposures and reported its proper functioning up to width of SR PSF of 10 nm. We see potentials of the method up to 5 nm FWHM.

P-S11-26-T1 Additive Processes for Micro Fabrication: Making an Impact with Inkjet

Dr. Kai Keller [1]

1. Notion Systems GmbH

The manufacturing of micro electronics is a wasteful undertaking. Introducing additive processes into micro production reduces waste and will play a mayor role in making the production of electronics more sustainable. In my presentation I will report on the recent developments in the area, provide application examples, and show where the current limitations are.

P-S11-27-T1 Micro/nano fabrication of Bio wells: Comparison between Nanoimprint lithography and nano 3D printing

Dr. Lubuna Shafeek [1], ***Dr. Salvatore Bagiante*** [1], ***Dr. Jack Merrin*** [1]

1. *Institute of Science and Technology Austria (ISTA)*

In this study, an attempt to conduct a comparative investigation of two fabrication techniques for bio well fabrication: nanoimprint lithography (NIL) and nano 3D printing. Major challenge for fabricating bio wells for biological application is to develop a sustainable and compatible methods with specific tools. In this research, we will evaluate the process flow related to product development, limitations, and suitability of these techniques for creating high-resolution, functional bio wells for biological applications. Current microfluidic devices are typically molded from polydimethylsiloxane (PDMS) on a glass substrate due to its transparency, biocompatibility. Nanoimprint lithography is a top-down fabrication method that utilizes a mold to transfer a pattern onto a substrate through mechanical deformation or imprinting. On the other hand, nano 3D printing is an additive manufacturing process that builds structures layer-by-layer from a liquid precursor using a technique called two-photon polymerization (2PP). In 2PP 3D printing, a high-power focused laser creates a nonlinear energy distribution centered at the laser focal point, whereby an excitation induces monomer crosslinking of the material which creates a three-dimensional nanostructure. Both techniques were performed under optimized conditions to ensure accurate and reproducible fabrication of bio wells.

P-S11-28-T1 Resist based Ion Beam Lithography with light ions from Liquid Metal Alloy Ion Sources

Dr. Achim Nadzeyka [1], ***Dr. Paul Mazarov*** [1], ***Mr. Torsten Richter*** [1], ***Dr. Michael Kahl*** [1]

1. *Raith GmbH*

Here we report about recent Ion Beam Lithography (IBL results on positive and negative resists like PMMA and HSQ employing light Si and Li ions from Liquid Metal Alloy Ion Sources (LMAIS). The experiments have been performed using a FIB-SEM tool based on a lithography architecture with laser interferometer stage (Raith VELION). LMAIS is a versatile FIB source technology that is capable to deliver various ion species. Light and heavy ions such as Silicon and Gold or Lithium and Bismuth are unified in a single source (AuGeSi or GaBiLi). Various ion species are emitted simultaneously from a single source and separated in a downstream Wien filter.

In this contribution we discuss our IBL results with respect to possible resist thickness, achievable minimum feature size, line edge roughness and proximity effect and compare them to typical EBL results.

P-S11-29-T1 Ion Beam Planarization Using Solvent-Free Polymer Coatings

Mr. Lukas Paul Lingenfelder [1]

1. *Leibniz Institute of Surface Engineering e.V. (IOM)*

This study presents new developments for ion beam planarization of optical surfaces. In ion beam planarization, thin, usually polymeric, sacrificial layers are applied to the surfaces to be planarized. Subsequently, an ion beam etching step is used to transfer the levelled surfaces into the optical surface. In general, the smoothing effect decreases very strongly with the spatial wavelength of the roughness components. This is caused by the loss of solvent in the photoresist during the coating step.

It is shown how the smoothing effect can be significantly increased by using a solvent-free nanoimprint resist and how larger spatial wavelengths can also be smoothed. The smoothing behavior is investigated for pre-structured Si wafers with line pattern of lateral structure sizes up to 450 µm and surface amplitude of 20 nm. The ion beam etching transfer is carried out with a broad beam ion source of the Kaufman type, whereby the influence of the etch selectivity (Si to photoresist) on the achievable degree of planarization is investigated. To further improve the planarization level and etch resistance of the resist UV flood exposure, pre-tempering, and post-tempering are examined.

P-S11-30-T1 3D Ice Lithography Software and Control

Mr. Joachim Lyngholm-Kjærby [1], ***Mr. Affan Kaysa Waafi*** [1], ***Dr. Anpan Han*** [1]

1. *Technical University of Denmark*

3D lithography has a huge potential in micro- and nanofabrication. 3D ice lithography (3DIL) complements TPL and FEBID. By performing a layer-by-layer lithography process, focused electron beams interact with condensed vapour films, creating voxels by cross-linking the organic components in each layer. This abstract presents 3DIL software and control.

P-S11-31-T1 SiOxNy Low Temperature Deposition at PECVD using Carbon-free Precursor

Mr. Youngju Ko [1], ***Mr. Hyeonjin Choi*** [2], ***Mr. Jaehee Kim*** [1], ***Mr. Jinmyeong Kim*** [2], ***Mr. Namgun Kim*** [1], ***Prof. Heeyeop Chae*** [2]

1. *Department of Semiconductor and Display Engineering, Sungkyunkwan University,* ***2.*** *School of Chemical Engineering, Sungkyunkwan University*

Several studies have explored Si source precursors for low-temperature deposition of SiOxNy. However, existing precursors have all exhibited carbon contamination issues, which hinder the attainment of high film purity and reduced carbon emissions. In this study, trisilylamine (TSA), a carbon-free precursor, is investigated for low-temperature deposition of SiOxNy to enhance film purity and minimize carbon emission. The characteristics of the deposited films were modulated by varying the ratio of Si source precursor to oxygen gas. Higher Si source ratios resulted in an increase in refractive index (RI) up to 1.7, approaching the properties of silicon nitride, while higher oxygen gas ratios led to a decrease in RI down to 1.55, approaching the properties of silicon oxide. Additionally, the deposition rate exhibited variations ranging from 30 to 60 nm/min depending on the gas and power variables. Our findings demonstrate that low-temperature deposition of SiOxNy using TSA through the plasma-enhanced chemical vapor deposition (PECVD) method is feasible. This research not only offers insights into the control of film properties by adjusting precursor and gas ratios but also presents a practical approach to achieve carbon-free SiOxNy deposition, enabling enhanced film purity and reduced carbon emissions.

P-S11-32-T1 AI-assisted design of charged particle optics

Dr. Aydin Sabouri [1], ***Dr. Carla Perez Martinez*** [1]

1. *University College London*

Accelerated charged particles have been widely used for micro and nanotechnology applications and in the semiconductor industry, ranging from mass spectroscopy systems to lithography and electron/ion microscopes. In the systems in which focusing of the beam is desired, it is important to consider the optical aberrations of the focusing column, such as spherical and chromatic aberrations, which significantly affect the resolution of the system. In order to achieve the optimum design for the charged particle options (CPO) system, artificial intelligence (AI)-based optimisation methods such as particle swarm optimisation (PSO) can be used. However, these methods usually require hundreds to thousands of simulations depending on the number of design variables.
In this study, the DA method is used to calculate the optical performance of an electrostatic Einzel lens consisting of three electrodes. The optimum efficiency is achieved by finding the optimal gap between the electrodes, the inner diameter of the electrodes, and the optimal operating voltage.
A code is developed for running automated simulations of the lenses with different geometries. The direction of geometric alterations to find the optimal design for the spot size, considering spherical and chromatic aberrations, is accomplished by utilising PSO and GA techniques.

P-S11-33-T1 Nonlinear parameter-evolution approach for achieving high aspect ratio in nanoscale etching.

Mr. Arjun Moothedath Sethumadhavan [1], ***Mr. Zhong Ren*** [1]

1. *Oxford Instruments*

Silicon-based periodic nanoscale structures can confine light in compact space, allowing for a high density of integrated optical components through band gap (effective refractive index) engineering. The critical dimension and profile of these high aspect ratio structures are essential to optical performance. This paper reports a nonlinear parameter evaluation with an exponential function for the nanoscale etching. The time-multiplexed process included deposition, polymer breakthrough and etching steps, utilizing C_4F_8-SF_6 chemistry. The key process parameters were systematically studied by experiments on a deep reactive ion etching tool. The optimized process provided a vertical profile with minimal undercut and bowing, and a high selectivity to an e-beam resist mask. As a result, the periodical nanostructures with an aspect ratio of up to 24:1 were fabricated on the wafer scale. The variation in trench width from top to bottom was approximately 3 nm. This technique allows for the realization of even higher aspect ratios by employing a thicker mask.

P-S11-34-T1 Fabrication of micro-patterned β-Ga2O3 thin films by selective solid-phase crystallization via room-temperature excimer laser annealing

Dr. Daishi Shiojiri [1], Dr. Satoru Kaneko [2], Mr. Ryoya Kai [3], Dr. Akifumi Matsuda [4], Prof. Mamoru Yoshimoto [3]

1. *Kanagawa Institute of Industrial Science and Technology,* ***2.*** *KISTEC,* ***3.*** *Department of Materials Science and Engineering, Tokyo Institute of Technology,* ***4.*** *Tokyo Institute of Technology*

We investigated the room-temperature (RT) fabrication of β-Ga_2O_3 crystalline thin films using the excimer laser annealing (ELA) process and its micro-patterning method. Amorphous Ga_2O_3 thin films were grown on sapphire substrates at RT by the pulsed laser deposition method. Amorphous precursor Ga_2O_3 films were irradiated by a non-focused KrF excimer laser at RT. The effect of the ELA conditions on the crystallinity and surface morphology of Ga_2O_3 thin films was investigated. The results of x-ray diffraction measurements indicated that highly uniaxially-oriented crystalline β-Ga_2O_3 thin films were obtained after RT ELA. As for the RT micro-patterning of β-Ga_2O_3 thin films, the grown amorphous Ga_2O_3 thin films were subsequently laser-annealed by irradiating the KrF excimer laser onto the film surface in air at RT through a mask, and then, wet-etching was carried out with H_3PO_4 solution and ultrasonic vibration to remove non-crystallized area. Formation of the micro-wall is thought to be caused by the selective etching of the amorphous phase. These micro-patterns on the sapphire substrates are expected to be applied to the fields of optoelectronic devices.

P-S11-35-T1 Enhancing Electroplating Uniformity for 30 nm Resolution Charts through Graphic Auxiliary Approach

Mr. Qiucheng Chen [1], Mr. Xujie Tong [1], Mr. Chengyang Mu [1], Ms. Qingxin Wu [1], Mr. Jun Zhao [1], Prof. Yifang Chen [1]

1. *Fudan university*

X-ray microscopy, like STXM and TXM, offers superior resolution and multi-scale imaging capabilities compared to traditional methods. The Fresnel zone plate is crucial for X-ray focusing and influences imaging quality. The resolution chart serves as a diagnostic tool for testing zone plate resolution. In this study, a novel approach is presented for fabricating a 30 nm resolution chart using electron beam lithography and electroplating. Monte Carlo simulations were employed to design an auxiliary ring, compensating for low current density during electroplating. The charts with the auxiliary ring exhibited more uniform electroplating thickness. These advancements have the potential to improve high-resolution X-ray imaging for future applications. This research contributes to the field of high-efficiency X-ray microscopy.

P-S11-36-T1 Nanofabrication of randomly distributed hole array for coherent diffraction imaging in soft X-ray

Mr. Xujie Tong [1], ***Mr. Chengyang Mu*** [1], ***Dr. Yijie Li*** [1], ***Prof. Yifang Chen*** [1]

1. *Fudan university*

Computational ghost imaging (CGI) method can perform intensity-only imaging with single pixel. However, a series of X-ray ghost imaging optics with large area (>1mm*1mm) and high quality are technically challenging, especially for those with small (<200nm) and dense feature. In this work, we propose a novel routine of random binary mask and gratings for X-ray ghost imaging. Corner proximity effect correction for each unit of the random binary mask was performed to ensure the pattern has square corners. The random binary mask (1.1mm*1.1mm) with square holes (200nm*200nm) and grating mask (1.5mm*1.5mm) with 460 small gratings (20μm*20μm) were obtained. With the feasibility of fabricating X-ray ghost imaging optics, cheap and low radiation dose X-ray ghost imaging technology will be expected to expand to X-ray tomography ghost imaging, X-ray diffraction microscopy ghost imaging, dark field ghost imaging, and isotope-labeled multipara metric ghost imaging.

P-S11-37-T1 Nanofabrication of 10 nm resolution compound Kinoform zone plate with high efficiency in soft X-ray

Mr. Xujie Tong [1], ***Mr. Chengyang Mu*** [1], ***Dr. Qiucheng Chen*** [1], ***Prof. Yifang Chen*** [1]

1. *Fudan university*

X-ray microscopy and spectroscopy with sub-10 nm resolution enable unique insights into integrated circuit, condensed matter and biological specimens. However, High-resolution X-ray lenses (<20nm) with non-ideal zone plate structure and metal material limit their diffractive focusing efficiency within 1-3%, especially in soft X-ray. Zone plates with parabolic shape, known as Kinoform lens, can achieve high focusing efficiency due to the continuous modulation of X-ray phase. Inspired by this, this work focuses on improving the focusing efficiency of 10 nm resolution X-ray microscopy by combing a 3-dimentional trapezoidal Kinoform lens with zone-doubling zone plate lens. The compound Kinoform zone plate lens with high efficiency and 10-nm resolution has been developed using greyscale electron beam lithography and atomic layer deposition. Systematic study of the effect of developing temperature and exposure dose were conducted. The developed lens possesses broad prospect of applications in high-resolution X-ray microscopy with high efficiency. The proposed high-resolution greyscale electron beam lithography method can also be applied to optical components in the visible band, such as metasurfaces, waveguides, etc.

P-S11-38-T1 UV-Nanoimprinting of Ceramics

Ms. Sonja Kopp [1], ***Dr. Abhijeet Lale*** [2], ***Ms. Viktorija Jonaityte*** [1], ***Dr. Michael Haslinger*** [1], ***Dr. Martin Schwentenwein*** [2], ***Prof. Francesco Moscato*** [3], ***Dr. Michael Muehlberger*** [1]

1. *PROFACTOR GmbH,* ***2.*** *Lithoz GmbH,* ***3.*** *Medical University of Vienna*

Ceramic 3D printing or Lithography-based Ceramic Manufacturing (LCM) is able to produce a wide range of ceramic parts for various applications ranging from medical to aerospace. Although the surface quality meets or exceeds the requirement for most applications and surface roughness R_a of 0,4µm can be achieved in the final part, in certain special cases it can be interesting to add well defined microstructures on the surface. We suggest that one way to achieve this is to use UV-nanoimprint lithography. On the one hand the LCM process is also based on UV-curing materials and on the other hand nanoimprinting is capable of also patterning non-flat surfaces. We will present the status of our nanoimprint process and address critical issues like adhesion and grain size growth during sintering.

P-S11-39-T1 Advanced electron-beam grayscale lithography by using optimized dose gradients in the pattern design

Dr. Kevin Hofhuis [1], ***Dr. Nazanin Samadi*** [1], ***Dr. Christian David*** [1], ***Dr. Analía Fernández Herrero*** [2], ***Mr. Bas Ketelaars*** [3], ***Dr. Christiaan Zonnevylle*** [3], ***Dr. Vitaliy A. Guzenko*** [1]

1. *Paul Scherrer Institute,* ***2.*** *Helmholtz-Zentrum Berlin für Materialien und Energie,* ***3.*** *Raith B.V.*

The implementation of newly developed dose gradient writing techniques in the Raith EBPG Plus system is discussed, enabling precise control over the dose in specific shapes and facilitating the creation of complex 3D structures. The authors present the initial outcomes of using these techniques, which demonstrate faster writing times and enhanced flexibility in generating customized grayscale patterns.

P-S11-40-T1 Fabrication and Characterization of High-Transmittance, Low-Resistance Transparent Devices based on AgNW using Nanoimprint Lithography

Mrs. YEONJOO HA [1], Dr. JaeJong Lee [1], Mr. Jee-Hoon Seo [1]

1. *Korea*

In this study, we investigated the effects of forming nanostructures on the surface of a substrate coated with AgNW and studied methods to create a low-resistance surface while maintaining high transparency. The resin used in the experiment was a mixture of AgNW and PMMA. The mixed resin was coated onto a glass wafer, and nanoimprinting experiments were conducted by applying varying levels of pressure using a nanopattern stamp. The changes in AgNW junctions were examined using scanning electron microscopy (SEM), and resistance measurements were taken at five points on the glass surface to observe resistance variations. Additionally, when AgNW was coated and the transparency was measured, no difference in transparency was observed. Furthermore, contact angle measurements were performed to assess the anti-reflection effect. When the contact angle of the glass wafer coated only with AgNW and the contact angle of the PMMA/AgNW mixed resin-coated wafer used in the experiment after nanoimprinting were compared, it was confirmed that the surface became more hydrophobic. Through this study, we were able to confirm the role of nanostructures in reducing AgNW resistance while maintaining transparency. Moreover, by creating a hydrophobic surface, we believe that this research can lead to further applications of functional glass.

P-S11-41-T1 Atomic Layer Etching of Silicon Nitride with Plasma Oxidation and HF/NH3 Selective Gas Phase Etching

Mr. Sangwoo Kim [1], ***Mr. Ohchel Kwon*** [2], ***Mr. Hyeongkwon Jeong*** [2], ***Mr. Suhwan Park*** [2], ***Mr. Gwanwoo Min*** [2], ***Ms. Hyunseo Shim*** [2], ***Prof. Heeyeop Chae*** [3]

1. *Department of Semiconductor and Display Engineering, Sungkyunkwan University,* ***2.*** *Samsung Electronics,* ***3.*** *School of Chemical Engineering, Sungkyunkwan University*

In this work, a new type of silicon nitride atomic layer etching (ALE) method was developed using plasma oxidation and HF/NH_3 selective gas phase etching (GPE) process. The silicon nitride surface was oxidized with O radical in O_2 plasma, and oxidized surface was selectively etched by HF/NH_3 GPE process. The O_2 plasma generated oxidation layer and the oxidation depth was about 8Å thickness at 240 seconds which showed self-limiting characteristic. The etch amount of silicon nitride and silicon oxide was investigated with dependence of HF and NH_3 GPE time. The main etchant gas containing HF and NH_3 is quickly reacted with silicon oxide, but the silicon nitride needs more time to start the reaction. At 2 seconds GPE process, the silicon nitride was hardly etched about 0.083Å but silicon oxide etch amount was about 19.7Å. The silicon nitride was almost not etched in short time GPE process, so oxidation layer could be etched selectively with this process. The cycle process of 2 seconds GPE was developed to confirm whether the oxidation layer was selectively or completely removed. Finally, constant etch rate per cycle (EPC) was observed in this cyclic process with plasma oxidation and HF/NH_3 selective GPE process.

P-S11-42-T1 Simulation study of three-dimensional grayscale ice lithography on amorphous solid water for blazed gratings

Mr. Jinyu Guo [1], Mr. Shuoqiu Tian [1], Mr. Rui Zheng [2], Ms. Shan Wu [2], Dr. Ding Zhao [2], Prof. Yifang Chen [1], Prof. Min Qiu [2], Mr. Wentao Yuan [1]

1. *Fudan university,* ***2.*** *Westlake University*

Based on former ice lithography research on amorphous solid water (ASW), the advantages of ice lithography (IL) methods in preparing delicate nanostructures have been confirmed tentatively. In order to amplify the advantages of ice lithography to the fullest, this paper reports for the first time our progress in fabricating three-dimensional linear blazed grating template structures by means of grayscale electron beam lithography (EBL) simulation on ASW, aiming to surmount the bottleneck of current fabrication technology and enable excellent fabrication of blazed grating templates with high diffraction efficiency at specific wavelength.

The fabrication method of blazed grating template structures is systematically investigated by means of contrast curves of ASW with the assistance of Monte Carlo simulation. By designing a reliable template combined with optimized dose distribution, the defects of significant proximity effect and uncontrollable exposure dose of conventional grayscale EBL performed on PMMA were basically avoided. The resulting profile of blazed wavelength around 1550 nm with less flaws was obtained. By characterizing the first-order diffraction efficiency, the dramatic advantage of utilizing ASW to fabricate different linear blazed gratings is further demonstrated.

P-S11-43-T1 Metallization of UHMW-PE Fibers by Supercritical CO2 Catalyzation toward Weavable Devices

Mr. Hikaru Kondo [1], Dr. Tomoyuki Kurioka [1], Dr. Wan-Ting Chiu [1], Dr. Chun-Yi Chen [1], Prof. Mark Chang [1], Ms. Machiko Yagaguchi [2], Ms. Arisa Jinno [2], Prof. Hiromichi Kurosu [2], Prof. Masato Sone [1]

1. *Tokyo Institute of Technology,* ***2.*** *Nara Women's University*

Weavable devices are multifunctional fabric-based devices prepared by weaving various functional fibers into a single piece of fabric. Functional fibers possessing decent electrical conductivity are essential for weavable devices, and this can be realized by metallization of polymer fibers. On the other hand, the adhesion between the metallized material and the polymer is reported to be significantly improve by a supercritical CO_2 ($scCO_2$) catalyzation process. In this study, ultra-high-molecular-weight polyethylene (UHMW-PE) fibers are selected because of the outstanding mechanical strengths, low density, chemical resistance, abrasion resistance, and impact resistance. Functionalization of UHMW-PE fibers by adding conductivity could be useful for medical and military applications. Ni-P is the coating to be metalized on the UHMW-PE for the decent electrical conductivity, excellent corrosion resistance and high mechanical strength. In addition, deposition of a Ni-P layer demonstrates the versatility as the sacrificial material in decoration of other nobler metallic materials and decoration of other functional materials by electroplating. By the $scCO_2$ catalyzation, presence of Pd catalyst inside the UHMW-PE structure was confirmed. The electrical resistance gradually decreased following an increase int eh Ni-P deposition time, and it reached 0.98 Ω after 60 min of the Ni-P deposition time.

P-S11-44-T1 PbS quantum dot thin film dry etching

Mr. Nicolas Le Brun [1], ***Dr. Gilles Cunge*** [2], ***Mr. Pascal Gouraud*** [3], ***Mrs. Camille Petit-Etienne*** [4], ***Mrs. Linda Parmigiani*** [3], ***Dr. Stéphane Allegret-Maret*** [3], ***Dr. Jonathan Steckel*** [3]

1. *PhD STUDENT,* ***2.*** *Univ. Grenoble Alpes, LTM, F-38054 Grenoble-France,* ***3.*** *STMicroelectronics,* ***4.*** *CNRS*

Detecting light towards the near Infrared (NIR) and Short-wave Infrared (SWIR) regions is a recent challenge for many manufacturers. Silicon having weak absorption properties at these wavelengths, new materials are investigated to build efficient image sensors for these specific regions of the light spectrum. Among them, PbS quantum dot thin films are particularly promising materials due to their tunable band gap, absorption properties and large-scale production availableness. However, patterning the active parts of photodiodes by plasma etching of this new material is challenging: the etching chemistry should be chosen to volatilize Pb and S without modifying the active part of the PbS photodiode and the etching profile should be anisotropic. We thus explore several plasma chemistries (H_2, Cl_2, HBr, N_2) to etch PbS films in high density plasmas. The etching mechanisms and etching profiles are investigated by XPS and TEM/EDX measurements, respectively. We show that halogen-based plasmas deteriorate the material by Cl and Br diffusion deep in the PbS film underneath the mask. By contrast, pure H_2 plasmas are efficient to etch PbS but lead to a high roughness. We then investigate H_2 based gas mixtures, which allow to produce interesting etching properties.

P-S11-45-T1 Preparation of gold nanoparticle-hydrogel composite by room temperature electron reduction for catalytic applications

Prof. Changjun Liu [1]

1. *Tianjin University*

An increasing research interest can be found on the preparation and application of metal-hydrogel composites. Herein, a room temperature electron reduction has been developed for the preparation of gold nanoparticle-hydrogel composite using argon glow discharge plasma as the cheap electron source. Compared with the thermal or chemical reduction methods, the room temperature electron reduction is simple, easy to manipulate, and compatible with the commonly used impregnation processes. It does not need the expensive or hazardous reducing agents. It can be easily turned on and off. The obtained composite exhibits an apparent blue appearance when it is viewed in transmission light. However, a uniform and highly reflective golden metallic appearance when it is viewed in reflected light. The scanning electron microscopical (SEM) analyses demonstrates that the gold nanoparticles are closely packed on the surface of hydrogel. The Au nanoparticle-hydrogel composite by room-temperature electron reduction shows a high activity for the reduction of methylene blue (MB) in the presence of $NaBH_4$. The plasmon characteristic of the composite suggests that it may have good activity for the photocatalytic conversion. It may have applications in the photo-electronic devices as well.

P-S11-46-T1 Parallel Printing of Nanoliter Droplets with PDMS Nozzles Under Fluorinated Liquid

Mr. Muhammad Awais Maqbool [1], ***Prof. Takayuki Shibata*** [1], ***Dr. Okamoto Shunya*** [1], ***Prof. Moeto Nagai*** [1]

1. *Toyohashi University of Technology*

In the three decades since its inception, microfluidics has advanced significantly. Droplet microfluidics has a wide range of applications in biology, medicine, chemistry, physics, and Material science. It allows for high throughput treatment with a few microliters of sample with/without a small number of cells. It has attracted interest in large-scale drug research. Fluorinated liquid (FC-40) prevents the evaporation of droplets, and the printing of aqueous emulsion droplets has increased in popularity. Recently, nL droplets have been printed with a single probe. However, their limitation is printing one droplet at once. The number of droplets can be increased by the parallelization of nozzles and the speed-up of a robot. We used an SLA 3D printer and made four parallel nozzles and demonstrated the printing of nL droplets with a cartesian robot by contact printing under FC-40 and characterized the parallel printing. Our system printed 4 droplets at once and the sizes are smaller than the previous techniques. It printed 300 droplets in 1 minute with a speed of 30 mm/sec and it can be further increased by increasing the velocity of the robot and flow rate.

P-S11-47-T1 Selective Atomic Layer Etching(ALE) of Germanium to Silicon using control parameter

Mr. Hyo Jun Kim [1], ***Mr. Hee-woong Shin*** [1], ***Dr. Chang Weon Lee*** [1]

1. *PSK*

Atomic Layer Etching(ALE) is promising technology that can remove ultra-thin materials throug.h at least one self-limiting reaction step to achieve lower atomic-scale process variation. Dry etching is preferred for next-generation semiconductor devices similar to anisotropic etching [1,2]. At present, the ALE for isotropic selective etching of Ge to Si has been reported [3]. However, the selective ALE Ge to Si method depends on the recipe and it is difficult to achieve. As is well known, Si-Si bond energy is 3.25eV, Si-Ge – 3.12eV, and Ge-Ge – 2.84eV it is easier to selectively etch Ge than Si. The selective etching characteristics of silicon, germanium subjected to a downstream NF3/NH3/N2 remote plasma. The reactive NF3 gas and pressure should be the most important parameters to drive selectivity and etch amounts. NF3 gas varied from 5 to 20sccm and from 100 to 300mTorr at the pressure. The source power, Chuck Temp, NH3 and N2 were initially held constant. Selectivity greater than 77:1 of Ge over Si was achieved using 5sccm NF3 gas, 100mTorr pressure.
In this study, selective Ge etching in different parameters were investigated. We found that low pressure, NF3 gas selectively etches Ge over Si.

P-S11-48-T1 Grayscale exposure challenges using direct-write laser exposure on thick photosensitive positive resist

Ms. Gerda Ekindorf [1], ***Dr. Christine Schuster*** [2], ***Mr. Dominique Colle*** [1], ***Dr. Peter Heyl*** [1], ***Dr. Anja Voigt*** [2]

1. *Heidelberg Instruments Microtechnik GmbH,* ***2.*** *micro resist technology GmbH*

Grayscale lithography is a manufacturing method to create 2.5 dimensional structures. Here, a photosensitive positive resist is exposed with spatially modulated intensity levels. These different intensity levels, also called gray values, can be exposed with a Direct Write Lithography System – DWL, manufactured by Heidelberg Instruments Microtechnik GmbH. The height of the created structure is limited by the nitrogen (N_2) bubble formation that deforms the structures in ultra-thick layers of commercially available DNQ-based photoresists. The new experimental photoresist mr-P 22G_XP manufactured by micro resist technology GmbH is designed for grayscale applications in very thick films. The test exposures made with a DWL 66^+
show good results by realizing structures over 100 µm in height without nitrogen bubbles. Controlled multiple exposure with low doses is necessary to create deep grayscale patterns in the resist. This can be done using “N-Over” (N times overlapping) DWL exposure mode. The resist-inherent bleaching during exposure allows reaching very deep into this positive resist. The other big challenge in grayscale lithography process is the shape optimization. Higher sensitivity of the thick positive photosensitive resist requires even more stability control of the environment and the lithography process.

P-S11-49-T1 3D-microstructured Interpenetrating networks with tuned thermal and mechanical properties

Dr. Dorothee Silbernagl [1], ***Dr. Paulina Szymoniak*** [1], ***Ms. Zeynab Tavasolyzadeh*** [1], ***Prof. Heinz Sturm*** [1], ***Dr. Ievgeniia Topolniak*** [1]

1. *Federal Institute for Material Research and Testing, BAM Berlin*

Multiphoton lithography (MPL) has recently attracted significant research interest as a versatile tool capable of producing 2D and 3D micro- and nanoscopic features with high spatial resolution. The integrity of MPL microstructures, or their ability to respond to external stimuli, is of critical importance. However, achieving the desired properties of fabricated microcomponents for a specific application remains a challenge.
In this work, we present new MPL materials based on epoxy-acrylate interpenetrating networks (IPNs). We aim at 3D microstructures, whose properties can be easily tuned by varying the ratio of the IPN components and fabrication parameters. The resulting library of 3D microstructures was investigated for their thermal and mechanical properties using highly-sensitive space-resolved methods. Flash scanning calorimetry revealed the influence of both, IPN composition and fabrication parameters, on glass transition temperature and material fragility. AFM force-distance curve and intermodulation methods were used to characterize the mechanical properties with a lateral resolution of 1 micron and 4 nm, respectively. The deformation, stiffness and elastic behaviour are discussed in detail in relation to the morphology. Moreover, we found that some 3D IPN microstructures exhibit fully elastic behaviour. Our funding encourages the further development of IPN systems as versatile and easily tuneable MPL materials.

P-S11-50-T1 Ni-P Electroless Plating of PET Parts with Complex 3D Structure by Supercritical CO2 Assisted Catalyzation

Ms. Ami Iwasaki [1], ***Mr. Po-Wei Cheng*** [1], ***Dr. Tomoyuki Kurioka*** [1], ***Dr. Chun-Yi Chen*** [1], ***Prof. Mark Chang*** [1], ***Prof. Kei Takase*** [2], ***Prof. Hiroshi Ishihata*** [2], ***Prof. Masato Sone*** [1]

1. *Tokyo Institute of Technology,* ***2.*** *Tohoku University*

In recent years, as electronic components have become increasingly miniaturized and complex, one of the methods used to form microstructures is the fusion of photolithography and plating technologies. Typical examples include MEMS technology and transfer methods. These technologies require electrolytic plating of a metal film as a conductive layer on photosensitive resin with complex shapes. Currently, the sputtering method is used for this process, but the sputtering method is very expensive in terms of equipment. Therefore, there is a demand for metal film deposition by wet methods such as electroless plating, which offers superior uniformity of deposition. However, the conventional electroless plating method has problems such as scratches and deformation caused by the pretreatment process and adhesion strength between the polymer material and the metal layer. To solve these problems, a catalytic process using supercritical carbon dioxide (sc-CO_2) as a solvent has been proposed, and in previous studies, electroless Ni-P plating on polyethylene terephthalate (PET) film structures has been realized. However, the application of sc-CO_2 catalyzed electroless plating on polymeric materials with practical 3D structures has not been investigated. In this presentation, we report the results of sc-CO_2 assisted catalytic Ni-P plating on PET samples with complex 3D structures.

P-S11-51-T1 Resolution enhancement techniques on a DUV Stepper for roll-to-roll nanofabrication of plasmonic solar light absorbers

Ms. Maria Serra González [1], ***Mr. Matthias Keil*** [1], ***Ms. Nastasia Okulova*** [2], ***Ms. Rucha A. Deshpande*** [1], ***Prof. Rafael Taboryski*** [1]

1. *Technical University of Denmark,* ***2.*** *Inmold*

We present a series of resolution enhancement techniques that enable the printing of patterns with critical dimensions (CD) that are half the specifications of a DUV stepper tool. These are a combination of off-axis dipole illumination, cross- triple-exposure and assist feature lines in the mask. The full wafer printing with the stepper tool, combined with roll-to-roll (R2R) extrusion, makes this process flow suitable for industrial use.
To demonstrate engineering of a plasmonic heat absorption metasurface , the R2R fabricated foils were metallized by 18 nm of aluminum . We show how the replicated structures present plasmonic resonances in the solar wavelength range, making them suitable for solar absorption applications . A hundred-meter roll containing the fabricated structures can be manufactured in less than 30 minutes, confirming the industrial capacity of this method.

P-S11-52-T1 Vacuum-Assisted filling of high aspect ratio Silicon trenches with Polymers for surface planarization for micromachining of complex microsystems.

Dr. Jose Fernandes [1], ***Mr. Tiago Oliveira*** [1], ***Mr. Helder Fonseca*** [1], ***Mr. Vitor Silva*** [1], ***Mr. Jose Rodrigues*** [1], ***Dr. Andrea Gouvea*** [1], ***Dr. Carlos Alberto Calaza Cabanas*** [1]

1. *International Iberian Nanotechnology Laboratory*

The micromachining of Silicon with Deep Reactive Ion Etching is one of the most crucial techniques used for the microfabrication of MEMS and other complex micro systems. High topographies and deep holes brought several new challenges that can block further processing, packaging and the integration of other devices. In this work a solution for filling cavities with polymers is presented. Such process allows the filling of high aspect ratio cavities with polymers allowing further processing in the same wafer. Complete filling of trenchs with high aspect ratio structures bigger than 30 was achieved. On this work several polymers were tested and compared. After the filling cavities with such polymer, an high selective RIE process is performed to promote further processing on the surface of the wafer without having big cavities. On the end of the process, such polymers are removed by O2 plasma or wet processes to clean and/or release the devices. With such technique, several diferent trenchs/structures with different depths can be fabricated avoiding issues like overetch, notching and depth difference in the same etching step. This technique also allow lift-off processes in a micromachined wafer without the usage of fancy photoresists and polymers.

P-S11-53-T1 Microfabrication of thin film structures by two-photon polymerization for in situ electron microscopy studies

Ms. Chloé Chemin [1], ***Prof. Babak Rezaei*** [1], ***Dr. Alice Bastos Da Silva Fanta*** [1], ***Dr. Ada-Ioana Bunea*** [1], ***Prof. Stephan Sylvest Keller*** [1], ***Prof. Thomas Willum Hansen*** [1]

1. *Technical University of Denmark*

Due to its excellent physical, chemical and electrochemical characteristics, pyrolytic carbon has emerged as a promising material for various technological applications. Graphitized carbon is obtained by pyrolysis of a polymer thin film. To fabricate pyrolytic carbon with the most promising properties, systematic and in depth understanding studies of the graphitization process are currently lacking. Transmisssion electron microscopy (TEM) is one of the most suitable tools for investigating the graphitization of polymer thin films during the thermal treatment process at the nano-scale. However, the preparation of polymer thin film samples for TEM remains a challenge.

This work presents the microfabrication of overhanging polymer thin film structures printed on commercial MEMS-based TEM heating chips (DENSsolution Wildfire) by two-photon polymerization (2PP) 3D printing . The fabrication of overhanging polymer structures with different geometries, i.e. fully supported films, films supported on one side, and strings with different widths, was optimized in terms of exposure dose and surface roughness. Thus, we demonstrated the successful 2PP fabrication of overhanging polymer thin films for in situ TEM studies, using a Nanoscribe Photonic Professional GT+ system. Further studies will investigate the conversion of these films into pyrolytic carbon.

P-S11-54-T1 Constant defocus approximation in mask data-preparation for grayscale patterning of microlens

Ms. Marie-Line Pourteau [1], ***Mr. Aurélien Fay*** [1], ***Mr. Sébastien Bérard-Bergery*** [2], ***Mr. Florian Tomaso*** [1], ***Mr. Rémi Coquand*** [1], ***Mr. Ujwol Palanchoke*** [1], ***Ms. Charlotte Beylier*** [2], ***Mr. Guillaume Claveau*** [2], ***Mr. Samir Guerroudj*** [2]

1. *Univ. Grenoble Alpes, CEA, Leti, F-38000 Grenoble, France,* ***2.*** *STMicroelectronics, 850 rue Jean Monnet, 38926 Crolles Cedex, France*

Grayscale lithography is a powerful technique to pattern complex 3D microstructures with various heights and slopes, in a resist material in a single-step process, with applications as varied as microfluidic, micro-optics, or MEMS components. The low contrast resist material is exposed to a spatially modulated exposure dose, thanks to a glass photomask with sub-resolutions chromium dots. Adjusting the dots size and location, one can control the final pattern shape in the resist.

During their long-term partnership on grayscale microlens, CEA-Leti and ST Microelectronics designed a grayscale I-line photomask with 2.6 µm pitch microlens patterns. An initial simplified lithographic model, based on the assumption that the incident aerial image is not progressively defocused by optical index changes, appeared to fail predicting resist bridge between the lenses base.

In the current work, we present an improved lithographic model that includes a simple constant defocus approximation and is able to reliably predict the resist bridging observed on microlenses processed with the first mask. Microlenses patterned with a new mask, designed according to the new model, have no more bridging. We thus experimentally show that one can avoid a complex exact simulation of the aerial image focusing within the resist.

P-S11-55-T1 Tailoring vertical sidewalls and draft angles for demolding in the same mold by direct write lithography in thick epoxy resist

Dr. Muhammad Refatul Haq [1], ***Dr. Helmut Schift*** [1]

1. *Paul Scherrer Institute*

Sidewall verticality in lithography is essential for high aspect ratio (HAR) microstructures, but often even more important when functional properties in a device, e.g., a microfluidic chip, have to be achieved. Now, vertical sidewalls are often detrimental, e.g., if the devices have to be produced with molding techniques. Therefore complicated geometries have always favored a defined so-called “draft angle” in the range of a few degrees. Unfortunately, current process technologies do not allow for precise tailoring of sidewall inclination and shape within a narrow range, presenting a challenge for device fabrication. We have found that DWL 66^{+} from Heidelberg Instruments Mikrotechnik GmbH can produce different sidewall angles depending on the write mode (WM) used. For systematic analysis, we exposed mr-DWL 40 from micro resist technology GmbH. We therefore employed a hybrid mode, i.e., by manually changing the objective lens and realigning by optical pattern recognition. After exposure, the resist is developed. We have found that for WM I sidewalls with positive slope (78°) and WM III for nearly vertical sidewalls (88°) can be achieved in 60 µm thick resist.

P-S11-56-T1 Room temperature imprint of water-based microparticle inks towards glass microfluidic devices

Dr. Muhammad Refatul Haq [1], ***Dr. Babak Mazinani*** [2], ***Prof. Vivek Subramanian*** [2], ***Dr. Helmut Schift*** [1]

1. *Paul Scherrer Institute,* ***2.*** *Ecole Polytechnique Federale de Lausanne (EPFL)*

Microfluidic devices in polymers have become widely used for diagnostic purposes, and process chains have been established to mold them by casting, hot embossing and injection molding. However, for many applications, glass devices would be favored, because of their higher chemical stability, their compatibility with other microfabrication processes that would allow for integration of different functionalities and the possibility to develop devices that could be easily reused. Recently, novel low-temperature glasses based on phosphate glass that are suitable for 3D printing have been developed and used via extrusion printing to realize fully-integrated functional microfluidic systems. Since the material is water-based, its solidification is purely based on the evaporation of the water during extrusion through a nozzle onto a hot bed. We have used this material for room temperature imprinting using PDMS molds.In both processes, a heating process was employed that first removes the binder from the green body, and then facilitates sintering together at higher temperature. For simple microfluidic devices with 100-200 µm wide channels, the shape is fully retained during demolding and annealing. The shrinkage is almost isotropic.

P-S11-57-FT Penning vacuum gauge with high-efficiency plasma source for a miniature ultra-high vacuum cell

Dr. Yuichi Kurashima [1], ***Dr. Taisei Motomura*** [1], ***Dr. Takashi Matsumae*** [1], ***Mr. Atsuhiko Maeda*** [1], ***Dr. Shinya Yanagimachi*** [1], ***Dr. Hideki TAKAGI*** [1], ***Mr. Naoto Oshima*** [2], ***Dr. Mitsuhiro Watanabe*** [2]

1. *National Institute of Advanced Industrial Science and Technology (AIST),* ***2.*** *Nihon University*

In recent years, miniaturization of quantum devices using cold atom is growing demand. An ultra-high vacuum environment is required for generating cold atom. Therefore, it become key issue to measure the inside pressure of a vacuum cell by a miniature ultra-high vacuum gauge. Penning vacuum gauge using Penning discharge can be powerful candidate of miniature ultra-high vacuum gauges because it possible to be miniaturized by the MEMS process. However, a distance between the electrodes becomes extremely narrow, resulting in extremely short electron flight distances, and collisions will hardly occur between electrons and residual gas molecules. As a result, the vacuum gauge with narrow electrodes is leading to deterioration of a discharge efficiency. Therefore, we have been proposed a miniature efficiency plasma source by a magnetic mirror trap with two opposing permanent magnets. In this study, we attempted to integrate a Penning vacuum gauge and a miniature vacuum cell for realization of the quantum device by cold atom, and evaluated the pressure dependence of the discharge current of the integrated vacuum gauge. As a result, the Penning vacuum gauge has been successfully integrated into a miniature vacuum cell, which can measure ultra-high vacuum.

P-S11-58-T1 The Effect of Damaged Layer Removal Process on Si Atomic Layer Etching

Mr. Namgun Kim [1], ***Mr. Whan Kyun Kim*** [1], ***Mr. Dongjun Shin*** [2], ***Dr. Jongkyu Kim*** [2], ***Mr. Kukhan Yoon*** [2], ***Mr. Youngju Ko*** [1], ***Prof. Heeyeop Chae*** [3]

1. *Department of Semiconductor and Display Engineering, Sungkyunkwan University,* ***2.*** *Samsung Electronics,* ***3.*** *School of Chemical Engineering, Sungkyunkwan University*

In this study, the effect of fluorocarbon plasma pretreatments was investigated for Si quasi-atomic layer etching (ALE) using a 300mm inductively coupled plasma (ICP) reactor. The Si surfaces were pretreated with CF_4 or CHF_3 fluorocarbon plasma, followed by ALE cycle processes involving Cl_2 plasma chlorination and Ar ion etching. The variation in ALE cycles and removal depth for RIE-damaged Si layers was changed by plasma pretreatment conditions. Significant fluorocarbon layers were observed on the Si substrate after fluorocarbon pretreatment. The CHF_3 plasma pretreatment showed a higher atomic percentage of fluorocarbon at 79.0% compared to the CF_4 plasma pretreatment at 59.1%. The etch per cycle (EPC) value of Si in the ALE window was measured at 5.5 Å/cycle with plasma pretreatment of CHF_3 and 6.2 Å/cycle with that of CF_4. The fluorocarbon layers generated by plasma pretreatments had a significant influence on the initial cycle of Si ALE, with plasma pretreatment of CHF_3 affecting up to 30 cycles and that of CF_4 affecting up to 20 cycles. This work highlights the importance of optimizing surface pretreatments for damaged layer removal in semiconductor manufacturing and provides insights into the impact of pretreatment process conditions on ALE performance.

P-S11-59-T1 Perspective of Unconventional Holographic Lithography and Ion Bombardment

Dr. Ying Liu [1]

1. *University of Science and Technology of China*

In the fabrication of diffraction gratings, holographic lithography (HL) and ion beam etching (IBE) are utilized in a conventional mode, where HL is used to form the photoresist (PR) grating as mask, and IBE is introduced to transfer the PR pattern into the grating substrate. In other words, no grating mask is used in HL, while a PR mask is necessary during IBE.

In this contribution I will review our recent progress of HL and IBE in an unconventional fashion, i.e., HL with an electron beam lithography (EBL)-written phase mask (PM) and IBE, also known as ion bombardment (IB), a maskless nanofabrication tool for self-organized nanostructures, respectively.

First, I will strengthen the synergy effect of HL and EBL, which is promising and suitable for the production of microstructures in patch. Second, IB is a bottom-up approach that generates self-organized nanostructures on surfaces with a period of ~100 nm. The degree of ordering of self-organized nanostructures is a key issue to be overcome. Our results of the enhancement of ordering of the nanoripples by bombarding bilayer systems indicate that not a periodic template but self-organized nanoripples on the top layer can guide the growth of the nanoripples on the underlying layer.

P-S11-60-T1 Nano-scale Zirconia Ceramics printed via Two-Photon-Polyemerization from a transparent nano-particle containing Feedstock

Dr. Johanna Sänger [1], ***Dr. Birte Riechers*** [2], ***Prof. Raúl Bermejo*** [1], ***Prof. Jens Günster*** [2]

1. *Chair of Structural and Functional Ceramics, Montanuniversität Leoben,* ***2.*** *Federal Institute for Material Research and Testing, BAM Berlin*

Vat-Polymerization promises the highest accuracy of all Additive Manufacturing (AM) technologies. The most detailed structures can be achieved with Two-Photon-Polymerization (2PP). To fabricate advanced technical ceramics such as alumina and zirconia with this technology via a powder processing route, ceramic powders are required. Those ceramic particles turn slurries opaque, which is contradictory to light-based vat polymerization techniques, especially to 2PP, where scattering hinders the photon transmission through the resin completely. In this work, nano-particles from ceramic-suspensions with a mean size of 5nm were selected to reduce the scattering at the particle sites in such way that a transparent heterogeneous resin can be formed. As result, the created mixture is suitable for 2PP with a ceramic particle fraction of up to 80wt%. This enabled the fabrication of yttria stabilized zirconia (YSZ) parts with a resolution of 500nm, the smallest for ceramic-AM reported so far. This ceramic “meta-material” possesses mechanical properties near the theoretical stiffness of zirconia and exhibited room temperature creep behavior. The reported results are based on the quality and stability of ceramic nano-particles suspension. This opens a way for powder processing in photon-based additive manufacturing and creates a way for ceramics and other non-polymer materials in high-resolution micro applications.

P-S11-61-T1 Broad beam ion erosion of silicon with metal-co-deposition: experimental and simulation results

Mr. Felix Linß [1], ***Dr. Carsten Bundesmann*** [1], ***Dr. Frank Frost*** [1]

1. *Leibniz Institute of Surface Engineering e.V. (IOM)*

Ion beam erosion has gained increasingly attention due to the ability to machine ultra precision surfaces. Ion beam erosion of silicon with simultaneous co-deposition of metal species favours the formation of surface patterns. These patterns occur on the nano-and micrometre scale. For industrial processes, precise control of the mechanisms contributing to the surface quality is very important. Therefore, it is necessary to determine the influence of the co-deposition materials mounted inside a vacuum vessel, especially on the surface roughness and the substrate removal rates.

In this study a broad beam ion source was utilized, so that parallel irradiation of the silicon samples and co-deposition material was ensured. It was operated with Argon at a low ion energy of 700 eV. The dependencies of roughness and pattern formation are reviewed and compared with additional simulation data. It could be shown, that silicide-forming metals activate the structuring of silicon. The silicon removal and the surface roughness depend on the co-deposition material. Supporting simulation data urge that the effect of altering the silicon removal is driven by the combination of sputtering and scattering properties of the co-deposition material. This indicates that this effect is self-sufficient and does not rely on the silicide formation.

P-S11-62-T3 Aptamer-Decorated Graphene Channel Array with Liquid-Gating for Sensing Cortisol Stress Hormone

Mr. Ali Gilani [1], ***Dr. Shokoofeh Sheibani*** [1], ***Dr. Johan Frédéric Longo*** [2], ***Dr. Ali Saeidi*** [2], ***Mr. Sadegh Kamaei Bahmaei*** [2], ***Mr. Yann Christophe Sprunger*** [2], ***Mr. Stefan Razvan Anton*** [3], ***Prof. George Sanciu*** [3], ***Prof. Adrian Mihai Ionescu*** [2]

1. *Ecole Polytechnique Federale de Lausanne (EPFL),* ***2.*** *EPFL,* ***3.*** *University POLITEHNICA of Bucharest*

The ability to detect cortisol hormone with high sensitivity and accuracy has significant implications for diagnosing and monitoring stress-related disorders. Also, graphene-based sensors have attracted considerable attention in recent years due to their exceptional electrical and mechanical properties. This study presents for the very first time a novel aptamer decorated graphene channel with liquid-gating, operating as a liquid-gate graphene FET (LGFET) to detect cortisol. The sensor employs two separated arrays of aptamers functionalized LGFET, one for specific binding measurement and the other for nonspecific binding measurement. Experiments carried out in a diluted PBS solution show a sensitivity of 38mV per decade of concentration, which improves near ~55mV, after differential subtraction. The sensor exhibits a linear response over a concentration range of 1nM to 1µM, with a detection limit of 1nM. The high sensitivity and specificity of GFET functionalized with aptamer make it a promising tool for the accurate and rapid detection of cortisol in clinical and research settings. Moreover, the use of proposed graphene as a sensing platform at the wafer scale opens up new opportunities for the industrial development of other 2D sensors for a wide range of applications in personalized healthcare.

P-S11-63-T3 2-Photon Lithography for bio-inspired 3D microstructures for in vitro neuroelectronic devices

Dr. Valeria Criscuolo [1], ***Ms. Claudia Latte Bovio*** [2], ***Prof. Francesca Santoro*** [1]

1. *Faculty of Electrical Engineering and IT, RWTH, Aachen 52074, Germany. Institute of Biological Information Processing—Bioelectronics, IBI-3, Forschungszentrum, Juelich 52428, Germany,* ***2.*** *Tissue Electronics, Istituto Italiano di Tecnologia, 80125 Naples, Italy. Dipartimento di Chimica, Materiali e Produzione Industriale, Università di Napoli Federico II, 80125 Naples, Italy*

Bioelectronic devices are electronic platforms that interact with biological systems, such as cells and tissues, used to monitor cellular electrical activity or modulate cellular behavior by applying an external electrical field. Here, the cell-device interface plays a crucial role for an effective electrical coupling.[1,2] In neuroelectronic applications, aimed at recapitulating neuronal communication and functions, it is imperative to take inspiration from the extremely complex architecture of the brain. Neurons interact with and respond to plenty of mechanical and topographical cues for the development of a functional nervous system[3]. Given this high complexity, recently 2-photon polymerization (2PP) lithography has emerged as the tool of choice for mimicking neurons´ features thanks to its high resolution, versatility, and design freedom[4,5]. Here we propose innovative approaches for the realization of 3D microstructures and scaffolds based on 2PP for neuroelectronic applications. In particular, 2PP enabled the realization of both conductive and non-conductive 3D structures through the choice of the functional material as well as microfabrication techniques. Such structures proved to be effective as smart bio-inspired interfaces. The fabrication of 3D electrodes with different levels of complexity will open the way to the possibility of sensing and/or stimulating cells and tissues in a more realistic environment.

P-S11-64-T3 Controlled wettability of mixed surfaces for enhanced water harvesting

Ms. Joyce Estephan [1], ***Mrs. Cécile Gourgon*** [1], ***Mr. Jean-Hervé Tortai*** [1], ***Mrs. Marie Panabière*** [1], ***Mrs. Camille Petit-Etienne*** [1], ***Mr. Léo Bon*** [1]

1. *CNRS*

Water scarcity is a global issue that scientists are trying to address by new solutions. Inspired by the Namib desert beetle, collecting atmospheric water appeared as a potential answer. In this study, we mimicked the beetle's surface, combining hydrophilic and hydrophobic zones. We prepared till now, four types of mixed surfaces using and combining different technologies such as lithography, plasma roughening and metal deposition. We studied different materials, patterns, roughnesses and morphologies. We then conducted water collection tests on our prepared mixed samples using homogeneous surfaces as references. Our results demonstrated that the mixed samples achieved higher water collection efficiency, particularly those with contact angles between 75° and 80°. To understand the results, departure drop volume was experimentally measured for each surface and compared with the theoretical calculated volume. The study will compare the findings with previous research to identify optimal surface parameters for harvesting fog and dew.

P-S11-65-T3 Leveraging The Elastic Deformability of Polydimethylsiloxane Microfluidic Channels for Efficient Intracellular Delivery

Dr. Hashim Alhmoud [1], ***Mr. Mohammed Alkhaled*** [1], ***Mr. Batuhan E. Kaynak*** [1], ***Prof. Mehmet Selim Hanay*** [1], ***Ms. Enise Kartal*** [1], ***Ms. Yagmur Ceren Alatas*** [1]

1. *Bilkent University*

The design of a modular lab-on-a-chip component with a small footprint for intracellular cargo delivery is presented. Using the mechanical implementation, a temporary constriction is formed within the microfluidic channel of an elastic polydimethylsiloxane (PDMS) microfluidic device. The constriction dimensions are tunable in real time down to a few micrometers. This constriction forces single cells to morphologically deform. This sudden deformation disrupts the cellular membrane, allowing bioactive cargo from the surrounding medium to permeate through the membrane along the concentration gradient. Unlike other transfection technologies that are limited to genetic material transport (lipid conjugates, lipid particles, etc.), this mode of transmembrane diffusion allows for the introduction of various types of bioactive cargo ranging in diversity from DNA/RNA sequences, to inorganic nanoparticles and small molecules. The method also preserves cell viability and function unlike other techniques such as electroporation and sonoporation. This device architecture has implications not only in modular rapid intracellular delivery, but also in the development of mechanical valves, micropumps, and flow redirection apparatus for microfluidics.

P-S11-66-T3 Microwave Sensors Integrated with 3D Microelectrodes to Eliminate Position-Dependent Particle Response in Microfluidics

Ms. Yagmur Ceren Alatas [1], ***Mr. Uzay Tefek*** [1], ***Mr. Burak Sari*** [2], ***Prof. Mehmet Selim Hanay*** [1]

1. *Bilkent University,* ***2.*** *Sabanci University*

Microwave sensors can be used to probe internal dielectric properties of microparticles and cells. Although sensors with coplanar electrode configuration are commonly used in microfluidics due to ease of fabrication, electric field along the height of microfluidic channel changes significantly; causing position-dependent sensitivity. One solution is using 3D electrodes at the walls of microfluidic channel to obtain uniform electric field, yet it is necessary to use high-conductivity electrodes at microwave frequencies. Here, we integrated metalized, 3D microelectrodes on microwave resonator for microparticle sensing. 3D microelectrodes were fabricated using SU8 and positioned at the sensing region of the resonator, in contact with microfluidic channel walls. Microwave resonator was excited at its resonance frequency and its phase and amplitude were tracked using custom built electronic circuitry. Microparticles were transferred to sensing region between SU8 microelectrodes through a PDMS microfluidic channel. Amplitude shift histogram obtained from an experiment with 20μm polystyrene particles demonstrates a sharp, central distribution indicating position-independent operation of the sensor.

P-S11-67-T3 Fabrication and characterization of Nafion/PANI composite membrane-based micropump for Insulin administration

Ms. Shatavisha Biswas [1], ***Mr. Arkaprava Datta*** [1], ***Prof. Tarun Kanti Bhattacharyya*** [1]

1. *Indian Institute of Technology, Kharagpur*

In this study, we report an Insulin Delivery System that consists of a dual-diaphragm IPMC-driven micropump and its electronics control module. Polyaniline impregnated Nafion composite membrane is used as the actuator of the micropump. This micropump employs two Nafion/PANI composite membranes on either side of the micropump chamber and nozzle/diffuser elements to control the fluid flow. The micropump structure is biocompatible and fabricated using UV lithographic process. The flow characterization of the device indicates that this IPMC-based device has a wide operating range (6.5 - 298 μL/min) and is tunable by altering the frequency and voltage.

P-S11-68-T3 A wearable microfluidic device with a built-in micropump for reliable sweat collection for health monitoring

Mr. Zhuodan Chen [1], ***Dr. Weihao Li*** [1], ***Prof. Xing Cheng*** [1]

1. *Southern University of Science and Technology*

Epidermal-fluidic devices have received increasing interest from researchers due to their great potential in health monitoring applications. These devices enable non-invasive biofluids collection and analysis of biomarkers such as sweat, which can provide information about changes in glucose, lactate, NaCl concentration, and the presence of some disease-related biochemical factors. Previous studies have demonstrated a sweat collector with a capillary burst valve (CBV) for a continuous, time-sequential sampling of excreted sweat. However, these designs have several limitations, for instance, natural pressure from the sweat gland cannot provide a stable long-term driving force, hindering continuous monitoring over extended periods. Further developments are needed for longer-duration, higher-volume sweat collection, and more specific sweat composition testing in health monitoring. In this study, we propose a novel microfluidic system comprising a programmable micropump and a multi-branched network. The network has multiple collection trees separated with gradient threshold pressure based on CBVs demonstrated, and a built-in micropump is designed to provide controllable driven force to meet demands in different scenarios. The sweat collector with a built-in micropump is expected to function reliably for sweat collection over an extended time period.

P-S11-69-T3 A planar integrated astable microfluidic circuit for square pressure waveform generation

Dr. Weihao Li [1], ***Mr. Zhuodan Chen*** [1], ***Prof. Xing Cheng*** [1]

1. *Southern University of Science and Technology*

The field of microfluidic networks, originating from microelectronics, still holds significant potential to be explored as inspired by the tremendous capabilities achieved by integrated electronic circuits. Previous research typically relied on pneumatic valves or multi-layer fabrication, leading to a dependence on bulky external controllers or the soft lithography paradigm, which both require lengthy fabrication periods and high costs. A promising solution to these issues is to use non-linear effects in microfluidics, allowing for functional responses due to passive features in the design. Moreover, the inclusion of a micropump in the system could foster greater integration and portability. In this study, we present a planar microfluidic circuit network fabricated by maskless lithography, incorporating designs such as resistors, capacitors, diodes, and transistors, all of which can ultimately be combined with a micropump module. In addition, the planar functional components demonstrate properties comparable to their electrical analogies in the network. An astable microfluidic multivibrator is demonstrated using the proposed designs to generate a square pressure wave. The technique presented in this work may present a facile route towards complex fluid pressure profile generation using microfabricated fluidic circuits analogous to well-studied electronic counterparts.

P-S11-70-T3 Fabrication of switchable biocompatible, nano-fluidic devices using a thermoresponsive polymer on nano-patterned surfaces

Mr. Christopher Bickmann [1], ***Dr. Christoph Robert Meinecke*** [1], ***Dr. Christian Helke*** [1], ***Ms. Susanne Hartmann*** [1], ***Dr. Till Korten*** [2], ***Prof. Stefan Diez*** [3], ***Dr. Danny Reuter*** [1]

1. *Technische Universität Chemnitz, Center for Microtechnologies, Reichenhainer Str. 70, 09126 Chemnitz, Germany,* ***2.*** *Physics of Life, Technische Universität Dresden, Dresden 01069, Germany,* ***3.*** *Technische Universität Dresden, B CUBE - Center for Molekular Bioengeneering*

Nanostructured surfaces are of great importance for various applications such as microfluidic and microanalytical devices, biosensors, or network-based biocomputation. Therefore, it is interesting to develop methods that enable the creation of structured surfaces with switchable and rewritable patterns. One approach is the selective deposition of stimuli-responsive materials, such as self-assembling monolayers (SAMs) or polymer brushes. In this study, we present a method for depositing and patterning the thermosensitive polymer poly(N-isopropylacrylamide) (PNIPAM) on nanostructured surfaces. These polymer brushes act as flow regulators in nanoscale microfluidic channels, allowing control over material transport. Two nanolithographic approaches were pursued to graft PNIPAM in the nano-dimensional channels. The first approach involved patterning the SAM using photoresist and lift-off processes, followed by selective deposition of the polymerization initiator. The second approach included depositing PNIPAM on the entire surface and then performing lithographic patterning through plasma etching. Both approaches were compared for their suitability in in situ patterning and functionalization inside nano-fluidic channels. The study successfully demonstrated the adaption of process steps for grafting PNIPAM onto nano-patterned glass surfaces and achieved reliable structuring of structures at the nanoscale. AFM and XPS analysis confirmed patterned growth of both the SAM and PNIPAM structures.

P-S11-71-T3 3D Integration of a micro-perforated membrane for combined in-situ electrical analysis and real time imaging of living cells.

Mr. Matthieu Sagot [1], ***Dr. Bastien Venzac*** [1], ***Mr. David Bourrier*** [1], ***Dr. Aurélie Lecestre*** [1], ***Mr. Adrian Laborde*** [1], ***Dr. Aline Cerf*** [2], ***Prof. Hervé Aubert*** [1], ***Prof. Christophe Vieu*** [1]

1. *LAAS-CNRS,* ***2.*** *SmartCatch*

In the context of liquid biopsy, the current main challenge is the extraction of the biological information through the capture of tumoral biomarkers from complex body fluids. These biomarkers, and more specifically Circulating Tumor Cells (CTCs), are usually present at very low concentrations compared to billions of peripheral blood cells. We aim to address this issue though the conception and fabrication of an integrated CTC capture, detection, and analysis device. In the last MNE edition, we presented the fabrication of a microperforated membrane device for cell capture with a label-free detection method using impedance spectroscopy. Now, we present a new clean room fabrication process for the device coupling cell capture with electrical detection and *in-situ* analysis, together with the development of a 3D printed integration chip (ICHIP) for live optical imaging. Altogether, the combination of these technological developments allows for live electrical and optical characterization of collected cells on a microperforated membrane.

P-S11-72-T3 Picking microorganisms by impedance flow Cytometry

Mrs. Mohadeseh Mozafari [1], ***Mr. Peer Erfle*** [1], ***Mr. Jonathan Block*** [2], ***Dr. Rainer Krull*** [2], ***Prof. Andreas Dietzel*** [3]

1. *Technische Universität Braunschweig, Institut für Mikrotechnik, Alte Salzdahlumer Str. 203, 38124 Braunschweig, Germany,* ***2.*** *BRICS Braunschweig Integrated Centre of Systems Biology,* ***3.*** *Institute of Microtechnology, Braunschweig, 38124, Germany*

Recent studies have highlighted the crucial role of electrogenic gut microorganisms in oxygen-deprived environments. However, our understanding of their function within the human intestinal microbiome remains incomplete. With the available, time-consuming screening methods same as the labeling methods with very limited sample throughput and low detection rates, the entire variety of bacteria is not yet accessible – leaving the largest proportion of the human gut biocenosis unexplored. Therefore, a label-free and real-time method is required by taking advantage of microtechnology to understand the properties of microorganisms in order to meet superior control over the enormous link between microbiota and health and disease issues. The objective of this research is to develop a microfabricated high-throughput bioelectrochemical flow cytometer able to pick out currently uncharted gut bacteria by their electrical properties. Based on impedance and polarizability a strong correlation between electrical properties accessible by microfluidic sensing and bacterial extracellular electron transfer will be established. A multi-frequency impedance measurement system shall be established in this novel impedance flow cytometer.

P-S11-73-T3 Rapid prototyping of self-filling microfluidic chips for Sars-CoV-2 RNA detection by isothermal amplification

Mr. Filip Staniszewski [1], ***Dr. Christina Schmidleithner*** [1], ***Dr. Stefan Schrittwieser*** [1], ***Ms. Barbara Posch*** [1], ***Dr. Lidiya Osinkina*** [2], ***Dr. Maximilian Westenthanner*** [2], ***Dr. Joachim Stehr*** [2], ***Dr. Johannes Peham*** [1]

1. *AIT Austrian Institute of Technology GmbH,* ***2.*** *HP*

The public interest in point-of-care devices, that require little user interaction or laboratory equipment, has dramatically increased since the Sars-CoV-2 pandemic. Here we propose a microfluidic design, AITmicro, that is based on capillary retention valves (CRVs) and enables controlled volume deposition independent of applied sample volume together with a pipeline for rapid prototyping. Filling of the chip requires only a disposable transfer pipette. For rapid deployment, a pipeline for accelerated prototyping was established, which can save up to 65% in costs compared to conventional prototyping. In this pipeline a set of microfluidic designs are milled an evaluated. Subsequently one design is injection molded and larger testing experiments are set up. Excluding the design process, the costs for our AITmicro chip with the prototyping pipeline were 5200 EUR (1000 chips) and required about 6 weeks. A LAMP assay for the detection of Sars-CoV-2 RNA was incorporated to highlight the diagnostic capability of AITmicro, achieving an LOD of 10 copies/µL. There, positive samples changed their color to yellow, while negative controls remained pink. In future, this microfluidic system can be combined with further assays to provide rapid and cost-effective pathogen detection at PCR-sensitivity without any further readout instruments or trained laboratory personnel.

P-S11-74-T3 Hydrocarbon-Mediated Shrinkage of Silicon Nitride Nanopores

Mr. Debmalya Roy [1], ***Mr. Aniruddha Guha*** [1], ***Dr. James Yates*** [2], ***Prof. Suman Chakraborty*** [1]

1. *Indian Institute of Technology, Kharagpur,* ***2.*** *ITQB NOVA*

Solid-state nanopores have found vital applications in biomolecular sensing and ionic circuitry, but their prospects rely on the development of precise fabrication techniques for obtaining the desired electrokinetic current characteristics required for the applications. We present a novel approach for fabricating nanopores in thin film dielectrics by employing hydrocarbon-based pore shrinkage with the electron beam from a transmission electron microscope (TEM). The method involves immersing a nanopore drilled using a focussed ion beam in ethanol, air-drying it, and then exposing it to the electron beam. The residual ethanol molecules aid in the deposition of hydrocarbons, which, combined with reflowing silicon nitride, contribute to pore shrinkage. Real-time visual feedback during the process enables precise control, allowing for the accurate shrinkage of pores with initial diameters exceeding 100 nm. Energy dispersive spectroscopy reveals enhanced carbon presence around the pore after ethanol exposure and shrinkage. This technique offers advantages over alternative methods in its ability to shrink large pores with high precision and provides a means to fine-tune nanopore sizes for applications such as biosensing. This would meaningfully contribute to advancements in the field of solid-state nanopore fabrication.

P-S11-75-T3 Reversible Manipulation of Effective Pore Diameter in Silicon Nitride Nanopores

Mr. Aniruddha Guha [1], ***Mr. Debmalya Roy*** [1], ***Dr. James Yates*** [2], ***Dr. Chirodeep Bakli*** [1], ***Prof. Suman Chakraborty*** [1]

1. *Indian Institute of Technology, Kharagpur,* ***2.*** *ITQB NOVA*

Engineered nanopores have gained increased popularity for their robustness and compatibility with standard fabrication techniques. Precise control of ionic transport through a nanopore using an external electric field has enabled advances in biopolymer sequencing, nanofluidic diodes, transistors, and nanofluidic memristors. However, in extreme confinements (sub-10 nm), ionic conductance varies non-linearly with changes in applied potential, particularly under stronger electric fields. This variability alters the effective pore opening and affects sequencing applications. Such inconsistencies make exploration of variations in ionic transport, especially at higher potentials, crucial for nanopore technologies. This study investigates the non-linear variations in ionic current using voltages higher than the conventional ranges and explores the underlying physics. Experiments employed single nanopores created via controlled dielectric breakdown in thinned silicon nitride membranes. A 1M KCl solution (pH 5.5 to 6) served as the electrolyte, and Ag/AgCl electrodes recorded the ionic current. Findings reveal a rapid current increase at higher potentials, contrasting with much lower values at lower potentials. This behaviour could be attributed to the formation and accumulation of Bjerrum pairs and immobile layers near the pore wall. Results of this study would help in tuning effective pore diameter through applied potential enhancing versatility of nanopores in various applications.

P-S11-76-T3 The Effects of 3D Nozzle Injection Shape on Precipitated Lipid Nanoparticles in a Low Aspect Ratio Lamination Mixer (LARM)

Mr. Ebrahim Taiedinejad [1], ***Ms. Alshaimaa Abdellatif*** [1], ***Prof. Andreas Dietzel*** [2]

1. *Technische Universität Braunschweig, Institut für Mikrotechnik, Alte Salzdahlumer Str. 203, 38124 Braunschweig, Germany,*

2. *Institute of Microtechnology, Braunschweig, 38124, Germany*

This safe and inexpensive carrier system allows for incorporating sensitive and poorly soluble active substances. The utilization of drug or carrier nanoparticles containing drug or mRNA molecules is becoming more prevalent in pharmaceutical formulations, with particle sizes and polydispersity being crucial parameters impacting bioavailability, pharmacokinetics, and pharmacology. The controlled and continuous production of nanoparticles can be achieved through microfluidic mixers, which offer specific conditions. A new 3D low aspect ratio microfluidic system ensures precise control of particle size and polydispersity index (PDI).
This study shows how using rectangular nozzle shapes with different sizes affects the SLNP size and PDI.
the ratio of aqueous to organic phases (Qaqueous/Qorganic) remained constant at 9 while Qaqueous+Qorganic increased from 200 µl/min to 1000 µl/min. With all nozzles with three different widths, the average particle size decreased from 200 nm to almost 120 nm. However, at a flow velocity greater than 400 µl/min, produced nanoparticles with a nozzle size of 500×30µm2 had a PDI below 0.1. This indicates that the production of monodisperse nanoparticles was more successful with bigger nozzle sizes

P-S11-77-T3 Development of an automatic reagent drip system for passive pumps

Prof. Katsuo Mogi [1], ***Mr. Reo Shimada*** [1], ***Mr. Hiroyuki Kimura*** [2], ***Mr. Naoki Takada*** [3]

1. *Tokyo Denki University,* ***2.*** *Kyoto Pharmaceutical University,* ***3.*** *National Institute of Advanced Industrial Science and Technology, Tsukuba*

A syringe pump is widely used as a means of injecting liquid into microchannels in microfluidic devices because that can pump liquids while maintaining a constant flow rate. However, syringe pump-based systems have several drawbacks such as pulsation at low flow rates, limited injection volume, large system size, high cost, and complicated piping. One effective solution to this problem is to use passive pumps to inject liquids into microchannels. The flow in the microchannel from the small droplet on the inlet port to the large droplet on the outlet port is generated according to the pressure difference due to surface tension. The passive pump generates a steady flow at low flow rates without expensive equipment and external tubing. On the other hand, reagent injection into a passive pump is an intermittent process, and manual reagent dropping is a burdensome task. Therefore, we developed a practical automatic reagent drip system. The system is capable of intermittent and long-term injection of droplets into microfluidic devices without human intervention.

P-S11-78-T3 Durable carbyne-coated micro and nanotextured surfaces for antibacterial control

Mr. Dimitris Nioras [1], ***Mr. Dionysia Kefallinou*** [1], ***Mr. Dimosthenis Ioannou*** [2], ***Dr. Andrey Brigadin*** [3], ***Dr. Angeliki Tserepi*** [2], ***Dr. Evangelos Gogolides*** [4]

1. *Institute of Nanoscience and Nanotechnology, NCSR "Demokritos",* ***2.*** *Institute of Nanoscience and Nanotechnology, NCSR Demokritos, Aghia Paraskevi 15341, Attiki, Greece,* ***3.*** *Swissimpianti Sagl, 6828 Balerna, Switzerland,* ***4.*** *NCSR Demokritos*

Our research aims to explore the mechanical robustness and bactericidal properties of micro and nano-textured polymeric surfaces developed using our dry plasma technology, subsequent to a Carbyne-enriched deposition. By introducing micro and nanostructures onto Poly(methyl methacrylate) (PMMA) surfaces via oxygen plasma treatment, we proceed to deposit a thin Carbyne-enriched film, approximately 30-40 nm in thickness. The inclusion of the Carbyne-enriched coating significantly enhances the hardness and durability of the textured surface. Prior studies have already demonstrated the remarkable antibacterial efficacy of our plasma-treated surfaces against *E. coli*. Building upon these findings, we envision the development of reusable bactericidal surfaces, that leverage the durability of the carbyne coating in combination with the bactericidal action of the plasma induced structures. This breakthrough holds immense significance in terms of public health, safety, early prognosis, and prevention of outbreaks.

P-S11-79-T3 On the Micromixing Mechanism by Active and Passive Methods

Prof. Levent Trabzon [1]

1. *Istanbul Technical University*

Advantages of microfluidic devices have had a significant effect on field of biomedical diagnostics, drug development, drug delivery and biomedical research industries In general, mixing enhancement methods can be categorized as passive and active methods. Main difference between two of these methods related to power consumption. Passive methods don't require external energy, while active methods use an external field to generate disturbance. In the passive method, the mixing process relies entirely on diffusion or chaotic advection. Besides, active mixers can be categorized by the types of external disturbance effects. Among all of them, based on the simplicity of fabrication and versatility of use, inertial based and EHD (electrohydrodynamic) technique are studied as a passive and active method, accordingly. Specially, design of geometry and position of electrodes are extensively studied in order to examine versatilitiy of mixing in passive and active micromixers. There is an enhanced mixing with sunflower geometry which is superposition of asymmetrical linear microchannel and straight circular microchannel. The longitudinal ones are giving very versatile mixing in a short distance with very low volt (8 V) and Re number (0.04). The findings are well matched with experimental results in mixing as seen in case of inertial mixing approach.

P-S11-80-T3 Micropatterned polymeric chips for enhanced production of the antibacterial compound TDA by Phaeobacter inhibens biofilms

Ms. Yuyan Liu [1], ***Dr. Ariadni Droumpali*** [1], ***Mr. Xavier Florensa*** [2], ***Prof. Paul Kempen*** [1], ***Dr. Maria Dimaki*** [2], ***Prof. Claus Sternberg*** [2], ***Prof. Lone Gram*** [2], ***Prof. Rafael Taboryski*** [2]

1. *DTU Nanolab,* ***2.*** *Technical University of Denmark*

Over the last three decades, there has been a rapid increase in fish supply demand, however, infection control is the main challenge for the aquaculture industry. Therefore, a sustainable solution for controlling infectious diseases is urgently needed. *Phaeobacter inhibens* marine bacteria can inhibit pathogens by producing the antibacterial compound tropodithietic acid (TDA).

In this study, we investigate the effect of different micropatterns on *Phaeobacter inhibens* growth and TDA production. A polymer material platform is beneficial for potential large-scale production, hence, cyclic olefin copolymer (COC) was selected for micropatterning. The fabrication step comprises lithography, electroplating, and molding (LIGA) processes.

Phaeobacter inhibens grow on polymeric surfaces with different micropatterns of planar, pit, and pillar surfaces. Bacteria on pit surfaces formed the highest amount of biofilm, surprisingly, the TDA production didn't follow biomass formation, and a significant enhancement in TDA production was found on the pillar surfaces.

Finally, finite element simulations were conducted to study the possible reasons for *Phaeobacter inhibens* biofilm growth and TDA synthesis.

P-S11-81-T3 Lab-on-a-phone – plasmonic biosensing in 3D scaffolds using a smartphone

Dr. Florian Laible [1], ***Ms. Melanie Sommer*** [1], ***Prof. Monika Fleischer*** [1]

1. *University of Tübingen*

Plasmonic biosensors are capable of very fast and sensitive detection of biomarkers. We present a low-cost lab-on-a-phone device to perform plasmonic shift sensing in point-of-care scenarios. Their active volume is a nanostructure-spiked 3D PDMS scaffold. For illumination and data collection as well as processing the smartphone is used. The plasmonic shift is measured by monitoring the color change (hue value in the HSV color space). We compare the HSV approach to spectrometric methods on refractive index shift measurements, present the prototype development and the pathway to an open-source low-cost point-of-care sensor.

P-S11-82-T3 Iridium oxide thin film electrodes for highly sensitive impedance biomass detection

Mr. Sven Meinen [1], ***Prof. Andreas Dietzel*** [1], ***Dr. Rainer Krull*** [2], ***Mr. Kevin Viebrock*** [2]

1. *Institute of Microtechnology, Technische Universität Braunschweig,* ***2.*** *Institute of Biochemical Engineering, Technische Universität Braunschweig*

In a previous work, an impedance sensor was developed for a capillary wave micro bioreactor consisting of four gold electrodes (4-point measurement in liquids) to measure the biomass in buffered media. However, for low densities of cells their contribution to the measured impedance was very small due to a high contact impedance of gold micro-electrodes. Therefore, electro deposited iridium oxide is investigated as alternative electrode material. With scanning electron microscopy and impedance measurements, the influence of deposition time on thin film morphologies and on impedance in buffer solution was studied in detail.

P-S11-83-T3 Fabrication of Surface Microstructures and Investigation of their Influence on the Interaction with Blood for Application in a Left Ventricular Assist Device

Ms. Marta Bonora [1], Mr. Stjepan Perak [2], Ms. Sonja Kopp [3], Ms. Sarah Linnemeier [1], Mr. Richard Benauer [4], Dr. Markus Lunzer [2], Prof. Francesco Moscato [1], Dr. Marcus Granegger [1], Dr. Michael Muehlberger [3]

1. *Medical University of Vienna,* ***2.*** *UpNano GmbH,* ***3.*** *PROFACTOR GmbH,* ***4.*** *bionic surface technologies GmbH*

Heart failure is the leading cause of death in Western countries and is increasingly challenged by the shortage of donor organs. Contemporary mechanical circulatory support (MCS) devices promote survival and improve the quality of life for HF patients. Rotodynamic blood pumps used as left ventricular assist devices (LVADs) constitute the largest proportion of clinically used MCS devices. The interaction of blood with the implant surface is a key aspect of the success of these devices, since thrombus formation can occur at the inner surfaces and must be avoided. Using computational fluid dynamics simulations, we establish an understanding of the detailed flow conditions within a novel pediatric LVAD with the aim of replicating these in a microfluidic setup that allows to test different surfaces and surface microstructures with respect to their thrombogenicity. We fabricate our microstructures using two-photon-polymerisation 3D printing and nanomprinting. We will report on the fabrication procedure of the microstructures and the microfluidic setup and present first experimental results relevant for our LVAD use case.

P-S11-84-T3 Development of a Microfluidic Lab-on-PCB Device to Preconcentrate Proteins through the Control of pH using Electrochemically Generated Acid

Ms. Grace Maxted [1], ***Prof. Pedro Estrela*** [1], ***Dr. Despina Moschou*** [1]

1. *University of Bath*

The work presented here reports an adaptable microfluidic module designed to perform a sample preparation step of protein preconcentration through isoelectric focusing (IEF) by using electrochemically generated acid (EGA) to form a pH gradient. The module has been designed for eventual integration into Lab-on-a-Chip (LoC) biosensors to increase analyte concentration and reduce contamination to improve function and limit of detection (LoD).

As per our previously published work, we use quantitative control of pH through the production of EGA using electropolymerised self-assembled monolayers (SAMs) on gold electrodes within an individually addressed printed circuit board (PCB) array. Fluorescence spectroscopy and electrochemistry were the primary methods used throughout, with potentiostats used to apply set potentials whilst a fluorescent dye was used alongside an optical setup.

We now present here the steps taken to test the capability of concentrating proteins in its original form and subsequent integration into a microfluidic system using micromachined channels. The data collected in its non-microfluidic form displays promising results for protein preconcentration, whilst the preliminary data for EGA in its microfluidic system showed encouraging developments with a slight adjustment of dye concentration.

Poster Session 1.2: Track3, Track4

P-S12-01-T3 Photolithographic production of smart water filters able to detect bacteria

Dr. Amparo Ferrer-Vilanova [1], ***Dr. Josune J. Ezenarro*** [1], ***Dr. Nuria Vigues*** [2], ***Prof. Jordi Mas*** [2], ***Dr. Gonzalo Guirado*** [2], ***Dr. Xavier Munoz-Berbel*** [3]

1. *Institute of Microelectronics of Barcelona (IMB-CNM-CSIC),* ***2.*** *Universitat Autònoma de Barcelona (UAB),* ***3.*** *Instituto de Microelectrónica de Barcelona (IMB-CNM, CSIC)*

Microbial detection in drinking water is a concerning issue nowadays, requiring periodical analysis. The techniques currently used are time consuming since they need sample transport to the laboratory. In order to diminish the response time, portable versions are being developed but most times, they need sample pre-treatment to provide good responses. A different strategy consists on the use of metabolic indicators, which are molecules that show a colour change in the presence of metabolically active bacteria. In this work, smart water filters for bacterial detection are produced through the incorporation of the metabolic indicator Prussian blue by using a photocatalytic process. These filters are sensible only to the presence of live bacteria, producing a clear colour change from blue to colourless due to the metabolic reduction of Prussian blue to the Prussian white form. To develop the measurements, an opto-fluidic membrane filter holder is used in order to pre-concentrate the bacteria in the water samples. Thus, smart filters produce detectable colour changes in less than 2 hours for bacterial concentrations of 10^4 CFU mL^{-1}, and in less than 5 hours for smaller concentrations, which are promising results when comparing with standard methods.

P-S12-02-T3 A novel method for real time monitoring of wetting transition of underwater superhydrophobic surfaces and membranes: Application in membrane desalination

Mr. Dimosthenis Ioannou [1]***, Dr. Kosmas Ellinas*** [2]***, Dr. Evangelos Gogolides*** [3]

1. *Institute of Nanoscience and Nanotechnology, NCSR Demokritos, Aghia Paraskevi 15341, Attiki, Greece,* ***2.*** *University of the aegean,* ***3.*** *NCSR Demokritos*

Underwater superhydrophobicity (SH), inspired greatly by the salvinia leaves, has become an important subject in scientific research because of the many applications in maritime engineering and water treatment since superhydrophobic surfaces feature anti-corrosive, anti-wetting and anti-fouling properties. In the world of membrane distillation (MD), SH membranes need to resist wetting and fouling and maintain a stable performance in terms of flux and salt rejection. However, wetting transitions on SH membranes are only indirectly assumed when the distillate conductivity increases and very few MD monitoring methods have been proposed.
Herein we present polytetrafluoroethylene (PTFE) membranes that have been rendered superhydrophobic after O_2 plasma nanotexturing followed by C_4F_8 plasma deposition. Going one step further, we introduce a novel method to study the stability of the superhydrophobic state, by monitoring the membrane surface in situ during MD using white light reflectance spectroscopy (WLRS). This method enables monitoring in real time with very fast acquisition speed at 50-200 ms. Using our method, and as revealed by the practically unaffected reflectance spectrum, we showcase the stability of the superhydrophobic state of our plasma treated membranes, compared to commercial membranes, for liquids of surface tension down to 39.1 mN/m

P-S12-03-T3 Intracranial Magnetic Stimulation Micro-coil Probes for Two-photon Excitation Microscopy

Mr. Xiyuan Liu [1], ***Dr. Kayeon Kim*** [2], ***Dr. Changsi Cai*** [2], ***Dr. Shelley Fried*** [3], ***Dr. Anpan Han*** [4]

1. *Technical university of Denmark,* ***2.*** *University of Copenhagen,* ***3.*** *Technical University of Denmark,* ***4.*** *DTU*

There are four additional challenges when using two-photon microscopy (2PM) together with micro-coil for in vivo neurostimulation; (i) low invasiveness; (ii) prevention of a large shadow obscuring 2PM imaging. (iii) consideration of the small working distance in 2PM system; (iv) parallel alignment of the micro-coil probe to pyramidal neurons (PNs) in layer 2. Taking on these challenges, we designed L-shaped vertical micro-coil probes dedicated to 2PM.

We introduced a multi-step Bosch process to eliminate the margin between the metal trace and the silicon edge. It also minimizes invasiveness due to its smaller width compared to our previous straight probes. The vertical cantilever is 600 to 900 μm long, facilitating operation under a small working distance in 2PM system. The shadow of the micro-coil is small enough to observe the somatic region of interest (Figure 2a). We applied 1 kHz half-sinusoid waveform at a repetition rate of 200Hz for stimulation, with a duration of 600 ms. The fluorescence signal changes were confined to neurons close to the coil, suggesting that the response to magnetic stimulation was spatially confined to the cortical regions in close proximity to the coil, consistent with previous findings.

P-S12-04-T3 The development of bile duct stent

Dr. Atushi Sekiguchi [1]

1. *Litho Tech Japan Corporation*

This approach involved creating a nano-mold using electron beam lithography and forming nanostructures using a nanoimprinting method. Lithography requires special facilities and equipment and entails high costs. Additionally, current nanoimprinting and lithographic technologies are generally suitable only for flat substrates; they are not designed to create nanostructures directly on the inner walls of a tubular substrate. In the present study, we used the atmospheric pressure low-temperature plasma method to develop a technology for imparting enhanced antifouling performance to the surfaces of tubular materials, regardless of substrate shape.

P-S12-05-T3 Evaluation of echinoid-shaped nanostructures for reusable mechano-bactericidal and bacterial filtration

Mr. Hee-Kyeong Kim [1], ***Prof. Young-Sam Cho*** [1], ***Prof. Hyun-Ha Park*** [1]

1. *wonkwang university*

Waterborne infections result from using contaminated drinking water, which is a serious danger to public health. People can easily expose to cholera, parasitic infections, and so on if they use contaminated water. In this study, a biocide-free echinoid-shaped aluminum oxide nanostructured surface was proposed. Mechano-bactericidal means that the nanostructure damages the bacterial membrane during the surface attachment stage. The proposed echinoid-shaped Al_2O_3 nanostructure can effectively kill the attached bacteria. The echinoid-shaped nanostructure surface mechano-bactericidal efficiency was shown against *E. coli* (97 ± 3.81 %) and S. aureus (80 ± 9.34 %). In addition, the echinoid-shaped nanostructure was well maintained even after thermal cleaning at 500 °C and showed high mechano-bactericidal activity (89 ± 6.86 %). In the case of the proposed echinoid-shaped nanostructure surface, it already has fine pores during the fabrication process. Therefore, the filtration experiment of bacteria through our proposed echinoid-shaped surface having interconnected fine pores showed high bacteria filtration (99.2 ± 0.3 %). The echinoid-shaped nanostructure has mechano-bactericidal activity about attached bacteria and filters out the bacteria to provide clean water. The proposed echinoid-shaped nanostructure surface is reusability via thermal treatment and could be one of the candidates for bacteria filtration apparatus.

P-S12-06-T3 Highly Flexible, Ultra-long SEEG Probes with IrOx Micro Electrodes Realized using Compact Bond Interfaces

Mr. Marc Keller [1], ***Prof. Oliver Paul*** [2], ***Dr. Patrick Ruther*** [1]

1. *IMTEK - University of Freiburg,* ***2.*** *IMTEK, University of Freiburg*

This study presents a novel fabrication and assembly process for flexible neural probes for clinical deep brain applications. Current state-of-the-art stereo-electroencephalography (SEEG) probes used in epilepsy diagnostics and Parkinson's disease treatment are characterized by a limited channel count and cause tissue reactions affecting their long-term recording performance. In contrast, micromachined neural probes offer larger electrode numbers and cause a reduced tissue response. They are however limited to cortical regions closer to the brain surface. To overcome these limitations, the proposed fabrication process enables 200-µm-wide flexible neural probes based on polyimide with lengths exceeding 30 cm. The probes consist of the components electrode array, extension section, and connector interface. The fabrication process involves lithography, thin-film deposition, reactive ion etching (RIE), and gold electroplating. Test structures used to evaluate the assembly process address the mechanical bond strength, bond yield, and contact resistance. The study demonstrates successful bonding of compact interfaces with a bond yield of 100% and excellent mechanical strength, i.e. the bonded interconnections withstand tensile forces up to $F_{\mathrm{max}} = 2.6 \pm 0.64$ N. This advanced fabrication and assembly process opens up possibilities for deep brain applications using micromachined neural probes of reduced cross-sections at increased channel count.

P-S12-07-T3 Reflectance-Based Optical Biosensor Platform with Residual-Layer-Free Nanoimprint Lithography

Dr. Junhyoung Ahn [1], ***Dr. Yunji Eom*** [1], ***Dr. Soonkeun Kwon*** [1], ***Dr. Hak-Jong Choi*** [1], ***Dr. SungHwi Lee*** [1], ***Dr. Hyungjun Lim*** [1], ***Dr. JaeJong Lee*** [1]

1. *Korea Institute of Machinery & Materials*

Nanoimprint lithography (NIL) is the simple process using stamp and UV or thermal curable resins for nanopatterning with low cost, high-throughput, and high resolution. Residual-layer-free NIL provides good performance of nano-scale structures functional arrangements with 2/3D layouts. We demonstrated nanohole patterns of 200 nm pore size using residual-layer-free NIL without further process for removing residual layers for reflectance biosensor. The reflectance peaks of gold substrate are enhanced to 8 times using the hexagonal hole patterns of diameter 200 nm, and pitch 400 nm. So, this substrate can be applied for immune reflectance biosensor with magnetic nanoparticles for pre-treatment.

P-S12-08-T3 Design and fabrication of polymer microstructures with embedded electrodes for 3D measurements

Mr. João Serra [1]***, Dr. João Ventura*** [2]***, Dr. Paulo Aguiar*** [3]***, Dr. Susana Cardoso De Freitas*** [4]***, Dr. Diana C. Leitao*** [5]

1. *Instituto Superior Técnico,* ***2.*** *IFIMUP - Instituto de Física de Materiais Avançados, Nanotecnologia e Fotónica da Universidade do Porto,* ***3.*** *i3S - Instituto de Investigação e Inovação em Saúde, Universidade do Porto,* ***4.*** *INESC Microsistemas e Nanotecnologias,* ***5.*** *Department of Applied Physics, Eindhoven University of Technology*

The ability to perform 3D mapping of electrical activity is increasingly relevant in biology and medicine. Self-assembly fabrication strategies can be employed to deliver 3D electrode arrangements from conventional planar designs, including taking advantage of intrinsic stress and/or thermal expansion coefficient mismatch between layers.

Here, we fabricate stress-actuated polyimide (PI) strips where microelectrodes can be embedded, forming the basis for 3D self-assembled MEAs. A curvature model based on the plane strain approximation was used to select the range of suitable thicknesses for the stress-inducing layer.

Spin-coated PI was patterned using UV photolithography and a TMA-based developer. PI was cured after each coating at 200 ºC for 30 minutes to enable multiple PI layers. AlSiCu was used as a sacrificial layer and a 200 nm SiO_2 underlayer was used as a stress-actuating layer. Au leads were fabricated between two PI layers to minimize damage during the bending process. The bending action did not occur immediately after release, requiring heating at 200 ºC for 30 minutes, presumably to soften the PI layer and allow it to relax into the curvature imposed by the stress. The underlying mechanisms and their impact on process design and electrode characteristics will be discussed.

P-S12-09-T3 Patterning of bio-doped silk films at wafer level for the sustainable and scalable production of biosensors

Dr. Sara Santiago Malagón [1], ***Dr. Marcin Procek*** [2], ***Dr. Augusto Márquez*** [1], ***Dr. Salvador David Aznar Cervantes*** [3], ***Dr. Gonzalo Guirado*** [4], ***Dr. Carlos Domínguez Horna*** [1], ***Dr. Xavier Munoz-Berbel*** [1]

1. *Instituto de Microelectrónica de Barcelona (IMB-CNM, CSIC),* ***2.*** *Department of Optoelectronics, Silesian University of Technology,* ***3.*** *instituto murciano de investigación y desarrollo agrario y medioambiental,* ***4.*** *Universitat Autònoma de Barcelona (UAB)*

Silk fibroin (SF) has emerged as a promising biopolymer for microfabrication processes due to its remarkable properties, including high processability, mechanical strength, stability, biocompatibility, biodegradability, and entrapment capacity. Its polymorphic crystalline structure enables it to function as a resist in lithographic processes, with the advantage of being fully sustainable and water-based.

This study presents a lithographic process, specifically e-beam lithography, for patterning SF films on a wafer level, which is particularly valuable for the large-scale production of highly sensitive and specific biosensors. The film thickness was precisely controlled through spin-coating, achieving values from 50nm to 600nm. Crystalline SF films were patterned using e-beam lithography as a positive resist and developed using water and submicrometer patterns below 800nm were successfully obtained.

Furthermore, the films were doped with enzymes, such as glucose oxidase and peroxidase, along with ABTS redox mediator. The doping conserved the resolution of the patterns while preserving the structural integrity and functionality of the biomolecules.

The SF technology holds great potential for biosensor development due to its scalability for mass production and long-term stability of enzymes in the SF matrix. Previous reports have indicated lifespans of up to 8 months under minimal storage conditions, such as drying and room-temperature.

P-S12-10-T3 Simultaneous detection of SARS-CoV-2 nucleoprotein and receptor-binding domain by a Multi-Area Reflectance Spectroscopy (MARS) immunosensor

Dr. Dimitra Tsounidi [1], Dr. Nikos Papanikolaou [1], Dr. Ioannis Raptis [1], Dr. Sotirios Kakabakos [1], Dr. Panagiota Petrou [1]

1. *NCSR Demokritos*

This work presents for the first time the fast and label-free simultaneous determination of Nucleoprotein (NP) and Receptor-Binding Domain (RBD) for SARS-CoV-2 diagnosis at the Point-of-Care implementing a biosensing device based on Multi Area Reflectance Spectroscopy (MARS) . Dual-analyte detection is achieved using silicon chips with two silicon dioxide areas of different thickness, each one functionalized with a specific antibody against NP and RBD, respectively. The two sensing areas are simultaneously illuminated, and the reflected interference spectrum collected is the combination of the spectra from the two areas. Processing of this spectrum, provides for the monitoring of biomolecular reactions taking place onto the two areas as increase of the respective biomolecular layer thickness. Both proteins are determined in 12 min following a two-step sandwich immunoassay with detection limits of 10 ng/mL. The assays are repeatable with intra- and inter-assay coefficients of variation lower than 10%. The biosensor developed is incorporated into a compact fully-automated bench-top reader along with a dedicated easy-to-use software. The short assay duration in combination with the excellent analytical performance and the small-sized device constitute the proposed analytical method suitable for application for the reliable SARS-CoV-2 diagnosis at the Point-of-Care.

P-S12-11-T3 3D printed microstructures as bacterial biofilm carriers

Mrs. Carmen Lopéz Vizcaino [1], Dr. Rocio Espinosa Portero [1], Dr. Sebastian J Kjeldgaard-Nintemann [1], Dr. Henriette Lyng-Røder [1], Dr. Ada-Ioana Bunea [2]

1. *University of Copenhagen,* ***2.*** *Technical University of Denmark*

Many bacteria can form biofilms, which are complex communities of microorganisms embedded in a self-secreted extracellular matrix composed primarily of polysaccharides and extracellular DNA. Biofilms can contain pathogenic bacteria, however, “good” bacteria, which can secrete useful compounds, can also form biofilms. The biofilm state typically confers enhanced resilience and enables the community to secrete the compounds of interest more quickly compared to planktonic bacteria, which when introduced into a new environment first need to overcome stressors and reach a stationary phase. Here, we explored the use of polymeric microstructures as biofilm carriers for two strains of lactic acid bacteria. The microstructures were fabricated by two-photon polymerization direct laser writing of an acrylic resin and contained three large grooves with a planar surface, or containing pits or pillars. Our results show that surface morphology influences bacterial attachment, as the lactic acid bacteria seem to prefer patterned surfaces, and particularly pits (Figure 3a). The lactic acid bacteria also prefer to attach to the pristine negatively-charged microstructure surface as opposed to positively charged surfaces. Future studies will focus on the fabrication of the microstructures in a biocompatible and biodegradable material, as well as optimizing the surface patterning for further enhancing bacterial attachment.

P-S12-12-T3 Evaluation of microneedle patches for improved intradermal delivery of molecularly-defined cancer vaccines

Dr. Francesco La Malfa [1], ***Dr. Koen van der Maaden*** [2], ***Prof. Ferry Ossendorp*** [2], ***Prof. Urs Staufer*** [3]

1. *TU Delft,* ***2.*** *Leiden University Medical Center,* ***3.*** *Delft University of technology*

Microneedle patches have emerged as a promising technology for targeted drug delivery through the skin. These patches, comprising an array of tiny needles, provide several advantages over conventional administration methods, including improved patient compliance, reduced pain, and avoidance of needle-related injuries and waste.

This study investigates the effect of various microneedle designs on skin penetration and drug delivery efficiency. Critical tip diameter, shape, cutting-edge angle, and length of the needle were investigated.

2-photon polymerization technique was employed as technique for the fabrication of master molds. Soft lithography technique was used to fabricate secondary molds in polydimethylsiloxane (PDMS). Finally, dissolvable microneedles were created by filling these secondary molds by means of centrifugation. Preliminary experiments involved the fabrication of such patches in polyvinylpyrrolidone via centrifugation method. Other dispensing methods will be tested in future as well. Different shapes (conical, tetragonal, hexagonal, and octagonal) will be evaluated together with tip diameter, cutting-edge angle, and length, to assess their impact on skin penetration and drug delivery.

The aim of this work is to contribute to the ongoing research on optimizing microneedle-based drug delivery systems. Finally, the proposed research seeks to enhance transdermal drug delivery and develop customized systems for different drugs and patient populations.

P-S12-13-T3 Biomolecular Gradient patterning on Cell-compatible Polymer Brushes

Mr. Yoan Mimoun [1], ***Dr. Emmanuelle Marie*** [1], ***Dr. Mathieu Morel*** [1]

1. *ECOLE NORMALE SUPERIEURE*

Molecular gradients play a key role in cell migration and differentiation. While polymer brushes offer specific grafting and dynamic control, obtaining continuous gradients of biomolecules remains limited. Our approach therefore combines polymer-coated coverslips with microfluidic gradient generators to create cell culture substrates with restricted domains exhibiting biomolecular gradients. Here we show a simple gradient transfer onto micrometric stripes achieved via streptavidin-biotin recognition, but the versatility of our platform offers customizable gradient shapes and compositions. Such platform could become a tool of choice for biological studies ranging from tumor metastasis to tissue regeneration.

P-S12-14-T3 Synthetic route of Au-Fe3O4 Janus nanoparticles for continuous separation and purification of targeted biomaterials

Dr. Yunji Eom [1], Dr. Hak-Jong Choi [2], Dr. Junhyoung Ahn [2], Dr. SungHwi Lee [2], Dr. CheolGi Kim [1], Dr. JaeJong Lee [2]

1. *Daegu Gyeongbuk Institute of Science & Technology,* ***2.*** *Korea Institute of Machinery & Materials*

We developed a synthetic route to prepare Au-Fe_3O_4 Janus nanoparticles(JNPs) for the continuous separation and purification of specific biomaterials. The JNPs were functionalized with hydrophilic chains and target material, allowing for strong and specific binding with the targeted biomaterials. The effectiveness of the JNPs separation system was demonstrated using biotin-PEG-thiol, PEG-functionalized dopamine, and streptavidin-functionalized polystyrene bead as targeting ligands, hydrophilic ligands, and artificial biomaterials, respectively, to demonstrate the effectiveness of the JNPs separation system.

P-S12-15-T3 Paper-based microfluidics with internal calibration as a rapid assay for the quantitative measurement of antidepressants

Mr. Esteban Builes-Münden [1], ***Ms. Monika Conrad*** [2], ***Mr. Markus Franz Wieghaus*** [3], ***Prof. Günter Gauglitz*** [2], ***Prof. Andreas Dietzel*** [1]

1. *Institute of Microtechnology, Braunschweig, 38124, Germany,* ***2.*** *IPTC - University of Tübingen,* ***3.*** *OFFIS - Institut für Informatik*

We developed a paper-based device for therapeutic drug monitoring (TDM) of the antidepressant Amitriptylin (AMT) for therapy dose optimization. Due to the small size of AMT, a typical sandwich assay cannot be carried out. Therefore, a binding inhibition test was implemented on femtosecond laser structured nitrocellulose paper. The results were analyzed by colorimetric evaluation using a smartphone application. Internal device calibration is required for an evaluation independent of light influences or cross reactivities. This was assured by establishing six different channels on the nitrocellulose paper and adding varied but well-defined amounts of the analyte AMT into each of them before the measurement can begin, a method called the standard addition method.

To achieve lower limits of detection (LOD) for environmental measurements of small analytes, a pre-incubation time of at least five minutes directly after the reaction with the conjugates is required. For this purpose, a switchable fluid barrier based on a mechanical bending actuation was developed. This switchable barrier is a key technical element to significantly increase the sensitivity of the detection.

P-S12-16-T3 Fabrication of flexible microsensor arrays with ASIC integration for respiratory monitoring

Mr. Maolei Zhou [1], ***Ms. Yadi Zhen*** [1], ***Prof. Andreas Dietzel*** [1]

1. *Institute of Microtechnology, Braunschweig, 38124, Germany*

Flexible sensor arrays for respiration monitoring used for premature infants require complex multilayer wiring within the sensor film since signal and supply lines for many sensor nodes have to be organized. ASIC chips embedded in the flexible system are needed to enable digitization and parallel readout of many sensors. A femtosecond-laser-assisted pulsed current electroplating technology was developed to establish reliable, cost-effective multilayer wiring and ASIC contact pad formation.

P-S12-17-T3 Recording of somatosensory evoked potentials by ultraconformable µEcoG multielectrodes array with 3D PEDOT:PSS micropillars-integrated microelectrodes

Ms. Alice Lunghi [1], ***Dr. Pierpaolo Greco*** [2], ***Dr. Mauro Murgia*** [1], ***Dr. Riccardo Viaro*** [2], ***Ms. Sonia Guzzo*** [1], ***Dr. Michele Di Lauro*** [1], ***Prof. Luciano Fadiga*** [2], ***Prof. Fabio Biscarini*** [1], ***Dr. Michele Bianchi*** [3]

1. *Istituto Italiano di Tecnologia,* ***2.*** *University of Ferrara,* ***3.*** *University of Modena and Reggio Emilia*

Recording neural signals is of outmost importance to understand how neurological disorders affect the normal functioning of neural tissue. To this end, devices capable to accurately discriminate between signals and noise are highly desired and lowering the impedance is an efficient method to achieve this goal. Impedance reduction can be obtained either by using conductive polymers, particularly PEDOT:PSS, as coating material for the recording electrodes or by increasing their electroactive surface area by surface micro- and nanopatterns. However, the combination of these two approaches has only been minimally explored.

In this work, I will present the design, fabrication and validation of an ultra-flexible µEcoGs multi-electrodes array (MEA) that, for the first time, explores the application of PEDOT:PSS micropillars in the field of *in vivo* neural recording. I will demonstrate the fabrication of a 3D soft PEDOT:PSS micropillars array and how these microstructures are effective in regulating electrochemical properties, as well as the integration of this array in an ultra-flexible µEcoGs MEA. Moreover, I will present demonstrate recording of somatosensory evoked potential in rat models. So far, the results suggest that the recording quality depends more on the surface geometry rather than on the chemical nature of the electrodes.

P-S12-18-T3 Investigating the effect of nanostructures effective shear modulus on the propagation of the neuronal growth cone

Dr. George Flamourakis [1], ***Ms. Selina Teurlings*** [1], ***Mr. Dimitri Kromm*** [1], ***Dr. Daan Brinks*** [1], ***Dr. Carlas Smith*** [1], ***Dr. Angelo Accardo*** [1]

1. *Delft University of technology*

3D neuronal cultures provide a more realistic representation of the brain's microenvironment compared to 2D cultures. The growth cone, which plays a crucial role in axonal outgrowth, is affected by the mechanical properties of the cellular environment. However, previous studies on growth cone architecture have primarily been limited to 2D glass slides, which do not mimic the brain tissue's properties. To address this limitation, we have used nano-pillar structures to create 3D neural cultures. Using two-photon polymerization (2PP), we fabricated different arrays of pillars with varying sizes and mechanical properties. These pillar arrays allowed us to investigate the influence of topographic and mechanical cues on the growth and behavior of neuronal growth cones derived from Neural Progenitor cells (NPCs). The experiments revealed that the pillar arrays created complex interconnected structures, with NPCs forming bridges and connections with neighboring clusters. Over time, the NPCs differentiated into immature neurons and extended axon-like structures expressing neuronal growth cones. We found that the effective shear modulus and topography of the pillar arrays influenced the morphology, differentiation, and growth cone structure of the NPCs. Future research using advanced imaging techniques aims to further explore the propagation of neuronal growth cones in these 3D cultures.

P-S12-19-T3 Nano-needles transform plant cells and tissues with high efficiency without tissue damage

Prof. Andy Kah Ping Tay [1]

1. *National University of Singapore*

Plant biotechnology is an important enabling tool to achieve food security. Genetic engineering of plants can be employed to generate crops and vegetables which generate much higher biomass while requiring less space, labour and raw materials to grow. Here, we describe a nano-needle platform which makes use of mechano-poration to achieve close to 100% transformation efficiency and cell viability in intact plant cells and plant tissues (Arabidopsis, Tobacco and Choy Sum). The platform is also integrated with a handheld clamp device to improve user-friendliness and facilitate use by untrained farmers without expensive and bulky equipment.

P-S12-20-T4 Versatile and highly efficient all-day radiative cooler based on optimized polymer-ceramic composite fabricated via facile process

Mr. Jaein Park [1], ***Mr. Dongwoo Chae*** [1], ***Mr. Hangyu Lim*** [1], ***Mr. Jisung Ha*** [1], ***Prof. heon lee*** [1]

1. *korea university*

Radiative cooling is a carbon-free, zero energy technology that can substitute various energy-consuming cooling systems such as air conditioners and auto-chillers for cooling heat-generating machines. Previous reports on radiative cooling have focused mainly on the cooling performance, thereby overlooking the applicability, structural complexity, manufacturing complexity, and certain physical properties of the cooler. In this study, we present an efficient, applicable, and facile-fabricated radiative cooler composed of poly(vinylidene fluoride-co-hexafluoro propene) (P(VDF-HFP)) and alumina (Al_2O_3). Apart from being fabricated in the form of a freestanding sheet with 97.5% solar reflectance and 94.8% infrared (IR) emissivity, the P(VDF-HFP)/Al_2O_3-based radiative cooler (PARC) can be applied to solid substrates via simple coating techniques. This shows that the PARC can be introduced in architecture, clothing, and other fields that demand cooling. The PARC‘s cooling performance is experimentally proven by a sub-ambient temperature drop of 5.8 □ and the cooling power of the PARC is calculated to be 125.6 Wm^{-2} under the AM1.5 global spectrum, which is superior to that of previously reported radiative cooling emitters.

P-S12-21-T4 Fluoropolymer based radiative cooler having High durability for external environment

Mr. Jisung Ha [1], ***Mr. Dongwoo Chae*** [1], ***Mr. Hangyu Lim*** [1], ***Mr. Jaein Park*** [1], ***Prof. heon lee*** [1]

1. *korea university*

Radiative cooling is next generation technology which can cool our living space than ambient temperature without energy consumption by reflecting sunlight (0.3-2.5um) and radiating the heat to the space (3K) through the atmosphere's window (8-13um). Due to the nature of the radiation cooling device that must be installed outside, we make a device that can be maintained for a long time because of its high durability character of fluoropolymer. A white and durable coating can be easily formed by dripping the solution. This cooler shows solar reflectivity of 92.5 % and emissivity of 91.7 % and its calculated cooling power is 95.6 W/m^2. This implies that it is possible to cool more than 11 degrees compared to the ambient temperature. Actual measurement results also showed similar results. Also, extra measurements were carried out in high temperature and chemical environments with ETFE cooler and control group of samples. At 120□, only ETFE film can decreases 24 degrees contrast to ambient temperature keeping the coating intact. Furthermore, when immersed into sulfuric acid below PH3, film was remained and its cooling performance was almost same. It is expected to apply for external device case which is frequently exposed to heat and chemical environment.

P-S12-22-T4 High-performance semi-transparent perovskite solar cells based on 3D-patterned FTO

Mr. sucheol ju [1], ***Mr. jaemin park*** [1], ***Prof. heon lee*** [1]

1. *korea university*

In semi-transparent perovskite solar cells (PSCs), the short-circuit current density (J_{SC}) greatly decreases with an increase in transmittance, and this results in a significant decrease in PCE. Our semi-transparent PSCs were fabricated by controlling the absorption layer thickness and aperture ratio using a 3D-structured FTO manufactured via direct printing and mist-CVD. This strategy has an advantage in that the aperture ratio (transmission/entire area) can be controlled easily by adjusting pattern specification. Also, the 3D-structured FTO enhanced the diffuse transmittance and shortened the carrier travel distance; further, it minimized the decrease in PCE because of an increase in transmittance. Our fully semi-transparent PSCs (F-PSCs) achieved a PCE of 12.0% to 14.6%, and an average visible transmittance (AVT) of 13.4% to 17.0%. These results demonstrate that the parameter of semi-transparent PSCs (transmittance and PCE) can be easily tailored to the application by controlling the specification of the pattern.

P-S12-23-T4 Deep Eutectic Solvent Supported Polymer-Based High Performance Anion Exchange Membrane for Alkaline Fuel Cells

Ms. Aida Barlybayeva [1]***, Dr. Bauyrzhan Myrzakhmetov*** [2]***, Mr. Mirat Karibayev*** [1]***, Dr. Almagul Mentbayeva*** [1]

1. *Department of Chemical and Materials Engineering, School of Engineering and Digital Sciences, Nazarbayev University,* ***2.*** *Laboratory of Advanced Materials and Systems for Energy Storage, Center for Energy and Advanced Materials Science, National Laboratory Astana, Nazarbayev University*

In this study, polymer electrolytes as potential AEMs were first prepared using the swelling method, where electrospun PVA nanofibers were fabricated via the electrospinning technique, followed by swelling in a series of DESs. To prepare the DES solutions, choline chloride (ChCl) and ethylene glycol (EG) were mixed at different molar ratios. The cross-linking of pure PVA fibers with glutaraldehyde in ethanol and DES uptake were successfully confirmed with a scanning electron microscope (see Figure 1). Moreover, Figure 1 C shows the formation of channels for ion conduction. However, although obtained fibers were crosslinked, there was a challenge with diluting DES in potassium hydroxide after immersion for 24 hours based on a weight loss of 49.5 %. In order to overcome this, the encapsulation method was suggested, which is based on the encapsulation of DES into the PVA solution by mixing them, varying the amount of DES added, and then preparing fibers using electrospinning. Encapsulation of DES in PVA nanofibers was preliminary confirmed by transmission electron microscope: PVA appears lighter due to its decreased density, proving that DES is present inside the fibers (see Figure 3).

P-S12-24-T4 Affordable and effective method for measuring key parameters of micro and nanostructured triboelectric energy harvesters

Dr. Luca Fachechi [1], ***Dr. Vincenzo Mastronardi*** [2], ***Dr. Laura Blasi*** [3], ***Dr. Gaia de Marzo*** [1], ***Prof. Massimo De Vittorio*** [2], ***Dr. Maria Teresa Todaro*** [4]

1. *Istituto Italiano di Tecnologia,* ***2.*** *Istituto Italiano di Tecnologia; Department of Innovation Engineering, Unisalento,* ***3.*** *National Research Council of Italy,* ***4.*** *Istituto Italiano di Tecnologia; Institute of Nanotechnology, CNR Lecce*

Triboelectric harvesters play an important role in mechanical energy harvesting. The analysis of these devices is not straightforward due to their output signal features. Here we propose a measurement method based on a cheap and compact custom electronic circuit, able to provide fast, reliable and accurate analysis of the device output voltage, current and generated power. Triboelectric energy harvesters based on carboxymethyl cellulose (CMC) porous aerogel films have been fabricated and analyzed by means of this approach. Short circuit current output signals have been compared with those obtained by using a commercial low noise current amplifier.

P-S12-25-T4 Improvement of Mechanical/Electrical Properties of Nano-Metal Film for Neural Electrode with Curing Rate Adjustment of Photosensitive Polyimide

Dr. HyungDal Park [1], ***Dr. Seonho Seok*** [2], ***Dr. Jinseok Kim*** [1]

1. *Korea Institute of Science and Technology,* **2.** *University-Paris-Saclay*

One of the main technologies that make up electroceuticals, which have recently attracted attention as a new treatment technology for intractable chronic diseases, is the neural interfaces. Basically, neural interfaces are implanted in the body, so high safety and reliability are required. In order to increase safety, it is fabricated based on flexible materials, and polyimide is used as one of the representative materials. Concerning reliability, it is demanded at first to improve the adhesion and electrical characteristics of the metal thin film deposited on the polyimide. For these purposes, it is common to approach by increasing surface roughness by attaching additional materials such as nanoparticles on deposited metal thin film or surface treatment method of fully cured polyimide. However, as a result, there is a limit to the characteristic retention period after the improvement of the adhesion with the metal thin film and the electrical properties. Accordingly, this paper presents a way to improve the mechanical/electrical properties of metal thin films by adjusting process steps and the curing conditions of PSPI (Photosensitive Polyimide), which is frequently used to implement flexible neural interfaces.

P-S12-26-T4 Eco-friendly transparent silk fibroin radiative cooling film for thermal management of optoelectronics

Ms. Ching Wen Hwang [1], ***Ms. Yu-Hsuan Chen*** [1], ***Prof. Dehui Wan*** [1]

1. *National Tsing Hua University*

Although transparent radiative cooling is a passive cooling strategy with practical applications and aesthetic appeal, complex manufacturing processes and the use of environmentally unfriendly thermal emitters remain latent problems. Herein, we developed eco-friendly transparent silk radiative cooling (TSRC) films, regenerated from natural silkworm cocoons, for zero-energy-consumption thermal management of optoelectronic devices. These TSRC films could dissipate heat radiatively through molecular vibrations of the protein backbone and side chains, while retaining the function and appearance of the associated devices, due to their high visible transparency. Theoretical and experimental investigations revealed that the thermal emission increased rapidly upon increasing the film thickness, but slowly thereafter to achieve saturation; nevertheless, the intrinsic solar absorption of silk in the ultraviolet and near-infrared regions also grew linearly, unavoidably weakening the cooling effect. After spectroscopic optimization, we improved the maximum cooling power during the daytime and nighttime to 77.6 and 101.7 W/m^2, respectively. Gratifyingly, the films had a remarkable effect on the cooling performance of electronic devices under sunlight. For example, the TSRC film provided a temperature drop of 5.1 °C for a smartphone during multitasking and charging, and 14 °C for a silicon solar panel with an improvement in the photoelectronic conversion efficiency (ca. 7%).

P-S12-27-T4 Effects of copper surface roughness on inkjet printing of PCB resist ink

Mr. KWON YONG SHIN [1], ***Dr. Sang-Ho Lee*** [1]

1. *Korea Institute of Industrial Technology*

The inkjet printing process is being considered as an alternative to dry film-based photolithography in the printed circuit board (PCB) manufacturing industry. Recently, several solder resist inks and etch resist inks for inkjet have been developed and commercialized for PCB production. Two types of copper foils are commonly used in PCB manufacturing: Electrodeposited and Rolled-annealed copper. Generally, copper foil surface is etched to be rougher to improve adhesion when laminated. It is an important study to investigate the uniform inkjet printing quality on the various copper surface roughness to apply the resist inks to PCB production. We investigated the effects of copper surface roughness on inkjet printing of resist inks. Three copper foils with different surface roughness and a solder resist ink were prepared. The printed resist ink showed different spread on the surface morphology and roughness, which affects the printing quality of the solder resist pattern. The printed solder resist ink pattern shows irregular edge profile and non-uniform thickness by increase of the surface roughness. For the copper foil of the lowest surface roughness, the average thickness and standard deviation was 6.16 ± 0.68 ㎛ and the thickness uniformity (CV) was 11.0.

P-S12-28-T4 On chip synthesis of Ag nanoparticles assisted by resonating microwave heating using a post-wall waveguide

Mr. Kaito Fujitani [1], ***Mr. Hiroshi Nakamura*** [1], ***Dr. Akinobu Yamaguchi*** [1], ***Dr. Mitsuyoshi Kishihara*** [2], ***Dr. Yuichi Utsumi*** [1]

1. *University of Hyogo,* ***2.*** *Okayama Prefectural University*

We demonstrated continuous on-chip synthesis of Ag nanoparticles by resonating microwave heating in a microchannel embedded in the post-wall waveguide designed to confine 24.125 GHz microwave radiation. This post-wall waveguide comprises metal columns (post-wall) instead of a conductor sidewall and easily introduces microchannels through the gaps between the metal columns. The waveguide length has been adjusted to achieve a resonance frequency of 24.125 GHz using the electromagnetic wave simulation, assuming the microchannel is filled with pure water. When microwaves with an input power of 4 W, a maximum temperature increase of 94 °C is observed, the result is about 12 °C higher than that of a microchip with non-resonant structures. In addition, using this system, we obtained Ag nanoparticles with about 20 nm by resonating microwave irradiation while controlling the flow rate at 0.7 μL/min. We evaluated the synthesized particle size using dynamic light scattering measurement. This estimated size is well correlated with the absorbance spectra results. Not only the precision synthesis of nanoparticles but also the high efficiency and automated chemical synthesis combined with multi-chemical unit operations are expected to be substantialized using this microwave microfluidics enhanced by the effect of microwave resonance.

Track3 - Micro/Nano Engineering for Life Sciences / Track4 - Micro/Nano Engineering for Physical and Chemical Applications

O-S63-T3-1 Electrode Design Using Multi-Material Topology Optimization for Accurate Measurement of Trans-Epithelial Electrical Resistance in Organ-on-a-Chip

Mr. Haruki Goda [1], Mr. Naoyuki Ishida [1], Dr. Kozo Furuta [1], Prof. Kazuhiro Izui [1], Prof. Fred van Keulen [2], Dr. Ken-ichiro Kamei [1], Prof. Toshiyuki Tsuchiya [1], Prof. Osamu Tabata [3], Dr. Yoshikazu HIRAI [1]

1. *Kyoto University,* ***2.*** *Delft University of technology,* ***3.*** *Kyoto University of Advanced Science*

Trans-epithelial electrical resistance (TEER) measurements are used in organ-on-a-chip (OoC) devices to estimate the barrier properties of cell layer. This measurement is performed using impedance spectroscopy based on the four-electrode configuration. Although the measured results are highly dependent on the electrode layout, there is no standard methodology for designing electrodes, that results in incorrect estimation of TEER. We present an electrode design method using a novel topology optimization that enables accurate TEER measurement in OoC. Numerical examples prove the success of maximizing the cell observation area while satisfying the constraint of measurement accuracy, demonstrating its advantage over conventional electrode layouts.

O-S63-T3-2 The dual role of topographical and mechanical cues: a multi-modal platform for in vitro mimicking of cardiac microenvironment

Ms. Denise Pagliara [1], ***Dr. Raffaele Vecchione*** [2], ***Prof. Paolo Antonio Netti*** [1]

1. *Università degli Studi di Napoli "Federico II",* ***2.*** *Istituto Italiano di Tecnologia*

Innovative *in vitro* models are required to better recapitulate the cardiac microenvironment in the study of cardiac functionality and pathology. In fact, the current literature focuses on the introduction of linear pattern for cardiac cells alignment and simple uniaxial stretch for mechanical stimulation, but these solutions are still far from an optimal mirroring of the cardiac tissue. The aim of the presented work is to build an *in vitro* platform able to better mimic the native cardiac features, by combining microfluidics to a multi-modal presentation of mechanical and topographical cues, in the form of biaxial mechanical load and radial micro-patterned structure, respectively. These cues are applied to a HL-1 cardiomyocytes culture to reveal how cells sense both stimuli. Notably, the results demonstrate that the simultaneous presentation of the overmentioned signals better recapitulates the native cardiac microenvironment, resulting in the increased cells response in terms of alignment and migration velocity. In light of this, the platform is able to induce cells rearrangement along with mechanical load, seamlessly recapitulating cardiac physiology and paving the way toward the meticulous investigations of cell-microenvironment synergy.

O-S63-T3-3 Engineering Ultrathin Si Membranes with sub-20 nm Pores at Wafer Scale

Dr. Cian Cummins [1], ***Dr. Sandeep Seema Saseendran*** [1], ***Mrs. Aurelie Humbert*** [1], ***Dr. Lubuna Shafeek*** [2], ***Dr. Salvatore Bagiante*** [3], ***Dr. Lucas Lindeboom*** [4], ***Dr. Fokko Wieringa*** [4], ***Dr. Roberto Garcia van der Westen*** [4], ***Dr. Swathi Suran*** [4], ***Dr. Jeroen Vollenbroek*** [5], ***Dr. Geert Langereis*** [4], ***Dr. Patrick van Deursen*** [4], ***Dr. Simone Severi*** [1]

1. *imec v.z.w.,* ***2.*** *ISTA,* ***3.*** *Institute of Science and Technology Austria (ISTA),* ***4.*** *Imec The Netherlands,* ***5.*** *University of Twente*

Ultrathin silicon membrane device layers with monodisperse nanopore geometries open exciting opportunities to manipulate, measure and detect species at the molecular level. In this work, we present a robust integration approach from imec's 200 mm fab producing 100 nm thick Si membrane device layers. The Si membranes are composed of dense 20 nm pore sizes patterned by block copolymers. Our technology development will be discussed with a view to possible applications in life science and sensing domains.

O-S63-T4-4 Focused gold ion beam for the fabrication of sub-100 nm length InGaZnO thin film transistors on flexible substrates

Dr. Elia Scattolo [1], ***Ms. Federica Catania*** [2], ***Mr. Alessandro Cian*** [1], ***Dr. Niko Muenzenrieder*** [2], ***Dr. Giuseppe Cantarella*** [3], ***Prof. Paolo Lugli*** [2], ***Prof. Luisa Petti*** [2], ***Mr. Damiano Giubertoni*** [1]

1. *FBK, Fondazione Bruno Kessler,* ***2.*** *Free University of Bozen,* ***3.*** *University of Modena and Reggio Emilia*

The utilization of metal oxide semiconductors, particularly indium-gallium-zinc oxide (IGZO), for the development of thin-film electronics on flexible substrates, holds significant promise in advancing lightweight and flexible systems. Although IGZO devices offer advantages in large-area fabrication, low-temperature manufacturing, and electrical performance, the relatively low carrier mobility of IGZO thin film transistors (TFTs) poses a limitation for high-speed data transmission and communication applications. To overcome this challenge, various scaling strategies have been employed to produce IGZO TFTs with ultra-thin channel lengths.

In this study, we present a novel approach to fabricate ultra-scaled IGZO TFTs on a free-standing polyimide foil by utilizing gold ion (Au+) focused ion beam (FIB) milling for metal contact patterning. The optimization of beam parameters was crucial to prevent ion contamination and damage to the underlying IGZO layer. By employing an Au+ beam accelerated at 35 kV, with a beam current of 8.2 pA and an ion fluence of 6000 μC/cm², we achieved a channel length of 78 nm. The reduction in channel length through FIB milling resulted in a remarkable carrier mobility of 3.06 $cm^2\ V^{-1}\ s^{-1}$ dand a drain current value of 685 μA at a gate-source voltage of 12 V.

O-S63-T4-5 PEDOT:PSS deposition in OECTs: inkjet printing, aerosol jet printing and spin coating

Ms. Giorgia Rinaldi [1], ***Dr. GIUSEPPE TARABELLA*** [2], ***Dr. Pasquale D'Angelo*** [2], ***Dr. Simone Luigi Marasso*** [2], ***Prof. Matteo Cocuzza*** [1], ***Prof. Fabrizio Pirri*** [1], ***Dr. Matteo Parmeggiani*** [1]

1. *Politecnico di Torino,* ***2.*** *CNR*

Additive manufacturing techniques have been developed to overcome the costly and complex silicon-based technologies and to be able to design electronics on flexible and plastic substrates. Furthermore, great interest has raised around organic electronic materials, due to their tunable electrical properties.
This work addresses for the first time the comparison of ink-jet printing, aerosol jet printing and spin coating for the deposition of an organic semiconductor, namely PEDOT:PSS, for OECT channels.
The devices were tested recording both transfer and output characteristics in a sodium chloride solution, effectively identifying aerosol jet printing as the method providing the best results.

Poster Session2.1: Track 2

P-S21-01-T2 Hollow Silicon-based Microneedle Array for Dermal Interstitial Fluid Extraction Fabricated by Only Dry Etching in Wafer Scale

Mr. Ali Gilani [1], ***Dr. Hervé Elettro*** [2], ***Mr. Nicolas Humblot*** [2], ***Prof. Adrian Mihai Ionescu*** [3]

1. *Ecole Polytechnique Federale de Lausanne (EPFL),* ***2.*** *xsensio,* ***3.*** *EPFL*

This study presents a dry etching technique for the fabrication of silicon-based hollow microneedle arrays (HMNAs) that are suitable for extracting dermal interstitial fluid (ISF). The proposed technique enables the production of long, sharp, and hollow needles with a length of ~500 µm on a 1mm thick silicon wafer. The holes in the needles have a size of 100 µm, allowing for efficient biofluid extraction. The fabrication process involves using a thick layer of silicon oxide as a dry etch mask on both sides of the silicon wafer. Needle formation is achieved on the front side, followed by hole formation from the backside using deep reactive ion etching. The sharpness of the needles is enhanced through careful optimization of the etching process. Mechanical endurance and ISF extraction capabilities of the HMNA are evaluated by inserting the needles into chicken meat, resulting in the successful extraction of 5 µL of ISF in 10 minutes. The study demonstrates the feasibility of the proposed HMNA fabrication technique and its potential for extracting ISF for diagnostic purposes.

P-S21-02-T2 Energy Efficient Coloration of Solar Panels

Mr. Oskar Darselius Berg [1], ***Mr. Markus Babin*** [2], ***Ms. Irina Vyalih*** [3], ***Ms. Nanna Lysgaard Andersen*** [2], ***Prof. Morten Madsen*** [3], ***Mr. Peter Behrensdorff Poulsen*** [2], ***Mr. Sune Thorsteinsson*** [2], ***Mr. Jan Stensborg*** [1]

1. *Stensborg A/S,* ***2.*** *DTU Electro, Department of Electrical and Photonics Engineering, Technical University of Denmark, Kgs. Lyngby, Denmark.,* ***3.*** *The University of Southern Denmark, Mads Clausen Institute*

The potential of using Distributed Bragg Reflectors on a foil to selectively reflect wavelengths while maintaining the efficiency of solar cells hidden behind it in the module provides great promise for colored solar cell module integration. This concept allows for widespread integration in cities, and everywhere a black solar module would provide a stark unwanted contrast to the surroundings.

ColorFoil achieves this by stacking dielectric layers using magnetron sputtering onto an index-matched sheet. Therefore, the sheet optically disappears into the encapsulant of the PV module-stack while selectively reflecting a narrow collection of wavelengths. Further enabling us to custom design specific colors, matching conventional colors of the built environment like “tile red”, “brick yellow” and “forest green”.

A reflection of a narrow selection of wavelengths does however pose challenges to color-perception. An increased viewing angle will red-shift the narrow peak to generate different coloration at high-, and even moderate angles. Using structured surfaces created with Stensborg’s Rolling NanoImprint Lithography (R-NIL) process, scattering widens the narrow reflection. This generates the perception of a wide reflection peak while maintaining the high efficiency of the solar cell.

In summary, colored solar modules can be completely integrated with buildings without significant performance loss.

P-S21-03-T2 Heavy metal ion detection by an impedance sensor based on Platinum nanoparticles/DNAzymes network

Dr. Evangelos Aslanidis [1], Dr. Evangelos Skotadis [1], Ms. Georgia Tzourmana [1], Ms. Chryssi Panagopoulou [1], Ms. Annita Rapesi [2], Dr. George Tsekenis [2], Dr. STAVROS CHATZANDROULIS [3], Prof. Dimitris Tsoukalas [4]

1. *Department of Applied Sciences, National Technical University of Athens, Zografou 15780, Greece,* ***2.*** *Biomedical Research Foundation of the Academy of Athens, Athens 11527, Greece,* ***3.*** *Institute of Nanoscience and Nanotechnology, NCSR Demokritos, Aghia Paraskevi 15341, Attiki, Greece,* ***4.*** *National Technical University of Athens*

In this work, we investigate the impedance response of a platinum nanoparticle (Pt NPs) network based biosensor featuring two distinctive DNAzymes species of different chemical modification groups (i.e amino and thiol modified), which enable their attachment on the Pt NP layer. The impedance Pt NP sensor fabrication process starts with the formation of two gold interdigitated electrodes with an electrode gap of 10 μm formed on oxidized silicon substrates. Pt NPs were then deposited using a modified DC magnetron system. A Pt NPs network sensor has proven to be a very effective platform for several applications while with the incorporation of DNAzymes they can detect heavy metal ions showing good sensitivity by monitoring the sensor's resistance response. The DNAzymes were functionalized onto the Pt NPs network. DNAzymes are double-stranded DNA engineered to catalyze to single-stranded DNA in the presence of the element to be detected. This change in DNAzymes modifies the overall sensors' impedance. The results shown that both techniques present a linear response range, for maximum concentrations up to 160 nM and 200 nM in the case of thiol and amino modified DNAzymes respectively. The devices also exhibit a great low limit of detection (LoD) of 12.5 nM.

P-S21-04-T2 Fabrication of Silicon nano-pillars to enlarge their implementation in future integrated circuits and systems

Dr. Alberto del Moral [1], ***Mr. Raul Ramos*** [1], ***Dr. Borja Sepúlveda*** [1], ***Dr. Esteve Amat*** [1]

1. *Institute of Microelectronics of Barcelona (IMB-CNM-CSIC)*

Vertical structures with high aspect ratio are being considered as future device configuration to be implemented in integrated circuits (ICs). Silicon nanowire-based transistors (NW) are promising architectures to achieve further gate length scaling down to 5 nm. Therefore, their device integration can yield new pathways for further ICs miniaturization. In this work, two fabrication processes for vertical architectures are presented based on different etching procedures: Reactive Ion Etching (RIE) and Metal Assisted Chemical Etching (MACE). The manufacturing process of vertical nano-pillars with a high aspect ratio is presented, including the strategies for its further implementation in ICs and CMOS devices.

P-S21-05-T2 Dual photoresist maskless UV photolithography process to fabricate 3D suspended microstructures for pyrolytic carbon microelectrodes

Mr. Mohammad Ramezannezhad [1], ***Prof. Babak Rezaei*** [1], ***Prof. Stephan Sylvest Keller*** [1]

1. *Technical University of Denmark*

SU-8 is a well-known negative tone resist which can be easily utilized to fabricate 3D microstructures, especially with pillars pattern. Also, it is possible to convert it into conductive carbon during a pyrolysis process at high temperature and use it as carbon microelectrode . It has always been a massive challenge to enhance the surface area of electrodes leading to higher signal and better performance. However, it is also possible to build a suspended layer on the top of the pillars to add even more surface area to the electrode. There have been few studies regarding 3D microelectrodes with a suspended layers. However, none of them was based on maskless lithography (MLA) approach which is a straightforward, and high throughput approach with flexibility in changing designs to pattern resists with a micron-scale resolution. In this study, fabrication of 3D suspended microstructure based on SU-8 and mr-DWL photoresists with maskless UV photolithography including addressing the suspended layer thickness is presented.

P-S21-06-T2 Mass Spectrometry by Single Mode Nanoelectromechanical Systems at Atmospheric Conditions

Mr. Batuhan E. Kaynak [1], Mr. Mohammed Alkhaled [1], Ms. Enise Kartal [1], Dr. Cenk Yanik [2], Prof. Mehmet Selim Hanay [1]

1. *Bilkent University,* ***2.*** *Sabanci University*

Nanoelectromechanical Systems Mass Spectrometry (NEMS-MS) is an emerging technique that is well-suited for measuring analytes that are challenging to measure with conventional mass spectrometry. Recent advances include conducted NEMS-MS at atmospheric conditions with unparalleled capture efficiencies. When the NEMS device is operated in air, it experiences dissipation, which poses challenges in utilizing the two-mode theory to accurately determine the mass and position of the landing analytes. The Paddle NEMS architecture has been developed to allow mass measurement using a single mode. The new NEMS device features a platform section with a uniform mode shape, allowing for direct correlation between the mass of the analyte and the frequency shift caused by its landing on the sensor. This eliminates the need for complex calculations and corrections associated with altered mode shapes in atmospheric conditions. Experimental validation confirmed the uniform mode shape and demonstrated the capability of the Paddle NEMS devices to measure nanoparticles with a single mechanical mode. The results highlight the potential of Paddle NEMS for mode shape independent mass sensing in atmospheric pressure NEMS-MS systems.

P-S21-07-T2 Tuneable refractive index polymer waveguides for photonic sensor platforms using wavelengths from 400 nm to 1650 nm.

Mr. Harry Biller [1], ***Dr. Mandy Sendel*** [1], ***Dr. Maik Gerngroß*** [1], ***Mr. Matthias Schirmer*** [1], ***Mr. Robin Kraft*** [2], ***Mr. Crispin Zawadzki*** [2]

1. *Allresist GmbH,* ***2.*** *Fraunhofer Heinrich Hertz Institute*

The PolyChrome Berlin research alliance provides a microchip platform for the realization of hybrid optical devices for use in sensing and analysis.
This microchip platform is based on a wide wavelength range from 400nm – 1650nm and the interaction of polymer and silicon nitride based optical waveguides in combination with hybrid integration.
The Polymer-based waveguides can be directly patterned into core-cladding structures using a negative tone photolithography mask.
To improve the performance of polymer waveguides, we are investigating the optimization of waveguide material compositions and refractive index engineering. The challenges are to achieve a sufficiently high refractive index contrast for the core and cladding, and to match the refractive index of the silica optical fiber for low coupling losses and attenuation.
We demonstrate waveguide polymers with tunable refractive index in the range n=1.41 to 1.49 with feature sizes of 1.0 µm core structures and attenuation of 1.0 dB/cm at 1550nm. Further research is underway to optimize the attenuation with a target of 0.5 dB/cm and to improve the long-term stability of the waveguide for the use of 400nm light sources.

P-S21-08-T2 A Method for the automated Replication of Diffractive Optical Elements with Strong Curvature

Mr. Constantin Rödel [1], ***Mr. Paul Kastl*** [1], ***Dr. Stefan Kühne*** [1], ***Mr. Johannes Wolf*** [2], ***Dr. Thomas Krist*** [3], ***Prof. Dirk Oberschmidt*** [1]

1. *Technische Universität Berlin,* ***2.*** *micro resist technology GmbH,* ***3.*** *NOB nano optics berlin GmbH*

Until now, replication of diffractive optical elements (DOEs) was limited to planar or weakly curved geometries. Strongly curved DOEs, with radii of curvature in the range of a few centimetres, significantly reduce the size of spectral devices by combining diffractive and imaging properties. Additionally, they reduce the alignment effort and the number of optical interfaces, thus increasing the system's efficiency.
In collaboration with Nano Optics Berlin NOB GmbH and micro resist technology GmbH, a device for the automated replication of strongly curved diffractive optics was developed at the TU-Berlin. This involves a multi-step thin-film replication process from ultra-precision manufactured masters into UV-curable hybrid polymers.
Two methods have been developed for the adjustment in six degrees of freedom in order to create a uniform gap and combat shrinkage of the hybrid polymer during curing. The mold halves are adjusted in x, y and c via optical means using measurement marks and Moiré-Fringes. Adjustment in a, b and z is done with a load cell array. Measurements
of microfeatures with an atomic force microscope show high accuracy of replica. Single order surface line scans on a scatterometer produce comparable intensity profiles. The transfer to industrial application is currently in preparation.

P-S21-09-T2 Batch Fabrication of nanoscale fin-type FETs using thermal Scanning Probe Lithography

Dr. Armin Knoll [1], ***Dr. Jana Chaaban*** [2], ***Dr. Nicholas Hendricks*** [2], ***Dr. Emine Cagin*** [2], ***Dr. Chloé Bureau-Oxton*** [1], ***Dr. Heiko Wolf*** [1], ***Mr. Daniel Widmer*** [1], ***Ms. Ute Drechsler*** [1]

1. *IBM Research Zurich,* ***2.*** *Heidelberg Instruments Nano AG*

Thermal Scanning Probe Lithography (t-SPL) has become a commercially available tool for the fabrication of simple nanoscale devices. The next important step of the technology is to demonstrate reliable batch fabrication of complex devices on chip to wafer scale.
Here we present our work towards batch fabricating arrays of field effect transistors on SOI substrates. Two innovations facilitate the task: 1) We use amorphous silicon in the transfer stack to absorb the laser light. This local heat source enables much faster writing of > 500 µm/s, and a much better line definition in laser written fields. 2) For gate overlay patterning the tool has to work on topography. Using the modeled resist thickness and measured topography, the tool subtracts the topography and adapts the write force according to the layer thickness. Thus, it operates as if it would pattern on a flat surface and all feedback loops can be applied. As a result, the tool precision and endurance is greatly enhanced. Devices with channel width down to 20 nm and gate overlay errors < 10 nm are demonstrated.

This work is an important step for t-SPL to develop towards a high precision, damage free, and fully automated lithography tool.

P-S21-10-T2 Low-cost nanostructures for contactless structural monitoring

Dr. Javier Bravo Larrea [1], ***Mr. Julio Peña*** [1]

1. *NAITEC*

In this work we use a combination of NIL and inkjet printing for reducing dramatically the cost of the nanostructured strain sensors for structural health monitoring. Laser interference lithography is used to obtain the original master with periodicity of the nanostructure easily tunable between 200 nm and 800 nm. From this master, multiple nanostructured are obtained by NIL and inkjet, and use as contactless strain sensors for structural health monitoring. The advantage of these labels compared to the ones obtaines by self-assembly or soft lithography is that all the light is reflected from the surface and the light does not interact with the material that is analized. Besides, the nanostructured surface is protected from the external environment.

P-S21-11-T2 Al-SWG reflectors for tuneable VIS filters and spectroscopy applications

Dr. Christian Helke [1], ***Mr. Christian Behl*** [2], ***Dr. Regine Behlert*** [2], ***Ms. Susanne Hartmann*** [3], ***Mr. Micha Haase*** [4], ***Dr. Jörg Martin*** [2], ***Dr. Danny Reuter*** [2], ***Dr. Karla Hiller*** [5]

1. *Fraunhofer ENAS, Technologie Campus 3, 09126 Chemnitz,* ***2.*** *Fraunhofer ENAS,* ***3.*** *Technische Universität Chemnitz, Center for Microtechnologies, Reichenhainer Str. 70, 09126 Chemnitz, Germany,* ***4.*** *Fraunhofer Institute for Electronic Nano Systems,* ***5.*** *Fraunhofer ENAS; Technische Universität Chemnitz, Center for Microtechnologies, Germany*

The authors present a subwavelength grating (SWG) reflector that provides a fixed reflector in a tunable Fabry-Pérot-Interferometer (FPI). It consists of a 25 nm thin aluminum layer that is nanostructured with 140 nm Al patches and a 200 nm pitch on 2 mm circular dies for the VIS range.

The manufacturing realized on 6” glass wafers by deposition of the 25 nm aluminum layer followed by electron beam lithography and etching. The exposure was carried out with a 50-keV-eBeam lithography tool Vistec SB254. The negative tone resist ma-N 1402 from Micro Resist Technology GmbH was exposed with 150 µC/cm² and 170 µC/cm² with a sizing factor of 20 nm, 10 nm and 0 nm. The pattern is transferred into the 25 nm aluminum layer by a chlorine dry RIE process (Sentech SI800 tool). The fabricated SWG reflectors show different CDs regarding their sizing factor.
Furthermore, we will present the dependency of the reflectance with respect to their fabricated CD, the sizing factor and the integration technology for MOEMS related applications. Exemplarily, the measured reflectivity is above 70 % for wavelengths > 550 nm and increases up to 85 % for wavelength 1000 nm.

P-S21-12-T2 Characterization of hybrid nanowire-MEMS force sensors using direct actuation

Mr. Bartosz Pruchnik [1], Mr. Krzysztof Kwoka [1], Dr. Tomasz Piasecki [1], Mr. Masoud Jedari Ghourichaei [2], Dr. Mehrdad Karimzadehkhouei [3], Mr. Cemal Aydogan [4], Prof. Ivo W. Rangelow [5], Prof. Halil Bayraktar [6], Prof. B. Erdem Alaca [2], Prof. Teodor Gotszalk [1]

1. *Department of Nanometrology, Wrocław University of Science and Technology, Wroclaw, 50-370, Poland,* ***2.*** *Department of Mechanical Engineering, Koç University, Istanbul, 34450, Turkey,* ***3.*** *Dept. of Mechanical Engineering, Koç University, Istanbul, 34450, Turkey,* ***4.*** *Institute of Micro- and Nanoelectronics, Ilmenau University of Technology, Ilmenau, 98693, Germany,* ***5.*** *Technische Universität Ilmenau,* ***6.*** *Dept. of Molecular Biology and Genetics, Istanbul Technical University, Maslak, Istanbul, 34467, Turkey*

We present the results of the GF characterization of novel hybrid planar force sensors including silicon nanowires using direct actuation method. Force sensor consists of the movable shuttle suspended on 8 springs and 4 sets of the nanowires allow ing to detect the magnitude and the direction of the force applied to the shuttle. We demonstrate the set-up and analysis of the the direct actuation method using nanomanipulators inside the SEM microscope chamber. The SEM was used for measuring the magnitude of the displacement of the shuttle. The response of the sensor to the shuttle movement along and perpendicular to the nanowire orientation were presented.

The analysis of the mechanical setup showed that to evaluate the gauge factor mechanical compliance of the chip mounting system has to be taken into account and carefully evaluated to achieve proper GF values. The nanowires in the sensor exhibited the GF of 20 which may be improved with the manufacturing process modification.

P-S21-13-T2 Understanding of Ta doping effect into the Sb2Te3 for high-speed phase change memory

Mr. jaemin park [1], ***Mr. sucheol ju*** [1], ***Prof. heon lee*** [1]

1. *korea university*

Phase change memory is highlighted as a leading candidate for storage class memory. In this study, a high-performance phase change memory material was designed for doping engineering of Ta element inside Sb2Te3. To optimize the Ta doping concentration, Ta doped Sb2Te3 with various concentrations was fabricated using a sputtering process. The phase change characteristics of the fabricated Ta-doped Sb2Te3 films of various concentrations were analyzed, and the crystallographic, structural, and electrical Ta doping effects inside Sb2Te3 were analyzed. By analyzing the Ta doping effect on Sb2Te3, it was shown that the crystallization temperature of the Sb2Te3 phase change material was increased and the grain growth was suppressed, thereby affecting the electrical conductivity. Through this, we demonstrated the optimized Ta doping concentration as a phase change memory material. A phase change memory was fabricated using optimized Ta0.41Sb2Te3 and confirmed to have fast set speed and low resistance drift characteristics. Through this study, the Ta doping effect of Sb2Te3 was closely analyzed and the optimal Ta doping concentration was demonstrated. It was confirmed that Ta-doped Sb2Te3 is a high-performance phase-change memory material applicable to next-generation storage class memory.

P-S21-14-T2 Direct Vacuum Wafer Bonding for 1310 nm Bidirectional Tunable MEMS VCSEL

Mr. Masoud Payandeh [1], ***Dr. Hitesh Kumar Sahoo*** [2], ***Dr. Elizaveta Semonova*** [2], ***Prof. Kresten Yvind*** [2]

1. *Technical university of Denmark,* ***2.*** *Technical University of Denmark*

Microelectromechanical system (MEMS) vertical cavity surface emitting lasers (VCSELs) have shown great promise as a light source for optical coherence tomography (OCT), mainly due to their small footprint, low power consumption, and potential for integration with endoscopes and other medical devices. MEMS VCSELs consist of three main parts, an active region that is sandwiched between two highly reflective mirrors. The actuation of one of these mirrors contributes to changing the length of the optical cavity and thus allows continuous tuning of the emitting wavelength. Achieving a high-speed ultra-broad tuning range MEMS VCSEL for swept source-OCT at 1300 nm could have significant implications for medical imaging, particularly in endoscopic settings where real-time 3-D imaging of large tissue volumes is critical. In this work, key results will include the achievement of novel optically pumped MEMS VCSEL devices with a tuning range larger than 100 nm at 1300 nm. To achieve such a tunable source for OCT, high-yield direct wafer bonding of SOI wafer to InP wafer is essential. We developed a process to achieve smooth clean bonding surfaces to improve direct vacuum wafer bonding.

P-S21-15-T2 Encapsulation Strategy for Ultrathin Electronics Incorporated in a Flexible Polymer Film

Mrs. Ulrike Passlack [1], ***Mr. Nicolai Simon*** [2], ***Prof. Volker Bucher*** [2], ***Dr. Christine Harendt*** [1], ***Prof. Joachim Burghartz*** [1]

1. *Institut für Mikroelektronik Stuttgart (IMS CHIPS),* ***2.*** *Institute for microsystems technolgoy (iMST)*

Miniaturized ultrathin electronics integrated into flexible polymer films for monitoring vital parameters or recording nerve signals are of particular interest in the medical sector. Reliability and longevity are paramount, especially for implantable systems that need to last as long as possible and withstand harsh environments.
This work summarizes the manufacturing of ultrathin systems-in-foil (SiF) and addresses critical process steps that contribute to system reliability. Because polyimide (PI) is used as the dielectric in which 30 µm back-thinned chips and sensors are embedded, an encapsulation strategy is required, as PI does not have high diffusion barrier to moisture or ions. Two methods, ceramic nanolaminates deposited by an atomic layer deposition (ALD) process and a polymer, the benzocyclobutene (BCB) deposited by a spin-coating process, are compared for their suitability with the state-of-the-art Parylene-C encapsulation.

P-S21-16-T2 Fabrication of GST metasurface spectral filters using nanoimprint lithography

Dr. Jorge Ramiro [1], ***Mr. Aritz Juarros*** [1], ***Dr. Rocio Ortiz*** [1], ***Mrs. Alazne Martinez*** [1], ***Dr. Borja Pozo*** [1]

1. *Tekniker*

The electromagnetic radiation received from space varies in spectrum with the relative velocity of the objects and their temperature, allowing the observation depending on the range of the spectrum analyzed. Therefore, it is sometimes desirable to collect light within a restricted wavelength spectrum. This can be done by using a selective filter that transmits or reflects the precise range of wavelengths. In this context, an actively tunable filter would allow imaging of the same object in several spectral ranges, each providing different information. Tunable metasurfaces are one of the best solutions for this kind of filters with operation in space. These filters incorporate active materials which allow their optical properties to be controlled by an external stimulus. Phase change material, such as chalcogenide glasses are examples of active materials used in this type of devices
In this work, in order to obtain tunable metasurfaces to be employed as spectral filters with work range in the infrared, an alternative route has been employed to avoid etching a noble metal (the formation of non-volatile halide products limits the ability to dry etch noble metals with standard equipment and process gases) and to include a more cost-effective technique like the nanoimprint lithography.

P-S21-17-T2 Shape-engineering of 2D TMD semiconductors via thermal-Scanning Probe Lithography

Mr. Giorgio Zambito [1], ***Dr. Matteo Gardella*** [1], ***Prof. Maria Caterina Giordano*** [1], ***Prof. Francesco Buatier de Mongeot*** [1]

1. *University of Genoa*

Two-dimensional (2D) materials have gained increasing interest in recent years, with a huge number of proof-of-concept devices shown for electronics and optoelectronics. The ability to arbitrarily engineer the shape of such materials is appealing, since it allows to obtain tailored optoelectronic responses and/or in-series devices with optimized geometries. In this work, we propose a novel process to additively fabricate deterministic MoS_2 nanocircuits thanks the combination of thermal Scanning Probe Lithography (t-SPL) and physical deposition method based on Ion Beam Sputtering (IBS). The confinement of MoS_2 inside the deterministic nanopatterns is demonstrated via micro-Raman spectroscopy and Kelvin Probe Force Microscopy, as well via a nanoscale electrical characterization via Conductive-AFM analysis. Finally, we show some preliminary results achieved exploiting grayscale lithography to tailor MoS_2 morphology by deterministic conformal transfer of flakes onto patterned polymer films, in order to observe strain-induced effects.

P-S21-18-T2 Room temperature bonding process of polydimethylsiloxane to titanium for biomedical applications

Ms. Lucrezia Maini [1], ***Mr. Roman Furrer*** [2], ***Prof. Christofer Hierold*** [1], ***Dr. Cosmin Roman*** [1]

1. *Micro- and Nanosystems, ETH Zurich, 8092, Switzerland,* ***2.*** *Transport at Nanoscale Interfaces, EMPA, Dübendorf, 8600, Switzerland*

Polydimethylsiloxane (PDMS) is a biocompatible material widely used in the biomedical engineering field for sensors encapsulation. Bonding of PDMS to metals is challenging due to their chemical reactivity. Of particular interest is titanium in the perspective of sensors integration on prostheses. In this work, we present a room temperature bonding process of a PDMS-based acoustic metamaterial membrane to a titanium plate. The sample is inspected through scanning electron microscope (SEM) images and ultrasonic measurements in the high frequency (50 MHz) regime. The results show good uniformity, with a limited amount of air bubbles (<5%) over the surface.

P-S21-19-T2 Harvesting the kinetic energy of raindrops with a microscale triboelectric nanogenerator

Dr. Ali Ghaffarinejad [1], ***Mr. Xabier Casas*** [2]

1. *Sensors and Smart Systems Group, Institute of Engineering, Hanze University of Applied Sciences,* ***2.*** *Consejo Superior de Investigaciones Científicas (CSIC),*

In this communication, we introduce a micro-scale energy converter optimized for harvesting the energy of raindrops. The device converts the kinetic energy of raindrops into electric energy and works based on the principles of triboelectric nanogenerators which employ electrostatic induction for power generation. Compared to other generators with centimeter-scale architecture discussed in the literature, the device does not waste any kinetic energy of falling drops due to its submillimeter design. In fact, the generator accumulates water collection and energy generation steps into a single step. With a total active area of 900 µm by 900 µm (L×L), the converter is the smallest triboelectric nanogenerator reported to date for harvesting the energy of drops. Experimental results show a harvested power of 76 W/m2 which is the highest reported in the literature to the best of our knowledge.

P-S21-20-T2 Scalable meta-projector for wide viewing angle 3D imaging

Mr. Gyeongtae Kim [1], ***Ms. Yeseul Kim*** [1], ***Ms. Jooyeong Yun*** [1], ***Prof. Junsuk Rho*** [1]

1. *pohang university of science and technology*

Unlike conventional cameras, depth cameras that can obtain 3D information of surrounding objects is expected to play an important role in next-generation computer vision. Depending on the purpose of usage, it is evaluated as accuracy, resolution, recognition speed, distance, and viewing angle. Among them, the viewing angle is an important performance in autonomous robots, augmented and virtual reality glasses, that require 3D information of objects located in a wide area ahead. Lidar have been used widely, a method of measuring the distance from the round-trip time-of-flight by scanning a laser light source, but requiring mechanical scanning. Here, we propose meta-projector to illuminate wide viewing angle without scanning, ~10K dot array over 180°, and reconstruct the depth from binocular parallax. Compared to using binocular parallax only, that is passive-stereo, the active-stereo incorporating meta-projector shows advantage on depth reconstruction for low-light environments and texture-less planes. As a proof-of-concept, we place face masks at wide viewing angle and estimate the depth. We demonstrate low-cost production of meta-projector using nanoimprint lithography. Once soft mold is replicated from master meta-projector, the high-index nanoparticles are embedded into UV-curable resin to enhance light manipulation efficiency. Such a scalable meta-projector shows its potential towards compact 3d imaging device.

P-S21-21-T2 Quantitative characterization of nanowire verticality using SEM images

Ms. ELENI STAI [1], ***Dr. Vassilios Constantoudis*** [1], ***Mr. Dimitris Nioras*** [1], ***Dr. Evangelos Gogolides*** [1]

1. *NCSR Demokritos*

During the last few decades, nanowires have been used in various fields of applications from electronics and photonics to bio-devices and energy harvesting systems. One of the critical properties of nanowire patterns is their alignment since it tunes the contact area with the attached body and hence the kind of the interaction that nanowires have with them. For example, when they are perfectly vertical, the contact area with the attached droplet or bacteria is minimized leading to the enhancement of their superhydrophobic or bactericidal behavior. Therefore, the quantitative characterization of nanowire verticality can empower the evaluation of their performance in many applications. In this work, we propose a novel methodology for characterizing quantitatively the verticality of nanowires (NWs) by analyzing top-down or tilted SEM images. The key idea of our approach is to exploit the link between the verticality of nanowires and the anisotropy of their projection on SEM images.

P-S21-22-T2 Permittivity-Based Microparticle Classification through Integration of Impedance Cytometry and Microwave Sensing

Mr. Uzay Tefek [1], ***Mr. Burak Sari*** [2], ***Dr. Hashim Alhmoud*** [1], ***Prof. Mehmet Selim Hanay*** [1]

1. *Bilkent University,* ***2.*** *Sabanci University*

Material identification at the single microparticle level plays a crucial role in environmental screening and advanced material manufacturing. However, current techniques like Raman and FTIR spectroscopy are expensive, non-portable, and time-consuming. High-throughput methods such as resistive pulse sensing lack material characterization. A complementary approach has been the use of high-frequency microwave resonant sensors that directly probe the dielectric permittivity of microparticles by overcoming ion screening effects and serving as a classification parameter.

Direct measurements of the permittivity of individual microparticles have proven to be challenging due to the convoluting effect of particle size on microwave signals. Accurate material classification requires determining the particle's geometric size and compensating for its effect. To address this challenge in measuring permittivity, we integrated a low-frequency impedance cytometry sensor with a high-frequency microwave capacitance sensor in a microfluidic chip. By normalizing the microwave signal using size-only information from impedance cytometry, we obtained a ratio that depends solely on the particle's permittivity.

The integrated sensing platform achieved over 94% accuracy in distinguishing between polystyrene and soda lime glass microparticles, despite their similar sizes and electrical characteristics. This technique has potential applications in environmental monitoring and pharmaceutical quality control. It can also be applied to single-cell analysis.

P-S21-23-T2 Metalenses for generation of Perfect Vortex Beams for telecom infrared applications

Dr. Daniele Bonaldo [1], ***Dr. Andrea Vogliardi*** [1], ***Dr. Gianluca Ruffato*** [1], ***Dr. Simone Dal Zilio*** [2], ***Prof. Filippo Romanato*** [1]

1. *University of Padova,* ***2.*** *CNR-IOM*

Metalenses are changing the way optical systems are designed and built. In the last ten years a lot of research showed their potential and now they should be tuned to a given application domain in order to generate innnovation. Fiber telecom techonology has been advancing Spatial Division Multiplexing as a way of increasing communication capacity, but efficient coupling methods of fibers' Orbital Angular Momentum (OAM) modes are needed. For such a task, the common Laguerre Gaussian beams are not optimal as their beam size increase considerably with OAM, giving bad coupling with a given fiber core size. Perfect Vortex Beams, instead, change slightly with OAM, but their generation is still under development. In this work, metalenses generating Perfect Vortex Beams (PVBs) at a telecom wavelength (1310 nm) have been designed, fabricated and characterized. Devices featured full dielectric silicon meta atoms, whose simultaneous control on propagation and geometric phase allowed for easy generation of two different PVBs and their vector superposition with the same device, depending on the input polarization. Metalenses were fabricated through standard electron beam lithography processes and characterized on a custom optical bench. Results showed generation of high quality PVBs.

P-S21-24-T2 Influence of the combination of ordered 2D and random 3D structures on the reaction of Al/Ni multilayer

Mr. Konrad Jaekel [1], ***Ms. Yesenia Haydee Sauni Camposano*** [1], ***Mr. Sebastian Matthes*** [1], ***Mr. Marcus Glaser*** [1], ***Prof. Jean Pierre Bergmann*** [1], ***Prof. Peter Schaaf*** [1], ***Prof. Jens Müller*** [1], ***Dr. Heike Bartsch*** [1]

1. *Technische Universität Ilmenau*

This study investigates the influence of surface structuring in nano- and micrometer range on the reaction kinetics of Al/Ni reactive multilayer systems. By employing KOH etching as macroscopic and black silicon (bSi) etching as nanoscopic structuring method on (100)-oriented Si wafers, well-defined lines and 3D nanostructures are created. Samples with different line depths (250 nm, 720 nm, and 1600 nm) are prepared and the applied bSi process is varied between 30 and 60 minutes. Following bSi formation, a thermal oxidation step is conducted, and Al/Ni reactive multilayers are deposited. Controlled ignition experiments, where conducted to monitor reaction propagation using a high-speed camera as well as the temperature with high-speed pyrometers. Results indicate that the depth of the 2D line structures influences reaction propagation, while the presence of 3D nanostructures enhances adhesion of the reacted multilayers. Reaction velocity and maximum temperature decrease compared to non-structured surfaces. Surface design emerges as a control parameter for tailored reaction kinetics and controlling reaction propagation in Al/Ni reactive multilayer systems. The findings open avenues for advanced reaction control using surface structuring, with broad implications for diverse applications. Ongoing investigations focus on understanding underlying mechanisms and optimizing nanostructured surface designs to enhance system performance.

P-S21-25-T2 Plasma etching and roughening of inclined objects, macroscopic surfaces and microfluidic channels: experiments and modelling

Dr. Athina S. Kastania [1], ***Mr. Sotiris Mouchtouris*** [1], ***Dr. Angelos Zeniou*** [1], ***George Kokkoris*** [2], ***Dr. Vassilios Constantoudis*** [1], ***Dr. Angeliki Tserepi*** [3], ***Dr. Gerburg Schider*** [4], ***Mr. Daniel Borstner*** [4], ***Mr. Philipp Melchior*** [4], ***Dr. Dieter Nees*** [4], ***Dr. Barbara Stadlober*** [4], ***Dr. Evangelos Gogolides*** [1]

1. *Institute of Nanoscience and Nanotechnology, NCSR "Demokritos",* ***2.*** *School of Chemical Engineering, National Technical University of Athens,* ***3.*** *Institute of Nanoscience and Nanotechnology, NCSR Demokritos,* ***4.*** *Joanneum Research Forschungsgesellschaft MbH*

Plasma processing of polymeric substrates induces surface roughness and its morphology depends on the exact substrate material and the plasma conditions. Substrates horizontally placed on the plasma reactor electrode have been well studied. However, the roughness formation potential on inclined polymeric surfaces inside a plasma reactor (such as microfluidic sidewalls) is not thoroughly investigated. For this purpose, tests are performed on various imprinted polymeric substrates and microfluidics placed at several angles θ with respect to the electrode. SEM imaging demonstrates roughness formation on the inclined etched surfaces, even at high tilting angles, exhibiting different morphology than the horizontal surfaces. A variation in surface roughness versus distance from the electrode is also found almost in all inclination angles –from an anisotropic pattern nearby the electrode to a more isotropic roughness away from it. This change is quantified through 2D Fourier analysis of SEM images. To illuminate this roughness variation, a modeling framework is utilized consisting of a reactor scale model and a Monte Carlo model for the particle trajectories calculation. Preliminary results demonstrate a local variation in ion energy and angular distributions arriving on the inclined surfaces, justifying the experimental observations. Applications include wetting control, regulating cell adhesion etc.

P-S21-26-T2 A Simple Fabrication Process for the Integration of Microfluidics on Si based Biosensors

Dr. Myrto-Kyriaki Filippidou [1], Mr. Aris Kanaris [1], Mr. Evangelos Aslanidis [2], Ms. Annita Rapesi [3], Mr. Sotirios Ntouskas [1], Dr. Evangelos Skotadis [2], Dr. George Tsekenis [3], Prof. Dimitris Tsoukalas [4], Dr. Angeliki Tserepi [1], Dr. STAVROS CHATZANDROULIS [1]

1. *Institute of Nanoscience and Nanotechnology, NCSR Demokritos, Aghia Paraskevi 15341, Attiki, Greece,* ***2.*** *Department of Applied Sciences, National Technical University of Athens, Zografou 15780, Greece,* ***3.*** *Biomedical Research Foundation of the Academy of Athens, Athens 11527, Greece,* ***4.*** *National Technical University of Athens*

Microfluidics technology is the basic technology used to realize Lab-on-Chips (LOCs), such as microlaboratories exhibiting several advantages including small sample volume, reduced analysis time, low manufacturing cost, greater sensitivity, and portability. One of the fields in which LOC devices are particularly useful is environmental monitoring and water pollution caused by heavy metal ions, pesticides or other contaminants which can easily pass in the human food chain. Thus combining of miniaturized microfluidic systems, with the appropriate detection scheme is a very promising tool for water safety and detection of water pollutants. Despite the great progress in the field, the biggest challenge is still the integration of all the necessary components (e.g. microfluidic channels, detection unit, heating elements, electrical connections, etc.) for the operation of the device on the same substrate targeting the realization of a completely autonomous Lab on Chip device which is lightweight, portable, low cost and can be used in both laboratory and on-site measurements. To this end, we present a rapid and simple fabrication method based on photolithography of dry photosensitive layers (dry resist) for the integration of a microfluidic channel network with an electrochemical detection scheme for the detection of water pollutants (e.g heavy metal ions).

P-S21-27-T2 Investigation on the effect of sharp corners of AZO gate and Al2O3 insulator in ZnO Thin Film Transistors

Mr. Jiale Zeng [1], ***Dr. Ben Rowlinson*** [2], ***Dr. Martin Ebert*** [3], ***Prof. Karol Kalna*** [4], ***Dr. Christian Patzig*** [5], ***Mr. Lutz Berthold*** [6], ***Prof. Harold Chong*** [7]

1. *jz2g19@soton.ac.uk,* ***2.*** *bdr1g15@soton.ac.uk,* ***3.*** *me1r18@soton.ac.uk,* ***4.*** *k.kalna@swansea.ac.uk,* ***5.*** *christian.patzig@imws.fraunhofer.de,* ***6.*** *lutz.berthold@imws.fraunhofer.de,* ***7.*** *hmhc@ecs.soton.ac.uk*

Sharp corners in MOSFET architecture can produce a localised high electric field that causes loss of gate control, threshold voltage (V_{TH}) shift, and gate oxide dielectric breakdown. One of the possible gate oxide dielectric breakdown phenomena can be explained by the percolation model, which states that local insulator materials could become conductive when subjected to a high electric field. Our previous research on ZnO thin-film transistors (TFTs) showed a gate leakage current of 2.7 μA and loss of gate voltage bias control beyond drain voltage of 9 V, both of which indicate gate oxide dielectric breakdown characteristics. In this work, combining experimental results and simulation, we confirmed that gate sharp corners can induce a strong electric field on the local dielectric layer, resulting in a loss of gate control and a threshold voltage shift. The simulation also predicts that the TFT can operate up to a gate-drain voltage (V_{GD}) of 70 V without the sharp corner of the AZO gate.

P-S21-28-T2 “Flow-Through”, low-temperature gas phase deposition for conformal coating of ultra-high aspect ratio polymer micro- and nanochannels

Mr. Manuel Müller [1], ***Mr. Jeremy Teuber*** [1], ***Mr. Rukan Nasri*** [1], ***Dr. Robert Zierold*** [1], ***Dr. Irene Fernandez-Cuesta*** [1]

1. *Universität Hamburg*

In this work, we present a method for selective coating of the inner walls of high aspect-ratio polymer micro- and nanochannels with inorganic material (Al_2O_3) by gas phase deposition (GPD) in a “*Flow-Through*” mode. Integrating metals and metal oxides into channel systems offers the introduction of catalytic, electrical, or optical functionalities and mechanical elements not native to the polymer template material. The herein implemented pressure gradient over the channel system sets up novel incubation and evacuation strategies to overcome the limitations of diffusion-based atomic layer deposition (ALD) or line-of-sight-based chemical vapor deposition (CVD). Complementary to the ALD methodology, alternating injections of precursors allow for a controlled growth of the material. However, this work aimed to achieve high growth rates with fast cycle times in high AR structures at reasonable homogeneities due to the utilization of high differential pressures and condensation in the channels. Low temperatures (< 110 °C) requirements for polymers posed an additional challenge for the deposition process. The highest aspect ratio achieved so far for microchannels is 5500, and the smallest channels coated with this method were 50 µm long 500 x 500 nm nanochannels integrated along microchannels with aspect ratio 1100.

P-S21-29-T2 Omega Active Cantilever for traceability of localized functional properties of nanostructures

Mr. Hans-Georg Pietscher [1], ***Mr. Aditya Suryadi Tan*** [1], ***Mr. Fabian Dietrich*** [1], ***Mr. Robert Reichert*** [1], ***Ms. Ewelina Gacka*** [2], ***Mr. Bartosz Pruchnik*** [2], ***Mr. Dominik Badura*** [2], ***Prof. Teodor Gotszalk*** [2], ***Dr. Stefanie Gutschmidt*** [3], ***Prof. Thomas Sattel*** [4], ***Dr. Virpi Korpelainen*** [5], ***Dr. Andrew Yacoot*** [6], ***Dr. Isaac Stricklin*** [7], ***Dr. Tito Busani*** [7], ***Ms. Jaqueline Stauffenberg*** [4], ***Prof. Thomas Fröhlich*** [8], ***Prof. Eberhard Manske*** [8], ***Prof. Ivo W. Rangelow*** [8]

1. *Nano analytik GmbH,* ***2.*** *Wroclaw University of Science and Technology,* ***3.*** *University of Canterbury,* ***4.*** *Ilmenau University of Technology,* ***5.*** *National Metrology Institute VTT MIKES,* ***6.*** *National Physical Laboratory,* ***7.*** *University of New Mexico,* ***8.*** *Technische Universität Ilmenau*

Fast, accurate and traceable High-Speed Scanning Probe Microscopy (HS□SPM) has great potential for use in identifying faulty nano□products across multistage production processes and offers the benefits of increased productivity and reduced wastage. Conventional scanning probe microscopy (SPM) is either too slow to cover large sample areas or if fast, it lacks positioning accuracy. The paper presents a comparison between numerical analysis and experiments of a direct-oscillating thermally driven active cantilever with integrated Wheatstone bridge piezoresistive readout sensors suitable for fast atomic force microscopy (AFM) and scanning probe lithography (SPL) as well as conductive atomic microscopy. Commercial finite element software was used to get the numerical results. In the paper, we present also the comparison between two cantilever shapes, namely the Classical Design and the Omega Design. We also compared the deflection response of both active cantilevers. Finally, an experimental setup based on the commercial AFM of nano analytik GmbH was used and results with respect to sensor sensitivity and piezoresistive Signal/Noise were measured for both Classical Design and Omega-Active cantilever design. AFM image on Celgard® oriented Polypropylene membrane exhibiting precise force control was measured with active cantilever Omega Design. This kind of cantilever is successfully integrated into an NFM-Machine.

P-S21-30-T2 Improving Dynamic Tracking Performance of Nanopositioning Stage for Defect Review System using Iterative Learning Control

Dr. Kyung-Rok Kim [1], ***Dr. HYUNCHANG KIM*** [1], ***Dr. Dongwoo Kang*** [1], ***Dr. Jaeyoung Kim*** [1]

1. *Korea Institute of Machinery & Materials*

A nano-positioning stage is a crucial technologyutilized in various fields such as inspection equipment, optical systems, and AFM[1-3]. In this paper, we apply iterative learning control (ILC) to enhance the dynamic tracking performance across the entire motion. ILC is a method derived from the concept that the performance in subsequent tasks can be improved by leveraging the outcomes of previous tasks [5, 6]. Ultra-precision XY stage is designed to decouple the motion along the x and y axes, a parallel compliant mechanism is designed. ILC is employed in conjunction with the PI feedback control. Scanning in XY plane is conducted by a scan motion in x-axis and step motion in y-axis. The scan motion with a maximum speed of 80μm/s and a constant velocity region of 5μm is given in x-axis while step motion with 80nm grid in given in y-axis. The experimental results obtained using PI control along and PI+ILC control is compared. In both case same PI control gain is applied. The results clearly demonstrate that ILC improved the tracking performance significantly. By applying ILC control, the 3-sigma errors in the x and y axes are reduced to 2.28nm and 3.76nm,

P-S21-31-T2 Soft contact pressure sensors based on randomly rough surfaces

Mr. Luigi Portaluri [1], ***Dr. Luciana Algieri*** [2], ***Mr. Marco Bruno*** [1], ***Prof. Massimo De Vittorio*** [1], ***Prof. Michele Scaraggi*** [1]

1. *Istituto Italiano di Tecnologia; Department of Innovation Engineering, Unisalento,* ***2.*** *Istituto Italiano di Tecnologia*

Nowadays, the availability of advanced rough contact mechanics theories enables the design of soft contact sensors based on randomly-rough surface structural functionalization. The latter is based on facile fabrication processes, when compared to standard microfabrication such as two photon soft lithography. In this work, we have compared the performance of soft contact capacitive sensors based on deterministic micro patterning with respect to the newly-developed random interfaces . The latter show superior sensitivity with respect to the former, as expected from the multiscale nature of the random roughness.

P-S21-32-T2 Etch residuals after dry etching AlN with CH4/BCl3/Ar over photoresist and overlapping metal layer

Mr. Nils Dittmar [1], ***Dr. Chris Stöckel*** [1], ***Mr. Micha Haase*** [1], ***Dr. Danny Reuter*** [1]

1. *Fraunhofer Institute for Electronic Nano Systems*

A dry etching process for AlN over photoresist was developed. The selectivity between AlN and photoresist was adjusted by the flow rate of CH4. The gas flow of other etching gases (BCl3 and Ar) were held constant. It was shown that a higher rate of CH4 creates thicker polymers on sidewalls. Using the etching process with 5 sccm CH4 for structuring AlN with overlapping metal generates peeled-off strings on the sidewalls and back-sputtered metal on top of the sidewalls. Both kind of residuals were treated with O2 plasma, which removed some of the residuals. Other means to completely remove the residuals were not successful.

P-S21-33-T2 Dimensional and mechanical control of submicrometric fibers using two-photon polymerization

Mr. Ianis DROBECQ [1], ***Mrs. Ophélie Thomas-Chemin*** [1], ***Mr. Pierre-Francois Calmon*** [1], ***Prof. Laurent Malaquin*** [1], ***Dr. Bastien Venzac*** [1]

1. *LAAS-CNRS*

In vivo, the extracellular matrix (ECM) surrounding cells exhibits fibrillary architecture whose biochemical, structural, and mechanical properties greatly influence cellular behaviours. Testing *in vitro* these mechanical contributions require the creation of microstructures reproducing the mechanics of the ECM, from individual fibre to more complex architectures. We investigated the fabrication of suspended fibres using 2PP with a Nanoscribe printer (Photonics professional GT2) and IP-Dip resin and performed a systematic study of the impact of process parameters on fibre dimensions using scanning electron microscopy (SEM). According to the beam theory, the spring constant strongly depends the lateral dimension of the fibres: a 10% relative error in the width of a fibre can change the spring constant by 45%. We are currently performing mechanical measurement by atomic force microscopy (AFM) on clamped-clamped square beams to correlate spring constants and dimensions. We simulated their deflections on Comsol software and found good accordance with the theory.

P-S21-34-T2 Microfabrication and Silicon Integration of Epitaxial Magnetic Shape Memory Films

Mr. Satyakam Kar [1], ***Mr. Lukas Fink*** [2], ***Prof. Kornelius Nielsch*** [1], ***Dr. Sebastian Fähler*** [2], ***Dr. Heiko Reith*** [1]

1. *Leibniz Institute for Solid State and Materials Research Dresden,* ***2.*** *Institute of Ion Beam Physics and Materials Research, Helmholtz-Zentrum Dresden-Rossendorf (HZDR)*

Magnetic shape memory alloys are an emerging class of smart materials that combine ferroelastic and ferromagnetic transitions to generate multifunctional properties like magnetic field induced actuation, multicaloric cooling, and thermomagnetic energy harvesting. These effects have been primarily studied in bulk and single-crystal systems. However, while progress has been made in understanding these effects, their application and integration in microsystems present two key challenges. Firstly, the suitability of microfabrication techniques for their films have not been investigated in detail. Secondly, the epitaxial growth of these films is until now only possible on expensive single crystal oxide substrates that are incompatible with state-of-the-art silicon microsystem technology.

In the current study, we address these challenges by investigating the microfabrication and silicon integration of epitaxial Ni-Mn-Ga-based Heusler films. We show that reactive ion etching of Ni-Mn-Ga films is unsuitable due to redeposition and the best results are obtained by ion-beam etching with adjusted sample-stage tilt. Finally, we demonstrate epitaxial integration of Ni-Mn-Ga films on Silicon substrate using a 4 nm $SrTiO_3$ buffer. This approach allows monolithic fabrication of partly freestanding structures using Silicon microtechnology.

P-S21-35-T2 Dependence of Structural Design on Effective Young's Modulus of Ti/Au Multi-Layered Micro-Cantilevers for MEMS Capacitive Accelerometers

Mr. Shunkai Watanabe [1], ***Dr. Tomoyuki Kurioka*** [1], ***Prof. Mark Chang*** [1], ***Dr. Chun-Yi Chen*** [1], ***Mr. Akira Onishi*** [1], ***Dr. Parthojit Chakraborty*** [1], ***Prof. Katsuyuki Machida*** [1], ***Prof. Hiroyuki Ito*** [1], ***Prof. Yoshihiro Miyake*** [1], ***Prof. Masato Sone*** [1]

1. *Tokyo Institute of Technology*

Gold materials are promising toward movable components in MEMS (micro electromechanical systems) capacitive accelerometers due to the high mass density. To enhance performance and achieve further miniaturization of the MEMS device, we focused on gold with a high mass density. Metallic materials are known to show the sample size effect, and mechanical properties may differ between bulk and microscale. Hence, it is necessary to investigate mechanical properties of gold materials on the micro-scale for applications in MEMS accelerometers. This study reports dependence of structural design on effective Young's modulus (E_{eff}). of Ti/Au multi-layered micro-cantilevers for MEMS capacitive accelerometers. A total of 240 Ti/Au multi-layered micro-cantilevers of different structural designs were prepared, and the E_{eff} was evaluated by a resonance frequency method and FEA (finite element analysis) simulations. From experimental and FEA simulations results, a higher E_{eff} was obtained for a smaller the gap between the bottom surface of the cantilever and the bottom electrode. In addition, in most micro-cantilevers, the E_{eff} decreased following an increase in the width. This results are an important factor in desighing MEMS components.

P-S21-36-T2 Closed loop error compensation of RADAR PCBs fabrication process using inkjet printing and interoperability methods

Mr. Abdalla Shahin [1], Mr. Helmut Zörrer [1], Mr. Peter Bauer [1], Mr. Gerald Stubauer [1], Dr. Benedikt Pressl [2], Dr. Rolf Schneider [3], Mr. Ferhat Aslan [3], Mr. Jochen Seeser [3]

1. *PROFACTOR GmbH,* ***2.*** *BESI Austria GmbH,* ***3.*** *Notion Systems GmbH*

Companies are eager to become more adaptable and improve their systems and network structures due to the increased global competition. To meet these expectations, they have to cope with the complexity of interconnected processes and have the flexibility to meet changing requirements [1]. This work focuses on the fabrication of RADAR printed circuit boards (PCBs) as part of the project TINKER where the main target is to enable error compensation and defect repair inline the fabrication process using inkjet printing. This is achieved through the use of a closed error compensation feedback loop and an interoperability structure to support data transfer among several partner companies.

P-S21-37-T2 Electronic integration of microchips via inkjet printing

Mr. Gerald Stubauer [1], ***Mr. Peter Bauer*** [1], ***Dr. Pavel Kulha*** [1], ***Dr. Michael Haslinger*** [1], ***Mr. David Hahn*** [2], ***Mr. Jochen Seeser*** [2], ***Mr. Christian Debatin*** [2], ***Dr. Alexander Fischer*** [3], ***Dr. Istvan Denes*** [3], ***Mr. Christian Geissler*** [4], ***Dr. Benedikt Pressl*** [5], ***Dr. Birgit Brandstätter*** [5], ***Dr. Dieter Holzinger*** [6], ***Dr. Doron Gurovich*** [7], ***Mr. Semyon Melamed*** [7]

1. *PROFACTOR GmbH,* ***2.*** *Notion Systems GmbH,* ***3.*** *Robert Bosch GmbH,* ***4.*** *INFINEON Technologies AG,* ***5.*** *BESI Austria GmbH,* ***6.*** *TIGER Coatings GmbH & Co KG,* ***7.*** *PV Nano Cell Ltd*

In this work, we show how to leverage inkjet printing in multiple assembly steps of a technology demonstrator for a RADAR sensor package. The demonstrator consists of a printed circuit board (PCB) with cavities where bare RADAR dies are placed directly with contacts facing up (instead of traditional approach using packaged flip-chip assemblies). Thus, a connection of the microstructure of the chip (130µm pitch) with the conducting path structures of the standard PCB can be achieved by inkjet printing of UV-curable dielectric filling material and conductive silver nanoparticle ink. The fabrication and validation of this demonstrator includes: a) Dispensing of adhesive and assembly of the microchip into the cavity and record of 3D data; b) Inkjet printing of polymer layers to fill remaining gaps in the cavity, record of 3D data and printing of additional layers until gaps are filled via a feedback loop; c) Contacting the microchip via inkjet printing of conductive lines; d) Electrical characterization of inkjet-printed electrical contacts to the microchip and e) Reliability tests of the contacts. The inkjet gap filling process and the electronic connection via inkjet printing will be shown in more detail and results of electrical characterization and reliability tests will be presented.

P-S21-38-T2 From Micro to Nano: Integrating cavities in monolithic nanopore Silicon membrane by improved Nanofabrication methods for various Applications

Mr. Sanjeev Vishal Kota [1], ***Prof. Rafael Taboryski*** [1], ***Prof. Henri Jansen*** [1], ***Prof. Jörg Hübner*** [1], ***Dr. Jesper Yue pan*** [1], ***Dr. Anil Thilsted*** [2]

1. *Technical University of Denmark,* ***2.*** *Spectro Inlets Aps*

The rampant consumption of fossil fuels has triggered an overwhelming release of greenhouse gases. As a response, technology development is targeting renewable energy sources, converting fossil fuels to renewables, and capturing CO_2 into sustainable gases and liquids. An enabling factor for this transition is a reliable in-line analysis of gaseous species strengthened by a user-friendly analyte sampling technique.

This study envisages a monolithic silicon membrane-based gas separator (SMS) fabrication with an embedded cavity and a well-defined capillary as an outlet channel. The SMS facilitates volatile organic compounds (VOC) separation from emission sources, ambient air, or industrial processes that reflects targeted gas composition, which is then analyzed using on-site monitoring equipment.

A coarse-tuned three-step DREM (Deposit, Remove, Etch Many Times) procedure was employed to create a silicon nanopore membrane of 4 µm deep, using SF_6/C_4F_8/Ar gas mixture. At low pressure, the subsequent isotropic etch process formed a 2µm buried cavity beneath the etched holes, featuring an opening width of 300 nm and pitch of 700 nm. An atomic layer deposited (ALD) alumina (Al_2O_3) hard mask with high etch selectivity for Silicon, measuring 50 nm, was utilized. A quantitative investigation of the etched samples was performed using scanning electron microscopy.

P-S21-39-T2 A ReRAM Optronic Physical Reservoir for Fashion Styles Recognition

Mr. Jiayi Li [1], ***Dr. Haider Abbas*** [1], ***Dr. Asif Ali*** [1], ***Dr. Xin Ju*** [2], ***Prof. Diing Shenp Ang*** [1]

1. *Nanyang Technological University,* ***2.*** *Agency for Science, Technology, and Research (A*STAR)*

We propose an ITO/HfO_x/TiN ReRAM crossbar device as a physical optronic reservoir (OR) for high-accuracy and simplified in-sensor computing. On static image classification, the OR can achieve 85% accuracy on the fashion-MNIST dataset, with just one trained readout layer. It also shows excellent robustness to device noise and variability—a significant standard deviation of 0.5 over normalized response yielded only 9% accuracy loss.

P-S21-40-T2 Optimisation of a physical reservoir computer's parameters using a genetic algorithm non-linear search

Dr. Claude Meffan [1], ***Mr. Taiki Ijima*** [2], ***Prof. Amit Banerjee*** [2], ***Dr. Jun Hirotani*** [2], ***Prof. Toshiyuki Tsuchiya*** [2]

1. *Kyoto Univeristy,* ***2.*** *Kyoto University*

In this work, we propose that a genetic algorithm can be used to optimise the parameters of a Surface Acoustic Wave (SAW) reservoir computing system. Using a SAW resonator as a physical processing neuron, we create and measure the performance of a time-delay reservoir computer, optimised by a manual search. Using this performance as a baseline, we then find the hyper-parameters of a genetic algorithm (mutation rate, population size, cross-over type) which allow for quick and automatic convergence. We discuss the nature of the converged parameters relative to the size of the search space and discuss how this tactic can be used in future physical reservoir computing systems.

P-S21-41-T2 Design, fabrication of a label-free sensor using a taquito-like MoS2 morphology as channel.

Ms. Wendy Martinez [1], ***Dr. Orfil González-Reynoso*** [1], ***Dr. Gregorio Guadalupe Carbajal-Arizaga*** [1], ***Dr. Barbara Cortese*** [2], ***Dr. Mario Alberto Garcia-Ramirez*** [1]

1. *Universidad de Guadalajara,* ***2.*** *Univeristà di Roma "La Sapienza"*

The Molybdenum disulfide electronic properties are structure dependent. Thereby, we develop a label-free sensor using a novel MoS_2 morphology called "taquito-like" as a detection channel.
In here, we synthesized MoS_2 structure through a hydrothermal method and place it on a Si/SiO_2 substrate, Subsequently, we deposit a Mo electrode in each side of the structure. The proximal portion was connected to voltage and the distal portion to the ground. The sensor was tested by electromagnetic field perturbances when it is in contact with different solutions. The solutions contain molecules commonly found in biogenic substances. The recorded data was conditioned and processed with separation algorithms such as (Blind Source Separation) in order to characterize the involved molecules.
In this work, we obtain a system capable to record and identify signals caused by the interaction between the molecules and the detector. The sensor returns a family curve that describes a molecule's set. The separation algorithm is responsible for identifying the curve that represents each molecule. Once the molecule signals are detached, it is possible to quantify the molecules amount in the analyzed solution.

P-S21-42-T2 Photo-switchable reconfigurable nanostructured surfaces for hemiwicking

Ms. Rucha A. Deshpande [1], ***Mr. Jesper Navne*** [2], ***Mr. Mathias Adelmark*** [1], ***Prof. Rafael Taboryski*** [1]

1. *Technical University of Denmark,* ***2.*** *DTU Nanolab*

In recent years, there is growing interest in switchable surfaces, where the liquid-solid interface reversibly can be photo-switched from a hydrophobic to hydrophilic state for smart applications. Here, the study is carried out for nanostructures composed of nanopillars in hexagonal pattern on Si and fused silica substrates coated with thin layers of photo-switchable layers of common materials viz. TiO_2 and ZnO. The dynamics of the flow and their engineered photo-switchable response based on Cassie Baxter relations is studied theoretically and experimentally. Our study focuses on the mechanism of the photoinduced flow of liquid on nanopatterned surfaces, with investigation of all key parameters including geometrical pattern, UV light of different wavelengths viz. 275, 300 and 365 nm, thickness and two common materials.

P-S21-43-T2 Improved gate oxide quality by making enhanced structure in sub-14nm DRAM

Mrs. hyojin park [1], ***Prof. Byoungdeog Choi*** [2]

1. *Sungkyunkwan University and Samsung Electronics,* ***2.*** *Department of Semiconductor and Display Engineering, Sungkyunkwan University*

As the node of DRAM products is advanced, it became important to improve gate oxide reliability. There are many causes according to the gate oxide reliability, usually oxide breakdown is occurred due to the strong electric field of corner Si substrate. So, to get over this, making a proper structure for gate oxide breakdown is most important and we usually focused on the thickness of dielectric. But there are limits, so we desperately need a novel way to overcome. In this paper, we suggested a new method that can improve gate oxide reliability by making a better structure in sub-14nm DRAM, and how it can reduce the gate oxide breakdown. With this experiment, we varied cleaning process times to make round structure and figured out the structure by TEM measurement, and the roundness of corner Si is increased by 27% and TDDB (Time dependent dielectric breakdown) is also increased by 3% even in case of 8% larger corner roundness in n-channel MOSFETs fabricated in the Samsung Electronics sub-14nm DRAM process.

P-S21-44-T2 Thermo-mechanical behaviour of different sealing materials used as encapsulants in Power Modules

Mrs. Chiara Spano [1], ***Mr. Giulio Galfré*** [1], ***Mr. Emilio Mattiuzzo*** [2], ***Mr. Lorenzo D'Ancona*** [2], ***Mrs. Valentina Bertana*** [1], ***Mr. Luciano Scaltrito*** [1], ***Mr. Sergio Ferrero*** [1]

1. *Politecnico di Torino,* ***2.*** *VISHAY Semiconductor Italiana S.P.A.*

Power modules are demanding higher power density and operating temperatures, so new designs and improved materials are necessary to guarantee a longer lifetime. Modules' main existing packages are Vacuum Potting Gel (VPG) with gel as sealing and Transfer Molding (TM) with Epoxy Molding Compound (EMC) as encapsulant. This work aims at demonstrating if power modules, with the same substrate but different sealings, may have different thermal behaviors at the same operating conditions. An Improvement in thermal resistance was recorded in TM. However, additional tests are investigating whether it is caused by EMC higher thermal conductivity or EMC different final warpage.

P-S21-45-T2 193 nm ArF lithography for high topology InP wafer processing

Mr. Aleksandr Zozulia [1], ***Dr. Jeroen Bolk*** [1], ***Dr. Samir Rihani*** [2], ***Dr. Graham Berry*** [2], ***Dr. Michael Robertson*** [2], ***Dr. John Rawsthorne*** [2], ***Prof. Kevin Williams*** [1], ***Dr. Yuqing Jiao*** [1]

1. *Eindhoven University of Technology,* ***2.*** *Huawei Technologies Research and Development (UK) Limited*

To increase the production volume and fabrication yield of InP membrane photonics, a process transition to 193 nm ArF lithography is needed. However, the thin ArF resist does not cover well high surface topology. In this work, we propose the process flow, which helps to enable using of the ArF lithography for the processing of high device topology InP wafers.

P-S21-46-T2 Design and fabrication of an opto-mechanical antenna in the NIR range

Mr. Daniyal Khoshmaram [1], ***Dr. Xavier Borrisé*** [2], ***Prof. Joan J. Garcia-Garcia*** [1], ***Mr. Raul Ruiz*** [1], ***Prof. Xavier Cartoixà*** [1], ***Prof. Gabriel Abadal*** [1]

1. *Universitat Autònoma de Barcelona (UAB),* ***2.*** *Institut Català de Nanociència i Nanotecnologia (ICN2)*

We present an innovative opto-mechanical antenna that combines a plasmonic optical nanoantenna with a microcantilever for direct transduction from the optical to the mechanical domain. Extending the concept of MEMSTENNA (combination of a MEMS and an antenna) to the near-infrared (NIR) range, this design offers enhanced frequency response and sensitivity for room temperature radiation detection.

The proposed device features a plasmonic optical dipole nanoantenna integrated into Au-coated silicon nitride triangular microcantilevers. By tuning the nanoantenna's dimensions, including length, width, supporting arm dimensions, and Si3N4 thickness, it exhibits resonance at 1.55 μm when illuminated by a focused laser.

Fabrication involves focused ion beam milling to define the nanoantenna structure and reduce the Si3N4 thickness, followed by assembly to form the opto-mechanical antenna. COMSOL Multiphysics RF simulations optimize the nanoantenna's dimensions, achieving a deep S11 notch at 1.55 μm.

Sensitivity analysis explores fabrication tolerances and Si3N4 thickness variations, revealing their influence on the antenna's response. Furthermore, RF and mechanics coupling in COMSOL enables calculation of the microcantilever deflection versus voltage characteristics.

Results demonstrate that a 70 mV voltage can be generated in the nanoantenna feed gap capacitance through a 0.5 W 1.55 μm laser beam.

P-S21-47-T2 A Hybrid Nanowire-MEMS Force Sensor

Dr. Mehrdad Karimzadehkhouei [1], ***Mr. Masoud Jedari Ghourichaei*** [1], ***Mr. Levent Demirkazik*** [1], ***Mr. Bartosz Pruchnik*** [2], ***Mr. Krzysztof Kwoka*** [2], ***Mr. Dominik Badura*** [2], ***Dr. Tomasz Piasecki*** [2], ***Dr. Onur Aydin*** [1], ***Dr. Bekir Aksoy*** [1], ***Mr. Cemal Aydogan*** [3], ***Dr. Gokhan Nadar*** [1], ***Prof. Ivo W. Rangelow*** [4], ***Prof. Arda Yalcinkaya*** [5], ***Prof. Halil Bayraktar*** [6], ***Prof. Teodor Gotszalk*** [2], ***Prof. B. Erdem Alaca*** [1]

1. *Department of Mechanical Engineering, Koç University, Istanbul, 34450, Turkey,* ***2.*** *Department of Nanometrology, Wrocław University of Science and Technology, Wroclaw, 50-370, Poland,* ***3.*** *Ins. of Precision Measurement and Sensor Technology, Ilmenau Uni. of Tech., Ilmenau, 98693, Germany,* ***4.*** *Technische Universität Ilmenau,* ***5.*** *Department of Electrical and Electronics Engineering, Boğaziçi University, Istanbul, 34342, Turkey,* ***6.*** *Dept. of Molecular Biology and Genetics, Istanbul Technical University, Maslak, Istanbul, 34467, Turkey*

Miniaturization of electromechanical sensors brings about significant advantages such as higher resonance frequencies and lower power requirements resulting in increased speed and sensitivity with higher signal-to-noise ratio. Equally important is the cost reduction due to wafer-level production. With the use of nanowires (NWs), these advantages can be fully exploited. As an interface to cells and tissues, NWs can serve as mechanical building blocks addressing issues such as cell differentiation, proliferation, adhesion, motility, and fate that are affected not only by chemical signals, but also by externally applied mechanical forces. In this study, fabrication of a multi-axis nanoelectromechanical system (NEMS) force sensor is reported that incorporates piezoresistive NWs. The sensor is intended to be utilized for the measurement of traction forces between live cells and the sensor surface. With micro and nanoscale components, the proposed sensor is a challenging integration platform.

P-S21-48-T2 Nano-Imprinting and Air Injection System: Enabling Nano Patterns on Curved Stamp Surfaces for Biotechnology Applications

Dr. SeokYoung Ji [1], ***Dr. Hyungjun Lim*** [1], ***Dr. Hak-Jong Choi*** [1], ***Dr. Junhyoung Ahn*** [1]

1. *Korea Institute of Machinery & Materials*

In the field of biotechnology, there is extensive research being conducted on the development of devices utilizing nano patterns. Among them, we have conducted research on process equipment for the fabrication of functional bio-application devices with nano patterns on curved surfaces. While significant advancements have been made in process technologies for fabricating nano patterns on flat substrates, implementing patterns on curved surfaces has been challenging. To address this difficulty, we have designed and implemented equipment that uses an inkjet-based system to realize nano patterns on stamps of various shapes such as curved, rectangular, and triangular. Using this equipment, we have successfully implemented 300 nm nano patterns on curved stamp surfaces. We believe that this process system equipment will play an important role in various biotechnology fields in the future.

P-S21-49-T2 Improved electrical performance of ZnO thin-film transistors using 2DEG with insertion of Al2O3 layer deposited by atomic layer deposition

Mr. Dongki Baek [1], ***Mr. Se-Hyeong Lee*** [1], ***Ms. So-Young Bak*** [1], ***Mr. Chan-Yeong Park*** [1], ***Mr. Hyeongrok Jang*** [1], ***Mr. Jinwoo Lee*** [1], ***Prof. Moonsuk Yi*** [1]

1. *Department of Electrical and Electronics Engineering, Pusan National University*

Traditional ZnO thin-film transistors (TFTs) with an ultra-thin active layer less than 10nm exhibit low carrier mobility due to low carrier density in the active layer when it is deposited using atomic layer deposition (ALD) at low growth temperatures (<200°C). To address this issue, we introduced a ZnO/Al_2O_3 heterojunction active layer. At the ZnO/Al_2O_3 heterojunction interface, a two-dimensional electron gas (2DEG) is formed, and supplies free carriers. All devices were fabricated at 150°C, and the overall thickness of the active layer was maintained at 6nm. The thickness of the Al_2O_3 layer was adjusted to evaluate its impact on performance. The optimized performance was achieved with a ZnO (5nm)/Al_2O_3 (1nm) and exhibit as a carrier mobility of 11.91cm^2/V·s, a subthreshold swing of 0.83V/dec, a threshold voltage of 8.48V, and an on-off current ratio of 2.09 x 10^6. Afterward, we will optimize the ZnO/Al_2O_3 TFT by adjusting the total thickness of the active layer, the thickness of the Al_2O_3 layer, and the growth temperature to improve the subthreshold swing and threshold voltage.

P-S21-50-T2 Characterization of Inkjet-printed Mask Pattern for Area-selective Atomic Layer Deposition Process

Mr. Jun Ho Yu [1], ***Dr. Sang-Ho Lee*** [1]

1. *Korea Institute of Industrial Technology*

Atomic layer deposition (ALD) is a nanoscale thin film deposition technique capable of producing highly conformal, dense, and low porosity film. It relies on alternating pulses of precursor gases and vapors to the substrate surface and subsequent chemisorption or surface reaction of the precursors. Unlike ALD, which involves reactions occurring over the entire surface, AS-ALD selectively inhibits thin film deposition on specific surfaces by utilizing surfaces with distinct chemical properties. This paper presents the inkjet printing technique for fabricating a two-layer ALD suppression mask pattern composed of a fluorocarbon (FC) thin film and photoresist (PR). To analyze the ALD inhibition effect of the mask patterns, surface analysis of the deposited layer was conducted using an AFM. As a result of AFM analysis, all surfaces before Al_2O_3 deposition showed fine-grain spreading topology. In the cases of the PR surfaces, even after Al_2O_3 deposition, surface morphology maintained a fine-grain spreading topology. However, FC-covered PR showed lumped and undulating surface including cavities along with the abrupt increase of Rq. A 6.5 nm thick Al_2O_3 thin film was successfully patterned by the proposed lift-off process using an inkjet-printed 1.28 μm thick FC/PR mask pattern.

P-S21-51-T2 Technology performance of silica nanoparticle deposition techniques over carbon-based substrates

Mrs. Ana Coloma Velez [1], ***Mrs. Michelle Cedeño*** [2], ***Mr. Xingqi Chan*** [3], ***Prof. Andreu Cabot*** [3], ***Prof. Manuel Domínguez-Pumar*** [1], ***Prof. Andriy Yaroshchuck*** [1], ***Prof. Alexandra Bermejo*** [1]

1. *Polytechnic University of Catalunya,* ***2.*** *PhD STUDENT,* ***3.*** *Catalonia Institute for Energy Research*

This work describes two techniques for depositing silica-based nanoporous layers onto various carbon-based materials. These can be scaffolds for low-cost, environmentally friendly energy harvesters.
353 nm diameter silica nanoparticles have been deposited onto three different carbon-based substrates. As deposition methods, two different techniques have been explored: electrospray and drop casting.
Electrospray technique involves a syringe pump connected to a high-voltage power supply, which creates a strong electric field between the capillary needle and a counter-electrode. The electric field induces formation of a Taylor cone at the needle tip due to surface tension. The flow rate and applied voltage were optimized depending on the solution type used for electrospray.
Drop casting consists in depositing a small volume of nanoparticle solution onto a tissue using a pipette or a syringe. The solution is carefully spread over the desired area, forming a thin film, which enables gradual evaporation of the solvent.

P-S21-52-T2 Circuit-level Macro Modeling for Behaviors of Hole Accumulated Current during ERS Operation in 3D Charge Trap Flash Memories

Dr. Sunghwan Cho [1], ***Prof. Byoungdeog Choi*** [2]

1. *Sungkyunkwan University and Samsung Electronics,* ***2.*** *Department of Electrical and Computer Engineering, Sungkyunkwan University*

In this paper, we developed circuit-level macro model as a framework for circuit simulation during erase operation in 3D charge trapping flash (CTF) memory device focusing on the behaviors of hole accumulated current at the bottom of the 3D channel. After analyzing the difference of channel electrostatic potential in the string which is attributed by the difference of hole barrier in ground select line (GSL), we derived a formula for the hole accumulated current by transforming the subthreshold current in BSIM-CMG model. To extract model parameters, we fitted our SPICE simulation results for 2 representative GSL conditions with TCAD simulation results and experimental data.

P-S21-53-T2 Damascene Versus Etch-Back Chemical Mechanical Planarization for Resistive Memory Crossbars Back-End-Of-Line Integration

Mr. Raphael Dawant [1], ***Mr. Mathieu Gaudreau*** [1], ***Mr. Marc-Antoine Roy*** [1], ***Mr. Javier Arias Zapata*** [1], ***Prof. Dominique Drouin*** [1], ***Prof. Serge Ecoffey*** [1]

1. *Université de Sherbrooke*

Memristive memories have gained attention for their compatibility with BEOL integration, particularly in in-memory computing applications. This study investigates two techniques, Damascene and Etch-back, for integrating memristive memory arrays in BEOL. TiOx-based resistive memory was fabricated using these techniques, with Damascene employing CMP on the metal and Etch-back using CMP on the dielectric. AFM measurements and FIB cross-sections revealed differences in metal dishing and trenching effects between the two approaches. The material choice for connecting the TiOx-based memory to the metallic electrode was limited, with TiN being utilized. Etch-back demonstrated an advantage by allowing the stacking of different metals, resulting in lower access resistance with the use of lower resistivity Al beneath TiN. In contrast, Damascene, the standard for electroplated Cu interconnections, exhibited trenching defects and filling voids. Devices from both approaches showed similar cycling behavior and performance. The study concludes that Etch-back exhibits greater potential due to its mitigation of trench effects, improving interface quality, and reducing access resistance. The comparative analysis focuses on CMOS integration suitability and explores the potential for 3D integration of crossbar arrays.

P-S21-54-T2 Resolution enhancement of Scanning Electron/Atomic Force Microscope images using a computational method based on Fourier spectra stitching

Ms. ELENI STAI [1], ***Dr. Vassilios Constantoudis*** [1], ***Dr. Andreas Kaidatzis*** [1], ***Dr. Evangelos Gogolides*** [1]

1. *NCSR Demokritos*

A great challenge in the characterization of multiscale hierarchical surfaces is that the widely used Scanning Probe Microscopy (SPM) images for their inspection depict only a limited range of their morphology scales. In order to overcome this challenge, we propose a computational method based on the hybridization of SPM images obtained with different magnifications, i.e. pixel size and measurement range. The method generates scale-enhanced images containing the scales and frequencies of the images of both high and low magnifications, ranging from the higher resolution (smaller pixel size) to the larger measurement range of the input images. The key process of the method is the stitching of the Fourier Spectra of the input images with different resolution so that we get a wide-scale Fourier spectrum. By inverting the obtained wide-scale Fourier spectrum and randomizing their phases, we derive an artificial scale-enhanced image of the full-scale surface morphology. The so-called Fourier Spectra Stitching (FSS) method can be applied in all types of SPM images of surfaces with stochastic morphologies.

P-S21-55-T2 Calculation of magnetic force between current-carrying circular and arbitrary shaped filament: segmentation method

Dr. Kirill Poletkin [1], ***Mr. Pavel Udalov*** [2], ***Dr. Alexei Lukin*** [2]

1. *Hefei University of Technology,* ***2.*** *Peter the Great St. Polytechnic University*

A new formula for calculation of magnetic force between current-carrying circle and line segment is derived by using Mutual Inductance Method. Using the fact that any curve can be interpolated by a set of line segments, a method for calculation of magnetic force between a circular filament and filament having an arbitrary shape in the space is proposed based on the derived analytical formulas (Segmentation Method). The proposed segmentation method was successfully applied to the calculation of the magnetic force between the circular filament and the following special curves such as polygons, and circles.

P-S21-56-T2 Fabrication of a thin-film adaptive electrostatic phase plate

Mr. Mathias Adelmark [1], ***Dr. Ada-Ioana Bunea*** [1], ***Dr. Marco Beleggia*** [1], ***Dr. Andrei Lavrinenko*** [1], ***Prof. Rafael Taboryski*** [1]

1. *Technical University of Denmark*

Electron beams have become essential for the fabrication and characterization of micro and nanostructured devices. To further improve and advance this technology, control of the electron beam phase is one of the key elements. For this purpose, adaptive phase plates (PP) are most promising. Here, we combine concepts from electrostatic and thin-film based PPs, and investigate the possibility of fabricating a thin membrane with electrodes on top. This, however, introduces new limitations, as the membrane must be as thin as possible, while maintaining the stability to support the electrode system. Thus, the fabrication needs to be optimized considering the limitations imposed by current cleanroom technology, requirements for implementation in a transmission electron microscope (TEM), and requirements for in-situ electric field adjustment. The design is intended for the condenser system of a typical TEM, where the beam size is ~50 µm. Furthermore, the PP is designed to interface with a commercial holder, as the relative beam positioning and electrode pads are well known. With the process flow established, the next step is to try it out experimentally and adjust as needed, paying particular attention to the electrode fabrication and silicon etching steps, which were identified as critical in the process.

P-S21-57-T2 Advanced micro- and nanoprobing combined with other analytical tools for characterizing semiconductor devices, MEMS and nanostructures

Dr. Anya Grushina [1]

1. *Imina Technologies*

Micro- and nanoprobing probing is typically used to electrically characterize devices or materials, but in combination with other analytical techniques it becomes a very powerful tool. For example, nanoprobing is used in combination with specialized signal processing equipment for in-situ SEM electrical failure analysis (EFA) of semiconductor devices. More examples include micromechanical testing, nanoindentation, AFM, etc. In this contribution, we are reviewing the state-of-the-art electrical probing combined with other techniques used to characterize different classes of devices and materials. We aim to offer insights about potential applications of nanoprobing and its combinations with other techniques for semiconductor device fabrication, materials science, and nanotechnology, and to support advances in a wide range of topics, from electronics and photonics to energy and healthcare.

P-S21-58-T2 Interfacing free-space beams and suspended silicon photonic waveguides with a low back-reflection fully etched grating coupler

Mr. Søren Engelberth Hansen [1], Dr. Guillermo Arregui [1], Mr. Ali Nawaz Babar [1], Mr. Marcus Albrechtsen [1], Dr. Babak Vosoughi Lahijani [1], Dr. Rasmus Ellebæk Christiansen [1], Dr. Søren Stobbe [1]

1. Technical University of Denmark

We present the development of a grating coupler with fully etched grating lines for suspended waveguide structures. The grating coupler is designed to couple with normal-incidence free-space beams with near-zero back-reflections. We present the measurement results of the fabricated device as well as the characterization method for obtaining the transmission and reflection characteristics based on a Fabry-Pérot resonator model in addition to windowed Fourier transforms.

P-S21-59-T2 Strain Rate Dependency of Mechanical Property in Micro-Compression of Electrodeposited Gold toward Design of MEMS Components

Mr. Shota Kanno [1], ***Mr. taro omura*** [1], ***Dr. Tomoyuki Kurioka*** [1], ***Dr. Chun-Yi Chen*** [1], ***Dr. Parthojit Chakraborty*** [1], ***Prof. Katsuyuki Machida*** [1], ***Prof. Hiroyuki Ito*** [1], ***Prof. Yoshihiro Miyake*** [1], ***Prof. Masato Sone*** [1], ***Prof. Mark Chang*** [1]

1. *Tokyo Institute of Technology*

Gold-based MEMS accelerometers are promising devices to simultaneously realize high sensitivity and miniaturization by suppressing the thermal-mechanical noise due to the high mass density of gold. Components in MEMS devices often have sizes on micro-scale or smaller, and metallic materials are reported to exhibit the sample size effect. Therefore, clarifying the micro-scale mechanical property is a prerequisite for design of MEMS components. On the other hand, mechanical properties of a metallic material obtained from a mechanical testing are dependent on the strain rate used in the measurement. In this study, strain rate dependency is evaluated for the design of movable components in MEMS deceives. In particular, the strain rate sensitivity is calculated from the yield stress values obtained from compression tests of micro-pillars with a square cross-section fabricated from electrodeposited gold by FIB. The compression test was conducted using three different strain rates. The strain rate dependency could be quantified as the strain rate sensitivity. For the three types of the micro-pillars evaluated in this study, there was no obvious difference in the strain rate sensitivity. Possible explanations are the properties of strain rate dependency in fcc metals and the effect of grain size.

P-S21-60-T2 Stable superhydrophilic and superhydrophobic surfaces incorporated inside ultra-thin vapor chambers for heat transfer applications

Ms. Efrosyni Tsounai [1]***, Ms. Vasiliki Tselepi*** [1]***, Dr. Evangelos Gogolides*** [2]***, Dr. Kosmas Ellinas*** [1]

1. *Department of food science and nutrition, School of the Environment, University of the Aegean, Ierou Lochou & Makrygianni St, 81400, Myrina, Lemnos, Greece,* ***2.*** *NCSR Demokritos*

The rapid development of a variety of portable and slim electronic devices have increased the requirements for the heat flux management beyond the limits of traditional air convection cooling. To this direction, several miniaturized, thermal management devices to cool high-power, compact electronic devices have been presented. However, most of the methods are related with efforts about flattened cylindrical metallic heat pipes.Only recently, microfabrication techniques have been extensively investigated as routes for the fabrication of cooling devices. Herein, we present the fabrication of an ultra-thin (109 μm, possibly the thinnest reported up to now) and flexible thermal diode utilizing phase-change heat transfer and self-propelled jumping droplet for heat regulation. The hierarchical micro-nanotopography is created by plasma micro-nanotexturing followed by PEG coating, to offer stable superhydrophilicity (<2^{o} for all three etching durations tested) enabling capillary filling to the evaporator area. For the superhydrophobic plate (SCA>165^{o}Hysteresis< 5^{o}, for etching time higher than 6 min) plasma micro-nanotexturing is followed by a Teflon spin coating deposition (Teflon™ AF), in order to enable sustainable dropwise condensation on the condenser surface.

P-S21-61-T2 Comprehensive Evaluation of Geometric Effects on Long-Term Structure Stability of Ti/Au Multi-Layered Micro-Cantilevers toward Gold-MEMS Capacitive Accelerometer

Mr. Ryosuke Miyai [1], ***Dr. Tomoyuki Kurioka*** [1], ***Dr. Chun-Yi Chen*** [1], ***Prof. Mark Chang*** [1], ***Mr. Akira Onishi*** [1], ***Dr. Parthojit Chakraborty*** [1], ***Prof. Katsuyuki Machida*** [1], ***Prof. Hiroyuki Ito*** [1], ***Prof. Yoshihiro Miyake*** [1], ***Prof. Masato Sone*** [1]

1. *Tokyo Institute of Technology*

In this study, geometric effects on the long-term structure stability of gold-based micr-ocantilevers toward MEMS capacitive accelerometers are evaluated by long-term vibration test. A total of 240 cantilevers with different width (*w*

[μm] = 8, 9, 10, 11, 12, 13, 15 and 20), length (*l* [μm] = 200, 400, 600, 800 and 1000), and six types of Ti/Au layered structures (three single-layered (SL) structures, two double-layered (DL) structures, and a triple-layered (TL) structure) were fabricated. The long-term vibration tests were performed at a frequency of 10 Hz and an acceleration of 1 G with a cycle number of 10^3–10^7. The structural stability was evaluated from the amount of change in the tip height before and after the vibration test. The *w* had an insignificant influence to the structural stability, and the tip height change was obviously dependent on both the *l* and *t*. The structural stability was better for micro-cantilevers with a shorter length, and reducing the thickness also contributed to an improved structural stability. In conclusion, the structural stability was confirmed to be affected by the geometry. This is a critical finding for the design of MEMS movable components.

P-S21-62-T2 Enhanced Fe-FET Performance with HZO and MoS2-Based Dielectric Structures for Non-volatile Memory

Mr. Jeehwan Lee [1], ***Mr. Do Kyung Yun*** [2], ***Prof. Woo Jong Yu*** [2]

1. *Department of Semiconductor and Display Engineering, Sungkyunkwan University,* ***2.*** *Department of Electrical and Computer Engineering, Sungkyunkwan University*

Ferroelectric devices have emerged due to lower power consumption, faster switching speeds and improved data retention. Moreover, HZO($Hf_{0.5}Zr_{0.5}O_2$) films have shown high permittivity, which refers to store electrical energy when an electric field is applied, high dielectric constant, making it suitable for applications such as in non-volatile memory devices and excellent endurance making them suitable for repeated switching cycles without degradation. HZO exhibits ferroelectric properties as structural changes occur due to stress between the electrode and the thin film. It has ferroelectric properties due to the change of crystal structure from the conventional monoclinic phase to the orthorhombic phase through heat treatment, and at a Zr composition ratio of 50%.

In this Study, We fabricated 10-nm-thick ferroelectric HZO thin films as a Ferroelectric dielectric with MoS_2 as a Semiconductor. HZO was deposited by Thermal-atomic layer deposition at 250°C with H_2O and a post annealing process at 500°C. The transfer characteristic of this Fe-FET was demonstrated with operating voltage that was smaller than 10 V, memory window about 0.5 V, and small subthreshold slope about 400 mV/dec. This $Hf_{0.5}Zr_{0.5}O_2$ Fe-FET Device can be attractive for various applications in advanced electronic devices.

P-S21-63-T2 Thermal characterization of IMS substrates with different design parameters for Power Modules Devices

Mrs. Chiara Spano [1], ***Mr. Giulio Galfré*** [1], ***Mr. Emilio Mattiuzzo*** [2], ***Mr. Lorenzo D'Ancona*** [2], ***Mr. Luciano Scaltrito*** [1], ***Mr. Sergio Ferrero*** [1], ***Mrs. Valentina Bertana*** [1]

1. *Politecnico di Torino,* ***2.*** *VISHAY Semiconductor Italiana S.P.A.*

Due to recent advancements in semiconductors, the thermal efficiency and reliability of power modules is getting higher. This work aims at evaluating improved substrates such as Insulated Metal Substrates (IMSs) to overcome possible materials mismatches due to thermal stresses. The effect of different IMS design parameters was evaluated through a Finite Element Analysis and then measured with an experimental set-up for assessing the thermal resistance (Rth) between the single die and the heatsink. IMS groups with the higher thermal conductivity showed values aligned with standard ceramic substrates, although material layers in IMS give different contributions inside the thermal dissipation.

P-S21-64-T2 PZT sensor compatible with the 2D piezo-scanners dedicated to 1550 nm long-range LIDAR

Mr. Laurent Mollard [1]

1. *University Grenoble Alpes, CEA, Leti*

This article presents the development of a PZT (lead zirconium titanate) sensor that can be integrated in-situ into our 2D piezoscanners. These piezoscanners are dedicated to LIDAR (Lighth Detection And Ranging) at 1550 nm and long range (>100 m). LIDAR is considered a crucial sensor for autonomous driving because it can provide high-density point clouds with precise three-dimensional information. Therefore, MEMS-LIDAR based on MEMS mirrors is the best candidate for long-range application. The system specification requires an average optical power of 2 W on the 2 × 2 mm2 side mirror. Therefore, eye safety is a key issue for 905 nm and 1550 nm lasers. Because the eye transmits 905 nm light to the retina, which is not the case at 1550 nm, the 905 nm laser is limited to 10 times less incident laser power than the 1550 nm laser, and therefore has a smaller detection range. However, even a wavelength of 1550 nm can cause eye damage, particularly in the case of a fixed beam. This article presents the fabriction of a PZT sensor integrated into a PZT cantilever to ensure that the mirror is moving. These cantilevers have similar dimensions, thickness and PZT material to the actuators.

P-S21-65-T2 High-throughput AFM inspection and metrology with “Quattro”- active cantilever

Mr. Aditya Suryadi Tan [1], ***Mr. Fabian Dietrich*** [1], ***Mr. Hans-Georg Pietscher*** [1], ***Prof. Teodor Gotszalk*** [2], ***Mr. Chuan Du*** [3], ***Dr. Xiang qian Zhou*** [3], ***Mr. Fangzhou Xia*** [4], ***Mr. Kamal Youcef-Toumi*** [4], ***Dr. Andrew Yacoot*** [5], ***Mr. Ho-Se Lee*** [6], ***Prof. Eberhard Manske*** [7], ***Dr. Thomas Kissinger*** [7], ***Prof. Thomas Fröhlich*** [7], ***Prof. Ivo W. Rangelow*** [7]

1. *Nano analytik GmbH,* ***2.*** *Wroclaw University of Science and Technology,* ***3.*** *Parcan NanoTech Co., Ltd.,* ***4.*** *Massachusetts Institute of Technology,* ***5.*** *National Physical Laboratory,* ***6.*** *SEUM tronics,* ***7.*** *Technische Universität Ilmenau*

Conventional AFM has not enough throughput for today’s large-scale semiconductor manufacturing. We are developing massively parallel cantilever systems for high-speed imaging and metrology. Such systems can contain thousands of scanning active cantilevers. Work is underway on the design and fabrication of the “Massively Parallel Microscope” arranged in a Quattro array. This technology employs existing nano analytik GmbH technology of active cantilevers, which allows the deflection and the actuation of each cantilever in the array to be sensed and to be controlled individually. Since each cantilever in the array represents a self-sustaining AFM hardware system for metrology and imaging, the multiple parallel probes are forming many AFM that is capable to work independently. The goal is to provide compact atomic force microscopes suitable for real-time wafer inspection processing based on the work of many AFM probes that may be practiced by parallel AFM systems that are capable to operate autonomously. Advanced work includes the development of massively parallel cantilever arrays. The main focus is on increasing the scan area for large wafers, masks, displays, or dies. Finally, we will discuss general considerations for implementing high-throughput cantilever platforms, as well as current limitations and future directions for high-throughput imaging and metrology technologies.

P-S21-66-T2 Direct ink writing of high-detail resolution cellulose structures

Mrs. Farnaz Rezaei [1], ***Prof. Jonas Lindh*** [1], ***Dr. Daniel Carlsson*** [2], ***Dr. Jimmy Hedin Dahlström*** [2], ***Prof. Stefan Johansson*** [1]

1. *Uppsala University,* ***2.*** *Cytiva*

Direct ink writing (DIW) is a 3D printing technique to fabricate structures layer by layer. DIW technique could be used for different applications, e.g., drug delivery, microfluidics, and separation science. In this project, cellulose acetate (CA) is chosen as a biodegradable ink to evaluate the possibility of printing with a high-detail resolution by changing printing parameters.

Ink with different viscosities (various amounts of CA with different molecular weights) is examined to achieve a few micrometer resolutions. According to the chosen ink, it is possible to change the size of the nozzle. Results indicate the structure printed with 10 % CA (50 kDa), and the nozzle with an inner diameter of 3 µm gives the highest resolution. However, various parameters could affect the printing results, by examining the evaluating the parameters it is possible to achieve a high-resolution cellulose structure.

P-S21-67-T2 A Study about Bump Non-Contact Failure of Flip Chip at sub-20nm DRAM

Mr. Dongsik Park [1], ***Mr. Kyo Seon Choi*** [2], ***Prof. Byoungdeog Choi*** [3]

1. *Sungkyunkwan University and Samsung Electronics,* ***2.*** *Samsung Electronics,* ***3.*** *Department of Semiconductor and Display Engineering, Sungkyunkwan University*

In this paper, we proposed “Bump Non-Contact Failure” model that occurs during the bump and the PCB bonding in the DRAM Flip-chip process. Also, how to improve its failure was introduced. As a result of TEM image analysis and bump fail test checked, the chip warpage is one of the important causes of the defect. Two improvement methods were presented. The defect rate can be reduced by Mount Force up test, because the solder area is easier to touch the PCB due to the strong pressing force. And, change of the solder height increases the possibility of contact because solder is more widespread in the bump compared to pillar area. These experiments were conducted with in sub 20nm technology in Samsung Electronics.

P-S21-68-T2 A study on the silicon dislocation in DRAM STI structure

Mr. Bonhwi Gu [1], ***Mr. Injae Bae*** [2], ***Prof. Byoungdeog Choi*** [3]

1. *Sungkyunkwan University and Samsung Electronics,* ***2.*** *Samsung Electronics,* ***3.*** *Sungkyunkwan University*

Silicon dislocation in DRAM is usually caused by thermal stress of insulators (silicon oxide, silazane) in shallow trench isolation (STI), which will result in fatal reliability issues. In fabrication process, many factors such as STI depth, STI width ratio, oxide/silazane film characteristics, etc., are considered to improve such failure. Despite those efforts, dislocation is still occurring intermittently. Here, we find another factor that is tensile stress induced by silicon nitride in STI and present a new design rule related to nitride. To prevent dislocation, we should forbid certain condition, which includes specific size of STI width mainly filled with nitride and ratio of STI width beside active region. This evaluation was performed with Samsung Electronics' 18nm node DRAM technology.

P-S21-69-T2 Spintronic Terahertz Emitter Integrated Microdevices for Terahertz Polarization Modulation

Dr. Zhongyang Bai [1], ***Dr. Tong Sun*** [1], ***Dr. Zhaoying Li*** [1], ***Dr. Dong Li*** [1], ***Prof. Tianxiao Nie*** [1], ***Prof. Youguang Zhang*** [1], ***Prof. Lianggong Wen*** [1]

1. *Beihang university*

A spintronic terahertz emitter (STE) that generates broadband terahertz (THz) pulses at room temperature has the advantages of low cost, large bandwidth, and high scalability To expand the functionality of spintronic terahertz devices, the integration of emerging terahertz metasurfaces with STE shows immense potential for device multifunctionality and miniaturization. However, the process complexity and low emission efficiency of metasurfaces-based spintronic terahertz devices remain the major challenge in achieving multifunctional integration. In this paper, we propose a novel spintronic meta-antenna array (SMA) device for terahertz polarization modulation. This device is realized by integrating patterned STE and metal block metasurfaces on the same substrate. A W/CoFeB/Pt ultrathin nanofilm stack has been deposited on the substrate with patterned STE arrays. This device provides polarization manipulation to terahertz waves, which exhibits promising potential in spintronic terahertz technology with controllable spatial characteristics.

P-S21-70-T2 Bioinspired Microfluidic Flow Sensors with Magnetic Artificial Cilia for Organ-on-Chip Applications

Mrs. Bhavana Venkataramanachar [1], Mr. Max Verhoef [1], Dr. Tanveer ul Islam [1], Prof. Jaap den Toonder [1]

1. *Eindhoven University of Technology*

Measuring flow in a microfluidic chip presents an inherent challenge of flow sensing at very small scales. The methods adopted presently either result in altering the fluid properties or require unsuitable additional bulky components. Inspired by the sensing ability of a hairlike microstructure existing in nature, called cilium, we present a novel microfluidic flow sensing concept using magnetic artificial cilia in a microfluidic chip. The cilium undergoes deflection due to an existing flow, which is sensed by a magnetic field sensor integrated in the chip. Here, we show the device fabrication and the basic proof-of-principle of this concept using experiments and simulations

P-S21-71-T2 Ultrathin Si nanostring resonators with widely tunable dynamic behaviour

Prof. Amit Banerjee [1], ***Mr. Wei Yu*** [1], ***Prof. Jun Hirotani*** [1], ***Prof. Toshiyuki Tsuchiya*** [1]

1. *Kyoto University*

Nanomechanical resonators devices are building blocks for a number of emerging technologies, such as ultra-sensitive sensing, efficient signal and information processing, quantum computing, etc. Moreover, nanoresonators made of atomic-scale materials (CNT, graphene, MoS_2, etc.) provide ultrawide electrostatic tunability of their resonance frequencies and dynamic behavior, offering a new paradigm for developing novel nanoelectronic applications of nanoresonators. In this work, we have developed ultrathin Si nanoresonator devices (~ 20 nm in thickness (t), and ~ 200 μm in length (L)) by conventional top-down microfabrication of single-crystal Si wafers and in the fabricated devices we observed wide electrostatic tuning of the resonance frequency (~ 70%) and the cubic-nonlinearity at room temperature using moderate gate-voltage. Such wide electrostatic tunability has not been achieved before in top-down microfabricated nanoresonator devices to the best of our knowledge. This research is expected to aid in the development of scalable fabrication process of widely tunable ultrathin resonators for commercial applications.

P-S21-72-T2 Fabrication of the atomically-stepped ultrasmooth conducting polymer thin film on the flexible transparent polyimide sheet

Prof. Mamoru Yoshimoto [1]

1. *Tokyo Institute of Technology*

In this work, we report fabrication of the 0.3nm-high atomically-stepped ultra-smooth conducting polymer thin film coated on the flexible transparent polyimide sheet by using the thermal nanoimprinting process. The transcription of 0.3 nm-high atomic-step and atomically flat terrace pattern of the sapphire (Al2O3 single crystal) wafer mold onto the Poly(3,4-ethylenedioxythiophene): poly(styrenesulfonate) (PEDOT: PSS) conducting polymer thin film surface was investigated under various nanoimprinting conditions. The atomic steps and terrace pattern corresponding to the mold could be transferred onto the PEDOT: PSS thin film spin-coated on the polyimide substrate for nanoimprinting at 260□ under 15 MPa for 40 min. The electrical resistance of the nanopatterned PEDOT: PSS thin film with 0.3 nm-high atomic steps remained almost unchanged after nanoimprinting at 260□.

P-S21-73-T2 PFIB Reworking: A Cost-Effective Solution for Repairing ASICs

Dr. Evgeny Demenev [1], ***Dr. David Novel*** [1], ***Dr. Lorenza Ferrario*** [1]

1. *FBK, Fondazione Bruno Kessler*

The Plasma Focused Ion Beam (PFIB) is a highly versatile tool extensively utilized in the semiconductor industry and material characterization for various applications. It offers a wide range of operations, including cross-sectioning, ion-polishing surfaces for EBSD analysis, preparation of TEM lamellae, analysis of failure mechanisms, wafer inspection, creation of nanopatterns (e.g., for photonics), and automatic slice and view capabilities. The focus of this study was to assess the effectiveness of the PFIB reworking technique on a considerable quantity of multi-channel ASICs that exhibited behavioural anomalies attributed to incorrect microfabrication tolerances. The results of the study demonstrated a significant improvement in yield through PFIB reworking, with almost 95% of the channels being fully functional compared to the initial 50% PFIB reworking proves to be a fast, reliable, and cost-effective method for circuit modification in ASICs. This technique is particularly valuable for testing modifications to ASIC designs prior to implementation in a new production run, thus minimizing production costs and risks. The strategies outlined in this study can provide guidance to enhance the yield of integrated circuits across various applications, including medical imaging detectors, astro-particle physics, MEMS, and telecommunications.

P-S21-74-T2 Adjustable arrangement of Polystyrene Micro Spheres by Using 3D Micro Printing and Colloidal Lithography

Mr. Li-En Kang [1], ***Mr. Yu-Sheng Xhieh*** [1], ***Prof. Yeeu-Chang Lee*** [1]

1. *Department of Mechanical Engineering, Chung Yuan Christian University*

Most of the microstructures used as light diffusers or anti-reflective coatings involves very expensive fabricate equipment. This paper presents a facile approach to the fabrication of 3D microstructures in any conceivable configuration. A micro-printing system based on UV curable epoxy was first used to create a template with a specific geometric arrangement. In this study, we created surface templates in three configurations, including a conventional grid, concentric circles, and a honeycomb arrangement of displaced hexagons. Polystyrene (PS) micro-spheres in a methanol mixture (1: 10) was applied over the template under vibration. The workpiece was then heated to 65°C for 5 minutes, causing the spheres to fuse and form a stable attachment with the underlying template for the creation of a PDMS soft mold. The diffusers fabricated by using the soft mold created interesting diffraction patterns when illuminated under 655nm laser light. In the future, we will work on tailoring these diffraction patterns by altering the underlying template and/or size of the PS spheres.

P-S21-75-T2 Calculation of magnetic stiffness over torque between two current-carrying circular filaments arbitrary oriented in the space

Dr. Kirill Poletkin [1]

1. *Hefei University of Technology*

A new set of formulas for calculation of magnetic stiffness over torque between two circular filaments arbitrarily oriented in space were derived by using Mutual Inductance Method (MIM) (Kalantarov- Zeitlin's method). Formulas are presented in an analytical form through integral expressions, whose kernel function is expressed in terms of the elliptic integrals of the first and second kinds. The derived new formulas were successfully validated by Grover's method (GM).

P-S21-76-T2 Synchronous vibration of 1×2 torsional micromirror array

Mr. Mikiya Oki [1], ***Prof. Amit Banerjee*** [1], ***Prof. Jun Hirotani*** [1], ***Prof. Toshiyuki Tsuchiya*** [1]

1. *Kyoto University*

We report a synchronized 1×2 torsional micromirror array for high speed, large scan angle, and large aperture optical devices. A MEMS torsional mirror is an optical device to control the angle of the incident laser using torsional vibration of supporting beams which connect the anchor and the mirror plate. The torsional mirror is key to miniaturizing spatial scanning systems such as endoscopes, Lidar, and laser projectors. However, the performance of applications using torsional micromirrors is limited because of the difficulty in achieving large deflection angle, large mirror size, and high resonant frequency at the same time despite its merit of being compact, light, and low power consumption. In our previous research, we report a micromirror array to achieve a large deflection angle, high resonant frequency, and large aperture but the variations in the vibration amplitude and phase were the problem. In this study, we propose a synchronizing method to reduce the variations and demonstrate it using a 1×2 torsional micromirror array.

P-S21-77-T2 Comparison of Pt- and W-based FEBID-grown nano-cones

Dr. Cristiano Glessi [1], ***Mr. Mike Simons*** [1], ***Ms. Aya Mahgoub*** [1], ***Mr. Toon van Marken*** [1], ***Dr. Cornelis Hagen*** [2]

1. *tu delft,* ***2.*** *Delft University of technology*

Focused Electron Beam-Induced Deposition (FEBID) can be used for the direct production of three-dimensional free-standing nano-structures. However, the precision, durability and production time of these structures are highly dependent on electron beam and precursor-gas parameters. Concentric nano-cones are explored as a case study, which are produced using two different FEBID precursors: $MeCpPtMe_3$ (deposition of PtC_x) and $W(CO)_6$ (deposition of W-C). We present a systematic comparison of the 3D patterning of these precursors and of the performance of the grown material under harsh electron exposure conditions.

P-S21-78-T2 Transport of Droplets via Magnetically-Responsive Microwall Arrays with Path-Guide

Ms. Soyeon Kwon [1], ***Prof. HYUN-TAEK LEE*** [1], ***Mr. Jihun Kim*** [1], ***Ms. Yoobin Do*** [1]

1. *INHA University*

Stimulus-responsive micropillars or microwalls have garnered significant attention in current research due to their wide range of potential applications in diverse fields, including micro mixers, micro pumps, droplet transportation, and surface manipulation. This study focuses on the development of activated microwalls and investigates their operation through the utilization of magnetic fields. Specifically, we explore the use of a periodic magnetic field generated by a Halbach array to enable controlled droplet transport, allowing for manipulation of both transport speed and path. In this research, a flexible microwall arrays responsive to magnetic fields was fabricated using soft lithography techniques. The fabrication process involved creating a master mold through maskless lithography and incorporating a magnetic-responsive composite material called carbonyl iron powder (CIP) into polydimethylsiloxane (PDMS). The microwalls achieved adjustable bending angles and significant bending variations, allowing for precise droplet transport. By comparing structures with linear patterned walls to those with droplet path-guide, it was found that the inclusion of path-guide prevented droplet detachment and enabled more accurate control over the droplet transport path. Through the manipulation of microwall patterns and magnetic field application, the trajectory of droplets was governed with precision, presenting a promising development for droplet control systems.

P-S21-79-T2 Direct Printing Process of High-Refractive-Index Polymer for Practical Fabrication of High-Performance Metasurfaces

Mr. Dong Kyo Oh [1], ***Mr. Joohoon Kim*** [1], ***Ms. Hyunjung Kang*** [1], ***Prof. Junsuk Rho*** [1]

1. *pohang university of science and technology*

Visible metasurfaces, with periodic nanostructures, enable precise control over electromagnetic waves for holography, lenses, and optical sensors. However, costly and time-consuming electron-beam lithography (EBL) hinders practical metasurface fabrication. Here, we present a direct printing method employing a polymer blended with high-refractive-index TiO2 nanoparticles for efficient metasurface fabrication. The effective refractive index is tailored up to 1.9 by adjusting nanoparticle concentration. Rigorous analysis optimizes metasurface designs, while direct printing on flexible substrates yields high-performance metasurfaces verified through diffraction efficiency measurements. We expect this approach can be extended to other functional materials, opening possibilities for the practical fabrication of highly efficient and multifunctional metasurfaces.

P-S21-80-T2 Design and Simulation of Miniatured Piezoresistive Diaphragm Pressure Sensor for High Vacuum Applications

Dr. Jian LU [1], ***Dr. Lan ZHANG*** [1], ***Dr. Yuichi Kurashima*** [1], ***Dr. Hideki TAKAGI*** [1]

1. *National Institute of Advanced Industrial Science and Technology (AIST)*

In situ monitoring of pressure variations by microelectromechanical system (MEMS) in pipes, vacuum chamber, etc. is one of the key technologies for industry 4.0. MEMS Pirani sensor has been well investigated in recent years with a full range of 0.1~1000 Pa and an extremely high resolution of 0.01 Pa, while it needs complicated calibration due to gas dependency and temperature dependency. An absolute MEMS capacitance vacuum sensor with a full range of 1~1000 Pa has been developed with an achievable resolution of 0.5 Pa and a sensitivity of 33.03 fF/Pa. However, it is difficult to be used under strong and high frequency electric fields, since the inductive current may induce noise or even breakdown the device. In this work, a piezoresistive diaphragm pressure sensor was proposed with miniatured size of 2.2 mm × 2.2 mm, which is expected to use in the pressure range of 1~100 Pa with good linearity and a resolution of better than 0.1 Pa. Finite element method by COMSOL Multiphysics^{R} was used to optimize the device geometries. The design and simulation results will be presented herein in detail. The device fabrication process and evaluation results will be discussed as well.

Poster Session2.2: Track 4

P-S22-01-T4 Design and development of a multi-sensor temperature gradient platform for accelerated characterisation of innovative materials for chemoresistive sensor applications

Dr. Andrea Gaiardo [1], ***Dr. Anze Sitar*** [1], ***Dr. Matteo Valt*** [1], ***Dr. Elia Scattolo*** [1], ***Dr. Alvise Bagolini*** [1], ***Dr. Pietro Tosato*** [1]

1. *FBK, Fondazione Bruno Kessler*

Nowadays, the need for advanced, compact and low-cost gas sensors for various applications has led to a sharp increase in research and development in this field. Among the various solid-state gas sensors studied, chemoresistive devices have attracted much attention due to their high versatility, including the possibility of synthesising novel nanostructured sensing materials with tuned chemical and physical properties, whose sensing performance is typically temperature dependent. The objective of this work was to provide a new platform for accelerated testing of the sensing performance of nanostructured semiconductors in thermoactivation mode. Specifically, a sensor based on a silicon MEMS micro-heater and equipped with multiple electrodes was designed to exploit the temperature distribution on a suspended membrane in order to measure the electrical properties of a sensing material at different working temperatures simultaneously. The device was developed through silicon microfabrication, using a stack of SiO2 and Si3N4 for the zero-stress suspended membrane and Pt for the heater and electrodes. The performance of the device was then positively tested using a thick film of SnO2 nanoparticles as a sensing material, whose sensing performance was characterised with respect to different concentrations of H2, ethanol and CO.

P-S22-02-T4 New optical detection method of home-made explosives based on lab on paper chemical sensors

Dr. Viktoriia Lastivka [1], Mr. Piotr Kasprzak [2], Mrs. Izabela Mazur [2], Mr. Piotr Baran [2], Mr. Wawrzyniec Pniewski [2], Prof. Ilona Grabowska-Jadach [1], Prof. Michal Chudy [1], Dr. Katarzyna Tokarska [3], Dr. Kamil Zukowski [3], Prof. Artur Dybko [1]

1. *Warsaw University of Technology,* ***2.*** *Military Institute of Armament Technology,* ***3.*** *CEZAMAT*

This paper presents a new fast colorimetric method for visual detection of home-made explosives, i.e. triacetone triperoxide (TATP), hexamethylene triperoxide diamine (HMTD). To the authors' best knowledge, this is the first paper describing such a colorimetric test. The chemical sensors were based on chromatography paper covered with wax. The very well-known starch iodide test was utilised. 10 ul of the sample was dropped on the central point of the sensor. Within one minute the sensing zone changed color into deep red/wine for TATP, and red/orange or HMTD. The sensors work up to the concentrations 0.01 mg/ml.

P-S22-03-T4 Cycling stability of elastomer composites for stretchable sensors

Ms. LINGYU liu [1], ***Dr. Thomas Kister*** [2], ***Prof. lola gonzalez-garcia*** [3], ***Prof. Tobias Kraus*** [4]

1. *INM – Leibniz Institute for New Materials, Saarbrücken, 66123, Germany,* ***2.*** *INM – Leibniz Institute for New Materials, Saarbrücken, 66123 Germany,* ***3.*** *INM-Leibniz Institute for New Materials, Campus D2 2, Saarbrücken, 66123, GermanyDepartment of Material Science and Engineering, Saarland University, Saarbrücken, 66123, Germany,* ***4.*** *INM-Leibniz Institute for New Materials, Campus D2 2, Saarbrücken, 66123, Germany; Colloid and Interface Chemistry, Saarland University, Saarbrücken, 66123, Germany*

Soft robotics and wearable electronics rely on stretchable actuators and sensors that can withstand cyclic loading under large strains. Materials with conductivities and/or piezoresistivities that are stable over many cycles are required. del Bosque A. *et al* developed highly stretchable sensors based on graphene nanoplatelet (GNP) reinforced polydimethylsiloxane for human motion monitoring.

Here, we study how the piezoresistance of such composites changes upon many tensile loading cycles. For this, pastes with graphene in liquid silicone precursors were prepared. We quantified the electrical conductivity of the resulting composites at different filling ratios using four probe resistivity measurement. The percolation limit of graphene in PDMS was approximately 12.5 wt%. We investigated the cycling stability of the 20 wt% composites which had a conductivity of around 10 S/m by exposing samples to strains of 10% and 20% for 300 cycles using a tensile testing machine and 2-point contact electrical measurements. After a rapid increase at the beginning the resistivity stabilized at higher cycling numbers.

The effects can be attributed to the presence of some irreversibility of graphene flakes during load-unloading, and to the viscoelastic behavior of the PDMS elastomer, which induces a delayed load-strain response, and thus, a delay in the electrical response.

P-S22-04-T4 Electroplating-based engineering of plasmonic nanorod metamaterials

Dr. Mihir Sahoo [1], ***Mr. Abhay Anand VS*** [1], ***Prof. Anshuman Kumar Srivastava*** [1]

1. *Indian Institute of Technology Bombay*

Electron beam lithography (EBL) is an effective technique for fabricating low-dimensional, reproducible nanostructures. Vertical cylindrical AuNR array fabrication is carried out via EBL, followed by metallization. Among various physical vapour deposition (PVD) techniques sputtering and e-beam evaporation techniques are popular due to the smooth and uniform thin film deposition of Au. However, the PVD techniques require a vacuum environment to deposit Au, which is costly, time-consuming, and thickness-limited. On the contrary, chemical deposition, i.e., electroplating deposit [1] with higher thickness in less time and at lower cost, becomes an alternative method for Au deposition. In this work, we present a detailed optimization for the electroplating-based fabrication of these metamaterials. We find that slightly acidic (6.0 < pH < 7.0) gold sulfite solution supports immersion deposition, which should be minimized to avoid uncontrolled Au deposition. Immersion deposition leads to plate-like (for smaller radius AuNR) or capped-like, i.e., mushroom (for higher radius AuNR) structure formation. The electroplating time and DC supply are the tuning parameters that decide the geometry of the vertically aligned AuNR array in area-dependent electroplating deposition. This work will have implications for developing plasmonic metamaterial-based sensors.

P-S22-05-T4 Solid-state ionic synaptic transistors for neuromorphic computing applications

Dr. Nerea Alayo [1]

1. *Catalan Institute of Energy Research*

In recent years, synaptic transistors have gained attention for analog computing, aiming to overcome the Von Neumann bottleneck in traditional digital computing. Synaptic transistors mimic biological neurons, improving energy efficiency and processor performance for brain-inspired computing. Electrolyte-Gated Transistors (EGTs) are a promising choice for synaptic transistors. However, current EGTs rely on unstable electrolytes or operate at high temperatures, causing integration challenges. To address this, the authors present a three-terminal thin-film EGT based on a ceramic electrolyte and a mixed ionic-electronic conducting channel able to work below 150ºC. In this EGT, a gate bias is applied to change the oxygen stoichiometry of the channel by pumping oxygen ions across the electrolyte. This technology is compatible with microfabrication processes, allowing for low-cost and large-scale production. The EGT first prototypes have been fabricated on oxide-based single crystal substrates. Nevertheless, the goal is to develop devices on silicon substrates to be compatible with existing microelectronics manufacturing processes. The presented EGT exhibits rapid and low-energy conductance at low temperatures, demonstrating synaptic characteristics such as short- and long-term plasticity, paired pulse facilitation, and spike timing-dependent plasticity. The proposed synaptic transistor holds great potential for enhancing energy efficiency and processor performance in information technology.

P-S22-06-T4 Color imaging-based Optomechanical system for gas sensing

Dr. Ferran Pujol-Vila [1], ***Dr. Mar Alvarez*** [2]

1. *Instituto de Microelectrónica de Barcelona (IMB-CNM, CSIC),* ***2.*** *Institute of Microelectronics of Barcelona (IMB-CNM-CSIC)*

We present the development- of a label-free colorimetric mechanical sensing platform for the remote quantification of VOC by image analysis. The platform is based on an array of bimorph optomechanical sensors (e.g. bridges) with structural coloration derived from the periodic nanostructuration of one of its surfaces. With this approach, the light diffraction on the photonic surface generates an associated structural coloration of the sensors that converts the induced mechanical motion into color shifts (mechanochromism). The bimorph optomechanical bridges are made of a layer of solvent resistance off-stoichiometry thiol-ene polymer (OSTE), and a PDMS layer, which have high swelling to solvents. During the detection of gases, the bimorph optomechancial cantilever experiment a bending due to the different swelling ratio of both materials. As a proof of concept, we demonstrate the detection of vapor of ethanol at different concentrations.

P-S22-07-T4 Benchmarking of ion-based nanopatterning techniques on stainless steel injection molding inlays for automotive applications

Mr. Florian Schlachter [1], ***Dr. Jens Bolten*** [1], ***Mrs. Olatz Adarraga*** [2], ***Dr. Yordan Georgiev*** [3], ***Mr. Tommy Schönherr*** [3], ***Ms. Ana Zuzuarregui*** [4], ***Mr. Evgenii Modin*** [4], ***Prof. Max Lemme*** [1]

1. *AMO GmbH,* ***2.*** *TECNALIA Basque Research and Technology Alliance (BRTA),* ***3.*** *Institute of Ion Beam Physics and Materials Research, Helmholtz-Zentrum Dresden-Rossendorf (HZDR),* ***4.*** *CICnanoGUNE-External Services Department, Basque Research and Technology Alliance (BRTA)*

We report on a novel approach for the nanotexturing of steel inlays for manufacturing automotive interior surfaces based on a combination of nanoimprint lithography (NIL) and an ion-based structuring process. The NIL produces the nanomask, while the latter transfers the nanopattern into a steel substrate. Reactive Ion Etching (RIE), Reactive Ion Beam Etching (RIBE) and Ion Milling have been benchmarked regarding their patterning capability in the steel substrate. We used UNE 1.2083 steel in our experiments, which is widely used as a mold material in the injection molding of plastic parts.

P-S22-08-T4 Optimization of the nanofabrication process of superhydrophobic fluidic concentrator coupled with metallic plasmonic nano-antennas for SERS analysis in the sub-femtomolar range.

Mr. Sofien Ramos [1], ***Mr. Victor Fabre*** [1], ***Mr. Matthieu Arribat*** [1], ***Ms. Aurélie Lecestre*** [1], ***Mr. Adrian Laborde*** [1], ***Mr. Franck Carcenac*** [1], ***Dr. Philippe Louarn*** [2], ***Prof. Christophe Vieu*** [3], ***Ms. Emmanuelle Trevisiol*** [4]

1. *LAAS-CNRS,* ***2.*** *IRAP,* ***3.*** *Toulouse University,* ***4.*** *TBI*

Self-assembled silicon nanopillars decorated with metallic nanoparticles have emerged as a reproducible SERS substrates. This study aims to optimize the fabrication process for SERS analysis by investigating two main factors: the surface density of hot spots and the enhancement factor. The surface density is influenced by the black silicon RIE process, while the enhancement factor depends on the morphology, the size and coupling of the decorated noble metal nanoparticles. We propose an optimization methodology for black silicon in non-cryogenic temperatures using RIE-ICP etching machines for SERS applications. We investigated the black silicon RIE parameters and the impact on nano-pillar over the wafer, as well as the influence of silver layer thickness and metal nanoparticle morphology. SERS detection of Rhodamine B (RhB) at sub-femtomolar concentration is performed using a specific device with a fluidic concentrator. Then hierarchical clustering algorithm extracts RhB spectra from 1650 recorded ones to determine the optimal nano-antenna configuration. The study focuses on the number of individual spectra resembling the Raman signature of the target molecule at sub-femtomolar concentration. We will present the main results at the conference and show that it is possible to find an optimal configuration for the etching parameters and thin film thickness.

P-S22-09-T4 Flexibly printed bioactive gold-polythiophene hybrid nanoparticles for electrochemical biosensing

Ms. Muniba Shahzad Bhatti [1], ***Ms. Indra Backes*** [2], ***Mr. Michael Alexander Horst Klos*** [1], ***Mr. Yannic Brasse*** [3], ***Prof. lola gonzalez-garcia*** [4], ***Prof. Tobias Kraus*** [1]

1. *INM-Leibniz Institute for New Materials, Campus D2 2, Saarbrücken, 66123, Germany; Colloid and Interface Chemistry, Saarland University, Saarbrücken, 66123, Germany,* ***2.*** *INM-Leibniz Institute for New Materials, Campus D2 2, Saarbrücken, 66123, Germany;,* ***3.*** *INM-Leibniz Institute for New Materials, Campus D2 2, Saarbrücken, 66123, Germany,* ***4.*** *INM-Leibniz Institute for New Materials, Campus D2 2, Saarbrücken, 66123, GermanyDepartment of Material Science and Engineering, Saarland University, Saarbrücken, 66123, Germany*

Conventional fabrication of electronically read-out biomedical sensors requires multi-step fabrication processes with thermal sintering and environmentally impactful chemicals to achieve sufficient electrical conductivity. Alternative processing methods such as inkjet printing waste less material and provide opportunities for bespoke designs.

In this contribution, we discuss printable gold nanoparticle (AuNPs) inks that become conductive immediately after deposition. A conductive polythiophene (P3KHT) was immobilized on quasi-spherical gold nanoparticles with a diameter of 74 ± 19 nm. The bioconjugation of Glucose oxidase (GOx) can be performed in solution prior deposition or on the surface of deposited AuNPs@P3KHT layer. In both cases, we found that the amine group of GOx was covalently bound to the functional carboxylate groups in the polymer side chain via EDC/NHS coupling, making the “bioink” suitable for glucose biosensing.

Colorimetric assays indicated that the AuNPs@P3KHT-Gox had a lower Michaelis Menten constant (K_m), indicating a higher enzymatic affinity towards glucose, than the free enzyme Gox. Electrochemical biosensors were fabricated by inkjet printing the AuNPs@P3KHT-GOx dispersion on PET (polyethylene terephthalate).

Our results indicate that AuNPs@P3KHT are suitable not only for glucose detection. They can be conjugated with other biologically relevant targets such as antibodies, oligonucleotides and peptidomimetics, for example for stem cell growth.

P-S22-10-T4 Development of Atomic Gold Decorated Polyaniline Derivative Electrodes toward Electrochemical Alcohol Sensing

Dr. Tomoyuki Kurioka [1], ***Mr. Keisuke Okamoto*** [1], ***Mr. Shohei Yoshida*** [1], ***Mr. Kengo Watanabe*** [1], ***Dr. Chun-Yi Chen*** [1], ***Dr. Parthojit Chakraborty*** [1], ***Prof. Takamichi Nakamoto*** [1], ***Prof. Masato Sone*** [1], ***Prof. Mark Chang*** [1]

1. *Tokyo Institute of Technology*

Electrochemical alcohol sensors are widely applied to many areas of industry. Their performance is related to electrode materials. Hybrid materials composed of atomic size gold clusters (Au_N, where N indicates the atomic size of the Au clusters) and polyaniline (PANI) are promising electrode materials. Generally, the electrocatalytic abilities of the hybrid materials are affected by their morphologies and nanostructures, which resulted from chemical structures of supporting materials. PANI derivatives, such as poly(*o*-methoxy aniline) (POMA) and poly(*o*-toluidine) (POT), also can serve as supporting matrices of noble metal nanoparticles. Therefore, Au_N-decorated PANI (Au_N/PANI) derivatives are also expected to be applicable to electrochemical alcohol sensing. In this presentation, we report Au_N/PANI derivative electrodes and their electrocatalytic abilities for 1-propanol (1-PrOH) oxidation.

Au_N/PANI derivative electrodes (i.e., Au_N/POMA and Au_N/POT) were fabricated by electrochemical polymerization of corresponding monomers followed by the atom-by-atom gold deposition process. Cyclic voltammetry (CV) measurements for 1-PrOH were performed in KOH aqueous solution using Au_N/PANI derivative electrodes (N = 1 or 2) to evaluate their electrocatalytic abilities. CV measurements proved that Au_N/POMA and Au_N/POT showed larger electrocatalytic abilities for 1-PrOH oxidation than Au_N/PANI, and Au_2/POT exhibited the highest eleccatalytic abilities in Au_N/PANI derivatives electrodes (N = 0, 1, or 2).

P-S22-11-T4 Light-controlled multimaterial microrobots for microscale pH sensing

Mr. Daniel Maher [1], ***Mr. Andreu Murillo Vilella*** [1], ***Mr. Marcin Piekarczyk*** [1], ***Dr. Colm Delaney*** [2], ***Dr. Larisa Florea*** [2], ***Prof. Rafael Taboryski*** [1], ***Dr. Ada-Ioana Bunea*** [1]

1. *Technical University of Denmark,* ***2.*** *Trinity College Dublin*

The sensing of chemicals in a microscale area is of great interest in many research and industrial applications. Microrobots that change shape depending on the presence of certain biomarkers or chemicals are promising options to accomplish this task. In this work, we present six designs for light-controlled multimaterial microrobots composed of a hard polymer backbone and a pH-responsive hydrogel. These microrobots can be fabricated entirely using two-photon polymerization 3D printing. The designs were formulated by considering factors such as microrobot size, ease of confirming visually when the target analyte/environment is encountered, and ease of alignment in a two-step printing process. When designing the microrobots, weight was a major constraint as they must be transported using optical trapping. The designs were tested by printing them with the backbone material only and were successfully manipulated using an optical trapping setup. From our current results, these microrobots seem promising for localized sensing applications in microscale regions.

P-S22-12-T4 High-Response Ethanol Gas Sensor Based on LaFeO3/In2O3 Composite

Prof. Zhenyu Yuan [1], ***Mr. Ninghao Chu*** [1]

1. *Northeastern University*

Abstract: Ethanol is a common industrial material and also a symbol of alcohol driving, so it is necessary to effectively detect ethanol gas. $LaFeO_3$, as a perovskite structured semiconductor has special catalytic activity, which can be used to improve the gas sensing performance of gas sensors. Therefore, we prepared pure $LaFeO_3$ and In_2O_3 as control groups (Sample1 and Sample2). Then, we add different mass amount $LaFeO_3$(0.02 g, 0.01 g, and 0.005 g) into the In_2O_3 hydrothermal reaction solution to prepare $LaFeO_3/In_2O_3$ composite (Sample3-Sample5).The $LaFeO_3/In_2O_3$ sensor exhibits selectivity for ethanol gas at the optimal operating temperature of 220□. The gas sensing performance of the In_2O_3 material composed by 0.01 g $LaFeO_3$ is the best, with a response of 147 to 100ppm ethanol gas at 220□ that is 2.8 times of the response of pure In_2O_3 sensor. The lower limit of detection is 500ppb. The response of Sample4 to ethanol gas at various concentrations is higher than that of other sensors, and it has continuity and long-term stability. The improvement of gas sensing performance of the sensor is mainly due to the Fermi level effect of the heterojunction, the catalytic effect of $LaFeO_3$ and the synergy between different components.

P-S22-13-T4 Study on Variation of Main luminescence centers in Eu Doped AlN Thin Films with Annealing Temperature Increasing

Mr. Yingda Qian [1], ***Prof. Xinwei Zhao*** [1]

1. *Department of Physics, Tokyo University of Science*

Phosphor-converted white LEDs have been successfully commercialized as solid-state lighting due to their high efficiency, small volume, and long lifetime, but lack of red emission and efficiency reduction between phosphors and chips also hinder its development. As a potential material for WLEDs, RE-doped nitride was selected. This paper, the low-temperature PLD method was used to grow the AlN: Eu thin film on Si(111) substrate. The proportion of Eu^{3+} and Eu^{2+} is regulated by changing the annealing temperature from 300 to 900 ^{o}C. The emission from Eu^{2+} and Eu^{3+} was measured by cathodoluminescence. The asymmetric emission peak originated from $^{5}D_{0} \rightarrow {}^{7}F_{2}$ transition of Eu^{3+} was fitted as Q1,Q2, and Q3 by gaussian function. At 900 □ annealing temperature, the area of Q2 is reversed and larger than Q3 and Q1. The defect excitation dominant type change can be attributed to the dissolution of Eu-O couple in the surface suddenly enhanced at 900 □. The N vacancies near the Eu ions are filled by O ions. The oxidation of Eu^{2+} from XANES can also prove the dissolution behavior at the surface. This study revealed the influence of defects and annealing temperature on the luminescence which gives instructions to the LED growth.

P-S22-14-T4 Spin valve effect in Fe3GeTe2/ZnO/Ni heterostructure with low resistance-area product

Mr. Whan Kyun Kim [1], ***Mr. Namgun Kim*** [1], ***Mr. Yong Ha Shin*** [2], ***Prof. Woo Jong Yu*** [2]

1. *Department of Semiconductor and Display Engineering, Sungkyunkwan University,* ***2.*** *Department of Electrical and Computer Engineering, Sungkyunkwan University*

2D van der Waals (vdW) magnetic materials, such as Fe_3GeTe_2 with its perpendicular magnetic anisotropy and metallic nature, have gained significant attention for their potential application in spintronic devices like spin valves. In this study, we inserted ZnO, a wide-band-gap semiconductor with a wurtzite structure, as a tunneling barrier for low resistance-area product (RA) magnetic tunnel junctions (MTJs) between Fe_3GeTe_2 and Ni to investigate the spin valve effect. Fe_3GeTe_2 and Ni exhibit perpendicular and in-plane magnetic anisotropy, respectively, causing the stray field around Ni to induce a spin direction change in Fe_3GeTe_2 in near zero magnetic field region. When a sufficient magnetic field is applied, an additional MR change is observed due to a complete spin direction change in Fe_3GeTe_2. We confirm an MR of 15.6 % at an RA of 37.6 kΩ/μm^2 at 2 K. The RA of our device is three times smaller compared to the previously reported Fe_3GeTe_2/InSe/Fe_3GeTe_2 spin valve with a comparable MR. Our findings demonstrate the potential of vdW layered magnetic materials as ferromagnetic electrodes in conventional MTJs.

P-S22-15-T4 4D printing of soft responsive polymer microstructures

Mr. Marcin Piekarczyk [1], ***Mr. Daniel Maher*** [1], ***Ms. Yekaterina Tskhe*** [2], ***Dr. Larisa Florea*** [2], ***Dr. Colm Delaney*** [2], ***Dr. Ada-Ioana Bunea*** [1]

1. *Technical University of Denmark,* ***2.*** *Trinity College Dublin*

Hydrogels have attracted attention in various biomedical fields due to their excellent biocompatibility, water absorption capacity, stimuli-responsive behaviour, and mechanical properties. However, traditional hydrogel fabrication methods have limitations in creating complex 3D geometries and functional dynamic behaviour required for successful applications. 4D printing, a new technology in additive manufacturing, has emerged as a promising approach to overcome these limitations. Our study demonstrates the potential of 4D printing of hydrogels, using the Nanoscribe Photonic Professional GT+ 3D printer and the two-photon polymerization (2PP) technique. We fabricated complex microstructures and characterized their response to different pH levels. The hydrogel material expresses reversible shape change behaviour between dry and wet states and exhibits swelling behaviour across different pH levels, expanding up to 40% in pH ~13 and 15% in pH ~2. Using the hydrogel material, ee designed and fabricated microrobotic scaffolds with a sensing element, as well as biomimetic cell structures. Both types of structures were designed and fabricated for further biomedical studies. Our findings demonstrate the potential of 4D printing of hydrogels for creating material systems capable of changing their shape, structure, or function directly off the printing bed, with potential applications in biomedical research and industry.

P-S22-16-T4 A novel Hall configuration with simplyfied design

Prof. Siya Lozanova [1], Dr. Avgust Ivanov [1], Mr. Martin Ralchev [1], Prof. Chavdar Roumenin [1]

1. *Institute of Robotics at Bulgarian Academy of Sciences*

An original Hall configuration with simplified design and orthogonal magnetic field activation is suggested. The device contains rectangular *n*-Si substrate. Three ohmic contacts are formed on each of the long sides. The prototype of the sensor is manufactured using IC technology by employing four masks. The resistivity of the *n*-Si substrate is $\rho \approx 7.5\Omega.cm$. A deep surrounding *p*-ring is also implemented around contacts. Thus, the surface current spreading is reduced and the transducer region is confined. The penetration of the current trajectories reaches about 30 μm. The increased sensitivity constituting $S_{RI} \approx 40V/AT$ is due to the decreased parasitic surface currents. Also the output electrodes are located out of the regions where the supply currents flow. The sensor resolution is about 80x135 μm^2. The output characteristics are linear and odd from the magnetic field and supply. The nonlinearity constitutes no more than $NL \leq 0.6$ % at field $\pm 0.7T \leq B$. The temperature coefficients of magnetosensitivity and resistance are respectively $TC_s \approx 0.1\%/°C$ and $TC_R \approx 1.1\%/°C$. In optimized operating mode, the minimum registered induction consists of $B_{min} \approx 16\mu T$. This ensure detailed mapping of the magnetic-field topology. The configuration having high performance is very promising for application in automobiles, industrial contactless automation, and especially, in robotics and robotised surgery.

P-S22-17-T4 A New sensor phenomenon in disordered systems under uniaxial pressure

Prof. Siya Lozanova [1], Mr. Martin Ralchev [1], Dr. Avgust Ivanov [1], Prof. Chavdar Roumenin [1]

1. *Institute of Robotics at Bulgarian Academy of Sciences*

The paper presents a sensor phenomenon determining the deformation state of rock structures with enhanced measurement sensitivity and accuracy. The discovered effect is an emission of micro-sized particles when exerting uniaxial pressure upon rocks and construction concrete. For the first time in non-regular systems – rocks and concretes, the directly proportional dependence between the amount of generated microparticles and the surface emitting them has been experimentally proven. A scaling coefficient has been introduced, which expresses the ratio of the particle-emitting surfaces of a formed measurement capacity in borehole of the massif and of laboratory specimen. By this coefficient, the number of particles obtained from the reference specimen for the relevant load forces, is multiplied. This scaling provides to adequately establish the deformation state in the borehole in accordance with the particle amounts obtained in it. The instrumental monitoring of the mineral microparticles in the borehole, referred to the pressure values, determines the pre-destruction and destruction conditions in the massifs. One of the numerous applications of the emission effect is in seismically active regions – to detect the folding of tectonic plates, fault activity and rock formations. This increases the possibility to obtain additional information about eventual prediction of earthquake processes.

P-S22-18-T4 Wafer-scale Fabrication of Infrared Metalenses using DUV lithography

Dr. Kai Sun [1], ***Dr. Xingzhao Yan*** [1], ***Mr. Chuang Sun*** [1], ***Dr. Jun-yu Ou*** [1], ***Prof. Otto Muskens*** [1]

1. *University of Southampton*

Wide field of view imaging at mid-infrared (MIR) range plays an important role in sensing temperature environment monitor, and military detection. Up to now, as the high absorption of the silicon and silica, a MIR imaging system is mainly made up of Si- or Ge-based optical components to realize high efficiency, which increases the cost of MIR imaging.

With the adoption of artificial metasurfaces, the metalenses are developed through phase-shifts control by different nano-features. Although metalenses have been widely demonstrated through e-beam lithography as lab solution, it is still challenging to DUV lithography and semiconductor process to make metalenses with suitability of mass production. Recently, we have demonstrated that wafer-scale metal oxide metasurface can be reliably manufactured using DUV lithography. In this work, we demonstrate Si-based infrared Metalens through DUV lithography and achieve Metalens on 8-inch substrates with more than 100 individual metalenses (12 mm diameter) on a single 200 mm Si substrate. In addition, the fabricated Metalens have the metasurface arrays as lens on one side and the moth-eye structure on the other side, achieving two metasurfaces on both sides. The fabrication process is compatible with large-scale manufacture and can accelerate Metalens commercialization from R&D to the premium market.

P-S22-19-T4 Acrylamide molecule detection by Surface-Enhanced Infrared Spectroscopy using resonant nanoantennas

Dr. Santos Merino [1], ***Dr. Jorge Ramiro*** [1], ***Dr. Alberto Villar*** [1], ***Dr. Ruth Diez*** [1], ***Dr. Iban Amenabar*** [2], ***Dr. Ralph Gay*** [3], ***Dr. Mario Zapata*** [4], ***Prof. Javier Aizpurua*** [4]

1. *Tekniker,* ***2.*** *CIC nanoGUNE,* ***3.*** *CIC nanogune,* ***4.*** *Materials Physics Center*

This work uses resonant Surface Enhanced Infrared Spectroscopy to develop a high-sensitive infrared absorption sensor to detect low concentrations of acrylamide in solution. To evaluate the potential of infrared absorption spectroscopy to detect acrylamide in water, the IR absorption spectra of acrylamide was simulated within the framework of density functional theory (DFT). The geometry of the gold antennas was optimized to provide effective coupling between the frequency of the plasmonic modes of the gold nanorod antennas and the target vibrational frequencies. Different geometries of nanoantennas with widths between 100 and 400 nm and lengths varying from 1.6 to 2.4 μm were fabricated on CaF_2 substrates using two different nanofabrication techniques: electron beam lithography and high resolution maskless lithography

P-S22-20-T4 Lowering dissipation in Electro-Optomechanical resonators for quantum transducing RF to optical signals

Dr. Enrico Serra [1], ***Dr. Michele Bonaldi*** [2], ***Dr. Antonio Borrielli*** [2], ***Prof. Giovanni Di Giuseppe*** [3], ***Dr. Nicola Malossi*** [3], ***Dr. Bruno Morana*** [4], ***Dr. Riccardo Natali*** [3], ***Dr. Paolo Piergentili*** [3], ***Prof. Lina Sarro*** [4], ***Prof. David Vitali*** [3]

1. *Istituto Nazionale di Fisica Nucleare, TIFPA, 38123 Povo (TN), Italy,* ***2.*** *Institute of Materials for Electronics and Magnetism, Nanoscience-Trento-FBK Division, 38123 Povo, Trento,* ***3.*** *Physics Division, School of Science and Technology, University of Camerino, I-62032 Camerino (MC), Italy,* ***4.*** *Dept. of Microelectronics and Computer Engineering /ECTM/EKL, Delft University of Technology, Feldmanweg 17, 2628 CT Delft, The Netherlands*

Optomechanics with nano/micro silicon/silicon nitride resonating devices is a growing field for the detection of extremely weak signals. The domain of application of these devices ranges from fundamental physics experiments to the search for quantum gravity effects or quantum technology applications. In fact, these devices can be functionalized with metallization and used as a testbed for exploring new ways of implementing quantum communication protocol. The mechanism involved in the conversion process is based on the capacitive modulation of the microwave/RF field by the displacement field of the nanomembrane that is in turn dispersively coupled to a high-finesse Fabry-Pérot optical cavity.

In this contribution, we describe the design and fabrication of the mechanical resonating part of the Electro-Optomechanical resonator for quantum transduction. The characterization of the mechanical Q-factor by a ring-down interferometric measurement demonstrates that the oscillator reaches quality factors of more than one million in the MHz range inside a vacuum chamber. The device can be effectively assembled with any read-out electrode and potentially used to transduce RF weak classical signals in a Nuclear-Magnetic-Resonace (NMR) apparatus. Currently, the system is optimized to be embedded into the optical cavity for the sympathetic ground state cooling of an LC resonating circuit.

P-S22-21-T4 Atomic PdxAuy Clusters Decorated Polyaniline for Electrochemical Sensing of 1-Propanol

Mr. Shohei Yoshida [1], Mr. Keisuke Okamoto [1], Dr. Tomoyuki Kurioka [1], Dr. Chun-Yi Chen [1], Dr. Parthojit Chakraborty [1], Prof. Takamichi Nakamoto [1], Prof. Masato Sone [1], Prof. Mark Chang [1]

1. *Tokyo Institute of Technology*

Electrochemical sensors are capable to fast-detect chemicals with a high sensitivity at a low cost. By these advantages, electrochemical sensors are promising for detections of biomolecules. In order to improve the sensitivity, catalytic electrodes composed noble metal clusters and conductive polymers as the supporting material are developed. Examples of the noble metal clusters are gold and palladium, and the conductive polymer could be polyaniline. In addition, reducing the size of the metal cluster is an effective strategy to improve the catalytic activity and reduce the cost. In this study, bi-atomic, tri-atomic and tetra atomic gold and palladium clusters decorated polyaniline electrodes were prepared, and their catalytic activities for the sensing of 1-propanol were evaluated. The results showed that the catalytic activity is higher for the even-numbered atomic pure palladium clusters than that of the odd-numbered atomic pure palladium clusters, which reveal the odd-even pattern effect. Next, for bi-atomic metal clusters, the catalytic properties were lower of heterogeneous bi-atomic metal clusters decorated PANI electrodes. On the other hand, for tri-atomic and tetra-atomic metal clusters, the catalytic activity was higher for heterogenous atomic metal clusters.

P-S22-22-T4 Fabrication and Characterization of Plasmon-Active Infra-Red Enhanced Micromembranes for Gas Diffusion Studies

Ms. Ketki Srivastava [1], ***Dr. Jasper Lozeman*** [1], ***Prof. Albert van den Berg*** [1], ***Dr. Ward van der Stam*** [2], ***Prof. Mathieu Odijk*** [1]

1. *University of Twente,* ***2.*** *Utrecht University*

Surface Enhanced Infra-Red Absorption Spectroscopy (SEIRAS) is a commonly used tool for obtaining chemical and biological information. Typical configurations include resonantly tuned microstructures on dielectric substrates, enhancing a certain region of interest in the mid-IR spectrum. In this work, we report an innovative method to fabricate plasmon-active porous micromembranes with an end use in applying them for studying gas diffusion. The membranes are fabricated on a 500 nm silicon-rich nitride (SiRN) layer using mask-less laser writing (MLW). We optimize the design of SEIRAS nanoslits and etch them completely to form porous micromembranes. The plasmonic activity is achieved by sputtering 50 nm gold (Au) on the fabricated porous micromembranes. Based on finite-difference time-domain (FDTD) simulations we show that the SEIRAS enhancement arises due to the collection of localized plasmons at the edges of the Au-SiRN microstructures. In addition to the fabrication, the optimization of the process flow is done by comparing electron-beam lithography (EBL) to MLW. We conclude that MLW is a better choice due to its durability during long etching processes, ease of use and reduced writing time when compared to EBL.

P-S22-23-T4 sensor technology development embedding nanoparticles

Mrs. Michelle Cedeño [1], ***Mrs. Ana Coloma Velez*** [1], ***Dr. Ramon Bragos*** [2], ***Prof. Manuel Domínguez-Pumar*** [2], ***Prof. Alexandra Bermejo*** [2]

1. *PhD STUDENT,* ***2.*** *Polytechnic University of Catalunya*

This work exhibits the development and analysis of a novel capacitive proximity sensor (CPS) based on the use of ceramic nanoparticles and common salt (NaCl), and the impact of the employed encapsulation layer on its sensing mechanism and performance. The proposed proximity sensor is composed of a simple aluminium electrode structure, a sensing layer based on SiO_2 nanoparticles and NaCl, and a *PDMS* layer as encapsulation layer. The characterisation has been carried out at room temperature within the sensing range (5-140 *mm*). The results of the impedance spectroscopy have been fitted using an equivalent circuit that models the electric behaviour of the proposed sensors. This approach reveals that the charge carrier's diffusion dominates the sensing mechanism. Furthermore, the comparison of the IS measurements show that PDMS encapsulation layer modifies the sensing performance of the device, affecting the impedance of the sensing layer, as expected. Nevertheless, it does not alter the trend of the electrical behaviour, thereby not indicating a change in the sensing mechanism. In particular, the results show that the proposed devices without and with encapsulation exhibit a detection distance of 140 *mm* with maximum capacitive sensitivities of $-40.2\%cm^{-1}$ and $-4740\%cm^{-1}$, respectively.

P-S22-24-T4 Advances in Micro- and Nanofluidic Devices for Vacuum Compatible UV Light Experiments

Mr. Manuel Müller [1], ***Dr. Irene Fernandez-Cuesta*** [1], ***Mr. Herbert Atrian Garcia*** [1], ***Mr. Jeremy Teuber*** [2], ***Mr. Rukan Nasri*** [1]

1. *Universität Hamburg,* ***2.*** *PhD STUDENT*

The aim of this project is to enable UV-based experiments including ultra-short laser pulses in vacuum through micro- and nano-fluidic systems. We coat fluidic chips with aluminium oxide using a flow-through gas phase deposition technique developed in our group and partially etch the chip. In this way we obtain physically encapsulated channels with wall thicknesses of 30 nm, which are suitable for integrating UV light and short pulsed light without degradation of the temporal resolution. We have demonstrated the feasibility of our approach by analysing the autofluorescence of DNA with excitation and emission light passing through the aluminium oxide layer on quartz. We have also demonstrated this fabrication principle in a polymer matrix fabricated by nanoimprint lithography. The disadvantage of these polymer fluidic chips is that their autofluorescence overlaps with the emission spectra of many relevant (bio)molecules. We are therefore transferring our approach to quartz substrates.

P-S22-25-T4 Enhancing Exciton Emission in Monolayer MoS2 using Electroplated Plasmonic Gold Nanodiscs

Mr. Abhay Anand [1], ***Dr. Mihir Sahoo*** [2], ***Prof. Anshuman Kumar Srivastava*** [1]

1. *Indian Institute of Technology Bombay,* ***2.*** *IIT Bombay*

Transition metal dichalcogenides (TMDCs) such as MoS_2 are semiconductors in the 2D material family, which gained attention due to their promising optical and electronic properties. Atomically thin thickness and low quantum yield are the main challenges which limit TMDC for practical applications. To tackle these challenges of TMDC and achieve effective manipulation of optical properties, integrating subwavelength plasmonic nanostructures with monolayer TMDCs is an effective solution. Plasmonic nanostructures can confine and enhance nearfield intensity during excitation.In this study, we employed electron beam lithography and electroplating techniques to fabricate an array of gold nanodisc (AuND) capable of significantly enhancing the photoluminescence (PL) of monolayer MoS_2. Monolayer MoS_2 placed on the gold nanodisc array exhibited an impressive photoluminescence enhancement of up to 150 times compared with the non-nanodisc region. To understand the mechanism behind this enhancement, we conducted FDTD simulations.

P-S22-26-T4 Determination of conventional and inverse magnetocaloric effect in iron oxide thin films

Mr. Dharohar Sahadot [1], ***Mr. Prakhar Gupta*** [1], ***Dr. Murtaza Bohra*** [1]

1. *Mahindra Ecole Centrale - School of Engineering, Mahindra University*

The heart of magnetic refrigeration technology is the working magnetocaloric materials that exhibit both the normal magnetocaloric effect (MCE) and inverse magnetocaloric effect (IMCE) over a wide temperature range. Currently, cost-effective various technological iron oxide material layers have been investigated due to their tunable MCE peaks at extended temperatures as a function of growth temperatures (T_G), paving the way to realise cooler-on-chip devices. Interestingly, IMCE are computed near the antiferromagnetic and Verwey transition temperatures, respectively, using a phenomenological model. The MCE of iron oxide layers is measured in terms of magnetic entropy change (ΔS_{max}) values (-0.06 to 0.11 J/kg-K) at relative tiny magnetic field of 0.5 kOe (See Fig 2). This study demonstrates that T_G variation is a main lever of action that enables external tuning of the soft magnetic and magnetocaloric properties which can eventually be used to create various magnetic ground states for MCE and IMCE functionalities.

P-S22-27-T4 Experimental Optical Cladding for Integrated Photonics with High-Contrast Polymer Waveguides

Mr. Omkar Bhalerao [1]

1. *AMO GmbH, Advanced Microelectronic Center Aachen*

In this work, we present an experimental optical cladding layer (SX AR-LWL 2.0) manufactured by Allresist GmbH and its compatibility with SU-8 processing, its simple patterning using i-line lithography, and its RI close to SiO2. The cladding layer thickness can be easily adjusted through dilution and the RI can be tuned by varying the composition, enabling flexibility in design and fabrication. We utilized the SU-8 2 formulation to fabricate bilayer waveguides (WGs) in an uncladded version exposed to the ambient environment and WGs cladded with the experimental resist. The bilayer SU-8 processing enables the fabrication of varying waveguide cross-sections on the same wafer. A cutback analysis of the cladded and uncladded WGs was performed to extract the total coupling losses along with the WG propagation loss. Our findings demonstrate that the cladded SU-8 WGs exhibit superior performance compared to the uncladded ones, with reduced propagation losses of approximately 1.4 dB. Our results hereby demonstrate the successful integration of the experimental optical cladding layer SX AR-LWL 2.0 in integrated photonic devices utilizing SU-8 WGs.

Track1 - Novel Developments in Nano/Micro Fabrication Methods and Processes / Track3 - Micro/Nano Engineering for Life Sciences

O-S81-T1-1 Advancements in Fabricating Polymer based Microring Resonators by Nanoimprint Lithography

Dr. Santhosh Pandian [1], ***Dr. Petri Karvinen*** [2], ***Dr. Heikki Rekola*** [2], ***Dr. Subhajit Bej*** [1], ***Dr. Paul Müllner*** [3], ***Dr. Eggeling Moritz*** [3], ***Dr. Rainer Hainberger*** [3], ***Prof. Tapio Niemi*** [1]

1. *Nanophotonics Research Group, Tampere University, Tampere,* ***2.*** *University of Eastern Finland, Joensuu,* ***3.*** *AIT Austrian Institute of Technology GmbH*

Polymeric materials for photonic integrated circuits (PIC) have attracted much interest over the past decades due to their unique properties, including low absorption, wide wavelength range, and simple and low-cost fabrication process. When compared to its counterparts (semiconductor materials), the polymer-based materials have the capability to fine tune their refractive index more easily. Polymeric materials also can incorporate active dopants, such as dyes providing optical gain, to realize devices with enhanced functionality. Advanced 3D structures are required to allow a high integration density of the photonic systems. Some of the classic examples of these systems are very large-scale integrated (VLSI) photonics and microring resonators (MRRs). Polymer based MRRs have been widely used in many applications ranging from optical communication and signal processing to sensing. One important field of application of polymer waveguide MRRs is biosensing, which is highly relevant for medical diagnostics, food analysis, and environmental monitoring due to its high sensitivity and real-time monitoring capabilities. Another interesting area for polymer waveguide MRRs is the realization of miniaturized ultrasonic detectors, which are key elements for photoacoustic imaging. These MRRs have been prepared using the established Nanoimprint Lithography (NIL) technique.

O-S81-T1-2 3D Ice Lithography

Dr. Bingdong Chang [1], ***Mr. Affan Kaysa Waafi*** [1], ***Mr. Joachim Lyngholm-Kjærby*** [1], ***Dr. Rubaiyet Haque*** [1], ***Prof. Anpan Han*** [1]

1. *Technical University of Denmark*

We report a novel 3D lithography strategy using condensed organic vapour thin films and electron beam exposure layer by layer. The process uses a focused electron beam to chemically cross-link the organic ice into a solid and shares software and CAD databases with industrial 3D printing. Guided by electron-matter-interaction simulations, we control the cross-linking thickness between 250 nm and 2 μm. The 3D prints contained up to 500 layers, and the smallest structures are 550-nm-wide. Our digital process complements two-photon lithography in three areas; (i) it is compatible with chemistry beyond photopolymers, (ii) we can print delicate suspended structures and tubes because our structures are not immersed in liquid resins that reside in cavities and destroy structures by interfacial forces, (iii) hanging structures are printed without sacrificial supports. Nanophotonics and microfluidics applications are demonstrated.

O-S81-T1-3 Manipulating droplet motion on superhydrophobic glass by contact electrification

Mr. Kuan-Ting Chen [1], ***Prof. Jiann Shieh*** [1]

1. *National United University*

The manipulation of water droplet movement has garnered significant attention due to its wide range of applications in various fields, such as self-cleaning, heat transfer, and energy harvesting. Various strategies involving both active methods and passive methods have been employed to drive droplet movement. However, a major challenge that remains is overcoming surface resistance to achieve fast movement over long distances. Recently, the generation of static charge through contact electrification has emerged as a promising approach for effective droplet manipulation. While the charging phenomenon has been shown to affect droplet sliding on surfaces and motion in air, the spontaneous repulsion between droplets on surfaces has not been identified, despite being observed in vapor-mediated systems or under external field conditions. Here, we present a spontaneous charging method for water droplets to repel each other on surfaces. We grew silica nanowires on a quartz plate to create a superhydrophobic glass. After contact electrification by injecting water, the generated static charge allows pure water droplets to repel each other, preventing them from merging and enabling droplets to become stuck on the surface and even move uphill. Remarkably, these charged droplets can travel at speeds exceeding a few centimeters per second over centimeter-scale distances.

O-S81-T3-4 Biodegradable Chitosan / Cellulose Nanocrystals free-standing device as a multifunctional sensor for health applications

Ms. Valentina Antonaci [1], ***Dr. Gaia de Marzo*** [1], ***Dr. Laura Blasi*** [2], ***Dr. Virgilio Brunetti*** [1], ***Dr. Francesco Rizzi*** [1], ***Prof. Massimo De Vittorio*** [1]

1. *Istituto Italiano di Tecnologia,* ***2.*** *National Research Council of Italy*

The fabrication of multifunctional piezoelectric materials represents a new frontier in sustainable and wearable devices. In this work, we study the combination of biodegradable optically active nanoparticles, cellulose nanocrystals, with a biodegradable piezoelectric polymer, chitosan. The CNCs solution were dropped onto the chitosan film obtaining a d_{33} of 13 pC/N by PFM, and used to fabricate a device with a d_{33} of 13,7 pC/N. This technology has the potential to produce, a biodegradable wearable multifunctional sensor able to sense both dynamic and static stimuli.

Papers

Novel Developments in Nano/Micro Fabrication Methods and Processes - Papers

Nano-antennas with decoupled transparent leads for opto-electronic studies

Melanie Sommer [a], Florian Laible [a], Kai Braun [b], Alfred J. Meixner [b], Monika Fleischer [a]
[a] Institute for Applied Physics and Center LISA+, University of Tübingen, Tübingen, 72076, Germany
[b] Institute of Physical and Theoretical Chemistry and Center LISA+, University of Tübingen, Tübingen, 72076, Germany
e-mail: melanie.sommer@uni-tuebingen.de

The integration of plasmonic nanoantennas with electrical circuits and optoelectronic devices is a promising way to keep up with further miniaturization and to improve their performances [1]. Subwavelength metal nanoparticles can exhibit localised surface plasmon polaritons (LSPPs) when illuminated with light. These LSPPs lead to high field enhancements around the nanoparticle especially at sharp corners and small gaps as well as hot electron generation. Two-dimensional (2D) materials can be included as well into optoelectronic devices, as they are extremely thin and exhibit excellent electric and optical properties that can be further boosted with plasmonic nanostructures [2]. Including plasmonic antennas to these systems is mainly done with many particles in random distributions or arrays. However, by using one nanostructure for both contacting and optical excitation one can measure e.g. current fluctuations under illumination directly where they happen. But this can be quite challenging. One has to overcome some obstacles to contact such a small antenna electrically, as the optical properties should not be disturbed by the leads. The common way is to place the leads at places with low near-field intensity [3]. This way the plasmonic properties of the antenna can be preserved. Using this approach, electrically driven antennas could be achieved [4] and the implementation of bow tie antennas into break junctions to investigate tunnelling currents and optical properties while changing the gap size of the bow tie is possible [5].

We developed a new process to contact single dimer antennas with indium tin oxide (ITO) [6]. ITO is already widely used as a material for transparent electrodes in optical devices. As it is also insulating at optical frequencies, it is an ideal material to contact plasmonic nanoantennas. By using ITO, the placement of the leads can be arbitrarily chosen, as the LSPPs stay localised, and the leads scatter very little light which can show up as noise in measurements.
The fabrication process is depicted in figure 1. In a first step the pattern of the dimer antenna consisting of a bow tie with leads is transferred into PMMA resist on an ITO covered glass slide with electron beam lithography (EBL). After the development, the gold deposition onto the sample is done by thermal evaporation. To keep the part for leads in the pattern free from gold, the sample is tilted by 10° with respect to the surface normal. The resist walls are now shadowed so the areas in the EBL pattern for the leads are not metallized. Next aluminium oxide is evaporated under normal incidence onto the full pattern as a mask for the following etching step. After the lift-off, the ITO layer is etched away with reactive ion etching (RIE) using an Argon plasma, leaving only the gold antennas with small ITO strips as leads on the glass substrate. The etch mask is then removed. Now a small gap can be introduced with focused helium ion beam milling to separate the contacts, and some reshaping of the bow tie can be done if necessary. A fabricated bow tie can be seen in figure 2 a).
Under dark field illumination the bow tie and the macroscopic gold leads appear bright, the ITO leads however hardly scatter light, so they are barely visible. By investigating the fabricated nanostructures with darkfield spectroscopy, one can see the plasmonic modes of the bow tie. In the spectrum in figure 2 b) three peaks can be seen. They are the three prominent modes of a bow tie, namely the base mode, anti-bonding mode and bonding mode. This confirms that the LSPPs can be excited, and the bow ties are optically decoupled from the leads. The nanoantennas can not only be measured optically, but also in combination with e.g. 2D materials, like graphene, on top to conduct transport measurements under optical excitation.

[1] Z. Liang et al., Plasmonics 9 (2014) 859–866.
[2] H. Wang et al., Nanoscale 12(15) (2020) 8095-8108.
[3] J. C. Prangsma et al., Nano Letters 12 (8) (2012) 3915-3919.
[4] J. Kern et al., Nature Photon 9 (2015), 582–586.
[5] C. M. Gruber et al., Nano Letters 20 (6) (2020) 4346-4353.
[6] M. Sommer et al., in preparation (2023).

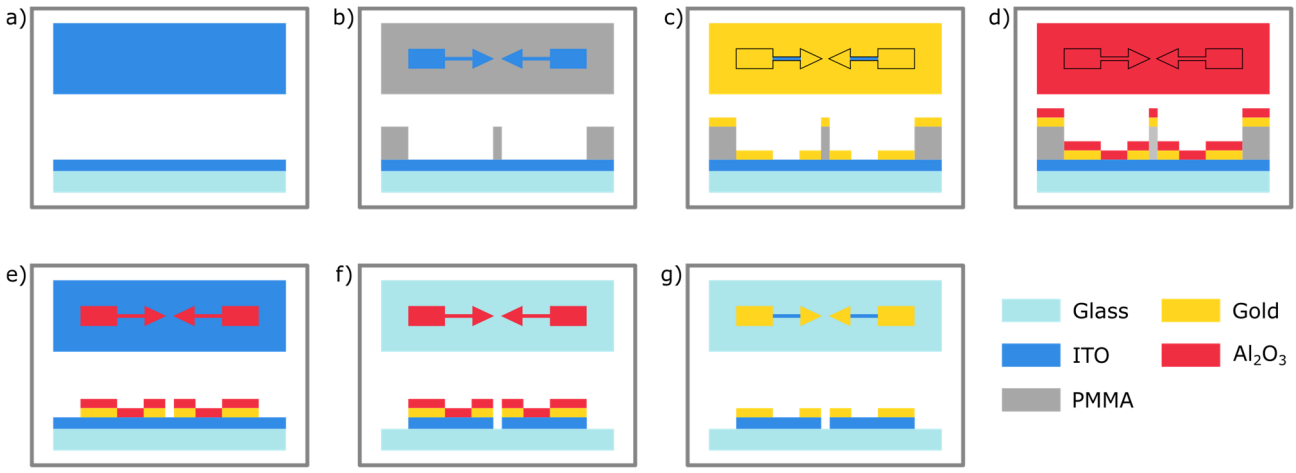

Figure 1. Steps of the fabrication process. a) Glass substrate with ITO layer. b) EBL and development. c) Gold evaporation with 10° tilt to the substrate normal, so parts of the pattern are shadowed by the resist. The sample is then tilted 10° in the other direction for a second gold deposition. A two-step evaporation was chosen to keep the connection between the bow tie and the substrate walls as thin as possible to ensure a clean lift-off. d) Aluminum oxide mask evaporation under normal incidence. e) Lift-off. f) ITO etching with RIE. g) Removal of etch mask and Helium ion milling for refinement of the bow tie shape and introduction of a small gap.

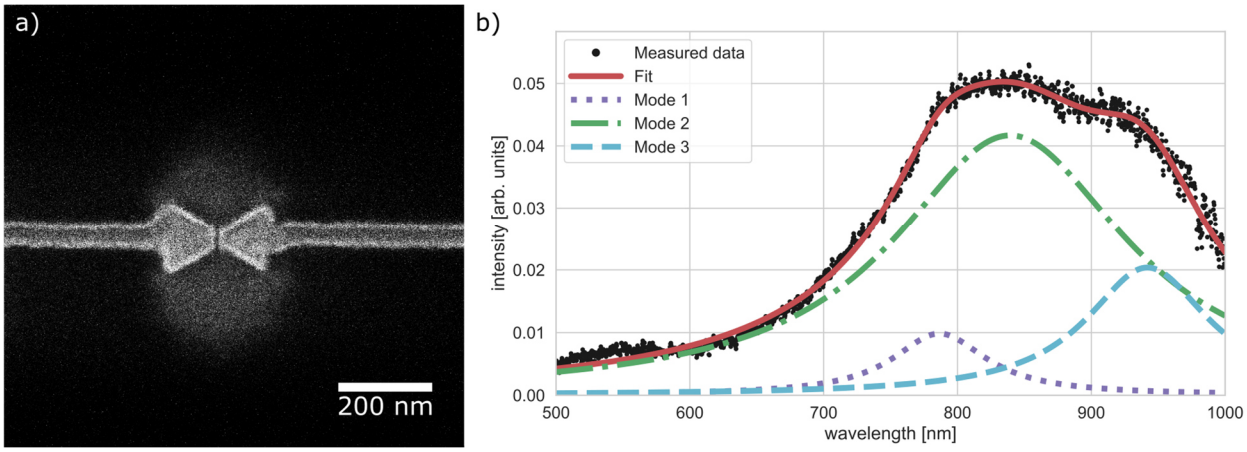

Figure 2. a) Helium ion microscope image of a gold bow tie with ITO leads after cutting the gap. b) Dark field reflection spectrum of a contacted bow tie. Three Lorentzian functions were fitted to the spectrum corresponding to the bow tie modes.

An effective and promising process for manufacturing nanofluidic channels in large scale

Wentao Yuan, Shuoqiu Tian and Yifang Chen

Nanolithography and Application Research Group, School of Information Science and Technology, Fudan University, Shanghai 200433, People's Republic of China
e-mail: yifangchen@fudan.edu.cn

Keywords: electron beam lithography, nanofluidic channel, high-density, chemical vapor deposition, self-sealing

Nanofluidic channels can find extensive applications in enzyme analysis [1], sensor [2], and nanofluidic chips [3]. Unfortunately, the manufacturing of nanofluidic channels still remains a challenge. So far, it has been reported that nanofluidic channels can be fabricated by nanoimprint, near-field electrospinning, imprinting-induced cracks, etc. However, at the stage for prototype, electron beam lithography (EBL) based processes are still needed in the areas of nanochannels owing to its advantages of high accuracy and mask less. In this work, a novel sealing method based on isotropic growth of silica on hydrogen silsesquioxan (HSQ) gratings prepared by EBL was used to fabricate inorganic nanofluidic channels with the channel-width of 60 nm.

Figure 1 presents a schematic diagram of the process flow for fabricating the inorganic nanofluidic channels. First, a 140 nm thick HSQ, supplied by Dow Corning, was spin coated on a double polished silicon wafer. Electron beam exposure was carried out by a beam-writer, JBX6300FS, supplied by Jeol Ltd., under the tension of 100 kV with the beam current of 500 pA, corresponding to the beam-spot size of 7-10 nm. The exposed HSQ was then developed in heated tetramethylammonium (TMAH) with the concentration of 0.25 mol/l for 1.5 min [4]. Finally, plasma-enhanced chemical vapor deposition (PECVD, Plasma100, Oxford) was applied to deposit a 200 nm thick silica film on the top side of the HSQ gratings at the speed of 1.2 nm/s. After deposition, the structural profiles of the fabricated HSQ gratings and nanofluidic channels were characterized by a scanning electron microscope (SEM, ZEISS Sigma 300 HD). Figure 2 presents the top and the cross-section view of the replicated HSQ grating. The width, the pitch and the height of this grating is 40 nm, 100 nm, and 140 nm respectively. After depositing silica, a serial of nanofluidic channels with high-density in the shape of pencil stub or spindle were formed, as shown in Figs 3a and 3b. Thanks to the short pitches, the open trenches in HSQ are gradually covered by the deposited silica, giving rise to a series of 200 nm tall nanochannels with the channel-width of 60 nm. It is worth mentioning that these nanochannels still have a flat upper surface.

By summery, this work has successfully developed a novel but simple process for high-density inorganic nanofluidic channels by depositing a silica film on HSQ gratings, replicated by electron beam lithography. The channel-width of the nanochannels can be further reduced through optimizing lithography parameters. Compared with traditional manufacturing methods, the proposed process, developed in this work for the nanofluidic channels has been greatly simplified. In addition, based on the high flexibility of electron beam lithography, nanofluidic channels can be precisely prepared into various shapes, such as rings, spirals, and any other shapes as needed.

[1] H. Sano et al., Lab on a Chip, 23 (2023) 727-736.
[2] D. Zhang et al., Small, 17 (2021) 2100495.
[3] H. Jeon et al., RSC Adv., 6 (2016) 46068.
[4] Y. Chen et al., Microelectron. Eng., 83 (2006) 4-9.

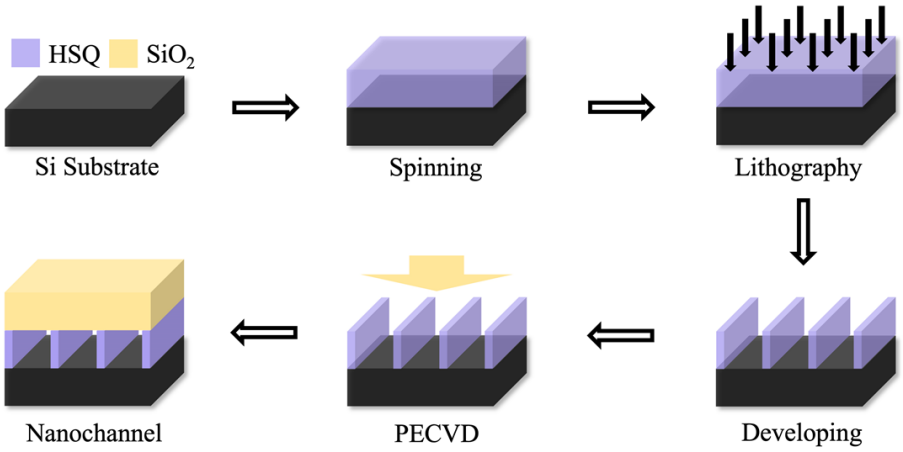

Figure 1. A schematic diagram describing the process flow

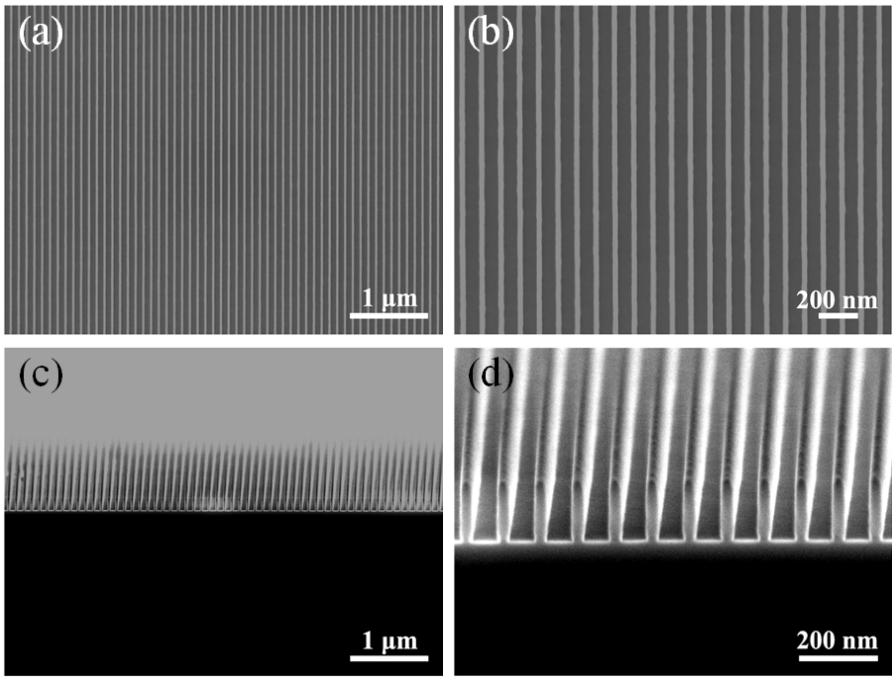

Figure 2. SEM images of the fabricated HSQ gratings. (a) and (b) top view of the HSQ gratings; (c) and (d) cross-section view of the HSQ gratings.

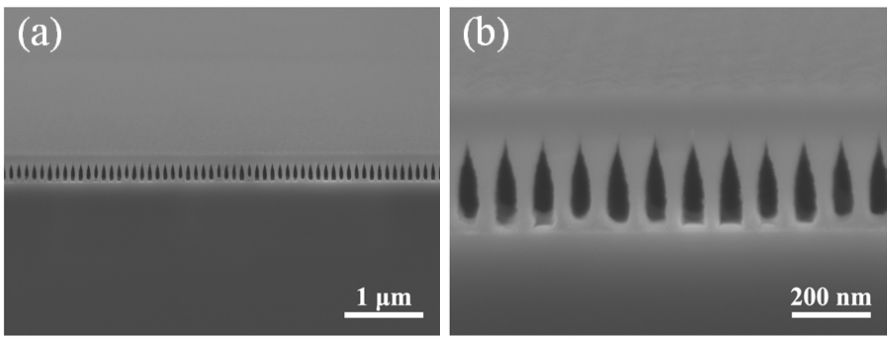

Figure 3. SEM images of the fabricated nanochannel

3D laser direct lithography for maskless patterning on large-format complex surfaces

Julian Hürtgen[a] , Serhiy Danylyuk[a], Arnold Gillner[a],

[a] Fraunhofer ILT – Institute for Laser Technology, Aachen, 52074, Germany
e-mail: julian.huertgen@ilt.fraunhofer.de

Photolithography plays a key role in micro/nano-manufacturing with a wide range of applications and outstanding importance to modern industry. While microlithographic patterning has conventionally been executed on flat substrates, mainly for producing computer chips and microcircuits, there are numerous applications that rely on curved surface fabrication of microcircuits or circuit-like components (i.e., curved waveguides, curved micro-optics, flexible electronics). For the production of these components, a mask is mandatory to protect selected areas during subsequent etching, deposition, or implantation operations. However, classical mask-based lithography is no longer possible for strongly curved substrates. Furthermore, the fabrication of resist masks for reproducible free-form structures is particularly challenging on nonplanar surfaces.

The presented system offers a new solution for maskless lithography on complex surfaces using a 5-axis direct laser writing tool (Fig. 1). The system consists of three linear and two rotary stages which are moved in a highly coordinated manner to guarantee precise alignment of the laser beam perpendicular to the curved surface throughout the entire exposure process. The laser optical system contains a UV laser diode with a wavelength of 405 nm collimated into a diffractive optical element (DOE) that converts the laser beam into a top hat profile. The beam size can be tuned between 50 and 5 µm using a removable beam expander, allowing to switch between different exposure strategies. A spray coating unit is integrated in the system to produce a homogeneous resist layer on complex substrates of a wide variety of materials. In addition, a camera detection system is included, to recognize previously written marker structures, enabling precise substrate-mask alignment for multiple photolithographic cycles.

The authors present the steps towards the fabrication of a three-dimensional optoelectronic device starting from a curved lens. The technique for producing a homogeneous resist film with minimal radial thickness variation on curved surfaces is explained. In addition, the reproducible fabrication of a resist mask for free-form structures with high edge quality is presented and different traversing strategies for direct laser lithography on 3D substrates are described. Furthermore, the writing of marker structures and the detection of them by utilizing the included camera optic system for a precise substrate-mask alignment is demonstrated.

Overall, this 5-axis 3D laser direct lithography system can fabricate homogenous resist layers and pattern structures with a resolution of 5 µm (Fig. 2) on complex surfaces with a radius of curvature of less than 23 mm (Fig. 3) and a maximum diameter of 150 mm to create a resist mask for subsequent processes, representing an important step towards the industrial production of three-dimensional optoelectronic devices.

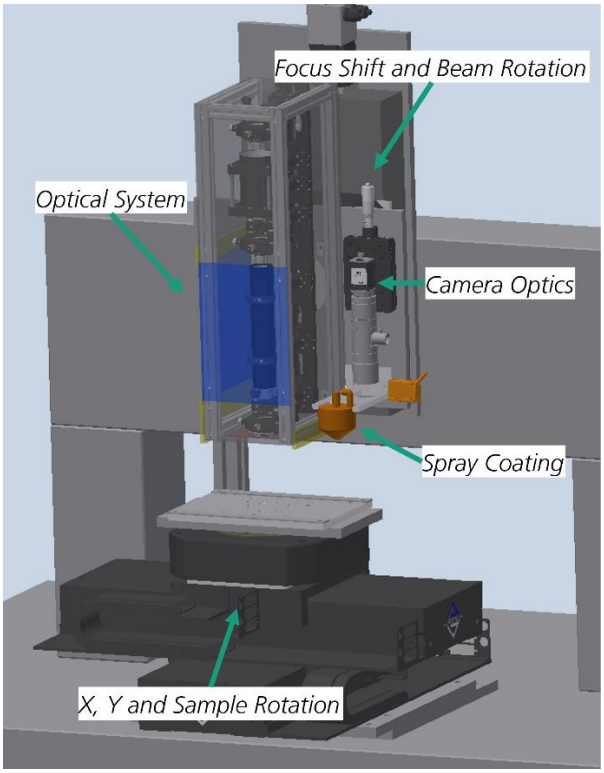

Figure 1. Schematic depiction of the overall assembly of the 5-axis 3D laser direct lithography system.

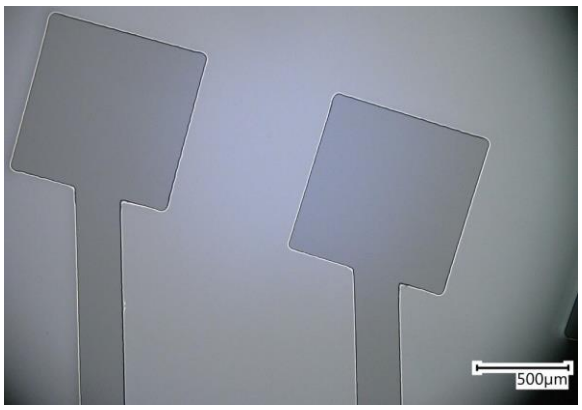

Figure 2. Light microscope image of exposed and developed structures on a resist bilayer.

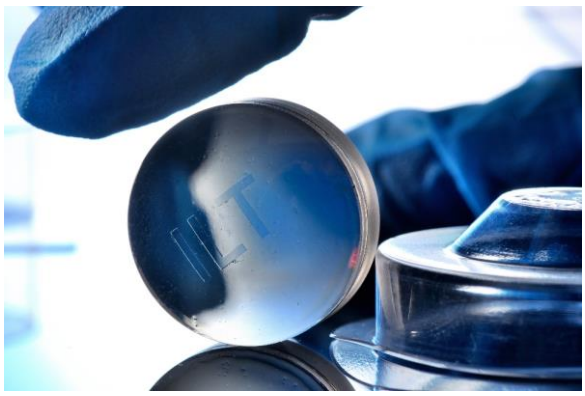

Figure 3. Image of a laser structured test layout on a convex 1-inch lens with a radius of curvature of 23 mm.

Millimeter-Scale Van Der Waals Graphene-MoS_2 Heterostructures Verified by Raman Spectroscopy

Nico Rademacher[a], Eros Reato[a,b], Annika Grundmann[c], Michael Heuken[c,d], Holger Kalisch[c], Andrei Vescan[c], Alwin Daus[a], Max C. Lemme[a,b]

[a] Chair of Electronic Devices, RWTH Aachen University, Aachen, 52074, Germany
[b] AMO GmbH, Advanced Microelectronic Center Aachen, Aachen, 52074, Germany
[c] Compound Semiconductor Technology, RWTH Aachen University, Aachen, 52074, Germany
[d] AIXTRON SE, Herzogenrath, 52134, Germany
E-Mail: max.lemme@eld.rwth-aachen.de

The coupling between 2D materials in van der Waals heterostructures influences the properties of the layer stack. Their interaction should ideally be probed non-destructively and with large-area mapping as the coupling especially in 2D materials transferred on top of each other cannot be assumed to be uniform. Raman spectroscopy is suitable to fulfil this task [1, 2], but studies often cover heterostructures of small flakes. Here we demonstrate millimeter-scale Raman mapping of graphene-MoS_2 heterostructures which have been assembled from large-area scalable films grown by chemical vapor deposition (CVD) methods. We perform statistical analyses of Raman spectra for up to mm^2-scale scans of the heterostructures which enables us to quantitatively evaluate the coupling between the two materials.

The graphene-MoS_2 heterostructure fabrication process is shown in Figure 1. Raman mappings were performed in areas with CVD graphene, CVD MoS_2, and their heterostructures before and after a post-fabrication annealing process (1 h in vacuum at 300 °C). Figure 2a displays an optical image of the measured area. Figure 2b shows spectra of single layer graphene (SLG), bilayer graphene (BLG), and a heterostructure, while Figure 2c-f shows Raman maps. The G peak position is the same for the graphene area and the heterostructure area, or before (Figure 2e) and after annealing (Figure 2f). However, the 2D peak positions differ between the graphene area and the heterostructure area after the annealing (Figure 2d), while there is no observable difference between them before annealing (Figure 2c). This indicates a change in the interaction between MoS_2 and graphene upon annealing, with the blue-shifted 2D peak position pointing to a closely-coupled heterostructure [1]. In fact, the Raman spectra not only change depending on the number of layers in graphene [2] and MoS_2 [3], but also in their heterostructures, where the 2D peak of graphene shifts similarly as it would for 2 layers of graphene [1]. No shift can be detected for the MoS_2 peaks because the multilayer MoS_2 films have a low sensitivity to such interface coupling [3].

We further statistically analyzed the distance between graphene G and the 2D peaks (Figure 3a) which allows us to define a threshold for close-coupling between the MoS_2 and graphene, i.e. the creation of a true heterostructure. We used Gaussian distribution fits and calculated their intersection resulting in a threshold at a Δ Pos(2D)-Pos(G) of about 1,100 cm^{-1}.

Histograms of the full width at half maximum (FWHM) of the graphene 2D peaks are shown in Figure 3b for the graphene and heterostructure regions. The FWHM for BLG is about twice that of SLG [4] or the heterostructure [1], enabling the distinction between BLG and a heterostructure

A heterostructure of approx. 40 mm^2 was fabricated (Figure 4a). The position of the graphene 2D peak is shown in Figure 4b and the distance between the graphene G and 2D peaks is shown in Figure 4c. Figure 4d shows our classification indicating a closely-coupled heterostructure in yellow and no interaction in blue using the 1,100 cm^{-1} limit. We hence identify areas with insufficient coupling between both 2D materials. This can be attributed to contamination that leads to a non-flatness of the 2D materials [5], which occur in typical wet-transfer processes like the one used here. This highlights the importance of locally evaluating the coupling of 2D materials in heterostructures, both for future technology improvements and heterostructure devices.

[1] K.-G. Zhou et al., *ACS Nano*, 8 (2014) 9914–9924
[2] A. Jorio et al., *ISRN Nanotechnology*, 2012 (2012) 1–16
[3] H. Li et al., *Adv. Funct. Mater.*, 22 (2012) 1385–1390
[4] A. C. Ferrari and D. M. Basko, *Nat Nanotechnol*, 8 (2013) 235–46
[5] Z. Cheng et al., *ACS Nano*,16 (2022) 5316-5324

Acknowledgments
This work was financially supported by the German Research Foundation (DFG) under the project 2D-NEMS (LE 2440/11-1).

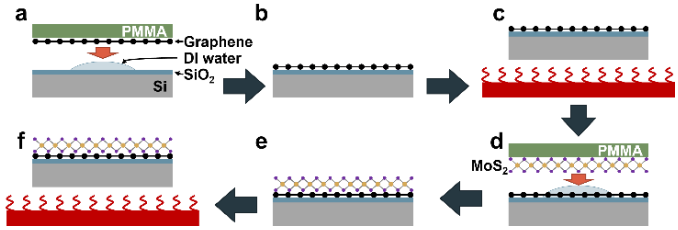

Figure 1: Fabrication process of the heterostructures: **a** Graphene with a mechanically supporting PMMA 950k A6 layer is wet transferred onto Si/SiO_2. **b** After PMMA removal. **c** Annealing of the Chip at 180°C for 10 min. **d** Wet transfer of multilayer MoS_2, also supported by PMMA 950k A6. **e** Removal of the PMMA. Raman measurements 'before annealing' were performed here. **f** Annealing of the heterostructure and Raman measurements 'after annealing'.

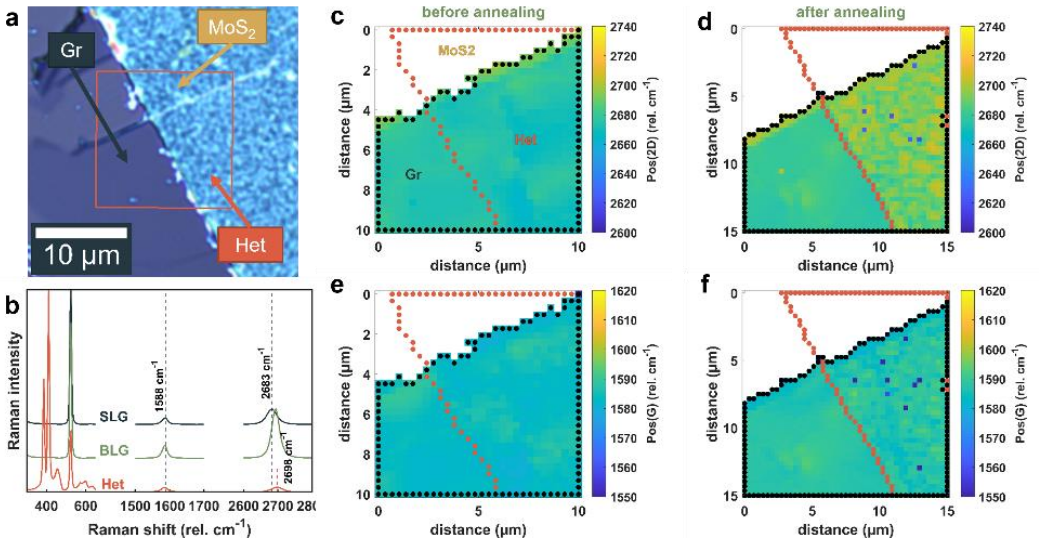

Figure 2: **a** Microscope image of the measured area (highlighted by the red frame). **b** Raman spectra of exemplary spots on single layer graphene (SLG), a bilayer graphene (BLG) and a heterostructure (Het). **c-f:** Position of the G and 2D peaks as a map. Black and red frame indicate graphene and MoS_2 locations, respectively. **c,d** 2D peak positions before and after annealing. **e,f** G peak positions before and after annealing.

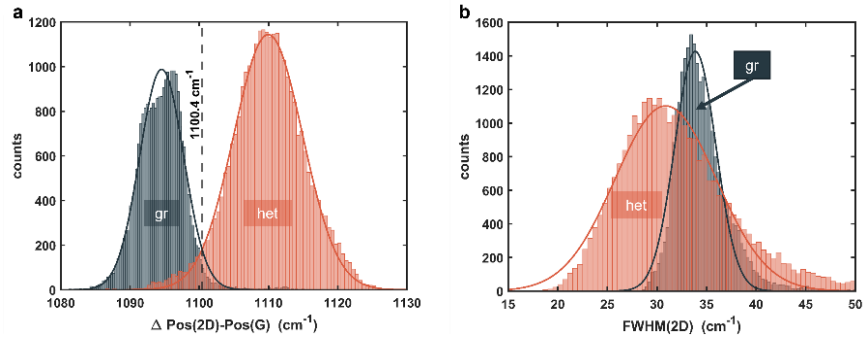

Figure 3: **a** Histogram of the difference (Δ) in peak position (Pos) for 2D and G peaks for the area in Figure 2, with Gaussian distribution fits and determination of their intersection. **b** Histogram of the FWHM(2D). Red and dark blue indicate the heterostructures (het) bare graphene (gr), respectively.

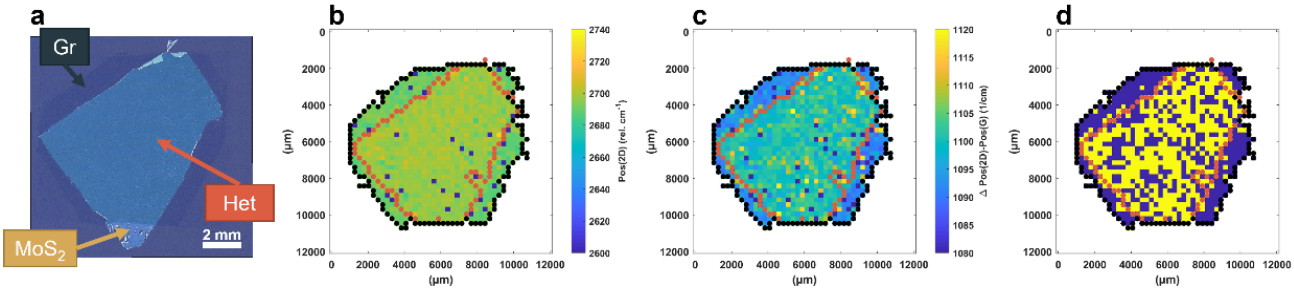

Figure 4: Large-area Raman measurement of the whole fabricated heterostructure: **a** Optical image of the measured area with a size of approx. 40 mm^2. **b-d** Black and red frame indicate graphene and MoS_2 locations. **b** Graphene 2D peak positions of the whole structure. **c** Difference (Δ) between the graphene G and 2D peaks positions. **d** Binary division of the data of b with values >1,100 cm^{-1} in yellow and the rest in blue.

Synthesis of super-flat graphene on substrates selected by molecular dynamics calculation

Satoru Kaneko [a, b], Takashi Tokumasu [c], Satomi Tanaka [a], Chihiro Kato [a], Manabu Yasui [a], Masahito Kurouchi [a], Daishi Shiojiri [a], Masahiko Mitsuhashi [a], Ruei-Sung Yu [d], Shigeo Yasuhara [e], Musa Can [f], Kripasindhu Sardar [g], Sumanta Kumar Sahoo [h], Masahiro Yoshimura [g], Akifumi Matsuda [b], Mamoru Yoshimoto [b]

[a] Kanagawa Institute of Industrial Science and Technology (KISTEC), Ebina, 243-0435, Japan
[b] Tokyo Institute of Technology,Yokohama, 226-8502, Japan
[c] Tohoku University, Sendai, 980-8577, Japan
[d] Asia University, Taichung, 41354, Taiwan
[e] Japan Advanced Chemicals, Sagamihara, 252-0243, Japan
[f] Istanbul University, Istanbul, 34134, Turkey
[g] National Cheng Kung University, Tainan, 701, Taiwan
[h] Radhakrishna Institute of Technology and Engineering, Bhubaneswar 752057, India
e-mail: satoru@kistec.jp

In order to select oxide films grown on silicon (Si), Schlom et.al. comprehensively investigate the thermodynamic stability of binary oxides on Si substrates[1]. Chemical reactions of oxide materials on Si surfaces are evaluated by Gibbs free energy. However, since the paper evaluates only thermodynamic stability, this method can not deal any crystallographic stability. The paper is essential for epitaxial growth of oxide film on Si substrates as mentioned in the paper. For epitaxial growth, we employ an absorption energy . The absorption energy is estimated by using a molecular dynamics, and we predict the orientation of crystal growth of oxide films on Si substrates, and experimental results agreed with the prediction[2].

In this study, the absorption energy was estimated on candidate substrates for graphene growth. The candidate substrates were silicon (Si), magnesium oxide (MgO), sapphire (Al_2O_3) and strontium titanate (STO), and as a carbon cluster, (1) six-ring membered carbon (6-ring), (2) 6 six-ring carbon (nano-graphene), as shown in figure1, were placed on the candidate substrates as a supercell. The absorption energy ($E_{absorption}$) was estimated by the difference of total energy of (1) substrate, (2) cluster and (3) supercell with

$$E_{absorption} = E_{sub} + E_{cluster} - E_{supercell},$$

as shown in figure2. The surfaces of substrates were optimized before the estimation of the absorption energy. Carbon films were experimentally deposited on the candidate substrates to compared with the simulation results.

Absorption energies were relatively stable on STO, MgO and Si substrates compared to Al_2O_3. After the structural optimization of supercells, 6-ring vertically stood up on Al_2O_3, Si(100) and MgO(001) substrates, and nano-graphene was distorted on Si(111) substrate. Both six-ring and nano-graphene flatly covered only the surface of STO substrate, as shown in figure 3. Carbon film was experimentally deposited on those candidate substrates in carbon dioxide (CO_2) atmosphere [3]. Carbon dioxide is extremely stable in the environment, but it can be a gentle oxidant at 900°C even in atmospheric environment, which is introduced by a paper published in 1864[4]. After deposition in CO_2 atmosphere, super-flat surface was verified on STO substrate with the roughness of ~ 70 pm[5]. Such a super-flat graphene is prepared by a chemical vapor deposition (CVD)[6,7]. A carbon film prepared by CVD method is post-annealed in CO_2 atmosphere, and show super-flat surface by selective etching amorphous carbon. CVD graphene usually contains intrinsic contamination on graphene surface during film growth, however PLD grew as-grown super-flat graphene without a post-annealing.

This study was supported in part by the Amada foundation under contract no. AF-2020227-B3, Tokyo Ohka Foundation for The Promotion of Science and technology no. 22117 and the Collaborative Research Project of the Institute of Fluid Science, Tohoku University.

Preferences

[1] K. J. Hubbard and D. G. Schlom, J. Mater. Res. 11 (1996) 2757.
[2] S. Kaneko et al., Appl. Surf. Sci. 586 (2022) 152776.
[3] S.Kaneko et al., ACS Omega

[4] M. H. Sainte-Claire Deville, Compt. Rend. 59 (1864) 873.
[5] S. Kaneko et al., Sci. Repo. 12 (2022) 15809.
[6] J. Zhang et al., Angew. Chem. Int. Ed.58 (2019) 14446.
[7] J. Zhang et al., ACS Nano 14 (2020) 10796.

Figure 1: Candidate substrates of Si, MgO, Al2O3 and STO and carbon cluster of six-ring and 7 six-ring (nano-graphene) carbon. Supercell was constructed by carbon cluster placed on candidate substrates.

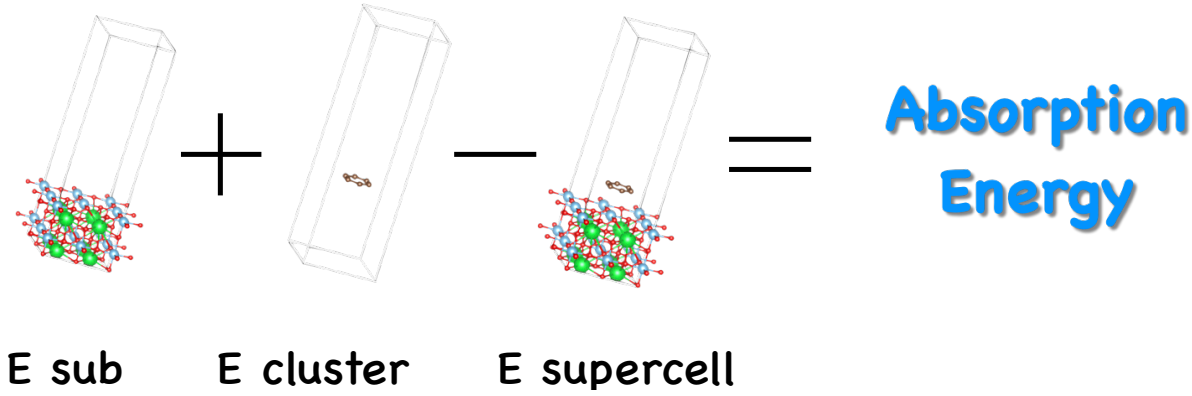

Figure 2: Absorption energy was estimated by total energy of substrate, carbon cluster and supercell.

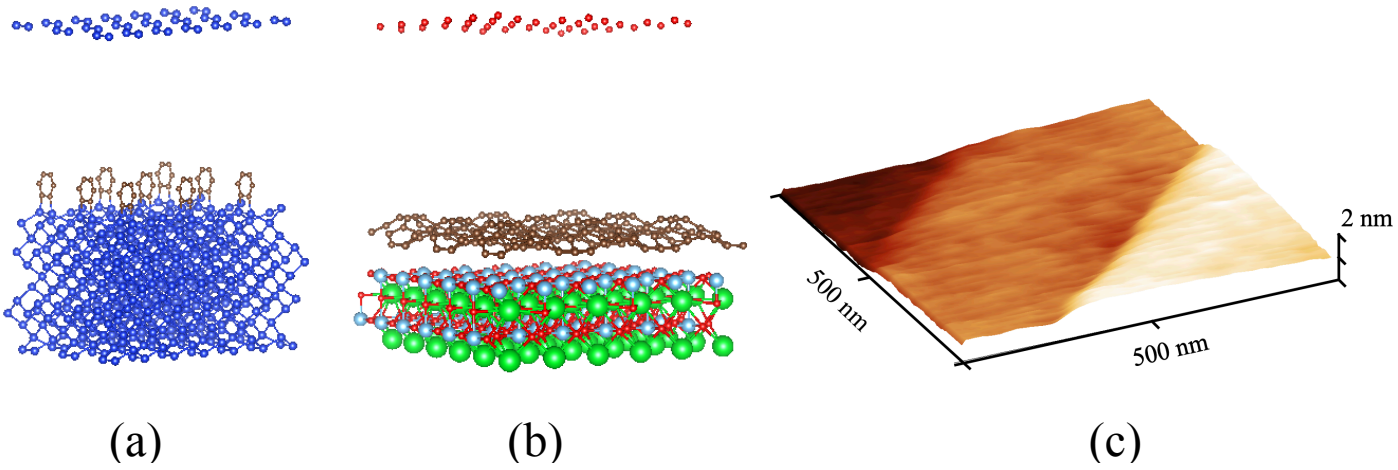

Figure 3: Structural optimization of (a) six-ring on Si(001) surface, (b) nano-graphene on STO(001) surface and (c) atomic force microscopy image of deposited carbon film.

Junctionless Nanowire Transistor: From Devices to Sensing Applications

Sayantan Ghosh [a,b], Muhammad Bilal Khan [a], Ahmad Echresh [a], Ulrich Kentsch [a], Slawomir Prucnal [a], Vaishali Vardhan [c], Subhajit Biswas [c], John Wenger [c], Stig Hellebust [c], Justin Holmes [c], Artur Erbe [a,b], Yordan M. Georgiev [a,d]
[a] Institute of Ion Beam Physics and Materials Research, Helmholtz-Zentrum Dresden-Rossendorf (HZDR), Dresden, 01328, Germany
[b] Technische Universität Dresden, Dresden, 01069, Germany
[c] School of Chemistry, University College Cork, T12 K8AF Cork, Ireland
[d] Institute of Electronics at Bulgarian Academy of Sciences, 72, Tsarigradsko Chausse Blvd., Sofia, 1784, Bulgaria
E-Mail: s.ghosh@hzdr.de

Keywords: Junctionless nanowire transistor, Ambipolar, Flash lamp annealing

Downscaling of complementary metal-oxide-semiconductor (CMOS) technology is fraught with difficulties. As a result, novel devices and circuits, sophisticated nanomaterials, and enhanced fabrication processes have become increasingly important in recent decades. Particularly, silicon nanowires have been employed effectively in innovative electronic devices, including sensors, solar cells and in logic circuitry. Due to their high surface to volume ratio, silicon nanowires have been demonstrated as energy efficient devices, which is the key for the next generation of information processing [1]. Field-effect-transistors based on silicon nanowires have been extensively used for sensing applications since the compact nanoscale structures allow excellent regulation of electrostatic potential across the nanowire channel [2]. One such nanowire concept is junctionless nanowire transistor (JNT) [3]. A JNT is a highly doped nanowire channel without p-n junctions, where the gate electrode regulates the flow of charge carriers. Silicon JNTs have shown excellent sensitivity to record-low concentrations of the protein streptavidin in liquid phase [4]. However, they have not yet been operated as gas sensors.

In this work, we report the fabrication and characterization of silicon-based JNT devices and their initial tests as gas sensors. Intrinsic silicon-on-insulator (SOI) substrates are ion-implanted with phosphorus (n-type) dopant. Millisecond range flash lamp annealing (FLA) is used for dopant activation and implantation defect healing. Top-down approach is carried out for nanowire fabrication using electron beam lithography patterning of the negative resist HSQ followed by reactive ion etching [5,6]. Successive processes of rapid thermal oxidation, nitrogen purge step and forming gas annealing are performed to create SiO_2 shell around the silicon nanowires. SiO_2 thickness is controlled by optimizating the time and temperature in these steps. UV lithography and metal evaporation are employed to create 50 nm thick Nickel contacts to the nanowires. Electrical characterization of these JNTs is performed by back-gating the nanowires. Unipolar device behavior is observed . However, these characteristics are changed after contact annealing leading to the ambipolarity in the devices. Two such transfer characteristics of JNTs based on unpassivated nanowires and nanowires with 3 nm SiO_2 shell are shown in Figure 1. These devices exhibit an on/off ratio of ~10^6. To further investigate the ambipolar nature of the silicon JNTs, output characteristics are measured, which shows Schottky barrier-based behavior of the devices (see Figure 2). Furthermore, van der Pauw and Hall Effect measurements are performed to determine their carrier concentration and hall mobility. Successive measurements of electrical characteristics of these devices are also performed in vacuum to compare them with the usual ambient measurements. Unfunctionalized JNTs are tested as sensors in purified air and NO_2 atmosphere. These sensor tests exhibited characteristic shifts in the transfer curve and a systematic increase and decrease of p- and n-type current, respectively, under the influence of NO_2 (Figure 3). These tests confirmed the potential suitability of the ambipolar JNT as sensors in gaseous environment. Additionally, these devices will be functionalized and tested for electrical detection of atmospheric free radicals.

[1] Amato, M., et al., Chemical Reviews, 2014. **114**(2): p. 1371-1412.
[2] Wan, J., et al., Microelectronic Engineering, 2009. **86**(4–6): p. 1238-1242.
[3] Colinge J P, et al. Nature Nanotech. 2010 **5** 225-229.
[4] Georgiev, Y. M., et al., Nanotechnology, 2019 **30** 324001 (8pp).
[5] Khan, M. B., et al., Applied Sciences, 2019. **9**(17).
[6] Khan, M. B., et al. 2020 Device Research Conference (DRC). IEEE, 2020.

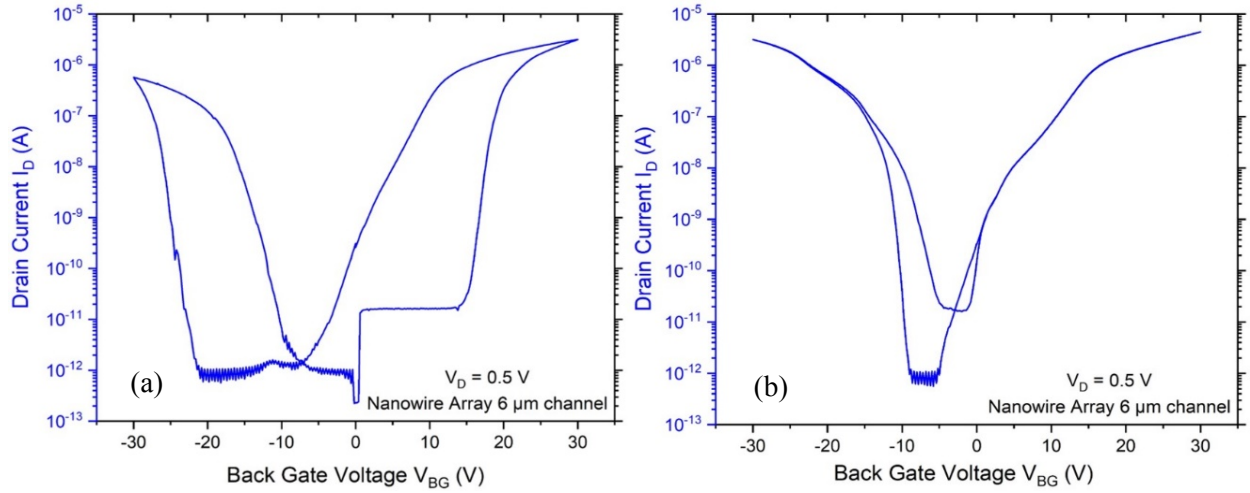

Figure 1. Transfer characteristics of (a) unpassivated and (b) 3 nm SiO_2 JNT devices.

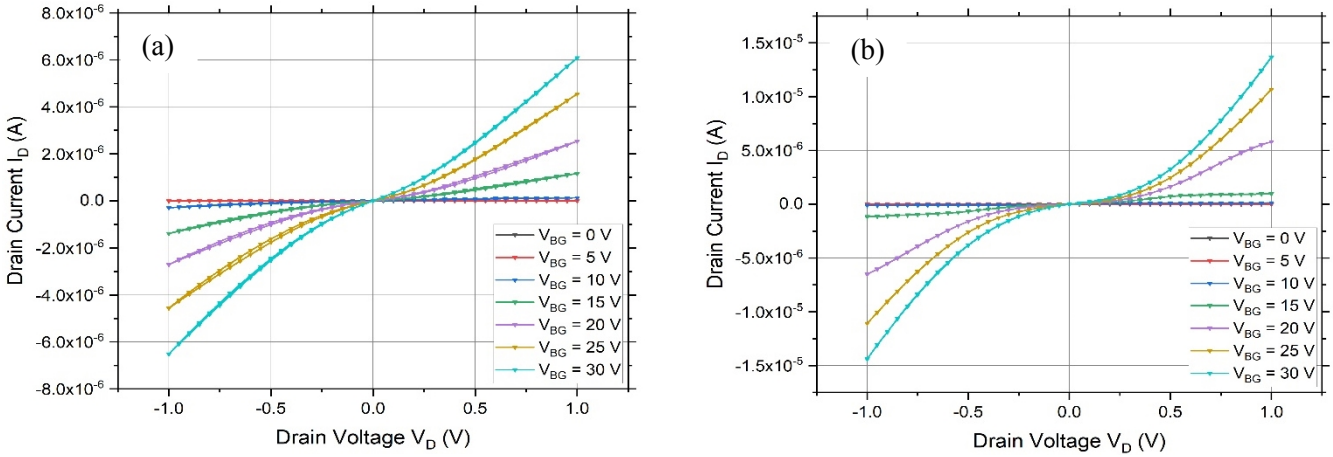

Figure 2. Output characteristics of (a) unpassivated and (b) 3 nm SiO_2 JNT devices. Back-gate voltage was varied to obtain the characteristics. The devices showed Schottky barrier based behaviour.

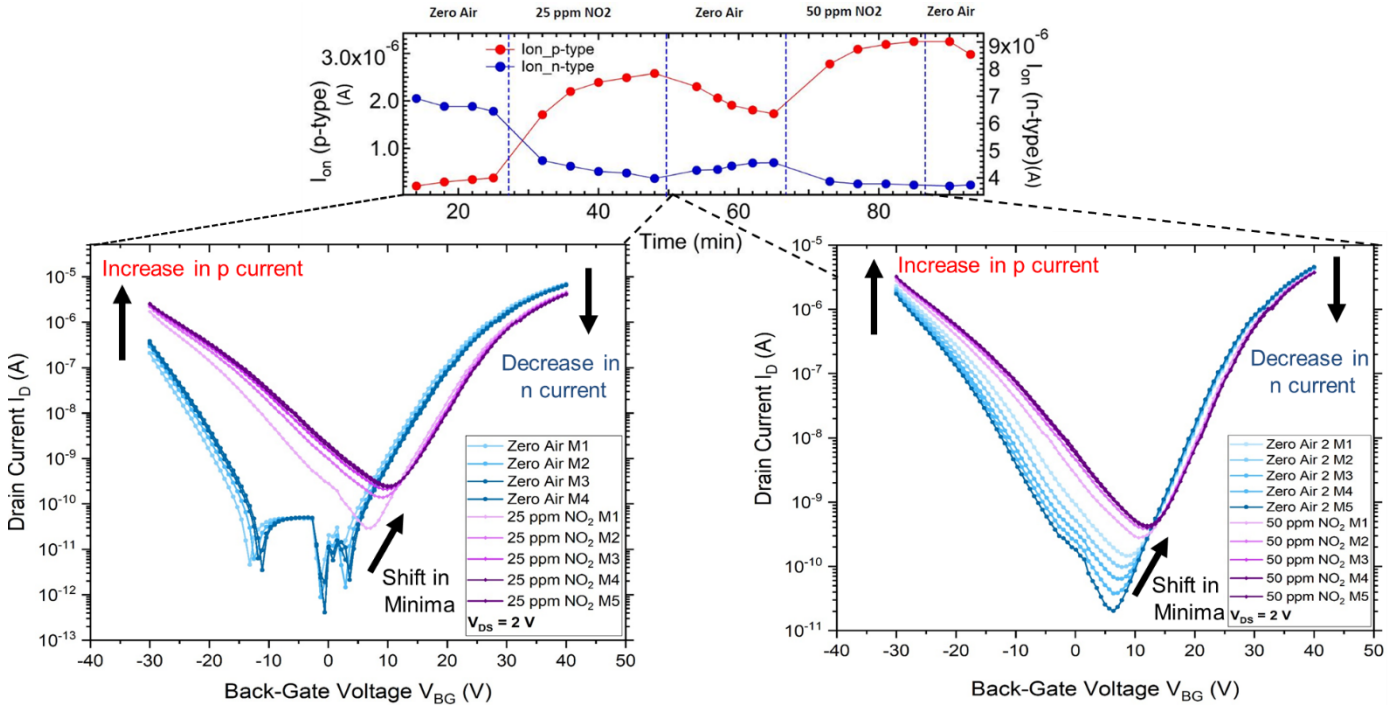

Figure 3. NO_2 sensor tests based on unfunctionalised JNTs. Characteristic shifts in the transfer curve are observed under the influence of NO_2 gas and purified air (termed as zero air). Adsorption of NO_2 gas on the surface of the JNT device induces charge transfer leading to the increase and decrease of hole and electron mediated currents, respectively.

Two-photon laser 3D printing enhancement by quantum dots and in-situ exchange

Ye Yu[a,c,d], Anatol Prudnikau[b,c], Vladimir Lesnyak[b], Man Ho Wong[c,d], Madhuri Chennur[c,d], Tanya Saxena[c,d], Josua Zscheile[c,d], Robert Kirchner[a,c,d]

[a] Institute of Semiconductors and Microsystems, Technische Universität Dresden, Nöthnitzer Straße 64, 01187 Dresden, Germany
[b] Physical Chemistry, Technische Universität Dresden, Zellescher Weg 19, 01069 Dresden, Germany
[c] Center for Advancing Electronics Dresden (cfaed), Technische Universität Dresden, Helmholtzstr. 18, 01069 Dresden, Germany
[d] HETEROMERGE GmbH, Gostritzer Str. 61, 01217 Dresden, Germany

robert.kirchner@heteromerge.com and vladimir.lesnyak1@tu-dresden.de

3D direct laser writing techniques have significantly been improved in the last decades in terms of available tools, processes and materials. Among the available technologies, two-photon polymerization (2PP) based 3D direct laser writing is one of the highest resolving and yet fast printing method being available today [1]. It has even reached industrial maturity in some fields of application. There is a broad spectrum of available tools and already demonstrated applications range from optics and photonics to fluidics and mechanics as well as to bioprinting. Today, one of the largest challenges is both the availability of different printing materials as well as the capability for their efficient printing. With both materials and tooling in place, functional 3D printing meaning the integration of multimodal entities, such as structural, optical, mechanical, electrical or magnetic ones, becomes possible in a single print run. In addition, synergistic integration of multiple properties in a single material is desired for reasons of efficiency.

In this contribution, we are approaching these needs by demonstrating a new print material based on an organic matrix typically used for 2PP printing and semiconductor quantum dots (QDs) being covalently integrated into this polymer matrix by suitable surface ligands [2]. We further demonstrate the capabilities of a novel print head system (HETEROMERGE MergeOne) that can do an automated in situ material exchange within a commercial 2PP system (Nanoscribe Photonic Professional GT2) without the need for manual operation. This paves the way towards high resolution functional micro additive fabrication. The printing material consists mainly of the organic monomer pentaerythritol triacrylate (PETA) forming a highly crosslinked polymer matrix upon 2PP. The polymerization is triggered mainly by the photoinitiator phenylbis(2,4,6-trimethylbenzoyl)phosphine oxide (BAPOs) as well as the presence of the QDs leading to a synergistic material enhancement. As a co-reactive ligand in this polymerization, mono-2-(methacryloyloxy)ethyl succinate (MMES) is used to modify the inorganic InP-based QDs for a homogenous matrix integration. Fig. 1 shows the respective chemical structures and Fig. 2 visualizes the matrix integration. The 2PP material containing QDs provided green and red photoluminescence, which can be used for color labelling, such as in security micro features [3]. Especially the green QDs enhanced material had a lower polymerization threshold as compared to the plain material. In effect, this enabled smaller voxel sizes, supporting a significant feature size reduction of about 32% compared to the plain material (Fig. 3), which is on par with much more sophisticated techniques like emission-depletion. The in-situ material exchange system consists of an open fluidic solution synchronously injecting and removing print material from the objective being hold in print material immersion [4-6]. Via this in-situ exchange of the printing material, multi-material 3D prints become possible (Fig. 4) with a high lateral alignment accuracy well below 500 nm, which is significantly better than the accuracy of 1-2 µm as it can be achieved by realignment after manual material exchange.

[1] V. Hahn et al., Adv. Funct. Mater. 30/26 (2020) 1907795
[2] Y. Yu et al., Adv. Mater. (2023) 2211702
[3] F. Mayer et al., Sci. Adv. 5/2 (2019) eaau916
[4] Y. Gao et al. Proc. SPIE 11677 (2021) 116770G
[5] R. Kirchner et al., Proc. MNE (2022) Track 2 / Session J
[6] R. Kirchner et al., Proc. SPIE PC12412 (2023) PC124120

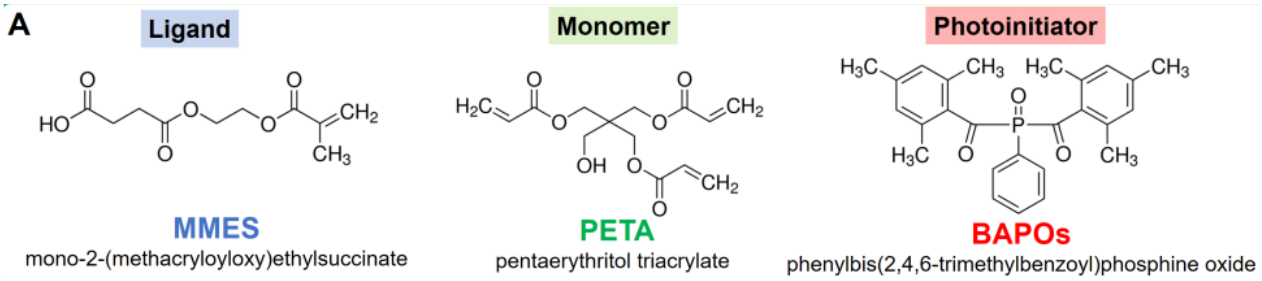

Figure 1. Chemical structure of MMES employed for the functionalization of QDs, PETA and BAPOs used as a monomer and a photoinitiator in 2PP, respectively.

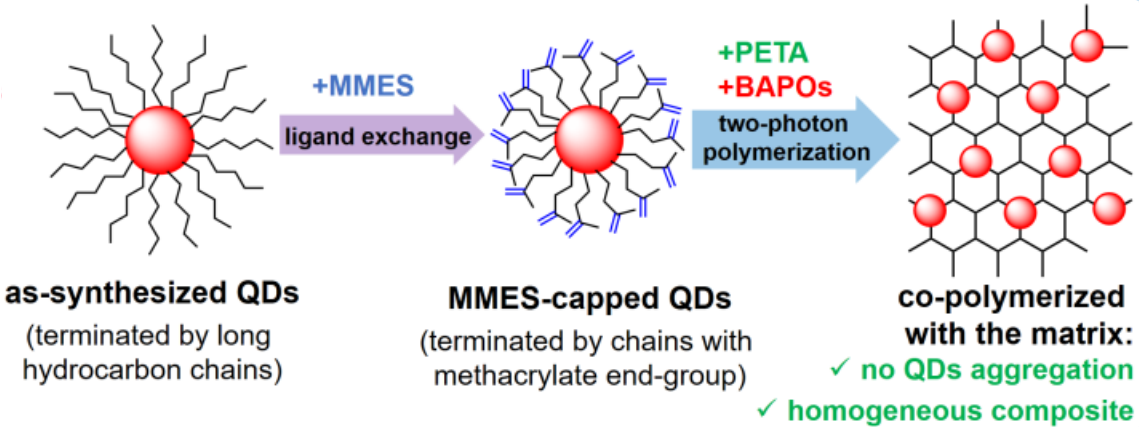

Figure 2. Superior matrix integration of the monomer-functionalized QDs due to MMES surface modification followed by copolymerization with PETA initiated by BAPOs.

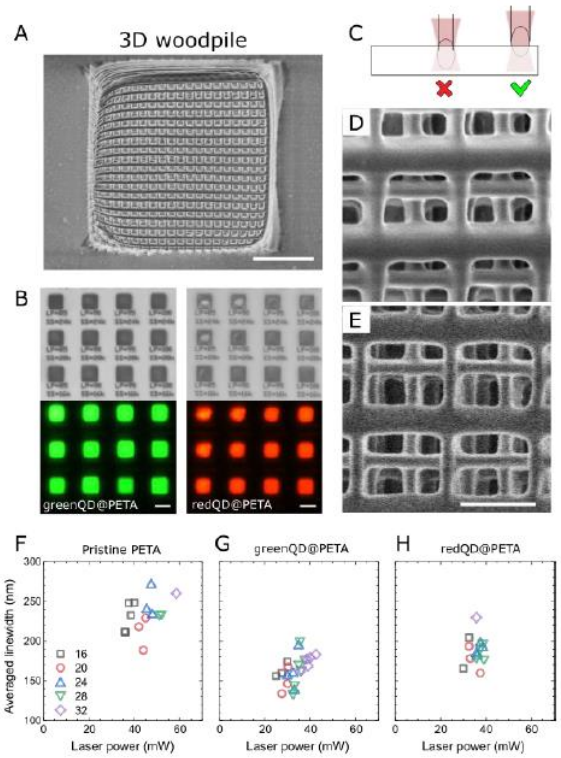

Figure 3. 2PP printed woodpile structure used for material evaluation as well as significantly reduced line width for green QDs.

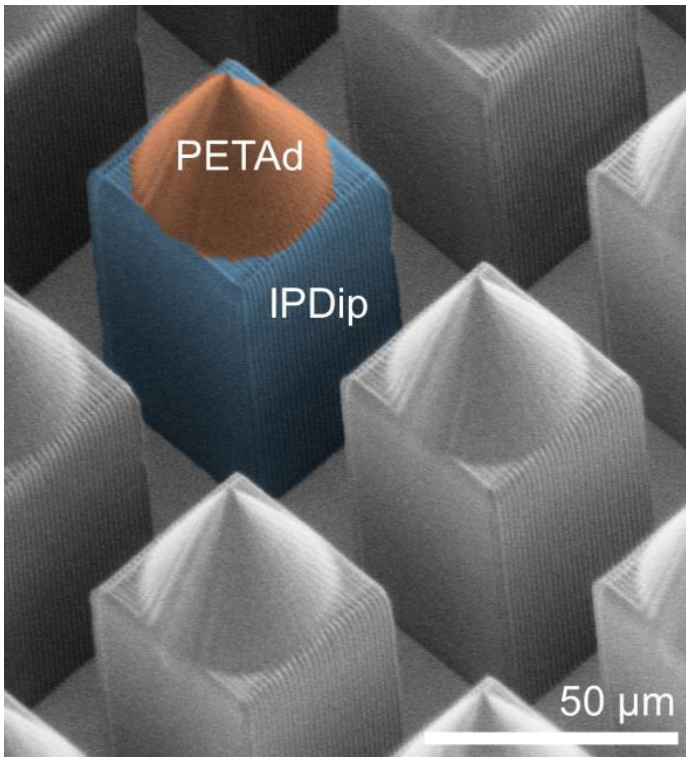

Figure 4. 2PP printed micro-needles made from commercial IPdip and layer dye doped PETA using in situ material replacement with high placement accuracy.

Combining thermal scanning probe lithography and dry etching for grayscale nanopatterns amplification in SiO_2

Berke Erbas[a], Ana Conde-Rubio[a,b], Xia Liu[a,c], Giovanni Boero[a], Juergen Brugger[a]

[a] Microsystems Laboratory, EPFL, 1015 Lausanne, Switzerland
[b] Institute of Materials Science of Barcelona ICMAB-CSIC, Campus UAB, Bellaterra 08193, Spain
[c] MIIT Key Laboratory for Low-Dimensional Quantum Structure and Devices, Beijing Institute of Technology, Beijing 100081, China
e-mail: juergen.brugger@epfl.ch

While nanolithography has historically focused on downscaling, there is now a growing interest in grayscale nanolithography for introducing or enhancing functionality in micro- and nanodevices through the creation of micro- and nanoscale 2.5D topographies with multiple depth levels. Interference and grayscale EBL are commonly used techniques to produce complex surface topographies, but have spatial resolutions limited to tens of nanometers due to diffraction or electron scattering. As an emerging technique, thermal scanning probe lithography (t-SPL) achieves single-digit nanometer spatial resolution and sub-nanometer depth control for grayscale nanofabrication, but it is limited to shallow depths typically below 100 nm [1]. t-SPL has been successfully implemented for sub-10 nm silicon binary nanopatterning [2], nanofluidic devices for precise particle separation [3], and sinusoidal gratings for enhanced optical diffraction [4]. Recently it also was used to induce local strain in 2D materials (2DMs) thanks to t-SPL's charge-free writing ability on materials that are sensitive to charged particles [5]. However, the performance and efficiency of devices are constrained by the limited depths and aspect ratios achievable with scanning probes. Previously, 3-fold amplification in depth profiles of binary patterns has been reported by dry etching-based transfer from thermally-sensitive polyphthalaldehyde (PPA) resist to SiO_2 dielectric layers [6]. However, the $C_4F_8/He/H_2$ plasma used for this depth amplification process also increases the surface roughness, up to 8 times, which in turn reduces the functional quality of the nanostructures for device integration.

Here, we combine t-SPL with dry etching to overcome the limitation in grayscale nanopatterning depth, and we demonstrate new dry etching process resulting in a significant increase in the aspect ratio of grayscale nanopatterns created on PPA polymers when transferred into SiO_2 dielectric layers (Fig. 1a). First, we create binary and sinusoidal nanopatterns having various aspect ratios in PPA by t-SPL with depths up to 40 nm. Due to the conical geometry of the t-SPL tip, we experimentally obtain the highest spatial resolutions for depths typically below 40 nm. Second, we amplify the aspect ratios of the "shallow" polymer patterns up to 10 times in a dry etch process when transferred into the underlying SiO_2 layer using CHF_3/SF_6 plasma (50/10 sccm). Our newly developed dry etch recipe enables the transfer without introducing additional surface roughness (Fig. 1b). This aspect ratio amplification is achieved without any distortion of the original shapes such as sinusoidal patterns in etching with up to 5 times depth amplification as shown in Fig. 2. At higher depth amplification distortion of the sinusoidal shapes begin to appear (see Fourier transforms of the measured topographies in Fig. 1c). We intend to use these structured dielectric surfaces as a platform to induce local strain in atomically thin 2DMs. As increased aspect ratios in sinusoidal patterns result in higher strain [5], we aim to achieve increased and deterministic local straining of 2DMs with precise nanolithography. This technique for the fabrication of the high aspect ratio and smooth grayscale dielectric nanostructures presented in this work has the potential to enable new photonic and nanoelectronics applications.

[1] A. W. Knoll et al., Advanced Materials 22 (2010) 3361-3365.
[2] Y. K. Ryu Cho et al. ACS Nano 11 (2017) 11890−11897.
[3] M. J. Skaug et al., Science 359 (2018) 1505–1508.
[4] N. Lassaline et al., Nature 582 (2020) 506–510.
[5] X. Liu et al., Nano Letters 20 (2020) 8250-8257.
[6] Y. Lisunova et al. Microelectronic Engineering 180 (2017) 20–24.

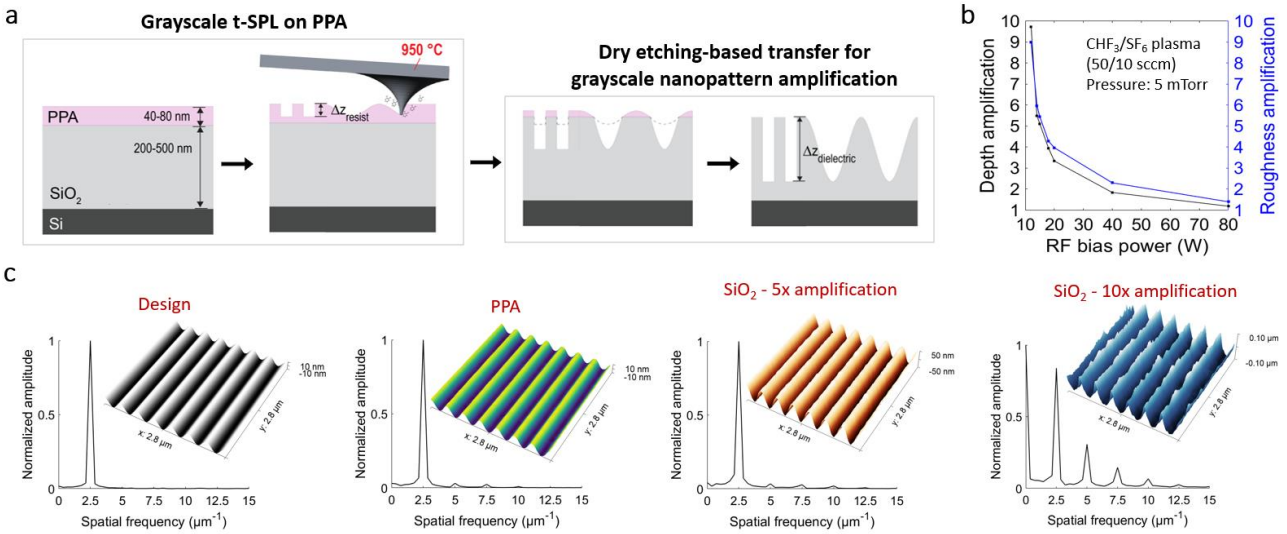

Figure 1. (a) Cross-sectional illustration of aspect ratio amplification for grayscale nanopatterns. The vertical amplification ($\Delta z_{dielectric}/\Delta z_{resist}$) results from the difference of etch rates between the PPA resist and the SiO_2 dielectric in CHF_3/SF_6 plasma. Images are not to scale. (b) Effect of RF bias power in the reactive ion etching process on depth amplification and the corresponding surface roughness amplification after dry etching. (c) Fourier transforms of grayscale design, the measured topographies on PPA and on SiO_2 dielectric layers after 5 times and 10 times depth amplifications. Fourier transforms are obtained along 140 lines on sinusoidal nanopatterns and then averaged.

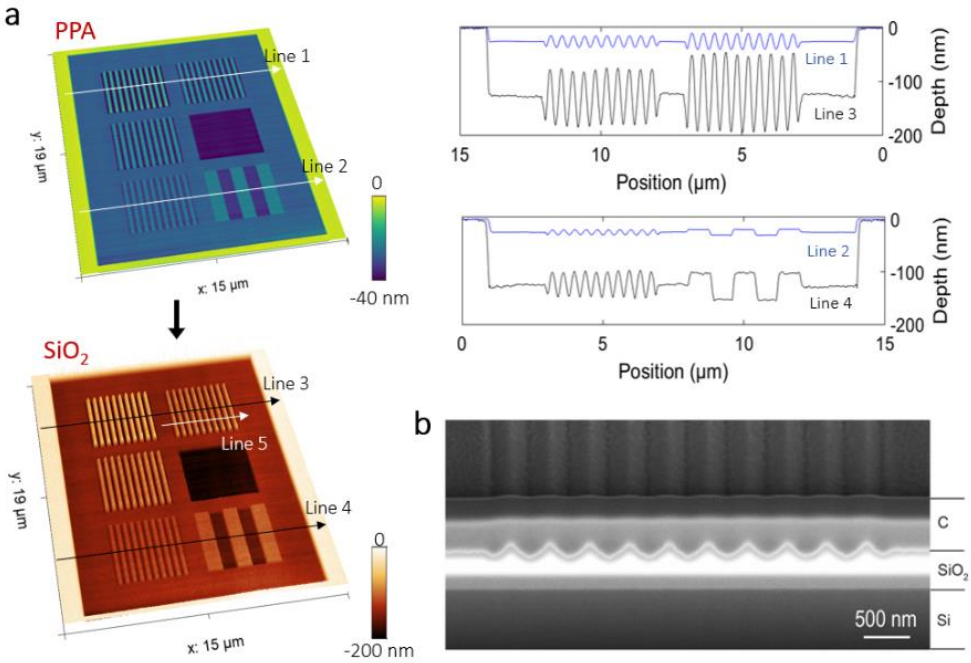

Figure 2. (a) AFM images and surface profile comparison of the nanostructures on PPA after t-SPL and SiO_2 after dry etching resulting in 5 times amplification in depth profiles. (b) FIB milled cross-sectional SEM image of sinusoidal nanostructures fabricated on SiO_2, corresponding to Line 5. The image is 54° tilt corrected.

Multi-process compatibility of hybrid polymers allowing advanced micro- and nano-patterning

J. Wolf, A. Schleunitz, M. Russew, G. Grützner
micro resist technology GmbH, Köpenicker Straße 325, D-12555 Berlin, Germany
e-mail: j.wolf@microresist.de

The material class of hybrid polymers is established for many years in industrial manufacturing processes as UV-curable polymer mostly used in replication technologies to manufacture permanent micro- and nano-optical pattern [1]. Among other benefits such as optical performance and physical stability, hybrid polymers e.g. endure reliability tests such as temperature cycling and temperature-humidity aging.

This makes hybrid polymers an attractive material candidate to be further explored in academic process research. With its proven qualification as a production material, any novel technologies employing the hybrid polymers can be transferred to industry even more quickly. This is important as market requirements change and hence alternative patterning technologies continue to develop. In this perspective, an exceptional advantage of the material class of the hybrid polymers is its multifunctionality resulting in a compatibility to various micro- and nano-fabrication processes using the very same material, e.g. OrmoComp®. Consequently, diversified process compatibility enables faster innovation cycles for example for micro-optics manufacture to go from rapid prototyping over small scale production to large scale mass fabrication using different schemes of micro- and nano-fabrication. In this context, we verified the hybrid polymer processing diversity beyond generic replication processes using the following material and process innovations:

1. Inkjet printing as alternative coating technique

A precondition for mass fabrication of optical pattern by replication is a uniform thin film to enable the reliable pattern transfer. Compared to standard spin coating, inkjet dispensing has advantages for thin film generation: coating of non-wafer or very large substrates is possible, effective material usage as less material is wasted and applying different film thicknesses according to demands of the pattern distribution. We demonstrate the solvent modified OrmoComp® of our inkjet compatible material InkOrmo which was adapted to form closed printed films in the 100 to 500 nm range.

2. 3D printing for mastering and prototyping

Furthermore, the hybrid polymer OrmoComp® can be easily employed in advanced laser-based additive manufacturing processes. With partners we prove the compatibility of OrmoComp® to standard two-photon polymerization (2PP) and advanced two-photon greyscale lithography (2GL) (Fig. 1). Those structures can be used as master original pattern in replication techniques when they are copied into working stamps [2]. But more importantly, they allow writing directly a prototype to validate device performance such as optical quality and design in the same material as already is used in high-volume manufacturing using wafer-scale replication technology.

3. Micro-Macro-Integration

Hybrid polymers have the ability to address cross-scale patterning from nm to mm and cm range. Hence, they are also recommended as semi-finished material and blanks. To enable mid- or large-scale production tasks by replication and imprinting, we recently assessed the hybrid polymers and established a 2-step replication process, where two different polymers fulfill different replication tasks: in a first step the macroscopic superstructure is replicated with an adapted version of OrmoClad. The micro-pattern is subsequently transferred as a thin film with OrmoComp® in the second step on top of the first replication step (Fig. 2). The components fabricated with this 2-step approach endure reliability tests (cycling test: -40 °C to 85 °C, 100 cycles and temperature humidity aging test 85 °C/ 85% RH, 1000 h).

4. i-line optical stepper lithography for alternative micro-patterning

The hybrid polymers are solvent free liquid formulations and remain liquid until UV-cured, therefore the micro-patterning with contact photolithography is challenging and usually results in a low resolution pattern transfer. To overcome these drawbacks and to enable a large scale production of micro-pattern, an i-line stepper with projection lithography was used to assess OrmoComp® [3]. To achieve the best pattern fidelity the material was exposed with a comparably very low dose of 10,5 J/cm² whereas the material is usually cured with doses above 500mJ/cm². To finalize the UV-curing of the hybrid polymer material, the developed pattern was subsequently flash exposed with >1J/cm². By doing so, 10 µm line and spaces with a side wall angle of 89.7° in a 22µm film made of OrmoComp® were achieved (Fig. 3). This novel patterning strategy can be used for the wafer-scale manufacture of micro-optics and patterned passivation layers.

[1] Gruetzner, G., et al. "UV-curable hybrid polymers for optical applications: technical challenges, industrial solutions, and future developments." Advanced Fabrication Technologies for Micro/Nano Optics and Photonics VII. Vol. 8974. SPIE, 2014.
[2] Schleunitz, Arne, et al. "Novel hybrid polymers for fabrication of advanced micro-optics." SPIE Newsroom (2017), doi.org/10.1117/2.1201703.006857.
[3] Koch, Matthias F., et al. "Advancing high resolution photolithography with hybrid polymers for wafer-scale manufacture of micro-optics and patterned passivation layers." Novel Patterning Technologies 2023. Vol. 12497. SPIE, 2023.

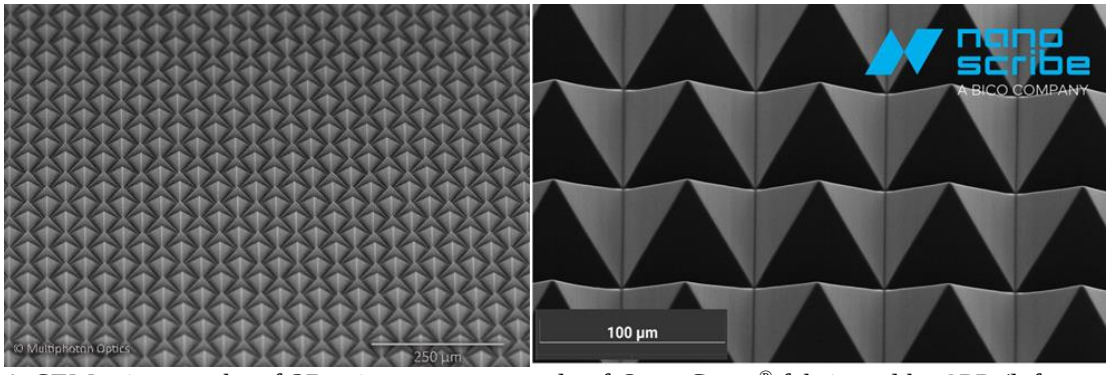

Figure 1. SEM micrographs of 3D micro-patterns made of OrmoComp® fabricated by 2PP (left, courtesy of Multiphoton Optics GmbH) and 2GL (right, courtesy of Nanoscribe GmbH & Co. KG) and thus demonstrating the multi-process compatibility of OrmoComp®

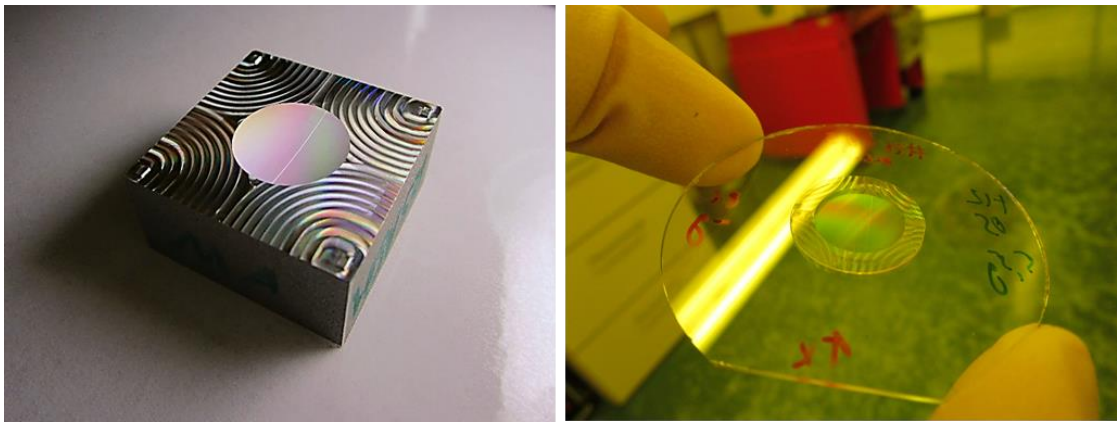

Figure 2. The ultra-precision machined master has a blazed grating on top of a spherical surface (left) and was replicated by a novel 2-step process (right). In a first step a modified OrmoClad_XP was used to replicate the macroscopic spherical surface as a preform. In the second step the grating pattern was replicated on top as thin film made of OrmoComp®.

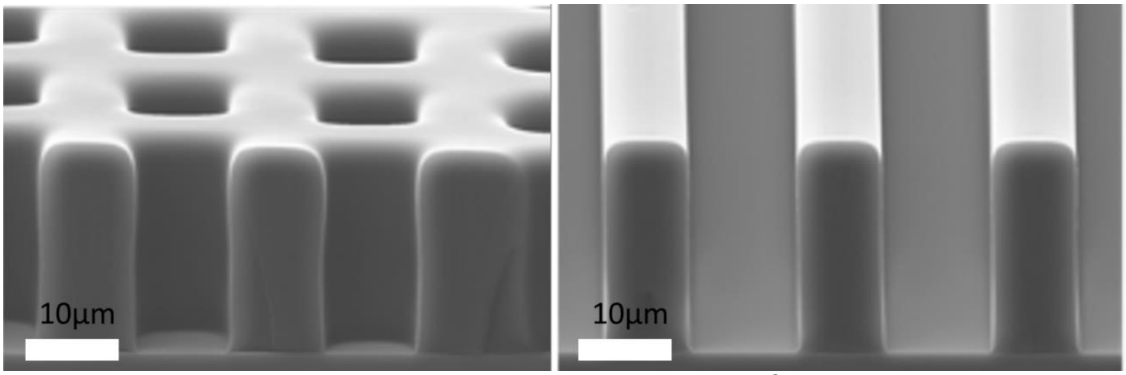

Figure 3. SEM micrographs of micro-patterns fabricated in OrmoComp® with a projection lithography i-line stepper using the following process innovation: to achieve maximum pattern resolution, the 22µm film was exposed with 10,5 mJ/cm² and subsequently after puddle development flash exposed to finalize the UV-curing of the material [3]

Greyscale lithography beyond 100 µm pattern depth facilitated by a novel photoresist and optimized processing

Christine Schuster [1], Marina Heinrich [1], Gerda Ekindorf [2], Anja Voigt [1], Arne Schleunitz [1], Gabi Grützner [1]

[1] micro resist technology GmbH, Koepenicker Str. 325, 12555 Berlin, Germany
[2] Heidelberg Instruments Mikrotechnik GmbH, Mittelgewannweg 27, 69123 Heidelberg, Germany
e-mail: c.schuster@microresist.de

Interest in greyscale lithography for the manufacture of complex 2.5D and freeform microstructures in photoresists is gaining further momentum, especially from industry for the fabrication of advanced micro-optical elements, such as refractive and diffractive lenses, blazed gratings, beam-shapers etc. The photoresist topography serves as pattern master or template for different methods of transferring the complex surface structures into materials for final, permanent applications. However, many such applications require large structure heights beyond 100 µm. Similar pattern height requirements are issued from manufacturers of components in other special applications such as organ-on-a-chip, or tumor-on-a-chip for drug validation. This height regime was not easily accessible until now by means of greyscale lithography in photoresists.
Considering these growing requirements we developed a novel greyscale positive photoresist, mr-P 22G_XP, designed with the aim to enable greyscale exposure of > 100 µm deep patterns. One of the challenges to overcome on the way to the dedicated material development was the trapping of nitrogen bubbles formed during photoresist exposure especially deeper in the resist film, eventually resulting in surface defects after resist development. This major issue has been drastically reduced and even overcome as will be presented.
Another challenge was to reduce the residual absorption after bleaching by exposure, as it occurs in this type of photoresist. The lower residual absorption in mr-P 22G_XP increases the light intensity penetrating into the thick-film resist, so that the light-induced solubility increase is still sufficient in deep levels of the resist film. This way higher pattern depths were achieved compared to generic photoresists, even more distinct at lower wavelengths such as 365 nm.
As a result of the presented work, the greyscale pattern depth limits in diazonaphthoquinone based photoresists have been pushed beyond 100 µm with the newly developed photoresist. For the first time, pattern depths of 100-120 µm were reproducibly possible in a photoresist generated by means of greyscale photolithography with a commercial and easily accessible set-up, such as laser direct writing (see Figure 1). Also LED exposure through greyscale masks (see Figure 2) with the mr-P 22G_XP resist formulation will be presented. This high resist pattern depth was obtained by a well-considered choice and evaluation of photoresist ingredients on one hand, and supported by careful lithography process adjustments on the other hand. With the gained know-how, in particular with laser direct writing, even deeper greyscale patterns of up to 150-160 µm seem within reach.

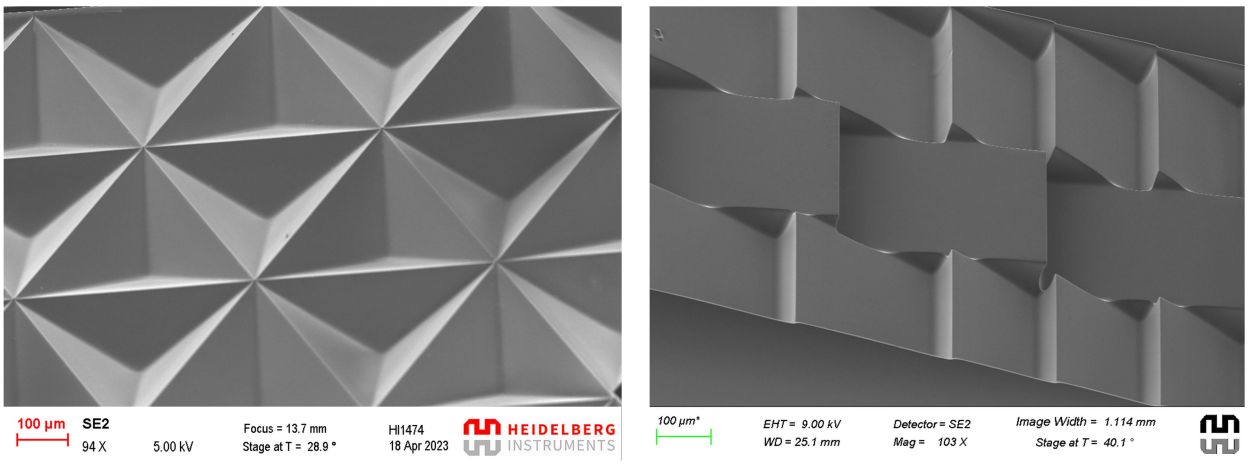

Figure 1. Exemplary greyscale structures in 120 µm thick positive photoresist mr-P 22G_XP, patterned with 405 nm Laser Direct Writing and development in 0.26N TMAH at Heidelberg Instruments Mikrotechnik GmbH: pattern depth = 117 µm (left) and 104 µm (right)

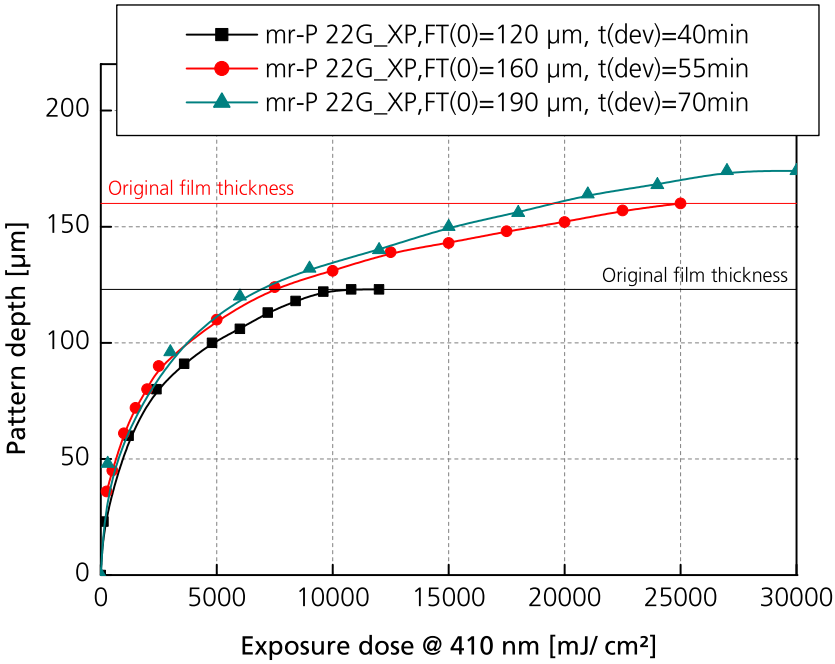

Figure 2. Response curves of mr-P 22G_XP in ~ 120 µm, ~ 160 µm, and ~ 190 µm film thickness – 410 nm LED exposure, development in 0.275N TMAH

Additive micro-structuring of non-planar optical waveguides for multifunctional neural interfaces

Marco Bianco[a,*], Antonio Balena[a], Marco Pisanello[b], Elisa Scarpa[a], Filippo Pisano[a], Barbara Spagnolo[a], Maria Samuela Andriani[a,c], Miroslav Stibůrek[d], Petra Kolbábková[d], Hana Uhlířová[d], Tomáš Čižmár[d,e,f,†], Ferruccio Pisanello[a,†], Massimo De Vittorio[a,c,†]

[a] Istituto Italiano di Tecnologia (IIT), Center for Biomolecular Nanotechnologies, Lecce, Italy.
[b] OptogeniX, Lecce, Italy.
[c] Dipartimento di Ingegneria dell'Innovazione, Università del Salento, Lecce, Italy.
[d] Complex Photonics, Institute of Scientific Instruments, Brno, Czech Republic.
[e] Leibniz Institute of Photonic Technology, Jena, Germany.
[f] Institute of Applied Optics, Friedrich Schiller University, Jena, Germany.
[*] Corresponding author. E-mail: marco.bianco@iit.it
† Co-last authors.

Microstructured implantable neural interfaces are essential tools which enable high-resolution mapping of neural circuits, long-term controlling and monitoring of brain activity, and provide a stable and biocompatible platform for developing effective treatments for neurological disorders [1]. The increasing complexity of neuroscience experiments has raised the demand for multifunctional devices able to detect the multifaceted nature of neural signals with cell specificity, as well as to attain specific neural therapies exploiting optical, electrical and thermal effects, or precise drug-delivery. The development of these tools poses a considerable challenge for the micro- and nano-fabrication community, as (i) integrating multiple functionalities on substrates with different geometries (cylindrical, planar, tapered, mixed) may require unconventional fabrication techniques, (ii) the materials employed should be biocompatible and ensure long-term stability, (iii) the devices need to be less invasive to minimize tissue damage and interference with neural functions.
In this work we propose an approach based on Two-Photon Polymerization (TPP) to manufacture arbitrary micro-patterns on non-planar optical fibers with different geometries, aiming at the integration of micro-electrodes, optical channels and microelectronic components directly on the surface of a low-invasiveness probe. The process exploits the aforementioned TPP approach combined with a 4-axis micromanipulator (Figure 1.a) to pattern the optical waveguide on the entire surface (Figure 1.b), conformal or masked deposition of different metallic and dielectric layers, wet etching and wire-bonding from the curved surface of the probe to an external circuit board for the external interfacing.
In particular, we describe (i) the fabrication of a fibertrode [2] (Figure 1.c), a probe based on a tapered optical fiber (TF) equipped with micro-electrodes for extracellular electrophysiology (Figure 1.d), and several optical channels for optogenetic activation of neurons, which can be individually addressed by exploiting the photonic properties of TFs [3] (Figure 1.e); (ii) the realization of a multifunctional probe based on a 45°-polished sideview optical fiber [4], for combined electrophysiology and holographic endoscopy in deep-brain (Figures 1.f-i); lastly, (iii) the integration of a thermistor on a TF (Figure 1.j) to probe temperature variations (Figure 1.k) during optogenetic stimulation, or related to physiological phenomena. Finally, we propose a bonding and encapsulation solution for the devices, based on a custom 3D-printed circuit board which allows the external interfacing and driving of the electrical and optical channels on the waveguides (Figure 1.l).
We believe that the possibilities offered by our approach will allow the integration of multiple functionalities on a single device, reducing clutter and stress on the animal and simplifying the implementation of elaborate neuroscience experiments.

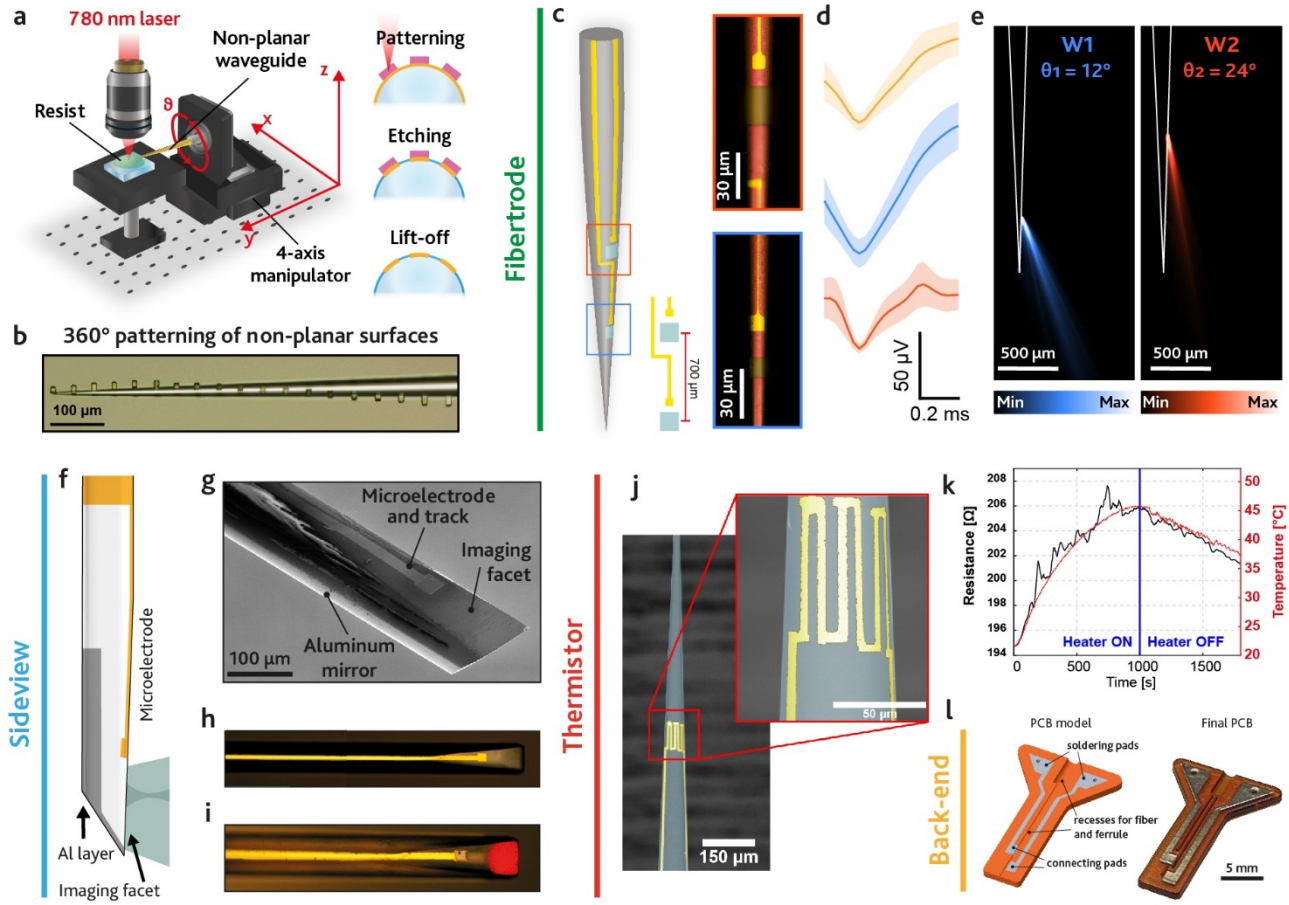

Figure 1. **(a)** Sketch of the TPP system and 4-axis manipulator proposed in this work. The polymerization of the resist allows defining polymeric masks to protect the metal layer from the subsequent wet etching processes. **(b)** Optical image showing the possibility to pattern the entire non-planar surface of a waveguide along its optical axis. **(c)** Sketched representation and optical images of a TF-based fibertrode featuring two optical windows and two microelectrodes. **(d)** Representative sorted waveforms of action potentials recorded with a fibertrode, bold line representing the mean, shaded area representing the standard deviation. **(e)** Fluorescence images showing the possibility to individually address each optical aperture by tuning the angle of the light injected in the fibertrode. **(f)** Schematic representation of a sideview probe, showing the 45°-polished surface with a layer of aluminum acting as a mirror, the imaging facet, and a microelectrode placed above it. **(g)** SEM micrograph of the final probe. **(h)** Close-up optical image of the sideview facet, showing gold microelectrode and track, and the imaging facet. **(i)** Image displaying light emission from the imaging facet when a red laser pointer is coupled to the distal end of the probe. **(j)** Colorized SEM micrograph showing the serpentine pattern of the thermistor. **(k)** Time trace of the simultaneous temperature measurement from a commercial temperature sensor (right y-axis) and change of the resistance of the thermistor integrated on the TF-based probe (left y-axis). Blue vertical line identifies the time at which the heater was turned off. **(l)** 3D rendering and final printed circuit board employed for the encapsulation of the probes presented in this work.

[1] H. Li et al., Microsyst Nanoeng 9, 4 (2023).
[2] B. Spagnolo, A. Balena et al., Nat Mater 21, 826–835 (2022).
[3] F. Pisano, M. Pisanello et al., Nat Methods 16, 1185–1192 (2019).
[4] M. Stibůrek et al., Nat Commun 14, 1897 (2023).

Guided Domino Lithography for Uniform Ultra-Sharp Nanoantenna Arrays

Dong Kyo Oh [a], Jaekyung Kim [a], Jihae Lee [b], Junsuk Rho [a,b,c,d]

[a] Department of Mechanical Engineering, Pohang University of Science and Technology (POSTECH), Pohang 37673, Republic of Korea
[b] Department of Chemical Engineering, Pohang University of Science and Technology (POSTECH), Pohang 37673, Republic of Korea
[c] POSCO-POSTECH-RIST Convergence Research Center for Flat Optics and Metaphotonics, Pohang 37673, Republic of Korea
[d] National Institute of Nanomaterials Technology (NINT), Pohang 37673, Republic of Korea
e-mail: jsrho@postech.ac.kr

Plasmonic nanoantenna platforms have gained significant attention due to their applications in optical sensors, quantum plasmonics, and other fields. To enable these applications, it is crucial to achieving a uniform and reliable fabrication of nanoantennas with a resolution in the single-digit-nanometer range. However, the improvement of process yield and uniformity of nanoantenna shapes across the entire fabrication area remains a major challenge. In this work, we present the guided domino lithography (GDL) method as a solution for the uniform fabrication of ultra-sharp nanoantenna arrays. [1] GDL involves utilizing the collapsing behavior of unstable photoresist nanostructures with a guide structure. By carefully controlling the collapsing process, we achieve the uniform fabrication of ultra-sharp bowtie photoresist masks.

To evaluate the effectiveness of the GDL technique, we directly compare the yields of conventional lithography and GDL under optimized electron beam exposure and development conditions, as shown in **Fig. 1**. Our experimental results demonstrate the superior performance of GDL in terms of yield and uniformity of nanoantenna shape across the entire fabrication area. In order to further validate the efficacy of the GDL method, we perform a rigorous analysis to investigate the electric field enhancement effect of ultra-sharp bowtie nanoantennas with different geometries. (**Fig. 2**) Our analysis confirms the significant electric field enhancement achieved by the fabricated nanoantennas, thus highlighting the potential of GDL for the practical manufacturing of single-digit-nanometer plasmonic nanoantennas.

In conclusion, we have presented the GDL method as a promising solution for the uniform fabrication of ultra-sharp nanoantenna arrays at the single-digit nanometer scale. Our results demonstrate the superior performance of GDL in terms of process yield and uniformity of nanoantenna shape compared to conventional lithography techniques. Moreover, our analysis confirms the significant electric field enhancement achieved by the fabricated nanoantennas. We believe that the GDL process holds great potential as a practical manufacturing method for single-digit-nanometer plasmonic nanoantennas, opening up new avenues for diverse quantum nanophotonic device applications. [2,3]

[1] D. K. Oh et al., Nanophotonics 12 (2023) 1435-1441.
[2] I. Kim et al., Mater. Today 39 (2020) 89-97.
[3] I. Kim et al., Microsyst. Nanoeng. 6 (2020) 65.

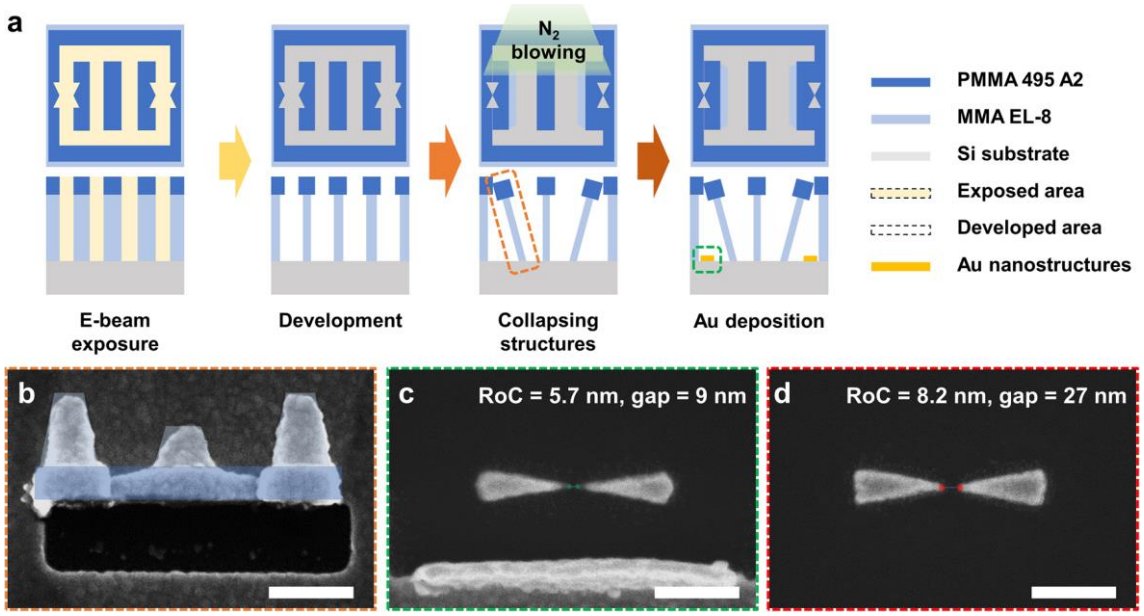

Figure 1. Overview of the guided domino lithography (GDL) process and comparison of ultra-sharp bowtie nanoantennas using GDL and electron beam lithography (EBL). All scale bars: 200 nm.

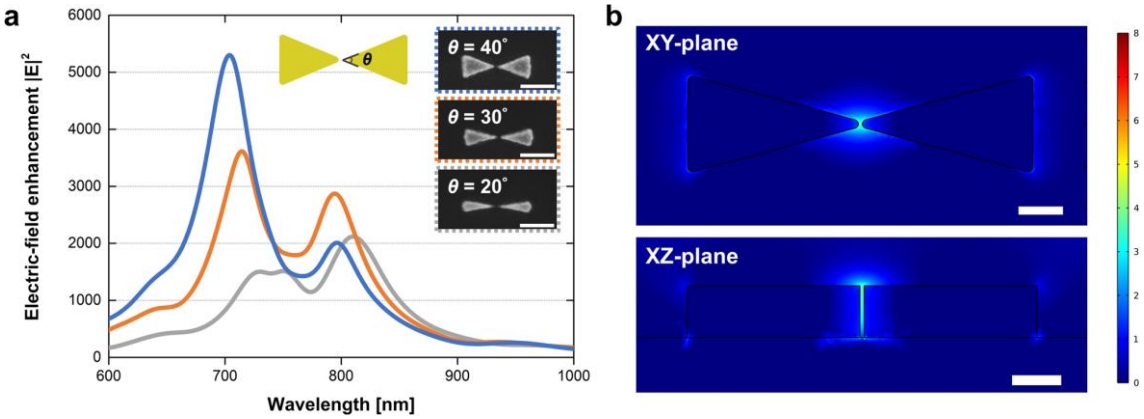

Figure 2. Electric field enhancement and field distribution of ultra-sharp bowtie nanoantennas with various angles. Scale bars in (a): 200nm. Scale bars in (b): 50 nm.

Intra-level Mix and Match Approach of the Photoresist mr-EBL 6000.5 using E-Beam and i-line Stepper Lithography for PICs

Sebastian Schermer [a], Markus Reinhardt [a], Christian Helke [a,b], Susanne Hartmann [b], Georg Heldt [a], Franz Tank [b], Anja Voigt [c] and Danny Reuter [a,b]

[a] Fraunhofer Institute for Electronic Nanosystems ENAS, 09126 Chemnitz, Germany
[b] Center for Microtechnologies (ZfM), Technical University of Chemnitz, 09126 Chemnitz, Germany
[c] Micro Resist Technology (mrt) GmbH, Köpenicker Str. 325, 12555 Berlin, Germany
e-mail: sebastian.schermer@enas.fraunhofer.de

In recent years, the miniaturization of modern integrated circuits (IC´s) and micro-electro-mechanical systems (MEMS) became more and more demanding. Complex structures with different sizes down to nanometer scale requires precision and high writing speeds at the same time. In order to achieve sub 100 nm structures, maskless writing tools such as electron beam (e-beam) lithography is used [1]. The downside of these sequential writing techniques are low writing speeds. To overcome those problems, one of the methods for complex pattern transfer is Mix and Match (M&M) lithography, which in general means the combination of exposures from two different lithographical devices on one wafer [2,3,4]. In contrast, we make use the intra-level mix and max approach (ILM&M). This approach combines at least two lithography techniques on just one resist layer. The main advantage of this hybrid lithography lies in an increased throughput of e-beam lithography since larger structures can be exposed with UV stepper lithography [2,3,4]. Since both lithography tools are used on the same resist layer, the resist has to be sensitive to both electron- and UV-radiation.

In this paper we describe the lithographic technique of exposing photonic integrated circuit (PIC) related structures such as waveguides, ring resonators and coupling structures within this ILM&M approach. Therefore, we combining electron beam lithography (VISTEC SB254, shaped beam, CD > 20 nm) and i-line stepper lithography (Nikon NSR 2205i11D, CD > 350 nm) on one resist layer. The “mr-EBL” series (from Micro Resist Technology, Germany) showed a great performance in structuring resist layers with e-beam systems with a sub-100 nm lateral resolution dependent on the layer thickness [5,6].

As a substrate 150 mm Si-wafer with a 500 nm Si_3N_4 layer on top was used. The mr-EBL 6000.5 resist with a thickness of 500 nm was applied via spin-coating followed by a softbake step. The exposure of different sized and shaped structures such as waveguides, ring resonators and coupling structures could be performed with either e-beam or i-line stepper. This way we are totally free by choosing the best exposure result for each structure type and combining them in one functioning PIC.

A PIC is a functioning circuit consisting of several optical components (e.g. lenses, waveguides and coupling structures) utilizing light for different purposes (e.g. sensing and information transfer). The structures will be transferred into the 500 nm thick Si_3N_4 layer after the lithography. An image of such a PIC device taken with an optical microscope is shown in figure 1. A 0.9 µm wide straight waveguide is broadened to 21.4 µm at both ends, where it is merged to a coupling structure. The coupling structure consists of a 17 x 33 hole array with square holes of 0.8 µm edge length separated by 0.4 µm wide crosspieces. In the middle of the waveguide, a 0.9 µm wide ring resonator structure is located beside the waveguide with a gap of 1 µm between ring resonator and waveguide.

In order to investigate optimal process parameter for both exposure tools, dose variations were done. The characterization were done with the Hitachi CS4800 CD-SEM to measure the dimensions of the waveguides and ring resonator structures exposed by the i-line stepper as well as the gap in between.

In Figure 2 SEM-images of the bottom right corner of the coupling structures as well as the waveguide is shown. Like expected, the holes written with the i-line stepper (a) are more rounded compared to the e-beam written ones (b). This is a result of the light diffraction on the stepper mask. In Fig. 2 (c) the waveguide next to the ring resonator is shown. We demonstrated clearly the ILM&M process possibility by using mr-EBL 6000.5 resist for i-line stepper lithography and e-beam lithography.

References:

[1] M. Hofmann et al., “Mix-and-match lithography and cryogenic etching for NIL template fabrication”, Microelectronic Engineering 224, (2020).
[2] C. H. Canpolat-Schmidt et al. „Lithographic performance of resist ma-N 1402 in an e-beam/i-line stepper intra-level mix and match approach”, European Mask and Lithography Conference, (2022).
[3] R. Jonckheere et al. “Electron beam / DUV intra-level mix-and-match lithography for random logic 0.25µm CMOS”, Microelectronic Engineering 27, 1-4, p.231-234, (1995).
[4] S. Magoshi et al. “Improved electron-beam/deep-ultraviolet intralevel Mix and Match lithography with 100 nm resolution“, Japanese Journal of Applied Physics Vol. 38, p.2169-2172, (1999).
[5] C. Martin et al. “Electron beam lithography at 10keV using an epoxy based high resolution negative resist”, Microelectronic Engineering 84, 5-8, p.1096-1099, (2007).
[6] A. J. Taal “mr-EBL: ultra-high sensitivity negative-tone electron beam resist for highly selective silicon etching and large-scale direct patterning of permanent structures”, Nanotechnology 32, (2021).

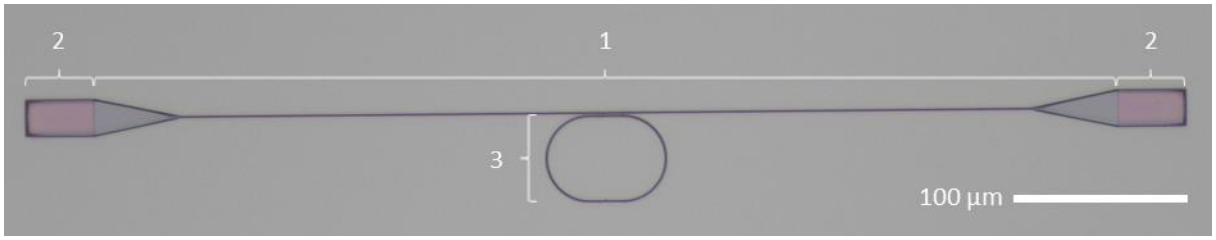

Fig. 1: Optical microscope image of (1) implemented waveguide with (2) coupling structures at both ends and (3) ring resonator structure beside the waveguide in the middle of the waveguide structure.

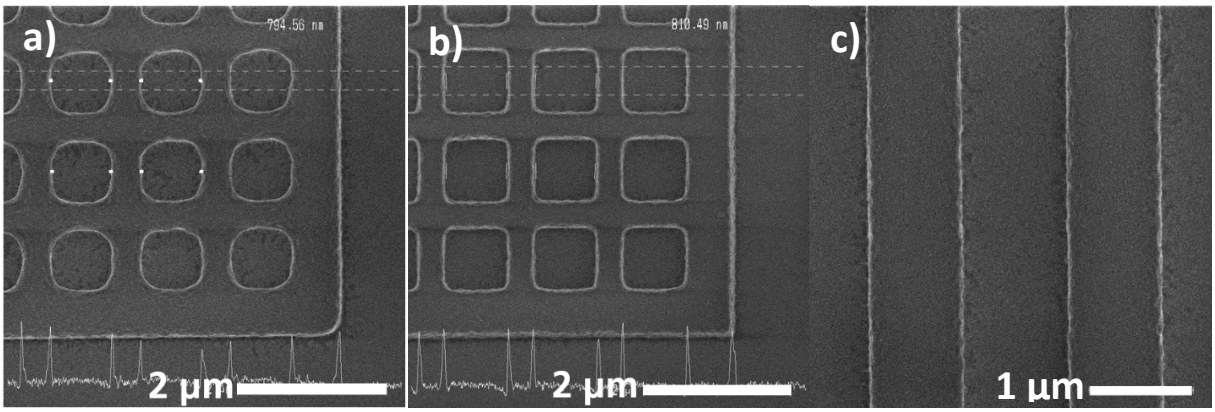

Fig. 2: CD-SEM images of coupling structures exposed by the i-line stepper (a) at an exposure dose of 360 mJ/cm² at focus zero and exposed by e-beam (b) at an exposure dose of 1.5 µC/cm². The Waveguide next to the ring resonator is shown in (c), exposed with i-line stepper and a dose of 420mJ/cm^2.

Novel Fabrication of Arbitrary Optical Probe Array by 4D Printing

Dominique Decanini [a], Abdelmounaim Harouri [a], Ayako Mizushima [b],
Jongho Park [c], Beomjoon Kim [c], Yoshio Mita [b,d] and Gilgueng Hwang [a,b,c,d]

[a] C2N/CNRS (UMR9001), Paris-Saclay University, FRANCE and
[b] Dept. of Electrical Engineering and Information Systems, The University of Tokyo, JAPAN and
[c] Institute of Industrial Science, The University of Tokyo, JAPAN and
[d] LIMMS/CNRS-IIS (IRL2820), The University of Tokyo, JAPAN
e-mail: hwang@if.t.u-tokyo.ac.jp

Probes are essential elements for electrical, mechanical or optical characterizations of biological or chemical samples. Particularly the optical probes are promising for near field sub-wavelength imaging technologies [1]. Various fabrication methods either on the optical fiber or on the cantilever have been proposed. However, their fabrications usually require sophisticated micro/nanofabrication technologies therefore batch production of optical probe array is challenging. In addition, solid structure inside optical probe could heat the probes by light absorption and loss of light through side wall of the optical probe. Fabrication of hollow optical probe surrounded by metallic mirrors could be an asset to efficient optical applications. Similar techniques typically the mold-casting method for the fabrication of biomedical optical microneedles could be considered for the fabrication of optical probe array [2]. Alternatively, 3D printing becomes also available for the direct fabrication of microprobes [3,4]. However, in either case, their surface coatings after fabrication could be time-consuming and difficult to guarantee to guide the optical path through the holes. Hollow microprobe could be fabricated by 3D printing but their developments of photoresist inside the holes could be challenging. In this work, we propose a novel fabrication of arbitrary optical probe array with 4D printing driven by surface tension assisted closing and consequent bonding of the closed structures by sputtering of metallic layers which serve as a mirror to reflect and guide the light through the aperture of microprobe.

Figure 1 shows the surface tension driven self-closing of U-shape micro ribbon structures. Vertically standing U-shape ribbon microstructures are fabricated by two-photon polymerization of photocurable Polydimethylsiloxane (PDMS) (Photonic professional GT+, Nanoscribe, GmbH) as described in the Ref [4]. Then the sample is kept in Isopropyl Alcohol (IPA) solution after development and rinsing. By evaporating the surrounding IPA, thanks to the surface tension, the structures self-deform their morphologies from U-shape to hollow microstructures by closing the upper edge of the structures. If the sample is completely dried, the closed microstructures remain to form microneedle-like shapes as shown in the Fig. 1. After drying them, to form the reflective layer of the surface, *Cr*/*Ni* 20/300nm were sputtered onto the surface of the assembled structures. The metallic layers serve for reflecting light to the openings of the structures and also for bonding the closed structures. Before this permanent bonding by metallization, the surface tension driven closing is reversible by wetting the closed structures with IPA. Figure 2 shows the reversible opening and closing processes of 100 structures by optical microscope images. Complete closings of 100 structures take around 2 seconds and openings take around 7 seconds. It should be noted here that both drying and opening were done in ambient temperature and pressure. This can be understood by the intrinsic reversible PDMS-PDMS bonding thus can take longer time to detach them by absorption of IPA through the porosity of PDMS. This reversibility should serve to further increase the quality of the 4D printing by redoing the assembly in case of the error or failure of assembly.

We finally demonstrate how the light transfers through these 4D printed optical probes. The sample was mounted onto an inverted optical microscope and the light was passing from the bottom of the sample in transmission mode. Figure 3 shows the microscope image that the light is exclusively passing through the openings of micro probes. This shows well that the structures are well assembled and the surface coated metal layers are well reflecting inner propagating lights so to successfully guide to the openings of structures. We believe that the proposed 4D printing process could open more applications requiring mass production of the hollow 3D micro structures for biomedical, microfluidic or optical applications. We aim to further miniaturize the optical aperture size by optimizing the dimensions and mechanical properties of the structures. This could also be promising to the applications such as the optical imaging of single cell/molecule.

[1] P. Achmari et al., OSA Continuum 4 (2021) 1143-1154.
[2] W. Xiaobin et al., Biomed. Opt. Exp. 13(2) (2022) 1045-1060.
[3] S.R. Dabbagh et al., iScience 24 (2021) 102012.
[4] M. Olowe et al., Pharmaceutics 14(12) (2022) 2693.
[5] D. Decanini et al., IEEE MEMS 2023.

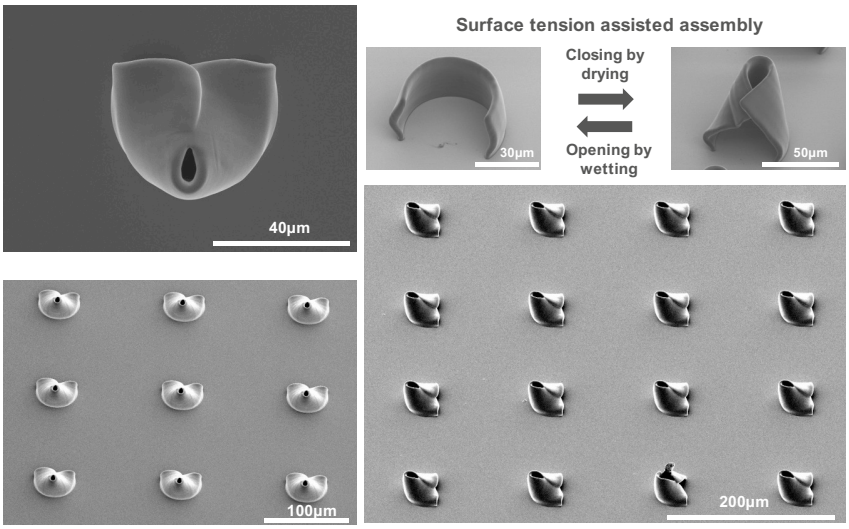

Figure 1. SEM images of the 4D fabricated optical probes by surface tension assisted closing. The U-shape ribbon structures are fabricated by two-photon absorption 3D nanolithography. Then they are closed by drying of surrounding medium to form the closed optical probe.

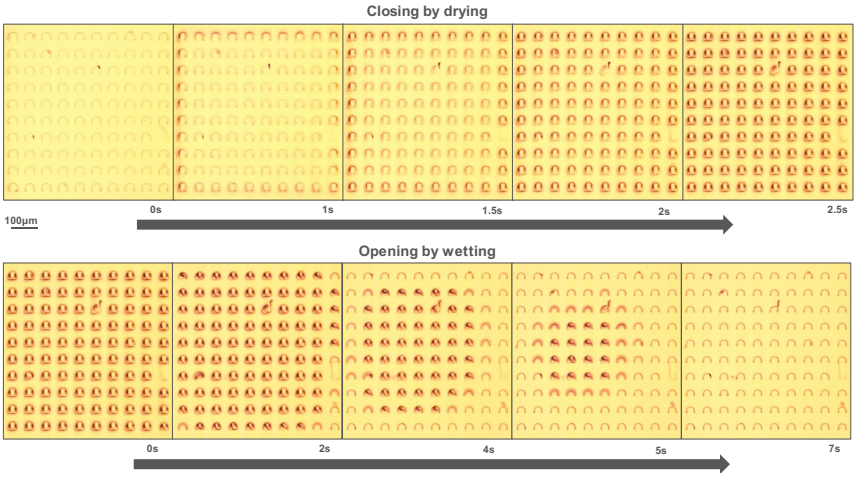

Figure 2. Optical microscope images of both the opening and the closing processes of 100 structures. The closing was successfully done by drying and the opening was done by wetting. This opening and closing processes are reversible.

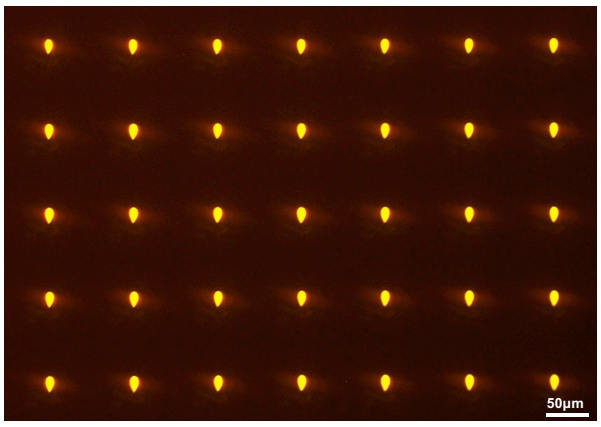

Figure 3. Light transmission through the openings of the 4D printed optical probes.

Multi-layer nanoimprint lithography material system for nanopattering of functional substrates

M. Lohse [a], M. Messerschmidt [a], N. Heidensohn [a], S. Grützner [a], A. Schleunitz [a], G. Grützner [a]

[a] micro resist technology GmbH, Berlin, 12555, Germany
e-mail: m.lohse@microresist.de

Nanofabrication technologies have moved from purely academic interest to industrial relevance for the last decades and enabled the miniaturization of devices in fields of application of non-semiconductor domains such as optics, photonics and life science applications. Especially in the fields of optics and photonics, nano patterning has proven to be an enabler for new fields of industrial research, such as augmented reality or meta lens application. In those emerging applications, high reliability and precision is required, as manipulating light is strongly dependent on the sizes and quality of the nano patterns where deviations from the optical design lead to an unacceptable loss in performance. In this context, nanoimprint lithography (NIL) plays a crucial role as fabrication technology with more and more demands, e.g. NIL into functional substrates in the context of high refractive optics or meta lens [1] applications. Hence the requirements for the imprint materials increase, leading to the need to compromise or find alternative processes. One of those innovations is using a multi-layer NIL approach. By separating the functionalities into multiple material systems (e.g. imprint performance and etch selectivity), the process gets more reliable and the manufacturer has a higher degree of freedom to operate.

In this presentation, we will show our view on industry driven imprint materials, their advantages and limitations and how a multilayer approach can overcome certain challenges in particular for non-classic substrates as are used for high RI glasses in augmented or virtual reality. We will present how a well-established lift-off process in photolithography that can be employed in the NIL context as well and how we were able to use a commercially available lift-off resist (LOR1a, Kayaku Advanced Materials) used in combination with a nanoimprint resist (mr-NIL210) for the fabrication of an etch mask on a full wafer scale (figure 1). Further, we will show that a classical imprint of mr-NIL213FC_XP can be combined with a lift-off layer and a deposited SiO_2-layer hard mask (see figure 2). The results will show that in a standard industrial etching process, such multi-layer stack can increase the imprint height significantly. Starting with an imprint height of 300nm, we were able to obtain an etching depth of 3µm, when combined with well-known metal-deposition technics and etching protocols. Coming from an initial imprint aspect ratio (AR) of roughly 1, this means that a 10-fold increase in AR was achieved [2]. While these examples have been used on silicon wafers, non-classical functional substrates such as TiO_2 or silicon nitride can be used for such approach as well, which potentially can lead towards pattern transfer in high refractive glasses.

While our described approach with this material system is particularly targeting NIL manufacturing industry, we strongly believe that it will enable academics to further push the technology and explore a multitude of options in terms of patterns and substrates, developing the novel processes beyond current industrial usage.

[1] C.A. Dirdal et al., Optics Express 28 (2020) 15542
[2] T. Handte et al., Micro Nano Eng 14 (2022) 100106

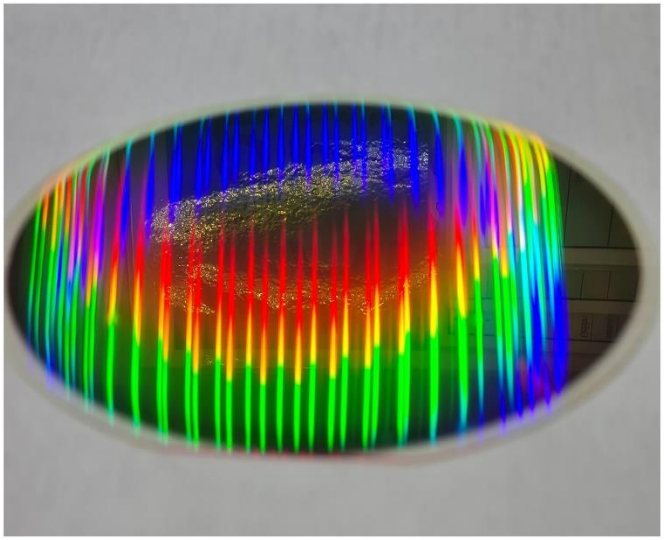

Figure 1 Fused silica wafer after the bilayer process chain and lift-off. The structures in the nanometer range lead to diffraction, reflection and resonance phenomena. [2]

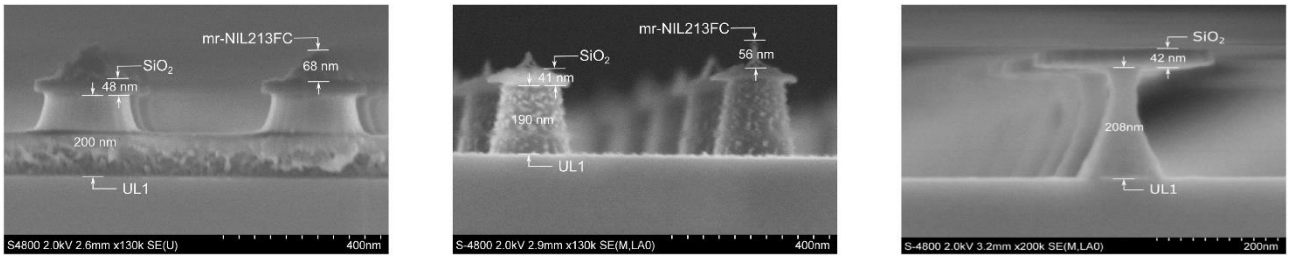

(a) 20 s (b) 50 s (c) 60 s

Figure 2. SEM images of the trilayer stack after opening of the intermediate SiO2 layer and creation of the undercut utilizing an ICPRIE O2 plasma after 20 s, 50 s and 60 s. [2]

Plasma Parameters Impact on Carbon Micro-lens Shape and Surface Roughness

Delia Ristoiu [a], Pierre Ducluzaux [a], Guillaume Claveau [a], Ece Aybeke [a], Etienne Mortini [a],

[a] STMicroelectronics, Crolles 38920, France
e-mail: delia.ristoiu@st.com

CMOS image sensor technologies are now extensively used in various fields such as machine vision, computational photography, augmented reality, digital healthcare, biomedical imaging. One of the main components of the image sensor are microlenses which allow light focalization onto the photodiode. Etched microlens are one of the most powerful techniques to achieve high surface fill factor and therefore maximize the quantum efficiency of the image sensor [1], [2].

Spherical microlenses are obtained by photoresist reflow and then they are transferred into a subjacent carbon-based layer by plasma etching. The purpose of this transfer process is to use shrink the lateral gap between microlenses, while maintaining the spherical shape. With respect to the previous papers [1,2], this study is focused on the plasma conditions impact on microlens shape and surface roughness.

Microlenses are etched in a CF_4 plasma, generated in a commercial CCP (capacitively coupled plasma) reactor using 2 plasma generators: a high frequency generator (HF power), and a low frequency generator (LF power) and a continuous negative high voltage generator (HVDC). In this study, a screening on CF4 flow, HF power, LF power, HVDC bias and pressure was performed and resulting microlens height, diagonal gap and roughness were analyzed.

Increasing CF_4 flow by 100 sccm has no impact on microlens height but increases the gap and the roughness. Gap increase is related to reduced polymerization rate due to shorter residence time. Meanwhile, a thinner polymer layer insures less surface protection against ion bombardment and leads to higher roughness.

Reducing HVDC by 650V has almost no impact on microlens shape, but significantly reduces roughness. Roughness reduction is related to HVDC impact on ion bombardment. Indeed, the HVDC generates balistical electrons into the plasma which will neutralize the substrate surface and thus increase the ion current. Reducing HVDC will contribute to ion current drop due to the electrostatic repulsion by the positively charged surface.

Increasing HF power by 500W has almost no impact on microlens shape or roughness (less than 10%). This behavior suggests that the CF_4 is totally dissociated such as further increase of the HF power has no effect on plasma density.

Reducing LF power by 500W has almost no impact on microlens shape (less than 10%) but leads to a significant roughness reduction. This result confirms that surface roughness is related to ion energy, high LF power leading to deeper ion implantation and higher roughness.

Increasing pressure by 70 mtorr leads to a very smooth surface, but the spherical shape is totally lost. At high pressure the residence time increases leading to high polymerization and smooth surface.

In conclusion, smooth microlens surface may be obtained either by using low ion energy (low LF, low HVDC) or by protecting the surface with thicker polymers (lower CF_4 flow, lower pressure). For the studied conditions, the microlens shape is not impacted by HVDC, LF and HF powers, but by the residence time: high residence time tends to increase height, while low residence time increases gap.

[1] Pin-Chieh Huang et al., e-Manufacturing & Design Collaboration Symposium (eMDC), 3-6 (2018).
[2] Delia Ristoiu et al., Proceedings of the SPIE, V 11326, p 113260O (9 pp.)

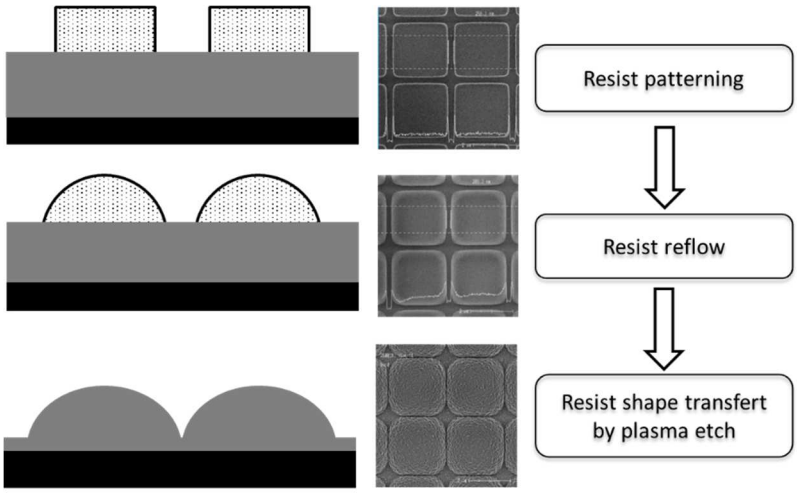

Figure 1. Etched microlens fabrication steps

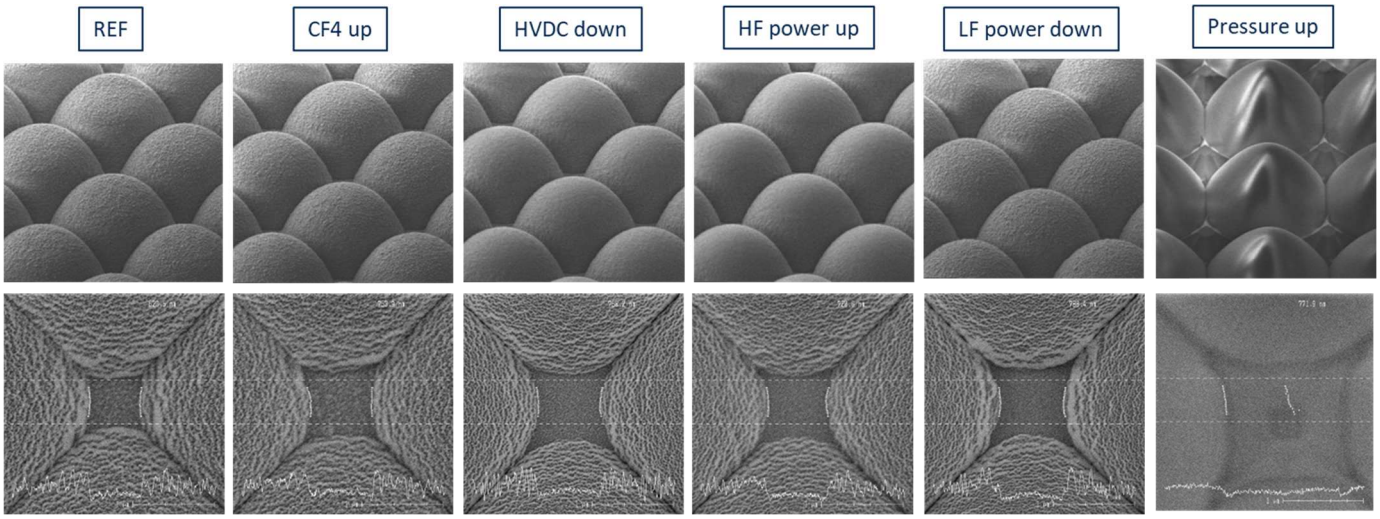

Figure 2. Impact of plasma parameters on Gap and Surface roughness (qualitative view)

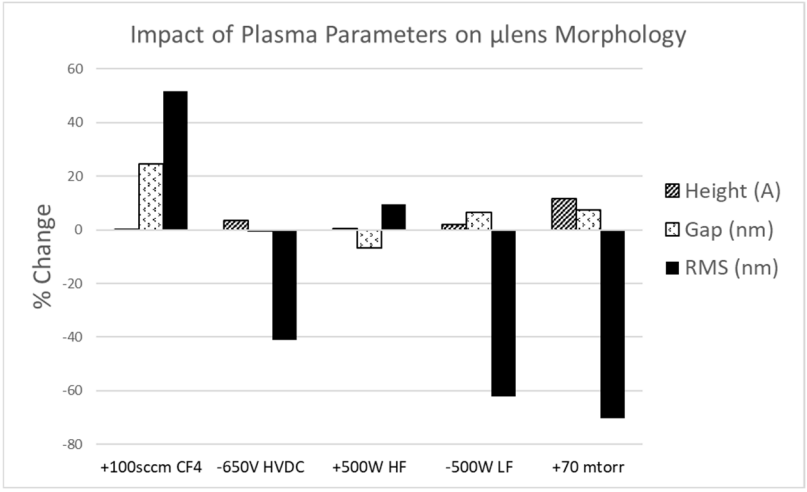

Figure 3. Impact of plasma parameters on microlens Shape and Roughness (quantitative view)

Blurred Electron Beam Induced Deposition for Direct Fabrication of Plasmonic Nanoantennas onto Tapered Optical Nanofibers towards Enhanced Single Photon Emission

A. Balena [a,b], C. Ding [b], M. D'Amato [b], M.F. Kashif [a], F. Pisano [a], M. Pisanello [c], G. De Marzo [a], M. De Vittorio [a,d,#], A. Bramati [b,#], F. Pisanello [a,#]

[a] Istituto Italiano di Tecnologia - Center for Biomolecular Nanotechnologies, Arnesano (LE), 73010, Italy
[b] Laboratoire Kastler Brossel, Sorbonne Université, CNRS, ENS-PSL Research University, Collège de France, Paris, 75005, France
[c] Optogenix s.r.l., Arnesano (LE), 73010, Italy
[d] Università del Salento – Dipartimento di Ingegneria dell'Innovazione, Lecce, 73100, Italy
[#] These authors jointly supervised the work
e-mail: antonio.balena@iit.it

Quantum emitters are of great interest for various applications in quantum photonics, sensing, and information processing, as they can produce on-demand single photons (SP) with high purity and brightness and sub-nanosecond lifetimes. Different material systems have been examined as potential options for SP sources (SPS)[1-3], including solid-state emitters such as organic molecules, color centers in diamonds, and quantum dots. Colloidal solid-state emitters, which have simple fabrication and can operate at room temperature, have a lifetime of the order of tens of nanoseconds and face challenges in efficiently extracting their photon emissions, which hinder their practical application. In this framework, optical nanofibers (ONFs)[4], which have a subwavelength diameter and strong evanescent field, offer a promising input/output platform to integrate SPS into photonic circuits. To further improve the SPS performance and SP collection efficiency, coupling with plasmonic nanostructures has been proposed [5]. Indeed, integrating SPS with plasmonic resonances in metallic low Q cavities provides a strong enhancement of the radiative rate of the emitter while acting as a redirecting element for the radiative field. However, deterministic methods to fabricate nanostructures directly on the ONF are not currently available, nor have been proposed. The techniques currently employed to realize an integrated SPS/ONF plasmonic system are based on separate or simultaneous drop-casting of the plasmonic particle and emitter [6-7], introducing a high degree of uncertainty in the positioning and orientation of the nanostructures on the ONF, as well as the reciprocal positioning with respect to the SPS. As a result, these methods fail to ensure the best coupling between the resonator and the ONF.
Here we introduce a bottom-up Electron Beam Induced Deposition (EBID) fabrication approach to directly pattern plasmonic nanoantennas onto ONFs (Fig 1.a), enabling sub-10 nm control over the position and the geometry of the realized structures. A specific aspect of the fabrication process is the exploitation of deliberate beam defocusing, obtained by the controlled blurring of the beam during the exposure: this is needed to reduce the electron flux over the exposed area, thus reducing the mechanical pressure exerted by the beam onto the ONF, that otherwise would prevent the correct result of the nanopatterning. In general, blurring of the beam is considered a detrimental condition for nanofabrication, but instead in this work, this strategy has been used to enable the patterning on these specific substrates, which are suspended, dielectric, and nanometric samples, while maintaining practically unaltered the composition of the nanostructure. We performed a thorough characterization of the deposited material by means of Scanning Electron Microscope inspection, Energy Dispersive X-Ray Spectroscopy, and Atomic Force Microscopy, while to optically characterize the properties of the interaction between the evanescent field guided by the ONF and a single nanopillar or two nanopillars separated by a nanogap, we measured the degree of polarization scattered light from a Near Infrared 785 nm laser beam. Two experimental configurations were investigated to measure how the intensity of the scattered light depends on the input polarization (Fig 1.b) and how, by fixing the input polarization of the beam, the light scattered from the structures is polarized (Fig 1.c). Moreover, we measured the spectral differences in the scattering of a supercontinuum laser from the two geometries, highlighting a redshift of the scattered signal for the nanoantenna configuration (Fig 1.d, left). The experimental results were confirmed by Finite Element Method (FEM) simulations (Fig 1.d, right), which also showed the redirecting effect on the radiative field, routed towards the collection channel represented by the ONF. These results showed how our approach presents a promising alternative to top-down fabrication methods for plasmonic nanostructures, which paves the way to improve the performances of SPS while promoting a more efficient SP collection via the ONF.

[1] Chatterjee A. et al., Nat. Rev. Phys., 3 (2021), 157-177.
[2] Kjaergaard M. et al., Annu. Rev. Condens. Matter Phys, 11 (2020), 369–95.
[3] Kimble H.J., Nature 453 (2008), 1023–1030.
[4] Pierini S. et al., ACS photonics, 7 (2020) 8, 2265–2272.
[5] Hugall J.T. et al., ACS Photonics, 5 (2018), 1, 43–53.
[6] Sugawara M. et al., Phys. Rev. Research 4 (2022), 043146.
[7] Shafi K.M. et al., Phys. Rev. Applied 19 (2023), 034008.

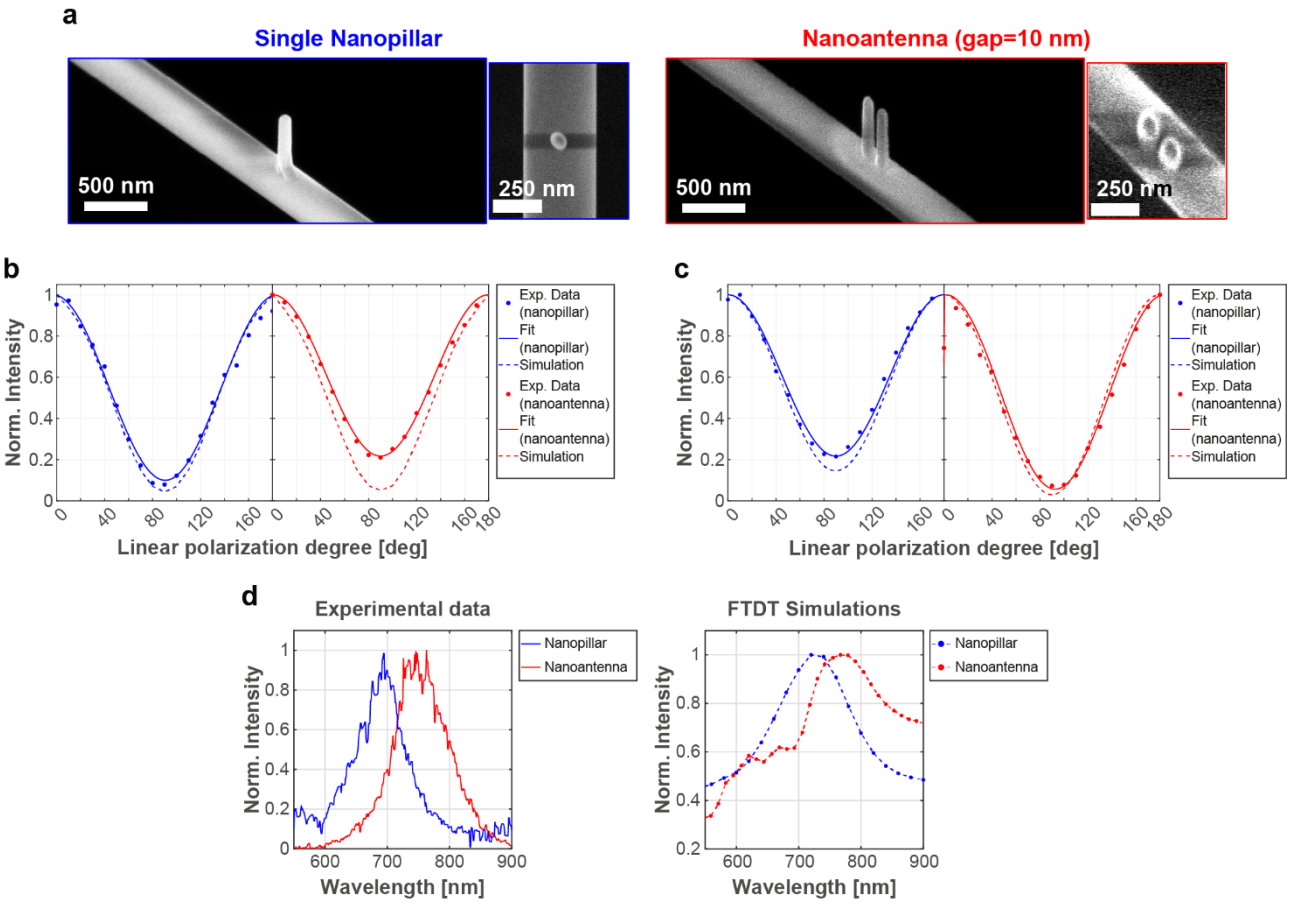

Figure 1. (**a)** SEM micrographs of a single nanopillar and a nanoantenna fabricated on a nanofiber. The inset shows the structures from the top, highlighting the nanometric size of the gap separating the pillars in the nanoantenna configuration**. (b)** Experimental response and FDTD simulations of the intensity dependence of the scattered light from the input polarization for both structures. **(c)** Experimental response and FDTD simulations of the intensity dependence from the detected polarization for both structures. **(d)** Experimental and FEM simulations of broadband spectral response of the two structures.

FEBID field emitters for vacuum nanoelectronics

Teodor Gotszalk [a], Ewelina Gacka [a], Bartosz Pruchnik [a] Piotr Kunicki [a], Krzysztof Kwoka [a], Tomasz Piasecki [a], Ivo W. Rangelow [b], Andrzej Sierakowski [c], Isaac Stricklin [d], Tito Busani [d]

[a] Department of Nanometrology, Wrocław University of Science and Technology, Wroclaw, 50-370, Poland
[b] Institute of Microelectronics and Photonics, Łukasiewicz Research Network, Warsaw, 02-668, Poland
[c] Institute of Micro- and Nanoelectronics, Ilmenau University of Technology, Ilmenau, 98693, Germany
[d] Department of Electrical and Computer Engineering, University of New Mexico, Albuquerque, NM 87131-1070, USA
e-mail: teodor.gotszalk@pwr.edu.pl

Field emission (FE) is emission of electrons induced by an electrostatic field. However, achieving high electrical fields (in the range of GV/m), making FE possible, involves structure biasing with high voltages (in the range of kV). This in turn causes a lot of problems with the device architecture. The solution to these problems is the structure miniaturization. There are reports about the FE between nanostructural electrodes fabricated in the focused electron beam induced deposition (FEBID) [1]. The technology mentioned above makes it possible to manufacture devices whose size is defined by the resolution of a scanning electron microscope in which the entire process is conducted [2,3]. Metrology of the FE from the FEBID nanostructures is quite challenging due to: i) relative high voltages (HVs) needed to induce the FE process ii) possible breakdown of the insulator structures iii) halo effect associated with the deposition of the FEBID nanowire making it really hard to identify, whether the FE takes place between the cathode and anode or between the metallic/carbon grains on the substrate.

In this paper we report FE conducted with use of the FEBID nanowires deposited on the so-called operational microelectromechanical system (opMEMS) microbridge (fig. 1). The opMEMS was a microbridge – 600 μm long, 40 nm thick structure suspended above an opening in the [110] silicon. The structure integrates three independent metal paths – two for displacement actuation, one to be cut for deposition of the FEBID electrodes [4]. Before the electrode deposition the device conductivity was tested. The conductivity tests were also performed after the electrodes were removed with FIB and measured in the same way. Area for the FEBID deposition was chosen in the middle of the bridge for symmetry purposes and to modulate the distance between the cathode and anode. Gap for the FE electrodes was milled in the gallium focused ion beam (FIB) process. Implantation on the structure edges (causing current leakage) was limited with introduction of photolithographically defined openings. FEBID pedestal was fabricated to increase the structure stiffness, the FIB fiducial marks were used to observe the distance between the cathode and electrode. We performed FE measurements in the tip-tip (fig. 2) and point-plane setup (fig. 3). The cathode and anode were fabricated out of Pt(C) material, which were also implanted with gallium ions. The electrodes were imaged between the measurements in order to analyze electrode structural changes [5]. We recorded FE in the range of up to 40 nA at the voltages ranging up to 60 V (fig. 4,5). Calculated Fowler-Nordheim curves confirmed FE process.

The National Science Centre has supported this work, Poland OPUS grant ”Nanometrology of Nottingham cooling effect using operational microelectromechanical systems” under project contract no. 2020/37/B/ST7/03792.

[1] Koops, H. W. P. *et al.* Additive electron-beam lithography. **2780**, 388–395
[2] Plank, H. *et al.* Focused electron beam-based 3D nanoprinting for scanning probe microscopy: A review. *Micromachines* **11**, (2020).
[3] Koops, H. W. P. Focused electron beam induced processing, a technology to develop and produce miniaturized electron- , IR , THz- , X-ray sources , high resolution detectors and sensors for IR- and X- ray tomography. *Procedia Eng.* **47**, 1460–1465 (2012).
[4] Koops, H. W. P., Gmbh, H. & Strasse, E. L. Focused Electron Beam Induced Processing renders at Room Temperature a Bose-Einstein Condensate in Koops-GranMat. *2015 28th Int. Vac. Nanoelectron. Conf.* 22–23 (2015) doi:10.1109/IVNC.2015.7225515.
[5] Edinger, K., Gotszalk, T. & Rangelow, I. W. Novel high resolution scanning thermal probe. *J. Vac. Sci. Technol. B* **19**, 2856–2860 (2001).

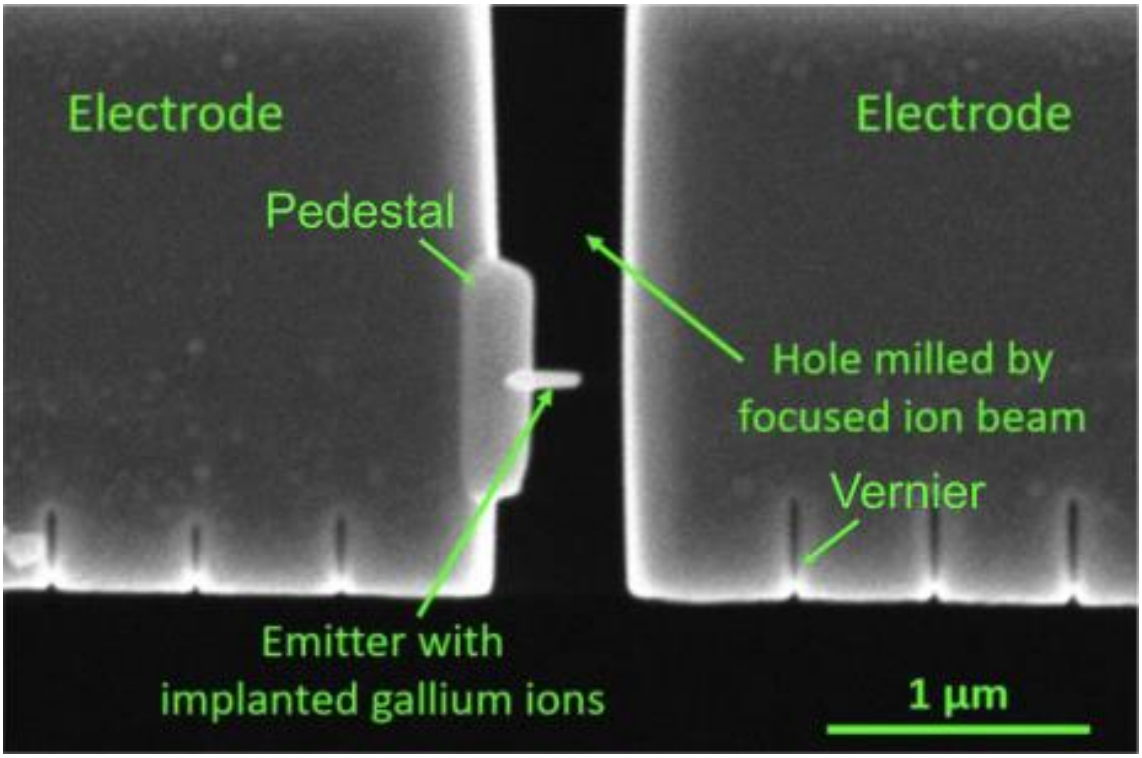

Figure 1. Model setup for FE measurements. All necessary components presented and denoted.
We fabricated two types of the FE structures: tip-tip and tip-plane. The first one is formed by a tip cathode and anode-fig. 2. The second one is created by the tip cathode and planar anode-fig. 3.

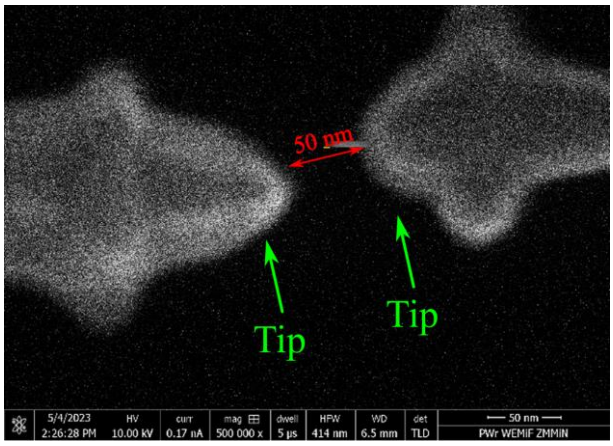

Figure 2 Tip cathode – tip anode setup

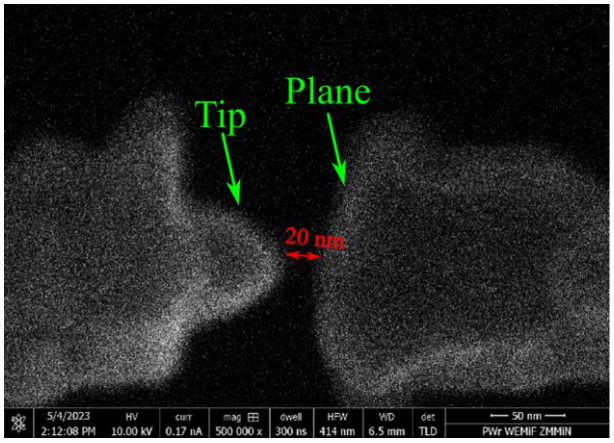

Figure 3. Tip cathode – planar anode setup

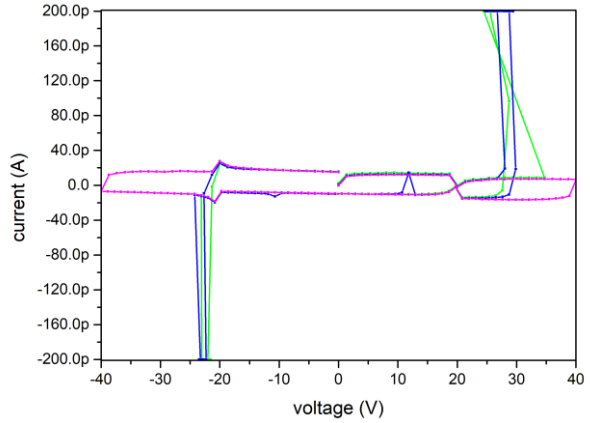

Figure 4. Single-sided FE from one of field electrodes in tip – tip setup

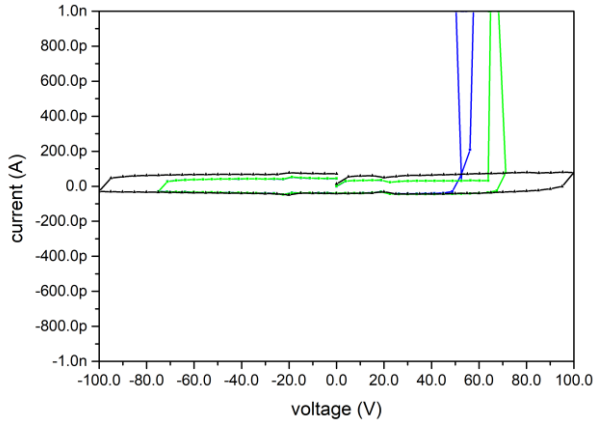

Figure 5. Single-sided FE from field electrode in tip – plane setup

Fabrication and Integration of Micro/Nano Structures, Devices and Systems - Papers

A spin-on-carbon/thin-metal based metasurface for broadband light modulation

Shuoqiu Tian and Yifang Chen*

Nanolithography and Application Research Group, State key lab of Asic and System, School of Information Science and Technology, Fudan University, Shanghai
e-mail: yifangchen@fudan.edu.cn

Keywords: plasmon hybridization, spin on carbon, metasurface, structural color, FP cavity

Metasurface is of great interest in nanophotonics for the ability to modulate light in subwavelength dimension. However, typical design strategy based on nanoscale metal antennas suffers from ohmic loss or challenging to fabricate. In this work, we introduce spin on carbon (SOC) to the design and fabrication of metasurface which greatly eases the above difficulties. As a proof of concept, a SOC/thin-metal based metasurface with chessboard configuration is developed. High aspect ratio nanopillars with widths under 50 nm in a large scale are acquired through electron beam lithography (EBL). A plasmon hybridization mechanism is established through finite difference and time domain (FDTD) simulations to interpret the tunable behavior in structural color as well as the wavelength-selective antireflection ability in visible and near infrared bands.

The proposed chessboard metasurface is schematically shown in Figure 1a. A 200 nm thick spin on carbon (SOC) layer is coated on silicon substrate to avoid generating plasmon modes between Au and Si substrate, above which lies SOC nanopillars with 300 nm height arranged in a hexagonal pattern. Au antennas of 40 nm thick above and below the nanopillars form Fabry-Perot (FP) cavities. Through the-state-of-art EBL process, followed by reactive ion etching (RIE), high quality metasurfaces with variant pitches are fabricated as shown in Figure 2. Simulations of reflection spectra are conducted in proposed chessboard metasurface with different height and pitches as shown in Figure 3. As shown in Figure 3a, by varying the height from 10 to 1000 nm (with a fixed pitch of 360 nm), the optical behavior of the metasurface can be divided into two regimes. When the height (h) is within 100 nm, the hybridization between top and bottom Au antennas dominates. When the height (h) is larger than 100 nm, the system behaves like a FP cavity. However, the reflection dip split into two branches near the wavelength of 1250 nm, which is a typical hybridization phenomenon. This hybridization, as shown in Figure 1b, is generated by the coexistence of LSPs and FP resonance, forming pairs of high-energy and low-energy hybridization modes. For varying pitches from 180 to 580 nm (with a fixed height of 300 nm), simulated reflection spectra are presented in Figure 3b. The dip around 1200 nm shifts greatly with the pitch, reflecting the existence of LSP mode. Figure 4a and b show the simulated and measured reflection spectra, respectively, in visible band. The measured results fit well with simulated ones thanks to nano pillars with perfect profile defined in SOC. It should be noticed that the wavelength of reflection peaks and dips changes regularly, resulting in different colors, which are filled in the measured spectra. Instead of visible band, reflection spectra in near infrared band are also simulated and measured as shown in Figure 4c and d, where results exhibit the same trend that the reflection dip red shift with increasing pitch. This indicates the existence of a LSP mode.

By summary, the proposed chessboard metasurface based on SOC/metals is systematically studied through FDTD simulations and experiments. Tunable plasmonic effect is demonstrated in both visible and near infrared band, showing controllable structure color and wavelength-selective antireflective ability, which is highly promising for use in perfect absorber, sensing and tunable filter. The developed SOC/metal metasurface should be of significant importance for future nanophotonic device, as a new family member.

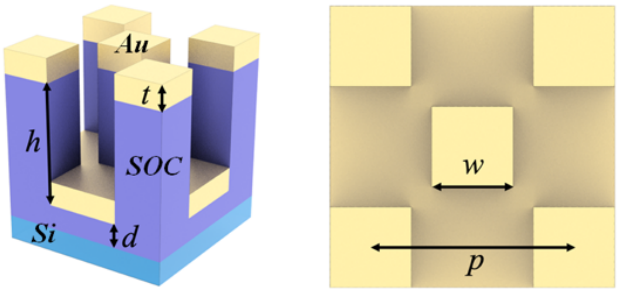

Figure 1. Schematic illustration of the proposed chessboard metasurface device.

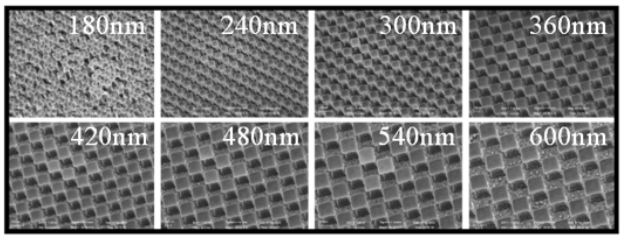

Figure 2. Tilted SEM image of fabricated chessboard metasurfaces.

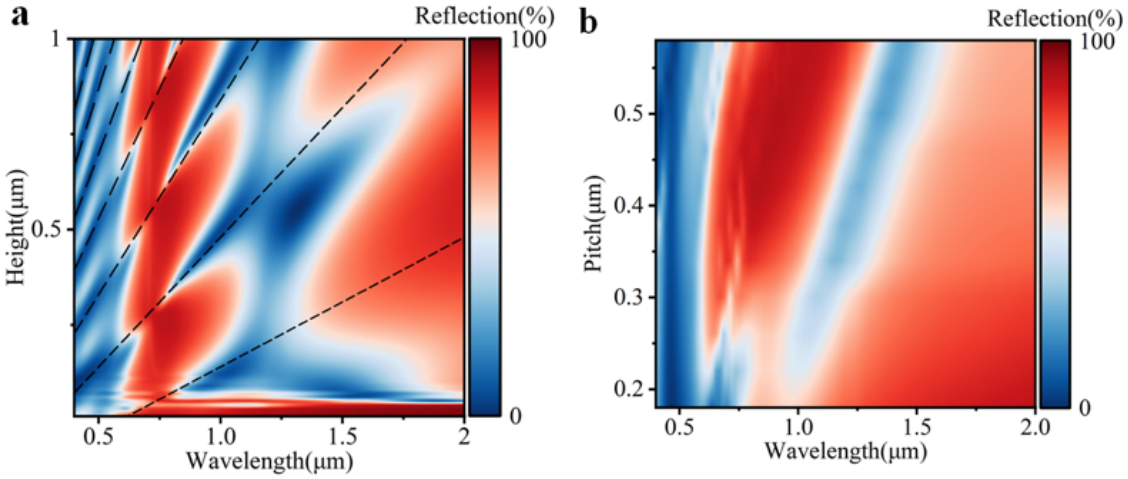

Figure 3. Simulated reflection spectra with different (a) height and (b) pitch.

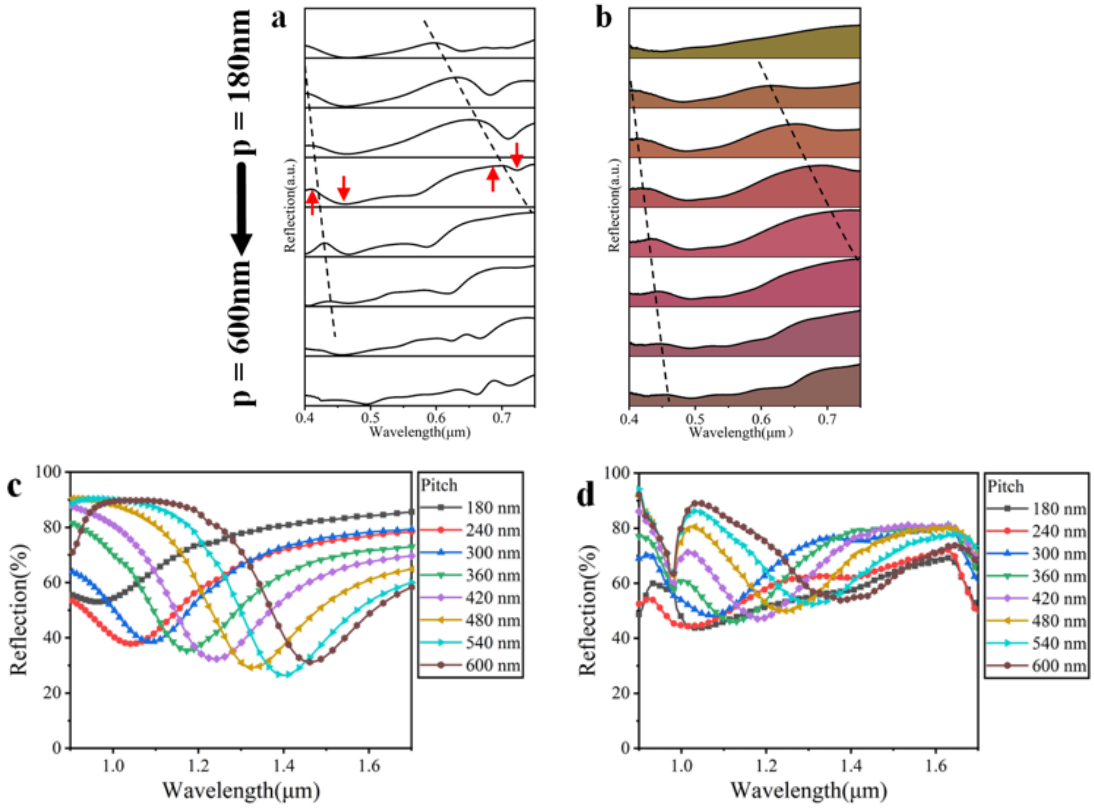

Figure 4. Simulated and measured reflection spectra in (a)-(b) visible and (c)-(d) near infrared band.

Durable Icephobic Superhydrophobic Silicon Nanowires Surfaces

Miika Heikkilä, Laura Fieber, Mehran Mirmohammadi, Ville Jokinen, Sami Franssila
Department of Chemistry and Materials Science, Aalto University, Micronova Nanofabrication Centre, 02150 Espoo, Finland
e-mail: mehran.mirmohammadi@aalto.fi

Introduction. Adhesion of ice on surfaces can be detrimental to windmill blades, power lines, airplanes, and sensors which motivates a search for icephobic surfaces. Superhydrophobic surfaces are effective at repelling liquid water through the Cassie-Baxter state, where an air pocket prevents the majority of the water from making contact with a solid. In many cases (but not all), superhydrophobicity can lead to time-delayed freezing or reduced adhesion strength of ice on the surface [1]. One definition of an icephobic surface is that the ice adhesion strength should be < 100 kPa, although for passive removal of ice, adhesion strengths < 20 kPa might be needed [2]. A key challenge is the durability of icephobicity: the ability to repel ice over multiple icing cycles. This has been achieved with superhydrophobic surfaces made from polymeric materials utilizing interfacial slippage [2], but it remains a challenge, especially for hard materials. Here we show durable superhydrophobic icephobic silicon surfaces utilizing a microscale protective Armor structure [3], monolithic nanowires, and protective hard coatings.

Experimental. Figure 1a shows the schematic for fabrication process of superhydrophobic silicon nanowires inside inverted-pyramidal structures. The process is composed of three main steps: lithography and silicon wet etching, metal-assisted chemical etching (MaCE), and titanium deposition to form titanium silicide with annealing. Nanoparticles (Ultra-Ever Dry, UED) coated planar silicon and Armor (inverted pyramid) were studied as two reference samples. The icephobicity was characterized by measuring the shear stress needed to separate a standardized block of ice from the surface. The ice block was created by filling a cylindrical Teflon mold (1 cm inner diameter, 2.2 cm outer diameter, and 2 cm height) with deionized water and freezing for 3 hours at -20 ± 1 °C and relative humidity of 65 ± 2 %. The shear adhesion force was then measured with a universal testing device (Instron 4204) with a modified sample holder (Fig. 1b). The measurement was done at room temperature within 10 seconds of removing the sample from the ice box and within 10 minutes of bringing the samples from the freezer using the ice box (verified by control experiments).

Results: Figure 2 shows the scanning electron microscopy (SEM) analysis (Fig. 2a-f) and icephobic properties (Fig. 2g) of all samples before and after ice adhesion measurements. All samples were extremely icephobic on the first icing cycle. Most samples had an adhesion so low that it did not even support the free weight of the ice block without any added external force. This self-supporting threshold was approximately 10 kPa, and all such cases have been plotted in Figure 2g as 10 kPa. After repeated icing-deicing cycles, the adhesion starts to increase due to wear. Our first result is the difference in durability between the Ultra-Ever Dry nanoparticle coated samples and the monolithic silicon nanowire samples. The nanoparticle samples had degraded to 40-45 kPa after the full 20 cycles due to the loss of the particles over the cycles, as shown in Figure 2b and c. The loss was also reflected in the wetting properties of the samples. The contact angle hysteresis (CAH) was initially 3°; after 20 cycles, it had increased to 32°.

All nanowire samples retain their icephobicity well over 20 cycles, but there are differences between the samples. After 20 cycles, the highest adhesion was on the plain nanowires (23 kPa), followed by titanium coated nanowires (20 kPa). The two best performing samples were the two annealed titanium samples. The titanium silicide sample annealed in argon atmosphere had a final ice adhesion strength of 16 kPa (structure in Fig. 2e). The best performing sample was sample annealed in nitrogen atmosphere which had both titanium silicide and titanium nitride. This sample's ice shear adhesion after 20 cycles was still below the 10 kPa self-supporting threshold, as seen in SEM images (structure in Fig. 2f).

Figure 3 shows X-ray diffraction analysis (XRD) of samples to research the effect of the annealing atmosphere (argon or nitrogen) and deposition method (EB evaporation or sputtering). All samples were annealed at 800 °C for 30 minutes. The effect of the annealing atmosphere is clear in Figure 3.; in argon, pure titanium silicide is formed, whereas in nitrogen, we get both titanium silicide as well as titanium nitride.

References

[1] Y. Shen, et al., Progress in Materials Science 103 (2019) 509-557.
[2] K. Golovin, et al., Science Advances 2 (2016) e1501496.
[3] Wang, D., et al., Nature 582 (2020) 55-59.

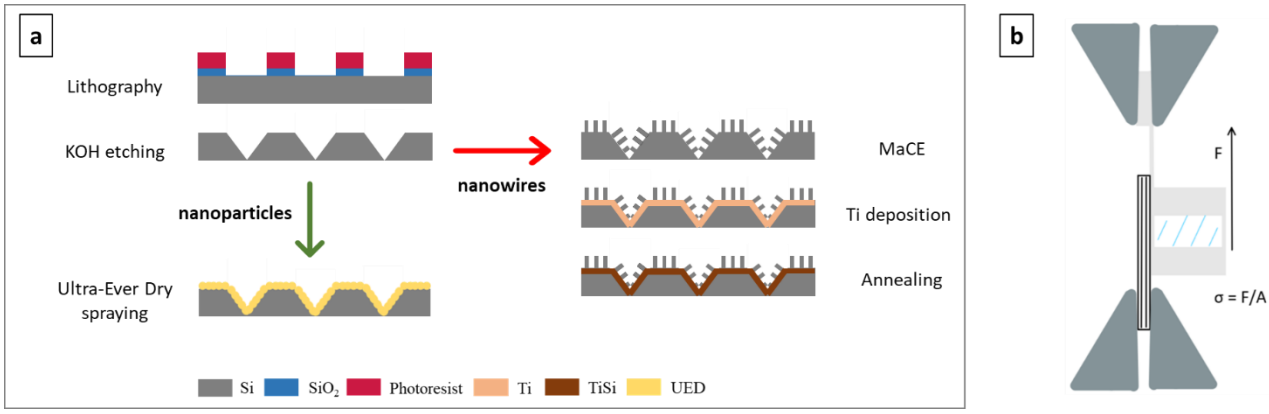

Figure 1. a) Fabrication process for silicon nanoparticles and nanowires inside inverted-pyramidal structures. b) Ice adhesion measurements setup.

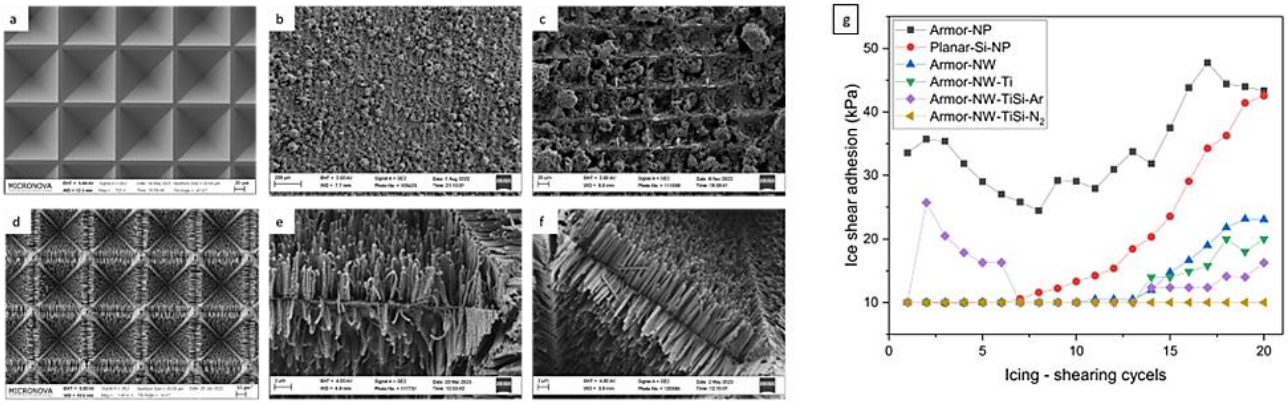

Figure 2. SEM micrographs of a) Armor (inverted pyramid), b) Armor nanoparticles (UED-coated) before, c) after ice adhesion test, d) Armor nanowires silicide before, e) annealed in argon, f) annealed in nitrogen after ice adhesion test. g) Ice shear adhesion of all investigated samples over the 20 icing-shearing cycles.

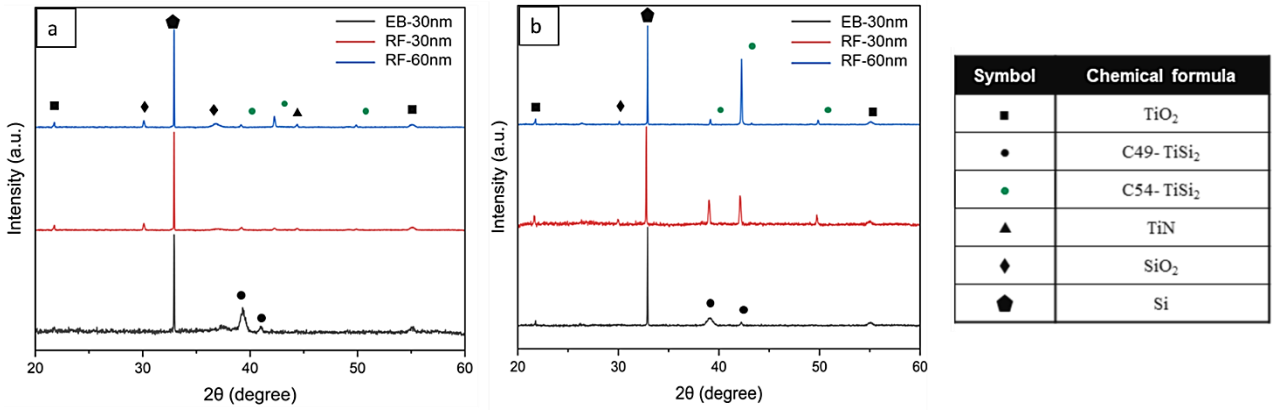

Symbol	Chemical formula
■	TiO_2
●	C49- $TiSi_2$
●	C54- $TiSi_2$
▲	TiN
♦	SiO_2
⬟	Si

Figure 3. XRD analysis of annealed EB evaporation and sputter titanium at different thicknesses in a) nitrogen and b) argon atmosphere.

3D Printing of Molecularly Imprinted Polymers by Digital Light Processing for antibiotics recovery

E. Camilli[a,b], W. Tang [d], I. Roppolo[a], F. Frascella[a], V. Bertana[b], M. Cocuzza[a,b,c], T. Minami[d], S L. Marasso[b,c]

[a] Department of Applied Science and Technology (DISAT), Politecnico di Torino, Corso Duca degli Abruzzi 24, 10129 Turin, Italy
[b] Chilab-Materials and Microsystems Laboratory, Department of Applied Science and Technology (DISAT), Politecnico Di Torino, Via Lungo Piazza d'Armi 6, 10034 Chivasso (Turin), Italy
[c] CNR-IMEM, Parco Area delle Scienze, 37a, 43124, Parma, Italy
[d] Institute of Industrial Science, The University of Tokyo, 4–6-1 Komaba, Meguro-ku, Tokyo 153–8505, Japan
e-mail: elena.camilli@polito.it

Molecularly Imprinted Polymers (MIPs) as artificial receptors have received considerable scientific attention in the past few decades, as material for biomimetic molecular recognition [1]. The preparation of an imprinted polymer involves the complexation, through covalent or non-covalent interactions, between a template molecule and a functional monomer, followed by polymerization in the presence of an excess of a crosslinking agent. The removal of the template from the resulting matrix leaves behind imprinted cavities, complementary at the atomic scale to the template molecules, thanks to the binding sites exhibited by the functional monomer. MIPs are nowadays employed in a large number of applications and fabricated in a variety of techniques, including photopolymerization methods [2], even though fabrication through additive manufacturing (AM) appears mostly as an unexplored field. The challenge of this work is in the employment of AM technology to realize 3D-printed MIP-based objects. A composite photocurable resin was developed to be suitable for a Digital Light Processing (DLP) printer, and optimized in order to reach reproducibility. The resin consists of Oxytetracycline (OTC, a broad-spectrum antibiotic) as the template molecule, methacrylic acid (MAA) as the functional monomer, Dipropylene Glycol Diacrylate (DPGDA) as the photopolymerizable crosslinker and Dimethyl sulfoxide (DMSO) as the solvent. The interaction mechanism between the carboxylic group of MAA and the hydroxyl and amide groups of OTC was computationally investigated through density functional theory (DFT) calculations [3], including the presence of DMSO (Figure 1). At first, multi-material disks were printed, consisting of a MIP 50 µm thick layer on a 500 µm thick support base of DPGDA. The thickness of the MIP layer was minimized to mimic a functionalization layer on a surface. Then, complex 3D filters were printed (Figure 2), entirely made of MIP resin. The samples were tested for OTC recovery from aqueous media, and the target adsorption was characterized by UV-Vis spectrophotometry (Figure 3).
In this work, DLP was employed to fabricate microstructured samples suited to characterize the material and investigate its capability in target recovery. Nonetheless, the described approach will be applied in the next future to develop a resin printable with a higher resolution technique, namely Two-Photon Polymerization, to obtain the patterning of MIPs at the nanoscale and thus the integration of MIPs in micro and nanosystems.

[1] J. J. Belbruno, Chemical Reviews, 119(1), 94–119 (2019)
[2] E. Paruli et al., ACS Applied Polymer Materials, 3(10), 4769–4790 (2021)
[3] S. Suryana et al., Molecules, 26(7), 1891 (2021)

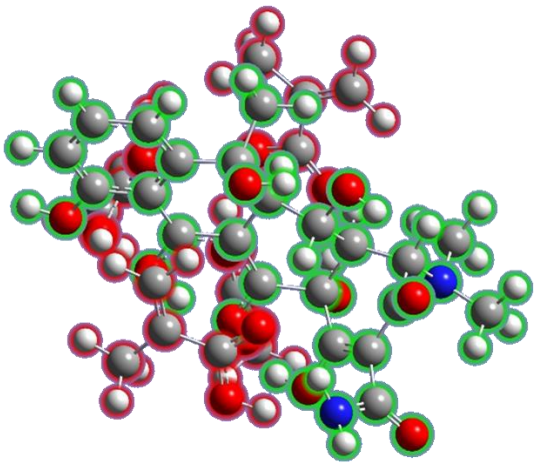

Figure 1. The complexation of Oxytetracycline (in green) and four molecules of Methacrylic Acid (in red), optimized by DFT calculation at the B3LYP(D3BJ)/def2SVP level.

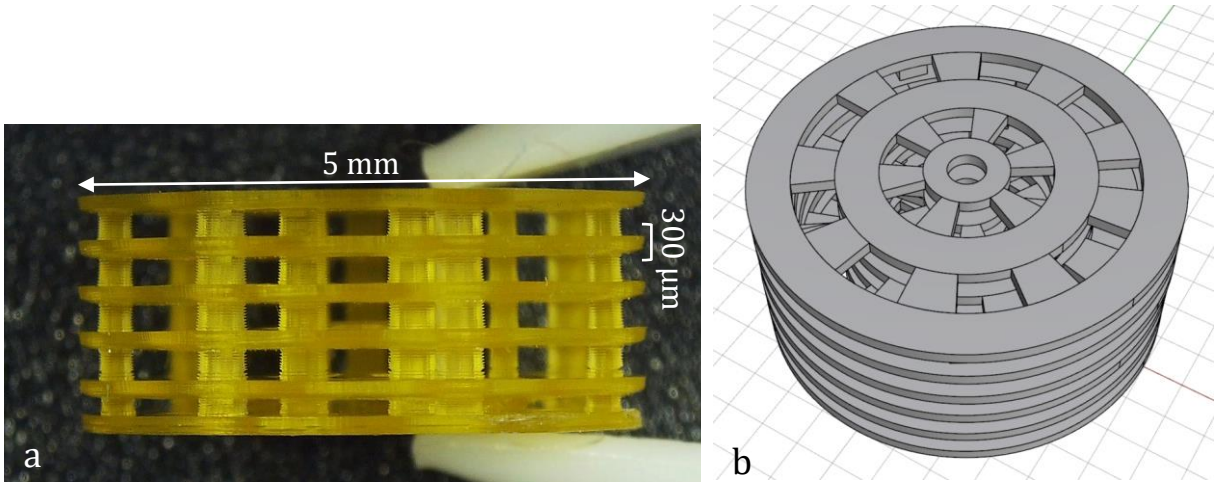

Figure 2. Side view picture (a) of the printed MIP filter, and the perspective view of the CAD drawing (b).

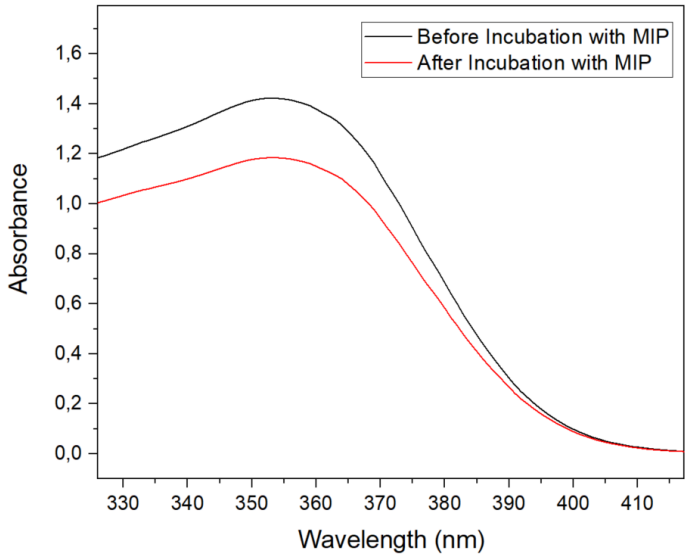

Figure 3. UV–Vis absorption spectra of the solution containing the target molecule (Oxytetracycline 100µM in deionized water), before and after being in contact with MIPs.

Fully inkjet printed and metallized waveguide antenna for RADAR application

Peter Bauer [a], Gerald Stubauer [a], Pavel Kulha [a], Michael J. Haslinger [a], Christian Debatin [b], Jochen Seeser [b], Alexander Fischer [c], Istvan Denes [c], Dieter Holzinger [d], Doron Gurovich [e], Semyon Melamed [e]

[a] PROFACTOR GmbH, Steyr-Gleink, 4407, Austria
[b] NOTION Systems GmbH, Schwetzingen, 68723, Germany
[c] ROBERT BOSCH GmbH, Renningen, 71272, Germany
[d] TIGER Coatings GmbH & Co KG, Wels, 4600, Austria
[e] PV Nano Cell Ltd, Migdal HaEmek, 23100, Israel
e-mail: peter.bauer@profactor.at

High performance RADAR sensors integrated in automotive vehicles are indispensable for modern mobility applications. Advanced-driver-assistance-systems (ADAS) as well as robotic cars rely on the detection of the environment and obstacles to secure the safety of the drivers and others [1]. Current bottlenecks of RADAR systems are the relevantly large size of such sensor devices, their weight and power consumption. Here complex 3D waveguide antennas are beneficial a highly efficient alternative to the commonly used 2D patch antenna arrays, with the potential advantages of the reduction of RF material, what can be associated with a reduction in costs and reduction of power consumption due to increased antenna efficiency [2].

Additive manufacturing, especially multi-material inkjet printing, opens the possibility for further miniaturization of the RADAR systems by a digital deposition of conductive interconnections and shielding (higher degree of customization). This makes it possible to fabricate complex 3D waveguide antenna structures with inner metallization with shorter production time and reduced waste. To this end, various 3D antenna structures are printed on PCBs and afterwards metallized by a precise overprinting with conductive Ink. Figure 1 shows printed waveguide antenna samples. Printing is performed with the TINKER-Pilot-Printer from NOTION (Figure 2), a multi-material printer which can be equipped with up to 4 printheads. TIGER developed a non-transparent UV-curable dielectric Ink (TIG 150/3.1K), used for building up the 3D antenna structure to meet radar waveguide requirements. PV Nano Cell developed the solvent based silver nanoparticle ink (I50TM-119) to achieve high conductive metal coating.

In this work we present the fabrication of metallized 3D waveguide antenna structures by multimaterial inkjet printing. The developed inkjet materials (TIG 150/3.1K, I50TM-119) as well as the TINKER-Pilot-Printer are presented in more detail. In addition, RADAR functionality testing of the inkjet printed 3D waveguide antenna structures, will be presented.

Acknowledgments
The project TINKER receives funding from the European Union's Horizon 2020 research and innovation programme under Grant Agreement No. 958472

References:

[1] https://resources.system-analysis.cadence.com/blog/msa2022-the-use-of-radar-technology-in-autonomous-vehicles
[2] B. O'Neal, 3D Printing Better Antennas for Millimeter-Wave Multi-Beam Applications, 3D Printing. (2019).

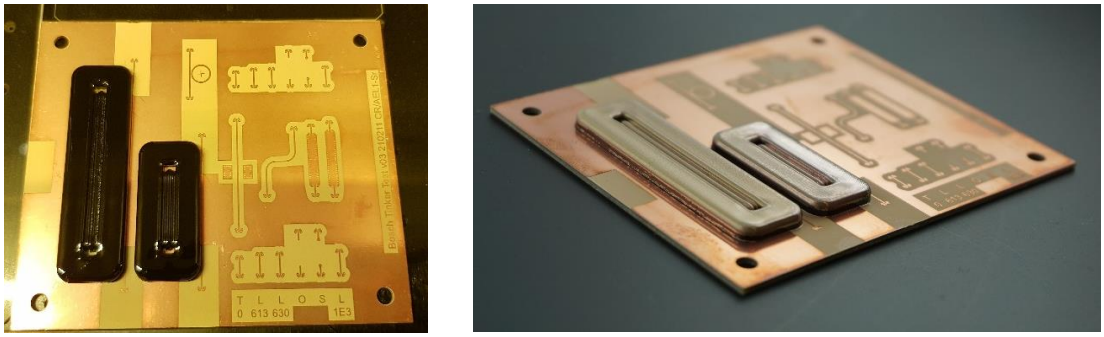

Figure 1. Inkjet Printed Waveguide structure (without cover) before (left) and after metallization (right) on a test circuit board

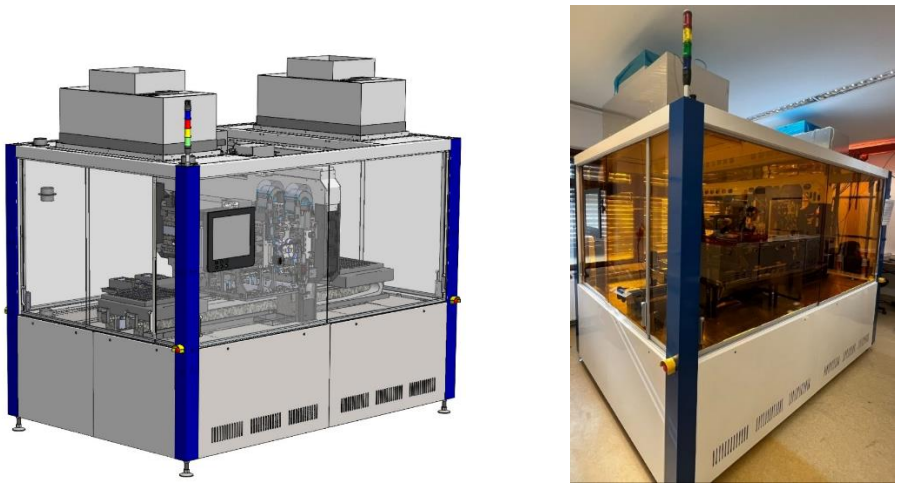

Figure 2. TINKER-Pilot-Printer: rendered image (left), built up printer (right)

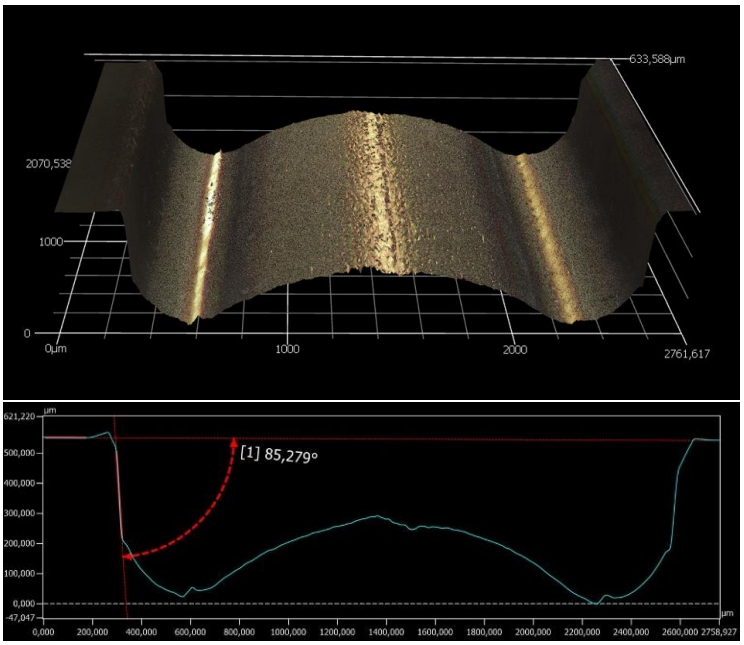

Figure 3. Metallized inner structure of printed waveguide antenna measured via Laser Scanning Microscope: overall structure (top), profile measurement incl. angle of printed wall (bottom)

Integrating top-down nanopatterning with bottom-up self-assembly to fabricate photonic cavities with atomic-scale dimensions

Ali Nawaz Babar [a,b], Thor August Schimmell Weis [a], Konstantinos Tsoukalas [a], Shima Kadkhodazadeh [b,c], Guillermo Arregui [a], Babak Vosoughi Lahijan [a,b], Søren Stobbe [a,b]

[a] Department of Electrical and Photonics Engineering, DTU Electro, Technical University of Denmark, B. 343, DK-2800 Kgs. Lyngby, Denmark.
[b] NanoPhoton - Center for Nanophotonics, Technical University of Denmark, B. 345A, DK-2800 Kgs. Lyngby, Denmark.
[c] DTU Nanolab, Technical University of Denmark, B. 347, DK-2800 Kgs. Lyngby, Denmark.
E-mail: anaba@dtu.dk

The two main techniques for fabricating nanostructures and functional devices are top-down nanopatterning and bottom-up self-assembly. Top-down nanopatterning offers precise control of pattern placement and scalability but is limited in achieving the smallest feature sizes [1]. Bottom-up self-assembly involves building blocks organizing themselves into functional structures through non-covalent interactions, offering atomic-scale resolution but less geometric freedom and production yield [2]. Combining the best of both approaches would be of great value to science and technology, especially nanophotonics because, on the one hand, light confinement is limited by the size of the smallest feature that can be fabricated [3, 4, 5] and, on the other hand, the potential of photonic technologies rely on the reliable fabrication of large-scale circuits [6]. An important proposed challenge is to confine light to unprecedented levels in air bowties with aspect ratios > 100 [3].

In this work, we use a novel method to fabricate photonic cavities with atomic-scale dimensions that use surface forces such as van der Waals, Casimir, and capillary forces [7] to self-assemble structures patterned only through lithography and etching [8]. The geometry and normalized electric field of the fundamental optical mode of our cavity design is shown in Fig 1a and 1b. The fundamental cavity mode has a resonance wavelength of λ = 1524 nm, a quality factor of $Q = 5 \times 10^4$, and a mode volume of $V = 3.4 \times 10^{-4}\ \lambda^3$. The extremely small mode volume stems from light confinement to a 2 nm air bowtie (Fig 1c and 1d).

We fabricate the designed air-bowtie nanobeam cavities in silicon-on-insulator wafers (Fig 2a) by self-assembling two halves initially separated by a gap g_f (Fig 2b) and suspended by two folded guided cantilevers. When the buried-oxide layer is etched, the two halves and springs are released, and the surface forces cause a deterministic collapse to form a 2 nm bowtie gap (Figs 2c and 2d). The resolution of the nanofabrication limits the absolute value of g_f. However, the relative distance between g_b and g_f is not limited by resolution, and, thus, the bowtie width, g, in the final device is limited only by surface roughness, enabling the realization of bowties with atomic-scale features (see high-resolution transmission electron microscope image in Fig 2d). Figure 2e shows the scattered far-field spectrum of a self-assembled cavity obtained with cross-polarized optical microscopy and its resonance fitted with a Fano lineshape. Our approach showcases the potential of integrating top-down nanopatterning and bottom-up self-assembly to realize photonic nanocavities with atomic-scale dimensions for applications such as single-photon nonlinearities and single-photon sources.

[1] J. H. Hah et al., J. Vac. Sci. Technol. B. 24, 2209–2213 (2006).
[2] Y. Min et al., Nat. Mater. 7, 527–538 (2008).
[3] H. Choi et al., Phys. Rev. Lett. 118, 223605 (2017).
[4] M. Albrechsten at al., Opt. Express 30, 15458-15469 (2022).
[5] M. Albrechsten at al., Nat. Commun. 13, 6281 (2022).
[6] N. Margalit et al. Appl. Phys. Lett. 118, 220501 (2021).
[7] G. Klimchitskaya et al., Rev. Mod. Phys. 81, 1827 (2009).
[8] A. N. Babar et al., arXiv. 2303.09610 (2023).

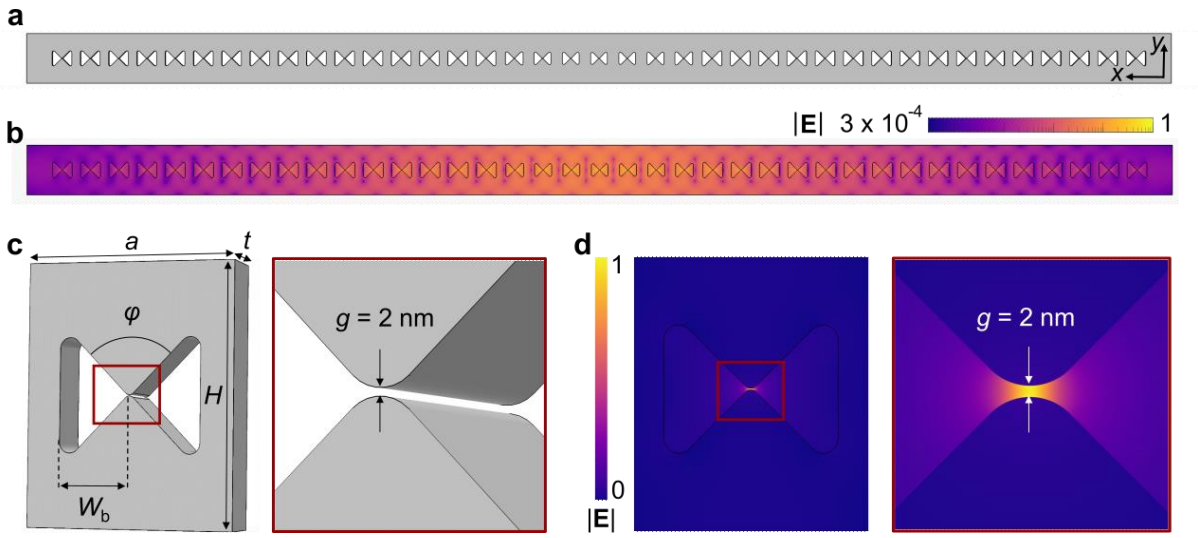

Figure 1. Design and geometry of a bowtie nanobeam cavity with atomic-scale dimensions. (a) The geometry of the bowtie nanobeam cavity. (b) The normalized electric field of the fundamental cavity mode, |**E**|, with a logarithmic color map. (c) The single bowtie unit cell with the following parameters: lattice constant, *a*, bowtie angle, φ, bowtie width, W_b, nanobeam width, *H*, and device-layer thickness, *t*. The inset illustrates the bowtie width, *g*, of 2 nm at the center of the bowtie. (d) . The normalized electric field of the fundamental cavity mode at the central bowtie unit cell with a linear color map. The inset illustrates the electric field tightly confined around the 2 nm bowtie width.

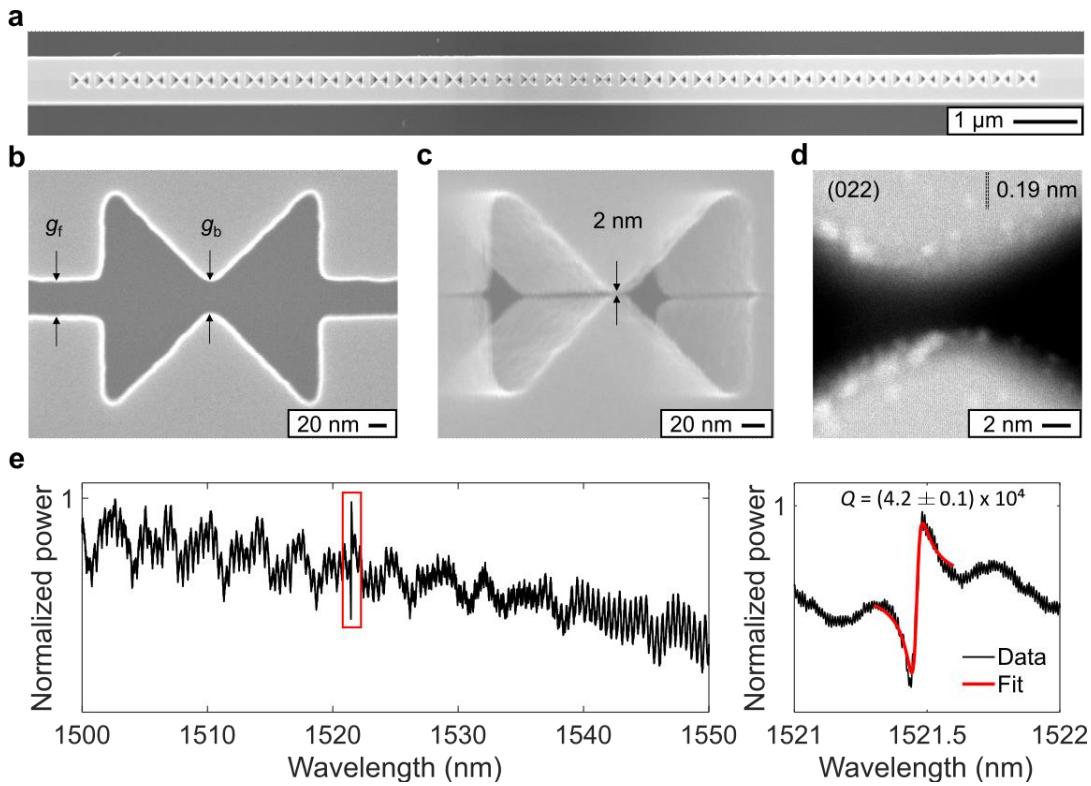

Figure 2. Fabrication and optical characterization of the self-assembled atomic-scale photonic cavities. (a) Tilted (20°) scanning electron microscope (SEM) image of a self-assembled nanobeam cavity. (b) Top-view SEM image of a single bowtie unit cell before self-assembly, with a fabricated gap, g_f, and a bowtie gap, g_b. (c) Tilted (20°) SEM image of a bowtie unit cell after self-assembly with an approximate bowtie width of 2 nm. (d) Top-view high-resolution transmission electron microscope image of the central region of the bowtie with an approximate 2 nm gap. The interplanar distance between the (022) silicon crystal planes is 0.19 nm. (e) Scattered far-field spectrum of a self-assembled nanobeam cavity measured using cross-polarized optical microscopy. The inset shows the resonance of the fundamental mode at the wavelength of 1521.5 nm, and a quality factor of $(4.2 \pm 0.1) \times 10^4$, extracted by fitting a Fano lineshape to the resonance.

Evaluation of the van der Waals force on the CNT Slipping Process in Transmission Electron Microscope

Keisuke Higashitani [a], Samel Jeong [a], Akada Keishi [a], Toshihiko Fujimori [a, b], Junichi Fujita [a]

[a] University of Tsukuba, Tsukuba, 305-8577, Japan
[b] Sumitomo Electric Industries, Ltd.,Osaka, 554-0022, Japan
e-mail: fujita.junichi.fu@u.tsukuba.ac.jp

The breaking strength of carbon nanotubes (CNTs) is reported to have over 100 GPa in a single CNT molecule. However, that of CNT bundle showed a significant decrease to ~60 GPa at the ten pieces of CNT [1][2]. In this case, the maximum breaking strength comes from the breaking of the CNT molecule rather than from the slipping between CNTs. On the other hand, the breaking strength of CNT fiber reached only ~4 GPa [3], where the crucial feature of the fracture cross-section showed the slipping of CNT molecules. That means the breaking strength of CNT fiber could have resulted from the van der Waals force between CNTs molecules in the fiber. Here, the slipping force between the CNTs depends on the contact length. Thus, the longer contact length gives the larger breaking strength against the CNT's slipping motion. We report the direct measurement and evaluation of the slipping force under the high-resolution TEM using a homemade piezo-driven TEM sample holder.

Fig. 1(a) shows the in-situ manipulation holder for driving the inter-CNT slipping. We used a commercially available nano-force measuring tungsten (W) probe (T-4-35, GGB Industries) for the in-situ tensile test. We attached the W probe to the tip of the holder, and the edge of CNT bundle was bonded at the tip of the the W probe using carbon contamination from the residual background hydrocarbon gas. The probe position was controlled in the sub-nm order using the bottom of the tube piezo device. In order to measure the slipping force between CNT bundles, the first step was to fabricate the measuring probe connecting with the counter CNT bundle on the Si substrate, as shown in **Fig. 1(b).** Then, we moved the CNT bundle on the probe to the counter CNT bundle, and adhered each other to have a certain contact length of 10 to 100 nm as shown in **Fig. 1(c)**. After establishing the bundle contact, we applied the tensile stress to the upward or downward direction to measure the probe's bending, as shown in **Fig. 1(d)**. All in-situ TEM operation was conducted with the 9 μA of the beam current under the accelerating voltage of 60 to 80 keV.

Fig. 2 shows the TEM images during the tensile test operation. The initial CNT bundles state of the pulling process shown in (a) has a contact length of 14.9 nm. Then, we moved the W probe with a constant velocity of 22 nm/s. As the probe drove to an upward, slipping and breaking of the contact suddenly occurred, and the probe position jumped up about 16 nm from the original position, and we estimate the slipping force to be 4.4 nN. Some of the strain-stress curves were summarized in **Fig. 3(a)**. The relationship between contact length and probe stress is shown in **Fig. 3(b)**. The counter CNT was composed of 3 pieces of CNT, and the tip of the tested bundle was also constructed with 2 or 3 pieces of CNT. Thus, if we assume the slipping of CNT occurs on the surface between the single CNTs, the slipping force will be approximately 0.26 N/m. Considering the typical CNT diameter in this experiment was about 2 nm, the breaking slipping stress of 27 nN with the 95 nm of contact length is identical to 7.7 GPa, which is weaker than the CNT molecules breaking strength. By extrapolation of the relation of bundle contact length and slipping force, the contact length of 1.54 μm could enlarge the breaking stress up to 100 GPa.

The defects that caused the bending and/or diameter mismatch, as well as the impurities adhered on the CNT body would weaken the van der Waals force and deteriorate the breaking strength of the CNT's fiber, but our experiment suggests only 2 micrometers of perfect contact length enables the production of ultra-high strength of CNT fiber.

Acknowledgment: This work was supported by Innovative Science and Technology Initiative for Security, ATLA, Japan (Grant Number JPJ004596).

[1] T. Fujimori, et al., Appl. Phys. Lett. 115, (2019) 023106
[2] Y. Bai, et al., Nat. Nanotechnol. 13, (2018) 589-595
[3] E. Gao, et al., Carbon, 138, (2018) 134-142

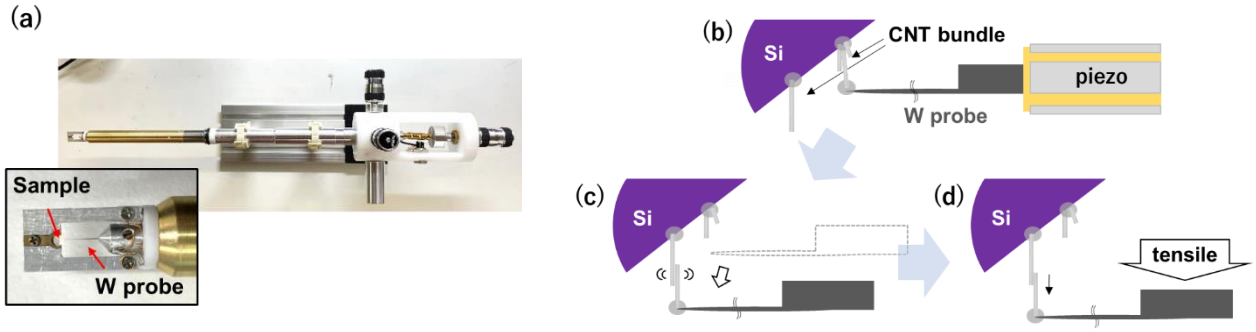

Figure 1. (a) Overview of in-situ TEM holder. **(b)-(d)** Illustration of tensile test operation. **(b)** Connecting the probe with the counter CNT bundle, then **(c)** moving the CNT bundle on the probe to the counter CNT bundle. **(d)** Applying the tensile stress.

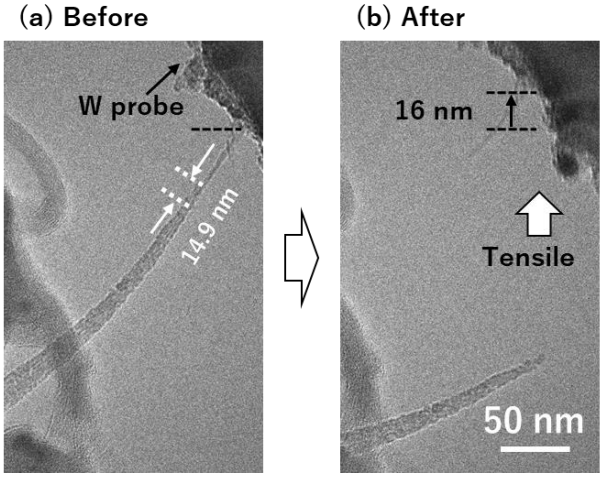

Figure 2. Tensile test between bundles before and after the slipping. The probe was moved at 22 nm/s in the upward direction and moved 16 nm at the moment of slipping.

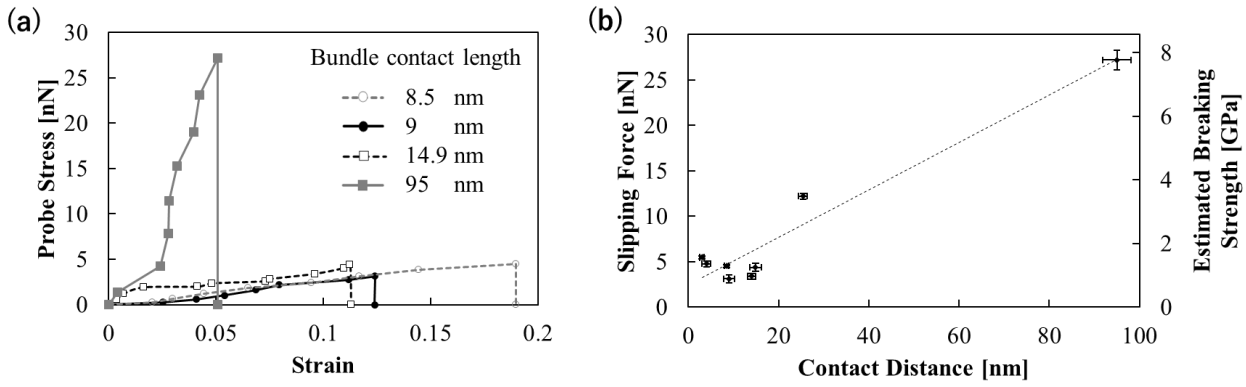

Figure 3. (a) Stress-train curves in multiple bundles. Four patterns of tensile tests were performed from a contact length of 8.5 nm to 95 nm. The caption corresponds to the contact length.
(b) Relationship between contact length between bundles and slipping force as well as estimated breaking strength, which is the slipping force divided by the cross-sectional area of the two CNTs.
The slope of the linear approximation is 0.26 N/m.

Conventional fabrication techniques with high yield for a tuneable room temperature single-electron transistor and field-effect transistor

Kai-Lin Chu, Faris Abualnaja, Wenkun He, Mervyn Jones, and Zahid Durrani
Department of Electrical and Electronic Engineering, Imperial College London, South Kensington, London, SW7 2AZ, United Kingdom
e-mail: kai-lin.chu21@imperial.ac.uk

Integrating complementary metal-oxide-semiconductor (CMOS) technologies and quantum devices has been of great interest in the development of quantum systems [1]. However, a low throughput and lack of reproducibility when combining these two technologies exists when fabricating these devices [1]. In this work conventional fabrication processes for CMOS devices have been used to produce room-temperature (RT) single-electron transistor (SET) quantum devices [2]. RT-SETs regulate the flow of one electron through tunnel barriers by shifting the electronic states of a quantum dot (QD) using an applied gate bias [3]. These hybrid devices may also operate as RT field-effect transistors (FETs) by tuning the gate bias. Using a modest research lab, we have achieved a relatively high throughput, where 66 FET-SET devices out of a possible 180 (~ 37%) across 4, 15 mm × 15 mm chips have been produced in a single run.

Each chip has a pattern that consists of 45 FET-SET devices divided into 9 equal groups (Fig. 1(a, b)). Each FET-SET device has a source, drain, and two gate terminals. Between source and drain, a 20 nm × 20 nm point-contact region is designed with gate electrodes separated by 200 nm on either side (Fig. 1(c)). A scanning-electron micrograph (SEM) of the completed device is shown in Fig. 1(d). The devices are made using silicon-on-insulator (SOI) material. The top-Si layer is heavily doped with phosphorous (P) dopant atoms using a spin-on-doping method followed by a rapid thermal annealing (RTA) process to activate the dopants. A bi-layer of PMMA is spin-coated on the top-Si layer and electron beam lithography (EBL) is used to define the pattern (Fig. 2 (a)). 30 nm of aluminium (Al) is then evaporated with a lift-off procedure to remove the PMMA. Reaction-ion etching (RIE) is used to transfer the pattern into the top-Si (Fig. 2(b)). After RIE, the Al mask is etched away, leaving behind the FET-SET pattern (Fig. 2(c)). Geometric oxidation at 1000 ºC is performed to partially oxidise the point-contact region leaving behind a Si-channel core (Fig. 2(d)). This step also embeds P dopant atoms into the surrounding SiO_2, forming the tunnel barriers and creating the device QD.

Figure 3(a) shows a colour map of the four 15 mm × 15 mm chips (Chip A, B, C, and D). RT FET-SET and FETs with very weak Coulomb diamonds are marked as a blue box, while the remaining non-gateable devices are marked as a yellow box. An average of 17 RT FET-SET/FETs are fabricated per 15 mm × 15 mm chip, producing an average yield of 37 % of functional transistors. Figure 3(b) shows the source-drain current (I_{ds}) vs. source-drain voltage (V_{ds}) for a RT FET-SET device at different gate biases (V_{gs}), with a gate threshold value V_{gs} = -5.5 V. The $|I_{ds}|$ vs. V_{gs} and V_{ds} characteristics for this same device is shown in Fig. 3(c). When V_{gs} is tuned to be near threshold, the device operates as a SET producing Coulomb diamonds (white lines). This RT SET-FET may be regarded as the bridge of applications between conventional FET and quantum devices.

Acknowledgements
The authors would like to acknowledge the Engineering and Physical Science Research Council (EPSRC). This research has received support from the UK EPSRC Single Atom Quantum Electronics project (EP/V030035/1).

References

[1] M. F. Gonzalez-Zalba, S. de Franceschi, E. Charbon, T. Meunier, M. Viner, AS. Dzurak, Nature Electronics, 4, 12 (2021), 872-884
[2] Z. A. K. Durrani, M. Jones, F. Abualnaja, C. Wang, M. Kaestner, S. Lenk, C. Lenk, I. W. Rangelow, and A. Andreev, Journal of Applied Physics, 124, 14 (2018) 144502.
[3] Z. A. K. Durrani, Single-electron devices and circuits in silicon. World Scientific (2009).

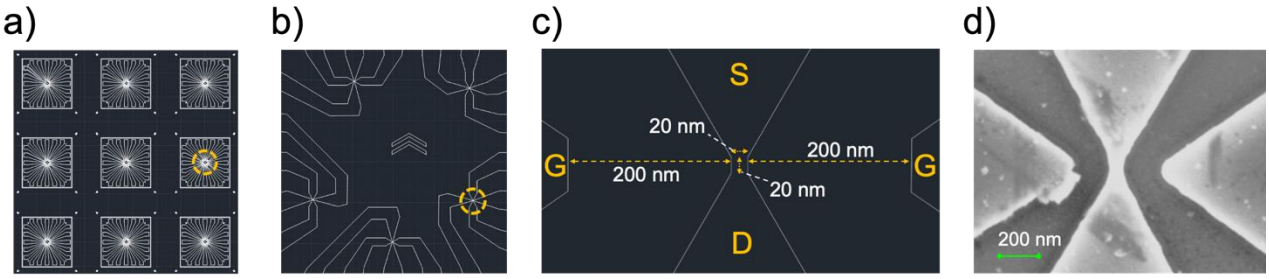

Figure 1: (a), (b) Layout and design of SETs. (c) SET source (S) and drain (D) point-contact dimensions and gate (G) distances are labelled. (d) SEM of a fabricated SET.

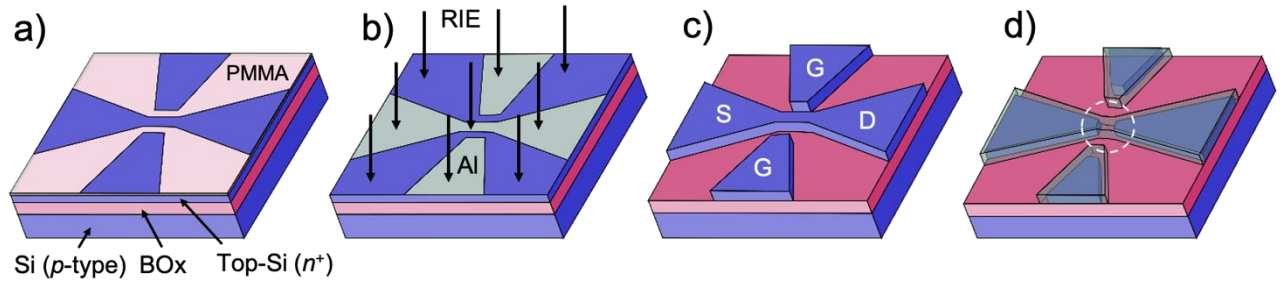

Figure 2: (a) EBL defined in bi-layer PMMA. (b) RIE with Al mask. (c) G, S, and D terminals are defined in top-Si layer. (d) Oxidation creates Si (n+) cores for S, D and G. In the point-contact region (dashed white circle) a Si-channel core and SiO_2 tunnel barriers with P donor atom QDs forms.

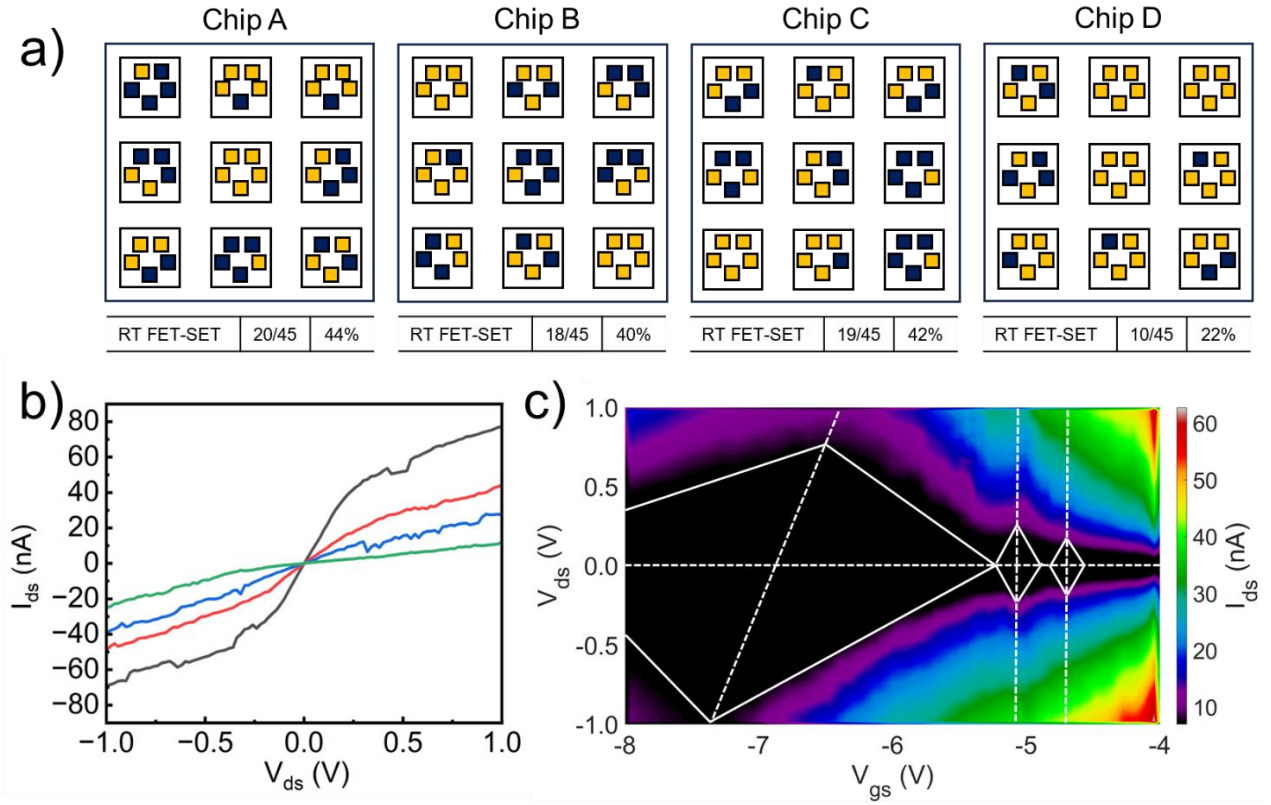

Figure 3: (a) Colour map for the four 15 mm × 15 mm chips A – D. RT FET-SET and FETs with weak Coulomb diamonds are coloured in blue, non-functioning devices are coloured in yellow. (b) FET I_{ds} vs. V_{ds} for V_{gs} = -4 V (black), -4.48 V (red), -5 V (blue), and -6.2 V (green). (c) $|I_{ds}|$ vs. V_{gs} and V_{ds} for a FET-SET device. Coulomb diamonds are marked in white. Dashed lines indicate diamond axis.

Structural and morphological study on a-Ge based nanostructures: dewetting from flat to patterned films

S. Freddi[a*], M. Gherardi[b], D. Chatain[c], G. Sfuncia[d], G. Nicotra[d], M. Bouabdellaoui[e,f], C. Barri[b], L. Fagiani[b], A. Fedorov[a], M. Abbarchi[e,f], M. Bollani[a]

[a] Institute of Photonics and Nanotechnology (IFN) – CNR, LNESS, Como, 22100, Italy
[b] Department of Physics, Politecnico di Milano, Milan, 20133, Italy
[c] Aix-Marseille Univ, CNRS, CINaM, 13009 Marseille, France
[d] Istituto per la microelettronica e microsistemi (IMM) -CNR, Catania, Italy
[e] Aix Marseille Univ, Université de Toulon, CNRS, IM2NP Marseille, France
[f] Solnil, 95 Rue de la République, Marseille, 13002, France

[*]e-mail: sonia.freddi@ifn.cnr.it

Thin solid films are usually metastable in the as-deposited state, and they will dewet or agglomerate to form islands when heated to sufficiently high temperatures. This process is driven by surface energy minimization and can occur via surface diffusion well below a film's melting temperature, especially when the film is very thin. During the thermal treatment, the thin film evolves forming at first holes, which expand on the thin film surface favoring the rupture of the film, by a process known as solid state dewetting (SSD). Isolated droplets can then grow from the film breaking [1,2].
Dewetted films can be exploited in several applications, including high-density magnetic recording media [3], flexible photonics [4], photocatalysis [5] or dielectric Mie resonator [6,7].
Among the dewetting systems reported in the literature, ultra-thin crystalline silicon-on-insulator (SOI) films have been largely studied and they have been considered as a model system for investigating and studying SSD. More recently, SiGe dewetting, i.e. SiGe structures directly formed on an electrically insulating and optically transparent substrate, has been efficiently exploited to realize arrays of nanostructures with typical footprint ranging from few nm up to several μm [8,9].
Germanium is a material of particular interest for photonic devices working at near and mid-infrared frequency. Therefore, the study and validation of a low-cost processing of Ge-based film, such as SSD, is of considerable interest for this kind of applications. Furthermore, thanks to its larger surface energy, Ge dewetting can be typically achieved at sensibly lower temperature with respect to Si, opening up the possibility to process this material exploiting simpler experimental set-ups. Despite the relevance of this material for photonics, the investigation of its dewetting features is not yet complete and a deep understanding of the process is still missing.
This work purpose is to study the morphological evolution of an amorphous-Ge-based thin film (a-Ge) and investigate morphological and structural properties of the dewetted islands. In detail, a-Ge has been deposited by MBE directly on thick thermal silicon oxide, whereas dewetting of a-Ge has been obtained by an annealing in the range between 600-700°C in UHV conditions in a home-made annealing machine. By a combination of in-situ reflection high-energy electron diffraction (RHEED) and by electron back scatter diffraction during high-temperature annealing, we clarify the initial crystallization dynamics of the Ge film. We complete the analysis by the structural characterization of the dewetted islands (ex situ, post-annealing) by high-resolution transmission electron microscopy (HR-TEM), atomic force microscopy (AFM) and scanning electron microscopy (SEM). Chemical composition has been assessed by electron energy loss spectroscopy (EELS). Different initial amorphous film thickness (range: 10 nm - 500 nm) and annealing treatments have been investigated to control the dewetting process of Ge (Figure 1). A full control over the final outcomes of the dewetting is obtained by introducing ad hoc features within the etched patches, thus guiding the dewetting fronts toward precise and reproducible shapes. So, to enhance the inherent spatial correlations into a true long-range ordering, SDD is also performed on a previously patterned a-Ge film achieved by a combination of e-beam lithography (EBL) and reactive ion etching (RIE). A systematic characterization of the germanium dewetting process in function of the Ge thickness, original pattern template, annealing temperature and annealing time will be presented.

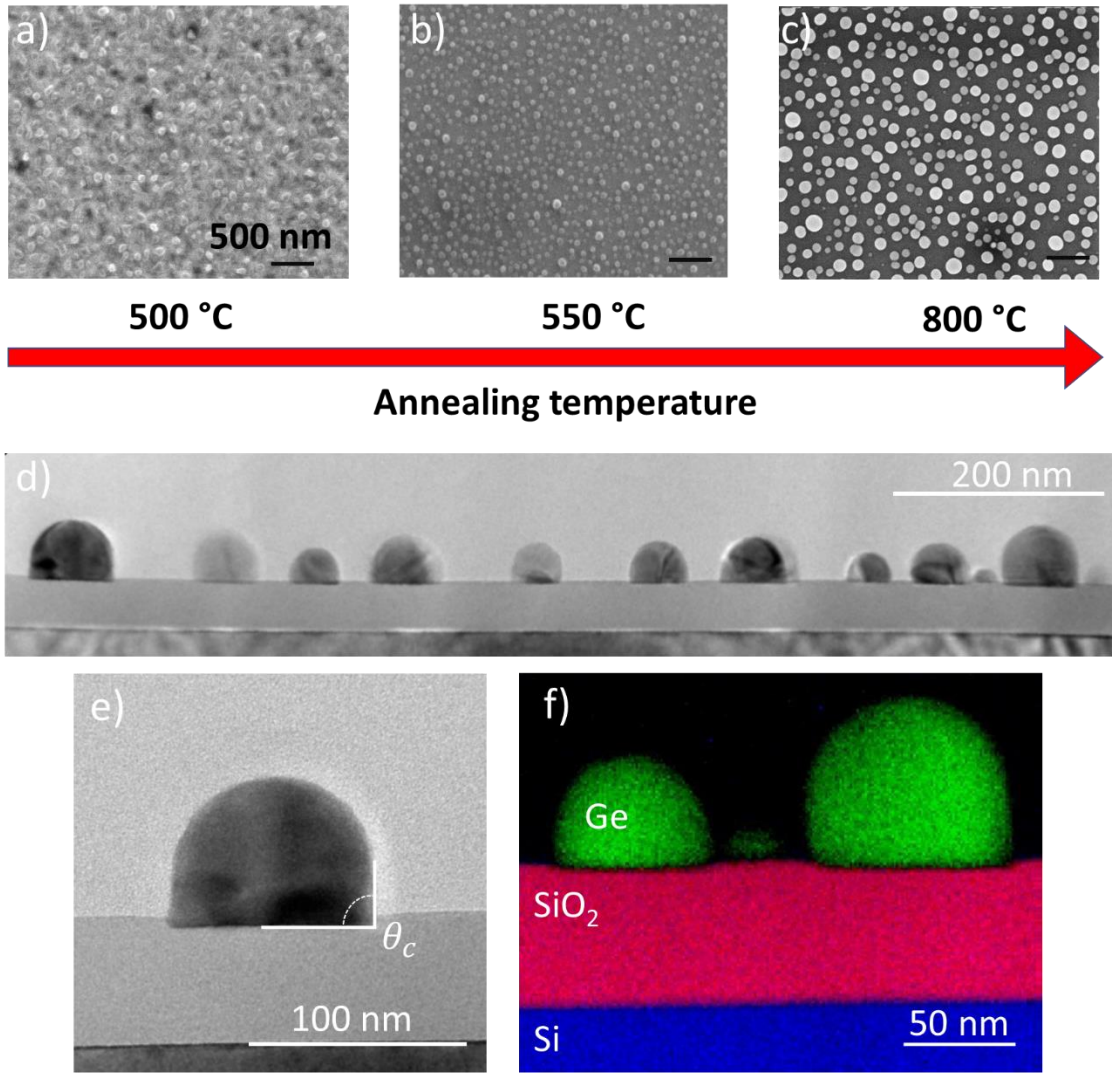

Figure 1. SEM images of an a-Ge sample, initial thickness of 10 nm, annealed for 15 minutes at 500°C (a), 550 °C (b), and 800°C (c). Complete dewetting achieved in (c). HR-TEM image of Ge crystalline island obtained by the annealing treatment of 15 minutes at 800°C (d). Contact angle of the dewetted island θ_C ~ 90° (e). EELS chemical map of the Ge island dewetted at 800°C for 15 min (f).

References

[1] F. Leroy et al., Surface Science Reports (2016), 71, 2, 391-409.
[2] M. Naffouti et al., Science Advances (2017), 3, 11, eaao1472.
[3] Y. J. Oh, et al., Small (2009), 5, 860–865.
[4] A. Benali et al., J. Phys.: Photonics (2020), 2, 015002.
[5] M. Altomare et al., Chem Sci (2016), 7(12), 6865-6886.
[6] N. Granchi et al., Opt Express (2023), 31, 5, 9007.
[7] N. Granchi et al., APL Photonics (2021), 6, 12, 126102.
[8] M. Bollani, et al., Nat Commun (2019), 10, 5632.
[9] M. Abbarchi et al., Microelectronic Engineering (2018), 190, 1-6.

Acknowledgements

This work is supported by the European Union Horizon 2020 program under grants No. 828890 – NARCISO and No. 964588 (XPIC) projects.

Dry release of MEMS Al_2O_3 origami for facet-based device integration with assistance of SU-8 reinforcement and folding stopping bars

J. Zhang[a], C. Strobel[b], T. Mikolajick[b], R. Kirchner[a]

[a] Technische Universität Dresden, Center for Advancing Electronics Dresden, Dresden, 01069, Germany
[b] Technische Universität Dresden, Institute of Semiconductors and Microsystems, Dresden, 01069, Germany
E-Mail: jianran.zhang@tu-dresden.de

Ever since the concept of micro-scale origami was proposed, there were many different techniques to fabricate various origami structures from micrometers to millimeters [1]. Previous works mainly focused on single device-functionality, such as microscale antennas, inductors, sensors, or actuators [2]. Our research introduced a dry release wafer-scale production method for Al_2O_3-based origami cubes enabling the integration of logic transistors and circuits on all facets, resulting in higher MEMS integration-density (Fig. 1) [3]. Al_2O_3 is patterned with 2 steps HF etching to have better carrier homogeneity (Fig.1a) and at the end released from Si by SF_6 plasma etching (Fig.1b). We addressed challenges related to folding behavior control using SiO_2 bars and careful origami designing. However, precise control of folding behaviors was still lacking, leading to problems like blocking of folding route or bending (Fig.1c). We then proposed further improvement in the paper [3]. This is a report updating results about the solution using stopping bars proposed in the paper (Fig.1d).

One major challenge is patterning such thick bars. Normal physical vapor deposition (PVD) combined with liftoff is too time-consuming, or costly, for an industry-compatible process. Alternatively, chemical vapor deposition (CVD) can be used, but it poses difficulties in liftoff, hence the required thick SiO_2 bars patterning need to be done with etching, which is even more difficult due to the selectivity of very thick SiO_2 and very thin Al_2O_3 origami and the extremely thin 2D materials involved. Thus, we explored the use of SU-8, a stable and strong material, that can withstand the SF_6 plasma. SU-8, with its thickness of a few micrometers, is easily patterned. We tested two approaches: patterning the bars after patterning Al_2O_3 and patterning the bars first. The advantage of the first approach is that all other processes can be completed before SU-8 patterning, except for releasing. The second approach requires etching protection on the device layer during Al_2O_3 patterning but provides extra protection during Al_2O_3 etching to prevent lateral etching towards the carrier. This extra protection could be crucial because lateral etching can cause shorted G and S/D on the origami substrate which poses a significant risk for circuit design afterward (Fig. 2a-e). The cause of this issue is the smaller Al_2O_3 structure resulting from lateral etching (Fig. 2f).

The main issue we encountered with SU-8 patterning was poor adhesion. In the first approach, due to the different heights of bars on bottom facets and sidewalls, they needed to be patterned separately using two different thicknesses of SU-8. However, the adhesion between the carrier surface, which had gone through complex processes, and SU-8 was compromised. As a result, during the development of SU-8 patterning on sidewalls, some patterned SU-8 on bottom facets became twisted by the developer (Fig. 3b). Additionally, severe bars delamination, breakage, and displacement were observed after treating the sample surface with 5 s 0.5% HF before releasing the carrier from the substrate using SF_6 plasma (Fig. 3c-e). In the 2nd approach, before the 2nd HF etching that was described in the previous paper [2], all bars are well patterned even after 3 h acetone dip for resist removal, Al_2O_3 appeared homogenous (Fig. 3f). However, after the second HF etching, the bars on sidewalls were almost completely lost (Fig. 3g, h). As we could still roughly see in Fig. 3h the facet structure, and the bars are actually still attached to it, hence the adhesion here is not the cause of bars loss, it should a full Al_2O_3 layer or contamination layer on Al_2O_3 peeling off taking the bars away with it.

To enhance the prevention of lateral etching, we determined that the two-step HF etching described in the previous paper was unnecessary. Instead, we found that applying only one HF etching with resist protection yielded excellent bar patterning. Building upon these results, we further improved the process by following the second approach. However, before HF etching, we introduced a thin SiO_2 cap on the SU-8 bars using the same mask. The carrier was then patterned using a longer single-step HF etching. Although the results of this attempt should be available before the conference, they could not be included here due to the abstract deadline.

[1] D. Karnaushenko et al., Adv. Mater. 2020, 32, 1902994
[2] A. Hiess et al., Fabrication of freestanding initial patterns for polymer actuated 3D micro-origami structures. Proc. 62nd EIPBN, 2018, Puerto Rico
[3] J. Zhang et al., Micro and Nano Engineering, 2023.March.19, 100179.

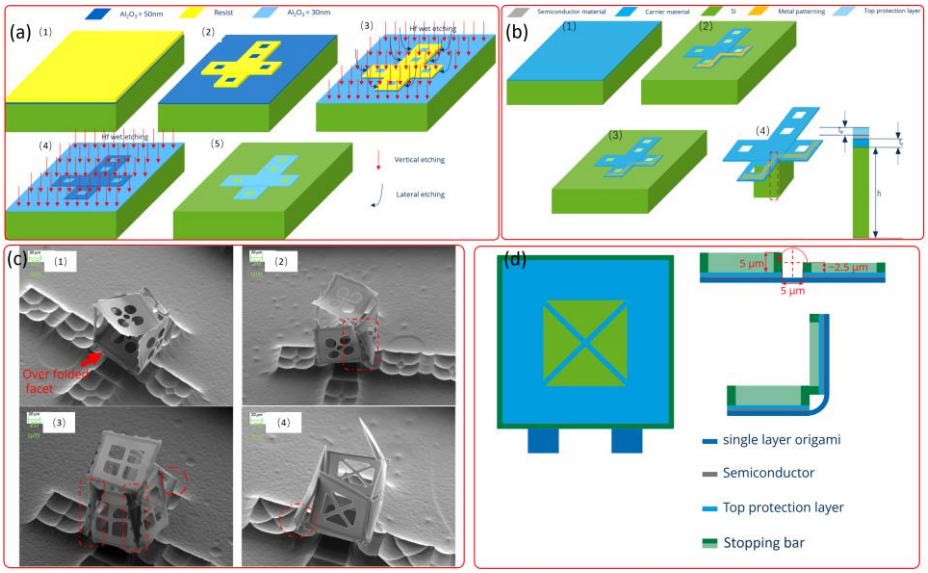

Figure 1. (a) two step HF etching for Al_2O_3 origami carrier patterning to achieved better carrier homogeneity, (a) Al_2O_3 origami cube releasing, (c) SEM images of typical results of optimized folding with SiO_2 bars, (d) improving folding control by patterning stopping bars at facet edges.

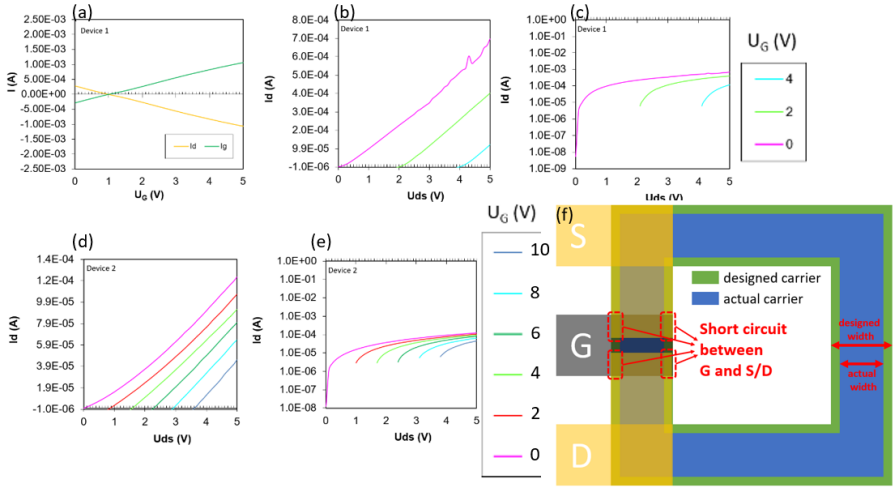

Figure 2. Electrical measurement results of (a) U_G-I_d-I_G of device 1, (b) U_{ds}-I_d of device 1, (c) U_{ds}-I_d of device 1 log graph, (d) U_{ds}-I_d of device 2, (e) U_{ds}-I_d of device 2 log graph. (f) reason of shorted G and S/D

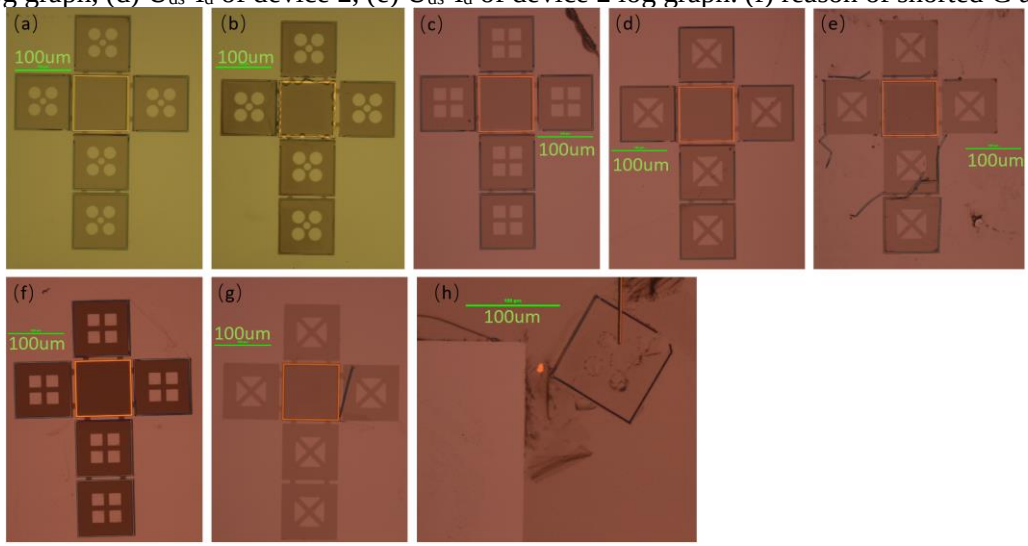

Figure 3. (a) well patterned SU-8 bars before short HF for approach 1, (b) patterned SU-8 on bottom facets twisted by the developer, (c) bar breakage after short HF, (d) bar delamination after short HF, (e) bar displacement after short HF, (f) well patterned bars even after 3 hours acetone dip for resist removal, (g) almost completely lost bars on sidewalls, (h) Al_2O_3 peeling off with bars still attach to it

Near-infrared photodetectors based on single germanium nanowires

Ahmad Echresh [a,b], Mohd Saif Shaikh [a], Manfred Helm [a,b], Artur Erbe [a,b], Yonder Berencén [a], Lars Rebohle [a], Yordan M. Georgiev [a,c]

[a] Institute of Ion Beam Physics and Materials Research, Helmholtz-Zentrum Dresden-Rossendorf (HZDR), Dresden, 01328, Germany
[b] Technische Universität Dresden, 01062 Dresden, Germany
[c] Institute of Electronics at the Bulgarian Academy of Sciences, Sofia, 1784, Bulgaria
e-mail: a.echresh@hzdr.de

Abstract

Germanium (Ge) is a promising candidate for designing near-infrared photodetectors because of its bandgap (0.66 eV), which induces a large absorption coefficient at near-infrared wavelengths. Also, Ge has excellent compatibility of parallel processing with silicon technology [1,2]. Photodetectors based on Ge material have been fabricated with different structures such as metal-semiconductor-metal (MSM) and p−n junctions. On the other hand, the observation of high responsivity in semiconductor nanowires with a high surface-to-volume ratio has attracted growing interest in using nanowires in photodetectors. So far, significant efforts have been made to fabricate single nanowire-based photodetectors with different materials such as Si, Ge, and GaN to achieve miniaturized devices with high responsivity and short response time [3-5]. Hence, Ge nanowires are an excellent candidate to fabricate single nanowire-based near-infrared photodetectors.

In this work, we report on the fabrication and characterization of an axial p−n junction along Ge nanowires. First, through a resist mask created by electron beam lithography (EBL), the top Ge layers of germanium-on-insulator (GeOI) substrates were locally doped with phosphorus ions using ion beam implantation followed by rear-side flash lamp annealing. Then, the single Ge nanowire-based photodetectors containing an axial p−n junction were fabricated using EBL and inductively coupled plasma reactive ion etching. The fabricated single Ge nanowire devices demonstrate the rectifying current−voltage characteristic of a p−n diode in dark conditions (see Fig. 1). Moreover, the photoresponse of the axial p−n junction-based photodetectors was investigated under light illumination with three different wavelengths: 637 nm, 785 nm, and 1550 nm. The measurements indicated that the fabricated photodetectors can be operated at zero bias and room temperature under ambient conditions (see Fig. 2a). A high responsivity of 3.7×10^{2} AW^{-1} and a detectivity of 1.9×10^{13} $cmHz^{1/2}W^{-1}$ were observed at zero bias under illumination of a 785 nm laser diode. The responsivity of the single Ge NW photodetectors was increased by applying a reverse bias of 1V (see Fig. 2b).

[1] L. Virot, D. Benedikovic, B. Szelag, et al. Opt. Express 25(2017), 19487–19496.
[2] W. Chen, R. Liang, S. Zhang, et al. Nano Res. 13(2020), 127–132.
[3] K. Das, S. Mukherjee, S. Manna, et al. Nanoscale (6)2014,11232–11239.
[4] S. Cuesta, M. Spies, V. Boureau, et al. Nano Lett. 19(2019), 5506−5514.
[5] S. Mukherjee, K. Das, S. Das, and S. K. Ray, ACS Photonics 5(2018), 4170−4178

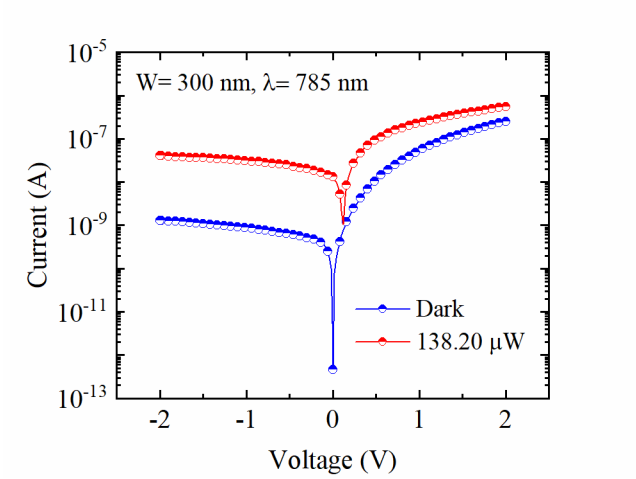

Figure 1. Semi-log current−voltage characteristics of a photodetector based on a single Ge nanowire of 300 nm width in dark conditions and under illumination of a 785 nm laser diode with a power of 138.2 µW.

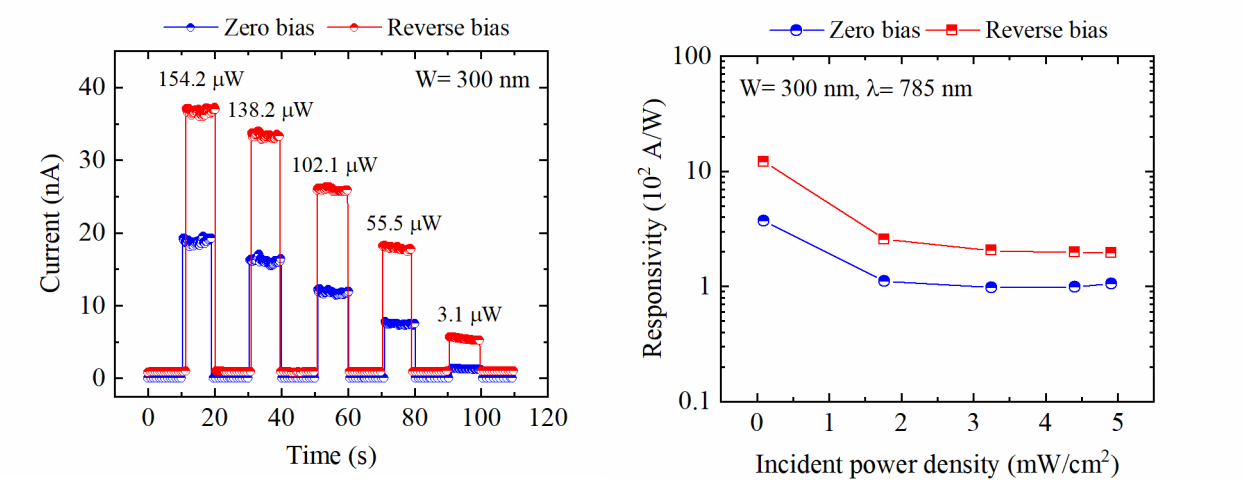

Figure 2. (a) Evolution of the photocurrent over time as a function of input laser power, (b) responsivity as a function of incident power density under illumination of a 785 nm laser diode.

The coexistence of volatile and non-volatile resistive switching in WTe_2 conductive bridge random access memory devices for neuromorphic computing

Haider Abbas, Asif Ali, Jiayi Li, and Diing Shenp Ang

School of Electrical and Electronic Engineering, Nanyang Technological University, Singapore 639798, Singapore
e-mail: edsang@ntu.edu.sg

1. Introduction

The computing efficiency in von Neumann architecture-based conventional computing systems is limited by the physical separation of memory and computing units. Neuromorphic computing offers a promising solution to overcome this so-called memory wall problem owing to its brain-inspired computing functionalities [1]. Emulating the synaptic plasticity of biological synapses is a crucial step for the practical realization of a neuromorphic computing system [2]. Conductive bridge random access memory (CBRAM) is a promising electronic synaptic device because it can emulate both short- and long-term synaptic plasticity functions of biological synapses [3]. In this work, we fabricated WTe_2 chalcogenide-based CBRAM devices that present the coexistence of volatile switching (VS) and non-volatile switching (NVS) with high uniformity. This coexistence of VS and NVS is exploited to mimic the short-term and long-term plasticity (STP/LTP) behaviors of the biological synapses.

2. Experimental

The memristor devices were fabricated on a thermally oxidized Si substrate such as SiO2/Si. A 10 nm thick Ti adhesion layer was deposited followed by the deposition of a 70 nm Pt bottom electrode (BE) using DC sputtering and thermal evaporator, respectively. For the switching medium, ~12 nm WTe_2 thin film was deposited on the Pt BE by RF sputtering. Finally, a 70 nm Ag top electrode (TE) was deposited by DC sputtering using a metal shadow mask to form the memristor cells having a structure of Ag/WTe_2/Pt. Fig 1 presents the complete experimental process and the device structure. Fig 1(a) shows the fabrication process with the experimental procedures used in this research. A schematic image of the cross-section of the Ag/WTe_2/Pt device is shown in Fig 1(b). For the electrical measurements, a Keithley 4200-SCS parameter analyzer was used. The bias was applied to the Ag TE keeping the Pt BE grounded, as shown in Fig 1(b).

3. Results and Discussions

The typical *I-V* characteristics of the device presenting NVS and VS behaviors are presented in Fig 2(a) and Fig 2(b), respectively. The device presented an electroforming-free switching. When the device undergoes a SET process with a higher current compliance (CC) the device exhibits NVS whereas, during low CC SET, the device shows VS. This is attributed to the formation of a strong/weak Ag conductive filament (CF) at high/low CC. The low CC limits the diffusion of Ag^+ ions into the switching layer thus forming a weaker CF which undergoes a self-rupture providing the VS. The self-relaxation behavior of the device was analyzed using AC pulse stimulation, as shown in Fig 2(c). The relaxation time of the electronic synapse for the given pulse was ~20 µs. Fig 3 shows the experimental demonstration of STP and LTP behaviors of the electronic synapse. In biological synapses, the repetition of the simulations for a longer time increases the concentration of Ca^{2+} ions causing structural changes in synaptic cleft which strengthens synaptic weight and prolongs its dissolution time. Similar behaviors are demonstrated by the WTe_2-based CBRAM where the weak stimulations (10 pulses) give rise to STP with a quicker forgetting (Figs 3(a,b)) whereas strong stimulations (30 pulses) lead to LTP with longer retention time (Figs 3(c,d)). Moreover, Fig 4(a) shows the transition from STP to LTP dependent on the stimulations. The pulse repetition-dependent transition from STP to LTP successfully mimics Atkinson and Shiffrin's biological model of memorization (Fig 4(b)) [4]. Furthermore, the device also presented LTP and LTD characteristics with a better linearity in synaptic weight modulation which is highly desirable for neuromorphic computing.

Acknowledgement

This work was supported by the Singapore Ministry of Education under Grant MOE-T2EP50120-0003

References

[1] I. Boybat et al., Nat Commun. 9 (2018) 2514.
[2] Y. Li, et al., J Phys D Appl Phys. 51 (2018) 503002.
[3] H. Abbas, et al., Micromachines 13 (2022) 725.
[4] R.C. Atkinson and R.M. Shiffrin, Psychology of Learning and Motivation - Advances in Research and Theory, 1968: pp. 89–195.

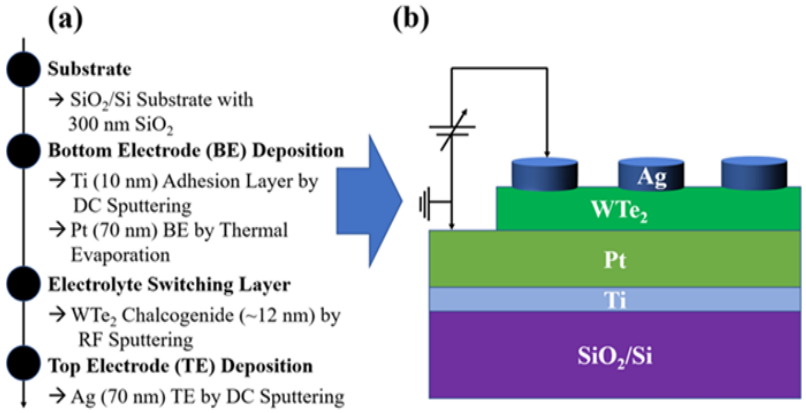

Figure 1. (a) Complete fabrication process and (b) corresponding cross-sectional schematic image of the fabricated CBRAM devices.

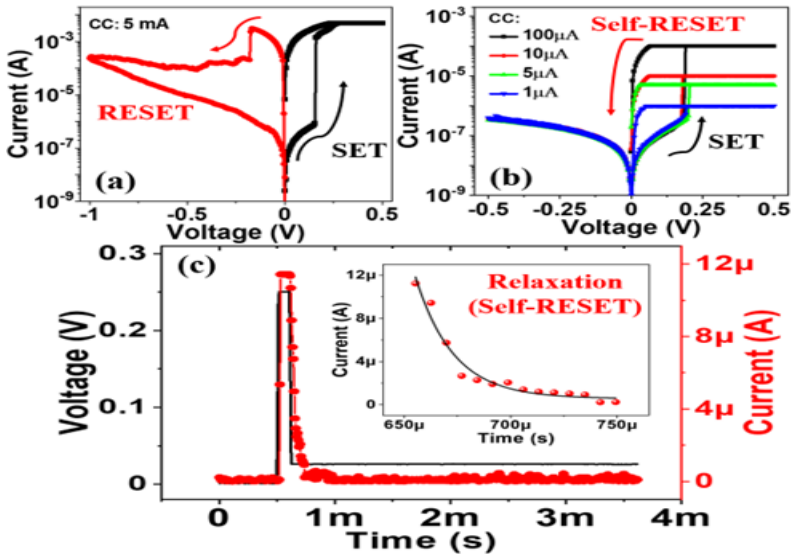

Figure 2. The typical I-V characteristics of the device presenting (a) NVS at higher CC and (b) VS at different CCs. (c) The self-relaxation characteristics of the device under pulse stimulation.

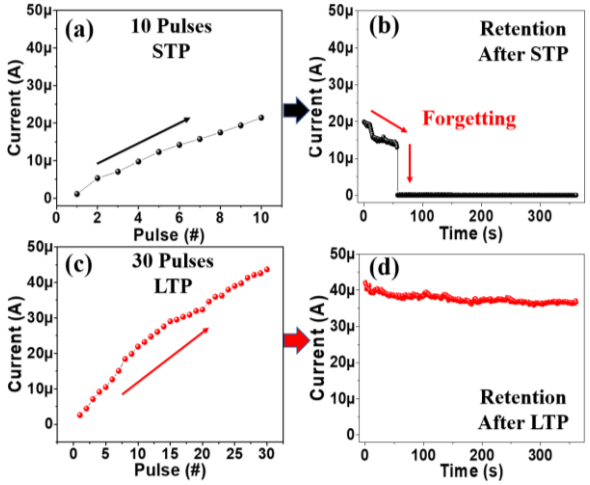

Figure 3. The Demonstration of STP and LTP behaviors in the CBRAM device. (a) Device current modulation with weak pulse stimulations (10 pulses) and (b) corresponding retention measurement after STP. (c) Current modulation with strong pulse stimulations (30 pulses) and (d) corresponding retention measurement after LTP.

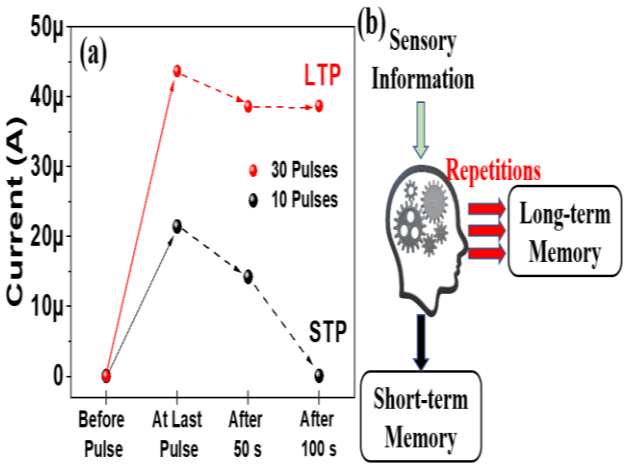

Figure 4. (a) Transition from STP to LTP under higher pulse repetitions. (b) Atkinson and Shiffrin's biological model of memorization.

Development of thermal rectification on asymmetric defect engineered graphene device

Islam Mohammad Razzakul [a], Afsal kareekunnam [a], Hiroshi Mizuta [a, b]
[a] Japan Advanced Institute of Science and Technology, 1-1 Asahidai, Nomi, 923-1211, Japan
[b] University of Southampton, Southampton, S0237XA, United Kingdom
e-mail: razzak@jaist.ac.jp

Purpose: This study investigates the use of asymmetric defect-engineered graphene nanostructure to develop thermal rectifiers for improving energy efficiency and enhanced device performance.
Novelty: The ability to precisely control the heat flow in a material is crucial for developing more energy-efficient technologies and reducing waste heat. In energy conversion processes, thermal rectifiers similar to electrical diodes allow heat to flow in a preferred direction, enabling more precise temperature control in electronic devices and leading to enhanced performance and efficiency. Graphene, in particular, is an ideal material for thermal rectification due to its unique properties such as high thermal conductivity, mechanical strength, and chemical stability. Therefore, making graphene thermal rectifiers is a key area of research for the advancement of many fields for thermal management. Thus, we have developed an asymmetric defect-engineered monolayer suspended graphene-based nanostructure and for the first time observed a thermal rectification ratio of 80%. According to the findings, monolayer graphene has significant potential to be used for developing high-performance thermal rectifiers to control heat flow and enhance performance in a variety of applications.
Results and Discussion: To fabricate the graphene thermal rectifier device, advanced graphene nanoelectromechanical systems (NEMS) technology was employed [1]. The process involved transferring chemical vapor deposited (CVD) graphene onto a SiO_2 (285 nm)/Si substrate, followed by creating electrode pads through the electron beam evaporation technique. In order to ensure good adhesion between the electrode layers and the substrate, the graphene beneath was removed with reactive ion etching (RIE) before the deposition of metal layers. After the fabrication of electrode pads, the resulting graphene was then cut into micro ribbons using electron beam lithography and O_2 plasma etching. For thermal rectification, an asymmetric defect-engineered graphene nanostructure was created by introducing a periodic pattern on the right half of the graphene ribbon. Finally, the graphene ribbon was suspended between two metallic thin film sensors (electrodes), forming an H shape. This was achieved by immersing the entire device in buffered hydrofluoric acid and subsequently dried through supercritical point drying procedure in order to prevent damage to the graphene. Figure 1 show the H shape of thermal rectifier devices, consisting of a suspended graphene ribbon with dimensions of 0.5 µ in length and 1.2 µ in width. The introduction of staggered square pattern in the graphene ribbon resulted in the formation of a narrow channel (see Fig. 1c), leading to an remarkable maximum thermal rectification. Conversely, the presence of isolated square defects (see Fig. 1b) in the graphene ribbon exhibits lower levels of rectification. To accurately measure the thermal transport properties in both directions (from the no-defect part to the defected part and vice versa), a high-precision 'differential thermal leakage' (DTL) method was developed (see Fig. 2a and b) [2]. The utilization of this technique effectively enabled the determination of temperature and defect structure dependencies of the thermal rectification ratio in graphene devices.
The asymmetric defect-engineered graphene devices exhibited an 80% increase in thermal conductivity when heat flowed from the defective region to the other side at a fixed environmental temperature of 150K (see Fig. 3a and b). The measurements also indicate that the efficiency of the thermal rectification can be enhanced by creating a larger temperature gradient between the heater and heat sink, or by decreasing the environmental temperature. On the other hand, the device without any engineered defects (see Fig. 1a) exhibited no significant variation in the heat flow. Temperature and space-dependent asymmetric phonon scattering and localization varying with the heat flux direction is found to be responsible for thermal rectification in the asymmetric defect-engineering suspended graphene nanostructure. These results highlight the potential of asymmetric defect engineering graphene application to enhance thermal rectification. This is an ongoing research work partly supported by the KAKENHI 20K20442 from the Japan Society for the Promotion of Science (JSPS).

[1] M.E. Schmidt et al., Small, 15(46) (2019) 1903025-1903032.
[2] F. Liu et al., Nano Future, 5(4) (2021) 045002-045014.

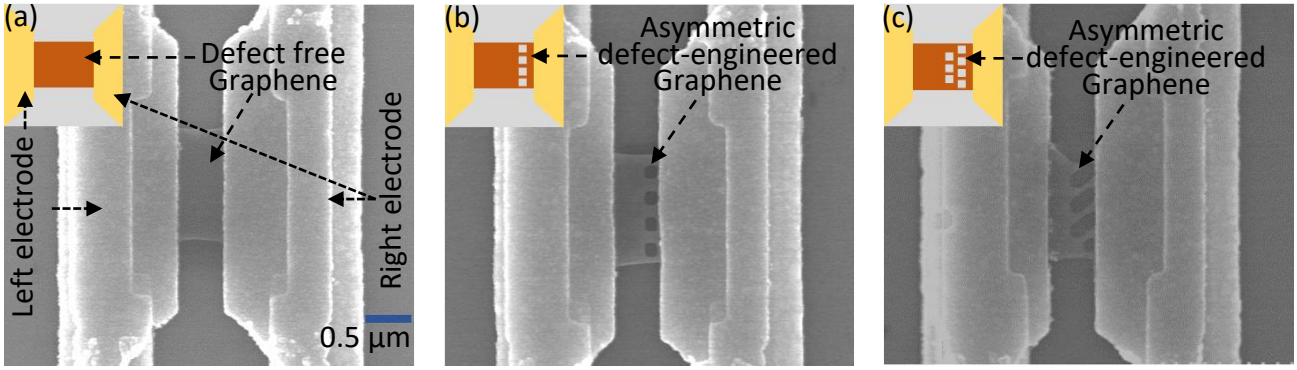

Figure 1. Scanning electron microscopy image of asymmetric defect-engineered suspended graphene device (a) non-defect and (b) square and (c) narrow channel generated from the staggered square pattern (inset show the schematic illustration of the devices).

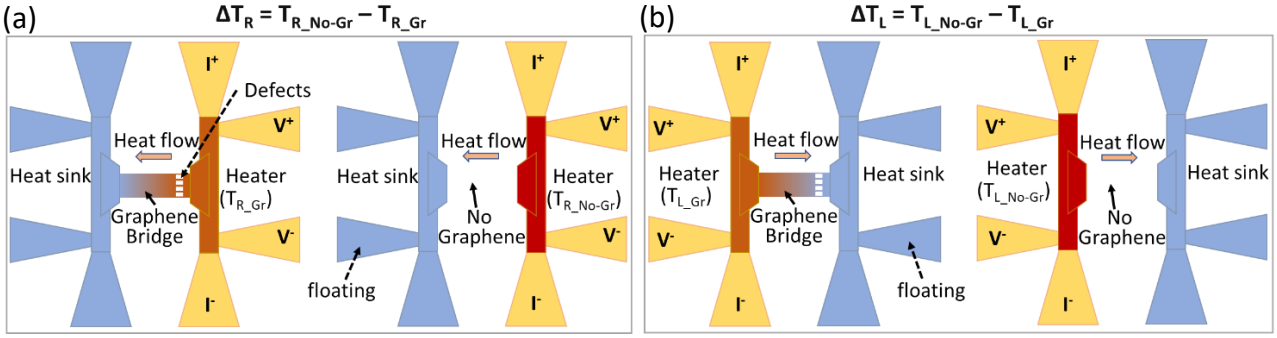

Figure 2. Schematic illustration of the DTL method to measure the heat flow in the graphene device. (a) ΔT_R is used to evaluate the heat flux from right to left and (b) ΔT_L for left to right. The temperature difference between the 'Graphene bridge' and 'No Graphene' condition is used to calculate ΔT_R and ΔT_L.

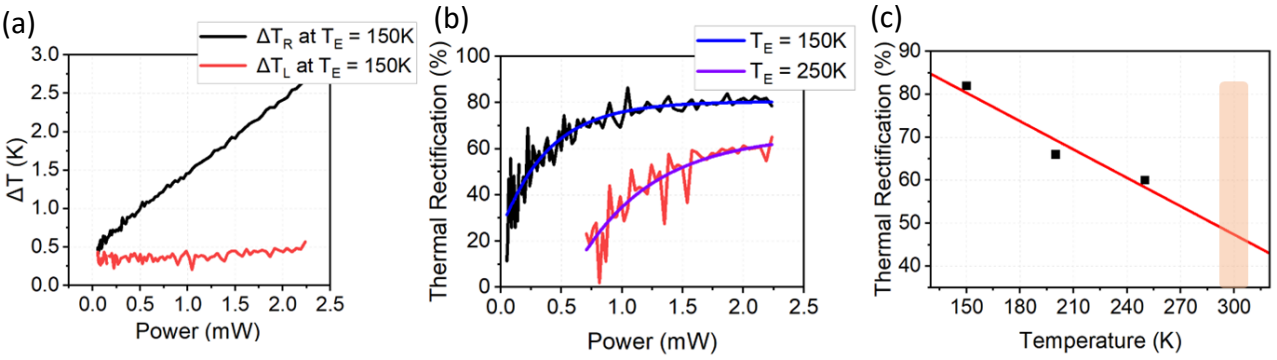

Figure 3. Thermal measurement results using DTL method at an environmental temperature (T_E) of 150K of the device shown in Fig. 1c. (a) The measured temperature difference in the left and right electrode with and without graphene ribbon in the devices. (b) Power dependence thermal rectification ratios at T_E of 150K (black line) and 250K (red line) are depicted. (c) Based on the observed result at 150K and 250K, it can be predicted that rectifications ratio of the asymmetric defect-engineered graphene device would fall around 45%. The results regarding the rectification ratio of square-shaped defect device at 150K was approximately 30%, data are not shown here.

2D BDiode – A Switchable Bidirectional Diode for Analog Electronic Circuits Fabricated Entirely from 2D Materials

Christian D. Matthus [a], Phanish Chava [b], Kenji Watanabe [c], Takashi Taniguchi [d], Thomas Mikolajick [e], and Artur Erbe [b]

[a] Chair for Circuit Design and Network Theory, Technische Universität Dresden, 01062 Dresden, Germany
[b] Institute of Ion Beam Physics and Materials Research, HZDR, 01328 Dresden, Germany
[c] Research Center for Functional Materials, [d] International Center for Materials Nanoarchitectonics, both National Institute for Materials Science, 1-1 Namiki, Tsukuba 305-0044, Japan
[e] Chair of Nanoelectronics, Technische Universität Dresden, 01062 Dresden, Germany
e-mail: christian.matthus@tu-dresden.de

The discovery of graphene and its analogous two-dimensional (2D) materials opened up the possibility of investigating electronic devices that are built entirely using heterostructures of different 2D materials [1]. Semiconducting 2D material-based heterostructures are of great interest due to their wide range of (opto)-electronic applications, especially for flexible electronics [2]. Recently, we reported a proof-of-concept device based on semiconducting WSe_2/MoS_2 heterojunction and showed the usability of such a device as a field effect transistor [3] as well as temperature sensor for cryogenic measurements [4]. Typically, sensor devices need analog frontend circuitry. Hence, there is a need for analog electronic devices based on 2D materials. Compared to conventional semiconductor devices, 2D materials enable the fabrication of hetero-interfaces with minimal defects owing to their atomically sharp surfaces. One example of the new opportunities of such material-based devices is the gate-induced switchability of a diode behavior due to the different current transport mechanisms, which is the focus of this work. Here, we demonstrate the applicability of a device we call 2D BDiode (switchable fully-**2D b**idirectional **diode**) based on a WSe_2/MoS_2 heterojunction encapsulated with insulating hexagonal boron nitride (h-BN) layers along with semi-metallic few-layered graphene (FLGr) as contact and backgate electrodes. In SPICE simulations we used the backgate for the demonstration of the potential of the device for applications like AC/DC conversion.

A top-view image and a schematic cross-section of the device are shown in Fig.1. The measurement setup is similar to the one we used for measurements on previously published devices and can be found elsewhere [3,4]. The frontgate voltage was grounded for all measurements. The obtained I-V characteristics are shown in Fig. 2. As one can see, the diode works like a conventional pn-diode in case of a negative backgate voltage while it changes to a reversely conducting, rectifying diode in case of positive backgate voltage. We ascribe this to different conduction mechanisms, i.e., band-to-band tunneling and drift-diffusion [3]. This device was modeled semi-empirically by adjusting the ideality factor, reverse saturation current and parasitic series and parallel resistances. A more detailed device description, measurement setup and understanding of the device behavior can be found in our previous reports [3,4]. The measured and modeled I-V characteristics in forward and reverse direction for the exemplarily selected backgate voltages of -7.5V and 5V are shown in Fig. 2.a-b. As a next step, we developed a SPICE building block (subcircuit) consisting of two 2D BDiodes in parallel: one for forward and one for reverse direction; the gate was modeled in a first order approximation by switches. Using this low-complexity model, the transition between forward and reverse characteristics is not modeled accurately while it fits very well for backgate voltages with absolute values significantly larger than zero. The model schematic is shown in Fig. 2.c. Finally, we applied this model for the design and (transient) simulation of circuit concepts with bidirectional working scenarios, which cannot be implemented with such a low number of devices in conventional CMOS. Few examples are shown below (Fig. 3) and include AC/DC, DC/AC converters, and charge pumps, which can handle negative as well as positive voltages. The switching between both operation scenarios takes place by changing the backgate voltage.

In summary, a fully-2D device was investigated and modeled for SPICE simulations. The simulations predict outstanding properties offering completely novel opportunities in analog circuit design.

References

[1] K. Novoselov et al. *Science* 353.6298 (2016)
[2] P. V. Pham et al. *Chemical Reviews* 122.6 (2022): 6514-6613.
[3] P. Chava et al. *2022 Device Research Conference (DRC)*. IEEE, 2022.
[4] C. D. Matthus et al. *Journal of the Electron Device Society* (under review), 2023.

Acknowledgements

Financial support by the European Social Fund and the Free State of Saxony in the project Re-Learning (project number 100382146 and by the Deutsche Forschungsgemeinschaft (DFG) FFlexCom Initiative (project number 270774198) as well as IHRS NANONET (project number VH-KO-606) is gratefully acknowledged.

Figures

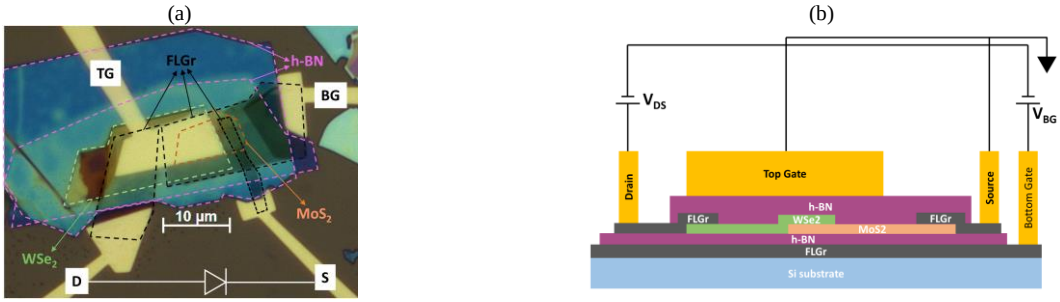

Figure 1. Top view microphotograph (a) and schematic cross section (b) of the investigated device (2D BDiode). [h-BN: hexagonal boron nitride; FLGr: few-layered graphene]

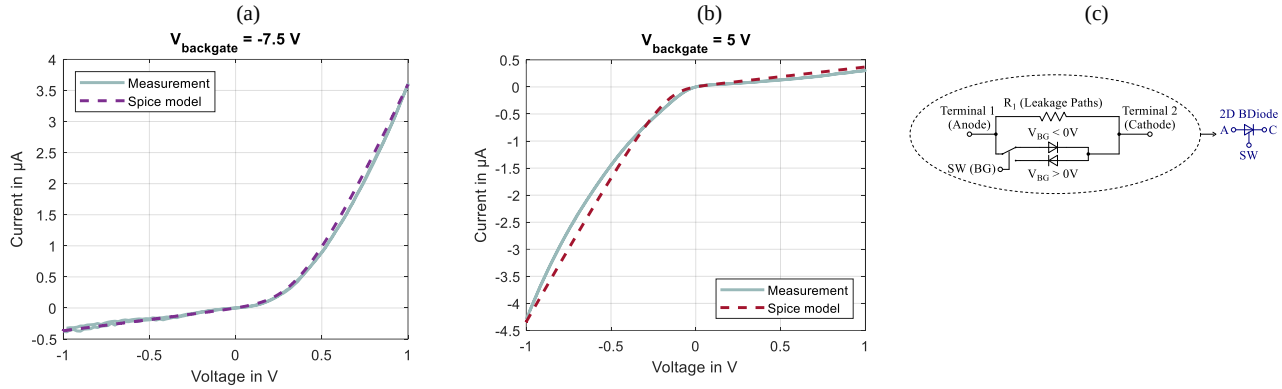

Figure 2. Measured I-V characteristics and semi-empirical model of the 2D BDiode for backgate voltage of -7.5V (a) and 5V (b) for SPICE simulations, and SPICE equivalent circuit and symbol (c).

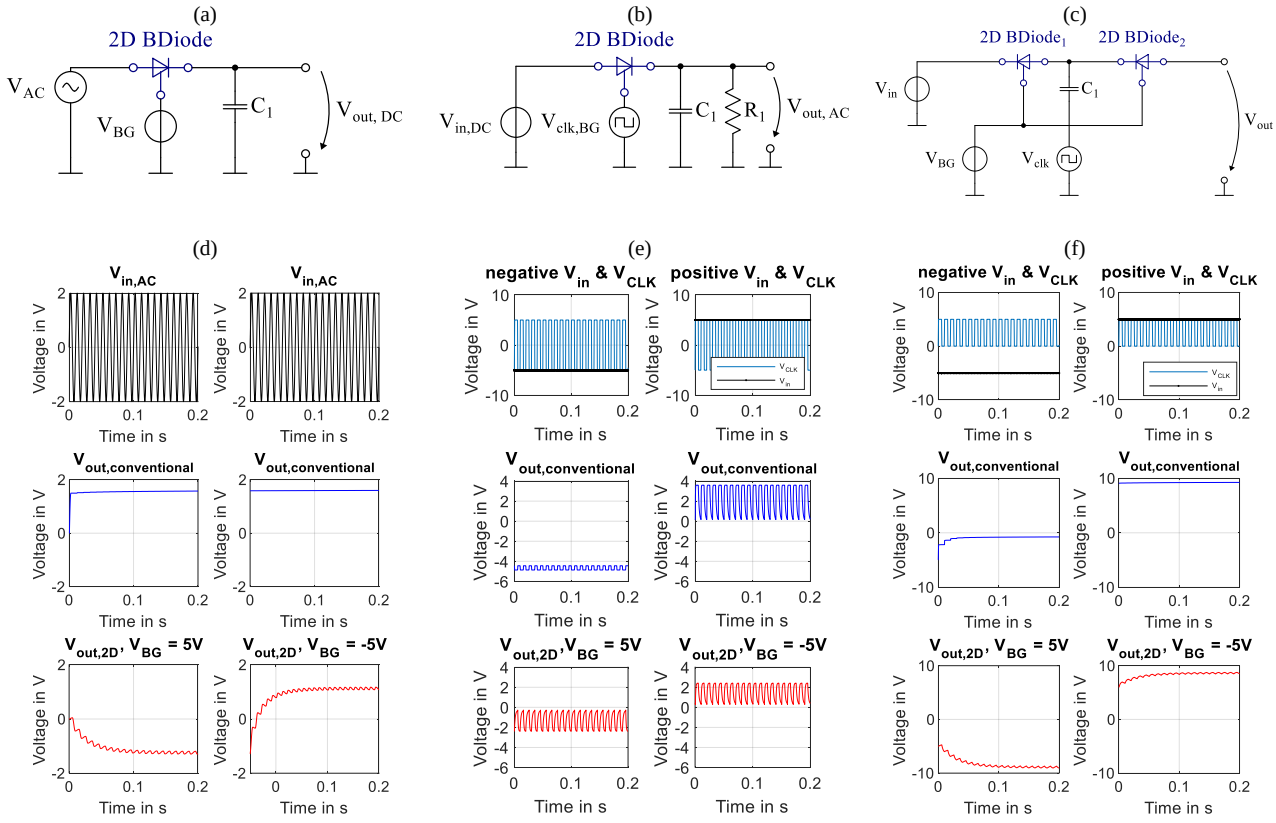

Figure 3. Schematics (a-c) and simulated transient characteristics (d-f) with conventional devices (ideal diode, MOSFET) and 2D-BDiode of an AC/DC converter based on a one-way rectifier (a,d), simplest DC/AC converter (b,e), and one stage charge pump (c,f) all for positive and negative input voltages (except rectifier).

Fabrication of electron transparent membranes and nanostructures in fluidic devices by nanoimprint lithography and *"Flow-Through"* gas phase deposition

Jeremy Teuber[a], Manuel Müller[a], Rukan Nasri[a], Judith Estengre-Pérez [a], Arwen R. Pearson[a], Irene Fernandez-Cuesta[a]

[a] Universität Hamburg, Physics Department, Hamburg, 22761, Germany
E-Mail: jteuber@physnet.uni-hamburg.de

Scanning electron microscopy (SEM) and transmission electron microscopy (TEM) allow the visualization and analysis of samples at nanometer resolution. The integration of liquid cells into these microscopy techniques has further extended their capabilities by enabling dynamic imaging and real-time analysis of samples under controlled flow conditions [1,2]. However, the use of liquid cells in SEM and TEM comes with limitations, such as their high cost, limited geometries and reliance on slit-like chambers formed by connecting two membranes with spacers in between.

In this work, we present a fabrication method to produce polymeric foils (<10 µm) which contains micro-, and nanofluidic structures selectively coated from the inside with Al_2O_3 by gas-phase deposition. These inorganic structures can be suspended by removing the polymer material from above and below. This allows the samples to be used as liquid cells for the investigation of the dynamic behavior of molecules in confined spaces, for example, with a TEM.

The fluidic devices are fabricated by direct UV nanoimprint lithography (NIL) [3]. Briefly, this uses photolithography and reactive ion etching (RIE) to first create a pattern on a silicon stamp which is then copied to a softer PDMS stamp. This PDMS stamp is used to imprint the fluidic devices. The design of the stamp is variable and versatile, and can be adapted to geometry of interest for the specific liquid cell. The method has the unique advantage of allowing the fabrication of liquid cells with reduced lateral dimensions (even down to nanochannels), and with complex 3D structures, with graded depths and widths. In the example shown in Fig. 1 (a), the fluidic device contains two microchannels which connect the inlet and outlet holes. These microchannels are interconnected by several nanochannels, as shown in Fig. 1 (b). To create the fluidic devices, the stamp is placed and aligned onto a polycarbonate plate which has been covered with a UV curable polymer (such as Ormostamp or mrNIL210 from micro resist technology GmbH) containing pre-patterned holes. The assembly is then cured with UV light, and the substrate and stamp are separated manually (Fig. 1 (a) step 2). Next, a polymer coverslip is used to seal the channel system of the fluidic device (Fig. 1 (a) step 3). To ensure a conformal coating of the inner walls with Al_2O_3, a specialized atomic layer deposition (ALD) reactor has been constructed which can be used in a "*Flow-Through"* mode [4]. The reactor's gas and vacuum ports match with the holes in the polycarbonate plate, allowing for connection to the imprinted fluidic circuit. By flowing the precursor gases with optimized conditions from one side of the microchannel to the other, a controllable pressure gradient is created. Using this method, we are able to achieve conformal Al_2O_3 coating of a variety of structures, including slits, chambers, and micro-, and nanochannels, with coating layer thickness possible from just a few nanometers to tens of micrometers. The precise control over the deposited Al_2O_3 thickness in the ALD process allows fine tuning of the wall thickness for applications requiring mechanical stability and electron transparency. This approach allows us to overcome the current limitations on liquid cell geometries to only slit-like chambers. In subsequent fabrication steps, the nanochannels or membranes can be selectively suspended by masking and reactive ion etching (RIE). Fig. 2 (c) and (d) show an example of a suspended, hollow Al_2O_3 membrane nanochannel with a cross-section of 500 x 500 nm and a suspended length of 20 µm.

To demonstrate the electron transparency of the Al_2O_3 membrane, we fabricated a TEM grid sample with an Al_2O_3 membrane deposited in our self-developed ALD reactor. We then deposited polystyrene beads above and below the Al_2O_3 membrane and imaged them with a SEM and with a TEM (Fig. 3 (a) and (b), respectively). Fig. 3 (a) shows two SEM images of the same area, obtained with two different detectors. The polystyrene beads below the membrane can only be detected using the secondary electron secondary ion (SESI) detector. Fig. 3 (b) shows the same sample at a different location imaged in transmission mode with a TEM. These results show that it is possible to image the beads through the Al_2O_3 membrane, and thus demonstrates its

electron transparency. To use this system as liquid cells in a TEM specimen holder, it is necessary to detach the structured and coated polymer foil from the substrate (shown in Fig. 1 (a) step 5) and cut it to 3 mm total diameter. Further results on the use of the samples inside a SEM and TEM will be shown at the conference.

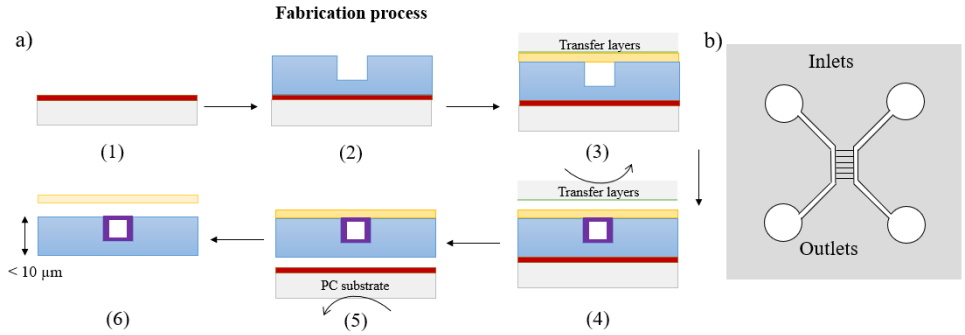

Figure 1. (a) Sketch of the sample fabrication process. A polycarbonate (PC) substrate is treated with perfluorooctyltrichlorosilane (1). The devices are made by casting a UV-curable polymer (2) on a substrate with holes. Then, using a soft stamp, the channels are patterned by UV nanoimprinting (2). A coverslip is used to seal the fluidic system (3). The sample is put in our self-built ALD reactor, and a Al_2O_3 layer is deposited on the inside of the enclosed channels (4). The transfer layer of the coverslip is removed. After coating the inner walls of the system, the PC substrate is removed (5). A structured and coated polymer foil (<10 µm) remains. Here the coverslip is etched by RIE (6). (b) shows a sketch of the fluidic structure on the substrate with inlets and outlets. The microchannels are connected via nanochannels.

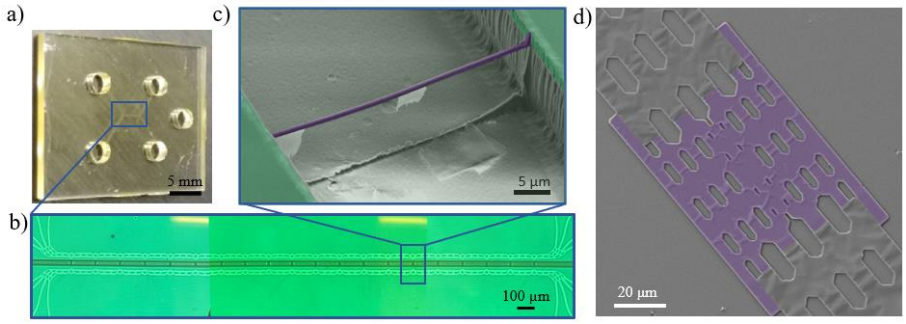

Figure 2. (a) These images show a close up of the fluidic structure on the PC substrate. To suspend the nanochannel, a trench is etched into the polymer by RIE (b). (c) shows the suspended nanochannel with a cross section of 500 x 500 nm and a suspended length of 20 µm. (d) shows a suspended Al_2O_3 membrane in a liquid cell.

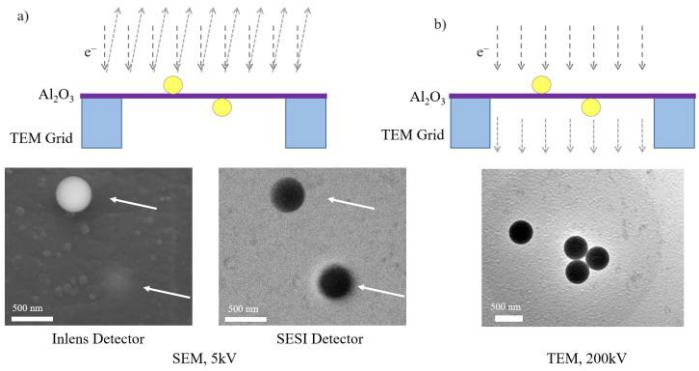

Figure 3. Electron microscope images of polystyrene beads placed on top and underneath an Al_2O_3 coated TEM grid. The sketches show the schematic structure of the TEM grid and the placed beads. Furthermore, it is illustrated how the electrons are scattered from the sample (a) or pass the membrane (b). The SEM images using a SESI detector in (a, right) show one polystyrene bead sitting on top of the Al_2O_3 layer and one underneath. With the Inlens detector (a, left) only the bead on top can be seen. (b) With the TEM all polystyrene beads can be observed, showing that the Al_2O_3 membrane is electron transparent.

[1] Yoon, A. et al. (2001). Dynamic Imaging of Nanostructures in an Electrolyte with a Scanning Electron Microscope. *Microscopy and Microanalysis, 27(1)*, 121-128. Doi 10.1017/S1431927620024769
[2] Meirong Li and Lan Ling., *ACS Nano* 2022, 16,15503-15511
[3] I. Fernandez-Cuesta et al., J. Vac. Sci. Technol. B (2011) 29 06F801.
[4] M. Müller et al., DE 102020102076A1 (2020) Hamburg, Germany, Deutsches Patent- und Markenamt.

The performance improvement of multi-layered ZnO/SnO_2 thin-film transistors by varying growth temperatures

Chan-Yeong Park [a], Se-Hyeong Lee [a], So-Young Bak [a], Dongki Baek [a], Hyeongrok Jang [a], Jinwoo Lee [a], Moonsuk Yi [a]

[a] Department of Electrical and Electronics Engineering, Pusan National University, Busan, 46241, Republic of Korea
e-mail: msyi@pusan.ac.kr

Amorphous oxide semiconductors (AOS), which are represented by amorphous indium-gallium-zinc oxide (a-IGZO), have received a lot of attention as an active layer material for thin-film transistors (TFTs) due to its high electron mobility, flexibility, transparency, and uniformity [1]. Despite these advantages, there is still demand for research on alternative materials owing to the scarcity and high price of indium. To reduce this high cost, tin (Sn) based active layer material like zinc-tin oxide (ZTO) has been actively researched as a substitute for indium-based TFT active layer material since tin is abundant in soil. ZTO is usually deposited via solution processing or vacuum-based techniques, such as pulsed laser deposition, sputtering, and atomic layer deposition (ALD). Among them, ALD provides precise control in nanometer scale using self-limiting reactions. Thus, this process has the advantages of excellent reproducibility and low defect density. However, conventional ZTO TFTs deposited using ALD have shown optimum performance at high annealing temperatures above 500℃, which disturbs their application on flexible substrates.

In this study, ZTO thin films were deposited with a multilayer structure to lower the process temperature to below 400℃ using ALD, and this temperature is suitable for application to flexible substrates [2]. When we deposited the active layer with binary ZnO and SnO_2 thin films separately to alternative a ternary ZTO thin film, a chemical reaction between the precursor and oxidant occurred at a relatively low temperature. Hence, ZnO and SnO_2 layers were deposited separately, the final process temperature was lowered through annealing and diffusion at 350℃ [3]. As shown in Figure 1, a multilayer structure was adopted to induce overall diffusion within the channel layer. For the deposition of the ZnO/SnO_2 thin films, diethylzinc (DEZ) and tetrakis(dimethylamino)tin (TDMASn) were used as precursors, and H_2O was used as an oxidant for both metal precursors. Each ALD ZnO and SnO_2 sequence consisted of DEZ pulse (with N_2 30sccm, for 0.3s) - DEZ purge (with N_2 30sccm, for 20s) - H_2O pulse (with N_2 30sccm, for 0.3s) - H_2O purge (with N_2 30sccm, for 20s), and TDMASn pulse (with N_2 30sccm, for 0.5s) - TDMASn purge (with N_2 30sccm, for 20s) - H_2O pulse (with N_2 30sccm, for 0.3s) - H_2O purge (with N_2 30sccm, for 20s) processes. The supercycle composed of 10 cycles of ZnO and 20 cycles of SnO_2 was repeated 6 times to deposit the multilayer structure. The multilayered ZnO/SnO_2 TFTs were fabricated in an inverted staggered structure as shown in Figure 2. To confirm the electrical performance of the fabricated TFTs according to the growth temperature, the deposition processes were performed at the growth temperature of 150℃, 180℃, and 200℃. After being deposited, the active layers were annealed at 350℃ for 1 hour.

The transfer curves of multilayered ZnO/SnO_2 TFTs according to growth temperature were presented in Figure 3. The electrical parameters such as carrier mobility (μ_{sat}), threshold voltage (V_{th}), on-off current ratio ($I_{ON/OFF}$), and subthreshold swing (S.S) were summarized in Table 1. The optimized performance was achieved at a growth temperature of 180℃ and exhibited as a carrier mobility of 8.09 $cm^2/V{\cdot}s$, a threshold voltage of 1.6V, an on/off current ratio of 2.63 x 10^7, and a subthreshold swing of 0.58V/dec. To analyze why the device is optimized at 180℃, X-ray photoelectron spectroscopy (XPS) was measured and O 1s peak deconvolution was conducted. As the growth temperature increased from 150℃ to 200℃, the results showed the reduction of M-OH bonding, which acts as a trap in the channel. However, the oxygen vacancy that serves as the carrier supplier in the channel exhibited higher results at 180℃ than at 200℃. Afterward, we intend to perform the optimization of the multilayered TFTs based on the cycle variation of Zn and Sn to improve the carrier mobility and overall performance, and the trend with respect to film thickness is also going to be examined.

[1] T. Kamiya, et al., Sci. Technol. Adv. Mater. 11 (2010), 044305.
[2] C. R. Allemang, et al., Adv. Electron. Mater. 6 (2020), 2000195.
[3] S. H. Lee, et al., Solid State Electron. 165 (2020), 107765.

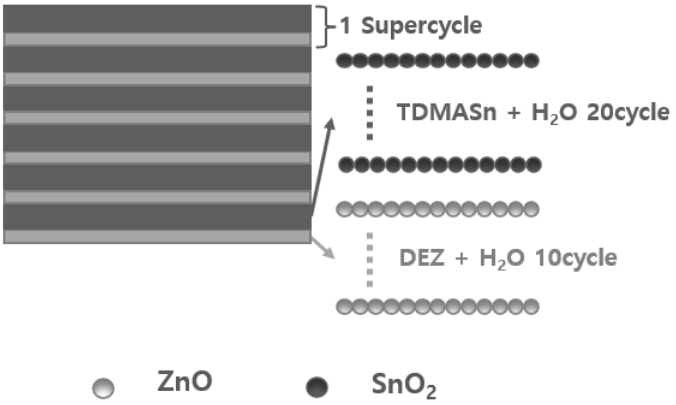

Figure 1. Deposition schematic of multilayered ZnO/SnO_2 supercycles

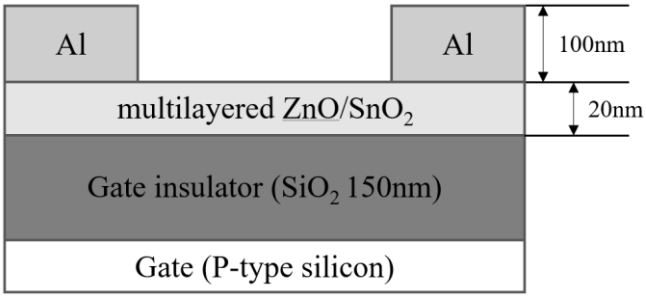

Figure 2. Cross-sectional schematic of multilayered ZnO/SnO_2 TFT

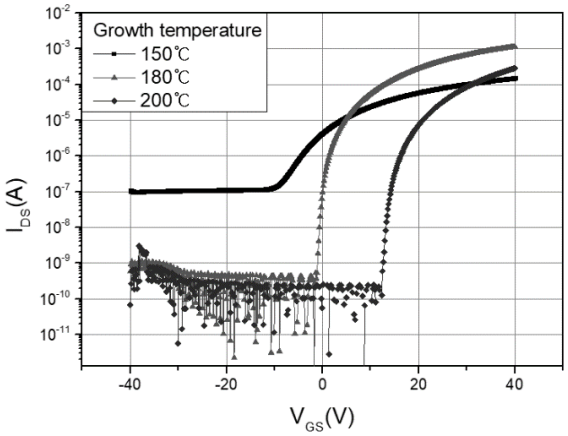

Figure 3. Transfer curves of multilayered ZnO/SnO_2 TFTs according to the growth temperature

	μ_{sat} ($cm^2/V \cdot s$)	$I_{ON/OFF}$	V_{th} (V)	SS (V/dec)
150°C	0.83	1.34×10^3	-4.32	>5
180°C	8.09	2.63×10^7	1.6	0.58
200°C	5.27	3.84×10^6	17.6	0.59

Table 1. Electrical parameters of multilayered ZnO/SnO_2 TFTs according to the growth temperature

Integration of hard magnetic materials in MEMS devices

F. Maspero [a], S. Cuccurullo [a], A. Plaza [a], F. Marson [a], O. Koplak [a], A. Del Giacco [a], M. Cocconcelli [a], G. Pavese [a], A. Cattoni [a], R. Bertacco [a]

[a] Politecnico di Milano - Department of Physics, Milan, 20133, Italy

e-mail: federico.maspero@polimi.it

The integration of piezoelectric and magnetic materials in micro-electro-mechanical systems (MEMS) enables several existing applications, ranging from energy harvesting [1] to magnetic field sensors [2]. Piezoelectric actuators are nowadays used in several commercial MEMS devices such as piezoelectric micromachined ultrasonic transducers while magnetic materials are not yet commonly integrated in MEMS devices.

Specifically, the deposition of hard permanent magnets at wafer level has been the topic of several research activities in the past decades. Magnetic layers of CoPt, FePt or Rare-earth-based magnets have been successfully deposited at wafer scale, reaching performances which are comparable to those of bulk materials. The integration of such magnetic compounds with MEMS has been one of the main goals of this research [3]. Due to the complexity of MEMS fabrication, only few examples of integration have been demonstrated in the past using complex fabrication processes and relatively bulky proof-of-concept devices.

In this work we demonstrate the integration of permanent micromagnets in MEMS devices using conventional lithography and pattern transfer techniques already in use in industry, and for different potential applications ranging from magnetometers [2] to energy harvester, but also focusing on new potential applications such as reconfigurable magnetic field sources obtained by displacing permanent magnets at the micro-scale.

We have designed proof-of-concept structures and optimized the fabrication process of the full devices. The optimizations concern: i) Deposition of a rare-earth-based magnetic materials by RF sputtering (SmCo and NdFeB); ii) Thermal treatment to enhance the magnetic characteristics of the magnetic layers; iii) Patterning of the magnetic thin films by optical lithography and ion beam etching employed to obtain micromagnets; iv) introduction of a passivation layer to protect the material from the subsequent process steps; v) release of the device and removal of passivation layer. An image of the final fabricated device is shown in Fig. 1. Thanks to this technology is possible to obtain strong magnetic fields at the microscale to bias and tune emerging applications in the field of magnonics and spintronics. This research is part of the EU project M&MEMS (Grant agreement 101070536 - https://mandmems.eu/).

[1] M.T. Bodduluri, T. Dankwort, T. Lisec, S. Grünzig, A. Khare, M. Ahmed, B. Gojdka., Micromachines,13(6), 863 (2022)
[2] F. Maspero, G. Gatani, S. Cuccurullo, R. Bertacco, 34th International Conference on Micro Electro Mechanical Systems (MEMS), p. 374-377 (2021).
[3] D. P. Arnold, Naigang Wang, J. Microelectromech. Syst., 18(6), 1255–1266 (2009).

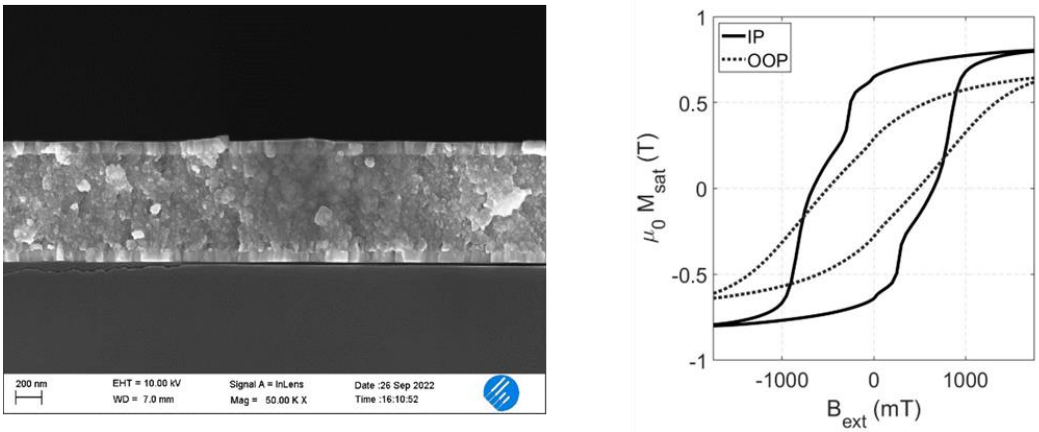

Figure 1. (Left) Cross-section of a 800nm-thick SmCo film deposited by magneton sputtering after post-annealing process and (Right) *In plane* (IP) and *out of plane* (OOP) magnetic hysteresis loops of the SmCo film.

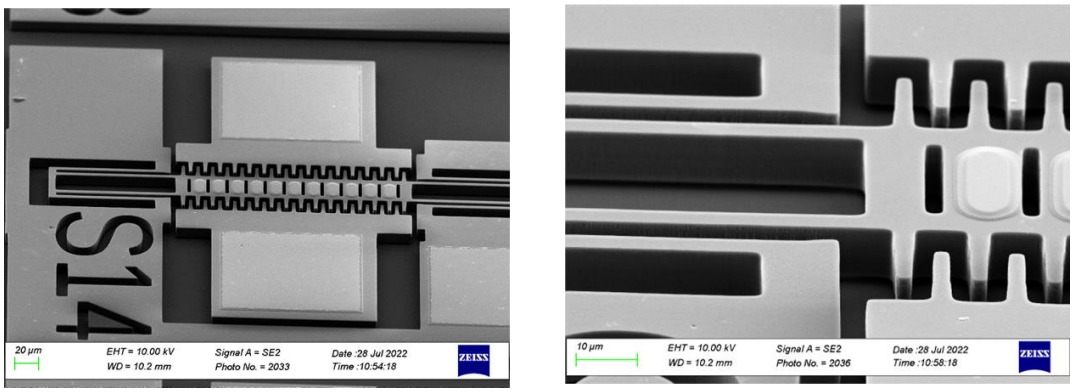

Figure 2. SEM images of micro-actuator with an array of permanent magnets on top. (Left) Full device overview. (Right) Zoom on the magnetic materials patches on top of the silicon resonator.

Simultaneous Estimation of dI/dV and dI/dz with Ultrafast feedback loop for Scanning Tunnelling Microscopy

Richa Mishra [a], S. O. R. Moheimani [a], James H. G. Owen [b], Ehud Fuchs [b], John N. Randall [b]

[a] The University of Texas at Dallas, Richardson, TX 75080 USA, Richardson, TX, 75080
e-mail: reza.moheimani@utdallas.edu.
[b] Zyvex Labs LLC, 1301 N Plano Rd., Richardson, Texas 75081
e-mail: ufuchs@zyvexlabs.com

Abstract:

The invention of the scanning tunneling microscope (STM) revolutionized our understanding and ability to manipulate surfaces at the atomic scale. The STM allowed scientists to visualize and manipulate individual atoms with unprecedented precision, extending our perception beyond the limits of the human senses. Soon after the discovery of STM, many new techniques emerged. Among them was scanning tunneling spectroscopy (STS) which provides electronic information of the surface[1].

The spectroscopic mapping of a surface can be obtained quickly by utilizing a feedback loop and adding a modulation signal to the DC bias voltage at a constant tunneling current. This technique allows for the acquisition of a dI/dV image simultaneously with the topography image for a given DC bias voltage. However, as noted in [2], there are two main drawbacks to this method. First, the resulting images are likely to be noisy (poor signal-to-noise ratio (SNR)) due to the small amplitude of the modulation voltage. Also, increasing the amplitude of the modulation voltage to obtain a better SNR may disrupt the feedback loop, resulting in the degradation of the topography image.

Another issue with conventional spectroscopy is that the tip-sample distance is constantly changing, making it difficult to capture I(V) information at very small voltages. We addressed this issue in [3] by closing the feedback loop on the natural logarithm of differential conductance, ln(dI/dV) as shown in Fig.1(a) and (b), instead of the natural logarithm of the tunneling current. In this approach, the tip-sample distance is regulated even when the applied sample DC bias voltage is zero, allowing for information about the engagement of electronic states for the full range of sample bias voltage. The I−V curve can be obtained orders of magnitude faster than the conventional spectroscopy method. The functionality of this closed-loop control system is ascertained by system-identification bode plots as shown in Fig.2.

We present a control technique to measure the topography of the surface and the local tunnel barrier height (dI/dz) simultaneously while the loop is closed on ln(dI/dV). We modulate the voltage and controller output with sinusoidal signals $v_m \sin(\omega_1 t)$, and $z_m \sin(\omega_2 t)$. The frequencies of the modulating signals should be above the closed-loop bandwidth of the system since the topography information lies in the low-frequency region. Also, ω_1 should not be a multiple of ω_2. We apply lock-in-amplifiers (LIA) tuned to ω_1 and ω_2 to the tunneling current to obtain dI/dV and dI/dz simultaneously, as shown in Fig.1(a). We need two modulating signals and two LIAs for this method. Next, we can also obtain dI/dV and dI/dz simultaneously by applying one modulation signal to the bias voltage and obtaining dI/dV at ω_1. Then we notch filter the tunneling current so that only the $2\omega_1$ frequency is passed and other harmonics are filtered out. As shown in Fig.1(b), we add this to the feedback channel. This $2\omega_1$ frequency propagates in the feedback loop and modulates controller output. Thus by applying two LIAs tuned at $2\omega_1$ to filtered tunneling current and controller output, we can obtain dI/dV and dz/dV. And by dividing the output of the LIAs, we can obtain dI/dz and dI/dV simultaneously using one modulation signal applied to the bias voltage and three LIAs. The topography, dI/dV, and dI/dz images with lithography, when the feedback loop is closed on ln(dI/dV), are shown in Fig.3.

[1] R. M. Feenstra, "Scanning tunneling spectroscopy," *Surface Science*, vol. 299, pp. 965–979, 1994.
[2] H. Alemansour, S. R. Moheimani, J. H. Owen, J. N. Randall, and E. Fuchs, "High signal-to-noise ratio differential conductance spectroscopy," *Journal of Vacuum Science & Technology B, Nanotechnology and Microelectronics: Materials, Processing, Measurement, and Phenomena*, vol. 39, no. 1, p. 010601, 2021.
[3] H. Alemansour, S. R. Moheimani, J. H. Owen, J. N. Randall, and E. Fuchs, "Ultrafast method for scanning tunneling spectroscopy," *Journal of Vacuum Science & Technology B, Nanotechnology and Microelectronics: Materials, Processing, Measurement, and Phenomena*, vol. 39, no. 4, p. 042802,

2021.

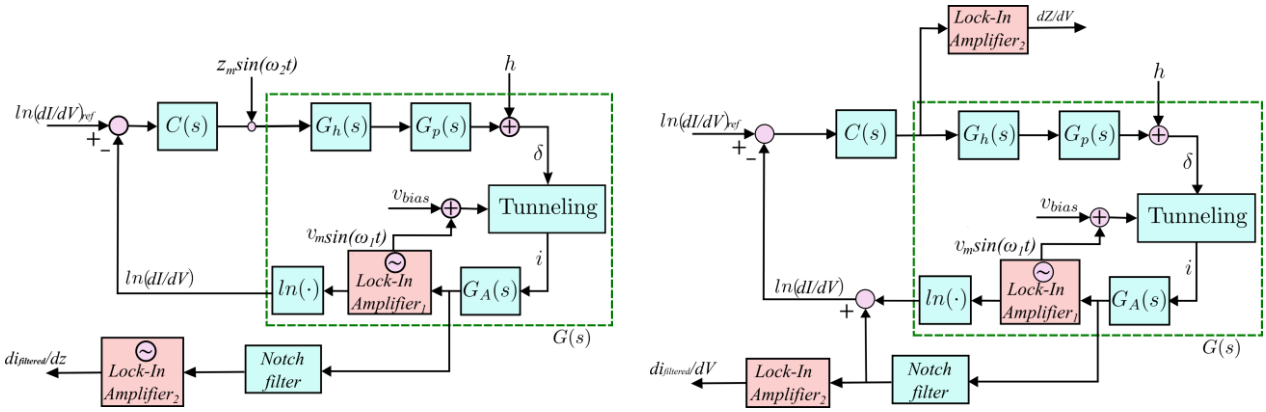

Figure 1. Control block diagram of an STM in the constant differential conductance mode. The modulation voltage $v_m \sin(\omega_1 t)$ is added to the sample bias voltage V_{bias} and the resulting current is then amplified by the preamplifier $G_A(s)$. The lock-in amplifier measures the in-phase component of the amplified current and sends it to the ZyVector for z-control of STM.

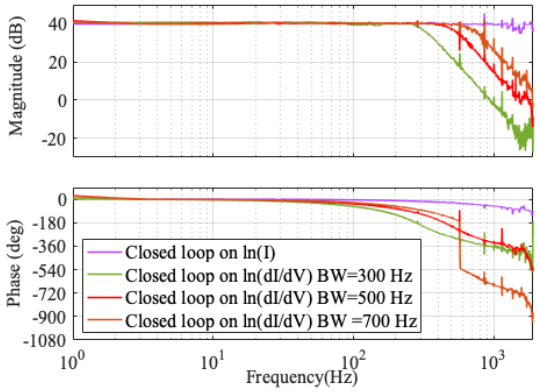

Figure 2. Experimentally obtained frequency responses of our STM system in the constant differential conductance mode. A 2 kHz modulation voltage with an amplitude of 0.8 V was applied to the -2.5 V dc bias voltage of the sample. The feedback loop was closed on the in-phase component with the setpoint value of 0.5 nA.

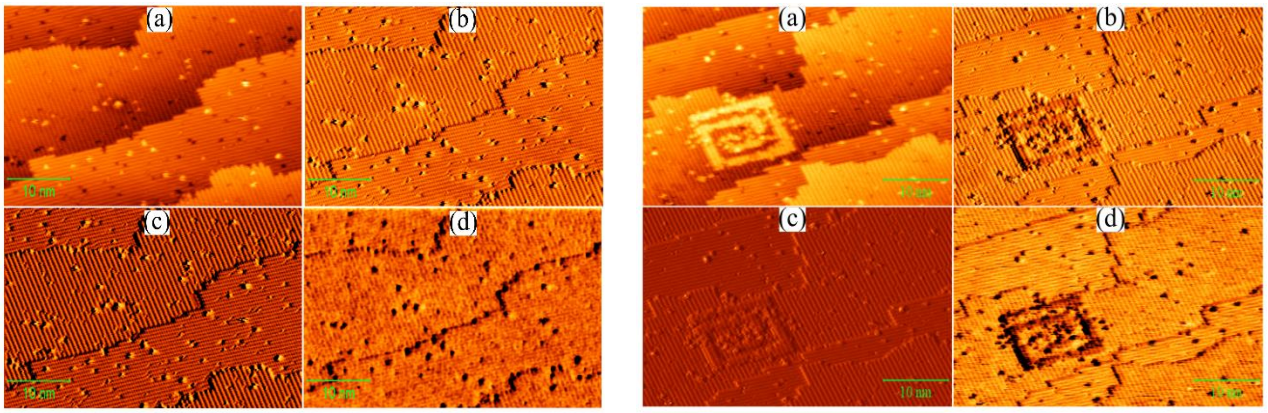

Figure 3. Imaging & Lithography using the Constant Differential Conductance (CDC) control method shown in Fig. 1(a). (a) Topography, (b) DC filtered current, (c) dI / dV image, (d) dI/dz image. All the images are obtained simultaneously. The spiral in the bottom left of the images at right was written using H Depassivation Lithography, under CDC control.

Through Silicon MEMS inspection with a near infrared laser scanning setup

Diogo E. Aguiam [a], Inês S. Garcia [a], Joana D. Santos [a], Filipe S. Alves [a]
[a] International Iberian Nanotechnology Laboratory, Braga, 4700-300, Portugal

Silicon-on-Insulator based MEMS device designs typically require bulk micromachining of both the device layer, to define springs and anchors, and electrostatic actuator and sensing electrodes, and the handle layer, to define structural supports and open backside cavities. The stacking of multiple microstructured silicon wafers is often used to combine structures in 3D MEMS devices [1] and in thin vacuum or pressure sealed packaging solutions [2]. To ensure reliable MEMS integration, the definition of alignment features between front and backside masks, and between multiple wafers, is required, as well as their validation through inspection [3]. Silicon has an absorption edge at 1.12 eV becoming opaque in the visible spectrum but mostly transparent in the near infrared region (λ>1100 nm), as illustrated in Figure 1. The high refractive index of this semiconductor material makes it somewhat reflective, resulting in high Fresnel losses at the interfaces. In addition, the absorption coefficient within the material increases with doping in conductive silicon substrates. Taking this optical behavior into consideration, a light beam in the near infrared will be able to propagate through the material, with transmitted signal attenuations observed at the interfaces between materials and through thick doped silicon materials.

In this work we present the concept and preliminary experimental validation of a near infrared laser scanning setup to inspect silicon encapsulated microstructures by measuring small variations of transmitted intensity. A schematic of the measurement setup is illustrated in Figure 2 A). A 1 mW collimated laser beam at λ=1550 nm (Thorlabs MCLS1) is shined through the silicon sample onto a negatively biased InGaAs photodiode (Thorlabs FGA01) covered by a ø100 µm pinhole. As the sample is scanned by an XY linear stage (Thorlabs DDS220), the light intensity through the sample is measured (Figure 2 B). The optical signal current is amplified using a transimpedance amplifier (FEMTO DLPCA-200). A lock-in amplifier (SR830) modulates the laser at 50 kHz and synchronously measures the amplitude and phase of the captured signal, which are acquired by a data acquisition system (Measurement Computing DT9836) together with the encoded stage positions. To evaluate the lateral resolution, the system a silicon structure with reducing width (Figure 3 A), showing good resolution down to <200 µm. To demonstrate the through silicon inspection concept of a real device, a MEMS custom stopper structure was scanned (Figure 3 B), and the system was able to see through the top and bottom silicon covers and distinguish the inner structure (Figure 3 C). The scanning stages enable sub-µm positioning but lateral resolution is limited by aliasing due to pinhole and photodiode apertures and scattering due to surface roughness. These preliminary results validate the measurement setup for inspection of processed samples and suggests it may also be used for non-destructive online inspection of wafers to confirm alignments of metal, SiO2 or photoresist marks, taking advantage of the sensitivity of the measurement method to detect the small variations of intensity due to Fresnel losses between these materials.````

Acknowledgements: This research was funded by the European Regional Development Fund (ERDF), through COMPETE 2020, Portugal 2020, under Project Future Door Panel (POCI 01-0247-FEDER-070118), and Project uPGRADE - Miniaturized Prototype for Gravity field Assessment using Distributed Earth-orbiting assets (reference POCI-01-0247-FEDER-045927); by the Portuguese Foundation for Science and Technology (FCT) under the UT Austin Portugal Program; and by the project Be.Neutral, with the reference n.º 644874240-00000016, co-funded by Component C5 – Capitalisation and Business Innovation under the Portuguese Resilience and Recovery Plan, through the NextGenerationEU Fund.

References:

[1] Miki, N., *et al*, (2003). Multi-stack silicon-direct wafer bonding for 3D MEMS manufacturing. Sensors and Actuators A: Physical, 103(1–2), 194–201.

[2] Wang, *et al*, (2019). Wafer-Level Vacuum Sealing by Transfer Bonding of Silicon Caps for Small Footprint and Ultra-Thin MEMS Packages. Journal of Microelectromechanical Systems, 28(3), 460–471.

[3] Lee, S. H., *et al*, (2011). Wafer-to-wafer alignment for three-dimensional integration: A review. In Journal of Microelectromechanical Systems (Vol. 20, Issue 4, pp. 885–898).

[4] Pierce, D. T., & Spicer, W. E. (1972). Electronic Structure of Amorphous Si from Photoemission and Optical Studies. Physical Review B, 5(8), 3017–3029. (RefractiveIndex.info, Pierce and Spicer 1972: α-Si; n,k 0.0103–2.07 µm)

[5] Degallaix, J. (2014). Absorption measurement of silicon: The introduction. Presented at GWADW 2014, June 2014.

[6] Riza, N. A. (2022). First Demonstration of Silicon Wafer Inspection Capability using Visible to Short-Wave Infrared CAOS Camera. Applied Industrial Optics (AIO) 2022, T1A.4.

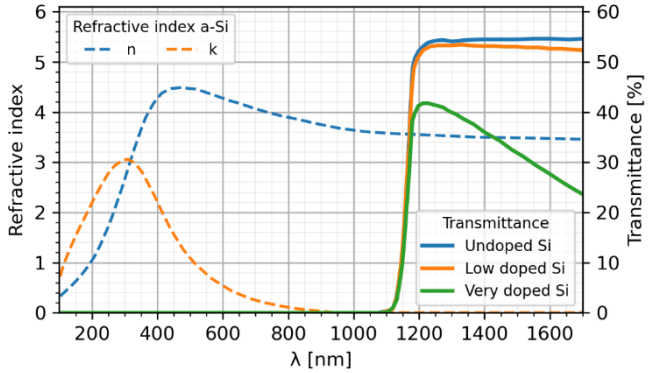

Figure 1. Complex refractive index (n-*i*k) and optical transmittance including Fresnel losses of silicon for different doping levels, extracted from [4,5].

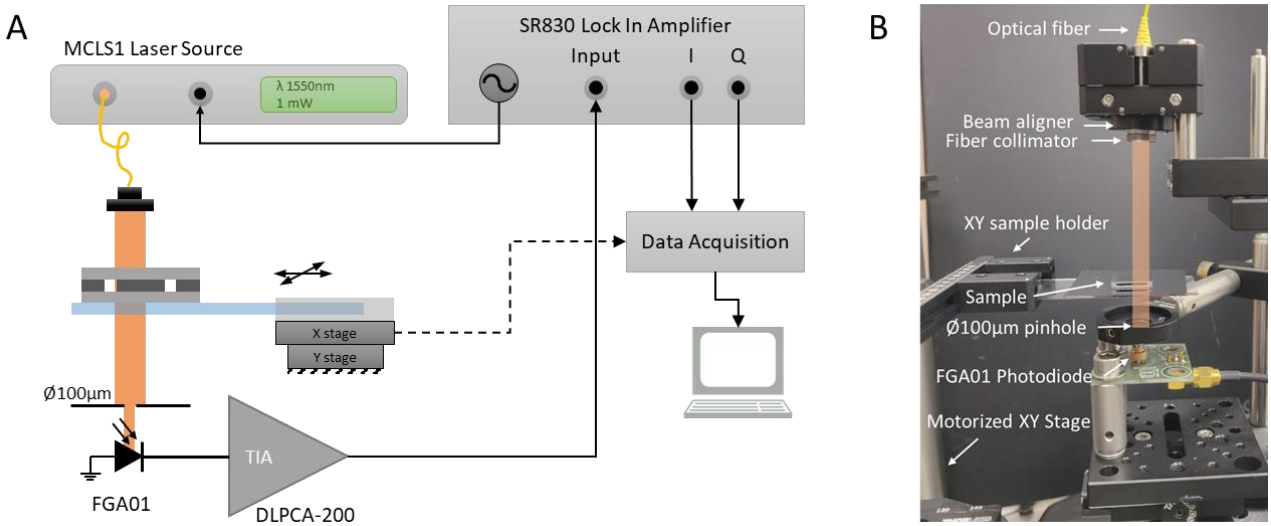

Figure 2. A) Schematic of the NIR scanning measurement setup. B) Photo of the optical scanning system and sample.

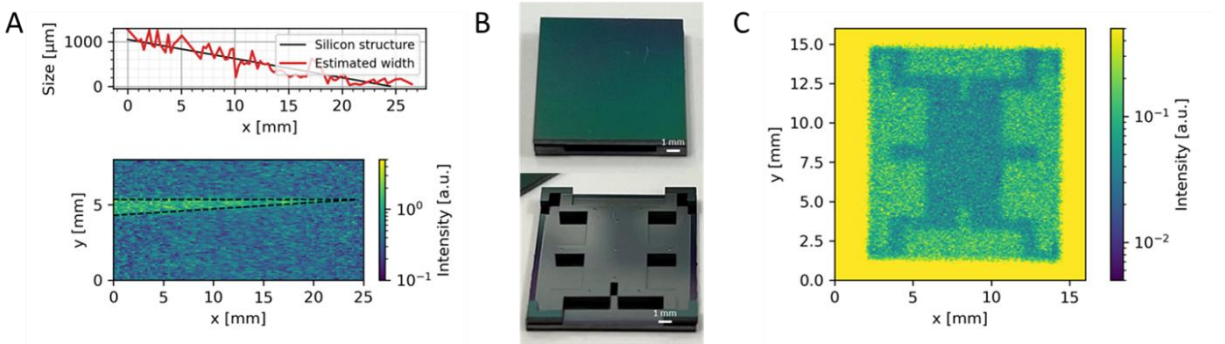

Figure 3. A) Measured signal scanning over a silicon structure with closing opening. B) Three stack silicon sample (top) and with cover removed (bottom). C) Measured intensity through the three structure sample.

Advanced defect detection procedure in immersion lithography for minimizing yield-killing defect classes through high sensitivity optical inspection, guided e-beam inspection, and AI technology by track parameters optimization

J. P. Nacenta Mendivil [a], M. Harumoto [b], K. Jullian [a], M. May [a], Y. Tanaka [b], A. Royer[a], F. Kouemeni-Tchouake [a], V. Masanes [a] , C. Couderc [a], L. Couturier [c] and R. Tiron [a]

[a] Univ. Grenoble Alpes, CEA, Leti, F-38000 Grenoble, France
[b] SCREEN Semiconductor Solutions Co., Ltd. 480-1 Takamiya-cho, Hikone, Shiga, Japan
[c]Applied Materials France, 864 Chem. des Fontaines, 38190 Bernin, France

e-mail: jorge-pablo.nacentamendivil@cea.fr

The continuous shrinking of semiconductor manufacturing nodes requires features with smaller critical dimensions and higher pattern density. This also necessitates better control and understanding of defectivity to successfully implement leading-edge processes. Moreover, as the node size decreases, potential yield-killing defectivity issues can coexist.
The usual patterned defectivity measurements consist of three stages: first, an optical inspection is conducted to obtain a mapping of possible defects through die-to-die comparison of optical signals combined with pattern coordinate information[1]. Second, a characterization of a number of the inspected defects is performed using SEM Review, which helps understand the different classes of defects resulting from our process. Finally, this information is used to train an AI algorithm capable of accurately recognizing and classifying each defect. Randomized statistical defect classification of a number of the inspected defects provides an idea of the contribution of each defect class to the total defectivity. However, there is a risk that main defect classes, which are prioritized for elimination, may often conceal less visible but nonetheless critical problems. Early detection of minority classes can enable co-optimization of multiple issues and expedite the fine-tuning of new and mature processes. Thus, to push defectivity optimization to its limit, a method for obtaining relevant statistical information about minority defects is essential, while adhering to the constraint of not increasing the sampling and machine time.
In this contribution, we present the results of a new defect inspection, review, and classification procedure that combines an extremely sensitive multi-attribute optical defect inspection with the use of ExtractAI™ technology (combining AI and guided e-beam inspection [2]) to rapidly search, map and classify yield-killing defects, regardless of their contribution to the total defectivity. Its relevance has been demonstrated in the simultaneous reduction of minority defects (embedded defects, microbridges, and watermarks) and majority not killer defects (residues) in an immersion lithography gate process targeting 28nm dense lines post-etch. In the first step, non-of-interest defects as residues, which are major contributors to total defectivity, have been understood without the need for SEM images and are systematically removed from the statistical analysis, allowing a focus on minor but significant killer contributors. In the second step, the co-optimization of these miner killer defects together with majority defects has been tackled, by tuning track process parameter in the exposure development step [3] resulting in a 95% reduction in total post-lithography defectivity as seen in Fig1. In addition, thanks to this new ExtractAI™ procedure, we have been able to gather sufficient statistical information about microbridging without increasing machine time. As shown in Figs 2a,b et c, this has helped us understand that the root cause arises from a specific resist residue redepositing mechanism in very specific areas of the die.

[1] W. Broadbent et al, Proc. SPIE 6607 660714 (2007).

[2] N. Cai et al. Proc. SPIE, Volume 9778, id. 977834 6 pp. (2016).

[3] J. P. Nacenta Mendivil et al. Proc. SPIE 12055, Advances in Patterning Materials and Processes XXXIX, 120550U (2022)

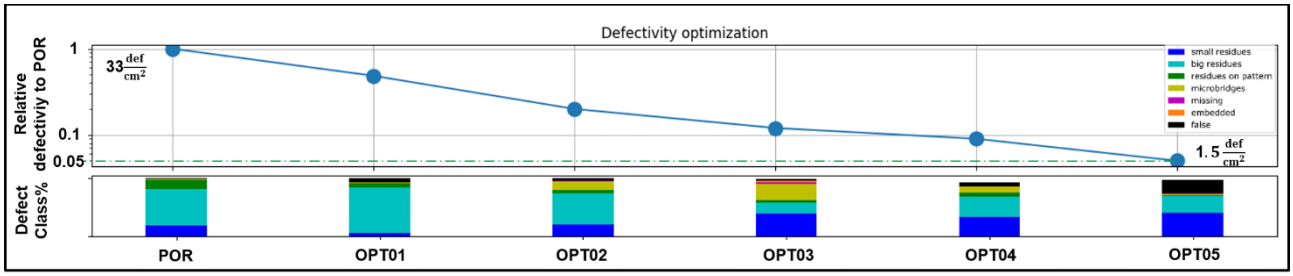

Figure 1. Progress in defectivity through track parameters optimization at the development step. The blue dots represent the initial defectivity (POR), and the series of optimized recipes (OPTxx) show the relative defectivity compared to POR. At the bottom, we observe the statistical distribution of defects for each defectivity measurement (500 reviewed defects). Changes in spin speed acceleration during DIW dispense (OPT01) had an effect on reducing small residues, which were manifested as non-killer defects. An appropriate DIW flow dispense helps reduce large residues (OPT02 & OPT03). The rinse and drying sequence (OPT04 & OPT05) also decreased the number of residues. With the assistance of ExtractAI™, a number of microbridges initially classified as minority defects were ultimately identified as main killer defects, allowing us to understand the effect of DIW flow and spin speed on them by rapidly tracking them on the wafer. Additionally, the impact on watermarks (missing patterns) and embedded defects could be observed. The former were eliminated by adjusting the scan speed during exposure, while the latter were ultimately understood as non-killer defects in post-etch analysis

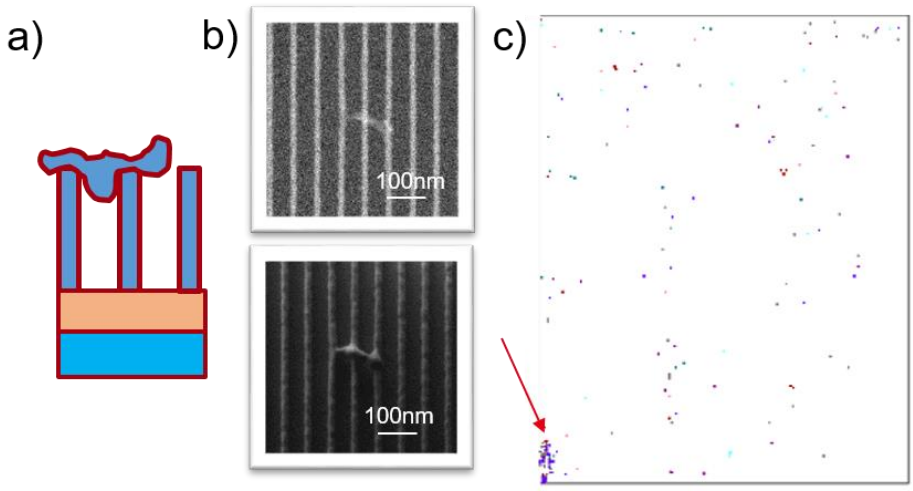

Figure 2. a) Schematic representation of a microbridge generated by a resist residue redeposited in a specific area of the die. b) SEM image showing the microbridge at high voltage (top) and low voltage (bottom) resulting from residue redepositing. c) Die stack of multiple wafers with a red arrow indicating a cluster of microbridges generated in the specific area of the die.

Design and All-In-One Etch of Silicon Metalens for Near-Infrared Focusing

Bingrui Lu [a], Søren Engelberth Hansen [a], Thor August Schimmell Weis [a],
Guillermo Arregui [a], Søren Stobbe [a]

[a] DTU Electro, Department of Electrical and Photonics Engineering,
Technical University of Denmark, Kgs. Lyngby, Denmark.
e-mail: binlu@dtu.dk, ssto@dtu.dk

Metalenses play an important role in the new generation of micro- and nano-optical systems. A metalens consists of a series of precisely engineered subwavelength nanostructures arranged on a flat surface to manipulate light properties such as amplitude and phase [1]. Because of their small footprint, planar geometry, and excellent optical performance, metalenses show great potential in applications from sensing, imaging, and communication to astronomy, quantum photonics, and virtual/augmented reality [1]. For applications that require high efficiency and low energy consumption, interests have shifted from plasmonic metalenses to all-dielectric ones in pursuit of lower absorption and scattering losses of dielectric material compared to metal. The development of dielectric metalenses poses a number of new nanofabrication challenges, such as material quality, substrate compatibility, and fabrication techniques together with fabrication tolerances. In our work, a metalens with an array of Si pillars in various diameters placed in a hexagonal lattice is designed for near-infrared (NIR) light focusing with the center wavelength of 1550 nm. The choice of silicon guarantees material quality and substrate compatibility thanks to the technologies from today's mature silicon industry. Meanwhile, a specially designed silicon deep-etching process developed in our cleanroom is optimized to obtain high-quality fabrication with precise control of the nanostructure geometries [2].

The hexagonal unit cell of the metalens contains Si pillars with a diameter of D and height of H, coated with an anti-reflective oxide layer as shown in Fig 1a and b. The nanopillars function by delaying the phase of an optical wavefront relative to other pillars of different diameters, which allows for arbitrary phase profiles to be generated if the relative phase difference spans 2π. Through iterative design space exploration in Fig 1 c and d, the lattice period of 450 nm, the height of 1.5 µm, and the pillar diameters from 140 nm to 356 nm are found to provide the required 2π phase span and sufficient feature sizes for fabrication. For a 330 µm wide metalens with a 110 µm beam waist of collimated Gaussian input, the focal lengths are simulated to be 884 µm, 806 µm, and 730 µm, respectively, for the wavelengths 1410 nm, 1550 nm, and 1690 nm.

For the high-precision fabrication of the silicon nanopillars, a simplified procedure of All-In-One etch is developed where the wet processes of lift-off and metal mask removal are avoided. An etching mask layer is deposited on the silicon substrate before a state-of-the-art high-resolution JEOL JBX-9500 FSZ E-Beam system is used to pattern 50 nm of CSAR resist. Before the exposure, a proximity effect correction (PEC) software, Beamfox Proximity, analyzes the pattern design and adjusts local exposure dosages to achieve the intended outcome of circular patterns in the correct dimensions. To avoid structural damage from the surface tension and other mechanical impacts of wet chemistry processing steps, a highly directional plasma dry etching process developed in DTU's cleanroom called CORE (Clear, Oxidize, Remove, and Etch) is optimized. It replaces the common fluorocarbon inhibitor in the Bosch deep etching with oxygen, making it a greener process for the environment. The nanopatterns are transferred from the resist to the etching mask, and then into the silicon substrate to form high-aspect-ratio pillars. Before the final step of anti-reflective oxide growth, the resist and the etching mask are both removed directly after the silicon CORE process in the same chamber.

The silicon metalens can be placed directly on top of other photonic circuits or components to form a 3D integrated system. The fabrication process developed in this work is fully compatible with the current silicon industry but with a greener execution. The metalens will be an essential component in the integration of optoelectronic circuits [3-5]. Further measurements and applications of the metalens will be presented.

[1] W. T. Chen et al., Nat. Rev. Mater. 5 (2020), 604–620.
[2] V. T. H. Nguyen et al., J. Vac. Sci. Technol. A 38 (2020), 053002.
[3] M. Albrechtsen et al., Nat Commun 13 (2022), 6281.
[4] S. E. Hansen et al., Opt. Express 31 (2023), 17424-17436.
[5] B. V. Lahijani et al., arXiv:2204.14257 [physics.optics].

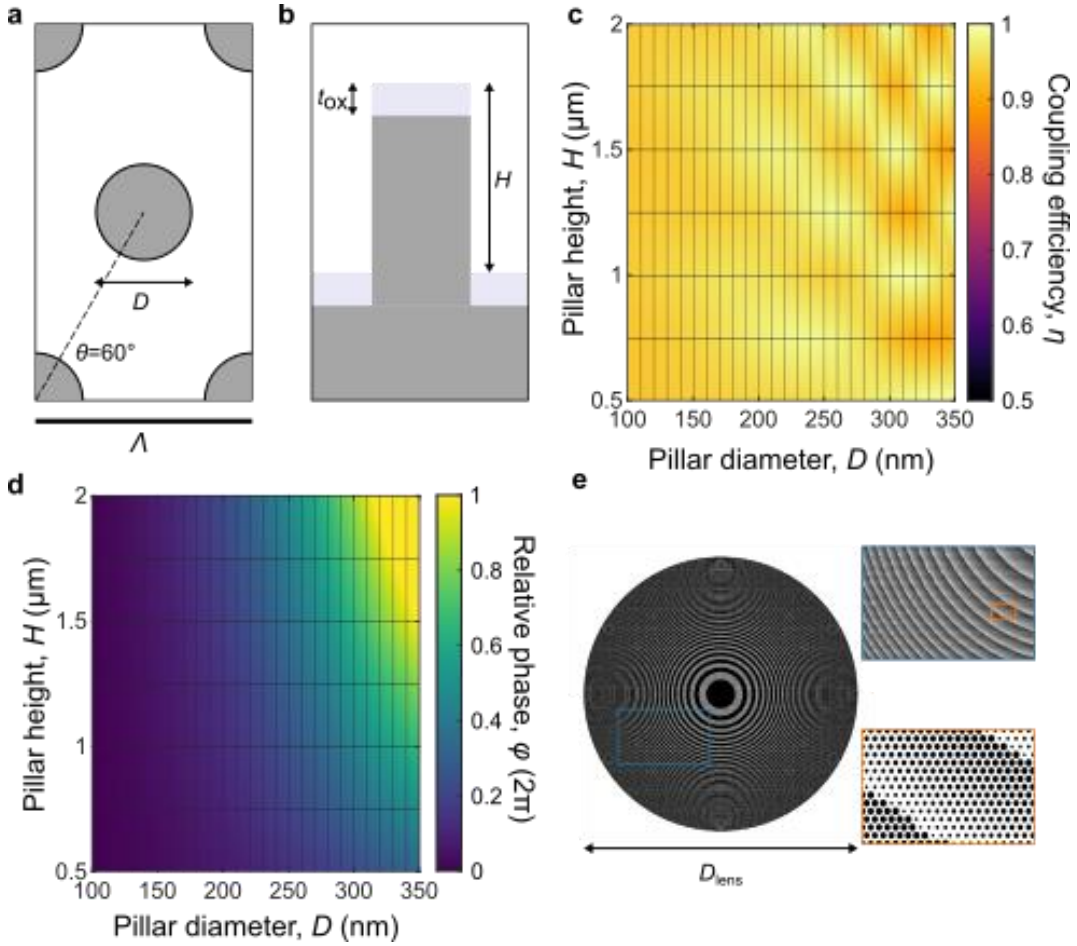

Figure 1. The design of the Si metalens. **a**, The hexagonal unit cell. **b**, Sideview of silicon pillars with height, *H*, and an oxide anti-reflection coating with thickness, t_{ox}. **c**, The coupling efficiency for different pillar diameters and heights.**d**, Design space of the relative phase compared to the smallest pillar diameter. **e**, The full metalens with a diameter of 330 μm.

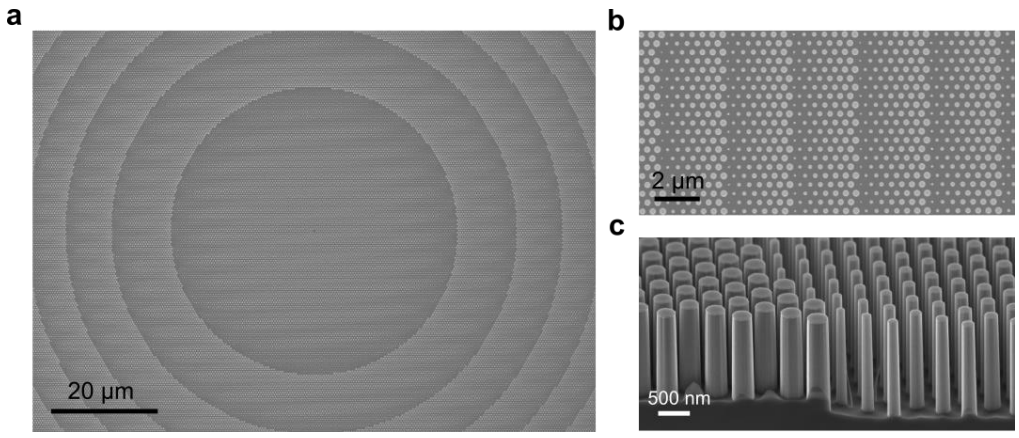

Figure 2. Scanning electron micrographs of fabricated silicon metalens. **a**-**b**, Topview images. **c**, tilted view.

Development of surface acoustic wave phase modulators for physical reservoir computing

Taiki Ijima[a], Claude Meffan [a], Amit Banerjee [a], Jun Hirotani [a] and Toshiyuki Tsuchiya [a]
[a] Kyoto University, Kyoto, 615-8540, Japan
e-mail: t_ijima@nms.me.kyoto-u.ac.jp

This paper proposes to utilize a surface acoustic wave (SAW) phase modulator for physical reservoir computing. SAW phase modulators with various designs with respect to a waveguide are fabricated, and their frequency responses are investigated. The measured results gave us beneficial information for optimization of the structural parameters. These can be regarded as hyperparameters in the SAW reservoir system. In the future, we intend to use these modulators as a physical reservoir system through a time-delayed feedback loop (Fig.1) [1].

Background

Recently, the power consumption in machine learning sector has been increasing because the amount of processed information especially in the cloud is also going up exponentially. Previously, both edge computing and physical reservoir computing were independently proposed as methods to address this problem [2][3]. These approaches have the potential to be merged by applying MEMS devices as a reservoir layer. The physical dynamics of this reservoir is mainly required to have two properties, non-linear behavior and mild attenuation. A SAW phase modulator has several characteristics which are advantageous regarding implementation into a physical reservoir computer [4]. The parameters in the devices such as the waveguide length and width may affect the learning performance. In this study, we fabricated devices with various designs and measured their frequency response to investigate its non-linearity and attenuation, and then examined the possibility to realize the system.

Descriptions of the SAW phase modulator

The SAW phase modulator in this research is based on a two-port delay line which has two opposite interdigital transducers (IDTs) on a piezoelectric material. SAWs are generated by applying a RF voltage signal to IDTs, which also receive a SAW to convert into electric power. In this design, they are fabricated on an X-cut lithium niobate (LN) wafer. The direction of SAW propagation is tilted 30 degrees relative to the Z-axis to reduce the SAW velocity. The center frequency, f_c, of the resonator is

$$f_c = \frac{v_{av}}{p} \quad (1)$$

where p is the period of the electrode fingers (Fig.2), and v_{av} is the average phase velocity of SAW. In this study, p is 11.7 μm and v_{av} is 3510 m/s. This gives the center frequency of ~300 MHz for the device. In between two IDTs, a waveguide that possesses long and narrow electrodes along the waveguide to modulate the phase of the SAW was inserted. (Fig.2). The phase modulation principle is the change of elastic constant of the piezoelectric LN substrate by applying a voltage [4]. The acoustic waveguide is defined by a SiN layer of 400 nm thickness which is deposited using plasma-enhanced chemical vapor deposition. IDTs and modulation electrodes are fabricated with an aluminum layer of 115 nm thickness which is deposited using an electron-beam evaporator.We prepared several devices with waveguide lengths of 5 mm, 10 mm, and 15 mm and widths of 10 μm and 18 μm in order to study the correlation among these parameters, modulation effects, and signal attenuation.

Results

For each design, the linear response without a modulation input was measured using a vector network analyzer and we confirmed the resonance peak at their center frequency decayed exponentially with the waveguide length while we observed mild relationship between the amplitude and the waveguide width (Fig.3). Furthermore, when the modulators were driven with a RF voltage signal at their center frequencies and applied 20 $V_{p\text{-}p}$ at 10 kHz frequency into the modulation electrodes, we observed the sideband power in the frequency spectrum of the output signals. From this outcome, we infer that the phase of the SAW was modulated.

[1] Appeltant, L et al., Nature Communications, 2(1), (2011) 468.
[2] Tanaka, G et al., Neural Networks, 115, (2019) 100-123.

[3] Shi, W et al., IEEE Internet of Things Journal, 3(5), (2016) 637-646.
[4] Shao, L et al., Nature Electronics, 5(6), (2022) 348-355.

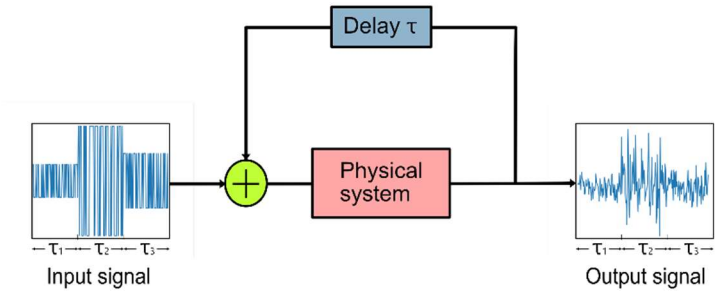

Figure 1. Physical reservoir system of time-delayed feedback loop

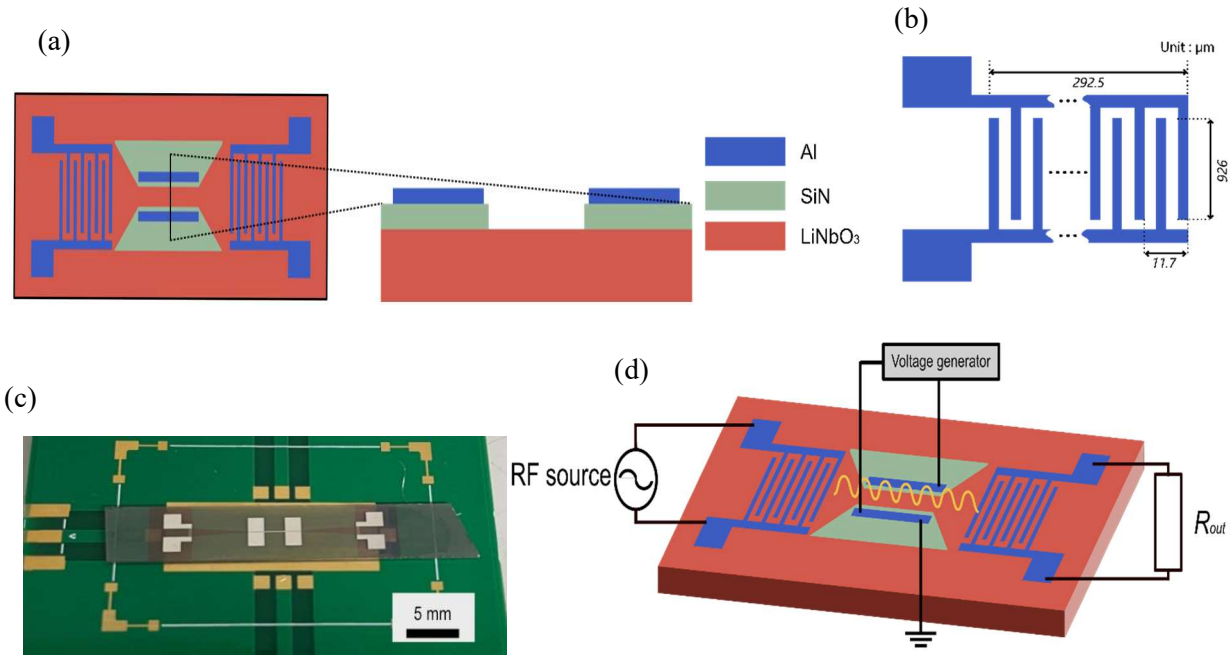

Figure 2. Design and fabrication of SAW phase modulator (a) Simplified illustration of SAW phase modulator with waveguide and cross-section of waveguide in modulation region (b) Interdigital transducer (IDT) (c) Fabricated SAW phase modulator (d) Configuration of SAW phase modulator

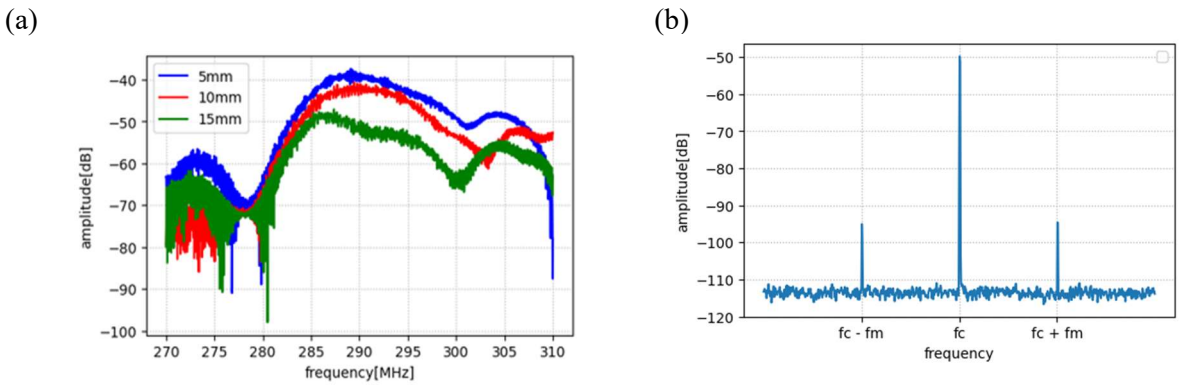

Figure 3. (a) Linear transmission spectrum of SAW phase modulators without modulation, showing scattering parameter (S_{21}) of 18 μm-wide waveguide for each waveguide length. (b) Frequency spectrum of modulated signal (f_c = 288.10 MHz, f_m = 10 kMz)

A silicon carbide (SiC) carbon nanotube (CNT) composite for high aspect ratio harsh environment MEMS

Jiarui Mo, Shreyas Shankar, Sten Vollebregt

Microelectronics Department, Delft University of Technology, Delft, 2628 CD, The Netherlands
e-mail: s.vollebregt@tudelft.nl

Silicon carbide (SiC) is a promising material for MEMS devices, especially for those aiming at harsh-environment applications due to its chemical inertness and excellent mechanical stability. However, the lack of a proper bulk fabrication process is a factor that impedes the development of SiC MEMS. Since most known wet etchants do not attack SiC [1], dry etching becomes mainstream in SiC processing. However, most reported dry etching methods suffer from low etching rates (typically ≤ 1 μm/min), non-vertical sidewalls, and rough etched surfaces [2-4]. In the case of surface micromachined SiC devices, structures are limited to thicknesses of several micrometres and low aspect ratios due to the limited thickness of the deposited SiC thin films [5-7].

Here, we propose to use an array of vertically aligned carbon nanotubes (CNT) reinforced by amorphous SiC as an alternative for high aspect ratio (HAR) SiC-based MEMS fabrication (fig. 1). As the growth of CNT is fast (μm/s) and vertically aligned, it addresses the problem of the low etch rate and non-vertical sidewalls brought by traditional SiC micromachining methods. Only a few nm-thin film of a-SiC is required to fill the CNT structure due to the small spacing between the CNT, which reduces deposition time.

The maximum aspect ratio we could achieve was 10 for a freestanding structure and 20 for a clamped beam. For higher dimensions, the CNT tends to bend. By performing transmission line measurements (TLM), we found that the electrical properties of the composite are dominated by the CNT ($\rho_{composite}$ = 0.7 Ω·cm, ρ_{CNT} = 0.2 Ω·cm). On the other hand, mechanical properties like Young's Modulus and compressive strength can be tuned over 3 orders of magnitude by varying the thickness of the a-SiC filler [8]. The Young's modulus increased from 200 MPa to 125 GPa from uncoated to 21 nm a-SiC coating, while the compressive strength increased from 1 MPa to 1.8 GPa.

Two different devices were fabricated using this approach. One is a chevron-shaped thermal actuator (fig. 2) tested up to 450°C without degradation [9]. The maximum displacement was 13.8 μm at 80 V; the device breaks down at higher bias due to local Joule heating. The other device is a capacitive accelerometer (fig. 3), for which the sensitivity scales with the device's thickness. The measured capacitance (fig 3. b) aligns with the designed value and changes with bias, indicating a successful release of the large 400 × 800 μm^2 perforated mass. The device was tested electrically up to 200°C due to the limitations of the probe station but remained mechanically stable up to 700°C. The device is currently being tested in a mechanical shaker. These results show that the a-SiC reinforced CNT array has good potential for fabricating HAR surface micromachined MEMS for harsh environment applications.

[1] D. Zhuang et al., Mater. Sci. Eng. R Rep., vol. 48, pp. 1-46, 2005.
[2] R. Liu et al., J. Cryst. Growth, vol. 531, p. 125351, 2020.
[3] K. M. Dowling et al., J. Microelectromech. Syst, vol. 26, pp. 135-142, 2016.
[4] A. A. Osipov et al., Sci. Rep, vol. 10, pp. 1-10, 2020.
[5] R. G. Azevedo et al., IEEE Sens, vol. 7, pp. 568-576, 2007.
[6] S. Rajgopal et al., in Proc. ICSCRM 2007, 859-862.
[7] A. V. Lim et al., IEEE Microw. Wirel. Compon. Lett, vol. 26, pp. 28-30, 2015.
[8] R.H. Poelma et al., Adv. Func. Matt., vol. 24, pp. 5737-57444, 2014.
[9] J. Mo et al., Proc. of IEEE MEMS, pp. 72-75, 2023

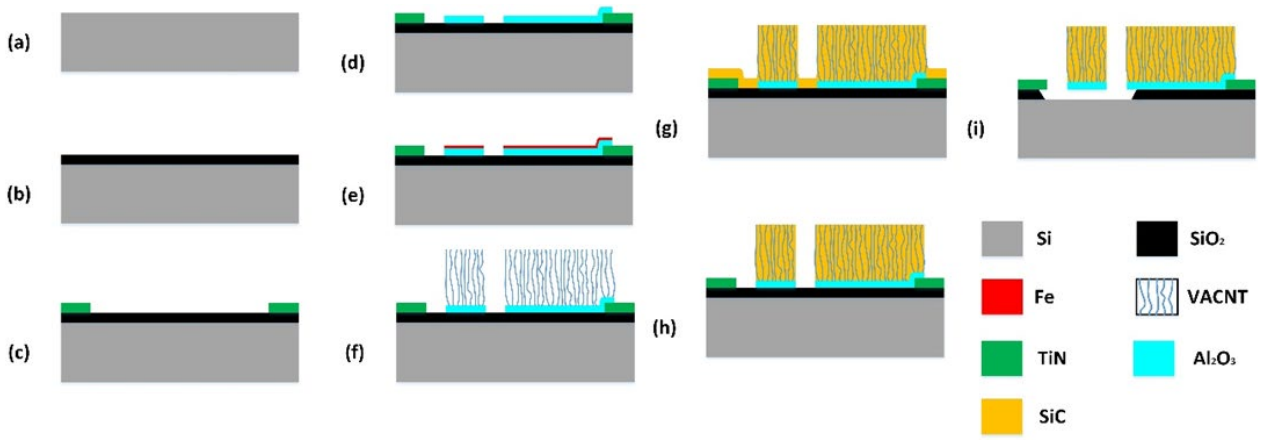

Figure 1. Process overview of the SiC-CNT composite: (a) Si substrate is used as starting material; (b) SiO_2 sacrificial layer is deposited; (c) TiN is sputtered as electrodes; (d)(e) Al_2O_3/Fe bilayer is evaporated, acting as diffusion barrier and catalyst, respectively; (f) CNT arrays are grown using the Fe; (g) The CNT array is infiltrated by a-SiC; (h) Floor layer removal by unmasked dry etching; (i) Vapour HF to release the structure.

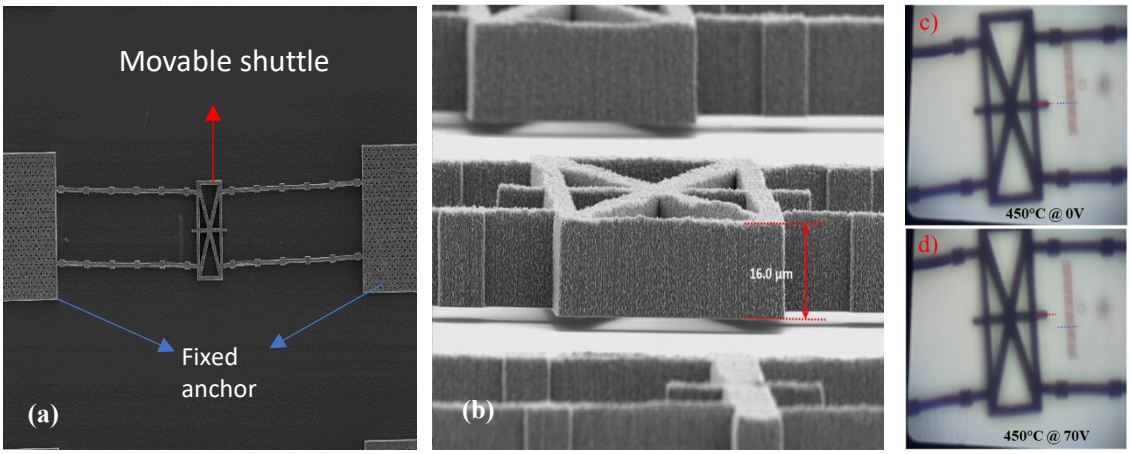

Figure 2. Chevron-shaped thermal actuator based on SiC-CNT composite. A) top view, b) side view, c) rest position at 450°C substrate temperature, d) 10 µm movement at 70V bias and 450°C substrate temperature.

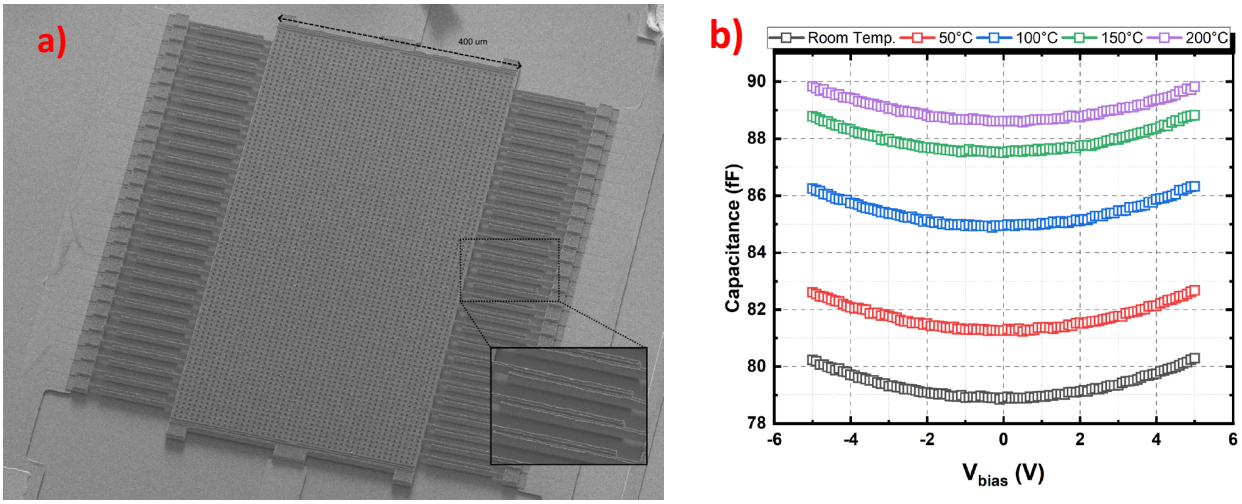

Figure 3. a) Top view of a 10 µm thick SiC-CNT composite MEMS capacitive accelerometer with 400x800 µm mass. The mass is perforated, allowing the vapour HF to release the large device. b) Capacitance between the fingers as a function of temperature and bias, demonstrating a successful release of the mass.

Parallel In-Plane Electrothermal Actuators

Yen Nee Ho, Aron Michael, Chee Yee Kwok, Cibby Pulikkaseril
UNSW Sydney, Kensington, 2052, Australia
e-mail: yennee.ho@unsw.edu.au

Progress Claims

This paper reports a novel electrothermal actuator with large in-plane displacement designed for MEMS-based pitch-tunable diffraction grating for beam steering applications such as in microlidar systems. The device consists of two sets of parallel electrothermal beams that pull and push a lever to produce large in-plane displacement. The actuator has been simulated, fabricated and tested. The results show that the actuator generates a large displacement of 177µm at a driving voltage of 6V. By increasing the number of parallel electrothermal beams, the actuator uniquely reduces power consumption while generating large displacement in comparison to the existing in-plane electrothermal actuators.

Background

A fully autonomous car has become technically feasible with the advancement of deep learning procedures for AI with LIDAR being the key component. Its social advantages are expected to be huge, centered on the removal of human error from driving. Current commercial solutions typically fall under scanning lidar systems [1]. However, they are bulky and power-hungry. Optical phased arrays are ideal, but they are not suited for long-range applications [2]. MEMS-based scanners are attractive as they are compact with high resonance frequency [3]. But the trade-offs between the aperture size, field of view and the resonance frequency are issues. MEMS-based pitch-tunable diffraction grating combining optical phased array and MEMS is a promising approach to address the issues. Such an approach requires an actuator with large in-plane displacement. Existing electrothermal in-plane actuators do not satisfy the necessary requirements [4]. In this work, a novel electrothermal actuator is developed that produces large displacement at relatively lower power consumption with high fill factor to satisfy the requirements.

Design

The proposed novel electrothermal actuator is illustrated in Fig 1. The device consists of two pushing actuators (PL and PB), which are comprised of parallel electrothermal beams, that pull the lever at A through a pulling beam (B1) and push the level at point B via a pushing beam (B2). This results in a rotation of the lever about point B, generating a displacement δ at point C. In this work, the electrothermal actuator with two (Design A) and four (Design B) parallel beams have been developed.

Fabrication

The fabrication process flow of the device is illustrated in Fig 2. It has been developed using standard photolithography with a single mask to define the device on an SOI wafer with a 5µm thick device layer and a 1µm thick BOX. The device layer is doped to a sheet resistance of 5Ω/□ using phosphorus diffusion. The contact metallization is patterned using gold (a). The front and the backside are patterned with Cr (b, c) to RIE the actuator and release (d) it down to the BOX (e) using deep RIE. To protect the front side during the backside etching, it is protected by C_4F_8 polymer (f).

Results

The fabricated actuators are shown in Fig 3(a) and (b). The displacement generated and power consumed by each actuator as a function of driving voltage are plotted in Fig 4(a) and (b). Design A generated an in-plane deflection of 81.2µm at a driving voltage of 6V dissipating 58.59mW. The power consumption is reduced to below 40mW with Design B for the same deflection. Design B dissipates less power when compared to Design A for deflections over 56.05µm, as indicated in Fig 4(b).

[1] High Definition Real-Time 3D LiDAR, Velodyne LiDAR, 2018.
[2] A. Yaacobi, J. Sun, M. Moresco, G. Leake, D. Coolbaugh, and M. R. Watts, “Integrated phased array for wide-angle beam steering,” Optics letters, vol. 39, no. 15, pp. 4575–4578, 2014.
[3] High-Performance Solid-State LiDAR, Innoviz Technologies, 2019.
[4] J. M. Maloney, D. L. DeVoe, and D. S. Schreiber, “Analysis and design of electrothermal actuators fabricated from single crystal silicon,” in ASME International Mechanical Engineering Congress and Exposition, vol. 19005. American Society of Mechanical Engineers, 2000, pp. 233–240.

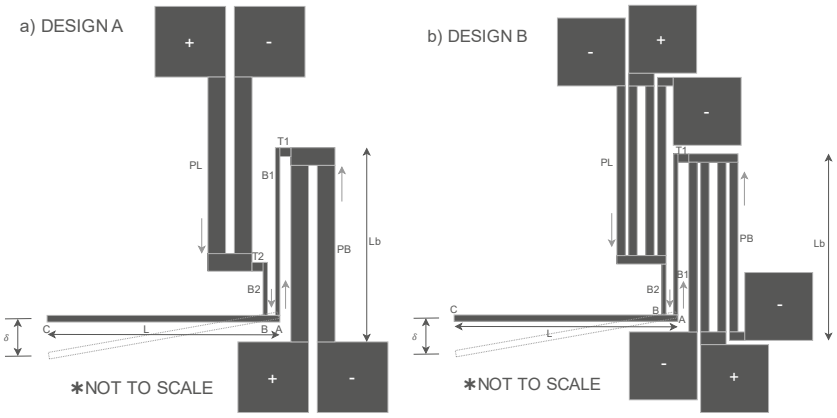

Figure 1. Schematic drawing of (a) Design A and (b) Design B actuators attached to a lever of length L via two spring beams B1 and B2.

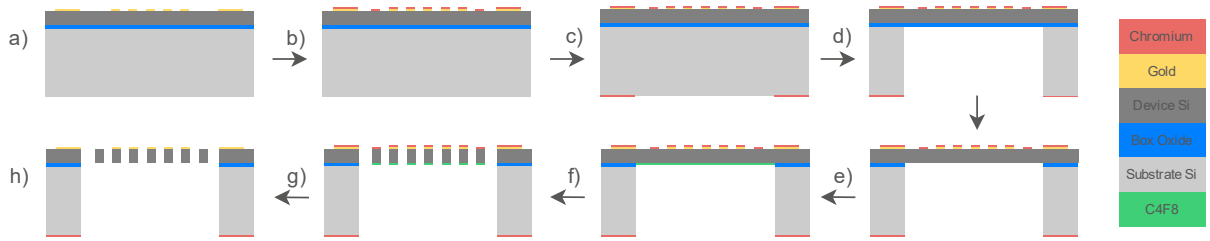

Figure 2. Fabrication process flow.

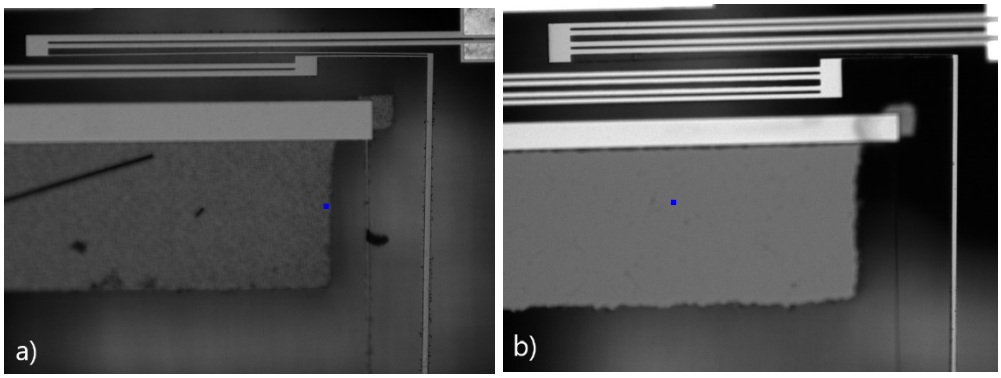

Figure 3. Microscopic images of fabricated and tested (a) Design A and (b) Design B actuators.

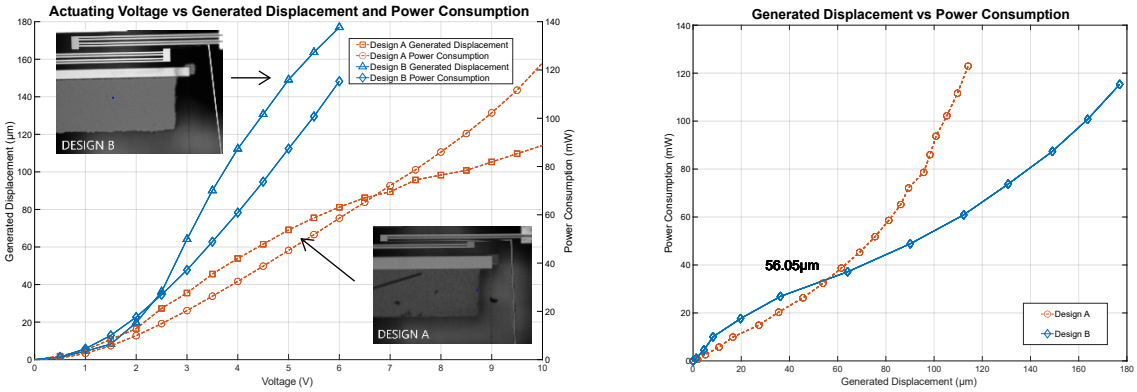

Figure 4. (a) Measured displacement and power consumption at various actuating voltages and (b) power consumption at various generated displacements with 5V actuation inset images for Designs A and B.

Fabrication of On-Chip Carbon Microelectrodes by Catalytic Graphitization of 3D Printed Polymers

Zoi Maria Papadopoulou, Swetha Vasudevan Kanakkottu, Babak Rezaei, Stephan Sylvest Keller
National Centre for Nano Fabrication and Characterization, DTU Nanolab, Technical University of Denmark, 2800 Lyngby, Denmark
email: zoipap@dtu.dk

Keywords: catalytic graphitization, additive manufacturing, pyrolytic carbon, CMEMS

The fabrication of carbon-based microelectromechanical systems (CMEMS) is an emerging field with wide applications ranging from medical devices and sensors to energy storage. Although photolithography combined with pyrolysis is the most established method for CMEMS fabrication, the technique has severe drawbacks that can be overcome by additive manufacturing. More specifically, by employing layer-by-layer 3D printing techniques for preparation of the precursor structures, the formation of on-chip 3D carbon micro structures with high aspect ratio in a two-step process is possible. Compared to the alternatives, this method reduces cost, time and complexity. The percentage of graphitization of the carbon material plays an important role for the electrical and electrochemical properties of the final device [1]. Here, we demonstrate that the addition of a catalyst to the 3D print resin can enhance its graphitization during pyrolysis, improving the electrochemical performance of the final on-chip microelectrodes.

In this study, a S140 PμSLA 3D printer (BMF, USA) was used in the first step of the process to print 3D polymer microstructures on Si substrates (Fig.1A). For this purpose, photocurable acrylic-based resin was mixed with iron chloride hexahydrate with 0.1% wt., 0.2% wt. and 0.5 % wt. to introduce iron ions at different concentrations in the precursor. The modified resin was printable for low concentrations of iron, where 0.5 wt. % was not sufficiently photocurable to print stable 3D structures. In the second step, the printed structures were pyrolyzed in a quartz tube furnace at 900^{o}C converting them into carbon. The fabricated microelectrodes were characterized by X-Ray photoelectron spectroscopy (XPS), Raman spectroscopy, Cyclic Voltammetry (CV) and Electrochemical Impedance Spectroscopy (EIS) using the standard potassium ferri-ferro cyanide redox probe at a concentration of 10 mM.

By introducing catalytic iron ions in the pristine resin, significant electrochemical and structural changes are observed. Firstly, by depth-probing the modified carbon with XPS, the presence of iron after pyrolysis was detected below the first layers of the sample (Fig. 2). Secondly, the catalytic properties of the iron ions were observed by Raman spectroscopy where the I_G/I_D ratio increased from 1.08 according to previous studies [2] to 1.12, evidencing higher degree of graphitization (Fig. 2). Thirdly, an improve in electrochemical performance was evident during CV, where peak-to-peak potential decreased and peak current increased for modified precursors. This suggests lower internal resistance caused by the enhanced graphitization. (Fig. 3). Lastly, during EIS the diameter of the semi-circle, which is proportional to the charge transfer resistance of the material, was drastically reduced, implying that a carbon electrode fabricated in presence of iron has better electrochemical properties.

In summary, the fabrication of on-chip carbon micro electrodes through additive manufacturing was possible after the precursor modification. The introduction of iron catalyst into the precursor, produced a lower internal resistance and improved the electrochemical performance.

[1] Thambiliyagodage C. J., et al. Carbon 134 (2011) 452-463

[2] Rezaei B et al. Materials & Design 193 (2020) 108834

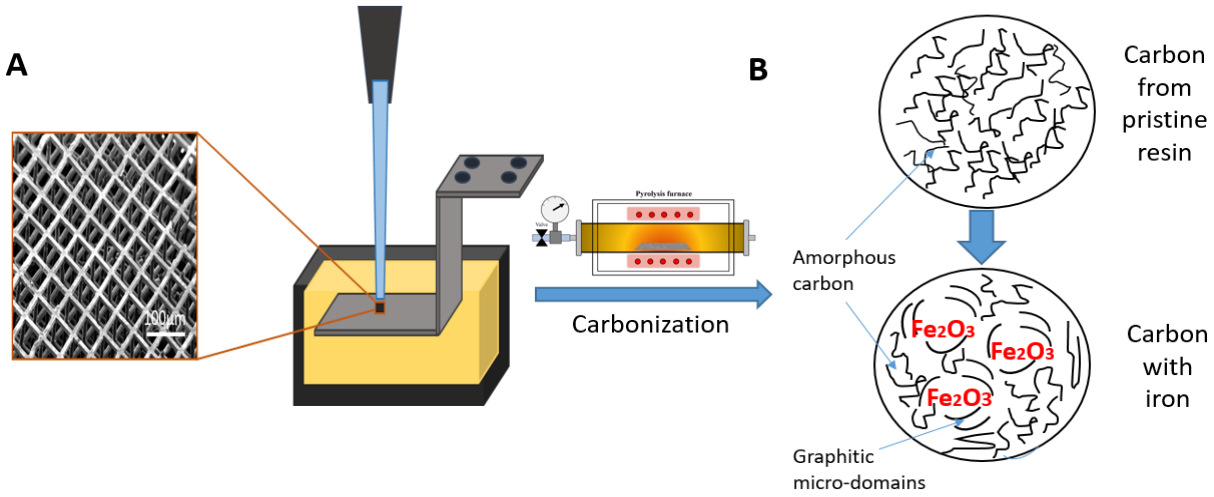

Figure 1. Modification of 3D print polymer precursor with iron ions for pyrolytic carbon micro electrodes fabrication. A) Illustration of 3D print method and pyrolysis process with SEM image derived from modified precursor. B) The carbon modification during pyrolysis after the addition of iron catalyst.

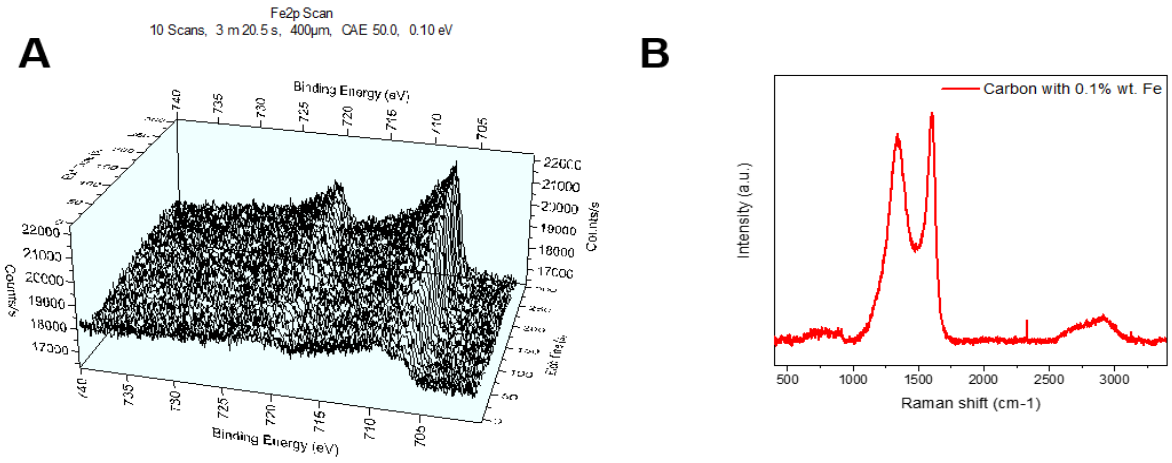

Figure 2. A) Depth-probing of the modified carbon with XPS verifying the presence of iron in the deepest layers of the structure. B) Raman spectroscopy demonstrates that modified precursor with iron produces amorphous carbon with graphitic micro-domains.

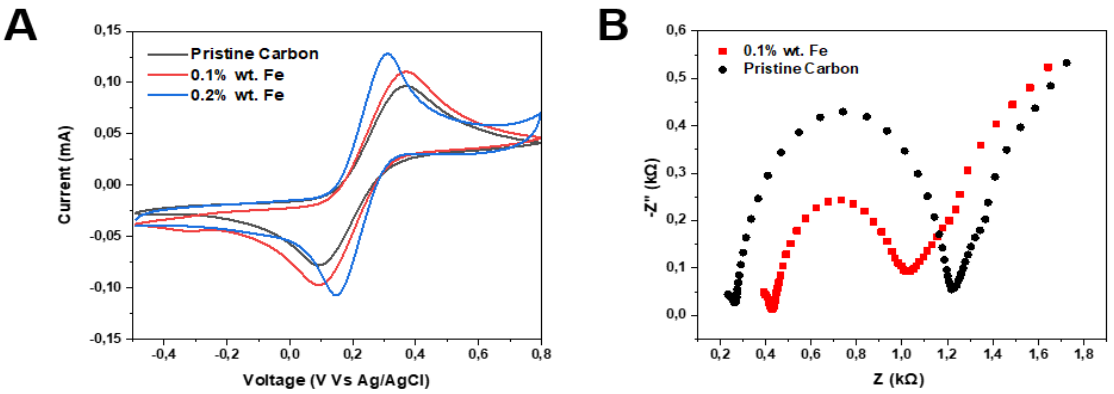

Figure 3. Electrochemical characterization of carbon micro electrodes using the standard potassium ferri-ferro cyanide redox probe of 10 mM. A) CV for carbon derived from pristine (black) and modified resin in two different concentrations (red, blue) at 10 mV/s scan rate B) EIS for electrodes fabricated with (red) and without iron at 0.1 wt.% (black).

Flexible photonic integrated circuit technology and characterization platform

Franz Tank [a], Julia Wecker [b], Chris Stoeckel [a,b], Christian Helke [a,b], Alexey Shaporin [b], Joerg Martin [b], Sebastian Schermer [b], Toni Großmann [b], Karla Hiller [a,b], Danny Reuter [a,b], Micha Haase [a,b], Alexander Weiß [b,]

[a] Chemnitz University of Technology, Center for Microtechnologies, Chemnitz, 09126, Germany
[b] Fraunhofer ENAS, Chemnitz, 09126, Germany
e-mail: franz.tank@zfm.tu-chemnitz.de

The authors present a flexible photonic integrated circuit technology and characterization platform (PIC-TCP) with silicon nitride Si_3N_4 as an optical transparent material with a spectral range from 400 nm to 2350 nm. The PIC-TCP is able to vary a large number of chip designs and characterize the photometric and spectral parameters automatically on wafer level scale with a minimum impact on time and resources. The flexible PIC-TCP is realized by using an automatic wafer prober with fibers and grating couplers based optical characterization setup. An efficient optical coupling of optimized grating structures is needed for this PIC-TCP, which includes a precise fabrication of subwavelength structures.
The authors present a technology flow for a low tolerance fabrication of grating couplers with a deviation of $½ \cdot (m_t - t_t) = 3$ nm and a slope of 3.2° (figure 1). The functionality of the PIC-TCP is shown at a PIC device, optimized for 1550 nm wavelength, including the coupling elements, waveguides and a ring resonator structure (figure 2). The optical bench is placed on a wafer prober for automatic wafer level mapping (figure 3). The functionality of the PIC-TCP is shown exemplary at ring resonators with a high Q-factor of > 10000 (figure 4).

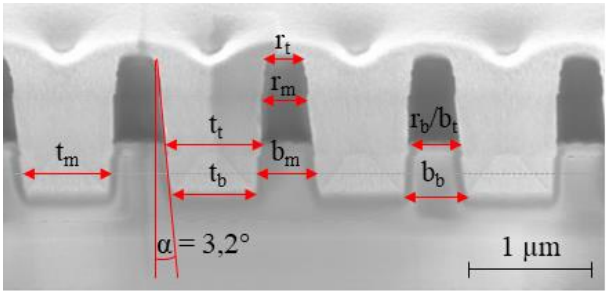

t_t = 794 nm b_t = 406 nm r_t = 282 nm
t_m = 739 nm b_m = 461 nm r_m = 344 nm
t_b = 655 nm b_b = 515 nm r_b = 406 nm

Figure 1: Cross section of a grating coupler for the PIC-TCP. Achieved trench width of 794 nm with a mask width (m_t) of 800 nm.

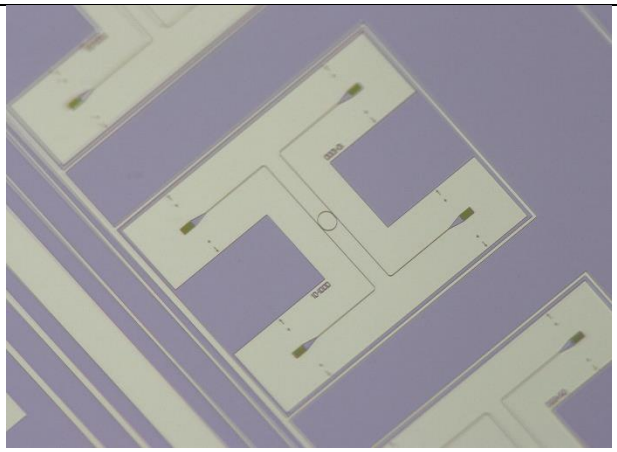

Figure 2: Microscope image of a PIC-TCP chip with grating coupler, waveguides and ring resonator.

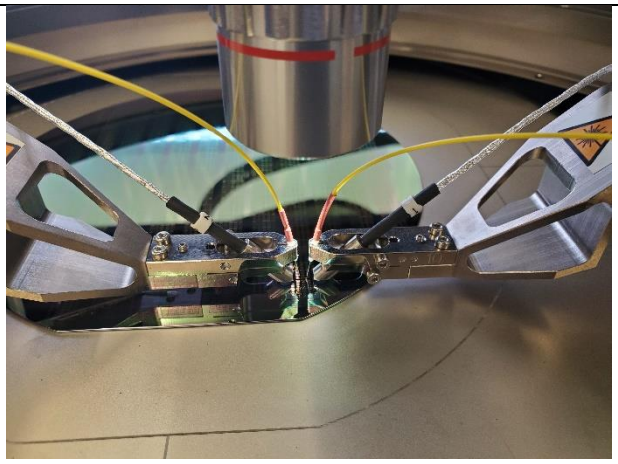

Figure 3: Wafer prober setup of the PIC-TCP.

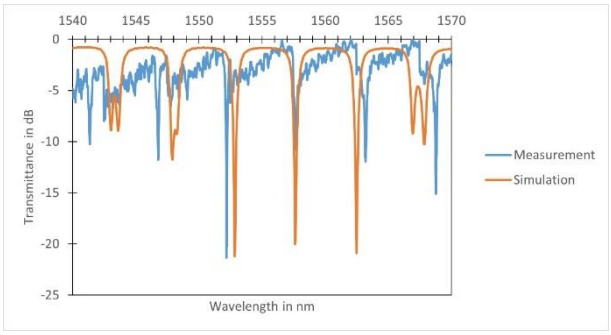

Figure 4: Comparison of the simulation and measurement of the optical transmission of a ring resonator PIC with a high q-factor > 10000 over the wavelength of 1540 nm to 1570 nm.

Plasmonic Metamaterial Absorber for MWIR and LWIR Bispectral Microbolometers

Alexander Litke [a], Elahe Zakizade [a], Marvin Michel [a], Sascha Weyers [a], Anna Lena Schall-Giesecke [a,b,c]

[a] Fraunhofer IMS, 47057 Duisburg, Germany
[b] University of Duisburg-Essen, 47057 Duisburg, Germany,
[c] Center for Nanointegration Duisburg-Essen (CENIDE), Carl-Benz-Strasse 199, 47057 Duisburg, Germany
e-mail: alexander.litke@ims.fraunhofer.de

Multispectral imaging in the infrared (IR) range has gained considerable attention due to its ability to visualize information from different regions of the electromagnetic spectrum. It enables applications such as remote gas sensing in the mid-wave infrared (MWIR) or simultaneous evaluation of different regions of the long-wave infrared (LWIR) for thermography. The development of suitable absorbers capable of selectively absorbing radiation in specific spectral ranges is crucial for multispectral uncooled imagers. In this work, we present Fourier transform infrared spectroscopy (FTIR) measurements and corresponding simulation results of fabricated plasmonic metamaterial absorbers (PMA) consisting of metal-insulator-metal-stacks (MIM) with periodically patterned top metal layers (Figure 1a). The FTIR-measurements show absorptances of more than 90 % for wavelengths ranging from the MWIR up to the LWIR. The choice of materials, deposition methods and patterning processes is suitable for the integration into the existing scalable nanotube microbolometer technology of Fraunhofer IMS (Figure 1b). The fabrication process is CMOS-compatible and carried out on 8-inch wafers.

MIM-PMAs were fabricated and evaluated with respect to their dimensions and applied dielectrics. Six patch sizes and SiO_2, Al_2O_3 and Ta_2O_5 as three dielectrics with different refractive indexes were used (Figure 1c). Figure 2a depicts exemplary FTIR-measurements and simulation results of PMAs with a patch size of 1.06 µm, which show distinct peaks with good agreement between FTIR-measurement and simulation. In Figure 2b the peak wavelengths of all fabricated PMAs are plotted as a function of their patch size. The spectra show high absorption maxima in a wavelength range from 2 µm to 9.5 µm, an interval more than 2 µm larger than reported in previous publications [1, 2]. Additional analytical calculations of the TM_{010}-mode using the Transmission Line Model (TLM) for microstrip antennas [3] show good qualitative agreement with the measurement results and the numerical simulations (Figure 2b, dotted lines), thus providing insight into the underlying physical principles: The wavelength of the absorption peak is a function of the patch size as well as the refractive index of the used dielectric. Accordingly, the control of geometry and material of MIM-PMAs enables a targeted selection of the absorption wavelength in both the MWIR and LWIR range depending on the intended application.

Furthermore, we fabricated bispectral MIM-PMAs consisting of patches with two different patch sizes arranged in a chessboard pattern (Figure 3b). The individual fields of this pattern correspond to the 12 µm nanotube microbolometers in shape and size. FTIR-measurements of these bispectral PMAs are demonstrated in Figure 3a. Two distinct absorption maxima marked as A and B in case of SiO_2 can be seen for each of the used dielectrics. In order to investigate the electric field distribution, numerical full wave simulations were performed. Figures 3c and 3d show the absolute values of the electric field on a cutting plane inside of the dielectric at wavelengths of 2.2 µm (A) and 3.3 µm (B). The field distributions provide evidence of the locally assignable origins of the peaks at the respective patches.

Overall, it was demonstrated that the fabricated PMAs exhibit absorptances of more than 90 % in a range from MWIR to LWIR depending on the lateral size of the patches and the refractive index of the dielectric. Bispectral PMAs have absorption spectra with two distinct maxima. Further developments aim at integrating the structures in microbolometers to enable multispectral imaging using an uncooled imager technology.

[1] T. Maier et al., Optics Letters 35 (2010) 3766.
[2] E. Zakizade et al., Proc. SPIE 12271 (2022).
[3] C. A. Balanis, Antenna theory: Analysis and design, Fourth edition (Chichester, West Sussex: Wiley Blackwell, 2016).

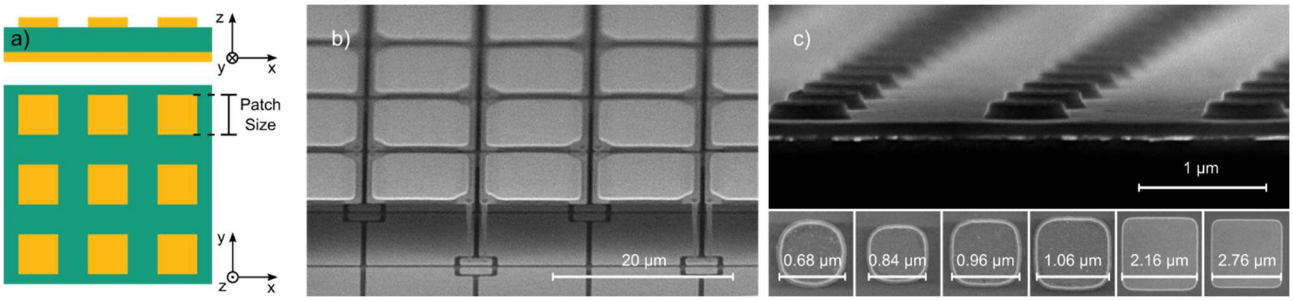

Figure 1. a) Schematic of a MIM-PMA with square-shaped micropatches as top layer. **b)** SEM-picture of Fraunhofer IMS' scalable nanotube microbolometers. **c)** SEM-pictures of the fabricated MIM-PMAs showing an aerial view as well as patches with all six sizes manufactured.

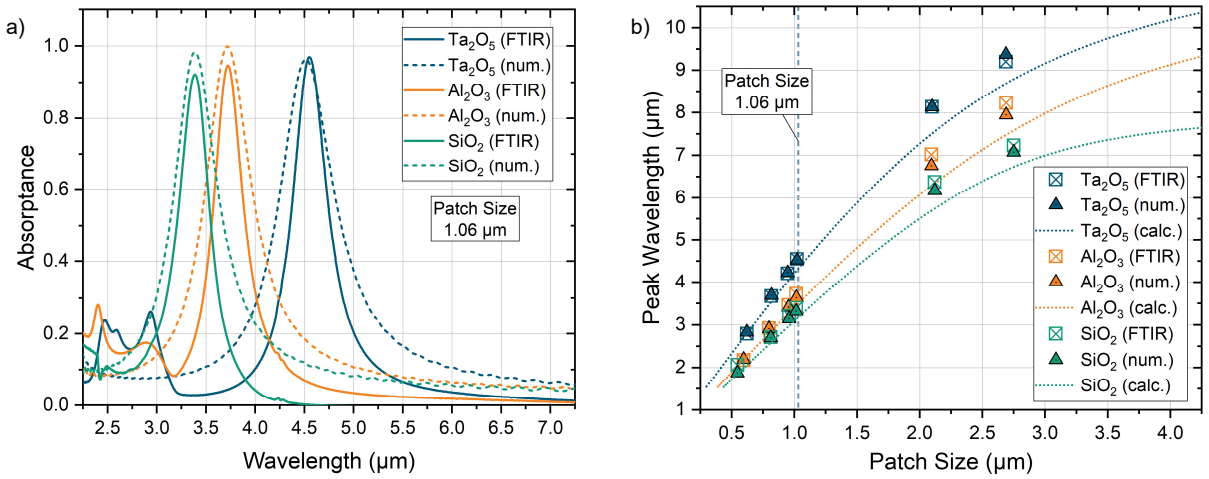

Figure 2. a) Comparison of the absorption spectra of MIM-PMAs with a patch size of 1.06 µm and three different dielectrics. FTIR-measurements (solid lines) as well as numerical simulations (dashed) are plotted. **b)** Peak wavelength as a function of patch size. FTIR-measurements, numerical simulations and results of analytical calculations using TLM are shown for all fabricated PMAs. The vertical dashed line marks the peaks of the spectra shown in a).

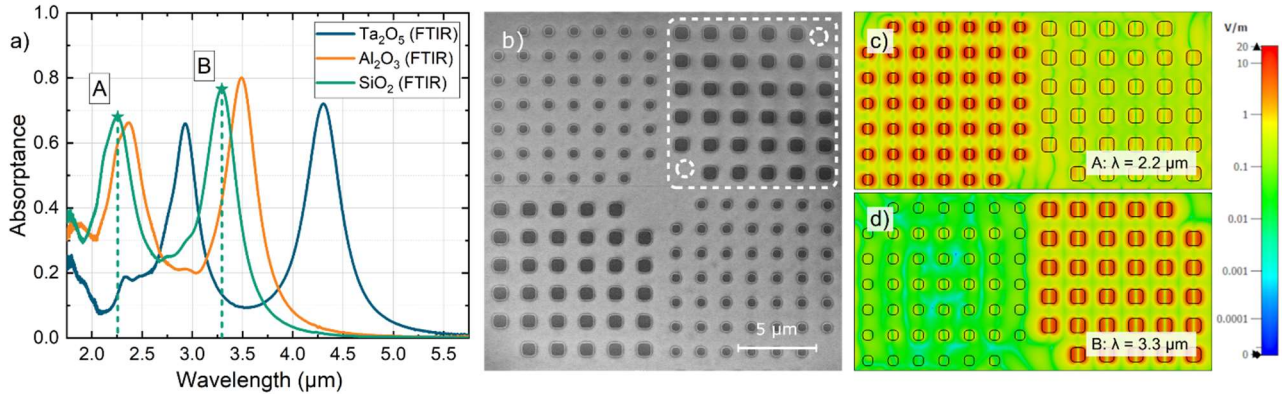

Figure 3. a) FTIR-measurements of the fabricated bispectral MIM-PMAs. Two distinct peaks can be seen for each dielectric. **b)** SEM-picture of the bispectral MIM-PMAs consisting of patches with two different sizes. The shape of one nanotube microbolometer is indicated in the upper right corner. **c)** and **d)** Simulated electric field distributions inside the dielectric at specific wavelengths, corresponding to the peaks marked as A and B in a). The distributions provide evidence of the locally assignable origins of the peaks.

Liquid crystal integrated multifunctional metasurfaces for photonic security platform

Gyeongtae Kim [a], Inki Kim [a], Jaehyuck Jang [b], Junsuk Rho [a,b,c]

[a] Department of Mechanical Engineering, Pohang University of Science and Technology (POSTECH), Pohang 37673, Republic of Korea
[b] Department of Chemical Engineering, Pohang University of Science and Technology (POSTECH), Pohang 37673, Republic of Korea
[c] National Institute of Nanomaterials Technology (NINT), Pohang, 37673, Republic of Korea
e-mail: jsrho@postech.ac.kr

In the information age, information security is very important before entering a hyperconnected society such as virtual reality. However, individual technological capabilities have also increased rapidly, resulting in a surge in counterfeiting technologies and attempts over the past few decades, for example, traditional optical security systems such as fluorescent materials and holograms are easily forged by digital printers. On the other hand, metamaterials have emerged with the recent development of nanofabrication, and their application as security systems has become active. Metamaterials are artificial materials made by arranging structures smaller than the wavelength of light, and have been widely studied because they can implement unusual light properties that have never been before by chemical properties of materials. Metasurfaces, a two-dimensional form of metamaterials, can control the amplitude, phase, and polarization of incident light, and many studies have shown that high-resolution structural colors, holograms, and polarization encoding are possible with metasurfaces [1]. However, previously implemented metasurfaces were expected to have numerous applications, but in fact, there are many limitations in actual applications because they are passive types after the device is fabricated. Some of the previously reported active metamaterials in the visible light were operated based on temperature, but practical applications are challenging due to the high price of active materials and difficulties in the process. On the other hand, liquid crystal is inexpensive, and can be operated at high speed through voltage. Liquid crystal has optical anisotropy, so it is possible to control refractive index and dielectric constant according to the applied voltage.

Here, we proposed liquid crystal-integrated multifunctional metasurfaces exhibiting up to four reflective spectra under white light, resulting in a high-resolution color-printed image. At the same time, if a laser light source is incident on the same metasurface, a polarized hologram which contain nine different polarizations is projected at far-field (Figure 1). To encode multiple holographic images with different polarization states, we adopt a pixelated metasurface to digitize a set of retrieved phase distribution from the image into a single meta-surface. These superpixels consist of four phase gradient meta-atomic groups that rotate clockwise or counterclockwise. The combination of groups of meta-atoms determines the polarization state of the reconstructed image covering entire Poincare sphere. The geometric parameters, i.e., length, width and in-plane rotation angle of anisotropic meta-atoms are designed to impart both spatially varying phase distribution and reflection spectrum, exploiting specifically designed geometric and propagation phase. Then, liquid crystal is integrated on multifunctional metasurfaces to actively manipulate polarization state of each component holographic images (Figure 2). The proposed multi-channel active metasurface-liquid crystal platform is a new optical device and has an important meaning in itself and is expected to be able to convert most of the passive metasurfaces into active [2]. As proof of concept, we devise an electrically tunable optical security platform using a multifunctional metasurface integrated with a liquid crystal. The optical security platform is double encrypted: a color print image decipherable by camera scan provides the first key and that information is used to fully unlock the double encrypted information via the projected vectorial holographic image as shown in Figure 3. These electrically tunable optical security platforms will provide a new path toward IoT sensors for security and anti-counterfeiting applications [3].

[1] G. Yoon et al., *ACS Nano*. **12**, 6421-6428 (2018)
[2] I. Kim et al., *Adv. Mater*. **32**, 2004664 (2020)
[3] I. Kim et al., *Nat. Commun*. **12**, 3614 (2021)

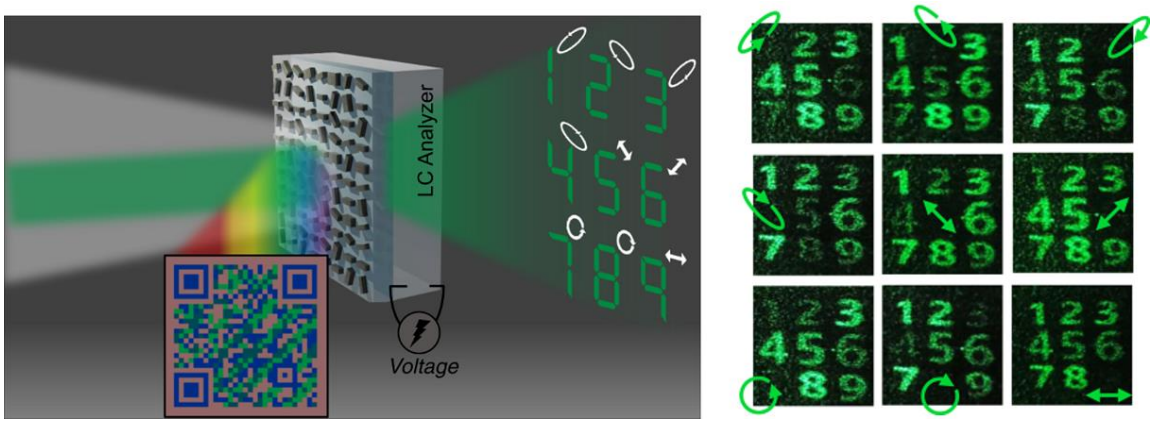

Figure 1. Dual mode metasurfaces with four reflective spectrum and nine polarization channels liquid-crystal for electrically tunable polarization states.

Figure 2. Fabricated liquid crystal-integrated metasurface device and optical setup to applying voltage.

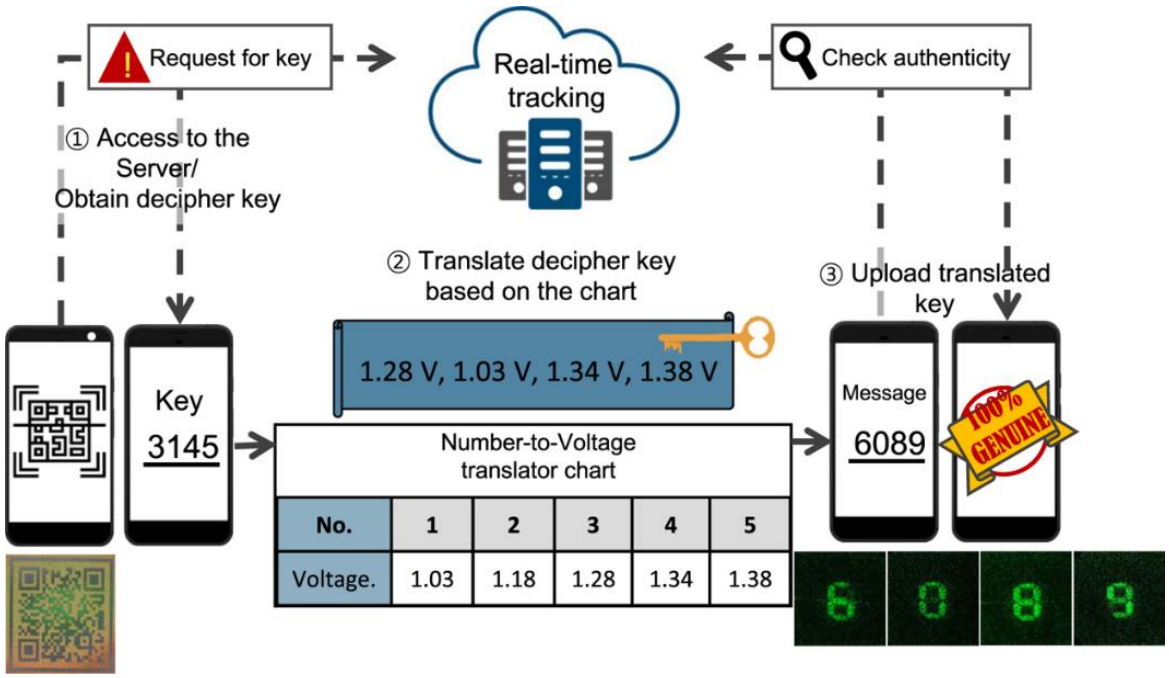

Figure 3. Two-level photonic security platform based on liquid crystal-assisted metasurface.

The state of the art and first glimpse of wood based printed electronics

Václav Procházka[a], Pavel Kulha[a], Thomas Geiger[b], Arjan Smit [c],André van Zomeren[c]

[a]PROFACTOR GmbH, Steyr, 4407, Austria
[b]Empa, Laboratory for Cellulose & Wood Materials, Überlandstrasse 129, 8600 Dübendorf, Switzerland
[c]TNO BCT group, Westerduinweg 3, 1755 LE Petten, The Netherlands#

*e-mail: vaclav.prochazka@profactor.at

Electronics manufacturing currently poses significant environmental pressures, such as resource scarcity, energy-intensive processes, and electronic waste accumulation. To address these concerns, the concept of green electronics has emerged, encompassing low-impact materials, energy optimization, and additive manufacturing. The HyPELignum project aims to demonstrate net-zero carbon emissions in electronics manufacturing through a holistic approach. By utilizing wood and wood-derived materials, which offer technical versatility and a low environmental footprint, the project aims to unlock the potential of additive manufacturing. HyPELignum will develop greener inks, adhesives, substrates and coatings, and introduce circularity through sustainable product design and a novel separation concept for improved recyclability. This paper focusses on the development of wood-based printed circuit boards (PCB) and the first attempts to print electronics on these important (or sustainable?) bio-based components (Fig.1).

Fractionation of a beech wood feedstock sample was performed using the Fabiola™ process (fractionation of biomass using low-temperature acetone), which applies mild process conditions [1] to obtain a lignin-rich cellulose pulp for the bio-based PCB (Figure 1) and a high purity and high-reactive lignin as input for: (i) the catalytic synthesis of fine chemical (inks and coating/impregnating resins), (ii) as polymeric (binder) in conductive inks (iii) as building block in the preparation of bio-based fire retardants. The biomass fractionation process has been optimized, particularly with regard to improving lignin yield and quality for these specific applications. In recent years, bio-based feedstock has been demonstrated as a valuable replacement of petroleum derived chemicals in the production of, among others acrylic acid, methacrylic acid as well as their esters. For example, production of acrylic acid via a catalytic conversion of glycerol [3] or lactic acid [4] has been reported while catalytic decarboxylation of itaconic acid or citric acid has been proposed for methacrylic acid production [5]

One intermediate product of the Fabiola-process is pulp with a high residual lignin content, which was disintegrated and processed into ligno cellulose nano-fibrils (l-CNF). A first printed ecoPCB demonstrator was fabricated based on l-CNF and is shown in Fig. 2. The substrate was formed by dewatering and hornification of the l-CNF under elevated temperature and pressure [6]. The Surface of the substrate provided non-soaking, stable properties to enable direct print with silver nanoparticle ink (i50TM from PV Nanocell), printed on Süss LP50 R&D inkjet printer. The bridge over NFC antennas consists of Tiger Black Ink for inkjet printing, which was printed on Stratasys Polyjet 3D printer. The integrated circuit for energy harvesting via NFC has been assembled, this provides enough power to lit the HyPELignum logo embedded into transparent Veroclear® layer preventing oxidation.

References

[1] Smit and Huijgen, Green Chem., 2017,19, 5505-5514. https://doi.org/10.1039/C7GC02379K
[2] Improved Process for the Organosolv Treatment of Lignocellulosic Biomass, Publication Number: WO2015/009145
[3] S.T. Wu et al., Catal. Rev. - Sci. Eng. 62 (2020) 481–523 https://doi.org/10.1080/01614940.2020.1719611.
[4] E. V. Makshina, et al., ChemCatChem. 11 (2019) 180–201. https://doi.org/10.1002/cctc.201801494.
[5] A. Bohre, et al., ACS Sustain. Chem. Eng. 9 (2021) 2902–2911. https://doi.org/10.1021/acssuschemeng.0c08914.
[6] Geiger, T. et al., Proceedings of the ECCM20, Lausanne, Switzerland (2022) 1458, https://doi.org/10.5075/epfl-298799_978-2-9701614-0-0

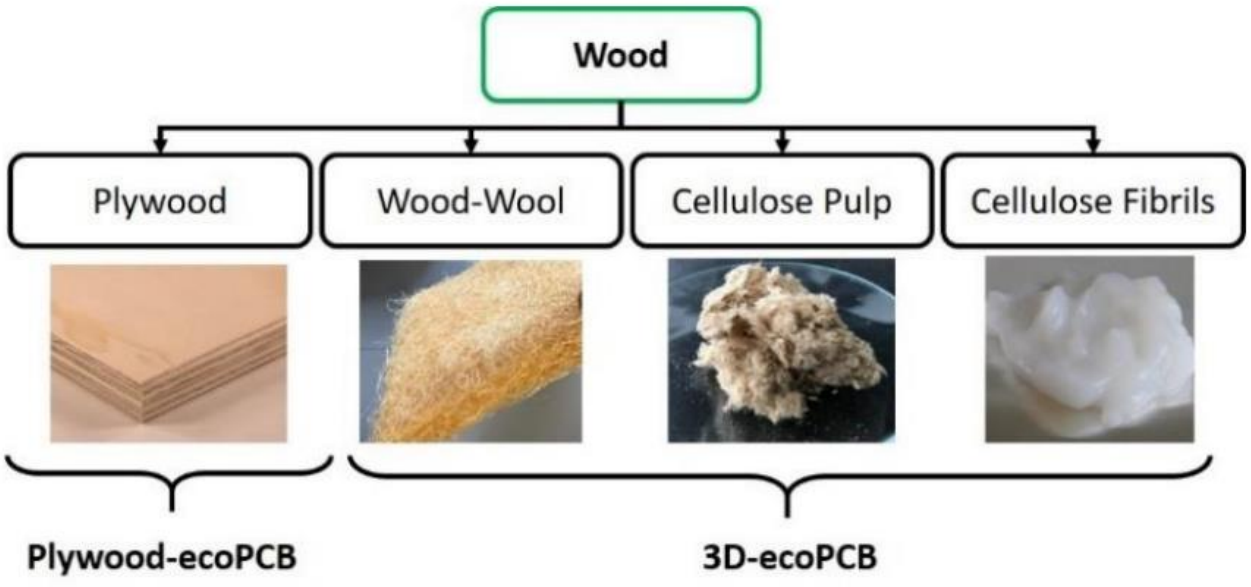

Figure 1. The schematic of wood products and derivates and their following use.

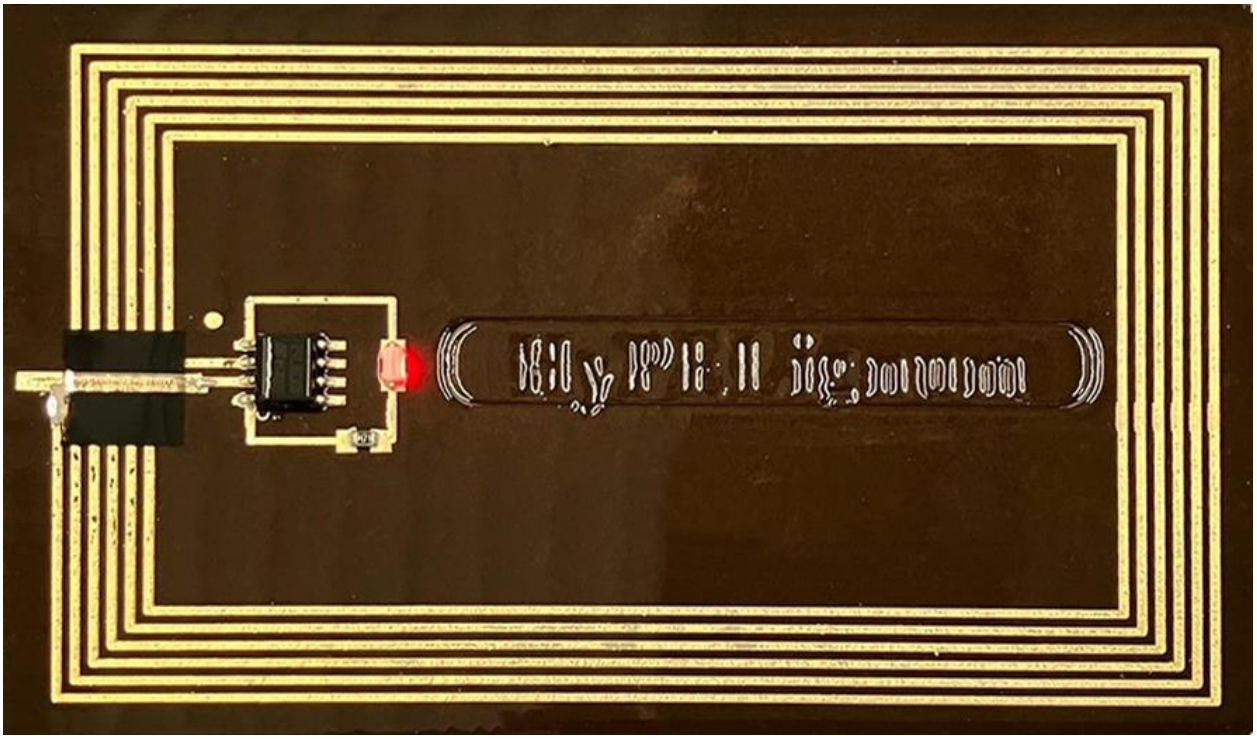

Figure 2. NFC energy harvesting PCB on (beech) wood-based lignocellulose board, created by Eleanor pre-extraction, Fabiola™ fractionation, hot-press and additive manufacturing.

Micro/Nano Engineering for the Life Sciences - Papers

High resolution µGrid-LED array with 15 µm pixels for optogenetic research

Eric Klein [a], Oliver Paul [a,b], Patrick Ruther [a,b]

[a] Department of Microsystems Engineering (IMTEK), University of Freiburg, Germany
[b] BrainLinks-BrainTools Center, University of Freiburg, Germany
e-mail: eric.klein@imtek.de

Purpose of the work
Micro light-emitting diodes (µLEDs) are among the most promising tools in optogenetics for precisely delivering light into tissue. State-of-the-art µLEDs realized on flexible substrates using laser lift-off are typically 50×50 µm^2 in size and arranged at a pitch of 100 µm or more [1,2]. Reliably realizing µLEDs with a footprint reduced to 15×15 µm^2 would enable researchers to precisely target much smaller brain structures than is currently possible, i.e. individual cells or even subcellular structures. This will increase the lateral resolution in optical stimulation and provide new opportunities in mapping neuronal circuits and investigating the interaction between cells. Furthermore, on a larger scale, the use of smaller µLEDs minimizes untargeted optical interactions by avoiding the unintentional stimulation of surrounding tissue. It is further expected to reduce tissue damage due to smaller implant dimensions.

Downsizing µLEDs on flexible polymer substrates to 15×15 µm² requires a lateral resolution in microfabrication way beyond the targeted µLED size. In particular n- and p-contacts of smallest footprints as well as the µLED contour itself have to be realized and aligned with respect to each other on non-planar substrates with structures typical 5 µm in thickness.

Novelty
In this study we present a novel µLED layout based on an established microfabrication process used so far for µLEDs with footprints of ≥50×50 µm² [3]. The process allows to decrease the emitter size of the µLEDs down to 15×15 µm², as schematically shown in Fig. 1. The µLEDs are arranged as a 3×3 grid array with a pitch of only 20 µm. The process flow of these µGrid-LEDs is summarized in Fig. 2. The two-layer interconnection lines and vias enable high-density connections to fit the pitch of the µGrid-LED array. While the lower metal layer (Metal 1) serves the interconnection within the µGrid-LED through electroplated vias, the main metal layer (Metal 2) runs along the slender probe shaft interfacing the probe to the peripheral instrumentation (Fig. 1(B)). In order to provide the highest possible amount of stimulation patterns, all µLEDs are independently controllable using a common n-contact, indicated by the blue line in Fig. 4.

Results
The µLED pixels provide a peak wavelength of 460 nm. They deliver an optical emittance of approximately 310 mW/mm² at 0.7 mA, corresponding to an optical power of 70 µW per µLED (Fig. 5 (A)). This emittance is comparable to that of a standard 50×50 µm² µLED for current densities below 2 A/mm^2. The emission angle of the miniaturized µLED is thereby reduced by up to 4° compared to our standard 5050 µm² µLEDs, as shown in Fig. 5 (B). The individual addressing capability of the µGrid-LED not only allows illumination of different sites but also enables the display of various patterns, as successfully demonstrated in Fig. 6.

References

[1] Gossler et al., J. Phys. D: Appl. Phys., 2014, vol. 47, pp. 205401
[2] Klein et. al., Front. Neurosci. 2018, vol. 12, pp. 569
[3] Klein et. al., IEEE MEMS'22 Conf., 2022, pp. 114-117

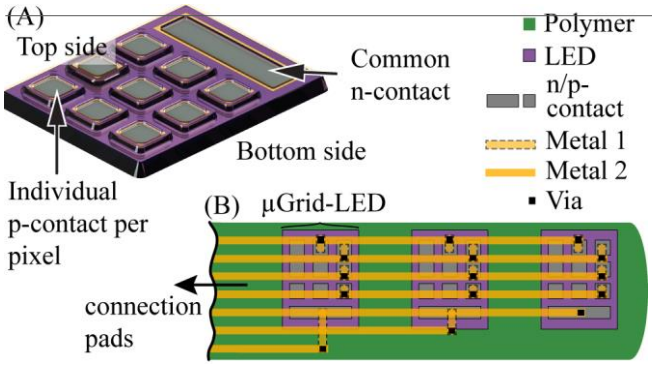

Figure 1: (A) Schematic of a µGrid-LED array with 3×3 pixels and (B) three µGRID-LEDs integrated in a flexible polymeric substrate, exemplarily showing the interconnection of the first four pixels.

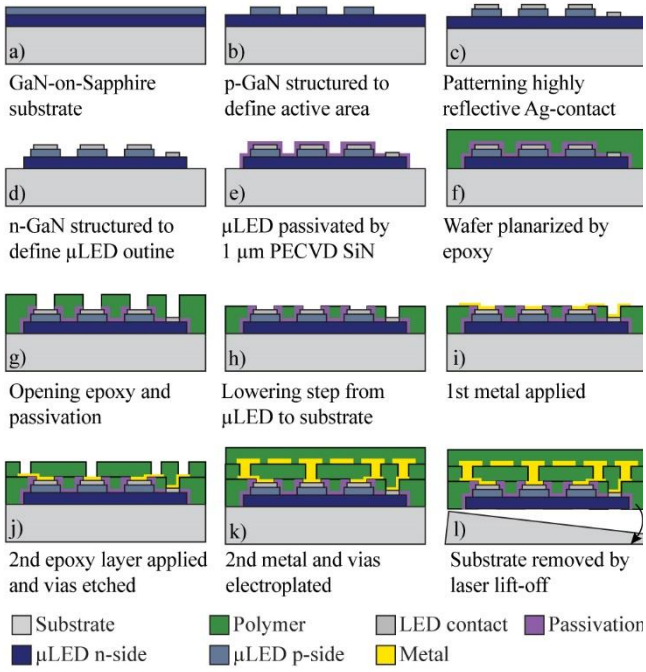

Figure 2: Schematic fabrication process for µGrid-LED arrays integrated into a flexible polymer substrate. In a) to e) µGrid-LEDs are fabricated while from f) to l) the flexible polymer substrate and the electrical interconnections are made.

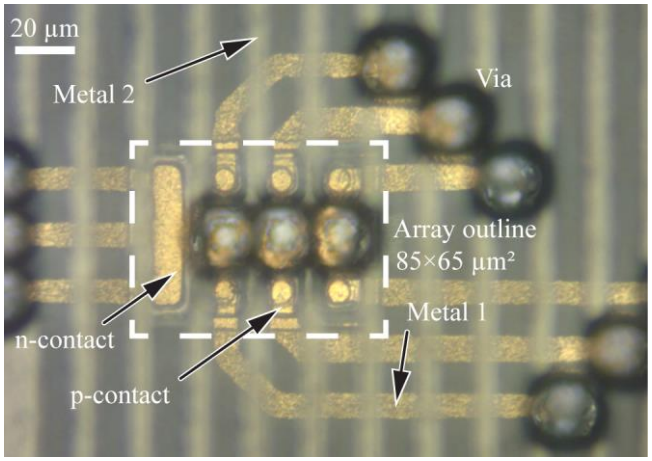

Figure 3: n- and p-interconnections interfacing the µGrid-LED with 2 metal layers (top view).

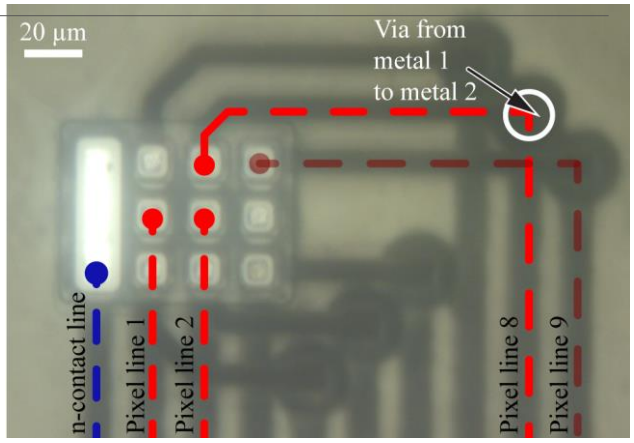

Figure 4: Addressing scheme of the µ-Grid LED (bottom view through the sapphire substrate).

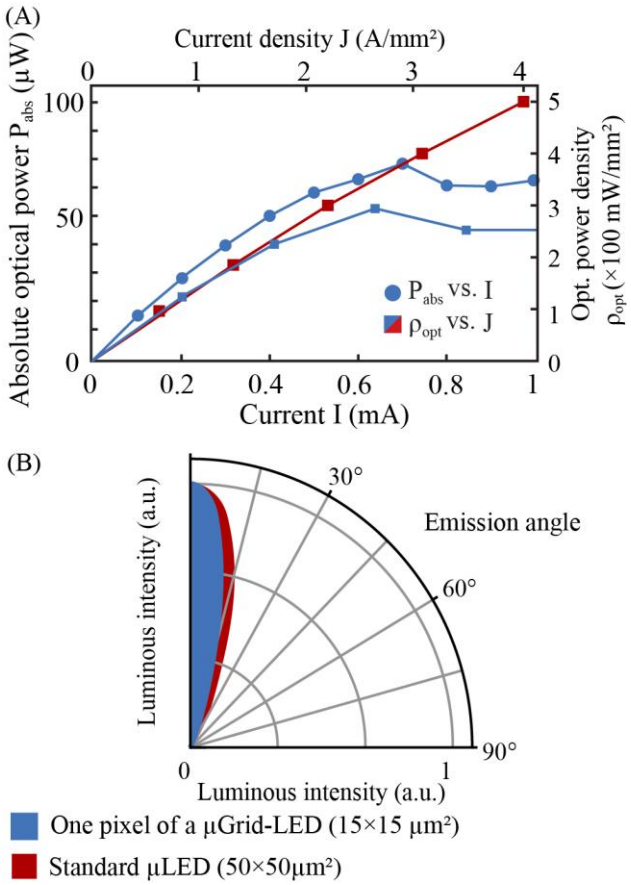

Figure 5: Optical characteristics of a single pixel compared to a standard 50×50 µm² µLED.

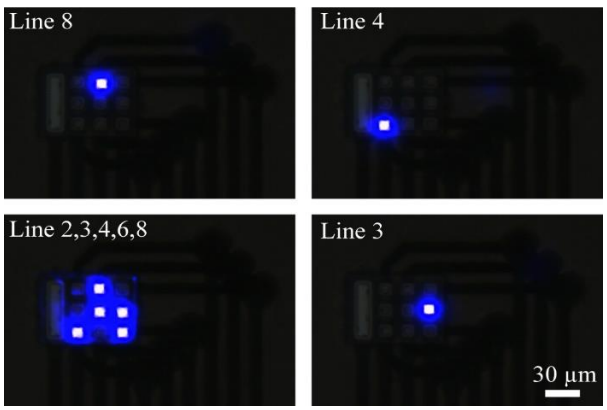

Figure 6: Different pixels active to stimulate different patterns.

A Microfluidic-Based Quantitative Analysis System for the Multiplexed Genetic Diagnosis of Viral Infections in Multiple Samples

Daigo Natsuhara [a], Shunya Okamoto [a], Moeto Nagai [a], Masaru Ihira [b], Takayuki Shibata [a]

[a] Toyohashi University of Technology, Toyohashi, 441-8122, Japan
[b] Fujita Health University, Toyoake, 470-1192, Japan
e-mail: d-natsuhara@mems.me.tut.ac.jp

A risk management strategy to address emerging and reemerging viral infectious diseases is a pressing global public health challenge. Early detection of viruses through rapid and accurate diagnostic technologies is preventing the spread of infection. Therefore, we have been developing a microfluidic diagnostic device for the multiplexed genetic diagnosis of multiple infectious viruses based on the loop-mediated isothermal amplification (LAMP) method in a single operation [1]. In this study, we developed a microfluidic-based quantitative analysis system for the detection of multiple nucleic acid targets in multiple samples. We demonstrated the ability of the developed system to assess the amounts of the DNAs of human herpesviruses.

Figure 1a shows the fabricated polydimethylsiloxane (PDMS)-based microfluidic device for the simultaneous diagnosis of multiple viral infections in two individual samples. The size of the fabricated device was approximately 35 mm in diameter. The five microchambers arranged in a circle were interconnected via two independent rectangular microchannels (202 μm in width and 109 μm in height). After introducing a mixture of nucleic acid (DNA or RNA) sample and gene amplification reagents using an electric pipette, the mixture was efficiently mixed while flowing through the mixing region. Subsequently, it was sequentially dispensed into an array of multiple reaction chambers by a pair of passive valves (Fig. 1b). After filling the reaction chambers, the device was immersed in a hot-water bath to amplify targeted nucleic acids through the LAMP reaction using primer sets that had been fixed in each reaction chamber (≈ 3 μL) beforehand.

Figure 2a is a typical experimental result showing the DNA amplification of herpes simplex virus type 1 (HSV-1) and type 2 (HSV-2) in reaction chambers connecting to each independent microfluidic network. Two types of specific LAMP primer sets (0.5 μL each) designed to amplify the DNA targets were pre-spotted and dried in each reaction chamber (Nos. 1, 3, 6, and 8 for HSV-1; Nos. 2, 4, 7, and 9 for HSV-2), whereas no primers were pre-spotted in chambers 5 and 10 as a negative control. The HSV-1 DNA sample mixed with the LAMP reagents (DNA concentration: 10^6 copies/μL) was introduced into the upper five reaction chambers. Meanwhile, the HSV-2 DNA sample (10^6 copies/μL) was introduced into the lower five microchambers. After dispensing the sample/reagent mixtures into all microchambers, the LAMP assay was conducted at 63°C for 60 min. Hydroxy naphthol blue (HNB) was used as an indicator for the visible colorimetric detection of the LAMP reaction. As expected, positive reactions, manifested by a color change of HNB from violet to sky blue, were clearly observed in the chambers 1 and 3 (HSV-1) after running the assay for 20 min, and subsequently, the chambers 7 and 9 (HSV-2) after 30 min. To obtain DNA amplification curves, the time-lapse images of the device were taken every 30 s during the LAMP assay using a home-made imaging equipment, and then a quantitative analysis of the time-dependent color change of each microchamber was performed by a home-made software. As shown in Fig. 2b, the change of the hue angle (Δh) in the CIELAB color space was plotted as a function of the reaction time, and then fitted precisely with a modified sigmoidal function.

To validate the availability of the developed quantitative analysis system, LAMP assays were performed using HSV-1 samples with different DNA concentrations ranging from 10^2–10^7 copies/μL. Figure 3a shows the obtained DNA amplification curves of different DNA concentrations of HSV-1. To enable quantitative LAMP analysis of targeted genes, the threshold time (Tt), which is defined as the initiation time of the detectable amplification reaction, was calculated as the maximum value of the second derivative of the fitting curves. Figure 3b shows standard curves for HSV-1 specific DNA, in which the calculated Tt values were plotted as a function of DNA concentration in a sample (n = 4). A strong negative correlation could be obtained ($R^2 = 0.970$) in the microfluidic devices (solid circle symbol). In addition, the Tt values obtained in the devices (3 μL each) were comparable to those (solid triangle symbol) obtained by real-time turbidity measurements of the conventional LAMP assays in the PCR tubes (25 μL each).

This research was partially supported by “Knowledge Hub Aichi”, Priority Research Project from Aichi Prefectural Government, Japan.

[1] D. Natsuhara et al., Sci. Rep. 12 (2022) 12852.

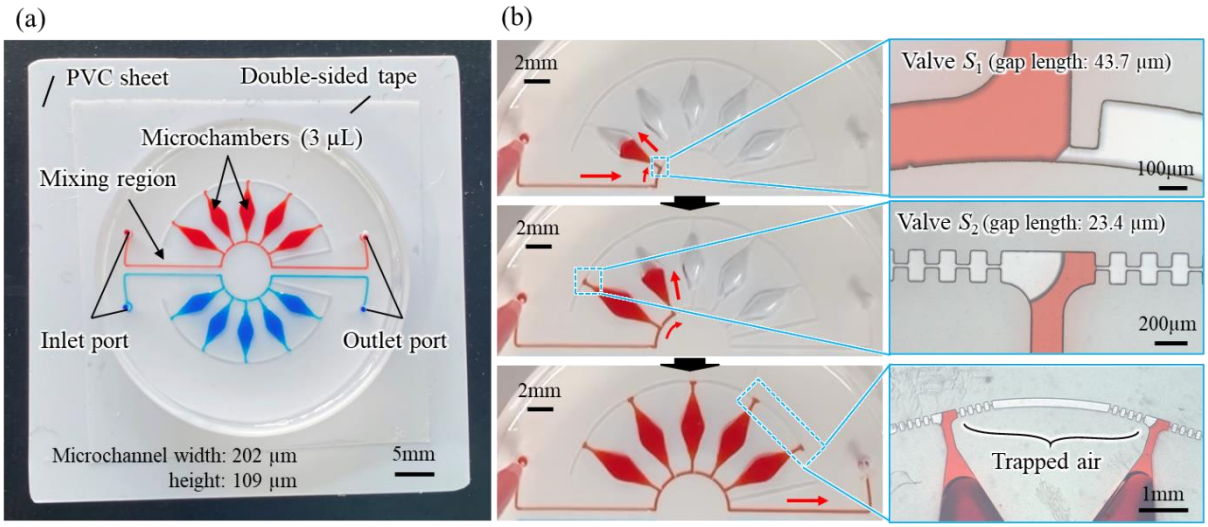

Figure 1. (a) Photograph of the fabricated PDMS microfluidic device for the diagnosis of multiple infectious disease in two samples. (b) Sequential dispensing of red-colored water into multiple chambers.

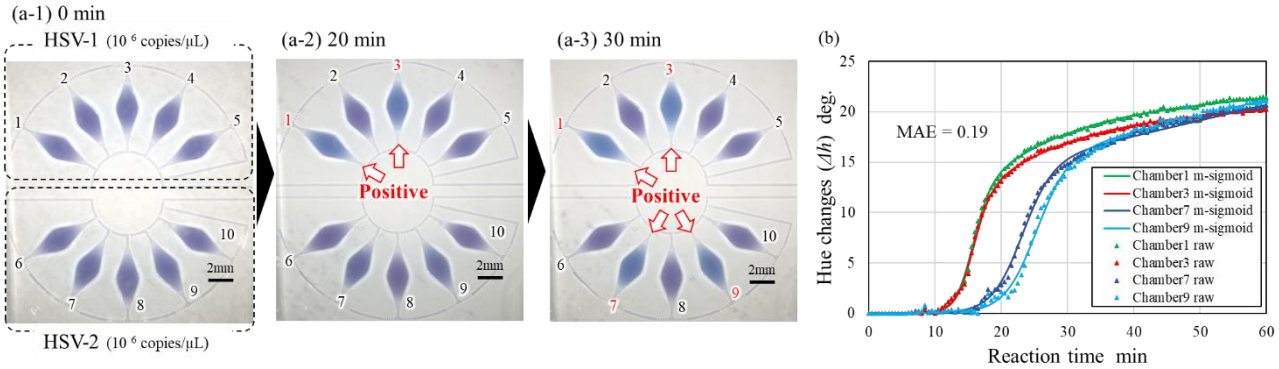

Figure 2. (a) Time-lapse images showing LAMP assay for the detection of HSV-1 and HSV-2 DNA (DNA concentration of 10^6 copies/μL). (b) DNA amplification curves fitted with a modified sigmoidal function.

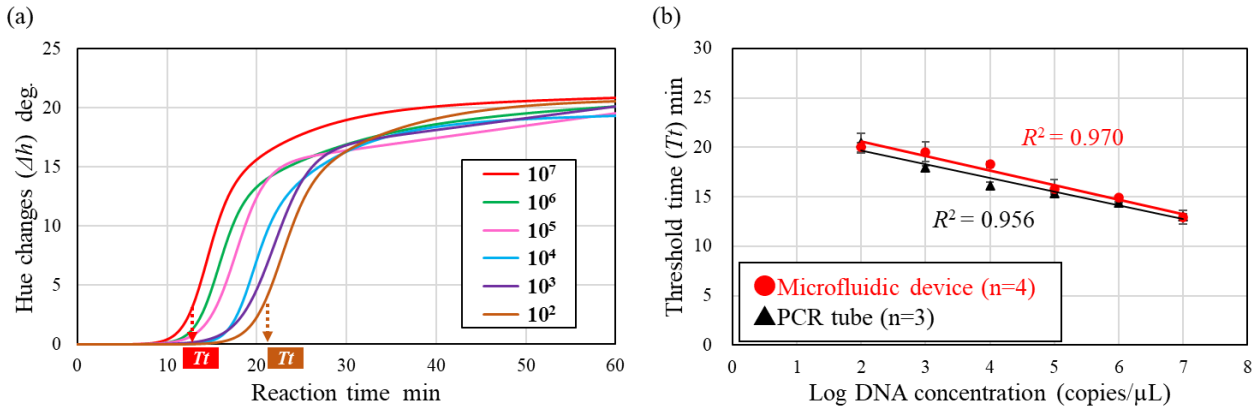

Figure 3. (a) DNA amplification curves of HSV-1 samples (10^2–10^7 copies/μL) fitted with a modified sigmoidal function. (b) Relation between viral DNA concentration and threshold time (*Tt*)

Motor protein driven, active, on-chip transport and detection of nanoscaled, biomolecular cargo

Tim Erichlandwehr[1,2], Marko Usaj[3], Alf Månsson[3], Irene Fernandez-Cuesta[1]

[1] Institut für Nanostruktur- und Festkörperphysik, Universität Hamburg, 20146 Hamburg, Germany
[2] Deutsches Elektronen-Synchroton (DESY), 22607 Hamburg, Germany
[3] Department of Chemistry and Biomedical Sciences, Linnaeus University, Kalmar, Sweden
e-mail: tim.erichlandwehr@desy.de

The combination of lab-on-a-chip platforms and on-chip sensors would have great potential for biomedical applications or environmental monitoring. The detection and controlled transport of small amounts of biomolecules remains a challenge. In this study, we investigate the integration of functional molecular motors with microfluidics to develop a hybrid and selective biochip platform. Motor proteins, such as Kinesin and Myosin, are able to facilitate motion from the nano- to macroscale and offer the potential to continuously capture molecules, while the fluidic circuit provides the ability to control and manipulate the liquid sample.[1][2][3] A device concept is sketched in figure 1. We coat hydrophobic surfaces with motor proteins that can propel actin filaments (AFs), by hydrolysis of ATP. These AFs can be funcationalized with biotin groups to capture analytes via a biotin-strepdavidin-biotin bridge. This way biotinylated biomolecules can be picked up by the AFs and transported to a site-of-interest by the motor proteins on the surface. The motor proteins need to be incubated on a hydrophobic surface to be in a conformation that allows for binding of AFs. The successful functionalizing of Si-based surfaces with motor proteins was achieved through gas-phase silanization with trimethylchlorosilane (TMCS), perfluoroctyltrichlorosilane (FOTCS), or perfluorodecyltrichlorosilane (FDDTCS) and was verified via water contact angle (WCA) measurements. The deposition of these silanes was done in a vacuum oven to allow for high-throughput sample preparation, compared to liquid silanization methods. We have developed a gas-phase silanization protocol that enables the functionalization of surfaces in a one-step process, in less than 30 minutes, with a variety of different silanes. For experiments, the WCA was adjusted to match the values used for similar studies in the literature.[4] The WCAs are shown in table 1. Another challenge during such capturing processes is the excessive binding of cargo to your transport shuttles, which leads to a termination of cargo transport. To combat this problem one can adjust the number of potential cargo binding sites. We successfully used myosin propelled, partially biotinylated actin filaments to selectively capture small fluorescently labeled DNA oligos. In Fig. 1 the capturing mechanism is schematically shown. Fig. 2 shows the selective binding of fluorescently labeled DNA molecules to AFs. Even after cargo loading, a significant fraction of filaments remain motile, which is essential for future application in on-chip diagnostic platforms. The preliminary fluidic chips for these measurements are fabricated using a simple UV-nanoimprint process from a master stamp, enabling the patterning of multiple levels and structure dimensions in less than 2 minutes. To address the challenge of maintaining filament motility during cargo loading, we have adjusted the number of "cargo binding sites" by using a ratio of biotinylated and non-biotinylated monomers during filament polymerization. Thus, this demonstrates the DNA capturing capabilities of motor protein-driven actin filaments, functionalized with biotin to enable cargo capture. Preliminary tests show that there is observable motility on flat Ormostamp structures, which enables its use during the fast, simple and cheap fabrication of fluidic devices for mobile applications.

REFERENCES:

[1] M. Persson, 1 Maria Gullberg, C. Tolf, A. Michael Lindberg, A. Månsson, A. Kocer "A Transportation of Nanoscale Cargoes by Myosin Propelled Actin Filaments," PLoS One. 8(2), Feb 21st 2013.

[2] P. Surendiran, C. R. Meinecke, A. Salhotra, G. Heldt, J. Zhu, A. Månsson, S. Diez, D. Reuter, H. Kugler, H. Linke, and T. Korten, “Solving Exact Cover Instances with Molecular-

MotorPowered Network-Based Biocomputation" ACS Nanosci. Au June 23rd 2022, 2, 5, 396–403.

[3] A. Salhotra, J. Zhu, P. Surendiran, C. R. Meinecke, R. Lyttleton, M. Ušaj, F. W. Lindberg, M. Norrby, H. Linke, A. Månsson, "Prolonged function and optimization of actomyosin motility for upscaled network-based biocomputation", New Journal of Physics, 23(8), 085005, Aug 16th 2021.

[4] F. W. Lindberg, M. Norrby, M. A. Rahman, A. Salhotra, H. Takatsuki, S. Jeppesen, H. Linke, A. Månsson "Controlled surface silanization for actin-myosin based nanodevices and biocompatibility of new polymer resists", Langmuir, 34(30), 8777-8784, July 3rd 2018.

[5] F. M. Esmek, T. Erichlandwehr, D. H.B. Mors, M. Czech-Sioli, M. Therrem, T. Günther, A.Grundhoff, N. Fischer, I. Fernandez-Cuesta "Real time, in-line optical mapping of single molecules of DNA", Bios and Bioel X, 9, 2021.

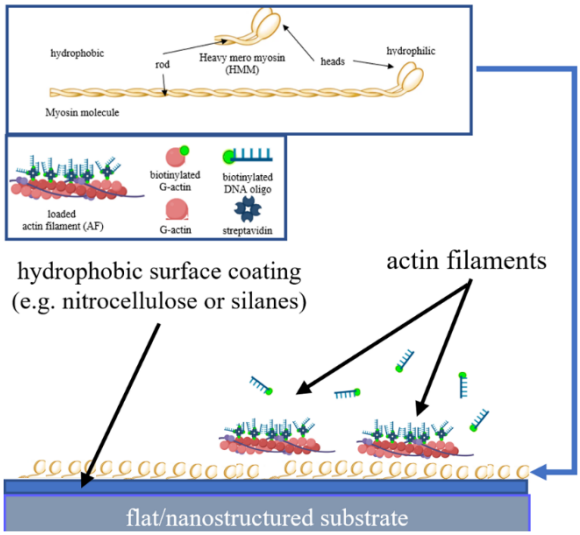

Figure 2: Schematic of basic cargo capturing platform. The substrate surface is coated with myosin II subunit heavy mero myosin (HMM). These molecules are produced by digesting full myosin II molecules with α-chemotrypsin and bind actin filaments, which can capture biotinylated cargo after incubation with streptavidin.

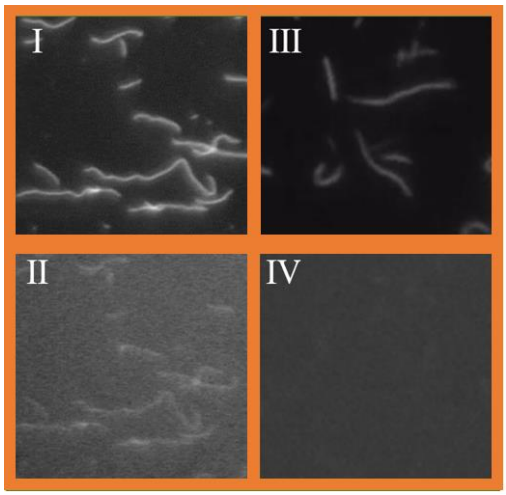

Figure 1: Fluorescence microscopy images of labeled actin filaments(AFs) using a CY3-filterset (I) and labeled DNA molecules loaded on the AFs imaged with a FITC-filterset (II). DNA cargo is visible along the entire filament. (III) and (IV) show a control sample without DNA cargo, imaged with the same filtersets, where just the filaments can be seen with the CY3- (III), but no signal is seen

Table 1: Summary of water contact angles (WCA) measured on glass surfaces after silanization. The used silane and silanization process parameters (Temperature and Pressure) are shown.

Silane	WCA [°]	Temperature [°C]	Pressure [mbar]
TMCS	83	22	150
FOTCS	90	50	400
FDDTCS	86	60	400

Adaptive resolution two-photon 3D printing with X-ray tomographic resolution optimization of ultracompact 3D microfluidics

Markus Lunzer [a], Andrew Nelson Butterfield [b], Konstantinos Karpos [c], Christian M. Schlepütz [d], Richard Kirian [c], Michael Heymann [b]

[a] UpNano GmbH, Vienna, 1030, Austria
[b] Institute of Biomaterials and Biomolecular Systems, University of Stuttgart, Stuttgart, 70569, Germany
[c] Department of Physics and The Biodesign Institute, Arizona State University, Tempe, AZ 85287, USA
[d] Swiss Light Source, Paul Scherrer Institute, Villigen, 5232, Switzerland
e-mail: markus.lunzer@upnano.com

Two-photon polymerization 3D printing (2PP) can build complex functional devices from submicron-scale volumetric units called voxels (Fig 1b) [1]. However, 2PP is a comparably slow method for generating bulk volumes due to its exceptionally high-resolution: a small voxel is scanned in a line-by-line fashion, hence print time scales with volume [2]. Faster printing can be achieved by increasing the rate of volume processed per time. This can be done by optical voxel enlargement: larger voxels can be spaced farther apart, thus fewer scan operations are required to polymerize a given volume per time resulting in faster print speeds, however, at the expense of print precision (Fig 1c). Nevertheless, in *adaptive resolution 2PP* precision is only applied in regions where it is structurally needed, increasing the throughput tremendously.
We demonstrate this method on the example of ultracompact 3D microfluidic devices, so-called gas dynamic virtual nozzle (GDVN) for serial fs-crystallography experiments (Fig 1a). A GDVN focuses a central liquid stream with an outer sheath of inert gas to generate a fine liquid jet with a diameter of only a few µm. These GDVNs deliver sample to X-ray free electron lasers by injecting crystal slurry as a fine jet into the X-ray interaction region (fig. 1a) [3]. X-ray beam pulses are just tens of femtoseconds long, brief enough to allow diffraction of the protein crystals by high-intensity radiation before they are vaporized. Thousands of diffraction patterns from separate, randomly oriented crystals are then combined to reconstruct the 3D structure [4].
The GDVN designs RN79 [5] (Fig 2a) and EuXFEL2012 [6] (Fig 3a) are fabricated at different *fine* and *coarse* print settings and combinations thereof. The CAD design is divided into regions of different print settings, with higher print speeds used where the lower precision doesn't impair functionality. For high resolution 3D print quality quantification synchrotron X-ray tomography (µCT) is applied, which gives valuable insights on both external and internal micro-features as well as surface topography. While scanning electron microscopy (SEM) is limited to viewing surface features, µCT can quantify fidelity and noninvasively reveal internal features (Fig 2b and c).
GDVN performance is characterized by jet measurements of length, speed and diameter, which are collected by analyzing jet images (Fig 2d). Representative phase diagrams showing the jet speeds and diameters for different gas and liquid flow combinations. The left edges of these diagrams, marked by the heavy lines, represent the drip-to-jet boundaries, which vary depending on the print settings used.
In refining regional print settings and hence the local resolution to match performance requirements ultra-rapid fabrication of functional devices becomes possible (Fig 3a and b). Such print time savings facilitate 2PP mass-production dramatically, as any loss in time is multiplied (Fig 3c).

[1] H.J. McLennan et al., Sci. Rep. 13 (2023) 562.
[2] M. Lunzer et al., Chem. Mater. 34 (2022) 3042−3052.
[3] D.P. DePonte et al., J. Phys. D. Appl. Phys. 41, (2008) 195505.
[4] H.N. Chapman et al., Nature 470, (2011) 73–78.
[5] R. Nazari et al. Opt. Exp., 28, (2020) 21749–21765.
[6] J. Knoška, et al., Nat. Commun. 11, (2020) 1–12.

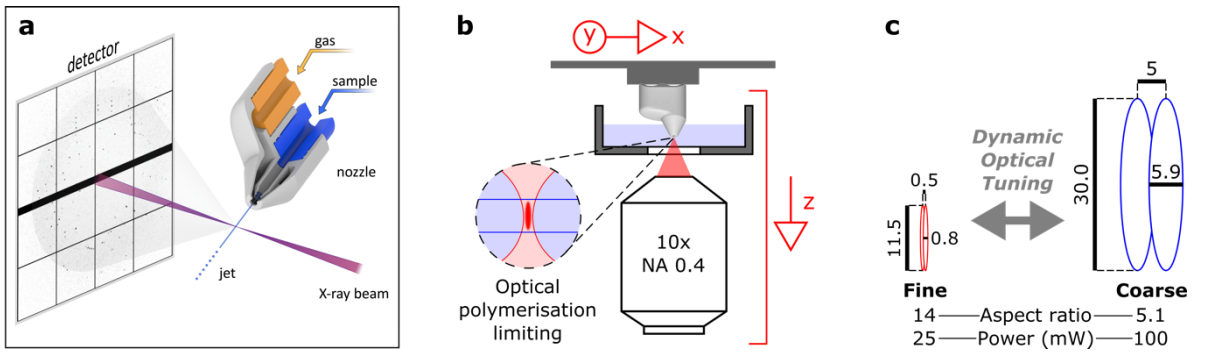

Figure 1. a) Micro-nozzles are critical devices in serial fs-crystallography experiments. Stable microjets are required to deliver protein microcrystals into the X-ray interaction region to obtain diffraction patterns. b) They can be produced using 2-photon lithography in Vat mode. c) By adjusting the voxel size and hatching distance, a choice between *fine* and *coarse* scan mode can be made on the fly to match local precision requirements. Lengths in µm.

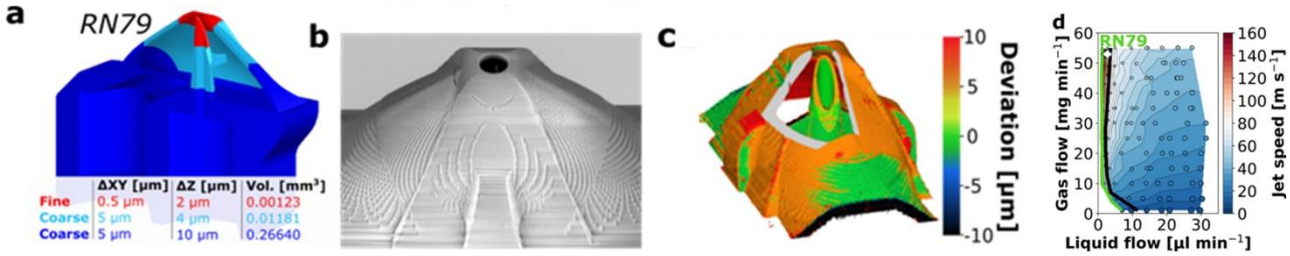

Figure 2. Throughput optimization of GDVN micro-nozzle RN79. a) CAD design of RN79 with assigned print parameter regions. (b) SEM and (c) µCT to validate accurate fabrication results. d) Jetting analysis confirm RN79 (green) to achieve a lower drip-to-jet boundary than reference EuXFEL2012 (black).

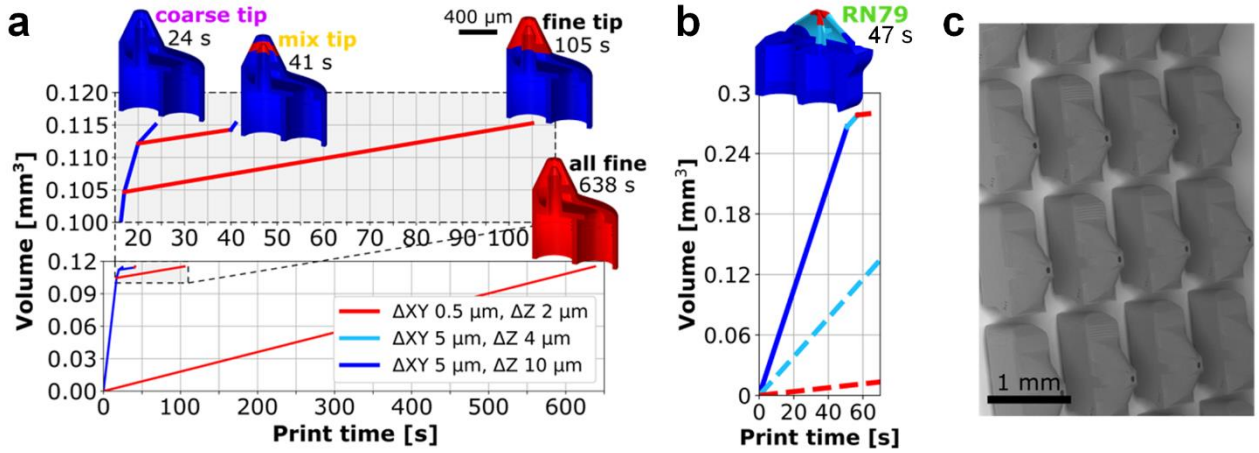

Figure 3. (a) In limiting high resolution *fine* mode voxels to only function-critical features fabrication time for EuXFEL2012 nozzles was reduced from over 602 to 33 s without compromising performance. (b) Time-optimized print settings yield high performing RN79 nozzles in only 63 s, compared to an all-*fine* mode print of 944 s. (c) Such print time savings facilitate mass-production vastly, as any loss in time is multiplied.

Tuning the mechanical properties and feature resolution of two-photon polymerized soft elastomeric 3D biomaterials for (neuro)mechanobiology

P.F.J. van Altena [a], A. Accardo [a]
[a] Department of Precision and Microsystems Engineering (PME), Delft University of Technology (TU Delft), Delft, 2628 CD Netherlands
e-mail: a.accardo@tudelft.nl

Two-photon polymerization (2PP) is a fabrication technique widely employed for the creation of engineered cell microenvironments [1,2]. From a technical point of view, there is a growing interest in soft materials compatible with the 2PP approach [3]. The field of neuromechanobiology can indeed benefit from employing soft materials in 2PP, as the mechanical properties and geometry of artificial 3D cell microenvironments mimicking the brain tissue, which features a Young's modulus of around 1 kPa, play a crucial role in the guidance of cell fate, phenotype, differentiation and migration [4]. The mechanical properties of 2PP printed constructs are highly dependent on the employed printing parameters (i.e. laser power, scanning speed, slicing and hatching distances). By tuning the stiffness of two-photon polymerized structures, reproducible 3D cell-instructive microenvironments featuring tunable mechanical properties can be employed to develop physiologically relevant in vitro models. In such context, the effect of the laser power on the stiffness of 2PP structures has been investigated for stiff materials (Young's moduli in the GPa range) [5], but not for soft materials (kPa and MPa range) [5].

In this work, the mechanical properties of a novel soft elastomeric polymer, IP-PDMS (a photosensitive type of PDMS), have been investigated [6]. To study the influence of the printing parameters on the mechanical properties of IP-PDMS, we employed optical-interferometer-based nanoindentation (Figure 1A) to characterise two-photon-polymerised structures manufactured with varying laser powers, scan speeds, slicing distances, and hatching distances. The nanoindentation experiments were performed on 3D-printed pedestals using spherically tipped probes in both air and aqueous environment. The minimum reported effective Young's modulus (YM) was 350 kPa, while the maximum one was 17.8 MPa. Figure 1B shows the influence of the scan speed and laser power on the YM. A clear decrease in YM is visible for increasing scan speeds and decreased laser powers. A linear relationship between IP-PDMS's YM and employed laser power was found with a similar slope for different scan speeds (not shown). In addition, we showed that, on average, water immersion lowered the YM by 5.4% (Figure 1C), a very important point as in the context of cell biology applications, the material must be employed within an aqueous environment. We also developed a printing strategy to determine the smallest achievable feature size and the maximum length of a double-clamped freestanding IP-PDMS beam (see Fig 2). These micrometric free-standing structures are an essential first step for the application of soft 3D prints in cell biology as their feature size should match the one of the cells under investigation [7]. The printing strategy is based on printing short hatch lines perpendicular to the longitudinal axis of the beam, to prevent collapse during printing. To assess these printed structures we performed a scanning electron microscopy morphological characterisation. The maximum length of a printed beam was 70 µm with a minimum width of 1.46 ± 0.11 µm and a thickness of 4.49 ± 0.05 µm (Figure 2A-D). The minimum beam width of 1.03 ± 0.02 µm was achieved for a beam length of 50 µm with a height of 3.00 ± 0.06 µm (Figure 2E-H).

In conclusion, the reported investigation of micron-scale two-photon-polymerized 3D IP-PDMS structures featuring tuneable mechanical properties paves the way for the application of this material in several cell biology applications, ranging from fundamental mechanobiology to in vitro disease modelling to tissue engineering.

References

[1] Q. Akolawala et al., *ACS Appl. Mater. Interfaces* **2022**, *14*, 20778.
[2] A. Sharaf et al., *Front. Bioeng. Biotechnol.* **2022**, *10*, 926642.
[3] A.I. Bunea et al., *Micro 2021, Vol. 1, Pages 164-180* **2021**, *1*, 164.
[4] L.C. Ransanz, P.F.J. van Altena,. et al., *Front. Bioeng. Biotechnol.* **2022**, *10,*1096054
[5] E. D. Lemma et al., *IEEE Trans. Nanotechnol.* **2017**, 23
[6] P.F.J. van Altena, A. Accardo, *Polymers* **2023**, 15, 1816.
[7] D. Fan et al., *Bioengineering (Basel)*. **2019**, 6, 113.

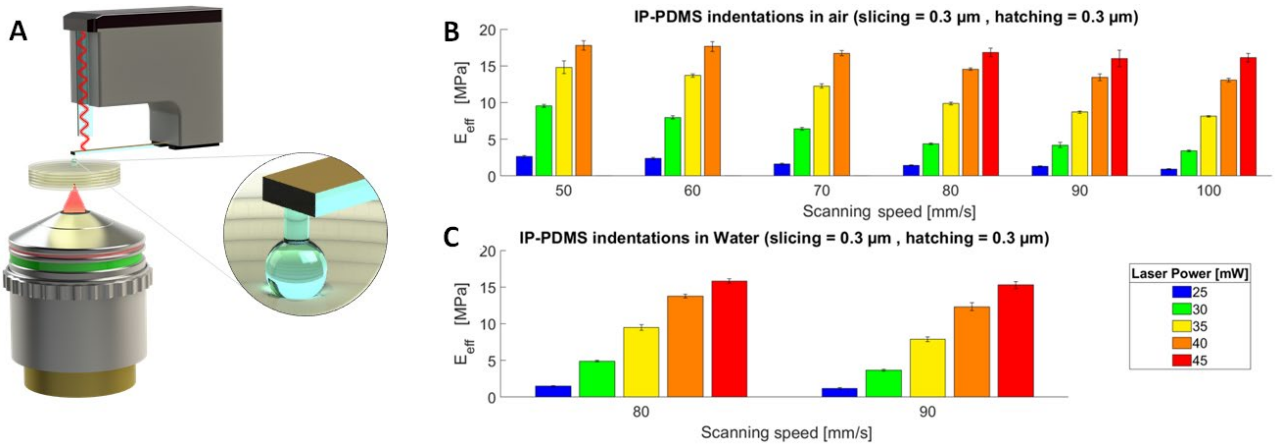

Figure 1. A) Illustration of the 2PP printing process and the nano-indentation process with the inset showing the spherical tip indenting an IP-PDMS pedestal. B) Results of the nano-indentation of IP-PDMS pedestals in air showing the influence of the scan speed and laser power on the YM. C) Influence of an aqueous environment on the YM.

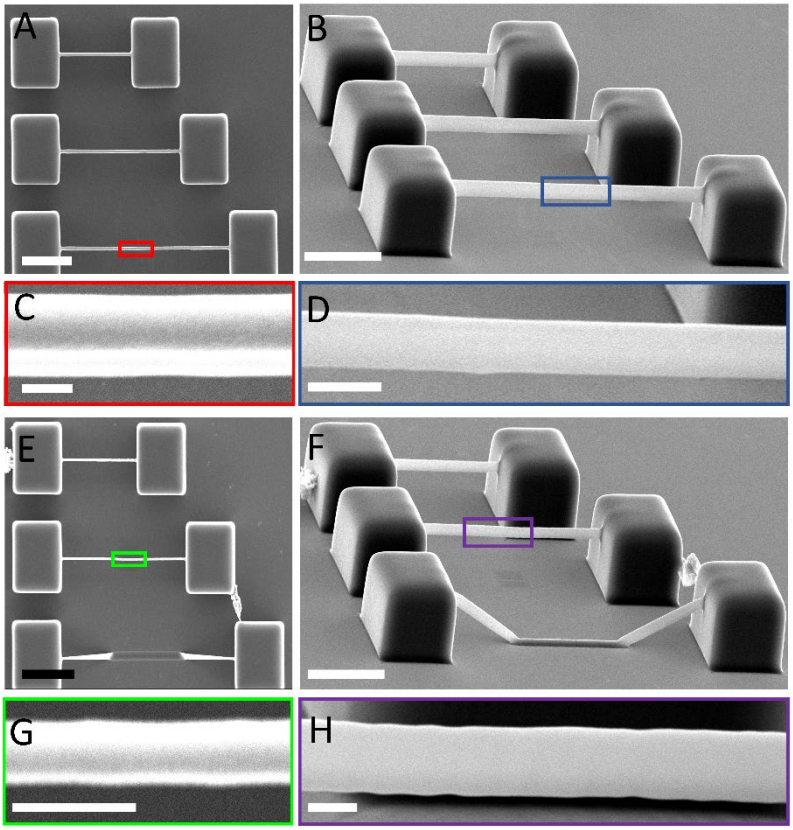

Figure 2. Representative SEM micrographs of 2PP-printed IP-PDMS beams. (A) Top view of beams with nominal lengths of 30, 50, and 70 µm and a nominal width of 1 µm (scalebar = 20 µm). (B) Tilt view of 65 degrees of the beams in A (scalebar = 20 µm). (C) Top view close-up of the beam with a length of 70 µm with an average width of 1.46 ± 0.11 µm (n = 3; scalebar = 1 µm). (D) Sixty-five-degree tilt view of the side of the printed beam indicated in B with a measured thickness of the beam of 4.49 ± 0.05 µm (n = 3; scalebar = 5 µm). (E) Top view of beams with nominal lengths of 30, 50, and 70 µm and a nominal width of 1 µm (scalebar = 20 µm). (F) Tilt view of 65 degrees of the same beams as in E (scalebar = 20 µm). (G) Top view close-up of the beam with a length of 50 µm with an average width of 1.03 ± 0.02 µm (n = 3; scalebar = 2 µm). (H) Sixty-five-degree angle view of the side of the printed beam indicated in F. The measured thickness of the beam is 3.00 ± 0.06 µm (n = 3; scalebar = 2 µm).

Biocompatible AIN Thin Films for Continuous Pulse Wave Velocity Assessment Applied to Cardiovascular Health

Angela-Tafadzwa Shumba[a,b], Suleyman Mahircan Demir[a,c], Gaia De Marzo[a], Valeria Carluccio[a], Vincenzo Mariano Mastronardi[a,b], Luca Fachechi[a], Francesco Rizzi[a], Paolo Motto Ros[c], Danilo Demarchi[c], Luigi Patrono[b], Massimo De Vittorio[a,b]

[a] Center for Biomolecular Nanotechnologies, Istituto Italiano di Tecnologia, Arnesano (LE), 73010, Italy
[b] Dipartimento Ingegneria dell'Innovazione @ Università del Salento, Lecce, 73100, Italy
[c] Department of Electronic and Telecommunications @ Politecnico di Torino, Turin, 10129, Italy
e-mail: angela.shumba@iit.it

One of the most prevalent health issues affecting first-world nations, including Italy, is cardiovascular diseases (CVDs), i.e., diseases affecting the heart and blood vessels. In Italy, over 40% of all deaths in 2022 were attributed to CVDs causing a considerable burden on healthcare infrastructures and institutions [1]. Developing innovative micro and nanoengineering solutions that facilitate the early detection and prevention of CVDs and efficient patient management to reduce the burden and improve patient care has been at the forefront of research and innovation activities in academia and industry. Traditional biomarkers, including heart rate (HR) and blood pressure (BP), have been obtained by various wearable sensing solutions and combined with other risk factors like age and sex to provide these services. However, pulse wave velocity (PWV), which offers critical insight into arterial stiffness directly correlating to CVDs, has emerged as an essential parameter that can significantly enhance their efficiency in recent years [2].

The typical tonometry method adopted in most commercial PWV devices involves compressing the blood vessels, causing discomfort, making it unsuitable for continuous assessment. It also typically requires well-trained technicians to operate the tonometry devices, limiting PWV analysis to specific laboratories and, in some instances, manual handling, reducing result reproducibility [2]. Piezoelectric sensors have also been adopted for PWV analysis in commercial devices [3], [4]; however, their bulky nature makes them unsuitable for continuous measurements. A smaller, 10x6x3cm piezoelectric nano transducer based on PVDF was also developed for PWV applications [5]. We, therefore, hypothesised that aluminium nitride (AIN) piezoelectric thin films are also suitable for PWV applications. Hence, this work demonstrates the application of flexible piezoelectric thin films to detect pulse waves and evaluate pulse wave velocity to develop comfortable and portable infrastructure for continuous PWV assessment.

The AlN piezoelectric sensor film (Fig 1) is grown on a thin Kapton foil making the sensor biocompatible, highly flexible, and thus suitable for long-term applications [6]. The shape of the sensor can be easily modified to suit the intended application-specific body surface thanks to the CMOS-compatible sensor microfabrication techniques. Here, a rectangular 2 cm × 1 cm structure is employed, significantly smaller than the one defined in [5]. The 26 µm thick multi-stack structure consists of Parylene, Kapton, an AlN interlayer, a molybdenum bottom electrode, AlN sensitive layer, and a molybdenum top electrode. The electrical characterisation of the patch is performed using an LCR meter, and the sensor's parallel capacitance and resistance are approximately ~3.28 nF and 2.75 MΩ, respectively. A FEM model was also set up to predict the sensor's response to a cardiovascular stimulus and create a digital twin of the device.

The piezoelectric sensors used to record pulse waves were first evaluated by simultaneously measuring heart electrical activity using an electrocardiogram (ECG) sensor (Olimelex) and pulse waves at different arterial sites using the fabricated sensors. The HR values obtained from the two devices revealed the successful detection of cardiac cycles using the fabricated sensors (Fig 2). Following the primary evaluation, the ECG device was removed to perform the PWV. The final test setup (Fig 3) includes a commercial charge amplifier and data acquisition (DAQ) device (Kistler 5165A) and an oscilloscope (Tektronix MDO4104-3) for visual signal verification. Offline processing and analysis of the collected measurements were performed using a custom algorithm defined in MATLAB software. Preliminary results (Fig 2) show that Carotid-Radial PWV (CR-PWV) obtained using our setup on a healthy subject within the 25-35 age group agrees with the selected, verified reference [7]. The design and validation of a custom electronic device to facilitate the production of a portable device with wireless capabilities are underway.

[1] C. Indolfi and G. Esposito, "Universal Health Care System and Cardiovascular Disease Burden in Italy," *Circulation*, vol. 145, no. 8, pp. 559–561, Feb. 2022, doi: 10.1161/CIRCULATIONAHA.121.057496.

[2] T. Pereira, C. Correia, and J. Cardoso, “Novel Methods for Pulse Wave Velocity Measurement.,” *J Med Biol Eng*, vol. 35, no. 5, pp. 555–565, 2015.
[3] M. H. N. van Velzen, R. J. Stolker, A. J. Loeve, S. P. Niehof, and E. G. Mik, “Comparison between pulse wave velocities measured using Complior and measured using Biopac,” *J Clin Monit Comput*, vol. 33, no. 2, pp. 241–247, 2019, doi: 10.1007/s10877-018-0165-9.
[4] J. J. Gagliardino *et al.*, “Arterial Stiffness: Its Relation with Prediabetes and Metabolic Syndrome and Possible Pathogenesis,” *J Clin Med*, vol. 10, no. 15, p. 3251, Jul. 2021, doi: 10.3390/jcm10153251.
[5] J. C. Murphy, K. Morrison, J. McLaughlin, G. Manoharan, and A. J. Adgey, “An Innovative Piezoelectric-Based Method for Measuring Pulse Wave Velocity in Patients With Hypertension,” *The Journal of Clinical Hypertension*, vol. 13, no. 7, pp. 497–505, Jul. 2011, doi: 10.1111/j.1751-7176.2011.00433.x.
[6] L. Natta *et al.*, “Conformable AlN Piezoelectric Sensors as a Non-invasive Approach for Swallowing Disorder Assessment,” *ACS Sens*, vol. 6, no. 5, pp. 1761–1769, May 2021, doi: 10.1021/acssensors.0c02339.
[7] G. L. Woolam, P. L. Schnur, C. Vallbona, and H. E. Hoff, “The Pulse Wave Velocity as an Early Indicator of Atherosclerosis in Diabetic Subjects,” *Circulation*, vol. 25, no. 3, pp. 533–539, Mar. 1962, doi: 10.1161/01.CIR.25.3.533.

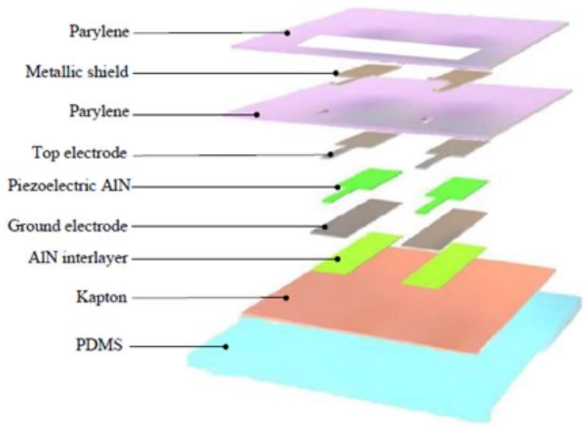

Figure 1. AIN thin film structure

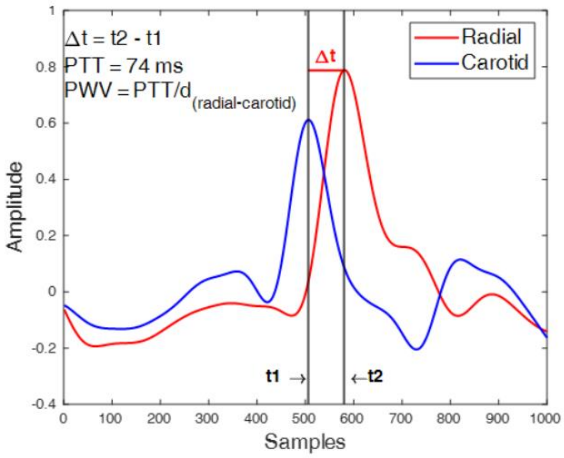

Figure 2. Carotid-Radial Pulse wave signals and PTT

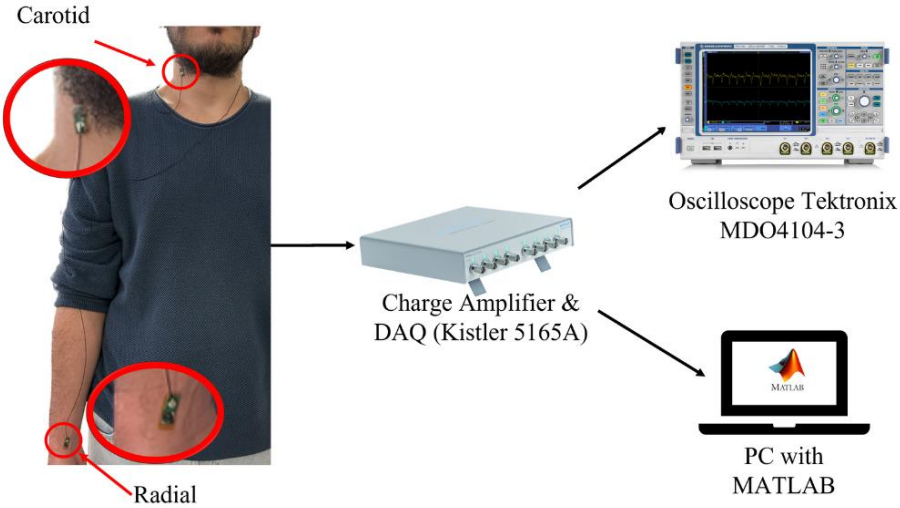

Figure 3. Experimental and pulse wave measurements setup

3D printed pyrolytic carbon microneedle biosensor for minimally invasive detection of TNF-α

Filip Angelov [a], Stephanie Ingemann Bisgaard [a], Jesper Yue Pan [a], Babak Rezaei [a], Yi Sun [b], Arto Heiskanen [b], Stephan Sylvest Keller [a]

[a] Technical University of Denmark, DTU Nanolab, 2800, Denmark
[b] Technical University of Denmark, DTU Health technology, 2800, Denmark
e-mail: suke@dtu.dk

In recent years, significant advancements in micro- and nanofabrication techniques have paved the way for highly sensitive and specific biosensing platforms, addressing the evolving needs of medical diagnostics. However, the development of a reliable biosensing solution utilizing the dermal interstitial fluid, – a biological medium available just beneath the epidermis, as a source of clinically relevant biomarkers remains challenging.

This study introduces an innovative microfabrication approach, utilizing projection micro stereolithography (PμSL) 3D printing for the engineering of pyrolytic carbon microneedle (PCMN) biosensors. Initially, the microneedles are digitally designed in Autodesk Fusion360 software (Fig 1A) and are segmented along the Z-axis in multiple image files (Fig 1A). Following, each image, corresponding to 20 μm in height is projected inside a chamber with UV photocurable resin layer-by-layer initiating polymerization. Subsequently, the printed microneedles undergo a process of pyrolysis at 900^{o}C in nitrogen atmosphere. This converts the photocured resin into pyrolytic carbon [1], resulting in an approximately 2-fold shrinkage in all dimensions of the structure, bringing the final length to 3 mm, while preserving the original shape and details of the microneedles (Fig 1B).

In order to achieve biosensing capabilities, the carbon surface was functionalized with gold nanoparticles (AuNP) by chronoamperometry at –200 mV in 3 mM $HAuCl_4$ for 20 sec, followed by covalent thiol crosslinking with primary amine-modified antibodies specific to TNF-α. TNF-a is a vital pro-inflammatory protein biomarker and holds important medical information for clinicians. These nanomaterials in addition to the PCMN itself allow for a dual functionality – as microstructure to capture target analyte in the skin and as a working electrode during subsequent electrochemical detection, which is done by a formation of a sandwich immunocomplex labelled with the catalytic enzyme horseradish peroxidase (HRP). In the presence of redox mediator – 2 mM hydroquinone and 1 mM H_2O_2 - the electrocatalytic signal can be detected via differential pulse voltammetry (DPV).

To confirm the successful integration of functional components, the PCMNs electrodes were thoroughly characterized using cyclic voltammetry (CV) and electrochemical impedance spectroscopy (EIS) with 10 mM ferri/ferro cyanide as a redox probe (Fig 3), as well as SEM (Fig 1C). Post AuNP deposition PCMN achieved peak-to peak separation ΔE = 113 mV ± 11.5 mV in CV and R_{CT} values of 270 Ω ± 53 Ω. The latter increased to up to 2920 Ω ± 187 Ω after the assembly of the complete biosensor, indicating successful integration of antibodies, successful formation of sandwich immunocomplex and labelling enzyme (Fig 3).

Extensive experimental validation was carried out in order to find optimal conditions for DPV measurements in order to evaluate the performance of the PCMN as biosensing electrode. It was found that the fabricated biosensors exhibit good sensitivity within the ng/mL range (Fig 4), positioning them as highly functional material for a wide range of biosensing applications.

This work represents a significant advancement in micro- and nanofabrication of microneedle biosensors. The conversion of the 3D printed microneedles to pyrolytic carbon ensures the retention of the original shape while imparting desirable properties for efficient and reliable biosensing. The integration of innovative fabrication methods, functionalization with specific bioreceptors, and thorough characterization sets the stage for groundbreaking biosensing platforms with immense potential in medical diagnostics and other sensing applications.

[1] Rezaei, B., Pan, J. Y., Gundlach, C., & Keller, S. S. (2020). Highly structured 3D pyrolytic carbon electrodes derived from additive manufacturing technology. *Materials & Design*, *193*, 108834. https://doi.org/10.1016/j.matdes.2020.108834

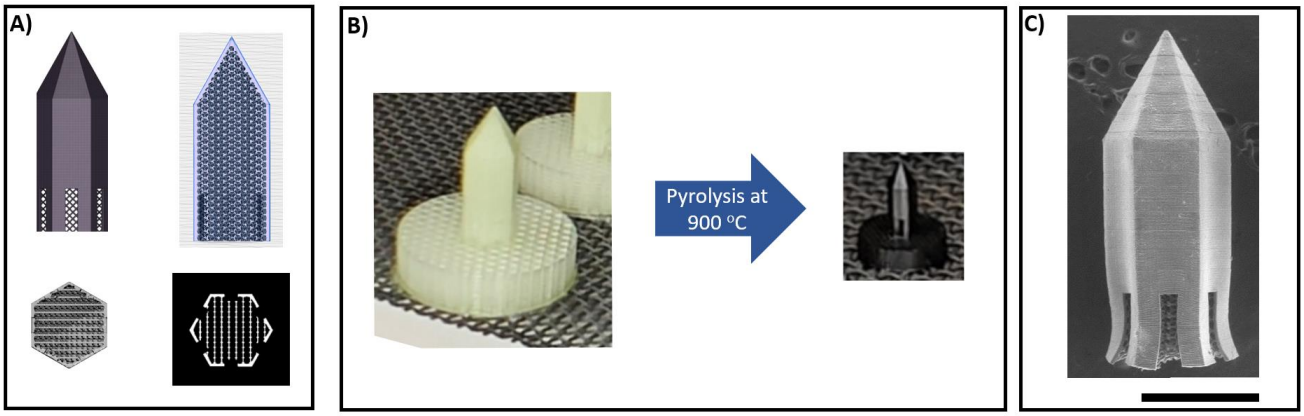

Figure 1. A) Rendering of the microneedle in Fusion 360 with visible cross sections along the vertical and horizontal axis. Bottom right – image from the segmentation fed into the 3D printer. B) MNs after 3D printing before and after pyrolysis. C) SEM image of the pyrolytic carbon microneedle after pyrolysis. Scale bar 1mm

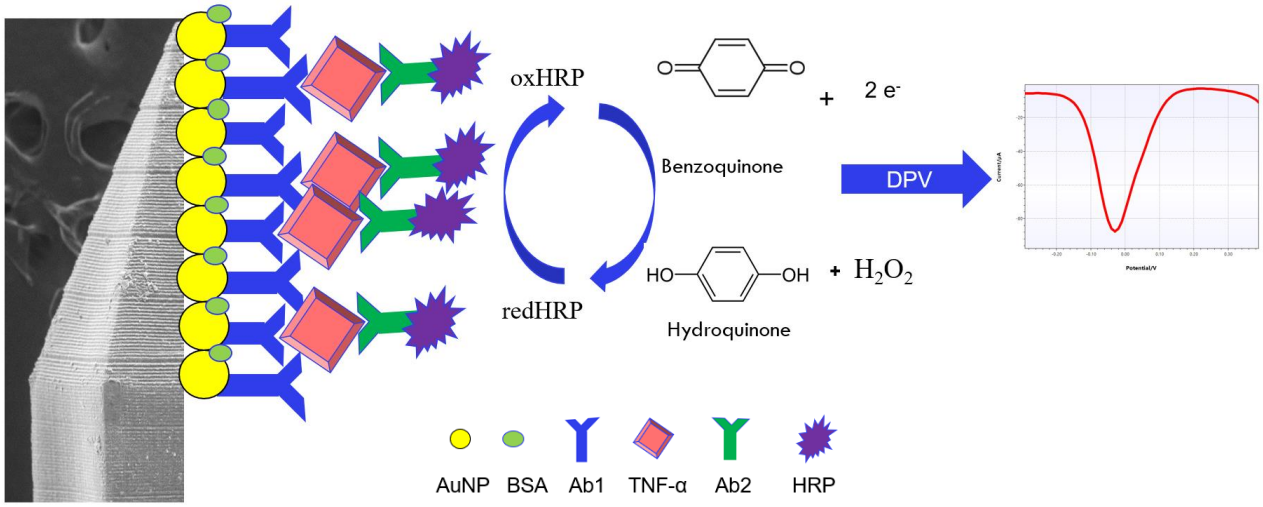

Figure 2. Structure of biosensing assay showing the construction of layers. AuNP are deposited on the carbon, linked to capture antibody, sensor is blocked by BSA, analyte is introduced, then 2nd antibody and HRP, which enables the DPV detection in the presence of H_2O_2 and hydroquinone, which is oxidized in the presence of HRP and reduced on electrode surface.

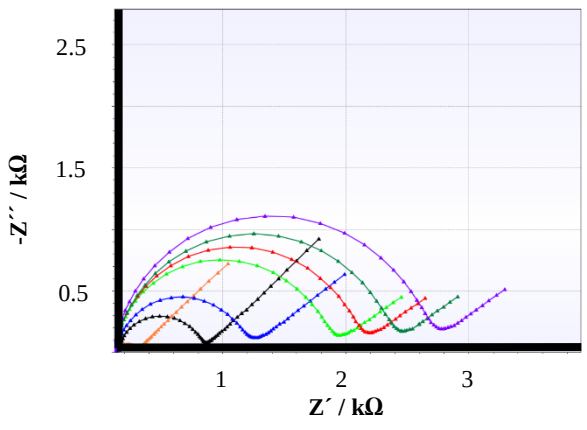

Figure 3. EIS in 10mM ferri/ferrocyanide of the different stages of functionalization of the biosensor. From left to right: AuNP, bare carbon, antibody 1, BSA, TNF-α, antibody 2, HRP.

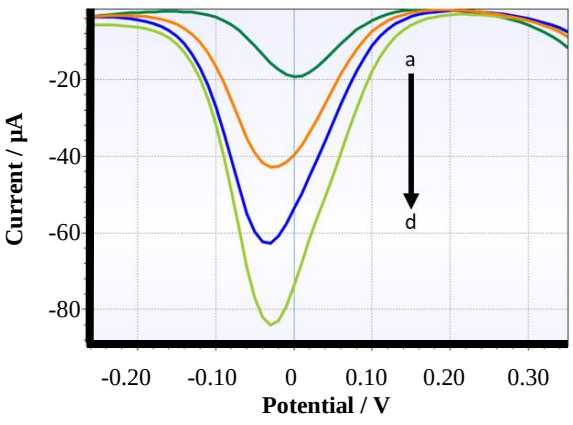

Figure 4. Detection of TNF-α via DPV. a) blank sample, b) 1 ng/mL, c) 10 ng/mL, d) 100 ng/mL

Growth of Vertically Aligned MoS_2 with Diffused SiO_x Film for Ag-Migration-Based Resistive Switching Devices

Jimin Lee [a], Sofía Cruces [a], Benny Ku [b], Satender Kataria [a], Ke Ran [c], Joachim Mayer [c,d], Alwin Daus [a], Max C. Lemme [a,b]

[a] Chair of Electronic Devices, RWTH Aachen University, Aachen, 52074, Germany, [b] AMO GmbH, Advanced Microelectronic Center Aachen, Aachen, 52074, Germany, [c] Central Facility for Electron Microscopy (GFE), RWTH Aachen University, Aachen, 52074, Germany, [d] Ernst Ruska-Centre for Microscopy and Spectroscopy with Electrons (ER-C 2), Forschungszentrum Jülich, Jülich, 52425, Germany

E-mail: max.lemme@eld.rwth-aachen.de; alwin.daus@eld.rwth-aachen.de

Introduction: Transition metal dichalcogenides (TMDs) are two-dimensional layered materials with van der Waals (vdW) inter-layer bonds [1]. MoS_2, a semiconducting TMD, can be obtained in high-quality small flakes or large-area thin films with variable electronic properties depending on the growth method [2]. Recently, it has been reported that the conversion of Mo thin-films into MoS_2 in sulfur atmosphere (sulfurization), can lead to scalable, large-area MoS_2 film growth [2]. Within this process, the vdW layer orientation (lateral or vertical) can be controlled by choosing an appropriate initial Mo film thickness [1]. However, the mechanism of orientation change and substrate dependence remains unclear. In resistive switching (RS) applications, the vdW gaps in MoS_2 facilitate ion movement, which is of particular interest when explored in compact vertical device architectures with small footprints [3-4]. Therefore, the layer orientation of MoS_2 is an important factor for RS, and the so far less-studied vertical alignment could be advantageous over the more common lateral layer arrangement. In this work, we compare vertically aligned (VA)-MoS_2 grown by sulfurization on SiO_2 and Au surfaces. We observe the formation of an amorphous SiO_x layer on top of the VA-MoS_2 thin film which can be attributed to Si and O diffusion from the substrate. In addition, we confirm that Ag ions can travel through the material stack leading to volatile RS.

VA-MoS_2 Growth/Device Fabrication: Fig. 1(a) shows the sulfurization process of VA-MoS_2. Sulfur powder and Mo thin films (~6 nm) on SiO_2/Si substrate (with and without pre-patterned Au electrodes) are placed upstream and in the center of the tube, respectively. Sulfur diffuses into the Mo film, creating MoS_2 while the temperature is kept at 800 °C for 30 min under 20 sccm Ar flow [5]. Figs. 1(b-c) present the device fabrication flow and an optical image of a fabricated device. The Ti/Au (5/50 nm) bottom electrode (BE) and Ag/Au (30/30 nm) top electrode (TE) are defined by photolithography, electron-beam evaporation, and lift-off. The Mo thin film is direct-current sputtered at 100 W and Ar flow with a chamber pressure of ~3×10^{-3} mbar.

Results/Discussion: Figs. 2(a-b) show the Raman spectra and a peak intensity ratio (E^1_{2g}/A_{1g}) map of the as-grown VA-MoS_2 film on SiO_2 and Au. E^1_{2g}/A_{1g} ratios of ~ 30% correspond to the formation of VA-MoS_2 layers [6]. Figs. 2(c-d) display high-resolution transmission electron microscopy (HRTEM) images with mostly VA-MoS_2 layers on SiO_2, while initial few layers on Au appear to be laterally oriented. We observe an amorphous layer between VA-MoS_2 and the TE [Fig. 2(e)] and confirm the presence of Si and O using high-angle annular dark-field (HAADF) scanning TEM and elemental mapping [Figs. 2(f-k)]. The SiO_x layer is formed from the SiO_2/Si substrate by solid-state reaction and atomic diffusion of Si and O at high temperatures, as previously reported [7], while potentially enhanced along the vdW gaps in the VA-MoS_2 layer. Furthermore, we performed current-voltage (I–V) characterization on Ag/SiO_x/VA-MoS_2/Au cross-point devices. Fig. 3(a) shows volatile RS in 10 subsequent voltage sweeps at 100 nA current compliance (CC). We found that the volatile RS originated from the formation of Ag-diffused conductive filaments in the VA-MoS_2/SiO_x layer, as traces of Ag ions were observed in the SiO_x layer [Figs. 2(e,k)]. Figs. 3(b-c) show the statistical analysis of on-threshold voltage ($V_{th,on}$) for different CCs and different areas of cross-point devices.

Conclusion: We synthesized VA-MoS_2 on SiO_2 and Au surfaces to explore the substrate dependence of the VA-MoS_2 layer orientation, obtaining different degrees of vertical alignment. A SiO_x layer was formed on top of VA-MoS_2. We further observed Ag migration through the stack upon electrical biasing leading to volatile RS. Thus, this study demonstrates the complex growth of VA-MoS_2. The impact of the substrate on the material stack and orientation as well as the precise implications for the RS behavior in memristive devices require further investigations.

Acknowledgments: Funding by the German BMBF through NEUROTEC 2 (16ME0399, 16ME0400, and 16ME0403) and NeuroSys (03ZU1106AA).

References: [1] Y. Jung et al., *Nano Lett.*, 14, 6842-6849 (2014). [2] W. Choi et al., *Mater. Today*, 20, 116-130 (2017). [3] M. Belete et al., *Adv. Electron. Mater.*, 6, 1900892 (2020). [4] D. Dev et al., *IEEE Electron Device Lett.*, 41, 936-939 (2020). [5] M. Belete et al., *ACS Appl. Nano Mater.*, 1, 11, 6197-6204 (2018). [6] D. Kong et al., *Nano Lett.*, 13, 1341-1347 (2013). [7] H. Liu et al., *Mater.*, 160 491-495 (2015).

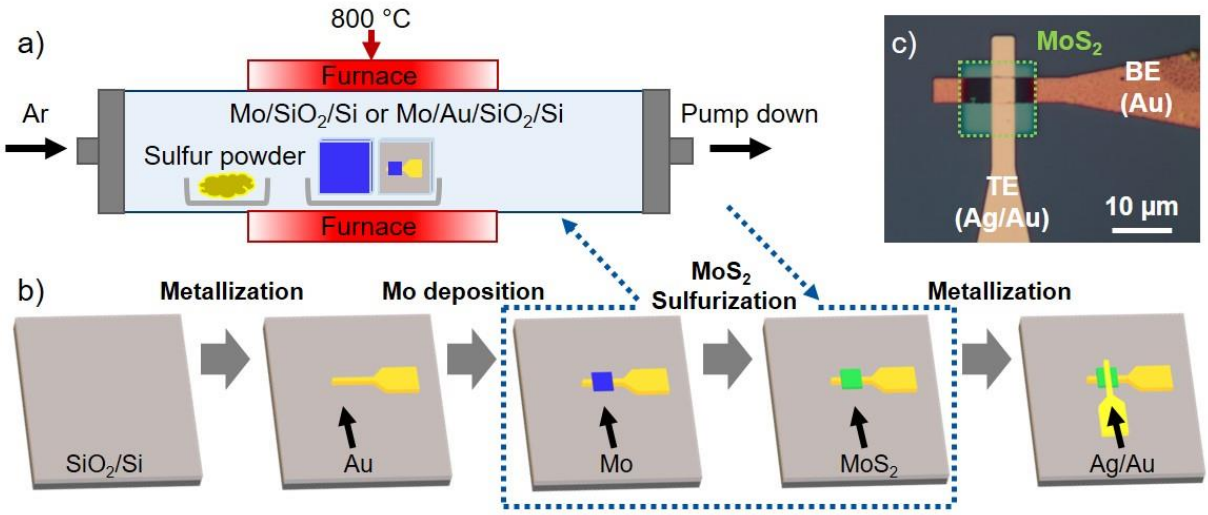

Figure 1. (a) Schematic of the sulfurization process of VA-MoS_2 films in a horizontal tube furnace. (b) Schematic of the fabrication process of a RS cross-point device. (c) Top-view optical microscope image of a fabricated device with an area of 16 μm^2.

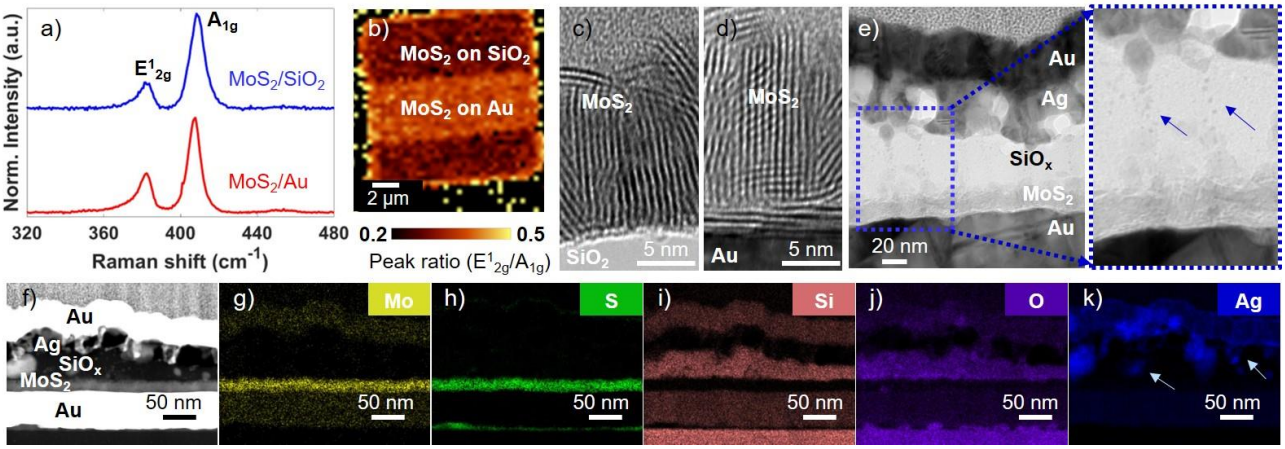

Figure 2. (a) Raman spectra from as-grown VA-MoS_2 films on SiO_2 and Au surfaces. (b) Raman map of the peak intensity ratio (E^1_{2g}/A_{1g}) from MoS_2/SiO_2 and MoS_2/Au. HRTEM showing VA-MoS_2 grown on (c) SiO_2 and (d) Au. (e) Cross-sectional TEM image of the RS device after 42 switching cycles at different CCs. The inset shows the magnified view of Ag traces in the material stack. (f) Cross-sectional HAADF STEM image of the resulting device. (g-k) Energy dispersive x-ray spectroscopy elemental mapping after RS measurement for Mo, S, Si, O, and Ag, respectively.

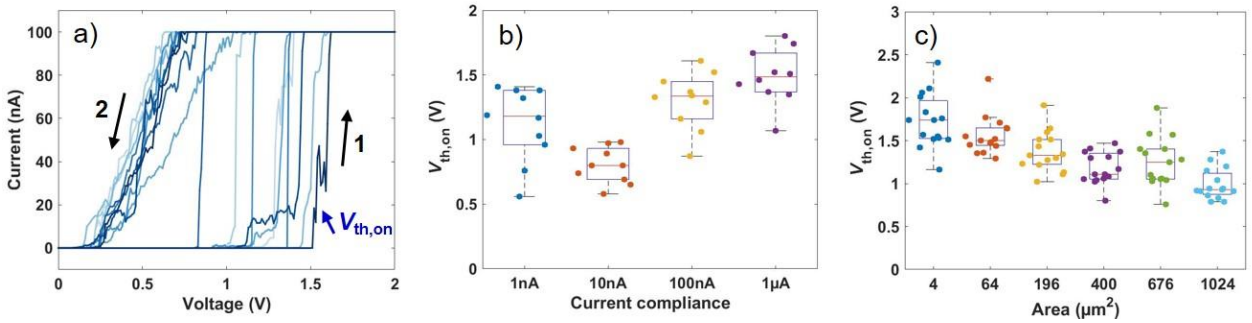

Figure 3. (a) 10 subsequent *I–V* curves of Ag/SiO_x/VA-MoS_2/Au cross-point device. The arrows 1 and 2 denote the voltage sweep direction. The rest points to $V_{th,on}$. Statistical analysis of $V_{th,on}$ for (b) different CCs on the same device with an area of 16 μm^2 for 10 subsequent volatile RS cycles, and (c) 1 μA CC on the different areas of the cross-point devices for 15 subsequent volatile RS cycles.

A method for measuring the d_{33} piezoelectric coefficient of soft thin films under weak loads

Gaia de Marzo [a], Valentina Antonaci [a, b], Luca Fachechi [a], Vincenzo Mariano Mastronardi [a, b], Maria Teresa Todaro [a, c], Luigi Portaluri [a, b], Antonio Qualtieri [a], Francesco Rizzi [a], Michele Scaraggi [a, b], Massimo De Vittorio [a, b]

[a] Center for Biomolecular Nanotechnologies, Istituto Italiano di Tecnologia, Arnesano (LE), 73010, Italy
[b] Department of Innovation Engineering, University of Salento, Lecce, 73100, Italy
[c] Institute of Nanotechnology, Consiglio Nazionale delle Ricerche, Lecce, 73100, Italy
e-mail: gaia.demarzo@iit.it

Piezoelectric soft thin films are key building blocks for skin compliant wearable sensors for monitoring health parameters, such as heartbeat, blood pressure, and breathing pace, due to their compactness, high sensitivity, low cost, and no power consumption [1], [2]. To optimize their performances and produce sensors that overcome state-of-the-art, it is necessary to systematically and accurately inspect their piezoelectric properties. This becomes very critical when the piezoelectric material is thin, flexible and soft. In these cases, it is of utmost importance the availability of a reliable, fast and easy-to-handle setup, allowing one to perform d_{33} coefficient measurements routinely by applying low forces to avoid any damage to the materials.
Among the techniques that exploit the inverse piezoelectric effect, Piezoresponse Force Microscopy (PFM) and Laser Interferometry (LI) are the most accurate to test the piezoelectric properties with high reliability [3][4]. However, they suffer from some drawbacks: (i) PFM is strongly influenced by electrostatic contributions and requires hours to extrapolate the value of d_{33} due to long measurements and computational analysis; (ii) LI is highly biased by environmental vibrations and involves efforts in sample preparation whose surface needs to be perfectly plane and reflective; (iii) both give information only on a nano or micrometric scale in the area confined under the tip or the laser beam. These aspects hinder their employment as routine analysis. On the other hand, a more straightforward approach is embodied by techniques exploiting the direct piezoelectric effect, which measures the charges developed when a known force is applied. Among these techniques, pneumatic methods are becoming popular, but they require complex setups and use single pulses to excite the signals, causing very high standard deviation and less reliability in the results [5]. Berlincourt or quasi-static methods overcome these issues by applying a pre-load and a sinusoidal force stimulus on the sample, consequently stimulating a sinusoidal electrical response that can be highly averaged to reduce uncertainty on the final result [6]. However, the non-planar and conductive sample clamps, working as electrodes, can induce strains on the thin films, generating d_{31} charge contribution or causing the accidental measurement of a triboelectric effect, which can be wrongly interpreted as piezoelectric signal [7]. Moreover, they exert forces higher than 1 N, bringing the risk of damage, or even simply deforming, the soft and thin material during the inspection itself.
To overcome all these limits, we developed an easy-to-handle and fast quasi-static measurement method that allows applying sinusoidal dynamic forces in a range between 2 mN and 30 mN. Measuring simultaneously the force applied and the charges generated by the thin film we can extrapolate the piezoelectric coefficient in considerably reduced time and with high reliability. The setup (Figure 1, 2 a and b) is essentially composed of a plane speaker acting as the actuator, a sensitive load cell for force measurement, a custom-made charge amplifier to read the sensor output, a device-embedded shielding film to avoid triboelectric effects and a surrounding Faraday cage to isolate charges generated by the environment. The setup was validated by correctly determining the known d_{33} coefficient of a commercially available Polyvinylidene difluoride (PVDF) foil (Figure 2c, 3a, d). Its versatility is demonstrated by measuring the d_{33} of a thin ceramic piezoelectric Aluminum Nitride (AlN) film (Figure 3 b, e) and of a thin Chitosan film, an innovative piezoelectric biopolymer (Figure 3 c, f). We envision that the employment of this approach to measure d_{33} routinely will boost innovation in the field of wearable sensors by supporting the investigation and improvement of piezoelectric thin film materials.

[1] L. Natta et al., ACS Sens. 6 (2021) 1761–17692021.
[2] Kim et al., Adv. Eng. Mater. 25 (2023) 2200873.
[3] E. Soergel, J. Phys. D: Appl. Phys. 44 (2011) 464003.
[4] G. J. T. Leighton et al., Smart Mater. Struct. 19, (2010) 065011.
[5] B. Toroń et al., Measurement 206 (2023) 112274.

[6] M. Stewart et al., Springer Series in Measurement Science and Technology (2014) 37–64.
[7] A. Šutka, et al., Adv. Mater. 32 (2020) 1–9.

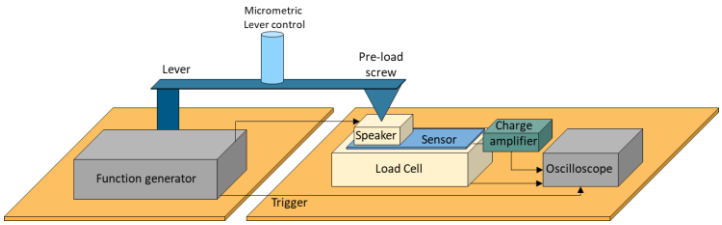

Figure 1. Scheme of the setup.

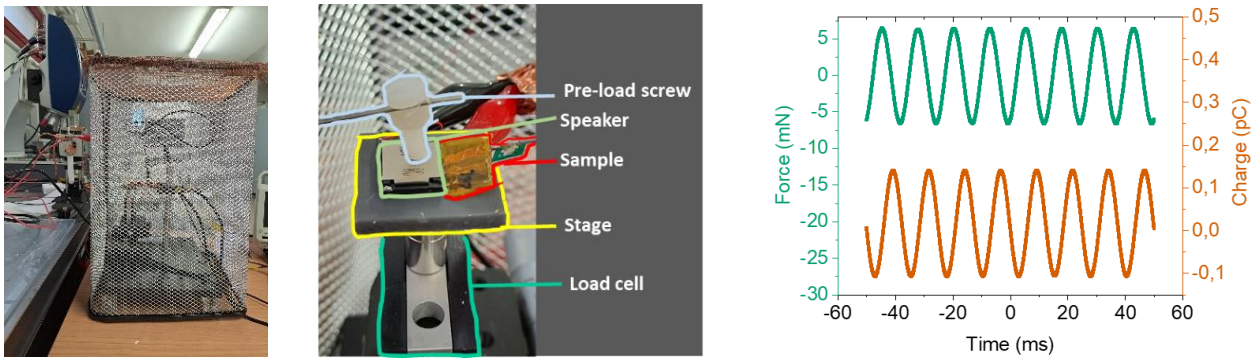

Figure 2. (a) The setup enclosed in a Faraday cage for the shielding of environmental charges. (b) The core part of the setup inside the Faraday cage. The samples placed on a stage mounted on the load cell for force measurement. The speaker placed on top of the samples and kept in position by the pre-load applied with a flat screw. (c) Example of Force and Charge signals acquired and averaged 64 times with the PVDF sample.

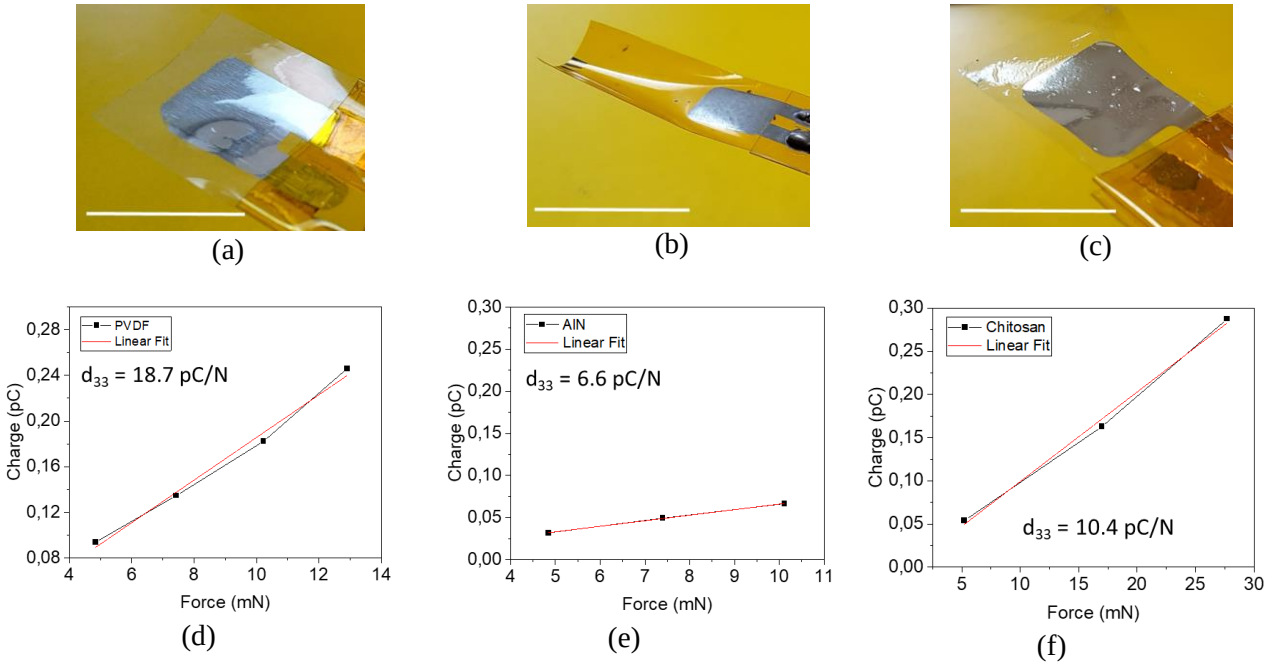

Figure 3. (a,b,c) Piezoelectric samples made respectively by PVDF, AlN, and Chitosan. The scale bar corresponds to 10 mm. (d,e,f) Plots of charges vs. forces and d33 calculation for the three samples measured.

Automatic markerless overlay with the NanoFrazor: towards batch-fabricated nanodevices

Jana Chaaban [a], A. Damyanova [a], J. Vergés [a], R. Erne [a], E. Çağin[a],

[a] Heidelberg Instruments Nano AG, Bändliweg 30, 8048 Zürich, Switzerland
e-mail: jana.chaaban@himt.ch

The NanoFrazor uses thermal scanning probe lithography (tSPL) for the simultaneous patterning and inspection of nanoscale structures as well as direct laser sublimation (DLS) for mix & match lithography to create nanodevices [1]. The technology has proven its value as an enabler of novel ultra-high resolution nanodevices [2], as well as an asset for improving the performance of existing device concepts [3]. The technology solves complex fabrication challenges by providing a way to achieve accurate markerless overlay, sub-nanometer precise 3D grayscale lithography, and the ability to integrate into inert atmospheres. The latter allows the further growth of the NanoFrazor into applications using sensitive material classes, which also benefit from this non-invasive technique with damage-free patterning capabilities.

Automation of the lithography steps carried out by the NanoFrazor is a natural next step in the expanding application space where the tool is used. In addition to making workflows for nanoelectronic device fabrication reliable and repeatable, and allowing unattended operation, automation is also a valuable training tool for novice users. Scripting functionality and unprecedented patterning endurance make automated, markerless overlay of arbitrary structures possible. Applications where high-resolution, critical features must be placed precisely on pre-existing structures (e.g. nanopillars on micro-posts, defined channels between FinFET source and drain contacts, …) benefit directly from this lithographic approach.

Here we present successfully implemented use-cases of automated, markerless overlay with the NanoFrazor, including nanopillars centered on pre-patterned matrices of microstructures. The overlay is shown to work even when the underlying structures are buried under resist layers, thanks to the highly sensitive in-situ reading capability of the tool. Using multiple reference points to calibrate for rotation and scaling errors on the substrate, the NanoFrazor software remains independent of the substrate placement and accuracy of the previous lithography steps. Once the substrate location and calibration are completed, design layouts of arbitrary shapes can be overlaid, patterned and simultaneously inspected, as shown in Figure 1. The inspection allows users to validate that the patterning has been carried out at the correct location and with a sufficient depth in the resist for subsequent processing. A lift-off step to produce the desired nanopillars on the micro-posts was validated using AFM and SEM imaging upon completion, as shown in Figure 2. In a second example, we combine the NanoFrazor's grayscale patterning capability with the automatic overlay process to integrate 47 grating couplers onto silicon waveguides to create unique, integrated nanophotonic devices, as seen in Figure 3.

[1] S. T. Howell et al., Microsyst Nanoeng 6, 21 (2020).
[2] M. J. Skaug et al., Science. 359 (6383), 1505–1508 (2018).
[3] X. Zheng et al., Nature Electronics 2, 17-25 (2019).

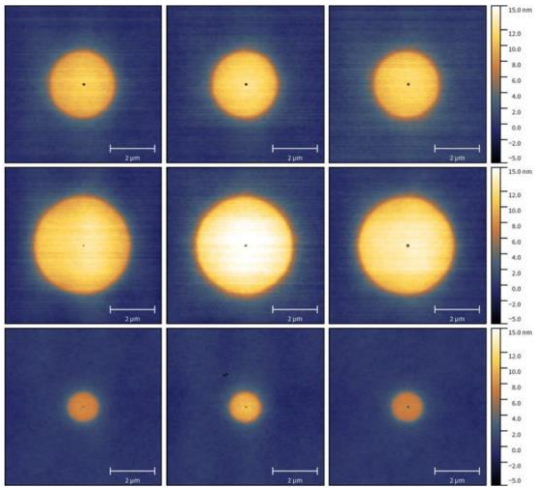

Figure 1. Example of automated overlay with the NanoFrazor, where a nanoscale circle was patterned in the center of a pre-existing micropillar in a repeated matrix. The circle is visible as a dark dot in the center, due to being created by sublimating thermal resist locally.

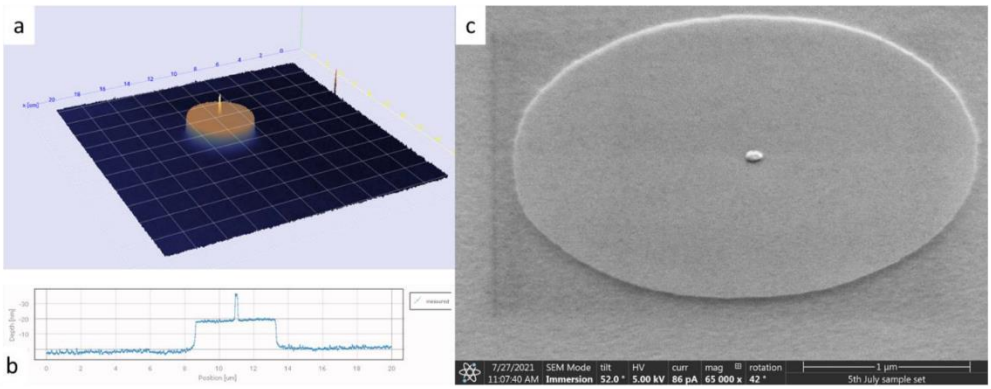

Figure 2. Characterization of nanopillars on micropillars through AFM, shown in 3D (a) and in profile (b). SEM micrograph of a nanopillar patterned at the center of a 2.5 µm high micro-post. The structures were obtained by lift-off processing following thermal scanning probe lithography with the NanoFrazor.

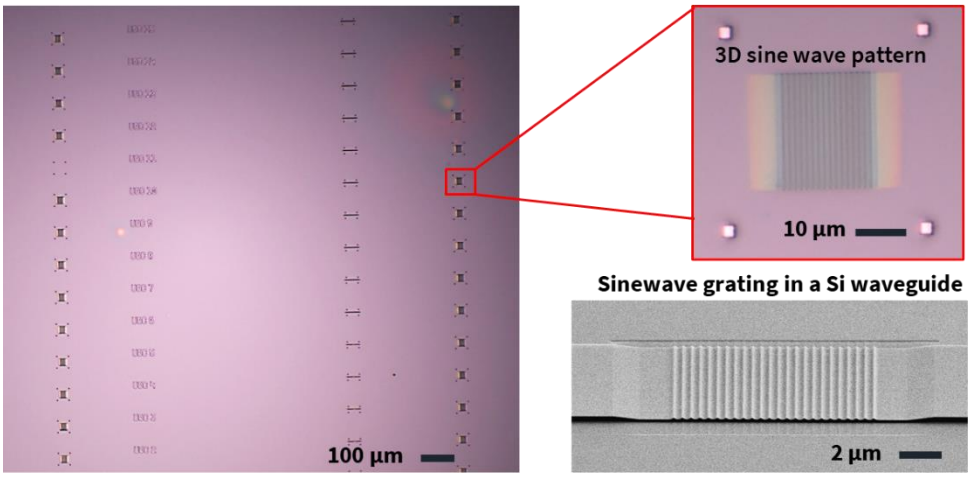

Figure 3. NanoFrazor-written grayscale sine wave structures (grating couplers), 47 in total, automatically aligned to markers on a Silicon substrate. The same markers will be used in a second lithography step for patterning and aligning waveguides using e-beam lithography. At the end of the fabrication process, the initial NanoFrazor-written grating couplers would be aligned to the beginning center, and end of the waveguides, as seen in the SEM image at the bottom right of this figure.

An electrochemical sensor for *Listeria monocytogenes* detection based on 3D printing and loop mediated isothermal amplification

Ane Rivas-Macho [a], Unai Eletxigerra [b], Ruth Diez [b], Santos Merino [b,c], Antton Sanjuan [d], M. Mounir Bou-Ali [d], Leire Ruiz [e,f], Javier del Campo [f,g], José Luis Vilas [e,f] , Felipe Goñi [a], Garbiñe Olabarria [a]

[a] Gaiker, GAIKER Technology Centre, Basque Research and Technology Alliance, Zamudio 48170, Spain
[b] Surface Chemistry and Nanotechnologies Unit, Tekniker, Eibar 20600, Spain
[c] Departamento de Electricidad y Electrónica, Universidad del País Vasco UPV/EHU, 48940 Leioa, Spain
[d] Fluid Mechanics Group, Mondragon University, Loramendi 4, Apdo. 23, 20500 Mondragon, Spain
[e] Macromolecular Chemistry Group, Department of Physical Chemistry, Faculty of Science and Technology, University of the Basque Country UPV/ EHU, 48940 Leioa, Spain
[f] Basque Center for Materials, Applications and Nanostructures, Martina Casiano Building, UPV/EHU Science Park, 48940 Leioa, Spain
[g] IKERBASQUE, Basque Foundation for Science, Plaza Euskadi, 5, Bilbao 48009, Spain
e-mail: santos.merino@tekniker.es

The food industry market has globalized so rapidly that there is an urgent need to improve the biological, chemical and physical monitoring of food quality control during all processes, from farm to fork. This trend in the industry raises the need to strengthen food safety by developing and implementing online quality control systems. Biological hazards caused by bacteria, viruses and their toxins constitute one of the most serious risks to consumer health. One of the microorganisms responsible for the greatest economic losses in the food sector is *Listeria monocytogenes* (LMO), which has a high incidence and persistence in the food industry and is very difficult to eradicate and eliminate from equipment and facilities. The consumption of contaminated food with LMO generates the disease known as listeriosis with a high rate of hospitalization (90%) and mortality (20–30%).

This research work describes the fabrication of a new integrated biosensor compatible with on-site detection of bacteria in low resources-settings. The sensor relies on the Loop Mediated Isothermal Amplification (LAMP) method for the amplification of the specific LMO nucleic acids sequence at a single temperature around 65ºC and subsequent electrochemical transduction mechanism for its detection. The electrochemical sensor is encapsulated in a microfluidic chamber, and it is compatible with an extraction-free method that has been validated with different spiked matrix food samples. The detection is achieved by adding the redox-active Methylene-Blue (MB) molecule to the LAMP reaction, which intercalates into the double-stranded DNA (ds-DNA) and monitoring its electroactivity by cyclic voltammetry. When the MB is free in solution, the molecule diffuses onto the surface of the working electrode and the redox reaction occurs unhindered, thus generating a current peak at specific potentials, indicative of a negative result. In the case of bacteria are present, the MB molecule intercalates into the polymerised ds-DNA, which restricts its electroactivity and almost no current peak is detected.

The gold microelectrodes were fabricated by UV-Lithography and gold lift off onto a silicon/silicon dioxide wafer and they were encapsulated into a microfluidic chamber manufactured by 3D printing using stereolithography and digital light processing. (Figure 1a). Computational fluid dynamics was used to design the chamber geometry, minimizing the bubbles formation and their presence around the microelectrodes. The biosensor was tested using LAMP product samples; 250 pg of LMO DNA as positive and PCR grade water as negative, obtaining a very reproducible voltammogram, with clear differences between both samples (Figure 1b) [1]. For a further validation of the device, three types of food samples spiked with different concentrations of LMO were tested: 25 mL or 25 g of dairy milk, fresh cheese and smoked salmon were spiked with 1050, 105 and 1 cfu. The three different samples of dairy milk with spiked LMO were successfully detected and the control sample (non-spiked food) was detected as negative. The same results were obtained for the samples of fresh cheese and smoked salmon, being able to detect as little as 1 cfu/25g of LMO (Figure 2).

Aiming to progress on a more versatile platform, a new chamber design was optimized by using a new clear resin, which is more transparent while lacks autofluorescence. Three different chamber volumes were manufactured and tested showing that LAMP reaction works, and positive results were detected by fluorescence (Figure 3). This new chamber design has been integrated with microelectrodes to get a dual platform which can operate under both transduction mechanisms, electrochemistry and fluorescence. Dual detection validation and sensitivity is now being developed and tested.

[1] A. Rivas-Macho et al. Heliyon 9, e12637 (2023)

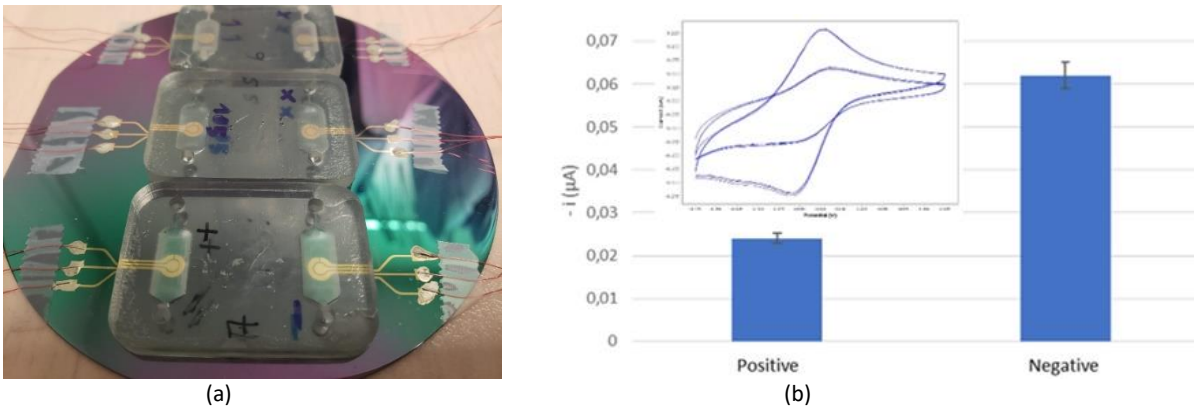

Figure 1. *(a) 3D printed chamber assembled onto the microelectrodes ready for measurement. (b) Validation of the assay for the electrochemical detection of Listeria monocytogenes in the microfluidic chamber. Voltammograms and peak currents for the positive and negative samples*

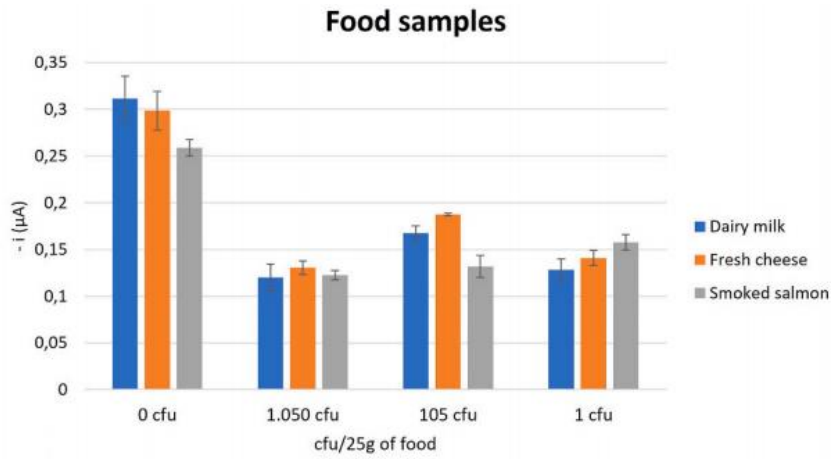

Figure 2. *Food sample validation: dairy milk results in blue, fresh cheese in orange and smoked sample in grey. Current peak represented on the left and L. monocytogenes cfu/25 g of food in the bottom.*

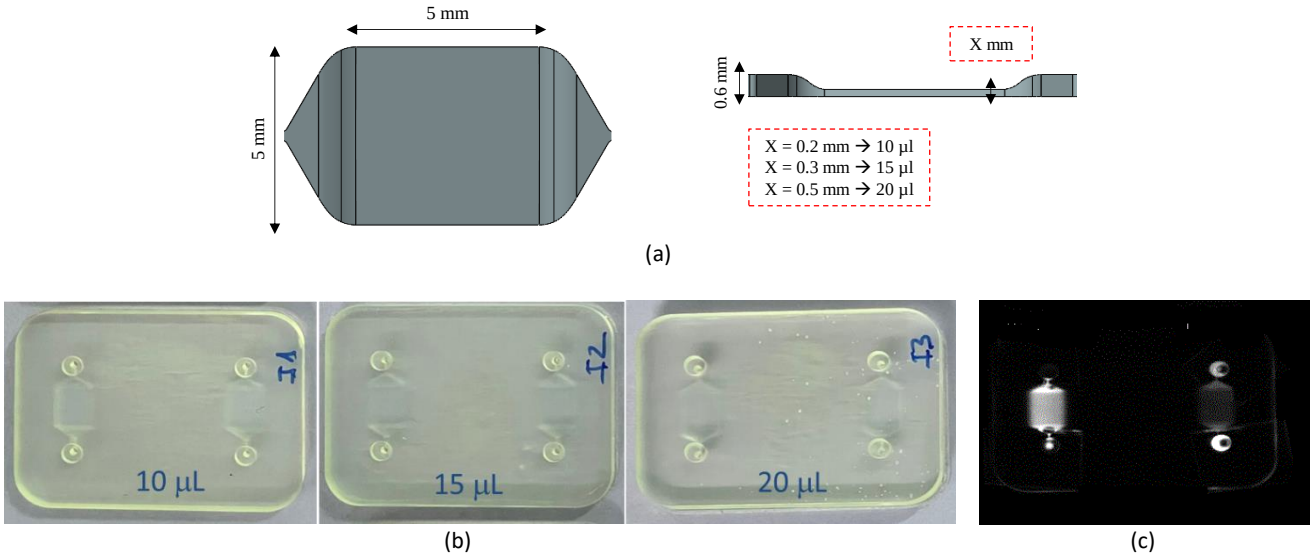

Figure 3. *(a) Geometrical design of the microfluidic chambers fabricated by 3D printing. (b) Different volumes of imprinted chambers in IFUN material. (c) Fluorescence analysis of L. Monocytogenes positive and negative samples.*

Auto-fluorescence suppression of 3D scaffolds fabricated via two-photon polymerization for cell biology applications

A. Sharaf [a], J.P. Frimat [b], G.J. Kremers [c], A. Accardo [a]

[a]Department of Precision and Microsystems Engineering, Faculty of Mechanical, Maritime and Materials Engineering (3mE), Delft University of Technology, Mekelweg 2, 2628 CD Delft, the Netherlands
[b]Department of Human Genetics, Leiden University Medical Center, 2333 ZA Leiden, the Netherlands
[c]Erasmus Optical Imaging Centre, Erasmus MC, 3015 GE Rotterdam, the Netherlands
e-mail: A.accardo@tudelft.nl

Fabrication of microscaffolds for fundamental cell mechanobiology studies has been substantially facilitated in recent years by innovative technologies such as two-photon polymerization (2PP). This microfabrication technique employs a near infrared (NIR) femtosecond-pulsed laser to fabricate, with nanometric resolution (up to 50 nm), microstructures that are predesigned via a computer aided design (CAD) software [1]. Even though 2PP has multiple benefits such as high resolution, reproducibility, and freedom of design of 3D micro-architectures, the fabricated microstructures usually suffer from high auto-fluorescence, which hinders fluorescence microscopy characterization of immunostained cells [2,3]. Since their fluorescence is much higher than that of the cell staining, it can block one or more of the 3 channels, blue (400-500 nm emission wavelength), green (500-600 nm emission wavelength), and red (600–800 nm emission wavelength), employed in fluorescence microscopy.

To overcome this limitation, we propose and compare two solutions that are relatively straightforward, inexpensive, and fast to employ in addition to being highly effective [4]: photo-bleaching, using a powerful point source, and photo-quenching, using a commercial photo-quencher known as Sudan Black B (SBB). This study compares, for the first time, the effectivity of these two solutions in the context of 2PP photoresins. The materials investigated are IP-L, IP-Dip, IP-S, and IP-PDMS, which are commercial acrylate or silicone based photoresins widely used in the field of 2PP. To investigate the performance of the proposed solutions the treatments were carried out on pedestals of 30x30x20 μm^3 (lxwxh) (Figure 1A). In addition, microchannels (Figure 1B) of 30 µm pore size and 3 µm thick walls and microcages (Figure 1C) of 30 µm pore size were fabricated, treated with both solutions, and cultured with the human neuroblastoma cell line (SH-SY5Y) to illustrate the degree of enhancement in terms of cell visualization by immunofluorescence microscopy. Photo-bleaching was carried out by exposing the microstructures to a powerful UV point source for 2 hours. Alternatively, quenching was performed by submerging the microstructures in a 0.3% w/v SBB solution for 2 hours to form a layer of adsorbed SBB on top of the microstructures that would absorb the photons emitted by them, thereby suppressing their auto-fluorescence. The effectivity of both solutions was measured by spectral analysis of the auto-fluorescence of the microstructures. The results showed that both solutions were comparable. The efficiency of bleaching ranged from 61.7% to 92.5% depending on the material and that of SBB quenching ranged from 33% to 95.4% (Figure 2). The adsorption of SBB on all materials yielded similar results except for IP-PDMS since it adhered poorly to structures fabricated using this material. This was significantly enhanced after a short oxygen plasma treatment of 30 seconds. Moreover, the Young's modulus of the bleached structures was measured before and after bleaching and was shown to increase on average by 59% for all materials. Finally, SH-SY5Y cells were cultured on the treated microstructures, differentiated for 3 days, and stained for Hoechst 33342 (blue staining for the nucleus), actin (green staining for the cytoskeleton), and paxillin (red staining for the focal adhesions) (Figure 3). Between the two solutions, bleaching was found to be more effective especially for what concerns the visualization of focal adhesions due to their small sizes (200-300 nm). Visualization of stained cells in microcages and microchannels treated with SBB proved to be challenging since the SBB layer deposited on top of the microstructures absorbed photons emitted by the staining of the cells.

In conclusion, this study provides a set of effective and straightforward solutions to solve the problem of auto-fluorescence that represents a major obstacle in cell biology studies using microstructures fabricated by 2PP.

[1] M. Emons et al., Opt. Mater. Express, OME. 2 (2012) 942–947.
[2] A. Sharaf et al., Front. Bioeng. Biotechnol. 10 (2022) 926642.
[3] A. Sharaf et al., Neural. Regen. Res. 18 (2023) 1709-1710.
[4] A. Sharaf et al., Micro and Nano Engineering 19 (2023) 100188.

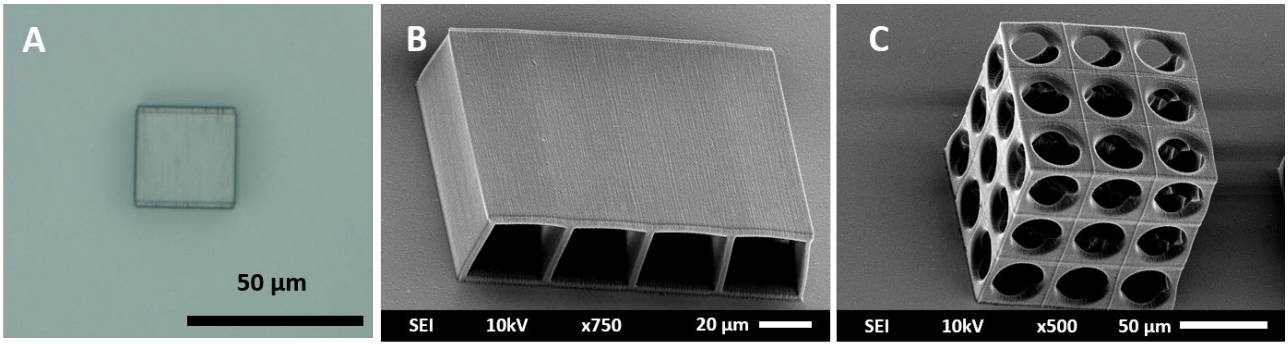

Figure 1. Representative optical microscope and SEM images of (A) IP-L pedestals, (B) IP-L microchannels, and (C) IP-L microcages.

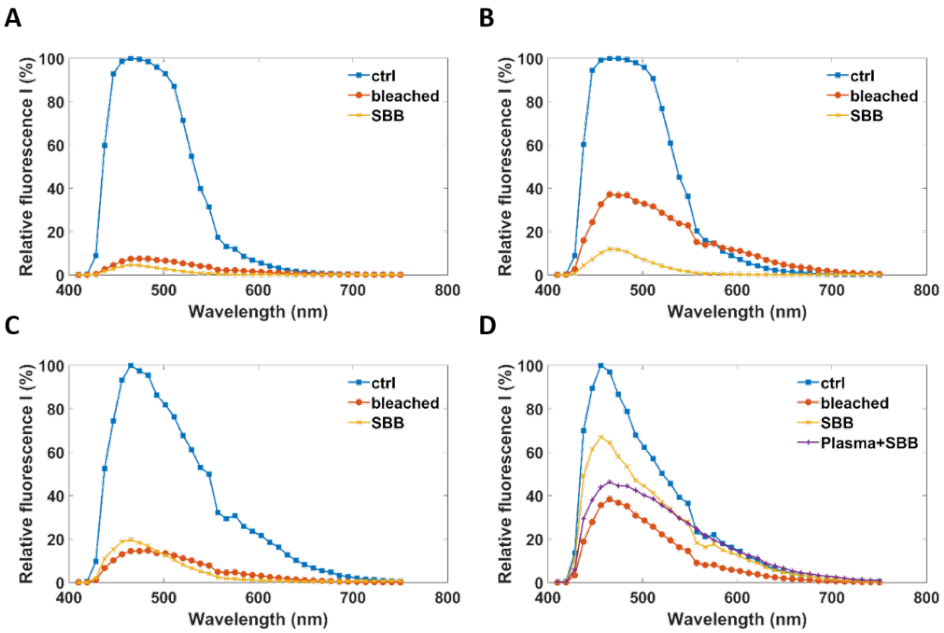

Figure 2. Spectral analysis showing the relative auto-fluorescence intensity (I) of (A) IP-L, (B) IP-Dip, (C) IP-S, and (D) IP-PDMS untreated (ctrl), bleached, and SBB quenched pedestals.

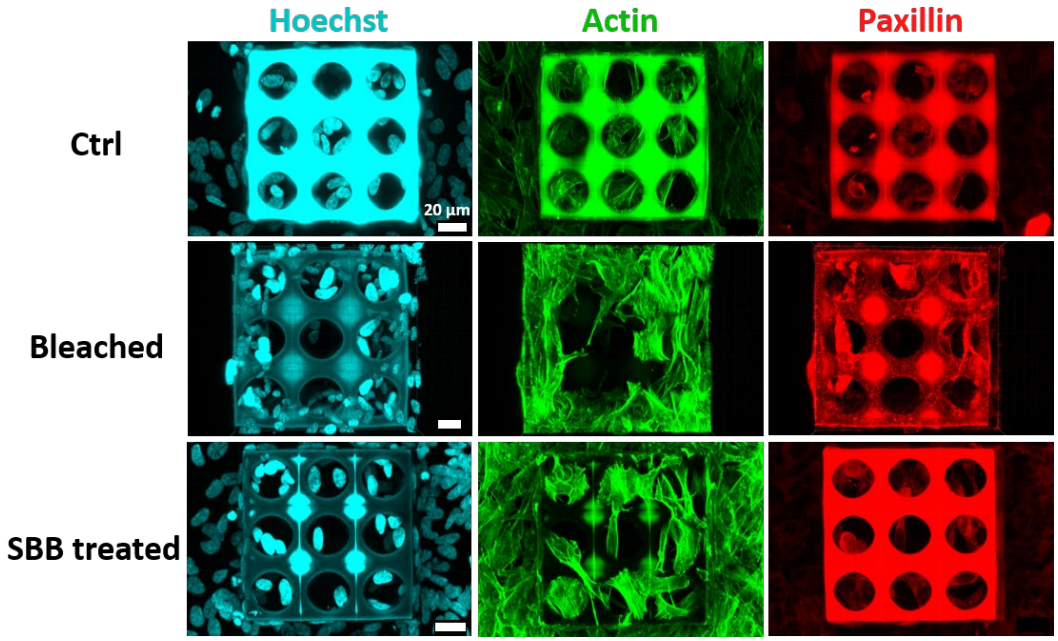

Figure 3. Zoomed in confocal microscope images of the top view of IP-L microcages (no treatment, bleached and SBB treated) colonized by differentiated SH-SY5Y cells. Hoechst staining (blue) is for nuclei; actin (green) depicts the cytoskeleton, and paxillin (red) depicts focal adhesions. Scale bar = 20 µm.

Microparticle-based Microneedles for mRNA delivery

Alessandro Attanasio[a,b], Raffaele Vecchione[b], Paolo Antonio Netti[a,b]

[a] Department of Chemical, Materials and Industrial Production Engineering (DICMaPI), University of Naples "Federico II" (Naples, 80138 Italy)
[b] Italian Institute of Technology (IIT) (Naples, 80125 Italy)
e-mail: alessandro.attanasio@unina.it

Gene therapy has attracted much attention in the very last years, due also to the pandemic worldwide situation. Use of DNA or RNA to induce a desired response of the organism, might result in achieving important therapeutic goals, so representing a solution for the treatment of several diseases. On the other hand, different factors hamper the administration of genetic material, due to its easy degradation, especially in the case of RNA, and the need to overcome extra and intracellular barriers [1]. Microneedles (MNs) are an ideal delivery platform capable of facing several challenges in the transdermal administration field. They permit to access to the intradermal route without reaching nerve endings, and enabling molecules with molecular mass > 500 Da to pass through the stratum corneum, the natural barrier of the human organism [2]. From the gene therapy point of view, MNs constitute an attractive technology within vaccines field since they can be used to deliver genetic material to the immune cell-rich environment of the epidermis [1]. MNs also can overcome some of the main limitations of conventional vaccines which require administration by trained healthcare personnel and storage at very low temperatures, being still an obstacle for rapid mass vaccination in developing countries, as happened for Ebola emergency [3]. Moreover, MNs represent an ideal solution for the patient compliance, which is limited by pain and needle-phobia discomfort [2].
Even if MNs came up in the state of art over twenty years ago, there are still challenging features with respect to the appropriate category. Polymer MNs are typically characterized by low drug loading limiting the number of applications and incomplete penetration in the skin, making the delivery less effective and not reproducible [2,4]. In addition, the stability of labile molecules is often affected by MNs fabrication process [5]. The current work aims to design and realize a MN-based technology patch able to provide complete indentation, namely implantation, and a low invasive fabrication procedure allowing the encapsulation of mRNA in an active form and its sustained release.
The proposed technological platform is constituted by a bi-compartmental array of microparticle-based MNs where a fast dissolvable tip together with slow release polymer microparticles (MPs) are assembled together and integrated onto polymethyl methacrylate (PMMA) pillars. Firstly, a MNs positive master was obtained by two photons lithography process (Nanoscribe system), achieving highly sharp tips. In order to enhance the mechanical stability of the master microcones, necessary feature for an optimal replica molding of the MNs PDMS stamp, a photopolymerized hexagonal pattern substrate was realized under the master MNs (Fig. 1a). PDMS stamps were first filled by casting with a fast dissolvable polymer (blend of HA and PVP) and then filled with drug-loaded PLGA MPs. In order to guarantee, simultaneously, mechanical robustness of the entire microneedle body and preserve the encapsulated drug, a gentle sintering process was necessary for the final MPs assembly (Fig. 1b). This process was developed, patented and then described in a previous work of the group [6]. PMMA pillars, realized by micromilling techinique, were used to lift the needles off from the stamp (Fig. 1 c-e). The pillars were supposed to deal with skin elasticity that is an opposing factor for the implantation of the MNs. Compression test and *ex vivo* pig skin implantation were used to characterize this MNs configuration achieving the intended outcomes (Fig. 2 a-d). Considering the showed results, the current work is presented as a novel and effective MNs platform to ensure implantation and mRNA delivery in a stable state leading to mass vaccination in painless and smart conditions, finally.

[1] T. Bauleth-Ramos *et al.*, Materials Today, 63 (2023) 239-287.
[2] E. Larraneta *et al.*, Materials Science and Engineering R, 104 (2016) 1–32.
[3] H. Yang *et al.*, Advanced Healthcare Materials, 6 (2017) 1600750.
[4] Q. Wang *et al.*, European Journal of Pharmaceutical Sciences, 66 (2015) 148-156.
[5] C. Di Natale *et al.*, Journal of Materials Chemistry B, (2020).
[6] R. de Alteriis *et al.*, Nature Scientific Reports, (2015) 5:12634.

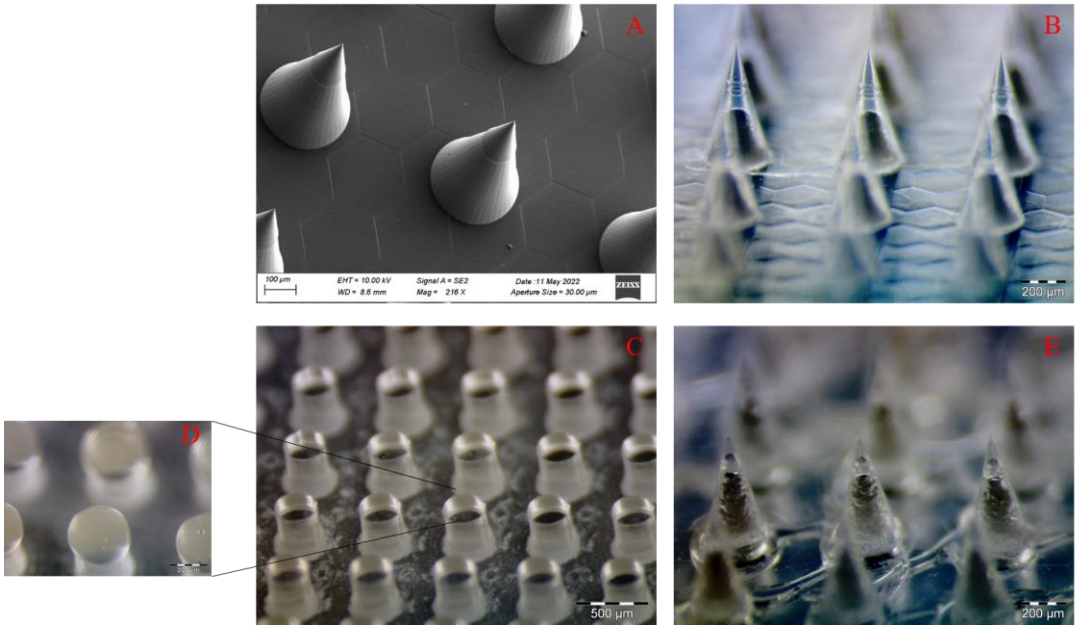

Figure 1. (a) MNs positive master. Compared to a previous work [5], laser and scan speed parameters were optimized to obtain the best resolution for the MNs tip (~ 1 µm). Hexagonal pattern acting as an interface between the cones and the glass substrate to ensure mechanical stability in the following replica molding process. (b) Microparticle-based MNs obtained by the patented sintering process (solvent/non-solvent vapour mixture at room temperature). (c) PMMA pillars. (d) close up showing the harvesting polymeric solution turned into a sticky state, added successively. (e) Final integration of Microparticle-based MNs and pillars.

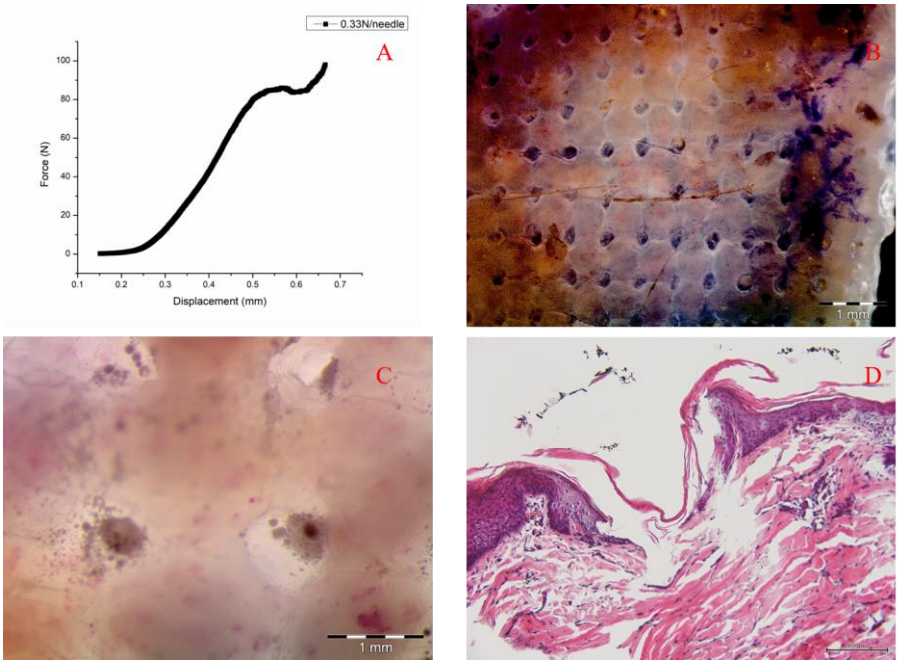

Figure 2. (a) Failure force of microparticle-based MNs (0.33N/needle). The compressive test was carried out by an Instron test station. The outcome is higher than skin resistance. (b-d) Implantation in *ex vivo* pig skin. Test carried out by a custom automated system.

Hybrid metal-dielectric non-planar optical neural interfaces for multifunctional monitoring of brain functions

M. S. Andriani[1,2,+,*], T. J. Parras [3,+], C. Montinaro[1], M. Bianco[1], A. Balena[1] , E. Cid[3], B. Spagnolo[1], M. Pisanello[4], F. Pisano[1], L. M. de La Prida[3,$], M. De Vittorio[1,2,$], F. Pisanello[1,$],

[1] Istituto Italiano di Tecnologia, Center for Biomolecular Nanotechnologies, 73010 Arnesano, Italy;
[2] Dipartimento di Ingegneria dell'Innovazione, Università del Salento, 73100 Lecce, Italy;
[3] Istituto Cajal, CSIC, 28002 Madrid, Spain;
[4] OptogeniX s.r.l., 73010 Arnesano, Italy. [+]Co-first authors [$]Co-last authors. * mariasamuela.andriani@iit.it

Micro and nanotechnologies are significantly supporting the development of integrated optoelectrical implantable devices, helping the neuroscience community to better control and monitor electrical and molecular events in the central nervous system. In particular, the ability to simultaneously modulate (optogenetics) and detect electrophysiological signals and/or functional fluorescence, using the single multimodal optic fiber in the same brain volume would enable unprecedented biomedical applications.

However, integrating bi-directional optical and electrophysiology channels on a single multimodal optical fiber represents a challenge. The ideal optoelectrical neural probe should indeed be able to: (i) deliver light for optogenetic control of neural activity, (ii) excite functional fluorescence, (iii) collect emitted photons, (iv) catch electrophysiology signals in its entire frequency range (100Hz-10kHz), and (v) provide spatial resolution for all the above-mentioned features. Planar micro e nanofabrication methods have been widely employed to fabricate implantable shanks for light delivery in scattering tissue, with in situ fabrication of solid-state waveguides or micro-light emitting diodes [1-3]. These devices can be coupled to photodetectors and single-photon avalanche photodiodes, enabling integrated light detection, also in free-moving mice [4]. However, the field would greatly benefit from a technology able to provide simultaneously bi-direction optical channels and electrophysiology capabilities.

In this study, we present a non-planar technology for establishing a hybrid metallic-dielectric light-guiding mechanism in tapered optical fibers neural implants. This enables the fabrication of integrated devices able to deliver and detect light from scattering brain tissue with high efficiency, together with the possibility of performing simultaneous extracellular electrophysiology.

A schematic representation of the implantable probe is displayed in **Figure 1a**, together with key fabrication steps in **panel b** and optical characterization in **panel c**. A tapered optical fiber conformally coated with a 200nm-thick Au layer is placed within a drop of IP-S photoresist and a fs-pulsed laser beam in a non-planar two-photon lithography (2PL) system employed to create a resist mask on the sections that should feature metallic confinement. The high aspect ratio of the voxel obtained with a high-NA low-magnification objective allows to generate steep resist walls with low surface-roughness on the non-planar surface of the taper. After wet-etching this results in a sharp transition between dielectric and metallic confinement of the guided modes (**Figure 1b**). Coupled with the ability of 2PL to obtain in-plain sub-diffraction resolution all-around the taper [4], the approach allows defining multiple sections of the waveguide that can exchange optical energy with the environment (**Figure 1c)**, to both deliver and collect light radiation from scattering brain tissue (**Figure 1d** shown 2-photon microscope image overlayed with the eye-guides lines, representing the collection pattern of the optical apertures). Through the same patterning method, electrodes for extracellular recording of neural activity can be integrated on the taper edge, in proximity of the optical apertures. Electrodes can be realized either directly on the metallic layers that act as waveguide cladding or through additional lithographic layers on a further conformal dielectric surface deposited on top of the device (see SEM details in **Figure 1e**). The impedance of the electrode can be controlled by changing its surface area.

Figures 2 and 3 display preliminary data collected by the realized probes. We confirmed the ability of the probes to record hippocampal ongoing oscillations (theta; 4-12 Hz) from awake transgenic mice expressing channelrhodopsin (ChR2) under the promoter Thy-1 (**Figure 2a**). Using optimal blue light stimulation, but not green light, we found population responses consistent with synchronous action potential firing from ChR2-expressing cells (**panel b**); arrowhead; data from three different probes is shown in **panel c**). In a separate set of experiments, we also tested the ability of our probes to record fluorometric signals in the somatosensory barrel cortex in response to air-puff whisker stimulation. **Figure 3** displays the first evidence of fluorescence variation over time and spike activity during multiple whiskers stimulation events, from a mouse expressing GCaMP6s in pyramidal cortical neurons under the promoter Thy-1.

To the best of our knowledge, the proposed approach represents the first evidence of the possibility to integrate electrophysiology and optical detection of neural activity within the same implantable device.

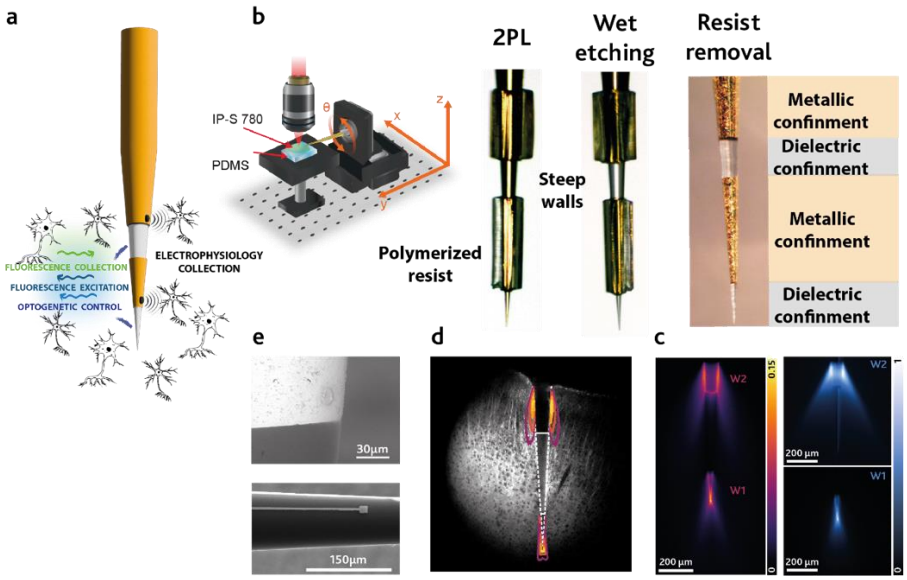

Figure 1 a) Implantable probe. **b)** Key fabrication steps. **c)** Optical characterization: collection (left), emission (right). **d)** shown 2-photon microscope image overlayed with the collection eye-guides lines. **e)** SEM electrodes images

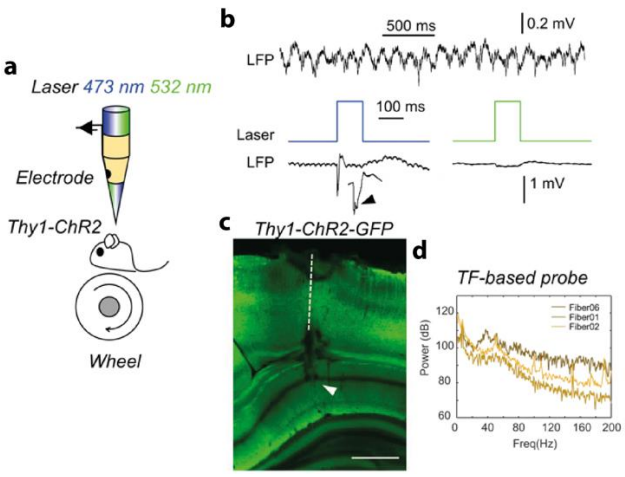

Figure 2 a) Schematic of the experimental setup for optogenetic tests in behaving Thy1-ChR2 mice running head-fixed on a wheel. **b)** Local field potential (LFP) oscillations and optogenetic responses recorded from the dorsal CA1 hippocampal region. **c)** Histological section showing the probe track. **d**) Power spectra of LFP signals collected from three different fibers.

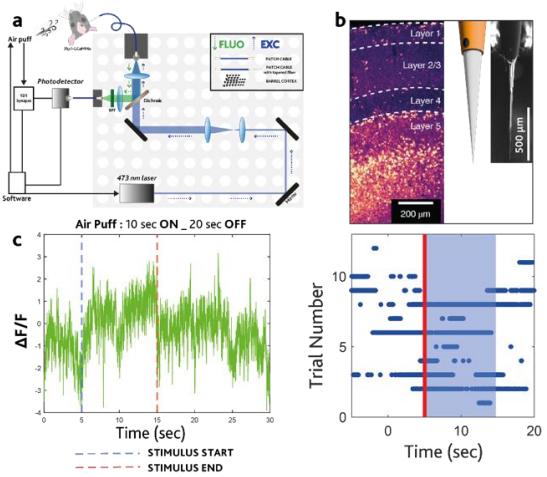

Figure 3 a) An air-puff whiskers stimulation system, implemented to trigger neural activity. **b)** Probe implanted to collect functional fluorescence and the correlated electrophysiology signal from the cortical column. **c)** Fluorescence variation over time (left) and spike activity (right) during multiple whiskers stimulation events

[1] A. Mohanty et al., *Nat Biomed Eng*, vol. 4, no. 2, pp. 223–231, Feb. 2020.
[2] W. D. Sacher *et al.*, *Opt Express*, vol. 27, no. 26, p. 37400, Dec. 2019.
[3] L. Lu *et al.*, *Proceedings of the National Academy of Sciences*, vol. 115, no. 7, Feb. 2018.
[4] A.S. Abdelfattah et al., *Neurophotonics*, 9(Suppl 1): 013001, Jan. 2022.
[5] B. Spagnolo, A. Balena et al., *Nat Mater*, vol. 21, no. 7, pp. 826–835, Jul. 2022.

Pyrolytic carbon microelectrodes for electrophysiological studies with retinal tissue

Pratik Kusumanchi [a], Jesper Guldsmed Madsen [b], Toke Bek [b], Rasmus Schmidt Davidsen [c], Stephan Sylvest Keller [a]

[a] DTU Nanolab, Technical University of Denmark, 2800 Lyngby, Denmark
[b] Institute of Clinical Medicine Ophthalmology, Aarhus University Hospital,8200 Aarhus N, Denmark
[c] Department of Electrical and Computer Engineering, Aarhus University,8000 Aarhus C, Denmark
email: prakus@dtu.dk, rasda@ece.au.dk,

Keywords: microelectrodes, pyrolytic carbon, electrophysiology.

Retinal degeneration due to age-related macular degeneration (AMD) and retinitis pigmentosa (RP) are the leading cause for blindness around the world. In the majority of cases the photoreceptor layer degenerates while the other neural networks retain their functionalities. Therefore, the overall aim of this project is to restore vision via a retinal implant replacing the photoreceptor layer. In such a device, 3D microelectrodes potentially provide high surface area and short distances to retinal neurons allowing for stimulation with largest electric fields upon application of an external voltage [1]. As a novelty, we evaluate pyrolytic carbon as a biocompatible electrode material for retinal implants [2]. More specifically, we develop a fabrication process for pyrolytic carbon microelectrodes based on patterning of high aspect ratio SU-8 structures followed by conversion into carbon electrodes using pyrolysis. For electrophysiological studies with retinal tissue, we have considered interdigitated carbon fingers with pillars as a format for local return electrode. With the aim to investigate threshold voltage for electrical stimulation with carbon.

Fig. 1 illustrates the fabrication process of 3D pyrolytic carbon microelectrodes. Firstly, a 15 µm thick film of SU-8 2035 was spin coated and patterned with UV photolithography followed by a second spin coating of 68 µm thick SU-8 2075 and UV pattering for the pillars. After subsequent post exposure bake, development, flood exposure of the SU-8 and a hard bake for 15-hours at 90°C, 3D precursor structures were obtained. A pyrolysis process was carried out in a quartz furnace at a temperature of 1050°C converting the SU-8 into carbon. Finally, gold was deposited to define the contact pads, and an SU-8 2005 passivation layer was patterned with UV lithography. For initial electrochemical testing, cyclic voltammetry is carried out in a 0.5 mM $K_3[Fe(CN)_6]$/ $K_4[Fe(CN)_6]$ electrolyte solution with an external Pt counter electrode and an Ag/AgCl reference electrode. The electrophysiological studies on excised porcine retinal tissue is carried out in (fig. 3 A) a 3D printed holder stacking the carbon chip, retinal tissue and a commercial microelectrode array (MEA, Blackrock CerePlex). Voltage pulses are supplied to the carbon chip and action potentials at the retinal ganglion cell (RGC) layer were recorded by the MEA.

As shown in the SEM image (fig. 2A, B) the required height (30 µm) and diameter (16 µm) of the carbon pillars were obtained with this fabrication process. The cyclic voltammograms (CV) as shown in fig 2C, demonstrates the excellent quality of carbon electrodes and confirm the electrical isolation between working and the return electrode (fig. 2C, read and blue). As expected, the peak current values nearly doubled when both sets of fingers (fig. 2C, black) were simultaneously connected as working electrode, confirming the successful fabrication of two independent and functional microelectrodes. First electrophysiological studies (fig. 3 A, B) show that the recorded signals being responses of the population of neurons (fig 3B, blue), here we observe action potentials appearing after the stimulus with a time delay and difference in amplitude indicating the behaviour of possible neuron activation (shown in arrows). Confirmation of such action potentials is done by repeating the experiment by adding a tetrodotoxin (TTX) chemical which blocks sodium channels in the tissue and preventing the possible phase change of neurons, thus no action potentials (fig. 3B, orange).

In summary, we established a custom-built setup for electrophysiological studies with retinal tissue using carbon microelectrodes and were able to record responses from neurons. Further statistical investigations on neuron action potential (latency, amplitude) are being carried out in the setup.

1. Thomas Flores et al, J. Neural Eng. Vol 15, pp.036011, 2018.
2. Davidsen R. S. et al., Micro and Nano Engineering, Vol. 2, pp. 110-116, 2019.

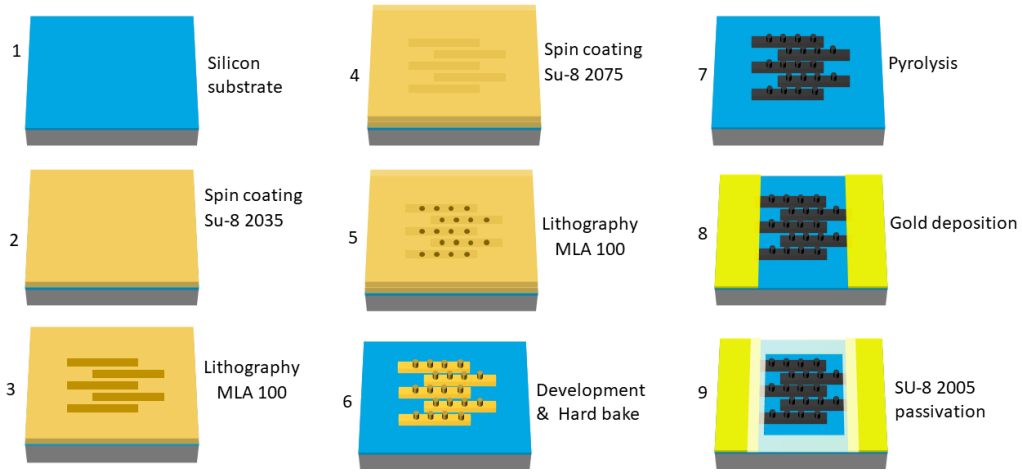

Figure 1: Fabrication process flow of 3D pyrolytic carbon microelectrode with interdigitated fingers, the gold was deposited for contacts and passivation of Su-8 2005 to project the carbon testing region.

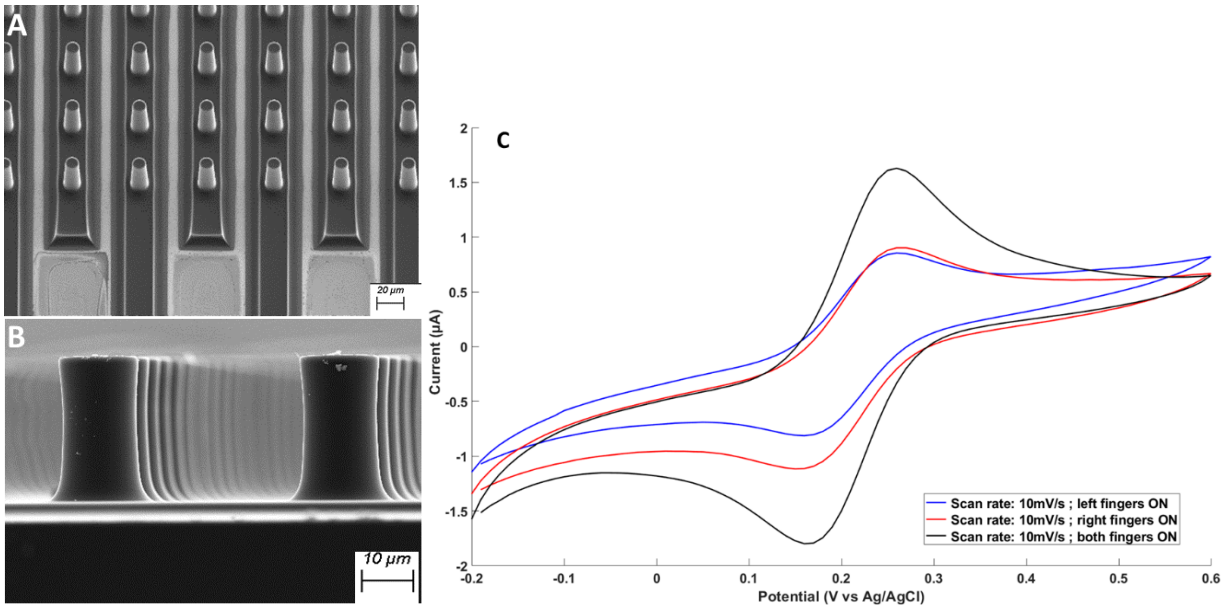

Figure 2: SEM images of, A) Carbon pillars on carbon base, B) pillars have a diameter of ~15 µm and a length of 30 µm. C) Cyclic voltammetry in 0.5mM $K_3[Fe(CN)_6]$/ $K_4[Fe(CN)_6]$ electrolyte solution at 10mV/s scan rate with an external platinum counter electrode and a Ag/AgCl reference electrode, the CVs indicate the individuality of finger by turning on one set at a time (red and blue) and the collective response (turning on both fingers, Black) is doubling the current.

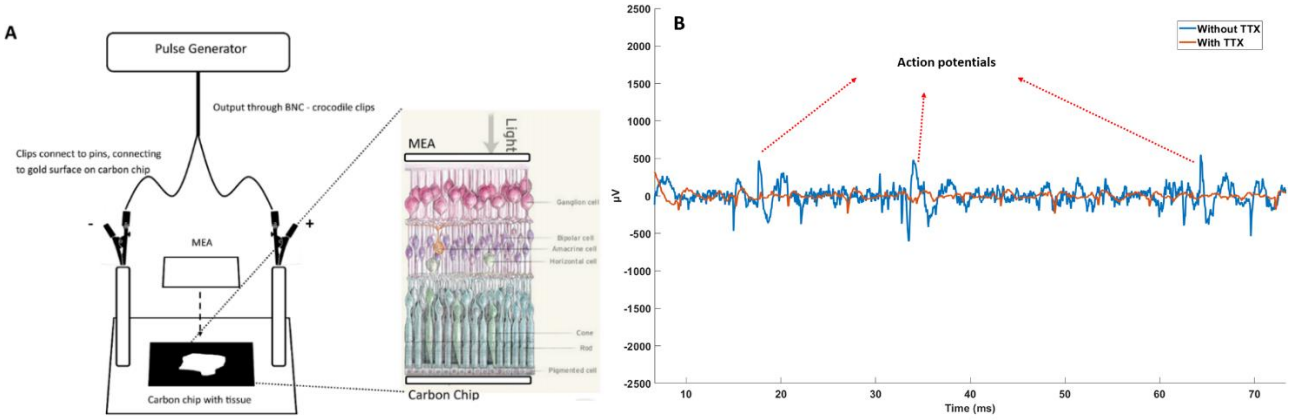

Figure 3: A) Schematic of the electrophysiology setup, with tissue and MEA are placed on carbon chip (with RGCs facing upwards) the carbon chip is supplied with pulses to stimulate the tissue and B) the raw data recording (Blue) shows the action potentials (arrows) detected by the MEA when external voltage is applied, the signals are absent with addition of TTX indicating sodium channel suppression thus no biological signals (orange).

Novel µfluidic Brain-on-Chip instructive µenvironments

Gulden Akcay, Jeroen van Venrooij, Regina Luttge
Neuro-Nanoscale Engineering, Department of Mechanical Engineering/Microsystems and Institute of Complex Molecular Systems, Eindhoven University of Technology, Eindhoven, 5600 MB, The Netherlands
e-mail: g.akcay@tue.nl

The human brain is a complex organized system made up of many different types of cells which process information. Considering plasticity and cellular interactions is a big challenge. Standard fabrication techniques including photo-patterning, lithography, and self-assembly are utilized for the manufacturing of microfluidic devices and also Organ on chip (OoC). Particularly, lithography is the most used technique, however, it is a cost-intensive process with complex and time-consuming operations performed in a clean room [1].

In that sense, 3D printing is becoming popular for microfluidic fabrication. This led researchers to explore 3D printing applications on OoC. 3D printing offers several advantages over its traditional manufacturing techniques such as more design freedom, able to print complex designs, reduction of waste products [2].

Integrating different cell types is one of the important parts but also creating 3D microenvironments, which mimic brain regional stiffness and layers. Having in vitro systems that provide translational models for human brain is the prime focus of Brain-on-chip (BoC) technology in this work.

We propose to use an actuator chip with different microfluidic “top layers”, which is a specific BoC design previously developed in our group [3]. This BoC is based on nine independent controlled microfluidic air-flow channels that can each locally actuate a polydimethylsiloxane (PDMS) membrane and are evenly distributed across the surface of the culture reservoir. We improved our chip design from a simple reservoir to 2 reservoirs connected with a central tunnel surrounding groves and feeding channels. We aimed to mimic the real brain in vivo conditions using the co-culturing method and different hydrogel layers.

We designed one of the top layers as being also beneficial to obtain defined hydrogel layers yielding a vertical stiffness gradient across. Another one has two steps of grooves surrounding the two reservoirs and the central tunnel. This structure results in pinning two stacked hydrogels to get defined layers that are up to 1 mm thick, which can be fed from the sidewall via the resulting feeding channels, which has a 0.2 mm opening to ease the nourishment of the hydrogel layers in order to allow the cell medium to reach out to the cells and the following layers effectively.

Our designs have been printed via 3D Printer (Formslabs, Form 3+) by using Clear v4 resin type. We used it as a mold to make a chip layer made of PDMS. To ease PDMS from the mold, Ease Release 200 (Mann Technologies) has been sprayed 15 to 20 cm from the mold surface, after leaving it fast dry under the fume hood for 5 min, PDMS (10:1) has been poured into the mold then after curing at 80°C in the oven overnight, PDMS has been peeled off the mold for being assembled with the actuator chip.

Figure 1 and 2 depicts the designs, molds, and results of molding the new actuator top layers. For initial culture tests, we mounted the reservoir layer which is shown in Figure 1 on a PDMS membrane of 10 µm thickness on a glass substrate and used iPS-derived human neurons to be cultured on a layer of GelMA as a 3D hydrogel scaffold. Cells were kept for 3 weeks in the culture to mature them. Synapse formation is illustrated in Figure 3, by staining the cells with MAP2, SYN-1, HOMER-1.

Next, we will assemble the newly designed PDMS top layers to the membrane layer of our actuator chip to provide instructive 3D microenvironments in progressing microphysiological systems studies.

[1] Rupal, B. S., Garcia, E. A., Ayranci, C., & Qureshi, A. J. *22*(1) (2018) 5-20.
[2] Carvalho, V. et al. 21(9) (2021) 3304.
[3] S. Xie, J. G. E. Gardeniers, and R. Luttge 28 (2018) 085011
[4] Akcay, Gulden, and Regina Luttge 12(2) (2021) 165

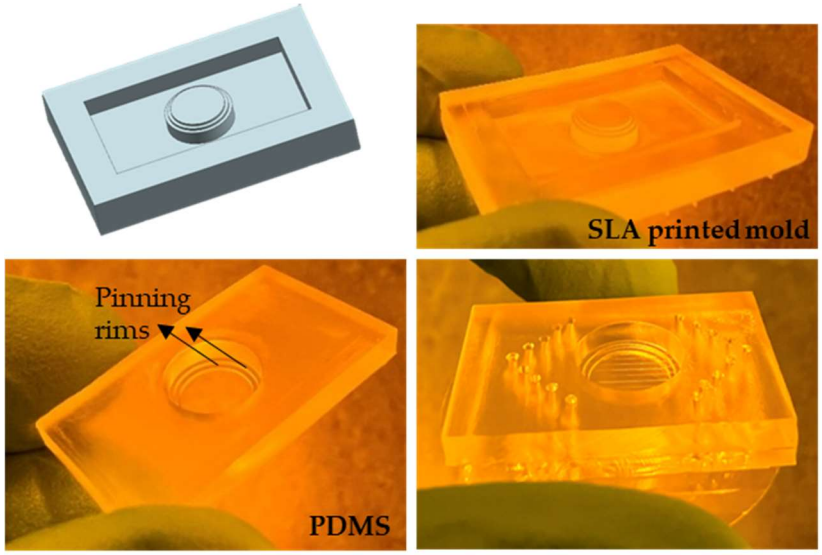

Figure 1. Fluidic design with pinning rims to obtain gel defined gel layers on top of each other.

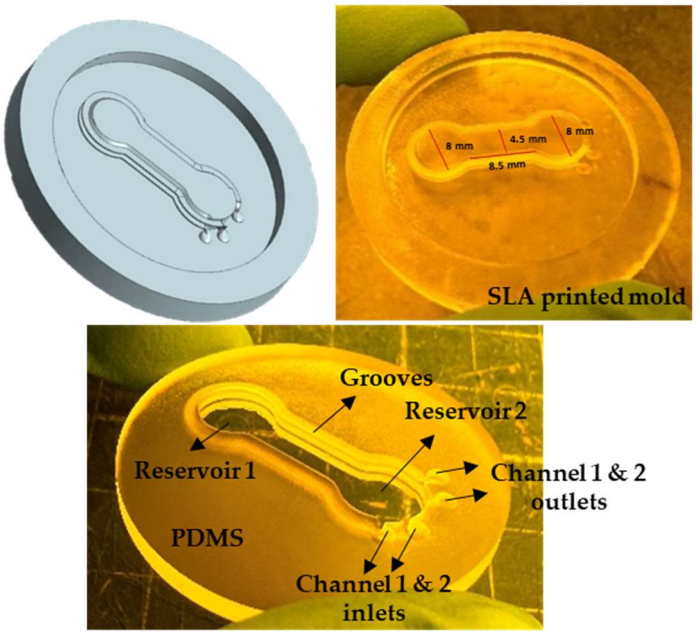

Figure 2. Fluidic design with microgrooves incorporated in the sidewalls of the channel allows us to pin a liquified gel in the z-direction while flowing along the channel upon insertion in one of the reservoirs at the channel endings.

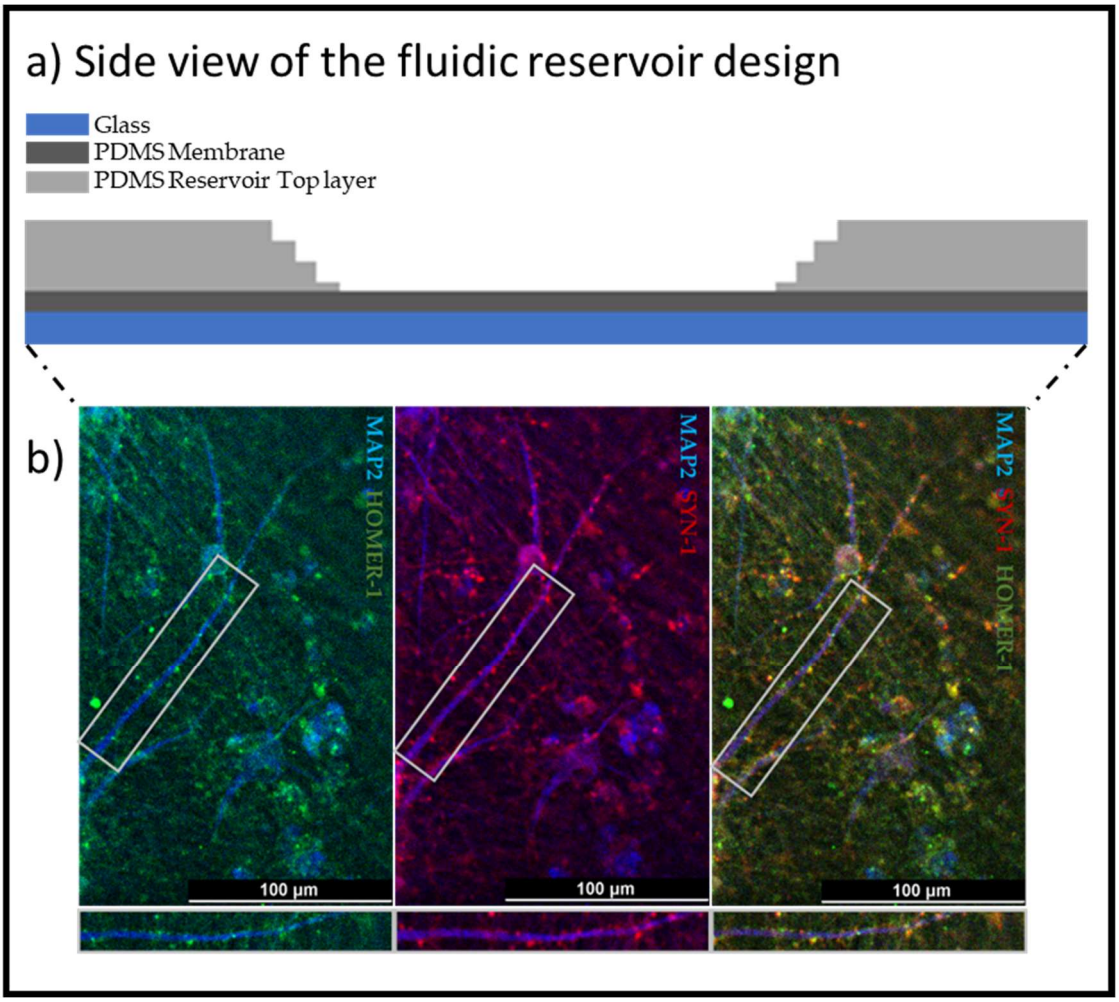

Figure 3. a) Side view of the fluidic design in Figure 1. **b)** iPS cell-derived human neurons form synapses in our fluidic design. (MAP2:Dentrite, SYN-1: Pre-synaptic marker, HOMER-1: Post-synaptic marker)

Micro/Nano Engineering for Physical and Chemical Applications - Papers

Group IV nanowires for nano-/optoelectronic and sensing applications

Muhammad Bilal Khan [a], Ahmad Echresh [a,b], Sayantan Ghosh [a,b], Oliver Steuer [a,b], Muhammad Moazzam Khan [a,b], Slawomir Prucnal [a], Lars Rebohle [a], Shengqiang Zhou [a], Manfred Helm [a,b], Artur Erbe [a,b], Yordan M. Georgiev [a,c],

[a] Institute of Ion Beam Physics and Materials Research, Helmholtz-Zentrum Dresden-Rossendorf (HZDR), Dresden, 01328, Germany
[b] Technische Universität Dresden, Dresden, 01062, Germany
[c] Institute of Electronics, Bulgarian Academy of Sciences, Sofia, 1784, Bulgaria

e-mail: y.georgiev@hzdr.de

Nanowires (NWs) based on group IV elements and alloys are promising excellent building blocks of variety of nanoelectronic, optoelectronic, photovoltaic, sensing, etc. devices. Beside the well-known advantages of the single-element Si and Ge NWs, such as superb electrical and mechanical properties and large surface area to volume ratio, the Si-Ge-Sn alloys (SiGe, GeSn and SiGeSn) offer a number of additional unique properties. With suitable Sn concentrations it is possible to achieve effective bandgap engineering and very high charge carrier mobilities for high-performance nanoelectronic devices as well as direct-bandgap Group IV semiconductors for optoelectronic applications. Therefore, the SiGeSn alloy systems would allow successful on-chip integration of nano- and optoelectronic devices, which makes them ideal candidates for post-Si applications.

In this work, we will briefly present the top-down fabrication of various group IV NWs: Si, Ge, SiGe, GeSn and SiGeSn (see Fig. 1) [1]. Such a wide range of nanowires, in conjunction with a variety of Sn contents in the alloyed systems, allows a flexible choice of nanowires with appropriate properties for different applications.

We will then discuss the challenging structural and electrical characterisation of the fabricated nanowires with special attention on the Hall Effect measurements using a novel six-contact Hall bar configuration (Fig. 2). This configuration permits to evaluate the electrical properties of even very small (20-30 nm) nanowires and reliably quantify their carrier concentration (n), Hall mobility (μ_H), and resistivity (ρ) [2].

The innovative nanoelectronic devices that we are targeting will also be discussed. These include junctionless nanowire transistors (JNTs) [3], reconfigurable field effect transistors (RFETs) [4] as well as nanowire phototransistors and photodetectors. We are in particular interested in Si JNTs for sensing application (see Fig. 3) [5] as well as in Ge, SiGe, GeSn and SiGeSn JNTs for digital logic. In the case of RFETs, we are working on Si, SiGe, GeSn and SiGeSn RFETs (see Fig. 4). Different configurations of such devices will be discussed together with their structural and electrical characterisation. The single-SiNW JNT phototransistors showed very high internal gain up to 35 for 860 nm illumination with very low light intensity (few pW) [6]. The photodetectors are based on single Ge NWs and demonstrated very high responsivity of 3.7×10^2 AW^{-1} and a high-frequency response of up to 1 MHz.

Acknowledgments: This work was partially supported by the German Bundesministerium für Bildung und Forschung (BMBF) under the project "ForMikro": Group IV heterostructures for high performance nanoelectronic devices (SiGeSn NanoFETs), Project-ID: 16ES1075, and by the European Union's Horizon 2020 Research and Innovation programme under the project RADICAL, Grant Agreement No. 899282. We gratefully acknowledge the HZDR Ion Beam Centre and nanofabrication facility NanoFaRo.

[1] A. Gangnaik et al., J. Vac. Sci. Technol. B 34 (2016) 041603.
[2] A. Echresh et al., Nanomaterials 11 (2021) 2917.
[3] Y. M. Georgiev et al., In Functional Nanomaterials and Devices for Electronics, Sensors and Energy Harvesting (Springer International Publishing AG, Cham, Switzerland, 2014) 367-388.
[4] M. B. Khan et al., Appl. Sci. 9(17) (2019) 3462.
[5] Y. M. Georgiev et al., Nanotechnology 30 (2019) 324001.
[6] S. Das et al., Appl. Phys. Lett. 108 (2016) 063113.

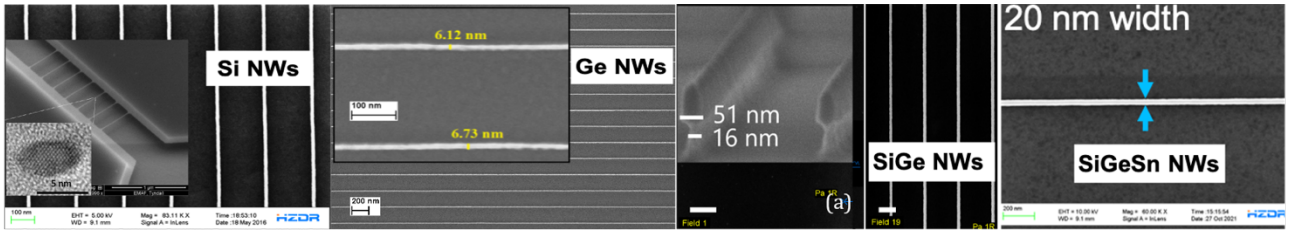

Figure 1. Collated scanning electron microscopy (SEM) micrographs of Si, Ge, SiGe and SiGeSn NWs.

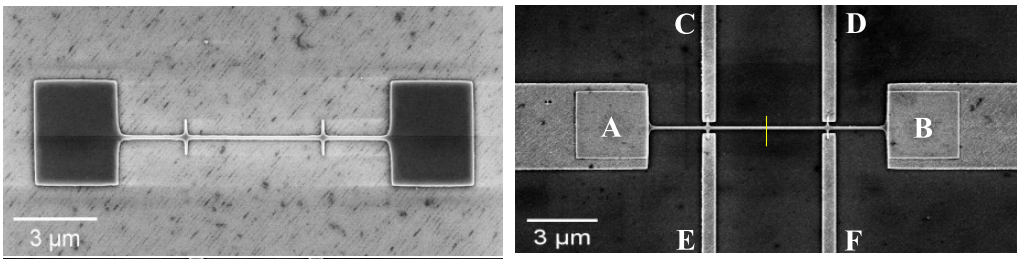

Figure 2. SEM micrographs of a GeNW with Ge contact pads and narrow Ge bars (left) and a fabricated device with the six-contact Hall bar configuration after metal deposition (right).

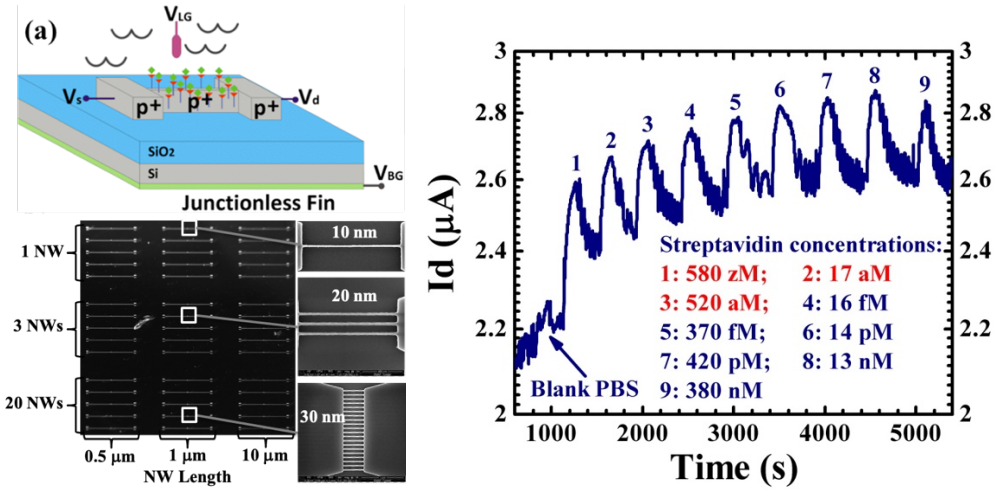

Figure 3. Si JNT sensors of different configurations (left) and results of detection of the protein streptavidin at nine different very low concentrations (right).

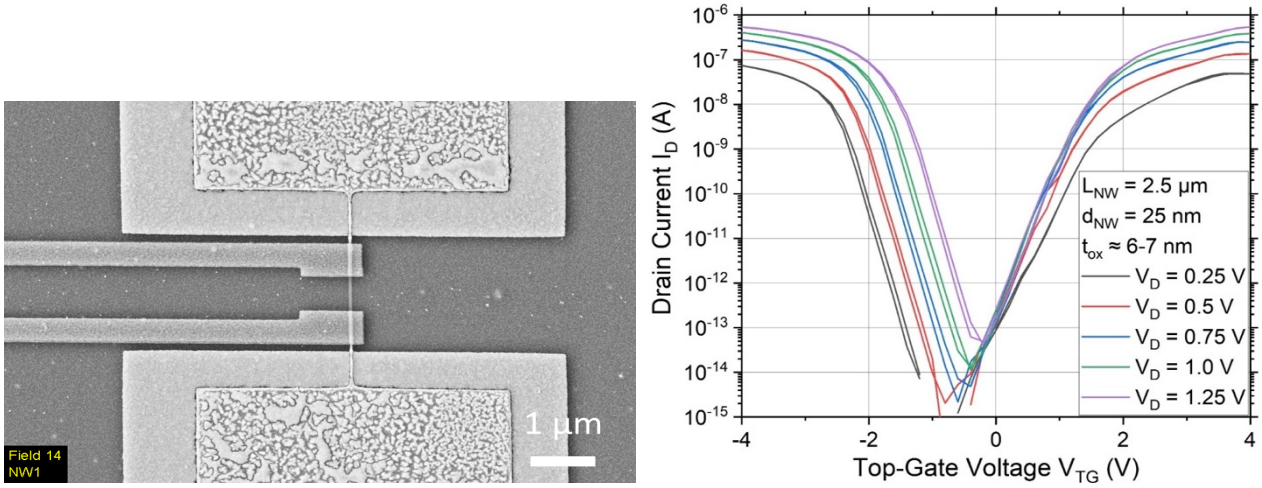

Figure 4. SEM micrograph of a SiNW RFET with two top gates (left) with its transfer characteristics (right).

Fabrication of self-powered wearable pressure sensing system based on PVDF-TrFE and ionic liquid

Chaeeun Lee, Changwoo Cho and Je Hoon Oh

Department of Mechanical Engineering and BK21 FOUR ERICA-ACE Center,
Hanyang University, Ansan, Gyeonggi-do, 15588, Republic of Korea
E-mail: jehoon@hanyang.ac.kr

Recently, flexible sensors have been utilized in various fields such as electronic fabrics, electronic skin, and healthcare monitoring systems. Among diverse types of sensors, ionic capacitive pressure sensors have been researched, which generate electrochemical double layers (EDLs) by introducing ionic liquids (ILs) composed of cations and anions into a polymer matrix [1]. Compared to conventional capacitive pressure sensors, ionic capacitive pressure sensors are characterized by higher sensitivity and faster response time. However, the devices used to process the signals from these sensors primarily depend on external power sources, such as batteries, which require periodic replacements. Therefore, the growing demand for sustainable alternative energy sources has increased, prompting extensive research into triboelectric nanogenerators (TENGs) as a promising solution [2]. Through periodic contact and separation, TENG converts mechanical energy into electrical energy, which can be stored and utilized to drive various devices.

In this work, we demonstrate a self-powered wearable pressure sensing system, which is composed of poly(vinylidene fluoride co-trifluoroethylene) (PVDF-TrFE) nanofiber-based TENG and an ionic capacitive pressure sensor based on an IL/PVDF-TrFE film. The TENG was used to harvest energy to provide power, and the ionic capacitive pressure sensor was used to detect pressure.

We fabricated flexible polymer-based electrodes by using multi-wall carbon nanotubes (MWCNTs) and polydimethylsiloxane (PDMS) [3]. To enhance surface adhesion, the mixing ratio of PDMS was set at 30:1. The MWCNTs/PDMS mixture was covered onto a mold with pyramidal patterns by doctor-blade casting, and the silver nanowires (AgNWs) solution was sprayed onto it (**Figure 1(a)**). The cured MWCNTs/PDMS/AgNWs composite was cut into 30×30 mm^2 and 10×10 mm^2 pieces and used as electrodes for the TENG and sensor, respectively. Electrospinning was employed to fabricate a PVDF-TrFE nanofiber membrane, which served as the friction layer for a TENG (**Figure 1(b and c)**). A mixture of PVDF-TrFE and [EMIM][TFSI], which is an ionic liquid, was spin-coated on the MWCNTs/PDMS/AgNWs composite to produce an ion-gel film, serving as the dielectric layer in sensor (**Figure 1(d and e)**).

To assess the power generation capabilities of the TENG with the PVDF-TrFE nanofiber membrane, the output voltage, short-circuit current, and power density were measured as a function of load resistance (**Figure 2(a)**). The power density was determined using the equation $P_D = I^2R/A$, where I is the short-circuit current, R is the external load resistance, and A is the contact area of the friction layer. The output voltage exhibited an increase with load resistance, whereas the short-circuit current displayed a decreasing trend. Notably, the power density demonstrated an exponential growth within the resistance range of 1 kΩ to 100 MΩ, followed by a decline at higher load resistances (>100 MΩ). The TENG attained a maximum power density of 5.07 W/m^2 at 200 MΩ. While the conventional capacitive pressure sensor induces capacitance change based on the variation in distance between its two electrodes, the ionic capacitive pressure sensor operates differently. When the electrode contacts with the IL/Polymer layer, the charged electrode attracts ions with opposite polarity, resulting in the formation of a nano-scale electric double layer (EDL) at the interface. This unique mechanism leads to a significantly higher capacitance change compared to the conventional capacitive pressure sensor [4]. Consequently, the sensitivity of the ionic capacitive pressure sensors using IL/PVDF-TrFE film was greater than that of the sensor with pristine PVDF-TrFE film (**Figure 2(b)**). In particular, when the composition ratio of PVDF-TrFE:[EMIM][TFIS] was 4:3 wt%, the sensor exhibited the highest sensitivity of 132.6 kPa^{-1} at the range from 0 to 1 kPa. The sensitivity of the ionic capacitive pressure sensors was observed to be remarkably high at low pressures, mainly owing to the rapid variation in contact area caused by the pyramidal shape of the electrodes.

To achieve the self-powered wearable sensing system, the TENG, ionic capacitive pressure sensor, and Arduino kit were attached to the glove. (**Figure 3(a)**). The TENG was connected to a battery, allowing the harvested energy to power the Arduino kit. The signal obtained from the ion capacitive pressure sensor was processed with an Arduino kit and displayed as pressure on a monitor. The pulse waveform obtained from the radial artery using this sensing system is shown in **Figure 3(b)**.

References

[1] L. Yang et al., Adv. Funct. Mater. (2023) 2303723.
[2] T. Bhatta et al., Nano Energy 81 (2021), 105670
[3] C. Lee et al., Compos. B. Eng. 255 (2023) 110622
[4] S. Zhang et al., Macromolecules 44 (2011), 940-949

Figures

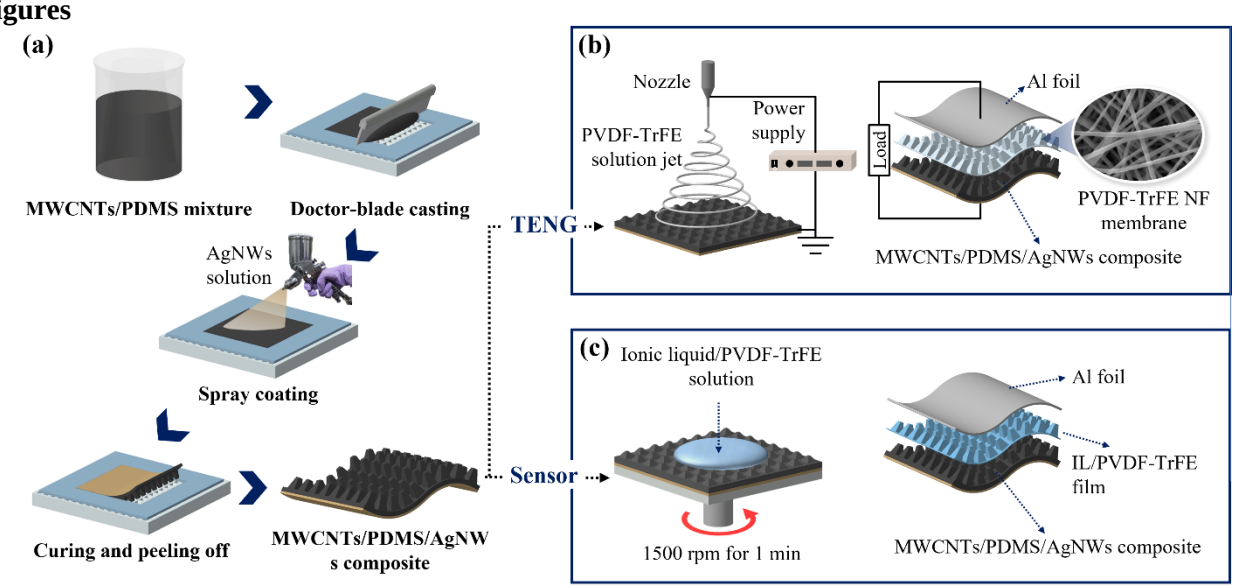

Figure 1. The fabrication process and structure of the TENG and ionic capacitive pressure sensor: **(a)** The process of preparing a flexible MWCNTs/PDMS/AgNWs composite electrode and the fabrication of **(b)** TENG and **(c)** ionic capacitive pressure sensor.

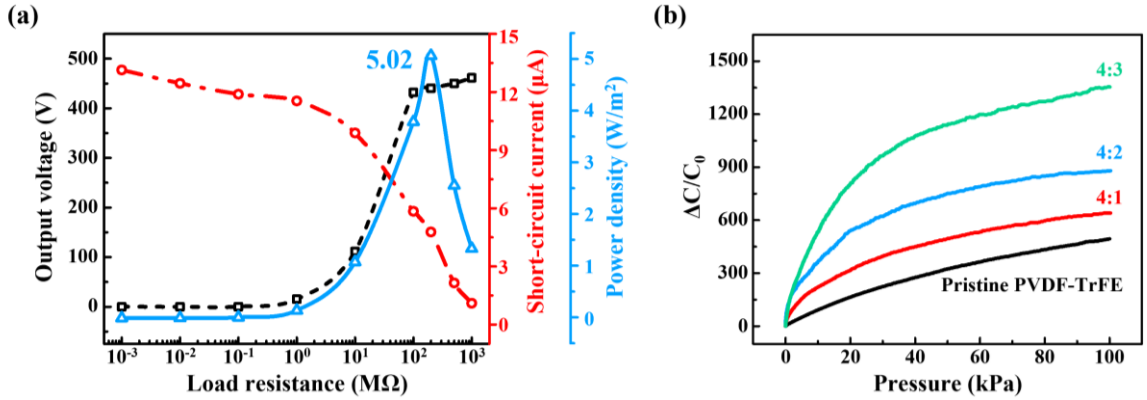

Figure 2. (a) Electrical performance of TENG and **(b)** capacitance variation of ionic capacitive pressure sensors with different composition ratios of PVDF-TrFE:[EMIM][TFIS].

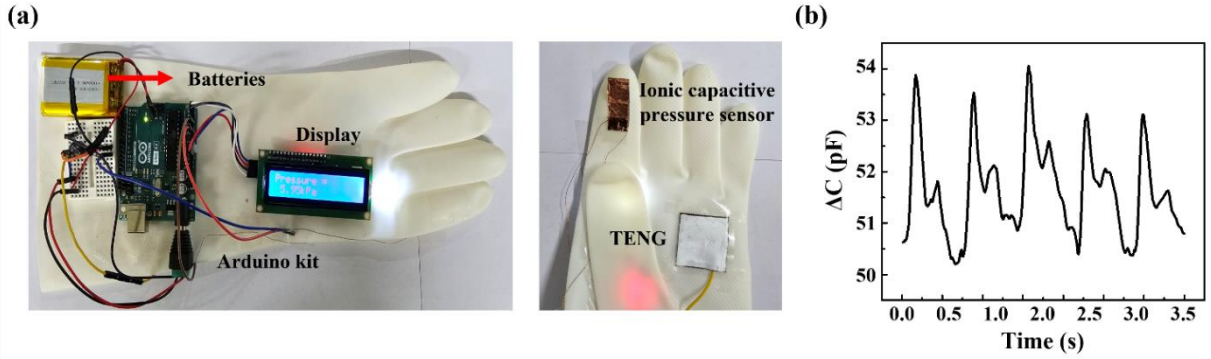

Figure 3. (a) Optical images of self-powered wearable sensing system and **(b)** capacitance signal change depended on the pulse of the radial artery.

Resonance tuning in plasmonic nanorings

W. Tao [a,b], F. Laible [a], A. Hmima [b], O. Guillot [a,b], T. Maurer [b], M. Fleischer [a]

[a] Institute for Applied Physics and Center LISA+, University of Tübingen, 72076 Tübingen, Germany
[b] Laboratory Light, Nanomaterials and Nanotechnologies – L2n, University of Technology of Troyes and CNRS EMR 7004, 10004 Troyes, France
e-mail: monika.fleischer@uni-tuebingen.de

Plasmonic nanostructures that act like optical antennas have become relevant building blocks for applications in opto-electronic devices, biomedical technologies, optical sensors, and nano-spectroscopy. Such nano-antennas are employed to concentrate the energy of electromagnetic radiation in the visible range in nanoscale volumes near the antenna surface, and to enhance and shape the radiation emanating from nano-emitters in their direct vicinity. The spectral properties of optical antennas can be noticeably modified via coupling effects. Near-field coupling between closely spaced antennas leads to strongly enhanced electric fields in the gap between them, as well as to hybridization of the plasmonic modes that results in a shift of the coupling mode to longer wavelengths. This effect can be used as a sensitive measure of the interparticle gap size in so-called plasmon rulers [1]. Likewise, in larger arrays of nano-antennas, the antenna dipoles can collectively couple in the far-field, leading to surface lattice resonances with a much narrower bandwidth than the individual particle plasmon resonances, and to potential Fano resonances due to their interference with the latter [2]. The present work aims at preparing plasmonic nano-rings on flexible polymer substrates using electron beam lithography and a transfer process based on a sacrificial layer. These flexible samples serve as an environment in which the coupling conditions between the antennas can be continuously and reversibly tuned by applying external strain. This way the evolution of the mode spectrum can be tracked, and the influence of the nanoring geometries on their deformation under strain is investigated.

Coupling effects have already been investigated in many studies [3]. In the majority of cases, different coupling conditions were created by preparing a large number of nominally identical nano-antennas with varying gap sizes. This allows for excellent statistics, however the inherent fabrication-related slight geometric variations between nanostructures hinder the extraction of the pure influence of the gap. Here, flexible substrates allow for evaluating the coupling behaviour of one and the same nano-dimer while only the gap is varied [4]. The present study goes one step further and in addition to the coupling behaviour also investigates the shape evolution of individual nano-rings on flexible substrates under strain [5]. This addresses the relevant scientific question whether one may safely assume that the nano-antennas are immobilized on the polymer while only the gap is varied, or the antenna shape itself is also influenced by strain.

In this work, gold nano-rings with different thicknesses and diameters are prepared on silicon substrates with a chromium sacrificial layer by electron beam lithography, see Fig. 1 [5]. In a process developed by the authors, the gold surface is then functionalized to improve adhesion to a layer of polydimethylsiloxane (PDMS), which is poured onto the surface and cured. In the following, the sacrificial layer is removed by wet chemical etching. Thus, the gold rings and PDMS are separated from the silicon support and form the new flexible sample. Strain is then reversibly applied to the device by mounting it in a stretching device with micrometre screws. The geometry of the nano-rings under strain is imaged in a scanning electron microscope, while the spectral properties of the nano-rings depending on the applied strain are monitored by reflection spectroscopy, cf. Fig. 2 and Fig. 3. Both localized surface plasmon resonances of the individual nano-rings and collective lattice resonances are observed and evaluated. By following the evolution of the modes and the nano-ring dimensions and comparing them with numerical simulations, conclusions on the influence of the nano-ring geometries on their deformability under local strain are drawn (see Fig. 4).

[1] P. K. Jain, W. Huang, M. A. El-Sayed, Nano Letters 7(7) (2007) 2080-2088.
[2] W. Tao, H. Hu, O. Guillot, T. Maurer, M. Fleischer, Advanced Photonics Research (2023) 2300012.
[3] F. Laible, A. Horneber, M. Fleischer, Advanced Optical Materials 9 (2021) 2100326.
[4] T. Maurer, J. Marae-Djouda, U. Cataldi, A. Gontier, G. Montay, Y. Madi, B. Panicaud, D. Macias, P.-M. Adam, G. Lévêque, T. Bürgi, R. Caputo, Frontiers of Materials Science 9 (2015) 170-177.
[5] W. Tao, F. Laible, A. Hmima, T. Maurer, M. Fleischer, Nano Convergence 10 (2023) 15.

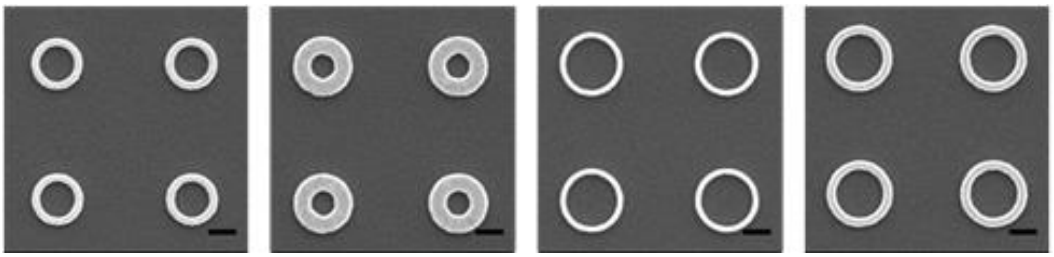

Figure 1. Scanning electron micrographs of lithographically prepared gold nano-rings with different parameters before the transfer to a flexible substrate, scale bar: 400 nm [W. Tao].

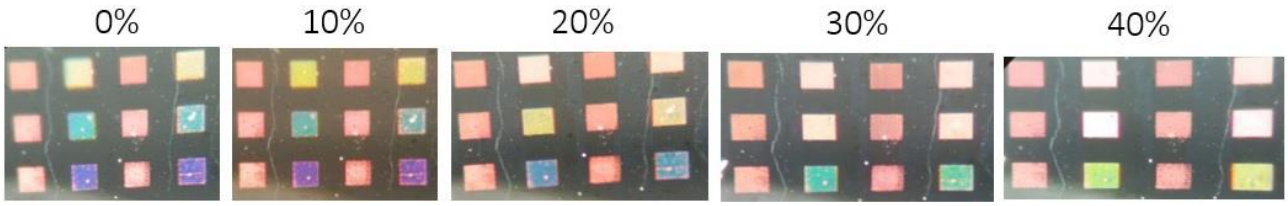

Figure 2. Changing dimensions of nano-disk arrays of originally (50 μm)^2 size on PDMS under increasing strain, and corresponding colour changes due to a shift of the surface lattice resonances [O. Guillot].

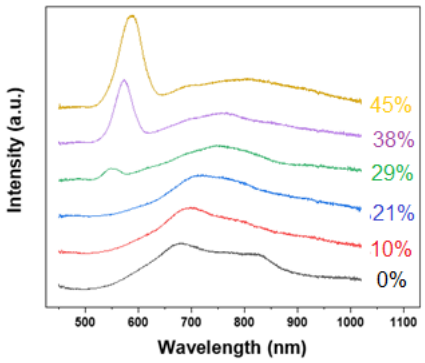

Figure 3. Reflection spectra of a nanoring array under illumination with transversally polarized light for different strain values [W. Tao].

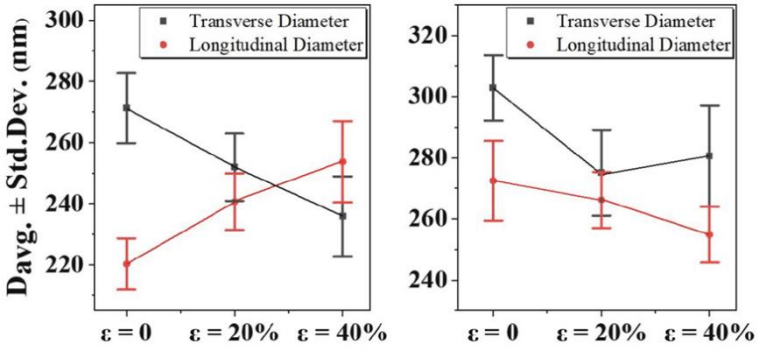

Figure 4. Evolution of the nano-ring diameters in the direction of and perpendicular to the applied strain; (left) the shape is deformed, (right) the shape remains mostly stable (modified after [5]).

Fabrication of silicon gratings for an X-ray free electron laser spectrometer

Joan Vila-Comamala[a], Elizabeth Skoropata[a], Cristian Svetina[a], Konstantins Jefimovs[a], Luc Patthey[a], Elia Razzoli[a], Christian David[a]

[a] Paul Scherrer Institut, Villigen PSI, 5232, Switzerland
e-mail: joan.vila-comamala@psi.ch

X-ray free electron lasers (FEL) deliver coherent, highly intense femtosecond X-ray pulses that enable unprecedented investigations of dynamic processes in matter [1]. To date, X-ray FEL pulses are mostly generated via self-amplified spontaneous emission (SASE), in which a high-energy electron beam passes through a chain of undulator magnets to produce the intense coherent X-ray pulses. The SASE process relies on the inherent fluctuations of the electron beam, resulting in a coherent emission that is further amplified in the last sections of the undulator. The inherent stochastic nature of SASE emission leads to a substantial shot-to-shot variation of the energy spectrum of the X-ray FEL pulses. A typical energy spectrum of single X-ray pulse is shown in figure 1(a), with a central X-ray energy of 930 eV and its typical bandwidth of about 2 %. Another characteristic of the SASE emission is the extremely spiky nature of energy spectra, resulting in a noise-like distribution of intense spikes on the top of a lower-amplitude background that varies shot-to-shot. As a result, online shot-to-shot characterization of the energy spectrum of X-ray SASE FEL pulses is crucial for enabling numerous femtosecond FEL investigations, especially for those in which the utilization of a monochromator is impractical. The use of a monochromator substantially stretches the femtosecond X-ray pulses, thus compromising the required temporal resolution to dynamically investigate atomic and molecular processes.

At the SwissFEL facility, located at the Paul Scherrer Institut in Switzerland, we are currently developing a high-resolution X-ray SASE FEL spectrometer that will be capable of providing online shot-to-shot energy spectra. Figure 1(b) illustrates the setup, wherein the incoming X-ray FEL pulses passes through a variable line spacing diffraction grating, also commonly known as a linear Fresnel zone plate. This grating will diffract a small portion of the X-ray intensity onto the detector, resulting in spatial spreading of the X-ray pulse energy spectrum due to diffraction. The SASE FEL spectrometer at the Athos undulator branch of the SwissFEL will cover X-ray energies ranging from 200 to 2000 eV. The diffraction gratings [2], which are one of the essential components of such instrument, are being produced on thin silicon membranes of 200 and 500 nm in thickness to ensure a high transmission of the X-ray beam, particularly at lower photon energies. The patterned area needs to be as large as the X-ray beam, up to 7×7 mm^2. In addition, a grating pitch down to 120 nm is required to obtain the high-energy resolution that enables resolving the spiky nature of SASE X-ray pulses. The gratings are being etched into the silicon membranes up to a thickness of 300 nm to ensure the required diffraction efficiencies up to 5 % in the entire photon energy range. In total, about 30 different grating design variations will be produced to cover the whole photon energy range of the Athos undulator and its special operational modes, such as two-color and large-bandwidth.

Taking into account all previous requirements, we have developed a simplified fabrication process combining electron beam lithography and silicon reactive ion etching [3], in which a 100 nm thin layer of PMMA resist is directly used as etching mask to transfer the pattern into the required thickness of silicon up to 300 nm. The steps of the fabrication process are schematically shown in figure 2 (a). In addition, the high-resolution e-beam lithography exposure has been optimized by the use of single pixel lines to minimize the exposure time down several hours to obtain the required patterned areas up to 7×7 mm^2. We will also discuss the exposure strategies to minimize any stitching errors in the final pattern that would severely compromise the energy resolution that the gratings are capable of delivering. Scanning electron image of the resulting silicon structures are shown in figure 2 (b), in which the remaining PMMA mask is visible on top of the silicon lines. In the near future, such gratings will be tested and implemented at the SwissFEL Athos SASE FEL spectrometer.

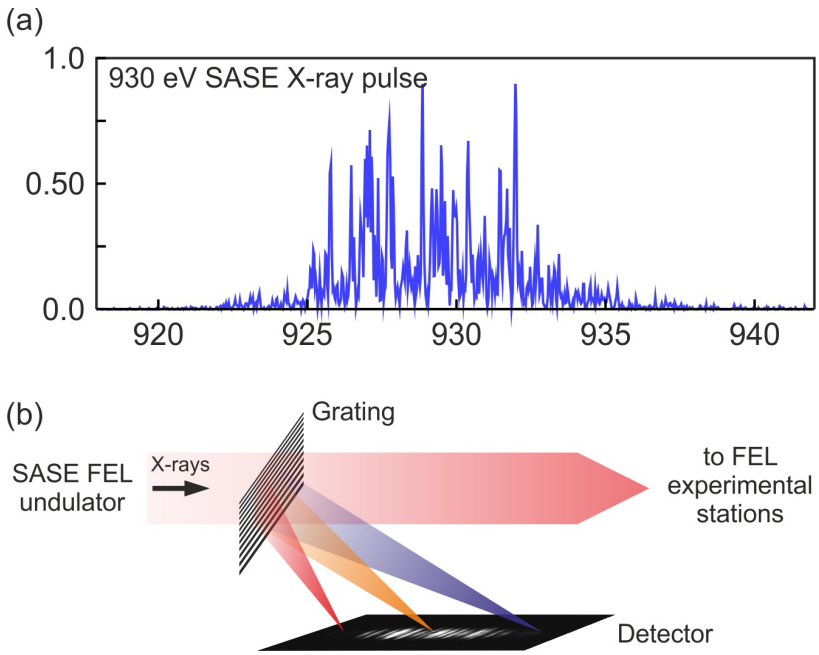

Figure 1. (a) Typical energy spectrum of X-ray FEL pulse generated by self-amplified spontaneous emission. The stochastic nature of the SASE process results in spiky energy spectrum with a typical bandwidth of about 2 %. (b) Schematic representation of the SASE spectrometer being developed at the SwissFEL (Paul Scherrer Institut, Switzerland). A variable line spacing diffraction grating is used to extract a small portion of the incoming X-ray beam to a detector, enabling the acquisition of the energy spectrum of the X-ray pulse on a shot-to-shot basis.

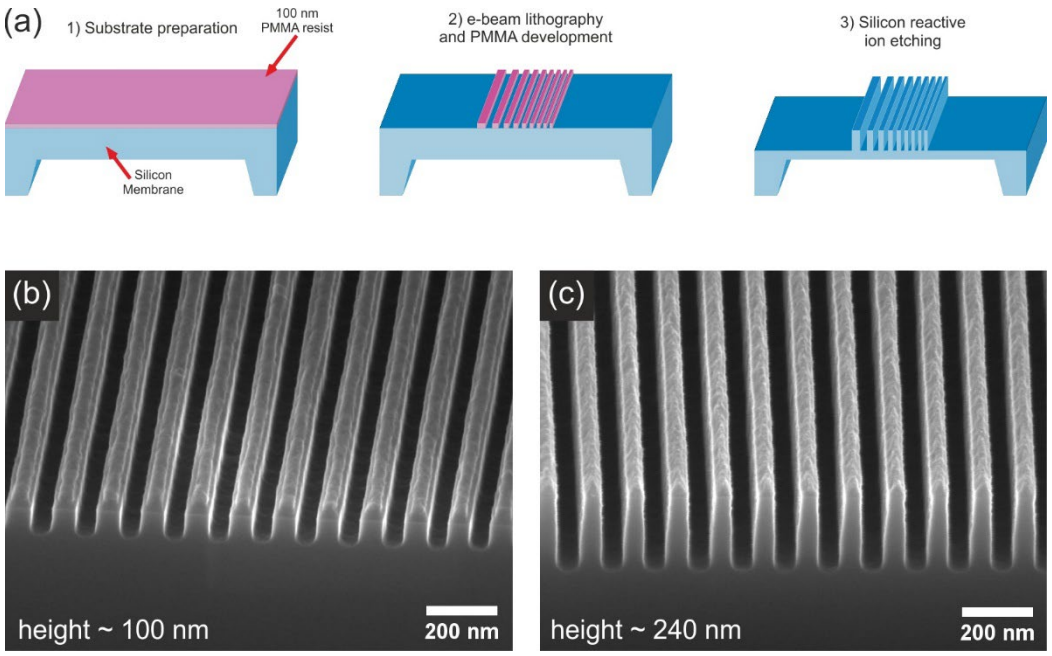

Figure 2. (a) Silicon grating fabrication: electron beam lithography on PMMA resist is combined with reactive ion etching of silicon. (b) and (c) Example of the 120 nm pitch grating etched into silicon to thickness of 100 and 240 nm, respectively. The remaining PMMA resist mask is visible on the top of the silicon lines.

[1] R. Abela et at., J. Synchrotron Rad. 26 (2019) 1073–1084.
[2] P. Karvinen et al., Opt. Lett. 37 (2012) 5073-5075.
[3] Z. Shi et al. Micromachines 11 (2020) 864.

Low-cost 3D printed diffractive optical elements for rapid prototyping

Daniel Fan*, Sejeong Kim

Department of Electrical and Electronic Engineering, University of Melbourne, Parkville, 3010, Australia
*e-mail: fan.d@unimelb.edu.au

Diffractive optical elements (D.O.E.) modify the phase of a propagating light beam, producing useful beam shapes such as Bessel beams, vortex beams, Airy beams, etc. These beams can find applications in object trapping, imaging, remote sensing, communications, microscopy, and so on. Commercial D.O.E.s can cost thousands of dollars making them unsuitable for prototyping and producing custom beam shapes. Spatial light modulators, while allowing freedom in arbitrary phase control, can be both bulky and expensive. Fabrication of D.O.E.s using two-photon polymerization, nanoimprint lithography, and other techniques require precise optimization of the fabrication process which can depend on the shape to be fabricated [1][2]. Post-processing might be required to reduce surface roughness such as via thermal reflow [2][3]. We present a simple fabrication process based on two-photon polymerization where two resins with similar refractive indices are combined so that fabrication tolerances are relaxed.

A traditional D.O.E. made from glass or polymer operating in air requires surface roughness much less than the wavelength of light (λ, Fig. 1a). By surrounding the D.O.E. (refractive index n_1) by another material with similar refractive index (refractive index n_2, Fig. 1b), the height of the D.O.E. (h) can be made larger according to the equation $\Delta\phi = \frac{2\pi h}{\lambda}(n_1 - n_2)$, where $\Delta\phi$ is the phase difference. Further, surface roughness requirements can also be relaxed [4]. Although this method was successfully used for D.O.E.s immersed in oil [4], the stringent requirement for $n_1 - n_2 = 0.002$ meant that it was necessary to measure the refractive index of both materials very accurately. Furthermore, using oil required leak-proof sealing of the liquid. Encapsulation within another resin was demonstrated [5] using an SLA 3D printer. However, stringent Δn meant tight processing tolerances such as humidity control and polymerization control. In this work, we use two-photon polymerization with IP-Dip2 (Nanoscribe GT2, Germany) to 3D print the D.O.E. structure. Then, we immerse it in IP-S resin, cover with a flat glass slide, and cure using one-photon UV light at 405 nm. In principle the IP-S can also be cured by two-photon polymerization which would allow fabrication of such multi-material structures within, for example, microfluidic channels. This process resulted in a good compromise between printing tolerances and refractive index tolerances.

At an operating wavelength of 594 nm, the cured IP-Dip2 ($n_1 = 1.547$ [5]) and cured IP-S ($n_2 = 1.507$ [6]) result in $n_1 - n_2 = 0.04$. For an $m = 1$ vortex plate, this gives a D.O.E. height of ~15 µm, compromising between precise refractive index and precise fabrication height. Simulations were performed using chirped z-transform (Fig. 2) [7], and the fabricated phase plate was placed in a collimated laser beam, followed by a focal length 150 mm lens, and the image recorded on a CMOS camera. The doughnut shaped intensity indicates a vortex beam was indeed produced with a central dark region of approximately 100 µm (Fig. 3), matching the simulated image. At high laser intensity the dark central region remained dark (Fig. 3c). This simple and robust fabrication scheme allows rapid prototyping of D.O.E.s for beam shaping research and development, with a wide variety of applications from microscopy (such as point-spread-function engineering) to telecommunications (such as orbital angular momentum encoding), optical tweezing and object manipulation, and so on.

[1] I.V.A.K. Reddy et al., Optica 9(6) (2022) 645-651.
[2] T. Blachowicz et al., e-Polymers (2021) DOI: 10.1515/epoly-2021-0061.
[3] N. Chidambaram et al., Adv. Mat. Tech. 2(5) (2017) 1700018.
[4] R. Orange-Kedem et al., Nat. Comm. 12 (2021) 3067.
[5] R. Orange-Kedem et al., arXiv:2303.15197 (2023).
[6] NanoGuide, https://support.nanoscribe.com/ (Retrieved 5/6/2023).
[7] T. Gissibl et al., Opt. Mat. Exp. 7(7) (2017), 2293-2298.
[8] L.M. Sanchez Brea, https://pypi.org/project/diffractio/ (2019).

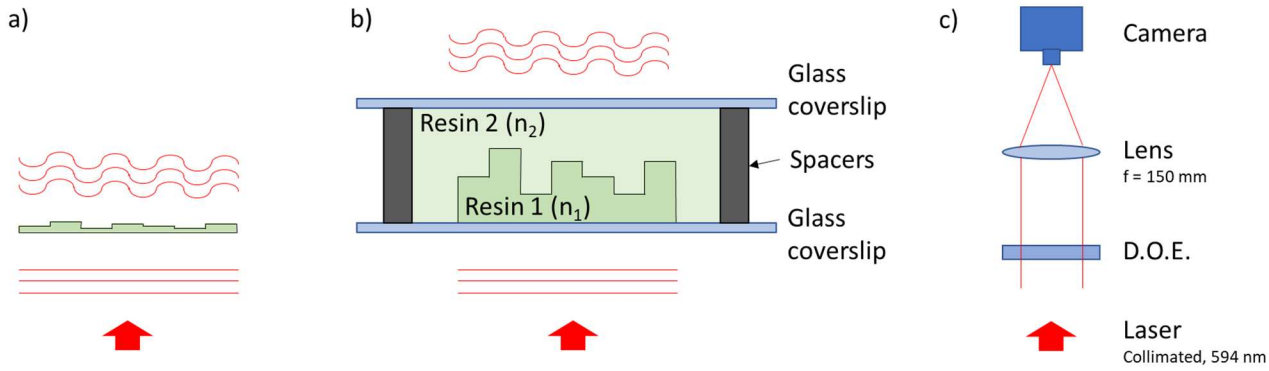

Figure 1. Schematic. a) A glass based D.O.E. in air requires roughness and surface topography << λ. b) By embedding a D.O.E. inside another material with a similar refractive index, the fabrication tolerances can be relaxed. c) Setup for characterizing vortex phase plate 3D printed using the presented scheme.

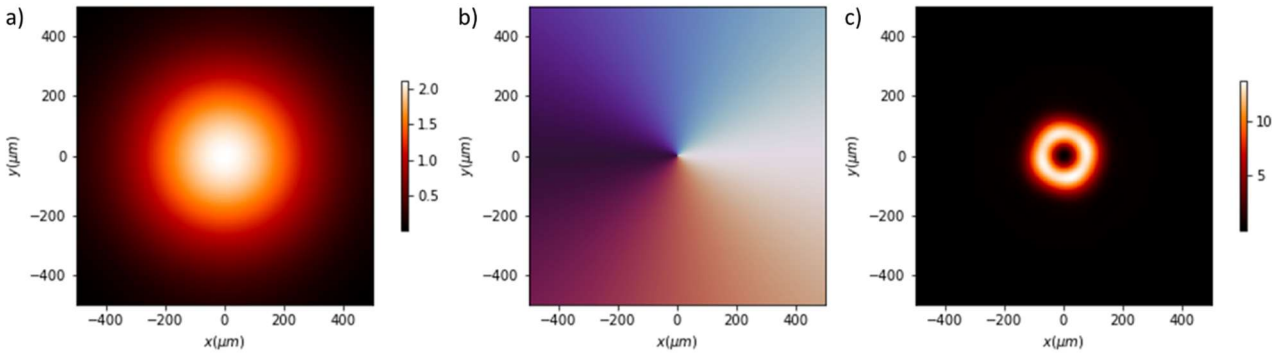

Figure 2. Simulation of beam propagation using chirped z-transform. a) Gaussian beam input from 594 nm laser. b) Phase profile of m = 1 vortex plate. c) Intensity at image plane after f = 150 mm lens showing the intensity minimum at the center of the vortex beam. Intensity values are arbitrary.

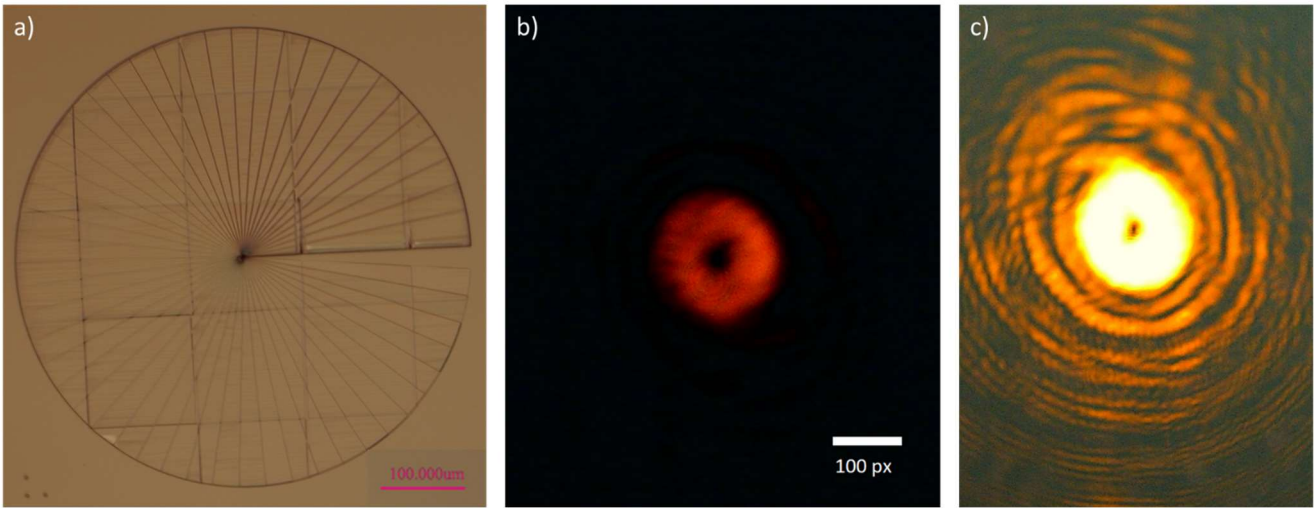

Figure 3. a) Two-photon polymerization fabricated m = 1 vortex phase plate (scale bar = 100 um). b) Intensity image on camera after collimated laser light at 594 nm wavelength passes through vortex phase plate followed by lens (f = 150 mm). c) At high laser intensity. Scale bar for a) is 100 µm. Scale bar for b) and c) is 100 pixels equaling 220 µm.

Bowtie photonic-crystal waveguides as strong light-matter interfaces

Guillermo Arregui [a], Ali Nawaz Babar [a,b], Anastasiia Vladimirova [a,b], Christian Anker Rosiek [a], Babak Vosoughi Lahijani [a,b], and Søren Stobbe [a,b]

[a] Department of Electrical and Photonics Engineering, DTU Electro, Technical University of Denmark, B. 343, DK-2800 Kgs. Lyngby, Denmark.
[b] NanoPhoton - Center for Nanophotonics, Technical University of Denmark, B. 345A, DK-2800 Kgs. Lyngby, Denmark.
e-mail: guibra@dtu.dk

The efficient emission of on-demand quantum states of light into propagating channels that can be interfaced with conventional passive photonic components is at the core of future on-chip quantum technologies. From this viewpoint, photonic-crystal waveguides (PhCWs) offer precise control over the optical environments that can host solid-state emitters. The light-matter interaction strength is governed by the local density of optical states (LDOS), which determines the Purcell factor. For an optimally oriented dipole-like emitter at position $\mathbf{r_0}$ in a PhCW, the LDOS reads [1],

$$\rho(\boldsymbol{r_0}, \omega) = \frac{n_g(\omega)}{\pi c} \frac{a}{\varepsilon(\boldsymbol{r_0}) V_{\text{cell}}} \qquad (1)$$

with $n_g = c/v_g$ the group index and $V_{\text{cell}} = ([\varepsilon(\boldsymbol{r_0})|\boldsymbol{E_k}(\boldsymbol{r_0})|^2])^{-1}$ the effective mode volume per unit cell of periodicity a. The traditional strategy to enhance the LDOS has been to target high n_g. However, backscattering due to unavoidable fabrication imperfection scales with n_g^2, leading to significant propagation losses, thus limiting the application of slow light for waveguide quantum electrodynamics (QED) experiments. Even waveguides built with photonic topological edge states, which had generated great expectations to combat backscattering, are bounded by the same limitation [2]. A less explored and alternative route to enhancing the LDOS is reducing the mode volume, V_{cell}, cf. Eq. (1), because it was believed that confinement in dielectrics was limited by the diffraction limit. Recent theoretical [3] and experimental developments in photonic nanocavities [4,5] have evidenced that the use of bowtie-like structures fosters light confinement down to features of size only limited by nanofabrication.

In this work, we investigate the use of bowtie structures to develop two-dimensional photonic-crystal waveguides (W1-BTs, Fig. 1(a)) allowing Purcell factors in the linear dispersion region ($n_g \sim 7$) that largely overcome those found on conventional W1 photonic-crystal waveguides (W1s, Fig. 1(b)) in the same dispersion region ($n_g \sim 8$). For example, a silicon bowtie of 10 nm, which is within reach with of our nanofabrication process [4], leads to a 15-fold enhancement of the LDOS (colormaps in Fig. 1(c)). However, the intense fields near the sidewalls of the narrow bowtie bridges may also promote roughness-induced scattering losses, compromising the performance of W1-BTs for waveguide QED experiments where fragile quantum states of light are manipulated. To address this issue, we fabricate suspended photonic circuits that include W1-BTs on a silicon-on-insulator platform with a 220 nm device-layer thickness and measure the wavelength-dependent propagation losses (Fig. 1(d)) using the cutback method [2]. We find a negligible enhancement of the waveguide losses with decreasing bowtie width and a 15-fold increase of the losses relative to conventional W1 waveguides in the linear dispersion region (approx. 2 dB/cm [2]), indicating that the presence of holes along the line defect plays a more significant role than the exact bowtie width. Despite this growth in the losses, short waveguide segments in near-unity transmission terminations, which we design, may still enable the operation of W1-BTs coupled to quantum dots [1] or to atomically thin materials [6] as broadband light-matter interfaces for the efficient generation of single photons with a large degree of quantum coherence.

[1] P. Lodahl et al., Rev. Mod. Phys. **87**, 347 (2015).
[2] C. Rosiek et al., Nat. Photon. **17**, 386 (2023).
[3] M. Albrechsten at al., Opt. Express **30**, 15458 (2022).
[4] M. Albrechsten at al., Nat. Commun. **13**, 6281 (2022).
[5] A. N. Babar et al., arXiv:2303.09610 (2023).
[6] E. V. Denning et al., Phys. Rev. B **105**, 085306 (2022).

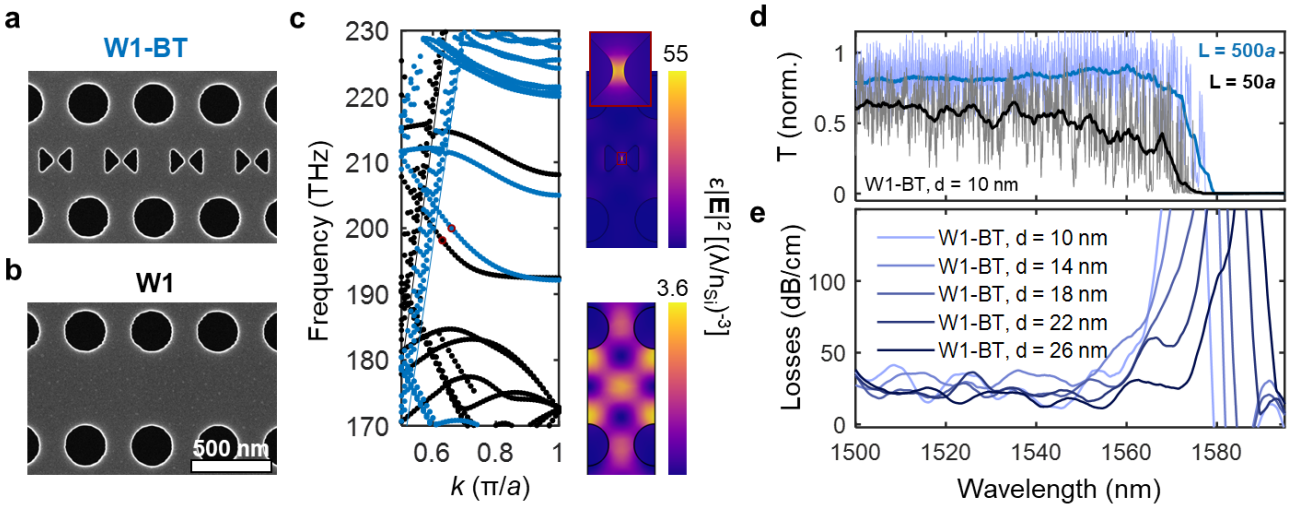

Figure 1. Two-dimensional bowtie photonic-crystal waveguides. (**a**,**b**) Scanning electron micrograph (SEM) of a suspended silicon bowtie photonic-crystal waveguide (W1-BT) and a conventional photonic-crystal waveguide (W1). (**c**) Dispersion diagrams of a W1-BT waveguide with bowtie width d = 10 nm (blue) and of a W1 waveguide (black). The normalized electric energy density of the Bloch mode highlighted in the dispersion with a red circle is given. (**d**) Optical transmission through suspended photonic circuits including W1-BT waveguide sections of 50 and 500-unit cells. (**e**) Propagation losses in W1-BT waveguides with different bowtie width.

qBIC-based metasurfaces on SOI for light polarization control

Luca Fagiani,[1,2] Luca Bolzonello,[3], Johann Osmond,[3] Domenico de Ceglia[4], Niek van Hulst,[3,5] Monica Bollani, [2] and Maria Antonietta Vincenti[4*]

1 Department of Physics, Politecnico di Milano, Milan, Italy
2 Istituto di Fotonica e Nanotecnologie-Consiglio Nazionale delle Ricerche (IFN-CNR), LNESS, Como, Italy
3ICFO - Institut de Ciencies Fotoniques, The Barcelona Institute of Science and Technology, Castelldefels, Barcelona, 08860 Spain
4Department of Information Engineering – University of Brescia, Via Branze 38, 25123 Brescia, Italy
5ICREA, Institució Catalana de Recerca i Estudis Avançats, Barcelona 08010, Spain

e-mail: maria.vicenti@unibs.it

Abstract: An ultra-compact integrated polarizer is presented, using quasi-bound states in continuum (q-BIC), which has been rarely demonstrated experimentally. The control is independent of the polarization state of the incoming light.

While most metasurfaces exploits phase manipulation of light, at the expense to depend on its frequency and polarization state, they can enable some other ways to control light properties, such as polarization through symmetry protected q-BIC. These structures possess then the advantage of the metastructures of being compact, integrable and easy to fabricate with an output polarization state which is independent of the input light state.

In our case the metasurface allowing for this result is SOI (Silicon on Insulator) based structure and formed by a series of pairs of Si bar lines with a broken symmetry and periodically repeated with a period of 500 nm over an area of 100um*100um, such as shown in Fig. 1. The pair is composed by a fixed width main bar line and the width of the second bar line can be varied to tune the frequency resonance.

To experimentally check its working, we have illuminated the qBIC polarizer with a normal incidence and rotating linear polarization beam and measured the polarization state of the transmitted output, for wavelengths ranging from 750 nm to 850 nm, as shown in Fig.2. We have studied the dependence of the output transmittance for TE and TM incoming light in function of 3 different asymmetry factors α and the comparison with simulated data is displayed in Fig3.

We can see that the incoming light polarization can be effectively suppressed and that we can choose the resulting polarization state to be TE or TM according to the operating wavelength. Moreover, it is shown that the resonance frequency of these structures can be tuned by changing the geometry parameter α.

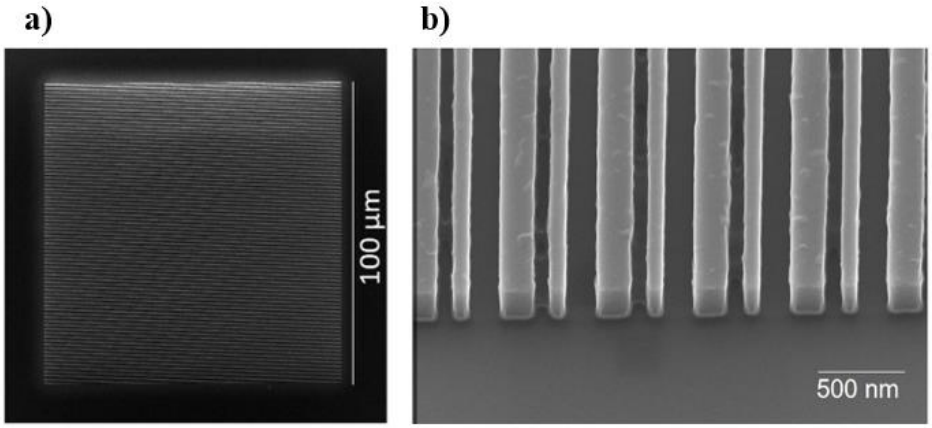

Figure 1. SEM images of the SOI metasurface of a) the patterned 100*100um^2 area and of b) detail of the section of the bar lines, with a period p=500 nm, bar line widths D_1 = 175 nm and D_2 = 87.5 nm for a corresponding asymmetry factor α = 0.5, and height h = 145 nm. SiO_2 layer is 2 µm thick.

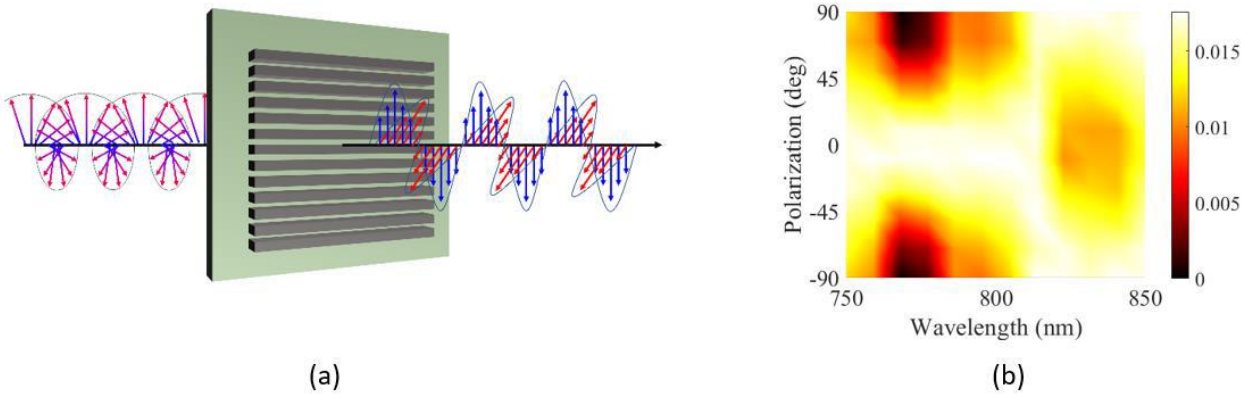

Figure 2. The q-BIC based SOI metasurface sketched in a) can convert the arbitrarily polarized incoming light into an output linearly polarized light. The transmittance spectra measured for an incoming linear polarized light is displayed in b).

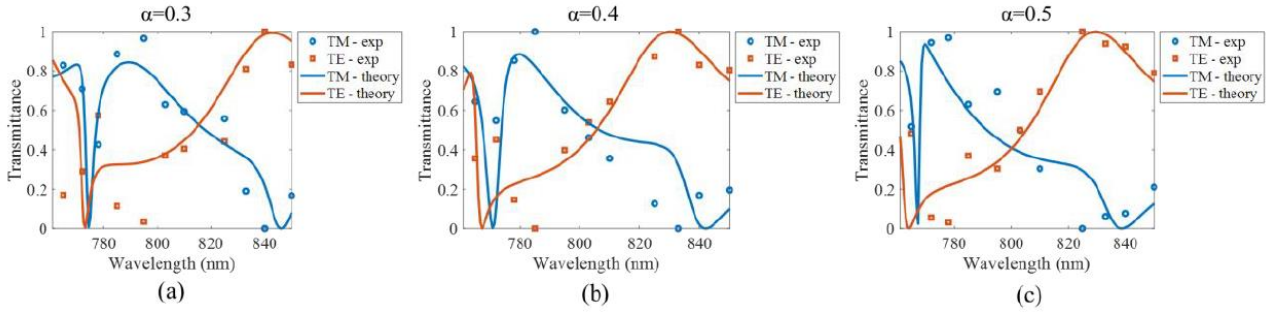

Figure 3. (a) Measured transmission spectra as a function of wavelength for an incoming linear polarized light with a polarization angle of 0º for TE to 90º for TM and the corresponding spectrum in (b) for TE (red dashed) and (c) for TM (black dashed) for different geometry α values.

High aspect ratio silicon-based micro- and nano-fabrication of optics for X-ray diagnostic imaging

Lucia Romano[a,b], Qihui Yu[a,b], Jelena Petrovic[a,b], Konstantins Jefimovs[b], Craig Lawley [a,b], Marco Stampanoni[a,b]

[a] Institute for Biomedical Engineering, University and ETH Zürich, 8092 Zürich, Switzerland
[b] Paul Scherrer Institut, 5232 Villigen PSI, Switzerland
e-mail: lucia.romano@psi.ch

X-ray Grating Interferometry based imaging is a very promising, fast growing and competitive technique for medical, material science and security applications [1]. The main bottleneck in gratings and X-ray optics fabrication is their high aspect ratio structure, whose quality and homogeneity over large areas strongly affect their performances.

This work reviews our approaches to gratings and X-ray optics fabrication by highlighting the possibilities of cutting edge micro- and nano-technologies for emerging applications from unique prototypes up to commercial devices. Our recent results in micro- and nano-fabrication processing on silicon substrates including lithography [2], deep reactive ion etching (DRIE) [2,3], fan-shaped gratings [4,5], metal assisted chemical etching (MacEtch) [6-9], metal casting [10] and Au electroplating [11] with bottom-up gold feature filling [12,13] are discussed, envisioning their advantages and drawbacks. The coupling of silicon etching at high aspect ratio and new metallization techniques represent a valid alternative to X-ray LIGA [14] for X-ray optics microfabrication, with the advantage of improved resolution and advanced manufacturing capabilities. Some examples (Fig. 1) are representative of our effective technological platform for X-ray optics fabrication with a large range of feature sizes and a sustainable manufacturing cost, useful for medical imaging systems with tube X-ray sources [15,16]. Our micro and nano-fabrication platform will boost not only the X-ray wavefront sensing and imaging but also many other applications can benefit of our approach for large area scaling up and integration, such as photonics, biological metamaterials, silicon metasurfaces, MEMS, VIAS, microfluidics and sensors.

References

[1] T. Weitkamp et al., Opt. Express 13 (2005) 6296-6304
[2] Z. Shi et al., Japanese Journal of Applied Physics 60 (2021) SCCA01
[3] Z. Shi et al., Micromachines 11 (2020) 864
[4] Z. Shi et al., Opt. Lett. 46 (2021) 3693-3696
[5] Z. Shi et al., Applied Surface Science 588 (2022) 152938
[6] L. Romano et al., Advanced Engineering Materials 22 (2020) 2000258
[7] L. Romano et al., Micromachines 11 (2020) 589
[8] L. Romano et al., Nanoscale Horizons 5 (2020) 869-879
[9] Z. Shi et al., Materials Science in Semiconductor Processing 157 (2023) 107311
[10] L. Romano et al., Journal of Vacuum Science & Technology B, Nanotechnology and Microelectronics: Materials, Processing, Measurement, and Phenomena 35 (2017) 06G302
[11] K. Jefimovs et al., Micromachines 12 (2021) 517
[12] D. Josell et al., Journal of The Electrochemical Society 168 (2021) 082508
[13] Z. Shi et al., Appl. Opt. 61 (2022) 3850-3854
[14] M. Richter et al., Journal of Micro/Nanopatterning, Materials, and Metrology 21 (2022) 024901
[15] J. Vila-Comamala et al., Opt. Express 29 (2021) 2049-2064
[16] M. Polikarpov et al., Scientific Reports 13 (2023) 9049

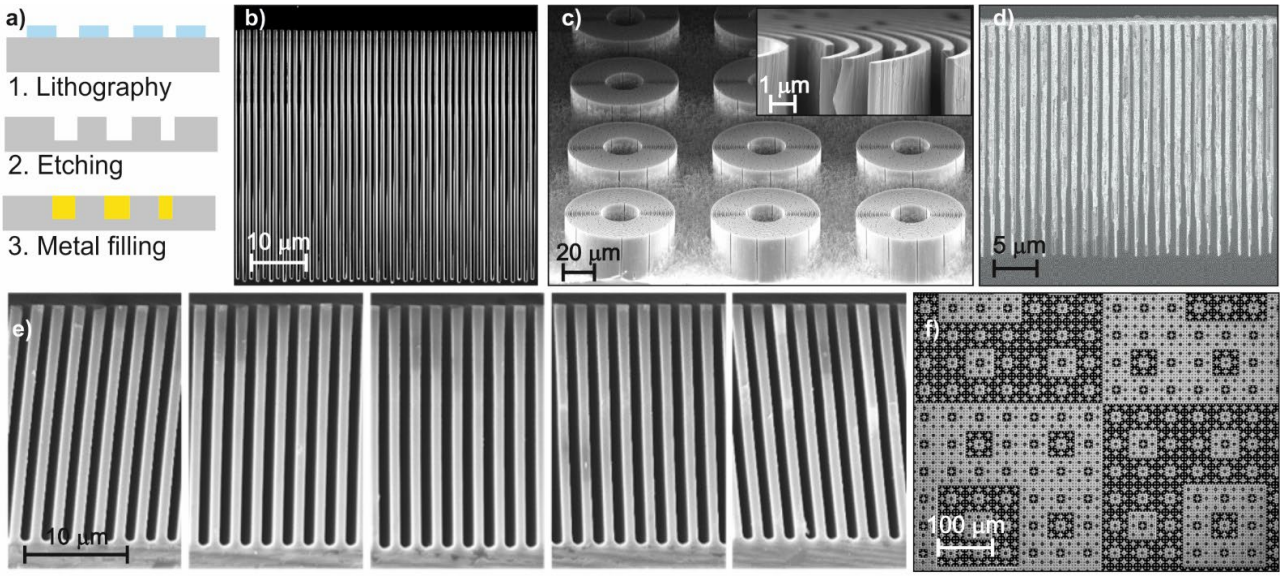

Figure 1. a) schematic of Si based manufacturing technology; b) SEM in cross section of DRIE grating in Si 4-inch wafer (pitch p=1.2 µm, structure height h=40 µm, A.R. 67:1) [3]; c) SEM in plan view of circular gratings array by MacEtch (p=1 µm, h=29 µm, A.R. 58:1, high magnification details in the insert [8]; d) SEM in cross section Au electroplated grating (p=1.2 µm, h=27 µm, A.R. 45:1) [11]; e) fan-shaped Si template, the images in cross section are representative of different distances from the optical axis. f) SEM in plan view of Au bottom up filled fractal pattern for focus characterizations of X-ray imaging systems [13].

MEMS Vibrometer for Structural Health Monitoring: Modeling and Characterization

Jan Niklas Haus, Zhengchun Zhu, Andreas Dietzel

Institute of Microtechnology, Technische Universität Braunschweig, Braunschweig, 38124, Germany
e-mail: j.haus@tu-braunschweig.de

For structural health monitoring (SHM), guided ultrasonic waves (GUWs) are used to detect, localize and quantify structural defects as cracks or delaminations in plate-like structures [1-4]. In the case of fiber metal laminates (FMLs), the observation of the inner layer's modal information is crucial due to the presence of multiple wave propagation modes [5]. To achieve visibility of GUWs at the inner layer of the structure, recent research suggests structure-integrable MEMS (micro-electro-mechanical system) vibrometers as a pickup [6], since the traditionally utilized structure-applied piezoelectric transducers cannot be integrated into the FML while maintaining functional compliance. According to [6], the inertial MEMS vibrometer could resolve ultrasonic bursts if operated in quasi-free frequency range. Due to the continuous nature of the oscillatory system, the bandwidth of the MEMS vibrometer is limited by its higher modes. If these modes are separated in frequency by structural and electrical design, the operational bandwidth could be enlarged. This requires a profound understanding of the inertial system's dynamic behavior.

In this work, the sensor's inertial system and its piezoresistive readout have been reshaped to better resolve GUWs with a center frequency of 100 kHz. A double-cantilever structure, yielding a piezoresistive Wheatstone half bridge (cf. Figure 1. (a)), has been selected as an oscillator. Electrical common mode rejection suppresses the torsional mode doubling the sensor's bandwidth. The electro-mechanical design is based on FEM (finite element method) modeling including modal and transient analyses. The resulting oscillator is microfabricated from silicon. It is experimentally characterized by its dynamic behavior obtained from a scanning laser vibrometer for the pico-scale and simultaneous electrical read out.

As a result of FEM modeling, the modal analysis of the oscillator reveals its different vibration modes and their corresponding frequencies, shown in Figure 1. (b). According to the result, the operational frequency bands of the MEMS vibrometer can be determined in theory. They are located between neighboring natural frequencies, such as between the first (approx. 60 kHz) and the second (approx. 220 kHz) natural frequency. During the experimental modal analysis, vibration modes consistent with the FEM results can be obtained, as presented in Figure 1. (c). Furthermore, as shown in Figure 2, the presence of torsional behavior at approx. 177 kHz can be observed by comparing the displacement amplitude spectra at two different detection points. However, at this frequency there is no significant peak in the amplitude spectrum of sensor's electrical output. In this case, it determines that with the double-cantilever design, although the torsional mode is still present, the associated electrical output of the sensor is greatly suppressed. Thus, the intended purpose of expanding the sensor's bandwidth is achieved.

In addition, the dynamic behavior of the oscillator under forced short-time vibrational displacement, as introduced by propagating GUW, is simulated by FEM transient analysis. Figure 3 (left) shows the comparison between the 100 kHz excitation as sensor input and the stress of a node located on one of the cantilevers representing the sensor output. The waveforms of the signals illustrate a high degree of linearity between them. Based on the piezoresistive effect, a theoretical linear relationship between the electrical signal output generated by the piezoresistive deformation and the vibration signal exists. This is confirmed by the experimental characterization result shown in Figure 3 (right).

As a conclusion, it could be demonstrated that the electrical output signal of the MEMS vibrometer can well represent the GUW-introduced displacement burst with a center frequency of 100 kHz. Moreover, from the comparison of simulation and the experimental results, it is reasonable to design the oscillator on the basis of FEM modeling. With the experimental insight into the micro-oscillator, the effects of non-ideal vibration conditions, and how they are compensated for by design, could be observed.

[1] R. Lammering et al., Lamb-wave based structural health monitoring in polymer composite (Springer, 2017)
[2] D. Balageas et al., Structural health monitoring (John Wiley & Sons, 2010).
[3] V. Giurgiutiu et al., Structural health monitoring: with piezoelectric wafer active sensors (Elsevier, 2007).
[4] Z. Su et al., Identification of damage using Lamb waves: from fundamentals to applications (Springer Science & Business Media, 2009).
[5] A. Volt et al., Fiber metal laminates: an introduction (Springer Science & Business Media, 2011)
[6] J. N. Haus et al., Sensors 22.14 (2022): 5368.

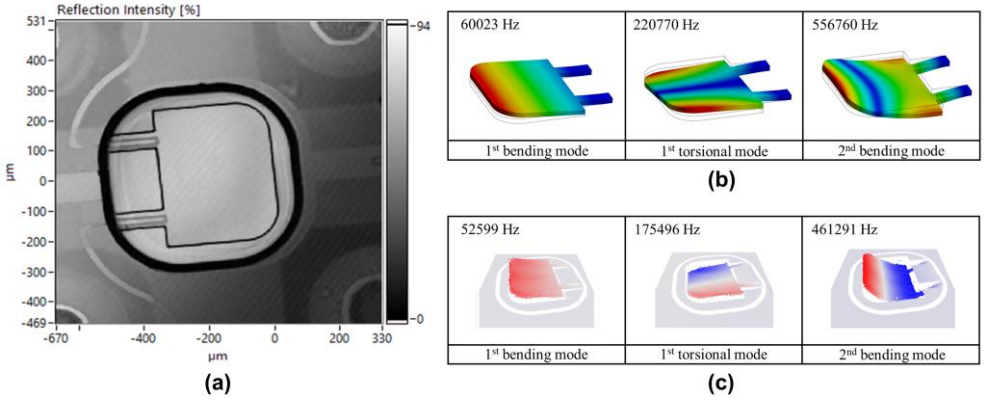

Figure 1. (a) Micrograph of ICP structured silicon oscillator with double-cantilever structure; (b) The first three vibration modes of the designed oscillator obtained by FEM modal analysis; (c) The first three vibration modes of the designed oscillator obtained by experimental modal analysis.

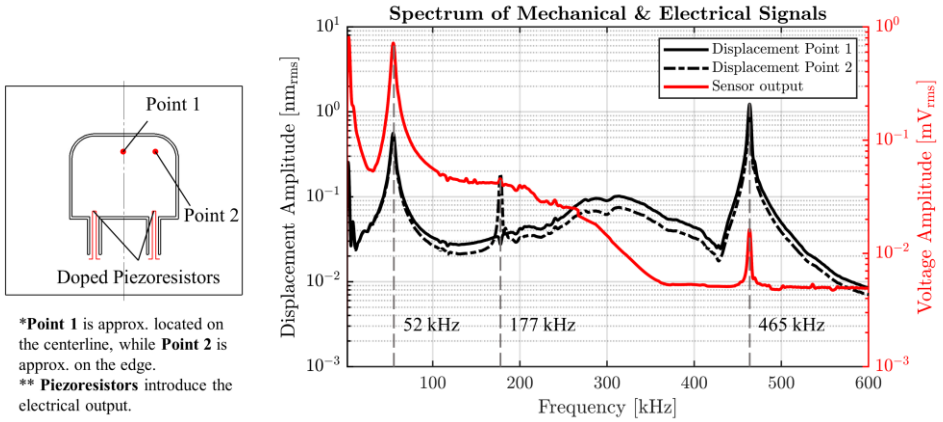

Figure 2. Schematic diagram of two displacement detection positions and illustration of piezoresistive read-out (left). Amplitude spectrum of the MEMS vibrometer's electrical output and displacement at selected positions (right) revealing the electrical suppression of the torsional mode.

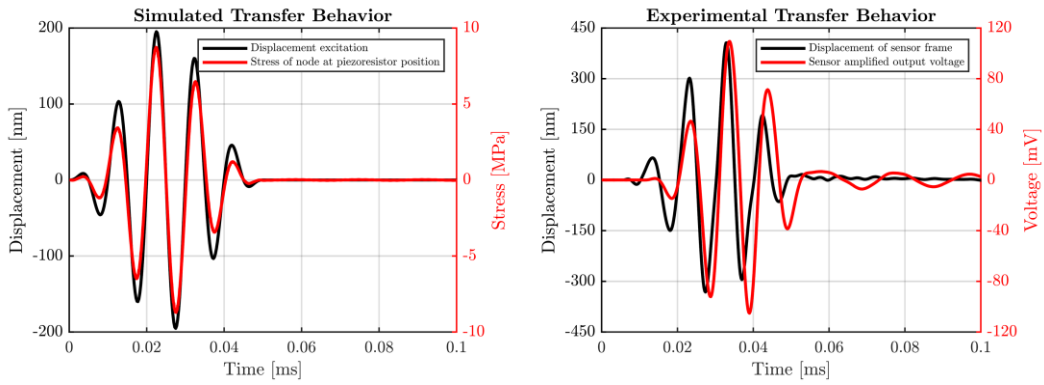

Figure 3. Comparison of the transfer behavior obtained from FEM simulation (left) with that obtained from experimental characterization (right), demonstrating the functional feasibility of the MEMS vibrometer.

Surface Lattice Resonances in Plasmonic Gold Nanocone Arrays

Lukas Lang, Monika Fleischer

Institute for Applied Physics and Center LISA$^+$, University of Tübingen, Tübingen, 72076, Germany
e-mail: lukas.lang@uni-tuebingen.de

Isolated plasmonic gold nanocones offer various interesting optical properties that may be utilized in the application in molecular or refractive index sensing studies. Two dominant localized surface plasmon resonance (LSPR) modes of dipolar character, namely the tip and base mode, are tunable by the geometry of the particles themselves. Electric near-field enhancements near strongly curved features like the tip enable excitation amplification of nearby molecular compounds [1]. The rather broad resonance linewidths of the single particles however complicate the detection of small differences in surrounding refractive index, demanding more narrow spectral features. As was already shown for e.g. plasmonic nanodiscs, the arrangement of radiating nanoparticles in regular arrays can lead to a significant alteration of the optical response, manifest in strongly reduced damping and modification of the particle polarizability [2, 3]. The emergence of so-called surface lattice resonances (SLRs) is however strongly dependent on the homogeneity of the medium, breaking down for large refractive index mismatches between substrate and superstrate. In this regard, there is much debate in literature on the stability of in-plane compared to out-of-plane oriented SLRs, while the latter are believed to be less sensitive due to stronger coupling between the single dipoles [4]. Thus, three-dimensional nanoparticles, such as gold nanocones, offering two dominant LSPR modes that are oriented in-plane as well as out-of-plane, depict ideal systems for comparing both SLR orientations in terms of their stability to the surrounding medium as well as for further use in molecular sensing applications.

To this end, gold nanocones are fabricated on a substrate according to the process depicted in Figure 1a). Starting with a cleaned glass substrate, an indium tin oxide (ITO) layer is deposited as adhesive agent as well as to provide an electrically conducting layer for examination under a scanning electron microscope (SEM). Next, a gold film is deposited by thermal evaporation whose thickness determines the height of the later formed cones. During a subsequent electron beam lithography step (EBL), a hole pattern is written into a PMMA resist layer on top of the gold film. Here, the geometry of the lattice and the size of the cone base can be chosen at will for the desired properties. After development of the resist, a thin aluminum oxide (Al_2O_3) layer is deposited via electron beam evaporation. The thickness of the film has to be adjusted to the gold layer, as it is etched at a different rate during the subsequent argon ion milling procedure. Here, the aluminum oxide discs act as an etch mask for the final formation of cone shaped gold particles (cf. Figure 1b)) and are entirely removed after sufficient etching.

Angle-resolved dark-field scattering measurements using collimated polarized white light reveal the drastic reshaping of spectral features and up to ten-fold narrowing of linewidths for the case of a square lattice of gold nanocones as compared to isolated particles (Figure 2a)). Dominant narrow scattering maxima corresponding to the excitation of SLRs are easily tunable by a mere change of the angle of incidence of the illumination light. Consequently, enhancement of quality factor and straightforward adjustability of the plasmon resonances enable tailoring of the system to specific application needs.
To illustrate the stronger coupling of individual dipole moments that occurs for out-of-plane excitation, Figure 2b) depicts extinction cross sections of a square gold nanocone lattice for s- and p-polarized oblique illumination. As can be described by a coupled driven harmonic oscillator model, spectral distortion is observable between different energy bands for both polarizations, while the energy splitting is enlarged for out-of-plane excitation. In this case, coupling occurs between the single particle LSPRs and the so-called Rayleigh-anomalies, meaning propagating light that is diffracted into the lattice plane, which are solely dependent on the lattice geometry. Altogether, the harnessing of SLRs can enable new pathways of tuning the properties of plasmonic systems to the desired needs and exceed the performance of single particles.

[1] C. Schäfer et al., Nanoscale, 5 (2013) 7861-7866.
[2] A. I. Väkeväinen et al., Nano Letters, 14 (2014) 1721-1727.
[3] V. G. Kravets et al., Chemical Reviews, 118 (2018) 5912-5951.
[4] M. J. Huttunen et al., Optics Express, 24 (2016) 28279-28298.

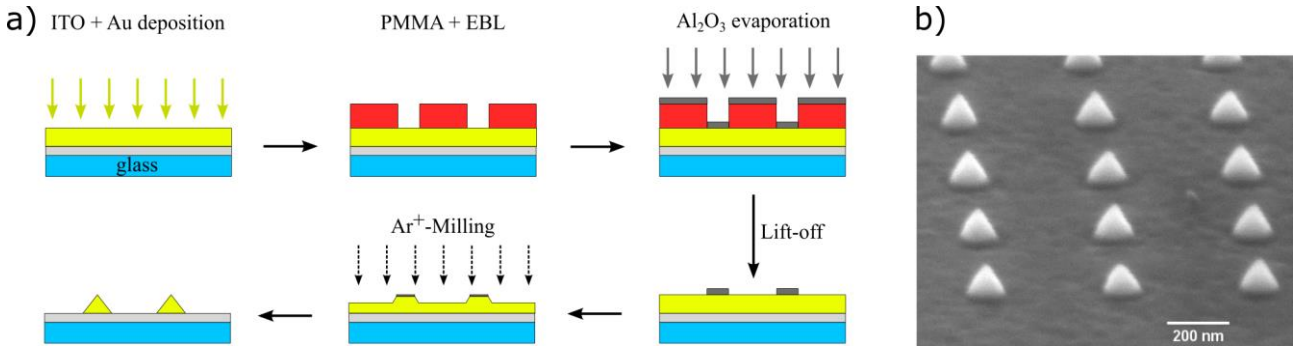

Figure 1. a) Fabrication process of gold nanocone arrays on glass/ITO substrates using electron beam lithography and argon ion milling. b) SEM image of a fabricated square gold nanocone array.

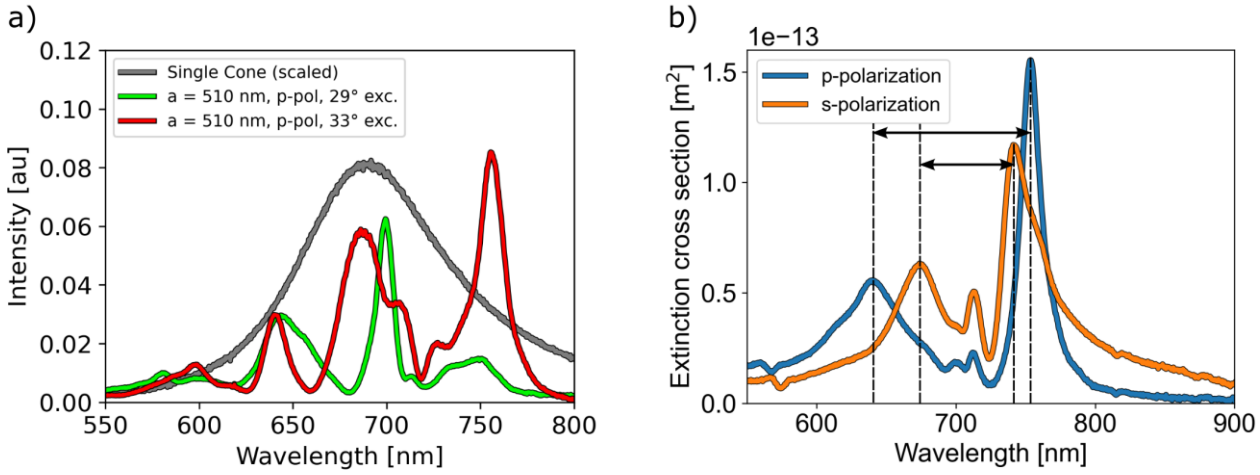

Figure 2. a) Dark field scattering spectra of a square gold nanocone array with period a = 510 nm and p-polarized white light illumination under 29° and 33° angles compared to isolated nanocone spectrum (single cone spectrum is taken with a dark field condenser with NA 0.95-0.8 and scaled for better comparability). b) Extinction cross sections of a square gold nanocone array with period a = 520 nm and p- and s-polarized white light illumination under 25° excitation angle. Arrows indicate stronger energy splitting for out-of-plane SLRs.

Highly sensitive pseudo-capacitive iontronic pressure sensor with MXene electrode to enhance ion intercalation

Changwoo Cho, Chaeeun Lee, and Je Hoon Oh

Department of Mechanical Engineering and BK21 FOUR ERICA-ACE Center,
Hanyang University, Ansan, Gyeonggi-do, 15588, Republic of Korea
E-mail: jehoon@hanyang.ac.kr

The increasing demand for electronic technologies in fields such as artificial intelligence, electronic skin, human-machine interaction, and the Internet of Things has led to a surge of investigation into wearable pressure sensors as an essential component for various human physiological applications [1]. Among various types of pressure sensors including piezoelectric, triboelectric, resistive, and capacitive, capacitive pressure sensors have garnered attention in numerous studies due to their advantages such as low pressure measurement, fast response, simple structure, and low power consumption. However, capacitive pressure sensors still face the challenge of low sensitivity due to small change in capacitance when pressure is applied.

Recent advancements have significantly improved the sensitivity of capacitive pressure sensors by employing ionic liquids (ILs)/polymer composites [2]. Unlike conventional capacitive pressure sensors, IL/Polymer composite-based capacitive pressure sensors form a nanometer-scale electrical double layer (EDL) at the interface of the electrode/composite when the electrode and composite are in contact, resulting in a high unit capacitance of several microfarads. Therefore, the larger the change in the contact area between the electrode and the IL/polymer composite, the greater the change in capacitance resulting in higher sensitivity. To enhance the variation in contact area with applied pressure, microstructuring of IL/polymer composite has been adopted in various studies [3]. However, achieving a higher level of sensitivity requires extremely fine microstructures, which involve costly processes that limit their implementation in low-cost, large-area devices. Meanwhile, cost-effective template methods have limitations in enhancing sensitivity due to the inherent difficulty of inducing a substantial change in the contact area.

MXene, a family of two-dimensional sheet materials and inorganic compounds consisting of transition-metal carbide and carbonitride, is emerging as an electrode material for tremendous electrochemical energy storage devices. In particular, the interlayer compound structure of MXene accommodates ions at high charge/discharge rates, making it an efficient ion intercalation electrode material in the field of capacitors [4].

In this work, we propose the iontronic capacitive pressure sensor with a microstructured IL/polymer composites dielectric layer and a $Ti_3C_2T_x$(MXene)-derived top electrode. The remarkable ionic intercalation property of the $Ti_3C_2T_x$ layer accelerates the formation of the EDL of the IL/polymer composite, resulting in a pseudo-capacitive effect. The fabricated sensor showed higher sensitivity than the iontronic pressure sensor with ordinary electrodes, and demonstrated commendable performance in various evaluation tests, exhibiting promising potential across a wide range of applications.

Figure 1 (a) shows a schematic of the fabrication process for MXene/PVA electrodes. Since the combination of PVA and KOH is well-established and widely used in electrical energy storage by speeding up the transfer of ions, we mixed MXene in the PVA/KOH solution to maximize the ion intercalation effect. With electrodes utilizing MXene, the ions in the IL/polymer composite quickly penetrate between the MXene layers and have a thinner EDL, leading to a larger volumetric capacitance than conventional electrodes (Figure 1(b)) [5]. Figure 2(a) shows the cyclic voltammetry curves of the electrodes. The volumetric capacitance of the PVA electrode is about 218 F/g, while the MXene/PVA electrode is about 805 F/g, demonstrating the ion storage capacity of MXene. In addition, the iontronic capacitive pressure sensor based on the MXene/PVA electrode exhibited about seven times higher sensitivity than the sensor with the conventional copper electrode (Figure 2(b)). As shown in Figure 3(a), the proposed sensor could detect a small pressure of about 0.25 Pa. Response time and recovery time were 43 and 48 ms, respectively, showing excellent performance (Figure 3(b)), and the sensor did not show any performance degradation during 10,000 loading-unloading cyclic tests (Figure 3(c)).

In summary, we present the pseudo-capacitive iontronic capacitive pressure sensor using IL/polymer as the dielectric layer and MXene/PVA as the electrode. The MXene/PVA electrodes can induce more ions by improving the intercalation speed of ions, and create thinner EDLs in IL/polymer composites, resulting in a higher volumetric capacitance compared to electrodes without MXene. The proposed sensor exhibited a notable sensitivity of 104 kPa^{-1}, and it was demonstrated that it showed excellent potential as a wearable pressure sensor through various sensing performance evaluations.

References

[1] Bijender et al., Sens. Bio-Sens. 33 (2021) 100434
[2] C. Cho et al., ACS Appl. Mater. Intercaces 15 (2023) 13625-13636
[3] N. Bai et al., ACS Nano 16 (2022) 4338-4347
[4] D. Gandla et al., ACS Omega 7 (2022) 7190-7198
[5] Q. Fan et al., J. Chem. Eng. 15 (2022) 131107

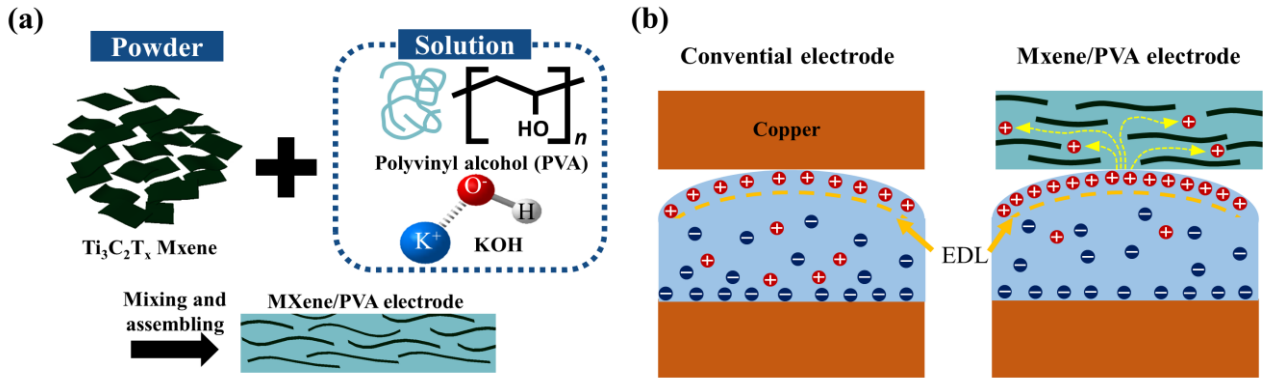

Figure 1. (a) Schematic of the fabrication process of MXene/PVA electrode and (b) comparison of an iontronic capacitive pressure sensor using conventional electrodes and MXene/PVA electrodes.

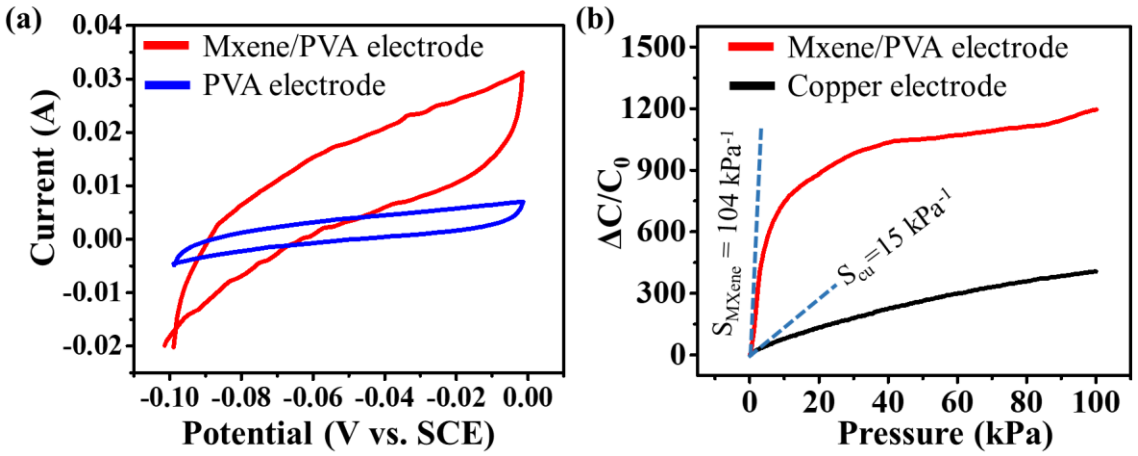

Figure 2. (a) Cyclic volummetric curve of MXene/PVA and PVA electrode and (b) relative capacitance variation graph for sensors with Mxene/PVA and copper electrode.

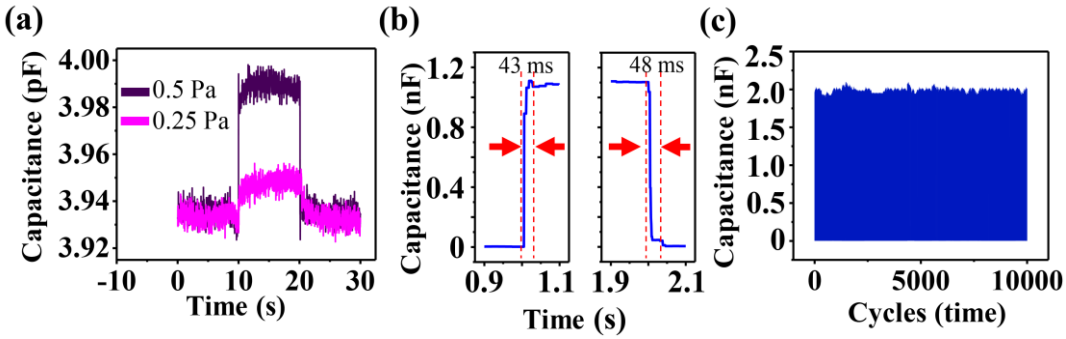

Figure 3. Performances of fabricated sensor: (a) Limit of detection, (b) response and recovery times, and (c) cyclic test.

Evaluation of highly sensitive vibration states of nanomechanical resonators in liquid using a convolutional neural network

Kazuki Bessho [a], Shin'ichi Warisawa [a], Reo Kometani [a]

[a] Graduate School of Frontier Sciences, The University of Tokyo
5-1-5, Kashiwanoha, Kashiwa-shi, Chiba 277-8563, Japan
e-mail: kbessho@s.h.k.u-tokyo.ac.jp

Keywords: Nanoelectromechanical systems, Nanomechanical resonator, Convolutional Neural Network, Grad-CAM, Solution concentration measurement, Acetone solution

Nanomechanical resonators can detect various small physical quantities with high sensitivity using changes in resonant characteristics. However, the measurement sensitivity is significantly reduced due to viscous damping in liquids. It has been suggested that in the measurement of physical quantities in vacuum, highly sensitive vibration states may exist in frequency bands other than the resonant frequency band [1]. This research applies this approach to measuring nanomechanical resonators in liquids, to identify the frequency bands and highly sensitive vibrational states that are useful for measurement. This research was carried out through the measurement of acetone concentration. Nanomechanical resonators placed in the liquid change their vibrational properties with changes in density and viscosity due to acetone concentration. A Convolutional neural network (CNN) model was used to analyze the vibration spectra.

Figure 1(a) shows scanning electron microscope (SEM) images of a nanomechanical resonator. The resonators were fabricated on a Si substrate by focused ion beam (FIB) ion implantation and wet etching, as shown in Fig. 1(b). The length and width of the resonator are 8.90 μm and 1.76 μm, respectively. Vibration spectra were measured using an optical heterodyne vibrometer, as shown in Fig .2(a). Photothermal excitation using a laser was used as the excitation method. First, the concentration classification capabilities of conventional measurement methods, which observe changes in resonance properties, and methods that estimate concentration changes by analyzing the vibration spectra using a CNN model were compared. Acetone solutions with concentrations of 2%, 3%, 3.5%, and 4% were used for the measurements, and the two methods were compared in terms of their ability to classify concentrations based on 2%. The CNN model used for the vibration spectrum analysis was a 34-layer residual network (ResNet) [2]. The measured vibration spectra consisted of 1400 data points and were trained as parameters in a 1D array. 300 vibration spectra of the center of the resonator were measured per acetone concentration, of which 200 were used as training data and 100 as test data. Figure. 2(b) shows results from the conventional method, while Fig. 3(a) shows results from the CNN-based method. The results indicated that a method using CNN can achieve higher sensitivity than conventional methods.

Gradient-weighted Class Activation Mapping (Grad-CAM) [3] was applied to confirm which frequency bands were important for classifying the 2% and 3.5% concentrations in the decision-making of the learning model. Grad-CAM is a method used to visualize the importance of each input parameter for the output of a CNN model. Grad-CAM was applied to all the test data used for training, and the results were averaged to output an importance score for each frequency. The Grad-CAM results are shown in Fig. 3(b). The results indicate that the high-frequency band from 12.5 to 13 MHz was most important for determining a concentration of 2%, while 7.7 MHz, close to the resonance frequency, was most important for determining a concentration of 3.5%. Next, vibration spectra were measured at several locations on the resonator, and amplitudes at frequencies of high importance were extracted from the spectra. By arranging the extracted amplitudes in the same order as the measurement positions, the vibration state at the frequencies of high importance was visualized. The measured positions on the resonator and the results of the vibration state measurements are shown in Figure 3(c). The results show that the amplitude is very small in the high-frequency band between 12.5 and 13 MHz, while the amplitude is large at 7.7 MHz, which is close to the resonance frequency. This result indicates that, in addition to the resonance state used in the conventional method, a vibration state with a very small amplitude may be useful in the measurement of nanomechanical resonators in liquids. More research is needed to determine the mechanism of low amplitude vibration conditions being highly sensitive.

[1] K. Tsumune, S. Warisawa and R. Kometani., 2022 Jpn. J.Appl. Phys. 61 SD1038
[2] Kaiming He et al., Proceedings of the IEEE Conference on Computer Vision and Pattern Recognition (CVPR), 2016, pp. 770-778
[3] R. Selvaraju et al., Proceedings of the IEEE International Conference on Computer Vision (ICCV), 2017, pp. 618-626

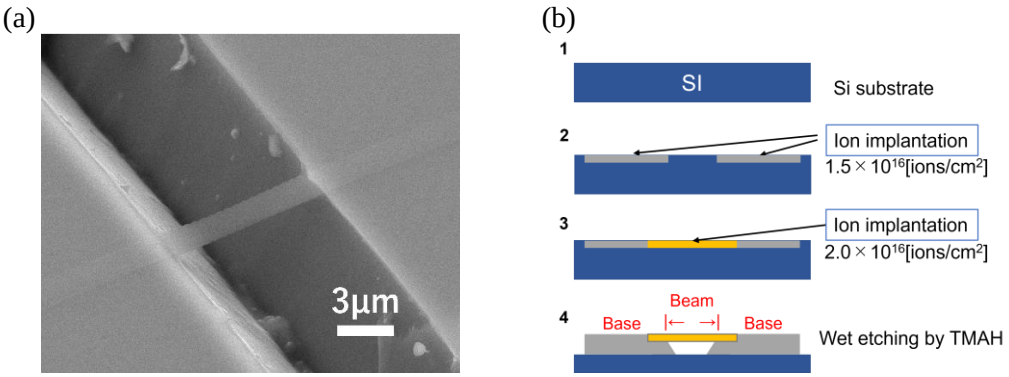

Figure 1. A nanomechanical resonator: (a) SEM image of a Si nanomechanical resonator, (b) Fabrication process of a nanomechanical resonator.

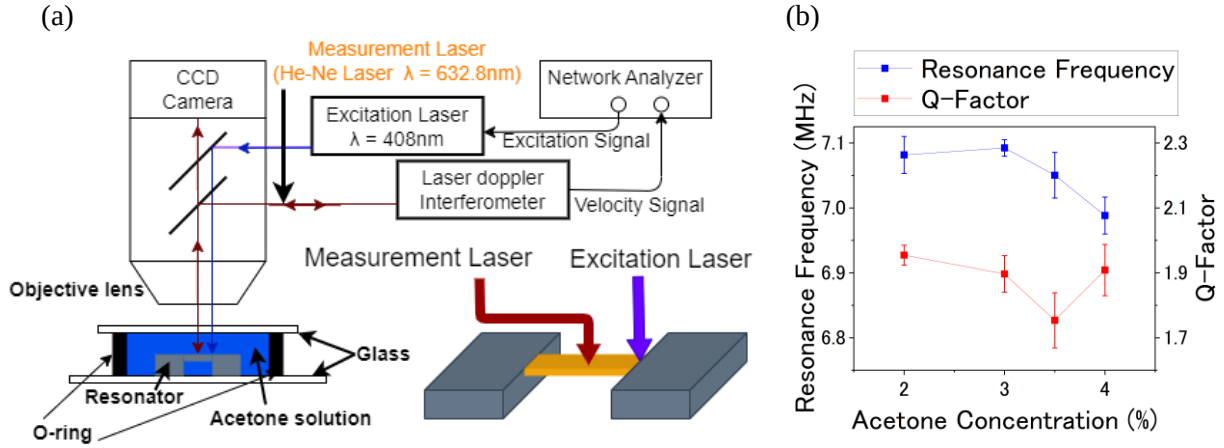

Figure 2. (a) Schematic of the vibration measurement system. (b) Resonant frequency and Q-Factor shift obtained from measurements of vibration spectrum using conventional methods.

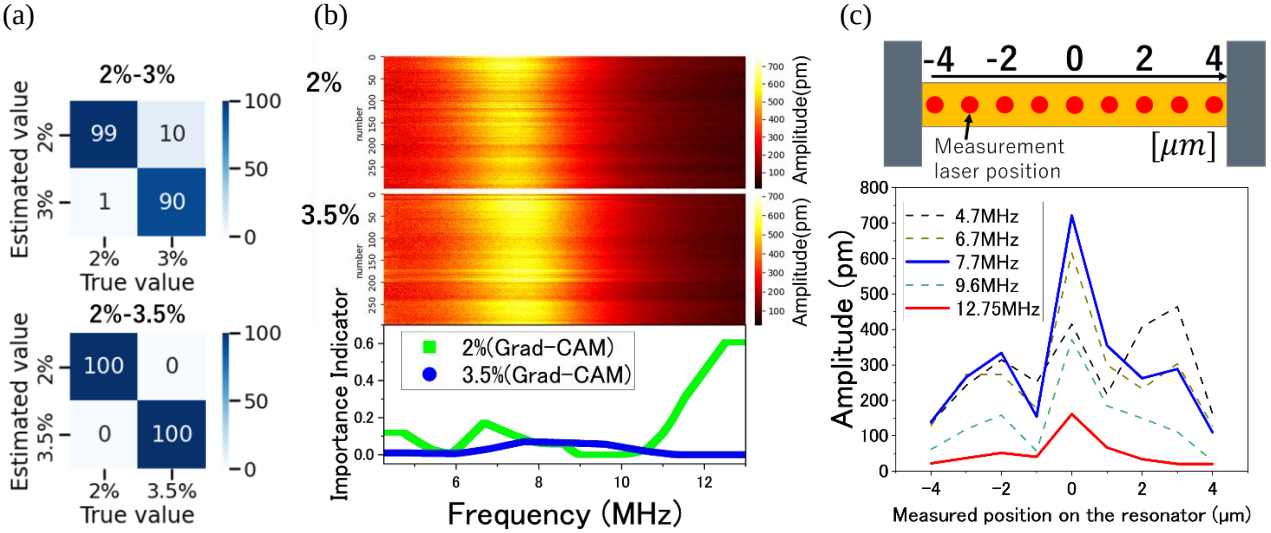

Figure 3. (a) Results of Resnet model classification for acetone concentration. (b) Heat map showing amplitude distribution of measured vibration spectra and Grad-CAM results for classification of 2% and 3.5% acetone concentration. (c) The upper figure is a schematic diagram showing the measurement position on the resonator during the vibration state measurement. The lower graph shows the measurement results of the resonator vibration state. The vibration state at 12.75 MHz out of 12.5-13 MHz, which was the most important for the 2% determination, is shown by the solid red line, and the vibration state at 7.7 MHz, which was the most important for the 3.5% determination, is shown by the solid blue line.

Scalable Si-based architectures obtained by templated solid state dewetting

S. Freddi[a], M. Gherardi[b], N. Granchi[c], A. Gatta Zini[b], A. Fedorov[a],
M. Abbarchi[d,e], A.Chiappini[a], M. A.Vincenti[f], F. Intonti[c], M. Bollani[a]*

[a] Institute of Photonics and Nanotechnology (IFN) – CNR, LNESS, Como, 22100, Italy
[b] Department of Physics, Politecnico di Milano, Milan, 20133, Italy
[c] Department of Physics and Astronomy and LENS, University of Florence, Sesto Fiorentino, Italy
[d] Aix Marseille Univ, CNRS, IM2NP 13397, Marseille, France
[e] Solnil 95 Rue de la République, Marseille 13002, France
[f] Department of Information Engineering, University of Brescia, Brescia, Italy

e-mail: monica.bollani@ifn.cnr.it

Silicon based nanocrystals represent a promising resource both for next generation electronic devices and for nano photonics applications. Their exploitation, however, requires precise size, shape, and position control [1]. Owing to their large surface area to volume ratio, thin semiconductor solid films are often unstable upon annealing. As such, under the action of surface diffusion, the film breaks eventually forming isolated islands when heated at temperature well below the melting temperature of the bulk material. This phenomenon, known as *solid state dewetting* (SSD), is one of the main factors impeding the use of ultra-thin silicon films on insulators (UT SOI) for the further miniaturization of electronic components. Here, we demonstrate the ultimate control of Si and SiGe based thin films dewetting for the precise formation of complex nano architectures, and their exploitation as dielectric nano antennas and field effect transistors wires [2,3]. The dielectric antennas are realized exploiting the SSD instability of thin solid films to form regular patterns of monocrystalline atomically smooth silicon and germanium nanostructures that cannot be realized with conventional methods. SSD, indeed, is a natural shape instability occurring in thin solid films when heated at high temperature: it transforms a flat layer in isolated islands in a timeframe independent from the sample size. However, its potential for applications based on complex pattern formation is still unexplored despite the manifold advantages it offers: a) it forms monocrystalline and facetted (atomically smooth) structures (size from ~nm up to ~10 μm), free from defects and from the typical rough ness produced by conventional etching methods; b) the islands are directly formed on an insulating substrate (SiO_2). Therefore, SSD can be efficiently exploited in all these fields to form perfectly ordered and complex nano architectures over large scales, as well as randomly organized, isolated islands. By properly combining e-beam lithographic (EBL) and reactive ion etching (RIE) processes, we can realize dewetted nanostructures that can play as Mie resonators [4,5,6]. One of the main key features of high refractive index dielectric Mie resonators is that their optical spectra display strong multipolar electric and magnetic resonances As a building material for such resonators Si or SiGe particles are very promising, since their absorption losses are very weak at visible and near infrared frequency. Furthermore, differently from metallic particles used in plasmonic e.g., gold silver, aluminum), they are compatible with silicon-based nanofabrication technologies being, therefore, more appealing for low-cost production and integration in electronic devices.

To understand the optical behavior of a single dewetted structure, we exploit a fabrication process in which arrays of islands are obtained through SSD of patterned Si or SiGe squares. Specifically, the resonator fabrication process starts from a silicon germanium on insulator with SiGe layers of 26 nm with a Ge content both of 20% and 30% on 7 nm Si layer itself on a 25 nm of SiO_2 box. The Ge content variation does not significantly modify the refractive index of the material, but it changes the dewetting dynamics. EBL is performed on negative resist at 30 KeV and the pattern exposed is transferred onto the sub strate by RIE with CF 4. Array of square patterns with lateral sizes varying from 200 nm to 700 nm and a periodicity of 3 μm are obtained. These samples are then annealed in a dedicated machine at temperature of 800°C, inducing the dewetting process, forming 3D shape islands due to surface energy minimization [Figure 1]. In contrast with more conventional top-down fabrication approaches where only cylinders can be obtained, this method enables a true 3 D shaping of the nano islands. The optical response of the nanoislands has also been evaluated by means of a commercial 3D finite element solver Comsol Multiphysics. The simulations revealed that islands support multiple resonances whose spectral position undergoes a significant red shift as the radius of the nanoparticle increases [Figure 2]. The results of the dark field spectroscopy show a good agreement between the simulation and the experimental data: the position of the peaks is perfectly reproduced, while the

mismatching with respect to the intensity can be ascribed to the asymmetry of the resonator shape respect to the simulated one.

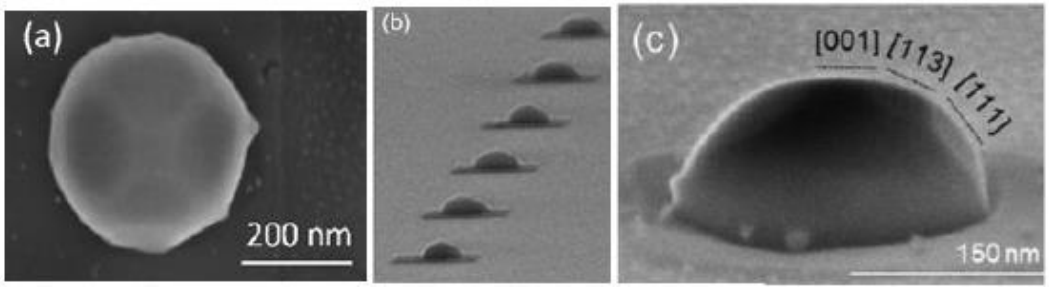

Figure 1: (a) SEM top view image of a single dewetted SiGe island. (b) SEM image of islands acquired with a tilt angle of 45 degrees to highlight the faceting of each scatter. (c) SEM image of a single island, where the faceting planes {001}, {113} and ,{111} are labelled.

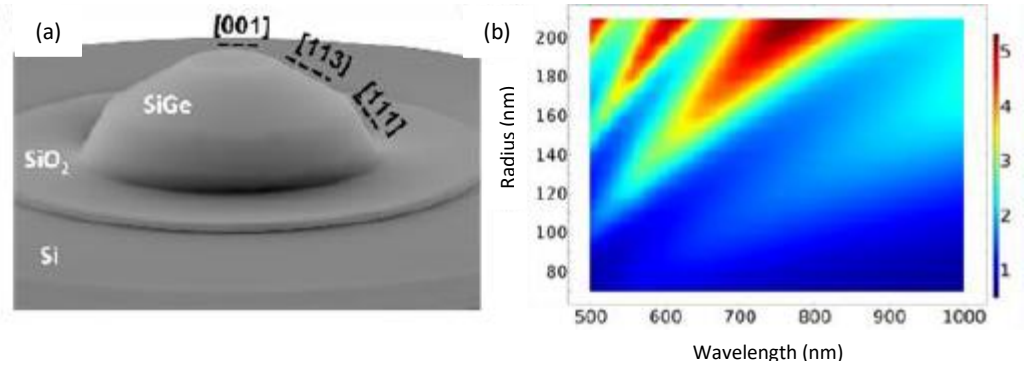

Figure 2: 3D sketch of resonator on the SiO_2 pedestal used for FEM simulation. The crystallographic planes are labelled. (b) FEM scattering cross section in function of the radius size and for a fixed aspect ratio of 0.6

Acknowledgements
This work is supported by the European Union Horizon 2020 program under grant No. 828890 – NARCISO Project and CNR "EPOCALE project (2022-2024).

References
[1] "Nanostructured Semiconductor Oxides for the Next Generation of Electronics and Functional Devices Properties and Applications" (2014), Pages 95-138
[2] M. Naffouti et al, Science Advances, (2017) Vol. 3, n°11, eaao1472
[3] M.Bollani, et al., Nature Comm.,(2019),10, 5632
[4] N. Granchi, et al., APL Photonics (2021), 6,12, 126102.
[5] L.Fagiani, et al., Opt. Mat. X, (2022), 13, 100116
[6] N.Granchi et al, Opt Express, (2023), 31, 5, 9007

Integration of Plasmonic Structures and Controlled Multimode Optical Fibers for Advanced Endoscopic Systems: Fabrication, Characterization, and Spatially Resolved SERS Enhancement

Linda Piscopo[a,b*], Liam Collard[b], Di Zheng [b], Filippo Pisano [b], Antonio Balena[b], Marco Pisanello[c], Massimo De Vittorio[a,b,+], Ferruccio Pisanello[b,+]

[a] Dipartimento di Ingegneria dell'Innovazione, Università del Salento, Lecce, 73100, Italy
[b] Istituto Italiano di Tecnologia, Center for Biomolecular Nanotechnologies, Arnesano,73010, Italy
[c] OptogeniX, Lecce, 73010, Italy
*Corresponding author. E-mail: linda.piscopo@iit.it, + co-last authors

Plasmonic structures, with their exceptional optical properties, have shown promise for the next generation of biosensors. These include neurochemical detection through surface-enhanced Raman spectroscopy [1][2], refractive index monitoring for label-free optical recording of neural activity [3] and wavevector-encoded detection of fluorescence [4]. Despite these sensing paradigms are challenging to be translated *in vivo*, the scientific community would highly benefit from the possibility of employing light-matter interactions to interface with brain cells in an endoscopic fashion.

To exploit the full potential and further enhance the detection capability of plasmonic endoscopy, thorough control of the excitation light is required. However, this is possible only in a microscopy-based sensing scheme, in which the plasmonic resonances can be efficiently excited by setting a specific operation point in the dispersion diagram by tuning both the in-plane component of the wave vector as well as the wavelength of the excitation field [5].

Here we propose a technological platform to translate plasmonics to neuroendoscopy (**Figure 1A**). To this aim, we have implemented a wavefront shaping method that allows controlling the coupling between guided modes in multimode fibers and plasmonic resonances both in the near field and the far field of metallic nanostructures fabricated on the distal fiber facet (**Figure 1B**). Through a phase modulation algorithm, it is possible to tailor key parameters of the excitation field: (i) its spatial confinement by engineering the intensity profile on the plasmonic facet, and (ii) its angular properties by acting directly in the far field plane (kx,ky)[6]. At the same time, the system employs a custom-made holographic system with a super-continuum light source (based on a 785 nm femtosecond pumping laser and a photonic crystal fiber), providing pico-second pulsed wavelength-tuneable shaped wavefronts at the input of the plasmonic fiber (**Figure 2A**). The ability to act simultaneously on the (kx,ky) space and the operative wavelength results in the possibility to set the working point of the coupling system in the dispersion diagram through the fiber.

We have applied this system to two plasmonic configurations for generating either propagating surface plasmon resonances (SPRs) as well as localized SPRs (**Figure 1C**). For testing propagating surface plasmons, we have fabricated elliptical nano-holes, in a gold layer deposited by electron-beam evaporation, by focused ion beam milling (FIB), which offers high resolution and repeatability in creating sub-diffraction apertures in metallic thin films. Scanning a focal spot on the nanostructured surface, through the fiber we recorded the propagation of plasmonic resonances in the metallic layer (**Figure 2B**).

Concerning localized SPR, we have tested the system in the context of spatially resolved SERS endoscopy. The facet of a MMF was equipped with nano-island nucleated directly on the facet by dewetting a thin gold film [2], following a random distribution and exhibiting a high coverage rate. The SERS response of the nanostructured fiber was tested in a Rhodamine 6G (R6G) solution, monitoring the intensity of the peak at 1510 cm-1 (**Figure 2C**) as we target different areas on the facet. The excitation wavelength was set at 785 nm, to address future applications *in vivo*, where a near-infrared light reduces the autofluorescence of the tissue.

In conclusion, the integration of plasmonic structures with multimode optical fibers controlled by holographic excitation using a spatial light modulator (SLMs) presents a promising avenue for developing plasmonic endoscopes. In this direction, we optimized a multispectral photonic system to study the dispersion curves of plasmonic structures and excite precise work points of the coupled system. We tested the system on different plasmonic geometries, targeting propagating and localized SPR and applied the wavefront shaping principles to obtain spatially-resolved endoscopic SERS.

[1] Vitol, E. A et al. (2009). In situ intracellular spectroscopy with surface enhanced Raman spectroscopy (SERS)-enabled nanopipettes. *ACS nano*, *3*(11), 3529-3536.

[2] Zheng, D. et al. (2023). Toward Plasmonic Neural Probes: SERS Detection of Neurotransmitters through Gold-Nanoislands-Decorated Tapered Optical Fibers with Sub-10 nm Gaps. Advanced Materials, 35(11), 2200902.
[3] Eddin, F. B. K. et al. (2022). Plasmonic Refractive Index Sensor Enhanced with Chitosan/Au Bilayer Thin Film for Dopamine Detection. *Biosensors*, *12*(12), 1124.
[4] Pisano, F. et al. (2022). Plasmonics on a Neural Implant: Engineering Light–Matter Interactions on the Nonplanar Surface of Tapered Optical Fibers. Advanced Optical Materials, 10(2), 2101649.
[5] de Waele, R. et al. (2009). Plasmon dispersion in coaxial waveguides from single-cavity optical transmission measurements. *Nano letters*, *9*(8), 2832-2837.
[6] Collard, L. et al. (2022). Holographic Manipulation of Nanostructured Fiber Optics Enables Spatially-Resolved, Reconfigurable Optical Control of Plasmonic Local Field Enhancement and SERS. Small, 18(23), 2200975.

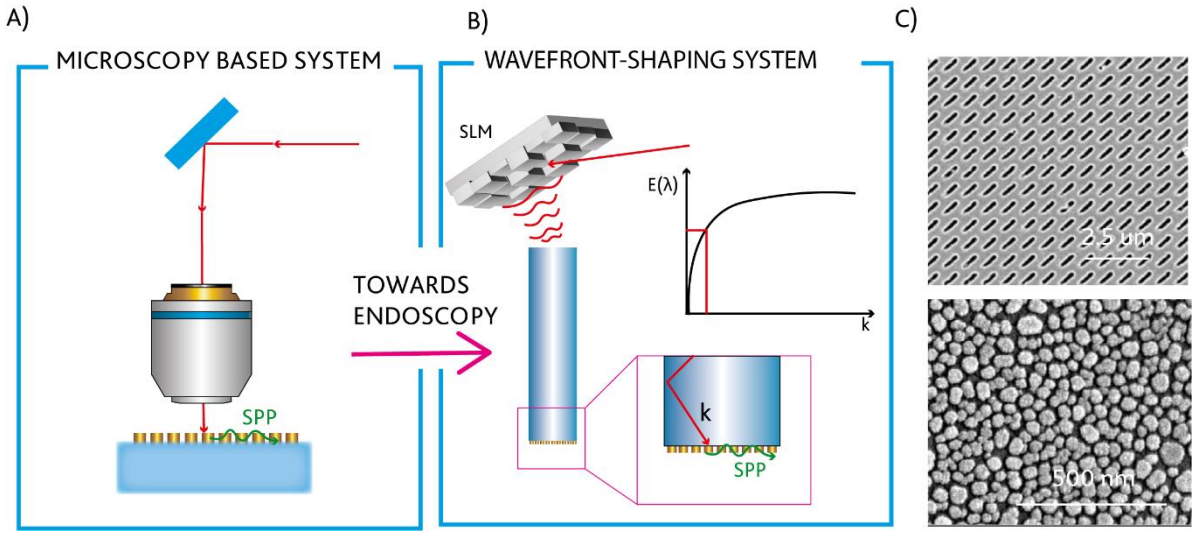

Figure 1: A) Schematic representation of the transition from classical optical setup for plasmonic structures excitation and B) endoscopic system based on optical plasmonic fiber. An example of dispersion curve is depicted. C) Plasmonic structures engineered on the facet of the MMF: gold nano-ellipses fabricated with Focused ion beam milling (top) and gold nano-islands obtained with planar dewetting.

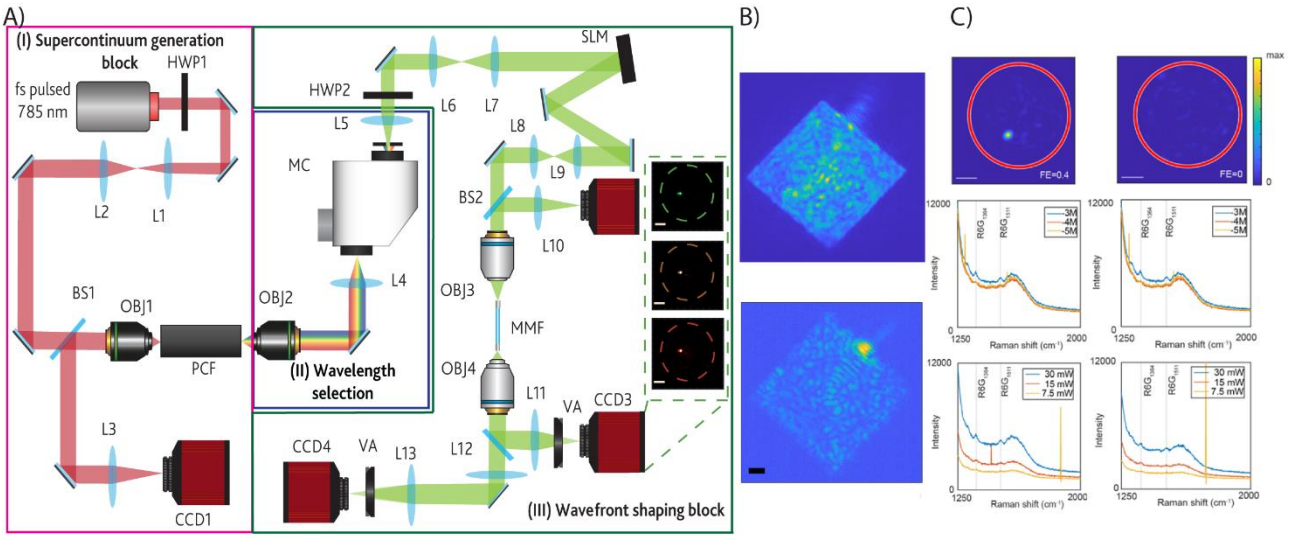

Figure 2: A) Schematic representation of the characterization setup. B) Propagation of surface plasmon resonance excited at different wavelengths, top 600 nm, bottom 633 nm. C) Rhodamine 6G SERS spectra collected with a plamonic fiber: exicitation point on the structures (left) and on a control region (right).

Towards photon-noise limited room temperature IR detection using optomechanical resonators

Martini P.[a] , Kanellopulos K.[a] , and Schmid S.[a]

[a] Institute of Sensor and Actuator Systems, TU Wien, Gusshausstrasse 27-29, 1040 Vienna, Austria
e-mail: silvan.schmid@tuwien.ac.at

The infrared (IR) portion of the electromagnetic spectrum holds many and important information about the interaction between radiation and matter. This information is of high value in many fields, ranging from fundamental research, industrial applications, to security scanning and medical imaging. The low energy carried by the photons in the IR range makes their detection challenging for room temperature detectors, and often in order to achieve the necessary sensitivity, thermal IR detectors make use of cryogenic cooling, e.g., with liquid helium which is a non-renewable natural resource [1].
A figure of merit for thermal detectors is the noise-equivalent power (NEP), which is defined as the absorbed power change that produces a signal equal to the total (rms) noise [2]. For an optomechanical resonator it can be calculated as:

$$NEP = \frac{\sqrt{2\tau}\,\sigma_y(\tau)}{\delta R}$$

where τ is the integration time at which the Allan deviation of the fractional frequency signal $\sigma_y(\tau)$ is measured and δR is the relative responsivity to the impinging power.
In this work, we propose a square drum resonator made of 50 nm thick silicon nitride (SiN) with a 5 nm thin film of platinum (Pt) deposited as a broadband IR absorber (~50% absorptance). The novelty of our work consists of the presence of a circular area where the Pt is not deposited. By using this particular design, we are able to significantly increase the responsivity of the structure, while keeping the photothermally induced noise coming from the readout laser low. This allows us to reach an NEP of hundreds of $pW/\sqrt{Hz}$, which is two orders of magnitude higher than the fundamental photon-noise limit of thermal detectors [3].
The responsivity measurements are shown in Fig 1a for different membrane sizes (L) and for multiple vibrational modes. The data are in good agreement with the predicted values from the analytical model [4]. Additionally, the validity of the analytical model was confirmed with FEM simulations (Fig 1b). The detector speed τ_{th} is also evaluated (Fig 2), showing again good agreement with the model.
Finally, the frequency stability of the devices is evaluated via the Allan deviation σ_y. Results show that the noise level is still two orders of magnitude higher that the theoretical one, which takes into account thermal fluctuation noise and thermomechanical noise [5-7] (see Fig 3).
The current NEP is therefore limited by the frequency stability of our nano-optomechanical platform. Efforts are underway to minimize the current sources of noise (thermal stability, flicker noise, electronic noise) to finally reach for the first time the photon-noise limit at room temperature.

[1] Rogalski, A. Infrared and Terahertz Detectors. (CRC Press, 2019).
[2] Kruse P.W. and Skatrud D.D., Uncooled Infrared Imaging Arrays and Systems (Academic Press, 1997).
[3] Kruse P.W., Uncooled Thermal Imaging. Arrays, Systems, and Applications (SPIE, 2001).
[4] Schmid, S., Villanueva, L. G., and Roukes, M. L., Fundamentals of Nanomechanical Resonators, 2nd edition, 2023, Springer.
[5] Sadeghi, P., Demir, A., Villanueva, L. G., Kähler, H. & Schmid, S. Frequency fluctuations in nanomechanical silicon nitride string resonators. Phys. Rev. B 102, 1–8 (2020).
[6] Snell, N., Zhang, C., Mu, G., Bouchard, A. and St-Gelais, R., 2022. Heat Transport in Silicon Nitride Drum Resonators and its Influence on Thermal Fluctuation-induced Frequency Noise. Physical Review Applied, 17(4), p.044019.
[7] Demir, A. & Hanay, M. S. Fundamental Sensitivity Limitations of Nanomechanical Resonant Sensors Due to Thermomechanical Noise. IEEE Sens. J. 20, 1947–1961 (2020)

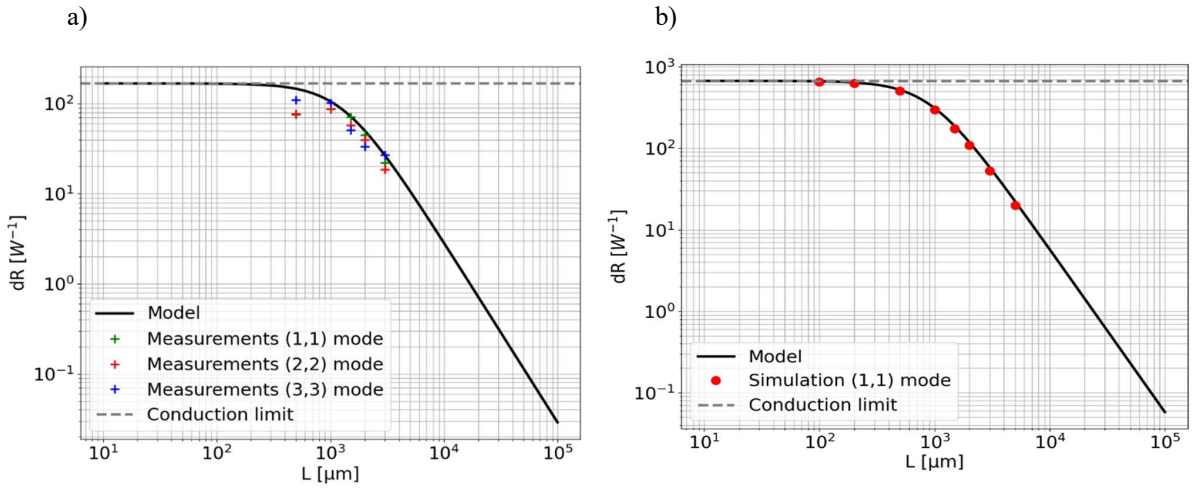

Figure 1. For each sample and mode, the responsivity is obtained at 4 different wavelengths (5.68 µm, 6.26 µm, 7.62 µm and 8.7 µm) by performing a linear fitting of the resonator frequency response to five different laser powers (ranging from 22.6 µW to 188µW) at every wavelength. The resulting average is plotted. Comparison between the measurements and analytical model (a). Comparison between model and FEM simulation for the case of a point-like heat source (b).

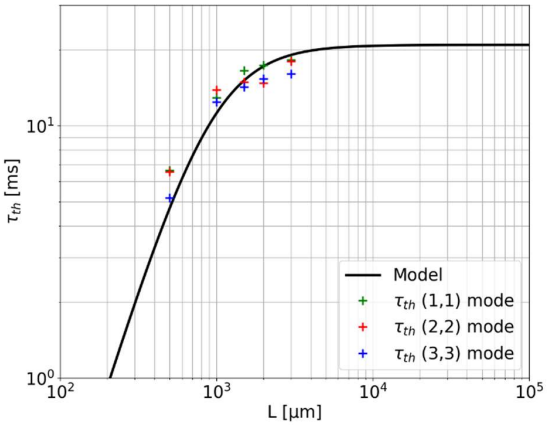

Figure 2. Thermal time constant measured for the drum resonators. For the bigger structures we reach the limit given by the radiative heat transfer, where τ_{th} is independent of membrane size.

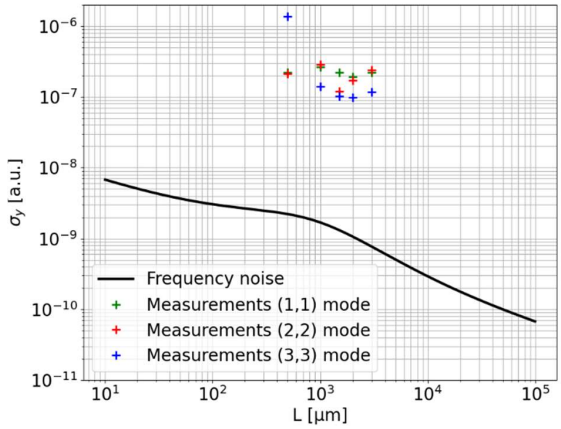

Figure 3. Comparison of the Allan deviation measured (coloured crosses) and theoretical (black line). The theoretical takes into account thermal fluctuation noise and thermomechanical noise.

Electrochemical analysis on the SERS structure using boehmite

Shunya Saegusa [a], Masayuki Naya [b], Takao Fukuoka [a], Yuichi Utsumi [a], Akinobu Yamaguchi [a]

[a] Laboratory of Advanced Science and Technology for Industry, University of Hyogo, Ako-gun, Hyogo, 678-1205, JAPAN
[b] Faculty of Science and Technology, Keio University, Yokohama, 223-0061, JAPAN
e-mail: saesae54@lasti.u-hyogo.ac.jp

Surface-enhanced Raman scattering (SERS) is a spectroscopic method that uses electric field enhancement to obtain highly sensitive Raman spectra [1]. This technique has potential applications in bioanalysis because of its high sensitivity and label-free measurements. However, it is difficult to fabricate structures that exhibit SERS activity because of the need to create nanogaps between nanoparticles of noble metals. We investigate microfluidic devices combined with SERS-active structures based on boehmite structures for potential applications in microbial analysis. This fabrication method is easy to fabricate and can achieve high sensitivity, wide area, and high resolution observation [2,3].

We have changed the fabrication method of noble metal layers from vapor deposition to magnetron sputtering to improve adhesion and stacking area [3], and fabricated this sensor into a microfluidic device as shown in Figure 1. Figure 2 shows the Raman spectra measured when the fabricated device was inter-fed with 4,4'-bipyridine (20 μM) and pure water at a flow rate of 0.1 mL/min, respectively. The Raman intensity increases with time because the amount of sample adsorbed on the hot spots of the gold nanoparticles increases with time. On the other hand, the adsorption of molecules on this gold surface is very strong. Even if pure water is pumped at a flow rate of 0.1 mL/min for 30 minutes, the sample cannot be removed from this sensor. In order to make the device reusable, we aim to create a desorbable label using redox desorption of thiolate bonds on the gold surface. In order to investigate the electrochemical reaction of this desorption, we report the results of analyzing the electrochemical reaction on a SERS substrate.

The SERS sensor was fabricated by sputtering an Au layer on a boehmite substrate. The boehmite was prepared by boiling a glass slide with an Al layer for 5 min. During sputtering, a metal mask was used to fabricate the electrode structures for cyclic voltammetry. The SERS structure was fabricated only for the working electrode. On the other hand, the reference electrode was made by sputtering Au followed by silver chloride paste. A 5 mm square dimethylpolysiloxane (PDMS) well was also prepared as a sample container.

We focused on the redox desorption of thiolate bonds on the Au surface as the desorption reaction. This bond has been used in some research cases for desorption of cells on electrodes [4]. In this study, cysteine was attached to the working electrode, and cyclic voltammetry was performed. Raman measurements were also performed during cyclic voltammetry to evaluate the dependence of cysteine-gold binding on the applied potential and desorption.

We believe that the above studies are important for maintaining the detection sensitivity of the SERS sensor.

1. K. Kneipp, Y. Wang, H. Kneipp, L. T. Perelman, I. Itzkan, R. R. Dasari, and M. S. Feld, , *Phys. Rev. Lett.*, 1997, **78**, 1667.
2. S. Yamazoe, M. Naya, M. Shiota, T. Morikawa, A. Kubo, T. Tani, T. Hishiki, T. Horiuchi, M. Suematsu, and M. Kajimura , *ACS Nano*, 2014, **8**, 6, 5622–5632.
3. T. Tanaka, S. Saegusa, M. Naya, T. Fukuoka, S. Amano, Y. Utsumi, and A. Yamaguchi, Journal of Photopolymer Science and Technology, 2022, **35**, (No.3), 249-253.
4. N. Mochizuki, T. Kakegawa, T. Osaki, N. Sadr, N. Kachouie, H. Suzuki, J. Fukuda, Journal of Tissue Engineering and Regenerative Medicine, 2012

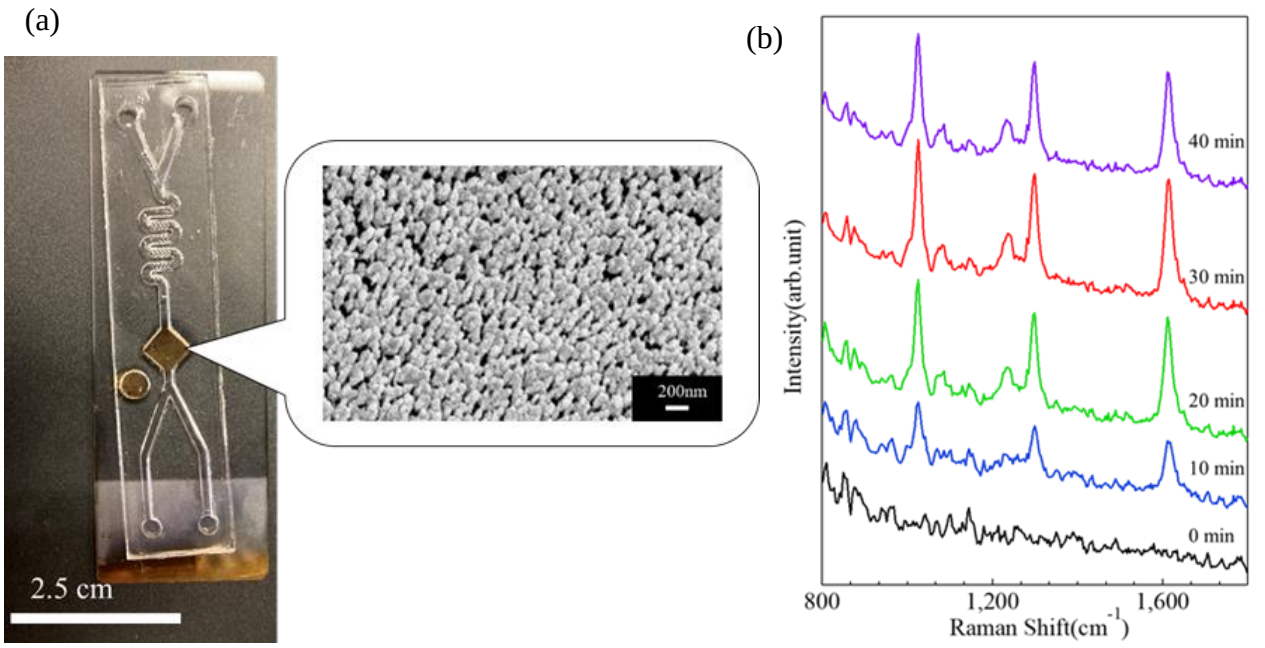

Figure 1. (a) Microfluidic device combined with SERS sensor and SEM image of SERS-active structure, (b) Changes in the intensity of Raman spectra with time

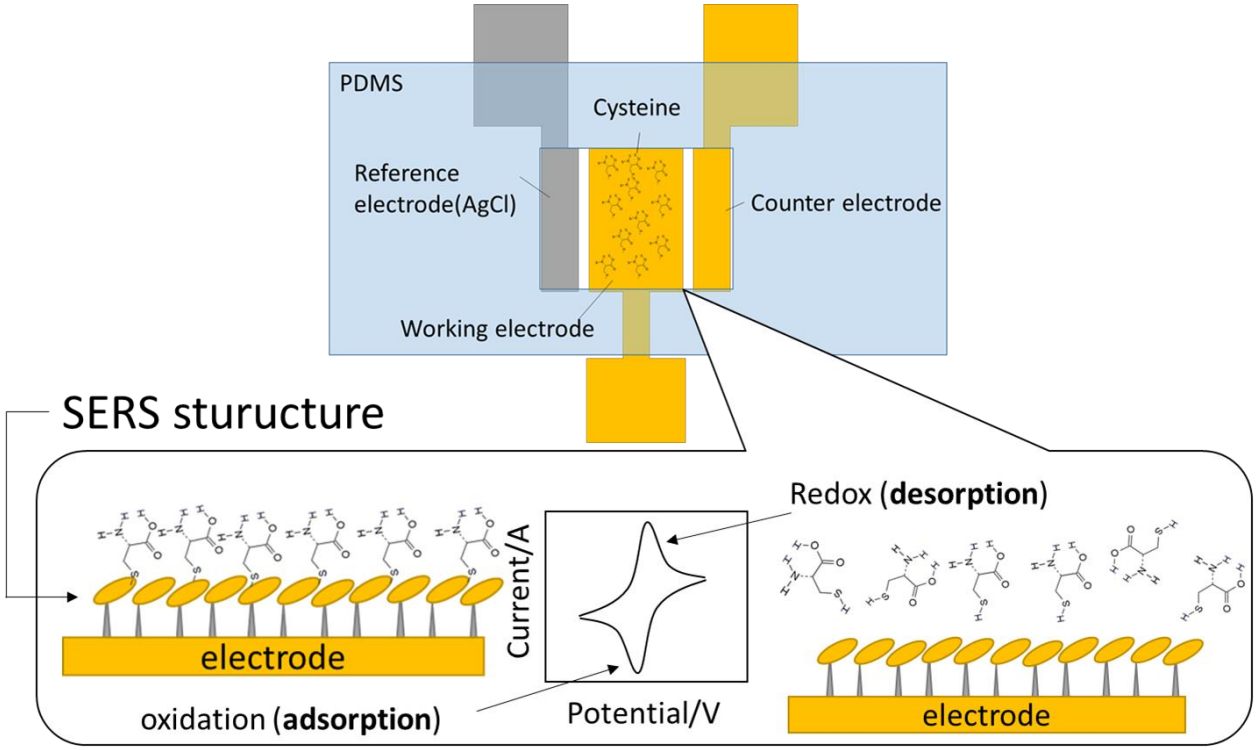

Figure 2. Chip design for studying the dependence of the bonding of adsorbed cysteine molecules

Focus Track - Next Generation Quantum Computing and related Materials - Papers

Nanofabrication methodology and optimization for photon extraction on diamonds' NV center

Mohammad Soltani[a], Behrooz Semnani[a], Abdolreza Pasharavesh[a], Vinodh Raj Rajagopal Muthu[a], Christopher Wilson[a], and Michal Bajcsy[a]
[a] Institute for Quantum Computing (IQC), University of Waterloo, Waterloo, ON, N2L 3G1, Canada
e-mail: m9soltan@uwaterloo.ca

Colour centers in diamonds are one of the highly promising candidates for quantum computing, communication and sensing[1]. Negatively charged nitrogen-vacancy centers (NV^- Centers) are explored as a solid-state spin qubit in particular, thanks to their extended spin coherence time[2]. However, due to the high refractive index contrast between diamond and air, excitation and collection of light from NV centers in diamond remains an outstanding challenge. A common approach is using solid-immersion lenses[3] which requires bulky optical setups or alternatively, enhanced collection of photons emitted by NV centers has been reported using nanofabricatted structures, including nanopillars[4], bullseye gratings[5], and , and GaP structures resulting from inverse design[6]. Here we explore the fabrication challenges their trade-offs with photon-extraction performance of two distinct approaches to such nanofabricated structures. The first approach uses plasmonic nanoantennas and does not require pattering into diamond. In contrast, in the second approach, we investigate the possibilities of improvement in nanofabrication processes for diamond nano-pillars, bullseye gratings and inverse-design metastructures shown in Fig. 1 and 2, respectively.

This works reports on our contributions to the design and fabrication of various nanostructures built with/ on the diamond, including plasmonic structures on top of the diamond and patterns made in the diamond itself, such as pillars, bullseye gratings and inverse metastructure on diamonds as shown in **Figure 1** and **2**, respectively.

One of the main issues associated with high-quality diamond samples is their small size and, thus, difficulty to handle. To cope with this situation, we designed and fabricated silicon-made pockets that allow us to mount the samples during processing. These handling pockets facilitate the spin coating on small dimensions samples and address aligning different parts of the diamond samples. For example, we fabricated plasmonic nanoantennas (Fig 1) on diamond pieces in such pockets using e-beam lithography followed by gold deposition and lift-off process.

Another outstanding challenge is the dry etching of bulk diamonds. We etched bullseye grating and inverse-design metastructures using directional inductively coupled plasma (ICP) of the Oxygen reactive ion etching optimized for quantum-grade diamond samples. We also tested the effect of mask materials and etching parameters for pillar structure etching morphology and investigated the impact of mask selectivity and morphology of etching. Aluminum hard-mask lift-off gives us better selectivity compared to Cr_2O_3. However, in most of the tries, micromasking effect occurred during the etching process for aluminum, while it was largely reduced for that of Cr_2O_3 (Fig. 3).

We also investigate the design's effect on reaching unconventional microneedle structures in diamonds. The design and materials selection allows us to make sharp-tip pillars suitable for other applications like biosensing or atomic force microscopy (AFM) tip patterning using diamond (Fig. 3, part c).
Our study of fabrication mechanisms is also suitable for other diamond-based devices with applications beyond quantum technologies.

References:
[1] C. Bradac et al., Nature Communications 10 (2019) 5625.
[2] J. Wrachtrup et al., Journal of Physics: Condensed Matter 18(2006) S807.
[3] T. Schroder et al., New Journal of Physics 13 (2011) 055017.
[4] T. Babinec et al., Nature Nanotechnology 5(2010) 195–199.
[5] L. Li et al., Nano letters 15(2015) 1493–1497.
[6] S. Chakravarthi et al., Optics 7(2020) 1805.

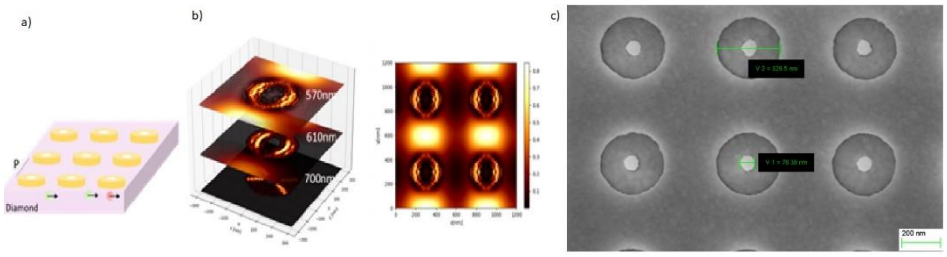

Figure 1. Plasmonic nanoantenna design for isolating individual NV centers in diamond a) Schematic of design b) Field distribution across the unit cell upon free space illumination c) SEM image of fabricated nano antenna before lift-off process.

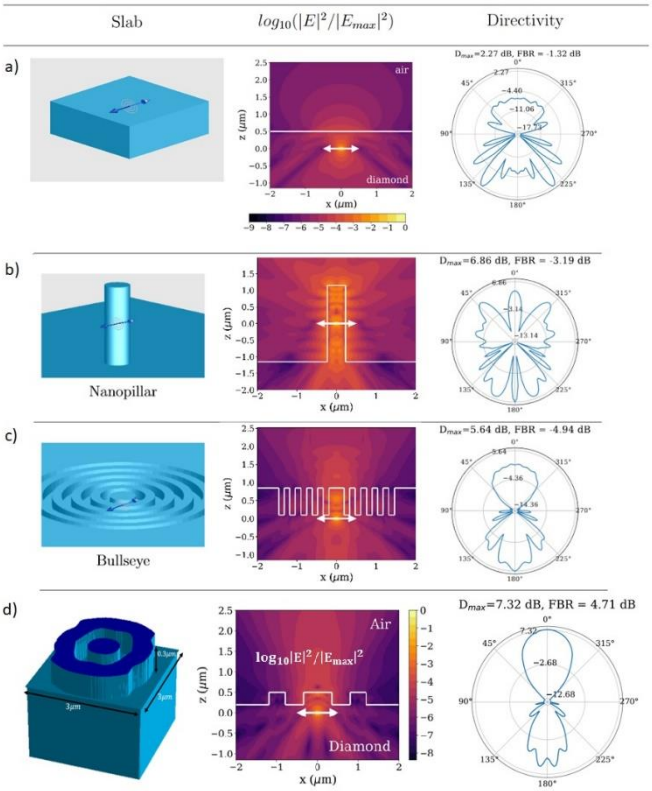

Figure 2. Photon extraction using diamond patterning methods and their effect on extraction efficiency a) diamond without patterning, b) with pillars, c) with bullseye and d) topology optimized hyper grating on top of the diamond.

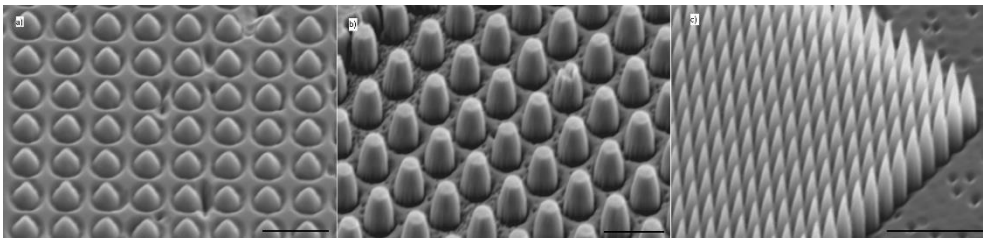

Figure 3. Different diamond pillar structures are etched in diamond using a lift-off process of hard mask followed by ICP-RIE oxygen plasma etching with a) Cr_2O_3 as a hard mask, b) and c) Aluminum as a hard mask, c) Shows sharp microneedles out of diamond by changing the design and materials selection (black scale bar represent 1μm).

Integrated superconducting single photon detectors for trapped ion quantum computers

Philipp L. Hoffmann [a], Alexander Fernández Scarioni [a], Sebastian Raupach [a], Peter Hinze [a], Thomas Weimann [a], Mark Bieler [a]

[a] Physikalisch-Technische Bundesanstalt (PTB), 38116 Braunschweig, Germany
e-mail: alexander.fernandez-scarioni@ptb.de

The readout of a qubit state in an ion trap architecture may be performed by observing the presence or absence of ion fluorescence. Typically, the fluorescence is analyzed by collecting the individual fluorescence photons in the ion trap and directing them out of the vacuum system using free-space optics to commercially available photon detectors [1]. This method is incompatible with the miniaturization, upscaling and cost reduction of ion trap chips required to increase the number of qubits in a trapped-ion quantum processor. One solution to this problem is to integrate the photon detectors directly into the read-out region of the ion trap. This has already been achieved by using a Superconducting Nanowire Single Photon Detector (SNSPD), which achieved a high average readout fidelity of the ion fluorescence photons [2-3]. It has also been shown that parallel readout fidelity with trap-integrated SNSPDs is affected by cross-talk (trapping rf potential) from ions in adjacent readout zones [2]. This can be improved by shielding the SNSPD from the trapping rf potential and by increasing the operating temperature of the SNSPD [3].

In this work, as a first step based on technology readily available in PTB's cleanroom facility, we pursue the use of niobium as a superconducting detector material for the SNSPD. Niobium has a bulk critical temperature of ~ 9 K, which is actually lower compared to other commonly used superconducting materials used in SNSPDs such as niobium nitride [4]. However, an advantage of using niobium is that we expect the intrinsic sensitivity to the fluorescence light below 500 nm to be one order of magnitude higher compared to wavelengths larger than 700 nm and two orders of magnitude for infrared [5]. This opens the prospect of intrinsically suppressing unwanted detections due to stray light at longer wavelengths or thermal background radiation by using an optimized bias current.

For this purpose, we have fabricated two main types of SNSPDs from sputtered 15 nm thick niobium films. The first type of these detectors (Figure 1.) consists of a meander structure where the lines of the meanders have a width of 120 nm and are separated by 80 nm. The length of the lines is 30 µm. The second type of detector (Figure 2.) is a "cheese" detector in which we have etched holes in an area of 30 µm x 30 µm. The holes have a diameter of 80 nm and are separated by 300 nm. This structure does not constitute a nanowire but a microwire with nanometer holes and we only refer to it as SNSPD for simplicity. Both detectors were made with the idea of having a large detection area and a well detectable electrical signal when switching from being super- to being normal conducting, which is important to efficiently detect fluorescence photons. Preliminary results from the first fabrication run showed that the critical temperature of the structures was ~4 K, which is well below the known critical temperature of bulk niobium ~9 K. We attributed this to the small thickness of the film and the presence of a Niobium oxide layer. To test the latter assumption, we made a second batch of detectors in which we passivated the niobium with a 2 nm layer of gold-palladium. With this passivation layer, the critical temperature increased to ~6 K, which is still well below the bulk niobium value. In the same fabrication run, we also fabricated single instead of meandered wires to control the process. The single wires showed an increased critical temperature of ~7.5 K compared to the meander structures (Figure 3.). Further investigation of the layers will allow us to understand why the critical temperature of the meander structures is lower than expected.

[1] J. E. Christensen et al., npj Quantum Information 6, 35 (2020)
[2] S. L. Todaro et al., Phys. Rev. Lett. 126, 010501 (2021)
[3] B. Hampel et al., arXiv:2302.01462v1 (2023)
[4] I. E. Zadeh et al., Appl. Phys. Lett. 118, 190502 (2021)
[5] Anthony Joseph Annunziata, "Single-Photon Detection, Kinetic Inductance, and Non-Equilibrium Dynamics in Niobium and Niobium Nitride Superconducting Nanowires," Yale University (2010).

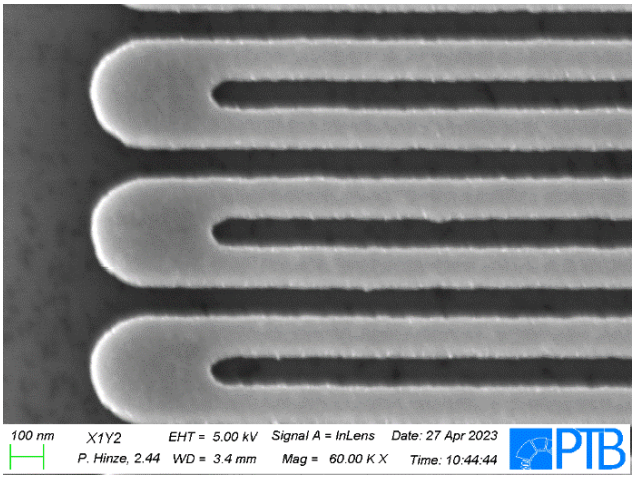

Figure 1. SEM picture of the meander type of SNSPD fabricated from a 15 nm thick sputtered niobium film. The width of the wires is targeted to be 120 nm and the separation is targeted to 80 nm.

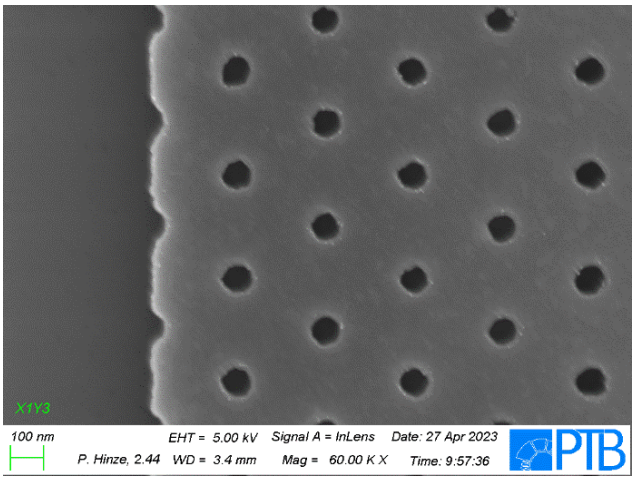

Figure 2. SEM picture of the “Cheese” type of SNSPD fabricated from a 15 nm thick sputtered niobium film. The holes have a targeted width of 80 nm and are separated by 120 nm.

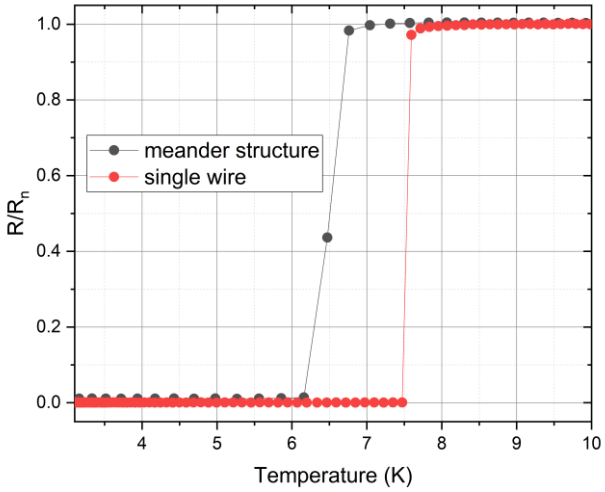

Figure 3. The measured resistance (normalized) as a function of the temperature obtained from the meander structure (black dots) and the single wire (red dots).

Poster Session1.1: Focus Track/Track1/Track3 - Papers

Recent Developments in Processing Large Area 2D Materials, Dielectrics, and Metals via CVD and ALD for Functional Applications

Nils Boysen [a], Rahel-Manuela Neubieser [a], Jan-Lucas Wree [b], David Zanders [b], Florian Zimmermann [c], Kai Oliver Brinkmann [c], Marvin Michel [a], Thomas Riedl [c], Anjana Devi [a,b]

[a] Fraunhofer IMS, 47057 Duisburg, Germany
[b] Inorganic Materials Chemistry, Ruhr University Bochum (RUB), 44801 Bochum, Germany
[c] Institute of Electronic Devices, University of Wuppertal, 42119 Wuppertal, Germany
e-mail: nils.boysen@ims.fraunhofer.de

Metal-organic chemical vapor deposition (MOCVD) and atomic layer deposition (ALD) are established in semiconductor manufacturing. Especially ALD, with its layer-by-layer fabrication capability reaching an unmatched conformality on intricate and high aspect-ratio structures, is gaining significant importance for the continuous downscaling of device dimensions. This not only requires advanced manufacturing tools and methods but also new and promising materials for semiconductor manufacturing. Among the different materials, high-k dielectrics, 2D materials or precious metals are in great demand to realize next-generation devices with complicated structures like gate all-around field effect transistors (GAA-FET). As both of the deposition methods are driven by chemical reactions of a precursor on the surface of the substrate in the vapor phase, a precise control of the precursor chemistry has to be ensured. Our joint research activities at RUB and IMS in collaboration with BUW has focused on the rational development of precursors and CVD/ALD processes for the realization of materials such as MoS_2, WS_2, Y_2O_3, Ag, Cu, Co among others, which are highly relevant for different micro- and optoelectronic applications.

The 2D materials MoS_2 and WS_2 have some unique opto-electronic properties which are especially prominent when monolayers of the materials are considered. In our recent studies, we have developed new Mo and W precursors with promising physico-chemical properties for the MOCVD of stoichiometric and crystalline MoS_2 and WS_2 thin films together with sulfur as the co-reactant at moderate process conditions on various substrates including glass.[1] The high quality of the WS_2 thin films obtained through a MOCVD process was confirmed by the promising functional properties of the layers. Not only could the films be used as a catalyst for the production of hydrogen but was also exploited for the selective sensing of NO_2, CO and NH_3 gas. For a scale-up of the processes to 200 mm wafers sizes, we developed a thermally driven ALD process with an amide-based Mo precursor at very low deposition temperature of 100 °C (Figure 1) on undoped silicate glass, thinned glass and Al_2O_3.[2] This not only enables the large-area deposition of MoS_2 on flexible substrates but can enable the fabrication of gas sensor structures in the future. For Y_2O_3, the new all-nitrogen based precursor chemistries enabled ALD in a wider deposition temperature range compared to established precursors and processes due to a significantly enhanced volatility of the precursor. The films were of high quality (Figure 2) and it was possible to alter the properties of the films employing molecularly engineered Y precursors.[3] In another important field, we focused on the development of Cu and Ag precursors for ALD applications.[4] Especially for next-generation solar cells, such as perovskite-based cells, conductive and at the same time transparent Ag films are needed which can be applied by highly scalable and atmospheric methods such as spatial ALD (SALD). Highly reactive and at the same time thermally stable precursors are still only scarcely available. In our recent studies, we investigated Cu and Ag precursors based on carbenes that are specifically tailored to provide a high thermal stability, while still enabling a high reactivity of the complexes. These new precursors were able to enable better-performing spatial ALD processes in terms of very low deposition temperatures (60 °C) and high growth rates. These features enabled the application of the SALD Ag films in organic solar cells as an electrode material for the first time (Figure 3). The ALD of transition metals like Co at low temperatures via thermal ALD is a challenge and recently for the first time we reported a new process for Co metal using alkyl-based reducing agents which delivered Co films with low resistivities.[5]

The representative contribution highlights the key findings of our research activities at RUB and IMS over the last years in the field of MOCVD and ALD. Together with this summary we provide valuable pathways on how to further advance the field to enable cutting-edge micro- and optoelectronic applications in the future.

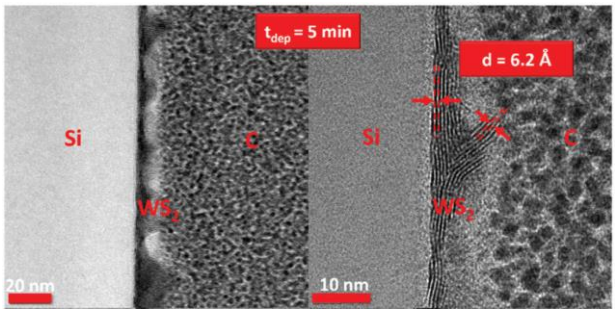

Figure 1. TEM images of MOCVD WS_2 films deposited on Si at a deposition temperature of 600 °C. Reproduced from Ref.[1b] with permission from the Royal Society of Chemistry.

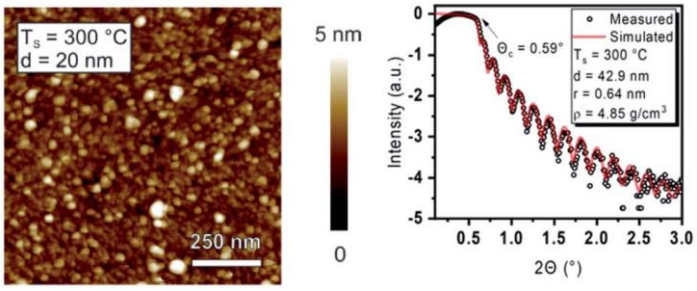

Figure 2. (left) AFM image and (right) XRR of Y_2O_3 a film deposited on Si at 300 °C. Reproduced from Ref.[3] with permission from the Royal Society of Chemistry.

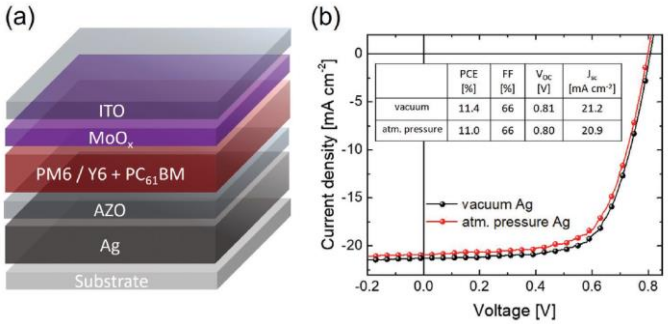

Figure 3. a) Image of the film stack used for the fabrication of the solar cell. The Ag layer has been deposited at 100 °C with the new carbene-based precursor. b) Characteristics of the solar cell.[4c]

[1] a) J.-L. Wree, E. Ciftyurek, D. Zanders, N. Boysen, A. Kostka, D. Rogalla, M. Kasischke, A. Ostendorf, K. Schierbaum, A. Devi, *Dalton Trans.* **2020**, *49*, 13462; b) J.-L. Wree, J.-P. Glauber, D. Öhl, A. Niesen, A. Kostka, D. Rogalla, W. Schuhmann, A. Devi, *J. Mater. Chem. C* **2021**, *9*, 10254.

[2] R.-M. Neubieser, J.-L. Wree, J. Jagosz, M. Becher, A. Ostendorf, A. Devi, C. Bock, M. Michel, A. Grabmaier, *Micro and Nano Engineering* **2022**, *15*, 100126.

[3] N. Boysen, D. Zanders, T. Berning, S. M. J. Beer, D. Rogalla, C. Bock, A. Devi, *RSC Adv.* **2021**, *11*, 2565.

[4] a) N. Boysen, T. Hasselmann, S. Karle, D. Rogalla, D. Theirich, M. Winter, T. Riedl, A. Devi, *Angew. Chem. Int. Ed.* **2018**, *57*, 16224; b) N. Boysen, B. Misimi, A. Muriqi, J.-L. Wree, T. Hasselmann, D. Rogalla, T. Haeger, D. Theirich, M. Nolan, T. Riedl et al., *Chem. Commun.* **2020**, *56*, 13752; c) T. Hasselmann, B. Misimi, N. Boysen, D. Zanders, J.-L. Wree, D. Rogalla, T. Haeger, F. Zimmermann, K. O. Brinkmann, S. Schädler et al., *Adv. Mater. Technol.* **2023**, *8*, 2200796.

[5] D. Zanders, J. Liu, J. Obenlüneschloß, C. Bock, D. Rogalla, L. Mai, M. Nolan, S. T. Barry, A. Devi, *Chem. Mater.* **2021**, 33, 5045.

Positioning accuracy of the direct laser lithography for a large-scale Fresnel Zone Plate

Viacheslav Vlasenko [a], Kahraman Keskinbora [a], Leonid Litvin [a], Michael Kahl [a], Jacco Houter [b]
[a] Raith GmbH, Dortmund, 44263, Germany
[b] Raith Laser Systems BV, St. Oedenrode, 5491 DC, The Netherlands
e-mail: viacheslav.vlasenko@raith.de

Large scale Fresnel Zone Plates (FZP) can be used to interferometrically measure the aspherical lens or mirror aberrations. In such measurements, it is crucial to manufacture the FZP which produces a precise spherical wavefront. Therefore, the positioning accuracy of the direct laser writer should satisfy a very strict tolerance. In this work a 100-mm-diameter FZP was fabricated on a glass substrate with maskless laser lithography technique and measured with a dedicated SEM based metrology tool. The production was carried out on a temperature-stabilized Raith PICOMASTER 200 direct laser writer tool. Extensive metrology results have proven that aspherical deviation of the FZP prepared with the laser beam writer was in the range of 100 nm across 100 mm distance.

Fresnel zone plates as diffractive optical devices are nowadays widely used in X-ray optics, holograms, photonics, and other fields of modern optics and photonics. Therefore, a broad and continuously evolving manufacturing ecosystem has been formed to satisfy the needs of various intended end results. Commonly used methods are electron- [1] or ion- [2] beam lithography, photolithography or even some modern femto-second laser techniques [3]. In this work, we have investigated the capabilities of maskless laser beam lithography (LBL) technique which has some advantages compared to aforementioned techniques as it is: i) more flexible compared to mask-based photolithography, ii) has a higher throughput than electron- and ion-beam lithography, iii) capable to deliver a sub-500 nm resolution and crucially, iv) without introducing stitching errors to the final device.

An initial experiment to write the complete FZP pattern using the Raith PICOMASTER 200 direct laser writer was carried out to obtain the processing and exposure parameters and to get a realistic view of the writing time. Figure 1 shows the results of that exposure with a width of the lines to be 527 nm and spaces 900 nm. On an image of the central zone and overall photo of the FZP no stitching errors are visible. Therefore, selected process parameters were considered to be satisfactory for further experiments as they provide required submicron resolution and intended duty cycle.

For positioning accuracy tests, the temperature of the lithography system including calibration plate and later the FZP substrate was stabilized to limit thermal drifts. Then, the tool mechanics was calibrated using a calibration standard. For the test itself, three vertical stripes, the first, middle and the last 4 % of the width of the zone plate pattern were written successively using the parameters obtained on the first stage. An alignment fiducial was introduced to mark the geometrical center of the pattern and to act as an anchor point for the metrology measurements. The glass plate was metallized with a nickel alloy using sputter coating.

For SEM metrology Raith CHIPSCANNER HS tool was used to make series of 10 measurements from the center of the fiducial mark to the center of the outer zones (Figure 2) in right, left, bottom and top directions. To determine the positioning accuracy the difference between the measured distance and the nominal distance was considered. The measurements were repeated after rotating the substrate by 180 degrees. The results have shown a very narrow spread around the mean value which confirms the high precision of the measurements. A summary of all the measurements is given in Figure 3. The most important value for the final application purpose was the difference of the measured mean values of horizontal and vertical diameter of the FZP which was less than 100 nm over its 100 mm size.

Considering that accuracy of the used metrological instrument was 100 nm, and that the calibration plate had the same specified accuracy of a 100 nm, we conclude that the selected LBL technique provides precision enough for patterning of FZP with desired aspherical tolerance of less than 100 nm over the whole 100 mm size of FZP. Further optical measurements on manufactured FZP are scheduled to prove this conclusion.

References

[1] J. Vila-Comamala; S. Gorelick *et all*, Opt. Express 2011, 19, 175–184.
[2] K Keskinbora, UT Sanli, M Baluktsian *et all*, Beilstein J. Nanotechnol. 2018, 9, 2049–2056.
[3] T. Jwad, S. Deng, H. Butt, S. Dimov, J. Micro Nano-Manuf. Mar 2018, 6(1): 011001.

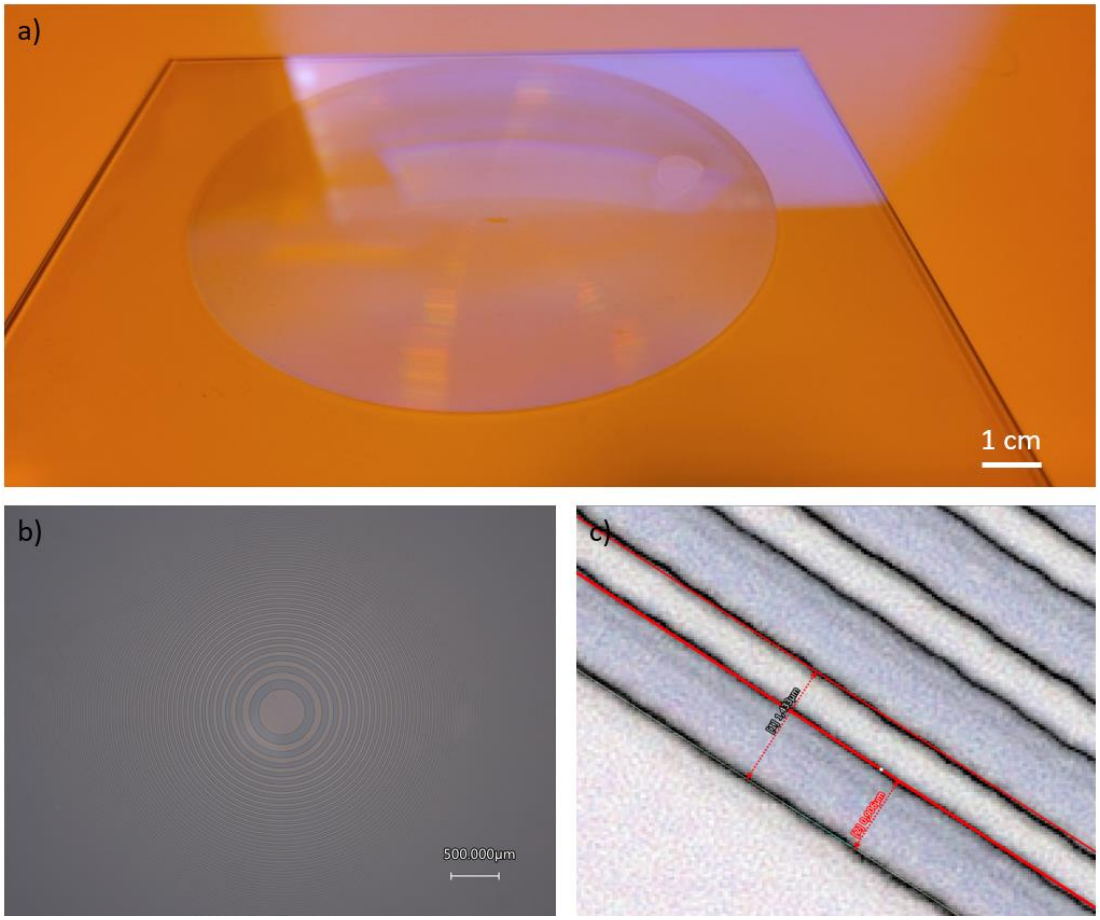

Figure 1. The images show a) the whole 100 mm wide FZP on the glass plate, b) the inner zones without any visible stitching errors, and c) a confocal image of the outermost zones in the bottom-left direction.

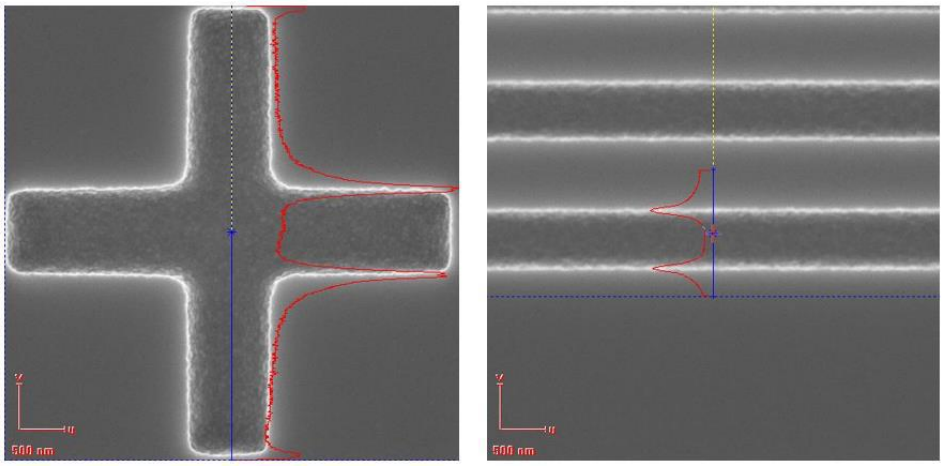

Figure 2. Left: Central marker. Right: Outermost zone in the bottom direction

Pattern Orientation	Center-Right (nm) CR	Center-Left (nm) CL	Center-Top (nm) CT	Center-Bottom (nm) CB	Diameter horizontal (nm) CR+CL	Diameter vertical (nm) CT+CB	Difference between vert. and hor. axes (nm)
Normal	316	82	403	95	398	498	100
Rotated by 180	145	281	130	391	426	521	95

Figure 3. Summary table of the measurement results. All values are the differences between the nominal and the measured value.

Realization of Highly Uniform Surface Functionalization and Applications to Organic Transistors

Ming Chen [ab], Xing Cheng *[ab]

[a] Department of Department of Materials Science and Engineering
Southern University of Science and Technology
Shenzhen, Guangdong 518055, China
[b] Shenzhen Key Laboratory for Nanoimprint Technology
Southern University of Science and Technology
Shenzhen, Guangdong 518055, China

e-mail: chengx@sustech.edu.cn

Abstract Text

The surface functionalization by self-assembled monolayers (SAMs) allows well control over the surface /interface physical properties and is currently employed in diverse applications, including nanoimprint lithography (NIL) [1], microelectromechanical systems (MEMS) [2], etc. Particularly, the surface functionalization is utilized during the fabrication flow of organic thin-film transistors (OTFTs) to reduce the dielectric to semiconductor interfacial trap states [3], improve the crystallinity of organic semiconductor thin films and modulate the threshold voltages [4-5]. Consequently, high-quality surface functionalization is greatly desired. However, the growth of SAMs is suffering from morphological defects due to the complexity of the fabrication processes, as observed by various groups [6-8]. The current work aims to optimize the SAM growth conditions, reduce the morphological defects and ultimately obtain the morphological defect-free surface functionalization.

Herein, the conventional vapor phase approach for SAM deposition is ameliorated and systematically investigated with 1H,1H,2H,2H-perfluorodecyltrichlorosilane (FDTS) as the SAM material. It is found that the utilization of addional glass petri dish could effectivelty reduce the contamination from the recation vessel and confine the FDTS vapor in localized area, finally realizing the morpholocal defect-free surface treatment (Fig. 1). The depostion parameters are determined based on the evaluation of saturated vapor pressure. Two morphological defects are indentified by varying the deposion temperature (T_D) and pressure (P_D), incluing the island structure and aggragation. The defects are eliminated after the optimization of the deposition variables. Particularly, deposition temperature of no less than 120 °C and deposition pressure of up to 0.02 bar are preferred for the highly uniform FDTS growth (Fig. 2). The successful depostion of FDTS is confirmed by the x-ray photoelectron spectroscopy and the monolayer feature is verified by the ellipsometer with the thickness of 1.31 nm. The FDTS growth could be deposited onto a 4-inch wafer, compatible with mass production of organic electronics. It is facinated that the growth protocal is universal for other frequently used SAMs, e.g., octadecyltrichlorosilane (OTS) and phenyltrichlorosilane (PTS). Finally, the surface functionalization is employed to the OTFTs. The device fabricated from defect-free SAMs shows a hole mobility of 1.79 $cm^2 V^{-1} s^{-1}$ which is 2.06 times to the devices with defective SAMs (Fig. 3). The current work imparts a general approach for morphological defect-free surface functionalization and is believed to provide valuable contribution to diverse engineering fields [9].

References

[1] L. J. Guo, Adv. Mater. 19 (2007) 495-513.
[2] F. W. DelRio et al., Nat. Mater. 4 (2005) 629-634.
[3] Z. Zhang et al., Adv. Funct. Mater. 25 (2015) 6122-6121.
[4] F. Zhang et al., Langmuir 34 (2018) 1109-1122.
[5] S. Kobayashi et al., Nat. Mater. 3 (2004) 317-322.
[6] B. C. Bunder et al., Langmuir 16 (2000) 7742-7751.
[7] X. Cao et al., Nanoscale 10 (2018) 378-385.
[8] W. Zhou et al., Appl. Surf. Sci. 155 (2008) 2885-2889.
[9] M. Chen et al., Adv. Mater. Interfaces 15 (2023) 2202453.

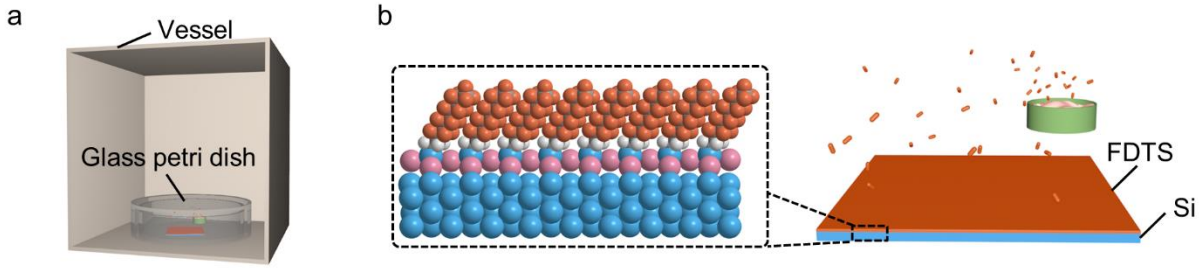

Figure 1. (a) The schematic diagram of the surface functionalization of FDTS. (b) The FDTS deposition inside the glass petri dish.

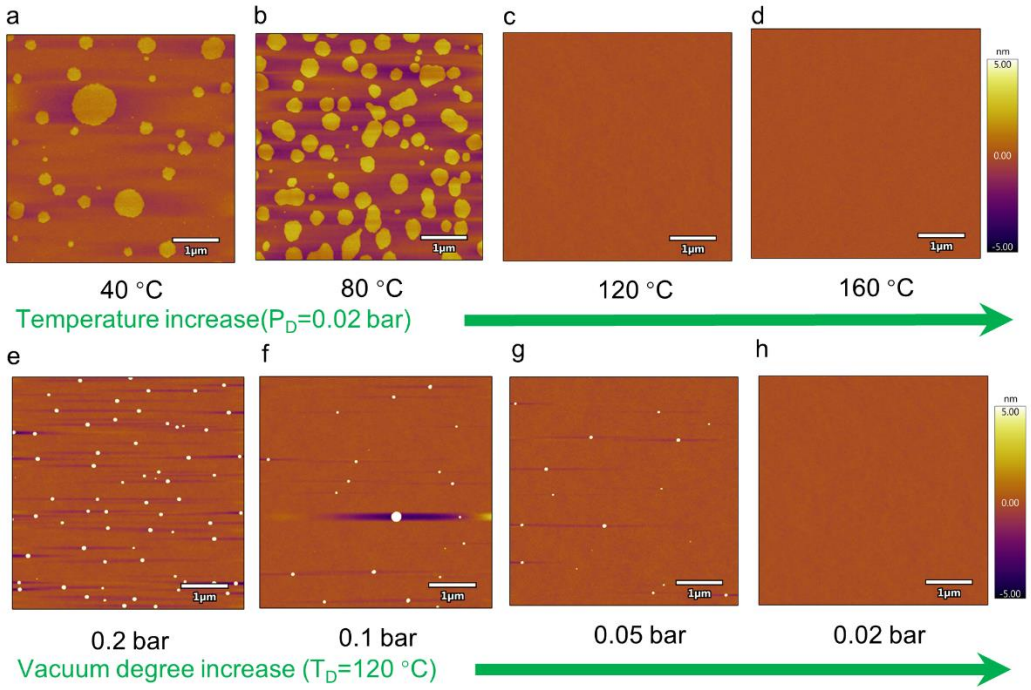

Figure 2. The atomic force microscopy images of FDTS by varying the deposition temperatures (a-d) and deposition pressures (e-h).

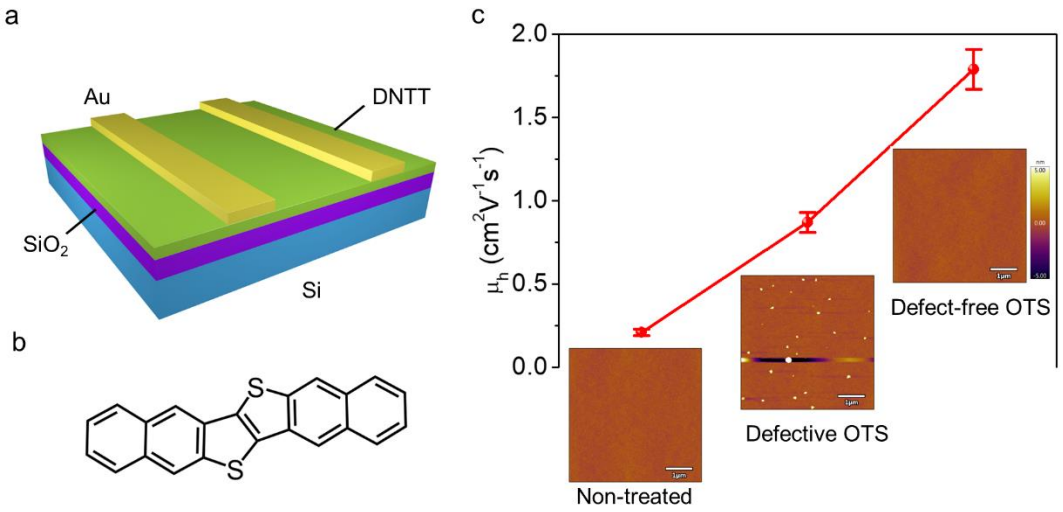

Figure 3. The application of high-quality surface functionalization to organic transistors. (a) The device structure. (b) The molecular structure of organic semiconductor. (c) The hole mobility of the transistor devices with different organic-dielectric interfaces.

Wafer scale fabrication of pyrolytic carbon sub-100 nm nanogap electrodes for electrochemistry by etching of insulating oxides

Nicolai Støvring [a], Jenny Emnéus [b], Arto Heiskanen [b], Stephan Sylvest Keller [a]

[a] National Centre for Nano Fabrication and Characterization, Kgs. Lyngby, 2800, Denmark
[b] Department of Biotechnology and Biomedicine, Kgs. Lyngby, 2800, Denmark
e-mail: nicosto@dtu.dk

Electrically separated electrodes with submicron/nanometer sized gaps are attractive in electrochemical sensing applications. Here, small gaps can induce redox cycling, a mechanism in which the same molecule of target analyte is reduced/oxidized multiple times amplifying the electrochemical signal many-fold [1]. Pyrolytic carbon presents itself as a desirable material in electrochemistry offering beneficial properties, such as being mechanically stable, chemically inert [2], and highly tailorable in terms of surface chemistry [3]
So far, nanometer gaps with pyrolytic carbon have only been achieved on single devices with processes that are not compatible with wafer scale cleanroom fabrication [4]. In this work, we show the current development of a process for wafer scale fabrication of sub-100 nm nanogap electrodes using a stacked layer approach with two pyrolytic carbon layers separated by insulating materials. Here, major challenges present themselves in terms of layer compatibility and stability during pyrolysis and etching.

To ensure adhesion of the pyrolytic carbon structures to the substrate during chemical and thermal treatment, adhesion structures were fabricated by patterning polycrystalline silicon and silicon dioxide for mechanical anchoring as shown in Figure 1a. Then, the first layer of pyrolytic carbon was deposited by defining a pattern in SU-8 followed by pyrolysis it at 900°C, resulting in an electrode with a thickness of 2.2 µm (Figure 1a). As a preliminary test, three insulating layers were deposited on the pyrolytic carbon and subjected to various treatments: 1) Al_2O_3 deposited using atomic layer deposition with 1000 cycles of 0.1 s TMA followed by 0.1 s H_2O (Picosun thermal ALD model R200); 2) SiO_2 deposited using reactive magnetron sputtering (KJLC PRO Line PVD75 thin film deposition cluster system) with a power of 140 W, pressure of 3 mTorr, Ar flow of 50 sccm and O_2 flow of 20 sccm; 3) SiN using reactive magnetron sputtering with a power of 120 W, pressure of 3 mTorr, Ar flow of 50 sccm and N_2 flow of 20 sccm (Figure 1b). A layer of 15 µm negative photoresist mr-DWL 5 was then patterned on top of this stack to both serve as the etch mask for the insulating layer and as second electrode after pyrolysis (Figure 1c). The wafers were then pyrolyzed at 880°C to achieve the second carbon layer. The amount of cracking and delamination between the three layers were determined using optical microscopy. SiO_2 and Al_2O_3 were determined to be the best candidates in terms of processing although they exhibited significant cracking and delamination. The pyrolysis also reduces the thickness of the Al_2O_3 layer to ~90 nm reducing the final gap, while the oxide thickness remained at ~95 nm. After pyrolysis, the wafers were subjected to a short descumming plasma process at 1000 W with N_2 80 mL/min and O_2 20 mL/min for 90 s. Finally, the wafers were subjected to a wet etch in 12.5% w/w Buffered Hydrofluoric Acid (BHF), for 2-5 minutes depending on the material and processing stage, to open holes in the oxide films (Figure 1d). After etching, some of the second layer of photoresist/pyrolytic carbon was found to delaminate from the first layer of the carbon and oxide.
To ensure successful stacking, several changes were implemented: The first pyrolysis temperature was increased to 1050°C and the second to 900°C to reduce the material shrinkage of the first layer during the second pyrolysis. In the oxide deposition step, an annealing of the carbon for 30 minutes before deposition of the oxide was implemented, resulting in formation of layers without any cracking or delamination after the second pyrolysis step. The resulting stacks are shown in Figure 2, while Figure 3 shows the result after both pyrolysis and wet etching for the different oxides.
By further tailoring the etching process as well as the design of the adhesion structures, we aim to achieve a significant increase in the adhesion of the pyrolytic carbon electrodes after etching. We are currently finalizing the process to optimize the yield by reducing delamination and will perform electrochemical redox cycling experiments in the near future.

[1] M. Odijk et al, *Electroanalysis*, vol. 20, no. 5, pp. 463–468, 2008.
[2] K. Kinoshita, *Carbon : electrochemical and physicochemical properties*. (1988, Chichester, New York, Brisbane, Toronto) .
[3] G. Pankratova et al, *Electrochim. Acta*, vol. 410, p. 139987, 2022.
[4] A. Salazar et al, *Microsystems Nanoeng.*, vol. 6, no. 1, 2020.

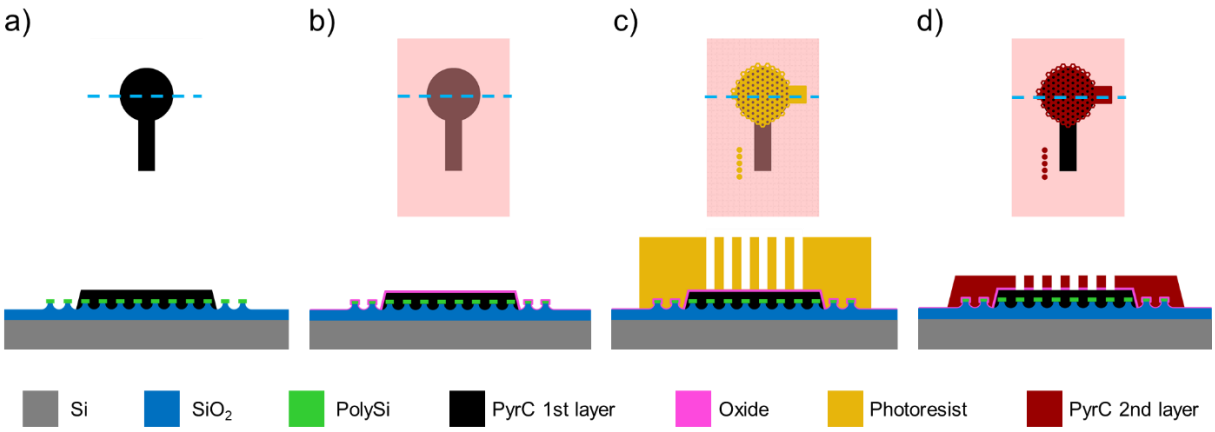

Figure 1. Process flow showing top and side view, where the side view is taken along the dashed line. 1a) First pyrolytic carbon layer on adhesion structure. b) Deposition of insulating oxide layer. c) Photolithography d) Pyrolysis of the photoresist and wet etching of the insulating oxide layer to create nanogaps.

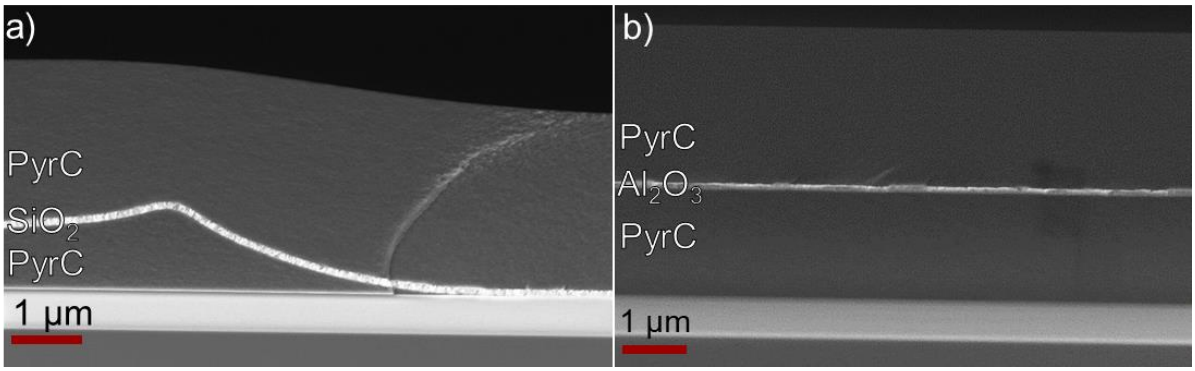

Figure 2. Cross Sections of the stack of layers for a) Pyrolytic Carbon/SiO_2/Pyrolytic Carbon with ~95 nm SiO_2 layer separating the carbon layers and b) Pyrolytic Carbon/ Al_2O_3/Pyrolytic Carbon with ~90 nm Al_2O_3 layer separating the carbon layers showing the successful stacking of the layer

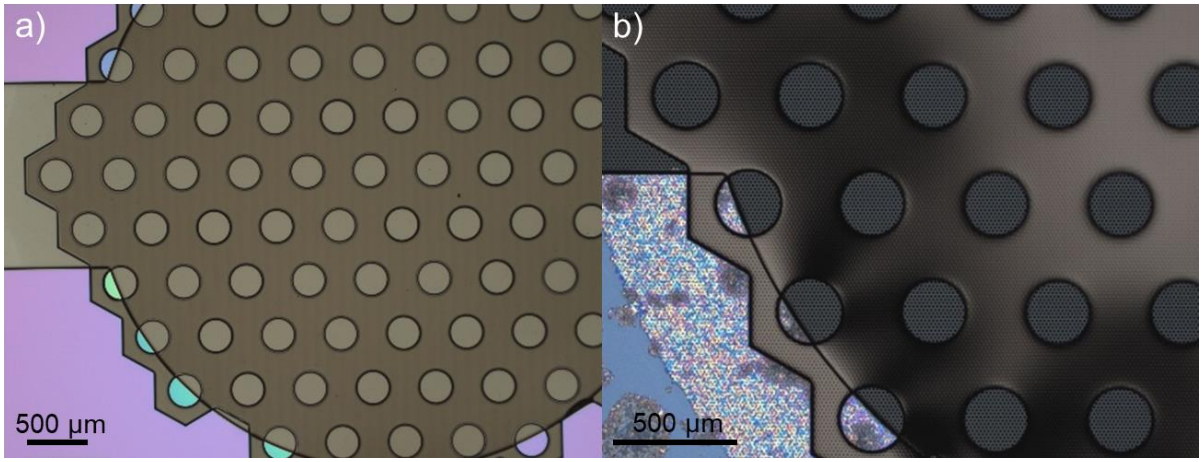

Figure 3. Optical micrographs of a) Pyrolytic Carbon/SiO_2/Pyrolytic Carbon and b) Pyrolytic Carbon/ Al_2O_3/Pyrolytic Carbon after BHF etching and pyrolysis.

Patterning of Novolac-based negative resist using EBL and its performance as etch mask for DRIE of silicon

Rahul Singh[a], Christian Vinther Bertelsen[a], Maria Dimaki[a], Winnie Edith Svendsen[a]

DTU Bioengineering, Danmarks Tekniske Universitet (DTU), 2800 Kongens Lyngby, Denmark

e-mail: cvbe@dtu.dk

Electron-beam lithography (EBL) is a pivotal tool in fabrication of nanoscale patterns which are widely used in the field of semiconductor devices and photonics [1]. Although both positive and negative tone resists are available for EBL, in certain cases, negative resists provide critical advantages over positive resists, for instance, reduction in writing time and high selectivity etch mask [2]. However, before using the resist with a particular EBL exposure system, a dose response optimization is necessary [3]. For instance, experimental results obtained from the dose test on AR-N 7520 negative resist were used to train an artificial neural network to predict the resist profile [4]. Furthermore, in a recent study, four negative EBL resists were compared for fabrication of large area gratings [5]. Results showed that AR-N 7520 and ma-N 2410 had comparable line edge roughness and no swelling was observed for both resists. An additional advantage of AR-N 7520 is that it acts as negative resists for both e-beam and i-line UV (365 nm) and hence allows mix and match processes where UV lithography is used for larger features and EBL for high resolution features. Such hybrid processes have the potential to reduce writing times and processing steps significantly [6]. Despite several works performed on AR-N 7520 resist, most of them are based on 30 kV exposure tools and lack robust study on efficacy of this resist as dry etch mask, particularly for deep reactive ion etching (DRIE) of silicon.

Therefore, in this work, firstly, an e-beam dose test is performed on AR-N 7520.17 (new) which is Novolac-based negative e-beam resist, using 100 kV EBL exposure system (JEOL JBX-9500FSZ). Secondly, DRIE of silicon is done using different AR-N 7520.17 patterns to study its performance as etch mask. The process steps, as shown in Figure 1, involve spin coating of 400 nm thick layer of the negative resist at 4000 rpm followed by soft bake at 85 °C for 60 seconds. Next, e-beam exposure is done at 100 kV and current value of 2 nA with exposure dose varying between 100-300 $\mu C/cm^2$. The resist is then developed in AZ 726MIF (2.38% TMAH) developer for 60 seconds and hard baked for 60 seconds at 85 °C. After the development and hard bake, DRIE of silicon is conducted for 120 seconds with 1000 W coil power and 20 W platen power. The flow rates of passivation gas (C_4H_8) and etch gas (SF_6) are 71 sccm and 44 sccm respectively. The resulting features after DRIE are 500-2000 nm tall silicon nanopillars of varying diameter and pitch. In Figure 2a, an SEM image of the resist pattern (dose 300 $\mu C/cm^2$) after development is shown where diameter of the individual pattern is 160 nm and gap 100 nm. The same pattern is then etched to obtain an array of silicon nanopillars as illustrated in Figure 2b. Similarly, even smaller features of diameter 90 nm are fabricated (Figure 3a) and then etched resulting in silicon nanopillars of same diameter (Figure 3b). The results show that, for both 160 nm and 90 nm diameter features, resist pattern as well as silicon nanopillars have vertical side walls. Furthermore, no significant damage to the resist layer is observed after the DRIE step. Similarly, dose test studies are performed on 200 nm thick AR-N 7520.11 resist and silicon dry etch selectivity for both resists is compared.

[1] C. Constancias et al., Electron Beam Lithography (John Wiley and Sons, 2013) 101–182.
[2] T. Borzenko et al., Microelectron. Eng. 86 (2009) 726–729.
[3] I. Kostic et al., in: J. Phys.: Conf. Ser. (IOP Publishing, 2022) 2240.
[4] E. Koleva et al., in: J. Phys.: Conf. Ser. (IOP Publishing, 2023) 2443.
[5] R. Andok et al., in: J. Phys.: Conf. Ser. (IOP Publishing, 2023) 2443.
[6] L.V. Jenni, L. Kumar, C. Hierold, Microelectron. Eng. 209 (2019) 10–15.

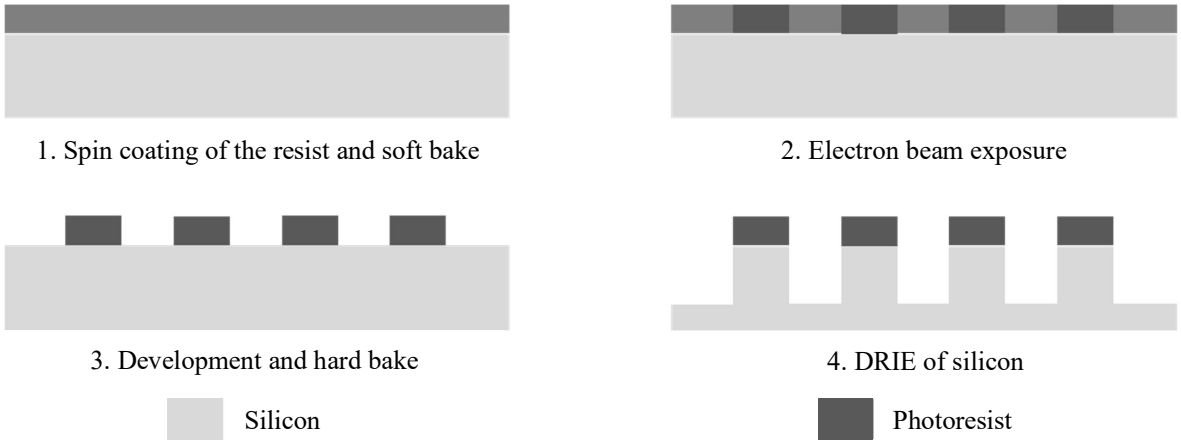

Figure 1. Process flow for patterning of the negative e-beam resist for DRIE of silicon.

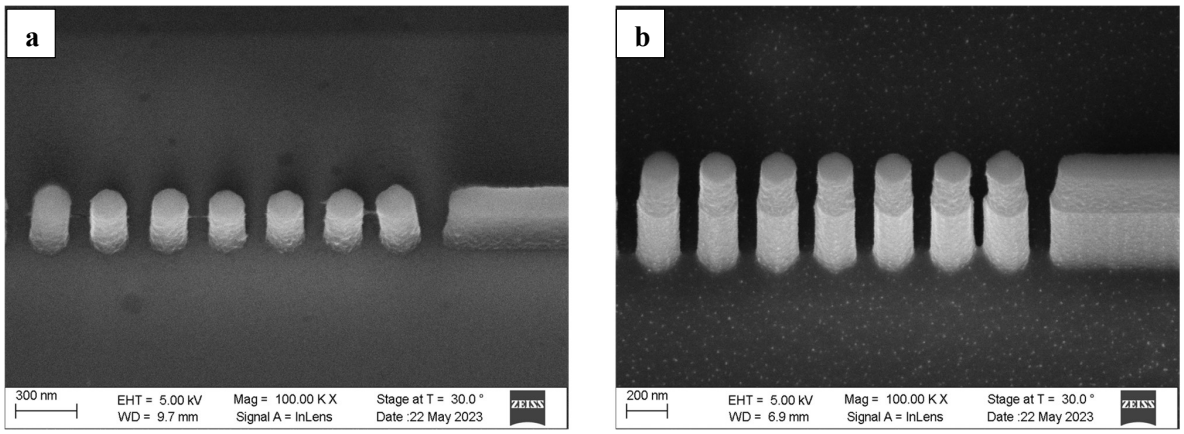

Figure 2. SEM images of 160 nm diameter features: a) resist structures after development; b) resist structures and etched silicon after DRIE.

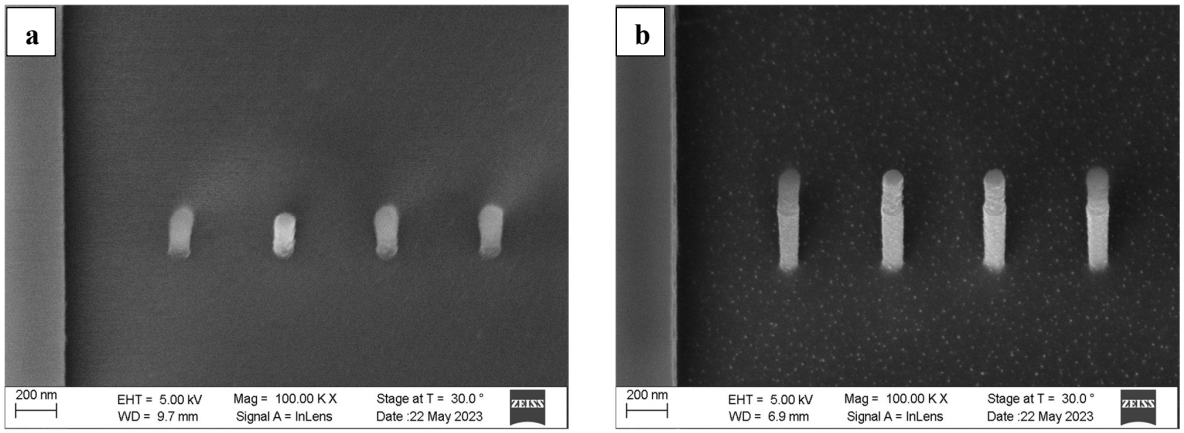

Figure 3. SEM images of 90 nm diameter features: a) resist structures after development; b) resist structures and etched silicon after DRIE.

Ion incidence angle-dependent pattern formation on AZ® 4562 photoresist by (reactive) ion beam etching

Tom Rüdiger [a], Martin Mitzschke [a], Carsten Bundesmann [a], Andrea Prager [a], Ying Liu [b], Bernd Abel [c], Agnes Schulze [a], Frank Frost [a]

[a] Leibniz Institute of Surface Engineering (IOM), Leipzig, 04318, Germany
[b] National Synchrotron Radiation Laboratory, University of Science and Technology of China, Hefei, 230029, P.R. China
[c] University of Leipzig, Faculty of Chemistry and Mineralogy, Leipzig, 04103, Germany
e-mail: tom.ruediger@iom-leipzig.de

Reactive ion beam etching (RIBE) is a key technology in our modern world. This versatile method can alter the surface morphology, the roughness and the chemical composition of the surface/near-surface area of various materials, e.g., metals, semiconductors and polymers [1]. Applications like semiconductor lithography, telescopes, high-performance mirrors as well as gratings for lasers are produced by RIBE or uses parts that are produced with this technique. This technology enables the smoothing of a surface or the creation of precise patterns at the surface [1,2].
A basic concept to manufacture a defined pattern is a pattern transfer utilizing photoresist. It is possible to structure the photoresist and transfer it in the substrate (e.g., SiO_2). Depending on the selectivity of the etch process the pattern can be stretched, compressed, or transferred unchanged. In order to achieve high performance of the manufactured optics it is necessary that there are no defects at the surface [3]. These defects could be nanopatterns like nanoholes, nanodots, ripples, triangular features, protrusions, or facets and were described previously [1,3,4].
Many studies investigated nanopatterns at inorganic surfaces and developed models that can explain their formation [4-6]. However, these nanopatterns are also observed at the surface of polymers and it is questionable if the existing models can deal with the complex issue of a non-monoatomic target and potentially the combination with a reactive ion beam, which causes fragmentation of the inserted reactive species.
In the presented work, nanopatterning on a commercially available photoresist with a wide range of ion incidence angles (0° - 75°) was investigated. Furthermore, the fluence (erosion time) and the etch gas were varied. The utilization of atomic force microscopy and scanning electron microscopy shows the emergence of nanopatterns (nanoholes, ripples, triangular features, protrusions, facets). The emergence of those nanopatterns and their shape depends on a wide range of ion incidence angles (see **Figure 1**) as well as the fluence (see **Figure 2**). The formed nanopatterns resembles those known from inorganic materials and leads to the assumption that local redeposition, surface viscous flow and dispersion plays an important role for the pattern formation on polymer surfaces. Spectroscopic ellipsometry shows that the thickness of the surface layer depends on the ion incidence angle but not on the fluence. In addition, it is possible to detect incidence angle- and fluence-depending trends in the chemical composition of the surface by means of X-ray photoelectron spectroscopy.

References:

[1] T. Rüdiger *et* al., Applied Surface Science 574 (2022) 151682.
[2] E. Rohkamm *et* al., Journal of Applied Physics 129 (2021) 223305.
[3] G. S. Oehrlein *et* al., Journal of Vacuum Science & Technology B 29 (2011) 010801.
[4] K. M. Loew *et* al., Physical Review E 100 (2019) 12801.
[5] M. Castro *et* al., Physical Review Letters 94 (2005) 16102.
[6] A. Moreno-Barrado *et* al., Physical Review B 91 (2015) 155303

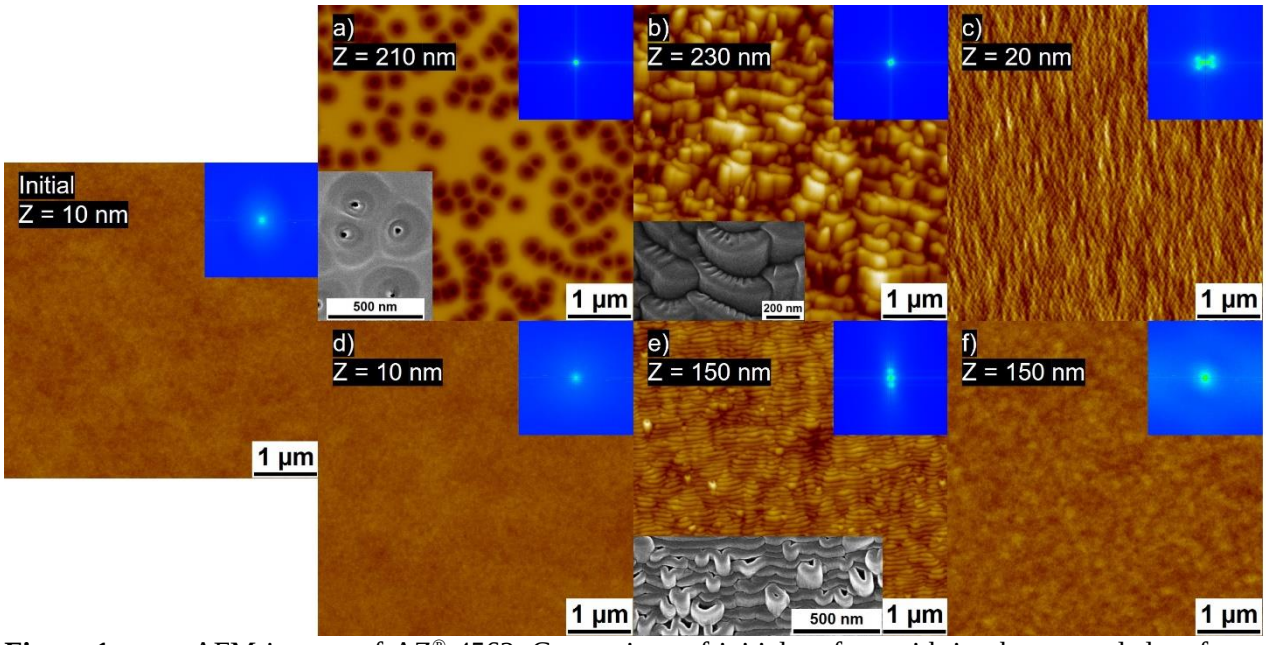

Figure 1: AFM images of AZ® 4562. Comparison of initial surface with ion beam eroded surfaces at various ion incidence angles: upper row: Ar (4 sccm 30 min): a) 0°, b) 55°, c) 70° lower row: O_2/CHF_3 (2 sccm each, 30 min): d) 0°, e) 55°, f) 70°. The insets show the corresponding FFT as well as SEM-images. The direction of the ion beam is from top to bottom.

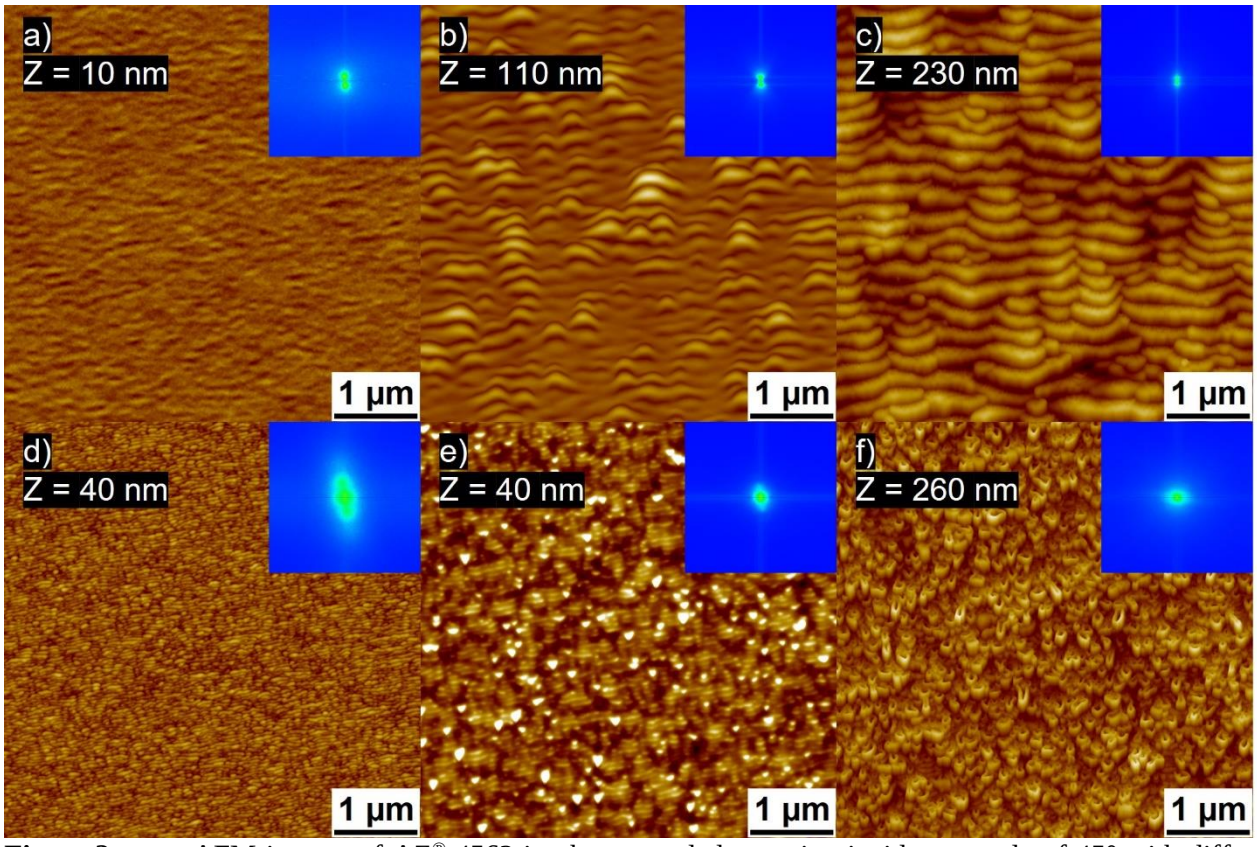

Figure 2: AFM images of AZ® 4562 ion beam eroded at an ion incidence angle of 45° with different etch gas and various erosion time. Upper row show surfaces eroded with Ar (4 sccm) for a) 10 min, b) 30 min and c) 60 min. The lower row show surfaces eroded with O_2/CHF_3 (2 sccm each) for d) 10 min, e) 30 min and f) 60 min. The corresponding FFT are shown as insets. The direction of the ion beam was top to bottom.

Selective ion-assisted nanostructuring process of silicon devices

A. Cian [a], E. Scattolo [a], M. Crivellari [a], J Llobet [bc], F. Pérez-Murano [b], L. Ferrario [a], D. Giubertoni [a]

[a] Sensors and Devices Center, Bruno Kessler Foundation, Trento, 38123, Italy
[b] Institute of Microelectronics of Barcelona (IMB-CNM CSIC), Bellaterra, 08193, Catalonia, Spain
[c] Alba CELLS Synchrotron, Cerdanyola, 08290, Catalonia, Spain
e-mail: acian@fbk.eu

In the latest years, it has been demonstrated that the implantation of specific ions can be used for controlled mask-less patterning of silicon substrates [1, 2]. This method can be easily implemented for the fabrication of elements such as silicon nanowires (SiNWs) mechanical resonators [3] and single-hole transistors [4] through the implantation of Gallium ions. This nanostructuring process relies on the focused ion beam implantation, followed by selective etching process in a solution.

In this work, we studied the benefits of employing a different species of ions in place of Ga+ FIB. We report the results obtained using a FIB column equipped with liquid metal alloy ion source (LMAIS), in particular with the focus on the impact of Au+ ions. We demonstrated that the implantation of Au+ in Si can replicate the variation in the etching rate of silicon in tetramethylammonium hydroxide (TMAH) solution. Ion fluences in the range of 1e15 – 1e17 ions/cm^2 are enough to dope the silicon substrate promoting the irradiated areas to act as a mask for the pattern transfer without a relevant sputtering effect.
Figures 1a and 1b show the SRIM expected depth profiles of Au in Si with different ion fluences for 35 and 70 keV irradiation energies, considering not only the implantation of Au ions but also the induced sputtering. These Monte Carlo simulations state that the substrates are affected by implantation within a depth of 20 nm approximately for 35 keV ion and 40 nm for 70 keV ions (see Figs 1). Scanning electron microscope imagines show that fluences lower than the saturation fluence (8.0e16 ions/cm^2) are enough to enable the masking effect of the irradiated areas. As it can be seen from the side view of two piled wires (see Fig 2b), it is possible to obtain suspended structures with just a fluence of 1e15 ions/cm^2.

Supported by the simulations and taking advantage of this behavior comparable to gallium-assisted etching, we have fabricated suspended silicon features stressing geometrical parameters such as minimum thickness, largest length of suspended elements and exploring complex layouts (see Figs 2).
The fine tuning of few beam parameters such as energy, fluence and writing strategy, allows to obtain suspended structures with critical dimensions (up to 35 nm large, 8.2 μm long and 16 nm thick) and with a plethora of possibilities in terms of layout (from SiNWs to hexagonal arrays).

The equivalent structures obtained by Ga+ implantation, has been proved to suffer from high resistance for electrical transduction due to amorphization of silicon and the incorporation of gallium within the irradiated volume [1]. As a result, these doped suspended structures doped have very low electrical and thermal conductivity [4]. However, the consequential annealing has been proved to induce the creation of nanocrystalline grain structures and improve the electrical conductivity. On going experiments (see Figs 3) are investigating the effects of high temperature treatments in a controlled environment in terms of gold concentration and of changes in the electrical properties of the implanted regions.

This work shows the versatility of this technological platform and sets the bases for using these devices for gas and bio-sensing with specific geometries and functionalization of the suspended structures.

[1] J. Brugger et al, Microelectronic Engineering, 35, (1997) 401-404
[2] B. Schmidt et al, Sens. Actuators Phys. 61, (1997) 369–373
[3] J Llobet et al, Nanotechnology 25 (2014) 135302
[4] J Llobet et al, Appl. Phys. Lett. 107, (2015) 223501
[5] P. Ferrando-Villalba et al, Nanotechnology 25(18), (2014) 185402

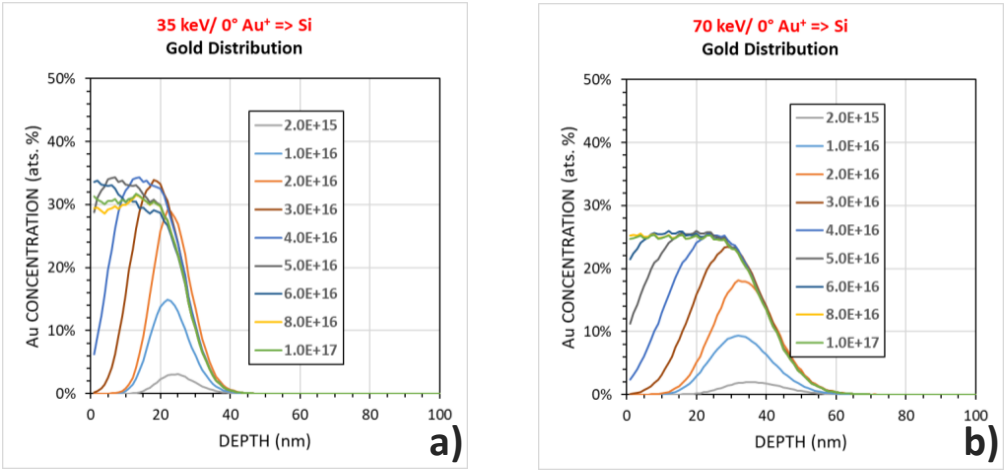

Figure 1. SRIM expected depth profiles of Au in Si with different ion fluences for 35 (a) and 70 keV (b) irradiation energies

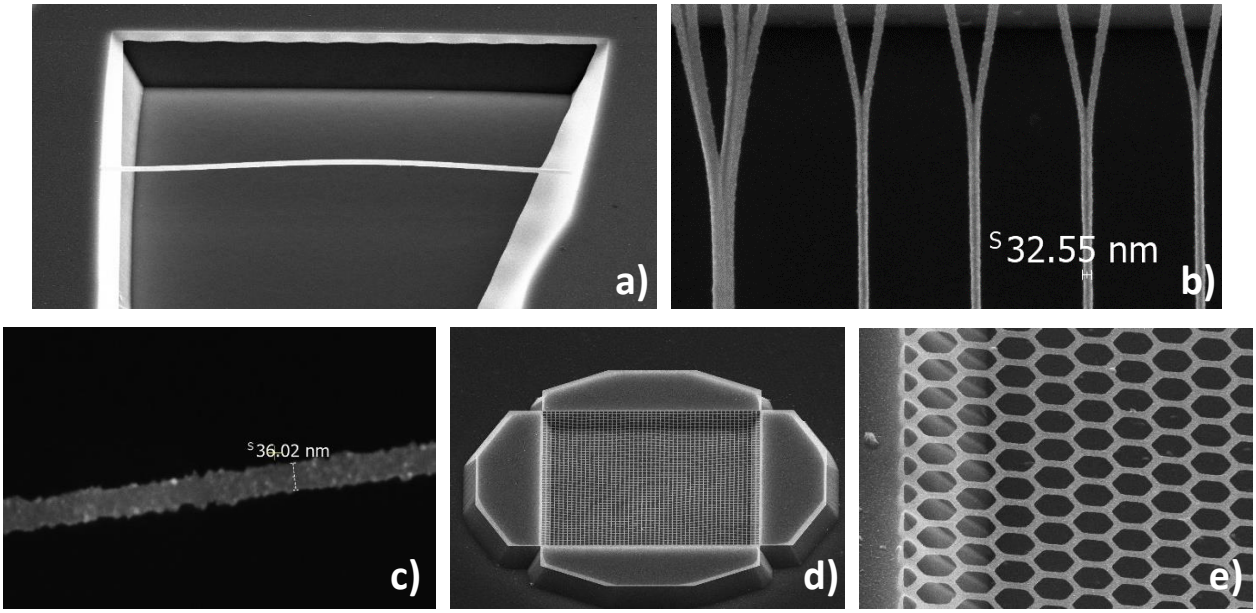

Figure 2. Examples of nanostructures obtained by Au+ implantation and consequential etching. Longest (a), thinner (b), smaller (c) and more complex suspended structures (d,e)

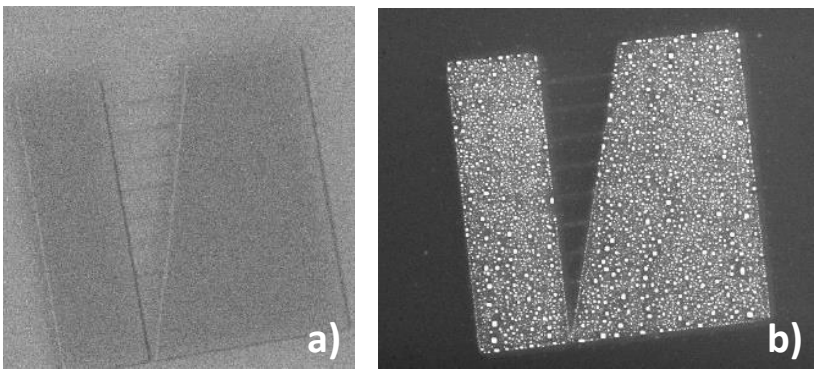

Figure 3. SEM images of the same pattern throughout the consequential steps of implantation (a) and annealing (b)

Plasma conversion of polydimethylsiloxane and perhydropolysilazane precursor layers by a pulsed atmospheric pressure plasma jet to a silicon oxide thin film

M. Rudolph[1], P. Birtel[1], T. Arnold[1,2], A. Prager[1], S. Naumov[1], U. Helmstedt[1], A. Anders[1,3], P. C. With[1]

[a] Leibniz Institute of Surface Engineering (IOM), Permoser Str. 15, 04318 Leipzig, Germany
[b] Faculty of Mechanical Science and Engineering, Institute of Manufacturing Science and Engineering, Technische Universität Dresden, 01062 Dresden, Germany
[c] Felix-Bloch Institute of Solid State Physics, Leipzig University, Linnéstr. 5, 04103 Leipzig, Germany
e-mail: patrick.with@iom-leipzig.de

The economical deposition of a barrier thin film material like silicon oxide onto flexible and thermally sensitive polymer substrates such as polyester foils is of great relevance to many applications, e.g., encapsulation of flexible photovoltaics, OLEDs and other flexible electronics. Common approaches to deposit metal or metalloid oxide thin films require either high processing temperatures >350 °C, e.g. in sol-gel methods and atmospheric pressure CVD which are not compatible with polyesters, or costly low pressure processes, e.g. CVD, ALD and PVD methods. Atmospheric pressure plasma treatment of materials is a flexible and efficient technology for the modification of surfaces. In some cases, such as in the activation of polymer surfaces, atmospheric pressure plasmas have become the tool of choice. For other purposes, such as the fabrication of thin films, the potential of atmospheric pressure plasmas is yet to be fully leveraged.

We discuss the conversion of perhydropolysilazane (PHPS) and polydimethylsiloxane (PDMS) layers to silicon oxide thin films using a pulsed atmospheric pressure plasma jet (pAPPJ) [1]. The precursor layers are spin-coated onto silicon wafers and polyethylene terephthalate (PET) substrates, before treating them with a microwave-excited pulsed atmospheric pressure plasma jet. By attenuated total reflection Fourier transform infrared spectroscopy (ATR-FTIR) the precursor decomposition and oxidation was followed, as shown in Fig. 1 for PHPS. Compared to PHPS reference films, the characteristic Si-H stretching peak intensity significantly decreased and a blue shift to higher wavenumbers was observed (2163–2172 cm^{-1}, $\Delta = 9$ cm^{-1}). This can be explained by a substitution of nitrogen with oxygen, which was also supported by DFT-calculated vibrational spectra of simplified ring structures (Fig. 1, c). Varying the scan velocity and the number of treatments resulted in various film compositions and morphologies, as determined by X-ray photoelectron spectroscopy (XPS) and scanning electron microscopy. It is suggested that three main processes contributing to the precursor decomposition and oxide formation mechanism (Fig. 2) based on mechanisms known from vacuum ultra violet-conversion of metal- and metalloid-containing molecular precursor compounds [2,3]: a) the decomposition of the precursor by plasma-produced species, in particular vacuum ultra violet photons from the argon excimer continuum; b) the oxidation of the surface from atmospheric oxygen and plasma-produced reactive oxygen species; c) the diffusion of oxygen into the film while gases produced from the precursor decomposition diffuse out of the film. Latter process is possibly facilitated by local plasma heating of the surface. Moreover, we show that the process is compatible with temperature-sensitive substrates such as polyethylene terephthalate (PET).

[1] M. Rudolph, P. Birtel, T. Arnold, A. Prager, S. Naumov, U. Helmstedt, A. Anders, P. C. With, Plasma. Process. and Polym., 20:e2200229, 2023.
[2] L. Prager, A. Dierdorf, H. Liebe, S. Naumov, S. Stojanovic, R. Heller, L. Wennrich, M. R. Buchmeiser, Chemistry, 13, 8522, 2007.
[3] P. C. With, J. Lehnert, L. Seifert, S. Dietrich, H. Krautscheid, S. Naumov, A. Prager, B. Abel, L. Prager, U. Helmstedt, Appl. Surf. Sci., 493, 525, 2019.

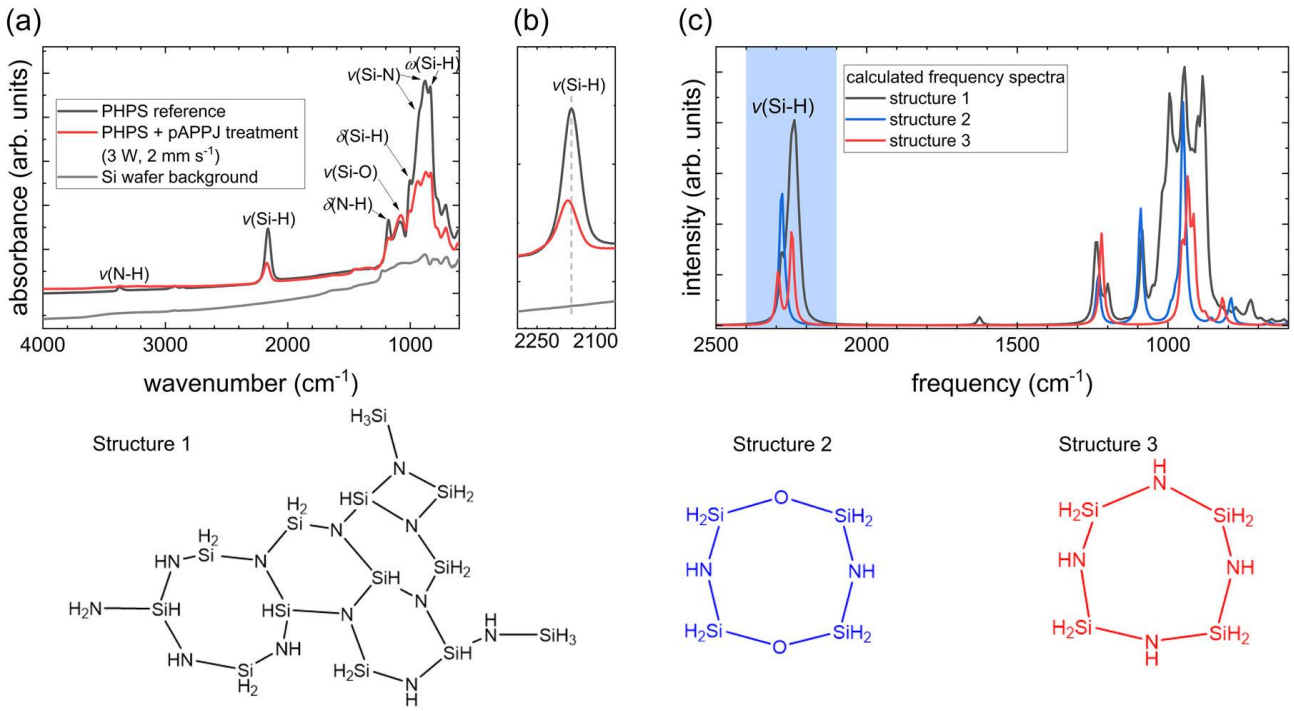

Figure 1. Attenuated total reflectance Fourier transform infrared spectroscopy spectra of PHPS precursor films on Si-wafer substrates before and after plasma treatment: (a) assignment of the characteristic vibration bands; (b) magnification of the *ν*(Si–H) region; (c) calculated PHPS spectrum for a complex ring structure as well as for simplified eight-ring structures with and without substitution of oxygen for nitrogen (corresponding structures are shown below the spectra).

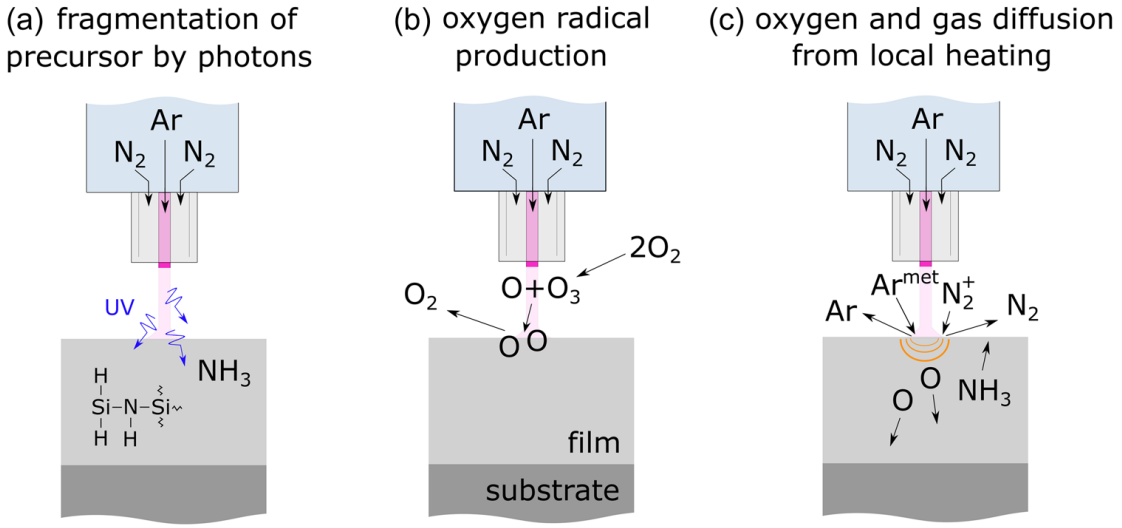

Figure 2. Suggested contributions to the conversion of the perhydropolysilazane (PHPS) precursor layer using an atmospheric pressure plasma jet. (a) The fragmentation of the precursor via energetic (vacuum ultra violet) photons. (b) The production of ozone or oxygen radicals from O_2 in the atmosphere that can react with the surface of the PHPS film. (c) The diffusion of these oxygen species into the precursor layer, consecutively oxidizing it. This step could be promoted by local heating of the surface by the plasma source. (c) is likely to be the rate-limiting process. Note that the selection of chemical species in the schematic is for illustrative purposes only and should not be understood as a comprehensive list of species.

Optical waveguides made of inkjet-able high refractive index materials using Nanoimprint Lithography

Michael J. Haslinger, Gerald Stubauer, Peter Bauer, Sebastian Kauscheder, Viktorija Jonaityte, Kateřina Masopustová, Sonja Kopp, Michael Mühlberger

[a] PROFACTOR GmbH, Im Stadtgut D1 | 4407 Steyr-Gleink | Austria
e-mail: Michael.Haslinger@profactor.at

Photonics-based devices are becoming increasingly important. 3D sensors are used in the automotive industry (LiDAR) to protect drivers, passengers, surrounding persons and objects from collisions and paving the way towards autonomous vehicles. Traditional LiDAR systems are made of moving components whose mechanical assembly makes them fragile, expensive and weighty.

An Optical Phased Array (OPA) LiDAR is a system which enables the beam steering without need for moving parts. The cost and size of the LiDAR can be significantly reduced while its performance (e.g. scanning speed, power efficiency, resolution) is improved thanks to the so-called solid-state beam steering.[1] In an OPA manipulation and guiding of light takes place in high refractive index waveguides. A modern approach to produce such waveguides and photonic integrated circuits of an OPA from functional materials is Nanoimprint Lithography (NIL). NIL is a micro- and nano-replication technology, which achieves very high resolution and allows for unattainable process flexibility. [2–3] By the use of high refractive index materials optical components like metalenses or waveguides and photonic integrated circuits can be directly fabricated in a single fabrication step. [4]

In this work we present the direct imprint of waveguide structures in various high refractive index materials from INKRON. The master design was done at CEA-Leti and is optimized for the refractive index of the resists. Master and master details can be seen in figure 1. Besides spin-coat-able materials, new developments of fully inkjet-able and imprint-able high refractive index materials will be presented. The RI of the materials is in the range of 1.7 to 1.9. Inkjet deposition of the resist is done with an LP50 inkjet printer or Dimatix DMP 2850 lab printer by using a number of different industrial inkjet printheads figure 2. Imprint is performed in a S&R tool at PROFACTOR in order to investigate material compatibility and stamp degradation which are important parameters and information for production processes and cost estimates.
The combination of digital material deposition by inkjet printing and UV-NIL is a very promising production technology for the future which achieves high quality imprints (figure 3). Inkjet printing enables a significantly higher efficiency in material application compared to spin coating. The one step manufacturing process of waveguides by using NIL and the combination of inkjet and NIL allows for a very sustainable manufacturing process.

Acknowledgments
The good cooperation in the TINKER project and the fruitful discussions with the partners EV Group, INKRON and LETI CEA are acknowledged. The project TINKER receives funding from the European Union's Horizon 2020 research and innovation programme under Grant Agreement No. 958472.

Literatur:

[1] https://www.eetimes.eu/cea-leti-goes-for-optical-phased-arrays-to-cut-lidar-cost/
[2] Schift, H., "Nanoimprint lithography: An old story in modern times? A review," J. Vac. Sci. Technol. B Microelectron. Nanometer Struct. 26(2), 458 (2008).
[3] Schift, H., "Nanoimprint lithography: 2D or not 2D? A review," Appl. Phys. A 121(2), 415–435 (2015).
[4] Einck, Vincent J., et al. "Scalable nanoimprint lithography process for manufacturing visible metasurfaces composed of high aspect ratio TiO2 meta-atoms." ACS Photonics 8.8 (2021): 2400-2409.

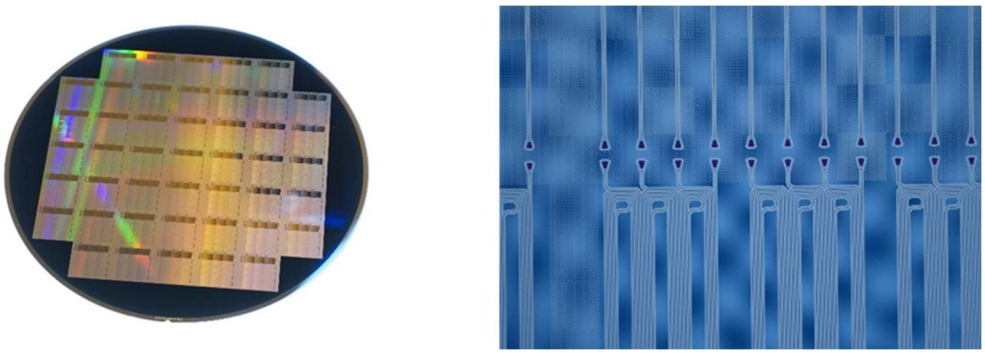

Figure 1. Left: Photonic integrated circuit test structures for the development of an imprint process. 200 mm PIC master was provided by CEA-Leti. Right: Microscope details of waveguide structures on the master.

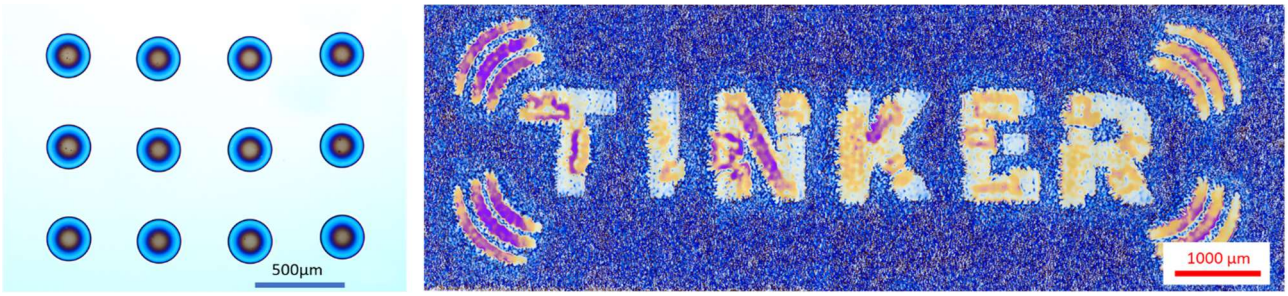

Figure 2. Left: Individual inkjet drops with 2.4 pl volume of IPO-912 resist deposited with a Dimatix DMP 2850 lab printer on a 100mm Si wafer demonstrating the good inkjet properties of the n =1.9 ink. Right: Image of TINKER logo printed with IPO-912 ink on a silicon wafer. The color impression was achieved by varying the printing resolution and therefore the layer thickness on the substrate.

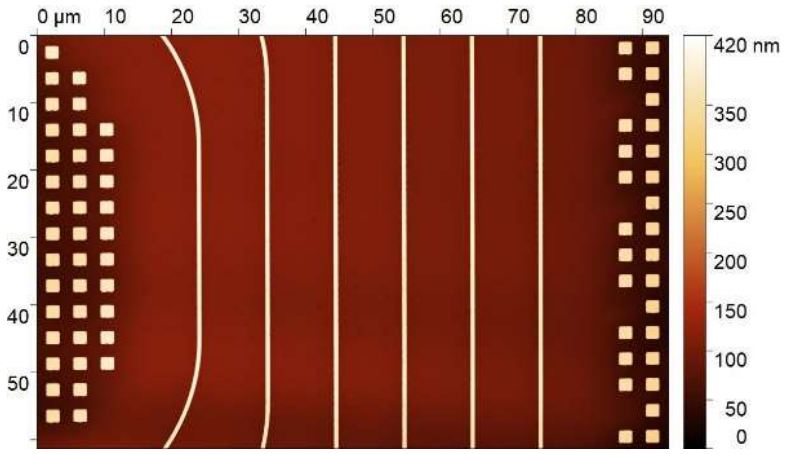

Figure 3. AFM image of imprinted waveguide structures in IPO-912 high refractive index resist. The image shows the high achievable quality.

No more macros: Open-source method for layout cell parameterization through feature recognition for procedural generation of lithography files

Tom Maslin [a], Stefanie Gutschmidt [a]

[a] University of Canterbury Department of Mechanical Engineering, Christchurch, 8041, New Zealand
e-mail: tom.maslin@pg.canterbury.ac.nz

Accurate modelling of the dynamics of micro-electro-mechanical-systems (MEMS) can be difficult due to challenges that come with the prediction of mechanical characteristics resulting from silicon-on-insulator fabrication methods. Investigations of MEMS dynamics therefore require experimental devices fabricated at the microscopic scale. However, access to micro- and nanoengineering foundries is often limited and it is then preferrable to produce many structures with unique dynamics for investigation on a single wafer. This emphasizes the need for a tool that enables researchers to quickly generate and modify lithography files throughout the design and fabrication process. To address this challenge, we develop a standalone, open-source Python application, FRiPL (Feature Recognition in Python for Lithography), that offers a low-to-no code interface for the purpose of creating and modifying parameterized cells (PCells) in graphic database system information interchange (GDSII) format, the industry standard for lithography files. This application has been tested for parallel use with KLayout [1], a free layout editor software, providing an intuitive user interface for procedural generation of structures with varying parameters.

The focus of our study is to enable rapid investigation of the dynamics of microscale piezoelectric coupled and uncoupled oscillators. To achieve this, we aim to maximize the number of geometric and coupling unique variations of devices on a single 4” silicon wafer. A no-code approach is to create a cell library of the oscillator shapes, and then instance each oscillator cell into a device cell within a common mount structure, which is in turn instanced into an overall wafer-level cell. This layout hierarchy is demonstrated in Figure 1. Free layout editors such as KLayout provide a means to do this with. However, manually creating this library is time-consuming, and modifying individual cells becomes arduous if changes are required. Instead, it is more efficient to define each oscillator as a parameterized cell (PCell) and procedurally generate the instances through scripting. Open-source toolboxes like gdspy [2] provide useful libraries for this approach, however, can quickly require more advanced scripting knowledge when working with geometries that don’t simply scale in 2D space. PHIDL [3] aims to reduce the required scripting necessary to utilize these open-source tools fully by offering built-in geometry libraries for scripting, whereas the current work aims to avoid scripting all together. Figure 2 details these conventional workflows along with the proposed method.

The presented work details the back-end Python architecture, utilizing the gdstk library [3], allowing for basic feature recognition and parameterization of a base oscillator shape, enabling procedural generation of geometrically distinct instances using a no-code interface. A ‘scaffold’ shape can be created using an existing layout editor, and the resultant GDSII file from that is fed into FRiPL for feature recognition. The tool allows for the parameterization of created geometries and the creation of parameterized rules between geometry features, which can then be modified through the comma separated values (CSV) file generated by the tool. This allows for exceptional control and tracking of unique device variations in much shorter timeframes than typical software-side PCell development. We have been able to create GDS files for 5 steps of lithography, for a wafer containing 951 devices (162 of which are geometrically distinct) in hours and can implement changes across all files in minutes. This involves defining oscillator numbers, dimensions, coupling, and even through-layer vias all through a csv worksheet in Microsoft Excel, requiring no coding. As a benchmark, the alternative script initially developed to achieve this using the method described in Figure 2b was over 700 lines of Python, which can fast be overwhelming.

[1] M. Köfferlein, KLayout, open-source software, Free Silicon Foundation, 2022.
[2] L. H. Gabrielli, gdspy/gdstk, open-source software, 2020.
[3] A. N. McCaughan et al., J. Vac. Sci. Technol, B 39 (2021).

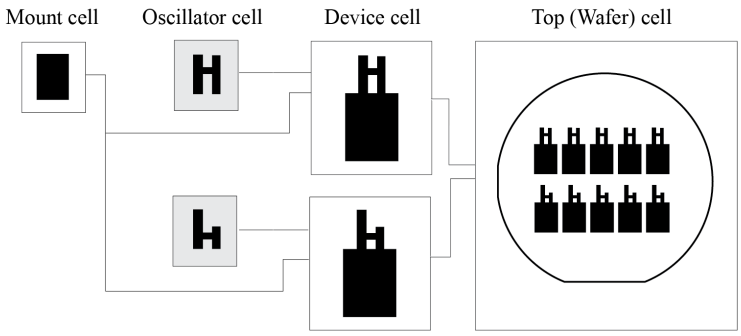

Figure 1. Hierarchal lithography layout showing two simplified unique oscillator cells with a common mount cell. Grey boxes indicate the cells either individually drawn with a layout editor or procedurally generated with programming for each geometrically unique instance.

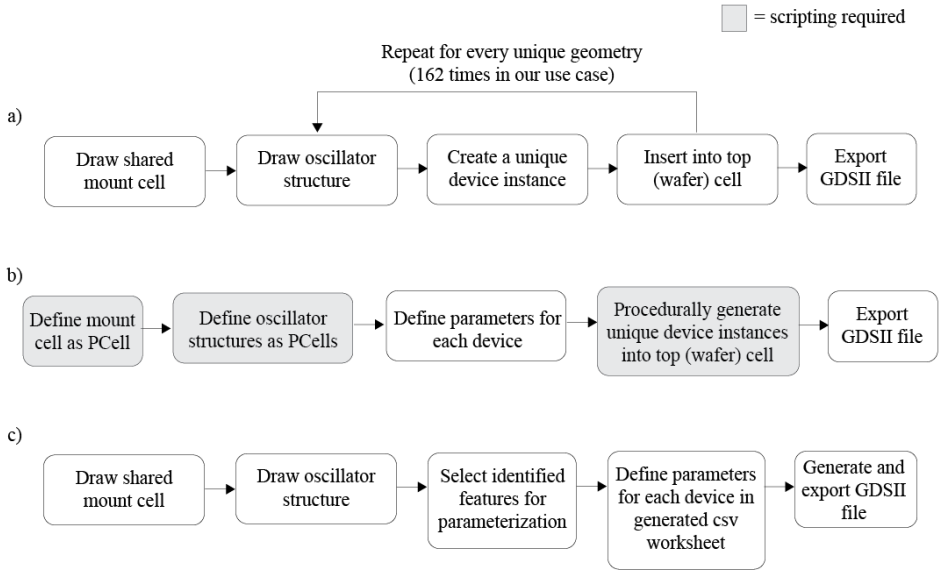

Figure 2. Simplified representations of workflows for achieving geometrically unique arrays a) No-code method using layout editor drawing tools, b) Scripting based parameterized cell method, c) new method for feature recognition and no-code parameterization.

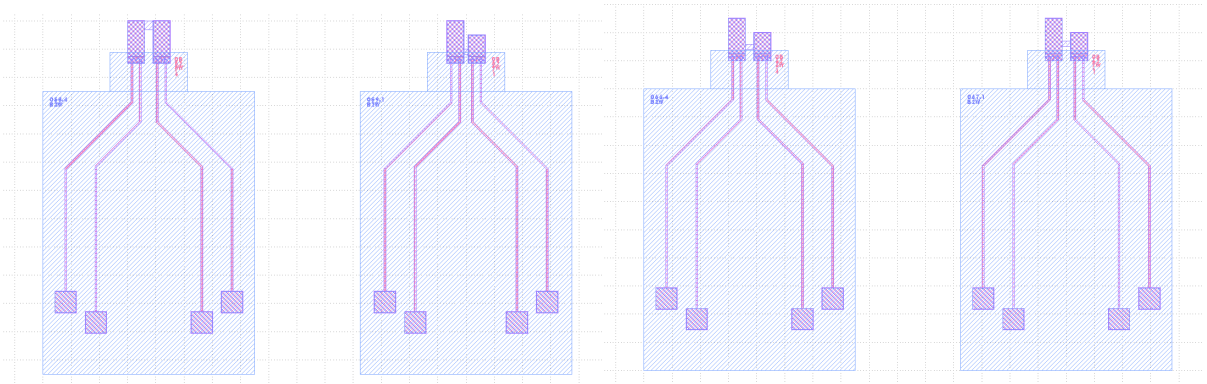

Figure 3. Four of the 162 device variants generated in the presented case, each with five layers of lithography. Observe the oscillator lengths, spacing, position of coupling beam, and electrode tracks are all updated between designs simply by modifying parameters in an Excel worksheet.

Degradable PVAc-graphene nanofibrous membrane for flexible piezocapacitive sensors

Debarun Sengupta [a], and Ajay Giri Prakash Kottapalli [a]

[a] Department of Bioinspired MEMS and Biomedical devices,
University of Groningen, Groningen, 9747 AG, the Netherlands
e-mail: debarun.sengupta@rug.nl

With growing life expectancy and a rise in the population with sedentary lifestyles, the load on existing healthcare infrastructure is expected to increase manifold in the next two decades. As per National Institute for Public Health and the Environment (RIVM), the number of centenarians will quadruple by 2040 [1]. Remote health monitoring and telemedicine will dominate the healthcare industry in the foreseeable future. The need of the hour is robust, reliable, sensitive, and inexpensive wearable sensors capable of providing intimate and detailed information regarding a person's physiological parameters. However, it is also critical that such sensors are environmentally friendly, and that production is sustainable. In this work, we present graphene-polyvinyl acetate (PVAc) electrospun nanofibrous membrane-based degradable piezocapacitive sensors for applications in wearables.

In our past work, the effect of graphene nanofiller addition on the dielectric response and pressure sensitivity has been reported [2]. It was observed that the 0.25 wt.% graphene-loaded PVAc nanofibrous membrane-based sensor demonstrated the maximum sensitivity. The sensor featured in this work comprises of 0.25 wt.% graphene-loaded electrospun nanofiber membrane sandwiched between two layers of fabric-based flexible electrodes. The schematic in Fig 1 shows the process steps involved in the fabrication of the nanofiber-based piezocapacitive sensor. The plot in Fig 2a compares the dielectric frequency response of 0.25 wt.% graphene-PVAc nanofiber membrane with a spin-coated membrane of the same composition. The mismatch of dielectric constants between the two cases can be explained by invoking the concept of a lower effective dielectric constant in porous materials owing to the presence of air voids. When such a porous material is subjected to external pressure, densification leads to an overall increase in the effective dielectric constant and this property can be employed for developing highly sensitive pressure sensors. The plots in Fig 2b show the compressive stress-strain characteristics of the encapsulated sensors assembly over 10 cycles of compressive loading. The sensor demonstrated a maximum hysteresis figure of ~ 4.93% at 10% compressive strain at a maximum pressure of 37.17 kPa. The plots in Fig 2c show the stress-strain characteristics of the nanofiber membrane for 10 cycles of uniaxial tensile loading and the tensile modulus nanofiber membrane was determined to be 212.69 MPa [2].

The sensor was subjected to a series of cyclic tactile pressure stimuli at different pressures and the plot in Fig 3a shows the relative capacitive change responses of the sensor for four distinct pressures. The plot in Fig 3b shows the pressure versus relative capacitive change responses of the sensor. Linear regression treatment revealed two distinct pressure regimes with sensitivity values of 0.01355 kPa^{-1} (~ 2.7 – 44 kPa) and 0.00653 kPa^{-1} (~ 56 – 319 kPa). The plot in Fig 3c shows the relative capacitance change response of the sensor to a series of 1000 cycles of tactile stimuli (at 10 N load) applied employing a PDMS model finger demonstrating the reliability of the sensor over prolonged use thus underscoring its robustness. To demonstrate the usability of the sensors in real-life applications, an ergonomic smart chair comprising six identical sensors placed at the bilateral scapula, gluteal, and hamstring regions is developed and tested. The schematic in Fig 3d shows the sensorized chair with an Arduino-based data acquisition system. The plots in Fig 3e compare the responses acquired from the sensors while a person sits leaning against the backrest (left plot) vs the same person sitting upright. The degradability of the sensors has been demonstrated previously [2] and it is expected that sensors similar to the one presented here will gain widespread acceptance for future applications in flexible electronics and wearable devices.

[1] "Life expectancy | Volksgezondheid Toekomst Verkenning." [Online]. Available: https://www.vtv2018.nl/en/life-expectancy.
[2] D. Sengupta et al., ACS Appl. Mater. Interfaces, vol. 15, (2023) 22351–22366.

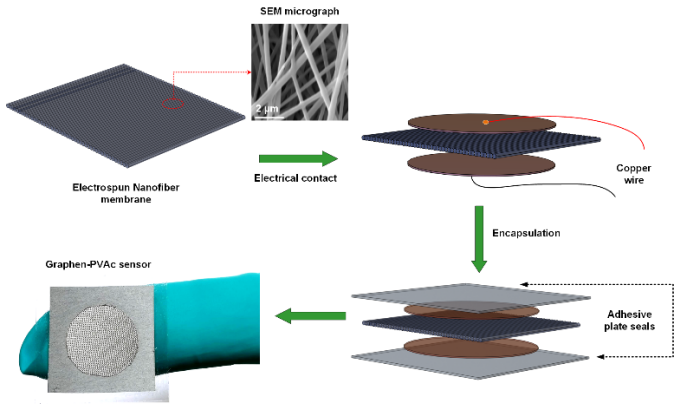

Figure 1. Schematic representation of process flow steps involved in the fabrication of PVAC-Graphene nanofiber based flexible piezocapacitive sensors.

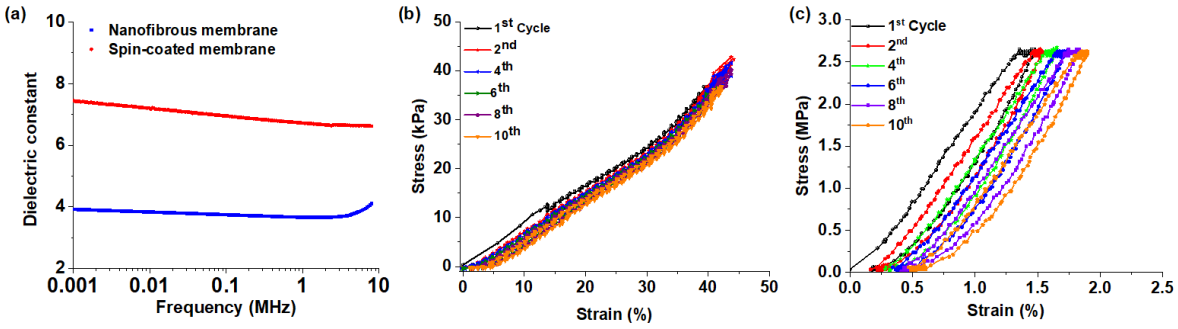

Figure 2. (a) Plots comparing the dielectric response of the 0.25 wt. % graphene-PVAC nanofibrous membrane with spin-coated membrane of the same composition; (b) Plot showing the stress-strain characteristics (compressive) of 1st, 2nd, 4th, 6th, 8th, and 10th cycles of the sensor assembly; (c) Plot showing the stress-strain characteristics (tensile) of 1st, 2nd, 4th, 6th, 8th, and 10th cycles of the nanofiber membrane.

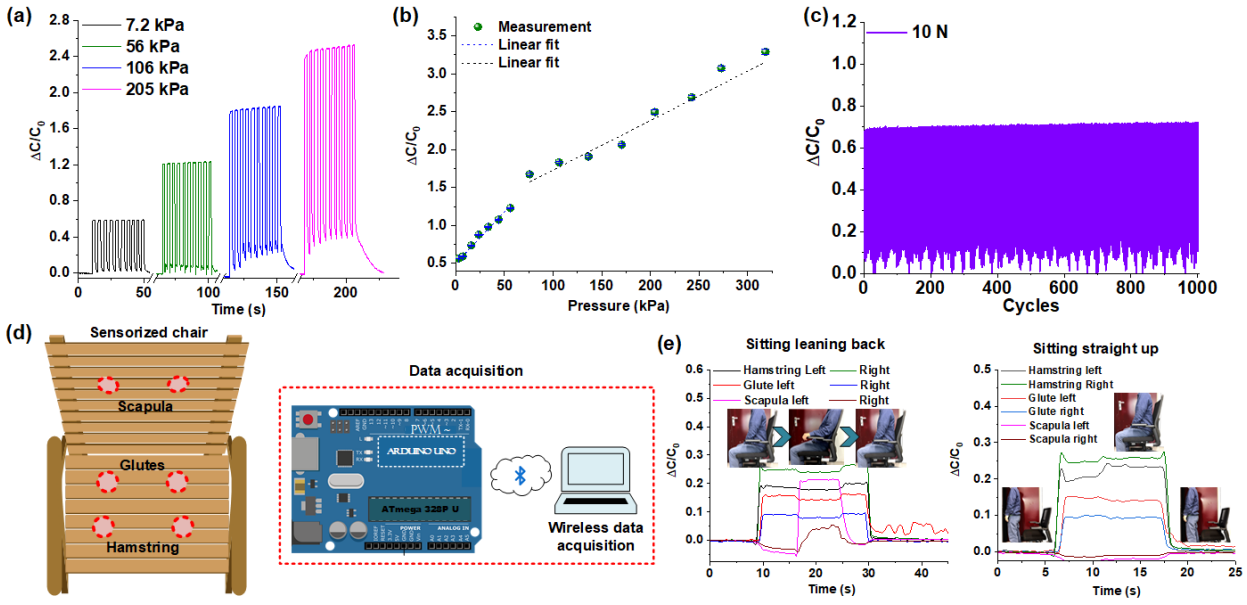

Figure 3. (a) Plot showing the relative capacitance change response of the sensor to four distinctive pressure stimuli; (b) Plot showing the pressure vs relative capacitance change response of the sensor; (c) Plot showing the relative capacitance change response of the sensor to 1000 cycles of uniaxial loading; (d) Schematic representation of the sensorized smart chair for posture monitoring; (e) Plots comparing the qualitative pressure distribution of a person sitting leaning back with the same person sitting upright.

SiO_2 & SiN_x Thin Film Deposition by Plasma Enhanced Spatial Atomic Layer Deposition Processes

Jaehee Kim [a, b], Hyeonjin Choi [d], Jinmyeong Kim [d], and Heeyeop Chae [c, d]*

[a] Department of Semiconductor Display Engineering, Sungkyunkwan University (SKKU), Suwon, 16419, Republic of Korea

[b] Semiconductor R&D Center, Samsung Electronics, Hwaseong 18448, Republic of Korea

[c] SKKU Advanced Institute of Nanotechnology (SAINT), Sungkyunkwan University (SKKU), Suwon, 16419, Republic of Korea

[d] School of Chemical Engineering, Sungkyunkwan University, Suwon, 16419, Republic of Korea

Tel.:82-31-290-7263, E -mail: hchae@skku.edu

Abstract

Atomic layer deposition (ALD) is the most advanced technology as producing ultrathin conformal films deposition with atomic-level precision, good uniformity and low surface roughness.[1,2] A major drawback of ALD is its low deposition rate, making ALD less utilization for process that require high throughput. An approach to overcome this drawback is spatial ALD, based on separating the precursors in space rather than in time. Since the elimination of purge steps, the spatial ALD allows high throughput without compromising the typical ALD features.[3,4] In this study, thin film deposition processes for dielectric SiO_2 and Si_3N_4 were developed by a spatially divided plasma enhanced atomic layer deposition (spatial PEALD) process. Trisilylamine (TSA, $N(SiH_3)_3$), Bis(tertiary-butylamino)silane (BTBAS, $[(CH_3)_3CNH]_2SiH_2$ were selected as silicon precursors, and NH_3 plasma was used as a reactant material. The ALD window of SiO_2 was observed in the temperature range of 125-150℃ and the chemical composition ratio in ALD window determined to be O/Si~1.92, as shown in Figure 1. Carbon components were identified as major impurities in the films. The impurities were reduced through high temperature, high plasma power, as shown in Figure 2. The growth per cycle (GPC) of the SiO2 and SiNx films were 1.33Å/cycle and 0.27Å/cycle at temperatures 150℃ respectively, as shown in Figure 3. The film characteristics of various process parameters were investigated according to the growth temperature, plasma power, and scanning speed of substrate. Finally the optimal deposition conditions with low impurities was found and the characteristics of SiO2 & SiNx thin films were confirmed. These results demonstrate the potential of spatial ALD combined with the intrinsic advantages of atomic layer deposition in the semiconductor industry.

References:

[1] J. Zhang et al., Nanomanuf. Metrol. 5(3) (2022) 191

[2] R. A. Ovanesyan et al., J. Vac. Sci. Technol. A 37(6) (2019) 060904

[3] P. Poodt et al., J. Vac. Sci. Technol. A 30(1) (2012) 010802

[4] D. Muñoz-Rojas et al., C. R. Phys. 18(7-8) (2017) 391-400

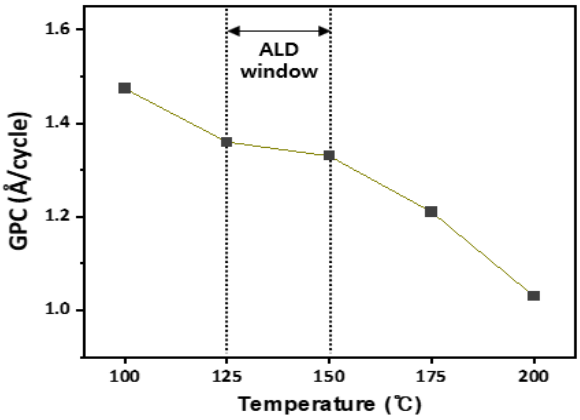

Figure 1. Growth rate of SiO_2 dependence on temperature using BTBAS precursor and O_2 plasma.

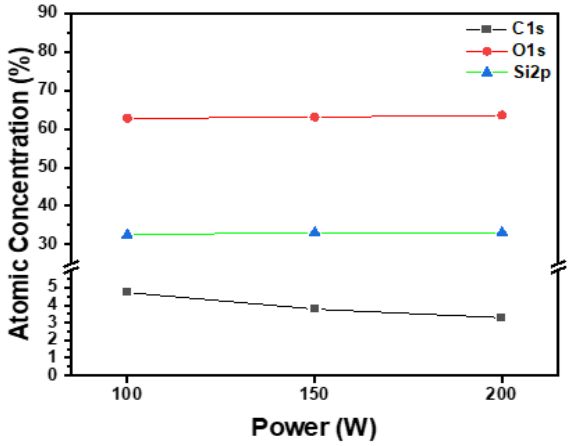

Figure 2. Composition ratio of SiO2 film dependence on Power

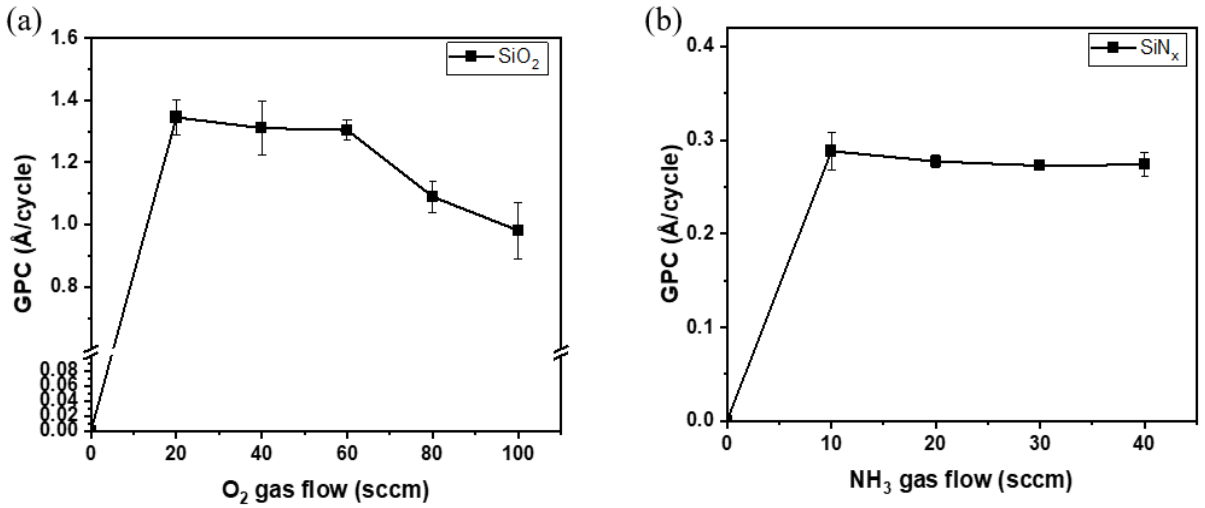

Figure 3. (a) Growth rate of SiO_2 dependence on O_2 plasma flow rate. (b) Growth rate of SiN_x dependence on NH_3 plasma flow rate.

Plasma Atomic Layer Etching of SiO_2 with Low-Global Warming Perfluoroisopropyl Vinyl Ether (PIPVE)

Jihye Kim [a,b], Hojin Kang [a], Minsuk Choi [a], Daeun Hong [a], Yongsun Cho [b], Junsik Hong [b], Heeyeop Chae [a,c,*]

[a] School of Chemical Engineering, Sungkyunkwan University (SKKU), Suwon, 16419, Republic of Korea
[b] Flash Yield Enhancement Team, Samsung Electronics, Pyeongtaek, 17786, Republic of Korea
[c] Department of Nano Science and Technology, SKKU Advanced Institute of Nanotechnology (SAINT), Sungkyunkwan University (SKKU), Suwon, 16419, Republic of Korea
e-mail: hchae@skku.edu

In this work, plasma atomic layer etching (ALE) was developed for SiO_2 with perfluoroisopropyl vinyl ether (PIPVE, $C_5F_{10}O$) and compared with conventional global warming C_4F_8 gas. PIPVE has a lower lifetime and global warming potential (GWP) of 3 which is significantly lower than that of C_4F_8, 9,540.[1],[2] ALE is a cyclic process that removes layers with atomic-scale precision and consists of a surface modification step and an etching step.[3],[4] In the surface modification step, SiO_2 surfaces were fluorinated with fluorocarbons generated from C_4F_8 or PIPVE plasmas. In the etching step, the fluorinated surface was etched by ions generated from Ar plasma.[5] The ALE window was observed in the bias voltage range of 20-27.5V for both C_4F_8 and PIPVE. The etch per cycle (EPC) of SiO_2 in the ALE window was determined to be 5.3 Å/cycle for C_4F_8 and 3.3 Å/cycle for PIPVE. The composition of the fluorocarbon layers on the SiO_2 surface was analyzed by X-ray photoelectron spectroscopy (XPS), and the F1s/C1s ratio was calculated using the F1s and C1s spectrum.[6,7] The PIPVE produces the lower than C_4F_8 the F1s/C1s ratio. The million metric ton carbon equivalent (MMTCE) of PIPVE was 49% lower than C_4F_8.[2] This work demonstrates that PIPVE can reduce global warming effects as compared to C_4F_8 and be used as potential etchants for ALE processes.

References

[1] Mocella, M. T., A current Assessment. MRS Online Proceedings Library (OPL), 447, 29. (1996)
[2] Environmental Protection Agency (EPA), 2013 Revisions to the Greenhouse Gas Reporting Rule and Final Confidentiality Determinations for New or Substantially Revised Data Elements (2013).
[3] T. Faraz, F. Roozeboom, H. Knoops, and W. Kessels, ECS J. Solid State Sci.Technol. 4, N5023 (2015).
[4] George, S. M., Accounts of Chemical Research, 53(6), 1151-1160 (2020)
[5] S. S. Kaler, Q. Lou, V. M. Donnelly, and D. J. Economou, J. Phys. D Appl. Phys. 50, 234001 (2017).
[6] T.H. Cha, Y.J. Kim, S.I. Lee, Y.G. Cho, and H.Y. Chae, J. Vac. Sci. Technol. A 37, 051302 (2019)
[7] Y.J. Kim, S.I. Lee, Y.G. Cho, S.E. Kim, and H.Y. Chae, J. Vac. Sci. Technol. A 38(2), 022606 (2020)

Name	Chemical Formula	Structure	GWP
Octafluorocyclobutane	C_4F_8	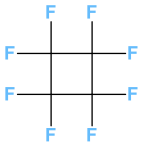	9,540
PIPVE (Perfluoroisopropyl vinyl ether)	$C_5F_{10}O$	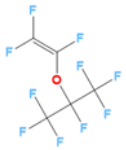	3

Table 1. Chemical Structures of C_4F_8 and PIPVE in This Study

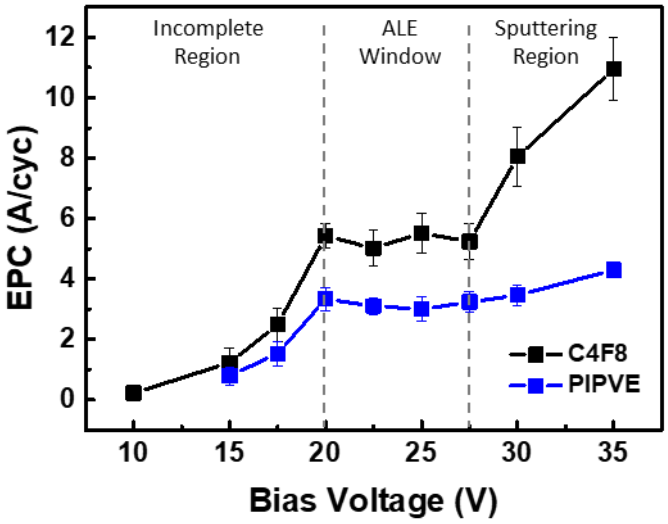

Figure 1. Etch per cycle of SiO2 using C4F8 and PIPVE in the fluorination step as function of bias voltage in the etching step using Ar plasma.

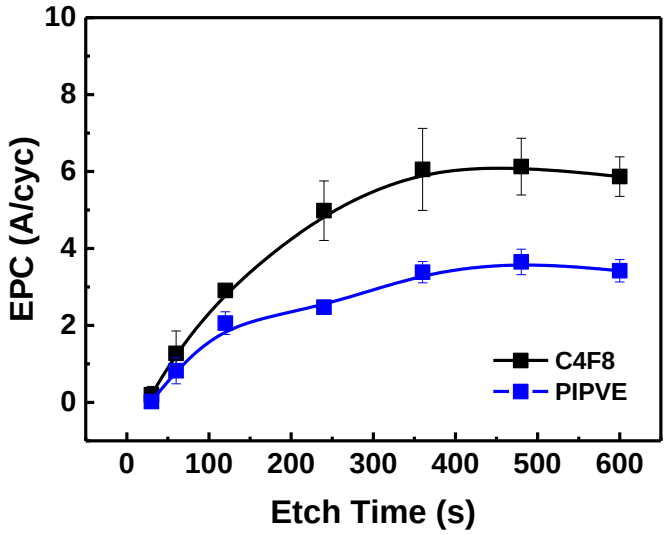

Figure 2. Etch per cycle of SiO2 using C4F8 and PIPVE in the fluorination step as function of etching time in the etching step using Ar plasma.

Fabrication of Flexible Transparent Silver Electrodes via Maskless Evaporation

Sihai Luo,[†] Enkui Lian, John C. deMello[*]

Department of Chemistry,
Norwegian University of Science and Technology (NTNU),
7491 Trondheim, Norway

e-mail: sihai.luo@ntnu.no

Abstract
We report template-patterned, flexible Transparent Electrodes (TEs) formed from an ultrathin silver film on top of a commercial optical adhesive – Norland Optical Adhesive 63 (NOA63). NOA63 is shown to be an effective base-layer for ultrathin silver films that advantageously prevents coalescence of vapour-deposited silver atoms into large, isolated islands (Volmer-Weber growth), and so aids the formation of ultrasmooth continuous films. 12-nm silver films on top of free-standing NOA63 combine high, haze-free visible-light transparency ($T \approx 60$ % at 550 nm) with low sheet-resistance ($\mathcal{R}_S \approx 16$ Ω/sq.), and exhibit excellent resilience to bending, making them attractive candidates for flexible TEs. Etching the NOA63 base-layer with an oxygen plasma before silver deposition causes the silver to laterally segregate into isolated pillars, resulting in a much higher sheet resistance than silver grown on pristine NOA63 ($\mathcal{R}_S > 8\times10^6$ Ω/sq.). Hence, by selectively etching NOA63 before metal deposition, insulating regions may be defined within an otherwise conducting silver film, resulting in a differentially conductive film that can serve as a patterned TE for flexible devices.

Introduction
The growing demand for flexible optoelectronic devices has generated a need for compliant, haze-free, stable, transparent electrodes (TEs) on thin, plastic substrates that exhibit high transparency and low sheet-resistance combined with excellent resilience under repeated flexing at bending diameters down to a few mm. [1,2] Transmittance and sheet-resistance requirements vary between applications: for instance, capacitive and resistive touch-panels require sheet resistances of a few hundred ohms per square (Ω/sq.) at 80 - 90 % transmittance, while (current-driven) solar cells and organic light-emitting diodes require sheet resistances of 10 – 50 Ω/sq. at similar transmittance levels. [3] For photodetectors, a sheet-resistance of < 100 W/sq. and a transmittance of > 50 % is needed for high bandwidth and responsivity, but in addition the electrode should exhibit an extremely low surface roughness to avoid the formation of conductive shunts that would otherwise increase leakage currents and reduce detectivity. [4,5] Beyond their physical properties, it is advantageous from a manufacturing perspective if the TEs can be deposited directly onto a flexible substrate (as opposed to it being necessary to first deposit onto a rigid substrate and then transfer to a flexible substrate afterwards). [8] It is also beneficial if the TE material can be patterned down to the few-micron level without recourse to time-consuming, costly, and environmentally harmful photolithography. [9]
Here we show that commercially sourced optical adhesive (OA)--NOA63 acts as an effective base-layer for ultrathin silver films that advantageously prevents coalescence of vapour-deposited metal atoms into large discrete islands (Volmer-Weber growth), and so aids the formation of ultra-smooth continuous films needed for TE applications. We show that ~12-nm films of silver on top of NOA63 combine high, haze-free transparency with low sheet-resistance, and exhibit excellent resilience to bending, making them attractive candidates for flexible TEs.

Results and discussion
The described procedure has several advantages over conventional methods for micropatterning metals such as shadow-mask evaporation and photolithography. In shadow-mask evaporation, gradual furring or deformation of the mask may occur due to adhesion of evaporated material, leading to a loss of patterning fidelity and a need for regular mask maintenance. In the method described here, a shadow-mask is used prior to metal deposition to spatially confine the oxygen plasma, but the mask is not damaged by the plasma treatment and does not require cleaning after use. Plasma etching moreover occurs isotropically, and therefore allows patterning right-up to the edge of the shadow-mask, avoiding the blurring and shadowing artefacts that are associated with shadow-mask evaporation. Photolithographic patterning of metals involves slow and costly multistep processes that have a substantial environmental impact in terms of both energy

consumption and hazardous reagent use. [9] Fabrication of the patterned OA/Ag electrodes reported here involves just four simple process steps (OA deposition, UV-curing, selective etching via a shadow-mask, metal deposition), making it easier to implement than photolithographic patterning, with a correspondingly lower environmental impact.

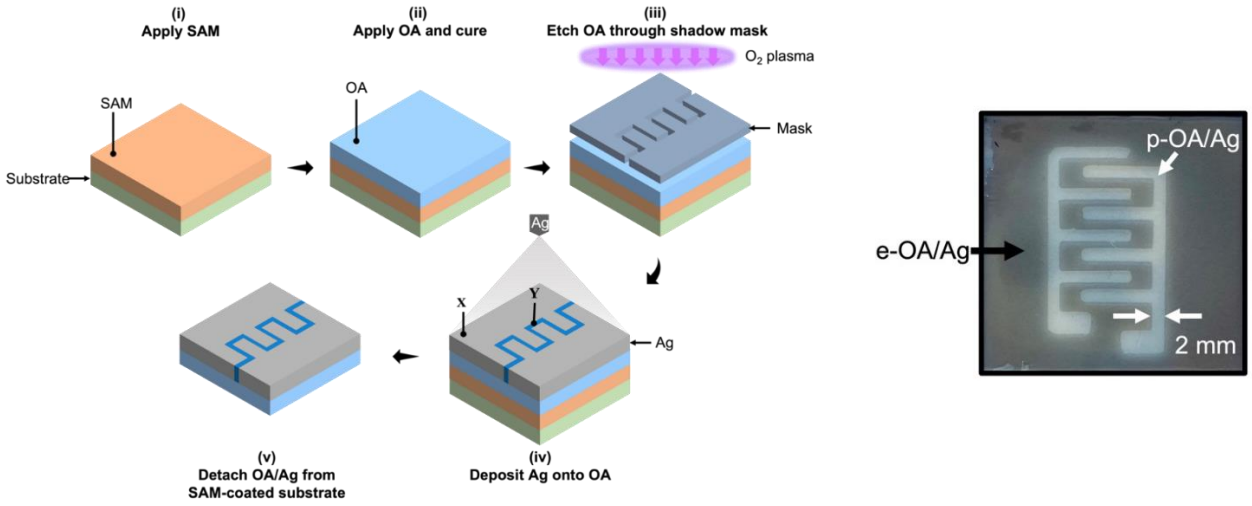

Figure 1. Schematic showing the fabrication procedure for patterned TEs. Insulating regions (Y) and conductive regions (X) (iv). Photo of patterned TEs. Insulating (e-OA/Ag) and conductive (p-OA/Ag) regions.

In contrast to both shadow-mask evaporation and photolithography, at the end of the OA/Ag patterning procedure, the TE surface is composed entirely of silver in both the conducting and the insulating regions. By selectively etching the OA layer prior to silver deposition, it is possible to define insulating regions within an otherwise conductive layer of silver, with the insulating regions being easily identified visually due to their substantially lower transmittance. The sharpness of the interface between the conducting and insulating regions is determined by the choice of shadow mask, see **Figure 2**. Using a rigid shadow mask allows vertical gaps to exist between the mask and the substrate, leading to ingress of the oxygen plasma into the shadow regions and unwanted broadening of the interface. The extent of the broadening is influenced by the etching time, with longer etches resulting in a more diffuse interface. Using a rigid shadow mask allows vertical gaps to exist between the mask and the substrate, leading to ingress of the oxygen plasma into the shadow regions and unwanted broadening of the e-OA/p-OA interface. The extent of the broadening is influenced by the etching time, with longer etches resulting in a more diffuse p-OA/e-OA interface, showing wider interfacial width.

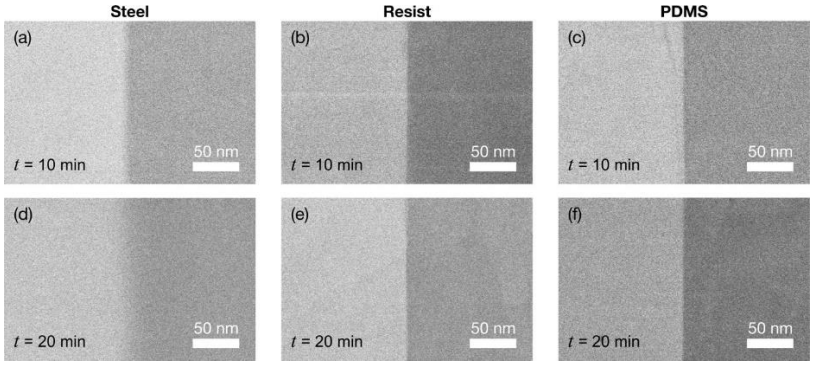

Figure 2. SEMs of etched/unetched interfaces using different masks, showing varied interfacial widths.

References

[1] T. Wang, K. Lu, Z. Xu, Z. Lin, T. Qiu, Z. Yang, H. Zheng, R. Yao, J. Peng, Crystals 2021, 11, 511.
[2] T. Sekitani, U. Zschieschang, H. Klauk, T. Someya, Nature Mater 2010, 9, 1015.
[3] H. G. Manning, C. G. da Rocha, C. O. Callaghan, M. S. Ferreira, J. J. Boland, Sci Rep 2019, 9, 11550.
[4] D. Baierl, B. Fabel, P. Lugli, G. Scarpa, Organic Electronics 2011, 12, 1669.
[5] A. Pierre, I. Deckman, P. B. Lechêne, A. C. Arias, Adv. Mater. 2015, 27, 6411.
[8] S. Ullah, X. Yang, H. Q. Ta, M. Hasan, A. Bachmatiuk, K. Tokarska, B. Trzebicka, L. Fu, M. H. Rummeli, *Nano Res.* **2021**, *14*, 3756.
[9] E. Mullen, M. A. Morris, *Nanomaterials* **2021**, *11*, 1085.

A Comparative Study of Granular Aluminium Deposition by Electron Beam Evaporator and Sputtering Techniques

Bruno Magalhaes [a], Rodolfo Previdi [a], Juan Servin [a], Lubuna Shafeek [a], Evgeniia Volobueva [a], Salvatore Bagiante [a]

[a] Institute of Science and Technology Austria
Nanofabrication Facility, Klosterneuburg, 3400 Austria
e-mail: bmartins@ist.ac.at

The deposition of granular aluminium thin films is an important process in many technical applications, including microelectronics [1], photovoltaics [1], sensors [2] and superconductivity [3]. The used deposition technique has a substantial impact on film qualities such as morphology, structure, and electrical conductivity. In this study, we analyze and evaluate the properties of granular aluminium deposited using two widely used deposition techniques: electron beam evaporator and sputtering. The electron beam evaporator uses a concentrated electron beam to thermally evaporate the aluminium target, whereas sputtering requires blasting the target with high-energy ions, which then condense on the substrate.

To compare the two deposition techniques, granular aluminium was deposited using identical parameters, with a focus on the influence of oxygen during deposition. Aluminum was first deposited in an oxygen-free atmosphere. The lack of oxygen aided in the preservation of the deposited aluminium's integrity, preventing the formation of oxide layers on the surface. This approach produced a pure aluminium deposition with low oxidation susceptibility. A continuous increase in oxygen pressure was evaluated in the following depositions. Because oxygen was introduced during deposition, a thin oxide layer formed on the surface of the deposited aluminium. This oxide layer acted as a protective barrier, preventing further oxidation of the underlying aluminium. Controlling the presence of oxygen during deposition revealed that the presence or absence of oxygen altered the characteristics of the deposited granular aluminium substantially. While oxygen-free deposition produced pure aluminium, regulated oxygen presence resulted in the creation of a protective oxide layer. The influence of the deposition technique was also evaluated.

SEM and AFM were used to investigate the morphology of the granular aluminium films for both deposition processes, yielding useful information on their surface properties, grain structures, and topography. SEM analysis gave high-resolution pictures that allowed for the imaging of grain boundaries, and film thickness, whereas AFM analysis provided nanoscale resolution that allowed for the evaluation of particle size distribution and, surface roughness. Using these complimentary methodologies, researchers gained a full understanding of the morphological features of granular aluminium films, allowing for future modification and development in their application-specific performance.

Four-point probe measurements were used to investigate the electrical properties of the granular aluminium films for both deposition processes, offering useful insights into their conductivity, resistivity, and electrical performance. Important electrical parameters such as the resistivity of the granular aluminium sheets were determined by examining the resistance and geometry of the probe setup. These electrical characterizations aided in understanding and optimizing the electrical behaviour of granular aluminium films for use in a variety of applications such as electronics, sensors, and energy storage.

In summary, the influence of oxygen during the deposition of granular aluminium plays a crucial role in determining the properties and performance of the deposited material independently of the deposition technique. Our comparative study reveals that while both electron beam evaporator and sputtering techniques

can produce granular aluminium films, there are subtle variations in their morphological, and electrical properties. Sputtering exhibits advantages in terms of lower resistivity and higher conductivity, likely due to its ability to produce films with stronger preferred crystallographic orientations. However, the electron beam evaporator may offer certain benefits such as simplicity of operation and higher surface roughness if required for specific applications. Ultimately, the choice of deposition technique depends on the desired film properties and the specific application requirements.

[1] A. Liu et al., Solar Energy Materials and Solar Cells 234 2022, 111447
[2] D. Dăscălescu et al., Chemosensors 9 2021
[3] R. Cohen et al. Physical Review 168.2 (1968) 444.

Measurement of short range PSF in EBL

J. Shapiro, M. Kahl, L.V. Litvin

Raith GmbH, Dortmund, 44263, Germany
e-mail: leonid.litvin@raith.de

Nowadays the simulated PSFs are often used for proximity effect correction and deliver rather acceptable result. However, sometimes inconsistencies occurred which could be overcome by adding additional heuristic term to simulated PSF [1]. The latter leads to the need for experimental verification of these PSFs. In this work we address the experimental measurement of PSFs with the purpose of developing a precise and reliable procedure.

The measurement of long- (LR) and mid-range (MR) parts of PSF can be easily achieved with established methods, e.g. [2], because these components have sizes which are usually larger than uncertainty introduced by resist thickness responsible for contrast formation in SEM. The short-range (SR) part of PSF can be very small, down to the size of few nanometers [3]. The lateral development of resist [4] and resist deformation during SEM imaging can considerably disturb the SR PSF. The measurement of SR PSF requires usually high-resolution SEM imaging of tiny amounts of resist under condition of essential noise of SEM signal. We decided that derivative of PSF - Line Spread Function (LSF) - is better suited for the purpose. LSF relies on exposure and width measurement of single pixel lines while traditional method [2] on that of single points. The width of line can be averaged along its length which makes the measurement more reliable and precise. Moreover, integration of LSF and normalization requirement can be used for validation.

In Fig 1 we show LSFs measured for Raith eLINE Plus by using 20 nm thick PMMA used as negative tone resist [5]. In case if the width of LSF exceeds the resist thickness (Fig 1a) the method works well. The normalization volume was 0.88, i.e., the contribution of all artefacts did not exceed 12% of its full volume. However, in case of finer beam diameter only part of LSF was measured (Fig 1b). The conclusion about size of PSF was not reliable. This happened due to lack of mechanical stability for developed line; narrow lines just were washed away because of too high aspect ratio. To overcome this a thinner resist should be used. We applied 13 nm HSQ resist and achieved a more convincing result (Fig 2). The electron beam of 350 pA generated the LSF of width of 10 nm with normalization volume close to 90%.
Our approach can be extended for complete PSF including SR, MR, and LR parts. It consisted in measuring LSF experimentally and approximating it by Gaussian and exponential terms.
In Figure 3 we demonstrate an LSF for a stack GaAs/CdTe/PMMA measured on 50 nm positive PMMA resist. Positive resist may distort the SR part, but for remaining parts our method delivered simple and easy way of measurement with good fidelity.
We conclude that the method of line exposures which backgrounds can be found in [4] works well for measurement of SR PSF in case of thin, negative resists. The essential distortion by lateral development that was found for PMMA [4] was not observed here. We managed to measure LSFs that were only 10 nm in width. We hope to explore even smaller PSFs by using thinner HSQ layers.

[1] G.G. Lopez et al., J. Vac. Sci. Technol. B 35 (2017) 06G505.
[2] S. Rishton et al., J. Vac. Sci. Technol. B 5 (1987) 135-141.
[3] V. Manfrinato et al., Nano Lett. 14 (2014) 4406-4412.
[4] S.V. Babin, A.A. Svintsov, Microelectron. Eng. 17 (1992) 417-420.
[5] H. Duan et al., J. Vac. Sci. Technol. B 28 (2010) C6C58-C6C62.

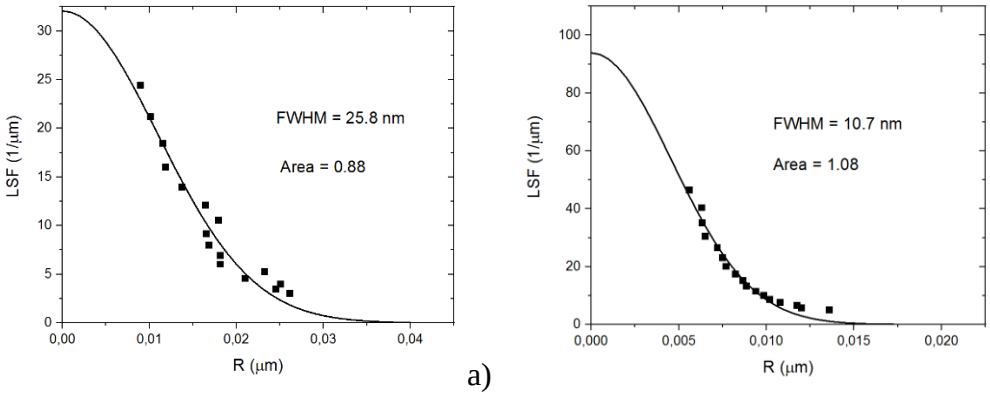

Figure 1. Measured SR LSFs (points) and Gaussian fit (lines) obtained for Raith eLINE Plus at 30kV on 20 nm thick PMMA used as negative resist: (a) – for beam current of 12 nA, (b) – for beam current of 350 pA.

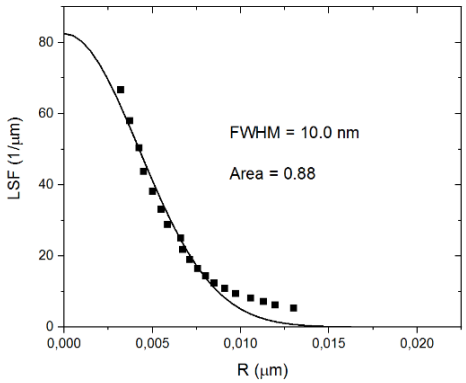

Figure 2. Measured SR LSF (points) and Gaussian fit to it (line) obtained for Raith eLINE Plus at 30 kV and at beam current of 350 pA on 13 nm thick HSQ resist.

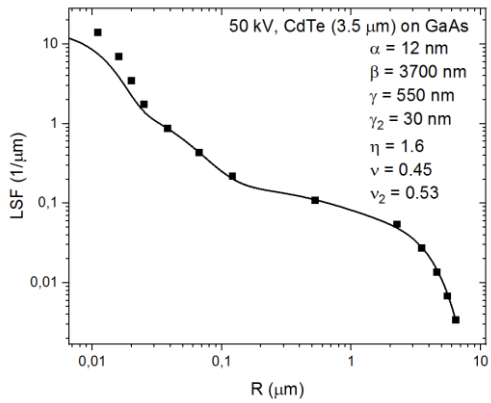

Figure 3. Measured complete LSF (points) for a stack GaAs/CdTe/PMMA and fit to it with function that includes two Gaussian and two exponential terms (line); Raith VOYAGER, 50 kV, 400 pA; resist thickness of 50 nm.

Micro/Nano fabrication of Bio wells: Comparison between Nanoimprint lithography and Nano 3D printing

Lubuna Shafeek[a], Jack Merrin[a], Salvatore Bagiante[a],
[a] Institute of Science and Technology Austria, Klosterneuburg, 3400, Austria
e-mail: lubuna.shafeek@ist.ac.at

Abstract
This study attempts to conduct a comparative investigation of two fabrication techniques for bio well fabrication: nanoimprint lithography (NIL) and Nano 3D printing. A major challenge for fabricating bio wells for biological applications is to develop a sustainable and compatible methods with specific tools. This research will evaluate the process flow related to product development, limitations, and suitability of these techniques for creating high-resolution, functional bio wells for biological applications. Current microfluidic devices are typically molded from polydimethylsiloxane (PDMS) on a glass substrate due to their transparency and biocompatibility[1]. Nanoimprint lithography is a top-down fabrication method that utilizes a mold to transfer a pattern onto a substrate through mechanical deformation or imprinting. On the other hand, Nano 3D printing is an additive manufacturing process that builds structures layer-by-layer from a liquid precursor using a technique called two-photon polymerization (2PP). In 2PP 3D printing, a high-power focused laser creates a nonlinear energy distribution centered at the laser focal point, whereby an excitation induces monomer crosslinking of the material, creating a three-dimensional nanostructure[2]. Both techniques were performed under optimized conditions to ensure bio wells' accurate and reproducible fabrication.

Method

Nanoimprint lithography method: Wafers fabricated by photolithography were used as templates (master wafers) for stamps with defined diameters and height[3]. The first step was to design the photomask using AutoCAD and convert the file to Gerber format using LINKCAD. A 5-inch quartz 1-micrometer resolution photo mask was fabricated from JD Photo Data, UK. To make the template for the PDMS stamp, spin coat a wafer with a 200-micron thick layer of SU8 GM1075 (Gersteltec, Switzerland) resist with a speed of 840 rpm followed by proper baking step. Once the wafer reached room temperature, the wafer was exposed at 1500mJ/cm^2 using EVG Mask Aligner 610 (EVG group, Austria) through a UV filter. After the exposure, a post exposure bakes at 95^{0}C for 1 hour. Propylene glycol methyl ether acetate (PGMEA) based developer was used to reveal the patterned structures. To get a clean structure and substrate surface, wafers were submerged in several baths of PGMEA before rinsing with isopropanol, followed by a hard bake of five minutes at 135°C (Fig 1). Before the stamp fabrication, the wafer surface was silanized with Trichloro-(1H, 1H, 2H, 2H-perfluoroctyl)-silane vapor over 12 hours (Fig 2). To make PDMS stamps, 50 g of elastomer and 5g curing agent (Sylgard 184) were mixed for 2 min in a Speedmixer, then poured into the master wafer and degassed in a desiccator then cured at 80°C overnights. Stamps with 9x9 mm cubes pressed into 12 mm diameter circle glass openings were made to transfer the pattern from the PDMS stamp to the Petri dishes. MY134 polymer (mypolymer.com) was used to make the bio compactable wells, two microliters of the MY 134 polymer were applied to the center of the dishes then pressed the PDMS stamp on onto the drop then, exposed the Petri dished with UV light for 2 hours in nitrogen atmosphere (Fig 3). Finally, the stamps were removed while pressing vertically down on PDMS (Fig 4).

Nano3D print method: Bio well dimensions of 200-micron diameter arrays were 3D printed on a NanoOne high-resolution 3D printer from biocompatible acrylate-based 2PP resins with the trade names Upflow (UpNano GmbH, Vienna, Austria). The required amount of Up flow was applied on the glass slide (Fig 5). Modeling of the 3D array was done within AutoCAD then the STL file format was imported into Think3D software (UpNano GmbH). The bio well array was printed in bottom-up mode using a 10×objective. An adapted print profile was used with a laser power setting of 400 mW to match the objective-material combination. Coarse printing mode was enabled for the optimal balance between printing resolution and speed. The final structure was achieved within a print time of 40 minutes (Fig 6). The bio well array was post processed and developed by sequential immersion PGMEA (1-Methoxy-2-propyl acetate) and isopropanol baths. Afterward, a post-curing step with UV light for 1 hour was required to get the final sample (Fig 7).

Result: Both techniques successfully created bio wells capable of accommodating cells and small volumes of liquids. The functionality of the bio wells was evaluated by examining their compatibility with biological samples and their ability to confine and manipulate fluids. Nano 3D printed bio wells offered superior resolution, precision, and versatility with high reproducibility. More surface characterization and multi-scale structures will be explored in the future.

Reference:

[1] Banik, S. et al. The revolution of PDMS microfluidics in cellular biology. Crit. Rev. Biotechnol. https://doi.org/10.1080/07388551. 2022.2034733 (2022).

[2] Rad, Z. F., Prewett, P. D. & Davies, G. J. High-resolution two-photon polymerization: The most versatile technique for the fabrication of microneedle arrays. Microsyst. Nanoeng. https://doi.org/10.1038/s41378-021-00298-3 (2021).

[3] J Renkawitz et al. Chapter 5 - Micro-engineered “pillar forests” to study cell migration in complex but controlled 3D environments, Methods in Cell Biology, Volume 147, ISSN 0091-679X, https://doi.org/10.1016/bs.mcb.2018.07.004

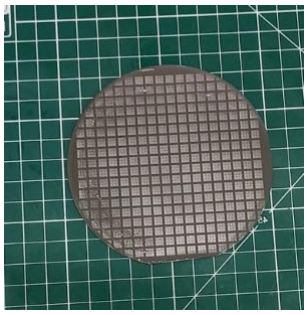

Fig1.
Master wafer

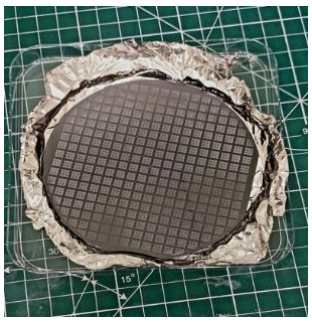

Fig 2.
Master wafer+PDMS

Fig 3.
PDMS stamp+MY134 polymer

Fig 4.
Bio polymer well

Fig 5.
Preparation of the sample

Fig 6.
Sample holder on the nano 3D printer

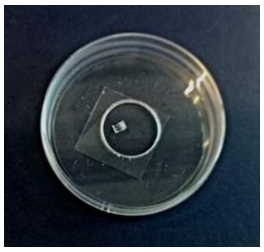

Fig 7.
3D printed bio well

Ion Beam Planarization using Solvent-Free Polymer Coatings

L. P. Lingenfelder [a], J. Zajadacz [a], G. Dornberg [a], A. Finzel [a], D. Schäfer [b], T. Hänsel [b], F. Frost [a]

[a] Leibniz-Institut für Oberflächenmodifizierung e.V. (IOM), Leipzig, 04318, Germany
[b] NTG Neue Technologien GmbH & Co. KG, Gelnhausen, 63571, Germany

e-mail: lukasp.lingenfelder@iom-leipzig.de

The manufacture of metal optics for high-precision optical processes is one of the key technologies in numerous growth markets. Coated or uncoated precision metal mirrors in various sizes and shapes are used wherever high performance, complex component shapes, temperature stability, low weight with high strength or simply the economic method of production preclude the use of glass optics. Such optics are manufactured on ultra-precise diamond turning machines, which guarantee the required surface accuracy for different surface shapes (flat, aspherical or free-form surfaces). However, diamond turning creates regular patterns (turning marks) on the machined surface and thus a residual roughness that limits the performance of the optics by scattering. One process to further reduce surface roughness is the process of ion beam planarization [1].

In ion beam planarization [2], thin, usually polymeric, sacrificial layers are applied to the surfaces to be planarized. Subsequently, an ion beam etching step is used to transfer the levelled surfaces into the optical surface (Figure 1). Thereby ideally the etch rate selectivity (substrate material to polymer layer) is set to about 1 by optimized ion beam parameters. Previous work has shown that this can reduce the roughness of diamond-turned NiP, for example, to approx. 30% of the initial value [3]. The degree of smoothing that can be achieved depends essentially on the leveling effect of the polymer layer, which is limited in particular by the evaporation of the solvent. In this study it is shown that the smoothing effect can be significantly increased by using a solvent-free nanoimprint resist and larger spatial wavelengths can also be smoothed. Due to the absence of a solvent, the coating can flow for up to several days after coating, filling long-wavelength structures better than solvent-containing coatings. The smoothing behavior is investigated for pre-structured Si wafers with line pattern of lateral structure sizes up to 450 µm and surface amplitude of 20 nm. The ion beam etching transfer is carried out with a broad beam ion source of the Kaufman type, whereby the influence of the etch selectivity (Si to photoresist) on the achievable degree of planarization is investigated.

The evolution of the surface topography of a typical Si test structure with 20 µm period during a complete planarization cycle (initial profile in Si (A), after resist coating (B) as well as (C) after adjusted ion beam planarization step) is summarized in Figure 2. The initial roughness of the Si-test structure was reduced here to 3.7% of the initial value in a single process run. Figure 3 shows the achievable degrees of planarization (DoP) as a function of the spatial wavelength (period) of the structures. Regardless of the period (here up to 30 µm), degrees of planarization < 10% can be achieved in this way, which is significantly better than when solvent-based photoresists are used. Additionally, Figure 4 illustrates the planarization results with a Ni-P sample.

Acknowledgements: The work was carried out within the joint project IONENPLAN, which was funded by the BMBF within the funding measure "KMU innovativ" (FKZ 02P19K551).

[1] Johnson, Leo F., and K. A. Ingersoll. "Ion polishing with the aid of a planarizing film." Applied Optics 22.8 (1983): 1165-1167.
[2] Frost, F., et al. "Large area smoothing of surfaces by ion bombardment: fundamentals and applications." Journal of Physics: Condensed Matter 21.22 (2009): 224026.
[3] Li, Yaguo, Hideo Takino, and Frank Frost. "Characteristics of diamond turned NiP smoothed with ion beam planarization technique." Journal of the European Optical Society-Rapid Publications 13 (2017): 1-5.

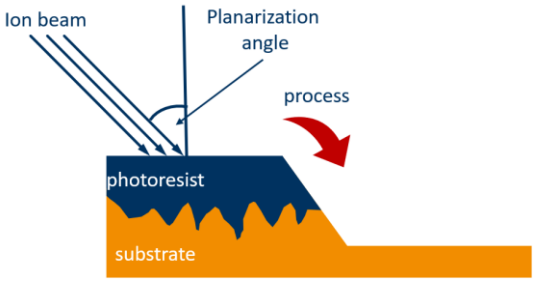

Figure 1. Schematic representation of the planarization process. A substrate material coated with photoresist is etched using RIBE. If the etch rate of the resist and the substrate are the same, the smooth surface of the resist is transferred into the substrate.

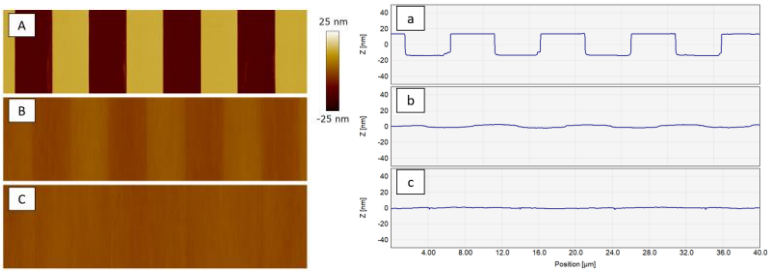

Figure 2. AFM 3D-images of a pre-structured Si-sample with a period of 20 µm before the planarization process (A) with an x-averaged profile (a); after coating with solvent-free resist (B) and (b); after RIBE etching step (C) and (c).

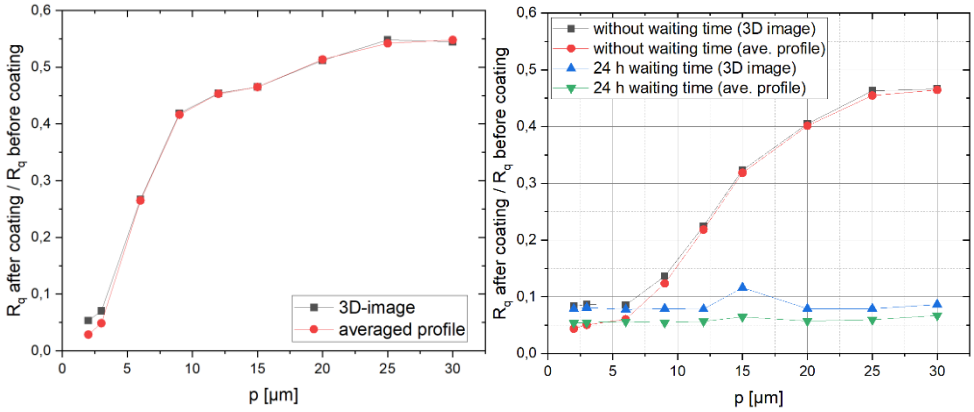

Figure 3. The degree of planarization (DoP) after applying the solvent-containing resist (left) and solvent-free resist (right) dependent on the lateral structure size is shown. Increased flowing-time of the solvent-free resist improves the DoP. The starting material was a silicon wafer structured with binary steps.

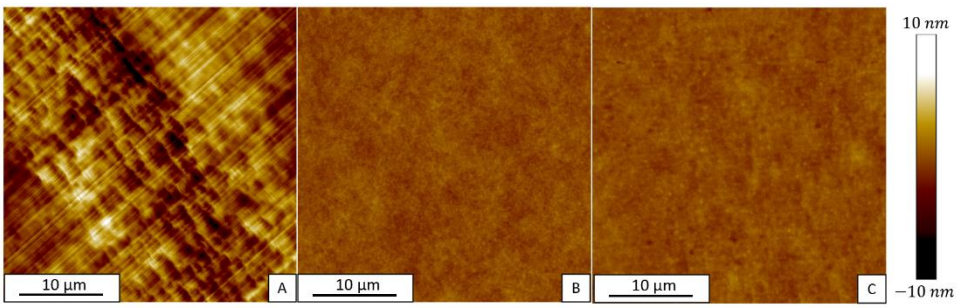

Figure 4. AFM images of a nickel-phosphorus sample before the planarization process (A), after coating with solvent-free resist (B), and after RIBE etching step (C).

SiOxNy Low Temperature Deposition at PECVD using Carbon-free Precursor

Youngju Ko [a], Hyeonjin Choi [b], Jaehee Kim [a], Jinmyeong Kim [b], Namgun Kim [a], and Heeyeop Chae [b,c]

[a] Department of Semiconductor and Display Engineering, Sungkyunkwan University (SKKU), Suwon 16419, Republic of Korea
[b] School of Chemical Engineering, Sungkyunkwan University (SKKU), Suwon 16419, Republic of Korea
[c] SKKU Advanced Institute of Nanotechnology (SAINT), Sungkyunkwan University (SKKU), Suwon 16419, Republic of Korea

e-mail: hchae@skku.edu

Silicon oxynitride (SiOxNy) finds extensive applications in various fields such as semiconductors, OLEDs, and solar cells [1]. In OLEDs, the demand for SiOxNy with excellent barrier properties and photo permeability is particularly high [2]. Organic layers integrated within OLEDs require thermal stability, necessitating low-temperature deposition processes. Several studies have explored Si source precursors for low-temperature deposition of SiOxNy [3,4]. However, existing precursors have all exhibited carbon contamination issues, which hinder the attainment of high film purity and reduced carbon emissions. In this study, trisilylamine (TSA), a carbon-free precursor, is investigated for low-temperature deposition of SiOxNy to enhance film purity and minimize carbon emission. The characteristics of the deposited films were modulated by varying the ratio of Si source precursor to oxygen gas. Higher Si source ratios resulted in an increase in refractive index (RI) up to 1.7, approaching the properties of silicon nitride, while higher oxygen gas ratios led to a decrease in RI down to 1.55, approaching the properties of silicon oxide. Additionally, the deposition rate exhibited variations ranging from 30 to 60 nm/min depending on the gas and power variables. Our findings demonstrate that low-temperature deposition of SiOxNy using TSA through the plasma-enhanced chemical vapor deposition (PECVD) method is feasible. This research not only offers insights into the control of film properties by adjusting precursor and gas ratios but also presents a practical approach to achieve carbon-free SiOxNy deposition, enabling enhanced film purity and reduced carbon emissions.

[1] Y. Shi et al, Micromachines 10 (2019) 552
[2] Y. Miao, SID International Symposium Digest of Technical Papers 51 (2020) 180-183
[3] J. H. Lee, J. Korean Phys. Soc. 48 (2006) 89-92
[4] F. M. Piras, Surface & Coatings Technology 202 (2008) 1606-1614

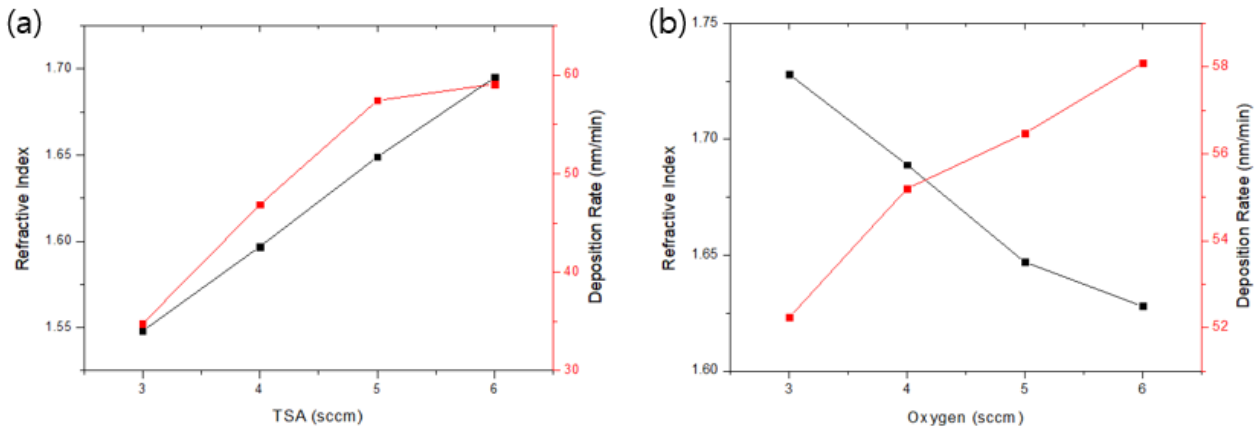

Figure 1. (a) Relationship between Refractive Index and Deposition Rate according to TSA flow rate. (b) Relationship between Refractive Index and Deposition Rate according to Oxygen flow rate.

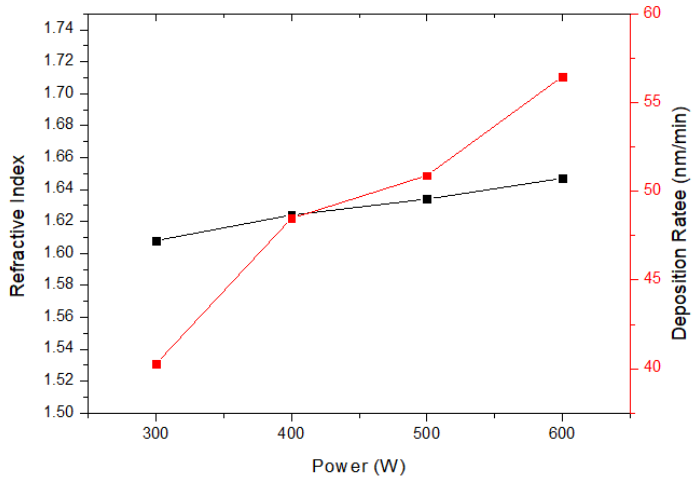

Figure 2. Changes in Refractive Index and Deposition Rate according to source power

Fabrication of micro-patterned β-Ga_2O_3 thin films by selective solid-phase crystallization via room-temperature excimer laser annealing

Daishi Shiojiri[*a], Satoru Kaneko [a,b], Ryoya Kai [b], Akifumi Matsuda [b], Mamoru Yoshimoto [b]

[a] Kanagawa Institute of Industrial Science and Technology,
705-1 Shimoimaizumi, Ebina-shi, Kanagawa, 243-0435, Japan
[b] Department of Materials Science and Engineering, Tokyo Institute of Technology,
4259 Nagatsuta, Midori-ku, Yokohama-shi, Kanagawa, 226-8502, Japan
[*]e-mail: d-shiojiri@kistec.jp

Wide band gap semiconductors have been extensively investigated for use in various device applications that take advantage of their excellent electronic and optical properties such as a combination of visible light transparency with electrical conductivity, high voltage resistance, and ultraviolet (UV) light emission and absorption. To extend the range of applications and create new functionality using the high-power deep UV light, it is necessary to exploit the semiconductors with band gap (E_g) > 4 eV.

Beta gallium oxide (monoclinic, a = 1.221 nm, b = 0.304 nm, c = 0.580 nm, β = 103.830º) has been identified as a potential wide band gap semiconductor with the E_g of 4.9 eV, and is often referred to as β-Ga_2O_3. Because of the excellent properties such as a combination of visible light transparency with electrical conductivity and high voltage resistance, those epitaxial films are promising for a wide variety of UV optoelectronic applications and future high-power devices such as deep-UV transparent conductive oxides [1], ultraviolet photodetectors [2], and high breakdown voltage field effect transistor devices [3]. To enable the ultrafine device applications of the β-Ga_2O_3 thin films, smooth surfaces and interfaces are required with good crystallinity and high orientation for the development of atomically controlled structures. Therefore, lower temperature material processing would suppress the mutual interdiffusion of the elements and thermal surface roughening. The low-temperature (LT) fabrication of crystalline thin films using a thermodynamically non-equilibrium process would also enable the development of metastable phases and atomically controlled structures as well as novel electronic functionalization. However, epitaxial β-Ga_2O_3 thin films have been mostly prepared by such a relatively high-temperature thin film processes (> 500ºC), and there are few reports on LT fabrication techniques for β-Ga_2O_3 crystalline thin films.

Excimer laser annealing (ELA) has been widely used for the solid-phase crystallization of amorphous thin films at low-temperature such as the manufacture of large area poly-Si thin-film transistors in industry. Laser annealing process exhibits advantages of high photon energy and a lack of thermal effects in the non-irradiated area. Moreover, interfacial reaction will be suppressed because of the ultra-short time pulse laser annealing [4]. The crystallinity, grain structures, and physical properties of thin films are also controllable due to the ELA conditions.

In this study, we investigated the room-temperature (RT) fabrication of β-Ga_2O_3 crystalline thin films using the ELA process and its micro-patterning method. The effect of the ELA conditions on the crystallinity, surface morphology, and optical properties of Ga_2O_3 thin films was investigated. Approximately 70-nm-thick amorphous Ga_2O_3 thin films were deposited on α-Al_2O_3 (0001) substrates at RT (~20ºC; not heated) by the pulsed laser deposition (PLD) method using a focused KrF excimer laser (λ: 248 nm, pulse duration: 20 ns, fluence: 1.5 J/cm^2) and a sintered β-Ga_2O_3 target (99.99% purity). The O_2 pressure of the PLD chamber was kept at 1.0×10^{-5} Torr (base pressure: ~10^{-9} Torr). The distance between the substrate and the target was 50 mm. The substrate was ultrasonically cleaned with acetone and ethanol and then dried by dry nitrogen prior to installation into an ultra-high vacuum PLD chamber. The grown thin films were subsequently laser-annealed by irradiating the non-focused KrF excimer laser onto the film surface in air at RT. The laser fluence was set in the 150 mJ/cm^2 range, and the number of the irradiated laser shots was 500 at 5 Hz during the ELA.

Figure 1 presents the XRD $2\theta/\omega$ patterns of the Ga_2O_3 thin films deposited on the α-Al_2O_3 (0001) substrates (a) before and (b) after ELA. Diffraction peaks derived from β-Ga_2O_3 ($\bar{2}$01) plane and (101) plane appeared after ELA (ICDD: 1-87-1901). This indicates that highly oriented crystalline β-Ga_2O_3 thin films were obtained by a combination of RT PLD and the subsequent ELA process.

The surface morphologies of the Ga_2O_3 films (a) before and (b) after ELA are shown in Figure 2. The crystallized films revealed a slightly roughened and cracked surface. This surface alternation is attributed to the volumetric shrinkage caused by crystallization and sintering by ELA.

RT micro-patterning of β-Ga_2O_3 thin films using RT ELA and subsequent RT wet etching was also investigated. Figure 3 presents the procedure of the β-Ga_2O_3 micro patterns on the α-Al_2O_3 substrate. An amorphous Ga_2O_3 thin film with the thickness of ~60–80 nm was deposited on an α-Al_2O_3 (0001) substrate at RT. The grown thin films were subsequently laser-annealed by irradiating the non-focused KrF excimer laser onto the film surface in air at RT through a mask of gold mesh, and then, wet etching was carried out with H_3PO_4 solution (40% concentration) and ultrasonic vibration for 30 min at RT to remove non-crystallized area. Figure 4 shows the cross-sectional height profile of the sample after etching. Formation of the micro-wall was caused by the selective etching of the amorphous phase. These micro-patterns on the sapphire substrates are seems to be applied to the fields of optoelectronic devices.

References

[1] E. G. Víllora et al., and K. Aoki, Appl. Phys. Lett. 92, (2008) 202120.
[2] T. Oshima et al., Jpn. J. Appl. Phys. 46, (2007) 7217.
[3] M. Higashiwaki et al., Appl. Phys. Lett. 100, (2012) 013504.
[4] T. Tsuchiya et al., J. Phys. Conf. Ser. 59, (2007) 224-229.

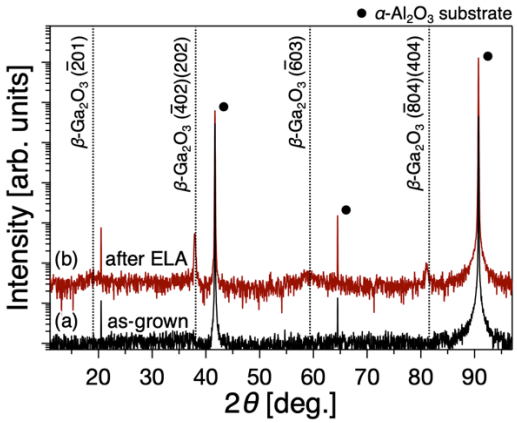

Figure 1 XRD $2\theta/\omega$ patterns of the Ga_2O_3 thin films (a) before and (b) after ELA.

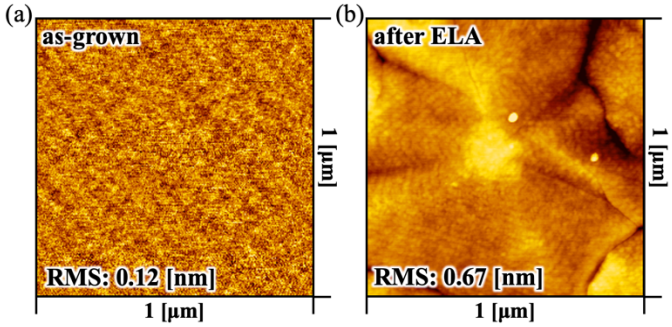

Figure 2 AFM images of (a) the as-grown and (b) the laser annealed Ga_2O_3 thin films.

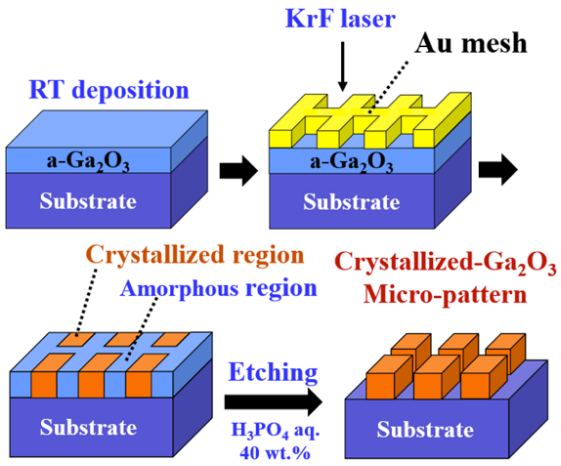

Figure 3 Procedure of the micro-patterned β-Ga_2O_3 thin film by ELA and wet etching.

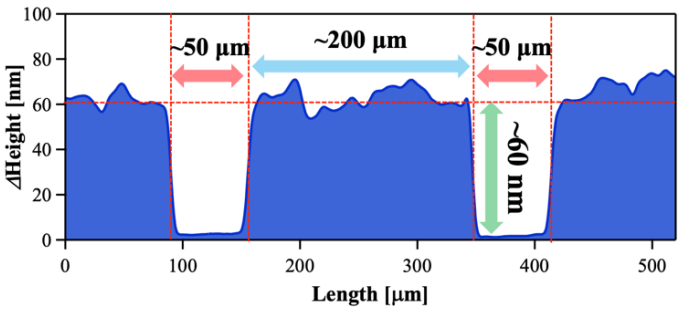

Figure 4 Cross-sectional profile of the micro-patterned β-Ga_2O_3 thin film.

Enhancing Electroplating Uniformity for 30 nm Resolution Charts through Graphic Auxiliary Approach

Qiucheng Chen, Xujie Tong, Chengyang mu, Qingxin Wu, Jun Zhao, Yifang Chen*

Nanolithography and Application Research Group, School of Information Science and Technology, Fudan University, Shanghai 200433, People's Republic of China
e-mail: yifangchen@fudan.edu.cn

Keywords: resolution chart, x ray, nanofabrication, Monte Carlo simulation, electroplating

X-ray microscopy, such as scanning transmitted (STXM) [1] and full-field transmitted (TXM) [2], offers superior resolution, non-destructive, non-contact and multi-scale imaging capabilities in contrast to traditional imaging methods. Fresnel zone plate, serving as an optical component for X-ray focusing, significantly influences imaging quality and contrast [3]. Furthermore, the resolution chart plays a crucial role as a diagnostic tool for testing the resolution of zone plates. However, during the electroplating of high-resolution charts, inadequate plating thickness may occur due to the low current density at narrow lines, resulting in adverse effects on high-resolution imaging quality.

This paper presents a novel approach for the fabrication of a 30 nm resolution chart by incorporating a graphic auxiliary design. The 30 nm resolution charts in this paper is fabricated by electron beam lithography and electroplating processes (Fig. 1). Firstly, a uniform layer of 1.5 μm thick PMMA resist (MW: 350 K) was spin-coated onto the membrane with a seed layer comprising 5 nm Cr/15 nm, followed by baking at 180 °C for 1 hour. Secondly, the resolution chart was exposed using the JEOL 6300FS e-beam writer at 100 kV, with a beam current of 500 pA. After exposure, the samples underwent development in a 1:3 mixture of methyl isobutyl ketone (MIBK) and iso-propyl alcohol (IPA) at 23 °C for 60 seconds. Lastly, the Au electroplating process employed a K3Au(SO3)2 electrolyte at 50 °C. Finally, a lift-off process was performed using 50 °C acetone for 10 minutes.

For the Monte Carlo simulations, the TRACER-BEAMER-LAB software provided by GenLSys Ltd was utilized. To enhance the current density during electroplating at the 30 nm linewidth, a compensating ring was introduced (Fig. 2b). However, the linewidth of the chart broadened from 30 nm (Fig. 2g) to 35 nm (Fig. 2h) due to proximity effects. An optimal auxiliary ring was designed (Fig. 2c) and preserved the desired 30 nm linewidth while incorporating the auxiliary design (Fig. 2i). Finally, the 30 nm resolution charts with and without the auxiliary ring were fabricated. The charts with an auxiliary ring (Fig. 3b) exhibit more uniform electroplating thickness compared to charts without an auxiliary ring (Fig. 3a).

This paper presents a novel approach utilizing Monte Carlo simulations to design an auxiliary ring, which effectively compensates for the electroplating speed while maintaining a high resolution of 30 nm for the test card. These advancements pave the way for promising prospects in high-resolution and high-efficiency X-ray imaging in the future.

Reference:

[1] H. Rarback, J.M. Kenney, J. Kirz, M.R. Howells, P. Chang, P.J. Coane, R. Feder, P.J. Houzego, D.P. Kern, D. Sayre, Recent Results from the Stony Brook Scanning Microscope, (1984) 203–216. https://doi.org/10.1007/978-3-540-38833-3_22.
[2] B. Niemann, D. Rudolph, G. Schmahl, X-ray microscopy with synchrotron radiation, Appl. Opt. 15 (1976) 1883. https://doi.org/10.1364/AO.15.001883.
[3] V. V. Lider, Zone Plates for X-Ray Focusing (Review), J. Surf. Investig. 11 (2017) 1113–1127. https://doi.org/10.1134/S1027451017060155.

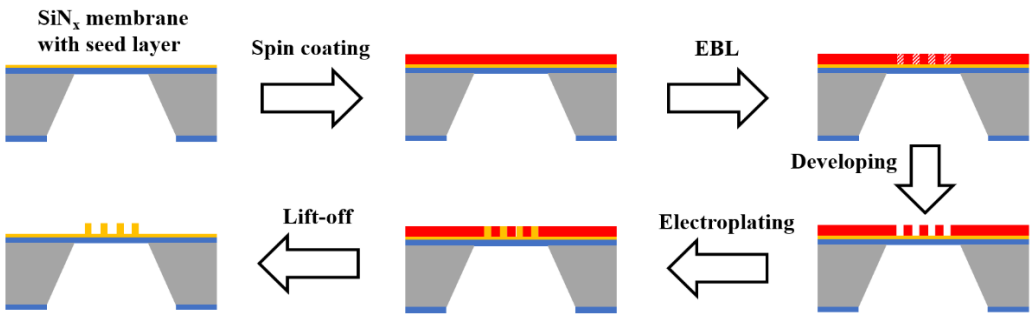

Figure 1. A schematic diagram describing the process flow.

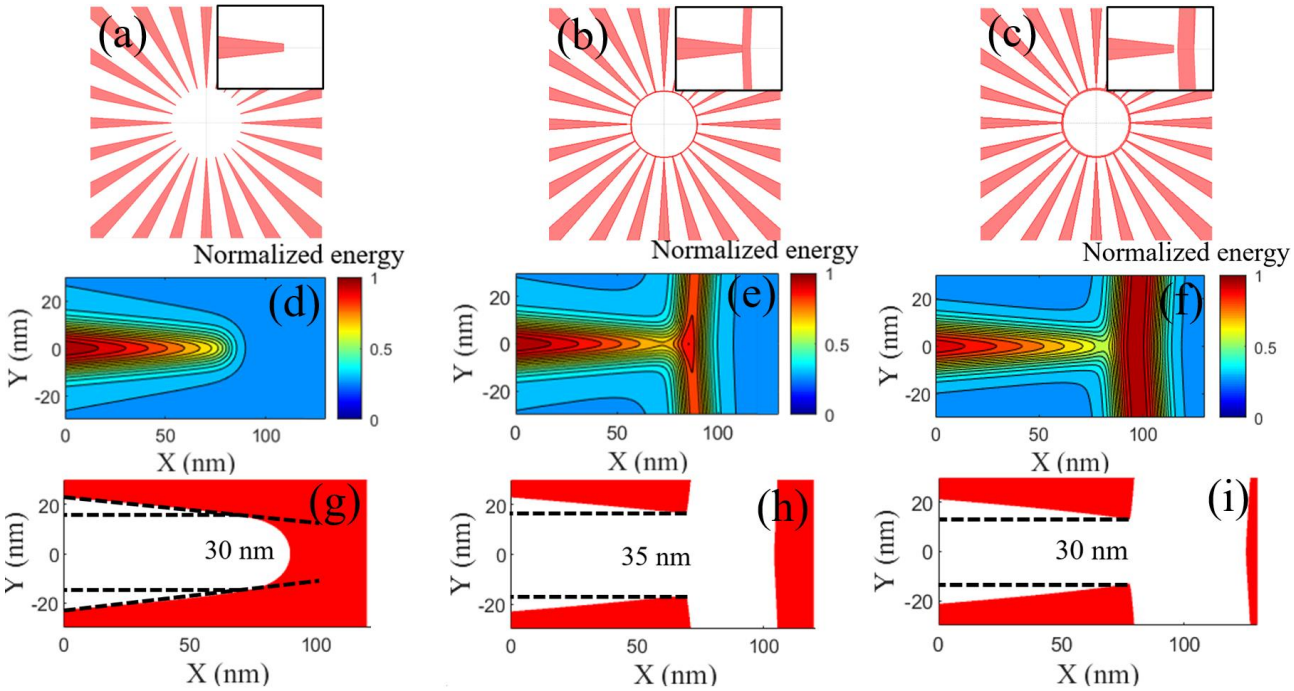

Figure 2. (a-c) EBL exposure layout pattern. (d-f) The deposited energy distribution (normalized) of a single star-shaped line after exposure in PMMA at middle height. (g-i) Resist profile after development at middle height. They correspond to lithography patterns without an auxiliary ring, with a 10 nm auxiliary ring, and with a 20 nm auxiliary ring and a 5 nm gap respectively.

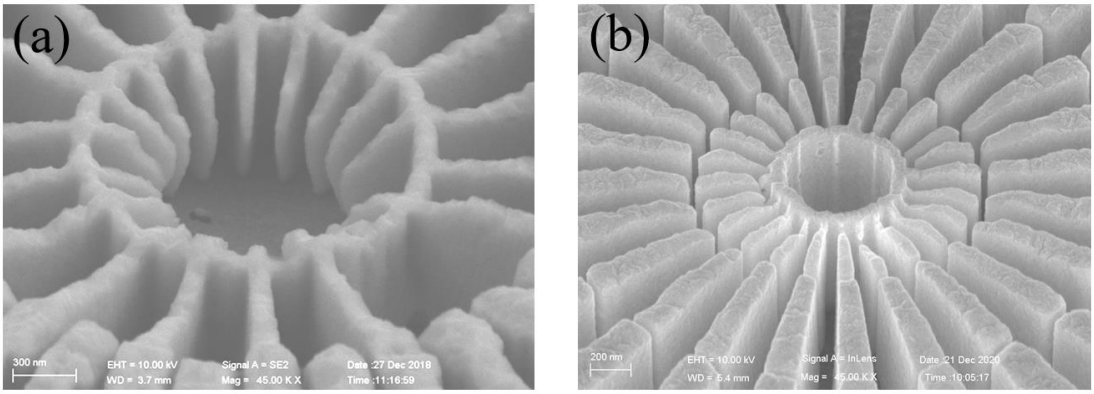

Figure 3. The SEM images of fabricated 30 nm resolution charts (a) without an auxiliary ring and (b) with an auxiliary ring.

Nanofabrication of randomly distributed hole array for coherent diffraction imaging in soft X-ray

Xujie Tong, Chengyang mu, Yijie Li and Yifang Chen*
Nanolithography and Application Research Group
School of Information Science and Technology, Fudan University, Shanghai 200433, China
* e-mail: yifangchen@fudan.edu.cn

Keywords: electron beam lithography, diffraction imaging, corner proximity effect correction, Au electroplating

Ghost imaging was originally called quantum correlation imaging, also known as single-pixel camera imaging, which is a new imaging technology as shown in Fig.1 (a). Computational ghost imaging (CGI) method can perform intensity-only imaging with single pixel. Compared with traditional X-ray imaging systems, X-ray CGI is more attractive due to its prominence of higher resolution, higher detectivity and more robustness. However, a series of X-ray ghost imaging optics with large area (>1mm*1mm) and high quality are technically challenging, especially for those with small (<200nm) and dense feature.

In this work, we propose a novel routine of random binary mask and gratings for X-ray ghost imaging (Fig.1 (b)). A 300-nm thick PMMA was spin coated on an in-house made 100-nm thick Si_3N_4 membrane with a pre-grown 5 nm Cr/10 nm Au as a seeding layer for electroplating. Electron beam exposure was carried out by JEOL 6300 FS at 100 kV. Development in THAM:IPA (1:3) was done at 23 °C for 1 min, then rinsed in de-ionized water for 30 seconds. Finally, the golden masks were formed by electroplating of Au using the replicated resist as the template in a $K_3Au(SO_3)_2$ electrolyte (10 g/L 50 °C). A constant current of 3 μA was applied in the plating for 5~10 min. A lift-off process in acetone was undertaken to wash away the resist.

Before the pattern transfer by Au electroplating, systematic study of the effect of dose distribution was conducted. Proximity effect correction for each unit of the random binary mask was carefully performed to ensure the pattern has square corners (Fig. 2 (a)). The dose of outer corner was decreased 10% by the software of BEAMER (GenLsys Ltd). The result was presented in Fig. 2 (b-d). For grating mask, periods of 460 small gratings vary between 200nm and 3700nm (Fig. 3(a)), which would be strongly affected by proximity effect. According to Fig. 1 (c), a process window was found at around 860μC/cm^2 to ensure that all grating can be prepared with good duty cycle. The results are shown in Fig. 3 (b-d). The micrographs of two masks after plating both show smooth surface and ideal duty cycle.

By summary, a novel and feasible method to fabricate X-ray ghost imaging optics by e-beam lithography has been attempted. The random binary mask (1.1mm*1.1mm) with square holes (200nm*200nm) and grating mask (1.5mm*1.5mm) with 460 small gratings (20μm*20μm) were obtained. With the feasibility of fabricating X-ray ghost imaging optics, cheap and low radiation dose X-ray ghost imaging technology will be expected to expand to X-ray tomography ghost imaging, X-ray diffraction microscopy ghost imaging, dark field ghost imaging, and isotope-labeled multipara metric ghost imaging.

[1] Z. Tan, H. Yu, R. Zhu, R. Lu, S. Han, C. Xue, S. Yang et al. Physical Review A. 106 (2022) 5.

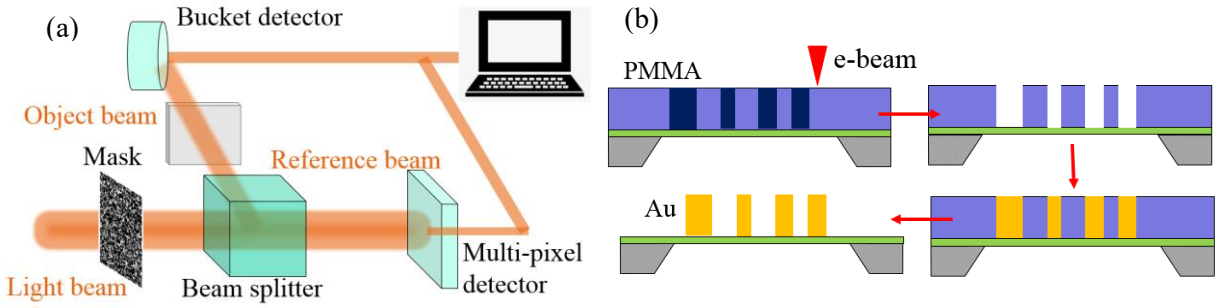

Fig.1 (a) The schematic of ghost imaging system; (b) The process flow.

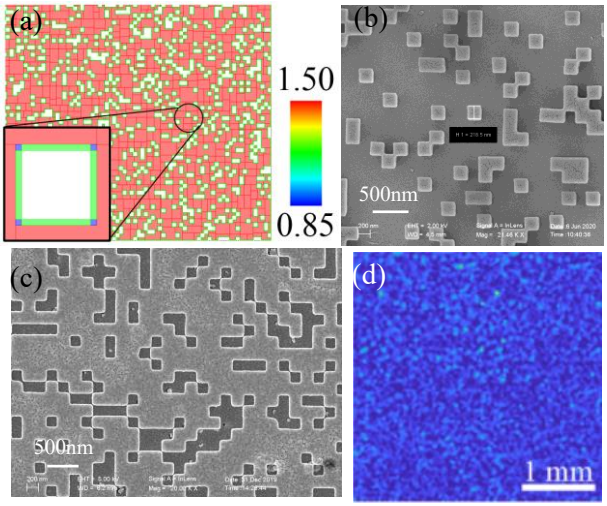

Fig.2 (a) Illustration of corner proximity effect correction of random binary mask; (b) Micrographs by scanning electron microscope of PMMA template; (c) Micrographs of random binary mask after electroplating. (d) Investigation on the characteristics of the speckle field with a 50 × 50 μm^2 square aperture in the optical path. Intensity distribution obtained by experiment[1].

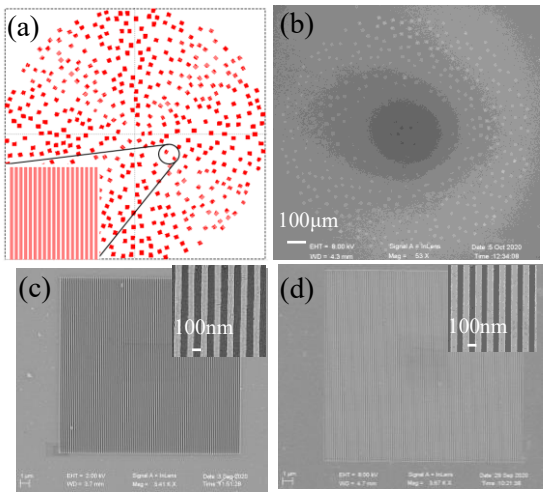

Fig.3 (a) Illustration of PMMA template of grating mask; (b) Micrographs of the whole grating mask after electroplating; (c) Micrographs by scanning electron microscope of PMMA template of single grating with a period of 200 nm; (d) Micrographs by scanning electron microscope of single grating with a period of 200 nm after electroplating.

Nanofabrication of 10 nm resolution compound Kinoform zone plate with high efficiency in soft X-ray

Xujie Tong, Chengyang Mu, Qiucheng Chen, and Yifang Chen*
Nanolithography and Application Research Group
School of Information Science and Technology, Fudan University, Shanghai 200433, China
e-mail: yifangchen@fudan.edu.cn

Keywords: 10 nm resolution, Kinoform lens, high focusing efficiency, grayscale electron beam lithography, 3D proximity effect correction, X-ray microscopy

X-ray microscopy and spectroscopy with sub-10 nm resolution enable unique insights into integrated circuit, condensed matter and biological specimens. High-resolution X-ray lenses (<20nm) have been successfully prepared by electron beam lithography (EBL) and atomic layer deposition (ALD)[1]. However, their non-ideal zone plate structure and metal material with high absorption coefficients limit their diffractive focusing efficiency within 1-3%, especially in soft X-ray. Our earlier work shows that zone plates with parabolic shape, known as Kinoform lens, can achieve high focusing efficiency due to the continuous modulation of X-ray phase. Inspired by this, this work focuses on improving the focusing efficiency of 10 nm resolution X-ray microscopy by combing a trapezoidal Kinoform lens with zone-doubling zone plate lens.

Fig. 1(a) schematically illustrates the process flow of the compound Kinoform zone plate (CKZP). A 450-nm thick SiOx-based hydrogen silsesquioxane (HSQ) was spin coated on an in-house made 300-nm thick Si_3N_4 membrane. 3D greyscale electron beam lithography (GS-EBL)[2] was carried out by a beam-writer, JBX-6300 FS at 100 kV with an e-beam of 7 nm in diameter. Hot developing (70°C) in TMAH: H_2O (1:3) was applied. Finally, the compound lens was formed by coating a 10-nm-thick HfO_2 on the surfaces of the HSQ-Kinoform zones by ALD. To achieve the parabolic shape for the zones as illustrated in Fig. 1(b), exposure dose distributions were calculated by software of TRACER and LAB (GenLsys Ltd). Systematic study of the effect of developing temperature and exposure dose were conducted, as shown in Fig. 1 (c). Contrast curve with developing temperature of 70°C shows lower contrast compared with that of 50°C, which contributes to the formation of Kinoform profile as well as the removal of residual resist. Ridges with sub-100 nm features shows robustness to exposure dose (Fig. 1(d)). A process window was found between 8000 $\mu C/cm^2$ and 9500 $\mu C/cm^2$ to ensure that all ridges can be prepared with good profile. The micrographs by scanning electron microscope in Fig. 2 (a-d) show smooth surface and ideal duty cycle of CKZP. The outmost zone can be clearly resolved with zone width of 10 nm and its aspect ratio reaches 45:1. Optical performance of CKZP were shown in Fig.3. It was proved that the intensity of the 2-nd focus spot of HfO_2-CKZP improves by 72% compared with that of HfO_2-ZP in the X-ray energy of 1200 eV. The insert graph shows direct soft X-ray imaging at 15 nm resolution by the fabricated 15 nm CKZP[2] at 1200 eV for the Siemens star.

By summary, a compound Kinoform zone plate lens with high efficiency was developed using greyscale electron beam lithography and atomic layer deposition. The developed lens possesses broad prospect of applications in high-resolution X-ray microscopy with high efficiency.

References:

[1] Vila-Comamala J, Gorelick S, Farm E, Kewish C M, Diaz A et al. Optics Express. 19 (2011) 175-184.
[2] Tong X, Chen Y, Mu C, Chen Q, Zhang X et al. Nanotechnology. 34 (2023) 21.

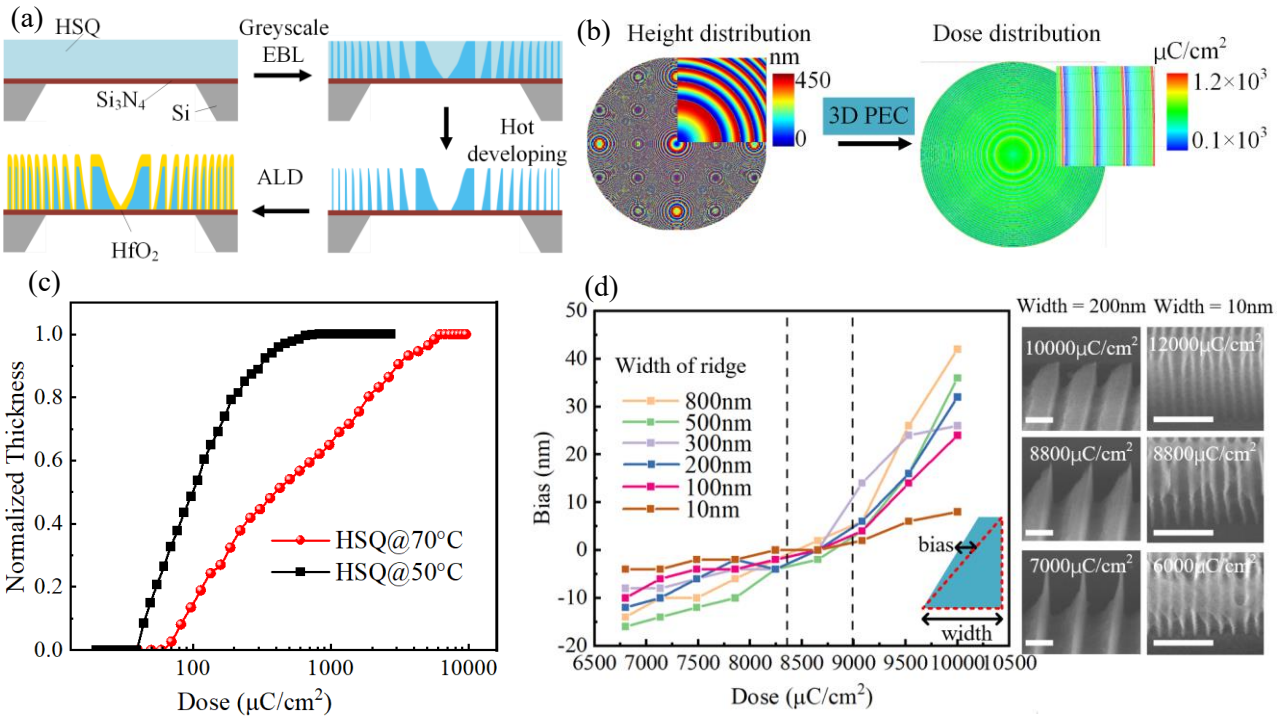

Fig.1 (a) The process flow; (b) Illustration of 3D PEC; (c) Contrast curves of HSQ at different developing temperature with developing time of 3 min; (d)Comparison curves of ridge width errors of HSQ-compond Kinoform zone plate with different periods. The scale bar is 200 nm.

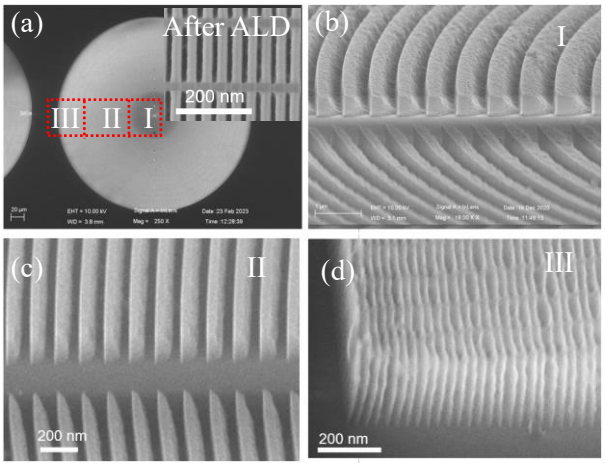

Fig.2 (a) Micrographs by scanning electron microscope of HSQ-compond Kinoform zone plate after HfO_2 coating; (b-d) The micrographs by SEM for the cross-sectional view at the tilt angle of 45° of the 10 nm zone template in HSQ before ALD.

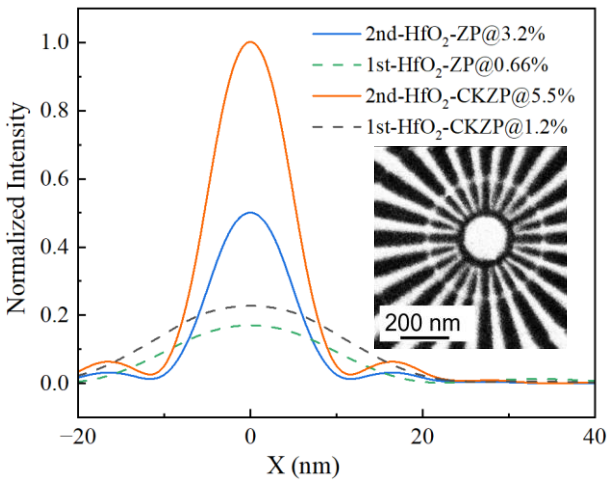

Fig.3 Calculation of the normalized intensities of the 1st and the 2nd order focal spots of zone plate and CKZP, respectively. The insert graph is the soft X-ray STXM image of the Siemens star, using the 15 nm HfO_2-HSQ-CKZP[2].

Atomic Layer Etching of Silicon Nitride with Plasma Oxidation and HF/NH3 Selective Gas Phase Etching

Sangwoo Kim [a, b], Ohchel Kwon [b], Hyeongkwon Jeong [b], Suhwan Park [b], Gwanwoo Min [b], Hyunseo Shim [c], and Heeyeop Chae [d, e]

[a] Department of Semiconductor and Display Engineering, College of Information and Communication Engineering (CICE), Sungkyunkwan University (SKKU), Suwon, 16419, Republic of Korea
[b] Global Manufacturing & Infra Technology, Samsung Electronics, Hwaseong, 18448, Republic of Korea
[c] Semiconductor R&D Center, Samsung Electronics, Hwaseong, 18448, Republic of Korea
[d] SKKU Advanced Institute of Nanotechnology (SAINT), Sungkyunkwan University (SKKU), Suwon, 16419, Republic of Korea
[e] School of Chemical Engineering, Sungkyunkwan University (SKKU), Suwon, 16419, Republic of Korea

e-mail: hchae@skku.edu

The atomic layer etching (ALE) methods of silicon nitride, which is used in various parts of the semiconductor manufacturing process, are being studied extensively. The current silicon nitride ALE techniques can be divided into ion bombardment [1], ammonium fluorosilicate (AFS) layer formation [2], and conversion etching [3]. In this work, a new type of silicon nitride atomic layer etching (ALE) method was developed using plasma oxidation and HF/NH_3 selective gas phase etching (GPE) process. The silicon nitride surface was oxidized with O radical in O_2 plasma, and oxidized surface was selectively etched by HF/NH_3 GPE process. The O_2 plasma generated oxidation layer on the silicon nitride surface. As shown in Figure 1(a), the oxidation depth was about 8Å thickness at 240 seconds which showed self-limiting characteristic. The percentage of O on silicon nitride surface was increased about 10.7% at the saturation point as shown in Figure 1(b). The etch amount of silicon nitride and silicon oxide was investigated with dependence of HF and NH_3 GPE time. The main etchant gas containing HF and NH_3 is quickly reacted with silicon oxide, but the silicon nitride needs more time to start the reaction compared to silicon oxide. At 2 seconds GPE process, the silicon nitride was hardly etched about 0.083Å but silicon oxide etch amount was about 19.7Å as shown in Figure 2. The silicon nitride was almost not etched in short time GPE process, so oxidation layer could be etched selectively with this short time process. The cycle process of 2 seconds GPE was developed to confirm whether the oxidation layer was selectively or completely removed. After three cycles of the GPE process, the oxidized silicon nitride thickness change was constant at around 7.98Å as shown in Figure 3(a), and the oxygen content was saturated at a level of 1.33% as shown in Figure 3(b). Therefore, it was determined that a minimum of three cycles GPE process was required to completely remove the oxidation layer and silicon nitride was almost not etched even after oxidation layer was fully removed. Finally, constant etch rate per cycle (EPC) was observed in this cyclic process with plasma oxidation and HF/NH_3 selective GPE process.

References

[1] Y. Ishii et al., Jpn. J. Appl. Phys. 56 (2017) 06HB07.
[2] K. Shinoda et al., J. Vac. Sci. Technol. A. 37 (2019) 051002.
[3] Aziz I. Abdulagatov et al., J. Vac. Sci. Technol. A. 38 (2020) 022607.

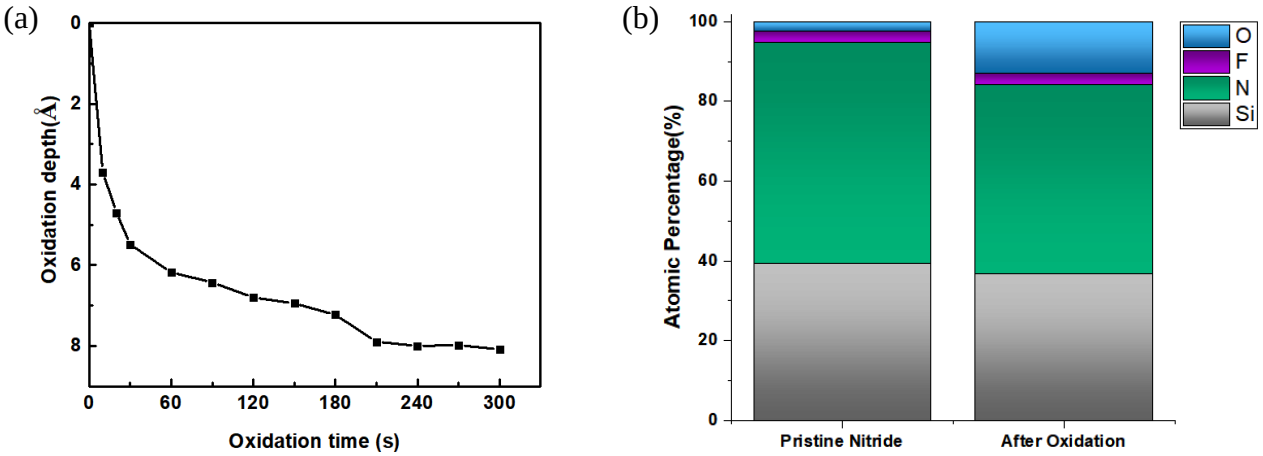

Figure 1. (a) Oxidation depth change as a function of oxidation time. (b) Surface composition of silicon nitride after 240s oxidation.

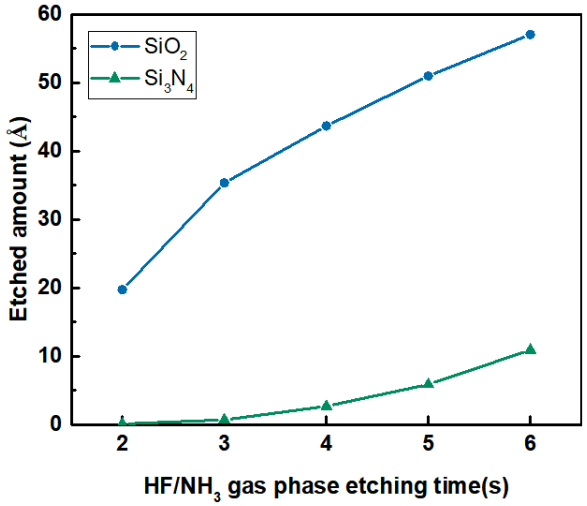

Figure 2. HF/NH3 gas phase etching time dependence of the silicon nitride and silicon oxide etched amount.

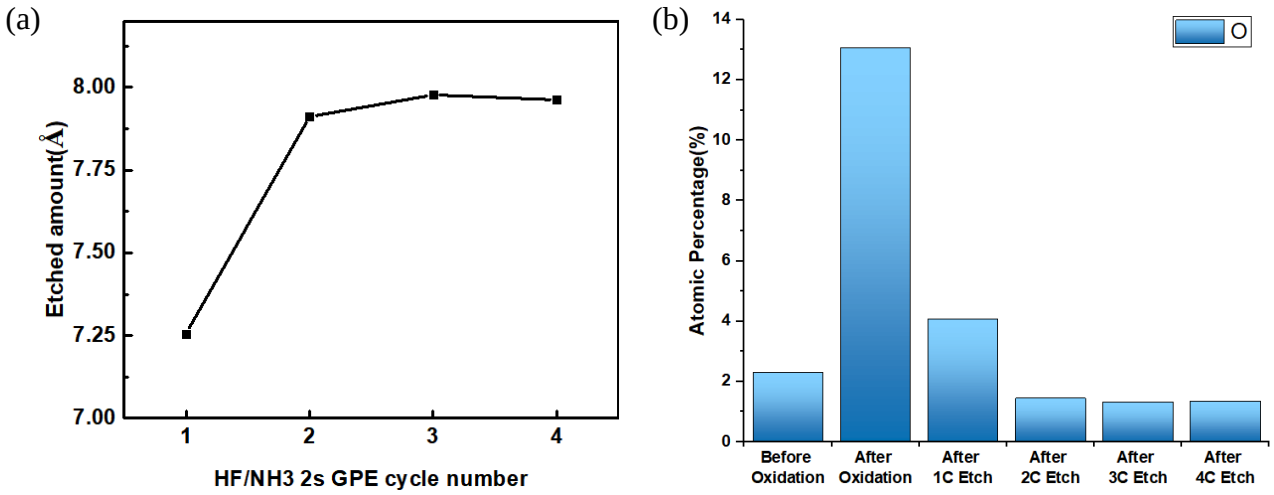

Figure 3. (a) Oxidized silicon nitride etched amount as a function of HF/NH3 2s GPE cycle number. (b) O atomic percentage change as a function of oxidation and HF/NH3 2s GPE cycle number.

Simulation study of three-dimensional grayscale ice lithography on amorphous solid water for blazed gratings

Jinyu Guo [a], Shuoqiu Tian [a], Wentao Yuan [a], Rui Zheng [b, c], Shan Wu [b, c], Ding Zhao [b, c], Yifang Chen [a,*] and Min Qiu [b, c, **]

[a] Nanolithography and Application Research Group, School of Information Science and Engineering, Fudan University, Shanghai 200433, China

[b] Key Laboratory of 3D Micro/Nano Fabrication and Characterization of Zhejiang Province, School of Engineering, Westlake University, Hangzhou 310024, China

[c] Institute of Advanced Technology, Westlake Institute for Advanced Study, Hangzhou 310024, China

e-mail: * yifangchen@fudan.edu.cn, ** qiu_lab@westlake.edu.cn

Abstract

Blazed grating is one of optical components with periodically inclined, subwavelength structures that enable to concentrate most diffracted light into a single narrow band in non-zero order with high diffraction efficiency and pleasurable image quality. To date, although a number of blazed gratings have been reported, their performance is still limited, owing to the capability limitation of electron beam lithography (EBL), which suffers from proximity effect. In recent years, EBL on amorphous solid water (ASW), known as ice lithography (IL), has emerged with the advantages in development-free, in-situ manufacturing and less proximity effect. The capability of 3D grayscale ice lithography has not yet been addressed. In this work, the feasibility of replicating blazed grating profiles by IL, with the maximum diffraction efficiency at 1550 nm for fiber optic communication is theoretically studied by using Monte Carlo simulation of IL, established in our earlier work [1, 2].

Fig. 1 schematically illustrates the fabrication process of the grayscale IL on ASW in an in-house developed cryogenic equipment of IL. Fig. 2 presents the normalized contrast curves for a 2-μm thick ASW and PMMA, respectively. The ASW exhibits a lower contrast than PMMA, which is considerably beneficial for grayscale IL. The designed cross-section structure of the blazed grating for 1550 nm wavelength is shown in Fig. 3. The pitch P is fixed to be 1 μm and the blazed angle α is designed as 50.8° to match the 1550 nm diffraction band, which is the biggest challenge in lithography for achieving such a specific facet. Grayscale EBL on both PMMA and ASW is carried out by Monte Carlo simulation. The theoretically replicated profiles are shown in Fig. 4. It can be seen that grayscale EBL on ASW fits the designed structure more closely than on PMMA. The theoretical cross-sectional shape of PMMA has an inward concave on the slope with an inclined sidewall due to proximity effect. By contrast, the slope facet of the blazed grating by IL on ASW has much better linearity, and the blazed angle is extremely close to the desired figure. No offset in the pitch direction can be observed between the designed structure and the simulated one. Fig. 5 shows simulated 3D structures of ASW and PMMA, respectively. Comparison of diffraction efficiency of blazed gratings by ASW and PMMA, respectively, is presented in Fig. 6, which shows the blazed wavelength of blazed grating on ASW be around 1550 nm and the diffraction efficiency peak remains at a high level, while for PMMA, the diffraction efficiency has a considerable blue shift in blazed wavelength, which causes a 10% loss in efficiency.

By summary, this paper proposes to apply grayscale e-beam lithography on amorphous solid water (IL) to replicate blazed grating templates. Numerical simulations demonstrate superior property of the blazed gratings by IL over EBL, which should offer a promising solution to the manufacturing of blazed gratings with high quality.

[1] J. Y. Guo, T. Liu, S. Q. Tian, W. T. Yuan, R. Zheng, S. Wu, D. Zhao, Y. F. Chen, and M. Qiu, A study of structural effect on the spectral property of metallic cross-hole array in mid-infrared wavelengths, Microelectron. Eng. 274 (2023).

[2] T. Liu, X. J. Tong, S. Q. Tian, Y. Y. Xie, M. S. Zhu, B. Feng, X. H. Pan, R. Zheng, S. Wu, D. Zhao, Y. F. Chen, B. R. Lu, and M. Qiu, Theoretical modeling of ice lithography on amorphous solid water, Nanoscale 14 (2022) 9045-9052.

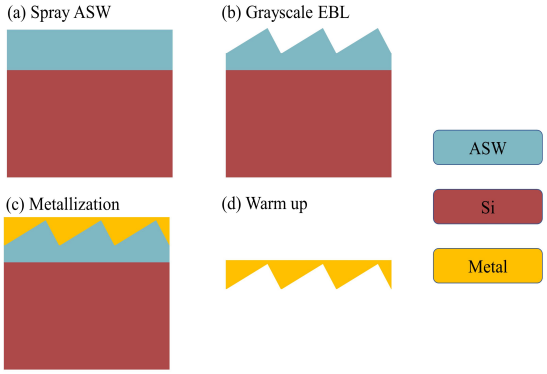

Figure 1. Schematic diagrams of the flow of grayscale EBL on ASW.

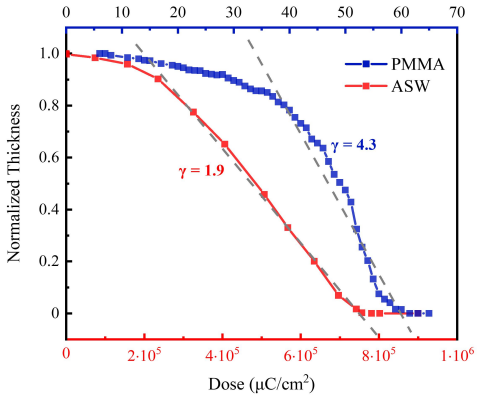

Figure 2. The normalized contrast curves for 2 μm thick ASW and PMMA.

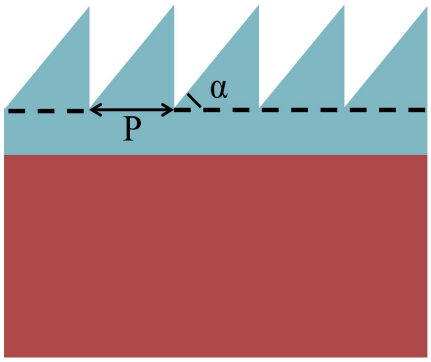

Figure 3. The layout of the section of the designed blazed grating template structure.

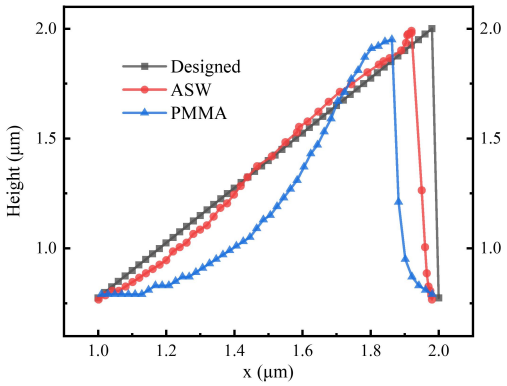

Figure 4. Comparison of detailed profile of single designed structure fabricated on ASW and PMMA .

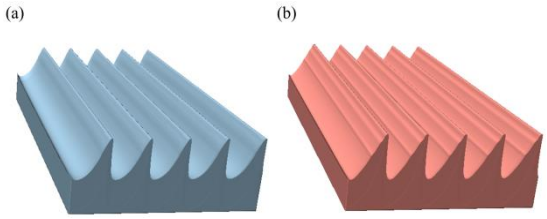

Figure 5. Comparison of the 3D profile of simulated blazed grating templates fabricated on PMMA (a) and ASW (b).

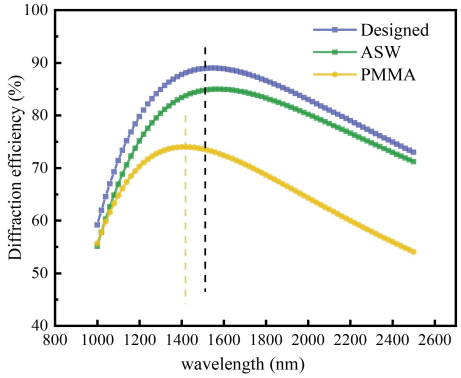

Figure 6. Comparison of diffraction efficiency of PMMA and ASW simulations of manufactured blazed gratings with theoretical one.

Metallization of UHMW-PE Fibers by Supercritical CO_2 Catalyzation toward Weavable Devices

Hikaru Kondo [a], Tomoyuki Kurioka [a], Wan-Ting Chiu [a], Chun-Yi Chen [a], Tso-Fu Mark Chang [a], Yamaguchi Machiko [b], Arisa Jinno [b], Hiromichi Kurosu [b], Masato Sone [a]

[a] Institute of Innovative Research, Tokyo Institute of Technology, Yokohama, 226-8503, Japan
[b] Cooperative Major in Human Centered Engineering, Nara Women's University, Nara 630-8506 Japan
e-mail: kondo@ames.pi.titech.ac.jp

Weavable devices are multifunctional fabric-based devices prepared by weaving various functional fibers into a single piece of fabric. Functional fibers possessing decent electrical conductivity are essential for weavable devices, and this can be realized by metallization of polymer fibers. [1] On the other hand, ensuring both sufficient electrical conductivity and stability in these metalized polymer fibers for practical device application remains challenging because of the difference in mechanical properties between the metal coating and polymer fiber, and this leads to insufficient adhesion between the two materials and defective results.

Recently, a metallization process by performing the catalyzation step of electroless plating in supercritical carbon dioxide ($scCO_2$) is reported to produce metallized polymers textiles possessing applicable electrical conductivity toward components in electronic devices and good adhesive properties between the metal coating and the polymer textile.[2] Nevertheless, it is necessary to metalize polymer fibers, instead of textiles, for design of weavable devices. Therefore, the purpose of this study is to functionalize fibers by adding conductivity to them. We also focused our attention on UHMW-PE fibers because of the recent interest in the realization of wearable devices.[3] Since UHMW-PE fibers are known for their excellent chemical and mechanical properties such as low density, chemical resistance, abrasion resistance, and impact resistance [4], functionalization of UHMW-PE fibers by adding conductivity could be useful for medical and military applications. However, there is limited reports on the functionalization of UHMW-PE fibers with electrical conductivity. Therefore, we aim to functionalize UHMW-PE fibers by Ni-P plating.

Surface morphologies of the Ni-P/UHMW-PE fibers were observed by an optical microscope (OM) as shown in Fig. 1. No obvious change was observed in the UHMW-PE fibers after the $scCO_2$ catalyzation step. Fig. 2 shows the elemental distribution of Pd on surfaces of the $scCO_2$ catalyzed UHMW-PE fibers by energy dispersive X-ray spectroscopy (EDS). The Pd signals are suggested to be originated the Pd catalyst. The EDS results confirmed successful decoration of Pd catalyst on to the UHMW-PE. Fig. 3 shows more detailed surface morphologies of the Ni-P/UHMW-PE with the plating time varied from 10 min to 60 min by scanning electron microscope (SEM) observations. The metallization appeared to be incomplete when the plating film was less than 15 min. When the plating time was increased to 30 min, complete coverage of Ni-P on the UHMW-PE fibers was confirmed. Fig. 4 shows the relationship between the electrical resistance of the Ni-P/UHMW-PE fibers and the plating time. The electrical resistance of the Ni-P/UHMW-PE fibers clearly decreased following an increase in the plating time. This result corresponded well the surface morphology results in Fig. 3.

In summary, UHMW-PE fibers were successfully metallized by electroless plating with the $scCO_2$ catalyzation. The Ni-P/UHMW-PE possessed decent electrical conductivity, and additional surface modifications by electrodeposition method would be possible. Also, by replacement reaction, the Ni-P could be replaced by a nobler metal to extend the application in varies field.

Acknowledgment
This work was supported by JSPS KAKENHI Grant Number JP21H01668 and JP21H00807.

References

[1] W.T. Chiu, Y. Tahara, C.Y. Chen, T.F.M. Chang, T. Hashimoto, H. Kurosu, M. Sone, Microelectron. Eng., 175 (2017) 34-37.
[2] K. Tokuoka, C.Y. Chen, T.F.M Chang, W.T. Chiu, H. Kurosu, M. Sone, Microelectron. Eng., 223 (2020) 111233.
[3] A.A. Candadai, E.J. Nadler, J.S. Burke, J.A. Weibel, A.M. Marconnet, scientific reports, (2021) 11:8705
[4] W. Zhang, Z. Hu, Y. Zhang, C. Lu, Y. Deng, Composites: Part B, 51 (20103) 276-281.

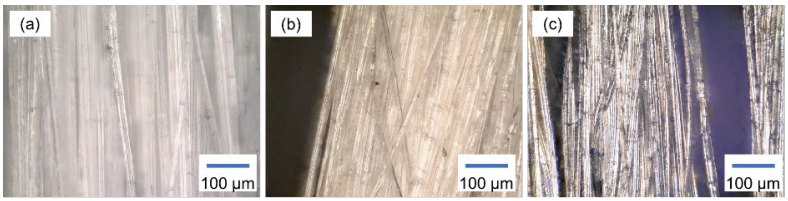

Figure 1. OM images of the (a) as-received UHMW-PE and (b) $scCO_2$ catalyzed UHMW-PE. UHMW-PE fiber and, (c) 10 min plated

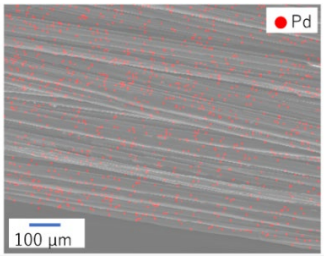

Figure 2. EDS mapping for palladium (Pd) on the catalyzed UHMW-PE

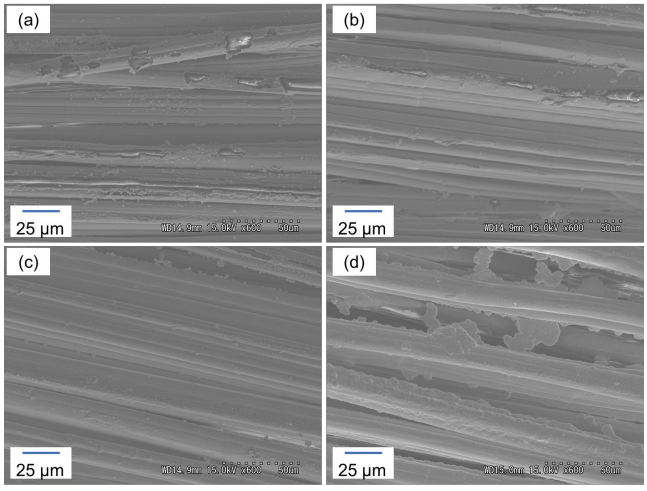

Figure 3. SEM images of the different plating time, (a) 10 min, (b) 15 min, (c) 30 min and, (d) 60 min.

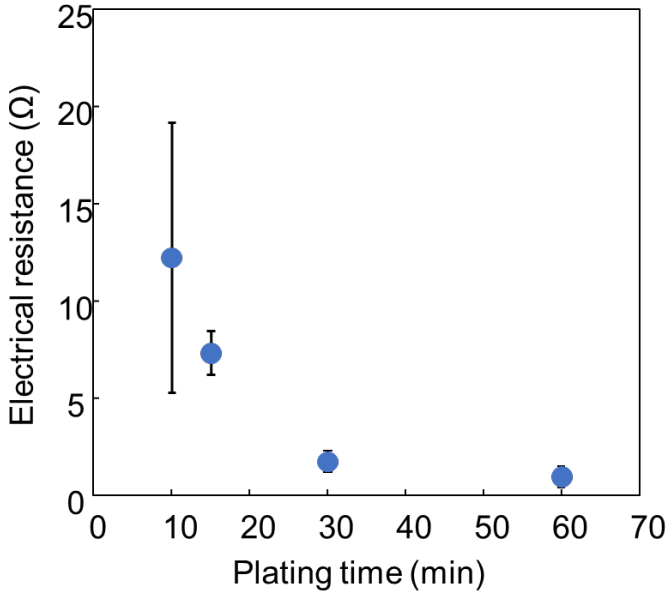

Figure 4. Relationship between the plating time and the electrical resistance of the Ni-P/UHMW-PE fibers.

Preparation of gold nanoparticle-hydrogel composite by room temperature electron reduction for catalytic applications

Min Fang [a], Chang-jun Liu [a,b]

[a] School of Chemical Engineering and Technology, Tianjin University, Tianjin 300072, China
[b] Collaborative Innovation Center of Chemical Science and Engineering, Tianjin 300072, China
e-mail: cjL@tju.edu.cn

Catalysis plays an extremely important role in production of chemicals and fuels. The use of catalyst has become one of the principals of green chemistry. With the developments of some specific catalytic applications, more and more uses of the soft supporting materials like peptides, polymers and hydrogels can be found in the literature. [1-4] Various technologies have been exploited for the preparation of the metal-soft material composite catalysts. A basic requirement of the such technologies is to operate at low temperatures to maintain the stability of the soft material. Considering the low temperature operation, our group has developed a room temperature electron reduction using the glow discharge plasma as the cheap source of electrons for the preparation of the catalysts with soft material as the support. [5-7]

Glow discharge is one of the cold plasma phenomena. It is normally operated at some vacuum. Compared with the thermal or chemical reduction methods, the room temperature electron reduction is simple, easy to manipulate, and compatible with the commonly used impregnation processes. It does not need the expensive or hazardous reducing agents. Argon, helium or even air can be used as the glow discharge forming gas. It can be easily turned on and off. [5-7] In this work, we report a preparation of gold nanoparticle-hydrogel composite by room temperature electron reduction. Figure 1 shows a schematical representative of the preparation of gold nanoparticle-hydrogel composite by room temperature electron reduction. A chloroauric acid solution ($HAuCl_4$) was loaded onto the surface of hydrogel dropwise. A glow discharge tube reactor (i.d.40 mm) was employed. The discharge tube is made of glass. Two metal electrodes are placed in the tube. The distance between the two electrodes was set at 100 mm. A dc high-voltage generator was used to generate glow discharge plasma. The hydrogel with the metal ion was placed in the center of the glow discharge tube that characterizes itself with highly energetic electrons at low gas temperature. The glow discharge was started at room temperature in this work. During the reduction, the gas temperature will have a slight increase but it is still in the room temperature range. Argon (>99.99% in purity) was used as the discharge-forming gas in this work. The pressure of the discharge tube was between 100 and 200 Pa. The applied voltage to the electrode was ca. 900V. To get enough metal loading, the electron reduction must be repeated for several ten times

Figure 2 shows the images of the obtained gold nanoparticle-hydrogel composite. The composite exhibits an apparent blue appearance when it is viewed in transmission light. However, a uniform and highly reflective golden metallic appearance when it is viewed in reflected light. The scanning electron microscopical (SEM) analyses were conducted to characterize the composite obtained. The SEM image demonstrates that the gold nanoparticles have been formed by the room temperature electron reduction. These nanoparticles are closely packed on the surface of hydrogel, as shown in Figure 3.

The Au nanoparticle-hydrogel composite by room-temperature electron reduction is an excellent catalyst for the reduction of methylene blue (MB) in the presence of $NaBH_4$, as shown in Figure 4. The absorption spectrum of MB was recorded as the evolution of reaction. The solution turns to be colorless from blue in 20 minutes. This confirms the gold nanoparticle-hydrogel composite is an excellent catalyst. From Figure 2c, the plasmon characteristic of the composite suggests it may have good activity for the photocatalytic conversion. It may have applications in the photo-electronic devices as well. We plan to confirm it in our future studies.

References

[1] W. Wang et al., Chem. Sci. 8 (2017) 3310-3324.
[2] J.K. Wychowaniecet al., Chem. Soc. Rev. 51 (2022) 9068-9126.
[3] Z. Wang et al., Chin. J. Catal. 42 (2021) 376–387.
[4] X. Lv et al., Euro. Polymer J. 182 (2023) 111713.
[5] C.-J. Liu et al., Chin. J. Catal. 37 (2016) 340–348.
[6] Z. Li et al., Carbohydrate Polymers 161 (2017) 270–276.
[7] Z. Wang et al., ACS Catal. 8 (2018) 2093−2110.

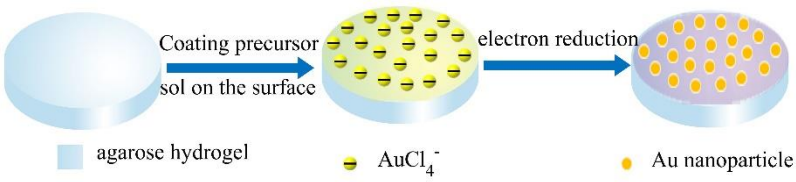

Figure 1. Schematical representative of the preparation of gold nanoparticle-hydrogel composite by room temperature electron reduction.

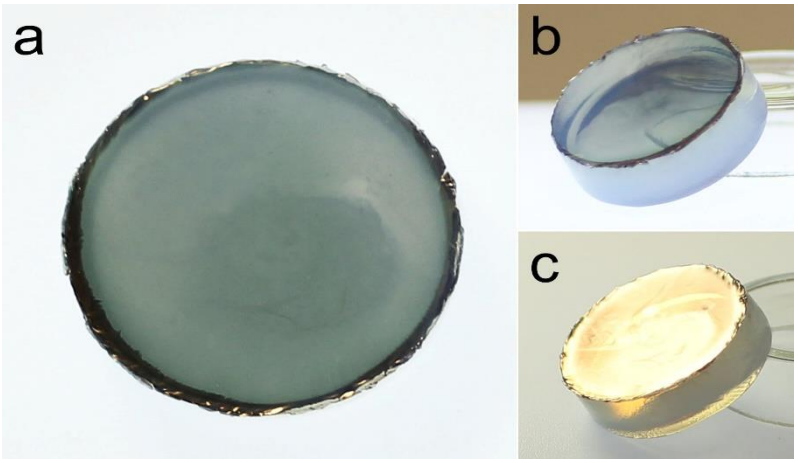

Figure 2. Images of the gold nanoparticle-hydrogel composite.

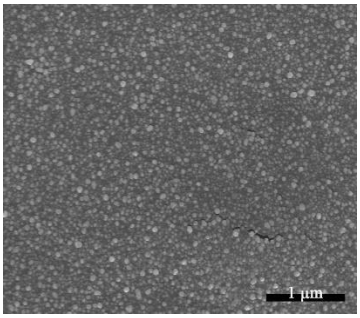

Figure 3. The SEM image of the gold nanoparticle-hydrogel composite.

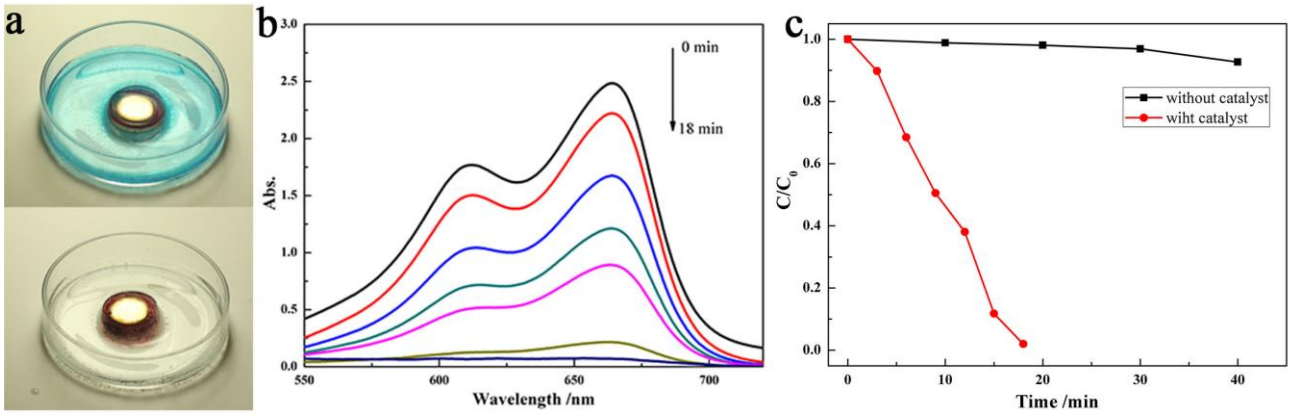

Figure 4. (a) Photographs of the MB solution with the composite catalyst before (up) and after 18 minutes (down). (b) UV-Vis spectra of MB reduced by the composite catalyst. (c) MB conversions with and without the composite catalyst.

Parallel Printing of Nanoliter Droplets with PDMS Nozzles Under Fluorinated Liquid

Muhammad Awais Maqbool [a], Shunya Okamoto [a], Takayuki Shibata [a], Moeto Nagai[a, b]
[a] Department of Mechanical Engineering, Toyohashi University of Technology
[b] Institute for Research on Next-generation Semiconductor and Sensing Science (IRES²),
E-mail: muhammad.awais.maqbool.me@tut.jp, awaisuet507@gmail.com, nagai@me.tut.ac.jp

Introduction:

Droplet microfluidics has a wide range of applications in biology, medicine, chemistry, and physics and it allows for high throughput treatment with a few microliters of sample with/without a small number of cells. It has attracted interest in large-scale drug research. Fluorinated liquid (FC-40) prevents the evaporation of droplets, and the printing of aqueous emulsion droplets has increased in popularity [1]. Recently, nL droplets have been printed with a single probe [2-3]. However, their limitation is printing one droplet at once. The increase in the number of droplets can be achieved by the parallelization of nozzles and the speed-up of a robot. We used a 3D printer and made four parallel nozzles and demonstrated the printing of nL droplets by contact printing under the fluorinated liquid and characterized the parallel printing.

Material and Methodology:

We designed a mold with a channel width of 200µm in CAD and printed it with an SLA 3D printer (Anycubic, Photon Ultra). The mold was replicated in PDMS with a base polymer to curing agent ratio of 10:1. After curing and cutting the device, the open side of the PDMS chip was bonded to a PDMS sheet. We cut at an angle and made sharp edges to reduce the contact area and surface tension. To print droplets autonomously, we made a droplet printer composed of a Cartesian robot (IAI, IK3-P6BBC31HHHS), microscope, and syringe pump (YMC, YSP-101) which was used to regulate a flow rate, Q and sizes of droplets, V_D (Fig.1a). Droplets were printed at a robot speed, V by contact printing method on a petri dish under FC-40 (Fig.1).

Results and Discussion:

Figs. 2(a),(b) show a PDMS printing head with sharp edges. Droplets were printed at various flow rates, Q. Droplets were printed at Q=3µL/min, V=10mm/s (Fig. 2c); Q=5µL/min, V=15mm/s (Fig. 2d); and Q=10µL/min, V=30mm/s (Fig. 2e). The smallest and greatest droplet sizes were 280µm (5.74nL) at Q=3µL/min, V=15 mm/s and 700µm (89.75nL) at Q=10µL/min, V=30 mm/s. We obtained the relationship between flow rate Q and speed V, as well as the size V_D and number of droplets, n. The results are depicted in Fig. 3 along with flow rate Q, and speed V. Droplet size increased with flow rate Q, this can be decreased by simultaneously raising the robot's speed. With increased speed V, there will be less time for droplets to become large and the robot will move to the next position and print out it before becoming larger. The size of the droplets, V_D is directly proportional to the flow rate Q and inversely proportional to the speed V.

Our system printed 4 times droplets at once and the sizes are smaller than the previous techniques [2-3]. There are some errors we are facing like all channel length does not remain equal because we are cutting manually by hand. Secondly, due to the softness and less thickness of the nozzle at outlets droplets position is disturbed when it comes down with high speed as you can see in Fig.2 (e).

Conclusion:

Parallel nozzles printed four droplets at a time underneath the fluorinated liquid while evaporation and contamination were prevented. The number of nozzles can be increased to 16, and a resister-type microfluidic nozzle will be added for creating chemical concentration gradients.

References:

[1] Zhu, Y., Piehowski, P.D., Zhao, R. et al. Nat Commun 9, 882(2018).
[2] Muhammad Awais Maqbool, et al., RoboMech Journal 2023 (Under review)
[3] Muhamamd Awais Maqbool, et al., IEEE MHS 2022 Paper ID: 2201 (In press).

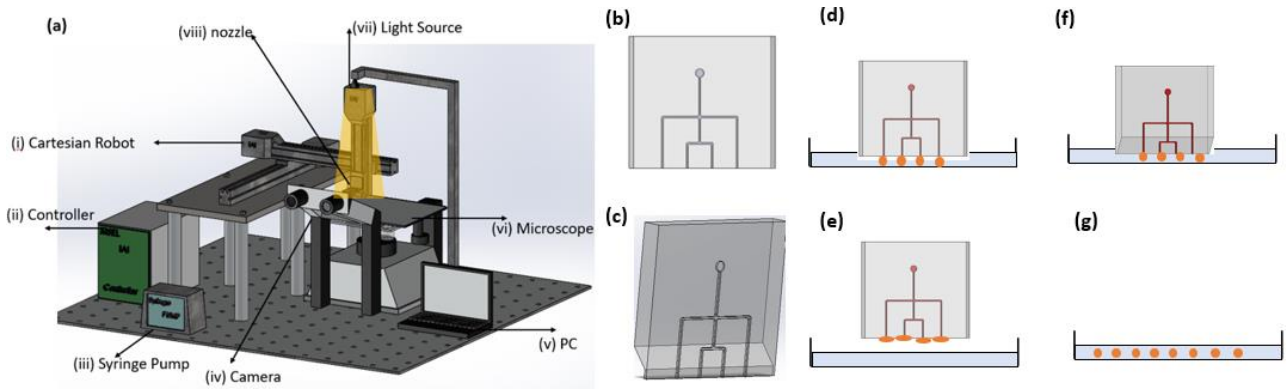

Fig. 1(a) Designed Setup Automated droplets printer with the Cartesian robot **(b)** Plane parallel nozzle. **(c)** Cut nozzle to make edges sharpened **(d)** Bring nozzle down to print droplets inside FC-40 **(e)** In the results droplets become flat with the surface of the nozzle **(f)** Nozzle with sharp edge bring down to print droplets inside the FC-40 **(g)** Printed droplets inside the FC-40

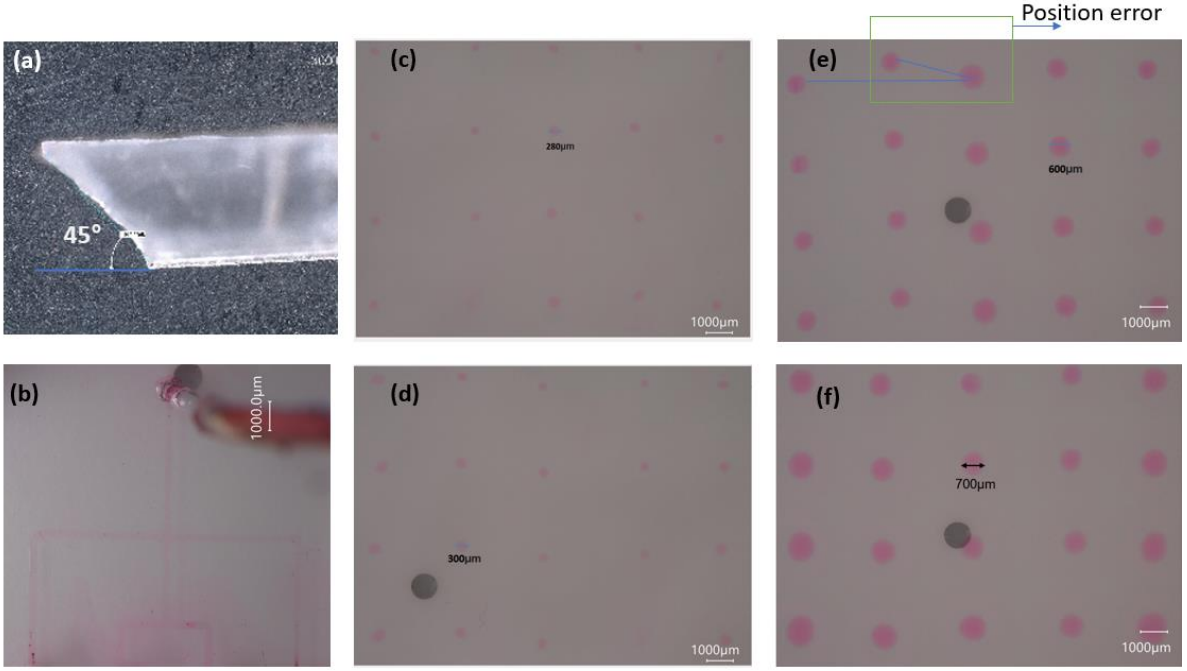

Fig.2 (a) Actual cutting nozzle to make edges sharpened. **(b)**Final chips nozzle with equal distribution of the fluid in channels taken by microscope. Contact printing droplet images taken with a microscope. **(c)***Q*= 3µL/min, *V*= 15mm/s **(d)** *Q*=3µL/min, *V*=10mm/s **(e)** *Q*=5µL/min, *V*=15mm/s **(f)***Q*=10µL/min, *V*=30mm/s.

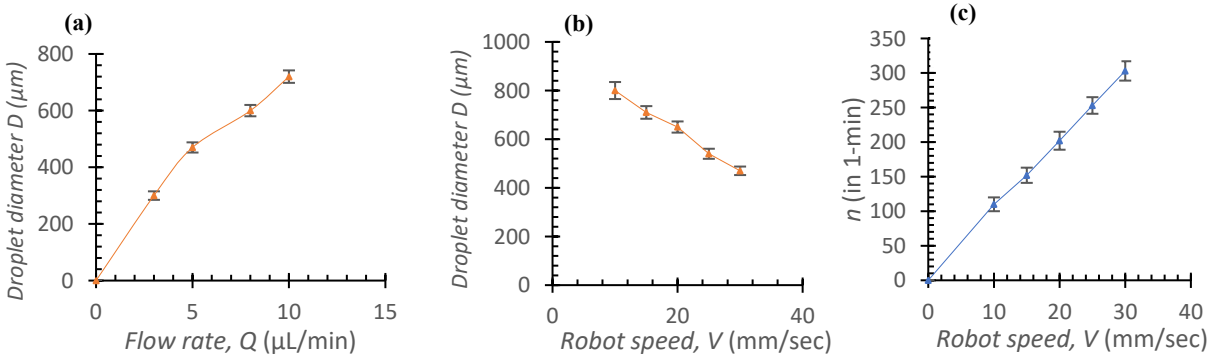

Fig. 3 The Size of the droplets and number of droplets in 1-min at various flow rates and speed of the robot. **(a)** Size of the droplet, how it varies with flow rate at constant speed (*V*=15mm/s). **(b)** Size of the droplets, how it changes with speed and vat constant flow rate (*Q*=10µL/min).**(c)** Number of droplets in 1-min *n* with different speed and constant flow rate.

Grayscale exposure challenges using direct-write laser exposure on thick photosensitive positive resist

G. Ekindorf [ab], C. Schuster [c], D. Collé [a], P. Heyl [a], A. Voigt [c]

[a] Heidelberg Instruments Mikrotechnik GmbH, Mittelgewannweg 27, 69123 Heidelberg, Germany
[b] Kirchhoff-Institut für Physik, Im Neuenheimer Feld 227, 69120 Heidelberg, Germany
[c] micro resist technology GmbH, Koepernicker Str. 325, 12555 Berlin, Germany

e-mail: gerda.ekindorf@heidelberg-instruments.com

Grayscale lithography is becoming increasingly popular as manufacturing method to create 2.5 dimensional structures in industry and research applications. Unlike binary lithography, the positive photoresist is not completely exposed down to the substrate surface, but spatially modulated intensity levels lead to a topography within the positive resist layer after developing. The intensity levels, also called gray values, can be easily created by using a Direct Write Lithography System – DWL, manufactured by Heidelberg Instruments Microtechnik GmbH. The tool is equipped with a laser (λ 405 nm, power 300 mW) and Spatial Light Modulator (SLM), allowing a fast laser light modulation between each exposed pixel. The SLM modulates the intensity of each pixel within the area according to input CAD data. A real-time autofocus system keeps each laser spot focused on the substrate while the stage on which it rests is moved by linear motors. The entire writing area is exposed stripe by stripe. The stripe width and pixel size depend on the focusing optics – the write mode. A large variety of structures like micro-lens arrays, Fresnel lenses, blazed gratings, holographic elements, diffractive optical elements (DOE) or parts for micro-electro-mechanical systems (MEMS) can be manufactured.

The height of the structures exposed with grayscale lithography is limited due to the chemistry behind positive photosensitive DNQ-based resists and the processing of them. The photoreaction that occurs during exposure of these resists leads to the release of nitrogen gas (N_2), which may form bubbles in the resist layer at certain depths, thereby limiting the maximum achievable pattern depth. In commercially available positive resists, this is typically observed in the 60-80 µm depth range. Additionally, coating such high film thickness is challenging, and often requires multiple coating and intermediate soft bake steps.

The new experimental positive photoresist mr-P 22G_XP [1] manufactured by micro resist technology GmbH is specially designed for grayscale applications in very thick films. Test exposures with DWL systems show good results by realizing structures over 100 µm in height (Figure 1.). Furthermore, the resist can be coated up to 120 µm in a single coating and up to 180 µm in double coating.

Exposing structures over 100 µm in height needs a specific writing strategy. A high intensity is needed to reach such depth. But a high dose in a single exposure leads to massive nitrogen bubble formation, or to burning of the resist. Controlled multiple overlapping exposures with relatively low doses are necessary to reach deep areas within the resist layer without defect. The DWL 66^+ used for the experiments already incorporates overlapping exposure methods, like N-Over and the more advanced CI-over, which were designed to eliminate stitching artifacts. By employing these exposure strategies, the rapid formation of nitrogen bubbles is prevented.

The reduction of the absorbance during exposure is a phenomenon known as bleaching effect. Higher transmittance helps to reach greater depth. The bleaching is more pronounced in the newly developed photoresist mr-P 22G_XP, and hence, favors even deeper patterns.

Not only, the process and the exposure strategy must be controlled carefully when using ultra-thick positive resist for grayscale lithography. The other challenge is the shape optimization. The non-linear response of the photoresist combined with proximity effects leads to shape differences between the CAD data and the resulting resist structures. While the resist response can easily be linearized with the help of contrast curves, proximity effects can be more intricate to compensate.

Finally, also the local environments like the clean room humidity and temperature stability strongly influence the final result and must be controlled precisely.

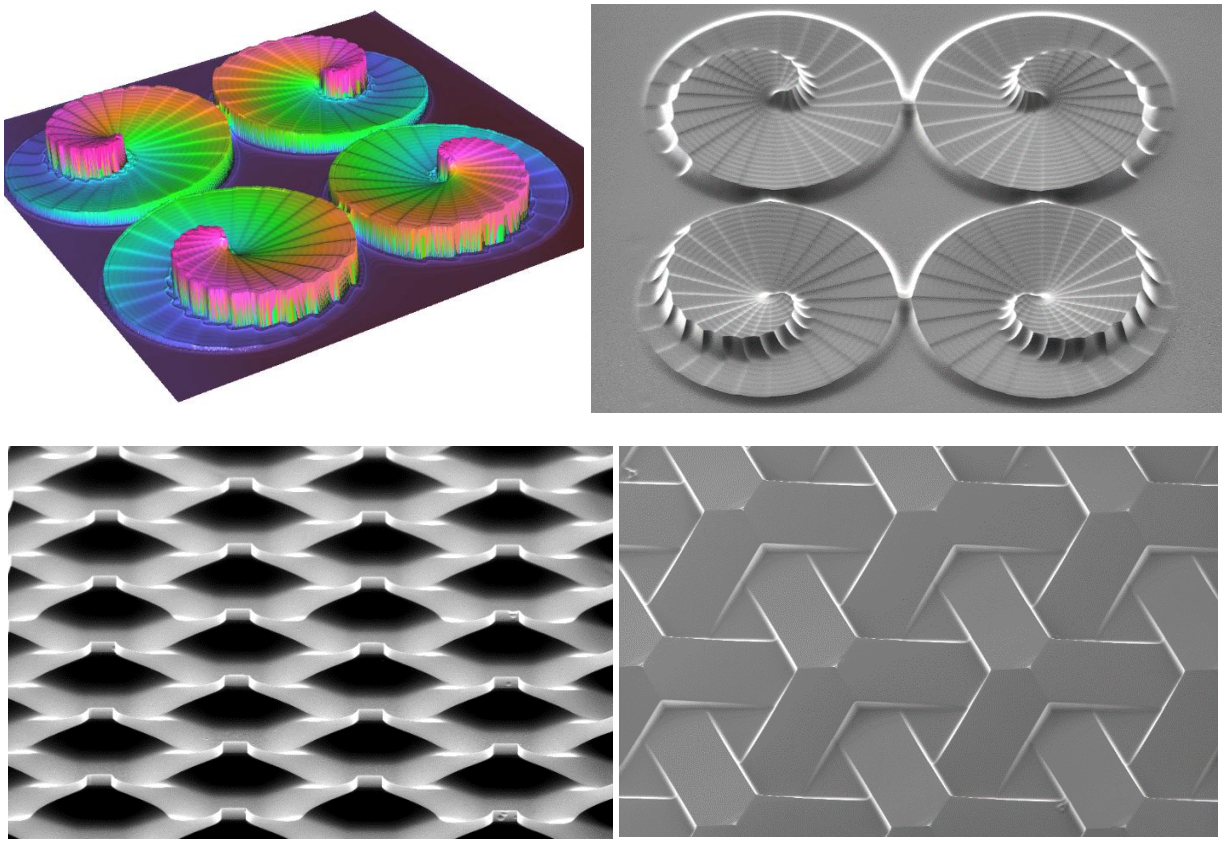

Figure 1.: DWL exposed grayscale structures in positive photosensitive resist mr-P 22G_XP.

[1] C. Schuster, G. Ekindorf, A. Voigt, A. Schleunitz, G. Grützner, *Pushing deep greyscale lithography beyond 100 µm pattern depth with a novel photoresist*, Proc. SPIE 12497, Novel Patterning Technologies 2023, 124970P (30 April 2023)
[2] D. Collé, G. Ekindorf, *Ultra-Thick Positive Photoresist Layers for Maskless Grayscale Lithography*, Proc. SPIE 12497, Novel Patterning Technologies 2023, 124970O (30 April 2023)

Ni-P Electroless Plating of PET Parts with Complex 3D Structure by Supercritical CO_2 Assisted Catalyzation

Ami Iwasaki [a], Po-Wei Cheng [a], Tomoyuki Kurioka [a], Chun-Yi Chen [a], Tso-Fu Mark Chang [a], Kei Takase [b], Hiroshi Ishihata [b], Masato Sone [a]

[a] Institute of Innovative Research, Tokyo Institute of Technology, Yokohama 226-8503 Japan
[b] Diagnostic Radiology, Tohoku University Graduate School of Medicine, Sendai 980-8575 Japan
[c] Division of Periodontology and Endodontology, Department of Ecological Dentistry, Tohoku University Graduate School of Dentistry, Sendai 980-8575, Japan
e-mail: iwasaki@ames.pi.titech.ac.jp

Recently, electronic components have become increasingly finer and more complex, and production methods have also become more complex. One of the methods used to create microstructures is the fusion of photolithography and plating technologies. Typical examples include MEMS technology, the LIGA process, and transfer methods. These technologies require the deposition of a metal film as a conductive layer on photosensitive resin with complex shapes by electroplating. Currently, the sputtering method is used for this process, but the sputtering method is very expensive in terms of equipment. Therefore, there is a demand for metal film deposition by the wet process, which has superior uniform deposition properties. However, the conventional electroless plating method, which is a wet process, requires pretreatment to deposit the catalyst on the surface of the polymer material and uses a strong acidic solvent, which may scratch the surface or deform its shape. Furthermore, the adhesion strength between the polymer material and the metal layer is insufficient. To overcome these problems, a catalyzation step using supercritical carbon dioxide (sc-CO_2) as the solvent is proposed.[1] The sc-CO_2-assisted catalyzation enables a deep impregnation of catalysts into the polymer material without the pretreatment step, and this enhances the adhesive properties of the deposited metal on the polymer. In previous studies, electroless Ni-P plating on polyethylene terephthalate (PET) film structures was achieved using sc-CO2-assisted catalysts.[1] However, the application of electroless plating using sc-CO_2 catalyst to 3D structured polymeric materials has not been explored. In this presentation, we report the results of sc-CO_2-assisted catalytic Ni-P plating on PET samples with complex 3D structures.

A PET base material with a concavo-convex structure was designed and fabricated on a fabrication machine. The Sc-CO_2 assisted catalytic process was performed in a high pressure reactor[1] containing palladium (II) hexafluoroacetylacetonate ($Pd(C_5HF_6O_2)_2$) as a palladium catalyst source at 70°C for 2 h. under 15 MPa, After the catalytic process, the samples were subjected to electroless Ni-P plating at 70°C for 10 min.

Figure 1 shows PET samples obtained before and after each treatment using the above method. As can be seen when compared to before treatment, undesirable swelling and cloudiness were observed in the PET samples. Furthermore, micrographs of the samples after the Sc-CO_2 catalyst treatment [Figure 2(a)] suggested that these were caused by microbubbles originating from the residual CO_2 in the PET. Furthermore, although metal was deposited on the sample, cracks appeared on the deposited metal due to accelerated expansion [Fig. 1(d), Fig. 2(b)]. Therefore, in the sc-CO_2 assisted catalyst treatment, we attempted to remove the residual CO_2 by controlling the operation of depressurization and temperature reduction and aging treatment. Specifically, after the catalyst treatment, the pressure in the reactor was cooled to room temperature while maintaining the pressure in the reactor, and then the pressure in the reactor was reduced to atmospheric pressure. PET samples collected from the reactor were stored under atmospheric pressure for 2 weeks, and then the same plating process was applied. The results before and after each of the above processes are shown in Figure 3. Figure 3(d) shows that Ni-P was well metallized on the PET surface, and the electrical resistance of Ni-P/PET was 8.7Ω, which is an acceptable value for electronic device applications. From these results, it can be concluded that the sc-CO_2-assisted catalyst is applicable to the metallization of PET materials with complex 3D structures.

Acknowledgement
This research is supported by the JSPS KAKENHI Grant Number JP21H01668, and based on the Cooperative Research Project of Research Center for Biomedical Engineering.

Reference

[1] P.-W. Cheng, C.-Y. Chen, T. Ichibayashi, T.-F.M. Chang, M. Sone, S. Nishimura, J. Supercrit. Fluids 180 (2022) 105455.

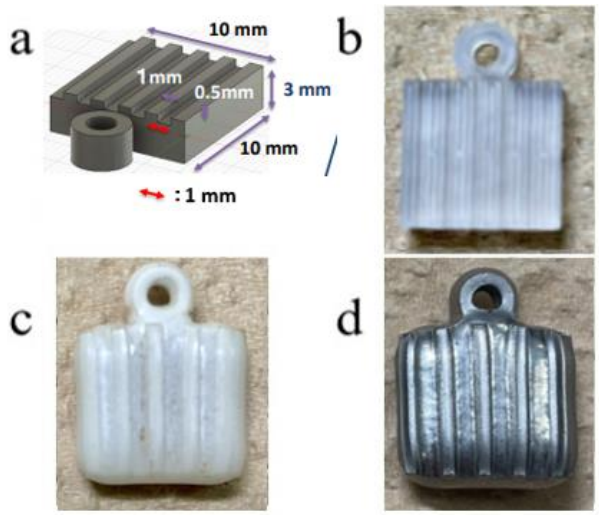

Fig. 1. (a) Design of the PET sample with a concavo-concave structure. Photos of the PET sample, (b) as prepared, (c) after catalyzation step, and (d) after electroless Ni-P plating.

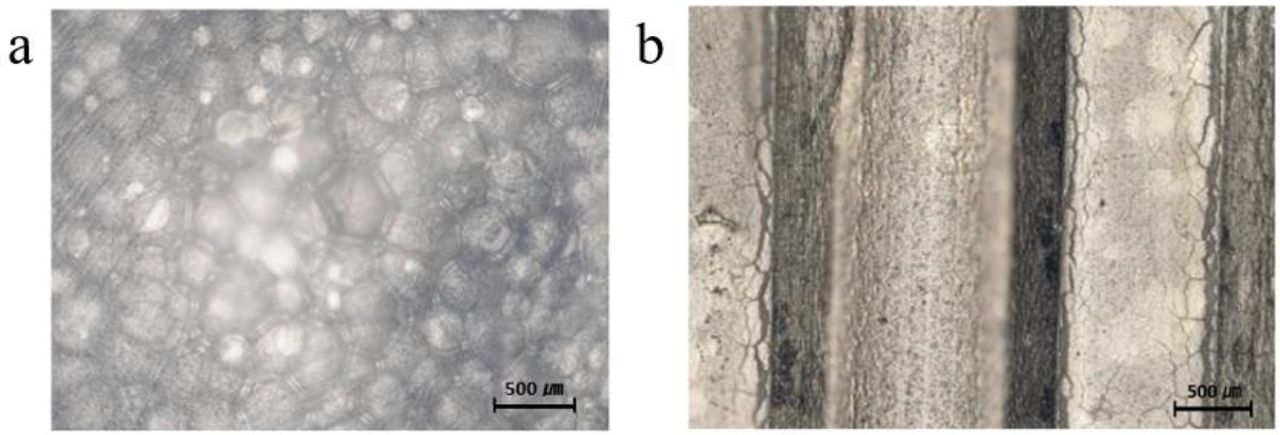

Fig. 2. (a) Optical micrograph of sample after sc-CO_2 assist catalyst treatment. (b) Optical micrograph of a sample after electroless plating process.

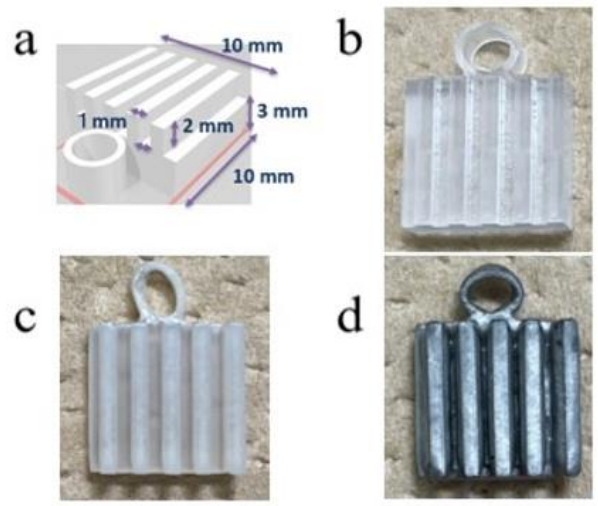

Fig. 3. (a) Design of the PET sample with a concavo-concave structure. Photos of the PET sample, (b) as prepared, (c) after catalyzation step, and (d) after electroless Ni-P plating.

Vacuum-Assisted filling of high aspect ratio Silicon trenches with Polymers for surface planarization for micromachining of complex microsystems.

J. Fernandes, T. Oliveira, V. Silva, H. Fonseca, J. Rodrigues, A. Gouvea, C. Calaza
International Iberian Nanotechnology Laboratory, Braga, 4715-330, Portugal
e-mail: jose.fernandes@inl.int

The micromachining of Silicon with Deep Reactive Ion Etching is one of the most crucial techniques used for the microfabrication of MEMS and other complex microsystems. High aspect ratio (HAR) trenches present several challenges that can compromise further processing, packaging, and the integration of other devices. Overcoming these challenges would allow the development of more complex and integrated micromachined microsystems. To overcome these issues, spray coating [1] or dry film [2] techniques have been widely used. However, these techniques still have several limitations. In spray coating, the coating is conformal to the trenches on the wafer, not allowing the complete usage of the surface with other materials, for example, for lift off processes. In dry film applications, air is encapsulated in the trenches and an etch-back step is not feasible. Other techniques like chemical mechanical planarization (CMP) have also been broadly used, though, the large non-uniformities and the non-selective process to expose the surface can complicate further process steps. A vacuum assisted filling of trenches in through silicon vias has the potential to be useful in the correction of the topography in heavy micromachined wafers [3,4,5]. Such a technique relies on the usage of a vacuum assisted process to extract the trapped air in the cavities followed by a spin coating [4]. Tunning the spin step at the end of the process can promote a different result and fill a cavity with polymer.

In this work, several polymers were experimented with to allow a full trench filling. Since the polymer will be subjected to high density plasmas in relatively high temperatures during Reactive Ion Etching processes, sputtering or even CVD processes, high temperature resistance is mandatory. Which makes the common photoresist not suitable for this application since the polymer should withstand a temperature of up to 300 C. The polymer should also be easily removed by O_2 plasma or by wet chemical etch, enabling the patterning of materials by RIE or Lift-Off for example. To test this solution, silicon wafers were prepared with high-aspect ratio structures by Deep Reactive Ion Etching using the Bosch Process, and were subjected to a vacuum assisted process inspired by the literature [3,4,5] and described in Figure 1. The viscosity of the polymer played an important role when using this process, since high viscosity polymers were not able to fill the cavities. Low viscosity polymers were more successful and presented reasonably conformal results in 8-inch wafers. In Figure 2, two different polymers used in this work are compared. The filling of structures with high aspect ratios larger than 30 were achieved. After filling the cavities with such polymer, a highly selective RIE process was performed to conduct further processing on the surface of the wafer, now with lower topography. The use of O_2 and CF_4 on a RIE system allows a high etch rate in the vertical direction while keeping the non-uniformity below 2% and a selectivity between polymer and silicon greater than 10.

The correction of the wafer topography enables further process development, as outlined in step 5 of Figure 1. This allows processes such as Lift-Off, since a planar surface is required for a conformal spin coating of LOR and photoresist (Figure 1 – (A)) and reactive Ion Etching (Figure 1 – (B)), that in the traditional method would require thick photoresists to overcome high-aspect-ratio structures, compromising the resolution. With the technique presented in this work, both processes are feasible, allowing the addition of other processing steps even when the wafer is micromachined with HAR structures.

[1] J. Linden, *et al*, Spray coating of PMMA for pattern transfer via electron beam lithography on surfaces with high topography, Microelectronic Engineering, Volume 88, Issue 8, 2011, 2030-2032.
[2] Till Huesgen, *et al*, Optimization and characterization of wafer-level adhesive bonding with patterned dry-film photoresist for 3D MEMS integration, Sensors, and Actuators A: Physical, Volume 162, Issue 1, 2010, 137-144.
[3] Xuyan Chen, *et al*, Fabrication and Electrical Characterization of High Aspect Ratio Through-Silicon Vias with Polyimide Liner for 3D Integration, Micromachines 2022, 13, 1147.
[4] Yingtao Ding, *et al*, Innovative polyimide liner deposition method for high-aspect-ratio and high-density through-silicon-vias (TSVs), Microelectronic Engineering, Volume 149, 2016, 78-84.
[5] Y. Yan, *et al*, "Study of Vacuum-Assisted Spin Coating of Polymer Liner for High-Aspect-Ratio Through-Silicon-Via Applications," in *IEEE Transactions on Components, Packaging and Manufacturing Technology*, vol. 6, no. 4, pp. 501-509, April 2016.

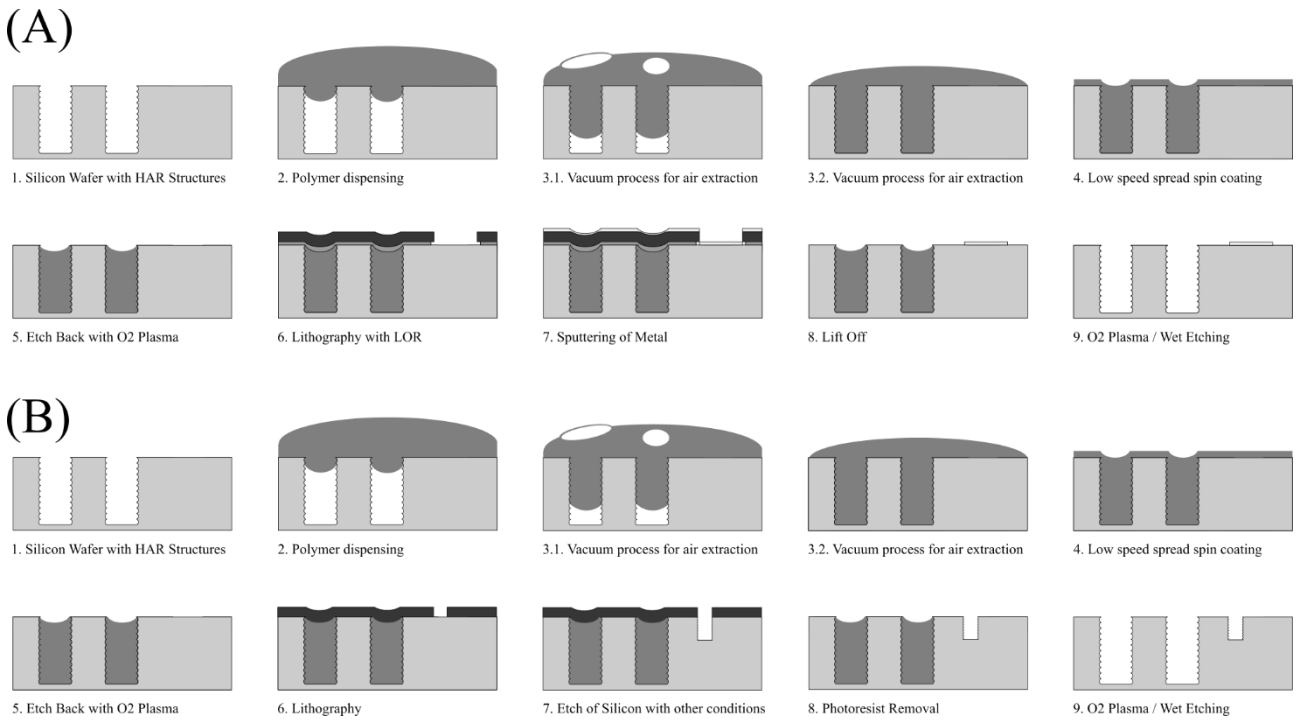

Figure 1. Process flow for topography correction with a vacuum assisted process used for: (A) lift off. (B) other etching depths.

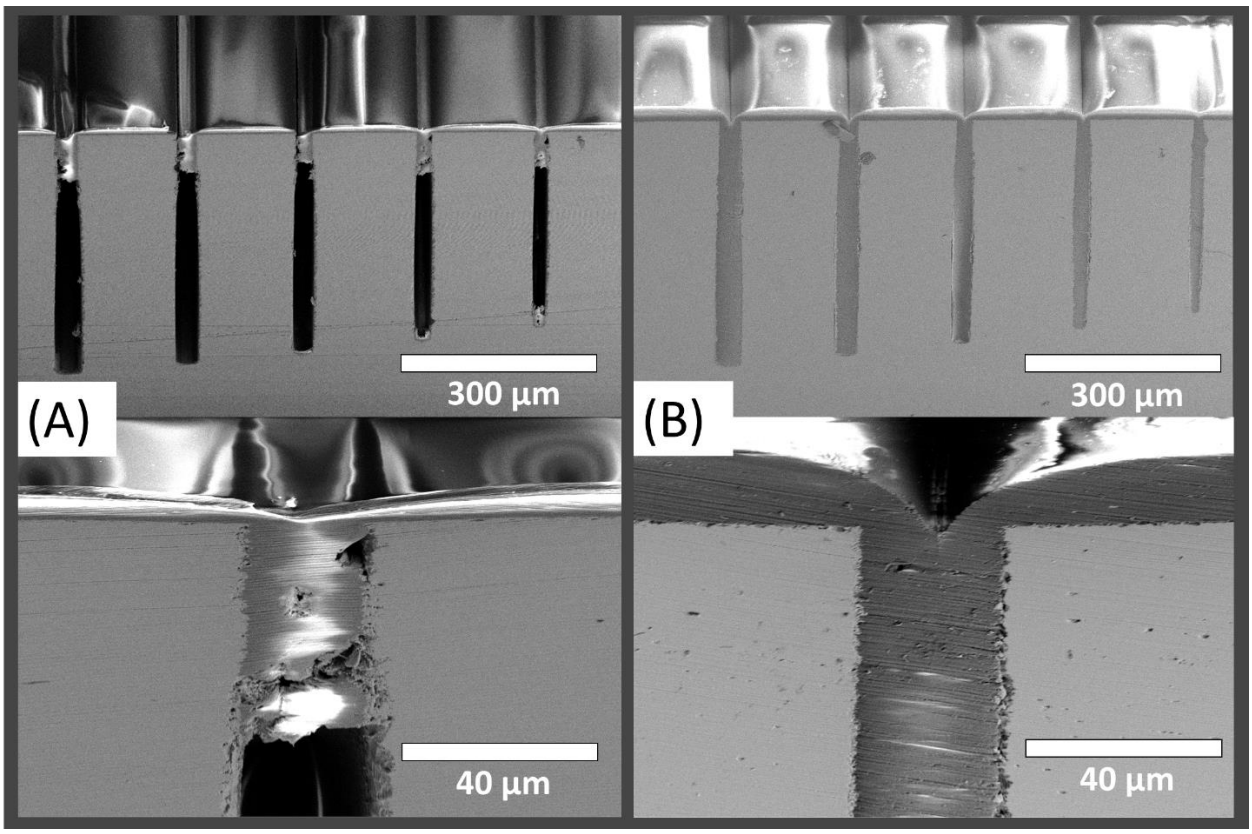

Figure 2. Polymer A vs Polymer B – Comparison of results when filling high aspect ratio trenches.

Microfabrication of thin film structures by two-photon polymerization for *in situ* electron microscopy studies

Chloé Chemin[a], Babak Rezaei[a], Alice Bastos da Silva Fanta[a], Ada-Ioana Bunea[a], Stephan Sylvest Keller[a], Thomas Willum Hansen[a]

[a] National Centre of Nano Fabrication and Characterization, DTU Nanolab, Technical University of Denmark, 2800 Lyngby, Denmark
e-mail: chlche@dtu.dk

Due to its excellent physical, chemical and electrochemical characteristics, pyrolytic carbon has emerged as a promising material for various technological applications [1]. Graphitized carbon is obtained through the pyrolysis of a polymer thin film. By tuning the pyrolysis conditions, the microstructure and thus the physicochemical properties of the derived carbon can be tailored. To fabricate pyrolytic carbon with the most promising properties, systematic and in depth understanding studies of the graphitization process are currently lacking. Transmisssion electron microscopy (TEM) is one of the most suitable tools for investigating the graphitization of polymer thin films during the thermal treatment process at the nano-scale [2]. Indeed, TEM offers the advantages of in situ analysis and revealing the nanostructure of pyrolytic carbon. However, the preparation of polymer thin film samples for TEM remains a challenge. This work presents the microfabrication of overhanging polymer thin film structures printed on MEMS-based TEM heating chips (DENSsolution Wildfire), a suitable substrate for in situ heating studies, by two-photon polymerization (2PP) 3D printing (**Fig. 1**) [3]. The fabrication of overhanging polymer structures with different geometries, i.e. fully supported films, films supported on one side, and strings with different widths, was optimized.

A Nanoscribe Photonic Professional GT+ system from Nanoscribe was used to fabricate overhanging polymer thin films of 1 µm thickness on either a 0.7 mm thick 30 × 30 mm^2 fused silica or on DENSsolutions chips as substrate. The microfabrication of thin films was done by direct laser writing of IP-Dip photoresist using 2PP with a Plan-APOCHROMAT 63×/1.40 Oil DIC objective. The system achieves two-photon excitation using a 780-nm frequency-femtosecond fiber laser source operating at a pulse length between 100 fs and 200 fs, a laser power ranging between 50 mW and 150 mW, and a repetition rate of 80 MHz. After printing, the samples were developed by a 20 min immersion in propylene glycol monomethyl ether acetate (PGMEA), followed by 5 min immersion in isopropanol. Finally, the structures were left to dry horizontally at room temperature.

To gain the optimal printing quality of the 2PP for a specific 3D pattern, the influence of different parameters such as laser power, scan speed, hatching distance and slicing distance on the uniformity and thinness of the derived polymer thin films was studied and optimized. The surface topography, dimensions, and surface roughness of the structures were examined by scanning electron microscopy (SEM) and atomic force microscopy (AFM).

Fig. 2 shows SEM images of three types of overhanging structures, each with a thickness of 1 µm, printed on silicon substrate by 2PP:

- Strings with a width of 1, 2, 3, and 4 µm and a length of 9 or 13 µm,
- Fully supported circles with diameters of 14, 15, 16, 17 µm,
- Circles supported on one side with diameters of 6, 7 and 8 µm.

Figure 2 shows the structures printed with optimized exposure settings, i.e. a laser power of 50% (100% corresponding to 150 mW) and a speed of 12000 µm/s, and default slicing and hatching distances, 0.3 µm and 0.2 µm respectively. The roughness of the structures was further tuned by optimizing the slicing and hatching distances, at the optimal laser power and scan speed. For a slicing distance of 0.2 µm, a low hatching distance of 0.1 µm resulted in the formation of bubbles in the polymer thin film (**Fig. 3a**), while for a larger hatching distance of 0.26 µm, the polymerization lines were visible (**Fig. 3c**), which could result in unstable structures during pyrolysis. Uniform polymer thin films were obtained with an intermediate hatching distance of 0.18 µm. In terms of surface quality. **Fig. 4** indicates that the sample fabricated with a slicing distance of 0.4 µm and a hatching distance of 0.1 µm has the lowest Root Mean Square (RMS) roughness.

To conclude, we demonstrated the successful 2PP fabrication of overhanging polymer thin films for *in situ* TEM studies. Further studies will investigate the conversion of these films into pyrolytic carbon.

[1] M. Fu et al., Mater. Chem. Front. 5 (2021) 2320-2327
[2] C. N. Shyam Kumar et al., Nanoscale 9 (2017) 12835-12842
[3] A.-I. Bunea et al., Micro 1 (2021) 164-180

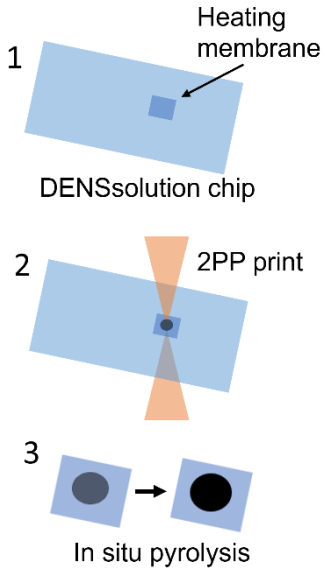

Figure 1. Schematic process flow of the graphitization on a MEMS heating chip. The polymer is printed by 2PP on the chip and the pyrolysis is studied by *in situ* TEM.

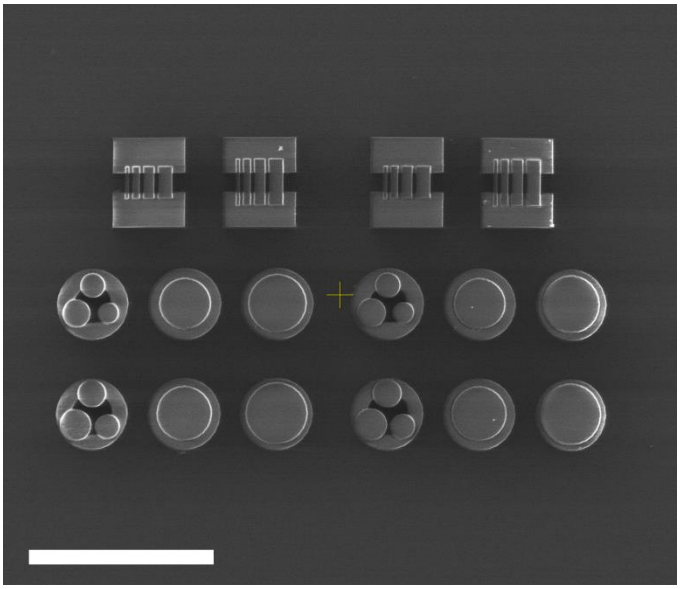

Figure 2. SEM image of the overhanging structures at a laser power of 50% and a scan speed of 12000 µm/s. The scale bar is 50 µm.

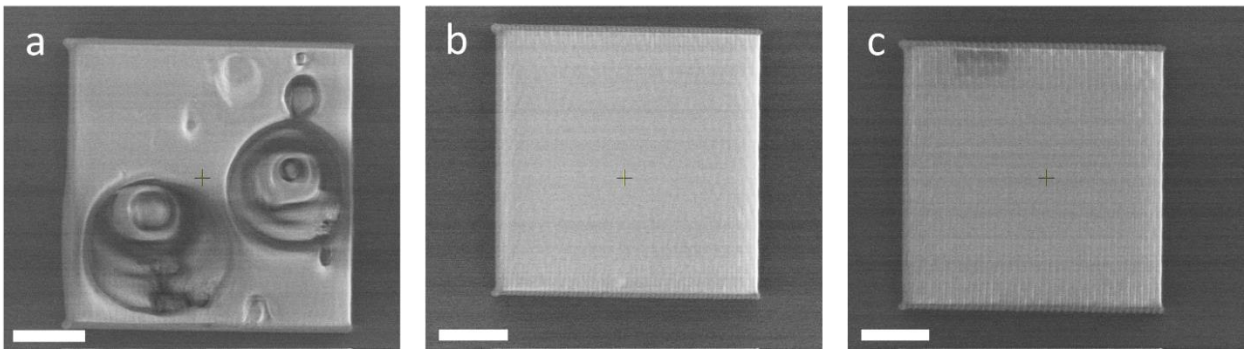

Figure 3. SEM images of a 20×20×0.9 µm cube printed at a laser power of 50%, a scan speed of 12000 µm/s, a slicing distance of 0.2 µm, and hatching distances of: a) 0.1 µm, b) 0.18 µm and c) 0.26 µm. The scale bar is 10 µm.

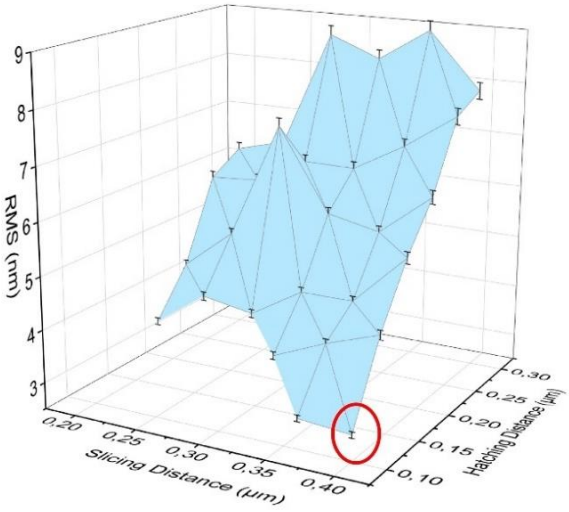

Figure 4. Graph of the RMS roughness values as a function of the hatching and slicing distances. The lowest RMS value is circled in red.

Constant defocus approximation in mask data-preparation for grayscale patterning of microlens

Marie-Line Pourteau [a], Aurélien Fay [a], Sébastien Bérard-Bergery [b], Florian Tomaso [a], Rémi Coquand [a], Ujwol Palanchoke [a], Charlotte Beylier [b], Guillaume Claveau [b], Samir Guerroudj [b]

[a] Univ. Grenoble Alpes, CEA, Leti, F-38000 Grenoble, France
[b] STMicroelectronics, 850 rue Jean Monnet, 38926 Crolles Cedex, France
e-mail: marie-line.pourteau@cea.fr

Grayscale lithography is a powerful technique to pattern 3D microstructures with various heights and slopes, in a resist material, with a single-step process. The complex profiles achievable are of interest for a wide range of applications such as microfluidic, micro-optics, or MEMS components [1-3]. The low contrast resist material is exposed to a spatially modulated exposure dose, leading to a variable resist height after development, either by direct writing process (laser-writing, e-beam lithography), but also by photolithography. In this case, the exposure dose is controlled by a glass photomask with sub-resolutions chromium dots. Adjusting their size and location, one can control the final pattern shape in the resist. To ensure the mask design meets the targeted pattern, data preparation using aerial image and resist development models is mandatory [4].

In 2021, CEA-Leti and ST Microelectronics continued their long-term partnership on grayscale patterning [4-6] and designed a grayscale photomask with 2.6 µm pitch microlens patterns. For data-preparation, in order to keep the lithographic numerical implementation simple, we used a simplified lithographic model based on the assumption (among others) that the incident light forming the aerial image propagates itself vertically through the resist, not being progressively defocused because of the change in optical indexes [7]. After exposure with an I-line stepper and resist development, however, resist bridge appeared between the lenses base, which was not consistent with the model prediction (Fig 1).

In the current work, we present an improved lithographic model that still requires only a limited computation time. Instead of simulating the exact progressive defocus, we chose to include a simple constant defocus approximation and are able to reliably predict the resist bridging observed on microlenses processed with the first mask (Fig 2). This improved model was used to design a new mask version. Finally, the microlenses patterned with this new mask have no more bridging (Fig 3). We thus experimentally show that a simple approximation of the defocus by a constant value is sufficient to predict the resist profile from a mask design, thus avoiding a complex and time-consuming exact simulation of the aerial image focusing within the resists.

[1] V. Nock et al., Microelectron. Eng. 85 (2008) 1077–1082.
[2] B. Morgan et al., J. Microelectromech. Syst. 13 (2004) 113–120.
[3] C. Waits et al., Sens. Actuators A, Phys. 119 (2005) 245–253.
[4] P. Chevalier et al., Proc. SPIE 10958 (2019) 109581E.
[5] N. Allouti et al., Proc. SPIE 10958 (2019) 1095809.
[6] U. Palanchoke et al., Proc. SPIE 12497 (2023) 124970N.
[7] P. Chevalier et al., Journal of Microelectromechanical Systems 30 (2021) 442-455

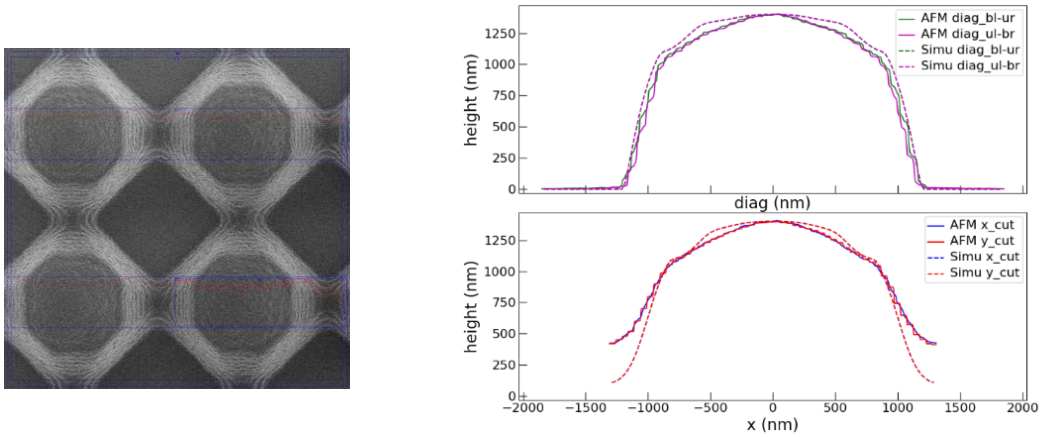

Figure 1. Patterns obtained with the initial version of the mask: (left) In-resist microlens top-view SEM imaging shows an important bridging – (right) Microlens profile AFM measurements are compared to simulated profiles, along diagonal axis (top) and x/y axis (bottom). Along x/y axis, the model does not predict the resist bridging.

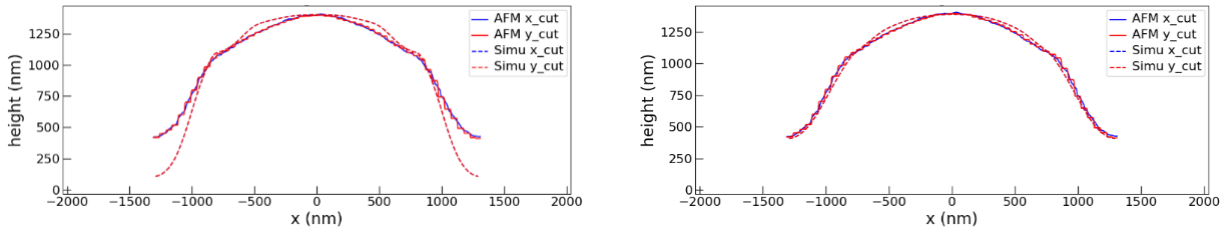

Figure 2. Microlens profile AFM measurements compared to profiles simulated using (left) the model with no defocus and (right) the model with constant defocus. In both cases, the resist is exposed with the initial version of the mask. The model fits well with the on-resist pattern profile when introducing a constant defocus value.

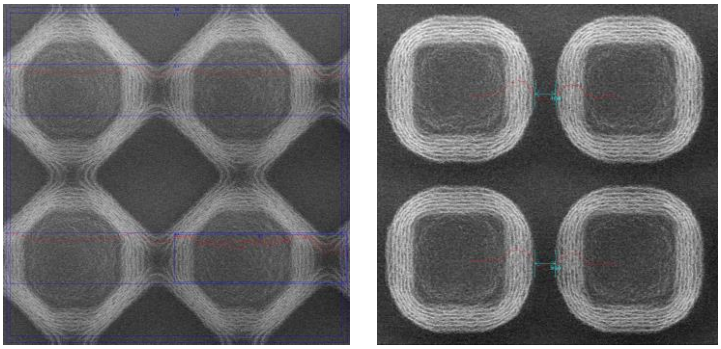

Figure 3. In-resist microlens top-view SEM imaging. Patterns are exposed with (left) the 1st version of the mask and (right) the improved version of the mask. In the later case, the bridging is removed.

Penning vacuum gauge with high-efficiency plasma source for a miniature ultra-high vacuum cell

Yuichi Kurashima [a], Taisei Motomura [a], Takashi Matsumae [a],
Atsuhiko Maeda [a], Sinya Yanagimachi [a], Hideki Takagi [a]
Naoto Oshima [b], Mitsuhiro Watanabe [b]

[a] National Institute of Advanced Industrial Science and Technology (AIST), Tsukuba, 305-8564, Japan
[b] Nihon University, Funabashi, 274-8501, Japan.
e-mail: y-kurashima@aist.go.jp

In recent years, miniaturization of quantum devices using cold atom is growing demand. An ultra-high vacuum environment is required for generating cold atom. Therefore, it become key issue to measure the inside pressure of a vacuum cell by a miniature ultra-high vacuum gauge. Penning vacuum gauge using Penning discharge can be powerful candidate of miniature ultra-high vacuum gauges because it possible to be miniaturized by the MEMS process [1, 2]. The principle is to generate a discharge by applying a DC high voltage between an anode and two cathodes. A degree of vacuum can be determined by measuring a discharge current because the discharge current is pressure dependent. However, a distance between the electrodes becomes extremely narrow in case of the miniature vacuum gauge, resulting in extremely short electron flight distances, and collisions will hardly occur between electrons and residual gas molecules. As a result, the vacuum gauge with narrow electrodes is leading to deterioration of a discharge efficiency. Therefore, we have been proposed a miniature efficiency plasma source by a magnetic mirror trap with two opposing permanent magnets [3]. In this study, we attempted to integrate a Penning vacuum gauge and a miniature vacuum cell for realization of the quantum device by cold atom, and evaluated the pressure dependence of the discharge current of the integrated vacuum gauge.

Three 0.4 mm thick Si and two 2 mm thick glass plates were prepared for integral of the penning vacuum gauge and cold atom generator cell. Several holes were fabricated for Si anode and cathode each other as shown in Fig.1(a). Two through-holes were fabricated in the glass insulated spacer. Bridges were fabricated between the two holes respectively so that the vacuum in the miniature ultra-high vacuum cell can be monitored with the integrated Penning vacuum gauge. A total of five layers of Si and glass plates were anodically bonded to each other. Figure 2 shows the arrangement and electrical wiring diagram for evaluating the discharge characteristic of the vacuum gauge integrated in the vacuum cell. Magnets embedded into a yoke were mounted outside the electrode section of the vacuum gauge. After setting up the integrated prototype structure in the vacuum chamber, the vacuum chamber was evacuated using a turbo molecular pump to make the integrated Penning vacuum gauge section under an ultra-high vacuum environment. The discharge current was measured for each vacuum level from 10^{-4} Pa to 10^{-6} Pa.

Figure 3(a) shows a picture of glow discharge inside the vacuum gauge at low vacuum pressure. Figure 3(b) shows the discharge current depends on the vacuum pressure. At a discharge voltage of 2 kV, the discharge current was 1,346 nA at 1.1×10^{-4} Pa, 134 nA at 1.1×10^{-5} Pa, and 13 nA at 1.1×10^{-6} Pa, respectively. It was found that the discharge current tends to decrease by about one order of magnitude as the vacuum decreases by one order of magnitude. This is because as the degree of vacuum decreases, the residual gas molecules become less ionized due to the decrease in residual gas molecules. At the same vacuum pressure, as the applied voltage decreased, the value of the discharge current also tended to decrease. We conclude that the Penning vacuum gauge has been successfully integrated into a miniature vacuum cell, which can measure ultra-high vacuum.

Acknowledgments: This work was partly supported by the Innovative Science and Technology Initiative for Security, Grant Number JPJ004596, ATLA, Japan.

References

[1] F. M. Penning, Physica 4 (1937) 71.
[2] T. Grzebyk, et al., Sens. Actuators A:Phys. 208 (2014) 113.
[3] Y. Kurashima et al., Sensors 23 (2023) 1040.

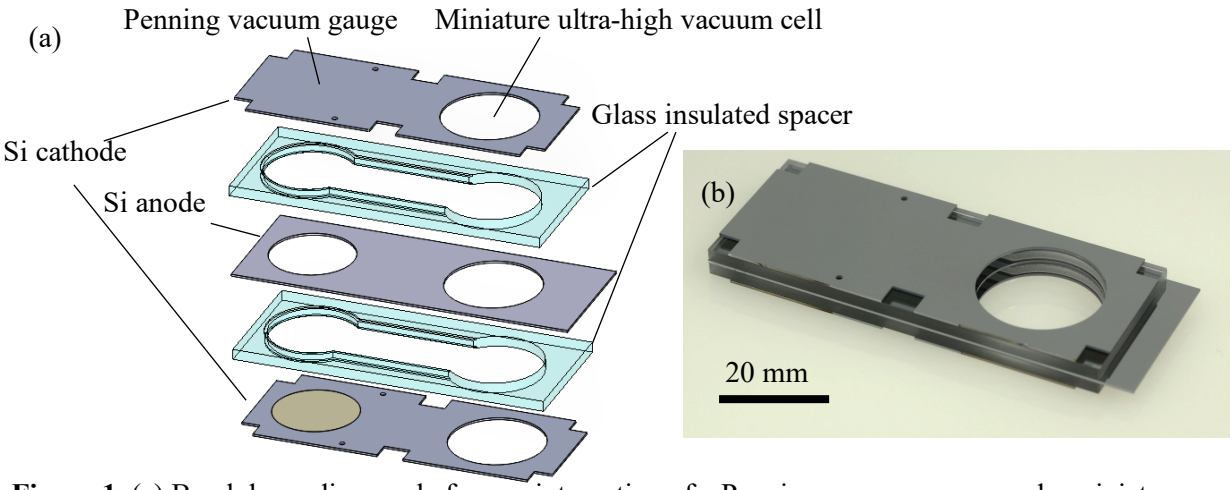

Figure 1. (a) Breakdown diagram before an integration of a Penning vacuum gauge and a miniature vacuum cell. (b) Realized integral structure of the vacuum gauge and the vacuum cell.

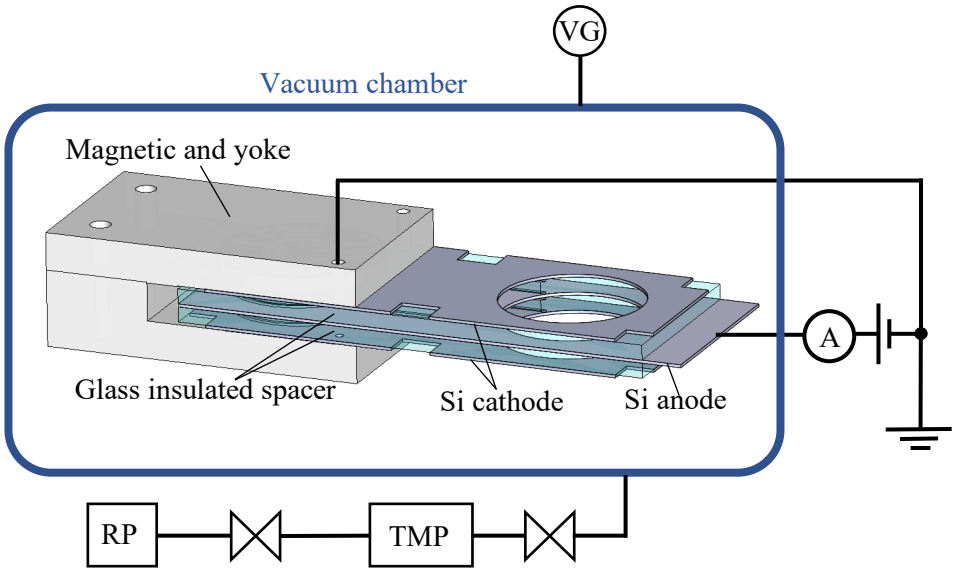

Figure 2. The arrangement and electrical wiring diagram for evaluating the discharge characteristic of the vacuum gauge integrated in the vacuum cell.

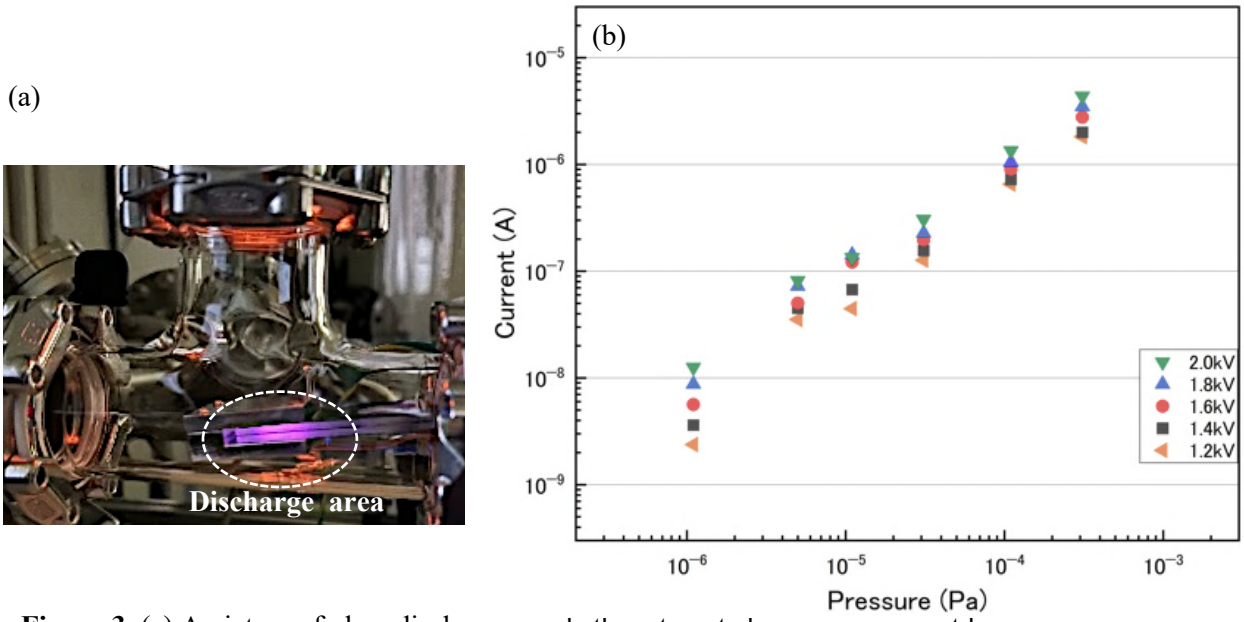

Figure 3. (a) A picture of glow discharge ınside the ıntegrated vacuum gauge at low vacuum pressure. (b) The discharge current depends on the vacuum pressures.

The Effect of Damaged Layer Removal Process on Si Atomic Layer Etching

Namgun Kim [a,b], Whankyun Kim [a,b], Dongjun Shin [b], Jongkyu Kim [b], Kukhan Yoon [b], Youngju Ko [a], and Heeyeop Chae [c,d,*]

[a] Department of Semiconductor and Display Engineering, Sungkyunkwan University (SKKU), Suwon 16419, Republic of Korea
[b] Semiconductor R&D Center, Samsung Electronics, Hwaseong 18448, Republic of Korea
[c] SKKU Advanced Institute of Nanotechnology (SAINT), Sungkyunkwan University (SKKU), Suwon 16419, Republic of Korea
[d] School of Chemical Engineering, Sungkyunkwan University (SKKU), Suwon 16419, Republic of Korea

e-mail: hchae@skku.edu

Atomic layer etching (ALE) is not widely used in the semiconductor manufacturing industry due to its low throughput, despite offering better control and selectivity compared to reactive ion etching (RIE) [1, 2]. The challenges of low throughput in ALE have been effectively developed by applying ALE selectively to critical layers following RIE processing [2, 3]. RIE can introduce damage layers that negatively affect the initial cycles of the ALE process, so fluorocarbon plasma pretreatment is commonly used to mitigate damage layers [4]. However, plasma pretreatment for ALE has not been extensively studied. In this study, the effect of fluorocarbon plasma pretreatments was investigated for Si quasi-ALE using a 300mm inductively coupled plasma (ICP) reactor. The Si surfaces were pretreated with CF_4 or CHF_3 fluorocarbon plasma, followed by ALE cycle processes involving Cl_2 plasma chlorination and Ar ion etching. The variation in ALE cycles and removal depth for RIE-damaged Si layers was changed by plasma pretreatment conditions, as shown in Figure 1(a). Significant fluorocarbon layers were observed on the Si substrate after fluorocarbon pretreatment. The CHF_3 plasma pretreatment showed a higher atomic percentage of fluorocarbon at 79.0% compared to the CF_4 plasma pretreatment at 59.1%, as shown in Figure 1.(b). The etch per cycle (EPC) value of Si in the ALE window was measured at 5.5 Å/cycle with plasma pretreatment of CHF_3 and 6.2 Å/cycle with that of CF_4, as shown in Figure 2. The fluorocarbon layers generated by plasma pretreatments had a significant influence on the initial cycle of Si ALE, with plasma pretreatment of CHF_3 affecting up to 30 cycles and that of CF_4 affecting up to 20 cycles, as shown in Figure 3. This work highlights the importance of optimizing surface pretreatments for damaged layer removal in semiconductor manufacturing and provides insights into the impact of pretreatment process conditions on ALE performance.

References

[1] K.J. Kanarik et al., J. Vac. Sci. Technol. A Vac. Surf. Film 33 (2015) 020802.
[2] C.T. Carver et al., ECS J. Solid State Sci. Technol. 4 (6) (2015) N5005–N5009.
[3] K.J. Kanarik et al., J. Phys. Chem. Lett. 9 (2018) 4814–4821.
[4] K. Koh et al., J. Vac. Sci. Technol. A: Vac. Surf. Films 36 (2018) 01B106.

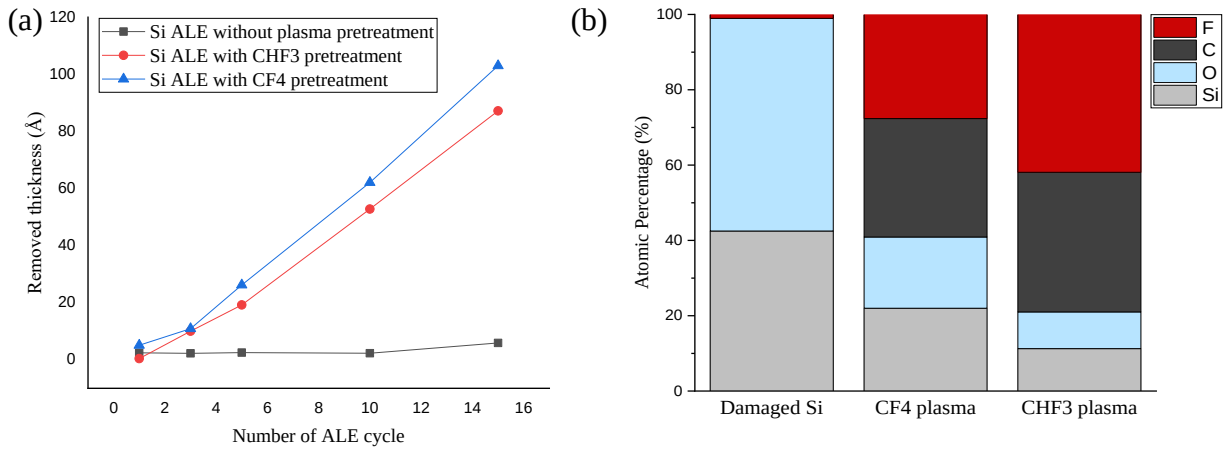

Figure 1. (a) Relationship between the number of ALE cycles and the removed thickness under various pretreatment conditions after RIE damage. (b) surface composition of damaged Si after CF4 or CHF3 plasma pretreatment.

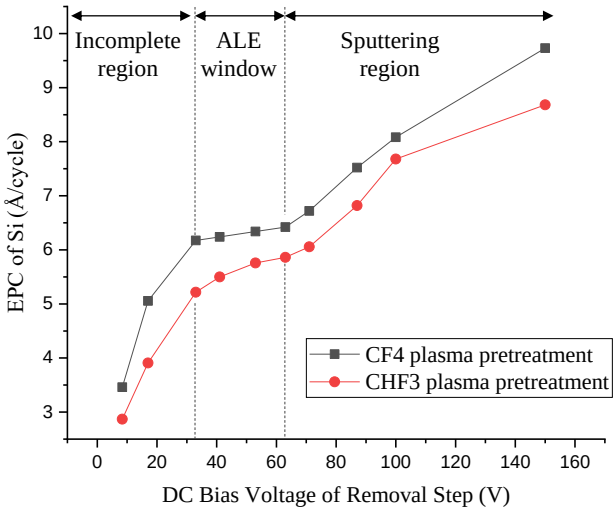

Figure 2. Etch per cycle of Si for CF4 and CHF3 plasma pretreatment as a function of DC bias voltage of removal step.

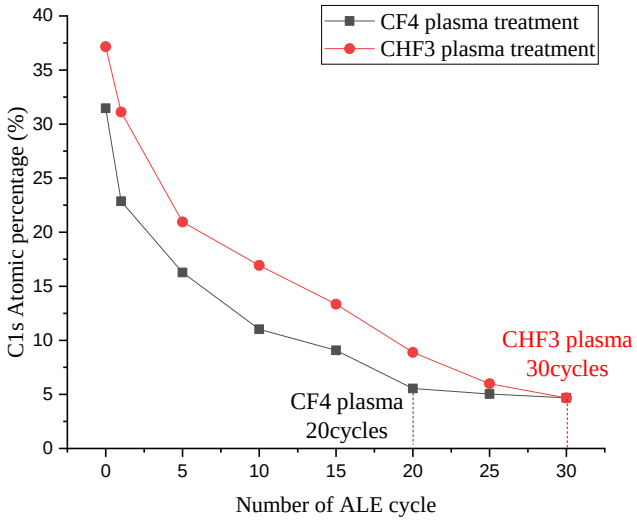

Figure 3. Change in C1s atomic percentage for CF4 and CHF3 plasma pretreatments as a function of ALE cycle number.

Perspective of Unconventional Holographic Lithography and Ion Bombardment

Ying Liu

National Synchrotron Radiation Laboratory, University of Science and Technology of China, Hefei, 230029, China
e-mail: liuychch@ustc.edu.cn

Thanks to the development of micro-/nanostructures, diverse micro-/nanofabrication methods emerge. There is no any single method that can fabricate all kinds of micro-/nanostructures. Thus, it is necessary to study both the integration of different methods to gain their synergy effects and the systematic investigation of a specific micro-/nanofabrication method.

In the fabrication of diffraction gratings, holographic lithography (HL) and ion beam etching (IBE) are utilized in a conventional fashion, where HL is used to form the photoresist (PR) grating as mask, and then IBE is introduced to transfer the PR pattern into the grating substrate. In other words, no grating mask is used in HL, while a PR mask is necessary during IBE for pattern transfer. Based on the fabrication of diffraction gratings for synchrotron and laser systems by using HL and IBE, in this contribution I will review our recent progress of HL and IBE in an unconventional fashion, i.e., HL with an electron beam lithography (EBL)-written phase mask (PM) and IBE, also known as ion bombardment (IB), a maskless nanofabrication tool for self-organized nanostructures, respectively.

First, regarding the HL using a PM written by EBL, we will strengthen the synergy effect of HL and EBL. The hybrid method exhibits the advantages of EBL in writing high-resolution patterns with an address grid of 0.1 nm and a flexible groove density distribution, and the feature of HL in printing VLSGs with high throughput. Meanwhile, the limitations of EBL in sequential mode and complex exposure optics during HL can be overcome. Moreover, dynamic exposure has been demonstrated to reduce Rowland ghosts during HL [1,2] (see Fig 1). Varied-line-spacing gratings with a central density larger than 3000 lines/mm and low stray light have been fabricated using this method [2] (see Fig 2). Our results also indicate that the hybrid method is promising and suitable for the production of microstructures, e.g., volume holographic gratings [3] in patch.

Second, IB is a bottom-up approach that generates self-organized nanostructures on surfaces of various solid materials without mask and with a period of ~100 nm, which is smaller than that of HL. The degree of ordering of self-organized nanostructures is a key issue to be overcome. We will demonstrate our findings of enhancing the ordering of IB-induced nanoripples by bombarding bilayer systems [4] (see Fig 3). This indicates that not a periodic template but the self-organized nanoripples on the top layer can guide the growth of the nanoripples on the underlying layer [5].

The work was funded by the Sino-German Centre for Research Promotion (GZ 983) and National Natural Science Foundation of China (11675169). Thanks for supports from colleagues at Friedrich Schiller University Jena providing EBL-written PMs, and Leibniz Institute of Surface Engineering.

[1] D. Lin, Soft X-ray varied-line-spacing gratings fabricated by dynamic near-field holography using a phase mask, Ph.D. Thesis, University of Science and Technology of China, 2020.
[2] D. Lin et al., J. Synchrotron Rad. 26 (2019) 1782–1789.
[3] M. V. Shishova et al., Appl. Opt. 60 (2021) A140–A142.
[4] J. Li et al., Nanotechnology 32 (2021) 385301.
[5] H. Li et al., Entropy 25 (2023) 170.

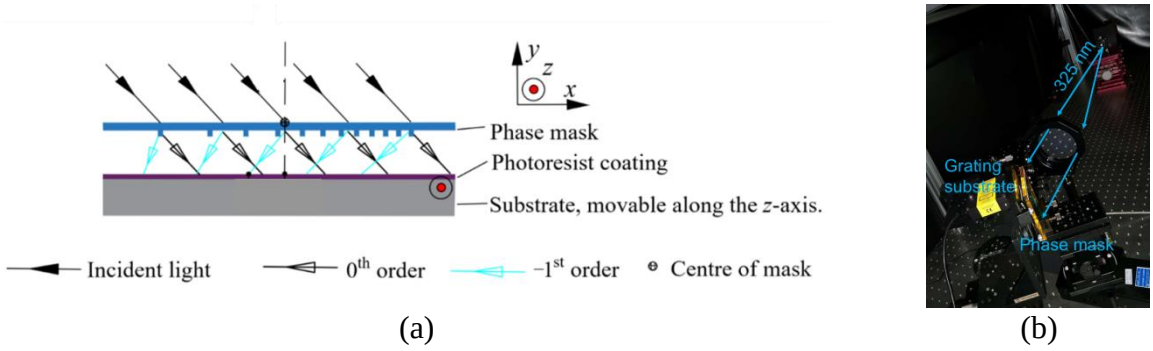

(a) (b)

Figure 1. (a) Schematic and (b) photo of the experimental setup of holographic lithography using an electron beam lithography-written phase mask for varied-line-spacing grating (VLSG) fabrication. The grating substrate can be displaced along the z axis during dynamic exposure, as shown in (a).

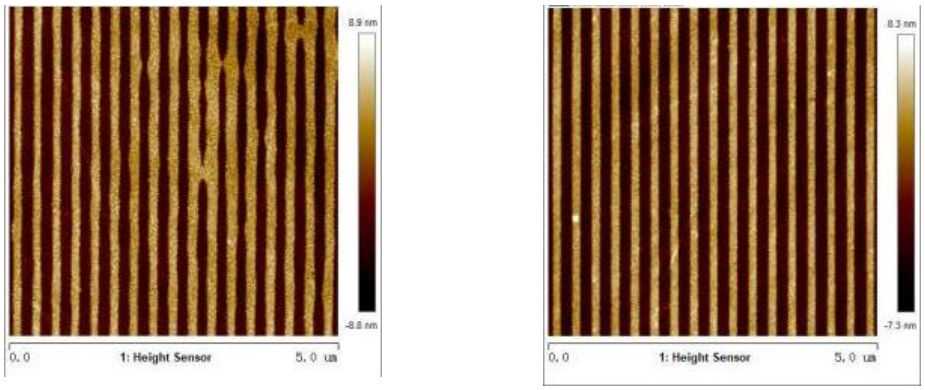

(a) (b)

Figure 2. AFM images of the gold-coated VLSGs with a central density of 3340 lines/mm and an area of 52 mm × 30 mm fabricated by (a) static and (b) dynamic exposure during holographic lithography with an EBL-written phase mask. The fabricated grating using dynamic exposure strategy features smoother line edge of gratings, leading to low stray light.

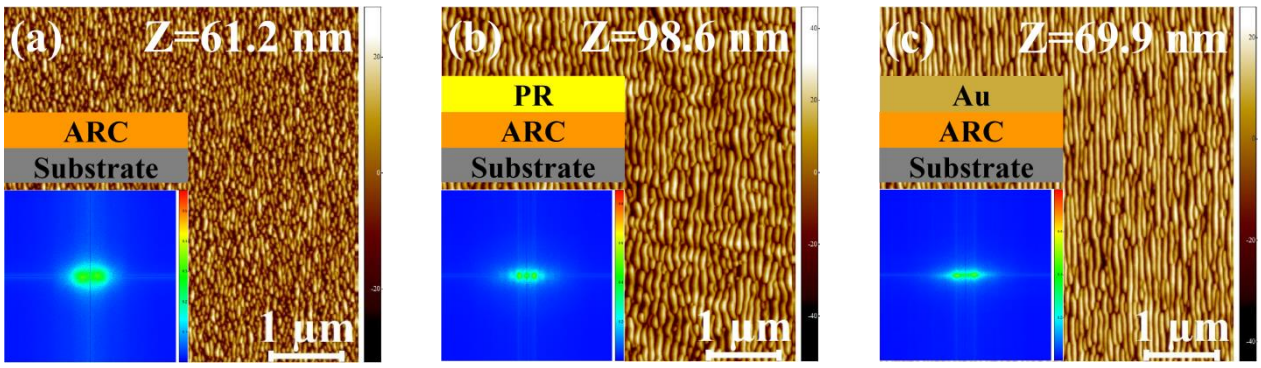

(a) (b) (c)

Figure 3. AFM images of nanoripples on (a) single antireflection coating (ARC), (b) photoresist/ARC, and (c) Au/ARC surfaces produced by ion bombardment. The degree of ordering of the nanoripples on the bilayer systems (b) and (c) is better than that of the well-developed ARC layer (a).

Broad beam ion erosion of silicon with metal-co-deposition: experimental and simulation results

Felix Linß [a], Carsten Bundesmann [a], Frank Frost [a]

[a] Leibniz Institute of Surface Engineering e.V. (IOM), Leipzig, 04318, Germany
e-mail: felix.linss@iom-leipzig.de

Ion beam erosion has gained increasing attention due to the ability to machine ultra precision surfaces. Especially in optical manufacturing, there is a rising demand for surface finishing with ion beam techniques. [1] For that, precise control of the mechanisms contributing to the surface quality is very important. Ion beam processing is operated inside a vacuum chamber. During the processing of samples, several other materials beside the samples can be eroded simultaneously ("co-deposited"). Examples are the chamber walls, sample holder or in-situ analytic devices. Ion beam erosion of Si with simultaneous co-deposition of metal species favours the formation of surface patterns. These patterns occur on the nano-and micrometre scale. [2] Since these patterns determine the properties of the processed surface, it is necessary to know the mechanisms of the patterning, especially the influence on the surface roughness and the substrate removal rates.

In this study a broad beam ion source was utilized, so that parallel irradiation of the Si samples and co-deposition material was ensured. It was operated with Ar at a low ion energy of 700 eV. A sample holder was utilized, which kept the co-deposition material ("target") at an angle of 45° to the substrate material. The setup can be seen in **Figure 1**. Si wafers were used as substrate material, and metal sheets as the targets. Atomic force microscopy, scanning electron microscopy and mechanical profilometry were used to examine the co-deposited surfaces. The dependencies of roughness and pattern formation are reviewed and compared with additional simulation data. These were carried out with the program *TRIM.SP*. For each target material, Ar ions sputtering the target material was simulated in the relevant setup. Additionally, the scattering of Ar ions from the target material was simulated.

It could be shown that ion beam erosion with simultaneous co-deposition can activate the patterning of Si. Ripple-like, well ordered, structures could be observed in the experiments with the silicide-forming materials Cr, Fe, Mo, Ni, Ta, and Ti. **Figure 2** presents the exemplary results for Ni, Mo, and Ta. Both, the AFM and SEM images show the patterning of the surface. For the ion beam co-deposition with Al, Cu, Si and Zn, no patterning was observed. Silicide formation is the driving mechanism for the patterning of Si. [3] Al and Zn do not form silicides, so no patterning occurred. The measured Si removal rates varied, depending on the co-deposited target material, as shown in **Figure 3a)**. The materials with higher atomic numbers tend to increase the Si removal. In contrast, for the materials with lower atomic numbers, the Si removal decreases. However, the removal change is independent of the atomic number, as the examples of Zn and Ta show. In **Figure 3b)** the simulation results are presented as the ratio of Ar ions scattered at the metal target to the sputtered and co-deposited metal target particles. A higher ratio implies more scattering, and thus more supply of Ar ions to erode the Si sample surface. If the ratio is lower, more metal target particles are deposited, and therefore a layer on the sample inhibits the erosion of the sample. Comparing the data with **Figure 3a)**, where the measured Si removal is presented, a good correlation is visible.

A correlation between the substrate removal rate and the co-deposition material has been postulated before. [3] The presented simulation data urges, that the Si removal is mainly influenced by the combination of sputtering and scattering properties of the co-deposition material. This indicates that this effect is self-sufficient and does not rely on the silicide formation.

[1] T. Hänsel et al., Vakuum in Forschung und Praxis 19 (5), 24 (2007).
[2] M. Engler, et al., Nanotechnology 25 (11), 115303 (2014).
[3] H. Hofsäss and K. Zhang, Nuclear Instruments and Methods in Physics Research Section B: Beam Interactions with Materials and Atoms 267 (16), 2731-2734 (2009).

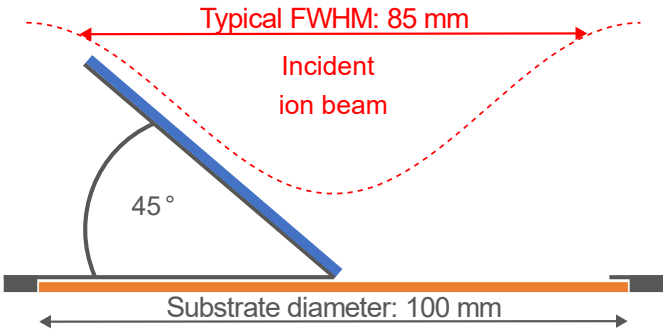

Figure 1. Experimental setup with the used angular arrangement. Blue marks the position of the co-deposition material ("target"), orange the position of the Si sample (wafer). The incident ion beam is marked as red, with its typical Gaussian-like-profile.

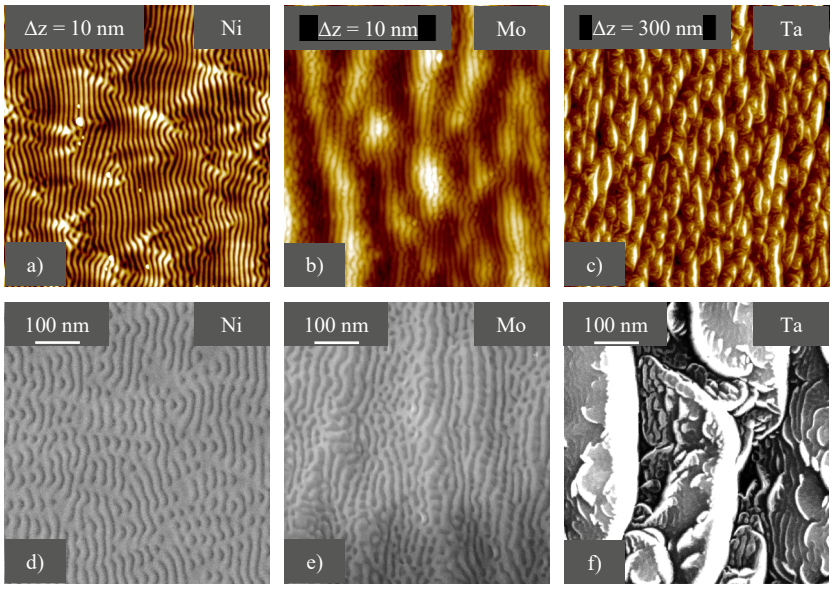

Figure 2. AFM (a - c) and SEM (d - f) images of ion beam co-deposited surfaces.

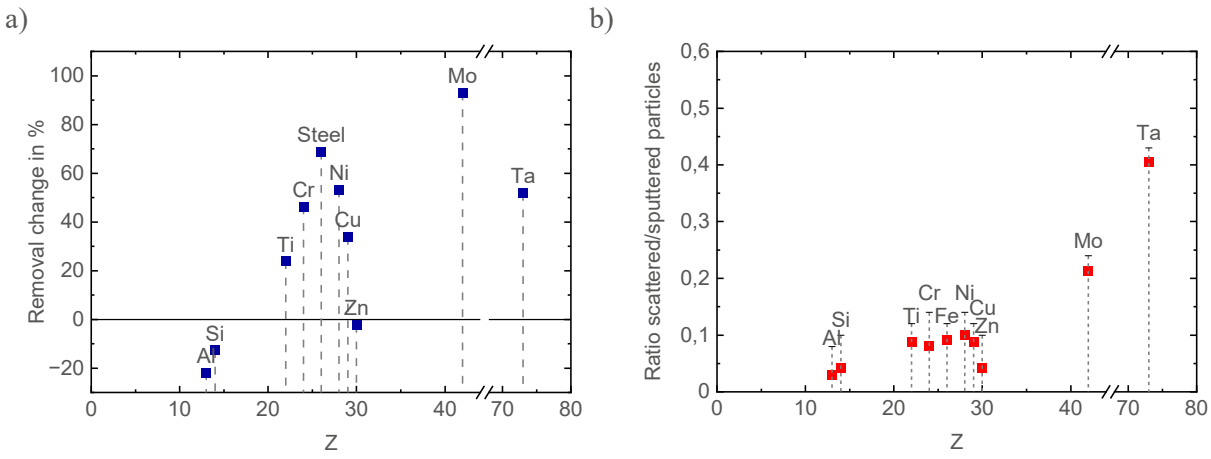

Figure 3. a) Measured data for the removal change induced by the respective co-deposition material. b) Simulated data for the ratio of scattered Ar ions in relation to the sputtered target particles.

2-Photon Lithography for bio-inspired 3D microstructures for in vitro neuroelectronic devices

Valeria Criscuolo [a, b], Claudia Latte Bovio [c,d], Francesca Santoro [a,b,c]

[a] Faculty of Electrical Engineering and IT, RWTH, Aachen 52074, Germany
[b] Institute of Biological Information Processing - Bioelectronics, IBI-3, Forschungszentrum, Juelich 52428, Germany
[c] Tissue Electronics, Istituto Italiano di Tecnologia, 80125 Naples, Italy
[d] Dipartimento di Chimica, Materiali e Produzione Industriale, Università di Napoli Federico II, 80125 Naples, Italy
e-mail: criscuolo@nei.rwth-aachen.de

Bioelectronic devices are electronic platforms that directly interact with biological systems, such as cells, tissues, or living systems, used to monitor cellular electrical activity or modulate cellular behavior by applying an external electrical field. In such applications, the cell-device interface plays a crucial role for an effective electrical coupling between the cell and the device [1], [2]. Furthermore, in neuroelectronic applications, aimed at recapitulating neuronal communication and functions, it is imperative to take inspiration from the extremely complex architecture of the brain. Neurons indeed interact with and respond to plenty of mechanical and topographical cues for the development of a functional nervous system [3]. Given the high complexity of the nervous system, recently 2-photon polymerization (2PP) lithography has emerged as the tool of choice for mimicking neurons´ features thanks to its high resolution, versatility, and design freedom [4], [5]. Here we propose innovative approaches for the realization of 3D microstructures and scaffolds based on 2PP for neuroelectronic applications. In particular, 2PP enabled the realization of both conductive and non-conductive 3D structures through the choice of the functional material as well as microfabrication techniques. Such structures proved to be effective as smart bio-inspired interfaces. The fabrication of 3D electrodes with different levels of complexity will open the way to the possibility of sensing and/or stimulating cells and tissues in a more realistic environment.

[1] G. Wrobel, et al., J. R. Soc. Interface, 2008, 5, 213–222.
[2] M. E. Spira, et al., Front. Neurosci. 2018, 12.
[3] A. Mariano, et al. Nanotechnology, 2022, 33, 492501.
[4] L. Caizhi, et al. Appl. Mater. Today, 2020, 19 100635
[5] F. A. Pennacchio, et al., J. Mater. Chem. B, 2018, 6, 7096.

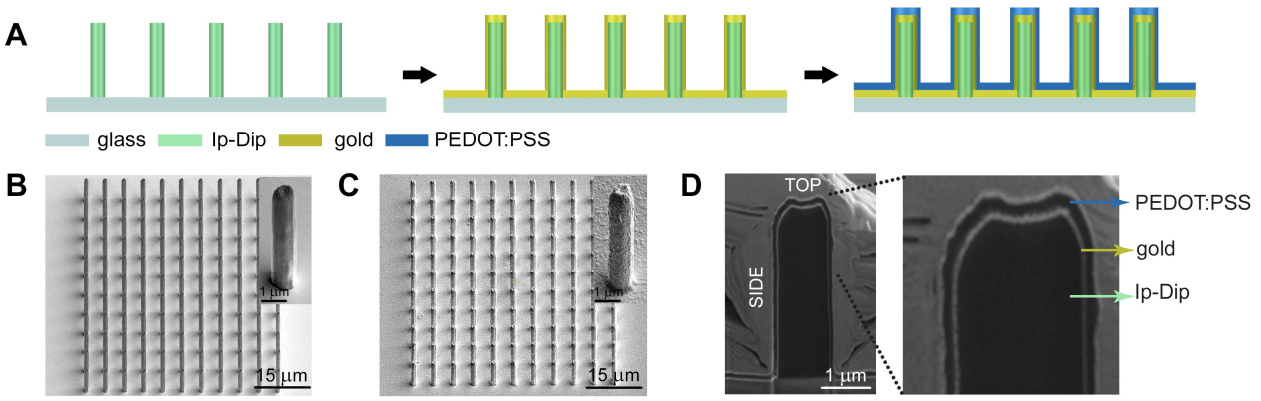

Figure 1. PEDOT:PSS micropillar arrays: (A) Schematics of fabrication of micropillars via 2PP, coating with gold, and electrodeposition of PEDOT:PSS. (B) Scanning electron micrographs of a representative array (height 5 mm, pitch 4 mm) before and (C) after PEDOT:PSS electrodeposition. (D) Scanning electron micrograph of a PEDOT:PSS-coated micropillar cross-section.

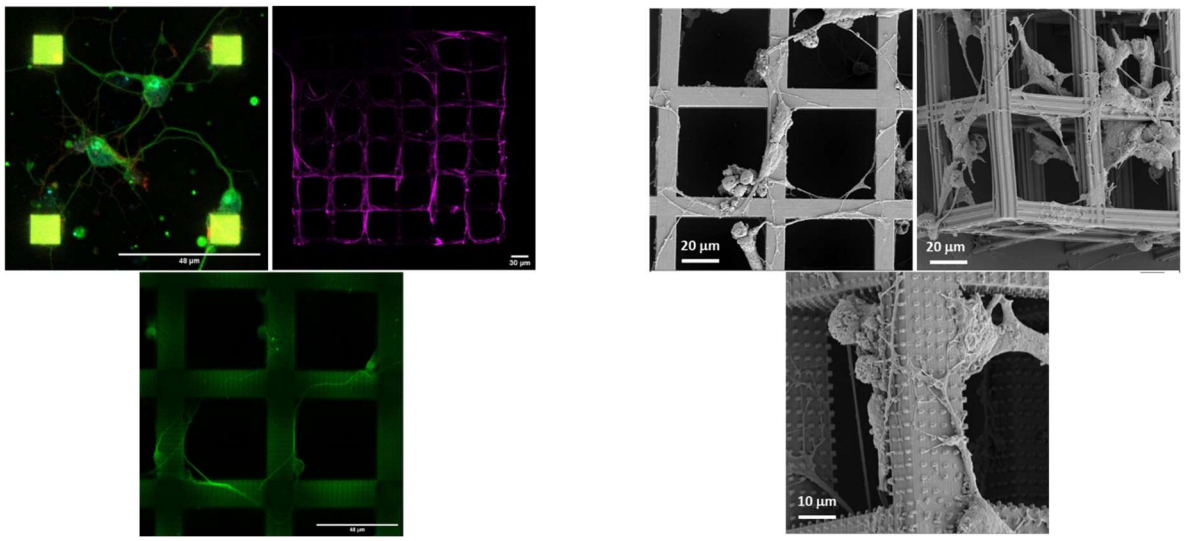

Figure 2. Primary neurons (left) and differentiated SH-SY5Y dells cultured on 3D cage-like scaffold featuring microgrooves and micropillars.

Leveraging The Elastic Deformability of Polydimethylsiloxane Microfluidic Channels for Efficient Intracellular Delivery

Hashim Alhmoud[a,b], and Mohammed Alkhaled[a,b], and Batuhan E. Kaynak[a,b], and Mehmet Selim Hanay[a,b]

[a] Department of Mechanical Engineering, Bilkent University, Ankara, 06800, Turkey
[b] National Nanotechnology Research Institute (UNAM), Ankara, 06800, Turkey
e-mail: hashim.alhmoud@bilkent.edu.tr

The design of a modular lab-on-a-chip component with a small footprint for intracellular cargo delivery is presented. Using the mechanical implementation, a temporary constriction is formed within the microfluidic channel of an elastic polydimethylsiloxane (PDMS) microfluidic device. The constriction dimensions are tunable in real time down to a few micrometers [1]. This constriction forces single cells to morphologically deform. This sudden deformation disrupts the cellular membrane, allowing bioactive cargo from the surrounding medium to permeate through the membrane along the concentration gradient [2]. Unlike other transfection technologies that are limited to genetic material transport (lipid conjugates, lipid particles, etc.), this mode of transmembrane diffusion allows for the introduction of various types of bioactive cargo ranging in diversity from DNA/RNA sequences, to inorganic nanoparticles and small molecules. The method also preserves cell viability unlike other techniques such as electroporation and sonoporation [3].

Although mechanical cell deformation as a means of intracellular delivery is not a new concept [4], the current state-of-the-art suffers from various issues such as low throughput and channel clogging after use [2]. Additionally, constrictions with fixed diameters can only process cells with a certain size-range. In this work we demonstrate that by controlling the constriction diameter in real time and on demand, 1) the device can process cell populations with different average diameters and maximize the delivery efficiency, and 2) any clogs that form from cell or debris clustering can be rapidly resolved by simply widening the constriction and momentarily increasing the flowrate.

The microfluidic devices are fabricated using conventional photolithography and cast molding in order to create a single 100 µm wide and 100 µm deep channel. The channel also consists of a region that is 1 mm long x 5 mm wide referred to as the compression region. The compression region is surrounded by two perpendicular pusher arms connected to linear actuators capable of applying compressive force against the compression region (Fig 1). By attenuating the compressive force applied by the linear actuators, a temporary constriction is formed in the body of the channel located in the compression region (Fig 2a).

Immortalized cells HEK293 FT, MDA-MB-231, MCF 7) suspended in transfection media consisting of PBS supplemented with 4% FBS and 1% Pluronic F-68 in addition to the desired cargo were injected into the device and flown through the channel at 12 µL/min. The constriction size was adjusted to compress the cells to 70% of their original size to maximize delivery while minimizing adverse effects. Subsequently we show the successful delivery of GFP-coding plasmids (Fig 2b, c), green-fluorescent 20 nm Au nanoparticles (Fig 3a-c), and 40kDa FITC-dextran with efficiencies up to ~80% and cell viabilities ~90% (Fig 3d).

This device architecture has implications not only in modular rapid intracellular delivery, but also in the development of mechanical valves, micropumps, and flow redirection apparatus for microfluidics. The use of mechanical compression in microfluidics is yet to be explored extensively but we imagine that this work will act as a first step towards similar implementations in the future.

[1] Alhmoud, H., et al. (2023). "Leveraging the elastic deformability of polydimethylsiloxane microfluidic channels for efficient intracellular delivery." Lab on a Chip 23(4): 714-726.
[2] Kang, G., et al. (2020). "Intracellular Nanomaterial Delivery via Spiral Hydroporation." ACS Nano 14(3): 3048-3058.
[3] Sherba, J. J., et al. (2020). "The effects of electroporation buffer composition on cell viability and electro-transfection efficiency." Scientific reports 10(1): 1-9.
[4] Sharei, A., et al. (2013). "A vector-free microfluidic platform for intracellular delivery." Proceedings of the National Academy of Sciences 110(6): 2082-2087.

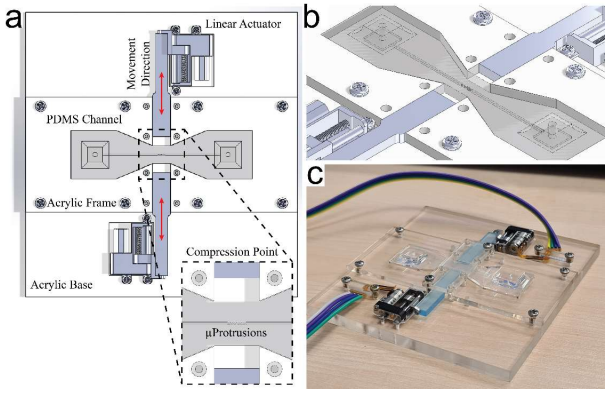

Figure 1. a-c) Schematic, render, and photograph of the device setup comprising the elastic microchannel, acrylic support frame, and a pair of miniature linear actuators. The inset describes the compression region.

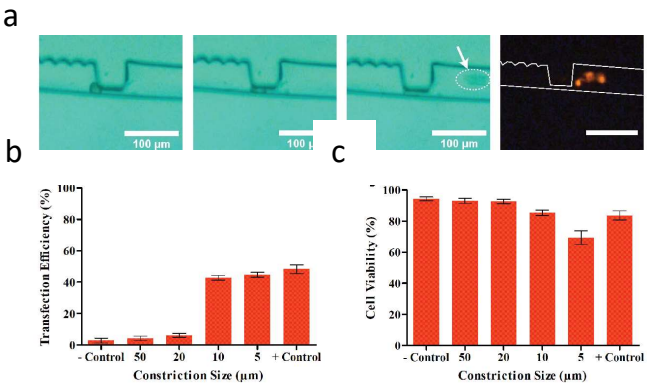

Figure 2. a) Series of optical/fluorescent microscope images showing the deformation of HEK293 cells through the constriction followed by the internalization of propidium iodide into the cell as a result. b) Graph depicting the relationship between constriction size and transfection efficiency of a GFP-coding plasmid into HEK293 cells. c) Shows the cell viability in relation to a decreasing constriction size.

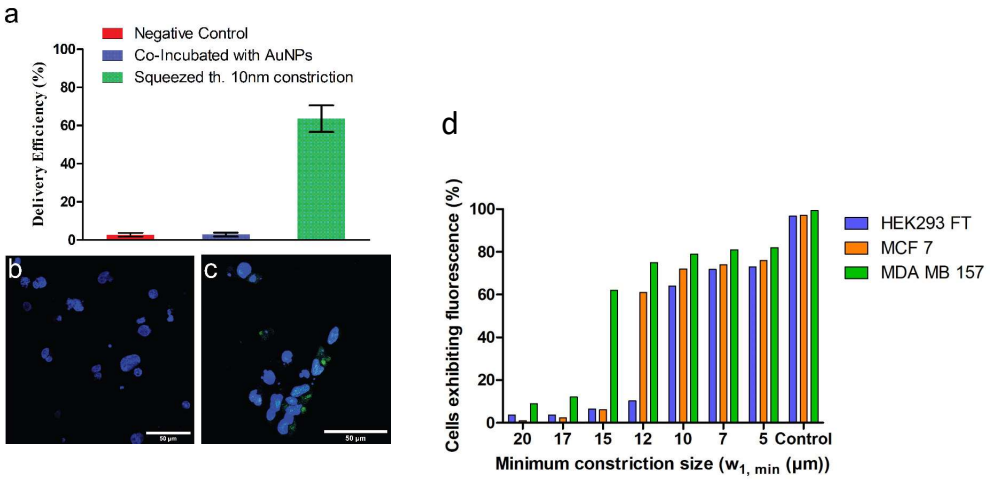

Figure 3. a) Graph representing the delivery efficiency of 20 nm Au nanoparticles in HEK293 cells after mechanical deformation. b-c) Fluorescence microscopy images showing the green fluorescing nanoparticles aggregating within the cellular cytoplasm as compared to the negative control. d) The relationship between the minimum constriction size and the delivery efficiency of 40kDa FITC-dextran to three separate cell lines.

Fabrication and characterization of Nafion/PANI composite membrane-based micropump for Insulin administration

Shatavisha Biswas[1], Arkaprava Datta[1], and Tarun Kanti Bhattacharyya[1]

[1]Indian Institute of Technology Kharagpur, Kharagpur, 721302, India
e-mail: tkb@ece.iitkgp.ac.in

This paper reports an Insulin Delivery System (IDS) that consists of an IPMC-driven micropump along with its electronic driving unit. The micropump utilizes two IPMC actuators and nozzle/diffuser elements to drive the fluid flow. The novelty of this device is that polyaniline (PANI) impregnated Nafion composite membrane is used as the actuator of the micropump. The fabricated membrane is dopped with Lithium for enhanced flow rate as compared to the conventional micropumps. Unlike other conductive polymers, PANI possesses mixed ionic and electronic conductivity, which promotes an enhanced ionic conductivity of composite PANI-Nafion membrane [1]. This Nafion/PANI composite membrane-driven micropump operates at a substantially lower driving voltage (<10V) than the piezoelectrically actuated micropump (> 30V applied voltage). The Nafion/PANI composite actuator causes the micropump to generate a significantly higher flow rate (188 µl/min) as compared to an earlier study, as reported by Mishra et. al. [2].

For the fabrication of the micropump, a circular through-hole (with the same dimension as the micropump chamber) is first formed in the silicon wafer using photolithography. The process involves patterning the wafer on both sides, followed by BHF etching, and finally, KOH etching to form the circular through-hole. Then, the nozzle/diffuser elements are fabricated by processing SU-8 2150 in the following steps: spin-coating, soft baking at 65^0C for 10 minutes and 95^0C for 2 hours, exposing the resist, post-baking at 65^0C for 5 minutes and at 95^0C for 30 minutes, developing using SU 8 developer and finally rinsing and drying.

For the fabrication of the actuator, liquid Nafion-117 solution is mixed with Dimethylformamide (DMF), in which PANI is further added. This solution is stirred and sonicated for an hour. The mixture is then poured into a petri dish and dried in a vacuum oven. Once it cools down, DI water is added to the petri dish, and finally, the fabricated membrane is extracted (Figure 1). Further, the membrane is doped with Lithium ions by dipping in Lithium chloride solution for 24 hours. Gold electrodes are deposited on both sides of the fabricated membrane using Magnetron Sputtering technique.

The deposited membrane is mounted on the micropump structure to analyze its vibrational performance. The schematic of the working principle and the final prototype of the micropump is depicted in Figure 2. It is to be noted that the maximum deflection, 98.2 µm, is observed when a 5V square wave is applied at 0.5 Hz (shown in Figure 3 (a)). Further, as seen in Fig. 3 (b)., with the application of 5V, 0.5Hz square wave, the flow rate of the micropump for Insulin attains a peak of 188 µl/min. The maximum flow of Insulin can go up to 298 µL/min (Fig. 3 (c)) when an 8V, 0.5Hz square wave is applied. The driving circuit of this IDS (shown in Fig 4) consists of the AD9850 DDS signal generator module, Arduino Uno microcontroller, LM741 operational amplifier, an OLED display and a rotary encoder module on the front panel to build a user-friendly interface.

References :

[1] O. A. Pyshkina et al., Colloid and Polymer Science, 297 (2019), 423-432.
[2] R. Mishra et al., Journal of Microelectromechanical Systems, 28(6) (2019), 987-996.

.

Figure 1. Synthesized Nafion/PANI composite membrane

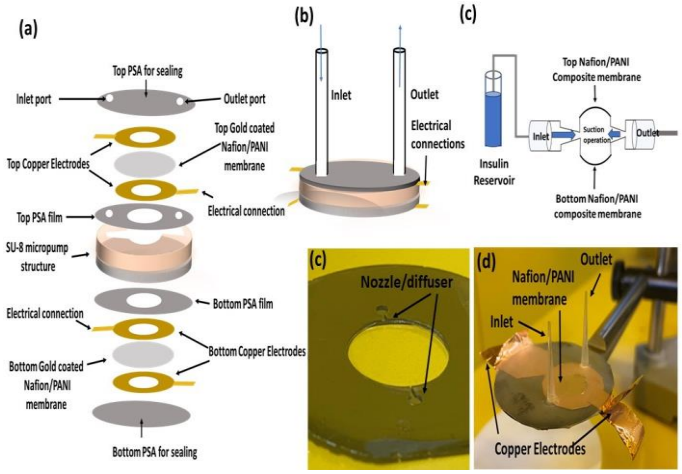

Figure 2. (a)-(b) Schematic of the insulin delivery system **(c)** Working principle **(d)** Top view of the dual actuator micropump structure **(e)** Assembled prototype of the insulin delivery system

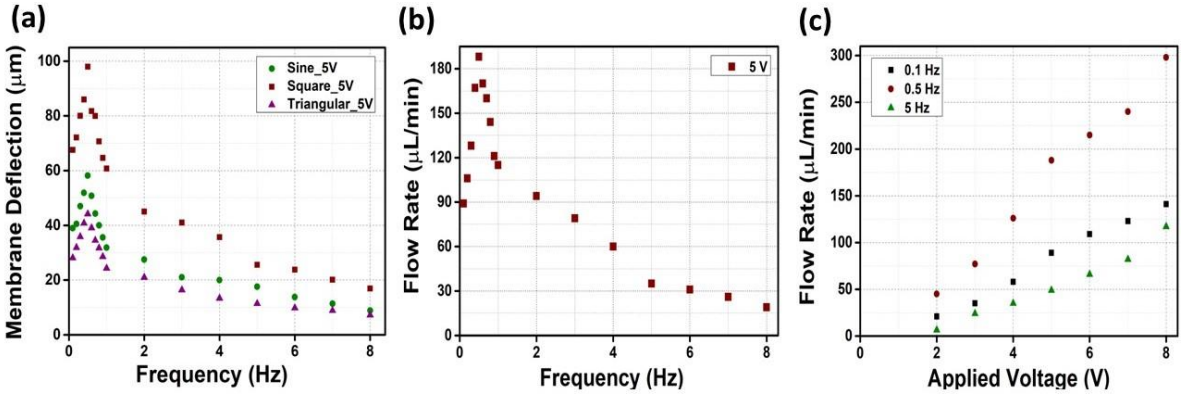

Figure 3. (a) Frequency response of Nafion/PANI membrane at 5V for different signals**,** Flow characteristics of the micropump for Insulin, **(b)** with increasing frequency at 5V square wave, **(c)** with increasing voltage at 0.1 Hz, 0.5 Hz and 5 Hz, square wave

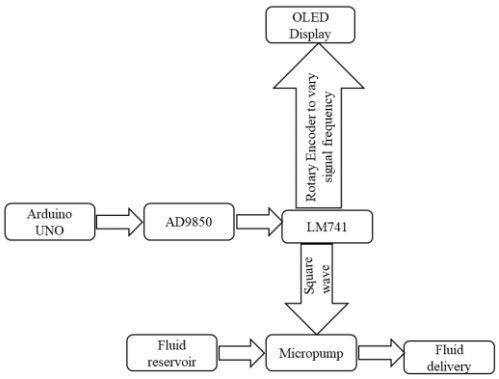

Figure 4. Electronics control module

A wearable microfluidic device with a built-in micropump for reliable sweat collection for health monitoring

Zhuodan Chen[a], Weihao Li[a], Xing Cheng[a]
[a] Southern University of Science and Technology , Shenzhen, 518055, China
e-mail: chengx@sustech.edu.cn

Keywords:
Wearable devices; Health monitoring; POCT; micropump;

Abstract

Epidermal-fluidic devices have received increasing interests from researchers due to their great potential in health monitoring applications[1].Typically, these devices contain a microfluidic network for the non-invasive biofluids collection and analysis of biomarkers such as sweat, which can provide information about changes in glucose, lactate ,NaCl concentration and the presence of some disease-related biochemical factors[2]. Previous studies have demonstrated a sweat collector with a capillary burst valve (CBV) for continuous, time-sequential sampling of excreted sweat [3, 4]. However, these designs have several limitations, for instance, natural pressure from the sweat gland cannot provide a stable long-term driving force, hindering continuous biomarker monitoring and analysis of disease-related biomarker changes over extended periods of time. Additionally, these passive platforms cannot accurately measure sweat composition, impeding the potential development of sweat detection in health monitoring. Consequently, further developments are needed for longer-duration, higher-volume sweat collection, and more specific sweat composition testing in health monitoring.

In this study, we propose a novel microfluidic system comprising a programmable micropump and a multi-branched network. Capillary burst valves (CBVs) are utilized to achieve a gradient threshold pressure by varying the width of the channel structure and the angle of channel divergence[5]. As depicted in Figure 1, our design incorporates 4 collection trees and each collection tree contains 4 chambers, providing a total volume of 48μL. The filling order of the chambers is represented as a, b, c, d, e. Initially, the sweat is introduced into the micropump and guided through the microchannels to fill the sweat collection trees sequentially. Once the chamber is filled, the pressure increases, facilitating the flow of sweat into the subsequent collection chamber. This process is repeated until all chambers in the collection tree are filled. Subsequently, the sweat passes through the gradient CBVs and enters the next collection tree. By following these steps, sweat secreted during different time periods is segregated and stored in separate chambers. Furthermore, Figure 1(b) presents an exploded view of the complete device, wherein the top layer encapsulates the microchannel layer, and a micropump with an integrated absorbing pad is positioned at the corner of the microchannel layer.

To fabricate the sweat collector, we utilize laser direct writing to pattern SU8. The specific fabrication process is illustrated in Figure 2. Additionally, Figure 3 illustrates device functionality with bule-dyed water introduced into the storage chambers in a time sequenced manner. Future work will focus on evaluating the device's performance in practical conditions, such as real-time, high-volume sweat collection for in-situ colorimetric testing, as well as the accurate analysis of sweat biomarkers when integrated with a high-throughput microfluidic platform. The sweat collector with built-in micropump is expected to function reliably for sweat collection over an extended time period.

References

[1] Yang, Y.R et al., Chemical Society Reviews, 2019. **48**(6): p. 1465-1491.
[2] Yang, D.S et al., Science (New York, N.Y.), 2023. **379**(6634): p. 760-761.
[3] Choi, J et al., Advanced Healthcare Materials, 2017. **6**(5).
[4] Koh, A et al.,Science Ttranslational Medicine, 2016. **8**(366).
[5] Cho, H. et al., Journal of Colloid and Interface Science, 2007. **306**(2): p. 379-385.

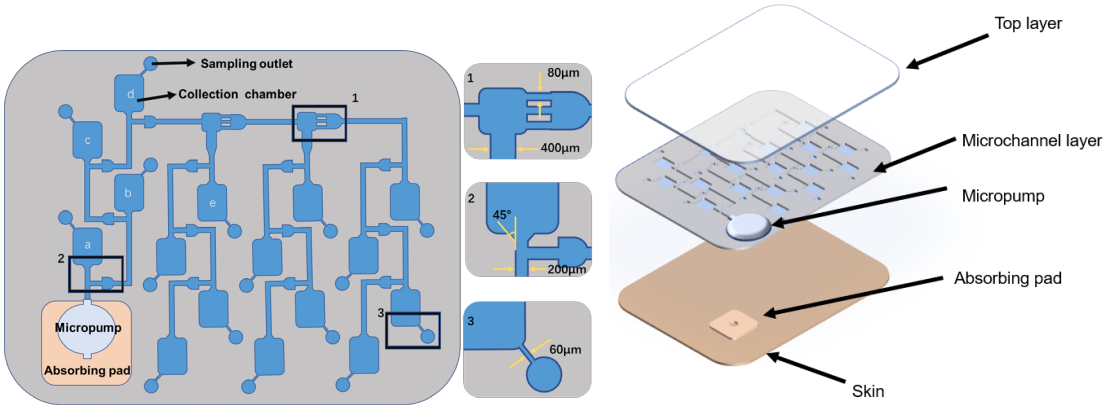

Figure 1. a) A schematic of the top-view of the sweat collector device; b) an exploded view of a complete device.

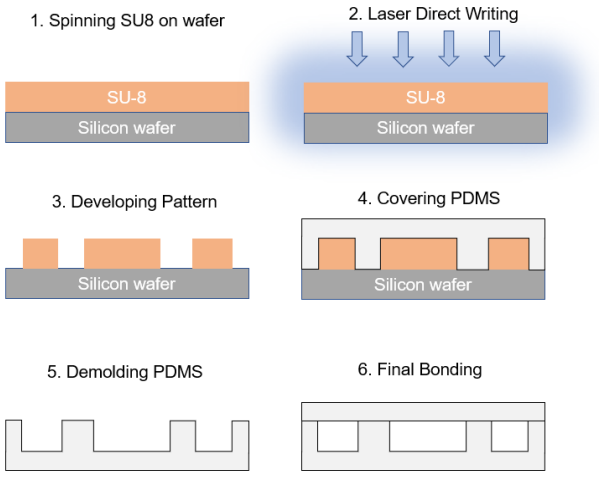

Figure 2. A schematic of fabrication process.

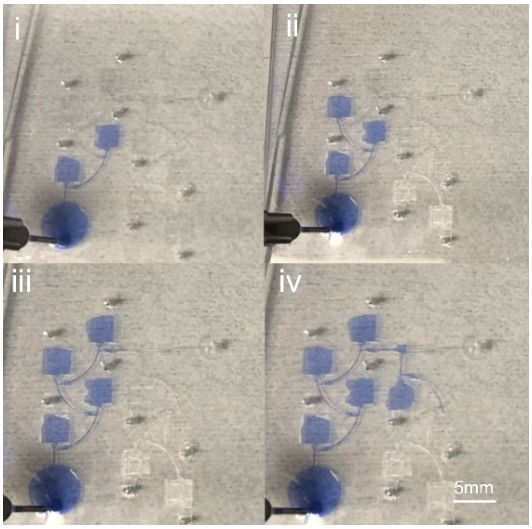

Figure 3. Photographs of a working device with blue water sequentially introduced into storage chambers.

A planar integrated astable microfluidic circuit for square pressure waveform generation

Weihao Li[a], Zhuodan Chen[a], and Xing Cheng[a]
[a] Southern University of Science and Technology, Shenzhen, 518055, China
e-mail: chengx@sustech.edu.cn

Key words:
Microfluidic circuit; Microfabrication; Non-linear microfluidics

Abstract

The field of microfluidic networks, originating from microelectronics, still holds significant potential to be explored as inspired by the tremendous capabilities achieved by integrated electronic circuits[1]. The fundamental principles of energy and mass conservations allow for analogies between fluid and electrical circuits, which have spurred a series of studies regarding the design, fabrication, and application of microfluidic circuits [2-4]. However, previous research typically relied on pneumatic valves or multi-layer fabrication, leading to a dependence on bulky external controllers or the soft lithography paradigm, which both require lengthy fabrication periods and high costs[5].

The challenge of realizing true lab-on-chip design remains unsolved, as current methods often fall into a "chip-in-lab" dilemma due to limitations in design paradigms and reliance on external facilities[6]. A promising solution to these issues is to use non-linear effects in microfluidics[7], allowing for functional responses due to passive features in the design. Moreover, the inclusion of a micropump in the system could foster greater integration and portability.

In this study, we present a planar microfluidic circuit network fabricated by maskless lithography, incorporating designs such as resistors, capacitors, diodes, and transistors, all of which can ultimately be combined with a micropump module. In addition, the planar functional components demonstrate properties comparable to their electrical analogies in the network. As depicted in Figure 1, the electrical elements and their microfluidic counterparts are illustrated, with the microfluidic components displayed in the top-view. Elastomeric membranes or cantilevers are employed to realize non-linear effects, thereby mimicking the behaviors of capacitors or transistors in fluidic circuits. Figure 2a and Figure 2b offer a specific example of an astable multivibrator, along with its input and output signal properties. The astable multivibrator could generate periodically changing voltage, whose period is determined by the specific values of the resistors and capacitors. As shown in Figure 2b, the theoretical output has the form of periodic square wave. In microfluidic network, this design could transform a constant pressure input into oscillating pressure output. Such flow controlling could be applied widely, for instances, chemical mixing, logic control, biomimetics and more.

To fabricate the proposed planar microfluidic circuit, we adopt the laser direct writing method on UV-PDMS (KER-4690). Figure 3a and 3b display the final layout pattern for the astable microfluidic circuit and a preliminarily fabricated device, respectively. In this work, we will elaborate on the characteristics of the proposed circuit components and the microfluidic astable multivibrator. Quantitative analysis will be carried out to evaluate the pressure output obtained by the astable fluidic circuit. The technique presented in this work may present a facile route towards complex fluid pressure profile generation using microfabricated fluidic circuit analogous to well-studied electronic counterparts.

References

[1] Whitesides, G.M., Nature, 2006. **442**(7101): p. 368.
[2] Thorsen, T. et al., SCIENCE, 2002. **298**(5593): p. 580-584.
[3] Leslie, D.C., et al., Nature Physics, 2009. **5**(3): p. 231.
[4] Mosadegh, B., et al., Nature physics, 2010. **6**(6): p. 433.
[5] Narayanamurthy, V., et al., RSC Advances, 2020. **10**(20): p. 11652-11680.
[6] Reyes, D.R., et al., Lab on a Chip, 2021. **21**(1): p. 9-21.
[7] Xia, H.M., et al., Lab on a Chip, 2021.21(7): p. 1241-1268.

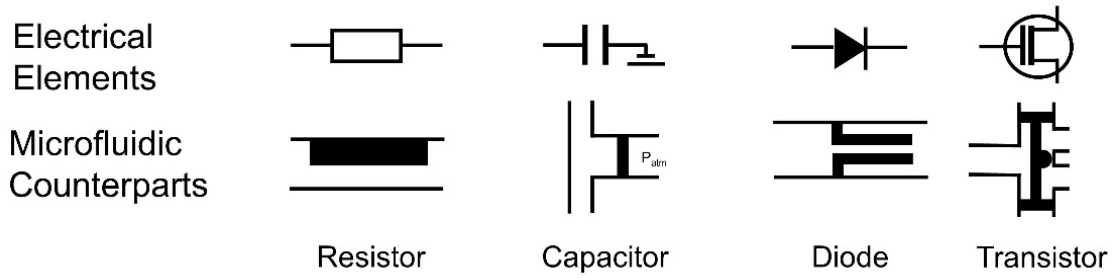

Figure 1. Electrical elements and the designs of their microfluidic counterpart in top-view.

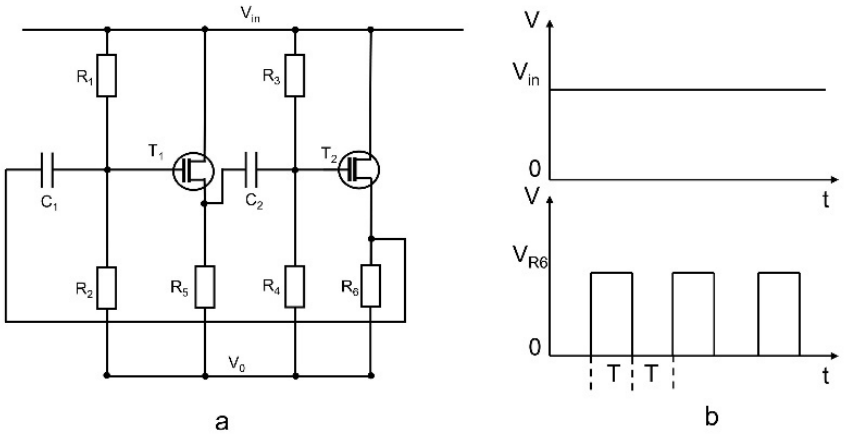

Figure 2. a) Astable multivibrator electrical circuit; b) input voltage and theoretical output voltage (V_{R6}).

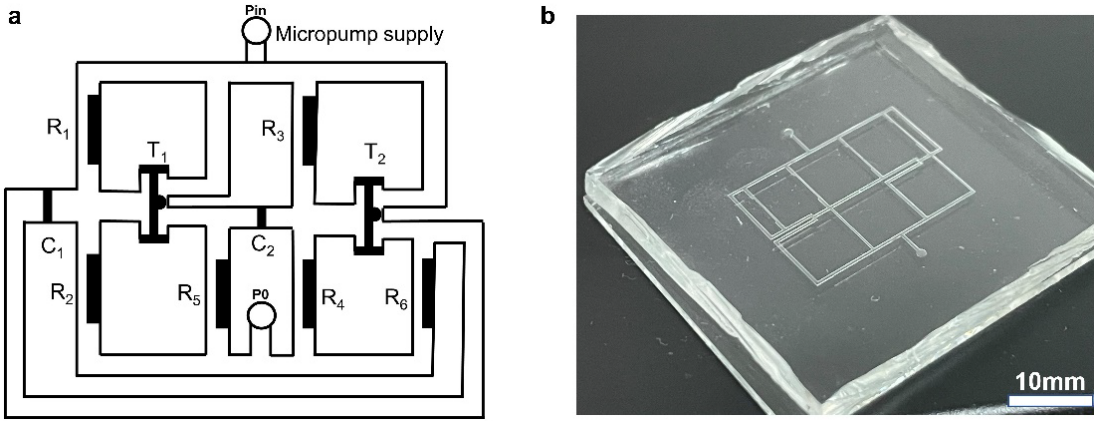

Figure 3. a) A layout pattern for astable multivibrator microfluidic circuit; b) a photograph of a preliminarily fabricated astable fluidic circuit based on PDMS.

Fabrication of switchable biocompatible, nano-fluidic devices using a thermoresponsive polymer on nano-patterned surfaces

Ch. Bickmann[1], Ch. Meinecke[1, 2], T. Korten[3], Ch. Helke[1,2], S. Hartmann[1], S. Diez[4], D. Reuter[1, 2]

[1] Center for Microtechnologies, Technische Universität Chemnitz, Chemnitz 09126, Germany,
[2] Fraunhofer Institute for Electronic Nanosystems (ENAS), Chemnitz 09126, Germany,
[3] Physics of Life, Technische Universität Dresden, Dresden 01069, Germany
[4] B CUBE, Technische Universität Dresden, Dresden 01069, Germany
e-mail: christopher.bickmann@zfm.tu-chemnitz.de

Nanostructured surfaces are of great importance for various applications such as microfluidic and microanalytical devices [1,2], biosensors [3], or network-based biocomputation [4]. Different techniques such as photolithography, micro-contact printing and dip-pen technology can be used to modify physicochemical properties such as wettability, charge and fluorescence. However, once a pattern is created, it cannot be easily changed, which limits the use of structured surfaces to a specific application. If new applications are needed, new microstructures have to be fabricated. Therefore, it is interesting to develop methods that enable the creation of structured surfaces with switchable and rewritable patterns. One approach is based on the selective deposition of stimuli-responsive materials that form self-assembling monolayers (SAMs) or polymer brushes. On such surfaces, the topographical and physicochemical properties can be locally controlled by externally manipulating the environmental conditions.

In this study, we present a method for depositing and patterning the thermosensitive polymer poly(N-isopropylacrylamide) (PNIPAM). Due to its thermoresponsive properties [5], these polymer brushes are intended to act as flow regulators in nanoscale microfluidic channels to control material transport through the nano network. For applications in biosensors and network-based biocomputation, it is desirable to dynamically switch the motion on or off in parts of the nanostructured device. To achieve this, two approaches were pursued based on nanolithographic methods to locally graft the thermosensitive polymer PNIPAM in the nano-dimensional channels. In both cases, a self-assembling monolayer (SAM) consisting of (3-Aminopropyl)-dimethylethoxysilane (APDMES) was bound to the hydroxyl group of the substrate surface and subsequently functionalized with the polymerization initiator α-Bromoisobutyryl bromide (BIBB). In the first approach (see figure 1), the SAM itself was patterned using a photoresist and a lift-off process, followed by the selective deposition of the initiator, which initiates substrate-induced atom transfer radical polymerization (SI-ATRP) for the growth of PNIPAM on the SAM structures. In the second approach, the covalently bonded PNIPAM layer was first deposited onto the whole surface using the previously described method. Then, a standard “top-down” lithographic patterning was carried out through oxygen plasma etching. Finally, both approaches were compared with regard to their suitability for in situ patterning and functionalization inside nano-fluidic channels.

The result of this study demonstrates the successful adaption of individual process steps for grafting PNIPAM onto nano-patterned glass surfaces. Additionally, essential structuring of molecular monolayers of the silane APDMES was achieved, with reliable structuring of structures a few hundred nanometers in size using the lift-off process. PNIPAM was also successfully grafted onto these nano-structured surfaces. The reaction time of the APDMES layer with the polymerization initiator BIBB and the composition of the reaction solution used were found to have the greatest influence of the processes. AFM and XPS analysis of the functionalized surfaces revealed patterned growth of both the SAM and the PNIPAM structures.

[1] K. Morikawa et al., Analytical Sciences. 32 (2016) 79-83.
[2] L. Ionov et al., Nano Letters. 6(9) (2006) 1982-1987.
[3] A. Minopoli et al., Advanced Materials Interfaces. 9(2) (2022) 2101133.
[4] D. V. Nicolau Jr. et al., Proc. Natl. Acad. Sci. USA. 113(10) (2016) 2591-2596.
[5] M. Heskins et al., Journal of Macromolecular Science. 2(8) (1968) 1441-1455.

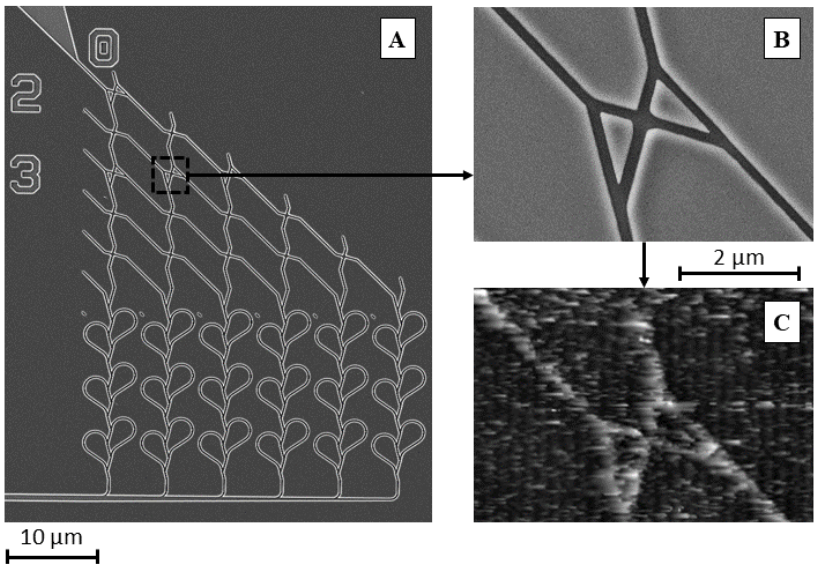

Figure 1. (A) shows a scanning electron microscope (SEM) image of a nano network of microfluidic channels patterned using electron beam lithography into a PMMA photoresist. (B) illustrates a junction within this network. (C) shows an atomic force microscopy (AFM) image of the junction after functionalization with PNIPAM and subsequent lift-off process.

Picking microorganisms by impedance flow cytometry

Mohadeseh Mozafari [a], Peer Erfle [a], Jonathan Block [b,c], Rainer Krull [c], Andreas Dietzel [a]
[a] Institute of Microtechnology, TU Braunschweig
[b] Braunschweig Integrated Centre of Systems Biology (BRICS), TU Braunschweig
[c] Institute of Biochemical Engineering, TU Braunschweig
e-mail: m.mozafari@tu-braunschweig

Purpose of the work: Recent studies have highlighted the crucial role of electrogenic gut microorganisms in oxygen-deprived environments [1]. However, our understanding of their function within the human intestinal microbiome remains incomplete. With the available, time-consuming screening methods same as the labeling methods with very limited sample throughput and low detection rates, the entire variety of bacteria is not yet accessible – leaving the largest proportion of the human gut biocenosis unexplored. Therefore, a label-free and real-time method is required with taking advantage of microtechnology to understand the properties of microorganisms in order to meet superior control over the enormous link between microbiota and health and disease issues. The objective of this research is to develop a microfabricated high-throughput bioelectrochemical flow cytometer able to pick out currently uncharted gut bacteria by their electrical properties. Based on impedance and polarizability a strong correlation between electrical properties accessible by microfluidic sensing and bacterial extracellular electron transfer will be established. A multi-frequency impedance measurement system shall be established in this novel impedance flow cytometer.
Background/ State of the art: A number of studies have been carried out in the recent past regarding the label-free investigations of single cells using flow cytometry [2], but research concerning microorganisms such as gut bacteria is still in the early stage. An impedance flow cytometry can give us detailed information about the properties as well as sorting or counting microorganisms in a specific solution [3]. With co-planar electrodes particles passing through the microchannel can be detected where the signal is sensitive to the distance from the electrodes [4]. In this work, a microchannel that has been fabricated using the Femto-second laser ablation will be sealed with the help of a thin PDMS layer to the layer containing the electrodes.
Description of the system: A thin PDMS layer was spin-coated on top of a glass wafer before microchannels were created using a Femto-second laser ablation method. Gold on top of a Titanium adhesion layer was sputtered on top of another glass wafer, and then structured by photolithography process to form co-planar microelectrodes. Both glass wafers were connected and sealed thanks to the PDMS layer in between (Fig. 1). In order to have an impedance flow cytometer, a microfluidics system was connected to HF2LI (Lock-in Amplifier- Zurich Instrument).
Experimental results: To ensure the appropriate measurement of bacterial suspensions and to prevent clogging of the microchannel, a sample treatment of cell dispersion followed by size exclusion filtration was developed (Fig. 2). This prevents bacterial aggregates from generating signals as they flow through the measurement channels, which form artifacts during signal evaluation. Preliminary experiments showed no effect of the treatment on cell viability, but further investigation with more refined methods and studies of the effect of surface structure integrity on signal quality is needed. After a leakage test on the microfluidics part of the system, first experiments with polystyrene beads (different sizes of 3, 5, and 10 μm) have been carried out. The signal analysis represents that the system is able to detect single particles when they are traveling through the sensing zone. Additionally, according to the study on the 10 μm polystyrene bead, the signal can provide information about the position (distance from the electrodes) of the particle inside of the sensing zone of the system. In the next step, the setup will be tested with bacteria, and after a successful detection of the bacteria, signal processing shall allow to extract the properties of the bacteria and to distinguish between different species.

[1] Naradasu et al. Frontiers in Microbiology 9, 3267. (2019)
[2] M. Li et al., RSC advances, vol. 11, 20944–20960 (2021)
[3] H. B. Steen, Journal of Microbiological Methods, 65–74, (2000)
[4] J. Cottet et al., Microfluid Nanofluid, p. 50, (2019)

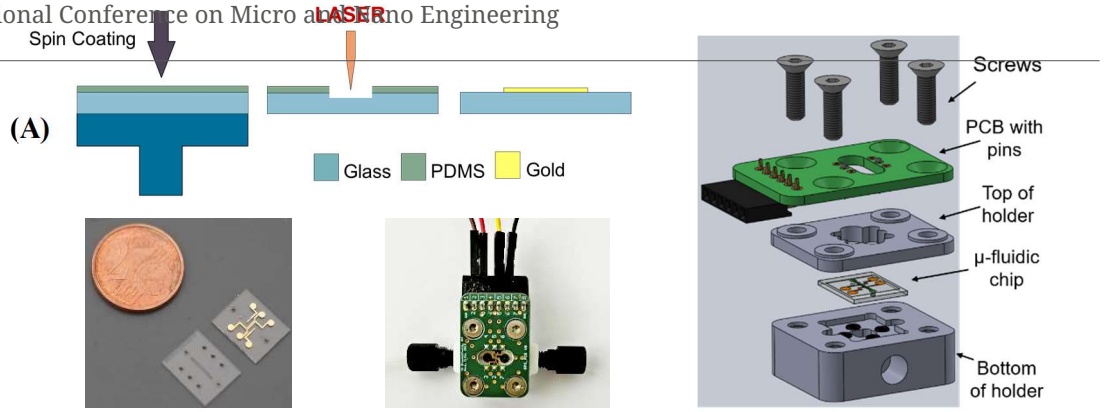

Figure 1. (A) schematic of the Microchannel fabrication plus the Gold electrodes (B) dissembled version of the microfluidics system with the electrical part (C, D) enclosing the system with the second glass substrate containing electrode inside of a holder and a PCB

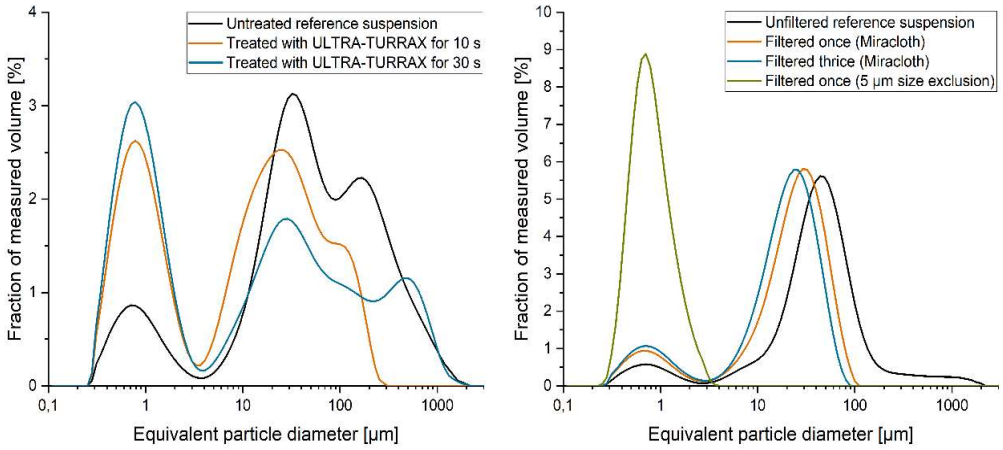

Figure 2. Sample treatment of bacterial suspensions with an ULTRA-TURRAX stirrer (A) and different filtering materials (B), fraction of measured volume over the equivalent particle diameter, equivalent particle diameters determined with laser diffraction spectroscopy

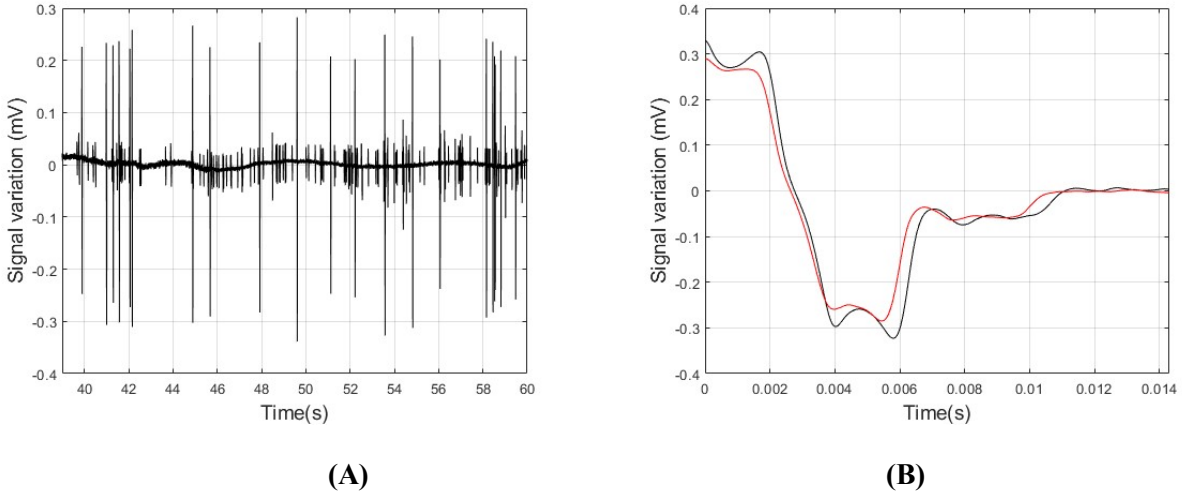

Figure 3. An early stage measurement of particle passing through the sensing zone (A) Measurement Signal Voltage: 3V, Frequency: 200KHz for a mixture of 5, and 10 μm polystyrene bead in PBS solution (B) Peak analyses in the signal which shows the different position of the particles inside of the microchannel

Rapid prototyping of self-filling microfluidic chips for SARS-CoV-2 RNA detection by isothermal amplification

Staniszewski F.[a], Schrittwieser S.[a], Schmidleithner C.[a], Posch B.[a], Osinkina L.[b], Westenthanner M.[b], Stehr J.[b], Peham J. R.[a]

[a]Molecular Diagnostics, AIT Austrian Institute of Technology GmbH, 1210 Vienna, Austria
[b] HP Health Solutions Germany GmbH, 82152 Martinsried, Germany
e-mail: filip.staniszewski@ait.ac.at

The public interest in point-of-care devices, that require little user interaction or laboratory equipment, has dramatically increased since the SARS-CoV-2 pandemic. Here we propose a pipeline for rapid prototyping together with a microfluidic design, *AITmicro*, that is based on capillary retention valves (CRVs) and enables controlled volume deposition independent of applied sample volume. A loop-mediated isothermal amplification (LAMP) assay for the detection of SARS-CoV-2 RNA was incorporated to highlight the diagnostic capability of *AITmicro*, achieving PCR-sensitivity without the need for trained personnel or readout instruments.

Introduction: As the SARS-CoV-2 pandemic spread, the need for rapid point-of-care diagnostic tools has increased dramatically. Although, many diagnostic methods, such as PCR-testing, were already realized, they still require a complex infrastructure that cannot be attained in a fast manner. The ideal assay would require no laboratory equipment or trained personnel and could be deployed fast. To this end, we developed a self-filling microfluidic chip, *AITmicro*, that only requires a transfer pipette to be filled and is therefore very user friendly. Filling of the diagnostic unit (*"reaction chamber"*) is independent of applied sample volume, which is realized by incorporating two capillary retention valves (CRV) [1]. For fast deployment, we established a pipeline for accelerated and cost-effective prototyping, which can be crucial for viral outbreak prevention.

Methods: Accelerated and cost-effective prototyping was realized by first micro-milling several designs (LPKF Protomat S103), which were evaluated regarding their microfluidic performance. In a second step, the optimal design – *AITmicro* – was injection molded (IM) by Protolabs (2.10 EUR per piece, Fig. 1a). Microfluidic chips were made from PMMA and sealed with adhesive foil (ARcare NB90106). In a final step, IM-chips were used in combination with a colorimetric LAMP assay for SARS-CoV-2 (E2019S, New England Biolabs) to highlight the diagnostic capability of *AITmicro*.

Results: A cost-effective pipeline for rapid prototyping as well as a self-filling chip for isothermal pathogen detection could be developed. We estimate that we could save up to 65% in costs by using our prototyping approach. In total, prototyping of *AITmicro* required 5200 EUR and 5-6 weeks in time (solid line, Fig. 1b). This included micro-milling of 10 designs (500 EUR), microfluidic evaluation (300 EUR) and injection molding of the final design, *AITmicro* (2200 EUR tooling and 2100 EUR for 1000 pieces). In *AITmicro* liqud flow is controlled by two CRVs. As equilibrium in pressure between the two CRVs is reached, which is when the inlet valve is completely drained, the flow of liquid stops (Fig. 1c). Therefore, AITmicro ensures the filling of the intermediate reaction chamber independent of applied sample volume. Finally, the diagnostic capability of *AITmicro* was achieved by incorporating a colorimetric SARS-CoV-2 LAMP assay, where amplification of the target results in change of color. While positive samples turn yellow (bright intensity in green channel), negative controls remain pink (dark intensity in green channel, Fig. 2). The readout (color change) does not require any instruments. Positive and negative samples are clearly distinguishable by the naked eye down to concentrations of 10 copies per µL (LOD). In future, this microfluidic system can be combined with further assays to provide rapid and cost-effective pathogen detection at PCR-sensitivity without any further readout instruments or trained laboratory personnel.

References:

[1] Juncker David et Al, *"Autonomous microfluidic capillary system"* Anal Chem., 74 (24) 6139-44, 2002.
[2] Brian A. Rabe, Constance Cepko, *"SARS-CoV-2 detection using isothermal amplification and a rapid, inexpensive protocol for sample inactivation and purification"* PNAS, vol. 117 (37) 24450- 58, 2020

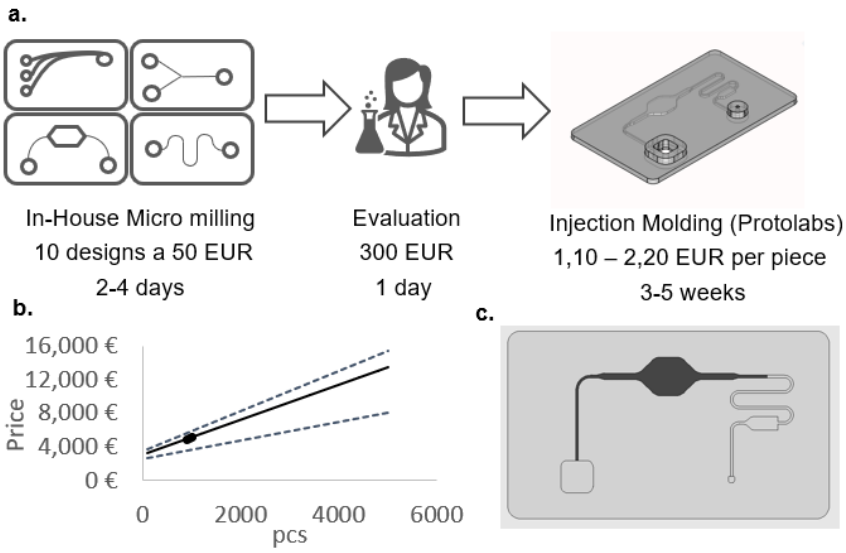

Figure 2. Rapid prototyping pipeline and AITmicro design a.) development of AITmicro and related costs; b.) cost estimation for rapid prototyping; solid, dashed lines and point represent costs of self-filling chip, minimal and maximal cost boundaries and cost for 1000 chips, respectively; c.) functionality of AITmicro: filling stops once pressure is equilibrated between the two CRVs.

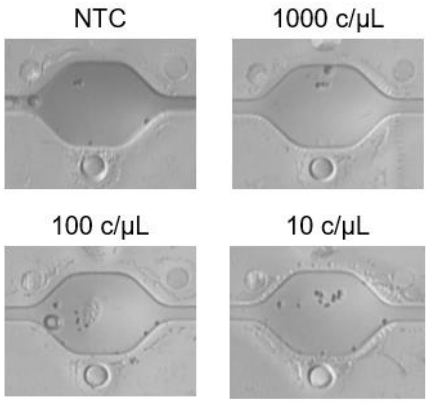

Figure 1. Colorimetric LAMP SARS-CoV-2 assay in AITmicro chip (grey-sacle represents only the green color channel). Positive samples change color to yellow (bright), while NTC remains pink (dark). The limit of detection (LOD) is 10 copies per µL.

Hydrocarbon-Mediated Shrinkage of Silicon Nitride Nanopores

Debmalya Roy [a], Aniruddha Guha [a], James Yates [c], Suman Chakraborty [a]

Indian Institute of Technology Kharagpur, Kharagpur, 721302, India
[b] ITQB NOVA, Oeiras, 2775-629, Portugal
e-mail: suman@mech.iitkgp.ac.in

Solid-state nanopores have come to prominence in a broad range of fields: from biomolecular sensing to applications in ionic circuits, where they function as fluid-based diodes, transistors, and memristors [1]. Many applications rely on characterization of the electrokinetic current flowing through the nanopore. However, the current is highly dependent on the size and morphology of the pore, making precise pore fabrication a crucial area of focus. A promising approach for the fabrication of nanopores of a desired pore size in thin film dielectrics involves the fabrication of larger nanopores, followed by their controlled shrinkage [2] - various methods have been explored for this[3]. One preferred method involves reflowing thin film material to refill the nanopore [4], another depends upon the deposition of foreign material around the pore [5]. In the former method, pore shrinkage occurs due to the viscous movement of the thin film material, driven by high energy. This energy can be supplied by sources such as electron or ion beams, lasers, or thermal heating, transforming the crystalline membrane into a viscous state that shrinks the pore due to surface tension [4]. The latter method relies on material deposition techniques such as: ALD, ion, vapour, or electrochemical depositions to introduce foreign material around the edges of the pore and thus shrinking it[3]. Methods employing an electron beam offer an inherent advantage over other approaches since they provide visual feedback during the shrinking process, enhancing fabrication control. Conversely, thermal or laser treatment techniques require extensive manual handling of the membranes, increasing the risk of physical damage. While electron beam methods have proven reliable for filling smaller pores in thicker films (and have demonstrated a greater potential for control), they struggle to achieve the same effect for larger pores, primarily due to their migration-based nature. Efforts have been made to exploit residual carbon inside the chamber of scanning electron microscopes for pore shrinking. It is worth noting that immersing pores in fluids like ethanol or deionized water for an extended period can also lead to pore shrinkage, but this method lacks precise control over the shrinking process [6]. Here we demonstrate a novel approach that employs hydrocarbon-based pore shrinkage using the electron beam from a transmission electron microscope. In this method, the pore is immersed in ethanol for approximately 10 minutes and then air-dried before exposing it to the electron beam. The residual ethanol molecules that adhere to the membrane aid in the deposition of hydrocarbons. When combined with the reflowing silicon nitride, these hydrocarbons contribute to the shrinkage of the pore. The real-time visual feedback provided during this approach enables precision and control, making it possible to shrink pores with diameters exceeding 100 nm with remarkable accuracy (figure:1). The compositions of the virgin membrane; the area around the initial pore; and the reflow region were recorded using energy dispersive spectroscopy, clearly indicating the enhanced presence of carbon around the pore following ethanol exposure (figure:3). This method can be used to fabricate and tune nanopores with a high degree of precision. These nanopores can then be used for biosensing and other applications.

[1] L. Xue, H. Yamazaki, R. Ren, M. Wanunu, A.P. Ivanov, J.B. Edel, Solid-state nanopore sensors, Nat. Rev. Mater. 5 (2020) 931–951.
[2] A.J. Storm, J.H. Chen, X.S. Ling, H.W. Zandbergen, C. Dekker, Fabrication of solid-state nanopores with single-nanometre precision, Nat. Mater. 2003 28. 2 (2003) 537–540.
[3] X. Lei, J. Zhang, H. Hong, Z. Yuan, Z. Liu, Controllable Shrinking Fabrication of Solid-State Nanopores, Micromachines. 13 (2022) 923.
[4] W. Asghar, A. Ilyas, J.A. Billo, S.M. Iqbal, Shrinking of Solid-state Nanopores by Direct Thermal Heating, (2011).
[5] H.K. Gatty et al., Highly efficient shrinkage of inverted-pyramid silicon nanopores by plasma-enhanced chemical vapor deposition technology, Nanotechnology. 27 (2016) 254005.
[6] Q. Li, Q. Zhao, B. Lu, H. Zhang, S. Liu, Z. Tang, L. Qu, R. Zhu, J. Zhang, L. You, F. Yang, D. Yu, Size evolution and surface characterization of solid-state nanopores in different aqueous solutions, Nanoscale. 4 (2012) 1572.

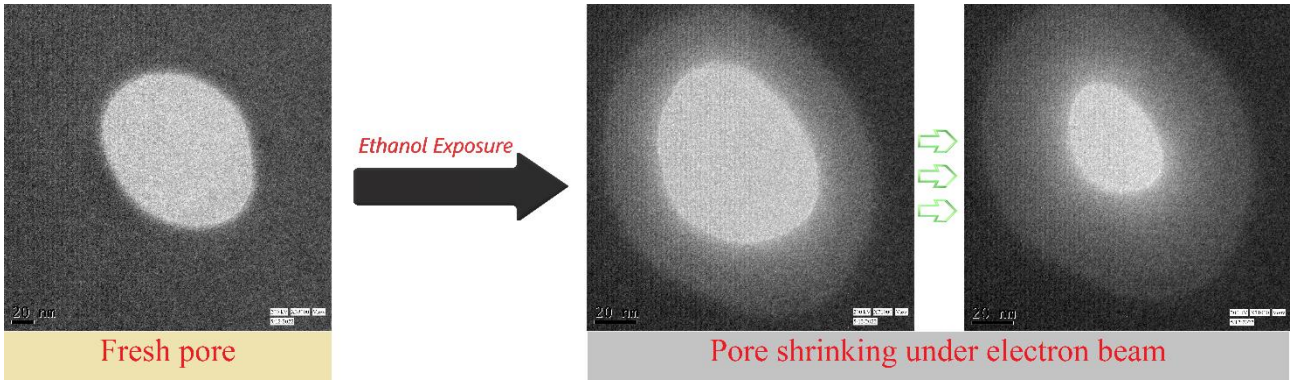

Figure 1. A fresh FIB drilled oval-shaped pore (150 nm x 120 nm) shrinking under an electron beam after being exposed to ethanol

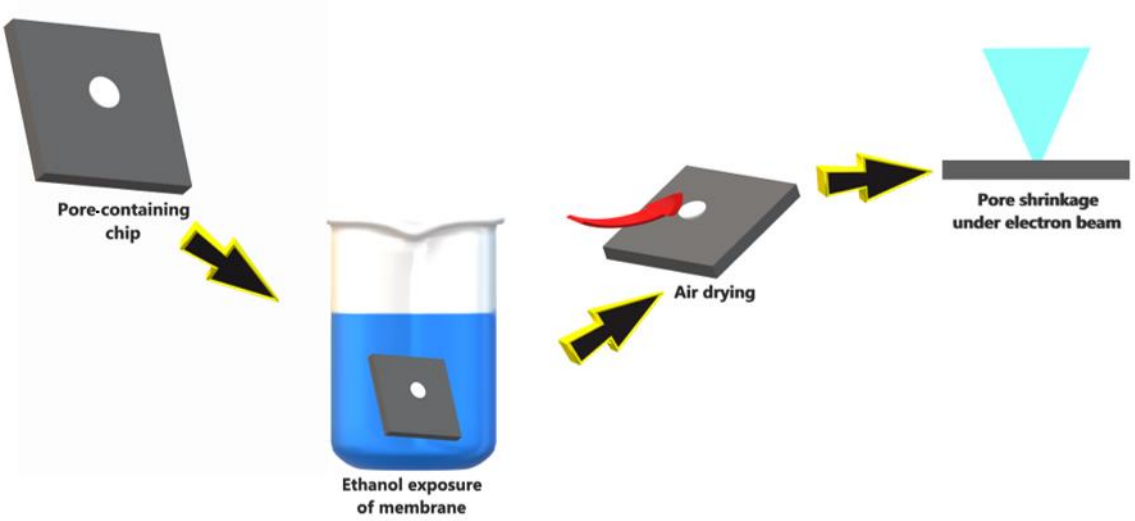

Figure 2. Process flow schematic showing different steps for shrinking a pore under electron beam

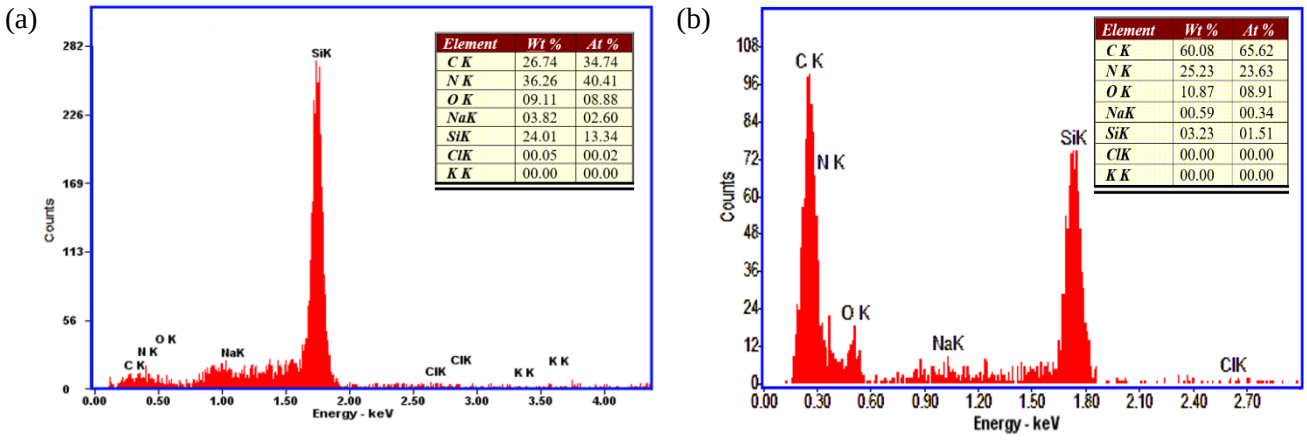

Figure 3. (a) EDS spectrum of pore-containing SiN_x membrane before ethanol exposure. (b) EDS spectrum of pore containing SiN_x membrane after ethanol exposure and pore shrinkage.

Reversible Manipulation of Effective Pore Diameter in Silicon Nitride Nanopores

Aniruddha Guha [a], Debmalya Roy [a], James Yates [b], Chirodeep Bakli [a], Suman Chakraborty [a]

[a] Indian Institute of Technology Kharagpur, Kharagpur, 721302, India
[b] ITQB NOVA, Oeiras, 2775-629, Portugal
e-mail: suman@mech.iitkgp.ac.in

Engineered nanopores are of interest due to their robustness and compatibility with standard fabrication techniques, making them a popular choice for single-molecule applications. Precise control over ionic transport through a nanopore under an external electric field has enabled advances in technologies such as biopolymer sequencing [1], nanofluidic diodes [2], transistors [3] and nanofluidic memristors [4] to name a few. Such applications are typically operated in lower bias ranges (in the range of -500 mV to +500 mV), where the pore size does not change much with a change in applied bias. Traditionally, a nanopore diameter is estimated from ionic conductance values, assuming ohmic behaviour [5]. However, with extreme confinements (nanopores with sub-10 nm diameters- ubiquitous in biomolecule sequencing applications and common for single particle detection), the ionic conductance values vary in a nonlinear fashion with changes in applied potential, especially with stronger applied electric fields [6]. This results in a variable effective pore opening that alters the blockade current values for sequencing applications. Considering the increased importance of nanopore technologies, it is crucial to explore and understand variations in ionic transport through a nanopore, including the changes in conductance that occur at higher applied potentials, which have remained relatively less explored. In this study, we have investigated nonlinear variations in ionic current by applying voltages outside of the conventional regimes, and we attempt to understand the physics underlying these variations. We also show how the traditionally estimated pore diameter varies with the applied potential (figure: 3) as non-ohmic behaviour is observed at higher voltages. Experiments were carried out using single nanopores that were created via controlled dielectric breakdown, in thinned regions milled by focused ion beam (FIB), in silicon nitride (SiN_x) membranes. We used 1M KCl solution (pH 5.5 to 6) as an electrolytic solution, and the ionic current passing through the pore was recorded using Ag/AgCl electrodes. Our experimental findings suggest that at higher applied potentials, the current increases much more rapidly than at lower applied potentials (figure: 2). Examining the voltage-current relationship over a larger range of applied potentials reveals extremely low current values at lower potentials in contrast to the disproportionately higher currents at higher potentials- resembling the voltage-gated nanopores found in living organisms. Such behaviour demonstrates an applied potential dependent effective pore diameter, and the same can be attributed to the formation and accumulation of Bjerrum pairs[7] within the sub-10 nm diameter pore as well as the formation of immobile layers adjacent to the pore wall. This combination reduces the effective pore size and allows very little current to flow through the pore at lower voltages. At higher applied voltages, the ion pairs break and mobilise, allowing for higher levels of ionic conductance. This also increases the effective pore opening making it capable of accommodating larger biomolecules. Establishing such control over tuning the effective pore diameter by varying the applied potential would make a single nanopore more versatile for sequencing and other applications that are currently being pioneered by the research community.

[1] J.J. Kasianowicz, E. Brandin, D. Branton, D.W. Deamer, Characterization of individual polynucleotide molecules using a membrane channel, Proc. Natl. Acad. Sci. 93 (1996) 13770–13773.
[2] R. Karnik et al., Rectification of Ionic Current in a Nanofluidic Diode, Nano Lett. 7 (2007) 547–551.
[3] E.B. Kalman, I. Vlassiouk, Z.S. Siwy, Nanofluidic Bipolar Transistors, Adv. Mater. 20 (2008) 293–297.
[4] Q. Sheng, Y. Xie, J. Li, X. Wang, J. Xue, Transporting an ionic-liquid/water mixture in a conical nanochannel: a nanofluidic memristor, Chem. Commun. 53 (2017) 6125–6127.
[5] H. Kwok, K. Briggs, V. Tabard-Cossa, Nanopore Fabrication by Controlled Dielectric Breakdown, PLoS One. 9 (2014) e92880.
[6] S. Ghosal, J.D. Sherwood, H.C. Chang, Solid-state nanopore hydrodynamics and transport, Biomicrofluidics. 13 (2019).
[7] N. Kavokine, P. Robin, L. Bocquet, Interaction confinement and electronic screening in two-dimensional nanofluidic channels, J. Chem. Phys. 157 (2022) 114703.

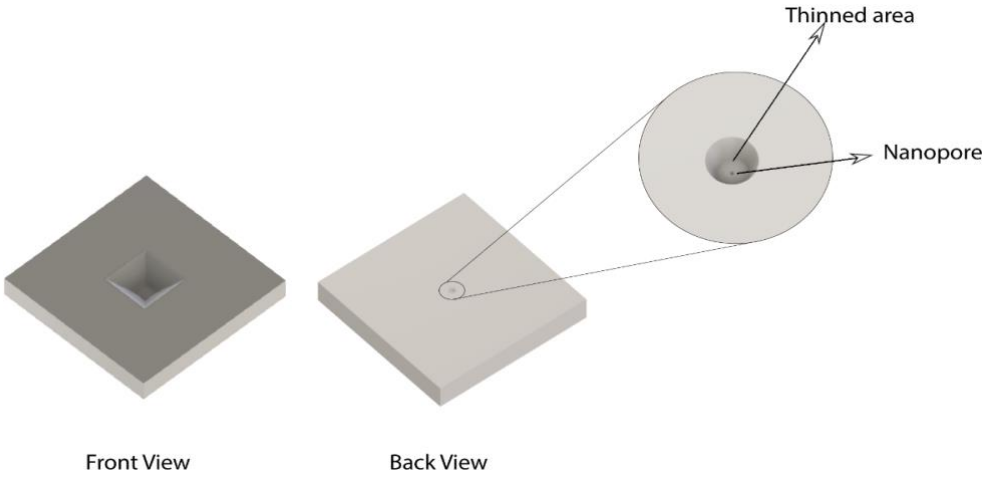

Figure 1. Schematic of nanopore fabricated inside a thinned region developed by FIB milling on a silicon nitride (SiN_x) membrane through controlled dielectric breakdown.

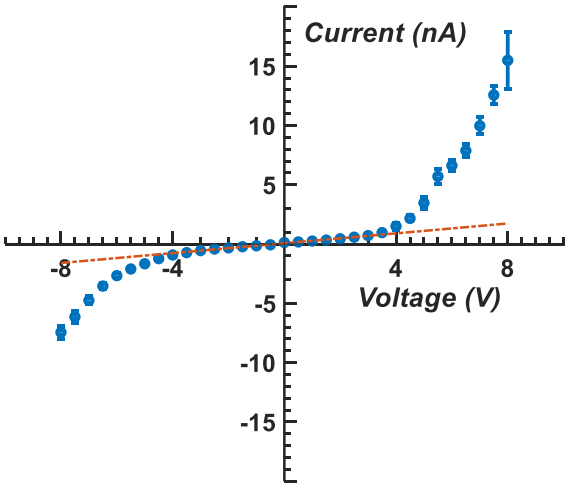

Figure 2. V-I response (blue) of the nanopore, sampled at every 500 mV, showing currents rectified at lower applied bias voltages and rapidly increasing for higher voltages. The line (red) describes the ohmic behaviour at low potentials, produced using linear fit from -1 V to +1 V.

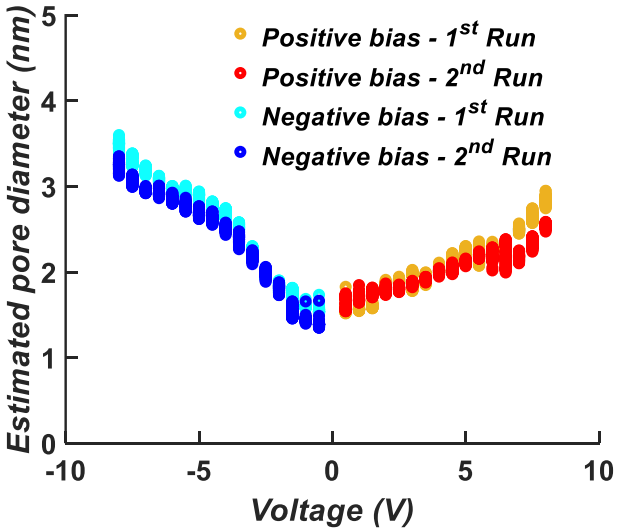

Figure 3. Pore sizes estimated at different voltages, sampled at every 500 mV. The increased measured pore sizes can be observed for higher voltages.

The Effects of 3D Nozzle Injection Shape on Precipitated Lipid Nanoparticles in a Low Aspect Ratio Lamination Mixer (LARM)

Ebrahim Taiedinejad [a, b], Alshaimaa Abdellatif [a,b] , Andreas Dietzel [a,b]

[a] Technische Universität Braunschweig, Institut für Mikrotechnik, Alte Salzdahlumer Str. 203, 38124 Braunschweig, Germany

[b] Zentrum für Pharmaverfahrenstechnik (PVZ) der Technischen Universität Braunschweig, Franz-Liszt-Str. 35a, 38106 Braunschweig

e-mail: e.taiedinejad@tu-braunschweig.de

• **Purpose of the work:** Did you know that lipid nanoparticles (LNPs) revolutionize drug delivery? This safe and inexpensive carrier system allows for the incorporation of sensitive and poorly soluble active substances. The utilization of drug nanoparticles or carrier nanoparticles containing drug or mRNA molecules is becoming more prevalent in pharmaceutical formulations, with particle sizes and polydispersity being crucial parameters that impact bioavailability, pharmacokinetics, and pharmacology. The controlled and continuous production of nanoparticles can be achieved through microfluidic mixers, which offer distinctive conditions. A new 3D low aspect ratio microfluidic system ensures precise control of particle size and polydispersity index (PDI).

This study shows how using rectangular nozzle shape with different size affects the SLNP size and PDI.

• **Background/ State of the art:** The principle of flow focusing in micro channels has already been used to successfully precipitate organic nanoparticles [1,2]. Institute of Microtechnology (IMT) at the Technical university of Braunschweig has strong background on the nanoparticle generation in the microfluidic channels [3–5] . Recently, a novel 3D microfluidic presented for continuous generating of small and monodisperse SLNPs without fouling (deposition of particles on the channel walls) [6]. Here the presented microfluidic channel was designed to distribute organic solvent properly in the channel centre with a narrow organic solvent layer thickness in order to increase the contact area between aqueous and organic solvent See (fig 1 ,2).

• **Results of the work:** This paper describes the effect of the nozzle size in the low aspect ratio lamination mixer (LARM) on the particle size and PDI when nozzle width increased from 10 µm to 30 µm (fig 2). The low aspect ratio of the rectangular nozzle increases the contact area between the organic and aqueous phases which reduces diffusive mixing time and which leads to the production of smaller and more monodisperse nanoparticles. A thin sheet of organic solvent in the middle of the channel facilitates fast and homogeneous mixing, which is crucial to the production of small and monodisperse nanoparticles.

As illustrated in Figure 3a, the ratio of aqueous to organic phases ($Q_{aqueous}/Q_{organic}$) remained constant at 9 while $Q_{aqueous}+Q_{organic}$ increased from 200 µl/min to 1000 µl/min. With all nozzles with three different width, the average particle size decreased from 200 nm to almost 120 nm. However, at a flow velocity greater than 400 µl/min, produced nanoparticles with a nozzle size of 500×30µm^2 had a PDI below 0.1. This indicates that the production of monodisperse nanoparticles was more successful with bigger nozzle sizes. In Figure 3b, it can be observed that there is a monotonic decrease in nanoparticle size with increasing $Q_{aqueous}/Q_{organic}$ from 20 to 100. Specifically, for the nozzle size of 500×30 µm^2, the particle size decreased from 160 nm to 80 nm with PDI below 0.1. For the nozzle sizes of 500×20 µm^2 and 500×10 µm^2, the particle sizes decreased from 210 nm to 90 nm and PDI increased to 0.17. In conclusion, whether ($Q_{aqueous}/Q_{organic}$ =9), or total flow increased from 20 to 60 ($Q_{organic}$ remained at 10µl/min), the generation of nanoparticles using a wider nozzle size resulted in better outcomes.

[1] A. Jahn, W.N. Vreeland, M. Gaitan, L.E. Locascio, Controlled vesicle self-assembly in microfluidic channels with hydrodynamic focusing, Journal of the American Chemical Society 126 (2004) 2674–2675.

[2] V. Génot, S. Desportes, C. Croushore, J.-P. Lefèvre, R.B. Pansu, J.A. Delaire, P.R. von Rohr, Synthesis of organic nanoparticles in a 3D flow focusing microreactor, Chemical Engineering Journal 161 (2010) 234–239.

[3] P. Erfle, J. Riewe, H. Bunjes, A. Dietzel, Optically monitored segmented flow for controlled ultra-fast mixing and nanoparticle precipitation, Microfluid Nanofluid 21 (2017). https://doi.org/10.1007/s10404-017-2016-2.

[4] P. Erfle, J. Riewe, H. Bunjes, A. Dietzel, Stabilized Production of Lipid Nanoparticles of Tunable Size in Taylor Flow Glass Devices with High-Surface-Quality 3D Microchannels, Micromachines 10 (2019).

[5] J. Riewe, P. Erfle, S. Melzig, A. Kwade, A. Dietzel, H. Bunjes, Antisolvent precipitation of lipid nanoparticles in microfluidic systems - A comparative study, International journal of pharmaceutics 579 (2020) 119167.

[6] P. Erfle, J. Riewe, H. Bunjes, A. Dietzel, Goodbye fouling: a unique coaxial lamination mixer (CLM) enabled by two-photon polymerization for the stable production of monodisperse drug carrier nanoparticles, Lab on a chip 21 (2021) 2178–2193. https://doi.org/10.1039/d1lc00047k.

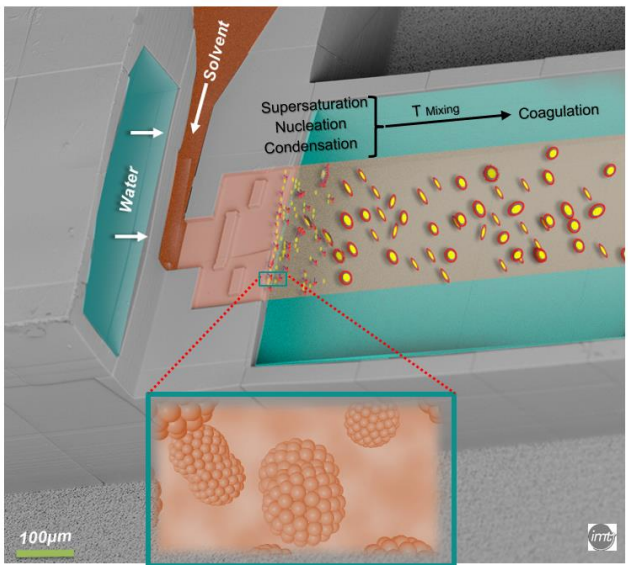

Figure 1. SEM images of key components of the LARLM. The microchannels are cut open to show their interior. Subsequent digital coloring (orange: organic phase, green: aqueous phase) illustrate the liquid flows after central injection

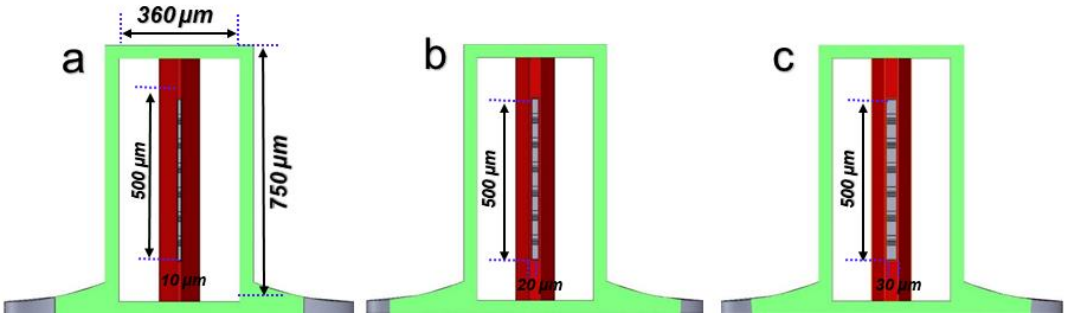

Figure 2. Front view reveals main channel with a size of 750×360 µm^2 and organic solvent nozzles with size of **(a)** 500×10 µm^2 **(b)** 500 ×20 µm^2 **(c)** 500×30 µm^2

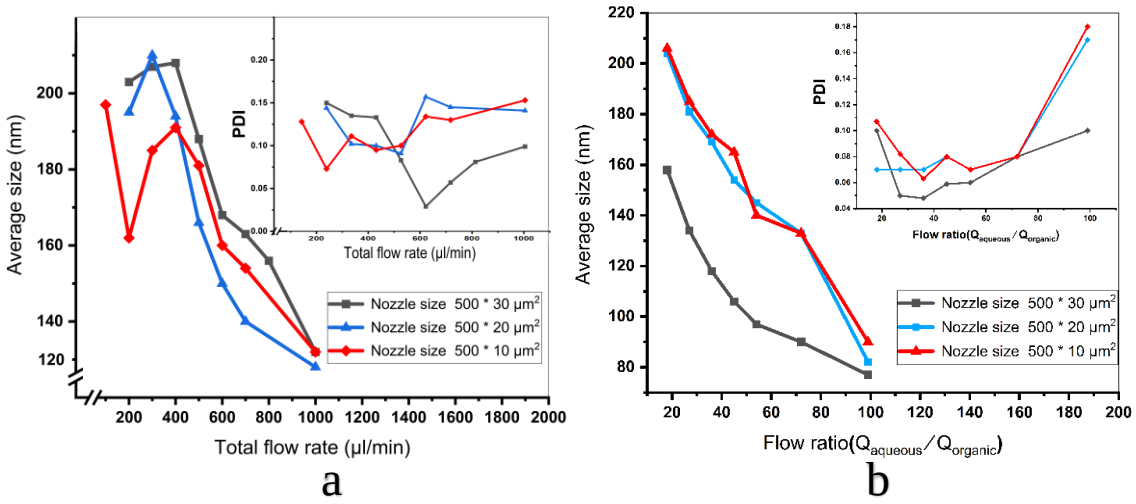

Figure 3. (a) Z-average and PDI as obtained for varied $Q_{aqueous}/Q_{organic}$ at constant $Q_{organic}$=10 µl/min **(b)** Z-average and PDI as obtained in constant $Q_{aqueous}/Q_{organic}$= 9 with increasing total flow rate from 200 to 1000 µl/min

Development of an automatic reagent drip system for passive pumps

Reo Shimada [a], Naoki Takada [b], Hiroyuki Kimura[c], Katsuo Mogi [a]
[a] Tokyo Denki University, Tokyo, 120-8551, Japan
[b] National Institute of Advanced Industrial Science and Technology, Tsukuba, 305-8564, Japan
[c] Kyoto Pharmaceutical University, Kyoto, 607-8414, Japan
e-mail: k-mogi@mail.dendai.ac.jp

Introduction: A syringe pump is widely used as a means of injecting liquid into microchannels in microfluidic devices because that can pump liquids while maintaining a constant flow rate. However, syringe pump-based systems have several drawbacks such as pulsation at low flow rates, limited injection volume, large system size, high cost, and complicated piping. One effective solution to this problem is to use passive pumps to inject liquids into microchannels. Figure 1 shows cross sectional view of the microchannel include a passive pump system. The flow in the microchannel from the small droplet on the inlet port to the large droplet on the outlet port is generated according to the pressure difference due to surface tension [1]. The passive pump generates a steady flow at low flow rates without expensive equipment and external tubing [2]. On the other hand, filling reagents into passive pumps is an intermittent dripping process, and manual reagent dropping is a burdensome task. Therefore, we developed a practical automatic reagent drip system. The system is capable of intermittent and long-term injection of droplets into microfluidic devices without human intervention.

Materials and methods:

Automatic reagent drip system: The automated reagent drip system developed in this study consists of a motorized micropipette that aspirates and dispenses liquid, and an arm robot that carries the micropipette. Figure 2 shows a prototype of the system. The arm robot has a minimal mechanism consisting of two driving parts. Simplifying the mechanism limits the number of failures points and increases reliability. We have developed an arm robot that satisfies the desired operating conditions at a reduced development cost by utilizing the drive unit of a commercially available compact CNC router machine (3018Pro, SainSmart). The base board used for wireless automatic control was the ESP32-DevKitC-32E (Espressif Systems, inc.). The pipette, which was used for this system as shown in figure 2, was a VIAFLO (INTEGRA, inc.); the VIAFLO uses an internal Bluetooth version. The prototype was controlled remotely by a PC using Wi-Fi and Bluetooth.

Microfluidic device for drip test: We use a model microchannel to demonstrate the automatic reagent drip system. The microchannel is a five-branch channel with one inlet and five outlets (Figure3). The inlet side is 500 μm in width, 100 μm in height, and 15 mm in length. Each blanch on the outlet side is 100 μm in width, 100 μm in height, and 15 mm in length. The microchannel structure was fabricated on a polydimethylsiloxane (PDMS) substrate with a thickness of 500 μm, 1 mm, and 2 mm by soft lithography. 1mm holes were punched at the inlet port and outlet ports on the PDMS substrate. And the substrate was bonded with a glass substrate by plasma surface treatment.

Reagents: In this demonstration, the fluid was observed by sending two kinds of dyes, red dye (*iroshizuku*, PILOT) and blue dye (*Quink*, PARKER).

Experimental: A microfluidic device for the drip test was set up in the prototype machine as shown in Figure 2. The microchannel in the device was filled with distilled water, and 40 μL of red and blue ink was dripped into the inlet port of the channel. Then, 20 μL of red and blue ink was dripped into the inlet port of the channel three times alternately for 60 minutes at 10-minute intervals. Images of dripped droplets were captured and the flow rate was calculated from the change in the droplet size. Additionally, the repeatability of the system was verified from images of the dripped positions.

Summary: The fabricated device was able to drip 20 μL of fluid into a microfluidic device continuously for 60 minutes under remote control. Furthermore, as a result of optimization for the purpose of operation, we succeeded in reducing the cost of the device. We are planning a biochemical experiment using a microfluidic device on the space station. Hence, we will use this drip system to verify the effect of a passive pump and aim to realize a liquid transfer system that does not depend on gravity.

[1] G. Walker; D. Beebe. A passive pumping method for microfluidic devices. Lab Chip, 2, (2002), 131-134.
[2] T. Pan; W. Wang; Ann. Biomed. From Cleanroom to Desktop: Emerging Micro-Nanofabrication Technology for Biomedical Applications. Eng., 39, (2011), 600-620.

コメントの追加 [MK1]: 小さい液滴側を球状にして、強調しましょう。
矢印が表面張力を表すのであれば太さは同じにしてください。圧力差であれば違う書き方が良いです。ヤング・ラプラスの式を参考にしてください。
≈0 とは？文中に説明を入れたほうが良いかも。

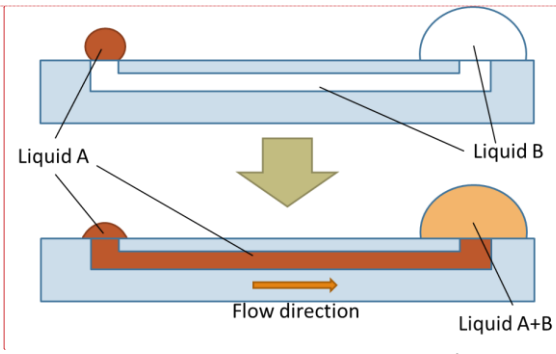

Figure 1. The passive pump driven by droplet surface tension.

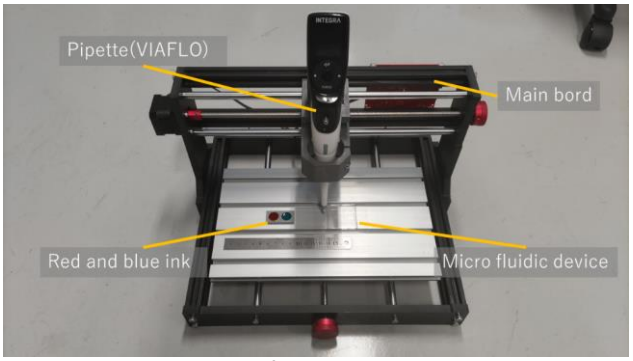

Figure 2. A prototype of an automatic reagent drip system.

コメントの追加 [MK2]: 図のフォントサイズを合わせる。

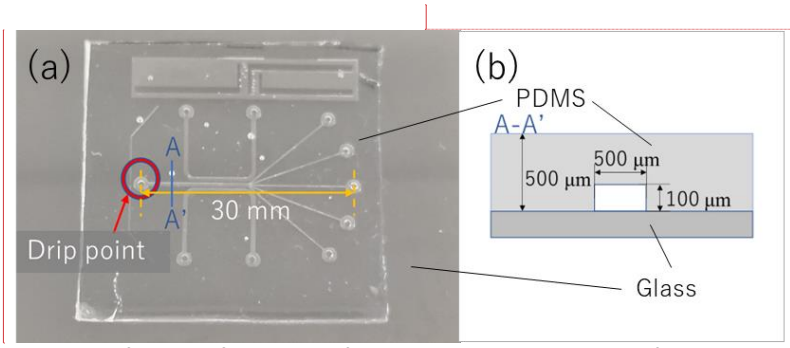

Figure 3. Autoline of the microfluidic device for this experiment and schematic of the cross-sectional view of the microchannel. (a): photo of a microfluidic device made of PDMS. (b): cross sectional view of the microchannel at A-A' shown in (a).

Durable carbyne-coated micro and nanotextured surfaces for antibacterial control

D. Nioras[1,2], D. Kefallinou[1,2], D. Ioannou[1,3], A. Brigadin[4], A. Tserepi[1], Evangelos Gogolides[*1]

[1]Institute of Nanoscience and Nanotechnology, NCSR "Demokritos" Aghia Paraskevi, Greece 15231

[2]Physics Department, National Technical University of Athens, Zografou Campus, Athens, Greece 15780

[3]School of Mechanical Engineering, National Technical University of Athens, Zografou, 15780, Attica, Greece

[4]Swissimpianti Sagl, 6828 Balerna, Switzerland

*e.gogolides@inn.demokritos.gr

Following the ground-breaking advancements in the field of Graphene, which led to the Nobel Prize in 2010, a multitude of new two-dimensional materials have emerged, holding great potential to revolutionize our daily lives in the near future. These materials exhibit a wide range of functionalities that can be exploited in applications spanning from mainstream microelectronics to antibacterial micro-fluidic devices. In this study, our focus is on a particular group of carbon allotropes called Carbynes, which contains alternating single and triple carbon bonds. Carbynes possess remarkable properties, with a reported Young modulus of 32.7 TPa, which surpasses that of diamond by 40 times [1]. Consequently, Carbynes are emerging as a new class of extraordinarily strong, tough, and lightweight materials, holding immense potential in various fields such as carbon-based material science, fabrics, sensors, electronics, and many more.

Our research aims to explore the mechanical robustness and bactericidal properties of micro and nano-textured polymeric surfaces developed using our dry plasma technology [2], subsequent to a Carbyne-enriched deposition. By introducing micro and nanostructures onto Poly(methyl methacrylate) (PMMA) surfaces via oxygen plasma treatment, we proceed to deposit a thin Carbyne-enriched film, approximately 30-40 nm in thickness (see Figure 1, a). The inclusion of the Carbyne-enriched coating significantly enhances the hardness and durability of the textured surface. Prior studies have already demonstrated the remarkable antibacterial efficacy [3] of our plasma-treated surfaces against *E. coli* (see Figure 1, b). Building upon these findings, we envision the development of reusable bactericidal surfaces with a significant killing effect at less than an hour, that leverage the durability of the carbyne coating in combination with the bactericidal action of the plasma induced structures (see Figure 1, c). This breakthrough holds immense significance in terms of public health, safety, early prognosis, and prevention of outbreaks.

This work has been funded by the T12EPA5-00067 Project 'Carbyne Films: Synthesis of a New Class of Carbon Allotrope and Novel Applications in Sensors and Biosensors (CarbyneSense). We thank A. Lukin for the useful discussions during the preparation of the proposal.

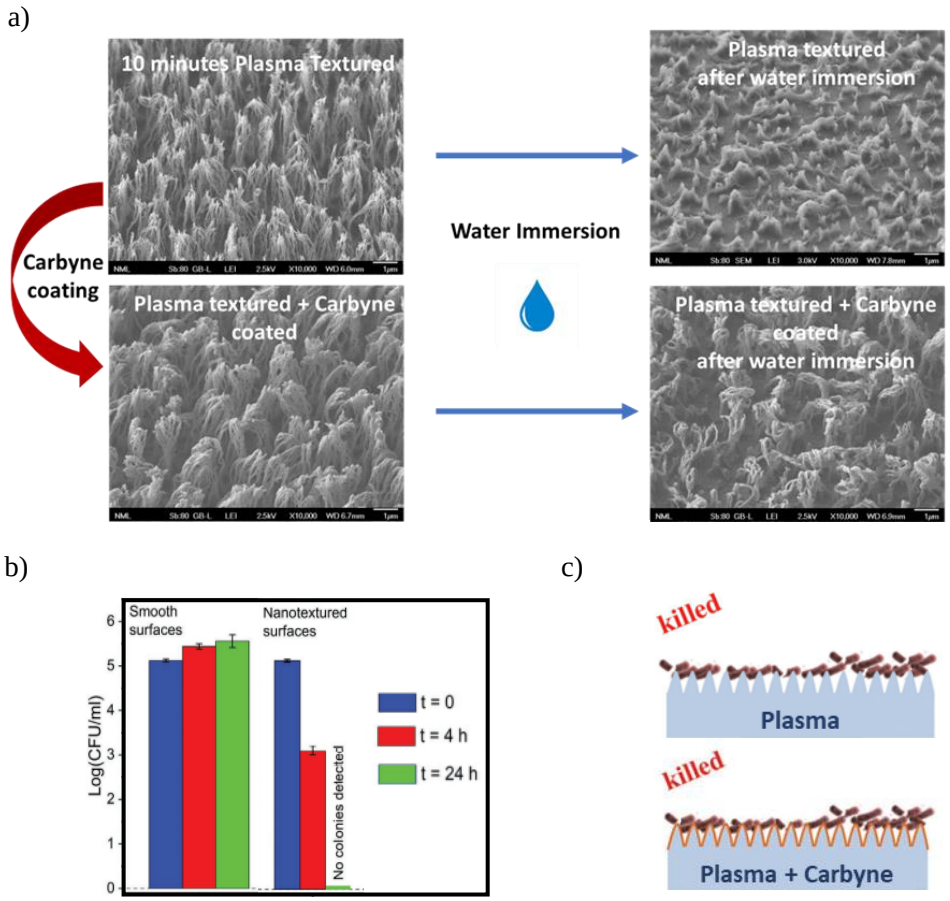

Figure 1: a) SEM image of PMMA surface nanotextured for 10 minutes in O_2 plasma, before and after Carbyne deposition, as well as before and after water immersion and drying. b) Results of the bactericidal action of untreated and plasma treated PMMA surfaces [3]. c) Illustration of the bactericidal action of the Carbyne coated surfaces.

[1] S. S. Sohn and J. W. Bode, "N-heterocyclic carbene catalyzed C-C bond cleavage in redox esterifications of chiral formylcyclopropanes," *Angew. Chemie - Int. Ed.*, vol. 45, no. 36, pp. 6021–6024, 2006.

[2] K. Tsougeni *et al.*, "Mechanisms of Oxygen Plasma Nanotexturing of Organic Polymer Surfaces : From Stable Super Hydrophilic to Super Hydrophobic Surfaces," vol. 25, no. 19, pp. 11748–11759, 2009.

[3] P. Dimitrakellis, K. Ellinas, G. D. Kaprou, D. C. Mastellos, A. Tserepi, and E. Gogolides, "Bactericidal Action of Smooth and Plasma Micro-Nanotextured Polymeric Surfaces with Varying Wettability, Enhanced by Incorporation of a Biocidal Agent," *Macromol. Mater. Eng.*, vol. n/a, no. n/a, p. 2000694, Feb. 2021.

Ευρωπαϊκή Ένωση
ΕΠΑνΕΚ 2014-2020
ΕΠΙΧΕΙΡΗΣΙΑΚΟ ΠΡΟΓΡΑΜΜΑ
ΑΝΤΑΓΩΝΙΣΤΙΚΟΤΗΤΑ
ΕΠΙΧΕΙΡΗΜΑΤΙΚΟΤΗΤΑ
ΚΑΙΝΟΤΟΜΙΑ
ΕΛΛΗΝΙΚΗ ΔΗΜΟΚΡΑΤΙΑ
ΥΠΟΥΡΓΕΙΟ
ΑΝΑΠΤΥΞΗΣ ΚΑΙ ΕΠΕΝΔΥΣΕΩΝ
ΓΕΝΙΚΗ ΓΡΑΜΜΑΤΕΙΑ
ΕΡΕΥΝΑΣ ΚΑΙ ΤΕΧΝΟΛΟΓΙΑΣ
ΕΣΠΑ
2014-2020
Με τη συγχρηματοδότηση της Ελλάδας και της Ευρωπαϊκής Ένωσης

Lab-on-a-phone – plasmonic biosensing in 3D scaffolds using a smartphone

Florian Laible [a], Melanie Sommer [a], Monika Fleischer [a]

[a] University of Tübingen, Institute for Applied Physics and Center for Light-Matter-Interaction, Sensors and Analytics LISA+, Tübingen, 72076, Germany
e-mail: florian.laible@uni-tuebingen.de

Plasmonic shift biosensors are capable of very fast and sensitive detection of biomarkers. The underlying mechanism of these sensors is the sensitivity of plasmonic nanoantennas to refractive index changes in their proximity. To create selective sensors the nanoparticles are functionalized with linker molecules that bind only to the analyte. The resonance wavelength shift caused by the refractive index changes around the nanoantennas can be directly and quantifiably linked to the amount of analyte which is present. The application areas of these plasmonic biosensors are diverse. They can e.g., be used to detect biomarkers indicating diseases or pathogens in drinking water.
In most cases, the nanoparticles are fabricated on flat 2D samples. The plasmonic resonance shifts are monitored by sophisticated optical setups using microscopes and spectrometers. This enables very low limits of detection, high sensitivities, and quantifiable results. The devices are however costly and, in most cases, difficult to transport. The number of nanoparticles contributing to sensing is limited by the field of view of the optical setup or by the available surface on the flat sample [1]. Their commercial success is however hindered by the relatively high cost of nanostructure fabrication and read-out devices.
However, there are advances to create point-of-care detectors for biomarker detection [2]. We aim to contribute to this line of thought by creating a handheld and accessible point-of-care sensor as an attachment for smartphones. The concept of the lab-on-a-phone is displayed in Figure 1. To achieve these goals, we introduce gold nanoparticle-spiked Polydimethylsiloxane (PDMS) 3D scaffolds. They are created by the sugar cube method, where liquid PDMS is poured on a sugar cube. The PDMS is cured, and the sugar is dissolved in water, see Figure 2 a) and b). This results in an open sponge with a very large and well accessible surface [3]. On the surface of the scaffold, gold nanoparticles are directly grown by emerging in a gold chloride ethylene glycol solution [4]. After the growth process, the color of the scaffolds visibly changed from white to red. The color represents the mean resonance wavelength of the nanostructures, see Figure 2 c) and d).
As the first proof of principle liquids with different refractive indices are added into the scaffold. The resulting resonance shift can be detected by a smartphone camera while using its flashlight for illumination. An example measurement can be seen in Figure 2 e). To increase the accessibility of the lab-on-a-phone, we want to use as much hardware and software of the smartphone as possible and use 3D printers to create brand and model-specific smartphone cases. These houses the test strip in the appropriate location and support a mirror. The test strips include a fluidic system and a 3D scaffold. The smartphone itself is used as a light source, detector, and computation unit. The resonance shift is detected via the color camera - no spectrometer is needed [5]. To quantify the color change, the raw data of the pixels are filtered and transferred into the HSV (hue, saturation, value) color space. Here the H value is given as an angle ranging from 0° to 360° representing the underlying color of the pixels. A change in color and therefore refractive index changes will be quantifiable by the change in H value. The saturation and value (brightness) of the color will not be considered.
The development of a prototype point-of-care sensor will be presented. A side-by-side comparison of the HSV sensing approach to common transmission spectroscopy measurements will be shown along with the first experiments detecting glycose in watery solutions. Finally, the pathway to progressing this approach to an open-source low-cost point-of-care sensor will be discussed.

[1] F. Laible, A. Horneber, and M. Fleischer, Localized surface plasmon resonance shift sensing, in: A. J. Meixner, M. Fleischer, D. P. Kern, eds., Optical Nanospectroscopy Applications (De Gruyter, Berlin/Boston, 2023) 101-139.
[2] C. Jin et al., Materials Today Bio, 14, 2022, 100263.
[3] S. Choi et al., ACS Appl. Mater. Interfaces 2011, 3, 4552–4556.
[4] A. Qualtieri et al., Microelectron. Eng. 84 (2010) 1435-1438.
[5] S. Mariani, et al. Advanced Functional Materials 31(26), (2021), 2100774.

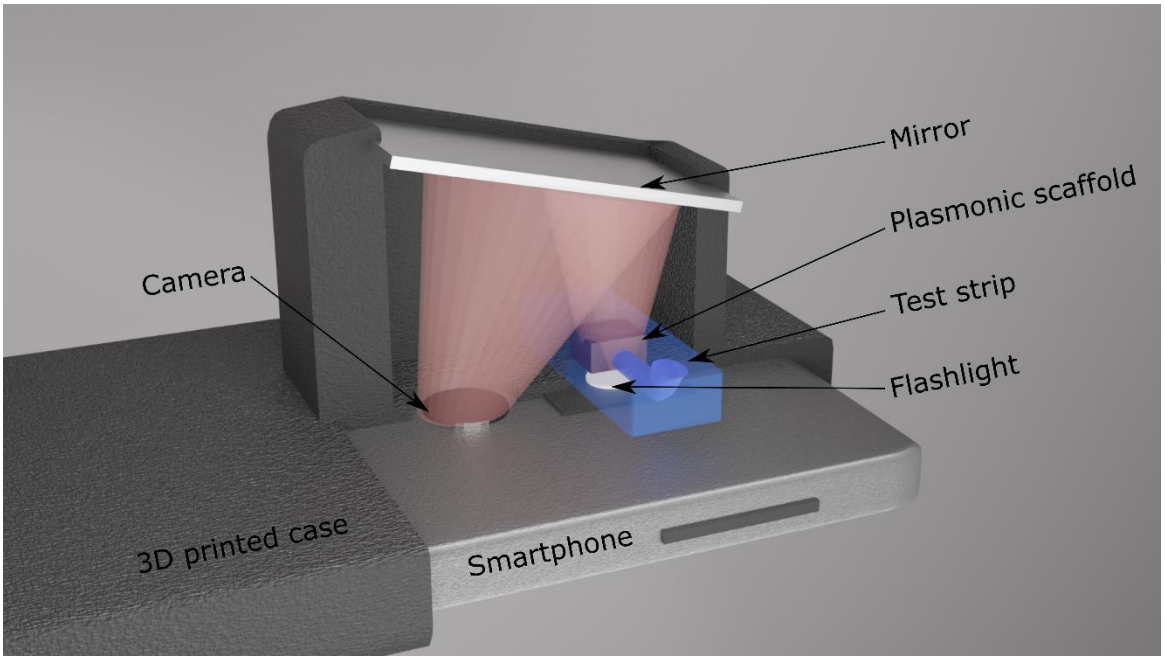

Figure 1. Illustration of the lab-on-a-phone concept

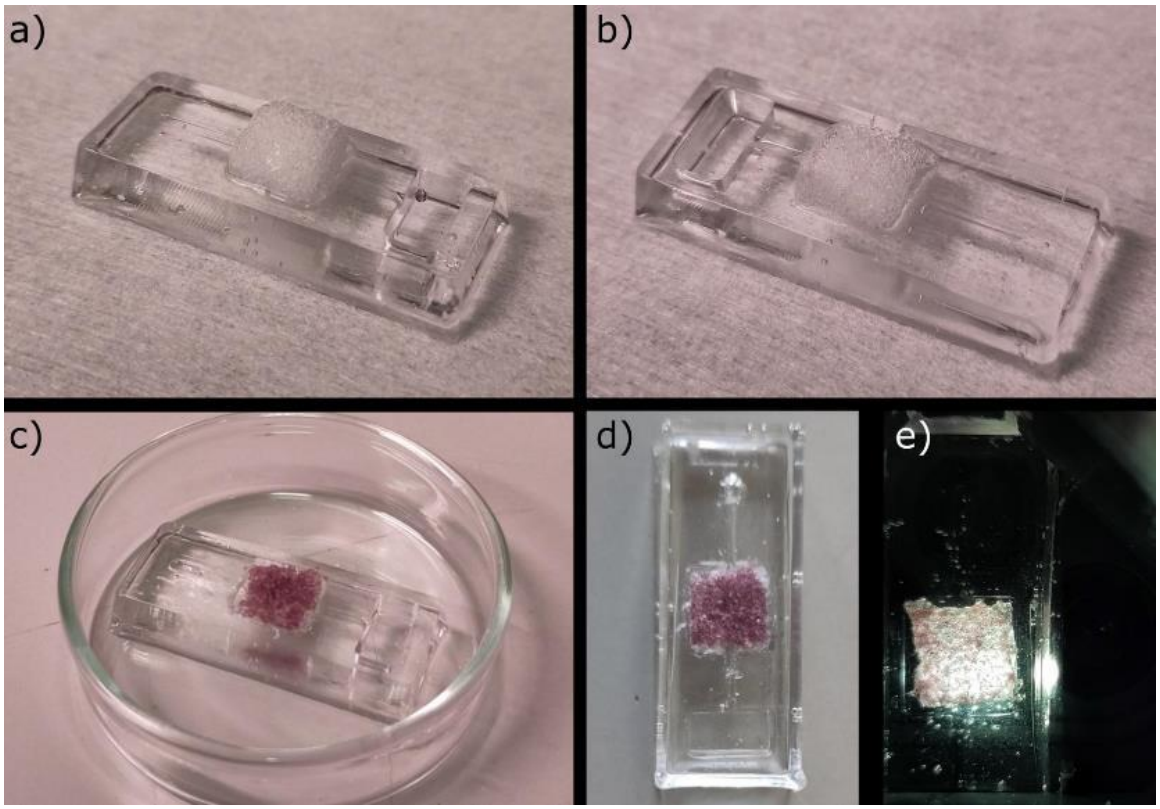

Figure 2. 3D scaffolds in test strips. a) Test strip with part of a liquid PDMS filled sugar cube. b) Test strip with solid PDMS scaffold. The sugar is already removed. c) Test strip after gold nanoparticle growth process. The gold nanoparticles lead to the color change of the scaffold. d) Top view of a finished test strip. A PDMS cap seals the fluidic device. e) Test strip image under measuring conditions in the lab-on-a-phone.

Iridium oxide thin film electrodes for highly sensitive impedance biomass detection

Sven Meinen[a,c], Kevin Viebrock[b,c], Rainer Krull[b,c], Andreas Dietzel*

[a]Institute of Microtechnology, Technische Universität Braunschweig, 38124 Braunschweig, Germany
[b]Institute of Biochemical Engineering, Technische Universität Braunschweig,38106 Braunschweig, Germany
[c]Center of Pharmaceutical Engineering, Technische Universität Braunschweig, 38106 Braunschweig, Germany
e-mail: s.meinen@tu-braunschweig.de

Novelty/ Progress Claims

Recently an impedance sensor was developed for a capillary wave micro bioreactor consisting of four gold electrodes (4-point measurement in liquids) to measure the biomass in buffered culture media [1]. However, for low biomass densities their contribution to the measured impedance was very small when using gold micro-electrodes with a high contact impedance. Therefore, electrodeposited iridium oxide was investigated as alternative electrode material. With scanning electron microscopy and electrical measurements the influence of deposition time on thin film morphologies and on contact impedance in buffer solution was studied in detail. Our results show a way to decisively increase biomass sensitivity.

State of the Art

Because of its electrochromic properties and high specific surface area, electrodeposited iridium oxide was often used for electrochemical sensor applications [2–4]. The deposition of iridium oxide was typically carried out according to the method described by Yamanka et al. [5]. The nucleation and film growth process has been extensively studied [6]. But, the surface morphologies depending on the duration of deposition and their influence on impedance when immersed in phosphate buffer saline (PBS) was not studied in detail before.

Description of the Method

Sputtered indium tin oxide (ITO) on a glass substrate was structured by photolithography to achieve circular test structures with an area of 18 mm^2. The iridium oxide was deposited from an iridium chloride solution using a potentiostat (Gamry Reference 600+) with a platinum wire counter electrode following the recipe from Yamanaka et al. [5] The voltage was cycled between -0.7 and 0.8 V vs. Ag/AgCl with 75 mV s^{-1}. Samples obtained after increasing numbers of deposition cycles were investigated with electrochemical impedance spectroscopy (EIS) using the same setup but in PBS and scanning electron microscopy.

Experimental Results

The SEM images (***Figure 1)*** show grain growth with increasing deposition time. The formation of iridium oxide starts with small crystallization nuclei (5 cycles) which grow rapidly (20 & 50 cycles) before different crystal grains coalesce (100 cycles). The images also show an increasing 3-dimensionality with progressing deposition time and thus increasing specific surface area. When different crystallization nuclei have grown and start to get in contact after 50-100 deposition cycles the increase surface area comes to an end as the grain sizes determined from micrographs clearly show (***Figure 2)***. The EIS of samples with different deposition times showed a decreasing impedance magnitude with deposition time over all frequencies. The impedance also decreases with increasing frequency for all samples. With longer deposition times, the impedance approaches a constant level even at lower frequencies. This is important because it extends the measurement range of the impedance sensor, since a constant electrode impedance is much easier to correct. At the constant level the impedance decreases from 17 (uncoated sample) to 15 kΩ (5-20 cycles), then reduces by about 40 % to 9 kΩ after 50 cycles. After 50 more cycles, the impedance decreases only by a further 1.5 kΩ. After 50-100 deposition cycles grain sizes do not grow anymore and also impedance reduction come to an end. With these results it appears promising to use this material for biomass sensing electrodes which can sense even very low concentrations of cells.

[1] Meinen et al., Integrated electrical impedance spectroscopy (EIS) sensor for monitoring viable biomass in microbioreactors, Contribution at MNE 2022 (poster)
[2] Frederick et al., 2020 J Neural Eng 17 56001
[3] Chapman et al., 2019 J Neural Eng 16001
[4] Bezbaruah et al., 2002 Analytical Chem 74 5726–5733
[5] Yamanaka., 1989 Jpn. J. Appl. Phys. 28 632–637
[6] Wu D et al, 2022 J. Electrochem. Soc. 169 92503

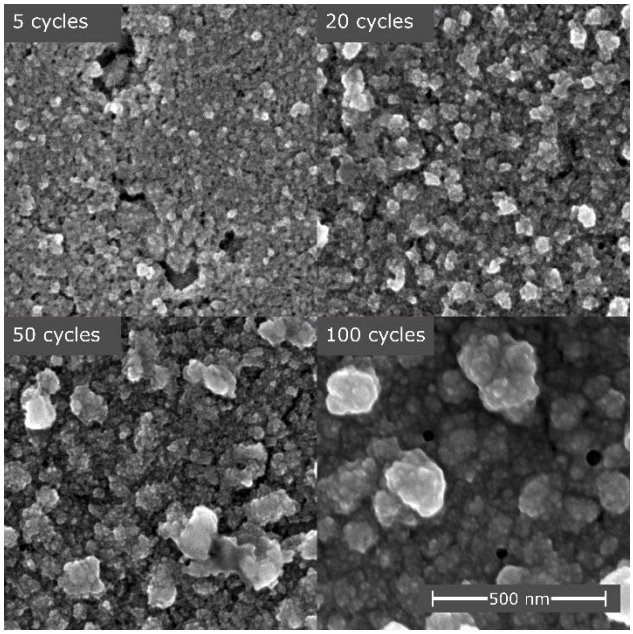

Figure 1. SEM Images of the growing iridium oxide grains

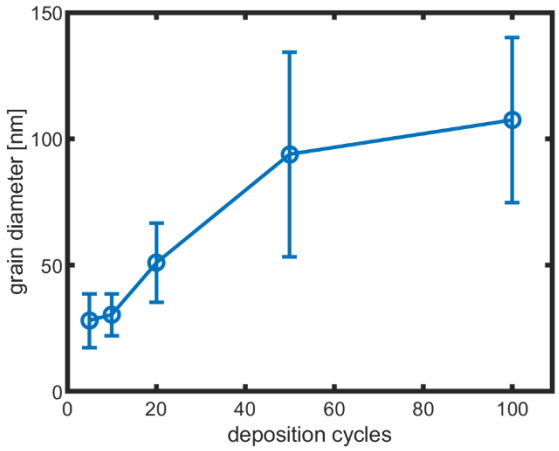

Figure 2. Grain sizes determined from SEM images

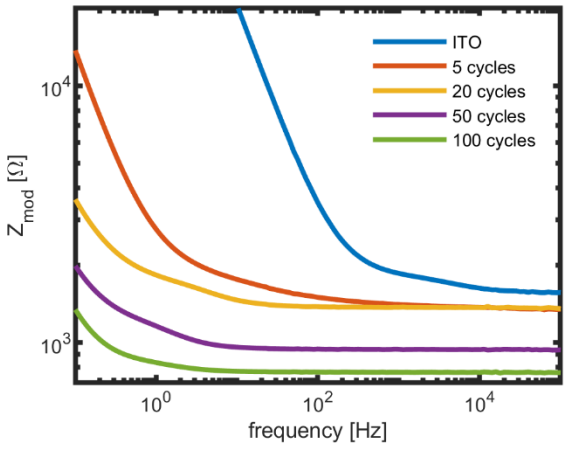

Figure 3. EIS in PBS vs. Ag/AgCl with samples deposited with different numbers of cycles

Poster Session 1.2: Track3, Track4 - Papers

Photolithographic production of smart water filters able to detect bacteria

Amparo Ferrer-Vilanova [a], Josune J. Ezenarro [a], Núria Vigués [b], Jordi Mas [b], Gonzalo Guirado [c] and Xavier Muñoz-Berbel [a].

[a] Institut de Microelectrònica de Barcelona (IMB-CNM, CSIC), Campus Universitat Autònoma de Barcelona, Cerdanyola del Vallès (Barcelona), 08193, Spain.
[b] Departament de Genètica I Microbiologia, Universitat Autònoma de Barcelona, Cerdanyola del Vallès (Barcelona), 08193, Spain.
[c] Departament de Química, Universitat Autònoma de Barcelona, Cerdanyola del Vallès (Barcelona), 08193, Spain.

e-mail: amparo.ferrer@imb-cnm.csic.es

The access to clean water is an essential factor for human life since pathogenic microorganisms present in drinking water may cause infections, diseases or even death. To avoid bacterial contamination in water, periodical analyses are required. However, golden standard methods for bacterial detection, e.g. cell plating and counting, the enzyme-linked immunosorbent assay (ELISA) or polymerase chain reaction (PCR), still rely on sample collection and transport to central laboratories, which delays time-to-result and decision making [1,2]. To solve this limitation, portable biosensors have been already developed based on DNA sensors or immune sensors [3], which faster but still requiring sample pre-treatment to provide reliable results. Alternatively, metabolic indicators consisting of electrochromic molecules that change of colour by the presence of live and metabolically active bacteria are now being employed in bacterial sensing in water samples, although they have not been implemented in portable version for in situ analysis.

Here, we present a strategy where filter membranes conventionally used to purify water are photolithographically processed to incorporate the metabolic indicator Prussian blue, which confer them sensitivity to the presence of bacteria. The bacterial detection mechanism is illustrated in Figure 1. That is, when live and metabolically active bacteria are retained in the filter, it changes of colour from deep blue to uncoloured by the metabolic reduction of the Prussian blue to its reduced Prussian white form. This process is selective and only live bacteria, and not dead ones, can produce the colour change. Thus, the change of colour of the smart filter confirms the presence of live and metabolically active bacteria on it, and consequently the microbial pollution of the treated water. In addition, if retained bacteria die, the Prussian white molecules in the filter are re-oxidized by environmental oxygen and it recovers its initial blue colour. This regeneration step allows the recycling of the filter, which can be used multiple times.

The photolithographic process for the production smart filter membranes is detailed in Figure 2. As shown, filters were immersed into a solution containing the two iron precursors, and after UV irradiation, an intense blue colour was produced on the filter surface. The photolithographic process allows the transference of patterns by using a simple photo-mask (Figure 3a), resulting in typical cubic Prussian blue crystals in the patterned region that are stably retained in the nitrocellulose matrix (Figure 3b). The filters were implemented in an opto-fluidic and high-performance membrane filter holder, which allows the pre-concentration of the bacteria in water and their detection in situ with integrated optical fibres (Figure 4a). Colour changes in the filter are therefore detected in situ with the opto-fluidic system, and in less than 2 hours, for bacterial concentrations of 10^4 CFU mL^{-1}, being possible to measure smaller concentrations in less than 5 hours (Figure 4b).

This technology was applied to the study of real water samples from different origin and compared to golden standard methods, i.e. cell plating and counting, providing promising results in the fast and in situ analysis of water.

[1] M- Bruma et al., JAP&T. 14 (2008) 196-202.
[2] Y. Liao et al., Micromachines. 11 (2020) 1079.
[3] R. Singh et al., Sensors and Actuators B- Chem. 197 (2014) 385-404.

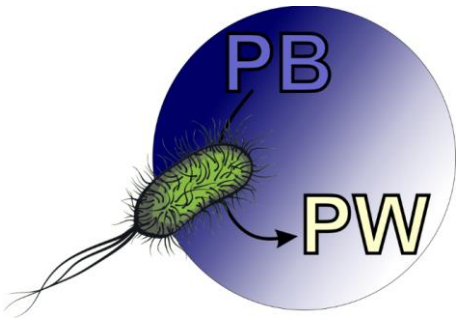

Figure 1. Scheme of the bacterial detection mechanism of the smart filters.

Figure 2. Scheme of the cyanotype procedure followed for the production of the smart filters.

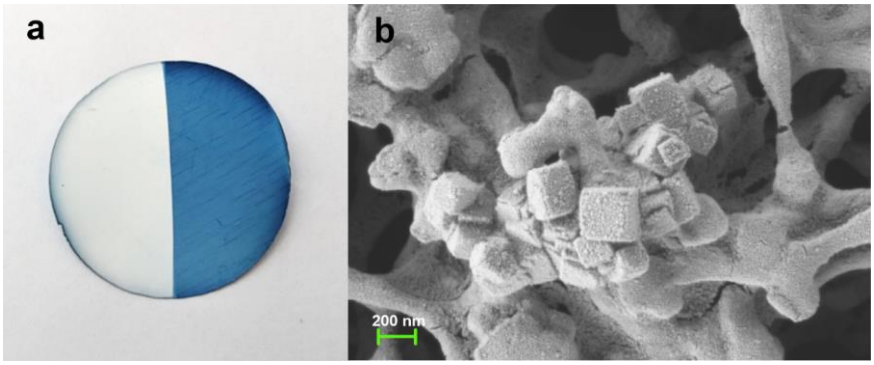

Figure 3. a) Picture of a smart filter modified in half with Prussian blue by using a mask. b) SEM images of the Prussian blue cubic structures present on the filters surface.

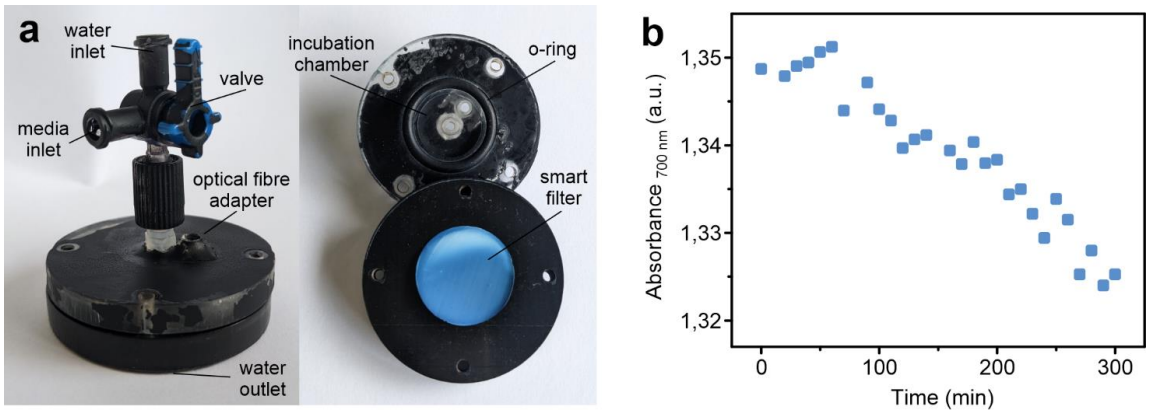

Figure 4. a) Scheme of the opto-fluidic membrane filter holder used for the bacterial detection. b) Bacterial-sensing kinetics response of the smart filters against a bacterial suspension of 10^3 CFU mL^{-1}.

A novel method for real time monitoring of wetting transition of underwater superhydrophobic surfaces and membranes: Application in membrane desalination

D. Ioannou [a], K. Ellinas [b], E. Gogolides [a]

[a] Institute of Nanoscience and Nanotechnology, NCSR Demokritos, Aghia Paraskevi 15341, Attiki, Greece
[b] Department of food science and nutrition, School of the Environment, University of the Aegean, Ierou Lochou & Makrygianni St, 81400, Myrina, Lemnos, Greece

e-mail: d.ioannou@inn.demokritos.gr

Underwater superhydrophobicity (SH), inspired greatly by the salvinia leaves, has become an important subject in scientific research because of the many applications in maritime engineering and water treatment since superhydrophobic surfaces feature anti-corrosive, anti-wetting and anti-fouling properties. In the world of membrane distillation (MD), SH membranes need to resist wetting and fouling and maintain a stable performance in terms of flux and salt rejection. However, wetting transitions on SH membranes are only indirectly assumed when the distillate conductivity increases (i.e. salt rejection decrease) and very few MD monitoring methods have been proposed.[1]

Herein we present polytetrafluoroethylene (PTFE) membranes that have been rendered superhydrophobic after O_2 plasma nanotexturing followed by C_4F_8 plasma deposition. Going one step further, we introduce a novel method to study the stability of the superhydrophobic state, by monitoring the membrane surface in situ during MD using white light reflectance spectroscopy (WLRS).[2,3] This method enables monitoring in real time with very fast acquisition speed at 50-200 ms.

Using WLRS, we showcase the stability of the superhydrophobic state of our plasma treated membranes compared to commercial membranes by lowering the surface tension of the saline feed solution with the gradual addition of sodium dodecyl sulfate (SDS). Untreated PTFE membrane's wetting properties fade, as indicated by reflectance decrease, for a liquid with surface tension of 55 mN/m (0.01mM). On the contrary, the plasma treated PTFE membrane exhibits stable superhydrophobicity both in static conditions and during MD, as revealed by the practically unaffected reflectance spectrum, for liquids of surface tension down to 39.1 mN/m, corresponding to 10 times higher SDS concentration (0.1mM).

[1] W. Barthlott et al., Adv. Mater. 22 (2010) 2325–2328.
[2] A. Smyrnakis et al., Adv. Mater. Interfaces. 9 (2022) 1–8.
[3] D. Ioannou et al., ACS Appl. Mater. Interfaces 15 (2023) 18493−18504

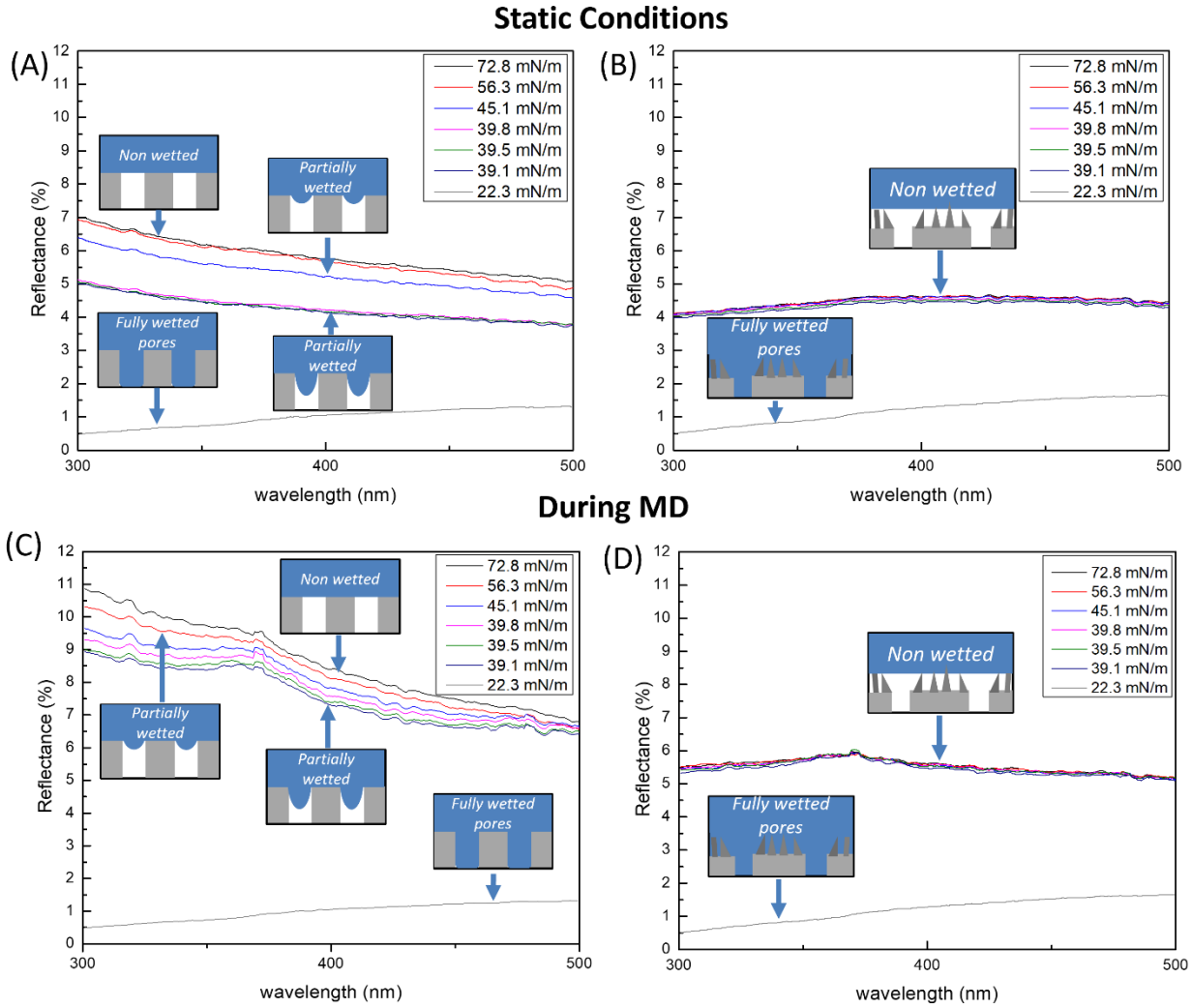

Figure 1. Reflectance spectra of untreated PTFE membrane (A) and plasma treated PTFE (B) at static conditions for different surface tensions corresponding to different SDS concentrations in the feed saline solution. (C) and (D) are the same spectra during MD. Notice that reflectance decreases along with the lowering of surface tension on untreated membranes in both cases. On the contrary in the case of plasma treated membranes reflectance remains almost completely stable down to 39.1 mN/m. Insets: schematics of the wetting states and their corresponding reflectance spectra; for the untreated membrane partial wetting occurs at 56.3 mN/m and gradually advances to full wetting while the plasma treated remains non-wetted down to 39.1 mN/m.

The development of bile duct stent having antifouling properties by using atmospheric pressure low-temperature plasma

Atsushi Sekiguchi[1*, 3], Masashi Yamamoto[2],
Hiroko Minami[3], Kimiyasu Aikawa[4]

1 Osaka Metropolitan University, Department of Physics and Electronics
11-1 Gakuen-cho, Naka-ku, Sakai, Osaka 599-8531, Japan

2 National Institute of Technology, Kagawa College,
Department of Electrical and Computer Engineering
335 Chokushi-cho, Takamatsu, Kagawa 761-8058, Japan

3 Litho Tech Japan corporation
2-6-6 Namiki, Kawaguchi, Saitama 332-0034, Japan

4 Saitama Medical University, International Medical Center
1397-1, Yamane, Hidaka, Saitama 350-1298, Japan

Biomimetics (or biomimicry) is a field of technologies based on imitating various functions and properties of organisms. Waterproof products, which are inspired by lotus leaves with super-water-repellent fine structures, are a well-known example of biomimetics. The present study examined the surface structure of snail shells, which exhibit oil repellency (oleophobic property). Snail shells have nanoporous structures with nanoholes on the scale of 200–400 nm. When water enters these nanoholes, the surface is covered by thin water films. The oil can be repelled by the water film. These structures are known as superhydrophilic nanostructures. An earlier report discussed our efforts to create such nanostructures using a nanoimprinting method and assessed the feasibility of application to the inner walls of biliary stents. This involves a labor-consuming two-stage process involving creating nanostructures on a film surface, then rolling the film into a tube. In addition, the nanoimprinting mold made via electron beam lithography is costly and unsuitable for mass production.

To overcome these issues, we sought to develop elemental technologies for providing antifouling properties to biliary stents, which are made of polyethylenes (PEs), by forming nanostructures directly on the inner surface, using atmospheric pressure low-temperature plasma. We formed nanostructures on the inner walls of PE tubes of varying diameters under varying plasma conditions. We then examined the resulting structures and effects of the antifouling properties thus imparted.

Keywords: Biomimetics, Snail shell structure, Super-nanohydrophilic (structure), Bile duct cancer, Biliary obstruction, Biliary stent, Atmospheric pressure low-temperature plasma

1. Introduction

Applying biomimetics, we sought to develop technologies to improve the antifouling properties of a substrate surface independent of substrate shape. Biomimetics seeks to create artificial structures that imitate diverse functions exhibited by living organisms [1–3]. As the saying goes, *There are no dirty snails*, snail shells have long been known to exhibit superior antifouling performance. Snail shells feature nanoporous surface structures on the scale of 200 nm–400 nm (Fig. 1).

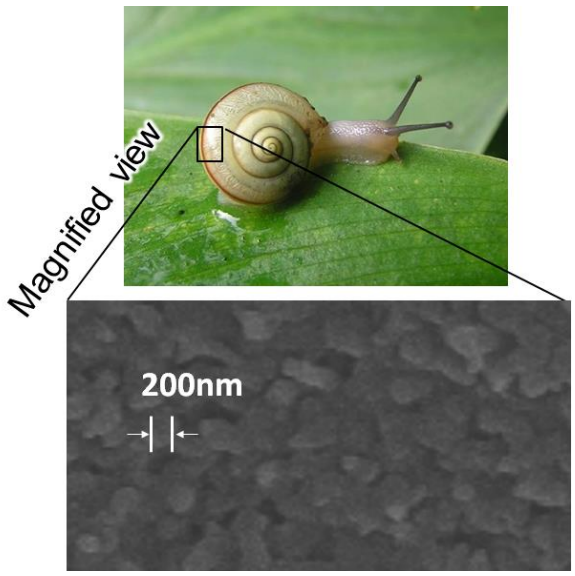

Fig. 1. Snail shell structure.

Water entering these nanoholes forms a thin film of water on the surface, which repels oil and other fouling substances. Referred to as superhydrophilic nanostructures, these films exhibit antifouling properties, repelling oils containing proteins, etc. (Fig. 2).

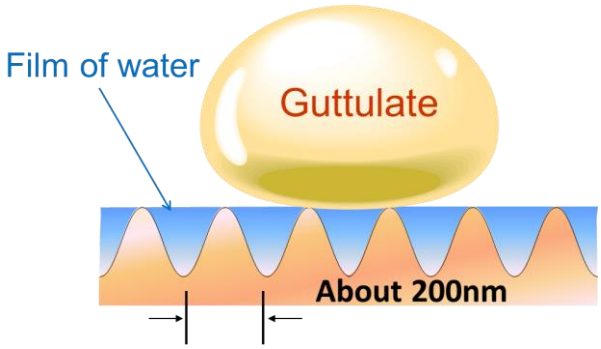

Fig. 2. Mechanism of the production of antifouling properties by superhydrophilic nanostructures.

Thus, we might expect to produce antifouling properties (super-nanohydrophilic effects) by forming such convex-concave nanoscale structures replicating snail shells on polymer surfaces. An earlier report discussed our efforts to form nanostructures on the surface of an acrylic polymer substrate by nanoimprinting, after which the polymer sheet was rolled into a tube to produce prototypes of biliary stents with antifouling properties [4–5]. However, this approach involved creating a nano-mold using electron beam lithography and forming nanostructures using a nanoimprinting method. Lithography requires special facilities and equipment and entails high costs. Additionally, current nanoimprinting and lithographic technologies are generally suitable only for flat substrates; they are not designed to create nanostructures directly on the inner walls of a tubular substrate. In the present study, we used the atmospheric pressure low-temperature plasma method [6–7] to develop a technology for imparting enhanced antifouling performance to the surfaces of tubular materials, regardless of substrate shape.

2. Biliary Stents with Antifouling Properties

Figure 3 shows the relative positions of the liver, gall bladder, and bile duct. Bile is a fluid secreted by the liver that activates lipase, a digestive enzyme that facilitates the dissolution of oils in water and assists in the digestion and absorption of lipids. The main constituents of bile are bilirubin (an end product of red-blood cell breakdown), cholesterol, and bile acid [8]. Bile is temporarily stored in the gall bladder before being excreted to the duodenum. Biliary strictures attributable to bile duct cancer [9] or bile duct obstructions inhibit the flow of bile from the gall bladder to the duodenum, bile may flow back into the liver, resulting in icterus or, if left untreated, even fatal hepatic failure. Treatment to secure a passage for bile flow often involves a surgical procedure called endoscopic biliary stenting (EBS) [10–11].

Two types of biliary stents are currently available: metallic stents and plastic stents [11]. Most EBS procedures involve plastic stents. Figure 4 is a photograph of a straight plastic stent. Each end has a flap, and each section of the tube beneath the flap has an opening.

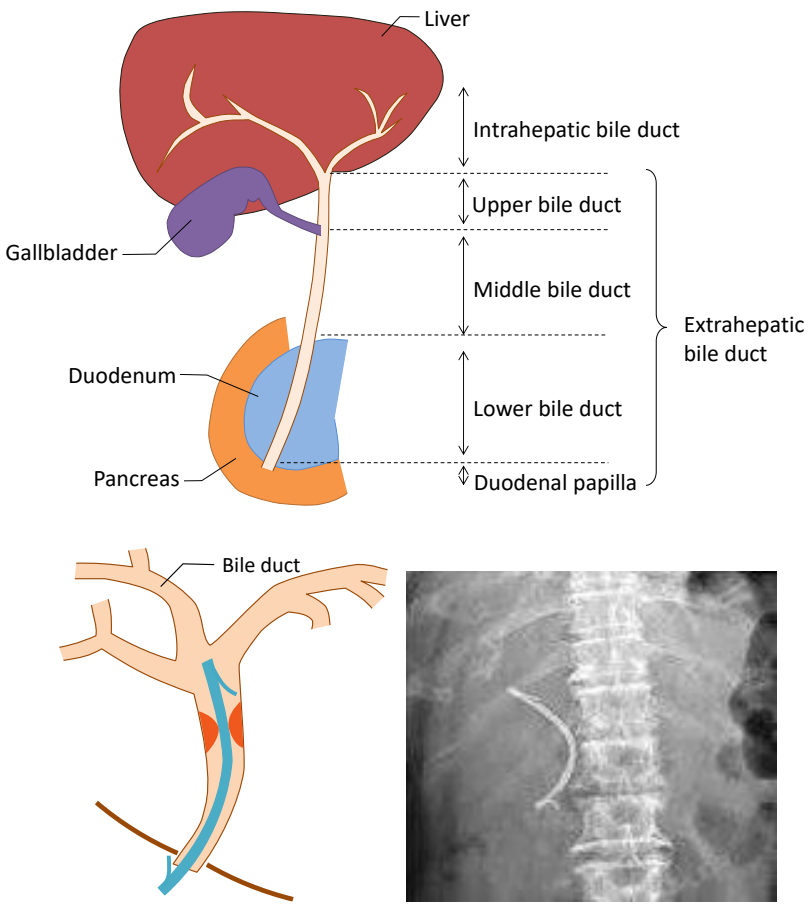

Fig. 3. Biliary tract structure and example of endoscopic biliary stenting procedure.

Fig. 4. Plastic stent (straight type, Boston Scientific Corporation).

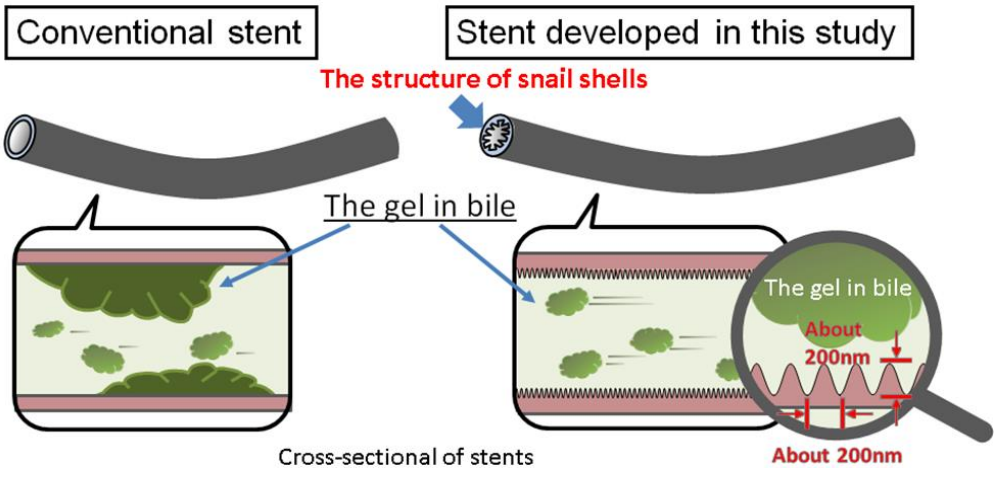

Fig. 5. Comparison of conventional stent and antifouling stent (schematic image).

Figure 5 is a schematic image comparing an antifouling stent to a conventional stent. In efforts to produce a surface that repels fluids containing oils, such as bile, we believed the structures found on snail shells, which exhibit super-nanohydrophilic effects in the presence of water, appeared likely to prove effective in creating an occlusion-resistant biliary stent.

We sought to develop elemental technologies for imparting antifouling properties to the inner walls of PE biliary stents by forming nanostructures directly onto the inner surface of polyethylene (PE) biliary stents with atmospheric pressure low-temperature plasma. We formed nanostructures on the inner walls of PE tubes of varying diameters under varying plasma conditions and examined the resulting structures and effects of the antifouling properties thus imparted.

3. Processing of Inner Walls of PE Tubes by the Atmospheric pressure low-temperature plasma Method

Atmospheric pressure low-temperature plasma can generally be categorized into two types: thermal equilibrium plasma (hot plasma) and nonequilibrium plasma (cold plasma) [12–13]. A representative example of the former is arc discharge, in which the plasma is at high temperature, with both electron temperature and gas temperature on the order of 10,000 K. The latter is represented by glow discharge. Although the electron temperature of the plasma is 10,000 K or more, the gas temperature is around room temperature. Given the high gas pressure (the high number of molecules in the gas state) at atmospheric pressure, the number of collisions between electrons and gas molecules is also high, tending to result in plasma in a state of thermal equilibrium. While PE biliary stents cannot be exposed to hot thermal plasma, we believe cold plasma that can be sustained near room temperature is suitable.

Two well-known examples of atmospheric pressure low-temperature plasma are streamer discharge and dielectric barrier discharge. Since a uniform spatial distribution of discharge inside the biliary stent is required, we chose to use an RF power supply as the power source and helium as the dielectric barrier discharge gas. This combination suppresses electron density and is sufficient to form atmospheric pressure plasma of uniform distribution at low temperatures [12]. The diagram in Figure 6 illustrates the principle of this apparatus. The basic components are the power source, electrodes, and a glass tube through which helium gas flows. Two electrodes are placed on the opposite sides of the glass tube facing each other at some distance from the glass tube. High-frequency power is applied to the electrodes to generate atmospheric pressure low-temperature plasma inside the glass tube. As shown in Figure

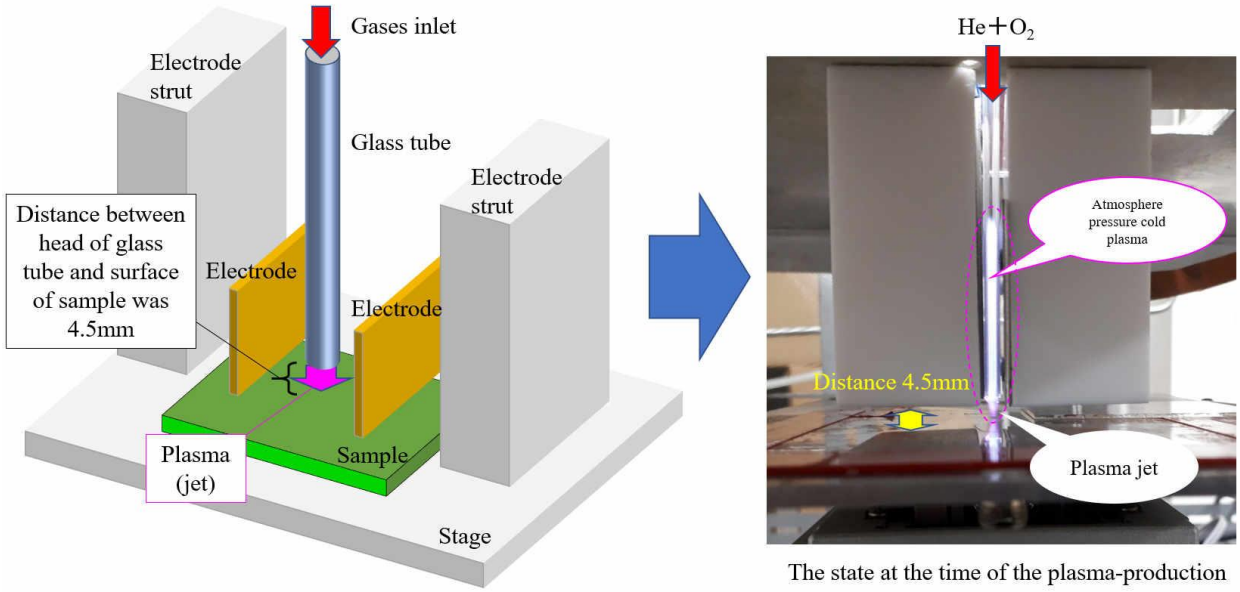

Fig. 6. Overview of the atmosphericc pressure low-temperature plasma generation unit and plasma being generated.

7, a PE tube is set in place of the glass tube. Plasma is generated inside the PE tube to form nanostructures directly onto the inner wall of the biliary stent.

When small amounts of oxygen are mixed into the He plasma, the dissociation of oxygen molecules generates atomic oxygen. Since the excitation level of atomic oxygen is the same as the metastable level of helium, previous studies suggest the Penning ionization reaction shown in the reaction formula below will occur. The oxidation reaction attributable to the atomic oxygen generated (O*) holds the promise of various applications for material surface processing technologies [13–14]. Mixing N_2 or NH_3 at concentrations of around 1 % in place of oxygen generates N radical (N*), amino radical (NH_2*), or imino radical (NH*), which can then be used to induce nitridation or amination of material surfaces [14–15].

$$He + electron \rightarrow He^* + electron \quad (1)$$

$$He^* + O_2 \rightarrow He + O^* + O^+ + electron \quad (2)$$

4. Experiment

4.1. Examining plasma generation conditions

We observed the state of plasma generation inside the tube for varied He and O_2 flow rates (Figure 8). The results showed a stable glow discharge can be formed at an He flow rate of 1.4 slm and O_2 flow rate of 2–10 sccm. We then adjusted the power to determine the conditions at which stable plasma can be achieved.

Figure 9 shows the dependency of glow discharge inception power on O_2 flow rate. The He flow rate was fixed at 1.4 slm. We found that at O_2 flow rates of 0–6 sccm, a glow discharge can be stably formed at a power of 20–100 W. This power range may be regarded as the process window for glow

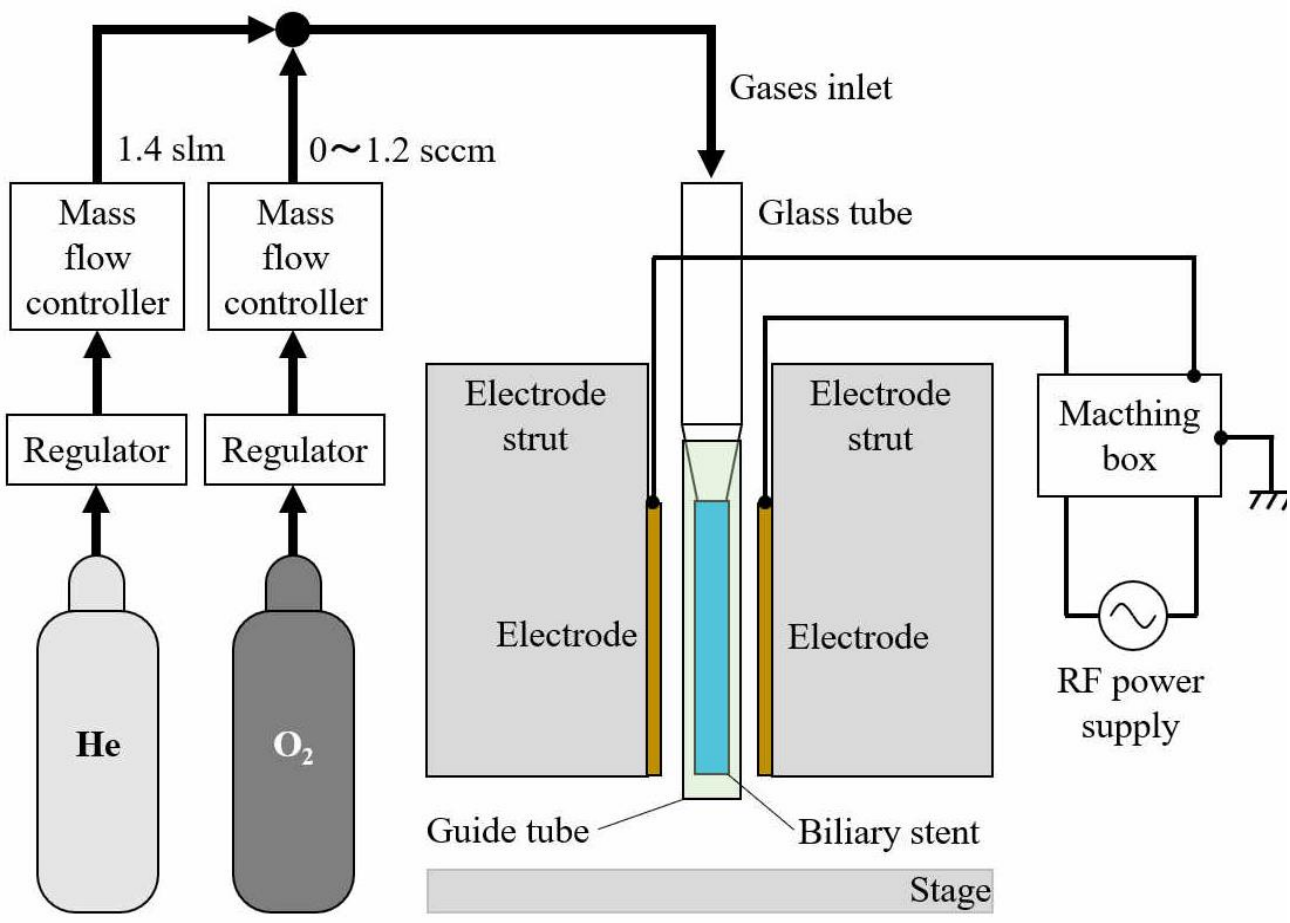

Fig. 7. Biliary stent plasma processing unit.

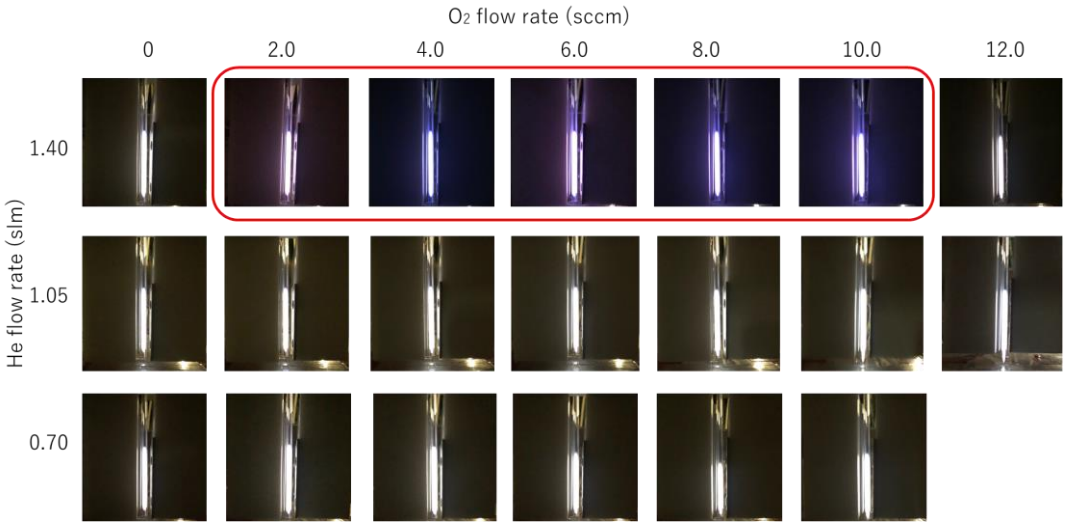

Fig. 8. State of plasma generation at various He and O_2 flow rates.

discharge inception. We surmised that stably forming a plasma inside the stent within this process window would allow processing of nanoporous structures on the inner wall of the stent.

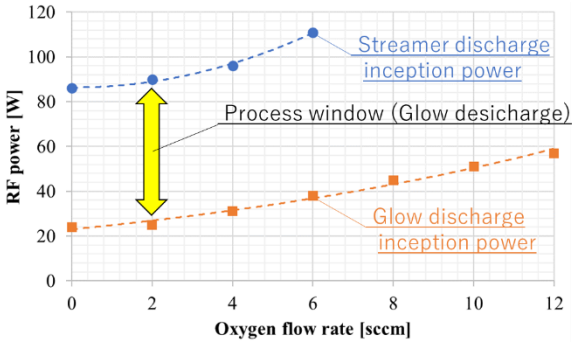

Fig. 9. Dependency of glow discharge inception power on O_2 flow rate (process window) at a fixed He flow rate of 1.4 slm.

Figure 10 shows photographs of the state of plasma formation within PE tubes of varying inner diameters. We achieved stable plasma formation with inner diameters of 2–4 mm.

4.2. Observations of plasma processed surfaces

To observe nanostructures on the inner walls of the PE tube, we rolled a piece of PE sheet into a tube and inserted it into a guide tube to simulate a PE biliary stent with an inner diameter of 2 mm, then exposed it to plasma processing. We observed the structures on the inner wall of the PE sheet via AFM (Figs. 11 and 12). We made observations for power settings of 45 W and 60 W. To prevent tube overheating due to plasma exposure, we limited the duration of a single plasma irradiation to 5 seconds and allowed cooling intervals of 30 seconds before subsequent irradiation. This irradiation cycle was repeated multiple times.

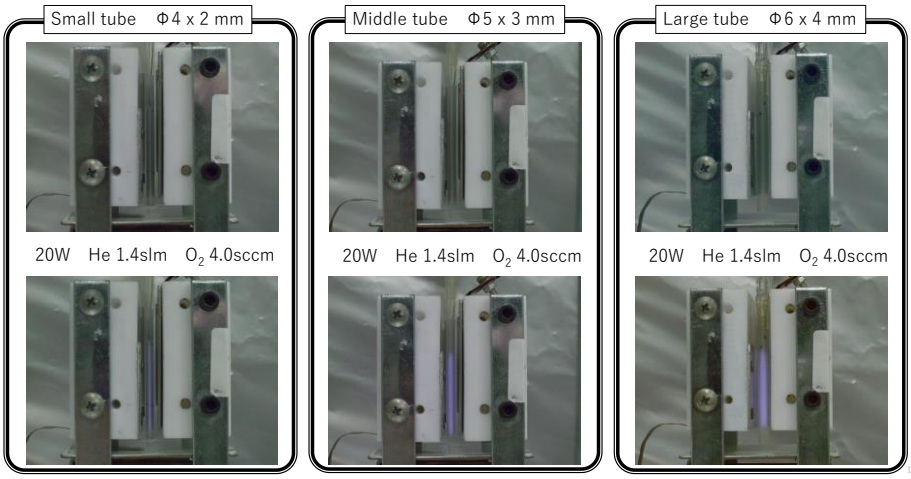

Fig. 10. State of plasma generation for different PE tube sizes.

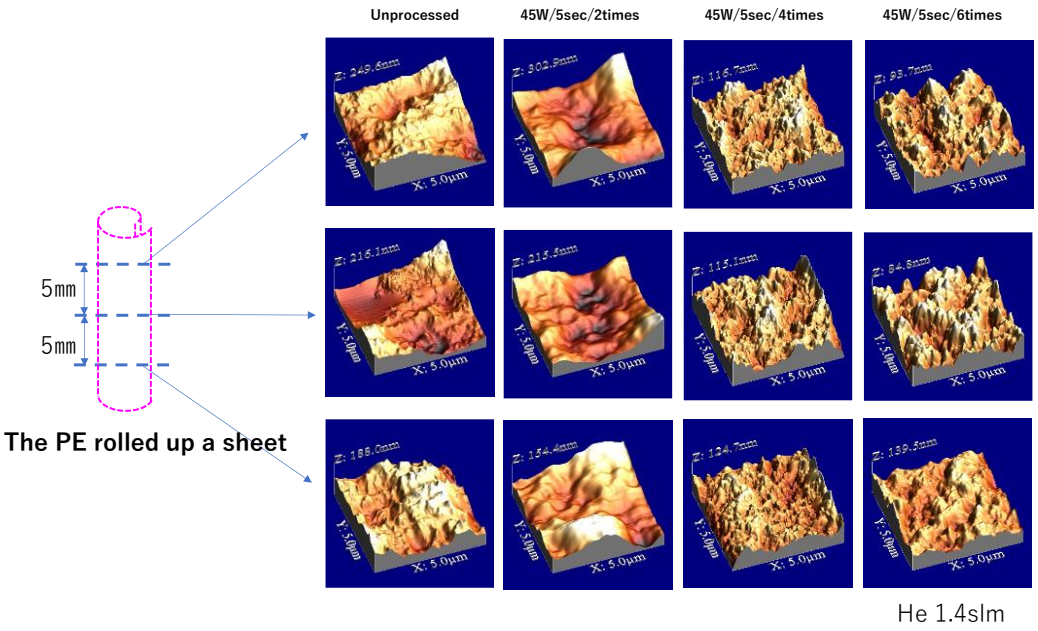

Fig. 11. Relationship between irradiation time and surface structures at 45 W and He flow rate of 1.4 slm.

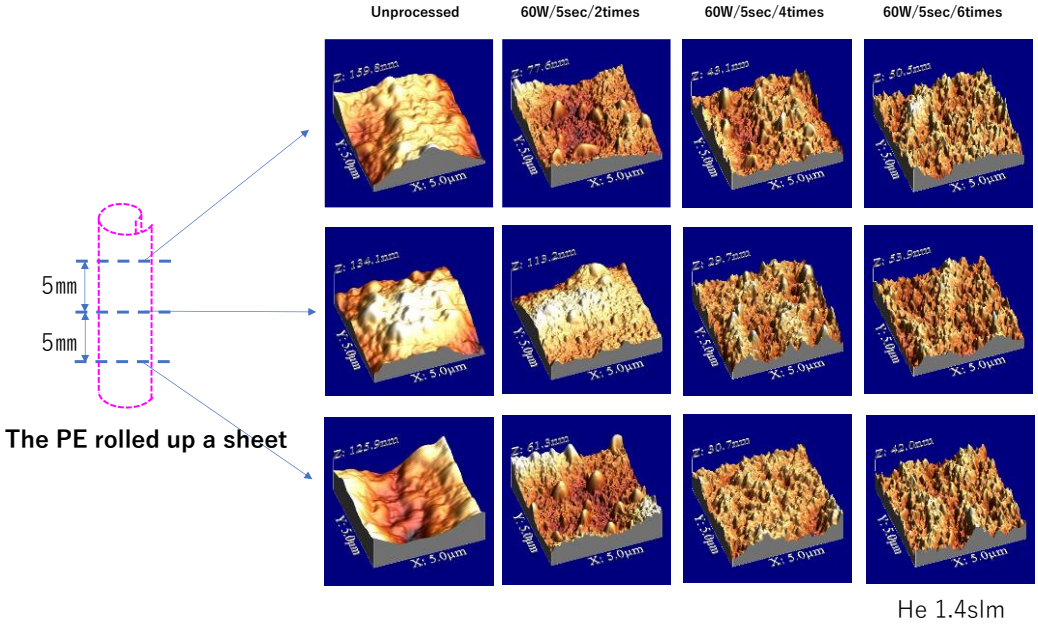

Fig. 12. Relationship between irradiation time and surface structures at 60 W and He flow rate of 1.4 slm.

Figure 11 shows the results of examination for irradiation at 45 W. Two irradiation cycles reduced surface roughness. Four to six irradiation cycles resulted in surfaces with satisfactory convex-concave nanoscale structures.

Figure 12 presents the results of examination for irradiation at 60 W. As with a power of 45 W, the nanostructures achieved after two irradiation cycles were insufficient. However, we could confirm that four to six irradiation cycles created surfaces with satisfactory convex-concave nanoscale structures.

These results indicated it was possible to form nanostructures on the inner wall of a stent by exposing it to plasma at a power of 45–60 W for four to six cycles for a duration of 5 seconds per cycle.

We examined the oil repellency of the inner wall of a PE tube of 2 mm in diameter processed with four cycles at an applied voltage of 45 W (Figure 13). According to the results, the contact angle was 107.7 degrees for unprocessed surfaces and

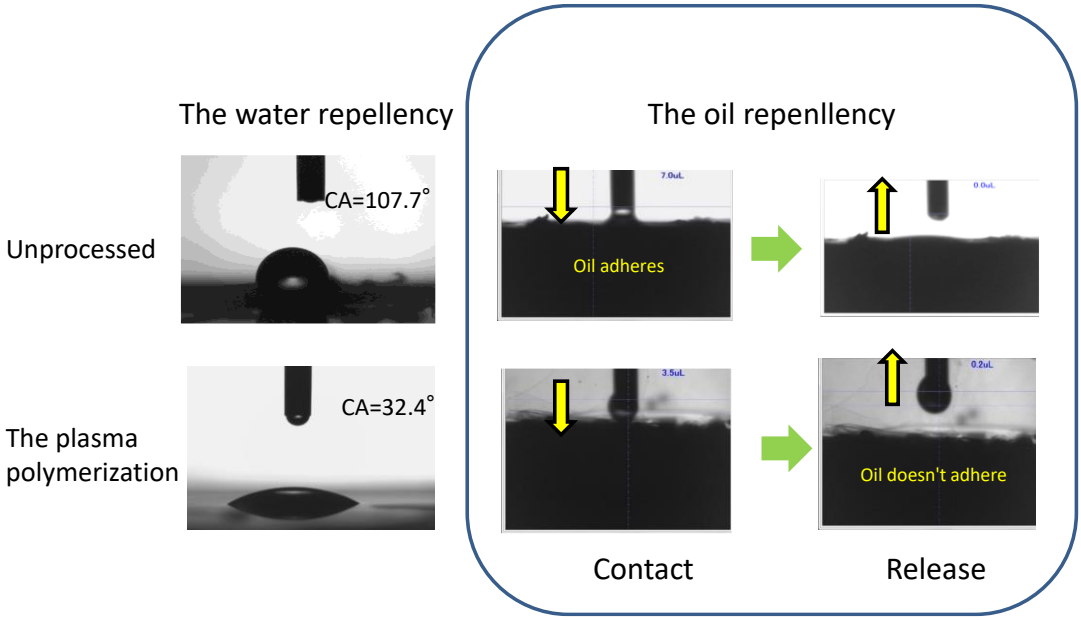

Fig. 13. Confirmation of water and oil repellency of inner stent walls.

32.4 degrees for plasma processed surfaces, which rendered them hydrophilic. We evaluated oil repellency in water and found that oil bound strongly to the unprocessed surfaces, while oil droplets failed to adhere to the plasma processed surfaces, confirming the oil repellent effects of the processed surfaces. We confirmed antifouling effects can be achieved through plasma processing.

4.3. Liquid passage test for PE stents

To evaluate the antifouling performance of PE tubes with nanostructures, we prepared an artificial bile solution from bovine bile powder and oil. The solution was prepared by dissolving a powder of bovine bile in pure water to achieve a concentration of 10 wt.%, adding lard to this solution at a concentration of 10 wt.%, and then heating to 40 °C. We used a pump to feed this artificial bile solution into PE tubes for observations of liquid passage. (Figure 14(a) is a photo of the apparatus used for the liquid passage test.) We allowed the bile solution to pass through the tube for 5 seconds at a flow rate of 6 mL/min, followed for 5 seconds by water. Then, once again, we passed the bile solution for 5 seconds, followed by water for 5 seconds. We observed the inner wall of the tube when water passed for the second time. For comparison, the photos show the tubes as the bile solution passes and as the water passes. We performed tests for tubes of three diameters: 2 mm, 3 mm, and 4 mm. The plasma processing conditions were four cycles of 10 seconds of irradiation and 10 cycles of 10 seconds of irradiation at 20 W and four cycles of 10 seconds of irradiation at 50 W. Under all processing conditions, we allowed a 30-second cooling interval after each 10-second plasma irradiation. Figure 14(b) presents the results of the liquid passage test.

The results confirmed that for unprocessed tubes of 2 or 3 mm in diameter, bile adhering to the inner wall of the tube was rinsed out with water. We observed no turbidity of the bile solution for surfaces processed by plasma for 10 cycles of 10 seconds of irradiation at 20 W and four cycles of 10 seconds of irradiation at 50 W; the surfaces were judged to have antifouling properties. For tubes of 4 mm in diameter, the amount of bile adhering to the inner wall was excessive, and the bile solution was confirmed to be turbid for all conditions.

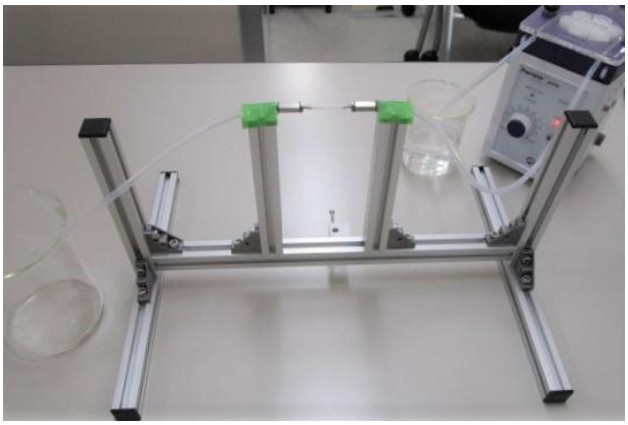

(a) External view of liquid passage test apparatus

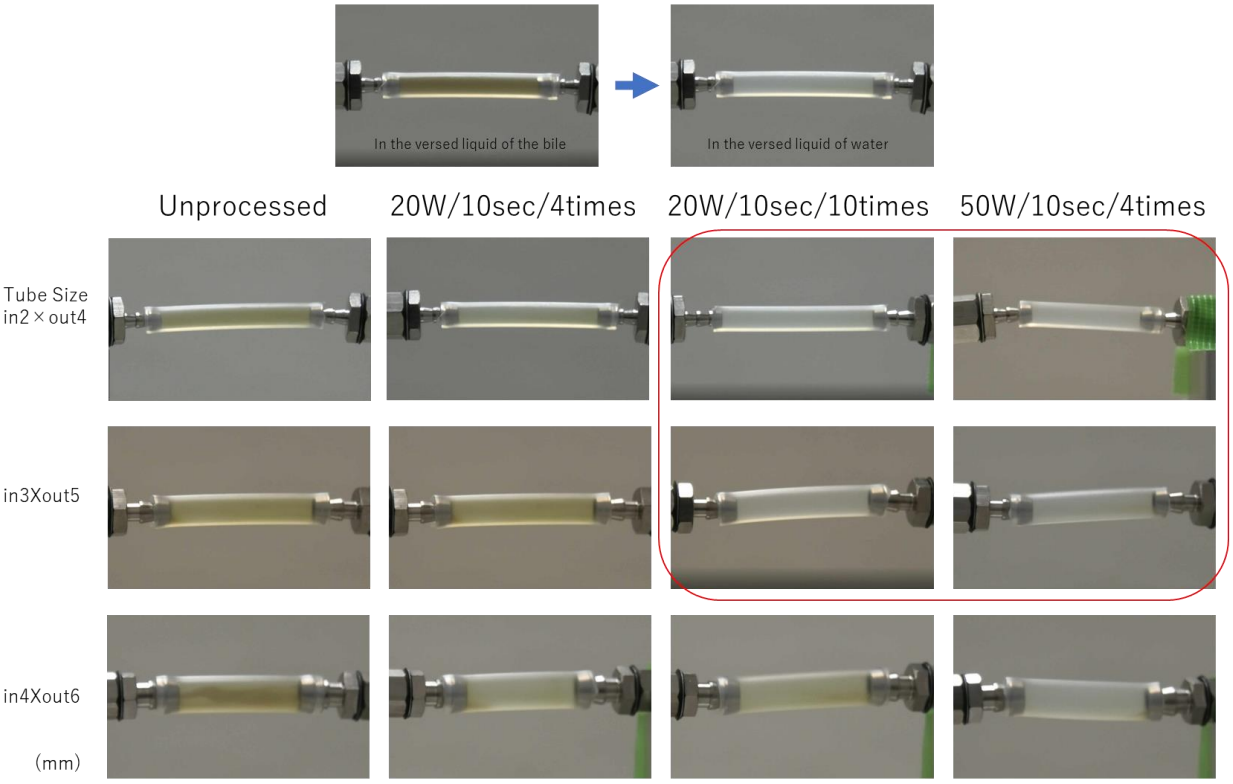

(b) Results of liquid passage test

Fig. 14. Apparatus and results of liquid passage test for mixed solution of bile + oil (lard).

5. Summary

We sought to develop elemental technologies for imparting antifouling properties to the inner walls of PE biliary stents by forming nanostructures directly onto the inner surface with atmospheric pressure low-temperature plasma. Nanostructures were formed on the inner walls of PE tubes having different diameters under varied plasma conditions, and the resulting structures and effects of the imparted antifouling properties were examined. The results show that plasma processing at an He flow rate of 1.4 slm, an O_2 flow rate of 0–6 sccm, and a power of 20–60 W forms satisfactory nanostructures on the inner walls of PE tubes that allow them to exhibit antifouling properties, especially oil repellency in water. In future studies, we plan to form nanostructures directly onto the inner surface of PE biliary stents with atmospheric pressure low-temperature plasma and confirm the imparted antifouling effects by performing animal experiments.

Acknowledgement

We wish to thank Mr. Hirano at HANACO Medical Corporation for supplying the PE biliary stents. This research was funded by 2018 revision manufacturing, commerce, service productivity improvement promotion subsidy.

References

1. M. Shimomura, "*Biomimetics, National Science Museum16*", Tokai University Press, **2** (2016).
2. J. knippers, K. G. Nickel, and T. Speck, "*Biomimetic Research for architecture and Building Construction, Biological Design and Integrative Structures, Biologically Inspired System Vol.9*", Springer, (2016) 69.
3. M. Kato, *J. Print. Sci. Technol.*, **48** (2011) 186.
4. A. Sekiguchi, Y. Matsumoto, H. Minami, T. Nishino, H. Tanigawa, K. Tokumaru, and F. Tsumori, J. Pohotopolym. Sci. Technol., **31** (2018) 121.
5. A. Sekiguchi, T. Nishino, M. Aikawa, Y. Matsumoto, H. Minami, K. Tokumaru, F. Tsumori, and H. Tanigawa, J. Pohotopolym. Sci. Technol., **32** (2019) 373.
6. C. Tendero, C. Tixier, P. Tristant, J. desmaison, and P. Leprince, Specctrochemica Acta, **B61** (2006) 2.
7. C. Jen-shin, J. Plasma Fusion Res., **82** (2006) 682.
8. G. Masselli, R. Manfredi, A. Vecchioli, and G. Gualdi, *Eur. Radiol.*, **18** (2008) 2213.
9. T. Tsuyuguchi, T. Takada, Y. Kawarada, Y. Nimura, K. Wada, M. Nagino, T. Mayumi, M. Yoshida, F. Miura, A. Tanaka, Y. Yamashita, M. Hirota, K. Hirata, H. Yasuda, Y. Kimura, S. Strasberg, H. Pitt, M. W. Büchler, H. Neuhaus, J. Belghiti, E. Santibanes, S-T. Fan, K-H. Liau, and V. Sachakul, *J. Hepatobiliary Pancreat Surg.*, **14** (2007) 35.
10. http://www.shimadahp.jp/section.php?x-vew=4&from=section&navi=3&sin=6.
    By Shimada hospital HP.
11. A. C. Smith, J. F. Dowsett, R. C. Rassell, A. R. Hartfield, and P. B. Cotton, *Lancet*, **344** (1994) 1655.
12. S. Kanazawa, M. Kogoma, T. Moriwaki, and S. Okazaki, J. Phys. D: Appl. Phys., **21** (1988) 838.
13. T. Murakami, J. Plasma Fusion Res., **92** (2016) 688.
14. M. Kogoma, Faculty of science and Techno., **58** (2007) 779.
15. M. Kogoma, J. Vac. Soc. Jpn. **51** (2008) 2.
16. T. Tsunoda, Jitsumu Hyomen Gijutsu, **34** (1987) 415.
17. T. Matsuoka, K. Sakaguchi, and C. Hata, J. Soc. Mat. Sci., Jpn, **51** (2002) 1038.
18. T. Ohiwa, K. Sumiya, S. Ogawa, and K. Takiguchi, Vaccum, (1981) 214.
19. G. W. Collins, S. A. Letts, E. M. Fearon, R. L. McEachern, and T. P. Bernat, Phys. Rev. Lett., **73** (1994) 708.
20. U. Cvelbar, S. Pejovnik, M. Mozetie, and A. Zalar, Applied Surface Science, **210** (2003) 255.

Evaluation of echinoid-shaped nanostructures for reusable mechano-bactericidal and bacterial filtration

Hee-Kyeong Kim [a], Young-Sam Cho [a,c], Hyun-Ha Park [b,c]

[a] Department of mechanical design engineering, college of Engineering, Wonkwang University,
[b] Department of mechanical engineering, college of Engineering, Wonkwang University
[c] MECHABIO Group, Wonkwang University
corresponding author e-mail: plmn130@wku.ac.kr

Abstract

Waterborne infections result from using contaminated drinking water, which is a serious danger to public health. People can easily expose to cholera, parasitic infections, and so on if they use contaminated water. In this study, a biocide-free echinoid-shaped aluminum oxide nanostructured surface was proposed. Mechano-bactericidal means that the nanostructure damages the bacterial membrane during the surface attachment stage. The proposed echinoid-shaped Al_2O_3 nanostructure can effectively kill the attached bacteria. The echinoid-shaped nanostructure surface mechano-bactericidal efficiency was shown against *E. coli* (97 ± 3.81 %) and S. aureus (80 ± 9.34 %). In addition, the echinoid-shaped nanostructure was well maintained even after thermal cleaning at 500 °C and showed high mechano-bactericidal activity (89 ± 6.86 %). In the case of the proposed echinoid-shaped nanostructure surface, it already has fine pores during the fabrication process. Therefore, the filtration experiment of bacteria through our proposed echinoid-shaped surface having interconnected fine pores showed high bacteria filtration (99.2 ± 0.3 %). The echinoid-shaped nanostructure has mechano-bactericidal activity about attached bacteria and filters out the bacteria to provide clean water. The proposed echinoid-shaped nanostructure surface is reusability via thermal treatment and could be one of the candidates for bacteria filtration apparatus.

Prepared an echinoid-shaped nanostructure

Echinoid-shaped nanostructure was prepared using Al powder (sub-10 μm) via a simple sintering process. Al powder suspension in water was prepared and 1.2 ml was dropped onto the sapphire wafer. The dropped Al suspension was dried at room temperature overnight to evaporate water, and it was sintered at 930 °C for 3 h via furnace, resulting in echinoid-shaped structures (named as "echinoid-nano"). The sample without an echinoid-shaped nanostructure for the control group was sintered at 800 °C for 30 min (named as "non-echinoid"). Figure 1 shows the fabrication process and surface characteristics of the sample.

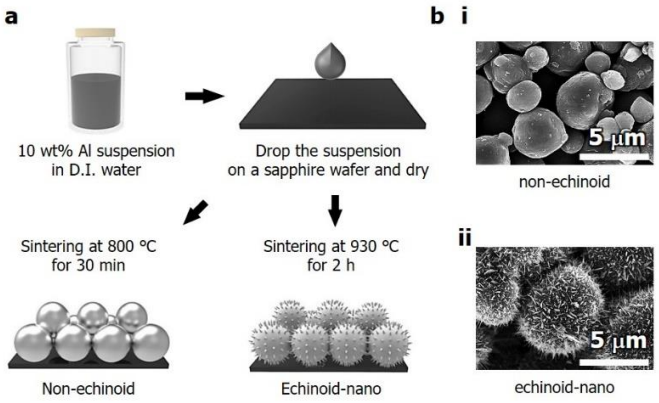

Figure 1. a) Fabrication process of echinoid-nano sample and b) SEM image of echinoid-nano surface.

Mechano-bactericidal test

The mechano-bactericidal activity of echinoid-nano and non-echinoid was evaluated using two types of bacteria with different membrane thicknesses (gram-negative *Escherichia coli* and gram-positive *Staphylococcus aureus*). Each sample was immersed in 2ml of bacteria suspension (DO_{600}; 0.1) and grown at 37 °C for 18 h. The samples were carefully rinsed for the unattached bacteria using sterile phosphate buffer saline (PBS). The washed samples were evaluated for bacterial survival via confocal and SEM (Fig. 2). In the case of *E. coil*, it was mostly dead (red staining), and the membrane of *E. coli* was stretching and penetrated by the echinoid-shaped nanostructure. Moreover, some live bacteria were observed in *S. aureus*, and only the deformation of the bacterial membrane by the nanostructure. The survival of *S. aureus* seems to resist nanostructures because they have a thick peptidoglycan layer in the membrane.

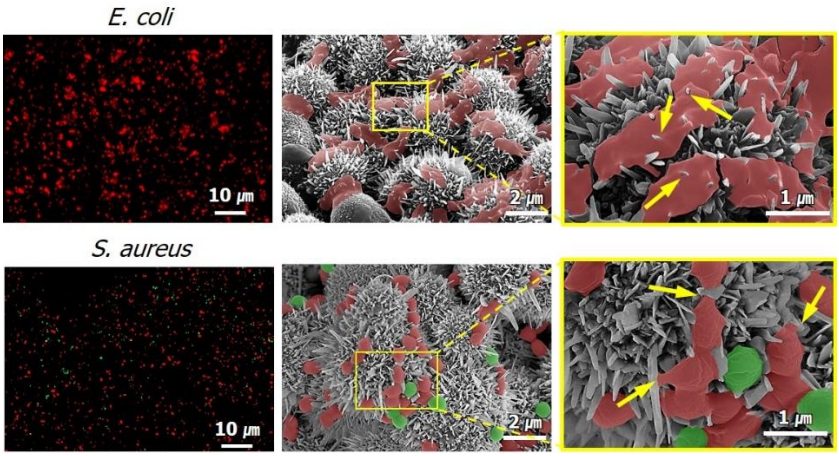

Figure 2. Representative fluorescence and SEM images of *E. coli* and *S. aureus*. The yellow arrow shows the deformation of bacteria membrane by nanostructure.

[1] Ivanova E. P. et al., small. 8 (2012) 2489-2494.
[2] Ivanova E. P. et al., Nature Reviews Microbiology. 19 (2021) 8-22

Highly Flexible, Ultra-long SEEG Probes with IrO_x Micro Electrodes Realized using Compact Bond Interfaces

M. Keller [a], O. Paul [a,b] and P. Ruther [a,b]

[a] Department of Microsystems Engineering (IMTEK), University of Freiburg, Freiburg, 79110, Germany
[b] BrainLinks-BrainTools Centre, University of Freiburg, Freiburg, 79110, Germany

Purpose of the work

Addressing deep brain regions in clinical applications remains a challenging technical endeavour. State-of-the-art stereo-electroencephalography (SEEG) probes used in epilepsy diagnostics or tremor treatment in Parkinson's patients are limited in channel count. Due to device dimensions exceeding 800 µm in diameter, they cause severe tissue reactions that negatively affect long-term recordings of single unit activity [1]. In contrast, micromachined neural probes provide large numbers of electrodes [2]. The use of polymeric substrates makes these tools mechanically flexible, which helps reducing tissue response [3,4]. However, standard fabrication processes enable probes with lengths of a few 10 mm only. These are applicable in cortical regions closer to the brain surface. In order to circumvent these limitations and enable deep brain clinical applications with micromachined neural probes of reduced cross section, we have developed an advanced fabrication and assembly process.

Novelty

The novel fabrication and assembly process enables 200-µm-wide flexible neural probes based on polyimide (PI) with lengths exceeding 300 mm. The neural probes are divided into three main components (ca. 15 µm thick), i.e. an IrO_x-based electrode array, an extension and a zero-insertion force (ZIF) interface (see Fig. 1(a,b)). The individual components with two metal layers sandwiched between three PI layers are fabricated separately on the wafer level and assembled using gold-gold thermocompression bonding. Thereby, the final probe lengths become independent of the size of the applied fabrication substrates. The MEMS process comprised of lithography, thin-film deposition, reactive ion etching (RIE), and gold electroplating steps is summarized in Fig. 1(c). A variety of dedicated test structures used to evaluate the assembly process, i.e. mechanical strength, bond yield and contact resistance, are shown in Fig. 2.

Results

Figure 3(a) shows a bond interface prior to assembly indicating vias (diam. 6 µm) between both metal layers. An ultra-long, highly flexible SEEG probe with 32 IrO_x-based electrodes and a total length of 350 mm is shown in Fig. 3(b) highlighting details of (i) bond interface, (ii) electrode array and (iii) ZIF interface. Scanning electron micrographs (SEM) of a bond interface and a focused ion beam (FIB) cut through a contact pad and 5-µm-wide interconnecting lines are given in Fig. 4(a,b). The cross-sectional dimensions of the implant are 200 µm × 15 µm. Using bond yield test structures similar to those introduced in [5] (Fig. 2(b)), a bond yield of 100 % was demonstrated. The contact resistance (Fig. 2(c)) as a function of bond pad dimensions varied between 20 and 80 µm is given in Fig. 4(c-i). The mechanical strength of 32 bonded pads (Fig. 2(a)) as a function of pad size P_w, pad arrangement, i.e. 4×8 or 2×16 arrays, and metal deposition method, i.e. sputter deposition and evaporation, is shown Fig. 4(c-ii to iv), respectively. The bonded interconnections withstand tensile forces up to $F_{max} = 2.6 \pm 0.64$ N ($n = 29$, pad size $P_w = 60$ µm).

[1] A. Carnicer-Lombarte et al., Front. Bioeng. Biotechnol. 9 (2021) 622524.
[2] C.M. Lopez et al., Proc. ISSCC, (2016), pp. 392-394.
[3] L. Luan et al., Neuron, 108 (2020), pp. 302-321.
[4] M. Vomero et al., Biomaterials, 281 (2022), pp. 121372.
[5] M. Odenthal et al., IEEE MEMS Conf 2023, pp. 409-412.

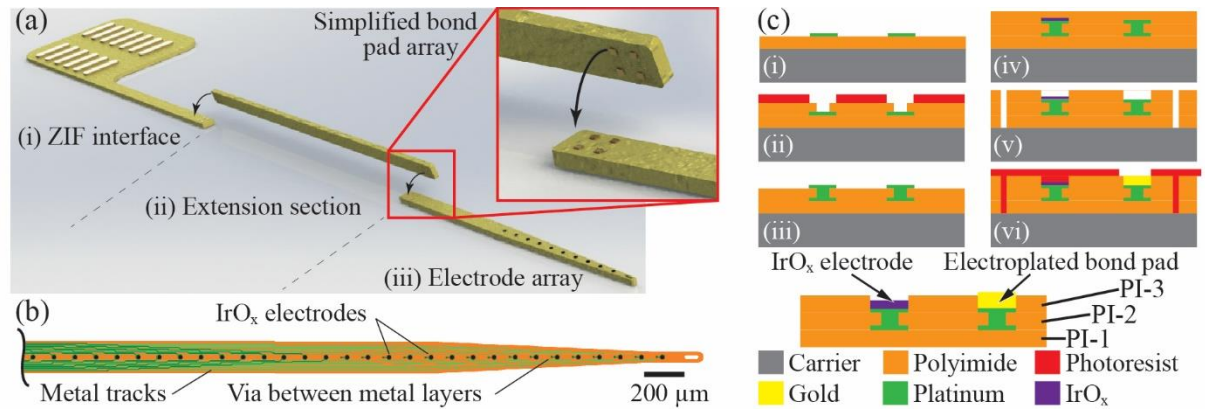

Figure 1: (a) Novel probe concept comprised of three main components assembled using thermocompression bonding. (b) Exemplary electrode array layout with 32 IrO_x electrodes. (c) Fabrication process using spin-coating of PI, physical vapor deposition of metal layers, RIE of PI layers and electroplating.

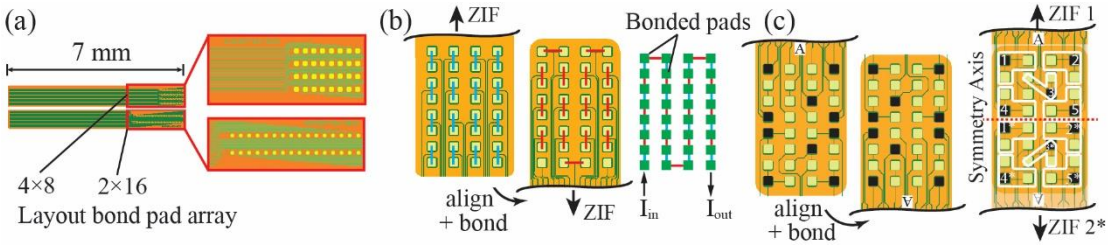

Figure 2: Test structures for evaluating (a) mechanical strength, (b) bond yield, and (d) contact resistance.

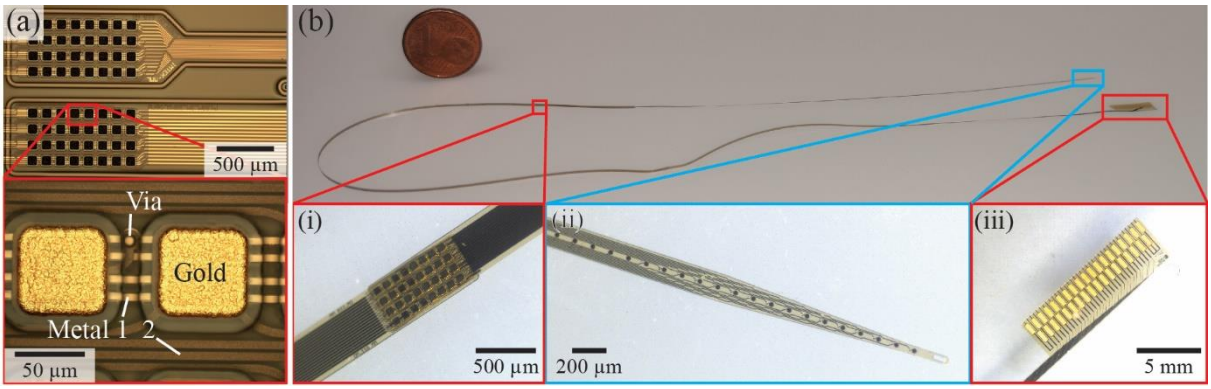

Figure 3: Fabrication results: (a) Details of electroplated bond pad arrays and (b) realized SEEG probe with total length of 35 cm (i) bonded pad array, (ii) IrO_x electrode array and (iii) ZIF interface.

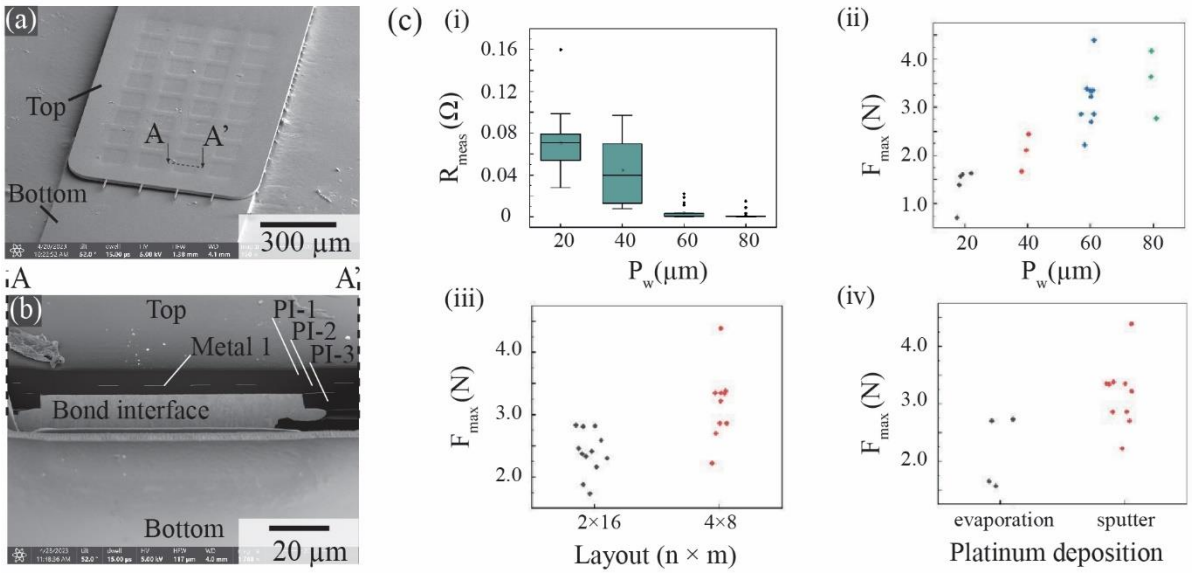

Figure 4: (a) SEM of bonded pad array and (b) FIB cut showing lines under pads. (c) Contact resistance R_{meas} vs. pad size P_w (i), and mechanical strength vs. P_w (ii), pad arrangement (iii), and deposition processes (iv).

Reflectance-Based Optical Biosensor Platform with Residual-Layer-Free Nanoimprint Lithography

Junhyoung Ahn[a,b], Yunji Eom[a,b], Soonkeun Kwon[a], Hak-Jong Choi[a], SungHwi Lee[c], Hyungjun Lim[a], JaeJong Lee[a,b]

[a] Department of Nano Manufacturing Technology, Korea Institute of Machinery & Materials, Daejeon, 34103, Republic of Korea
[b] Critical Disease Diagnostics Convergence Research Center, Korea Research Institute of Bioscience & Biotechnology, Daejeon, 34141, Republic of Korea
[c] Department of Robotics & Mechatronics, Korea Institute of Machinery & Materials, Daejeon, 34103, Republic of Korea
e-mail: ajh@kimm.re.kr

A reflectance biosensor is a type of biosensor that uses plasmonics about the interaction between light and metallic nanostructures to detect and analyze biomolecules like DNA, RNA, proteins, viruses, and bacteria. These biosensors are typically fabricated on metallic nanoparticles or nanopatterns, such as gold or silver, for the plasmonic signal generation. When light is directed to the nanoparticles, the plasmons at the surface of the particle are exited, producing a characteristic spectral signal. When a target binds on the nanoparticles or nanostructures, a shift plasmon resonance frequency was shown as spectral signal caused by the local refractive index changes [1]. Nanoimprint lithography (NIL), which was first demonstrated by S.Y. Chou [2], is a high-resolution patterning process using the fabrication to make nanometer-scale patterns on various surfaces, such as film, metal, and silicon. This fabrication involves using a stamp, usually made of a hard material like silicon and metal, to transfer a pattern onto surfaces by mechanical deformation. The process can be used to create a various nanopatterns, such as lines, dots, holes, and pillars. NIL has several advantages over other patterning process such as E-beam lithography and photolithography. It can not only achieve high-resolution to sub-10 nm typically and can be used to pattern a large area at one time, but also a relatively low-cost and fast process, making it attractive for large-scale manufacturing. [3].
The fabrication of optical biosensor using NIL has been widely researched because it has the high resolution, large-area patterning, and low-cost process. Lee et al developed ad optical biosensor using peptide-immobilized nanopillar structures for label-free detection of viruses with thermal NIL technique [4]. Jiang et al., presented a novel pressure free NIL technique by simply employing a very thin PDMS stamp with a spin-on-glass (SOG) HSQ material for localized surface plasmon resonance (LSPR) biosensor [5]. Likewise, various nanostructures patterns using NIL have been fabricated for biomedical detection and biological applications.
In this study, we demonstrate the simple, low-cost, and time-saving method for the fabrication of reflectance substrate using residual-layer-free NIL. The hole nanostructure patterns of 200 nm diameter, 400 nm depth, and 400 nm pitch were fabricated on Au surface using UV NIL without further process for removing residual layers for reflectance biosensor application. Gold surfaces have the reflectance peaks of 286 nm, 370 nm, and 433 nm, and the peaks are enhanced by residual-layer-free NIL hole pattern. The reflectance peaks are shifted by 100 nm magnetic nanoparticles. This substrate can be applied for immune reflectance biosensor with magnetic nanoparticles for target pre-treatment.

[1] H. Altug et al., Nat. Nanotech. 17 (2022) 5-16.
[2] S.Y. Chou et al., Appl. Phys. Lett. 67 (1995) 3114.
[3] S. Barcelo et al., Nano Converg. 3 (2016) 21.
[4] W.S. Lee et al., Biochip J. 15 (2021) 260-267.
[5] S. Jiang et al., Sens. Actuators B Chem. 242 (2017) 47-55.

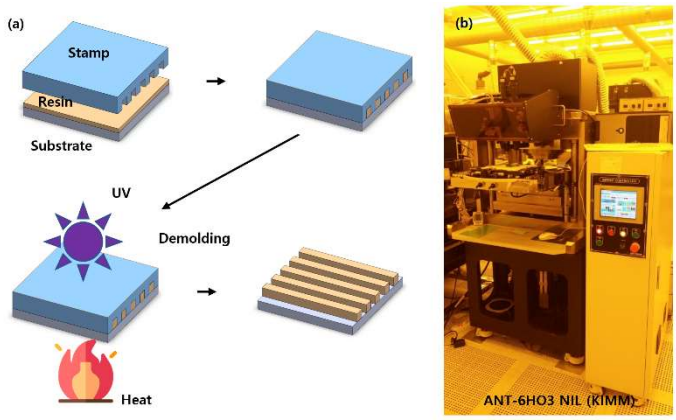

Figure 1. (a) Scheme of nanoimprint lithography, and (b) ANT-6HO3 UV/thermal nanoimprint lithography (developed by KIMM)

Figure 2. Photograph image of the reflectance chip with 3 mm sample loading well.

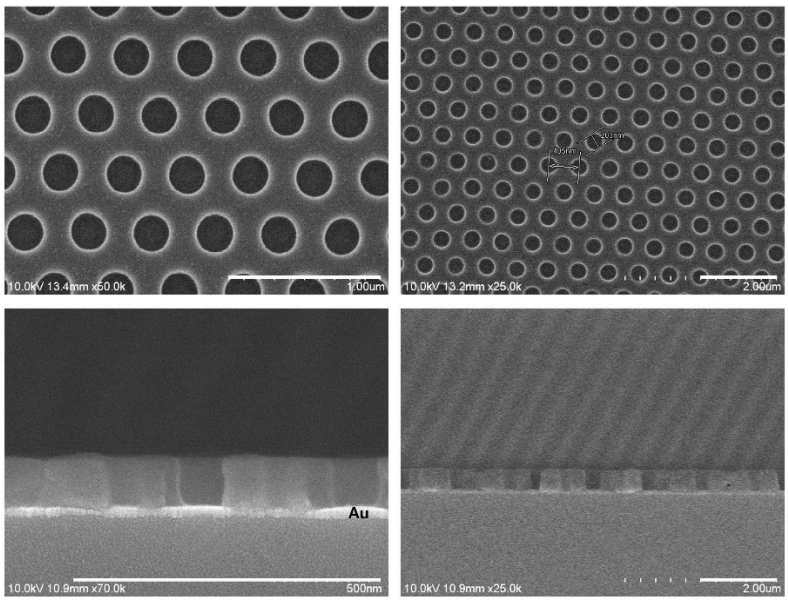

Figure 3. SEM images of the reflectance chip with Ti 2 nm adhesion layer and Au 20 nm reflectance layer (the white scale bar is 1 um)

Design and fabrication of polymer microstructures with embedded electrodes for 3D measurements

Joao M. Serra [a,b], Joao Ventura [c], Paulo Aguiar [d], Susana Cardoso [a,b], Diana C. Leitao [e]

[a] Instituto Superior Técnico, Lisbon, 1049-001, Portugal
[b] INESC Microsistemas e Nanotecnologias, Lisbon, 1000-029, Portugal
[c] IFIMUP, Porto, 4169-007, Portugal
[d] i3S - Instituto de Investigação e Inovação em Saúde da Universidade do Porto, Porto, 4200-135, Portugal
[e] Department of Applied Physics, Eindhoven University of Technology, Eindhoven, Netherlands
e-mail: joaompsserra@tecnico.ulisboa.pt

The ability to perform 3D mapping of electrical activity is increasingly relevant in biology and medicine, as 3D *in vitro* cultures behave much closer to *in vivo* systems than the more commonly used 2D [1]. Recent developments in 3D Microelectrode Array (MEA) platforms allow non-intrusive recordings of cell activity, through the use of microneedles [2], 3D printed structures [3] or mechanically actuated flexible materials [1]. Alternatively, self-assembling can be employed to deliver 3D arrangements starting from conventional planar designs [4]. For example, controlled bending of polymer layers can be achieved by taking advantage of intrinsic stress and/or thermal expansion coefficient mismatch between engineered layers [5,6].

Here, we fabricate stress-actuated polyimide strips where microelectrodes can be embedded, thus forming the basis for 3D self-assembled MEAs. We use polyimide (PI) for its biocompatibility and resistance to microfabrication processes [1]. To guide the process design, a curvature model based on the plane strain approximation was used to select the range of suitable thicknesses for the stress-inducing layer (Fig. 1), starting from available thin film materials. The impact of the PI layer thickness was also accounted for, where a trade-off between mechanical stability and the ability to undergo stress-based actuation has to be met.

Spin-coated PI was patterned using UV photolithography. The photoresist development and polyimide etching that defines the structures to be actuated (Fig. 2a) were done simultaneously using a TMA-based developer. PI was cured after each coating at 200 ºC for 30 minutes to enable coating and patterning of multiple PI layers. AlSiCu 150 nm was used as a sacrificial layer. Au leads and electrodes are fabricated in between two 3.34 μm PI layers, thus minimizing damage due to the bending process (Fig. 2b). As stress-actuator layer, a sputtered 200 nm SiO_2 underlayer was used, with an expected radius of curvature of R = 232 μm (Fig. 1a). However, we observed that the bending action did not occur immediately after release, and it was necessary to heat the sample at 200 ºC for 30 minutes. Most likely, the PI layer has to soften in order to relax into the curvature imposed by the bending structures [5]. The underlying mechanisms and their impact on both the process design and final electrode characteristics will be discussed. As an example, R = 350 ± 11 μm was obtained for a total PI thickness of 6.68 μm (Figs. 2c, d), larger than predicted by the model, pointing to deviations from plane strain conditions. In fact, the lateral size and geometry of the structures and intrinsic dependences of material properties (e.g. Young's modulus, Poisson ratio) on temperature were not accounted for in this simple approximation. Nevertheless, we successfully demonstrate embedding of Au electrodes in these bendable PI structures (Fig. 2e). Further optimizations are required, as a resistance increase of the test leads from 486.1 ± 6.8 Ω to 1497.1 ± 8.8 Ω was observed after release from the sacrificial layer.
This work sets the stepping stones to deliver 3D MEAs obtained from planar designs and conventional microfabrication techniques, enabling its application in electrical measurements of 3D neuronal cultures.

Acknowledgements: FCT for ID/05367/2020 through plurianual BASE and PROGRAMATICO, SFRH/BD/145160/2019, PTDC/NAN-MAT/31688/2017, NORTE-01-0145-FEDER-22090.

[1] D.A. Soscia et al., *Lab Chip. 20* (2020) 901–911
[2] B. Rostami et al., *2022 IEEE Sensors* (2022): pp. 1–4.
[3] J.M. Castro et al., *2023 IEEE 36th Int. Conf. Micro Electro Mech. Syst.*, (2023) pp. 315–318.
[4] B. Singh et al., *Npj Flex. Electron. 6* (2022) 1–9
[5] S. Agarwal et al, *Macromol. Mater. Eng. 304* (2019) 1–19
[6] R.M.R. Pinto et al., *Adv. Eng. Mater. 21* (2019) 1–11

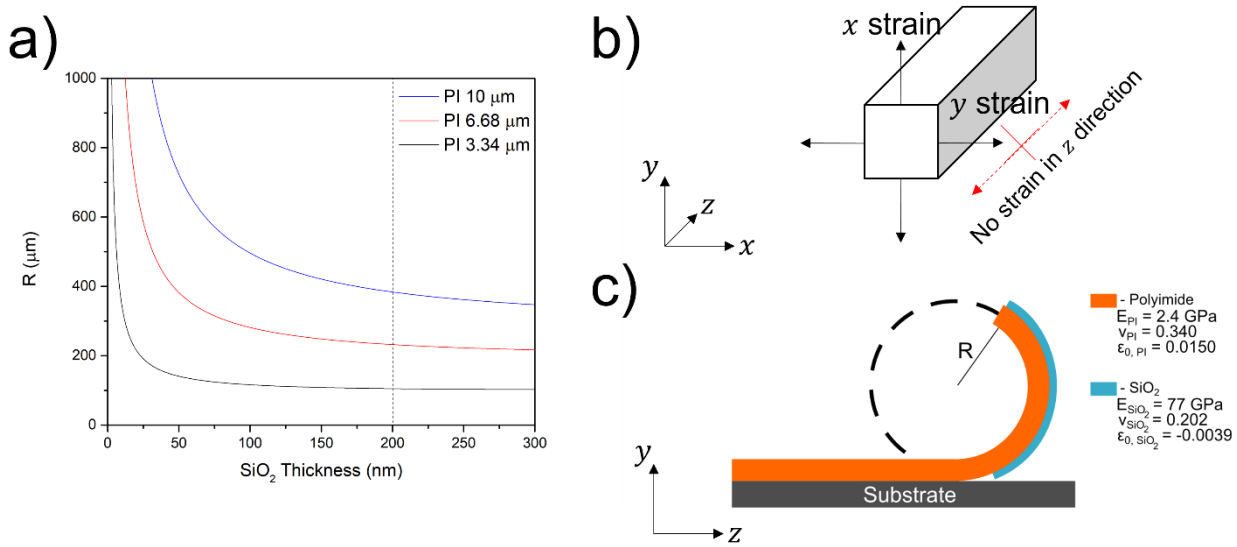

Figure 1. (a) Dependence of the curvature radius on the thickness of SiO_2 and PI obtained from the model to describe stress-induced bending. The expected values for 200 nm SiO_2 employed on the process is highlighted by the line. (b) Plane strain conditions. (c) Schematics of the plane strain model system with input materials parameters.

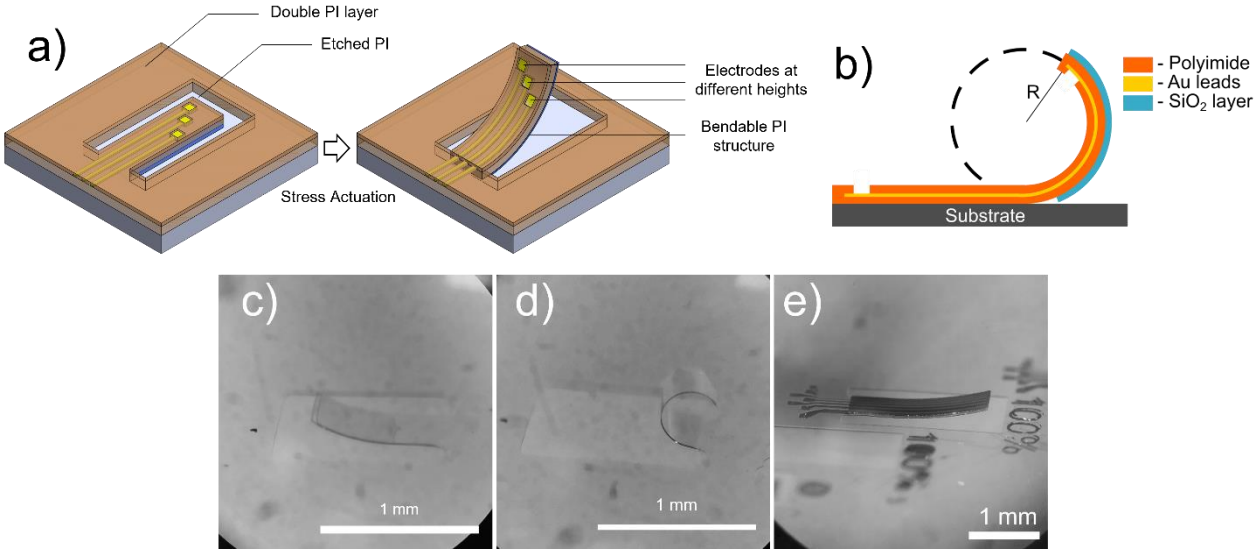

Figure 2. (a) Schematic diagram of the design of stress-actuated structures with electrodes to be positioned at different heights by bending of the polymer layer and (b) side view of the 3D structures with underlying SiO_2 stress layer and Au electrodes embedded between 2 PI layers of the same thickness. (c) PI strip after releasing from the sacrificial layer and (d) after heating the sample to further activate the bending action. (e) Example of a structure without SiO_2 underlayer but with 45 nm Au leads in between the 2 PI layers.

Patterning of bio-doped silk films at wafer level for the sustainable and scalable production of biosensors

Sara Santiago [a*], Augusto Márquez[a], Marcin Procek[b], Salvador David Aznar Cervantes[c], Gonzalo Guirado[d] , Carlos Domínguez Horna[a] Xavier Muñoz-Berbel [a]

[a] Instituto de Microelectrónica de Barcelona. Centro Nacional de Microelectrónica (IMB-CNM, CSIC), Cerdanyola del Vallés, Barcelona, 08193, Spain

[b] Department of Optoelectronics, Silesian University of Technology, 2 Krzywoustego Str., 44-100 Gliwice, Poland

[c] Instituto Murciano de Investigación y Desarrollo Medioambiental (IMIDA), San Pedro del Pinatar, Murcia, 30740, Spain

[d] Departamento de Química. Facultat de Ciencias. Campus Universidad Autónoma de Barcelona (UAB). Cerdanyola del Vallés, Barcelona, 08193, Spain

e-mail: sara.santiago@imb-cnm.csic.es

Silk fibroin (SF) is a natural bioprotein that has attracted attention for its potential use in microfabrication processes due to its high processability, mechanical, thermal and chemical stability, biocompatibility, biodegradability and entrapment capacity. [1,2] The polymorphic crystalline structure of SF is a key property because confer it the capacity to act as a positive or negative resist in lithographic processes. By manipulating the SF sample during processing, it is possible to modify its internal structure. Initially, the structure consists of amorphous domains that give it hydrophilic properties. However, through a process called water annealing, the material can be organized into crystalline structures (specifically β-sheet and α-helix), resulting in a fully hydrophobic nature. [3] Using photolithographic techniques, the crystalline structure can be reversed back to its amorphous state by exposing it to a high-energy electron beam. As a result, when treated with water as a developer, the regions irradiated by the electron beam are eliminated. This allows for the creation of high-resolution patterns on the silk films. The remarkable aspect of this process is its complete sustainability and reliance on water as a developer. [4]

Furthermore, silk fibroin serves as an exceptional polymer framework for maintaining the effectiveness of bio-dopants like enzymes and fluorescent proteins, even when exposed to challenging environmental circumstances. [5,6]

In this work, we have demonstrated the potential use of silk fibroin (SF) as a biocompatible and ecofriendly positive photoresist material with high resolution that avoids the use of harsh chemicals by means of a lithographic process (i.e. e-beam lithography) for the patterning of SF films at wafer level, which is of special interest for the fabrication at large scale of highly sensitive and specific biosensors. [7]

First, SF film thickness deposited on SiO_2 wafers were finely tuned by spin coating adjusting the SF concentration and spinning conditions, obtaining values from 50 nm to 600 nm with a standard deviation < 5%. After a fast crystallization step (<5 hours), crystalline SF films where patterned by E-beam lithography (positive resist) and revealed with water (100 $\mu C \cdot cm^{-2}$ dose and 10 keV acceleration voltage), being possible to obtain sub-micrometric patterns below 800 nm. (see Fig. 1 and Fig. 2) The same process was repeated doping the films with the enzymes glucose oxidase and peroxidase, and the redox mediator ABTS, obtaining similar resolution magnitudes without compromising the structural integrity and function of the biomolecules. [8] The activity of the entrapped enzymes and ABTS molecules could be determined by coupling optical fibers to detect the color change proportional to glucose concentration. (see Fig. 3)

The SF technology is of high interest in biosensors development for the potential scalability of the technology to mass production, and for the high stability of the enzymes in the SF matrix, where long lifespan close to 8 months have been already reported with minimal storage restrictions (i.e. dried and at room temperature).

[1] Q. Van Le et al., Polymers. 11 (2019) 1933-1965.
[2] M. Hang et al., Progress in Polymer Sciece. 46 (2015) 86-110.
[3] D. L. Kaplan et al., Acta Biomaterials. 6 (2010) 1380-1387.
[4] F. Omenetto, et al., Nature Nanotechnology. 9 (2014) 306-310.
[5] F. Omenetto, et al., J Control Release. 219 (2015)
[6] F. Omenetto, et al., Biomacromolecules 10 (2009) 1032-1042.
[7] C. Domínguez, et al. SPIE-Intl Soc Optical Eng (2019)
[8] A. Márquez. Alginate and silk fibroin based technologies for biosensing. Ph D. Thesis. Group of Chemical Transducers. Institute of Microelectronics of Barcelona. Centro Nacional de Microelectrónica (IMB-CNM, CSIC), 2019.
[9] A. Márquez. Proceedings. 2 (2018) 886-890.

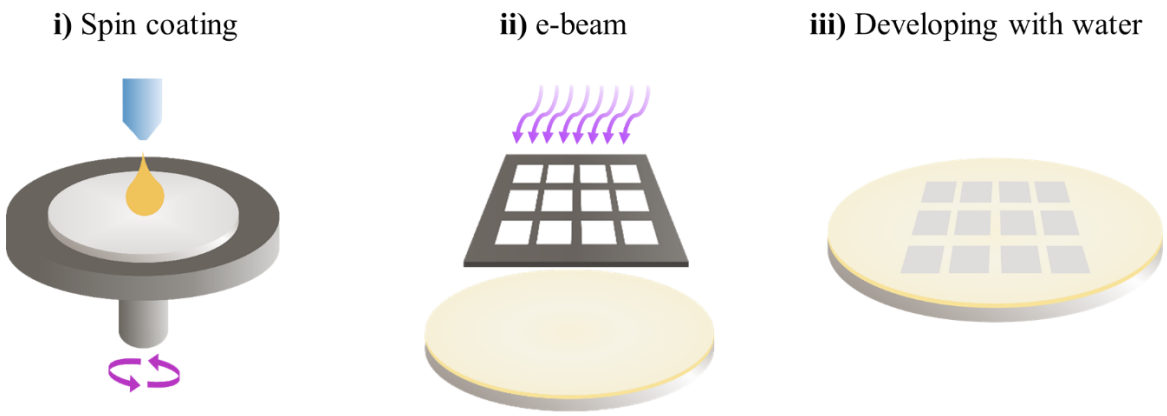

Figure 1. Fabrication steps of sub-micron patterned silk fibroin films on wafer level by e-beam photolithography.

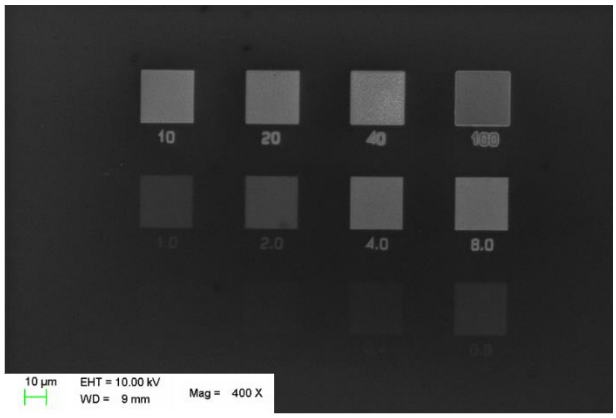

Figure 2. SEM image of patterned silk fibroin using a 10 keV 100µC·cm^{-2} e-beam dose.

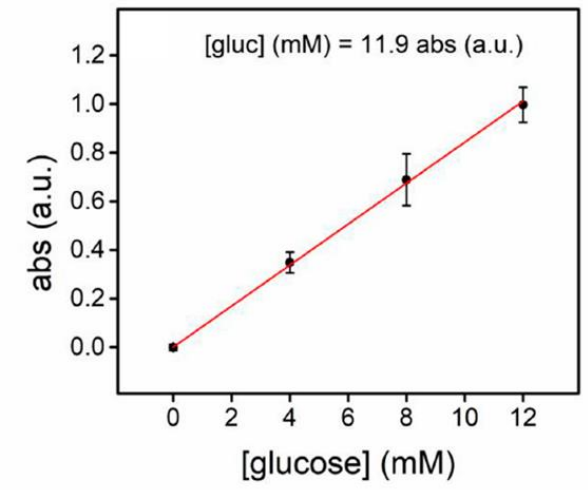

Figure 3. Detection and quantification of glucose using silk fibroin doped with glucose oxidase, peroxidase and ABTS redox mediator by UV-Vis spectroscopy.

Evaluation of microneedle patches for improved intradermal delivery of molecularly-defined cancer vaccines

Francesco La Malfa [a], Koen van der Maaden [b], Ferry Ossendorp [b], Urs Staufer [a]

[a] Department of Precision and Microsystems Engineering, Delft University of Technology, Delft, 2628 CD, the Netherlands.
[b] Department of Immunology, Leiden University Medical Center, Leiden, 2300 RC, the Netherlands

e-mail: U.Staufer@tudelft.nl

Microneedle patches (MNPs) have emerged as a promising technology for delivering drugs and vaccines through the skin. These patches consist of an array of tiny needles that penetrate the outermost layer of the skin, known as the stratum corneum, enabling intradermal delivery of therapeutic agents. MNPs offer a versatile platform for drug delivery, capable of administering various therapeutics such as small molecules and vaccines [1]. Their advantages over conventional administration routes include improved patient compliance, reduced pain, elimination of needle-phobia, and avoidance of needle-stick injuries and hazardous waste. Additionally, MNPs bypass the first-pass metabolism (after oral administration drugs first passes through the stomach and liver) and allow for sustained release of drugs, enhancing drug bioavailability and efficacy [2].
This study aims to investigate the effect of microneedle shape on skin penetration and drug delivery efficiency; specifically, to design and fabricate MNPs with different parameters and to evaluate the skin penetration depth and pattern of each shape. The study aims to answer four research questions:

1. what is the critical tip diameter for human skin piercing;
2. what is the best design, in terms of shape and cutting planes, for skin piercing and penetration depth;
3. what is the effect of the microneedle angle cutting edge on skin piercing;
4. what is the effect of the microneedle length on penetration depth;

In order to test and verify concepts that can address the research questions, master molds for MNPs were successfully fabricated using 2-photon polymerization (2PP), allowing for the precise printing of highly complex shapes. These molds were made using an acrylate-based polymer resin. Subsequently, secondary molds were produced by casting polydimethylsiloxane (PDMS) with a base/curing agent ratio of 10:1. The quality of both primary and secondary molds was assessed through confocal and secondary electron microscopy. Preliminary experiments involved the fabrication of MNPs using polyvinylpyrrolidone (PVP) via a centrifugation method (see Fig 3). Here, PVP was used as a proxy for the drug containing matrix that shall be employed later on.
The evaluation of different microneedle shapes is an ongoing area of investigation with significant potential to advance transdermal drug delivery. Although microneedles have proven effective in penetrating the stratum corneum and enhancing drug delivery, the optimal shape and size to maximize these outcomes are still subjects of ongoing research and debate. The proposed study aims to contribute to this research by evaluating different microneedle shapes, including conical, tetragonal, hexagonal, and octagonal designs (see Fig 1), with the objective of determining the shape that optimally influences both the amount and rate of drug delivery. Secondarily, the effect of different tip diameters (3, 10, 20, 30, 50 µm) is evaluated (see Fig 2): sharper tips require the application of less force to penetrate the skin [3]. Additionally, the effect of different cutting-edge values (between 5.4° and 29°) is evaluated for skin's penetration purposes [4] by changing the diameter at the base of the needle (50, 100, 150, 200 µm - see Fig 1). Finally, the length of the microneedles (250, 350, 500, 650 µm) will help us to understand what is its impact on skin's penetration [5] and drug delivery.
The various penetration experiments are currently underway, and data collection and analysis are actively ongoing. The results of these experiments will be reported and discussed at the conference. The outcome of this research could potentially lead to the development of new and improved microneedle-based drug delivery systems that are optimized for several types of drugs and different patient populations.

[1] K. Van der Maaden *et al*, JCR, 161 (2012) 645-655
[2] Y. Tian, Ji. Lee *et al*., J. Pharm. Sci. 111 (2022) 1070-1080
[3] A.M. Römgens *et al*., J. Mech, Behav, Biomed. Mater. 40 (2014) 397-405
[4] H. Peidong *et al.*, J. Mech. Sci. 65 (2012), 157-167
[5] F.J. Verbaan *et al*., J. Control. Release, 117 (2007) 238–245

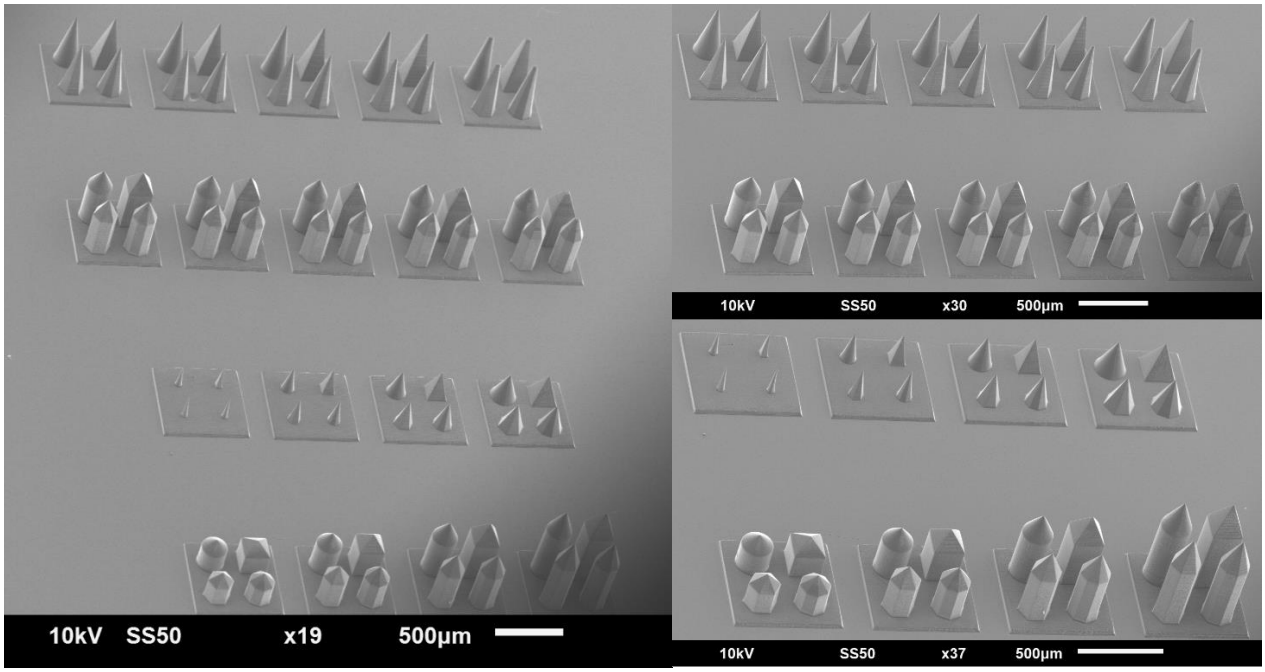

Figure 1.SEM imaging. Left: Example of microneedles fabricated by 2PP. From top to bottom, change of needle parameters: shape and tip diameter (1st and 2nd rows), diameter and cutting edge (3rd), length (4th). Right: Particular of the print instances.

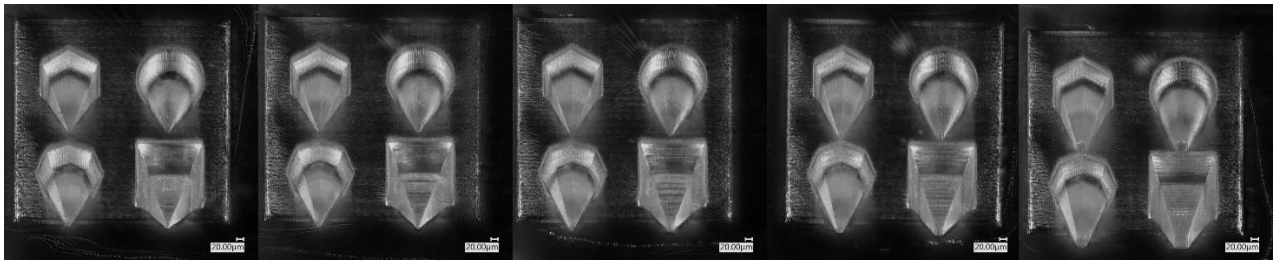

Figure 2. High resolution digital microscopy imaging. From left to right: change of tip diameter.

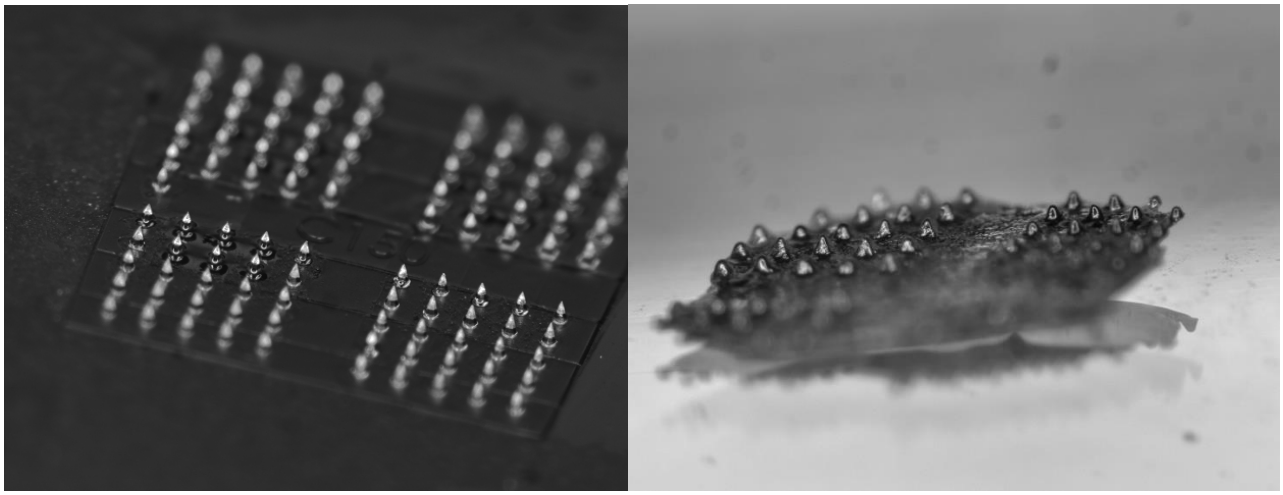

Figure 3. Confocal microscopy imaging. Left: Master mold of four 5x5 microneedle patches after demolding. Right: First dissolvable microneedle patch fabricated in PVP by centrifugation method.

Biomolecular Gradient patterning on Cell-compatible Polymer Brushes

Yoan Mimoun [a], Emmanuelle Marie [a], Mathieu Morel [a]

[a] UMR 8640 PASTEUR, Department of Chemistry, Ecole Normale Supérieure, PSL University, Sorbonne Université, CNRS, 24 rue Lhomond, 75005 Paris, France
e-mail : mathieu.morel@ens.psl.eu

Molecular gradients are ubiquitous in living organisms, and understanding the biological responses to these gradients is fundamental to the study of cell differentiation, morphogenesis or metastatic behavior of certain tumors. Particularly, substrate-bound gradients are critical in adhesion and migration processes involved in such phenomenon. Multiple methods have been developed to graft molecules on a surface [1], among which polymer brushes are of particular interest as they can be engineered for specific grafting of biomolecules but can also be dynamically controlled to present or hide these molecules of interest using an external trigger like temperature or light [2]. However, their complex patterning is often limited to "digital gradients", i.e. local domains of a given concentration with a tunable size or density. On the contrary, microfluidics allows to precisely control the chemical environment in space and time, and is therefore a tool of choice to generate continuous gradients of biomolecules [3].

Our strategy is to combine substrates coated with polymer brushes, alternating reactive and passive domains, and a diffusion-based microfluidic gradient generators [4] to obtain cell culture substrates with restricted domains grafted with continuous gradient of biomolecules (Streptavidin, RGD peptides, chemotactic factors…). Briefly, deep-UV etching is used to pattern free regions in a uniform layer of inert and anti-fouling polymer. A second uniform coating is then obtained in the etched regions with polymers bearing specific recognition moieties. Then a membrane-integrating microdevice is reversibly sealed on the polymer-coated coverslip, creating a closed chamber in which the gradient is formed by diffusion between a source and a sink channel (**Fig. 1**).

Here, a fluorescently-labeled streptavidin (Strep-Alexa-555) gradient was generated for 2 hours over a PLL-g-PEG coverslip patterned with HS-PEG-Biotin stripes. The coverslip was then detached from the device and rinsed; the highly specific streptavidin-biotin recognition ensured a one-step transfer of the concentration gradient to the stripes (**Fig. 2** and **Fig. 3**). Interestingly, another coverslip could immediately be sealed on the microdevice for sequential preparation of patterned substrates. By simply changing the orientation of the stripes relative to the gradient, a different pattern can be obtained on the coverslip, advantageously switching from stepwise gradients to continuous gradients confined to lines.

We are currently using this platform with other polymeric substrates, like PLL-PEG-N_3 allowing more versatility of the grafted object (click chemistry of DBCO-conjugated molecules) and a controlled reactivity. In addition, the geometry of the microfluidic device can be adapted to tune the gradient shape, and source and sink channels added to obtain complex chemical patterns. Our platform could thus become an invaluable tool to study the effects of biomolecular gradients on cellular haptotaxis or tissue development and differentiation.

[1] S. G. Ricoult, et al., Front. Bioeng. Biotechnol. 3 (2015) 1–12.
[2] F. Dalier, et al., Biomacromolecules. 17 (2016) 1727–1736.
[3] T. M. Keenan et al., Lab Chip. 8 (2007) 34–57.
[4] M. Morel, et al., Lab Chip. 12 (2012) 1340–1346.

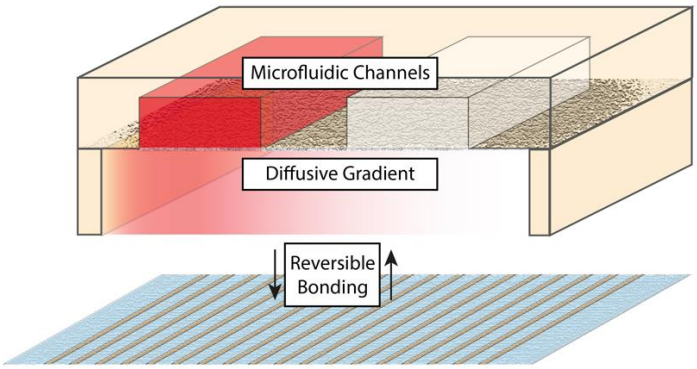

Figure 1. Schematic of the reversible bonding of the microfluidic gradient generator on a micropatterned polymer-coated substrate. A gradient of biomolecules is formed by diffusion through a porous membrane embedded in the microchannels and specifically binds to the pattern.

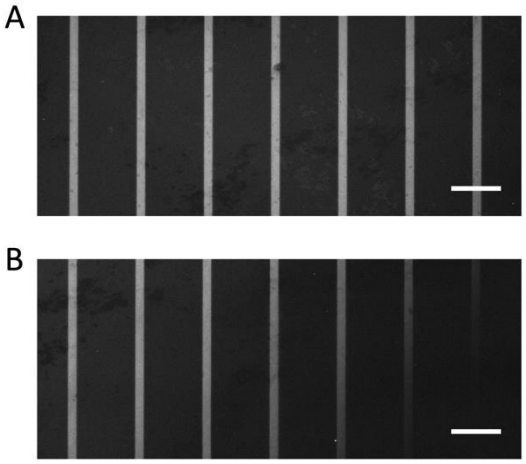

Figure 2. Epifluorescence microscopy images of PLL-g-PEG / SH-PEG-Biotin patterned coverlip functionnalized by Streptavidin-Alexa 555 (2h incubation). A) Uniform concentration. B) Left-to-right gradient. Scale bars 100 µm.

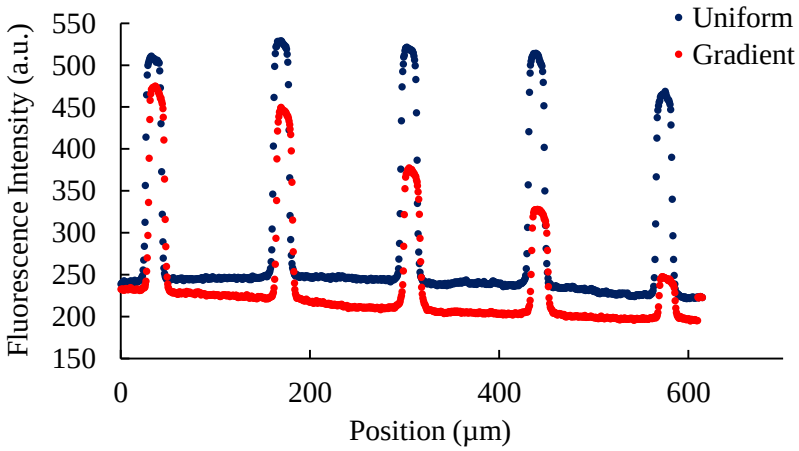

Figure 3. Linescans of fluorescence intensity of stripes-patterned coverslips functionnalized by Streptavidin-Alexa 555, with a uniform concentration (blue dots) or a gradient (red dots).

Synthetic route of Au-Fe_3O_4 Janus nanoparticles for continuous separation and purification of targeted biomaterials

Yunji Eom [a], Hak-Jong Choi [b], Junhyoung Ahn [b], SungHwi Lee [b], CheolGi Kim [a], Jaejong Lee [b]

[a] Daegu Gyeongbuk Institute of Science and Technology, Daegu, 42988, Republic of Korea
[b] Korea Institute of Machinery and Materials, Daejeon, 34103, Republic of Korea
e-mail: jjlee@kimm.re.kr

Magnetic nanoparticles (MNPs) have received significant attention in bio-applications, including hyperthermia, drug delivery, and biosensors. Recently, MNPs have emerged as a promising candidate for the separation and purification of biomaterials, such as proteins, DNA, and exosomes, for disease diagnosis and treatment [1,2]. Magnetic separation is a useful technology for obtaining specific biomaterials from whole blood or urine because of its simple process, high yield, and non-toxicity to biomaterials [3]. However, this separation method often results in particle aggregation caused by multiple binding sites on the particle surface, leading to reduced purity of the target material due to the insertion of undesired biomaterials or cluster precipitation.

In this work, we present a synthetic route for the preparation of Au-Fe_3O_4 Janus nanoparticles (JNPs) for the continuous separation and purification of specific biomaterials. Firstly, Au nanocrystals were synthesized by reducing $HAuCl_4$. Then, Fe_3O_4 NPs were attached to the Au surface using the thermal decomposition of $Fe(CO)_5$, as described in the literature, to synthesize Au-Fe_3O_4 JNPs capped with oleic acid (Fig 1) [4]. Each ligand on the surface of Fe_3O_4 and Au was continuously exchanged with a hydrophilic chain (PEG, COOH, etc.) functionalized catechol group and a target material (antibody) functionalized thiol group, which enables specific and strong binding between the targeted biomaterials and JNPs. The target material on the Au surface was attached to the surface of the targeted biomaterials. The hydrophilic chain on the opposite side of the JNPs can provide high dispersibility in aqueous solution and self-passivation to prevent undesired agglomeration between biomaterials and JNPs. In this study, we employed biotin-PEG-thiol, PEG-functionalized dopamine, and streptavidin-functionalized polystyrene (PS) bead as targeting ligands, hydrophilic ligands, and artificial biomaterials, respectively, to demonstrate the effectiveness of the JNPs separation system (Fig 2).

To analyze the structural and morphological properties, we investigated the as-synthesized and ligand-exchanged JNPs using transmission electron microscopy (TEM). Then, we observed the magnetic properties of JNPs using a vibrating sample magnetometer (VSM). Finally, we measured the dispersibility of JNPs before and after binding with the PS bead using a home-made dispersion analysis system and scanning electron microscopy (SEM). Our results demonstrate that the JNPs separation system is well-operated, with high dispersibility that enables easy movement and continuous process for separation by magnetic force.

[1] Jeonghyo Kim et al., ACS Appl. Mater. Interfaces.10 (2018) 1435-1438.
[2] Isabel Gessne et al., Scientific Reports, 9 (2019) 2069.
[3] Huilin Shao et al., Nature Communications, 6 (2015) 6999.
[4] Youngmin Lee et al., Angew. Chem. Int. Ed., 49 (2010) 1271-1274.

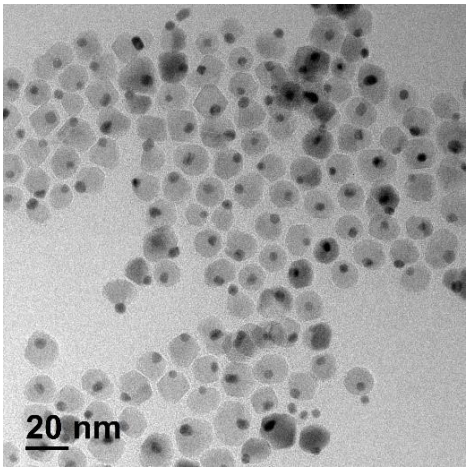

Figure 1. TEM image of synthesized Au-Fe_3O_4 Janus nanoparticles. The dark gray indicates Au nanoparticles and the light gray indicates Fe_3O_4 nanoparticles. The average size is 4.5 nm and 14.4 nm for Au and Fe_3O_4 nanoparticles respectively.

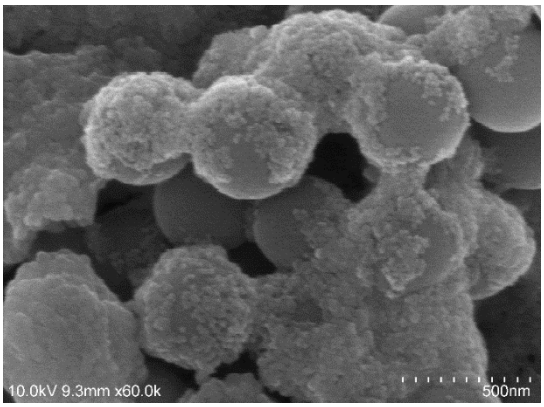

Figure 2. SEM image of polystyrene beads covered with Au-Fe_3O_4 Janus nanoparticles which were conjugated through biotin and streptavidin interaction.

Paper-based microfluidics with internal calibration as a rapid assay for the quantitative measurement of antidepressants

Esteban Builes-Münden[a], Monika Conrad[b], Günter Gauglitz[b], Markus Wieghaus[c], Andreas Dietzel[a]

[a] Institut für Mikrotechnik, Technische Universität Braunschweig, 38106, Germany
[b] Institut für physikalische und theoretische Chemie, Universität Tübingen, 72076, Germany
[c] OFFIS - Institut für Informatik, F&E Bereich Gesundheit, Gruppe Automatisierungs- und Integrationstechnik

e-mail: esteban.builes-muenden@tu-braunschweig.de

Paper-based instruments provide fast, economical and portable solutions for analyte detection, particularly in the areas of point-of-care (POC) diagnostics, environmental monitoring, food safety and forensics [1]. However, quantification of analyte concentrations with low molecular weight (<1000 Da) with internal calibration present an as yet unsolved challenge with regard to the development, manufacture, calibration and read out of the paper-based tests.

We developed a paper-based device (see Fig. 1) for therapeutic drug monitoring (TDM) of the antidepressant Amitriptylin (AMT) for therapy dose optimization [2]. Due to the small size of AMT, a typical sandwich assay cannot be carried out for catching the analytes at the test zone. Therefore, a binding inhibition test was implemented on femtosecond laser structured nitrocellulose paper (Figure 1). A calibration curve obtained with such a device is displayed in Figure 2. The results were analyzed by colorimetric evaluation using a smartphone application. Internal device calibration is required for an evaluation independent of light influences or cross reactivities. This was assured by establishing six different channels on the nitrocellulose paper and adding varied but well-defined amounts of the analyte AMT into each of them before the measurement can begin, a method called the standard addition method.

Laser structuring of different channels on the device was achieved using cold laser ablation through ultra-short pulses in the femtosecond range [3]. This process locally removes the nitrocellulose material almost without adding thermal energy. The frequency-doubled Yb: KGW-solid-state laser (Light Conversion Pharos, Lithuania) emitting at 1030 nm wavelength with a repetition rate of 600 kHz, laser power of 6.74 W and laser writing speed of 2400 mm/s was focused on the nitrocellulose paper for complete removal between the channels and partial ablation of the polyester carrier material below the paper. The laser scanning strategy was optimized for lower energy consumption and short production time.

To achieve lower limits of detection (LOD) for environmental measurements of small analytes, a pre-incubation time of at least five minutes directly after the reaction with the conjugates is required. For this purpose, a switchable fluid barrier based on a mechanical bending actuation was developed. A narrow gap perpendicular to the channel was realized by high resolution laser ablation to interrupt the channel over its entire width. This gap completely stops the sample fluid before it reaches the reaction zones. It could be demonstrated that this gap can be overcome by bending the paper device (see Figure 3) when a bridge between the two ends of the barrier is created and the fluid continues flowing to the test and control zones. This switchable barrier is a key technical element to significantly increase the sensitivity of the detection.

[1] E. Noviana et al. (2021), Chemical reviews n. 19, 121, pp. 11835–11885.
[2] M. Conrad et al. (2023), Mikrochimica acta n. 2, 190, p. 62.
[3] L. Hecht et al. (2016), Microelectronic Engineering, 158, pp. 52–58.

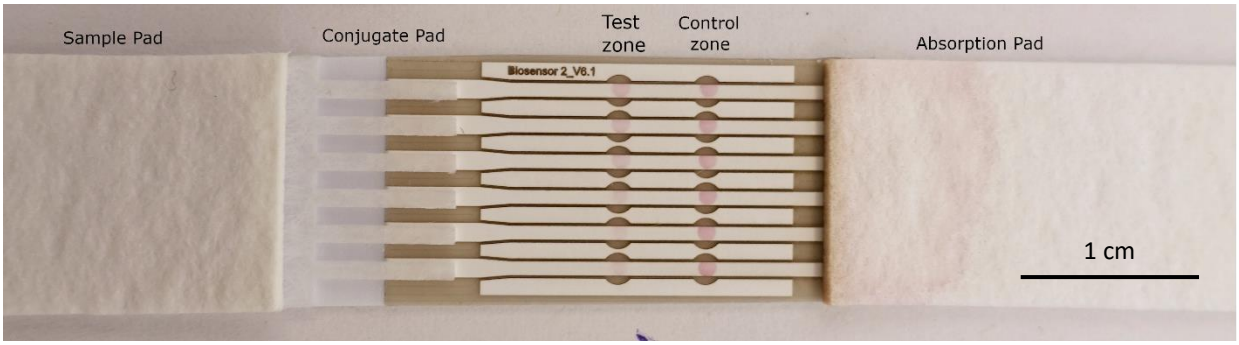

Figure 1. Multichannel device based on nitrocellulose paper with pads for sampling and absorption used for a measurement of 10 µg/L AMT. The decreasing color from top to bottom in the test zones of the channels is due to increasing amounts of added standards to the sample on the structured conjugate pad.

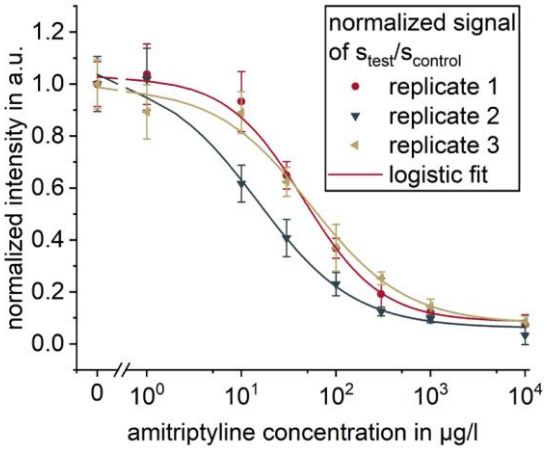

Figure 2. Calibration curve of the AMT measurement device based on a binding inhibition test

Figure 3. The mechanically switchable flow barrier can define a pre-incubation time within the nitrocellulose channel system

Recording of somatosensory evoked potentials by ultraconformable µEcoG multielectrode array with 3D PEDOT:PSS micropillar-integrated microelectrodes

Alice Lunghi [a, b], Pierpaolo Greco [b], Mauro Murgia [a, c], Riccardo Viaro [b], Sonia Guzzo [a, b], Michele Di Lauro [a], Luciano Fadiga [a, b], Fabio Biscarini [a, d], Michele Bianchi [a, d].

[a] Center for Translational Neurophysiology of Speech and Communication (CTNSC), Italian Institute of Technology, Ferrara, 44121, Italy
[b] Section of Physiology, University of Ferrara, Ferrara, 44121, Italy
[d] Institute for Nanostructured Materials (ISMN), National Research Council, Bologna, 40129, Italy
[c] Life Science Department, University of Modena and Reggio Emilia, Modena, 41125, Italy

e-mail: alice.lunghi@iit.it

Understanding how electrical signals are transmitted in the central and peripheral nervous systems is of utmost importance to clarify how neurological disorders affect the normal functioning of our neural tissues. To this end, technology platforms that enable the recording of neural signals are needed, and devices capable of accurate detection are highly desired [1]. The ability of a neural recording interface to discriminate between what is signal and what is not (*i.e.* noise) can be described through the signal-to-noise ratio (SNR), which can, in turn, be considered as the figure of merit for defining the quality of a device's performance [2, 3] Among strategies to improve SNR, the use of conductive polymers (CPs) has emerged as one of the most successful approaches [1]. The popularity of conductive polymers can be attributed to some of their unique properties, such as mixed ion-electronic conduction, processability in water, biocompatibility, and, in particular, low impedance [4]. Since impedance contributes to thermal noise, reducing its value is a simple approach to increase SNR [2]. Since spatial resolution is another key factor in precision neural recording, multi-electrode arrays (MEAs) with CPs microelectrodes currently represent the state of the art [5, 6]. However, because impedance is inversely proportional to electrode area, it remains a challenge to simultaneously achieve small electrode size and low impedance [7]. An interesting but little-explored strategy to overcome this mismatch is the use of mico- and nanopatterned CPs to increase the electroactive surface area (ESA) of electrodes while maintaining their small size [8, 9].

Here, I will report the design, fabrication and validation of an ultra-flexible µEcoGs MEA that, for the first time, explores the application of CPs micropillars in the field of in vivo neural recording. In our group, we have demonstrated the fabrication of soft 3D poly(3,4-polyethylendioxytiophene) polystyrene sulfonate (PEDOT:PSS) micropillar arrays and how these microstructures are effective in regulating important electrical and electrochemical properties of the resulting electrodes [8]. Different micropillar geometries, in fact, lead to different modulation of impedance, capacitance, and ESA, as shown in Figure 1A. As these are all essential characteristics for recording electrodes [1, 2], the ability to adjust them by changing the geometry of micropillars (*i.e.* diameter, height, and spacing) supports the potential benefits of implementing micropatterned CPs in the field of neural recording. In addition, the biocompatibility of the micropillar arrays was evaluated by assessing the viability and differentiation of SH-SY5Y cells (human neuroblastoma) cultured on these substrates. SH-SY5Y cells were found to interact tightly with the micropillars (Fig. 1B), making these substrates suitable for *in vivo* applications. Leveraging these promising results, we designed a µEcoGs MEA in which 3D PEDOT:PSS micropillars are integrated into the microelectrodes (Fig. 1C). In order to study how the micropatterned CPs affect the recording ability of the electrodes, we designed two distinct types of electrodes with micropillars of 7 or 4 µm diameter. The aspect ratio of the micropillars was 1 in both cases. We designed a fabrication process combining several techniques, resulting in the multistep procedure outlined in Fig. 1D. Briefly, the PDMS layer is encapsulated between two PET sheets and then a thin Ti/Au metal layer is deposited. The

connections, tracks and microelectrodes are obtained by IR laser ablation. Before electrodeposition of the PEDOT:PSS, the device is coated with a SU-8 protective layer that is selectively etched to expose only the microelectrodes and the connections. To precisely control the amount of charge deposited, electrodeposition was achieved by chronoculometry. The extreme flexibility of the devices is achieved by arranging the electrodes on a thin layer of PDMS (~80 µm) and is critical to ensure intimate contact between the surface of the somatosensory cortex and the electrodes, improving the quality of the recording [5]. Micropatterned µEcoGs MEAs have been shown to correctly record somatosensory evoked potentials (SEPs) in rat models (Fig. 1E); in particular, those equipped with 3D micropillars showed higher SNR than their non-micropatterned counterparts. Interestingly, the results obtained so far suggest that the recording quality depends more on the surface geometry (*i.e.* the presence of the micropillars) than on the chemical nature of the electrode (Au or PEDOT:PSS). Further investigations are currently underway to improve the understanding of the role and contribution of pattern and CP in the recording.

Bibliography

[1] M. Bianchi *et al.* Adv. Science 2022, 9, 2104701
[2] C. Boehler *et al.* Nat. Protoc. 15, 3557-3578 (2020)
[3] M.Vomero *et al.* Scientific reports, 2017, 7:40332
[4] D. T. Simon *et al.* Chem Rev. 2016, 116, 13009-13041
[5] M. Vomero *et al.* Biomaterials 255 (2020) 120178
[6] D. Khodagholy *et al.* Nature Nueroscience, 18, 310-315 (2015)
[7] D. A. Koutsouras *et al.* ChemElectroChem 2017, 4, 2321-2327
[8] A. Lunghi *et al.* Adv. Mater. Interfaces 9, 2200709, (2022)
[9] J. Yang *et al.* Sensors and Actuators A, 113 (2004). 204-211

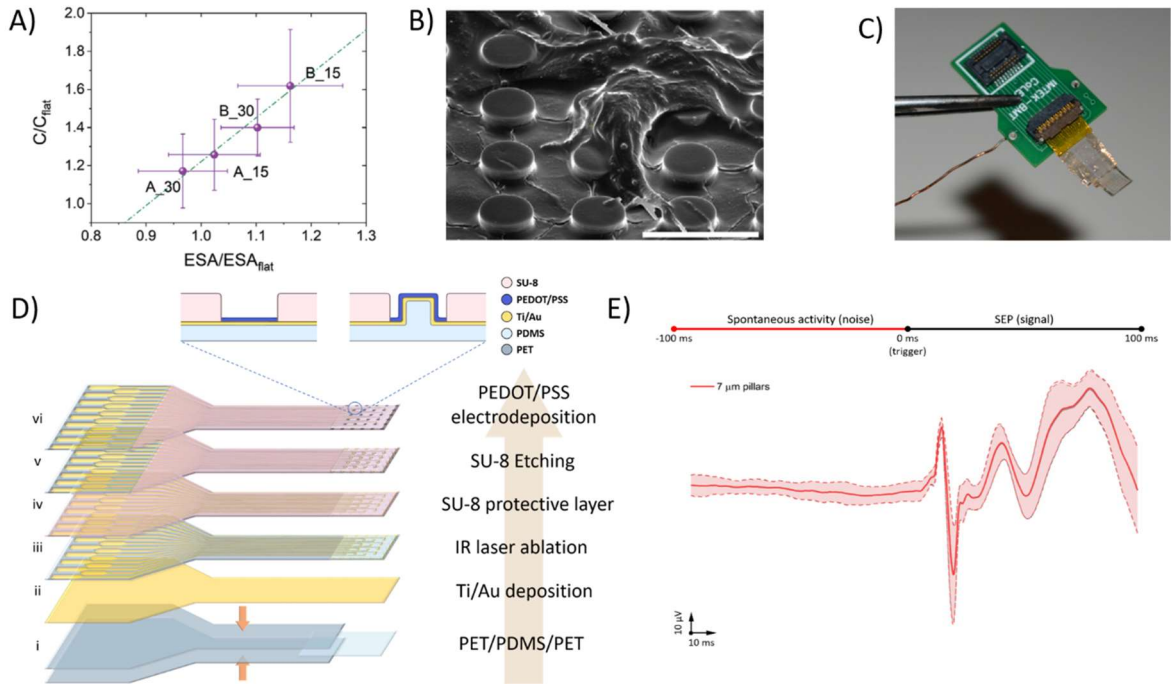

Figure 1. A) Correlation plot between normalized capacitance and normalized ESA of different 3D PEDOT:PSS micropillars electrodes; B) scanning electron micrograph of SH-SY5Y cells interacting with PEDOT:PSS micropillars (scale bar 20 µm); C) optical micrograph of an ultra-flexible µEcoGs MEA; D) schematic of the fabrication process with cross section view of the electrodes and E) representative SEPs recorded with a µEcoGs MEA from 7 µm micropillars electrodes of. A) and B) adapted from A. Lunghi *et al.* Adv. Mater. Interfaces 9, 2200709, (2022)

Investigating the effect of nanostructures effective shear modulus on the propagation of the neuronal growth cone

George Flamourakis [a], Selina Teurlings [b], Dimitri Kromm [c], Daan Brinks [b], Carlas Smith [c], Angelo Accardo [a]
[a] Department of Precision and Microsystems Engineering, Delft University of Technology, Delft, 2628 CD, the Netherlands
[b] Departments of Imaging Physics, Delft University of Technology, Delft, 2628 CJ, the Netherlands
[c] Delft Center of Systems and Control, Delft University of Technology, Delft, 2628 CD, the Netherlands
e-mail: A.Accardo@tudelft.nl

3D neuronal cultures are more physiologically relevant than 2D ones because they more closely resemble the *in vivo* physiological microenvironment, including the extracellular matrix, cellular connections, and signaling cascades, thus having a direct influence on cell survival, differentiation, and functionality [1]. The neuronal growth cone (NGC) is the most important cytoskeletal structure involved in axonal outgrowth, the process by means of which neurons probe the surrounding brain extracellular matrix to target other cells [2]. The mechanical properties of the cellular micro-environment of developing neurons can influence the signalling and motility of NGCs. Nonetheless, the evolution of this architecture is so far investigated almost exclusively on conventional 2D glass slides. This configuration hinders the possibility for the growth cone to probe more biomimetic 3D microenvironments, and features a Young's modulus (i.e. stiffness) in the range of ≈70 GPa which is much higher than the Young's modulus of the brain tissue (kPa).
The use of micro and nano-pillar structures is one method for producing 3D neural cultures, as shown recently by our group in presence of primary microglia [3]. In this work, we employed two-photon-polymerization (2PP) to create different pillar arrays in order to asses the effect of topographic and mechanical cues on the propagation of NGCs of induced pluripotent stem cell (iPSC) derived neurons. By altering the shape (i.e. diameter, spacing, and height) and fabrication parameters (i.e. laser power, scanning speed), the shear effective modulus (i.e. the shear modulus sensed by cells when crawling over a carpet of compliant structures) of the micropillar arrays can be tailored [3]. In this study, 5 different sub-micrometer pillar arrays were fabricated via 2PP with a fixed diameter of 0.5 μm, gap of 1 μm and varying height of 0.6 μm to 5 μm, leading to a theoretical effective shear moduli from 500 kPa to 35 MPa.Whole array micro-compression testing showed that higher pillars exhibit higher deformation than the shorter ones in respect to an axial force. More specifically, stress- strain curves reveals that 2.3 and 3.3 um high nanopillars undergo deformation at 5% strain and after ~ 30% strain they start to touch each other (thus the steeper slope of the diagram, **Figure 1**). Afterwards, the arrays were seeded with human iPSC derived Neuronal Progenitor Cells (NPCs) and were differentiated into neurons for a period of 4 to 8 weeks. Scanning Electron Microscopy (SEM) micrographs provided a detailed visual representation of the remarkable level of cell organization and coordination. The cell arrangement showcases a complex interconnected structure, where the NPCs form bridges and connections with neighboring clusters, creating an intricate web-like network with varied cell morphologies, ranging from elongated to spindle-shaped forms in presence of different micro/nano-pillar morphologies (**Figure 2A-E**). Neuronal growth cone structures were observed after 2 weeks on 3.3 μm height nanopillar array (**Figure 2F**). To further asses the differentiation process, neuron-specific beta tubulin III (Tuj-1) and F-actin cytoskeleton immunofluorescent markers were observed under a confocal microscope (**Figure 3**) revealing that NPCs are differentiated into immature neurons after the first 2 weeks with multiple neuronal networks being visible. Those results clearly indicate the impact that effective shear modulus has on the morphology of NPCs, their differentiation and their NGCs structure.
In summary, nanopillars were fabricated via 2PP and employed to study how different effective shear moduli and topographies can affect the phenotype of differentiated NPCs as well as their growth cones. We showed that cells create big cluster on the arrays and after 2 weeks of differentiation they start to form axon-like structures that express Tuj-1 and are extended from the spheres outwards. In the next future, super-resolution microscopy will be employed to unveil the propagation of neuronal growth cone of the neurons and ultimately connect the effect that different mechanical and topographic environments have on its propagation.

References

[1] Ransanz et al., Front. Bioeng. Biotechnol. 10, (2022) 1096054
[2] Lowery et al., Nat. Rev. Mol. Cell. Biol. 10, (2009) 332–343
[3] Sharaf et al., Front. Bioeng. Biotechnol. 10, (2022) 926642

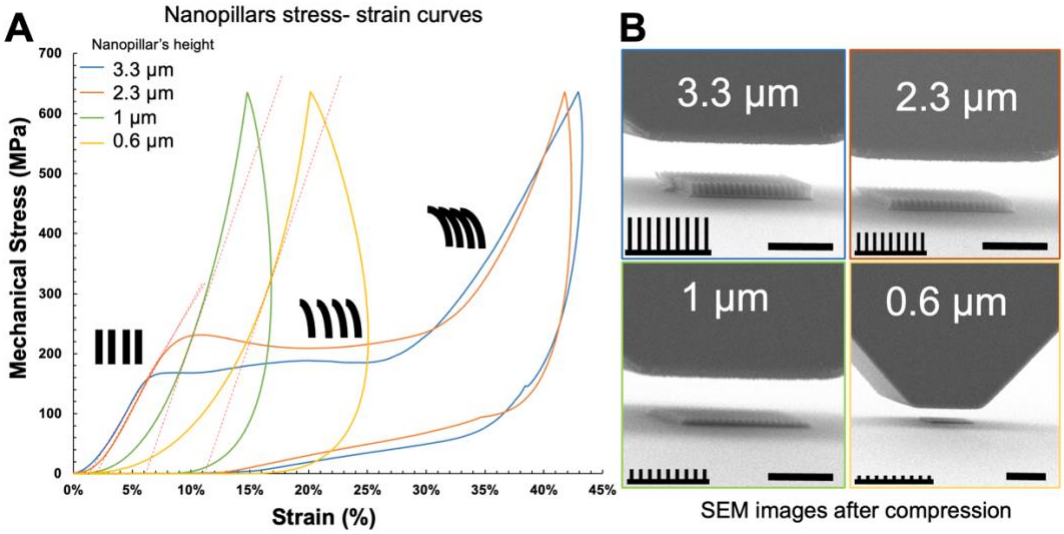

Figure 1. Micro-compression testing of 4 different arrays of nanopillars. A) Stress strain curves of the different height arrays. B) SEM images of the deformed pillars after the compression test. Scale bars correspond to 50µm. Array: 20 x 20 pillars (30 x 30 μm^2).

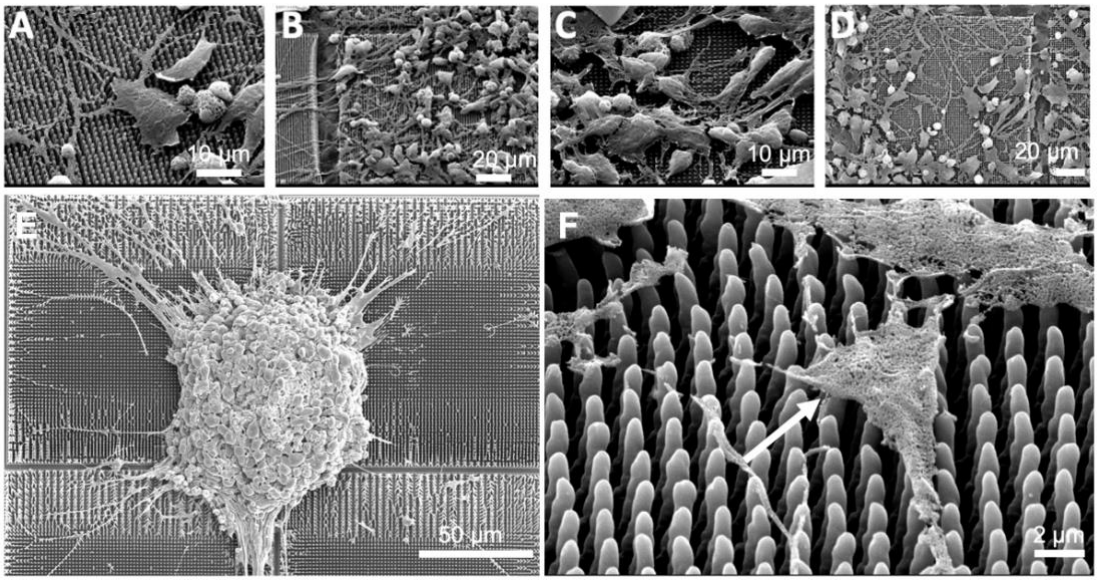

Figure 2. NPCs cultured on nanopillars arrays featuring A) 3.3 µm height, B) 2.3 µm height, C) 1 µm height and D) 0.6 µm height after 1 week of culture. E) 5 µm height nanopillars after 2 weeks in culture. F) Potential growth cone structure after 2 weeks on 3.3 µm height nanopillar array.

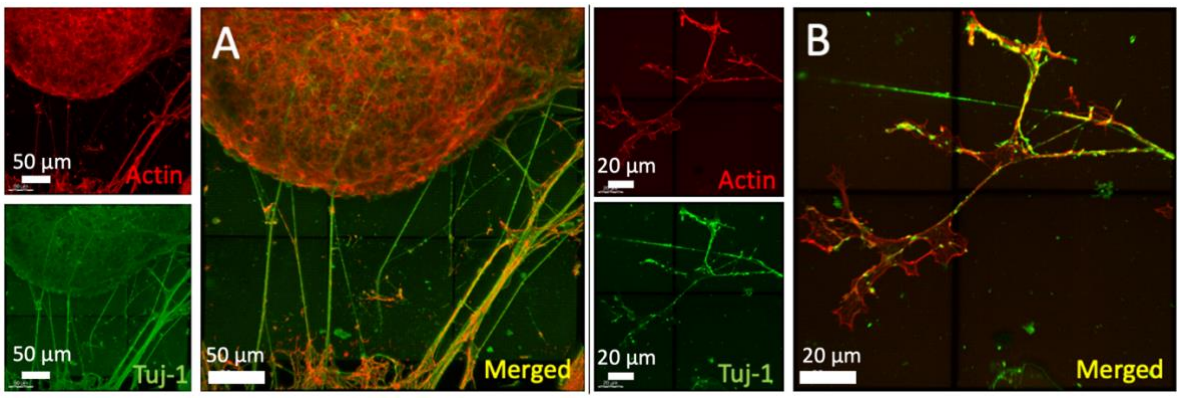

Figure 3.Confocal images of NPCs on nanopillars arrays after 2 weeks of differentiation. A) merged image of NPCs spheroid on top of the 3 µm high nano-pillar array and B) single cell on top of 1 µm height nano-pillar array.

Fluoropolymer based radiative cooler having High durability for external environment

Jisung Ha [a], Dongwoo Chae [a], Hangyu Lim [a], Jaein Park [a], Heon Lee [a]

[a] Department of Materials Science and Engineering, Korea University, Anam-ro 145, Seonguk-gu, Seoul, 02841, Republic of Korea

e-mail: nanoimprint@naver.com

Radiative cooling is next generation technology which can cool our living space than ambient temperature without energy consumption by reflecting sunlight (0.3-2.5um) and radiating the heat to the space (3K) through the atmosphere's window (8-13um). Due to the nature of the radiation cooling device that must be installed outside, we make a device that can be maintained for a long time because of its high durability character of fluoropolymer. A white and durable coating can be easily formed by dripping the solution. This cooler shows solar reflectivity of 92.5 % and emissivity of 91.7 % and its calculated cooling power is 95.6 W/m2. This implies that it is possible to cool more than 11 degrees compared to the ambient temperature. Actual measurement results also showed similar results. Also, extra measurements were carried out in high temperature and chemical environments with ETFE cooler and control group of samples. At 120℃, only ETFE film can decreases 24 degrees contrast to ambient temperature keeping the coating intact. Furthermore, when immersed into sulfuric acid below PH3, film was remained and its cooling performance was almost same. It is expected to apply for external device case which is frequently exposed to heat and chemical environment.

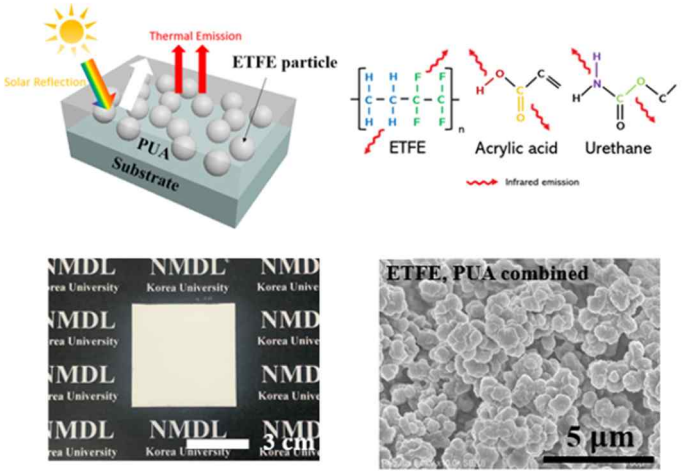

Figure 1. Schematic, Visual, Sem image of ETFE containing radiative cooling material

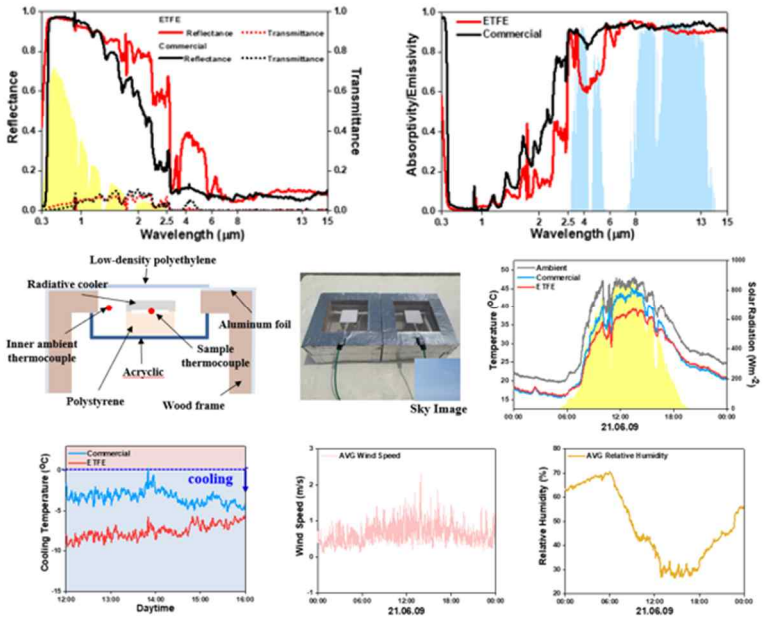

Figure 2. Optical properties of radiative cooling material and outdoor measurement chamber and result of measurement

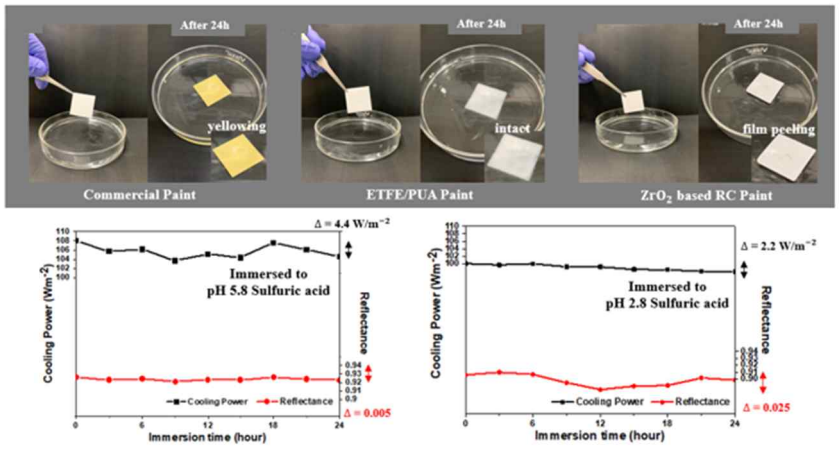

Figure 3. Chemical test data of ETFE containing radiative cooling material and control group of samples

Affordable and effective method for measuring key parameters of micro and nanostructured triboelectric energy harvesters

Luca Fachechi [a], Vincenzo Mariano Mastronardi [b,a], Laura Blasi [c,a], Gaia de Marzo [a], Massimo De Vittorio [a,b], Maria Teresa Todaro [d,a]

[a] Center for Biomolecular Nanotechnologies, Istituto Italiano di Tecnologia, Arnesano (LE), 73010, Italy
[b] Department of Innovation Engineering, University of Salento, Lecce, 73100, Italy
[c] CNR-IMM Istituto per la Microelettronica ed i Microsistemi, Lecce, 73100, Italy
[d] Istituto di Nanotecnologia Consiglio Nazionale delle Ricerche, Lecce, 73100, Italy
e-mail: luca.fachechi@iit.it

In recent years mechanical energy harvesting has gained attention as a promising method to capture energy from movements and environmental vibrations and to convert it into electrical energy for charging batteries and powering microdevices and autonomous sensors. Energy harvesters based on the triboelectric effect represent a new technology for mechanical-to-electrical energy conversion with several compelling features, including simple structure, lightweight, low cost, biocompatibility, and the possibility to choose the materials in a wide range. The triboelectricity mechanism arises from the periodic physical contact, i.e. compression and friction, between two materials with different electron affinities. By accurately engineering the device structure/architecture, these charges can be effectively harvested and extracted into an external circuit. Recently, thanks to the nanotechnology advances, significant efforts have been made to improve the performances of triboelectric harvesters and to maximize the output power obtained from triboelectrification. As the charge density on the triboelectric layers has a significant impact on the output of these devices, several techniques have been explored for micro and nanostructuring the involved materials [1], demonstrating that surface modification positively affects their performances. This has increased further the research interest on this topic. However the analysis of the key figures of merit of this class of devices, i.e. open circuit voltage, short circuit current and power transfer behavior versus external loads, is not straightforward. In fact these devices usually present a high internal impedance, high voltages and low output currents [2, 3]. Typically, triboelectric harvesters voltages are measured by a digital oscilloscope, even if the source impedance of these devices is above the input impedance of most of the commercially available oscilloscopes. This results in output signals being strongly attenuated. On the other side, peak short circuit currents of these devices can be as low as a few nA and then they require the exploitation of high gain current-to-voltage converters in order to exceed the detection limit of the oscilloscopes. Another point concerns the current peaks features which are very sharp and then wide bandwidth instrumentation is needed for a correct signal detection. In the literature, short circuit currents measurements are performed by using expensive and bulky commercially available instruments like SR570 low-noise current preamplifier (LNCP) [4] or VersaSTAT 3 potentiostat [5]. Here we propose a measurement method based on a differential amplifier scheme for the inspection of triboelectric energy harvesters. The core of this approach is represented by a cheap electronic circuit implemented on a compact (4×2.8) cm^2 PCB board, able to provide a fast, reliable and accurate analysis of the key figures of merit of this class of devices. Fig. 1 shows the built-up measurement setup consisting of an actuator working in vertical contact-separation mode, driven by a function generator. The actuator is able to provide forces in the 1 N-10 N range, calibrated by using commercially available force-sensing resistors. The triboelectric device under test is connected to a digital oscilloscope by means of the developed circuit for either voltage or current measurements.

Triboelectric energy harvesters based on thin films of carboxymethyl cellulose (CMC) porous aerogels and poly(dimethyl siloxane) (PDMS) have been fabricated. A device representative image and its schematic structure is reported in Fig. 1. These devices have been analyzed by exploiting the proposed measurement method, as reported in Fig. 2. Fig. 2a and 2b show the device output open circuit voltage and the short circuit current, respectively. Experimental results in terms of short circuit current have been compared with those obtained by using a commercial low noise current amplifier. Fig. 2c and 2d report a zoomed view of the current peaks acquired on short time scale, with the implemented experimental setup and by using a commercial low noise current preamplifier (DLPCA-200), respectively. This approach represents a rapid and accurate method for analysis and comparison of triboelectric devices with different characteristics allowing significant developments and applications in this research field.

[1] Y.J. Zu et al., Adv. Mat. Technologies 6(3) (2021) 2000916.
[2] R. Walden et al. Chemical Engineering Journal Advances 9 (2022), 100237.
[3] S. Lu et al., Nano Energy 87 (2021) 106137.
[4] H. J. J. Hwang, Micromachines 9(12) (2018).
[5] Q. Zhang, *Adv. Func. Materials* 28 (2018) 1706365.

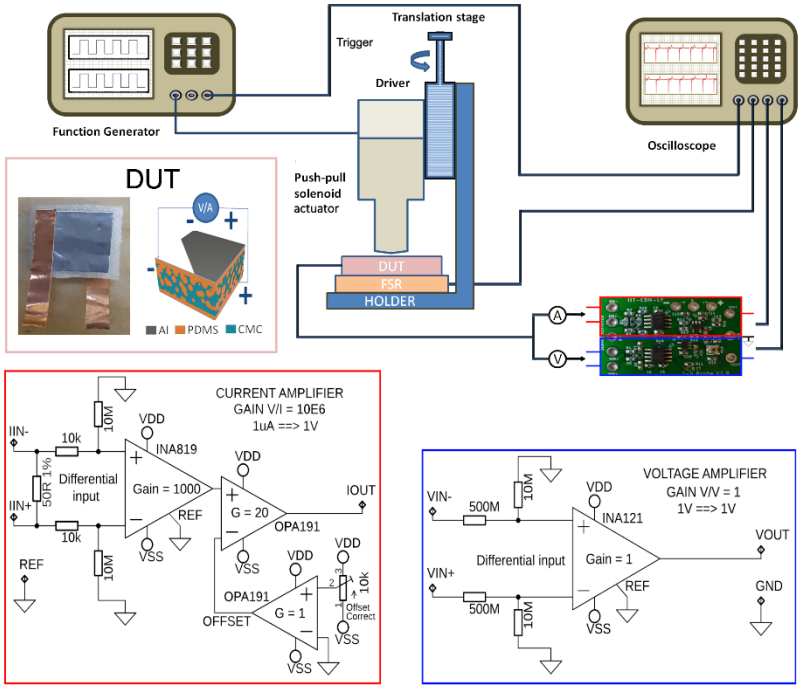

Figure 1. Measurement setup with highlighted the simplified schematic of the current (red) and voltage (blue) circuits and the fabricated triboelectric energy harvester under test.

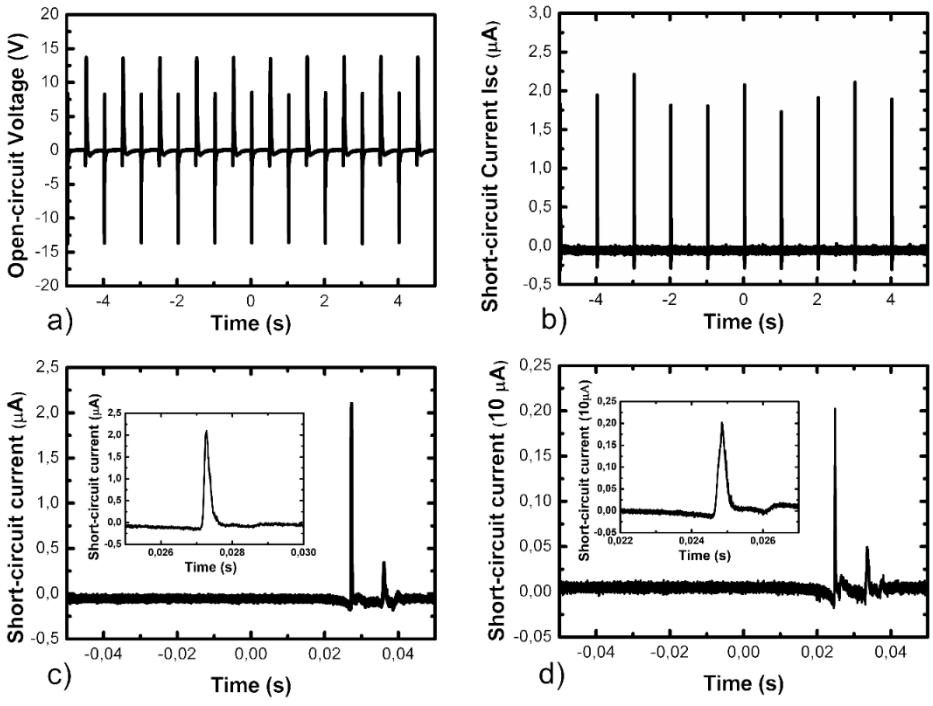

Figure 2. Open circuit voltage a) and short-circuit current b) acquired by the developed circuit; magnified views of short circuit currents acquired by the developed circuit c) and by the commercial low noise current amplifier d).

Improvement of Mechanical/Electrical Properties of Nano-Metal Film for Neural Electrode with Curing Rate Adjustment of Photosensitive Polyimide

HyungDal Park [a†], Seonho Seok [b*], Jinseok Kim [a*]

[a] Center for Bionics, Korea Institute of Science and Technology, 02792 Seoul, Republic of Korea
[b] Center for Nanoscience and Nanotechnology (C2N), University-Paris-Saclay, 91400 Orsay, France
e-mail: seonho.seok@u-psud.fr, jinseok@kist.re.kr

Recently, research on Electroceuticals has been actively conducted as a new treatment technology for intractable chronic diseases, and one of the main technologies that make up Electroceuticals is the neural interfaces. Basically, neural interfaces require high safety and reliability because body implantation is inevitable. In terms of safety, neural interfaces are fabricated based on flexible polymer-based materials to minimize mechanical mismatch with nerves or tissues, and polyimide is used as a representative material (Fig. 1(a)) [1]. It is sufficient to secure safety in the body compared to rigid or brittle materials just by configuring the main components of the neural interfaces with flexible materials. Concerning the reliability, it is demanded at first to improve the adhesion and electrical characteristics of the metal thin film deposited on the polyimide. For these purposes, it is common to approach by increasing surface roughness by attaching additional materials such as nanoparticles on deposited metal thin film or surface treatment method of fully cured polyimide [2, 3]. However, as a result, there is a limit to characteristic retention period after the improvement of the adhesion with the metal thin film and the electrical properties. Accordingly, this paper presents a way to improve the mechanical/electrical properties of metal thin films by adjusting process steps and the curing conditions of PSPI (Photosensitive Polyimide), which is frequently used to implement flexible neural interfaces.

For experimental verification, samples composed of PSPI and Au thin films have been fabricated using the MEMS process as follow; a 5 μm thick PSPI pattern was formed on a piranha cleaned silicon wafer, deposited Au 3000Å, and then a PR mask was formed for a dry etching mask, and the same shapes of Au layer as PSPI by dry etching with ICP-RIE were formed. The 1st PSPI sample was fully cured at 300°C for 1 hour before Au deposition, and the 2nd and 3rd PSPI samples were partially cured at 200°C for 20 minutes and then completed Au patterning. Thereafter, the 2nd sample has undergone a surface treatment with asher after partial curing and the 3rd sample has been subjected to additional PSPI full curing. The fabrication result is shown in Fig. 1 (b).

As shown in Figure 2, SEM photography and EDS measurements were conducted to evaluate the surface characteristics depending on PSPI curing conditions, and it was clearly confirmed that the roughness of the Au surface changed whether the PSPI was fully cured before Au deposition. In addition, after Au patterning, it was found that grain boundaries were formed on the surface of Au in a sample without PSPI full curing process. Also, through the EDS measurement, it was confirmed that the deformation of the Au surface or the redeposition of other materials did not occur.

Peel-off experiments using Scotch tape were conducted to evaluate the adhesion force of the Au thin film to PSPI. The Au thin film adhesion of the sample that underwent PSPI full curing process after Au patterning increased significantly as shown in Fig. 3(a). Note that the gold electrode was not debonded from the PSPI substrate but the tape is detatched from the gold electrode and thus the measured force is the maximum value of the scotch tape test. In addition, through the sheet resistance measurement of each sample, it was confirmed that it had a lower resistance and a smaller standard deviation under full curing after partial curing, as shown in Figure 3(b). As a result, we have improved the mechanical/electrical properties of nano-thick gold thin film by relativizing partial curing and full curing process with the time of depositing Au on PSPI. Based on these results, we plan to conduct further research on securing safety and stability through preclinical verification experiments.

[1] Christopher J. Bettinger, et al., "Recent advances in neural interfaces—Materials chemistry to clinical translation.", MRS bulletin 45.8 (2020) 655-668.
[2] Marco Cen-Puc, et al., "An assessment of surface treatments for adhesion of polyimide thin films.", Polymers 13.12 (2021) 1955.
[3] Jessamyn A. Fairfield, "Nanostructured materials for neural electrical interfaces.", Advanced Functional Materials 28.12 (2018) 1701145.

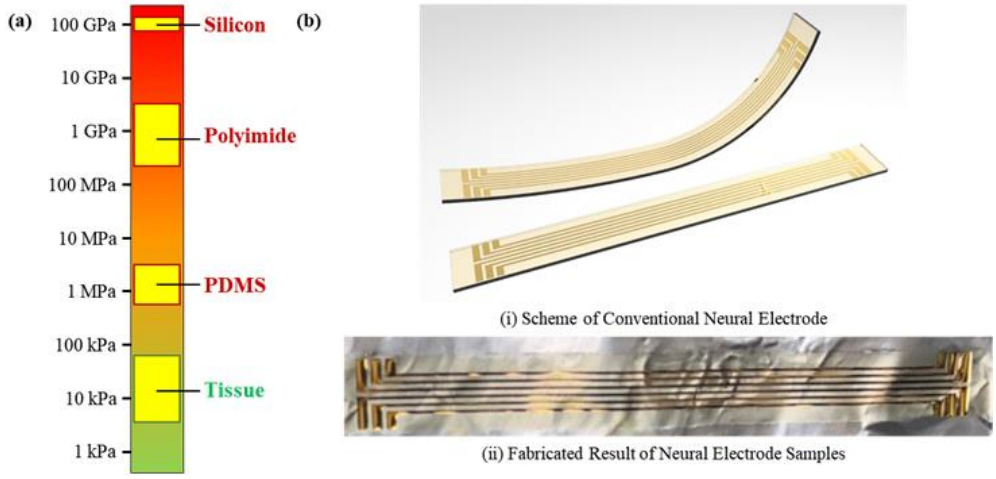

Figure 1. (a) Neural interface main material type and stiffness distribution, (b) Scheme and fabricated result of conventional neural electrode.

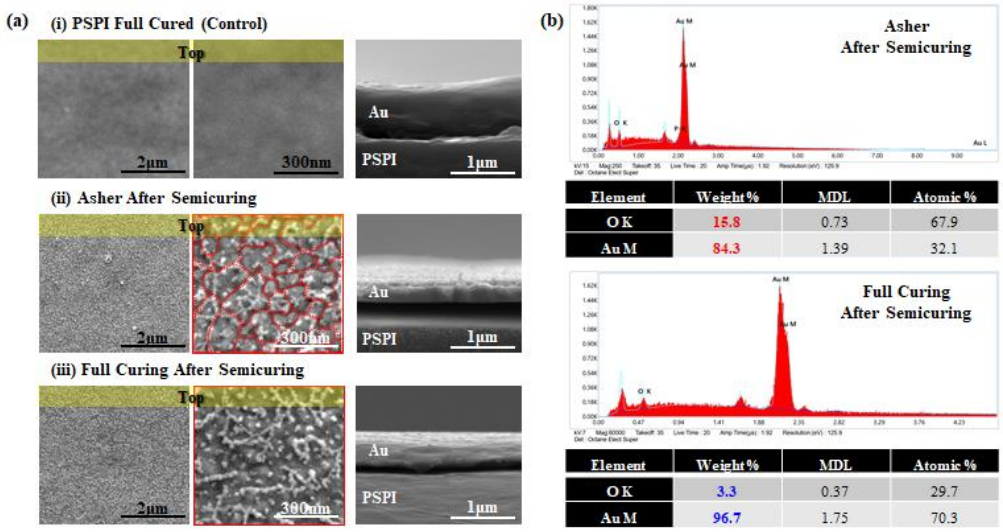

Figure 2. Fabrication results by PSPI curing conditions. (a) SEM images; (i) Basic PSPI full curing condition sample; (ii) After Au patterning, Asher treatment sample; (iii) After Au patterning, PSPI full curing sample, (b) EDS results of two different PSPI curing conditions.

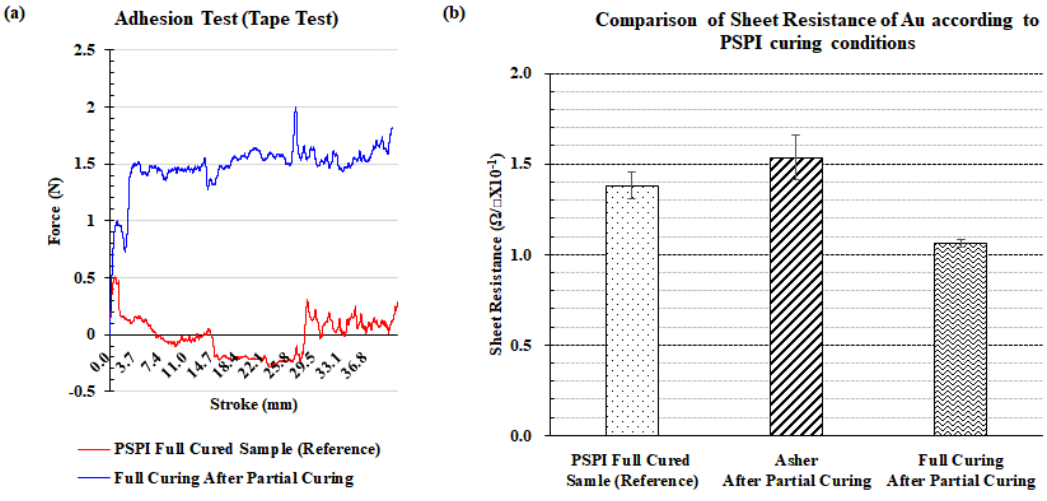

Figure 3. Adhesion and sheet resistance valuation results by PSPI curing conditions. (a) adhesion between PSPI and Au with peel off test, (b) Sheet resistance measurements.

Eco-friendly transparent silk fibroin radiative cooling film for thermal management of optoelectronics

Ching-Wen Hwang [a], Yu-Hsuan Chen [a], Dehui Wan [a]*

[a] Institute of Biomedical Engineering, National Tsing Hua University, Hsinchu, 300, Taiwan
e-mail: dhwan@mx.nthu.edu.tw

Heat is a main element that influences the efficiency of electronic devices; for example, greater than 55% of electronic device failures have been caused by high temperatures. Especially, for optoelectronic devices, the heat generated in the process of converting light to electrical energy, or the reverse energy conversion, significantly decreases the efficiency. These heat issues are even serious under intense sunlight. Therefore, there is much room for improvement in the thermal management of electronic devices. Transparent radiative cooling as a passive cooling strategy that no extra energy is required during cooling processes with practical applications and aesthetic appeal has received greater attention recently. However, the complexity of manufacturing processes and the use of non-eco-friendly polymers remain latent problems.[1]

In this study, we developed natural transparent silk radiative cooling (TSRC) films that can be coated readily onto optoelectronic devices. A schematic representation of our approach for the transformation of visibly opaque silk cocoons into TSRC films for passive cooling of optoelectronics (e.g., smartphones and solar panels) is shown in **Fig. 1**. During the regenerated process, the fibrous morphology and the secondary structure of the silk fibroin protein are disrupted. However, the molecular structure remains, thereby ensuring high broadband emissivity in the MIR region. We used optical photos, scanning electron microscopy (SEM) and atomic force microscopy (AFM) to investigate the typical appearances and morphologies of silk cocoons and TSRC films (**Fig. 2**). For a silk cocoon (**Fig. 2a**), we observed a compact fibrous structure (**Fig. 2b, c**). In contrast, the regenerated TSRC film was visibly transparent (**Fig. 2d**). **Fig. 2e, f** further confirm the presence of a homogeneous, flat TSRC film, without any noticeable fibrous or porous structures. Next, we recorded the spectra of a silk cocoon and TSRC films having various thicknesses to examine the optical properties of the TSRC films compared with a cocoon (**Fig. 3**). In **Fig. 3a**, the silk cocoon displayed high average VIS reflectance, up to 0.76, due to strong scattering at the air–fiber interfaces. In contrast, the UV–VIS–NIR reflectance of the TSRC films decreased sharply to only 0.07, originating from the flat interfaces between the TSRC films and the air. **Fig. 3b** reveals that, compared with the low transparency of the cocoon, the average transmittances of the 8-μm-thick TSRC film reached 0.91 in the VIS region (0.4–0.8 μm) and 0.90 in the range of operating wavelengths of Si-based solar panels (0.3–1.1 μm), matching the high-transparency requirements for optoelectronic devices. More importantly, as shown in **Fig. 3c**, the MIR emittance grew upon increasing the film thickness, which contributed the radiative heat dissipation. Nevertheless, the absorptances in the UV and NIR bands also increased slightly upon increasing the thickness, potentially resulting in additional solar absorption. Therefore, we further obtained the optimal TSRC film theoretically (**Fig. 4**). In **Fig. 4a**, T_{TSRC} and T_{amb} are the surface temperature of the TSRC film and the ambient air temperature, respectively; $P_{cooling}$ is the net cooling power; P_{rad} is the total radiated power of the TSRC film; $P_{atm}(T_{amb})$ is the incident absorbed power from the atmospheric radiatio; P_{sun} is the incident solar power; and $P_{cond+conv}$ is the cooling power lost through conduction and convection. In other words, P_{rad} is the positive factor, and both P_{sun} and P_{atm} are negative factors of the net cooling power. The overall cooling capacity and the optimal thickness could be determined by finding the maximal $P_{cooling}$ and minimal T_{equ} based on the UV–VIS–NIR and MIR spectra (**Fig. 4b**). We also performed theoretical calculations of the cooling power and temperature reduction at various ambient temperatures to imitate the effects of different working conditions (e.g., seasons, day/night, and heat interference from other equipment) of electronic devices (**Fig. 4c**). Afterwards, we experimentally examined the cooling performance of the films on electronic devices under sunlight. For example, the TSRC film provided a remarkable temperature drop of 14 °C (**Fig. 5a**) for a solar panel with an improvement in the photoelectronic conversion efficiency (ca. 7%, **Fig. 5b**). The cooling performance of the TSRC film on a smartphone will be reported in the conference.

[1] K. W. Lee et al., Adv. Funct. Mater. 32 (2021) 2105882.

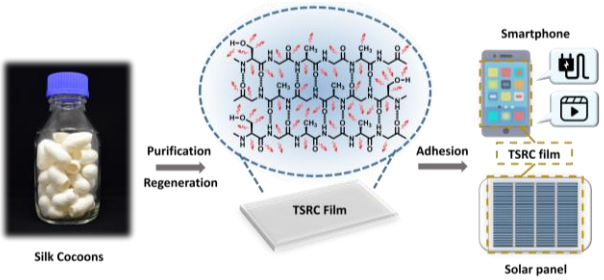

Figure 1. Schematic representation of the transformation of opaque cocoons into a eco-friendly transparent silk radiative cooling film and its application to the radiative cooling of electronic devices.

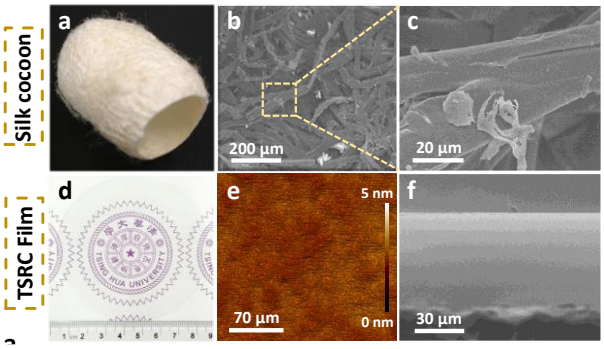

Figure 2. Appearance and morphology of TSRC films. (a-c) (a) Photograph of a cocoon and SEM images of (b) the fibrous structure and (c) a single fibril of a cocoon. (d-f) (d) Photograph, (e) top-view AFM image, and (f) cross-sectional SEM image of the TSRC film.

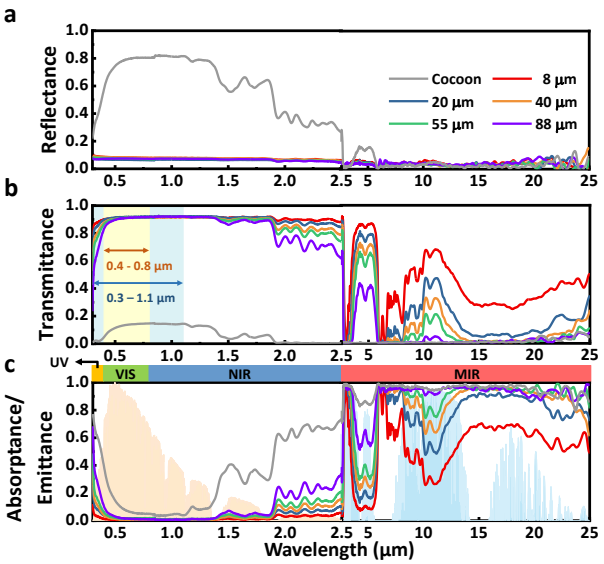

Figure 3. Optical performance of TSRC films. (a) Reflectance, (b) transmittance, and (c) absorptance/emittance spectra of a cocoon and TSRC films, recorded over the UV (0.3–0.4 μm), VIS (0.4–0.8 μm), NIR (0.8–2.5 μm), and MIR (2.5–25 μm) regions.

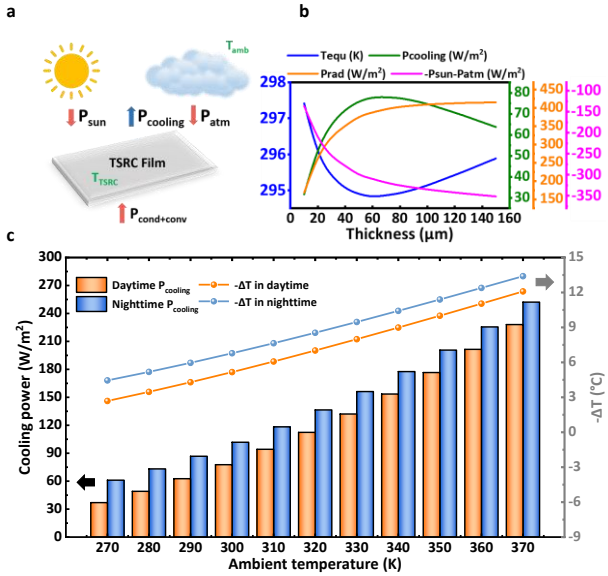

Figure 4. Theoretical cooling performance of the TSRC film. (a) Schematic representation of the parameters within $P_{cooling}$ of the TSRC film. (b) Values of the parameters related to the cooling performance of the TSRC film. (c) Cooling power and -ΔT of TSRC film, calculated under different ambient temperatures, where the -ΔT = T_{amb} - T_{TSRC}.

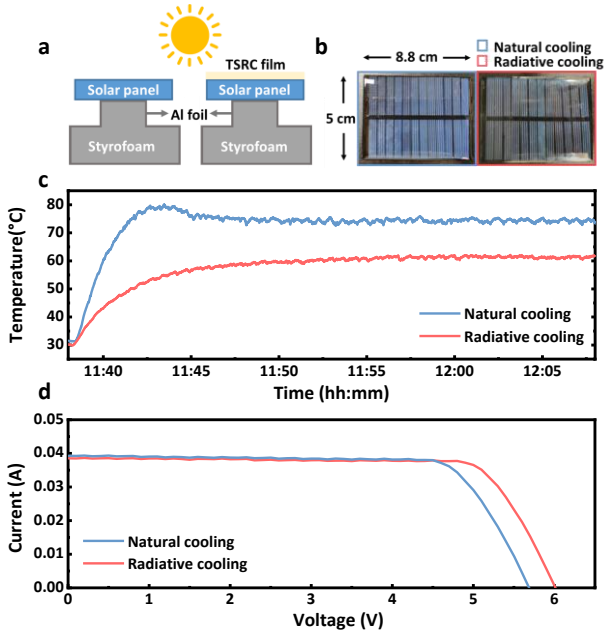

Figure 5. Cooling performance of the TSRC film on a polycrystalline Si solar panel. (a) Schematic representation of the experimental setu. (b) Photographs of the solar panel with (radiative cooling sample, red box) and without (natural cooling sample, red box) a TSRC film. (c, d) (c) Thermal measurement and (d) current–voltage curves of both samples.

Effects of copper surface roughness on inkjet printing of PCB resist ink

Kwon-Yong Shin, Sang-Ho Lee

Korea Institute of Industrial Technology, Ansan city, 15588, Korea
e-mail: sholee7@kitech.re.kr

The inkjet printing process is being considered as an alternative to dry film-based photolithography in the printed circuit board (PCB) manufacturing industry. The advantage of inkjet printing is that it is an alternative process, greatly reducing material waste as compared to a traditional lithographic process. Photomasks are eliminated along with associated process costs and storage requirements. Also, the downstream developing process step is also eliminated, which can reduce water, energy, and waste treatment processes. Recently, several solder resist inks and etch resist inks have been developed and commercialized for PCB production.

Two types of copper foils are commonly used in PCB manufacturing: Electrodeposited and Rolled-annealed copper. Generally, copper foil surface is etched to be rougher to improve adhesion when laminated. On high-speed PCBs above 1GHz, rougher copper surface increases insertion loss, and the resistance slows down the signals. The average surface roughness of copper foils was ranged from ~ 1 to ~ 8 ㎛. It is an important study to investigate the uniform inkjet printing quality on the various copper surface roughness to apply the resist inks to PCB production [1-3].

In this study, we investigated the effects of copper surface roughness on inkjet printing of PCB resist inks. Three copper foils with different surface roughness and a solder resist ink (DiPaMat SM G01, AGFA) were prepared for inkjet printing. The center-line average roughness (Ra) and peak-to-valley roughness (Rp-v) of the three different copper substrates were 0.084, 0.745, 0.561 ㎛ and 3.551, 1.317, 9.323 ㎛, respectively. The substrate surface was treated using O_2 plasma system to obtain a hydrophilic surface before printing process. The surface energy of the three different copper substrates were 49.8, 55.6, 55.8 mJ/m2, respectively, after O2 plasma surface treatment for 30 seconds. Finally, to test the uniformity of the resist thin film coating, the solder resist ink was printed in a 3 × 3 rectangular patterns with a width of 3 mm and a length of 10 mm on a 10 × 10 mm2 copper foil substrate. The deposited resist ink showed different spread on the surface morphology and roughness of the copper foils, which affects the printing quality of the solder resist pattern. The printed solder resist ink pattern shows irregular edge profile and non-uniform thickness by increase of the surface roughness. For the copper foil of the lowest surface roughness, the average thickness and standard deviation of the printed insulation thin film was 6.16 ± 0.68 ㎛ and the thickness uniformity (CV) was 11.0

[1] S.P. Morgan, Effect of surface roughness on eddy current losses at microwave frequencies, J. Applied Physics, p. 352, v. 20, 1949.
[2] John A. Marshall, Measuring Copper Surface Roughness for High Speed Applications, IPC, 2015.
[3] W. Li and D. Y. Li, On the correlation between surface roughness and work function in copper, J. Chemical Physics, 122, 064708, 2005.

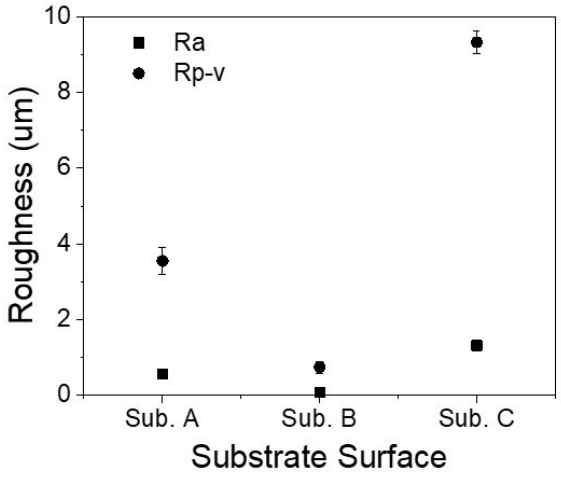

Figure 1. Surface roughness (Ra and Rp-v) of three copper foil.

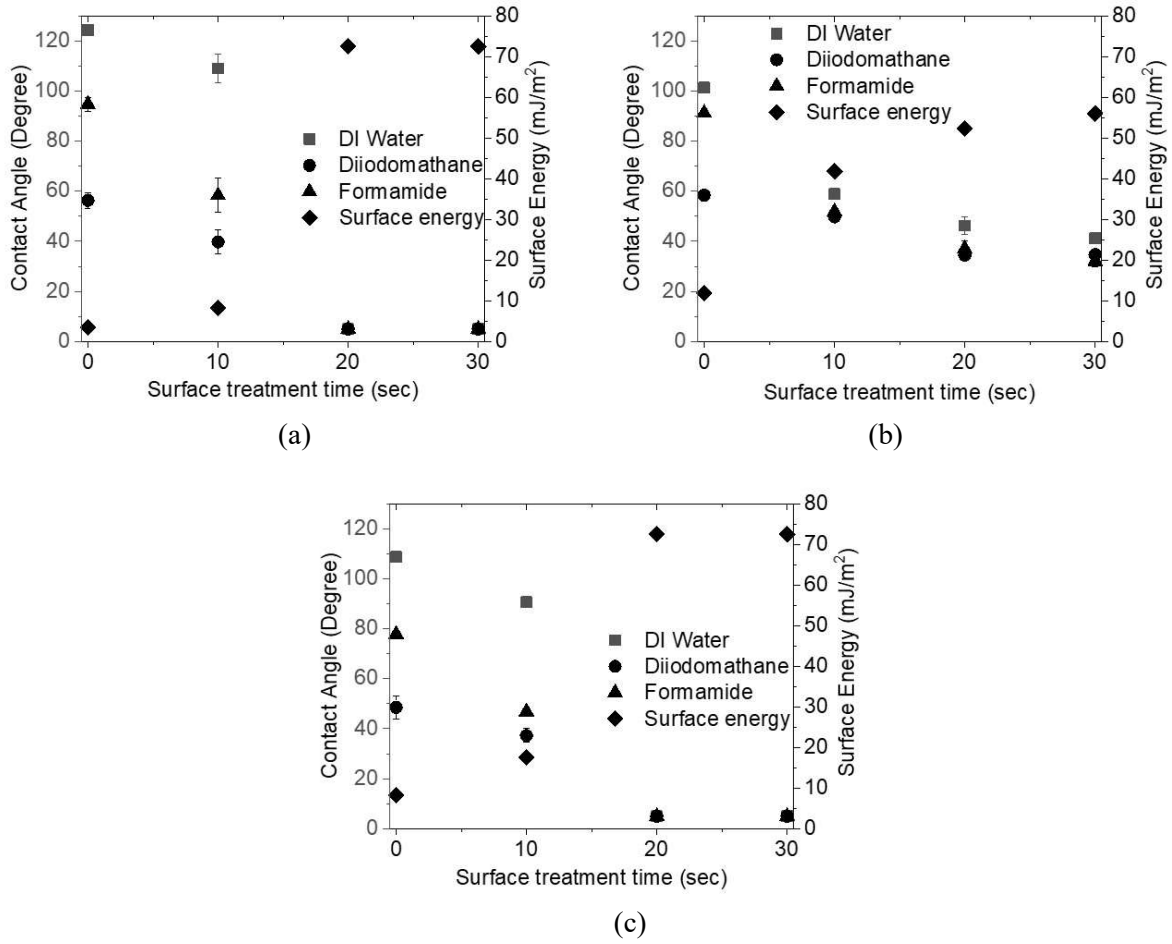

Figure 2. Contact angle and surface energy change according to the substrate treatment time with O_2 plasma system: (a) Sub. A, (b) Sub. B, (c) Sub. C.

On-chip synthesis of Ag nanoparticles assisted by resonating microwave heating using a post-wall waveguide

Kaito Fujitani [a], Hiroshi Nakamura [b], Akinobu Yamaguchi [a], Mitsuyoshi Kishihara [b], Yuichi Utsumi [b]

[a] University of Hyogo; 3-1-2 Koto, Kamigori-cho, Ako-gun, Hyogo, 678-1205, Japan
[b] Okayama Prefectural University; 111 Kuboki, Soja-shi, Okayama, 719-1197, Japan
e-mail: kit1129@lasti.u-hyogo.ac.jp

Chemical synthesis using microwave heating has been widely studied and applied in various fields owing to its high reaction speeds and yields. However, it is difficult to obtain multiple sequential and combinatorial syntheses with a small amount of source reagents, because the reaction fields must be isolated by metal plates. To solve these problems, one of the candidates is the application of a lab-on-a-chip or microreactor system. Unfortunately, there are few reports which can achieve chemical synthesis using microwave-microfluidics consisting of microwave heating structures combined with microfluidics due to inefficient microwave heating efficiency [1]. In this study, we demonstrate on-chip Ag nanoparticles by microwave-induced reaction in a microchannel inside a post-wall waveguide designed to confine 24.125 GHz microwave radiation. In particular, this device's heating efficiency was increased by microwave heating effect for adapting various microwave chemical syntheses. In addition, we have investigated this device's characteristics.

To consist of the microwave system which can achieve high microwave heating efficiency in a microchannel coupled with a post-wall waveguide and easy integration with other chemical operations, dimethylpolysiloxane (PDMS) was used as the structural material due to its high formability, high chemical stability, and visible light transmission. Microwave heating efficiency was increased by adjusting the waveguide length and achieving a resonance frequency of 24 GHz. In addition, it is sandwiched between an ITO sputtered glass and a brass sheet to form a waveguide. Using these materials, reaction monitoring during microwave irradiation becomes possible. A temperature rise simulation using COMSOL Multiphysics, frequency characteristics evaluation, and temperature measurement evaluated the prototyped device's performance. In addition, to demonstrate continuous on-chip synthesis of Ag nanoparticles by microwave heating using this microwave system, we prepared a mixed solution of 0.1 mL of 0.1M $AgNO_3$aq, 1 w/v% of polyvinyl pyridine, and 5.0 mL of ethanol. The flow rate was controlled at 0.7 μL/min.

Figure 1 shows the diagram of the designed microwave microfluidics coupled with a post-wall waveguide. A microchannel and the side walls of a post-wall waveguide are formed on two sheets of PDMS fabricated by a 3D printer (Fig. 1(a)). In addition, the post-wall waveguide is formed by sandwiching the dielectric material from the top and bottom as shown in Fig 1(b). As a result of the temperature distribution simulation when the microchannel is filled with water, the thermal energy locally heats the inside of a microchannel (Fig. 1(c)). Figure 2 shows the experimental setup for microwave irradiation with an input power of 4.0 W. 24.125 GHz microwave emitted from the Gunn oscillator is amplified by a power amplifier and emitted to the microchip with an output of 4 W. Also, the microwave reflected to the amplifier is blocked by an isolator installed between the amplifier output and the post-wall waveguide. As a result of water temperature measurement using a fiber-optic thermometer, the temperature rose to more than 94 °C. This result is about 12 °C higher than that of a microchip with non-resonant structures [2,3]. Using this device, we have synthesized Ag nanoparticles by resonating microwave heating. Figure 3(a) shows the absorbance spectra of Ag nanoparticles when the flow rate is controlled at 0.7 μL/min by the syringe pump and microwave irradiation with an input power of 4.0 W. The absorbance peak of Ag nanoparticles is observed at 401 nm. This result shows the range of particle size is 20 nm ± 10 nm [4]. In addition, as the result of dynamic light scattering, a scattering intensity peak is observed around a particle diameter of 19 nm (Fig. 3(b)). This result is consistent with the particle distribution obtained by the absorbance measurements. Not only the precision synthesis of nanoparticles but also the high efficiency and automated chemical synthesis combined with multiple chemical unit operations are expected to be substantialized using this device.

REFERENCES

[1] L. Jasinka et al, Sensors, 21, 5 (2021) 1710.
[2] K. Fujitani, et al, Sens. Mater., 33,12 (2021) 4399-4408.
[3] R. Tanaka, et al, Jpn. J. Appl. Phys., 62, SG (2023) SG1027.
[4] G.A. Martínez-Castañon, et al, J. Nanopart. Res., 10 (2008) 1343-1348.

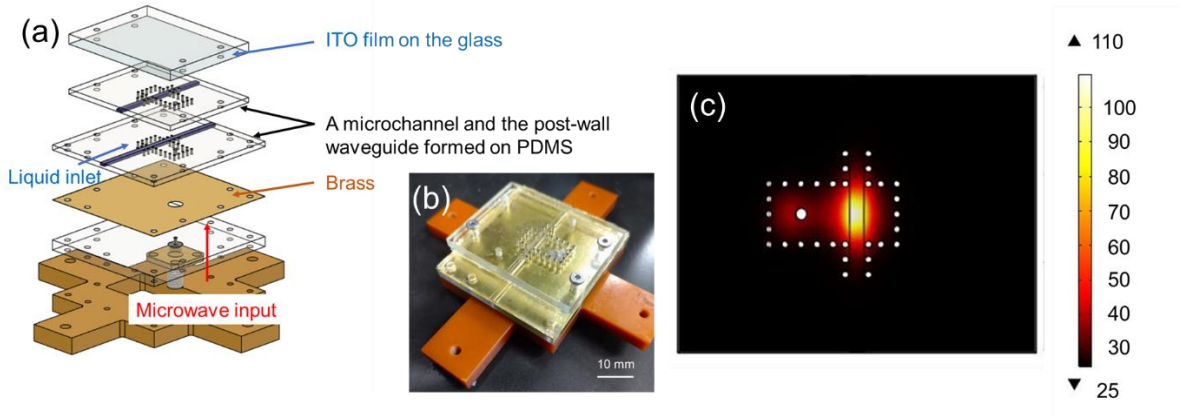

Figure 1. (a) The diagram of the designed microchip coupled with the post-wall waveguide. (b) Photograph of the prototyped microwave microfluidics. (c) Temperature distribution of water during 24.125 GHz microwave irradiation simulated using COMSOL Multiphysics.

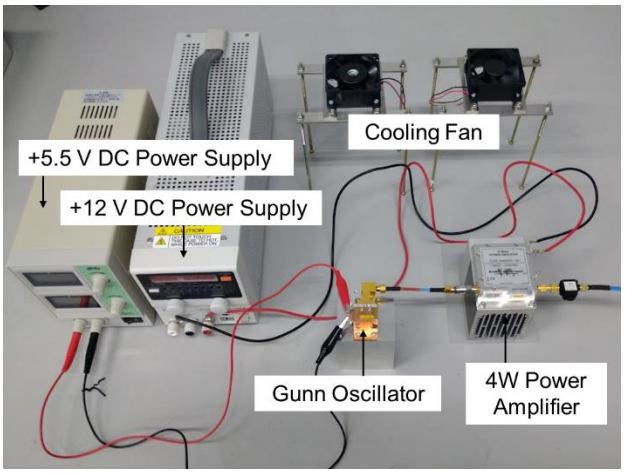

Figure 2. Photograph of experimental setup for microwave irradiation with an input power of 4.0 W.

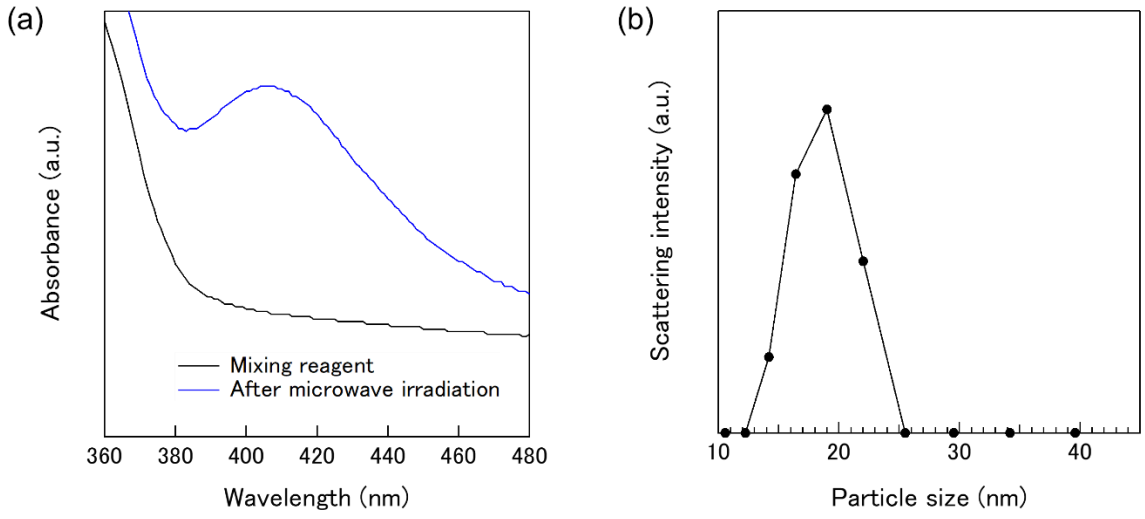

Figure 3. (a) Absorbance spectra and (b) dynamic light scattering measurement for Ag nanoparticles solution synthesized by a mixed solution of 0.1mM of $AgNO_3$, polyvinylpyrrolidone, and ethanol.

Micro/Nano Engineering for Life Sciences / Track4 - Micro/Nano Engineering for Physical and Chemical Applications - Papers

Electrode Design Using Multi-Material Topology Optimization for Accurate Measurement of Trans-Epithelial Electrical Resistance in Organ-on-a-Chip

H. Goda[a], N. Ishida[a], K. Furuta[a], K. Izui[a], F. van Keulen[b], K. Kamei[a], T. Tsuchiya[a], O. Tabata[c], Y. Hirai[a]

[a] Kyoto University, Kyoto, 615-8540, Japan
[b] Delft University of Technology, Delft, 2600 AA, The Netherlands
[c] Kyoto University of Advanced Science, Kyoto, 615-8577, Japan
e-mail: hirai@me.kyoto-u.ac.jp

Trans-epithelial electrical resistance (TEER) measurements are used in organ-on-a-chip (OoC) devices to estimate the barrier properties of a tissue or cell layer. This measurement is performed using impedance spectroscopy based on the four-electrode configuration. Although the measured results are highly dependent on the electrode layout, there is no standard methodology for designing electrodes, that results in incorrect estimation of TEER. We present an electrode design method using a novel topology optimization that enables accurate TEER measurement in microfluidic OoC. Several numerical examples prove the success of maximizing the cell observation area while satisfying the constraint of measurement accuracy, demonstrating its advantage over conventional electrode layouts.

Purpose of the work; Microfluidic OoCs an alternative way to screen drug candidates in a tissue- and organ-level context *in vitro* [1]. TEER is a widely used quantitative method for real-time assessment of tissue viability and barrier function by the measurement of the electrical resistance across the cellular monolayer (Fig. 1). However, due to the lack of proper electrode design method, accurate TEER measurement in OoC remains technically challenging. Furthermore, several numerical simulations performed to compensate the TEER measurements using the calibration curve [2], comparison of TEER results across OoCs is still difficult. Therefore, we propose an electrode design method using topology optimization, which optimizes the distribution of material density of the electrode within a design domain by fulfilling design variables that minimize or maximize an objective function in Fig. 2.

Novelty of the work; For an accurate TEER measurement, we experimentally demonstrated that the electrodes in the cell chamber must be appropriately designed to generate a uniform current density throughout the barrier tissue [3]. Although previous works have achieved the electrode design that generates uniform current density, the current carrying (CC) and voltage pick-up (PU) electrodes for the four-electrode configuration typically hinder the visualizing of the cell (Fig. 1c). The present topology optimization solves this trade-off in electrode design, i.e., achieving both a large observation area and uniform current density. In addition, multi-material topology optimization, which is generally applied to different material properties [4], is employed to optimize both CC and PU electrodes simultaneously. Here these electrodes have the same material property (i.e., electrical conductivity) but serve different purposes in the impedance spectroscopy. To address this technical issue on the existing multi-material topology optimization, we propose a new design domain using a two-layer structure with an inner and outer electrode layer to distinguish between the CC and PU electrodes (Fig. 2).

Results of the work; The topology optimization of the electrode layout for gut-on-a-chip was performed using COMSOL Multiphysics software. In the topology optimized result, the material density θ close to 0 is defined as electrode domains (Fig. 3). The electrode domain overlapped in the inner and outer layers is the CC electrode, and the remaining electrode domain in the inner layer is the PU electrode. Our topology optimization obtained both electrodes layout individually, allowing the visualization of the cell monolayer along the longitudinal axis of the cell chamber owing to the large observation area. Next, comparing the result with the electrode layouts demonstrated in the previous work (i.e., manually designed/optimized layouts) [3], the topology optimized layout has achieved both a larger observation area and a more uniform sensitivity distribution which is equivalent to the uniform current density (Fig. 4). Furthermore, this topology optimization method is applicable to other OoCs, allowing for a large observation area while maintaining the uniform sensitivity distribution (Fig. 5). These results demonstrate the validity of the present topology optimization and will lead to the estimation of a quantitative TEER for easy comparison of different OoC devices or organ models.

[1] D.E. Ingber, Nat. Rev. Cancer **23** (2022) 467-491
[2] O.Y.F. Henry et al., Lab Chip **17** (2017) 2264-2271
[3] T. Miyazaki et al., in Proc. IEEE MEMS 2021, Online (25-29 January, 2021) 411-414
[4] O. Sigmund, Comput. Methods Appl. Mech. Eng. **190** (2001) 6605-6627

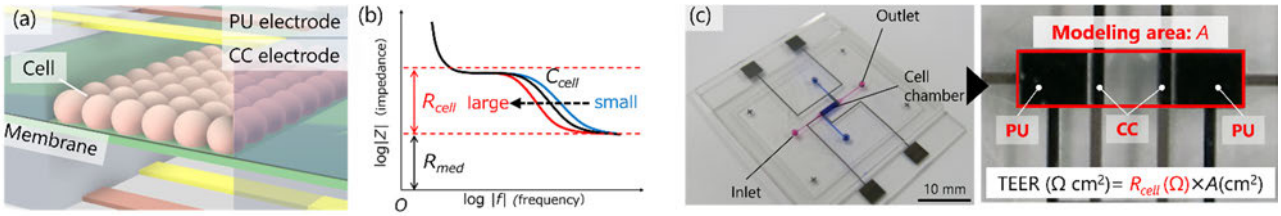

Figure 1. (a) Schematic illustration of TEER measurement in a microfluidic OoC. (b) Typical impedance spectra to estimate TEER. TEER is derived by fitting an equivalent circuit model to spectra. (c) Photograph of the microfluidic OoC used for the optimization. The black area corresponds to the Au-electrodes.

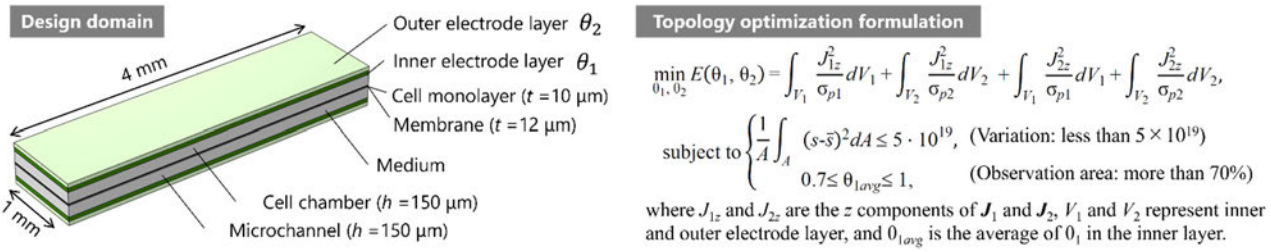

Figure 2. Two-layer structure consisting of an inner and outer electrode layer for the design domain. In this paper, objective function employs energy dissipation $E(\theta_1, \theta_2)$ at each electrode layers. σ_{p1} and σ_{p2} are the conductivity of the inner and outer layer, s is the sensitivity defined by the current density of $\boldsymbol{J}_1$ and $\boldsymbol{J}_2$.

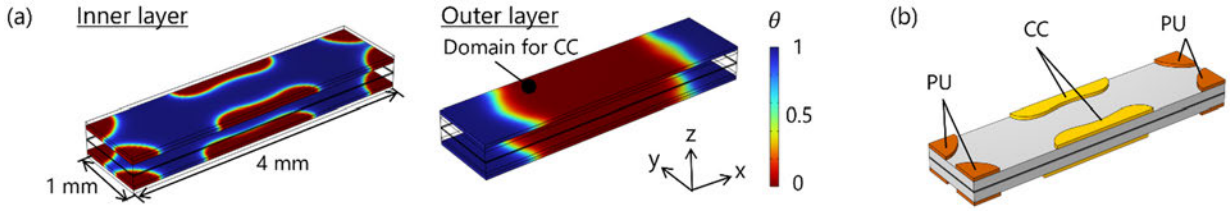

Figure 3. (a) Topology optimized inner and outer layers. (b) Final electrode layout. To determine the final electrode layout, the electrode is defined by the domain with the material density θ less than 0.5.

Pattern	A	B	C (in Fig. 1c)	Optimized
Electrode layout	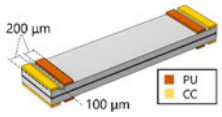	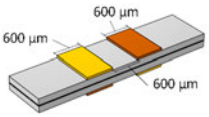	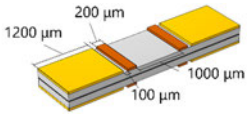	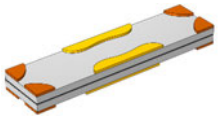
Sensitivity distribution	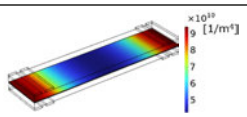	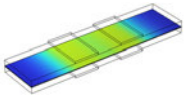	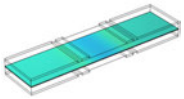	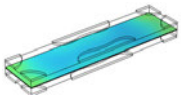
RSD	29%	15%	2.2%	4.7%
Observation area	80%	70%	30%	73%

Figure 4. Comparison of the uniformity of sensitivity distribution and observation area. Uniformity is evaluated by the relative standard deviation (RSD) of sensitivity distribution. Highly accurate TEER result can be obtained when the RSD is less than approximately 5%. Pattern C is the manually optimized layout.

Reference [5]		Reference [6]	
Original (RSD: 1.8%) Observation area: 4.7%	Optimized (RSD: 5%) Observation area: **73%**	Original (RSD: 0.2%) Observation area: 46%	Optimized (RSD: 1.3%) Observation area: **82%**
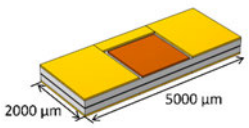	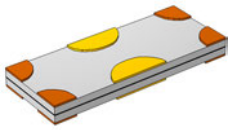	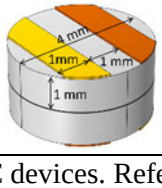	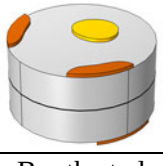

Figure 5. Optimized electrode layout applied to other OoC devices. References: [5] R. Booth et al., Lab Chip **12** (2012) 1784-1792, [6] P.-H. Yang et al., Chin. J. Anal. Chem. **50** (2022) 97-101.

The dual role of topographical and mechanical cues: a multi-modal platform for *in vitro* mimicking of cardiac microenvironment

Denise Pagliara[a,b], Raffaele Vecchione[b], Paolo Antonio Netti[a,b]

[a] Department of Chemical, Materials and Industrial Production Engineering (DICMaPI), University of Naples "Federico II" (Naples, 80138 Italy)
[b] Italian Institute of Technology (IIT) (Naples, 80125 Italy)
e-mail: denise.pagliara@unina.it

Cardiovascular and heart diseases are globally considered two of the most impacting problems impairing human health. Notably, disfunction of cardiac and vascular systems are yearly responsible for 17.9 million of death, as reported by the World Health Organization [1]. In this view, the development of specific treatments is crucial to limit these increasing numbers. *In vitro* reproduction of cardiac models provides the possibility to study the pathway of gene expression during cell stretching [2] or reproducing the biomechanical microenvironment in decellularized constructs towards a patient-specific *in vitro* modelling [3]. Despite such promising results, an accurate recapitulation of the cardiac tissue requires to grow aligned cell populations, as the cardiac tissue functionality depends on the anisotropy of the myocardial fibre rearrangement. Additionally, the mechanical machinery of the cardiac tissue is strongly affecting the cardiomyocytes activity [4] [5], which is a combination of longitudinal, circumferential and radial components of myocardial tissue deformation field [6]. As a result, simple uniaxial stress is not representative of the cardiomyocytes response in the mechano-sensing processes.

In this perspective, the current work aims to implement a microfluidic device for an efficient introduction of biochemical stimuli, in which a cardiomyocytes culture is ordered in a radial micropattern logic. Then, the native cardiac biomechanical microenvironment is mirrored by introducing a controlled biaxial stimulation to the aligned cardiomyocytes. The platform is a multilayer microfluidic device to merge biochemical and mechanical stimulation. The mechanical unit consists of a deformable membrane placed on top of a hollowed circular ring with a central pillar: here the application of vacuum lowers the membrane in the cavity, while the pillar blocks the vertical displacement, applying a biaxial planar stretch (*Fig. 1a-c*). The deformable area of the membrane is enriched with a radial micropattern (*Fig. 1d*), achieving cell alignment. Well-established techniques of microfabrication are coupled to a new photolithography approach, allowing to directly pattern photoresist on flexible polymethylmethacrylate (PMMA) substrate, facilitating the transfer of the micropattern into the microfluidic device and allowing for the non-trivial alignment to the central pillar (*Fig. 1e*).

Furthermore, the device has been implemented to stimulate a culture of HL-1 rat cardiomyocytes. The radial micropattern induces both HL-1 nuclei and actin fibres alignment (*Fig. 2a-c*). Cell tracking during biaxial stimulation (1h) demonstrates that cells sense the mechanical load applied through the flat deformable substrate, aligning their migration trajectories to the main direction of stimulation (*Fig. 3a-b*). Such trajectories alignment is furtherly improved in the case of cell seeded on patterned substrates (*Fig. 3c*). The response of HL-1 to such mechanical stimulation is additionally characterised by the distribution of cell velocities, which are considerably enhanced after biaxial deformation and even further improved for cell aligned on patterned substrates (*Fig. 3d*). These findings demonstrates that the proposed microfluidic platform can combine both topographic and mechanical signals, which are strong regulators of cardiomyocytes behaviour.

For these reasons, the current work provides a convincing platform to explore the cell-cell and cell-microenvironment interaction in the cardiac tissue, whose first applications pave the way to go deeply in the cardiac physiology and pathology, as well as for drug testing.

[1] World Health Organization, https://www.who.int/health-topics/cardiovascular-diseases#tab=tab_1.
[2] D. Frank *et al.*, Hypertension, 51 (2008) 309-318.
[3] J. Schwan *et al.*, Sci Rep, 6 (2016) 32068.
[4] K. D. Dwyer *et al.*, Bioactive Materials, 6 (2021) 2198-2220.
[5] G. Zhao *et al.*, ACS Appl Bio Mater, 2 (2019) 3508-3519.
[6] B. Bijnens *et al.*, *Fetal Diagnosis and Therapy*, 32 (2012) 5-16.

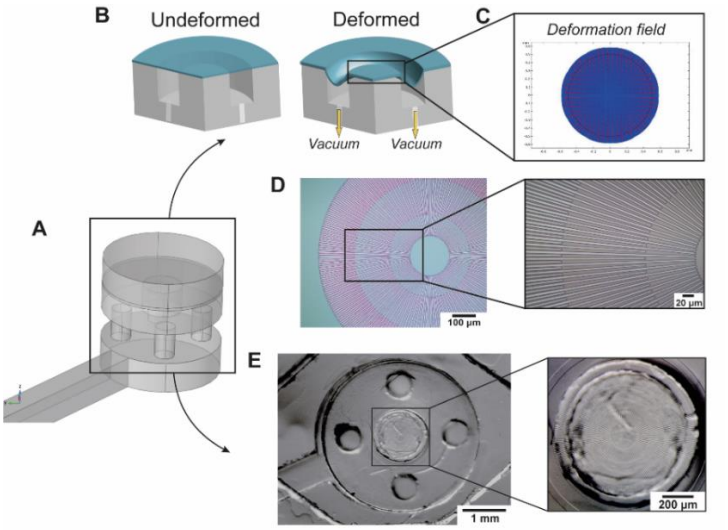

Figure 1. The microfluidic platform logic (A). A section of the device chamber shows how the vacuum induces the mechanical deformation of the flexible membrane (B), while a field of biaxial planar stretch arises on the central pillar (C). The flexible membrane is micro-patterned (D) and integrated in the platform for the mechanical stimulation (E).

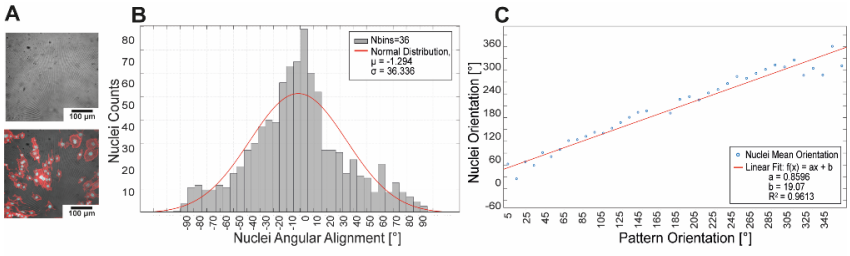

Figure 2. Device-seeded HL-1 cardiomyocytes adhere and align to the micro-pattern, as shown by brightfield and fluorescence images of nuclei (in cyan) and actin (in red) (A). The histogram of nuclei angle variation from the main direction of the micro-pattern demonstrates that cells feel the topographic signal (B). The nuclei orientation is following the pattern orientation, as demonstrated by the data linear fitting (C).

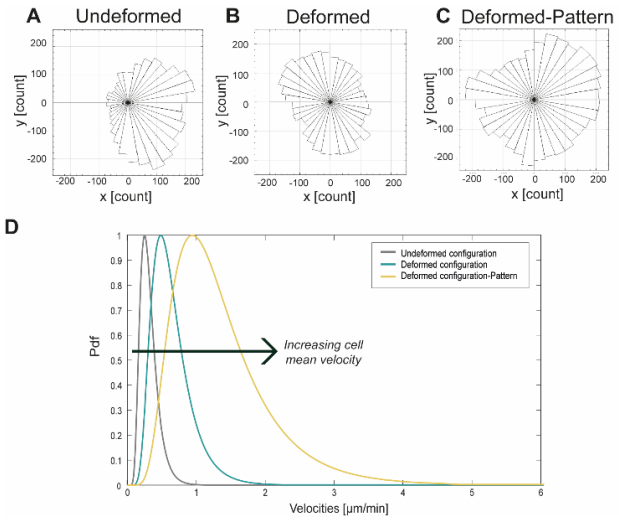

Figure 3. Cells migration tracking over 1 h shows that the cell trajectories rearrange from random to radial configuration when the cells move from undeformed (A) to deformed status (B). The micro-pattern enhances the cell migration alignment to the main direction of deformation (C). Along with trajectories orientation, cell migration velocity is improved after mechanical deformation on the patterned flexible substrate (D).

Focused gold ion beam for the fabrication of sub-100 nm length InGaZnO thin film transistors on flexible substrates

E. Scattolo [a], F. Catania [b], A. Cian [a], N. Münzenrieder [b], and G. Cantarella [c], P. Lugli [b], L. Petti [b], D. Giubertoni [a]

[a] Sensors and Devices Center, Bruno Kessler Foundation, Trento, 38123, Italy
[b] Faculty of Engineering, Free University of Bozen-Bolzano, Bozen-Bolzano, 39100, Italy
[c] Department of Physics, Informatics and Mathematics, University of Modena and Reggio Emilia, Modena, 41125, Italy
e-mail: escattolo@fbk.eu

Abstract

The realization of thin-film electronics on flexible substrates utilizing metal oxide semiconductor, specifically indium-gallium-zinc oxide (IGZO), holds great potential for the advancement of lightweight and flexible systems [1-2]. IGZO devices exhibit a favorable balance between large-area fabrication, low-temperature manufacturing, and electrical performance. However, a limitation in the development of high-speed thin-film devices for data transmission and communication arises from the relatively low carrier mobility of IGZO thin film transistors (TFTs), typically around 10 cm^2/Vs when manufactured at room temperature [3]. To address the need for high-speed IGZO-based thin-film devices on these substrates, various scaling strategies have been employed to produce MOS devices with ultra-thin channel length? [4-6]. To achieve higher resolution, Ga-ion based focused ion beam (FIB) techniques have been utilized to mill a top-metal contacts, resulting in scaling down to a channel length of 160 nm, which currently represents the shortest length achieved in IGZO TFTs [5].

Further reduction in channel length can be accomplished by employing alternative ions in FIB instrumentation. In this research, ultra-scaled IGZO TFTs were fabricated on a free-standing polyimide foil by utilizing Au^+ ions for metal contacts milling, as depicted in Fig.1a. Optimization of the beam parameters was crucial to prevent excessive ion contamination and damage to the underlying IGZO layer [7-8]. The patterning process was performed using an Au^+ beam accelerated at 35 kV, with a beam current of 8.2 pA and an ion fluence of 6000 $\mu C/cm^2$, resulting in a channel length of 78 nm, as illustrated in Fig.1b-c. The reduction in channel length through FIB milling led to a drain current value of 685 µA at a gate-source voltage of 12 V. The high drain current value obtained can be attributed not only to the scaling process but probably also to the implantation of Au ions in the IGZO. Monte Carlo simulations have confirmed that the Au ion contamination contributes to an enhanced IGZO conductivity, resulting in significantly improved carrier mobility of 3.06 $cm^2\ V^{-1}\ s^{-1}$.

Scaling the channel length of IGZO TFTs using Au FIB has demonstrated to be a viable approach for enhancing carrier mobility to a level compatible with data transmission applications. Furthermore, the increase in carrier mobility is not solely due to the scaling of the channel size but also the augmented IGZO conductivity resulting from gold implantation, indicating the multifaceted nature of FIB as a scaling method.

[1] A. Nathan et al, Flexible Electronics, Proc. IEEE 100, 1486–1517 (2012)
[2] F. Catania et al, J. Phys. D: Appl. Phys. 55, 323002 (2022)
[3] H. Yabuta et al, Appl. Phys. Lett. 89 (2006)
[4] N. Münzenrieder, et al, IEEE Trans. Electron Devices 60, 2815–2820 (2013)
[5] N. Münzenrieder et al, Flexible Printed Electron. 5, 015007 (2020)
[6] Petti et al, IEEE Trans. Electron Devices 65, 3796–3802 (2018)
[7] D. Giubertoni et al, MIPRO IEEE, (2020)
[8] E. Scattolo et al, Sensors 23 (2023)

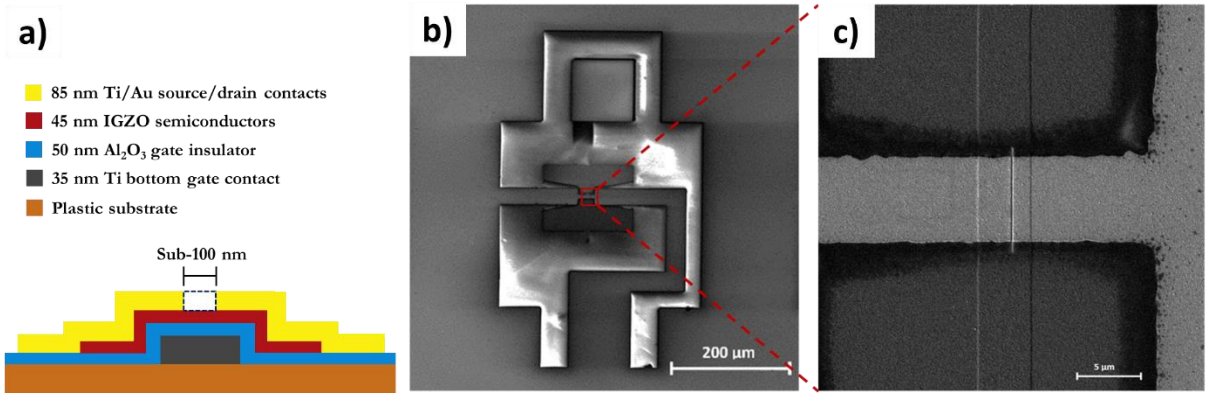

Fig. 1 - Fabrication process and materials used for short-channel IGZO electronics: a) cross-section of the fabricated IGZO thin film transistors (TFTs), as well as top-view SEM image of the fabricated IGZO TFTs (b) and of the patterned channel by Au ion beam (c).

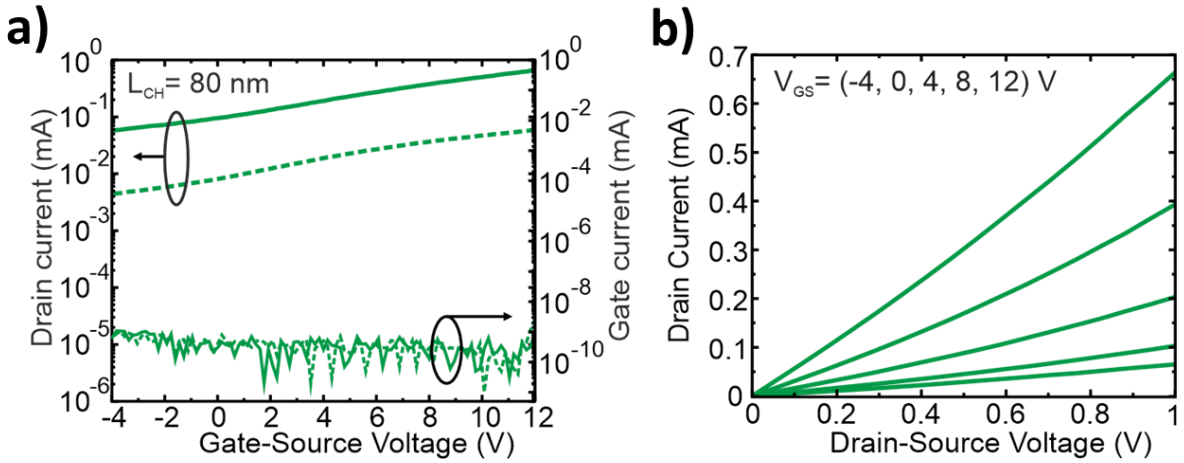

Fig. 2 – Direct current performance of Au- milled TFT. a) transfer characteristic represented by the drain current and gate current as function of the applied gate-source voltage, b) output characteristic represented by drain current at increasing value of gate-source voltage and drain-source voltage.

PEDOT:PSS deposition in OECTs: inkjet printing, aerosol jet printing and spin coating

Giorgia Rinaldi [a], Giuseppe Tarabella [b], Pasquale D'Angelo [b], Simone Marasso [a,b], Matteo Cocuzza [a,b], Fabrizio C. Pirri [a,c], Matteo Parmeggiani [a]

[a] Chilab–Materials and Microsystems Laboratory, Department of Applied Science and Technology (DISAT), Politecnico di Torino, Via Lungo Piazza d'Armi 6, 10034 Turin, Italy
[b] Institute of Materials for Electronics and Magnetism, IMEM-CNR, Parco Area delle Scienze 37/A, 43124 Parma, Italy
[c] Center for Sustainable Future Technologies, Italian Institute of Technology, Via Livorno 60, 10144 Turin, Italy
e-mail: giorgia.rinaldi@polito.it

Nowadays, new functionalities are integrated into everyday objects, creating the need for a multiplicity of different substrates for transistor design and new low-cost fabrication techniques. Silicon technologies require expensive clean-room fabrication processes, which are not compatible with the flexible and plastic substrates employed for applications such as wearable health monitoring. As a result, additive manufacturing techniques have become a major topic of interest due to their ability to reproduce patterns on a wide variety of substrates using different inks. These techniques are fast, easy to use and inexpensive, paving the way to printed electronics [1], [2].
Organic electronics is an emerging field, thanks to the possibility of low-cost fabrication and large area production of organic electronic materials and their tunable electrical properties. Among them, organic mixed ionic-electronic conductors (OMIECs) have been developed for their ability to transduce biological ionic signals, bridging electronic and biological worlds [2]–[4]. In this study, poly(3,4-ethylenedioxythiophene) polystyrene sulfonate (PEDOT:PSS) has been chosen as channel material for OECTs due to its stability, high conductivity and biocompatibility. In addition, it can be deposited by means of low-cost techniques, such as inkjet printing and aerosol jet printing [1], [2].
This work focuses on the comparison of ink-jet printing, aerosol jet printing and spin coating for the deposition of PEDOT:PSS for OECT channels, effectively identifying aerosol jet printing as the method providing the best results. In this study, spin coating is addressed as a reference technique for the process, as it is the most well-established one among those considered [4]. Differently, inkjet printing [2] and aerosol jet printing [1] are discussed as an innovative and promising pathway for the next generation of OECT devices. To the best of our knowledge, this is the first study addressing the comparison among these deposition methods for PEDOT:PSS as a channel material in OECTs.
The OECT devices were fabricated on a Si/SiO_2 substrate using common cleanroom techniques, in particular a two-mask photolithographic process was used for Au/Ti electrodes. They were designed with a W/L ratio of 30 and a channel length of 10 μm; the geometry of the devices is shown in figure 1.
The ink was formulated adding 1% wt of (3-glycidyloxypropyl)trimethoxysilane (GOPS), 5% wt of ethylene glycol and 0.5% wt of 4-dodecylbenzenesulfonic acid (DBSA) to a commercial water-based PEDOT:PSS ink (Clevios 1000). After the ink deposition, the devices have been placed on a hot plate at 120°C for 15 minutes in order to allow the evaporation of the solvent. In addition, a postdeposition treatment by thermal annealing at 150°C for 30 minutes has been applied to the devices.
From the analysis of the results, the best performance seems to be provided by the aerosol jet printed devices. Figures 2 and 3 present respectively the transcharacteristic and output characteristic of the three devices for a period of $0.5\,s$. As shown in figure 2, inkjet-printed devices present the best switching performance, as the OFF current is more than one order of magnitude lower than in the other two devices. However, as shown in figure 3, the aerosol jet printed device shows the highest I_{on}/I_{off} ratio as the maximum ON current is more than 4 times larger in the aerosol jet printed device than in inkjet printed one.

[1] G. Tarabella et al., Flex. Print. Electron. 5 (2020) 014005
[2] G. Mattana et al., Advanced Materials Technologies 2 (2017) 1700063
[3] M. Parmeggiani et al., Micromachines 14 (2023) 460
[4] J. Rivnay et al., Nature Reviews Materials 3 (2018) 17086

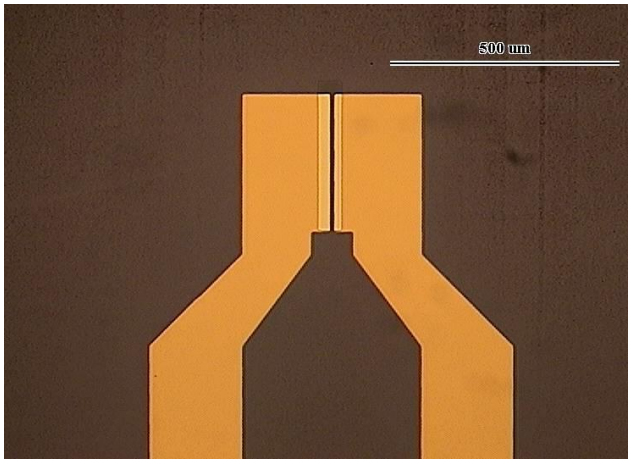

Figure 1: Geometry of the source and drain electrodes

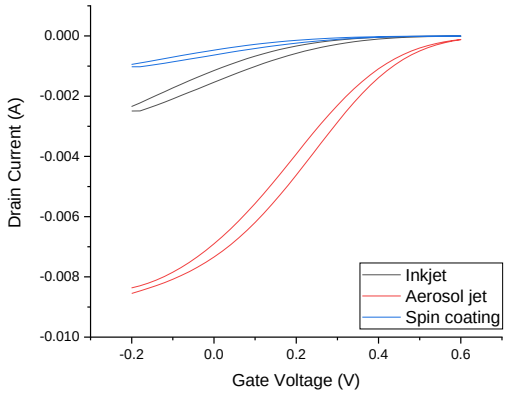

Figure 2: transcharacteristic for a period of 0.5 s

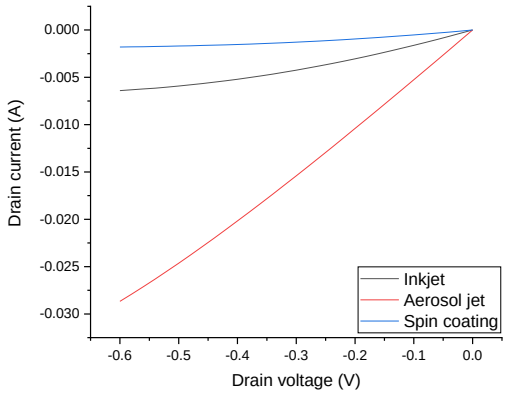

Figure 3: Output characteristic for $V_{gs} = -0.2\ V$ and a period of 0.5 s

Poster Session2.1: Track 2 - Papers

Energy Efficient Coloration of Solar Panels Using Structured Surfaces to Reduce Angular Dependency of Appearance

Oskar Darselius Berg [a], Markus Babin [b], Irina Vyalih [c], Nanna Lysgaard Andersen [b], Morten Madsen [c], Peter Behrensdorff Poulsen [b], Sune Thorsteinsson [b], Jan Stensborg [a]

[a] Stensborg A/S, Risø Huse 50, 4000 Roskilde, Denmark
[b] DTU Risø Campus, Fredriksborgvej 399, 4000 Roskilde, Denmark
[c] Mads Clausen Institute University of Southern Denmark (SDU), Alsion 2, 6400 Sønderborg, Denmark
e-mail: odb@stensborg.com

The worldwide transition to green electricity has brought attraction to the use of photovoltaic panels on buildings, both for building-attached (BAPV) and building-integrated (BIPV) applications. A major obstacle for PV on buildings is the lack of possibilities for aesthetic integration.

During the past years, a variety of colored PV solutions has entered the market and significantly improved the possibilities of architectural integration. Most solutions are based on pigments, leading to power losses between 20-50 % due to light absorption. Distributed Bragg Reflectors (DBR) on the other hand, are used to selectively reflect specific wavelengths has been shown to achieve power losses of less than 10%. This is close to previously established theoretical coloration efficiency limits [1], [2], which have shown that almost all colors can be attained with less than 10% power loss when using two 40 nm wide reflection spectra. It has also been shown that silicon has a close-to-optimal bandgap for the coloration of single-junction solar cells.

A narrow reflection of wavelengths does pose challenges to uniform color appearance. An increased viewing angle will blue-shift the narrow peak to generate different colorations at high, and even moderate angles [3].

An implementation of DBRs has been demonstrated on the inside of the glass coatings with a good color appearance in [3] and has been commercialized e.g. by Swissinso with limited color vision and large angle dependencies in the color appearance. Depositing the DBR on the glass however has disadvantages as large area vacuum deposition machinery is needed, and the producers of PV modules have less flexibility for sizing in the production.

The project ColorFoil aims to solve these issues by stacking using magnetron sputtering thin-film layers onto an index-matched foil, utilizing the aforementioned simple Bragg model. Thereby the sheet optically disappears into the encapsulant of the PV module, while selectively reflecting a narrow collection of wavelengths (see Figure 1). [3] Further, ColorFoil enables custom designs of specific colors, matching conventional colors of the built environment such as “tile red”, “brick yellow” and “forest green”.

Furthermore, the thin-film layers on foil instead of glass allow for the structuring of the foil surface to scatter reflected light. Utilizing the wide range of available structured surfaces created with Stensborg’s Rolling Nanoimprint Lithography (R-NIL) process (see Figure 2), the scattering is able to widen the narrow reflection peak. [4] This generates the perception of angular independent color (wide reflection peak) while maintaining the high efficiency of the solar cell.

For preliminary testing, three different diffuser structures have been fabricated by Stensborg, coated with a thin layer of gold and laminated behind satinated glass, as is common in BIPV. The surface reflections are then measured using an in-plane gonioreflectometer at DTU. [5] Figure 3 shows the bi-directional reflectance distribution function (BRDF) of the different structures for an incidence angle of 15°. As can be seen from the figure, introduction of a diffuser structure on the foil significantly increases diffuse reflections from the samples

Conformal sputtering of DBRS on the structured foil is currently being tested by SDU and will be presented at the conference alongside further measurements of the reflection properties.

[1] G. Peharz and A. Ulm, Renewable Energy 129 (2018) 299-308
[2] J. Halme and P. Mäkinen, Energy & Environmental Science 12 (2019) 1274-1285
[3] B. Bläsi, T. Kroyer, T. Kuhn, and O. Höhn, IEEE J. Photovoltaics 5 (2021) 1305–1311
[4] R. Singh Petersen, J. Stensborg, L. Yde, K. Petersons, MNE (2022)
[5] M. Babin, A. A. Santamaria Lancia, A. Thorseth, and S. Thorsteinsson, Proc. 37th EUPVSEC (2020) 1136-1142

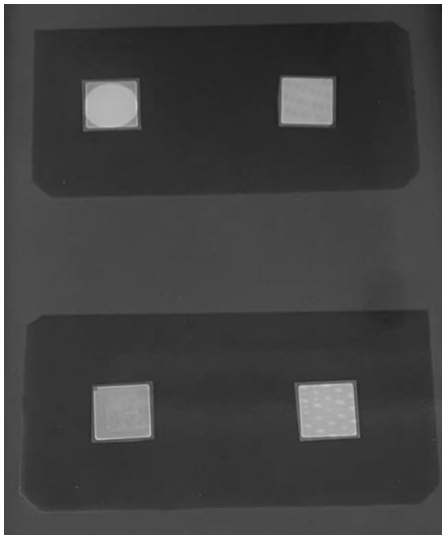

Figure 1. Structured foils from Stensborg with deposited DBR.

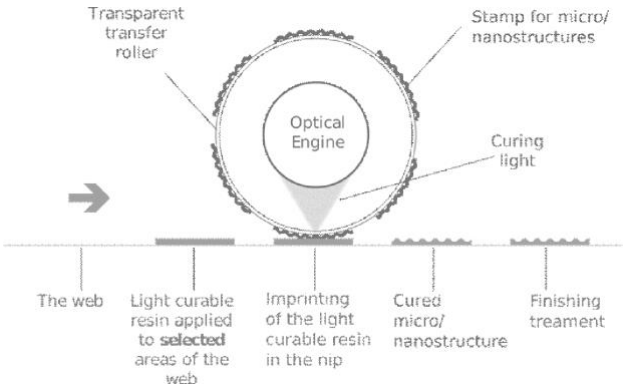

Figure 2. Schematic for a typical flow utilizing the novel optical engine.

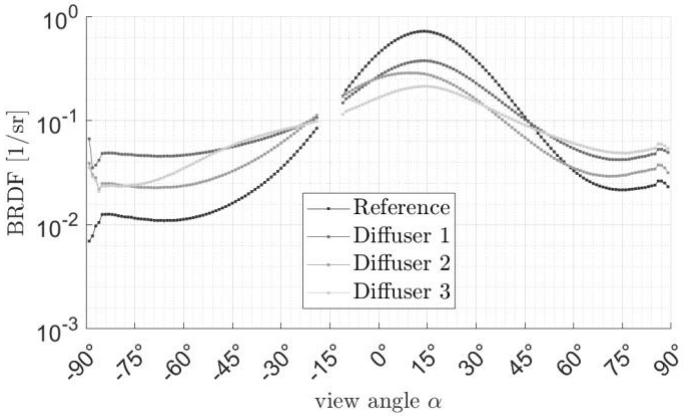

Figure 3. Preliminary results for the BRDF of DBRs sputtered on foils without (left) and with (right) a diffuser structure

Heavy metal ion detection by an impedance sensor based on Platinum nanoparticles/DNAzymes network

E. Aslanidis[1], E. Skotadis[1], G. Tzourmana[1], Chryssi Panagopoulou[1], A. Rapesi[1, 2], G. Tsekenis[2], S. Chatzandroulis[3] and D. Tsoukalas[1]

1 Department of Applied Physics, National Technical University of Athens, 15780 Zografou, Greece
2 Biomedical Research Foundation of the Academy of Athens, Athens, Greece
3 Institute of Nanoscience and Nanotechnology, NCSR Demokritos, Aghia Paraskevi 15341, Attiki, Greece
e-mail: dtsouk@central.ntua.gr

Heavy metal ions, such as Lead (Pb), Chromium (Cr), Cadmium (Cd) etc. present a serious environmental threat when found in soil and water; thus their accurate and fast detection poses a major challenge. Although several detection methods have been proposed in the literature [1], they are both expensive and time consuming. In this work, we investigate the impedance response of a platinum nanoparticle (Pt NPs) network based biosensor featuring two distinctive DNAzymes species of different chemical modification groups (i.e amino and thiol modified), which enable their attachment on the Pt NP layer.

A Pt NPs network sensor has proven to be a very effective platform for several applications while with the incorporation of DNAzymes they can detect heavy metal ions showing good sensitivity by monitoring the sensor's resistance response [2].

The impedance Pt NP sensor fabrication process starts with the formation of two gold interdigitated electrodes (IDE), 50 nm thick, with an electrode gap of 10 μm were formed on oxidized silicon substrates, using conventional photolithography and e-gun evaporation techniques. Pt NPs were then deposited using a modified DC magnetron system; the system allows control over Pt NPs diameter (herein 4 nm) as well as that of surface coverage. In this case, NP surface coverage was 49% which is right below the percolation threshold and results in inter-particle distance of few nm. After the Pt NPs deposition follows the DNAzymes functionalization with two distinctive DNAzymes. DNAzymes are double-stranded DNA engineered to catalyze to single-stranded DNA in the presence of the element to be detected (Figure 1). This change in DNAzymes modifies the overall impedance of the sensors. The bio-sensing devices were characterized by measuring changes in impedance using an HP 4284A precision LCR meter. The applied voltage consisted of 0.5 V DC bias while the oscillation amplitude was 50 mV at frequencies from 500 to 50000 Hz. Characterizing the sensors through impedance can give greater sensitivities due to the binding of DNAzymes onto Pt NPs. As a first step, a buffer solution was drop-casted on top of the bio-sensors. Then, a buffer solution containing a known heavy-metal ion concentration was drop-casted on the sensor, resulting in an increase of device impedance as shown in Figure 2. Figure 3 compares the sensitivity of the two different DNAzymes for varying Pb^{2+} concentrations. Amino modified DNAzymes showcase higher sensitivity when compared to the thiol modified DNAzymes; this can be related to the variations between the two chemical modifications and the quality of their attachment on the NP layer. Thiol modified DNAzymes are immobilized only on the PtNPs while the amino modified DNAzymes are immobilized both on the PtNPs as well as on the free surface of SiO_2. Therefore, in the case of amino modified DNAzymes there are many sites between the PtNPs where the DNAzymes are dense. The consequence of that is that during detection and when catalyzed into single strands, they result in the large increase of impedance. On the other hand, thiol-modified DNAzymes are only immobilized on Pt NPs, resulting in the gaps between PtNPs containing sparse DNAzymes (compared to amino-modified ones) and the change of impedance upon detection is smaller (Figure 3). Both techniques present a linear response range, for maximum concentrations up to 160 nM and 200 nM in the case of thiol and amino modified DNAzymes respectively. The devices also exhibit a low limit of detection (LoD) of 12.5 nM, in agreement with the permitted levels of Pb^{2+} for the EU [3].

This research has been co-financed by the European Regional Development Fund of the European Union and Greek national funds through the Operational Program Competitiveness, Entrepreneurship and Innovation, under the call RESEARCH – CREATE – INNOVATE (project code: T2EΔK-02144)

[1] Zhao Y., Yavari, K., Wang, Y., Van Cappellen, P., Liu, J. Deployment of functional DNA-based biosensors for environmental water analysis, Trends in Analytical Chemistry (2022) 153, 116639.
[2] Skotadis E., Tsekenis, G., Chatzipetrou, M., Zergioti, I., Tsoukalas, D. Heavy metal ion detection using DNAzyme-modified platinum nanoparticle networks, Sensors and Actuators B: Chemical 239 (2017): 962-969.

[3] Official journal of the European Union, Directive (EU) 2020/2184 of the European Parliament and of the Council of 16 December 2020, on the quality of water intended for human consumption

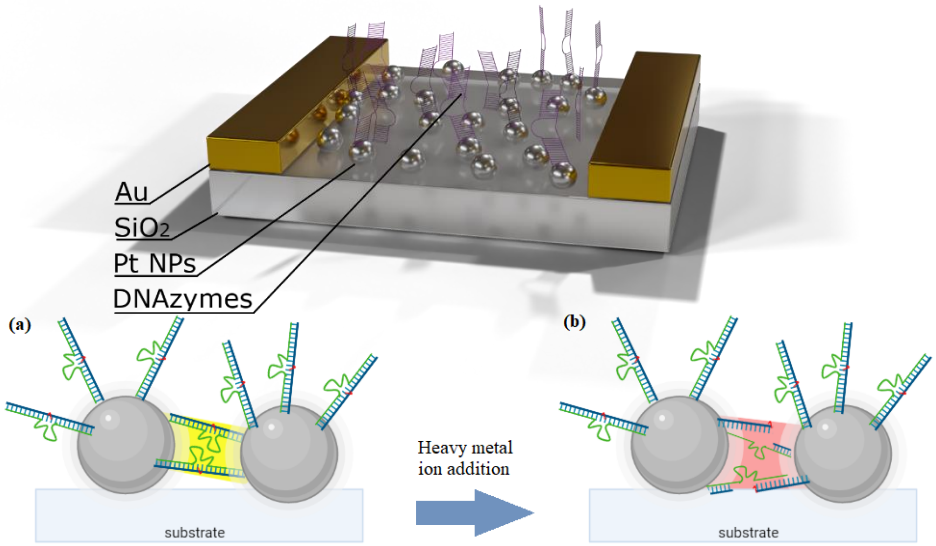

Figure 1. Top: Schematic representation of the biosensor. Bottom: Schematic representation of a) DNAzyme immobilization on PtNPs and b) their single-stranded catalysis in the presence of heavy metal ions

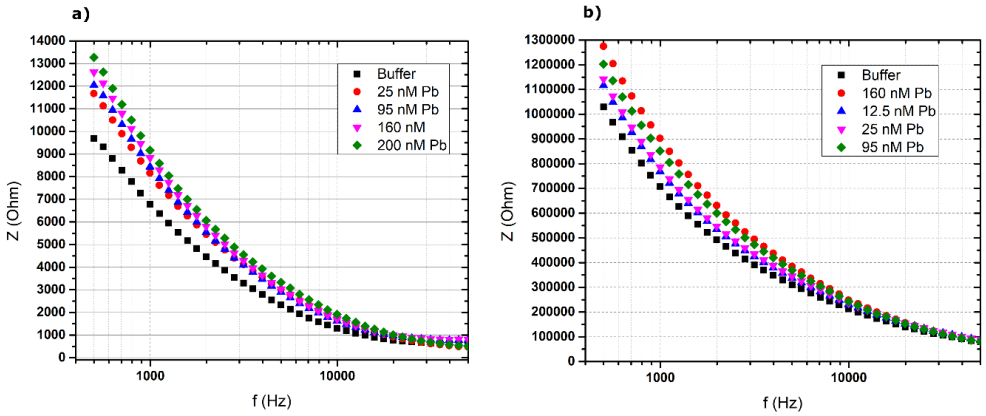

Figure 2. Impedance-frequency graphs of different Pb^{2+} concentrations a) amino modified DNAzymes b) thiol modified DNAzymes.

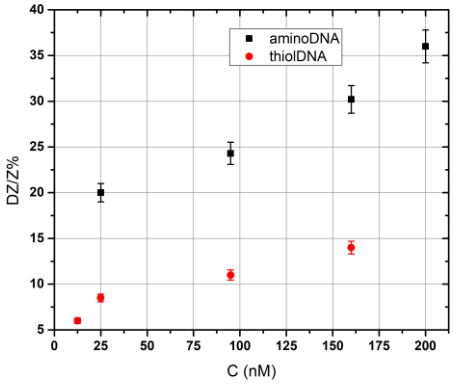

Figure 3. Relative impedance changes for different Pb^{2+} concentrations of the two immobilization techniques

Fabrication of Silicon nano-pillars to enlarge their implementation in future integrated circuits and systems

A. del Moral [a], R. Ramos [a], B. Sepúlveda [a] and E. Amat [a]

[a] Institute of Microelectronics of Barcelona (IMB-CNM, CSIC), 08193 Bellaterra, Spain.
Corresponding author e-mail: alberto.delmoral@imb-cnm.csic.es

Vertical structures with high aspect ratio are being considered as future device configuration to be implemented in integrated circuits (ICs). In this work, two fabrication processes for vertical architectures are presented based on different etching procedures: Reactive Ion Etching (RIE) and Metal Assisted Chemical Etching (MACE).

Silicon nanowire-based transistors (NW) are promising architectures to achieve further gate length scaling down to 5 nm. NWs can be manufactured in horizontal and vertical (vNW) configurations [1]. IRDS 2022 predicts vertical structures as the next step for the ultra-scaled technology nodes, due to its almost negligible impact of the contacted pitch [2]. While 2D layouts are still used in circuit design, with deep scaling it can eventually hit physical limits beyond the 10 nm technology node. Therefore, device/circuit integration in the third dimension (3D) can yield new pathways for further ICs miniaturization. The main benefits of vNW are: significant reduction of area consumption, i.e. larger device density, and (2) less short channel effects (SCEs) due to its gate-all-around (GAA) configuration. Moreover, vNWs are acquiring relevance in wide research scenarios: sensors (e.g. radiation and biomedical), thanks to their larger effective area [3]; in the Internet of Things (IoT) framework, due to their low power consumption [4]; for neuromorphic circuits, because of their high integration level; and high-performance for quantum technologies, due to its inherent charge confinement over the NW [5].

In this contribution the manufacturing process of vertical nano-pillars with a high aspect ratio is presented, including the strategies for its further implementation in ICs and CMOS devices. The main challenge of the process is the fabrication of large aspect-ratio structures, and thus this is the topic here addressed. Out of the scope of this contribution is the device doping, which could be achieved by epitaxial growth process. Two approaches are followed to pattern vNW. Fig. 1.a presents the RIE-based approach, where by depositing polystyrene nanospheres (A.*i*) with a colloidal self-assembly, followed by RIE silicon etching (A.*ii*) pillars are patterned. This technique is a low cost, fast, large patterning area, with a broad choice of nanospheres sizes and arrays [6]. Fig. 1.b shows the CMOS-compatible technique based on MACE, where a metal layer is used as natural mask. This is a useful method due to its high anisotropy. Focusing on a CMOS compatible procedure, a TiN layer is used as a catalyst [7] instead of the non-CMOS based on Au [8]. As polystyrene nanospheres do not endure the high temperatures used during the TiN deposition, silica nanospheres are used in this case (B.*i*), and after the TiN deposition (B.*ii*) they are peeled out (B.*iii*). To pattern the structure an optimized solution [8] of hydrogen peroxide (H_2O_2) and Hydrofluoric acid (HF) is used to etch away the silicon under the catalyst metal layer (B.*iv*). Fig. 2 shows the deposited nanospheres for both manufacturing procedures. Fig. 3.a and Fig. 3.b presents SEM images of the 60 nm diameter nano-pillars obtained by the RIE approach. Fig. 3.c summarizes the optimized nanopillar height as function of etching time for a RIE process at 350W and 0ºC. Once the pillar is patterned, the CMOS integration process towards a functional MOSFET device is performed as indicated in Fig. 4; this procedure has been already developed in previous works [9].

In summary, we present the strategies to manufacture vertical structures with large aspect ratio. Two CMOS approximations are presented: one based on patterning by using colloidal particles and RIE etching procedure, and one based on colloidal particles and MACE wet-etching.

References

[1] D. Yakimets *et al.*, *Device Res. Conf.*, pp. 133–134, 2014.
[2] IEEE, "International Roadmap for Devices and Systems (IRDS)," 2022. [Online]. https://irds.ieee.org/.
[3] M.-A. Doucey and S. Carrara, *Trends Biotechnol.*, vol. 37 **(1)**, pp. 86–99, 2019.
[4] A. V.-Y. Thean *et al.*, *Symp. VLSI Technol.*, pp. T26–T27, 2015.
[5] S. M. Frolov *et al.*, *MRS Bull.*, vol. 38 **(10)**, pp. 809–815, 2013.
[6] Y. Zhang, "Opto-Magneto-Electrical Nanoactuators for Wireless Cell Stimulation," 2020.
[7] J. D. Kim *et al.*, *ACS Appl. Mater. Interfaces*, vol. 11 **(30)**, pp. 27371–27377, 2019.
[8] Y. Jeong *et al.*, *Sci. Rep.*, vol. 9 **(1)**, p. 15914, 2019.
[9] A. del Moral *et al.*, *Semicond. Sci. Technol.*, vol. 37, p. 125014, 2022.

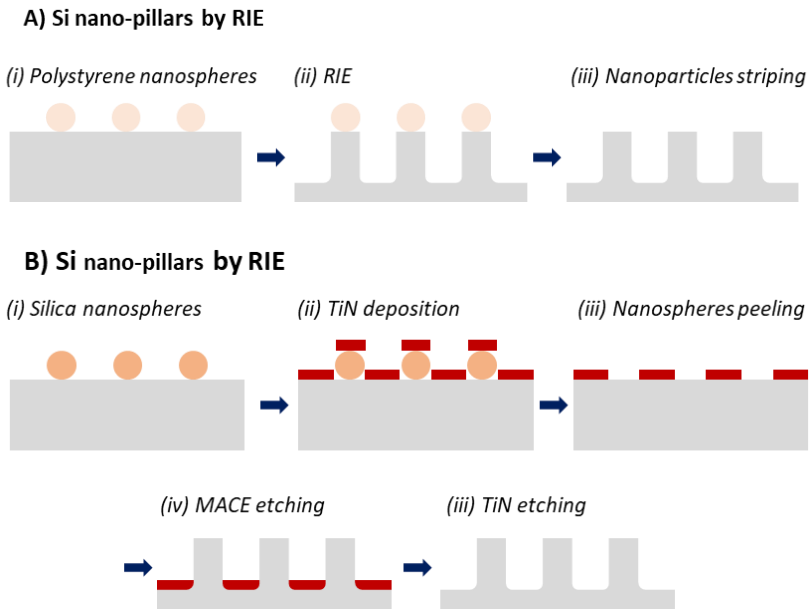

Fig. 1. Manufacturing processes to pattern Si nano-pillars by two different approaches: by means of (A) RIE and (B) MACE etching.

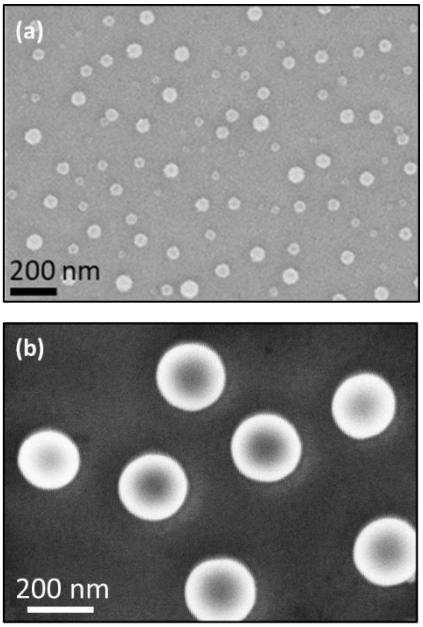

Fig. 2. Deposited nanospheres as mask: (a) 60 nm polystyrene and (b) 200 nm silica.

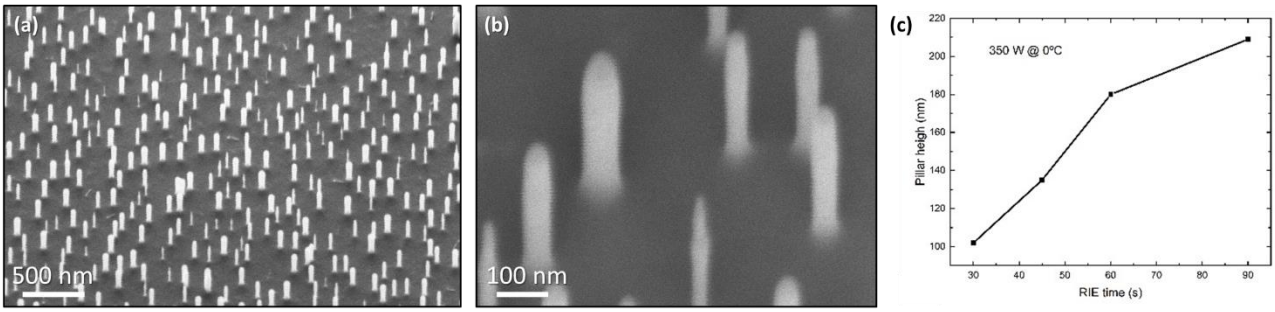

Fig. 3. (a) Tilted SEM image of the nano-pillars in average distribution after RIE, (b) closer SEM view of the nano-pillars in the same process step and (c) relation of pillar height for different etching times.

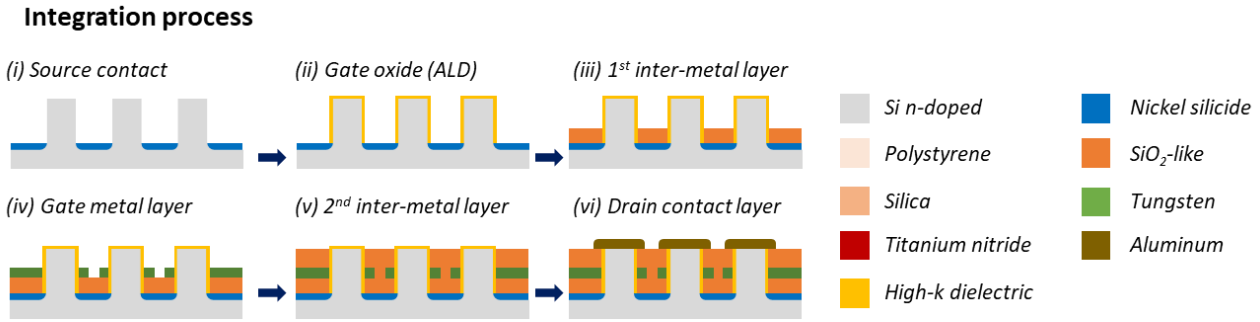

Fig. 4. Summary of the integration process after Si nano-pillar patterning: (*i*) Nickel silicide source contact, (*ii*) gate oxide by ALD, (*iii*) 1st inter-metal layer deposition by means of spin-coating and annealing, (*iv*) gate layer deposition and patterning, (*v*) 2nd inter-metal layer deposition and (*vi*) drain contact fabrication.

Dual photoresist maskless UV photolithography process to fabricate 3D suspended microstructures for pyrolytic carbon microelectrodes

Mohammad Ramezannezhad, Babak Rezaei, Stephan Sylvest Keller
DTU Nanolab, Technical University of Denmark, 2800 Lyngby, Denmark
email: mohram@dtu.dk

Keywords: 3D structure, microelectrode, pyrolytic carbon, SU-8, mr-DWL, Maskless lithography

SU-8 is a well-known negative tone resist which can be easily utilized to fabricate 3D microstructures, especially with pillars pattern [1]. Also, it is possible to convert it into conductive carbon during a pyrolysis process at high temperature and use it as carbon microelectrode [2]. It has always been a massive challenge to enhance the surface area of electrodes leading to higher signal and better performance. However, it is also possible to build a suspended layer on the top of the pillars to add even more surface area to the electrode. There have been few studies regarding 3D microelectrodes with a suspended layers [3] [4]. However, none of them was based on maskless lithography (MLA) approach which is a straightforward, and high throughput approach with flexibility in changing designs to pattern resists with a micron-scale resolution. In this study, fabrication of 3D suspended microstructure based on SU-8 and mr-DWL photoresists with maskless UV photolithography including addressing the suspended layer thickness is presented.

The schematic process flow for 3D suspended microstructure fabrication is shown in figure 1. Firstly, a 600 nm oxide layer was grown by the LPCVD method on a silicon wafer. Then, 15 µm SU-8 2035 (MicroChem Co) were spin-coated as the initial layer. In the following, the layer was soft baked for 15 min at 50 ˚C, exposed at 250 mJ/cm^2, and baked again for 2 h at 50 ˚C as the post exposure bake (PEB). For the second layer, SU-8 2075 was used to spin-coat the 100 µm layer, baked for 5 h at 50 ˚C, exposed at 240 mJ/cm^2, and baked again for 2 h at 50 ˚C. A maskless aligner with a wavelength of 365 nm (MLA 100, Heidelberg instruments) was utilized to fabricate first and second SU-8 layer. For the second layer, three different pillars diameter including 20 µm, 40 µm, and 80 µm are considered. The mr-DWL 40 photoresist (Micro resist technology Co.) was utilized for suspended layer fabrication. To confine the curing process exclusively to the top layer, a different type of mask-less aligner (MLA 150, Heidelberg instruments) was employed due to the distinct exposure wavelength of mr-DWL (405 nm). Mr-DWL 40 was spin coated at a thickness of approximately 25-30 µm followed by 1h soft bake (SB) at 50 ˚C. Then, the layer was exposed at 80 mJ/cm^2 and kept at 50 ˚C for 1 h for the PEB. Next, the samples were developed in the mr-Dev 600 solution and rinsed with Isopropyl Alcohol (IPA). At the end, the wafers were exposed at 250 mJ/cm^2 in the flood-exposure mode, and hard baked for 15 h at 90 ˚C. During the SEM characterization, it was observed that the final thickness of the suspended layer was significantly larger than the expected values. It could be related to migration of the photoinitiators at the interface of 2nd and 3rd layers during the fabrication steps of 3rd layer. For the subsequent pyrolysis step, the high thickness of the 3rd layer is a challenge and will result rupture and delamination of the electrodes. Therefore, the influence of the most significant process parameters on the final thickness of the suspended layer were systematically investigated (figure 2).

According to the results in figure 2, the exposure dose of the 3rd layer is the most critical parameter to achieve a reduction of the thickness of the suspended layer. Therefore, the effect of the exposure dose was investigated in more detail. The measured thickness of the suspended layer for different doses is presented in the SEM images (figure 3). According to figure 3 (f), the thickness of the suspended layer is significantly reduced for a lower dose. However, at the lowest dose of 10 mJ/cm^2, delamination of the suspended layer was observed for pillar diameters below 80 µm (e)).

In summary, the influence of different process parameters on the final thickness of suspended layers was studied. According to the results, it was concluded that the exposure dose of the suspend layer is the most important parameter. Next, we will investigate the effect of the dose value on the actual pyrolytic carbon.

[1] Amato et al,. Microelectronic. Engineering. 98 (2012) 483-487.
[2] Y.M. Hassan et al,. Journal of Analytical and Applied Pyrolysis 125 (2017) 91–99

[3] S. Hemanth,. Carbon N. Y., 121 (2017), pp. 226-234

[4] Mantis et al,. Carbon 179 (2021) 579-589.

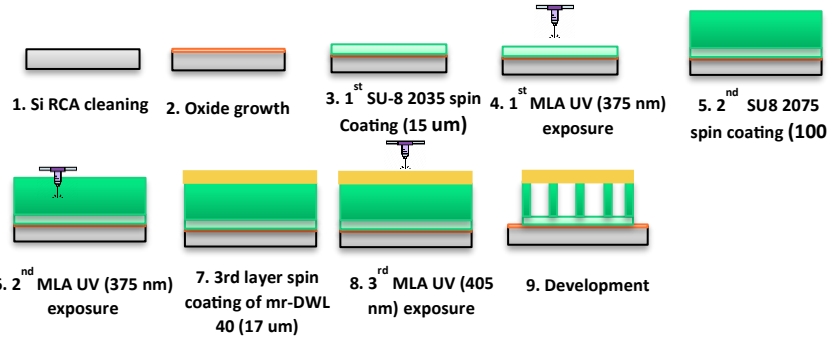

Figure 1. The schematic process flow for 3D suspended microstructure fabrication

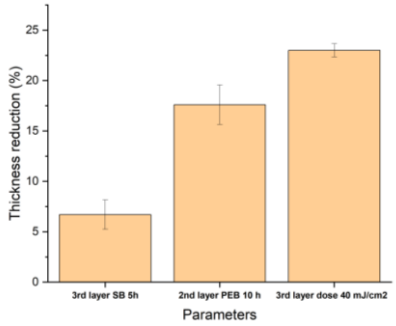

Figure 2. The effect of different parameters on thickness reduction of suspended layer

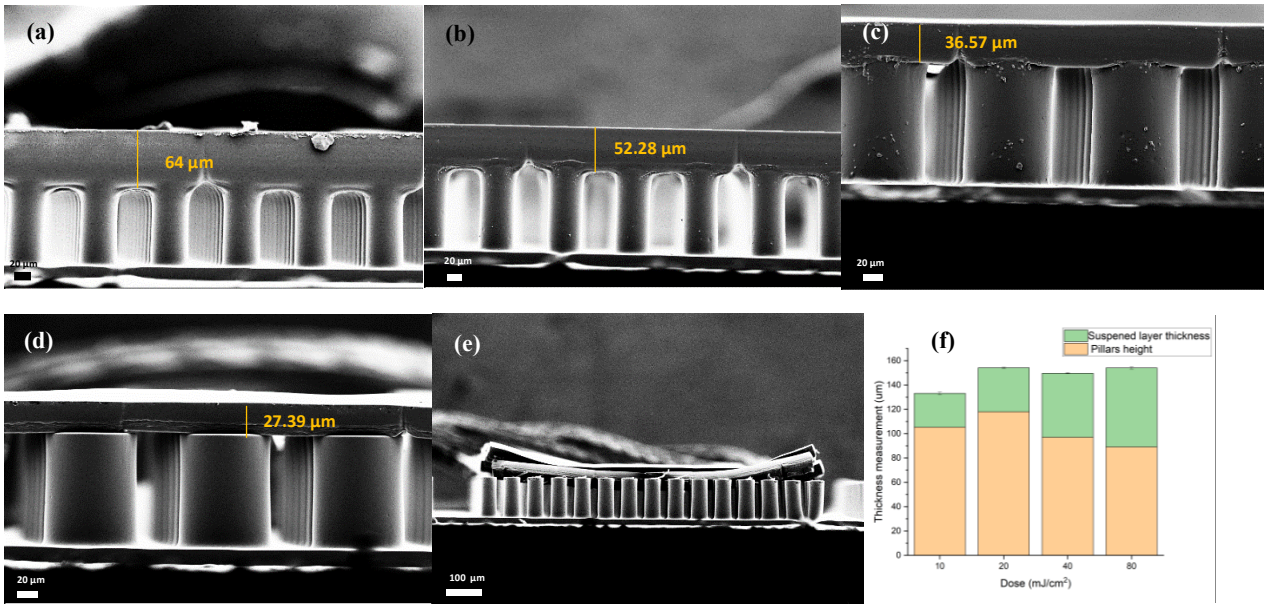

Figure 3. SEM images of 3D suspended microstructures fabricated in different exposed doses for the suspended layer. The suspended layer thickness measurement for (a) 80 mJ/cm^2, (b) 40 mJ/cm^2, (c) 20 mJ/cm^2, and (d) 10 mJ/cm^2 samples. (e) The example of suspended layer collapsing for 40 µm pillars with the dose of 10 mJ/cm^2. (f) The effect of suspended layer dose on the final height of pillars and thickness of suspended layer

Acknowledgements

The authors gratefully acknowledge the funding support from European Research Council under the Horizon 2020 framework programme grant no. 772370-PHOENEEX.

MASS SPECTROMETRY BY SINGLE MODE NANOELECTROMECHANICAL SYSTEMS AT ATMOSPHERIC CONDITIONS

19th International Conference on Micro and Nano Engineering

Batuhan E. Kaynak[1,2], Mohammed Alkhaled[1,2], Enise Kartal[1,2], Cenk Yanik[3], and M. Selim Hanay[1,2,*]

[1]Department of Mechanical Engineering, Bilkent University, 06800 Ankara Türkiye
[2]UNAM - Institute of Material Science and Technology, Bilkent University, 06800 Ankara Türkiye
[3]SUNUM, Sabancı University NAnotechnology Research and Application Center, 34956 Istanbul Türkiye

INTRODUCTION

- Nanoelectromechanical Systems Mass Spectrometry (NEMS-MS) is an emerging technique that is well-suited for measuring analytes that are challenging to measure with conventional mass spectrometry.
- Recent advances include conducted NEMS-MS at atmospheric conditions with unparalleled capture efficiencies.
- When the NEMS device is operated in air, it experiences dissipation, which poses challenges in utilizing the two-mode theory to accurately determine the mass and position of the landing analytes.
- The Paddle NEMS architecture has been developed to allow mass measurement using a single mode.

KEY TAKEAWAYS

- The new NEMS device features a platform section with a uniform mode shape, allowing for direct correlation between the mass of the analyte and the frequency shift caused by its landing on the sensor. This eliminates the need for complex calculations and corrections associated with altered mode shapes in atmospheric conditions.
- Experimental validation confirmed the uniform mode shape and demonstrated the capability of the Paddle NEMS devices to measure nanoparticles with a single mechanical mode.
- The results highlight the potential of Paddle NEMS for mode shape independent mass sensing in atmospheric pressure NEMS-MS systems.

DEVICE ARCHITECTURE AND MODE SHAPE SIMULATIONS

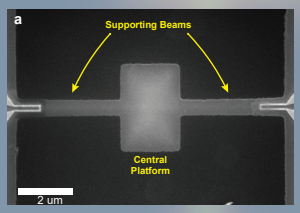

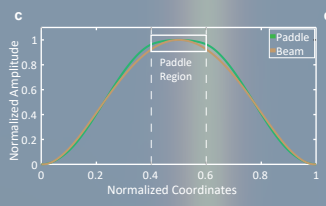

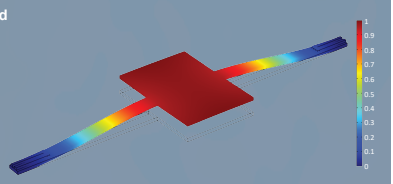

ELECTROSTATIC FOCUSING & PLL DATA

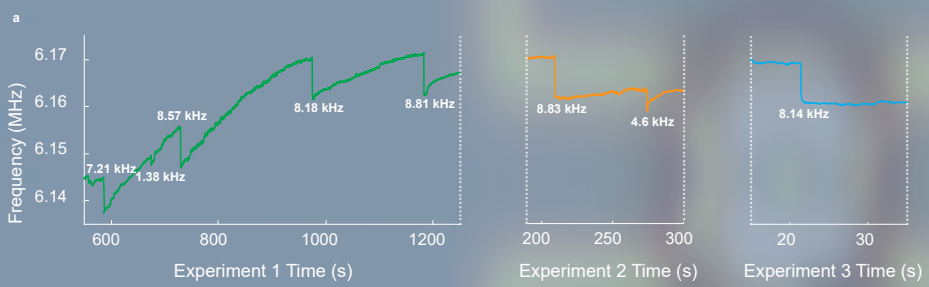

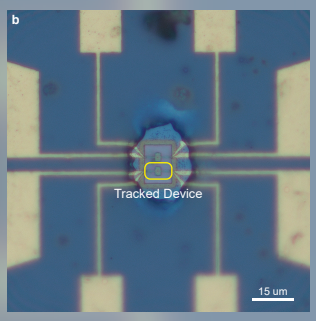

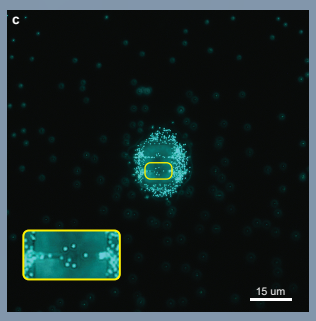

PLL & DIAMETER SPECTRA OF 200 nm F-PSNP

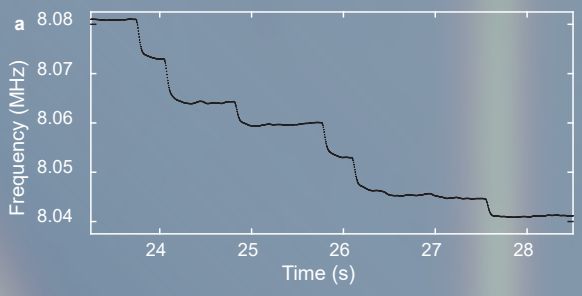

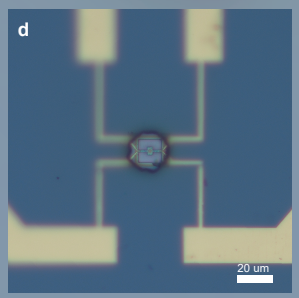

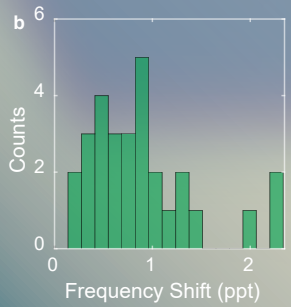

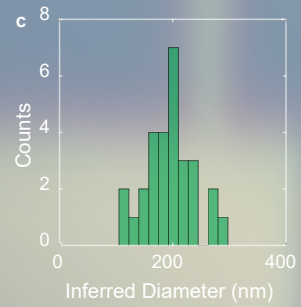

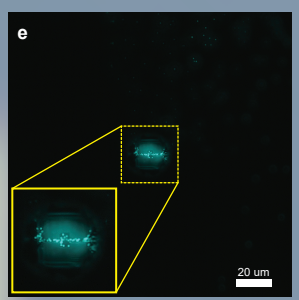

PLL & DIAMETER SPECTRA OF 40 nm GNP

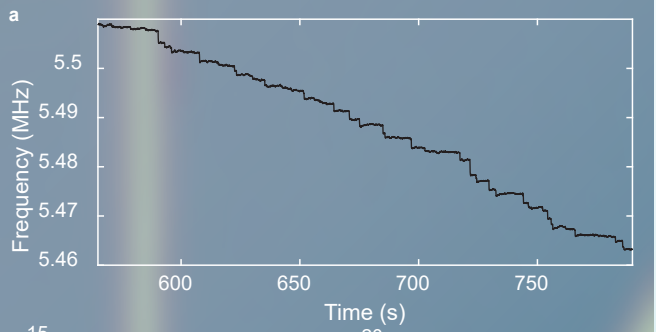

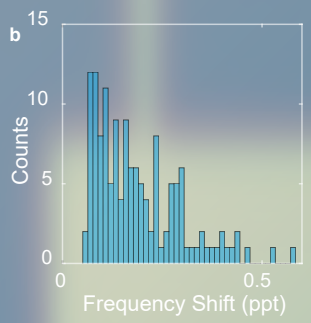

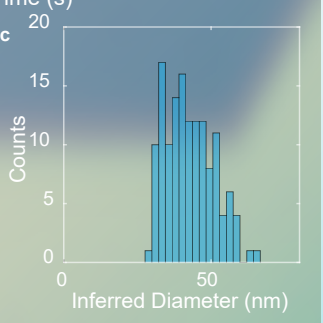

OUR RESEARCH GROUP

Led by Dr. Selim Hanay, Hanay Research Group is specialized in Nanoelectromechanical systems (NEMS), Microfluidics and Microwave sensors

678

* E-mail: selimhanay@bilkent.edu.tr

PRESENTER

Enise Kartal (MSc Student)

Department of Mechanical Engineering & UNAM - National Nanotechnology Research Center, Bilkent University, Ankara Türkiye

REFERENCES

B. E. Kaynak, M. Alkhaled, E. Kartal, C. Yanik, and M. S. Hanay, 'Atmospheric Pressure Mass Spectrometry by Single-Mode Nanoelectromechanical Systems', arXiv preprint arXiv:2306. 13227, 2023.

Scan here for Arxiv preprint

FUNDING

Supported by the Scientific and Technological Research Council of Turkey, grant no EEEAG-119E503

Received funding from the European Research Council under the European Union's Horizon 2020 research and innovation programme (grant no 758769)

A Method for the automated Replication of Diffractive Optical Elements with Strong Curvature

P. Kastl [a], C. Rödel [a], S. Kühne [a], J. Wolf [b], T. Krist [c], D. Oberschmidt [a]

[a] Technische Universität Berlin, Micro and Precision Devices, 10587 Berlin, Germany
[b] micro resist technology GmbH, 12555 Berlin
[c] NOB Nano Optics Berlin GmbH, 10627 Berlin
e-mail: kastl@mfg.tu-berlin.de

The production of diffraction grating masters with micro- and nano-features has required a high level of expertise since Rowland's first successful attempts up to the present day. Still, optically outstanding gratings are rather expensive one-offs.

Traditionally, a variety of replication processes made it possible to economically produce optical components as replicas from conventionally machined masters, which in turn results in more affordable spectrometric systems. Additionally, customers most often request batches of identical diffractive optical elements (DOEs) with strong curvature to equip their systems.

Until now, replication was limited to planar or weakly curved geometries. Strongly curved diffractive optical elements with radii of curvature in the range of a few centimeters significantly reduce the size of spectral devices. Furthermore, by combining diffractive and imaging properties, DOE with strong curvature reduce the alignment effort and the number of optical interfaces, thus increasing the system's overall efficiency.

In collaboration with Nano Optics Berlin NOB GmbH and micro resist technology GmbH, a device for the automated replication of strongly curved diffractive optics was developed at the Technical University Berlin (see Fig. 1). This involves a multi-step thin-film replication process (see Fig. 2) from ultra-precision manufactured masters into UV-curable hybrid polymers (see Fig. 3). In order to achieve a concave replica from a concave master and a convex replica from a convex master an intermediate stamp is necessary. Soft stamps are not ideally suited for subsequent handling in the developed process and do not provide the same accuracy as hard stamps [1]. To create hard stamps from masters and subsequently replicas from stamps hybrid polymer is used.

Hybrid polymer is well suited for the fabrication of micro structures [2]. The curing of hybrid polymers with UV-light unfortunately involves shrinkage to some degree (around 7 vol.-%). It was shown, that this shrinkage can be controlled in a two-step replication process [3] by applying a thin-film whose absolute shrinkage is relatively small. Therefore, it is important to create a thin and uniform gap between master and substrate.

Two methods have been developed for the adjustment in six degrees of freedom in order to create a uniform gap and combat shrinkage of the hybrid polymer during curing. The mold halves are adjusted in x, y and c via optical means using measurement marks and Moiré-Fringes. Adjustment in a, b and z is done with a load cell array. Measurements of microfeatures with an atomic force microscope show high accuracy of replica. Single order surface line scans on a scatterometer produce comparable intensity profiles. The transfer to industrial application is currently in preparation.

[1] Kwon, B.; Kim, J. H.: Importance of Molds for Nanoimprint Lithography: Hard, Soft, and Hybrid Molds. Journal of Nanoscience (2016) 2016, S. 1–12.
[2] Schleunitz, A.; Klein, J. J.; Houbertz, R.; Vogler, M.; Gruetzner, G.: Towards high precision manufacturing of 3D optical components using UV-curable hybrid polymers. Optical Interconnects XV, SPIE, 2015, S. 73–81.
[3] Grützner, S.; Wolf, J.; Kastl, P.; Rolón, D. A.; Kühne, S.; Oberschmidt, D.; Löchel, B.; Schleunitz, A.; Grützner, G.: Two-step replicated Nano Optical Pattern on curved Surfaces for Spectrometer Components. Turin, Italy, 2021.

Figure 1. Close-up of the replication process inside the device.

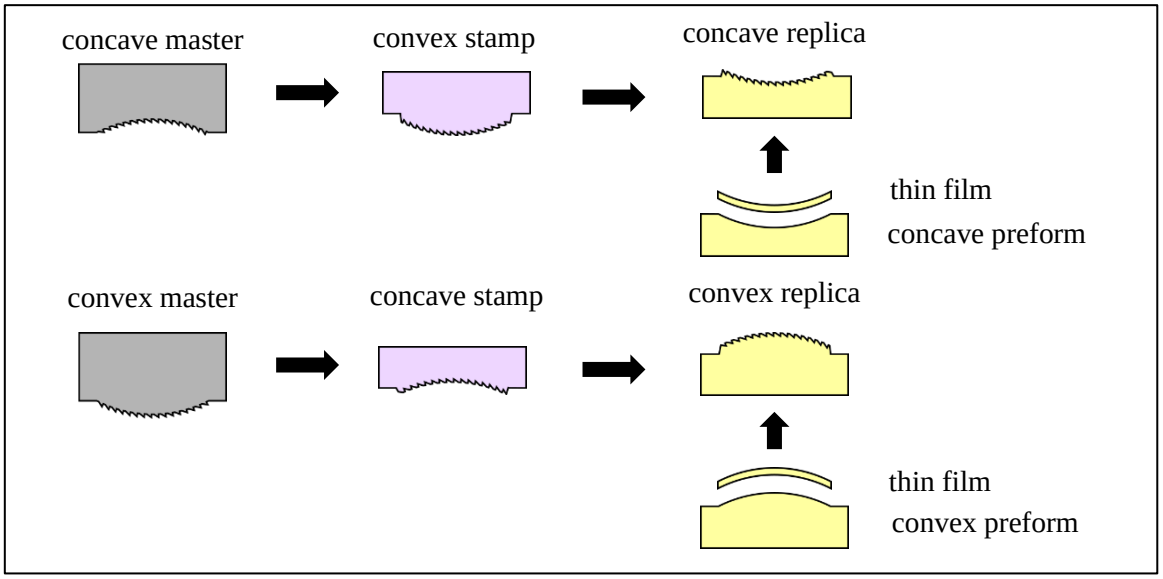

Figure 2. Overview of the replication process.

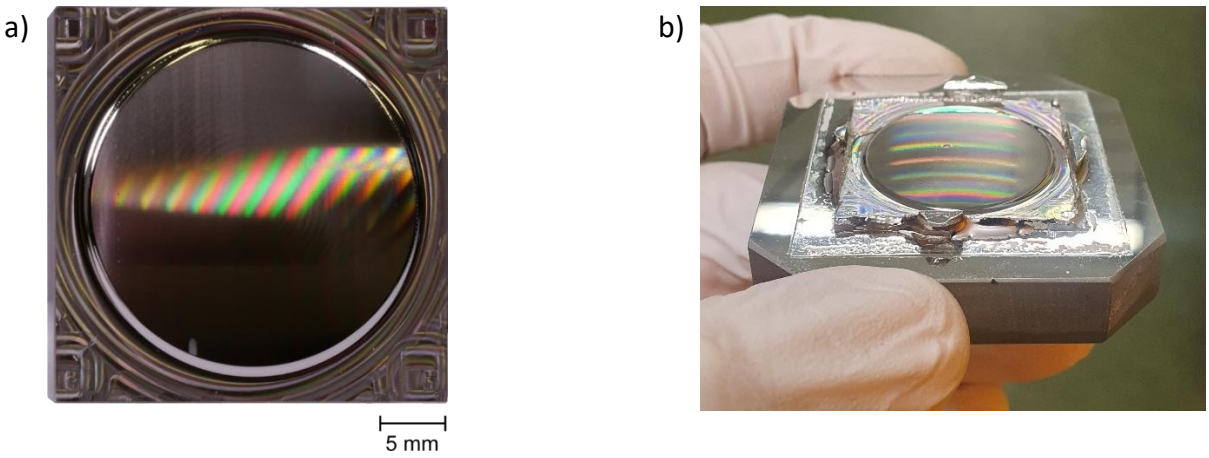

Figure 3. Photographs of a DOE master (a) and its replica (b).

Al-SWG reflectors for tuneable VIS filters and spectroscopy applications

Christian Helke [a,b], Christian Behl [a], Regine Behlert [a], Susanne Hartmann [b], Micha Haase [a,b], Jörg Martin [a], Danny Reuter [a,b] and Karla Hiller [a,b]

[a] Fraunhofer Institute for Electronic Nano Systems (ENAS), Chemnitz, 09126, Germany
[b] Technische Universität Chemnitz, Center for Microtechnologies (ZfM), Chemnitz, 09126, Germany
e-mail: christian.helke@enas.fraunhofer.de

A further development of miniaturized spectrometry systems is achievable by miniaturized tunable Fabry-Pérot-Interferometers (FPI). A main part of the FPI is the reflector, which is usually realized as a Bragg reflector consisting of an alternating dielectric layer stack with high and low refractive index layers [1,2]. To achieve high reflectivity an adequate material property homogeneity for each layer within the layer stack is needed. For stacks with larger number of layers, the integration with MEMS processes is challenging. Particularly, stack structuring and the achievement of process compatibility to a fabrication process for moveable FPI-MEMS structures are important. An alternative to the alternating layer stack reflector is a nanostructured subwavelength grating (SWG) reflector. These SWG reflectors indicate equivalent performance by using only one layer leading to a minimized reflector topology complexity, but the targeting critical dimension (CD) of the SWG itself become more and more challenging. In our previous work we showed LP-Si_3N_4 membraned based SWG reflectors as 424 nm nanostructured holes in a 200 nm LP-Si_3N_4 membrane and as 142 nm nanostructured 50 nm thin aluminum polygons on top of 150 nm LP-Si_3N_4 membranes [3] for the spectral wavelength range of 550 nm to 600 nm showing a reflectance of up to 99 %.

In this contribution we present a less complex SWG reflector that can act as the fixed reflector, consists of a 25 nm thin aluminum layer that is nanostructured for reflectivity in the VIS range. The array of nanostructures is designed as 2 mm circular dies consisting of 140 nm Al patches with 200 nm pitch.
The manufacturing of the SWG reflectors is realized on 6" glass wafers by deposition of the 25 nm aluminum layer followed by electron beam lithography and etching. The exposure was carried out with a 50-keV-eBeam lithography tool Vistec SB254 working very productively according to the shape-beam principle. The negative tone resist ma-N 1402 from Micro Resist Technology GmbH was exposed with 150 µC/cm² and 170 µC/cm² with a sizing factor of 20 nm, 10 nm and 0 nm of the SWG layout. Afterwards the pattern is transferred into the 25 nm aluminum layer by a chlorine dry RIE process at a Sentech SI800 tool and a followed resist strip.
The fabricated SWG reflectors show different CDs regarding their sizing factor. As an example, the 150 µC/cm² exposure with sizing factor variation is shown in Figure 1. The SWG CD varying from 140 nm (sizing 0 nm) to 115 nm (sizing 20 nm) within the pitch of 200 nm.

Spectral characterization of the manufactured SWG reflectors after etching and resist removal is done by using a FTIR Bruker Vertex 70 spectrometer with an aperture of 0.5 mm and 64 scans. FTIR transmission spectra is processed using SpectraGryph software. Assuming that the layers are free of absorption, the resulting reflectivity of the SWG reflectors is given by R = 1-T.
An example of the measured reflectivity of a SWG reflector exposed with 150 µC/cm² and 170 µC/cm² and a sizing factor of 0 nm is shown in Figure 2. The measured reflectance is above 70 % for wavelengths larger than 550 nm and increases up to the measured wavelength of 1000 nm. Both fabricated SWGs show the same spectral behavior.

We will present the dependency of the reflectance characterization with respect to their fabricated CD, the sizing factor and the possible integration technology for MOEMS related applications.

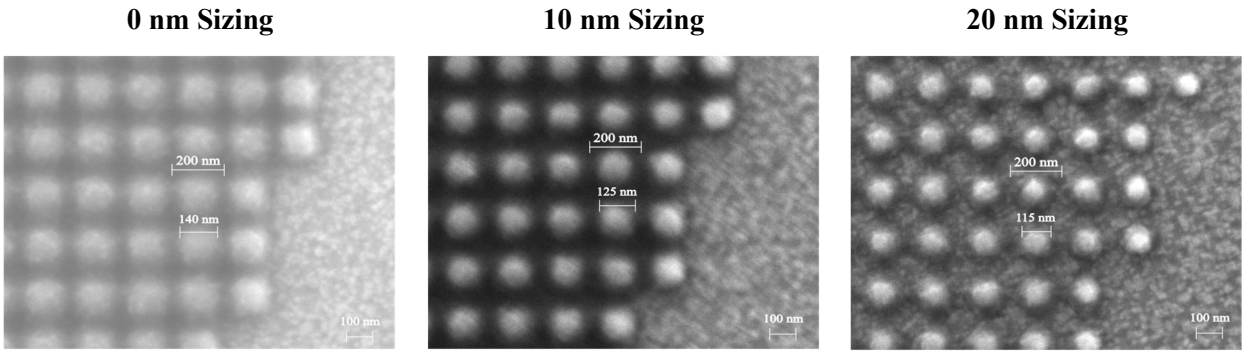

Figure 1. SEM images after E-Beam exposure with 150 µC/cm², 200 nm pitch, 140 nm CD and the three sizing factors of 0 nm, 10 nm and 20 nm.

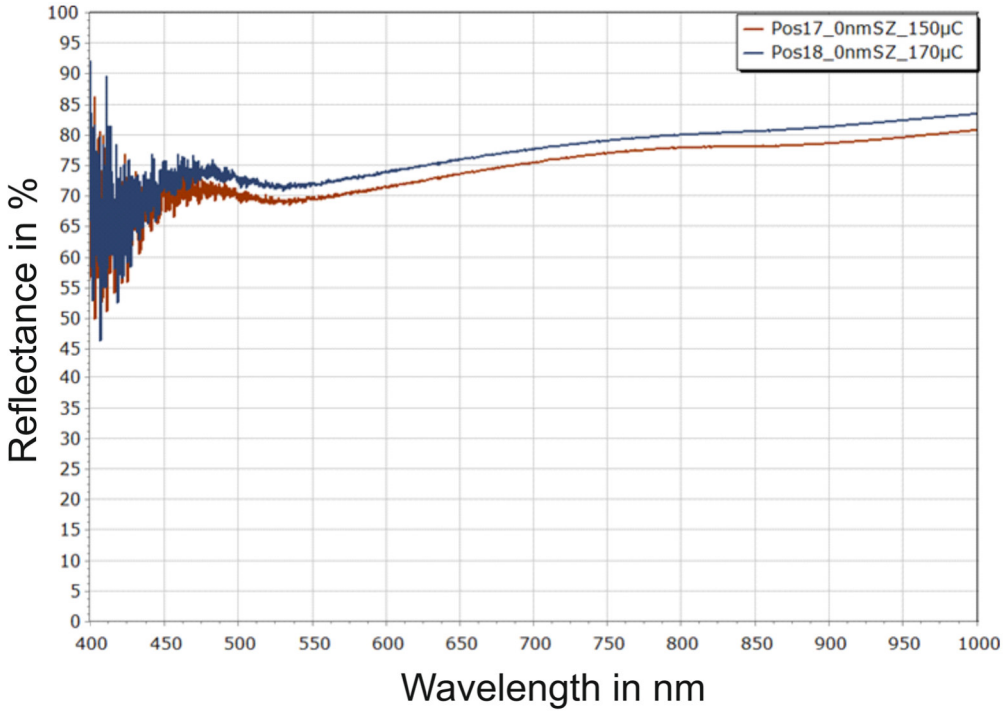

Figure 2. Reflectance of fabricate SWGs with 150 µC/cm² and 170 µC/cm² with 0 nm sizing factor.

[1] M. Ebermann et al. “Next generation of highly miniaturized Bulk-MEMS Fabry-Pérot Filters for infrared microspectrometers”, Transducers 2019 Conference, Berlin, Germany, June 23-27, 2019, pp 470-473
[2] M. Tuohiniemi et al. “MOEMS FPI with point-anchored Si-air mirrors for middle infrared”. Journal of Micro-mechanics and Microengineering 24, 2014, pp. 1–9
[3] C. Helke et al. “Challenges of nanostructure integration in Fabry-Pérot interferometers as alternative to Bragg reflectors: an example for Match 1:1-, eBeam-, and nanoimprint lithography", Proc. SPIE 10446, 33rd European Mask and Lithography Conference, 104460J (2017).10.1088/2053-1591/aaed10

Characterization of hybrid nanowire-MEMS force sensors using direct actuation

Bartosz Pruchnik[a], Krzysztof Kwoka[a], Tomasz Piasecki[a], Masoud Jedari Ghourichaei[b], Mehrdad Karimzadehkhouei[b,e], Cemal Aydogan[c], Ivo W. Rangelow[c,d], Halil Bayraktar[f], B. Erdem Alaca[b,e,g], Teodor Gotszalk[a]

[a] Department of Nanometrology, Wrocław University of Science and Technology, Wroclaw, 50-370, Poland
[b] Dept. of Mechanical Engineering, Koç University, Istanbul, 34450, Turkey
[c] Institute of Precision Measurement and Sensor Technology, Ilmenau University of Technology, Ilmenau, 98693, Germany
[d] nano analytik GmbH, Ehrenberg Str. 3, 98693-Ilmenau, Germany
[e] n²STAR-Koç University Nanofabrication and Nanocharacterization Center for Scientific and Technological Advanced Research, Koç University, Istanbul, 34450, Turkey
[f] Dept. of Molecular Biology and Genetics, Istanbul Technical University, Maslak, Istanbul, 34467, Turkey
[g] Surface Science and Technology Center (KUYTAM), Koç University, Istanbul, 34450, Turkey
e-mail: tomasz.piasecki@pwr.edu.pl

Piezoresistive detection is an established method for detecting and measurement of strain, force, pressure or other mechanical quantities. Devices equipped with piezoresistive sensing components have to be characterized to establish the gauge factor (GF) of the piezoresistors. We present the results of the GF characterization of novel hybrid planar force sensors using direct actuation method.

Single force sensor (figure 1) consists of the movable shuttle suspended on 8 springs allowing for its planar movement depending on the force applied to the shuttle. The movement is detected piezoresistively by 4 sets of the nanowires at four sides of the shuttle. The electrical readout of the nanowires strain would allow to detect the magnitude and the direction of the force applied to the shuttle. The advantages resulting from the use of the nanowires should result in high values of the GF compared to traditional silicon piezoresistors.

Due to the small dimensions of the movable structure there is no simple method for sensors calibration. We propose the direct actuation method using nanomanipulators inside the SEM microscope chamber, as shown in figure 2. Two Kleindiek MM3A manipulators with probes were used to provide the electrical contact to the nanowires. The Easylift probe being the accessory to the FEI Helios NanoLab 600 SEM/FIB system was used to apply the force the movable shuttle. Resistance was measured using Keithley 2001 mustimeters connected externally to the probes. The SEM was used for measuring the magnitude of the displacement of the shuttle.

Exemplary results are shown in figures 3 and 4. One of the experiments relied on the shuttle movement along the direction of the nanowires that the electrical contact was made to. The dependence of the resistance changes on the shuttle movement is shown in figure 3. In the second of experiments the movement was perpendicular to the direction of the nanowires. Due to the geometry of such movement the nanowires were elongated if the shuttle was moved either way from the resting point, as shown in figure 4.

The initial GF evaluation based on the results shown in figure 3 resulted in very low GF of 2.15, which was much lower than expected for the silicon nanowire [1]. Closer inspection of the behaviour of one of the springs suspending the shuttle revealed that the force applied to the shuttle moved also the whole chip due to the mechanical compliance of the chip mounting system in the SEM chamber. That movement allowed to evaluate the relation between the spring constants of the mechanically compliant parts of the measurement system (figure 6) resulting in the conclusion that only 10% of the observed displacement of the shuttle was related to the strain in the springs and nanowires suspending the shuttle and the rest was the result of the compliance of the rest of the setup. Taking that into account the GF of the nanowires was evaluated as 21.5. Such value shows the benefit of using nanowires for the force sensing as it is greater than geometric GF. Further improvements of the fabrication technology should lead to further improvement of the GF approaching the best results reported in the literature.

This work is supported by the Polish National Centre for Research and Development grant no. 01PT/0002/21 “piezoIoTMEMS” and Tübitak under grant numbers 120N361 and 118C155.

[1] B. E. Alaca and M. Karimzadehkhouei, Piezoresistive nanowire-based electromechanical sensors, Encyclopedia of Sensors and Biosensors (First Edition), Elsevier 2023, Pages 555-566.
[2] L. Wang, S. Kiu, X. Feng, C. Zhang, L. Zhu, j. Zhai, Y. Quin, Z L Wang, Flexoelectrocnis of centrosymmetric semiconductors, Nature Nanotechnology 15 (2020) 661-667

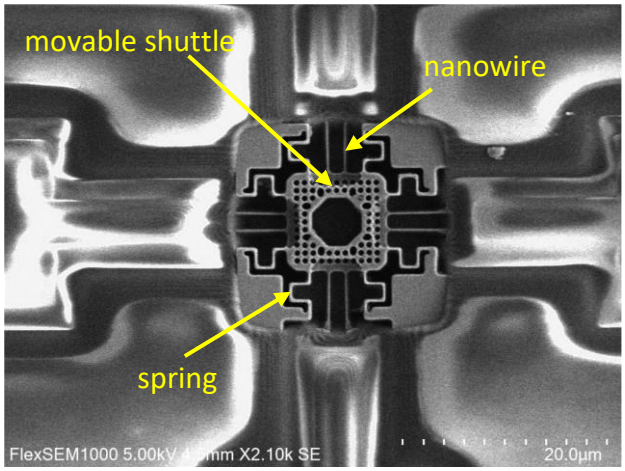

Figure 1. SEM image of the hybrid nanowire MEMS force sensor with movable shuttle suspended on 8 springs with 4 sets of piezoresistive nanowires.

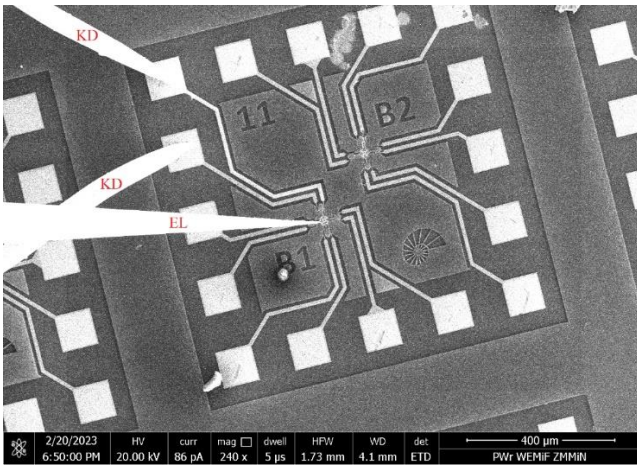

Figure 2. SEM image of the hybrid nanowire force sensor structure with nanoprobes used for electrical contact and actuation.

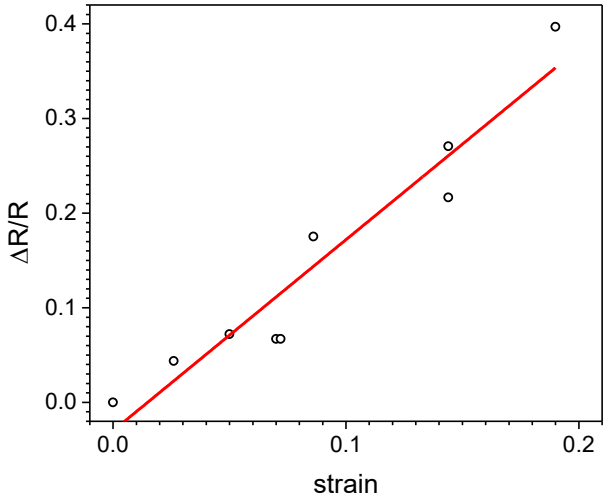

Figure 3. Direct measurement of the GF based on the apparent strain induced by the actuating probe movement and relative change of the resistance.

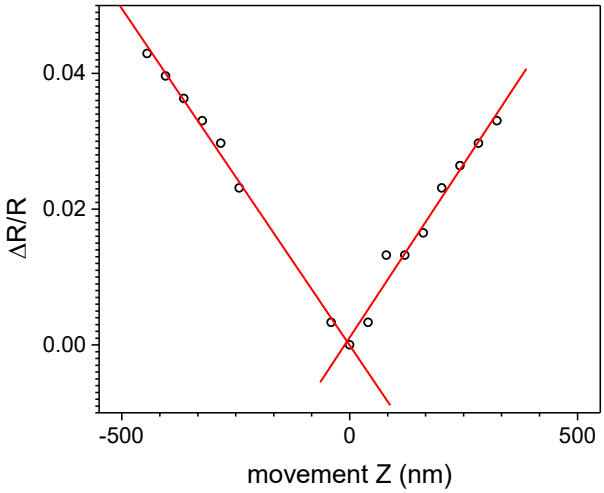

Figure 4. Relative change of the horizontal nanowire during the actuation perpendicular to the direction of the nanowire.

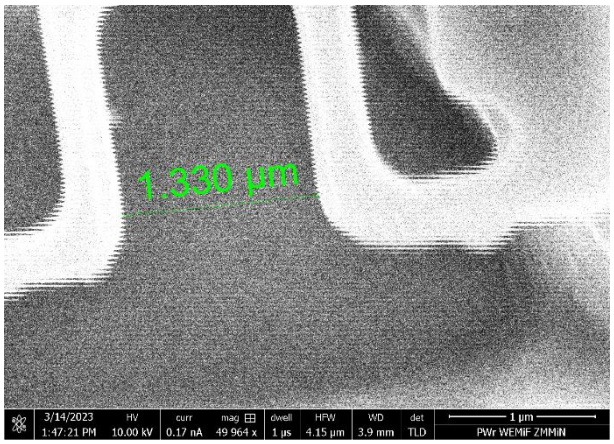

Figure 5. SEM image of the part of the movable shuttle spring allowing to determine the spring system stiffnesses and correction factor for the GF evaluation.

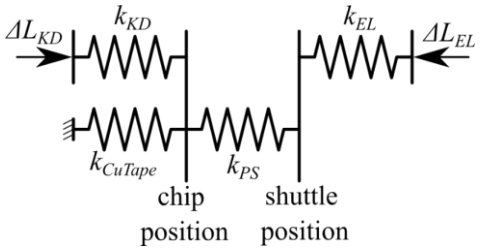

Figure 6. Schematic representing the elastic components of the whole measurement system taking into account the mechanical compliance of the DUT mounting.

Direct Vacuum Wafer Bonding for 1310 nm Bidirectional Tunable MEMS VCSEL

Masoud Payandeh [a], Hitesh Kumar Sahoo [a], Elizaveta Semenova [a], and Kresten Yvind [a]

[a] Department of Electrical and Photonic Engineering, Technical University of Denmark, Lyngby, 2800, Denmark
e-mail: maspa@dtu.dk

Micro electromechanical system (MEMS) vertical cavity surface emitting lasers (VCSELs) have shown great promise as a light source for optical coherence tomography (OCT), particularly due to their small footprint, low power consumption, and potential for integration with endoscopes and other medical devices [1,2]. Wavelength tuning range and adjustable repetition rate to tailor the image resolution, imaging range, and imaging speed are the advantages of MEMS VCSELs-based swept source-OCT. Due to the inverse relationship between axial resolution and laser tuning range, a wide tuning range of typically >100 nm is essential [2]. The tuning range is mainly limited by the free spectral range, gain bandwidth, and mirrors reflection bandwidth. To achieve wide and fast tunability, the device designs differ in many ways, including mirror design, MEMS structure, tuning mechanisms, cavity designs, and pumping mechanisms.

In our design shown in Figure 1-a, a highly reflective DBR mirror and high contrast grating (HCG) mirror (see Figure 1-b) along with III-V active material are used to define the cavity of the MEMS VCSELs. The actuation of HCG mirrors contributes to changing the length of the optical cavity and thus allows continuous tuning of the emitting wavelength. The MEMS VCSEL devices have two cavities, a semiconductor cavity that contains the active region and an air cavity. The two cavities are coupled strongly with each other, and the tuning ratio can be altered by controlling the coupling between the air and semiconductor regions. There are three different configurations for the MEMS VCSEL structures [2]: semiconductor-coupled cavity (SCC), extended cavity (EC), and air-coupled cavity (ACC). In this work, the focus is on EC lasers, in which the air cavity is formed by an etched hole in the spacer layer, and anti-reflective (AR) coating layers are used to couple the semiconductor and air cavities. We compare the simulation results of the three configurations and show that the EC structure with 140 nm tuning range represents a compromise between SCC and ACC designs as shown in Figure 2.

Two wafers are used to fabricate MEMS VCSELs - an SOI wafer and an InP wafer. Electron-beam lithography along with dry etching is used to define the HCG mirror on the SOI wafer, see Figure 1-b. Spacer layers (a thin SiO_2 layer and thick Poly-Si layer) with an air-gap opening is defined on top of the SOI wafer. As the Poly-Si surface is the top layer for bonding to InP wafer, this surface must be clean and smooth enough (Roughness < 3 nm) to achieve a proper bonding. Chemical mechanical polishing provides such a smooth Si surface as is shown in Figure 3-a. HF vapor phase etching is used for etching the SiO_2 layer underneath the HCG structure to release the MEMS membrane. Quantum Wells (QWs) as active layers for the MEMS VCSEL are grown on an InP wafer. To have the EC MEMS VCSELs, two AR layers (TiO_2 and SiO_2) are sputtered on the InP. The top layer is SiO_2 which is the bonding surface and must be smooth enough. We optimized the sputtering process to achieve a smooth SiO_2 surface for bonding, Figure 3-b shows the roughness of SiO_2 antireflection layer.

Direct wafer bonding can often be a superior bonding method compared to other techniques like polymer adhesive bonding, eutectic bonding, or anodic bonding, depending on the specific application requirements. Direct bonding can offer several advantages, such as: Improved bond strength, better thermal and mechanical stability, and lower contamination risk. However, direct bonding requires specific surface conditions, including an ultra-clean and smooth hydrophilic surface, and typically requires an intermediate thin layer and an annealing step to form strong covalent links. Al_2O_3 is an excellent choice to be used as the intermediate layer in direct wafer bonding [1]. Figure 3-c shows the direct vacuum bonding yield of a polished SOI wafer stack to an InP wafer with antireflection coating layers on it. In this figure, the InP substrate is removed by wet etching and high bonding yield of antireflection coating layers to SOI wafer is visible.

[1] H. K. Sahoo et al., "Tunable MEMS VCSEL on Silicon Substrate," in *IEEE Journal of Selected Topics in Quantum Electronics*, vol. 25, no. 6, pp. 1-7, Nov.-Dec. 2019.
[3] P. Qiao et al., "Wavelength-Swept VCSELs," in *IEEE Journal of Selected Topics in Quantum Electronics*, vol. 23, no. 6, pp. 1-16, Nov.-Dec. 2017.

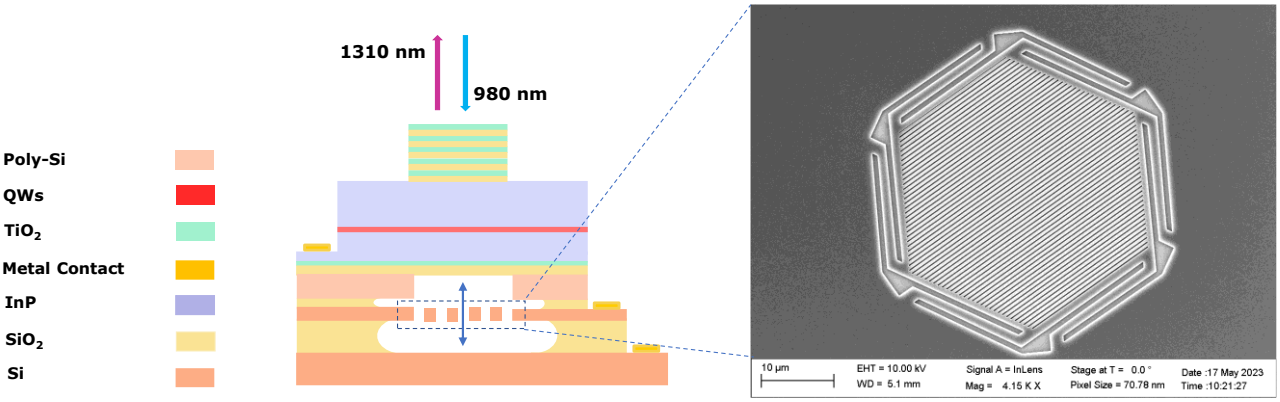

(a) (b)

Figure 1. (a) Cross section schematic of optically pumped MEMS VCSELs and (b) SEM image top view of high contrast grating mirror on Si with .

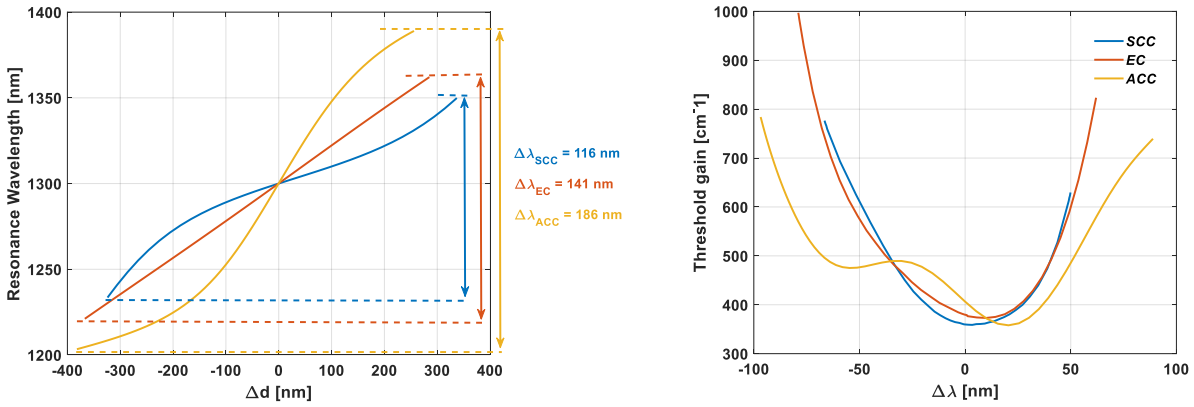

(a) (b)

Figure 2. Device simulation results, (a) Tuning diagrams of the resonance wavelengths as functions of the tuning distances Δd for the SCC (blue), EC (orange), and ACC (yellow) designs. (b) The threshold material gain as functions of the tuning wavelength for all designs.

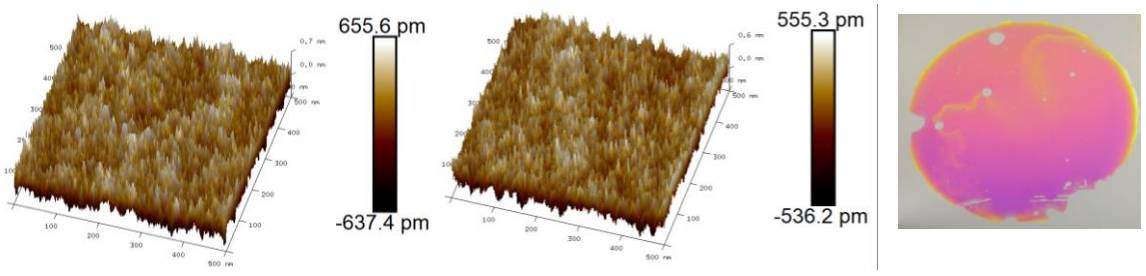

(a) (b) (c)

Figure 3. AFM images showing the surface roughness (Average Roughness, Rq) of (a) LPCVD Poly-Si after the polishing process (0.19 nm) and (b) SiO_2 by the modified sputtering process (0.16 nm). (c) Yield of direct vacuum bonding a SOI wafer (square shape) to an InP wafer (2'') with AR coating layers after removing the InP substrate.

Fabrication of GST metasurface spectral filters using nanoimprint lithography

Jorge Ramiro [a], Aritz Juarros [a], Rocío Ortiz [b], Alazne Martinez [c], Borja Pozo [c]

[a] Surface Chemistry and Nanotechnologies Unit, Tekniker, Eibar 20600, Spain
[b] Plasma Coating Technologies Unit, Tekniker, Eibar 20600, Spain
[c] Electronics and Communications Unit, Tekniker, Eibar 20600, Spain
e-mail: jorge.ramiro@tekniker.es

The electromagnetic radiation received from space objects varies in spectrum with the relative velocity of the object and its temperature, allowing the observation of different types of objects or fragments of objects depending on the range of the spectrum analyzed. For this reason, it is sometimes desirable to collect light within a restricted wavelength spectrum. This can be done by using a selective filter that transmits or reflects the precise range of wavelengths. In this context, an actively tunable filter would allow imaging of the same object in several spectral ranges, each providing different information. Tunable metasurfaces are one of the best solutions for this kind of filters with operation in space as they do not contain mechanical parts that may break or lose accuracy or functionality. These filters incorporate active materials which allow their optical properties to be controlled by an external stimulus. Phase change material, such as chalcogenide glasses are examples of active materials used in this type of devices.

For instance, one of the most successful developments in this field consists in the fabrication of a continuously tunable, all solid-state narrowband phase-change metasurface filter based on a $Ge_2Sb_2Te_5$ (GST) embedded plasmonic nanohole array, which operates across the 3–5 μm thermal imaging waveband [1]. Continuous, reconfigurable tuning was achieved by exploiting intermediate GST phases via optical switching with a single nanosecond laser pulse. The fabrication route in that approach consisted of deposition of a thin layer of Ag, direct-write UV laser lithography of a photoresist, dry-etching of the Ag with an inductively coupled plasma and a final GST deposition step.

In this work, to obtain tunable metasurfaces with work range in the infrared, an alternative route (Fig. 1) has been employed to avoid etching a noble metal (the formation of non-volatile halide products limits the ability to dry etch noble metals with standard equipment and process gases [2]) and to include a more cost-effective technique like the nanoimprint lithography (NIL). Firstly, a thin layer (60 nm) of GST was deposited by magnetron sputtering on a CaF2 substrate. Afterwards, a UV-NIL photoresist (mr-NIL213FC-200nm XP, from Microresist) was spin coated and the UV-NIL step was carried out using a PDMS stamp obtained as a replica of a SiO2 on Si master fabricated by direct-write UV-laser lithography with the desired dimensions (patterning area of 15 mm x 15 mm, hexagonal array of pillars with a diameter of 720 nm and period of 1.8 μm). After etching of the resist residual layer, GST was dry etched using a CHF_3/O_2 chemistry [3] in an Oxford Plasmalab 80+. Subsequently, a 60 nm gold layer was deposited using e-beam evaporation (AJA International. ATC-Orion-8E UHV) and lift-off of the UV-NIL resist was carried out using DMSO.

After cleaning with acetone and IPA, the filter was characterized by SEM showing the homogeneity of the obtained pattern on a large area (Fig. 2) and the good definition of the areas containing the noble metal and the chalcogenide glass (Fig. 3).

References

[1] M.N. Julian et al., Optica 7 (2020) 746-754.
[2] T.S. Choi et al., ECS J. Solid State Sci. Technol. 4 (2014) N3084.
[3] G. Feng et al. Electrochemical and Solid State Letters 10 (2007) D47-D50.

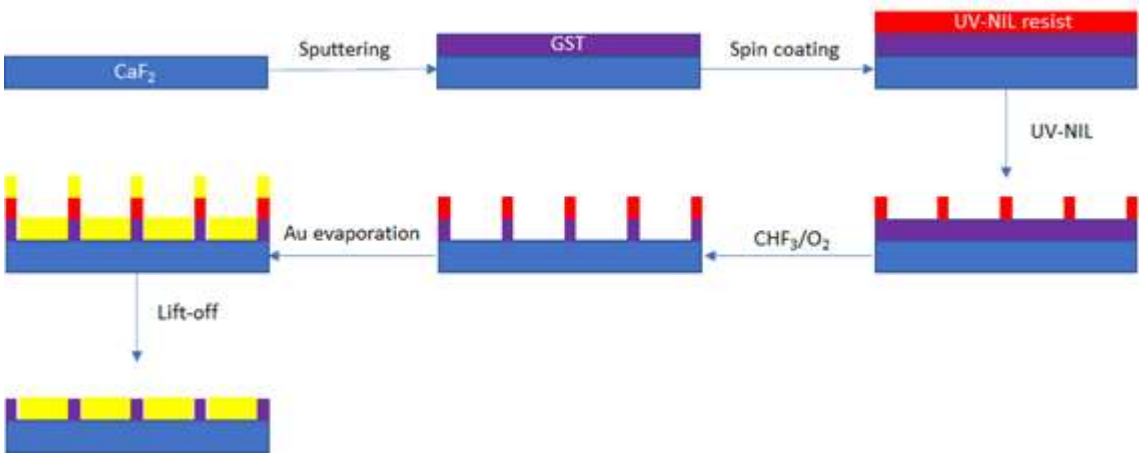

Figure 1. Scheme of fabrication of the metasurface filter based on GST embedded on gold.

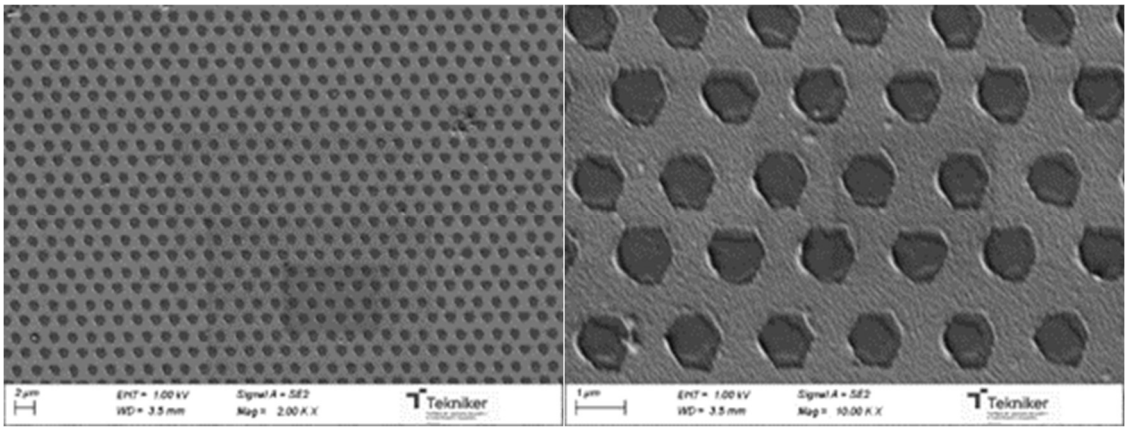

Figure 2. SEM photographs of GST structures embedded on Au.

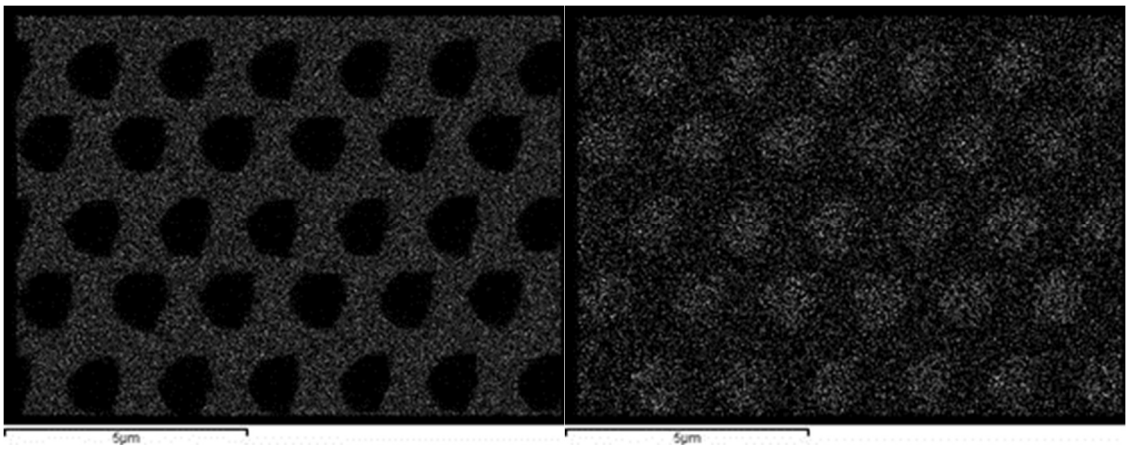

Figure 3. Distribution of the Au element (left) and Te element (right) from EDS/SEM analysis.

Room temperature bonding process of polydimethylsiloxane to titanium for biomedical applications

Lucrezia Maini [a], Roman Furrer [b], Christofer Hierold [a], Cosmin Roman [a]

[a] Micro- and Nanosystems, ETH Zurich, Zurich, 8092, Switzerland
[b] Transport at Nanoscale Interfaces, EMPA, Dübendorf, 8600, Switzerland
e-mail: lucrezia.maini@micro.mavt.ethz.ch

Polydimethylsiloxane (PDMS) is a material widely used in implantable devices due to its high biocompatibility and ease at fabrication.
While bonding of PDMS to glass or to PDMS itself has been developed and optimized, bonding to metals remains challenging and difficult. Most recent literature work shows the applicability of UV curable epoxies, combined with a surface functionalization step, for promoting the adhesion of PDMS on gold [1], [2]. However, while gold is a noble metal, there is limited literature for other types of metals, which are chemically more reactive. An important example with great potential in the biomedical field is titanium. In this case, there are only few precedents where high working temperatures (~1100 °C) are required, in order to promote adhesion [3]. This approach is limited when heat sensitive structures, rather than plain PDMS, are involved (e.g. embedded sensors and/or electrical components). Transferring and bonding of PDMS to titanium at room temperature can enable different applications with PDMS-based sensors, such as flexible electronics and biocompatible encapsulation solutions on prosthetic implants, to name a few.

In this work, we present a new fabrication process for bonding of a flexible acoustic metamaterial membrane made of PDMS (10:1 crosslink ratio) and silicon (Si) micropillars to titanium-grade 5 (see Fig. 1). The potential of the metamaterial membrane as temperature sensor on bone prostheses is explored elsewhere [4]. While this process was partially based on state of the art for bonding of gold and PDMS alone, here we optimized it for titanium, and we demonstrate its applicability at room temperature, with more complex PDMS-based sensors (PDMS-Si 2D metamaterials).

The transfer and bonding process consists of three steps: (1) PDMS activation with oxygen plasma, in order to expose hydroxyl groups; (2) functionalization of the PDMS with (3-Aminopropyl)triethoxysilane (APTES), to have amine groups as mediators; (3) bonding to the titanium substrate, previously coated with a UV-curable epoxy (NOA74). Transfer and bonding of the PDMS metamaterial is effectuated at room temperature. The success of the functionalization step (1) was verified with contact angle measurements between deionized water and the top surface of the PDMS based membrane (see Fig. 2).

As shown in Figs. 1 and 3, the evaluation of the bonding process was performed by scanning electron microscope (SEM) images of the cross section and through high-frequency (50 MHz) ultrasonic measurements [5]. The cross-section shows a uniform distribution of the NOA74 at the interface between the PDMS membrane and the Ti plate, therefore no visible air pockets were qualitatively detectable (see Fig. 1).
The ultrasonic measurements were taken in pulse-echo reflection mode and a 2D spatial map along the z direction of the root mean square (rms) voltage, normalized by the averaged value, was extracted (see Fig. 4). With this method, we were able to analyze the outcome of the bonding and better evaluate the interface between the membrane and the Ti backplate. In the example shown in Fig. 4, some air bubbles were visible in few locations. However, these air bubbles occupy less than 5% of the total surface area of the sample, which do not significantly affect the adhesion process.

[1] M. Agostini et al., APL Materials, 7.8 (2019), 081108.
[2] A. Borok et al., Biosensors, 11.8 (2021), 292.
[3] C.Y.K. Lung et al., Surface Interfac Anal, 47.1 (2015), 105-112.
[4] L. Maini et al., Submitted to Science Advances, 2023.
[5] T. Marhenke et al., IEEE Trans. Ultrason. Ferroelectr. Freq. Control, 67(3) (2020), 651-663.

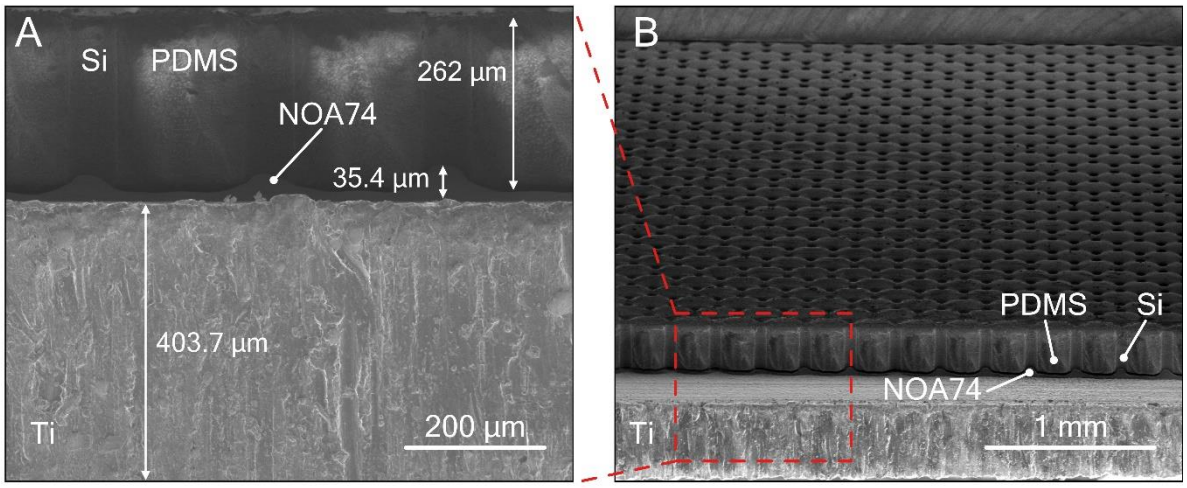

Figure 1. Side view (A) and top view (B) of PDMS based metamaterial membrane on Ti (SEM). The distribution of the NOA74 completely fills the gap in this image, without visible voids.

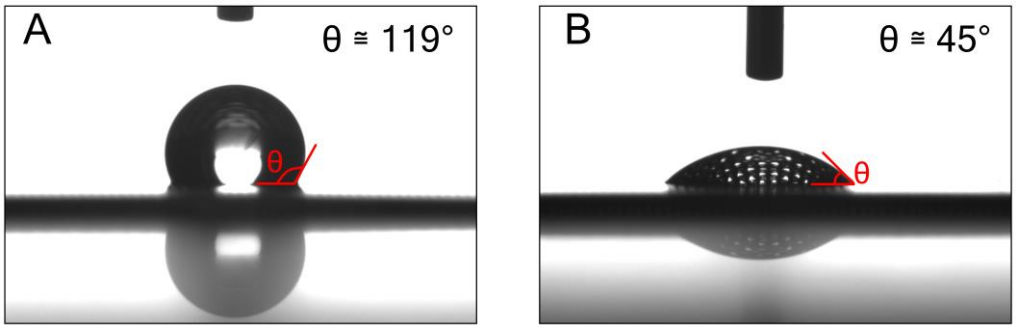

Figure 2. PDMS based metamaterial membrane before (A) and after (B) APTES functionalization; in red, measured contact angle (θ).

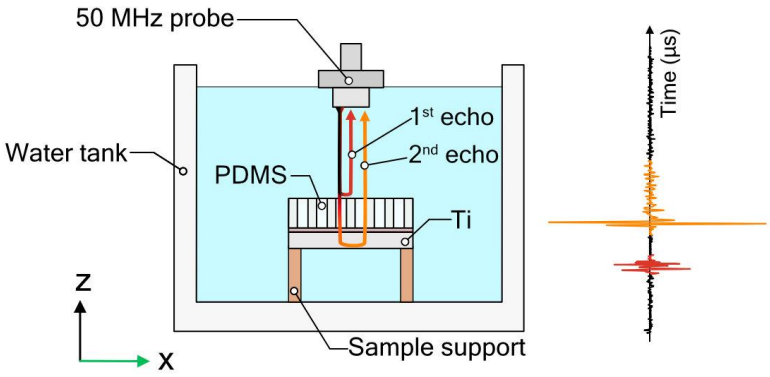

Figure 3. Ultrasonic set-up and recorded echoes for assessment of bonding technique to Ti.

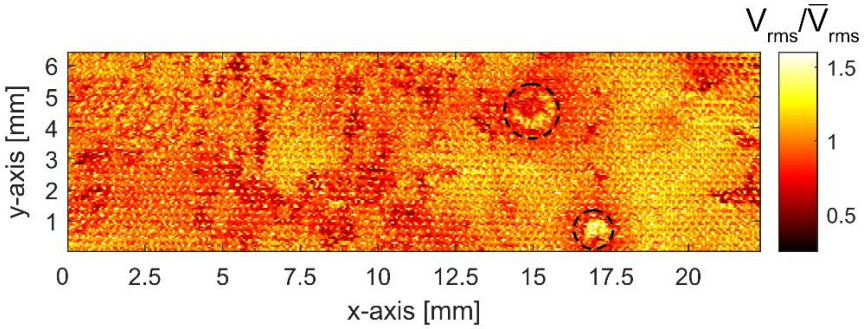

Figure 4. C-scan example of metamaterial surface close to Ti interface showing the ratio of the rms of the recorded voltage with the averaged value ($V_{rms}/\overline{V}_{rms}$), in reflection. Air-bubbles are distinguishable (dashed black circles), yet they occupy less than <5% of the sample area.

Scalable meta-projector for wide viewing angle 3D imaging

Gyeongtae Kim [a], Yeseul Kim [a], Jooyeong Yun [a], Junsuk Rho [a,b,c,d]

[a] Department of Mechanical Engineering, Pohang University of Science and Technology (POSTECH), Pohang, 37673, Republic of Korea
[b] Department of Chemical Engineering, Pohang University of Science and Technology (POSTECH), Pohang 37673, Republic of Korea
[c] POSCO-POSTECH-RIST Convergence Research Center for Flat Optics and Metaphotonics, Pohang, 37673, Republic of Korea
[d] National Institute of Nanomaterials Technology (NINT), Pohang, 37673, Republic of Korea
e-mail: jsrho@postech.ac.kr

Unlike conventional cameras that obtain only 2D intensity information of objects, technology that can obtain 3D information of surrounding objects is expected to play an important role in next-generation computer vision. Depending on the purpose of use, it is evaluated for its performance such as accuracy, resolution, recognition speed, distance, and viewing angle, and various types of depth recognition cameras have been developed. Among them, the viewing angle is a very important performance in autonomous robots, augmented and virtual reality glasses, that require three-dimensional information of objects located in a wide area ahead. Lidar and multi-camera methods have been used for wide-angle three-dimensional imaging. A lidar is a method of measuring the distance from the round-trip flight time of light by scanning a laser light source, requiring a pulse laser, a very sensitive sensor, and a mechanical or electronical scanning device [1]. The multi-camera method, based on binocular parallax, is preferred at personal distance within 3~5 meters, but there is a disadvantage in that depth reconstruction performance is low for low-light environments and texture-less planes. With the aid of additional illumination module, it is reported that the projected light patterns can be used to reduce artifact in depth reconstruction by engraving virtual texture on texture-less objects [2]. However, conventional projector based on spatial light modulators (SLMs) and diffractive optical elements (DOEs) are suffer from limited projection angle due to their large pixel size, where diffraction angle is inversely proportional to pixel pitch.

Metasurfaces, arrays of subwavelength nanostructures, are getting attention for their extraordinary light manipulation performance demonstrating potentials in wide range of flat optical applications, such as lenses, holograms, and beam steering devices. Here, we propose a metasurface-based projector, i.e., meta-projector, to illuminate wide viewing angle without scanning, in specific ~10K dot array over 180° (Figure 1). The metasurface is composed of periodic supercells, where each supercell is composed of array of anisotropic nanopillars with different in-plane rotation angle. Such geometrically birefringent nanopillars exhibiting strong light confinement are capable of producing designed phase retardation which is twice the in-plane rotation angle. The phase retrieval problem is conducted on spatial frequency domain which corresponds to the far-field propagation pattern. The designed frequency domains are spanning over every propagatable regime excluding evanescent regime with the aid of subwavelength pixel pitch of metasurface, satisfying Nyquist sampling theorem. The repeated supercells play an important rule to sample the continuous spatial frequency into discretized dot-like patterns over 180°. As a proof-of-concept, we reconstruct the depth from binocular parallax using stereo camera setup. With the aid of proposed meta-projector, the depth information of the face masks at wide viewing angle is reconstructed (Figure 2). Notably, we demonstrate low-cost production of meta-projector using nanoimprint lithography (Figure 3). Once the meta-projectors are transferred to PDMS-based soft mold, the coated UV-curable resin itself can be used as meta-projector structures. However, the discrepancy of efficiency is severe due to weak light confinement. Therefore, we embedded high-index nanoparticles into UV-curable resin to enhance light manipulation efficiency. Such a high-throughput and high-efficiency meta-projector on any arbitrary substrates shows its potential towards compact 3D imaging device [3].

[1] J. Park et al., *Nat. Nanotechnol*. **16**, 69-76 (2021)
[2] S.-H. Baek et al., IEEE/CVF CVPR, Nashville, TN, USA, 5753-5763 (2021).
[3] G. Kim et al., *Nat. Commun*. **13**, 5920 (2022)

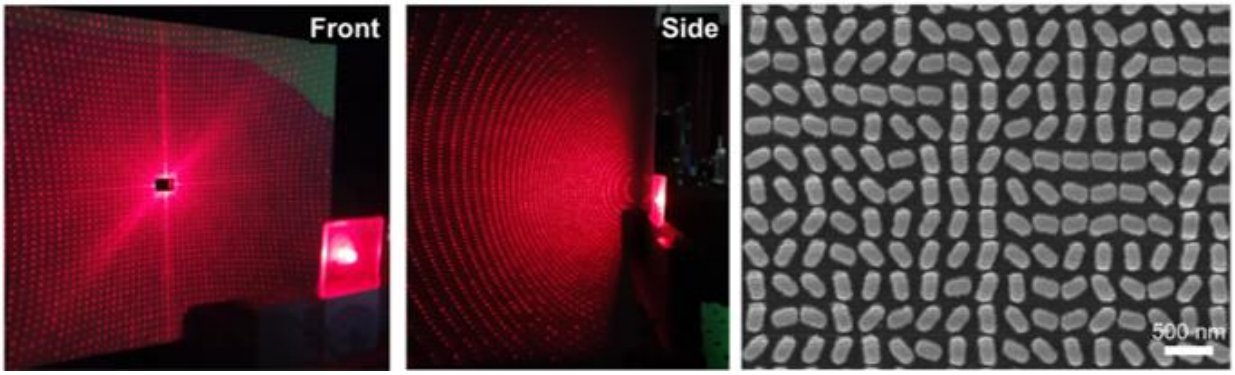

Figure 1. Metasurface-based projector illuminates ~10K points over the entire 180° angle.

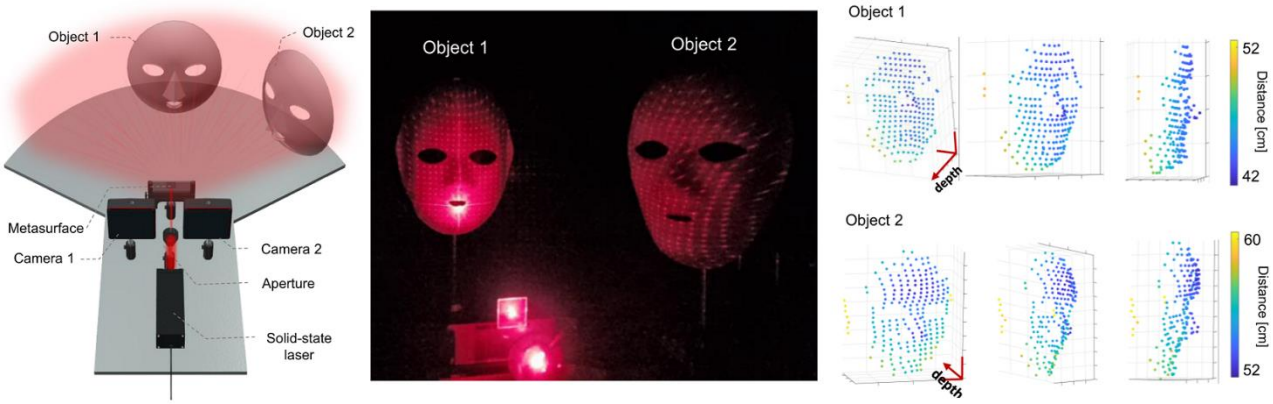

Figure 2. Metasurface-assisted stereo 3D imaging system and reconstructed depth map.

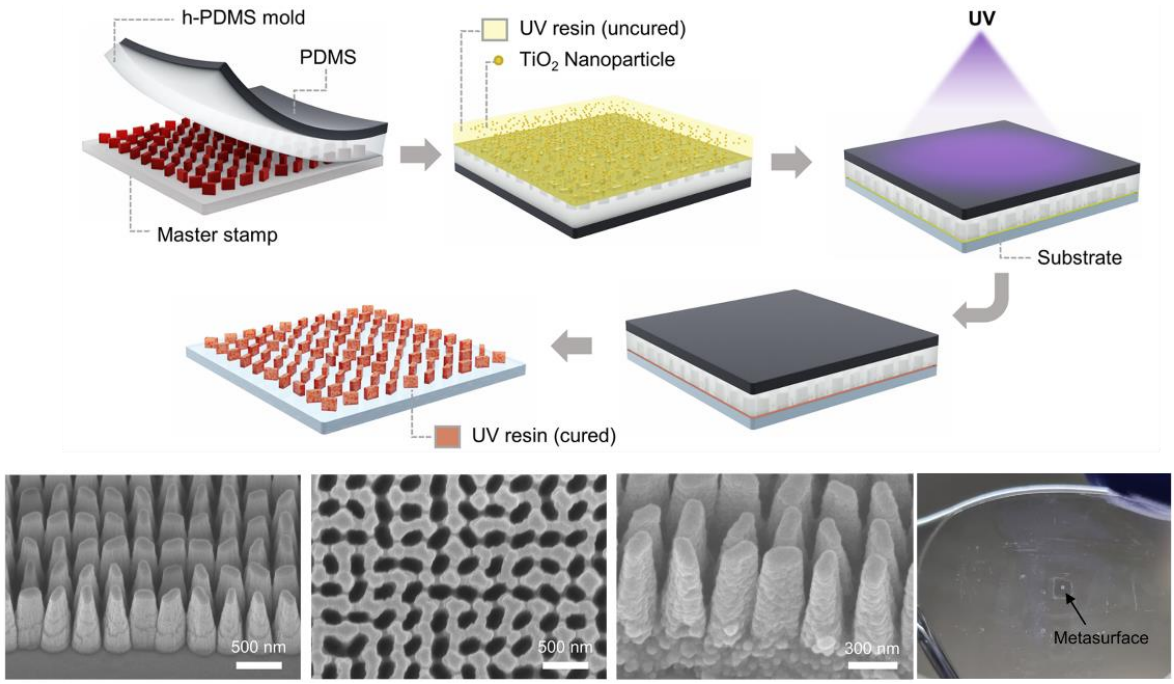

Figure 3. High-throughput fabrication of metasurfaces with nanoparticle-embedded-resin-based imprinting.

Quantitative characterization of nanowire verticality using SEM images

E. Stai[a,b], V. Constantoudis[a,c], D. Nioras[a,d], E. Gogolides[a,c],

[a] Institute of Nanoscience and Nanotechnology, NCSR Demokritos, Aghia Paraskevi 15341, Attiki, Greece
[b] Department of Physics, National and Kapodistrian University of Athens, Athens, Greece
[c] Nanometrisis p.c., Agia Paraskevi, Attiki 15310, Greece
[d] Physics Department, National Technical University of Athens, Zografou Campus, Athens, Greece
e-mail: e.stai@inn.demokritos.gr

During the last few decades, nanowires have been used in various fields of applications from electronics and photonics[1] to bio-devices[2] and energy harvesting systems. One of the critical properties of nanowire patterns is their alignment since it tunes the contact area with the attached body and hence the kind of the interaction that nanowires have with them. For example, when they are perfectly vertical, the contact area with the attached droplet or bacteria is minimized leading to the enhancement of their superhydrophobic or bactericidal behavior. Therefore, the quantitative characterization of nanowire verticality can empower the evaluation of their performance in many applications.

The main technique used for the inspection of nanostructured surfaces is Scanning Electron Microscopy (SEM) which however suffers from the fact that depicts a 3D surface as a 2D image. Hence, it is not a straightforward task to quantify the verticality of the nanowires on a surface (which is a 3D feature) by using SEM images (which is 2D). The obvious solution is to obtain and inspect cross-section SEM images. This can cause damage on the depicted nanowires and also usually cannot provide sufficient statistical data for reliable conclusions.

In this work, we propose a novel methodology for characterizing quantitatively the verticality of nanowires (NWs) by analyzing top-down or tilted SEM images. The key idea of our approach is to exploit the link between the verticality of nanowires and the anisotropy of their projection on SEM images. The depiction of a fully vertical NW with cylindrical shape on a top-down SEM image is isotropic since it has the circular shape of its cross-section. When it is declined from verticality, SEM image also shows a part of its axis indicating local anisotropy. Therefore, the deviation from full verticality can be quantified by an index characterizing the anisotropy of NW spots on top-down SEM images (see Fig.1). On the other side, we can also use titled SEM image for verticality characterization. In this case, the anisotropy of SEM images is correlated positively with the NW verticality. When NWs deviate from verticality and exhibit a spectrum of slopes and shapes, the anisotropy of their spots on images is reduced or even eliminated. By computing the 2D Fourier Transform (FT) of the SEM images, we can measure the anisotropy of the low-frequency part of FT to quantify the degree of nanowire verticality. In particular, we pose a threshold on FT values and identify the low-frequency region in 2D Fourier space with Fourier amplitudes higher than this threshold. The anisotropy ratio A is calculated by dividing the lowest radius of this region over the biggest one. In top-down SEM images, when $A<1$ we have anisotropic FT, quantifying the degree of deviation from full NW verticality. On the other hand, A close to 1 means that FT and therefore the SEM image are isotropic concluding better NW verticality. In the case of tilted SEM images, the inference process is conversed: $A<1$ means surface anisotropy and therefore NW verticality whereas A close to 1 leads to the conclusion that NWs deviate from verticality.

The above-described methodology can be also applied in the case we want to identify the presence of vertical-like NWs or their damage. The damage of NWs can be quantified by an decrease of A from 1 to less than 1 values in top-down SEM images. Alternatively, in tilted SEM images the NW damage is marked by a transition towards higher A values close to 1.

In Figure 2 there is an application of the method that uses tilted SEM images shown PMMA surfaces with nanowires after plasma etching for 10min before (a) and after immersion in water (b). One can clearly notice the increase of A from less than 1 value to 1 extracted by the analysis of 2D Fourier spectrum shown in c) and d) respectively which indicate the damage of NWs after water immersion.

[1] S. Chang, G. Lee, Y. Song, Recent Advances in Vertically Aligned Nanowires for Photonics Applications, Micromachines. 11 (2020) 726. https://doi.org/10.3390/mi11080726.
[2] M. Lard, H. Linke, C.N. Prinz, Biosensing using arrays of vertical semiconductor nanowires: mechanosensing and biomarker detection, Nanotechnology. 30 (2019) 214003. https://doi.org/10.1088/1361-6528/ab0326.

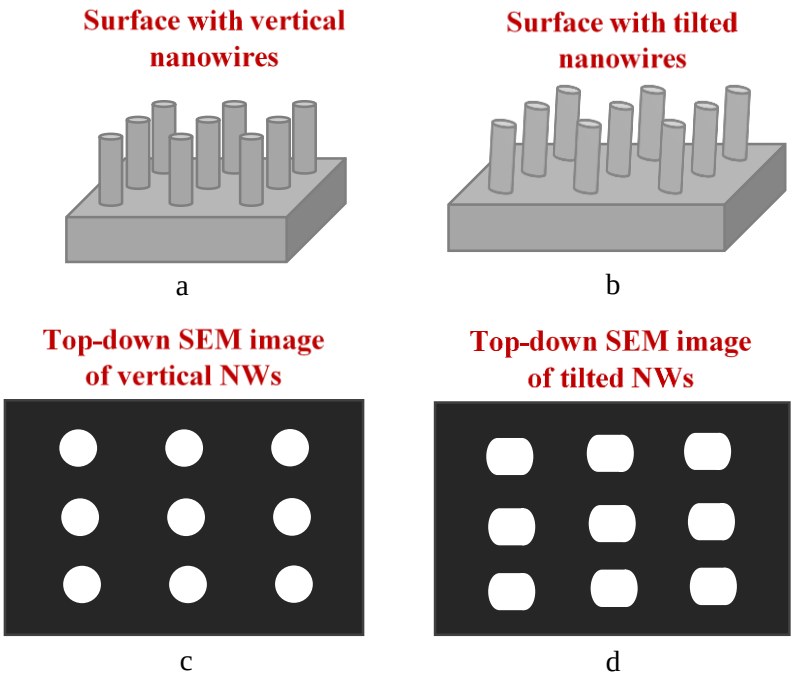

Figure 1. Schematic representation of the key idea of the proposed methodology: In a) we show a pattern with vertical NWs, while in b) with tilted NWs. In c) and d) the depictions of these surfaces in top-down SEM images are shown respectively demonstrating the link of NW verticality with image anisotropy.

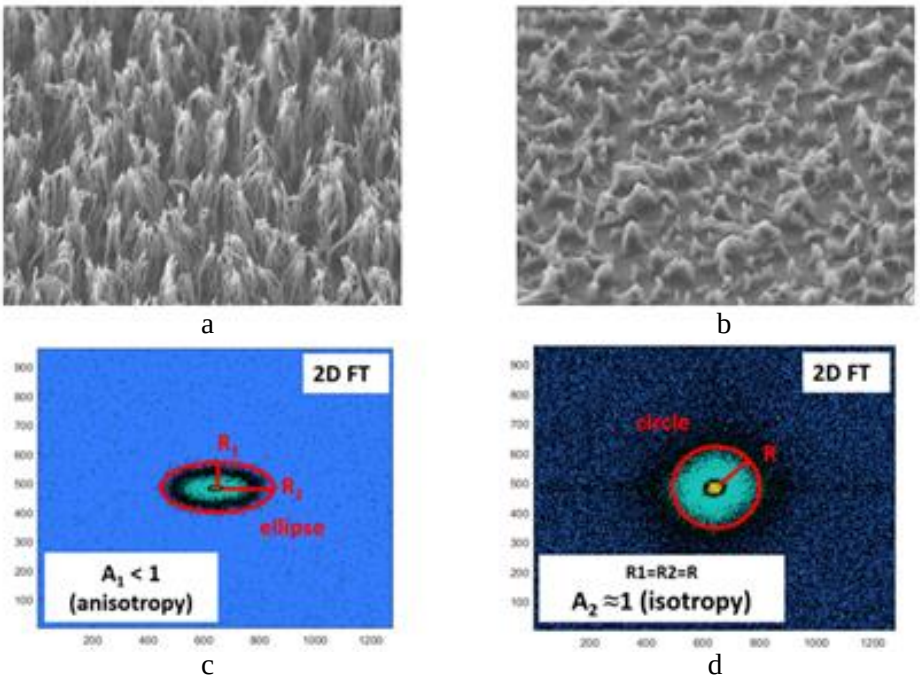

Figure 2. Tilted SEM images shown PMMA surfaces with nanowires after plasma etching for 10min before (a) and after immersion in water (b). In c), d) the 2D Fourier spectra of a) and b) SEM images are displayed accordingly. One can clearly notice the increase of A from A_1 <1 value to $A_2 \approx 1$ extracted by the analysis of shown in c) and d) respectively.

Acknowledgement
This work has been funded by the ERANET Project 'Carbyne Films: Synthesis of a New Class of Carbon Allotrope and Novel Applications in Sensors and Biosensors (CarbyneSense)', MIS 5161208.

Influence of the combination of ordered 2D and random 3D structures on the reaction of Al/Ni multilayer

K. Jaekel [a], Y.H. Sauni Camposano [b], S. Matthes [b], P Schaaf [b], J. Müller [a], H. Bartsch [a]

[a] Technische Universität Ilmenau (TU Ilmenau), Department of Electrical Engineering and Information Technology Gustav-Kirchhoff-Str. 1, 98693 Ilmenau, Germany
[b] Technische Universität Ilmenau (TU Ilmenau), Chair Materials for Electrical Engineering and Electronics, Institute of Materials Science and Engineering, TU Ilmenau, Gustav-Kirchhoff-Str. 5, 98693 Ilmenau, Germany
e-mail: konrad.jaekel@tu-ilmenau.de

Reactive multilayer (RML) or reactive nanolaminates, are regarded as reactive materials consisting of alternating layers of different elements or alloys. The primary characteristic of RMLs is their ability to release stored chemical energy in an exothermic, self-sustained and self-propagating reaction when stimulated by an external energy source, such as heat, mechanical pressure, or an electrical pulse. The stored energy is released during a phase formation which is leading to rapid heat generation and high temperatures. How the propagation and heat release is influenced by the multilayer parameters, like bilayer spacing, total thickness, atomic ratio and intermixed zone, is already widely studied and published [1]. The heat dissipation as a function of the substrate surface quality is another parameter, which can be used to control the reaction propagation [2].

The presented work exploits the effect of surface structure and substrate thermal properties on the reaction kinetics. A combination of KOH etched lines and black silicon (bSi) is applied on the surface. The combination of KOH etching to create 2D lines in Si <100>, along with a subsequent bSi process to generate 3D nanostructures, offers a unique platform for understanding the interplay between structure morphology and reaction dynamics. To fabricate the samples, (100)-oriented Si wafers were used as substrates. A patterned SiO2 mask, obtained using thermal oxidation, lithography, and reactive ion etching (RIE), enabled the generation of well-defined line widths of 30 µm, 50 µm, and 80 µm respectively, as well as different orientations to the main flat (Figure 1a, left side). Three sets of samples with different line depths, around 250 nm, 720 nm, and 1600 nm, were prepared. Two samples, featuring each depth of 250 nm and 720 nm, were produced, while the sample with 1600 nm deep valleys was a single sample. The KOH etched samples were then subjected to a bSi process, which produced 3D nanostructures on the Si surface, visible in Figure 1a, right side. This process was applied for respectively 30 min or for 60 min on a sample with 250 nm and 720 nm deep line structures. The wafer with 1600 nm depth was processed 30 min in this RIE process. bSi formation introduces surface roughening on the nanometer scale additional to the line structure in micrometer scale on to the sample. Following the formation of the nanostructured bSi surface, the samples were subjected to thermal oxidation to create a 1 µm thick oxide layer. This oxide layer served as a thermal insulation layer and facilitated a reaction of the subsequent deposited Al/Ni RMLs. Both, the oxide layer and the deposited RMLs are shown in Figure 1b.

Our analysis focused on assessing the reaction behavior of the samples through controlled ignition experiments. The ignition of the Al/Ni RML was achieved through an electrical stimulation, triggering the self-sustained reaction of the reactive layers. By monitoring reaction propagation with high-speed camera (FASTCAM SA-X2 type 480k, Photron) and measuring temperature curves with high-speed pyrometer (KGA series 840, Kleiber), we evaluated the influence of the surface morphology on the reaction kinetics. The depth of the 2D line structures exhibited interrupting effect on the reaction propagation, see Figure 2. The presence of 3D nanostructures on the Si surface resulted in improved adhesion of the reacted multilayers, specifically for the 60 min processed samples, visible in Figure 2. The reaction velocity, and the maximum temperature decreased in comparison to the Al/Ni reaction of free-standing multilayers [3].

Our findings provide valuable insights a new control parameter: the use of surface designing of a tailored reaction kinetics of Al/Ni RML systems. The changed reaction behavior observed in our study holds promise for the development of advanced reaction control, and structuring as a new tool for stopping the reaction propagation. Further investigations are under way to fully comprehend the underlying mechanisms and optimize the design of nanostructured surfaces for improved performance in various applications.

[1] S.Q. Arlington et al., Annu. Rev. Mater. Res. 52 (2022) 219–248.
[2] B. Liu et al., Applied Surface Science 546 (2021) 1–19.
[3] K. Jaekel et al., Effect of line structures on the self-propagating reaction of Al/Ni multilayer, in: 2022 IEEE 9th Electronics System-Integration Technology Conference (ESTC), Sibiu, Romania, IEEE, Piscataway, NJ, 2022, pp. 379–382.

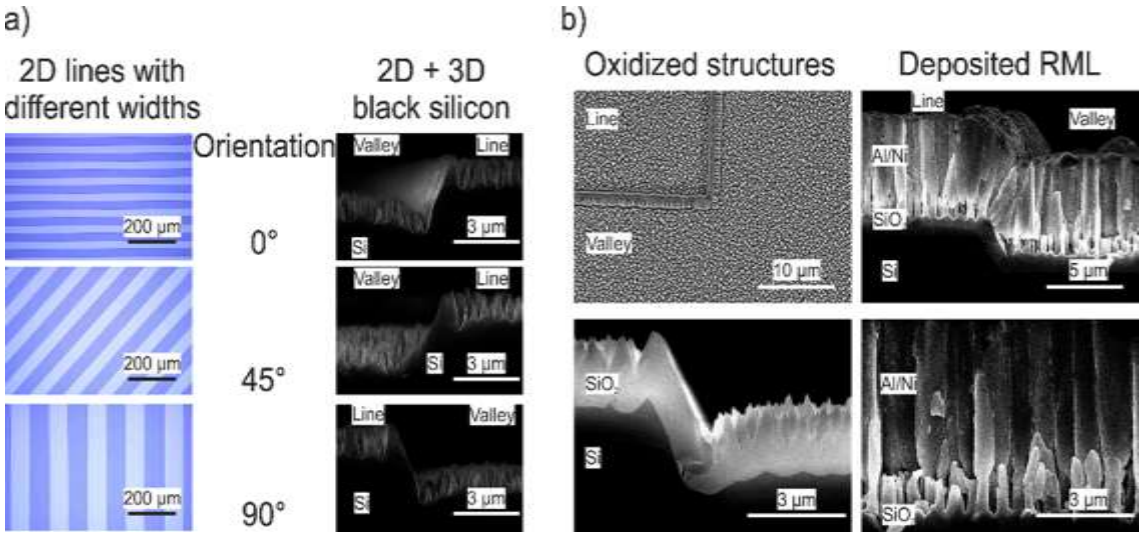

Figure 1. a) Top view of line structures with 30 µm ,50 µm and 80 µm widths and the three orientations 0°, 45° and 90°, as well as cross-sections of the combined 2D and 3D structures. b) Top view and cross-section of the oxidized structures and a side view of the Al/Ni multilayers deposited on the structures.

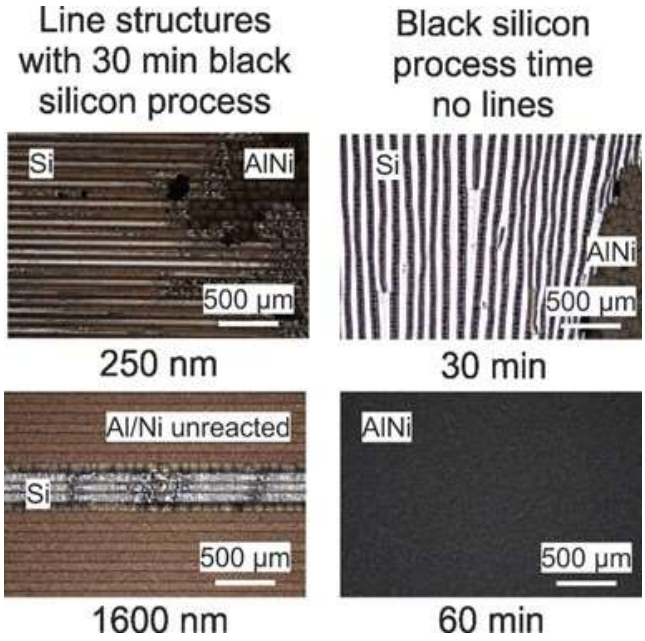

Figure 2. Light microscope images after the reaction of the Al/Ni multilayers showing the effect of different line depths and black Si process time.

A Simple Fabrication Process for the Integration of Microfluidics on Si based Biosensors

M.K. Filippidou [a], A.I. Kanaris [a], E. Aslanidis [b], A. Rapesi [b, c], S. Ntouskas [a], E. Skotadis [b], G. Tsekenis [c], D. Tsoukalas[b], A. Tserepi [a], S. Chatzandroulis [a] *

[a] Institute of Nanoscience and Nanotechnology, NCSR ''Demokritos'', Aghia Paraskevi 15310, Greece
[b] Department of Applied Sciences, National Technical University of Athens, Zografou 15780, Greece
[c] Biomedical Research Foundation of the Academy of Athens, Athens 11527, Greece
e-mail: s.chatzandroulis@inn.demokritos.gr

Microfluidics technology is the basic technology used to realize Lab-on-Chips (LOCs), such as microlaboratories exhibiting several advantages including small sample volume, reduced analysis time, low manufacturing cost, greater sensitivity, and portability [1, 2]. One of the fields in which LOC devices are particularly useful is environmental monitoring and water pollution caused by heavy metal ions, pesticides or other contaminants which can easily pass in the human food chain. Thus combining of miniaturized microfluidic systems, with the appropriate detection scheme is a very promising tool for water safety and detection of water pollutants [3].

Despite the great progress in the field [4], the biggest challenge is still the integration of all the necessary components (e.g. microfluidic channels, detection unit, heating elements, electrical connections, etc.) for the operation of the device on the same substrate targeting the realization of a completely autonomous Lab on Chip device which is lightweight, portable, low cost and can be used in both laboratory and on-site measurements. The solution can be provided by combining microfluidics technology and electrochemical sensing. To this end, we present a rapid and simple fabrication method based on photolithography of dry photosensitive layers (dry resist) for the integration of a microfluidic channel network with an electrochemical detection scheme for the detection of water pollutants (e.g heavy metal ions).

In particular, silicon (Si) substrates, on which an insulating layer of silicon dioxide (SiO_2) 3000 Å thick is thermally grown, are used to implement the microfluidic device, while the microchannel of the proposed microfluidic device has a unit (square wave channel with two inputs: one for the sample and the second for the buffer solution) for the passive mixing of the sample with the buffer solution and a detection unit which includes an array of biosensors. The microchannel fabrication process, is the following: first an array of six IDEs is deposited on a Si/SiO_2 substrate, consisting of an adhesive 10 nm thick Ti layer and 40 nm thick Au layer. The IDEs are patterned through lithography having inter-finger spacing of 10μm. Afterwards, a 1st layer of a dry resist film, approximately 80 μm thick, is deposited on the Si/SiO_2 substrate using a laminator, with its temperature adjusted at 105 °C (Fig 1a step A). The device is then heated for 1 hour at 90 ^{o}C, while after this step the device again passes through the laminator under the same conditions as before to deposit the 2nd layer of dry resist (Fig 1a step B). After the photolithography step (exposure for about 1 min and immersion in the appropriate developer for about 10-15 minutes inside an ultrasound bath), the patterning of the microchannel is achieved (Fig 1a step C). The device is then heated at 130 °C for approximately 1h and the microfluidic device is ready to be used (Fig 1b) after the fabrication of the biosensors and sealing (a polyolefin film coated on one side with a silicone adhesive).

The biosensors are realized as six pairs of Au interdigitated electrodes (IDEs) on which platinum nanoparticles (PtNPs) are deposited followed by immobilization of the DNAzymes. The PtNPs have a mean diameter of 4 nm and are deposited between the IDEs using a modified DC magnetron sputtering system that allows the control of the surface density covered by the PtNPs. The surface coverage of the PtNPS is close to 49%, which results in an interparticle distance of few nm. The biosensor operation principle is based on the fact that the presence of pollutants (e.g. metal ions) will lead to the cleavage of the DNAzyme double strand which will result to a resistance change thus enabling detection.

As a proof of concept, real time detection of Pb^{2+},which is is one of the most dangerous heavy metal ions, with a concentration down to 5 μM, is shown in Fig 2a. In Figure 2b the microfluidic device inside the chip holder ready to be used is presented. The proposed fabrication method is highly flexible and easy and is easily transferrable to other applications.

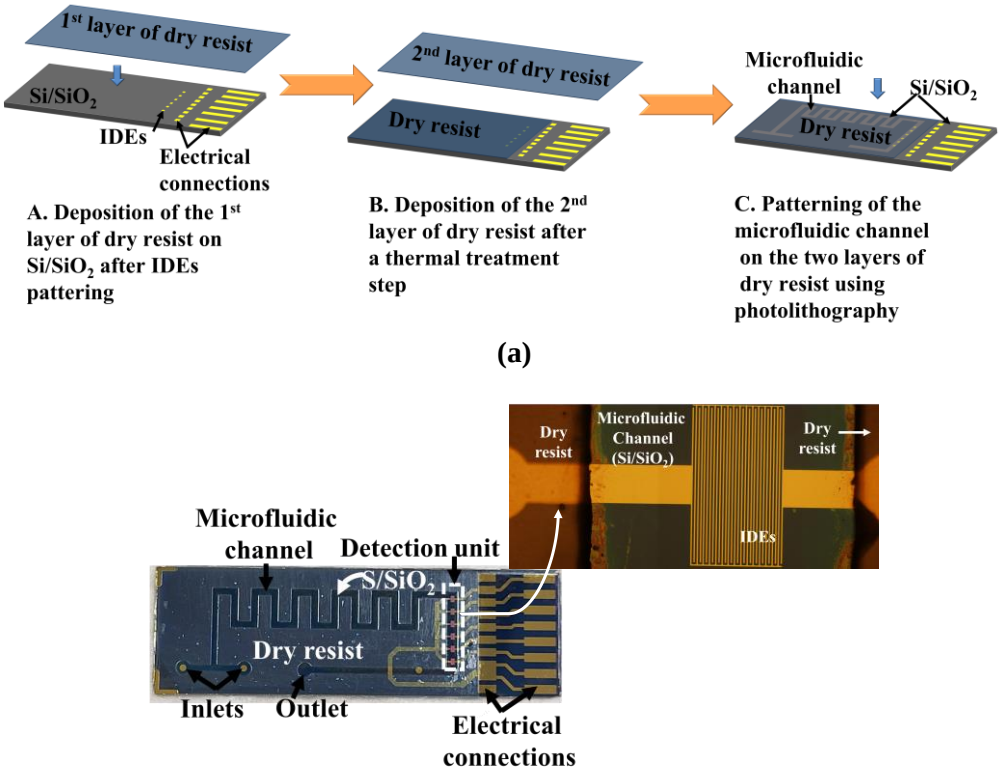

Figure 1. (a) Schematic representation of the fabrication process of the microfluidic device on Si/SiO_2 substrates, where 2 layers of dry resist are used for the patterning of the channel. **(b)** The image of the final device is also depicted. Inset: optical microscopy image of the IDEs inside the microfluidic channel (10 x magnification

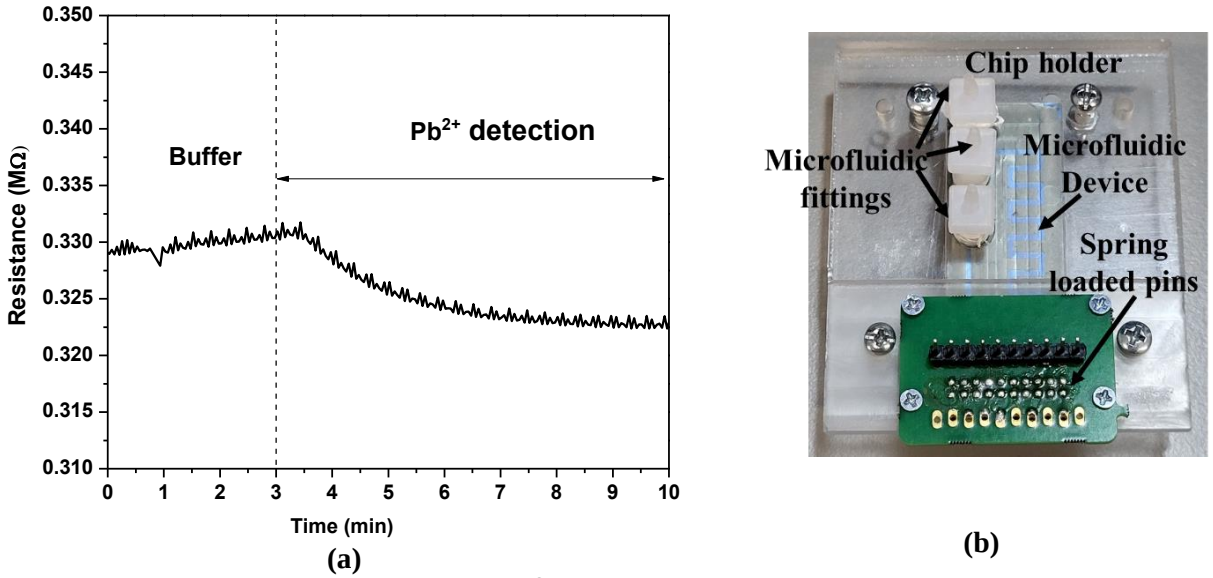

Figure 2. (a) Real time measurement of Pb^{2+} using the proposed PtNPs/DNAzyme biosensor. **(b)** The microfluidic device inside the chip holder ready to be used. The spring loaded pins used for the electrical measurement are also depicted.

[1] H. Becker and C. Gärtner, part of the Methods in Molecular Biology book series (MIMB,volume 1547) (Clifton, N.J.) (2017) 3-21.
[2] G. Luka et al., Sensors 15 (2015) 30011-30031.
[3] V. Karthik et al., Chemosphere 299 (2022) 134427.
[4] P.K. Rai et al., Sens. Actuators A: Physical 347 (2022) 113926.

Investigation on the effect of sharp corners of AZO gate and Al_2O_3 insulator in ZnO Thin Film Transistors

J. Zeng [a], B.D. Rowlinson [a], M. Ebert [a], K. Kalna [b], C. Patzig [c], L. Berthold [c] and H.M.H. Chong [a]

[a] School of Electronics and Computer Science, University of Southampton, SO17 1BJ, UK
[b] NanoDeCo Group, Dept. of Electronic & Electrical Engineering, Faculty of Science & Engineering, Swansea University, SA2 8PP, UK
[c] Fraunhofer Institute for Microstructure of Materials and Systems, 06120 Halle (Saale), Germany
e-mail: jz2g19@soton.ac.uk

Introduction

Sharp corners in a MOSFET architecture can produce a localised high electric field that causes a loss of gate control, a threshold voltage (V_{TH}) shift, and a gate oxide dielectric breakdown [1]. One of the possible gate oxide dielectric breakdown phenomena can be explained by the percolation model, which states that local insulator materials could become conductive when subjected to a high electric field [2-4]. Our previous research on ZnO thin-film transistors (TFTs) [5] showed a gate leakage current of 2.7 µA and the loss of gate voltage bias control beyond a drain voltage of 9 V, both of which indicate gate oxide dielectric breakdown characteristics. In this work, we combine the experimental results of our ZnO TFTs with a simulation study of the fabricated gate structure to determine the gate oxide dielectric breakdown.

Fabrication

The ZnO TFT (Fig. 1. (a)) is fabricated on a 150 mm wafer with a 100 nm thermally grown oxide. A 40 nm layer of 5% Al-doped ZnO (AZO) is deposited by thermal atomic layer deposition (ALD) at 175℃, a HCl wet-etching process is used to define the bottom-gate electrode. A 30 nm Al_2O_3 gate insulator and a 40 nm ZnO channel layer are contiguously deposited by plasma-enhanced ALD (PEALD), without breaking vacuum. Both layers are patterned by wet etching. The passivation layer, a 30 nm Al_2O_3, is deposited by PEALD at 150℃. Source/drain (S/D) vias are selectively wet etched [6]. A 40 nm layer of 2% AZO is deposited by thermal ALD to act as S/D contacts. Finally, 100 nm evaporated Al is lifted off as the S/D electrodes.

Results

The transmission electron microscopy (TEM) image (Fig. 1. (b)) shows gate sharp corners (blue dotted area). Wafers are immersed in deionized (DI) water after the etching process. The undesired undercut is created by the diluted etchant solution repeatedly etching the gate. The I_{DS}-V_{GS} characteristics (Fig. 2. (a)) shows that the gate is losing control of channel conduction with increasing drain voltage and, finally, the transistor characteristic diminishes at a drain voltage of 15 V. The corresponding gate leakage current, I_{GS} (Fig. 2. (b)), is 2.7 µA. By comparing the simulation of TFT (Fig. 3. (a)), the rectangle gate) and with the real experimental TFT (the gate with sharp corners), the rectangle gate model shows a $-4\ V$ threshold voltage (V_{TH}) shift. Through simulated electric field distribution (Fig. 3. (b-c)), the formation process of the percolation leakage path is observed, and the breakdown voltage can be predicted from the simulation. The typical breakdown field value for PEALD Al_2O_3 is 9 ± 0.5 MV/cm [7]. Because of the sharp gate corners in the TFT, the simulation result shows that the breakdown field of our PEALD Al_2O_3 is only 5 MV/cm. The sharp gate corner induced breakdown of 24 V is predicted to be 70 V in the TFT without the sharp gate corner (Fig. 2. (d)), which is a substantially larger breakdown voltage.

Conclusions

Gate sharp corners induce a strong electric field into the local dielectric layer, resulting in a loss of gate control and a threshold voltage shift. The simulations also predicts that the TFT operates up to 70 V without the sharp corner of the AZO gate.

[1] F. Palumbo, et al., Adv. Funct. Mater., vol. 30, no. 18, pp. 1900657, (2020)
[2] L. Ji, et al., Nature Materials, vol.16, no. 1, pp. 127–131, (2017)
[3] X. Li, et al., Appl. Phys. Lett., vol. 93, no. 7, pp. 072903, (2008)
[4] N. Raghavan, et al., Microelectron. Reliab., vol. 54, no. 55, pp. 847-860, (2014)
[5] B. D. Rowlinson, J. Zeng, H. M. H. Chong, et al., MNE 2022, Leuven, Belgium, (2022)
[6] B. D. Rowlinson, H. M. H. Chong, et al., MNE 2021, Turin, Italy, (2021)
[7] K. B. Jinesh, et al., J. Electrochem. Soc., vol. 158, no. 2, pp. G21, (2011)

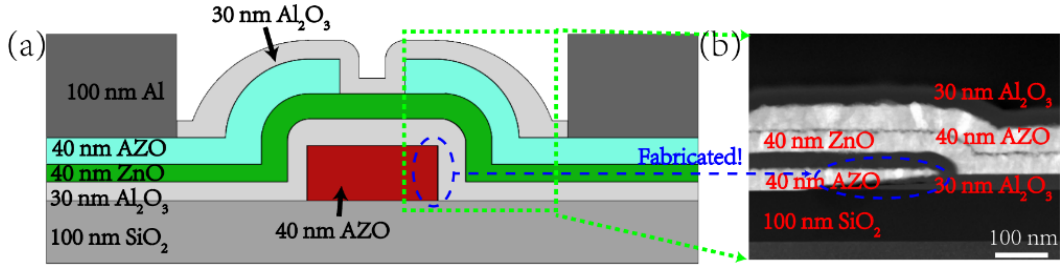

Figure 1. (a) Schematic of the ZnO Thin-Film Transistor (TFT) (W/L = 50/3 μm). A green dotted area indicates the area of the TEM cross-section view **(b)** that shows gate sharp corner structure (blue dotted).

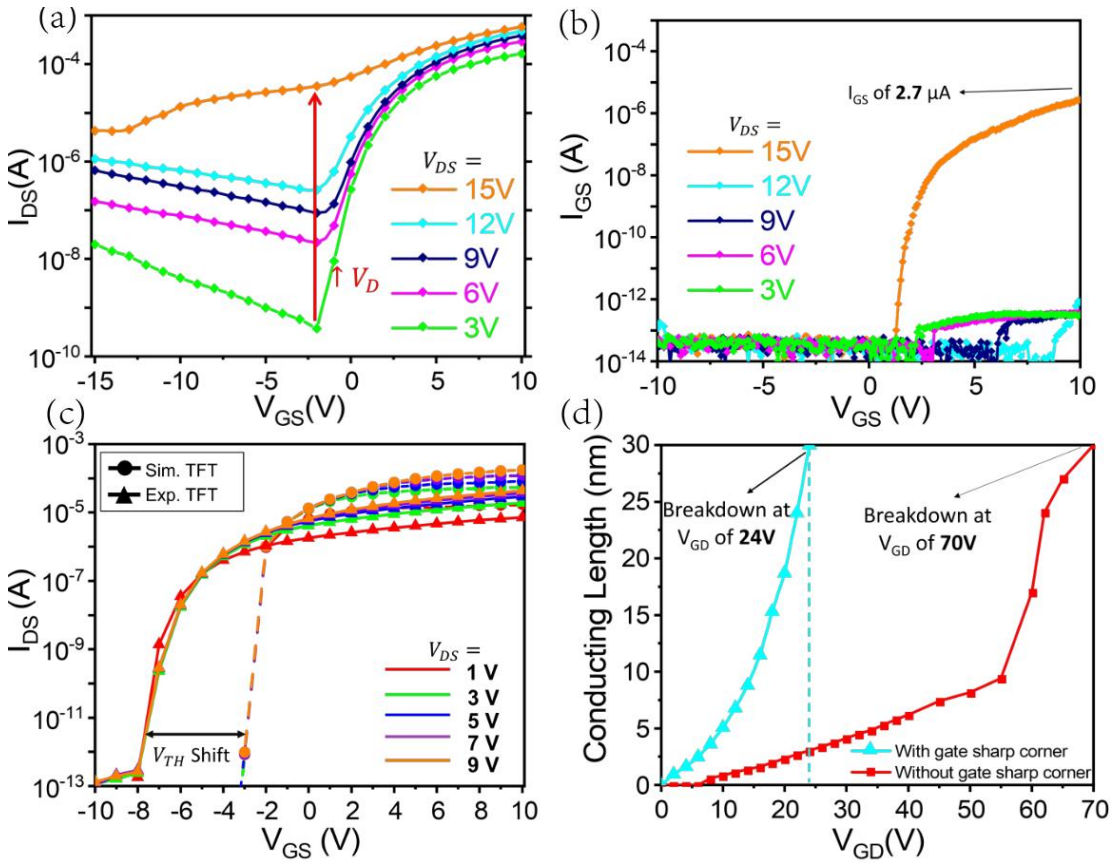

Figure 2. (a) V_{GS} against I_{DS} characteristics at indicated V_{DS}. **(b)** Gate leakage current, I_{GS}, against V_{GS} at indicated V_{DS}. **(c)** I_{DS}-V_{GS} characteristics comparing simulations and experimental data. **(d)** The simulated conducting length versus V_{GD} predicting a breakdown voltage in the TFT.

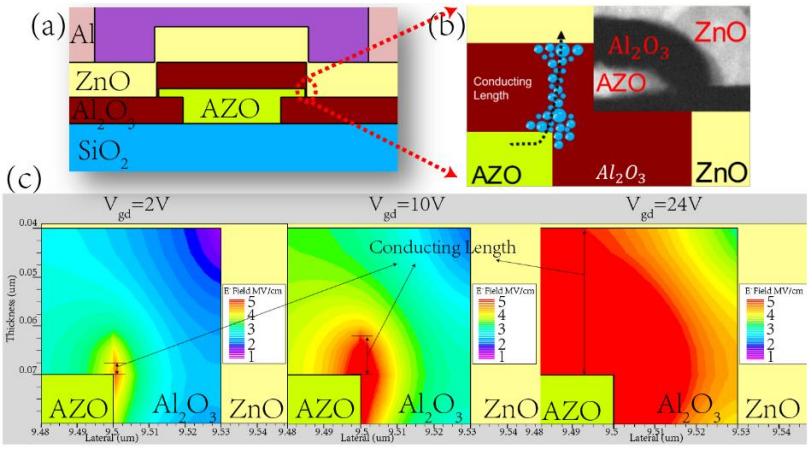

Figure 3. (a) The simulation model with a gate sharp corner. **(b)** Schematic diagram of the conducting path across the Al_2O_3 layer (inset: TEM of the AZO gate) **(c)** The simulation result on electric field distribution in the dielectric layer showing a conducting length grow with a higher applied voltage.

"*Flow-Through*", low-temperature gas phase deposition for conformal coating of ultra-high aspect ratio polymer micro- and nanochannels

Manuel Müller [a], Jeremy Teuber [a], Rukan Nasri [a], Robert Zierold [a], Irene Fernandez-Cuesta [a]

[a] Universität Hamburg, Physics Department, Hamburg, 22761, Germany
e-mail: manuel.mueller@physnet.uni-hamburg.de

In this work, we present a method for selective coating of the inner walls of high aspect-ratio polymer micro- and nanochannels with inorganic material (Al_2O_3) by gas phase deposition (GPD) in a "*Flow-Through*" mode [1]. Integrating metals and metal oxides into channel systems offers the introduction of catalytic, electrical, or optical functionalities and mechanical elements not native to the polymer template material. However, the defect and pin-hole-free integration in enclosed ultra-high aspect-ratio (AR) structures, especially the homogenous and conformal deposition, remains a challenge [2, 3]. Low process temperatures (< 110 °C) required to coat engineering polymers without deformation are an additional challenge for the deposition process.

The herein presented flow-trough gas phase deposition (FTGPD) process uses a pressure gradient over the channel system for novel incubation and evacuation strategies to overcome the limitations of diffusion-based atomic layer deposition (ALD) or line-of-sight-based chemical vapor deposition (CVD). Complementary to the ALD methodology, alternating injections of precursors allow for a controlled growth of the material. However, this work aimed to achieve high growth rates with fast cycle times in high AR structures at reasonable homogeneities due to the utilization of high differential pressures and condensation in the channels. Adjusting the parameters to a specific geometry ultimately allows for switching between CVD and ALD growth rates depending on the need for precision coating or high growth rates. A material system for nanoimprinted polymer micro- and nanochannels was developed for the process evaluation and applications. Ormostamp® or mrNIL-210® (microresist technology GmbH) are used to define the channel structure via nanoimprinting on a polycarbonate (PC) substrate. A mrNIL-210® coverslip foil (< 3 µm) is bonded to the imprinted sample to enclose the channel system. A PC carrier foil mechanically supports the thin foil during the ALD process to avoid bending into the channel micro- and nanostructures. A separation layer between the polymer and the PC carrier foil allows for removal after the process. Masked reactive ion etching removes the coverslip completely of partially, for direct observation of the deposited material or post processing.

In Figure 1, the reactor chamber (a) and an exemplary polymer sample with imprinted micro- and nanochannels with a bonded coverslip (b) are shown. The chamber is designed as a multi-purpose-reactor and is suited not only for our *"Flow-Through"* gas phase deposition but also for standard, diffusion-based chamber ALD. By mounting the sample via gaskets to the chamber ports, the sample holes are defined as in- and outlets (c, e, g) and the precursor injection is selectively directed to flow into and along the channels. A pressure gradient can be applied by pulsing gas precursor or nitrogen into the inlet and maintaining vacuum pump conditions at the outlet (d, f, h). This allows for a "Pressure-Gradient-Assisted-Incubation" (PGAI) (c, d) and "N_2 Purge Incubation" (N_2PI) (g, h). The N_2PI allows the distribution of already injected precursor without further introducing new precursor, thus minimizing excessive precursor accumulation at the inlets requiring long evacuation times.

In Figure 2 shows the results of FTGPD processes with implemented PGAI and N_2PI at the hand of selected microchannel structures with increasing effective aspect ratios (EAR). The EAR of the channels successfully coated by FTGPD range from hundreds to several thousand (width (w) and height (h) in micrometre scale, length (l) in the centimetre scale, $EAR = l(w+d)/(2wd)$). In (a) a representative meandering channel is shown, which is used to achieve centimetre long channels within a device. The growth per cycle (GPC) was deducted by measuring the layer thickness from FIB cross sections (c) along the channel length. It is plotted in (b) for Process 1 (PGAI & Evac., solid line) and Process 2 with AR-adjusted higher process times (PGAI & Evac. & N_2PI, dashed line). Higher deposition rates

emphasize the effect of decreasing GPC for increasing ARs with the same recipe. The N_2PI shows promising results to achieve higher deposition rates around 1-2 nm/cycle with better homogeneity along the channels, as shown by comparing both processes (purple). The highest aspect ratio achieved so far for microchannels is 5500, and the smallest channels coated with this method were 50 µm long 500 x 500 nm nanochannels integrated along microchannels with aspect ratio 1100.

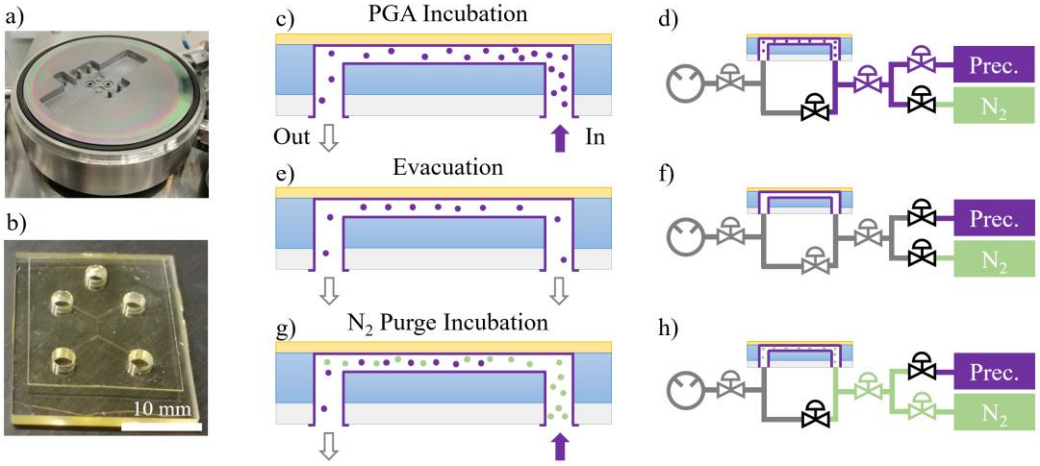

Figure 1. (a) Photo of the multi-purpose-process chamber and (b) exemplary polymer sample and (c,e,g) schematic cross section of the channel system during the process with imprinted micro- and nanochannels (blue) and coverslip (yellow). Mounting the channel system defines the holes as in- and outlets (c, e, g) with respect to the valve system of the reactor (d, f, h). The channel inlet can be selectively subjected to precursor or N_2 pulses while the outlet maintains vacuum. This allows for the modes of "PGAI" (c, d) and "N_2PI" (g, h). The "Evacuation" (e, f) can be performed on both channel sides simultaneously with an optional N_2 purge (not shown).

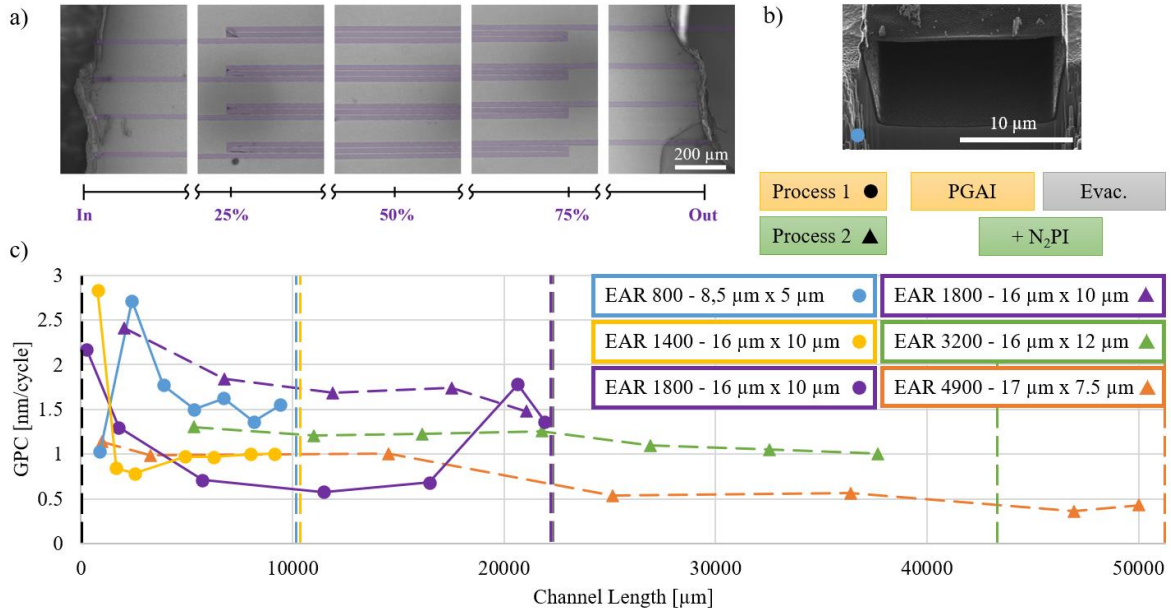

Figure 2. (a) SEM images of a 2.2 cm long meandering microchannel sample after the FTGPD process and coverslip removal, (b) GPC results for two processes at 105 °C and different microchannel geometries and measured by FIB cross-sections (c) at multiple positions along the channel from inlet to outlet (vertical lines) are shown. Three samples for Process 1 (circle, solid line) and Process 2 (triangle, dashed line) are shown with increasing EAR. All high aspect ratio channels are successfully coated on the inside without clogging. The added N_2PI function and AR-adjusted times in Process 2 show better deposition homogeneity and reduction of in- and outlet GPC spikes.

[1] M. Müller et al., DE 102020102076A1 (2020) Hamburg, Germany, DPMA.
[2] V. Cremers et al., Applied Physics Reviews (2019) 6(2) 021302.
[3] J. Yim et al., Phys. Chem. Chem. Phys. (2022) 24, 8645-8660.

Improving Dynamic Tracking Performance of Nanopositioning Stage for Defect Review Imaging System using Iterative Learning Control

Kyung-Rok Kim [a], Hyunchang Kim [a], Dongwoo Kang [a], Jaeyoung Kim [a]

[a] Department of Flexible and Printed Electronics, Korea Institute of Machinery and Materials(KIMM), Daejeon, 34103, Republic of Korea
e-mail: hckim0128@kimm.re.kr,

Abstract
A nano-positioning stage is a crucial technology extensively utilized in various fields such as inspection equipment, optical systems, and atomic force microscopy (AFM) [1-3]. In a previous study [4], we proposed an ultra-precision XY stage that employs a decoupled parallel compliant mechanism driven by a piezoelectric stack actuator. By implementing proportional double integral (PII) feedback control, we achieved a tracking error performance of ±3nm in the constant velocity region. However, significant errors persisted during the acceleration and deceleration periods.
In this paper, we apply iterative learning control (ILC) to enhance the dynamic tracking performance across the entire motion profile. ILC is a method derived from the concept that the performance in subsequent tasks can be improved by leveraging the outcomes of previous tasks [5, 6]. The objective of ILC is to attain better transient tracking performance by utilizing error information obtained from previous iterations,
Figure 1 illustrates the ultra-precision XY stage utilized in this study. To decouple the motion along the x and y axes, a parallel compliant mechanism is designed. Piezoelectric stack actuators are installed in both axes to provide a maximum displacement of 14.9um. Displacement is measured using a capacitive sensor. The XY stage is installed on top of the ZTilt stage, but we won't delve into its details since it remains fixed during the motion along the x and y axes proceed. Figure 2 presents the block diagram of the applied controller. Iterative learning control is employed in conjunction with the conventional proportional-integral feedback control loop. The ILC input for the current iteration is computed from the error of the previous iteration, which is stored in memory. The ILC input is adjusted by modifying the loop gain L and Q filter. The resulting ILC input is added before the PI controller. The experiment is progressed by employing the motion profile depicted in Figure 2. Scanning in XY plane is conducted by a scan motion in x axes and step motion in y axes.
The motion profile along the x-axis involves a scanning motion with a maximum speed of 80um/s and a constant velocity region of 5um. Simultaneously, the motion profile along the y-axis consists of step movements of 80nm step while the x-axis is in the acceleration region. Figure 3 compares the experimental results obtained using PI control along and PI+ILC control. In both case same PI control gain is applied. The results clearly demonstrate that when only proportional-integral control is utilized, a significant error peak occurs in the acceleration region of the step motion along the y-axis. Additionally, the x-axis fails to accurately follow the desired motion profile. Conversely, when iterative learning control is implemented, the tracking performance improves in both the x and y axes. By applying ILC control, the 3-sigma errors in the x and y axes are reduced to 2.28nm and 3.76nm, respectively.

Acknowledgement
This research has been supported by the National Research Program, 'Development and support of ultra precision UHV stage and system integration' (Grant NB1830), funded by the National Research Council of Science & Technology(NST), and Government-funded Research Program (Grant NK242E) funded by the Korea Institute of Machinery & Materials(KIMM).

[1] GU, Lei, et al. Journal of Micromechanics and Microengineering, 16.7(2006): 1349
[2] Schitter, George, et al. IEEE transactions on Control Systems Technology, 15.5(2007): 906-915.
[3] Gorman, J. J. Springer, Cham. (2016): 295-324
[4] KIM, Jaeyoung, et al. IEEE Access, 9 (2021): 88931-88941.
[5] Bristow, Douglas A. IEEE control systems magazine, 26.3(2006): 96-114.
[6] Fine, Benjamin T., et al. 2009 American Control Conference. IEEE, (2009): 931-936.

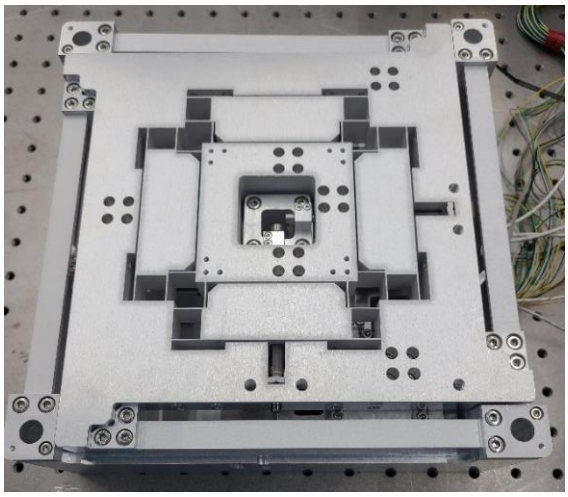

Figure 1. Ultra-precision nano-positioning XY stage driven by a piezoelectric stack actuator.

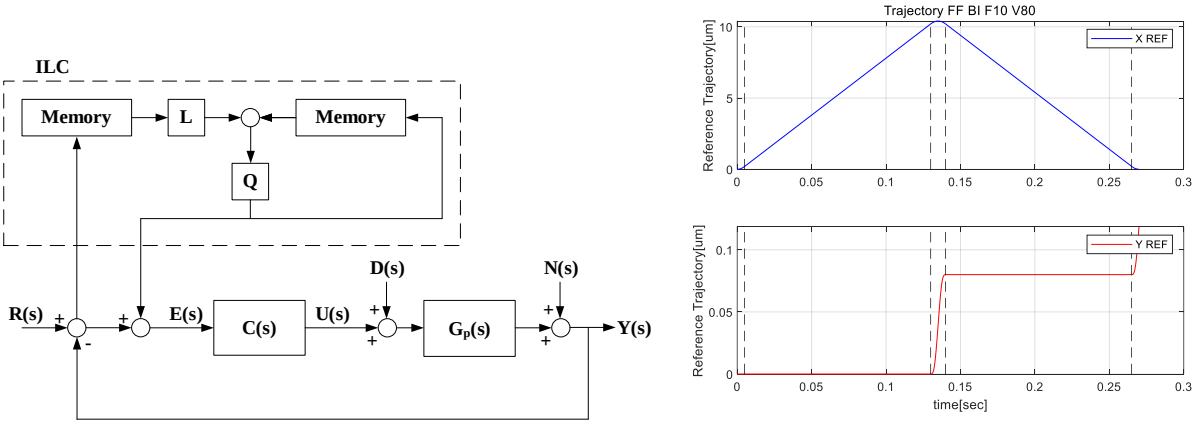

Figure 2. Block diagram of proportional integral controller with iterative learning control algorithm(left) and applied motion profile(right).

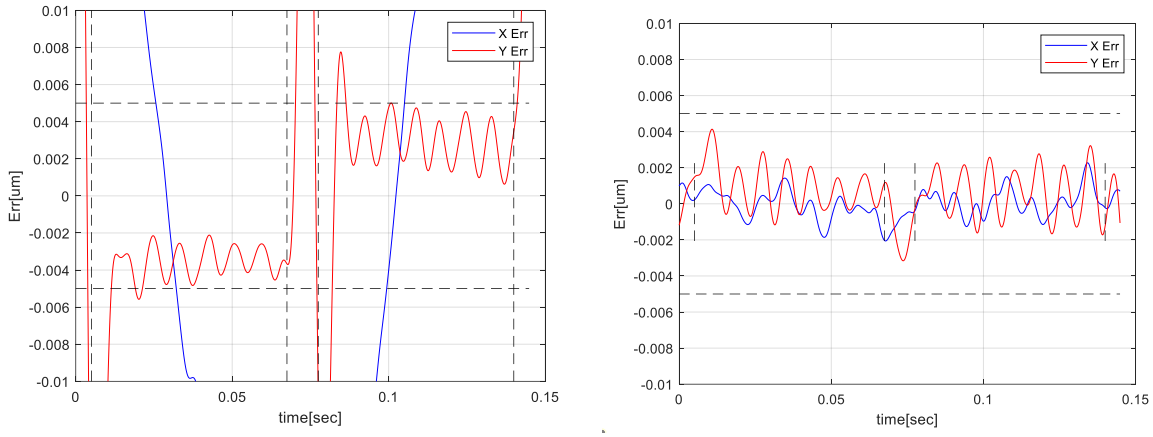

Figure 3. Dynamic tracking performance of PI control only case (left) and PI+ILC control(right).

Soft contact pressure sensors based on randomly rough surfaces

Luigi Portaluri[a,b], Luciana Algieri[a,b], Marco Bruno[a,b], Massimo De Vittorio[a,b], Michele Scaraggi[a,b]

[a] Center for Biomolecular Nanotechnologies, Istituto Italiano di Tecnologia, Arnesano (LE), 73010, Italy
[b] Department of Innovation Engineering, University of Salento, Lecce, 73100, Italy
e-mail: michele.scaraggi@unisalento.it
e-mail: massimo.devittorio@iit.it

Soft contacts are ubiquitously adopted in macro- to micro- and nano-electromechanical systems, from automotive industry to energy and robotics, including stretchable electronics for translational medicine applications [1]. Contact mechanics properties such as friction, adhesion, thermal and electrical contact resistance, to cite few, do strictly depend on the roughness and rheological properties of the mating surfaces, and can be nowadays (computationally-easily) predicted recurring to mean field formulations of the contact mechanics [2]. Therefore, the availability of such mean field theories enables the design of bio-interfaces and -sensors based on randomly rough surfaces, typically characterized by a facile microfabrication compared to standard soft lithography microfabrication of deterministic topographies.
In this work, we adopted randomly rough surfaces to develop capacitance-based soft contact pressure sensors. We compared their performance with those of capacitive soft contact pressure sensors based on deterministic topography, with similar root mean square roughness of the random surfaces. We observe that, as recently experimentally shown [3], the contact area, among the different interface properties, can be strongly affected by the local shear stresses acting in the true contact domains [3], therefore, capacitive soft contact pressure sensor measurements can be affected by the contact friction. Here we provide our fundamental contribution in the direction of shedding light, with accurate experimental tribometry experiments, on the role of frictional stresses and roughness randomicity on the capacitance formation. In particular, a home-made opto-electro-mechanical tribometer (Figure 1a) has been designed in order to detect, here for dry interactions, the true contact area (at optical magnification) and the contact capacitance as a function of the applied load, both during static and sliding contact. The interface is made by an ITO-coated, optically smooth microscope slide (ITO thickness of 25 nm) in contact with either a *i)* randomly rough self-affine or *ii)* deterministically-patterned PDMS layer with back electrode, the latter in adhesive contact on the top of a PDMS dome (Figure 1b). Both dome and layer share the same rheological properties. The surfaces have a root mean square roughness of ≈15 μm for both random and deterministic pattern (the power spectral density of the random roughness is reported in the inset of Figure 1b, whereas the deterministic pattern is constituted by a square array, with lattice distance 200 μm, of hemispheres with radius 50 μm). The contact area and the capacitance, the latter a measure of interface gap, is reported as a function of the applied normal load in Figure 1c, where the black (blue) line is for the deterministic (random) topography. We observe that the capacitance range (sensitivity) is larger for the random roughness with respect to the deterministic pattern. In Figure 1e) and f) we show the optically acquired true contact domains for the random and deterministic roughness case, respectively. Different colours identify different simply connected contact patches. We note that a larger contact area is coupled with a smaller average interface separation [2], thus an enhanced capacitance range, in agreement with our experimental findings.

[1] R.B. Mishra et al., Advanced Materials Technologies 6, (2021),2001023.
[2] M. Scaraggi et al., Journal of Chemical Physics 143 (2015), 224111.
[3] R. Sahli et al., PNAS, 115 (2018) 471-476.

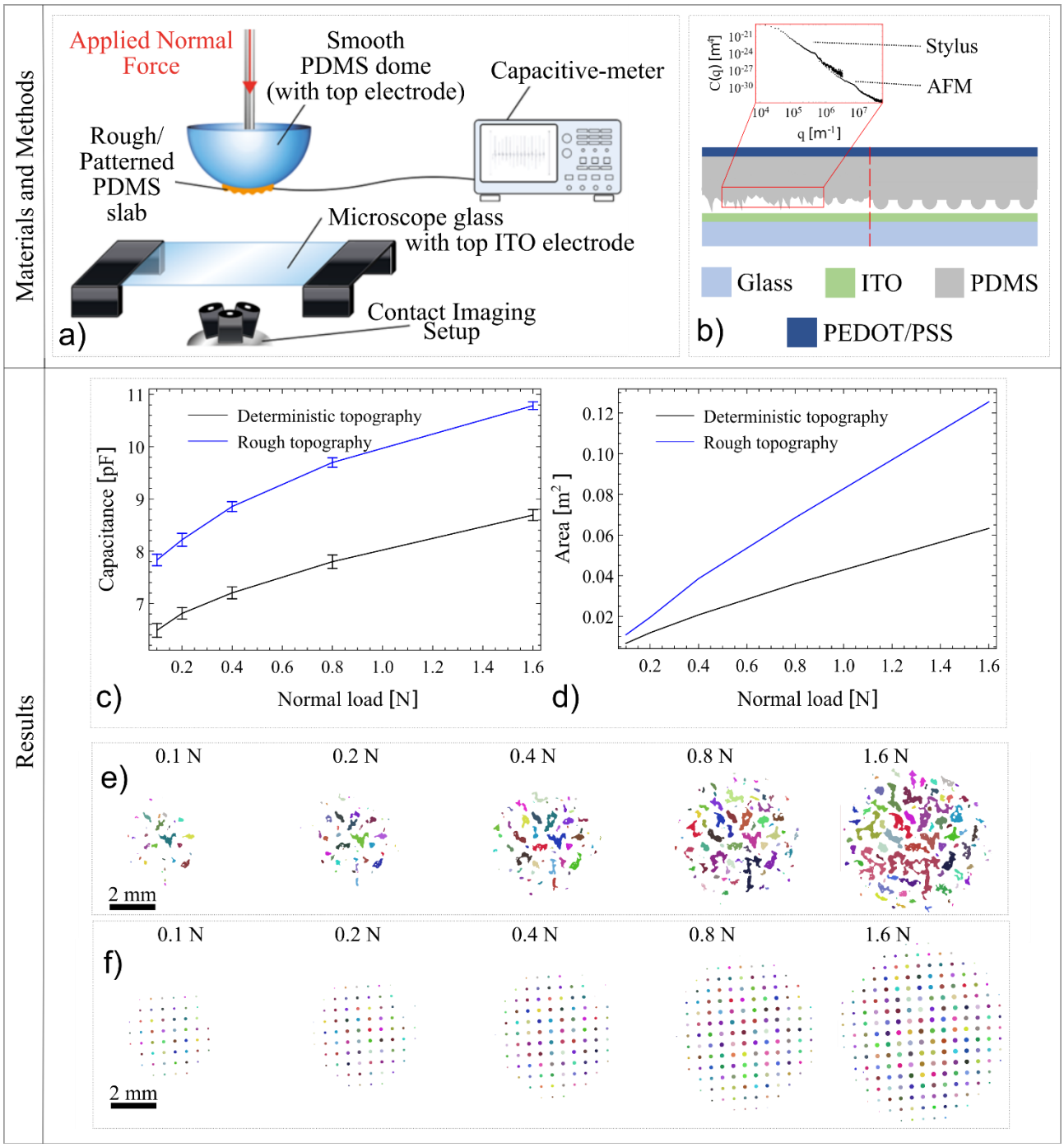

Figure 1. (a) Schematic of the opto-electro-mechanical tribometer adopted in this study. (b) Contact interface, as made by an ITO-coated, optically smooth microscope slide in contact with a randomly (left) or deterministically (right) rough PDMS layer with back electrode. (c) Contact area (right) and the capacitance (left) as a function of the applied normal load. (e) and f) optically acquired contact domains for the random and deterministic case, respectively (at different loads).

Short abstract:

Nowadays, the availability of advanced rough contact mechanics theories enables the design of soft contact sensors based on randomly-rough surface structural functionalization. The latter is based on facile fabrication processes, when compared to standard micro-fabrication such as two-photon soft lithography. In this work, we have compared the performance of soft contact capacitive sensors based on deterministic micro-patterning with respect to the newly-developed random interfaces. The latter show superior sensitivity with respect to the former, as expected from the multiscale nature of the random roughness.

Etch residuals after dry etching AlN with $CH_4/BCl_3/Ar$ over photoresist and overlapping metal layer

Nils Dittmar[a], Chris Stöckel[a,b], Micha Haase[a,b], Danny Reuter[a,b]

[a]Fraunhofer Institute for Electronic Nano Systems, Chemnitz, 09126, Germany
[b]University of Technology Chemnitz, Chemnitz, 09126, Germany
e-mail: nils.dittmar@enas.fraunhofer.de

AlN is used in various kind of technologies due to its outstanding electromechanical properties. Applications are MEMS resonators [1], waveguides [2], UV-LEDs [3] and others. AlN is often etched over hardmask e.g. SiO_2 [1] or Ni [2]. Removing these hardmasks after etching might damage the AlN layer due to the physical energy of the ions in case of dry etch processes. Wet etching might also attack AlN especially when using TMAH containing chemistry. If the application requires buried cavities, wet chemistry is challenging to remove from within the cavities.
In this work, AlN is structured over photoresist to avoid these effects. Instead, a remote O_2 plasma can be used to remove the mask. Nevertheless, the selectivity between AlN and photoresist has to be high to enable a reasonable thickness of the photoresist. In this work, the CH_4 content was adjusted in the AlN dry etching process to achieve high selectivity.

The experiments were done in an ICP chamber using $CH_4/BCl_3/Ar$ chemistry. The etching tool was AMAT Centura 5200. The samples were 200 mm Si wafers, on which AlN was deposited with and without metal layer on top. The metal layer was patterned by ion beam etching and overlapped the AlN structures to different degrees up to 600 nm. That means the patterned metal layer was not completely protected by photoresist and therefore etched in some structures while etching AlN. A scanning electron microscope was used to inspect the surfaces.

In the experiments without metal layer, the CH_4 content was varied between 0 sccm and 40 sccm. The results of the experiments (fig.1 and fig. 2) have shown a decrease of the AlN etch rate from 2 nm/s to 1 nm/s and photoresist etch rate from 1.4 nm/s to zero with increasing CH_4 content. These results proved, that the selectivity between AlN and photoresist can be influenced by CH_4 content. In fact, there was a growing polymer layer on the photoresist at maximum CH_4 flow rate. As seen in figure 1, etch residuals (presumably generated by CH_4) are on the sidewalls of the AlN structures and their thickness is decreasing from figure 1 a) to d) with decreasing CH_4 content. These residuals were removable by wet chemistry (TMAH), which attacks AlN and therefore might actually work as lift-off.
In the following experiments, a process (Fig. 1c) with low CH_4 content (5 sccm) was chosen and the process was applied on the wafers with the patterned metal layer to identify the influence of the metal. In the AlN etch process metal particles were back-sputtered to the photoresist sidewalls and stuck there after removing the photoresist (fig. 3). This was especially noticeably at structures with a high amount of overlapping metal. Furthermore, thin strings peeled off the sidewalls and protruded into the structures (fig. 4). Structures with less or no overlapping metal had less of these strings. It was noticed that they got thinner after 60 min of O_2 plasma but could not be completely removed. It is assumed that the O_2 plasma removed carbon polymers sticking to the sidewalls while the residuals with metal content remained. Etching without CH_4 (Fig. 1d) avoided the generation of these strings, since no carbon was introduced into the chamber. Therefore, it was concluded that a combination of CH_4 and metal might generate these strings.
Further processes were evaluated to remove these metallic etch residuals. A variation of dry etching processes were applied in a microwave remote plasma chamber: O_2, O_2/CF_4, O_2/H_2O, H_2/He, H_2/N_2. Since these tests had no visible effect, further procedures and chemistries have to be tested.

[1] J. Yang et al., Micromachines 6 (2015) 281-290
[2] X. Liu et al., Vacuum 116 (2015) 158-162
[3] Q. Zhang et al., Sci Rep 12 (2022) 7230

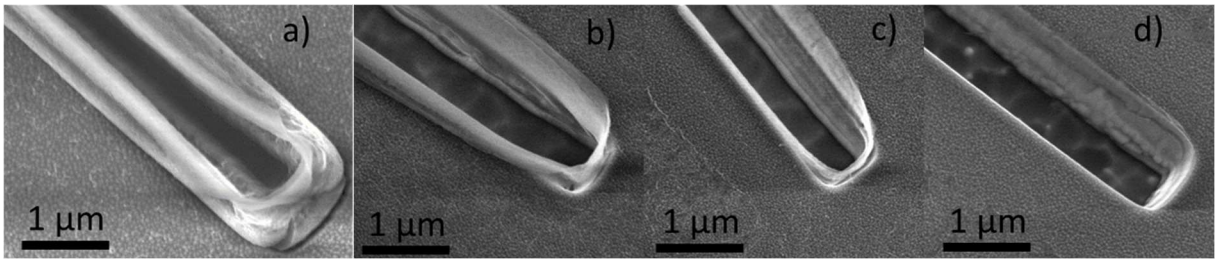

Figure 1. Thickness of sidewall polymers depending on CH_4 flow in AlN dry etching: a) 20 sccm, b) 10 sccm, c) 5 sccm and d) without CH_4. At 40 sccm CH_4 polymers grew over the whole surface.

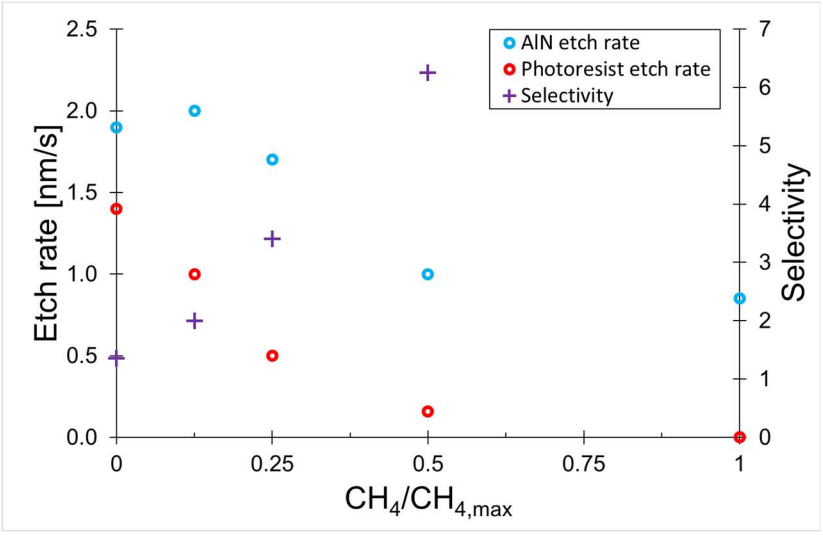

Figure 2. Etch rates for AlN (blue dots) and photoresist (red dots) as well as selectivity (violet crosses) over relative CH_4 content.

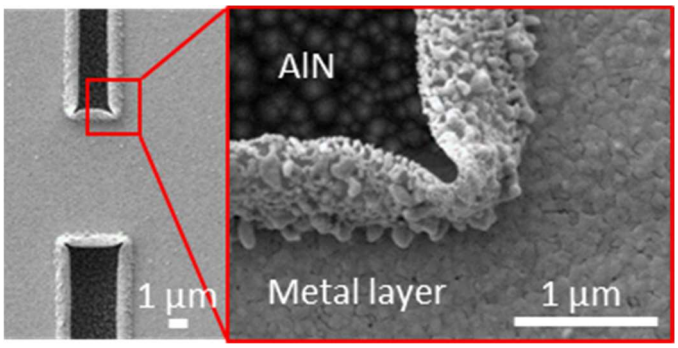

Figure 3. Presumably back-sputtered metal on the sidewalls of an RIE etched AlN structure after removing photoresist by O_2 plasma.

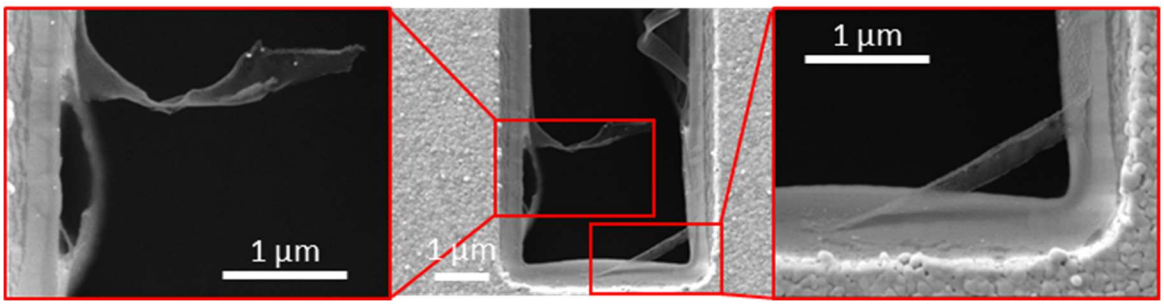

Figure 4. Peeled-off strings at sidewalls of RIE etched AlN structures after Si-DRIE and removing photoresist by O_2 plasma.

Dimensional and mechanical control of submicrometric fibers using two-photon polymerization

Ianis Drobecq, Ophélie Thomas-Chemin, Pierre-François Calmon, Laurent Malaquin, Bastien Venzac
LAAS-CNRS, Toulouse, 31400, France
e-mail : ianis.drobecq@laas.fr

In vivo, the extracellular matrix (ECM) surrounding cells exhibits fibrillary architecture whose biochemical, structural, and mechanical properties greatly influence cellular behaviours. In soft tissues, the ECM is composed of protein fibres, ranging in diameter from a few hundred nanometres to a few micrometres and low stiffness when bent and deformed.[1] The mechanical properties and dimensions of these fibres have a significant impact on the behaviour of cells as they directly contribute to cellular adhesion and to the distribution of forces and deformations in the tissue. Testing *in vitro* these contributions require the creation of microstructures reproducing the mechanics of the ECM, from individual fibre to more complex architectures. Two-photon polymerization (2PP) has already been used to produce 3D fibrillary structures on a small scale, with fibres down to 200nm in diameter.[2] However, existing microenvironment models did not address the mechanical properties of fibres at the cellular scale. In this work, we focused on this aspect through the control of fibre dimensions, which will allow us to control the rigidity of our 3D scaffolds.

We investigated the fabrication of suspended fibres using 2PP with a Nanoscribe printer (Photonics professional GT2) and IP-Dip resin and performed a systematic study of the impact of process parameters on fibre dimensions using scanning electron microscopy (SEM) and mechanical properties using atomic force microscopy (AFM). Several parameters can affect the final dimension of an object compared to its design [3], such as the spacing between two laser passes horizontally (hatching) and vertically (slicing), as well as laser power from 2mW to 88mW and 24 mm/s scan speed, or the laser path strategy. Through this systematic study, we could decipher the dependence of the fibre's dimensions and stability with process parameters. We designed a test structure ***(fig. 1)*** in which horizontal and vertical fibres and ribbons are printed between rigid supports, with varying dose, hatching, slicing or number of path (leading to fibres for single path and ribbons for multiple paths). Using SEM, the dimensions were measured for all these combinations.

Among its results, we observed a different evolution between the width and height of the fibres depending on the dose and regardless of the configuration. Horizontal fibres were printed for laser power above 21% (18mW) and vertical fibres above 27% (23mW), with minimal sections of 260x480nm² and 260x450nm² respectively**.** ***(fig. 2)*** No traces of fibres during development were visible under these powers. At increasing power, the fibre height (h) increases faster that the width (w). For ribbons, above 0.2 µm of hatching, we obtained independent fibres at 40% of power (35mW). ***(fig. 3)*** Below these values, the larger the hatching, the more the ribbon shrinks: as the energy density decreases, the lower cross-linkable degree lead to an increased shrinkage of the resin. Finally, we highlighted the printer robustness thanks to weak relative error in our measurement on N = 6 objects printed per batch and N = 4 batches.

According to the beam theory,[4] the spring constant strongly depends the lateral dimension of the fibres. ***(fig. 4)*** A 10% relative error in the width of a fibre can change the spring constant by 45%. Controlling precisely the fibre fabrication process is thus critical to create reproducible and well controlled models for cell culture. To complement this study, we are currently performing mechanical measurement by atomic force microscopy (AFM) on clamped-clamped square beams to correlate spring constants (k) and dimensions (width and length). We simulated, on Comsol software, their deflections submitted to a 50nN load force on a point in centre of the upper face. Analysis has been done on 0.5, 1, 1.5, 2 µm beam widths. In accordance with the theory, we found deflection of 138, 12, 2 and 0.65 nm respectively. Next experiments will aim to confirm the results obtained from the theory and the analytical model through mechanical measurements conducted by AFM.

[1] Shen, Z. L., Dodge, M. R., Kahn, H., Ballarini, R. & Eppell, S. J. In Vitro Fracture Testing of Submicron Diameter Collagen Fibril Specimens. *Biophys. J.* **99**, 1986–1995 (2010).
[2] Klein, F. *et al.* Elastic 3D Scaffolds: Elastic Fully Three-dimensional Microstructure Scaffolds for Cell Force Measurements (Adv. Mater. 8/2010). *Adv. Mater.* **22**, (2010).
[3] Hu, Q. *et al.* The influence of printing parameters on multi-material two-photon polymerisation based micro additive manufacturing. *Addit. Manuf.* **51**, 102575 (2022).
[4] Roark, R. J., Young, W. C. & Saunders, H. Formulas for Stress and Strain – 5th Edition. *J. Mech. Des.* **101**, 173 (1979).

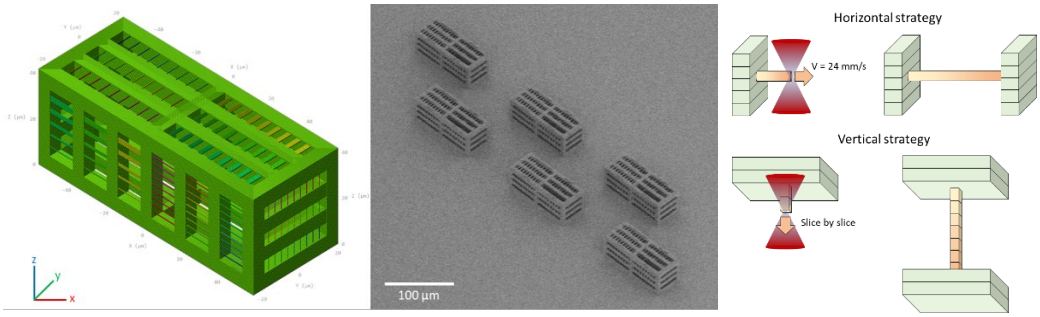

Figure 1: CAD file of calibration object (Left), SEM micrograph (middle) and illustration of the laser trajectory

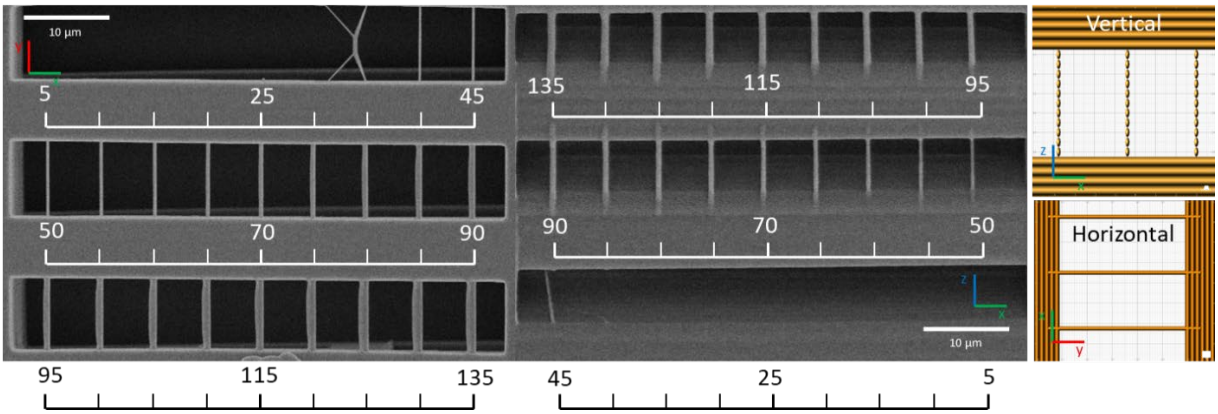

Figure 2: SEM micrograph of horizontal fiber with power laser scale (% of 65mW) (left), vertical fiber (middle) among laser power and design strategy of fibers (right)

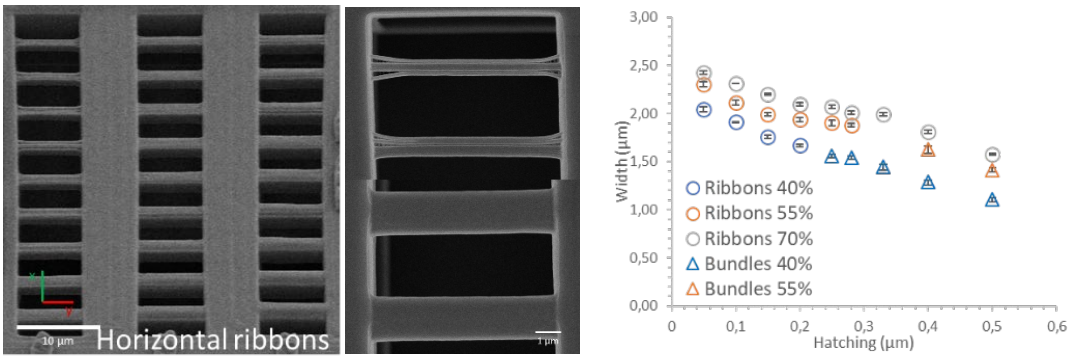

Figure 3: SEM micrograph of horizontal ribbons (left) zoom on bundles and ribbons (middle) and graph of ribbons width depending of hatching (right)

$$I = \frac{bh^3}{12} \qquad \delta(x) = \frac{F}{k(x)} = \frac{Fx^3}{12EI} - \frac{FLx^2}{16EI}$$

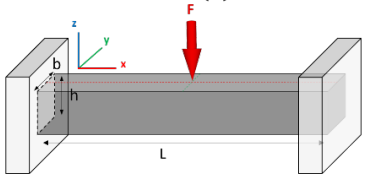

I : moment of inertia
δ : deflection where $x = \frac{L}{2}$
F : force applied
k : spring constant

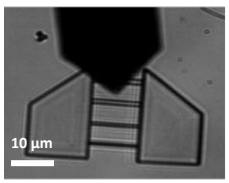

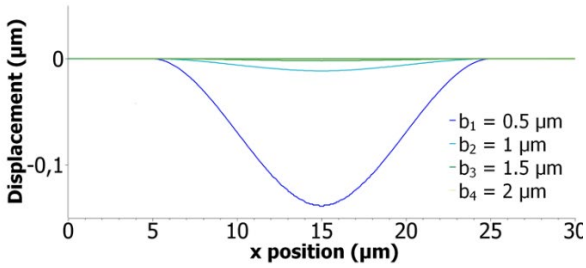

Figure 4: Schematics of a beam subjected to an axial force (left), brightfield micrograph of mechanical test performed by AFM (middle), beams displacement for various beam cross sections values with a 50 nN load force (COMSOL simulation) (right).

Microfabrication and Silicon Integration of Epitaxial Magnetic Shape Memory Films

Satyakam Kar [a b c], Lukas Fink[b a c], Kornelius Nielsch [a c], Sebastian Fähler [b], Heiko Reith [a]

[a] Leibniz IFW Dresden, Institute for Metallic Materials, Dresden, 01069, Germany
[b] Helmholtz-Zentrum Dresden-Rossendorf, Institute of Ion Beam Physics and Materials Research, Dresden, 01328, Germany
[c] TU Dresden, Institute of Materials Science, Dresden, 01062, Germany
e-mail: s.kar@ifw-dresden.de

Magnetic shape memory alloys are an emerging class of smart materials that combine ferroelastic and ferromagnetic transitions to generate multifunctional properties like magnetic field induced actuation [1], multicaloric cooling [2] and thermomagnetic energy harvesting [3]. These effects have been primarily studied in bulk and single crystal systems. However, while progress has been made in understanding these effects, their application and integration in microsystems present two key challenges. Firstly, the suitability of microfabrication techniques for their films has not been investigated in detail. Secondly, the epitaxial growth of these films is until now only possible on expensive single crystal oxide substrates [4] that are incompatible with state-of-the-art silicon microsystem technology. In the current study, we address these challenges by investigating the microfabrication and silicon integration of epitaxial Ni-Mn-Ga-based Heusler films.

For microfabrication of Ni-Mn-Ga films, we performed laser photolithography and tested reactive ion etching (RIE) using Ar and SF_6 plasma. The etching process results in etch rates of up to 100 nm/min. However, redeposition around the patterned structures are observed. Depending on a flat or undercut photoresist profile, redeposition creates 'fences' around the patterns (see Fig 1a), or a layer on top of the pattern (see Fig 1b). To avoid redeposition, we tested Ar ion beam etching (IBE) and tilting of the sample stage. However, tilting the sample results in a varying etch rate close to the masked area due to the shadowing of the ion beam by the photoresist. This problem is exemplarily shown in the FIB cross-section of a film partially etched at 15° tilt angle (see Fig 2a). Finally, we developed a two-step ion-beam etching process to obtain clean patterned structures (see Fig 2b).

To test the integration of epitaxial Ni-Mn-Ga films into Si-based microsystems, we deposited films on Si (001) based substrates with a 4 nm thick $SrTiO_3$ (001) buffer layer. The obtained films have the characteristic martensite phase microstructure [4] (see Fig 3a) and epitaxial growth is confirmed by XRD pole figure measurement. Lastly, we followed our previously optimized microfabrication process to obtain patterned structures on silicon-on-insulator (SOI) substrate (see Figs 3b and c).Furthermore, partly freestanding double-beam cantilevers with electrical contact pads are fabricated on SOI substrate by under-etching the top Si layer using XeF_2 etching (see Fig 3d). The cantilever can actuate by Joule heating using the thermal shape memory effect [5]. Our approach, therefore, successfully integrates an emerging multifunctional material with industry-compatible silicon microtechnology.

[1] A. Sozinov et al., Appl. Phys. Lett. 102 (2013) 021902.
[2] T. Gottschall et al., Nat. Mater. 17 (2018) 929–934.
[3] M. Gueltig et al., Adv. Energy Mater. 7 (2017) 1601879.
[4] A. Backen et al., Adv. Eng. Mater. 14 (2012) 696–709.
[5] M. Kohl et al., Appl. Phys. Lett. 104 (2014) 043111.

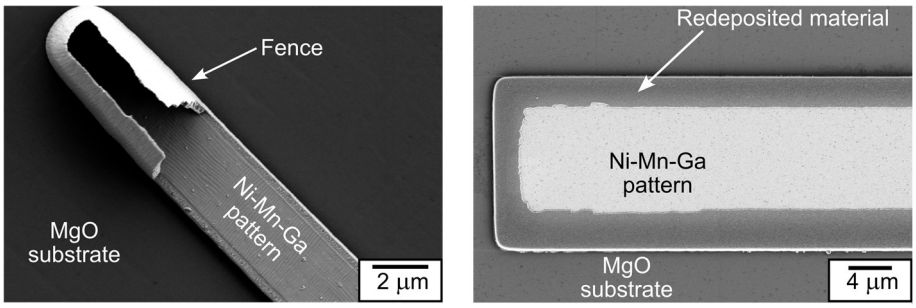

Figure 1. SEM images of Ni-Mn-Ga patterns obtained after reactive ion etching using (a) flat photoresist mask profile and (b) undercut photoresist mask profile. Redeposition 'fence' is seen in (a) around the pattern. Redeposited material on top of pattern is observed in (b).

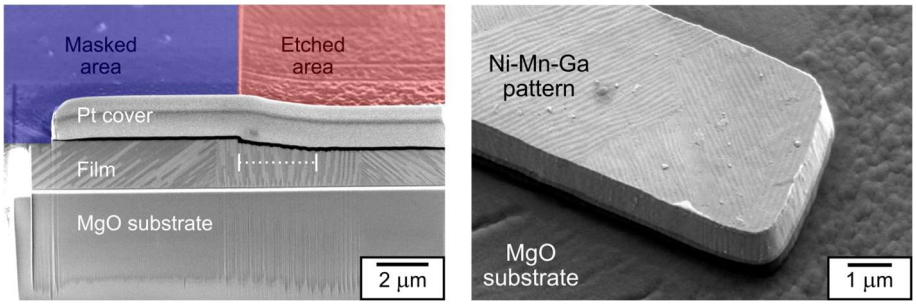

Figure 2. (a) FIB cross-section SEM image of partially ion-beam etched Ni-Mn-Ga film using 15° tilt. The etched depth reduces close to the masked area. This region is highlighted by white dotted line. (b) SEM image (45° tilted) of Ni-Mn-Ga pattern after an optimized two-step ion beam etching process. The pattern edges are sharp and free from redeposition.

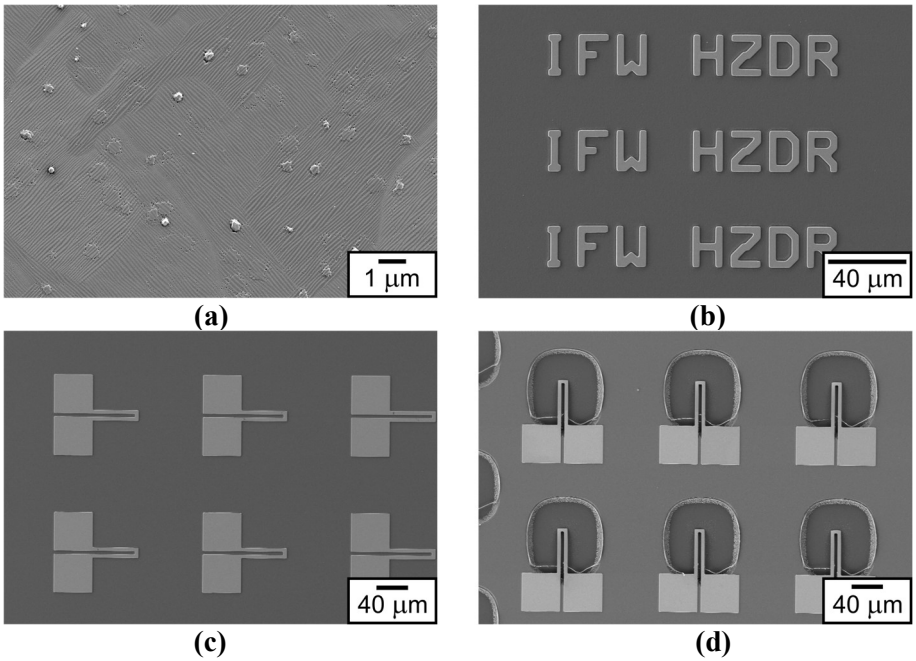

Figure 3. SEM images of (a) martensite phase microstructure observed in epitaxial Ni-Mn-Ga film grown on SOI substrate, (b, c) Ni-Mn-Ga patterns obtained using the optimized ion-beam etching process, (d) partly freestanding Ni-Mn-Ga cantilevers obtained after XeF_2 etching the top Si layer of SOI substrate.

Dependence of Structural Design on Effective Young's Modulus of Ti/Au Multi-Layered Micro-Cantilevers for MEMS Capacitive Accelerometers

Shunkai Watanabe, Tomoyuki Kurioka, Chun-Yi Chen, Tso-Fu Mark Chang, Akira Onishi, Parthojit Chakraborty, Katsuyuki Machida, Hiroyuki Ito, Yoshihiro Miyake, Masato Sone

Tokyo Institute of Technology, Yokohama, 226-8503, Japan
e-mail: watanabe@ames.pi.titech.ac.jp

Gold materials are promising toward movable components in MEMS (micro electromechanical systems) capacitive accelerometers due to the high mass density. The performance of a capacitive accelerometer is greatly influenced by the Brownian noise, and the Brownian noise is dependent on the overall mass of the component. Through usages of a high mass density material, performance enhancement and further miniaturization of the MEMS device could be achieved simultaneously. In fact, the performance of MEMS accelerometers utilizing a Ti/Au multi-layered design is reported to be significantly improved as reported in a previous study [1]. On the other hand, metallic materials are known to show the sample size effect [2], which the mechanical property changes as the size is reduced to micro-scale or smaller. Hence, it is necessary to investigate mechanical properties of gold materials on the micro-scale for applications in MEMS accelerometers. In specific, the Young's modulus is an important design parameter for MEMS components.

In a previous study on the Young's modulus of a Ti/Au multi-layered micro-cantilever [3], the Young's modulus was reported to be dependent on the geometry of the micro-cantilever, and this Young's modulus is the effective Young's modulus (E_{eff}). In another study, the structural stability of the Ti/Au multi-layered micro-cantilever was found to be affected by the design of the fixed-end [4]. Findings reported in these two studies suggest that structural designs including designs of the cantilever body and the fixed end are all factors influencing the E_{eff}. In this study, effects of the dimensions of the Ti/Au multi-layered micro-cantilever and the gap between the bottom surface of the cantilever and the bottom electrode (d_{gap}) on the E_{eff} are investigated.

A total of 240 Ti/Au multi-layered micro-cantilevers of different structural designs were prepared, and the E_{eff} was evaluated by a resonance frequency method [3] and FEA (finite element analysis) simulations. Fig. 1(a) shows a schematic of the resonance frequency method. Fig. 1(b) shows a schematic view of the Ti/Au multi-layered micro-cantilever. The samples are named as XX-#1-#2. The XX's are SL, DL and TL representing a single, double, and triple Ti/Au layered design, respectively. The #1 indicates the overall Au layer(s) thickness in micrometer. The #2 indicates the distance of the d_{gap} in micrometer. The lengths were 200, 400, 600, 800, and 1000 μm, and the widths were 8, 9, 10, 11, 12, 13, 15 and 20 μm. In addition, FEA simulations were also conducted to determine the resonance frequency using COMSOL Multiphysics Simulation software. The "Eigenfrequency" study was used in the COMSOL simulation.

Fig. 2(a) shows plots of the resonance frequency versus $1/L^2$ obtained by the experiments for SL-12-9 micro-cantilevers. The E_{eff} was calculated from the slope of the linear asymptote. The E_{eff} obtained experimentally are summarized in Fig. 2(b). Generally, a higher E_{eff} was obtained for a smaller d_{gap}. In addition, in most micro-cantilevers, the E_{eff} decreased following an increase in the width.

Fig. 3(a) shows plots of the resonance frequency versus $1/L^2$ obtained by COMSOL simulation for SL-12-9 micro-cantilevers. The E_{eff} obtained by COMSOL simulation are summarized in Fig. 3(b). A slight increase in the E_{eff} was observed following a decrease in the d_{gap} and micro-cantilevers with a narrower width. The observed trend for effective Young's modulus to decreasing the d_{gap} is similar to the experiment results.

Acknowledgement
The authors would like to thank T. Sakai and S. Iida, T. Konishi, NTT-AT Corp., for their technical support. This work was supported by JST, CREST Grant Number JPMJCR21C5, Japan.

References
[1] D. Yamane et al., Appl. Phys. Lett., 104 (2014) 074102.
[2] T. Nagoshi et al., Mater. Lett., 117 (2014) 256.
[3] H. Nakajima et al., in Proc. of 2017 IEEE NEMS, Los Angeles, CA, USA, 2017, pp. 264-267.
[4] M. Teranishi et al., Microelectron. Eng., 187-188 (2018) 105-109.

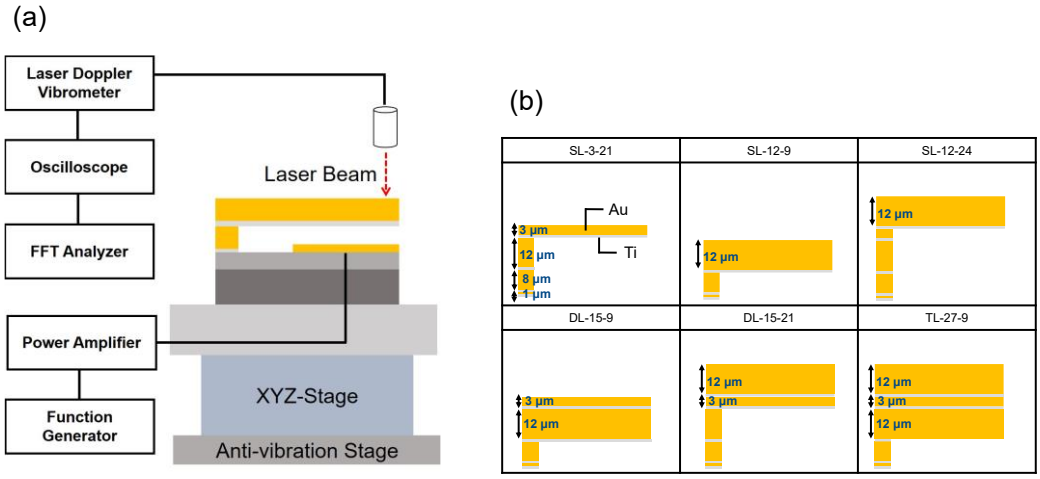

Figure 1. (a) Resonance frequency measurement equipment and (b) schematic view of the Ti/Au cantilever from the side.

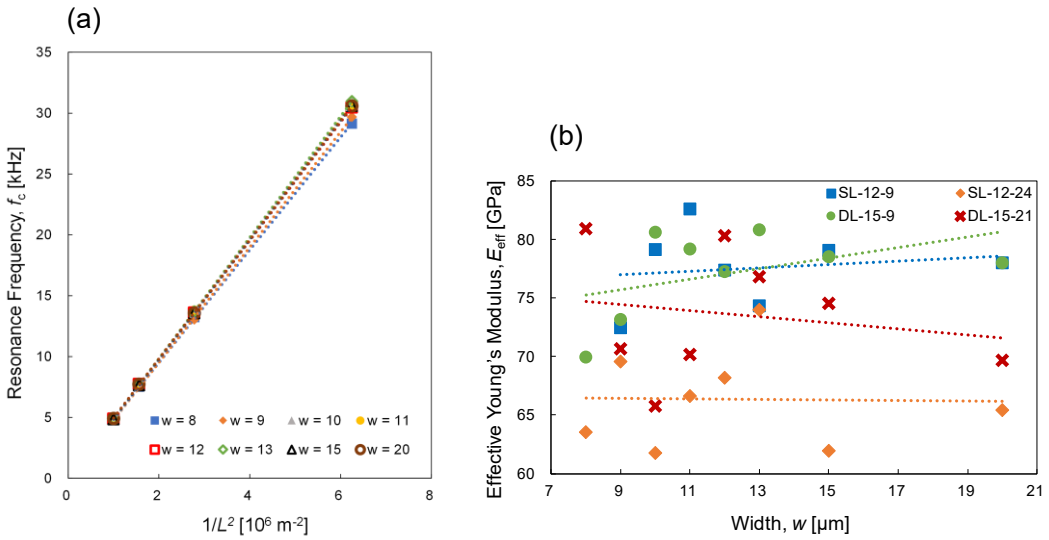

Figure 2. (a) The resonance frequency of SL-12-9 obtained by the experiment plots against $1/L^2$ and (b) the effective Young's modulus plots against width of cantilevers in resonance frequency method.

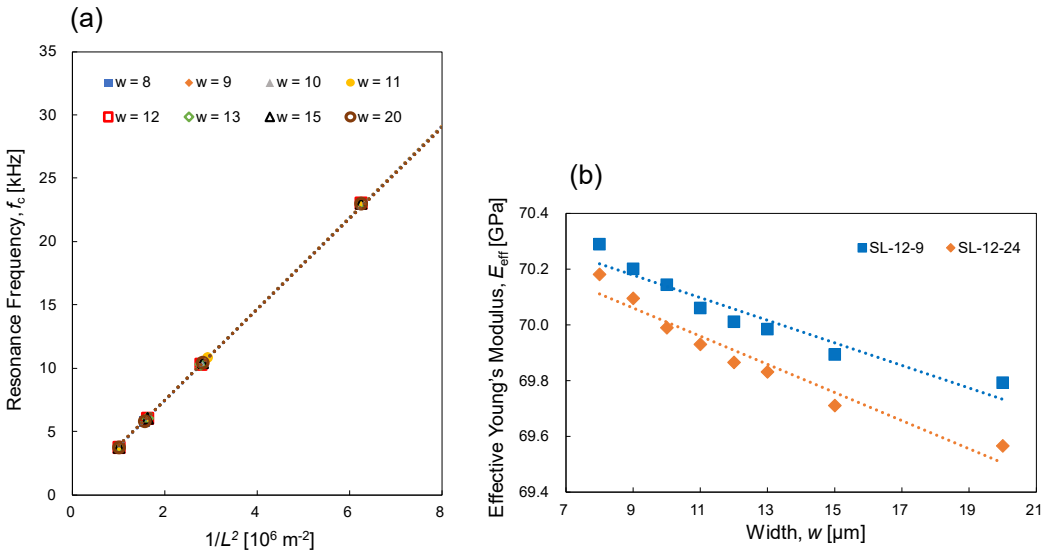

Figure 3. (a) The resonance frequency of SL-12-9 obtained by COMSOL simulation plots against $1/L^2$ and (b) the effective Young's modulus plots against width of cantilevers in COMSOL simulation.

Closed loop error compensation of RADAR PCBs fabrication process using inkjet printing and interoperability methods

Abdalla Shahin [a], Helmut Zörrer [a], Peter Bauer [a], Gerald Stubauer [a], Benedikt Pressl [b], Rolf Schneider [c], Ferhat Aslan [c], Jochen Seeser [c]

[a] PROFACTOR GmbH, Steyr-Gleink, 4407, Austria
[b] BESI Austria GmbH, Radfeld, 6241, Austria
[c] NOTION Systems GmbH, Schwetzingen, 68723, Germany
e-mail: abdalla.shahin@profactor.at

Companies are eager to become more adaptable and improve their systems and network structures due to the increased global competition. To meet these expectations, they have to cope with the complexity of interconnected processes and have the flexibility to meet changing requirements [1]. This work focuses on the fabrication of RADAR printed circuit boards (PCBs) as part of the project TINKER where the main target is to enable error compensation and defect repair inline the fabrication process using inkjet printing. This is achieved through the use of a closed error compensation feedback loop and an interoperability structure to support data transfer among several partner companies.

The fabrication process starts at BESI with placing the bare RADAR die into a cavity in the PCB, where a precise amount of non-conductive adhesive (NCA) was dispensed (Figure 1). During placement the NCA spreads through the cavity and due to imperfections in the PCB geometry and the dispensing pattern, the resulting gap filling is non-uniform. Planarity of the NCA is imperative to ensure a high-quality substrate for subsequent inkjet processing steps, for example, for printing connection patterns with conductive inks. After curing the NCA, BESI inspects the PCBs with high-resolution imaging and topology measurements and forwards the data to PROFACTOR. Here, samples are classified into three categories: good, spoiled or defective. “Good” samples have sufficient planarity to allow direct printing of the connection pattern. For “Spoiled” or “Defective” samples, PROFACTOR will generate suitable data for the corrective actions required to repair such defects, i.e., fitting printing layers to fill the missing NCA volume. PROFACTOR’s printing jobs are then sent to the TINKER pilot-printer at NOTION. The processed samples are returned to BESI for inspection. This constitutes the closed loop for error correction as depicted in Figure 2. If a sample is still defective, it undergoes another defect repair step in which the corrective actions are estimated by the error compensation algorithms based on the samples’ inspection images.

To be able to let the pilot systems interact seamlessly, a semantic interoperability framework is developed. It supports the loose coupling of the systems by providing a software service that supports the exchange of data and commands through semantic unification. The transfer of data within the pilot line is achieved through cloud folders using a time stamp and an ID for each PCB so that the data retrieval process can run without errors. In each PCB folder, subfolders are named featuring a unique step number, the data provider and the kind of data in that subfolder. Finally, when all operations are completed for the respective PCB, a ‘results’ folder is created containing the final inspection results and signaling that the entire PCB folder can be moved to an archive.

Acknowledgments
The project TINKER receives funding from the European Union’s Horizon 2020 research and innovation programme under Grant Agreement No. 958472

References:
[1] G. Weichhart, W. Guédria, Y. Naudet; *Supporting interoperability in complex adaptive enterprise systems: A domain specific language approach*; Data & Knowledge Engineering 105, 2016, 90-106; DOI: 10.1016/j.datak.2016.04.001.

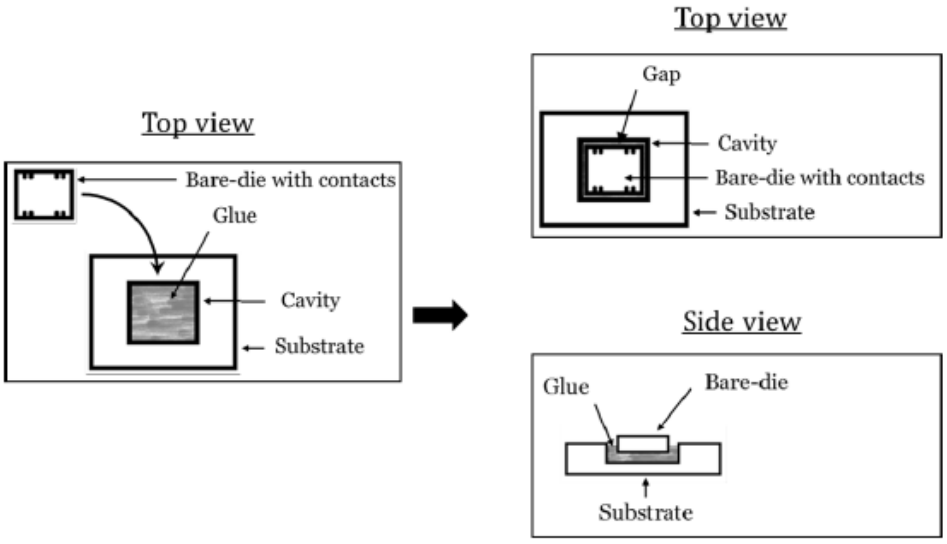

Figure 1. Pick and Place process of a RADAR bare die inside a PCB cavity done by BESI

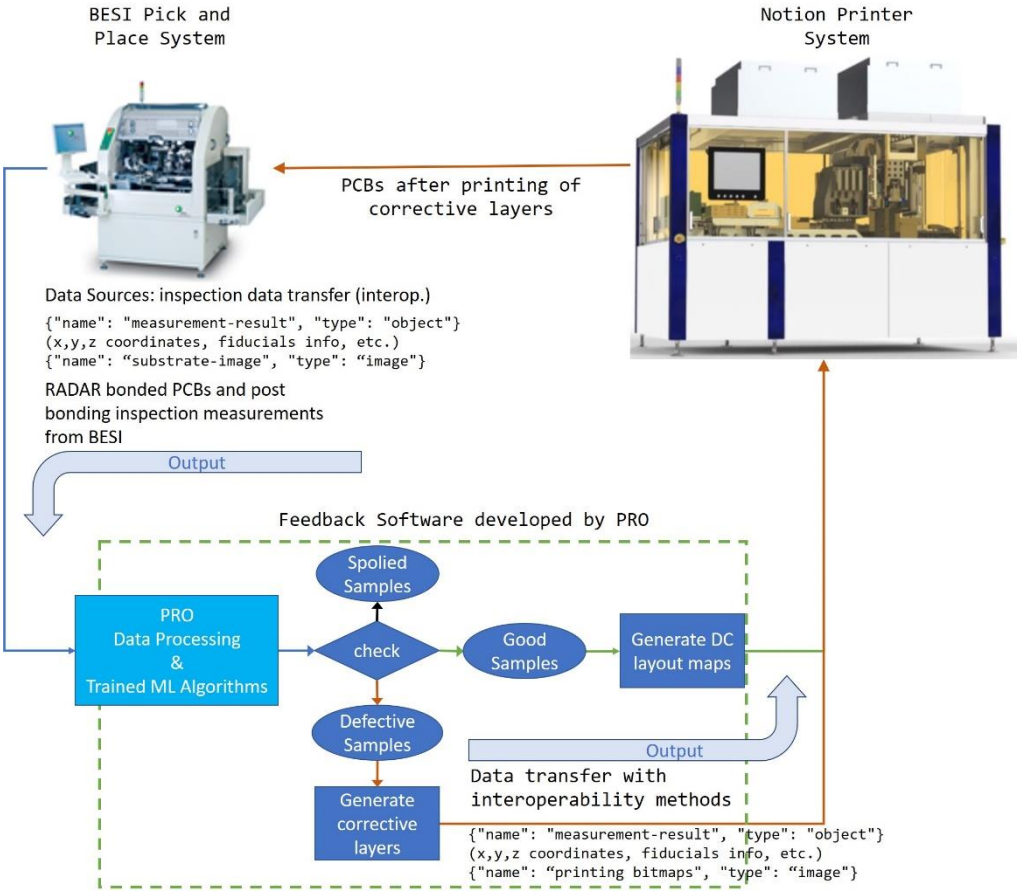

Figure 2. The closed loop diagram for error compensation of RADAR PCBs using inkjet printing

Electronic integration of microchips via inkjet printing

Gerald Stubauer [a], Peter Bauer [a], Pavel Kulha [a], Michael J. Haslinger [a], David Hahn [b], Jochen Seeser [b], Christian Debatin [b], Alexander Fischer [c], Istvan Denes [c], Christian Geissler [d], Benedikt Pressl [e], Birgit Brandstätter [e], Dieter Holzinger [f], Doron Gurovich [g], Semyon Melamed [g]

[a] PROFACTOR GmbH, Steyr-Gleink, 4407, Austria
[b] NOTION Systems GmbH, Schwetzingen, 68723, Germany
[c] ROBERT BOSCH GmbH, Renningen, 71272, Germany
[d] INFINEON Technologies AG, Regensburg, 93049, Germany
[e] BESI Austria GmbH, Radfeld, 6241, Austria
[f] TIGER Coatings GmbH & Co KG, Wels, 4600, Austria
[g] PV Nano Cell Ltd, Migdal HaEmek, 23100, Israel
e-mail: gerald.stubauer@profactor.at

Autonomous driving and self-driving cars represent one prominent example for the use of microelectronics and sensors, most importantly RADAR and LIDAR sensors [1]. The public awareness and the industrial need for further miniaturization of such sensor packages is the main driver of ongoing efforts in the automotive sector to be able to integrate such devices into the car body like in the bumpers and head lamps instead of attaching them. Safety (for the driver and others) is the most important key aspect of the automotive sector. Therefore, high-value and high-performance sensor systems are required for advanced driver-assistance systems (ADAS) as well as robotic cars. The large size of such sensor devices, their weight and power consumption are current issues of RADAR systems within cars. These can be overcome by the cost- and resource efficient pathway for RADAR sensor package integration via additive manufacturing processes like inkjet printing.
Here, we show how to leverage inkjet printing in multiple assembly steps of a technology demonstrator for a RADAR sensor package. The demonstrator consists of a printed circuit board (PCB) with cavities where bare RADAR dies are placed directly with contacts facing up (**Figure *1***), instead of a traditional approach using packaged flip-chip assemblies. Thus, a connection of the microstructure of the chip (130µm pitch) with the conducting path structures of the standard PCB (**Figure 2**) can be achieved by inkjet printing of dielectric filling material and electrically conductive ink. The fabrication and validation of this demonstrator includes multiple steps:

- Dispensing of adhesive and assembly of the microchip into the cavity and record of 3D data
- Inkjet printing of polymer layers to fill remaining gaps in the cavity, record of 3D data and printing of additional layers until gaps are filled evenly via a feedback loop
- Contacting of the microchip via inkjet printing of conductive lines
- Electrical characterization of the inkjet-printed electrical contacts to the microchip
- Reliability tests of the contacts

The daisy chain silicon die layout was designed and manufactured by INFINEON and a packaging design (fan-out structure) and the PCB were designed by BOSCH. The assembly process was developed by BESI and the inkjet materials were developed by TIGER (polymer based dielectric ink with low shrinkage) and PV Nano Cell (solvent based nanoparticle ink with high conductivity). An automated generation of printing data and the inkjet printing process were introduced by PROFACTOR and implemented and optimized by NOTION on the TINKER-Pilot-Printer (**Figure *3***). In this work, the inkjet gap filling process and the electronic connection via inkjet printing are shown in more detail and results of electrical characterization and reliability tests will be presented.

Acknowledgments
The project TINKER receives funding from the European Union's Horizon 2020 research and innovation programme under Grant Agreement No. 958472

References:

[1] https://resources.system-analysis.cadence.com/blog/msa2022-the-use-of-radar-technology-in-autonomous-vehicles

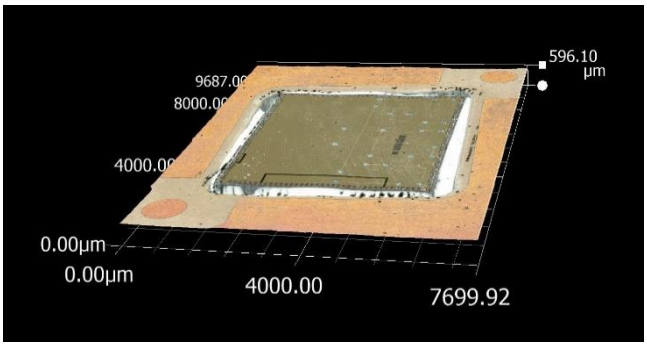

Figure 1. 3D image of a microchip assembled in the cavity of a printed circuit board before electronic integration.

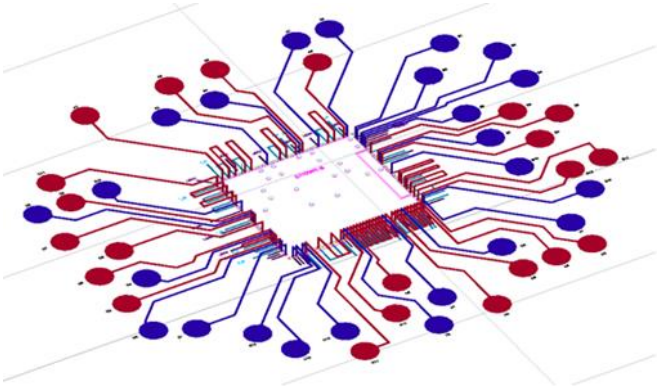

Figure 2. Layout of a contacted daisy chain die in the cavity.

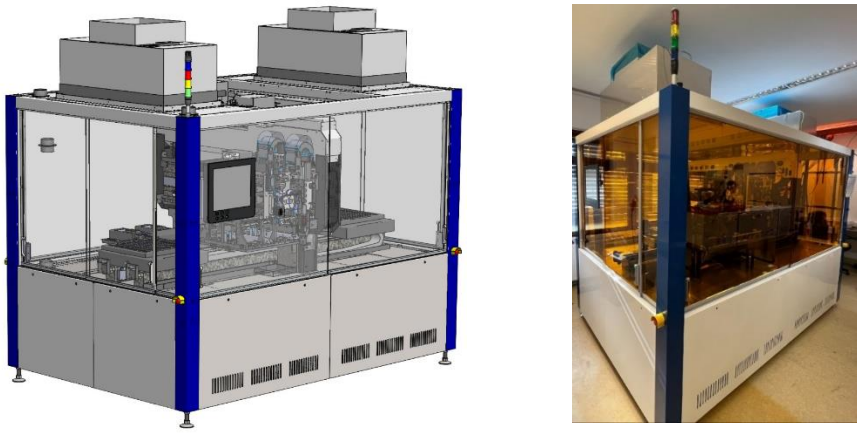

Figure 3. TINKER-Pilot-Printer rendered image (left), built up printer (right)

From Micro to Nano: Integrating cavities in monolithic nanopore Silicon membrane by improved Nanofabrication methods for various Applications

Sanjeev Vishal [a], Henri Jansen [a] , Jesper Yue Pan [a], Jörg Hübner [a], Anil Thilsted [b], Rafael Taboryski [a]

[a] DTU Nanolab, Technical University of Denmark, 2800 Lyngby, Denmark
[b]Spectro Inlets Aps, Ole Maaløes Vej 3, 2200 København Denmark

email: sanvis@dtu.dk

Keywords: Membrane, Green process, Nanofabrication, Silicon, Deep reactive ion etching, DRIE, Gas analysis.

Abstract:

The rampant consumption of fossil fuels has triggered an overwhelming release of greenhouse gases. As a response, technology development is targeting renewable energy sources, converting fossil fuels to renewables, and capturing CO_2 into sustainable gases and liquids. An enabling factor for this transition is a reliable in-line analysis of gaseous species strengthened by a user-friendly analyte sampling technique.

This study envisages a monolithic silicon membrane-based gas separator (SMS) fabrication with an embedded cavity and a well-defined capillary as an outlet channel. The SMS facilitates volatile organic compounds (VOC) separation from emission sources, ambient air, or industrial processes that reflects targeted gas composition, which is then analyzed using on-site monitoring equipment.

A coarse-tuned three-step DREM (Deposit, Remove, Etch Many Times) procedure was employed to create a silicon nanopore membrane of 4 µm deep, using SF_6/C_4F_8/Ar gas mixture. At low pressure, the subsequent isotropic etch process formed a 2µm buried cavity beneath the etched holes, featuring an opening width of 300 nm and pitch of 700 nm. An atomic layer deposited (ALD) alumina (Al_2O_3) hard mask with high etch selectivity for Silicon, measuring 50 nm, was utilized. A quantitative investigation of the etched samples was performed using scanning electron microscopy.

Materials and Methods:

A 50 nm thin alumina film was deposited on a silicon wafer at 200 °C using trimethylaluminum (TMA) and H2O as precursors by ALD (Picosun R200 ALD). Silicon wafers (150 mm diameter, DSP, 5–10 Ω cm phosphorus-doped n-type, 500 µm thick, ⟨100⟩ orientation) were coated with 65nm bottom anti-reflective coating (BARC) and DUV resist, then the nanopatterns were inscribed by deep UV (DUV) lithography (Canon FPA-3000 EX4) with 248nm KrF exposure laser source. The smallest critical dimensions were 300 nm holes with a 700 nm pitch [1]. After patterning of photoresist and BARC removal, the continuous etch process is performed in an inductively coupled plasma (ICP) (SPTS) to etch alumina. A chlorine plasma was generated at low pressure using BCl_3 and Cl_2 gases with a 2:1 gas ratio at low platen power of 10W with 500 W coil power. The reason for choosing BCl3 as one of the feed gases was reflected in the fact that it was primarily used for the etching of materials that are covered with native oxides in the form of BCl_xO_y.

The two-step deep reactive ion etching (DRIE) procedure was conducted in a dual-source setup (DRIE Pegasus, SPTS) in a sequential switching mode. A vital feature of this method is that each step is interconnected with precise gas flow adjustments, which enhances controllability and nanoscale

precision and minimizes anomalies. Initially, the nanoholes were anisotropically etched using the DREM [2] process with the optimized process parameters. This process has been tuned to retain more passivation on the sidewalls necessary during the second DRIE step. The second DRIE step consists of passivation fortifying and bottom polymer removal at very low pressure, followed by an isotropic etch. The passivation fortifying by C4F8 is required to make stronger polymer-protected sidewalls. Then the horizontal passivation at the bottom of the holes is etched with high directionality preserving the sidewall passivation and furnishing a path for the long-run isotropic etch process. Finally, the isotropic etch process at low pressures forms interconnected cavities beneath the etched holes, as shown in Fig 1. An outlet channel was etched from the other side by patterning a hole with different diameters on the alumina layer connecting to the cavity as a last step by DRIE etch process. The etched samples are characterized using scanning electron microscopy (SEM, Supra V60, Zeiss) that allows for a 10 nm resolution.

Results and discussions:

In summary, by experimental exploration, and theoretical studies, a fabrication technique for SMS has been studied based on a tuned DREM process, which features mass-fabrication and wafer-level. Also, DOE reveals the influence of process parameters on etch rate and sidewall profile.

References:

[1] Keil, M., Wetzel, A. E., Wu, K., Khomtchenko, E., Urbankova, J., Boisen, A., Rindzevicius, T., Bunea, A. I., & Taboryski, R. J. (2021). Large plasmonic color metasurfaces fabricated by super-resolution deep UV lithography. Nanoscale Advances, 3(8), 2236-2244.

[2] Chang, B. (2018). Technology Development of 3D Silicon Plasma Etching Processes for Novel Devices and Applications. Technical University of Denmark.

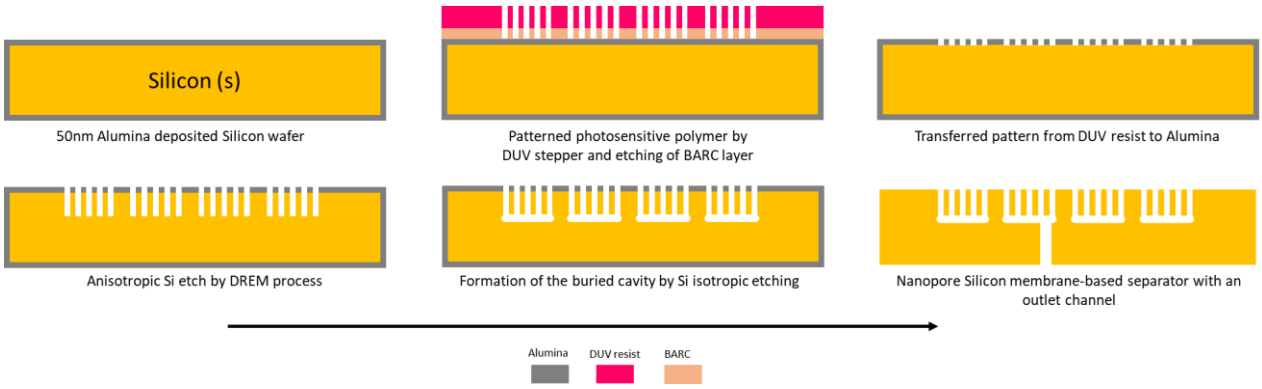

Figure 1: Schematic of the process flow for fabricating a nanopore Silicon membrane-based separator (SMS).

A ReRAM Optronic Physical Reservoir for Fashion Styles Recognition

Jiayi Li [a], Haider Abbas [a], Asif Ali [a], Xin Ju [b], and Diing Shenp Ang [a]*

[a] Nanyang Technological University, Singapore, 639798, Singapore
[b] Agency for Science, Technology, and Research (A*STAR), Singapore, 138634, Singapore
*e-mail: edsang@ntu.edu.sg

1. Introduction

Emerging resistive switching memories have shown great potential for in-memory computing applications, such as deep neural network acceleration [1], neuromorphic and physical reservoir computing [2,3]. Here, we demonstrate a micro optronic reservoir (OR) system based on the ITO/HfOx/TiN memristive crossbar device to reduce the software and hardware overhead of image classification task (Figure 1). The system comprises an input layer feeding the image parallelly into the OR using LED light pulses. The OR outputs are then fed into a trained readout layer for classification. The system showed good accuracy on the fashion-MNIST (f-MNIST) dataset [4] and excellent robustness to ReRAM device noise and variation.

2. Experimental

Device Fabrication

A 300 nm thick SiO_2 grown on Si was used as substrate. After cleaning, the active stack was deposited. 30 nm of TiN was deposited at room temperature by electron-beam evaporation. The bottom TiN electrode was defined by optical lithography and inductive coupled plasma reactive ion etching (ICP-RIE). 7 nm of HfO_2 was deposited at 150 °C with tetrakis(ethyl methylamino) hafnium (IV) and H_2O vapor by atomic layer deposition. Then, 60 nm of ITO (commercial, 99.9% target with a 90:10 In_2O_3:SnO_2 weight ratio) was deposited at room temperature by RF sputter. The top ITO electrode was then defined by optical lithography and ICP-RIE, with the HfO_2 acting as an etch stop layer. The opening for contact pad was then defined by ICP-RIE of the HfO_2 layer. No annealing was carried out. The area of the cross-point is 8 μm^2. The microscope image and schematic of the device structure are shown in Figure 2 (a) and (b), respectively.

Electrical Characterization

The devices were tested by Keithley SCS-4200 semiconductor analyzer. A broadband white light was supplied by a LED light as shown in Figure 2(c). The device demonstrates good repeatability and low operating voltage (average set/reset voltages are –0.28 V and 0.69 V, respectively). After set, the device can be momentarily reset by a light pulse, after which it shows a gradual recovery back to the set state. The decrease and recovery of the current are hypothesized to arise from light induced recombination and reformation of vacancy-interstitial defects, respectively [5].

3. Results and Discussions

The short-term memory of light induced reset may be exploited for reservoir computing of temporal light pulses. By inputting different light-pulse patterns, the device can demonstrate distinct output currents in accordance with the input patterns. Figure 3(a) shows the normalized output current after each predefined interval for a series of 3-bit pulse patterns. After the last interval, all 8 states resulting from the 3-bit pulse patterns are distinguishable. Figure 3(b) shows the simulated OR output for the “Boot” image from the f-MNIST dataset. Device noise and variability are accounted for by assuming each normalized output to be Gaussian distributed with a pre-assigned standard deviation σ.

Figure 4(a) shows the classification results for a logistic-regression trained readout layer (σ = 0.025), with an overall accuracy of 85% for all 10 classes in f-MNIST. Especially, the accuracy for boots, bags, and sneakers reached 95%. Figure 4(b) shows the overall accuracy as a function of σ. Even with a significant σ of 0.5, the accuracy is maintained at ~76%, proving the system’s robustness against device noise and variability. The error bar in the inset also shows little cycle-to-cycle variation for different simulation runs.

Acknowledgements

This work is supported by the Singapore Ministry of Education under Research Grant MOE-T2EP50120-0003.

References

[1] P. Yao *et al.* Nature. **577** (2020). [2] W. Wang *et al.* Sci Adv. **4** (2018). [3]Y. Zhong *et al.* Nature Electronics. (2022). [4] H. Xiao *et al.* arXiv preprint arXiv:1708.07747. (2017). [5] M.Y. Hassan and D.S. Ang: ACS Appl. Mat. Inter. **11** (2019).

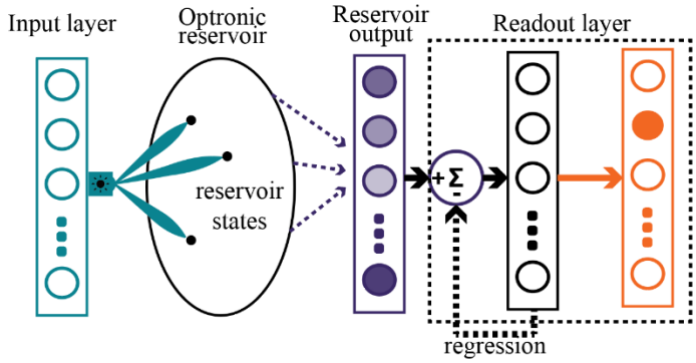

Figure 1 Optronic reservoir system for image classification. The reservoir is a 28×28 crossbar array (simulated) of ITO/HfO_x/TiN ReRAM devices. The readout layer comprises 10 output neurons (corresponding to 10 classes of the f-MNIST dataset) and 7840 synapses.

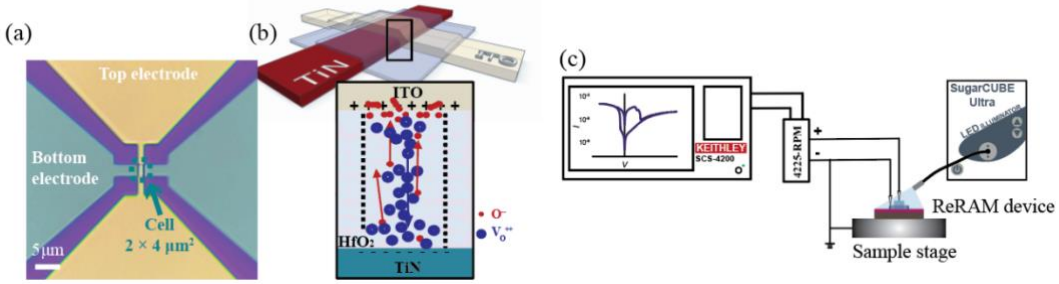

Figure 2 (a) Optical microscope image of our ITO/HfO_x/TiN ReRAM crossbar device. (b) Schematic of device structure. Inset: Oxygen vacancies and interstitials distributed across HfO_x. (c) Device characterization setup.

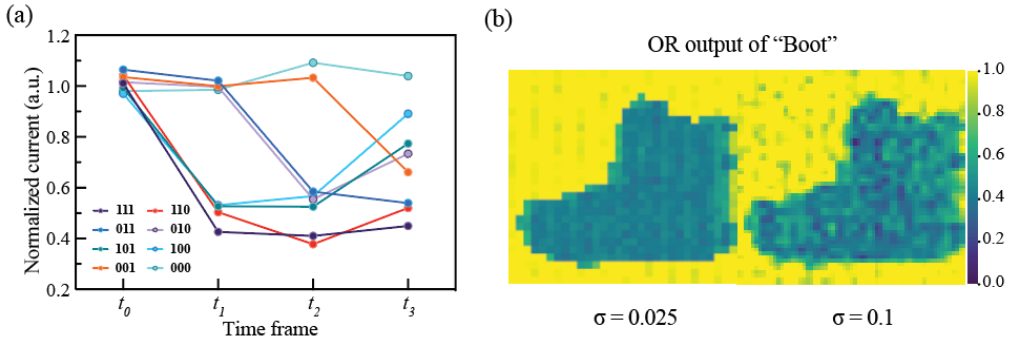

Figure 3. (a) Average optronic reservoir response of 3-bit light-pulse patterns read at different time intervals between pulses. (b) Example of reservoir output with device noise and variation.

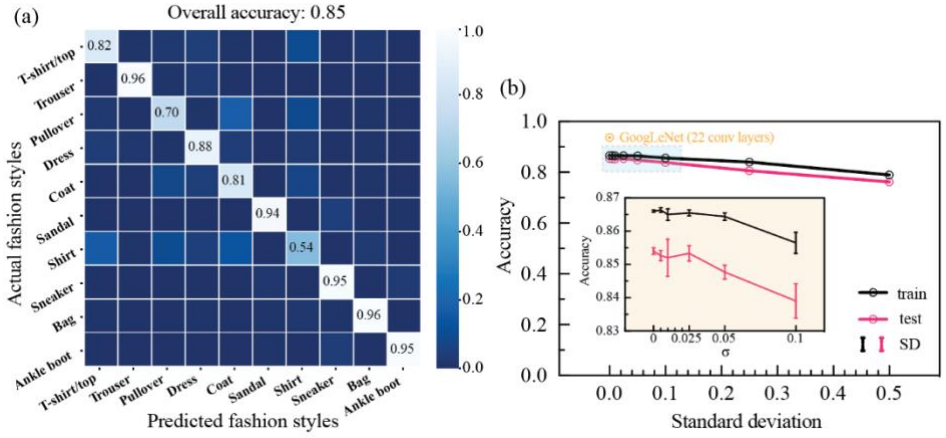

Figure 4. (a) Confusion matrix for all 10 classes in the f-MNIST dataset (80% training, 20% testing). (b) Overall accuracy as a function of standard deviation σ for device noise and variability (assumed to be Gaussian distributed). The accuracy for GoogLeNet is also shown for comparison. Inset: Accuracy for σ up to 0.1. Lines show mean values and error bars denote one standard deviation.

Optimisation of a physical reservoir computer's parameters using a genetic algorithm non-linear search

Claude Meffan [a], Taiki Ijima[a], Amit Banerjee[a], Jun Hirotani [a], Toshiyuki Tsuchiya[a]

[a] Kyoto University, Kyoto, 615-8540, Japan

e-mail: claudemeffan@gmail.com

In this work, we propose that a genetic algorithm can be used to optimise the parameters of a Surface Acoustic Wave (SAW) reservoir computing system. Using a SAW resonator as a physical processing neuron, we create and measure the performance of a time-delay reservoir computer, optimised by a manual search. Using this performance as a baseline, we then find the hyper-parameters of a genetic algorithm (mutation rate, population size, cross-over type) which allow for quick and automatic convergence. We discuss the nature of the converged parameters relative to the size of the search space and discuss how this tactic can be used in future physical reservoir computing systems.

Background

In the past, Surface Acoustic Wave (SAW) devices were used for lightweight and efficient signal processing [1]. However, due to the small non-linear coefficients of piezoelectric materials [2], SAW information processors have generally been considered inefficient for non-linear processing tasks, for example convolution, and classification tasks . Despite this, efforts to create SAW processors have continued, as they can operate at very high frequency and are very small and lightweight compared to optical devices.

Reservoir computing is a neural network algorithm which reduces the complexity of the training process. Recently, the concept of a time-multiplexed reservoir computer was proposed, allowing many different novel implementations of Physical reservoir computers to be feasible [3]. Physical Reservoir Computers are a neural network in which the neurons and interconnecting weights are embodied by sensors, actuators, or other physical systems which provide the essential functions of the network. In addition to being power efficient, using non-linear sensors or actuators as processing neurons also allows for direct input of physical stimuli into a neural network.

Results

Recently, we demonstrated that a 39 MHz SAW resonator device could perform non-linear classification tasks (Figure 1). This was achieved by integrating the resonator into a time-delayed positive feedback loop, to create the previously discussed time-multiplexed reservoir computer. While this result demonstrates that SAW devices can indeed perform complex non-linear processing, the optimization of the various network parameters was arduous and manual. In this work, we propose that a genetic algorithm (Figure 2) can be used to optimize the performance of the reservoir computer. Using the previously identified performance as a benchmark, we examine the effect of population size, mutation rate, and gene cross-over type on the convergence of the genetic algorithm, when using a 24-bits chromosome. The results, shown in Figure 3, show that the mutation rate (Figure 5 **c**) has the largest effect on the convergence of the system. A 5% mutation rate provided rapid convergence to the optimal parameters. The generational population size (Figure 5 **a**), and cross-over type, (Figure 5 **b**), were also influential but were less sensitive to change. In the future, we wish to use this system to examine a wider range of SAW devices for reservoir computing purposes.

[1] C. Campbell, *Surface Acoustic Wave Devices and Their Signal Processing Applications*. Elsevier, 2012.
[2] L. Shao *et al.*, "Electrical Control of Surface Acoustic Waves," *ArXiv210101626 Phys. Physicsquant-Ph*, Mar. 2022, Accessed: Mar. 17, 2022. [Online]. Available: http://arxiv.org/abs/2101.01626
[3] G. Tanaka *et al.*, "Recent advances in physical reservoir computing: A review," *Neural Netw.*, vol. 115, pp. 100–123, Jul. 2019, doi: 10.1016/j.neunet.2019.03.005.

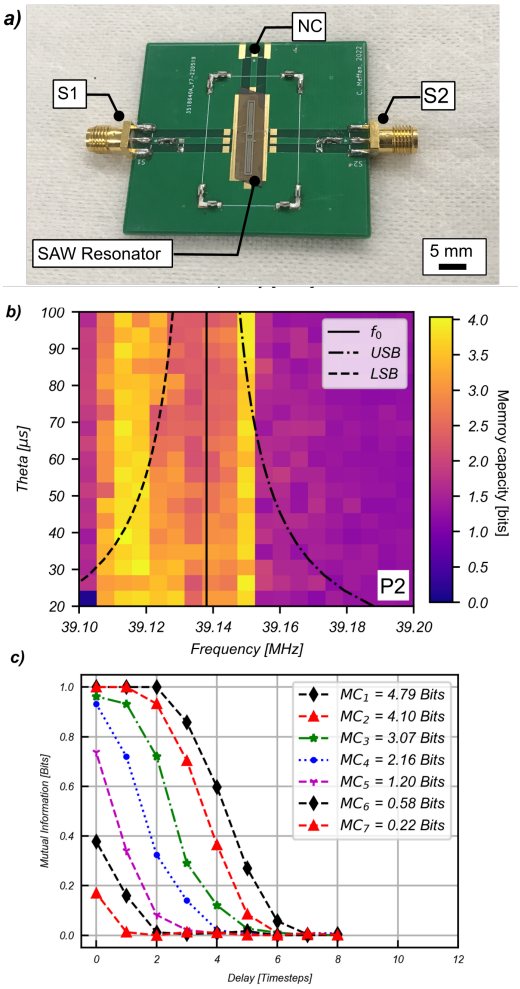

Figure 1: *The results of the time delayed binary parity task.* ***a)*** *The SAW resonator device used as a neuron in the physical reservoir computing system.* ***b)*** *The memory capacity (Shannon information content) of the reservoir as a function of resonator frequency and input rate.* ***c)*** *The memory capacity of reservoir for the binary parity tasks, of increasing order.*

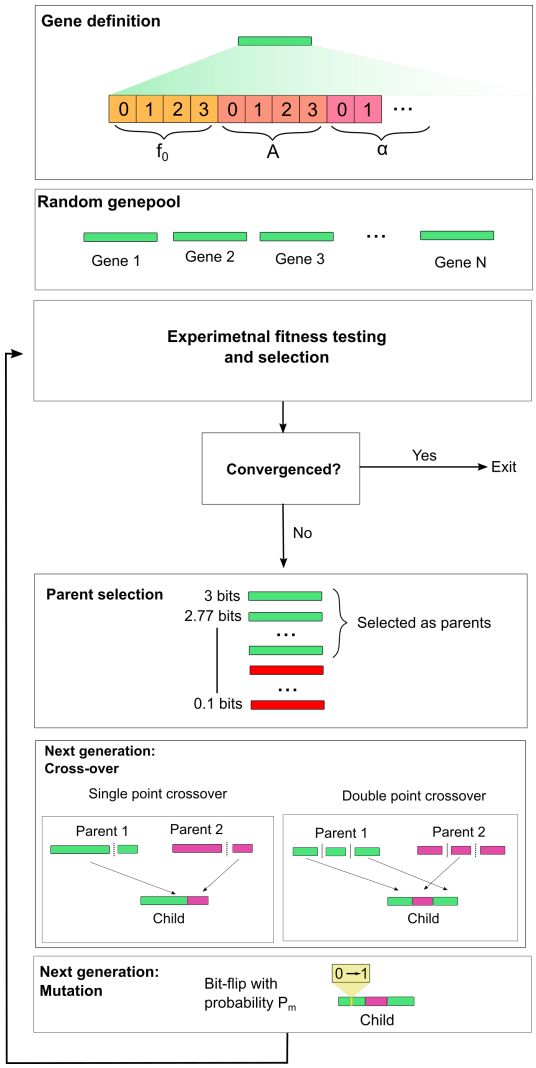

Figure 2: *A description of the genetic algorithm optimization process, used in this work to optimize the hyper-parameters of the SAW reservoir computer. In this work a 24-bit chromosome is used, containing 6 different parameters of the reservoir computer. In the future, longer, and more densely packed chromosome will be used for more precise results.*

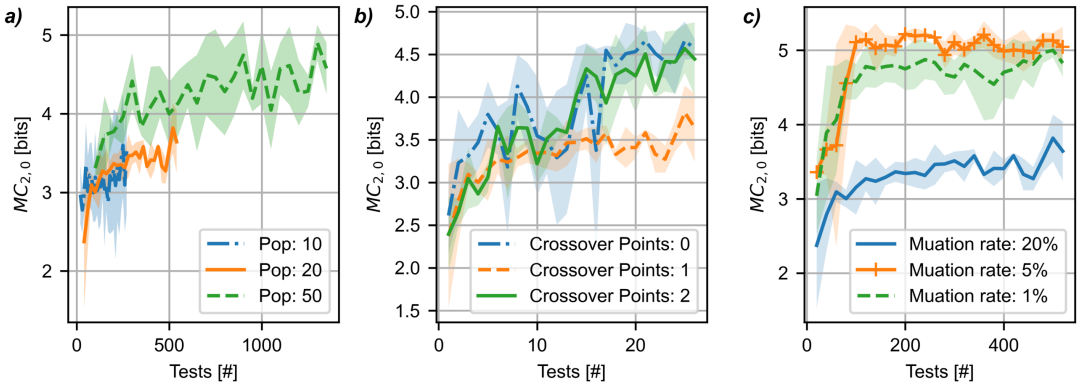

Figure 3*: The convergence of the genetic algorithm to the known high performance hyperparameters for the SAW reservoir compute. Lines represents the average of 3 tests, the shaded areas show the standard deviation.* ***a)*** *Population sizes of ~50 converge quickly to the known maximum performance (5 bits).* ***b)*** *The type of crossover type does not appear to substantially impact the convergence, however 0 point and 2 point do appear to outperform single point crossover.* ***c)*** *Mutation rate appears to be the most critical hyper-parameter in the convergence of the genetic algorithm. Rates of ~5% appear to allow the fastest and most reliable convergence.*

Design, fabrication, and characterization of a label-free sensor using a taquito-like MoS2 morphology as channel.

Martínez-Angeles W. L [a], González-Reynoso O [a], Carbajal-Arizaga G [c], Cortese, B [b], and García-Ramírez M.A [a].

[a] Universidad de Guadalajara, Guadalajara, 44100, México
[b] CNR-Nanotec, Università Sapienza, 00185 Roma, Italy
e-mail: mario.garcia@academicos.udg.mx

The Molybdenum disulfide is a member of Transition Metal Dichacogenides Family. The MoS2 structure consists of two layers of Sulphur atoms and one layer of Molybdenum between them (S-Mo-S) [1]. The intra-layer bond, sulfur-molybdenum, is covalent and the layers are bonded by Van der Waals interactions [2]. This allows the MoS2 to feature different kinds of morphologies with different electronic properties [3]. Thereby, we develop a label-free sensor using a novel MoS2 structure derivative of a morphology called "taquito-like" (Fig. 1) as a detection channel. In here, we synthesized MoS2 structure through a hydrothermal method and place it on a Si/SiO2 substrate, Subsequently, we deposit a Mo electrode in each side of the structure. The proximal portion was connected to voltage and the distal portion to the ground. The sensor was tested by electromagnetic field perturbances when it is in contact with different solutions; these solutions contain molecules commonly found in biogenic substances. The recorded data was conditioned and processed with separation algorithms (such as Blind Source Separation) in order to characterize the involved molecules.
In this work, we obtain a system capable to record and identify signals caused by the interaction between the molecules and the detector. The sensor returns a family curve that describes a molecule's set. The separation algorithm is responsible for identifying the curve that represents each molecule. Once the molecule signals are detached, it is possible to quantify the molecules amount in the analyzed solution.

[1] T. Nawz, A. Safdar, M. Hussain, D. Sung Lee, & M. Siyar. (2020). Graphene to advanced MoS2: a review of structure, synthesis, and optoelectronic device application. *Crystals*, *10*(10), 902.
[2] R. Dickinson and L. Pauling. The crystal structure of molybdenite. Journal999
of the American Chemical Society, 45(6):1466–1471, 1923
[3] Samy, O., Zeng, S., Birowosuto, M. D., & El Moutaouakil, A. (2021). A Review on MoS2 properties, synthesis, sensing applications and challenges. *Crystals*, *11*(4), 355.

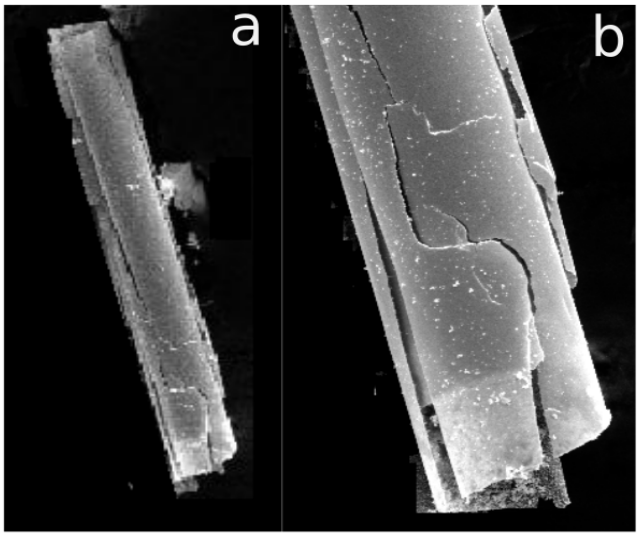

Figure 1. SEM image of taquito-like morphology, a) represents the hole morphology while b) is a close-up of the structure in which we can observe the MoS2 rolled-up structure.

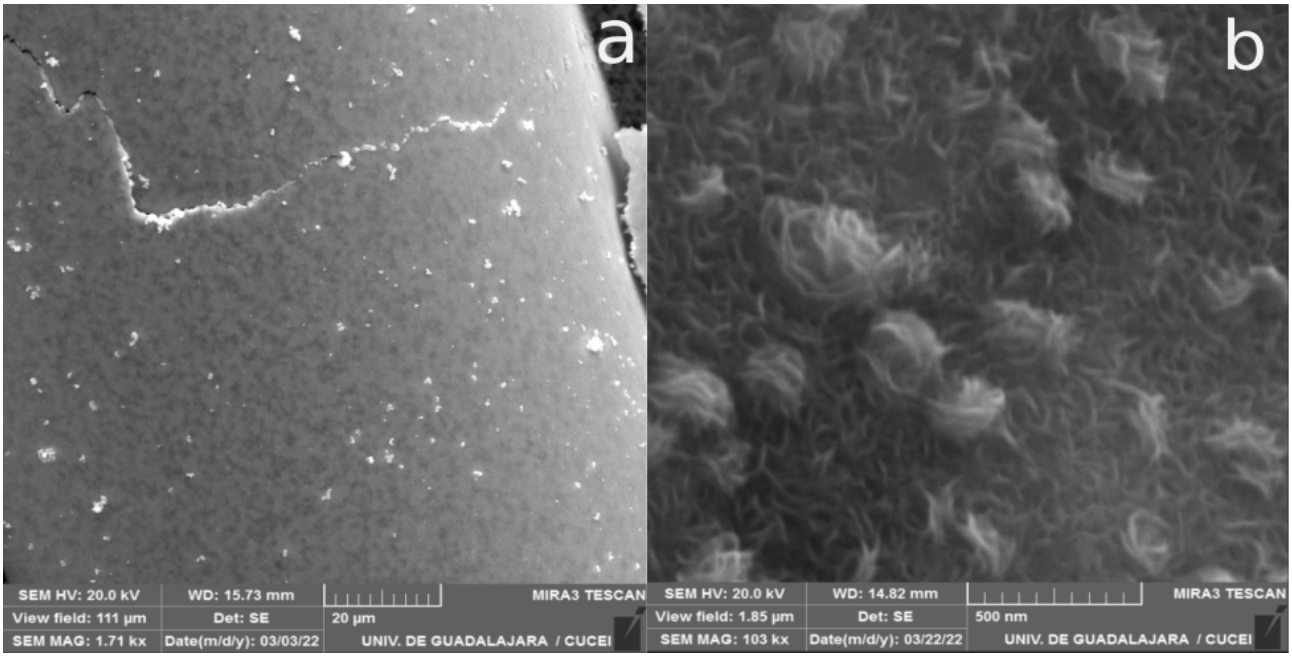

Figure 2. SEM image of MoS2 taquito-like a depicts the anverse surface and b) the obverse surface.

Improved gate oxide quality by making enhanced structure in sub-14nm DRAM

Hyojin Park [a, b], Byoungdeog Choi [b]

[a] DRAM Process Architecture team, Samsung Electronics, Hwaseong-si, 18448, Korea
[b] Sungkyunkwan University, Suwon-si, 16419, Korea
e-mail: bdchoi@skku.edu

Abstract
As the node of DRAM products is advanced, it became important to improve gate oxide reliability. There are many causes according to the gate oxide reliability, usually oxide breakdown is occurred due to the strong electric field of corner Si substrate. So, to get over this, making a proper structure for gate oxide breakdown is most important and we usually focused on the thickness of dielectric. But there are limits, so we desperately need a novel way to overcome. In this paper, we suggested a new method that can improve gate oxide reliability by making a better structure in sub-14nm DRAM, and how it can reduce the gate oxide breakdown. With this experiment, we varied cleaning process times to make round structure and figured out the structure by TEM measurement, and the roundness of corner Si is increased by 27% and TDDB (Time dependent dielectric breakdown) is also increased by 3% even in case of 8% larger corner roundness in n-channel MOSFETs fabricated in the Samsung Electronics sub-14nm DRAM process.

Introduction

As the size of device is shrunk, gate oxide reliability are occurring as an important problem in DRAM products. There are various models of gate oxide breakdown, and it is generally known that the high trap density in a specific area between Si and gate oxide is acting as making the percolation path, which causes gate oxide breakdown [1, 2]. To get over this, it became important to increase gate oxide thickness [3]. However, as the physical dimension of gate insulator structure is decreased so far, gate structure is becoming unfavorable to gate reliability, and it raised concerns about gate oxide breakdown in sub-14nm DRAM. To overcome this problem regardless of structure limits, redesigned process is required, and we found out a new way to improve the gate oxide reliability.

Experiment and results

Among various types of thick oxide transistor, the weak transistor of gate oxide reliability has several characteristics like formation of a highest electrical field and the lower electrical gate oxide thickness compared to other gate structure. Based on this, we defined the structure lowering electric field is the key parameter to improve gate oxide reliability, so focused on making round corner of gate [4, 5]. To increase roundness of Si corner, we tested wet cleaning times and made the gate structure with various corner size. In the experiment, we evaluated the various process times (decreasing 20 to 60 seconds) and analyzed the structure with TEM. As a result, according to the decreasing 1st wet cleaning time, corner roundness is increased 27% of reference as shown in Figs 1 and table I. We could figure out this is because the process is focused on oxide removal of STI (Shallow trench isolation) rather than etching Si as shown in oxide recess of table II. So, when the 1st process time is lower, Si substrate is much exposed to wet chemicals during 2nd process time and it make round corner of Si like as shown in Figs 2. To figure out round corner effect in gate oxide reliability, we demonstrated TDDB test in n-channel MOSFETs fabricated in the Samsung Electronics sub-14nm DRAM process. And it is verified that TDDB is improved by 3% even in case of 8% larger corner roundness gate structure like in Figs 3.

[1] Stathis. J, Journal of Applied Physics, Vol. 86 No. 10 (1999) 5757–5766.
[2] Degraeve, Robin, et al., IEEE Transactions on Electron Devices Vol. 45 No.2 (1998) 472-481
[3] J. W. McPherson, 2016 IEEE International Reliability Physics Symposium (IRPS, Pasadena, 2016).
[3] Tai-su Park, International Electron Devices Meeting, Technical Digest (IEEE, San Francisco, 1996) 163-1918.
[4] Tseng, Po-Hao, and Jenn-Gwo Hwu., Solid-state electronics Vol. 91 (2014) 100-105.

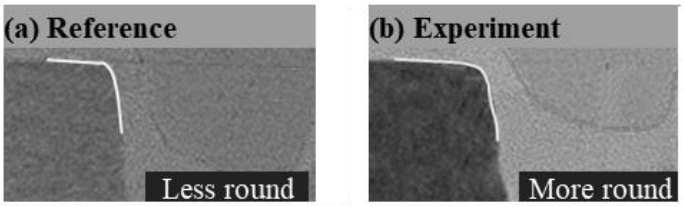

Figure 1. Changing Si corner profile according to the cleaning time in TEM measurement: (a)reference (b)decreasing processing time (60seconds).

Table I. Process flow of experiment.

	Process content	Conditions
Process-1	Wet cleaning	Variable
Process-2	Wet cleaning	Fixed

Table II. Variation in Si corner roundness and oxide recess in STI by various chemical etching times (unit : second).

Time(s) / Item	-60s	-40s	-20s	Ref.
Corner roundness (a.u)	1.37	1.14	1.12	1.0
Oxide recess (a.u)	0.56	0.59	0.85	1.0

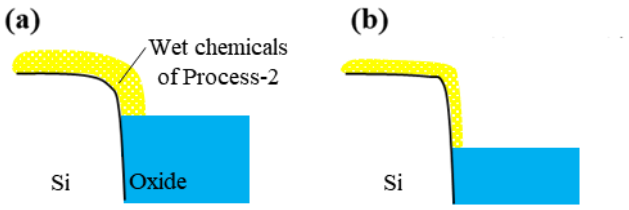

Figure 2. Diagram about how to change corner roundness according to oxide recess: (a)low recess (b)high recess. As oxide recess is increased during process-1, wet chemical is less crowded in Si during process-2.

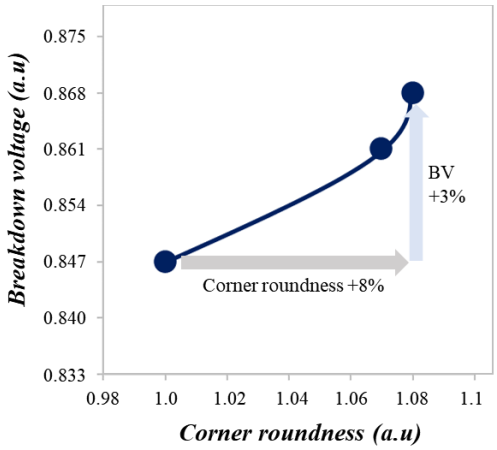

Figure 3. TDDB test by changing gate corner roundness.

Thermo-mechanical behaviour of different sealing materials used as encapsulants in Power Modules

Spano Chiara [a, b], Galfrè Giulio [a], Mattiuzzo Emilio [b], D'Ancona Lorenzo [b], Bertana Valentina [a], Luciano Scaltrito [a], Ferrero Sergio [a]

[a] Politecnico di Torino, Torino, 10129, Italy
[b] VISHAY Semiconductor Italiana S.p.A, Borgaro Torinese, 10071, Italy
e-mail: chiara.spano@polito.it

Thanks to latest advancements in semiconductors, the power density and the operating temperatures of power modules are becoming a key point, especially for the automotive market. At the same time, a higher reliability of the package is demanded to guarantee a longer lifetime. Consequently, improved materials and a novel designed thermal management system are crucial topics that are encouraging the development of new assembly technologies.

Power modules are made up by a substrate, whose purpose is to accommodate the semiconductors, and a package to protect the inner components from the environment and to increase the robustness of the system [1]. The main existing packages are based on two encapsulation technologies: Vacuum Potting Gel (VPG), with a gel as sealing, and Transfer Molding (TM), with Epoxy Molding Compound (EMC) as encapsulant. A schematic cross section is represented in **Figure 1** for both the concepts.

VPG consists of filling a protective plastic casing with silicone dielectric gel, so that the entire substrate and the soldered components are fully covered. The silicone layer owns a low viscosity behavior, optimal insulation properties and short curing times. Differently, the TM technology consists in injecting thermosetting pellets of EMC at high temperature (175°C) in a mold, where the substrates with assembled components are placed. A flow of epoxy covers everything until it crosslinks and solidifies in a unique compact body, followed by a cycle of Post Molding Cure (PMC) to toughen the material. TM is advantageous to save costs (no housing required), improve compactness and increase reliability through a higher moisture withstand [2].

This work aims at demonstrating if power modules, with the same substrate and electrical configuration but different sealing materials, may have different thermal behaviors at the same operating conditions. Indeed, for investigating this condition, two types of modules have been assembled with the same substrate and dice but different packages: sample A (package: gel sealing + plastic case) and sample B (package: EMC).

An evaluation of the Thermal Resistance junction to heatsink ($Rth_{j\text{-}s}$) has been previously simulated with a Finite Elements Analysis (FEA), on both the packages, and then assessed through an experimental test.

FEA has been configured and run in Comsol Multiphysics software, where the power modules were set as in the practical measurements. Therefore, modules have been evaluated as mounted on a copper plate with an interposed thermal grease 40 µm thick layer and, the whole system was fixed onto an aluminum water heatsink with an inlet water temperature of 18°C and a flow rate of 2 m^3h^{-1}. In terms of mesh, a fine tetrahedral geometry has been applied to the substrate and the soldered components, while a coarser one was generated for the remaining larger elements. The setup representation for VPG model is shown in **Figure 2**.

A pure thermal FEA shows that, although the EMC owns declared thermal conductivity values ($\lambda_{k\ EMC}$ = 0.9 $Wm^{-1}K^{-1}$) higher than gel sealing ($\lambda_{k\ gel}$= 0.1 $Wm^{-1}K^{-1}$), the heat transfer seems to be not sufficient to significantly change the temperature on the dice and affect the values of $Rth_{j\text{-}s}$, as visible in **Figure 3**. However, the experimental measurements of $Rth_{j\text{-}s}$ have provided different values, demonstrating an improvement in the thermal dissipation for the molding encapsulation (sample B). Indeed, applying 100W on each die, the test yields values in sample B that are approximately 20% lower than sample A. The reasons of this discrepancy are being investigated in order to understand if this variation is related to a difference in thermal conductivity of the sealings or to a slightly higher shrinkage of the EMC, as result of the TM and PMC temperature processes. As a matter of fact, a different final warpage of the product could influence the contact of the module with the thermal grease, affecting the thermal distribution in the materials layers' stack, as demonstrated also in literature [3].

[1] J. Broughton et al., J. Electron. Packag. 140 (2018) 40801 1-11.
[2] J. Schuderer et al.,10th International Conference on Integrated Power Electronics Systems (2018) 1-6.
[3] Y. J. Chen et al.,14th International Microsystems, Packaging, Assembly and Circuits Technology Conference (2019) 120-123.

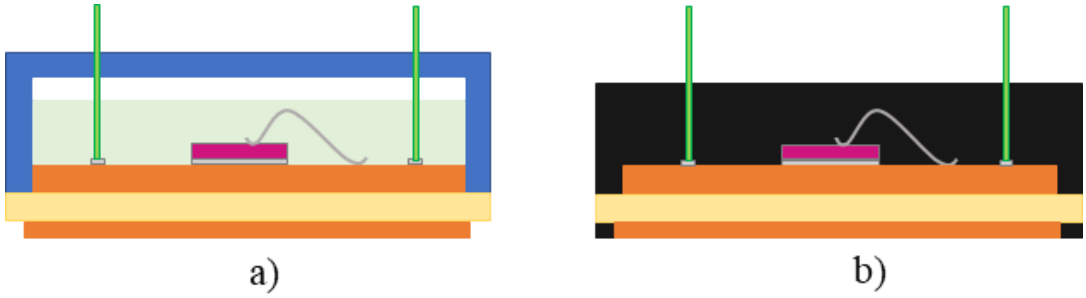

Figure 1: Cross section of both modules: a) VPG module (sample A) is composed from above by an external box, gel layer and the substrate. b) TM module (sample B) is composed from above by an EMC block and the substrate.

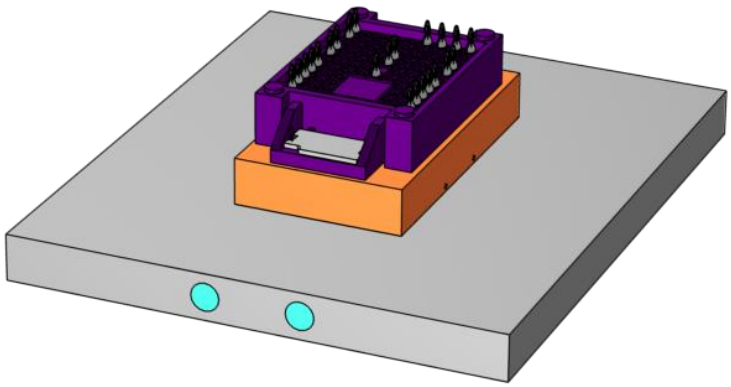

Figure 2: 3D representation of the experimental setup: VPG module is in purple, copper plate in orange and water heatsink in grey.

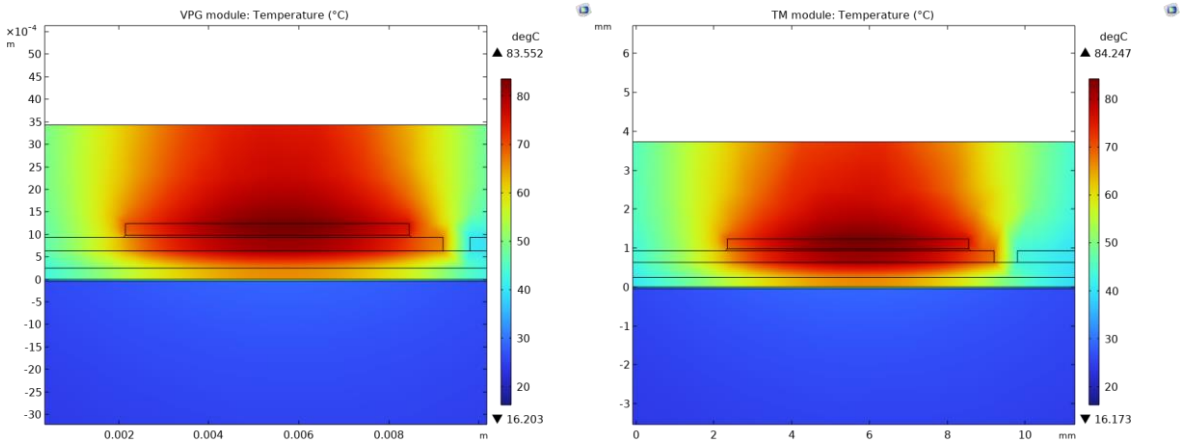

(A) (B)

Figure 3: 2D thermal plots across the maximum temperature cross section of both modules: sample A on the left and sample B on the right.

193 nm ArF lithography for high topology InP wafer processing

A. Zozulia[a], J. Bolk[a], S. Rihani[b], G. Berry[b], M. Robertson[b], J. Rawsthorne[b], K. A. Williams[a] and Y. Jiao[a]

[a] Eindhoven Hendrik Casimir Institute (EHCI), Eindhoven University of Technology, 5600MB Eindhoven, The Netherlands
[b] Huawei Technologies Research & Development (UK) Ltd, IP5 3RE Ipswich, UK
e-mail: a.zozulia@tue.nl

The trend in miniaturization of photonic integrated circuits (PICs) has led to the development of InP membrane photonics, which brings together the advantages of highly confined sub-micron waveguides and monolithic integration of lasers [1]. One of the factors limiting the scaling towards mass production of membrane photonic integrated circuits is a complex technological process, including patterning of features with critical dimension <200 nm, an alignment tolerance of <50 nm and low sidewall roughness. These requirements can be met by electron beam lithography (EBL) [2]; however, with EBL, the manufacturing volume is limited by long writing times. In addition resist coating and development for EBL are often done manually, compromising reproducibility.

In this work, we explored the possibility of using an ASML PAS5500 /1100B DUV scanner for the fabrication of active membrane PICs on a 3-inch wafer scale. The use of a 193 nm ArF lithography for the fabrication of passive membrane PICs has been previously reported [3]. However, the fabrication of active-passive circuits was a challenge due to the high surface topology of active elements (the height of a laser mesa is 920 nm together with a hard mask). The reason is that the 193 nm DUV resist stack is very thin (225 nm) and after development it leaves a non-uniform profile around topology (see Figure 1a). The non-uniformity is coming from the bottom anti-reflection coating (BARC), which is used to increase resist resolution and acts as an adhesion promotor, however it is non-conformal and can become several times the nominal thickness over topology. Therefore, two problems emerge. First, the hard mask cannot be fully etched at the bottom of the topology. Second, the semiconductor becomes exposed at the top of the topology, where the resist stack is thinner than nominal and thus the hard mask gets stripped faster (Figure 1b).

To solve the first problem, we removed the BARC from the stack. To improve the adhesion of the resist, we used HMDS primer, which is a conformal monolayer and does not create the same profile around topology as BARC. We did not observe resolution problems caused by the absence of BARC. To solve the second problem, we used a thicker hard mask at the step of forming the initial topology and did not remove it before depositing extra hard mask for the overlay patterning. The schematic process flow is shown on Figure 2. To validate the process, it was used for fabrication of InP PICs. In this process, the first layer was etched through 720 nm of p-doped InP with 200 nm of SiNx as the hard mask. Subsequently, an overlay lithography was made on top of existing topology, and the second layer was etched in 300-nm thick InGaAsP. On Figure 3 an angled view of structures fabricated with this new 2-layer process are shown. Comparing Figures 3b and 1b, we observe, that, as the result of the improved process, the top part of the structure is fully protected by SiNx, while the second layer is fully open with smooth edge everywhere close to the first layer structures.

In conclusion, we have demonstrated that 193 nm ArF lithography can be used in the fabrication of active membrane photonic circuits with ~1um of topology. This result opens the way to highly scalable mass production of InP membrane photonics.

Acknowledgements
This work was supported by the Huawei research grant HDMI.

References

[1] Y. Jiao *et al.*, "InP membrane integrated photonics research," *Semicond. Sci. Technol.*, vol. 36, no. 1, p. 013001, Jan. 2020, doi: 10.1088/1361-6641/abcadd.
[2] Y. Jiao *et al.*, "Vertical and Smooth Single-Step Reactive Ion Etching Process for InP Membrane Waveguides," *J. Electrochem. Soc.*, vol. 162, no. 8, pp. E90–E95, 2015, doi: 10.1149/2.0371508jes.
[3] J. Van Engelen, S. Reniers, J. Bolk, K. Williams, J. Van Der Tol, and Y. Jiao, "Low Loss InP Membrane Photonic Integrated Circuits Enabled by 193-nm Deep UV Lithography," in *2019 Compound Semiconductor Week (CSW)*, Nara, Japan: IEEE, May 2019, pp. 1–2. doi: 10.1109/ICIPRM.2019.8819069.

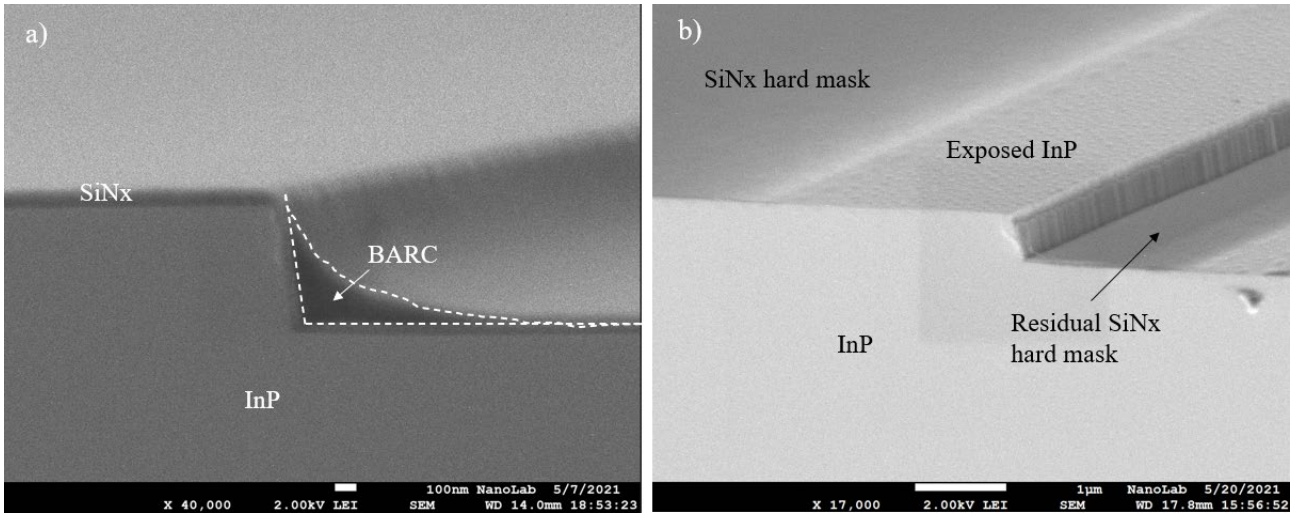

Figure 1. a) Cross-section of the InP wafer with topology. The DUV resist was patterned and developed, however the BARC stays, forming an extra mask close to the tall structures. b) Same cross-section after SiNx hard mask etching. On top of the step, InP is exposed due to thin resist. At the bottom, residual SiNx stays in places, where it was masked by non-uniform BARC.

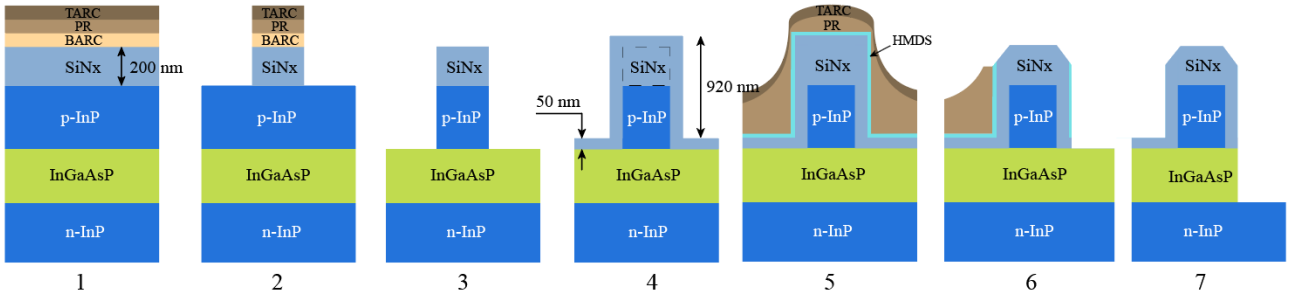

Figure 2. Schematic process flow. 1: On the plain wafer, 200 nm SiNx is deposited as hard mask and 3-layer DUV coating is applied. PR: photoresist. TARC: top anti-reflection coating. 2: after development, SiNx is etched by low pressure CHF3/O2 reactive ion etching (RIE) process. 3: InP is etched, using SiNx as the hard mask. 4: After the InP etching, an extra 50 nm SiNx deposited on top of 200 nm left from the previous step (old mask is shown in dashed line). 5: HDMS is used instead of BARC for the next layer DUV coating. 6: after development, patterning of SiNx is possible anywhere close to the high topology structures 7: Final topology after patterning SiNx mask and etching InGaAsP.

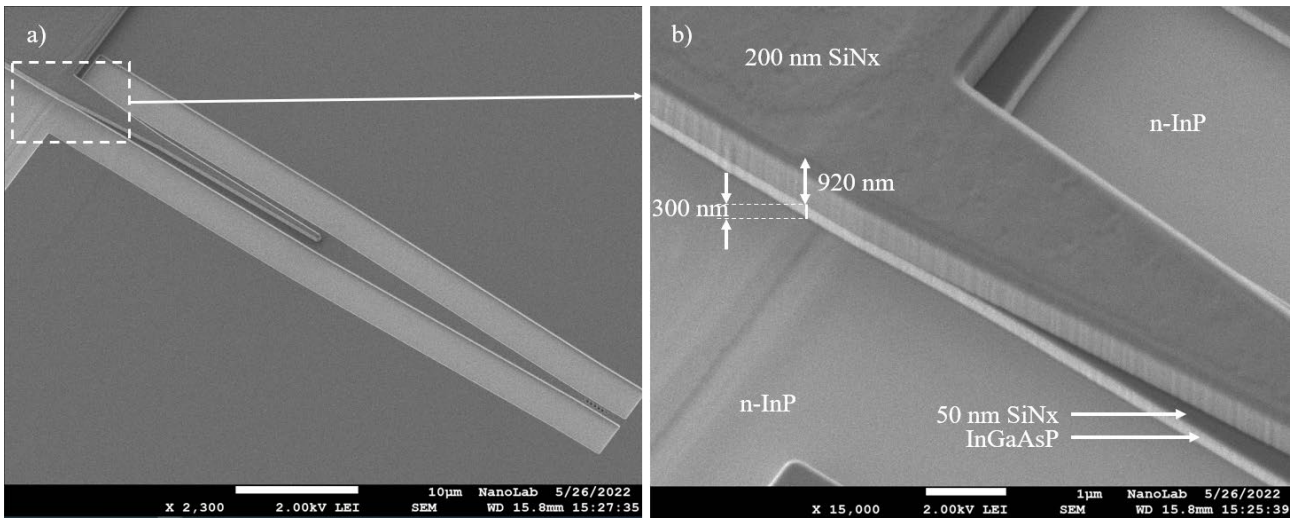

Figure 3. a) Bird's eye view of the 2-layer device fabricated with ArF lithography after second layer etching. b) Inset magnified. Second layer structures are patterned with varying distance to the first layer. The opening is clear and with smooth edge as close as 50 nm (second layer mask thickness) to the first layer topology.

Design and fabrication of an opto-mechanical antenna in the NIR range

Daniyal Khosh Maram[a], Xavier Borrisé[b], Joan Garcia[a], Raul Ruiz[a], Xavier Cartoixà[a], Gabriel Abadal[a]
[a] Dept. Enginyeria Electrònica, Campus UAB, 08193-Bellaterra, Spain; [b] Catalan Institute of Nanoscience and Nanotechnology (ICN2) and Barcelona Institute of Science and Technology (BIST), Barcelona, Spain
e-mail: Daniyal.KhoshMaram@uab.cat

The integration of mechanical elements into a radiofrequency antenna structure has been shown to enable the direct transduction from the electromagnetic domain to the mechanical domain. In a device fulfilling this particular characteristic named MEMSTENNA (combination of a MEMS and an antenna) [1], [2], both static and dynamic actuation have been induced remotely to drive a capacitive MEMS structure without using any local source of energy. The extension of the MEMSTENNA concept to the 1-10 THz range has been proposed to detect radiation in this region of the spectrum with an improved frequency response at room temperature [3]. In this work, we propose to extend even further the MEMSTENNA concept to the near-infrared optical range. Thus, here we present an opto-mechanical antenna that combines a plasmonic optical nanoantenna [4] with a microcantilever. Our proposed device structure consists of a NIR optical dipole nanoantenna (λ=1.55 μm) integrated in one of the metal sides of the free-end of two Au-coated silicon nitride triangular microcantilevers, as shown in (Fig. 1a). The dipole nanoantenna geometry is defined by its two components' length and width (L_1, L_2, W_1) as well as the dimensions of the supporting arms (L_{Arm1}, L_{Arm2}, W_2) which connect the dipole components to the microcantilevers. The Si_3N_4 thickness in the nanoantenna area is also considered as a design parameter. Both components of the nanoantenna are parallelly placed at a gap distance in an overlap area in the feed region of the antenna, defining a transduction capacitance that will load the nanoantenna (Fig.1b). Then, when the nanoantenna is illuminated by a focused 1.55 μm laser, a voltage is induced in the feed gap area which provides an electrostatic force with a dc component that will make the microcantilever to statically deflect. Fabrication process of the optical nano-antenna is carried out on commercially available tipless AFM microcantilevers (Fig. 2a) and starts by removing their 35 nm Au top layer and reducing their Si_3N_4 thickness in a certain region of their free end, by means of focused ion beam (FIB) milling (Fig. 2b). Then, FIB milling is also used to define one of the nanoantenna's component structure at one of the microcantilevers, by completely removing the Si_3N_4 and bottom Au layers (Fig. 2c). This process is repeated to define the second nanoantenna component and finally the two processed microcantilevers with their nanostructured tips are placed close to each other to form the optical nanoantenna device (Fig. 2d). SEM images of Figure 3 show one of the components of a fabricated nanoantenna prototype. To model and simulate the nanoantenna the COMSOL Multiphysics RF module has been used. Simulation conditions are characterized by a lumped port excitation and spherical perfect match layer (PML) as boundary condition. Optimal mesh is achieved by frequency domain RF adaptive mesh and adaptive frequency sweep. S_{11} has been used as the design parameter to obtain the optimal design dimensions for the nanoantenna to resonate at 1.55 μm (193.41 THz). Thus, deepest S_{11} notch is achieved for L_1=820 nm, L_2=850 nm, L_{Arm1}=720 nm, L_{Arm2}=750 nm, W_1=W_2=100 nm, and 140 nm Si_3N_4 thickness as shown in Fig 4a (bold blue curve). An analysis of the 50 nm fabrication tolerance effect on the S_{11} vs. frequency curves has been also carried out. Then, for instance, we have calculated a maximum sensitivity value of $\partial S_{11}/\partial L_{1,2}$ = -0.0753 db/nm at f=193.41 THz from the family of curves shown in Figs 4.a. Moreover, S_{11} is almost insensitive to Si_3N_4 thickness variations between 250 nm and 600 nm but presents a maximum sensitivity of $\partial S_{11}/\partial t_{Si3N4}$ = -0.18 db/nm around 150 nm as shown in Fig 4b. Finally, we have coupled RF and mechanics COMSOL physics and we have calculated the microcantilever deflection vs. voltage characteristic (Fig. 4c). Then, a 70 mV voltage will be generated in the nanoantenna feed gap by a 0.5 W, λ=1.55 μm focused laser beam with a gaussian profile, for a gap=5 nm.
This work was funded by Spain's Ministerio de Ciencia, Innovación y Universidades under Grant No. PID2021-127840NB-I00 (MICINN/AEI/FEDER, UE).

[1] R. Ruiz, J. Bonache, G. Abadal. "A flexible dipole antenna for direct transduction of microwave radiated power into DC mechanical deflection." Sensors and Actuators A: Physical 340 (2022): 113536.
[2] R. Ruiz, G. Abadal. "Direct Transduction from Radiofrequency Radiated Power to Static and Dynamic Flexural Mechanical Modes." 2021 21st International Conference on Solid-State Sensors, Actuators and Microsystems (Transducers). IEEE, 2021.
[3] C. Belacel, Y. Todorov, S. Barbieri, D. Gacemi, I. Favero, C. Sirtori. "Optomechanical terahertz detection with single meta-atom resonator." Nature communications 8, no. 1 (2017): 1578.
[4] J. Dorfmuller, R. Vogelgesang, W. Khunsin, C. Rockstuhl, C. Etrich, K. Kern. "Plasmonic nanowire antennas: experiment, simulation, and theory." Nano letters 10, no. 9 (2010): 3596-3603.

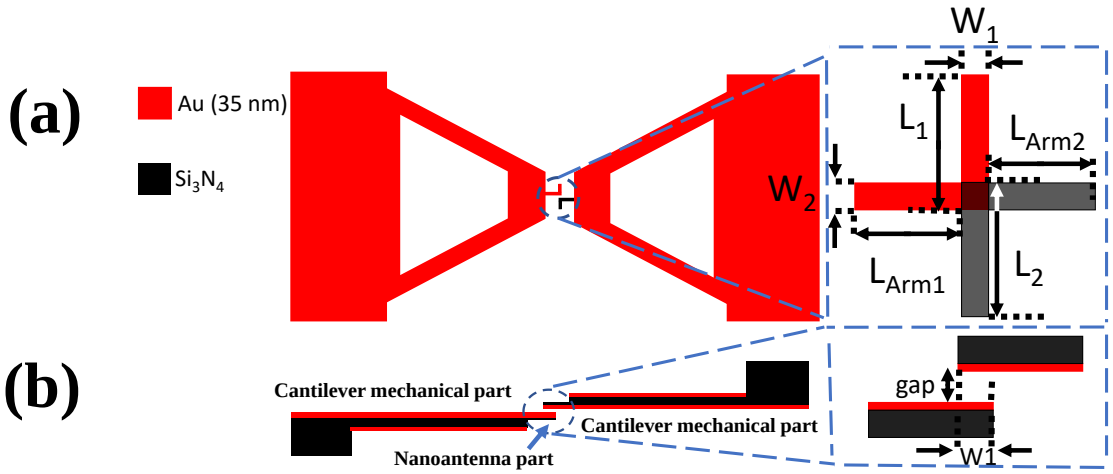

Figure 1: Schematic top (a) and side (b) views of the proposed structure including nano-antenna and microcantilever.

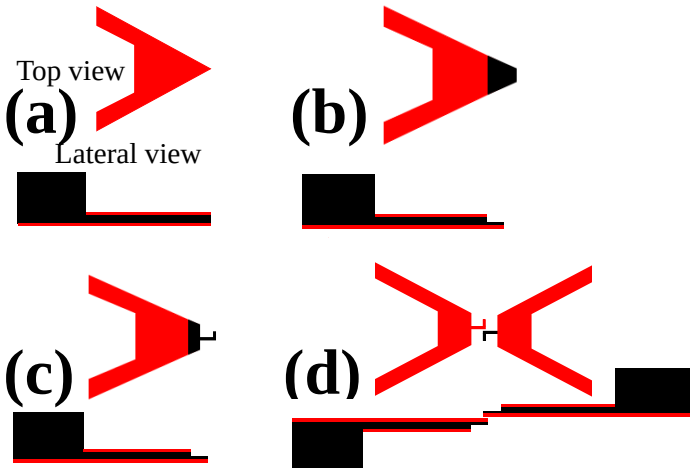

Figure 2: *FIB based fabrication process steps of the proposed structure. Commercial AFM microcantilevers (www.nanoandmore.com/AFM-Probe-PNP-TR-TL-Au)*

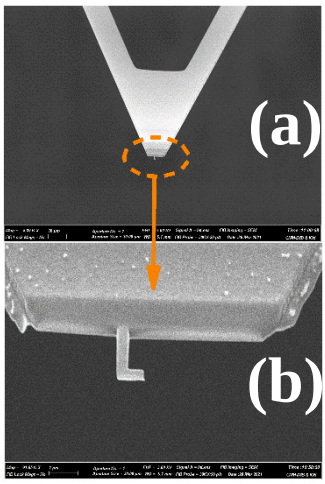

Figure 3: *SEM images of one of the fabricated nanoantenna's component.*

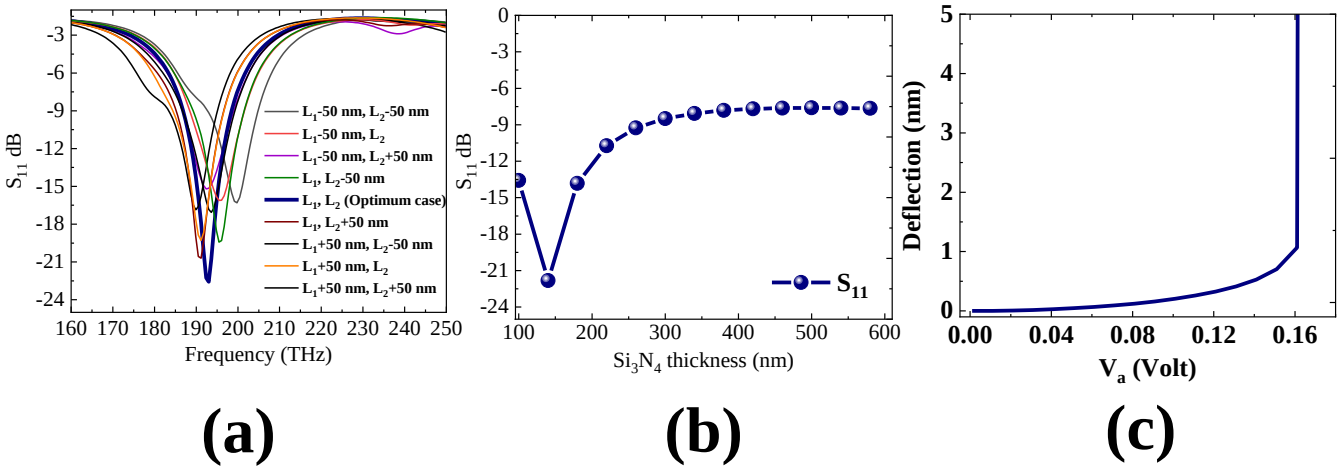

Figure 4: *S_{11} vs frequency curves obtained from COMSOL simulation, for 8 different dispersive values of L1 and L2 around the optimum case (a), S_{11} vs Si_3N_4 thickness at 193.41 THz (λ=1.55 μm) (b). Free end displacement of one of the microcantilever component as a function of the voltage induced in the feed gap area of the nanoantenna (c).*

A Hybrid Nanowire-MEMS Force Sensor

Mehrdad Karimzadehkhouei [a,f], Masoud Jedari Ghourichaei [a], Levent Demirkazik [a], Bartosz Pruchnik [b], Krzysztof Kwoka [b], Dominik Badura [b], Tomasz Piasecki [b], Onur Aydin [a], Bekir Aksoy [a], Cemal Aydogan [c], Gokhan Nadar [a], Ivo W. Rangelow [c,g], Arda D. Yalcinkaya [d], Halil Bayraktar [e], Teodor Gotszalk [b], and B. Erdem Alaca [a,f,h]

[a] Department of Mechanical Engineering, Koç University, Istanbul, 34450, Turkey
[b] Department of Nanometrology, Wrocław University of Science and Technology, Wroclaw, 50-370, Poland
[c] Ins. of Precision Measurement and Sensor Technology, Ilmenau Uni. of Tech., Ilmenau, 98693, Germany
[d] Department of Electrical and Electronics Engineering, Boğaziçi University, Istanbul, 34342, Turkey
[e] Dept. of Molecular Biology and Genetics, Istanbul Technical University, Maslak, Istanbul, 34467, Turkey
[f] n²STAR-Koç University Nanofabrication and Nanocharacterization Center for Scientific and Technological Advanced Research, Koç University, Istanbul, 34450, Turkey
[g] nano analytik GmbH, Ehrenberg Str. 3, 98693-Ilmenau, Germany
[h] Surface Science and Technology Center (KUYTAM), Koç University, Istanbul, 34450, Turkey
e-mail: mkarimzadeh@ku.edu.tr

Miniaturization of electromechanical sensors brings about significant advantages such as higher resonance frequencies and lower power requirements resulting in increased speed and sensitivity with higher signal-to-noise ratio. Equally important is the cost reduction due to wafer-level production. With the use of nanowires (NWs), these advantages can be fully exploited [1]. As an interface to cells and tissues, NWs can serve as mechanical building blocks addressing issues such as cell differentiation, proliferation, adhesion, motility, and fate that are affected not only by chemical signals, but also by externally applied mechanical forces [2]. In this study, fabrication of a multi-axis nanoelectromechanical system (NEMS) force sensor is reported that incorporates piezoresistive NWs. The sensor is intended to be utilized for the measurement of traction forces between live cells and the sensor surface. With micro and nanoscale components, the proposed sensor is a challenging integration platform.

Sensor architecture consists of three components: i) The proof mass is designed to interact with the cells and transfer the traction force to the NWs. It has in-plane dimensions of 10×10 μm^2 and a thickness of 2 μm. ii) piezoresistive NWs with their cross-sectional area ranging from 250×250 nm^2 to 550×550 nm^2 and their length in the range of 2 μm to 5 μm. iii) Retaining springs are designed to prevent out-of-plane movement of the platform and impart a certain in-plane stiffness to the sensor, Fig 1(g). Stresses generated in NWs can thus be measured. With four piezoresistive NW bridges on all sides of the interaction platform, the direction and the magnitude of the traction force can be quantified.

Fabrication is performed using 4-inch silicon on insulator (SOI) (100) wafers with p-type doping and a resistivity of 20-30 Ω.cm. The device layer, buried oxide (BOX) layer, and handle layer thicknesses are of 2±0.5 μm, 2 μm±5%, and 500±10 μm, respectively. The fabrication process flow depicted in Fig 1 consists of the following steps: (a) Initial deep silicon etch generating the proof mass and springs, (b) Second deep silicon etch for the definition of NWs, (c) Doping (p-type) of NWs to a level of 10^{17} cm^{-3} for optimizing the piezoresistive transduction. Pads, not visible in the particular cross-section of Fig 1, are doped to a level of 10^{20} cm^{-3}, (d) Metallization through lift-off is carried out for signal lines, (e) HF vapor etch of the BOX layer to release the proof mass, and (f) encapsulation of the sensor/packaging.

The response of the NWs to the mechanical actuation is tested in the setup shown in Fig 2(a). The resistance of the NWs changed with observed movement as shown in Fig 2(b) reaching piezoresistive gage factor (GF) of 20. The successful release of the shuttle opened the path for the real-time electromechanical characterization of the sensor. The pressure-sensing capabilities of the sensor are investigated utilizing the test setup shown in Fig 3(a). A pneumatic tubing is attached to a pipette tip with a tip diameter of 500 μm and mounted perpendicular to the surface to a micropositioner. The tip is placed on top of the proof mass using the overhead microscope. Nitrogen gas at 1 bar is used to provide pressure for four cycles, and electrical readouts are taken (Keysight B1500A). As the placement of the tip generates an almost ideal seal, the accumulated gasses are released through a vent valve. Under 1 bar of applied pressure, a 0.87% current increase is measured on the NWs across four cycles, which is depicted in Fig 3(b).

This work is supported by Tübitak under grant numbers 120N361 and 118C155.

[1] B. E. Alaca and M. Karimzadehkhouei, Piezoresistive nanowire-based electromechanical sensors, Encyclopedia of Sensors and Biosensors (First Edition), Elsevier 2023, Pages 555-566.
[2] Roca-Cusachs, P., Conte, V. and Trepat, X., Nature cell biology 19:7(2017) 742-751.

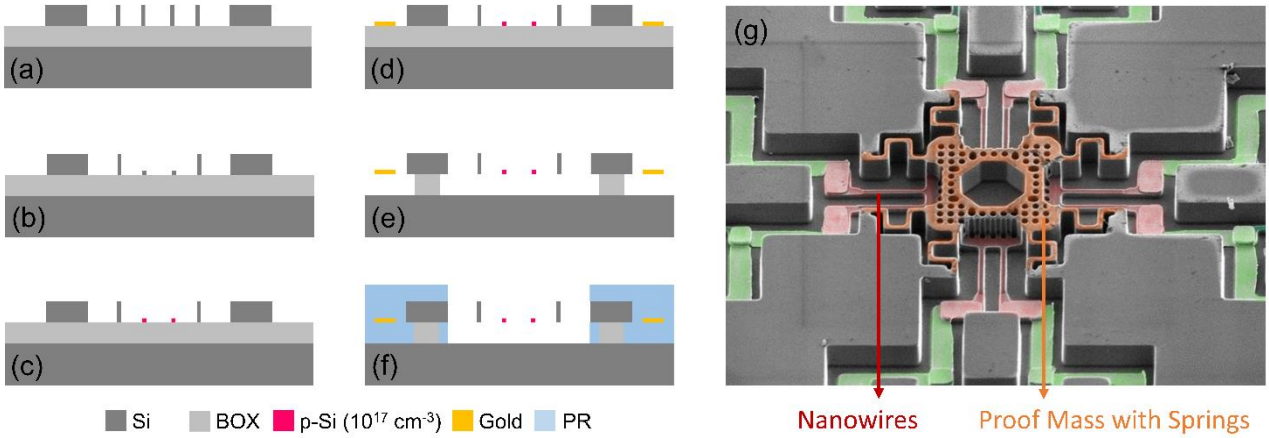

Figure 1. (a)-(f) Fabrication process flow steps, and (g) SEM image of the center region of the fabricated sensor with its parts including piezoresistive NWs and proof mass with springs.

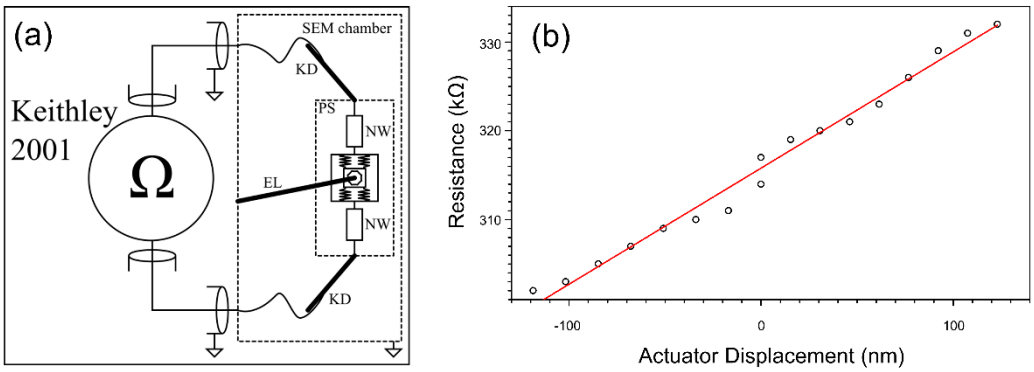

Figure 2. (a) Simplified schematic, and (b) results of the NW piezoresistive gage factor measurements. (Measurements are conducted in the chamber of FEI Helios NanoLab 600 FIB/SEM system with Kleindiek MM3A manipulators (KD) and EasyLift probe (EL).)

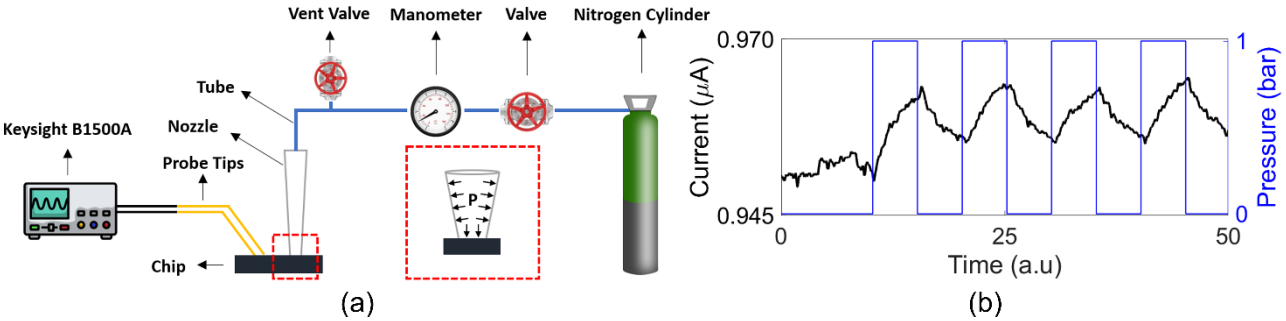

Figure 3. (a) Schematic of pressure sensing setup, and (b) Test results for an external pressure of 1 bar applied to the proof mass.

Improved electrical performance of ZnO thin-film transistors using 2DEG with insertion of Al_2O_3 layer deposited by atomic layer deposition

Dongki Baek [a], Se-Hyeong Lee [a], So-Young Bak [a], Chan-Yeong Park [a], Hyeongrok Jang [a], Jinwoo Lee [a], Moonsuk Yi [a]

[a] Department of Electronics Engineering, Pusan National University, Busan, 46241, Republic of Korea
e-mail: msyi@pusan.ac.kr

As the size of mobile devices becomes smaller and the demand for transparent flexible displays increases, there is a need for mobile displays to satisfy certain specifications, such as ultra-thinness, high-resolution and low process temperature for next-generation displays [1]. ZnO has been widely studied as an active layer material for traditional thin-film transistors(TFTs) due to its high carrier mobility (~10 $cm^2/V{\cdot}s$) and wide bandgap (3.2eV) for high-resolution and transparent displays. However, ultra-thin ZnO TFTs with a channel thickness <10nm, show low carrier mobility caused by low carrier density [2]. The high process temperature required to overcome low carrier density interferes with the application of the flexible substrate with a low thermal budget. Therefore, a two-dimensional electron gas (2DEG) generated at the ZnO/Al_2O_3 heterojunction interface can be used to improve carrier mobility by providing free carriers in ultra-thin film ZnO transistors at low temperatures.

In this work, we focused on generating carriers by 2DEG to improve the performance of 6nm ultra-thin ZnO TFTs. Figure 1 shows fabricated ZnO and ZnO/Al_2O_3 heterostructure TFTs at a low temperature (150°C) via atomic layer deposition (ALD) technique. ZnO TFTs are reference devices, and all TFTs are inverted staggered structure. In figure 1, 2DEG is created at the ZnO/Al_2O_3 heterojunction interface. To create 2DEG, a high reductive agent Tri-Methyl Aluminium (TMA) is used. During the growth of Al_2O_3 layer, TMA reduces the ZnO, leading to the creation of oxygen vacancies, which are a major source of free carriers [3]. These free carriers are confined at the heterojunction interface, resulting in the formation of 2DEG.

The generation of 2DEG is well demonstrated in Figure 2. In the case of 6nm ZnO TFTs, carrier mobility, subthreshold swing (S.S), threshold voltage (V_{th}), and on-off current ratio ($I_{ON/OFF}$) are 0.49$cm^2/V{\cdot}s$, 0.84V/dec, 38.08V, and 1.99×10^4 respectively. The high threshold voltage indicates a lack of carriers due to the ultra-thin ZnO thickness. Furthermore, it exhibits low carrier mobility caused by low carrier density and high resistivity. However, in the case of ZnO (5nm)/ Al_2O_3 (1nm) TFTs, there is a significant improvement in the parameters, with values of 11.91$cm^2/V{\cdot}s$, 0.83V/dec, 8.48V, and 2.09×10^6 respectively. The threshold voltage decreased by 30V, and the carrier mobility increased by 20 times. This notable improvement can be attributed to the supply of carriers, which were insufficient in the 6nm ZnO TFTs. In other words, 2DEG due to oxygen vacancies generated during the growth of Al_2O_3 layer provided free carriers.

We increased the thickness of the Al_2O_3 layer to investigate the effect of the Al_2O_3 layer thickness. The most notable feature of the ZnO (4nm)/ Al_2O_3 (2nm) TFTs, with an increased thickness of Al_2O_3 layer, is that the off current reaches 10^{-6} A. This value is 3 orders of magnitude higher than the off current of ZnO and ZnO (5nm)/ Al_2O_3 (1nm), which have an off current of 10^{-9}A. In addition, the relatively higher currents in all V_{gs} regions compare to ZnO (5nm)/ Al_2O_3 (1nm) TFTs indicate the presence of more oxygen vacancies. However, unlike ZnO (5nm)/ Al_2O_3 (1nm), which has improved carrier mobility and threshold voltage due to 2DEG generated by oxygen vacancies, more oxygen vacancies generated in ZnO (4nm)/ Al_2O_3 (2nm) no longer have a positive effect on carrier mobility improvement. Rather, as the thickness of Al_2O_3 layer increases, both carrier mobility and subthreshold swing deteriorate significantly. These results can be attributed to the fact that oxygen vacancies are confined within ~0.62nm into the ZnO layer from the ZnO/Al_2O_3 heterojunction interface, and Al_2O_3 is generally used as an insulator [3]. The electrons created by many oxygen vacancies confined at the ZnO/Al_2O_3 heterojunction interface are easily pushed out by a negative gate voltage, increasing the off current. Additionally, as the thickness of Al_2O_3 layer increases, the insulation performance improves and tunneling effect decreases. Therefore, carrier mobility and subthreshold swing deteriorate as the thickness of Al_2O_3 layer increase. Each parameter is summarized in Table 1.

Afterward, the ZnO/Al_2O_3 TFTs will be optimized by adjusting the total thickness of the active layer, the thickness of the Al_2O_3 layer, and the growth temperature to improve subthreshold swing and threshold voltage.

[1] K. Nomura et al., nature 432 (2004) 488-492.
[2] C.H. Ahn et al., Surf. Interface Anal. 42 (2010): 955-958.
[3] H.J. Lee et al., Adv. Electron. Mater. 7 (2021) 2000876.

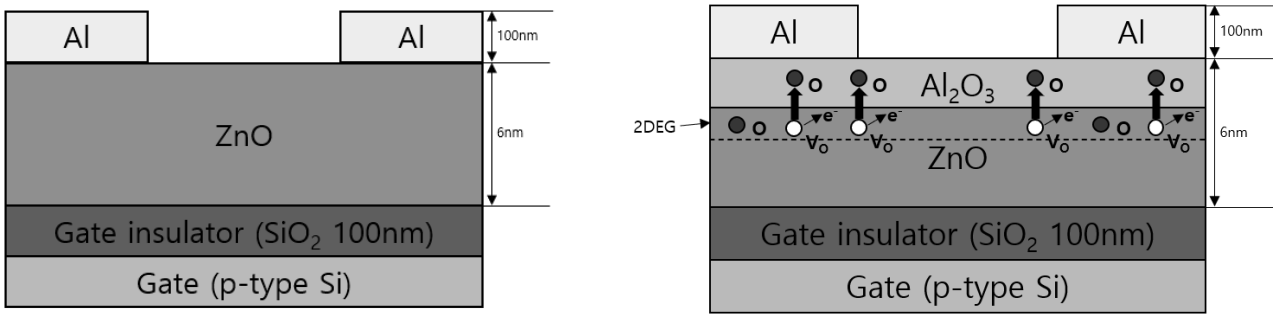

Figure 1. Schematic of ZnO and ZnO/Al_2O_3 TFTs

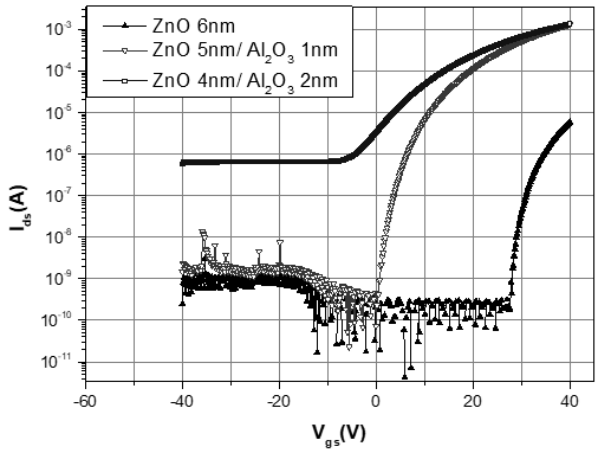

Figure 2. Transfer curve of ZnO and ZnO/Al_2O_3 TFTs

	Mobility [$cm^2/V{\cdot}s$]	S.S [V/dec]	V_{th} [V]	$I_{ON/OFF}$
ZnO 6nm	0.49	0.84	38.08	1.99×10^4
ZnO (5nm)/Al_2O_3 (1nm)	11.91	0.83	8.48	2.09×10^6
ZnO (4nm)/Al_2O_3 (2nm)	6.82	-	-	2.09×10^3

Table 1. Electrical parameters of ZnO and ZnO/Al_2O_3 TFTs

Technology performance of silica nanoparticle deposition techniques over carbon-based substrates

Ana Coloma Vélez [a], Michelle Cedeño Mata [a], Xingqi Chan [b], Andreu Cabot [b], Andriy Yaroshchuk [a], Manuel Domínguez-Pumar [a], Sandra Bermejo [a].
[a] Polytechnic University of Catalonia, Barcelona, 08034, Spain
[b] Catalonia Institute for Energy Research - IREC, Barcelona, 08930, Spain
e-mail: ana.gabriela.coloma@upc.edu

In recent years, nanotechnology has emerged as a promising field with numerous applications across various scientific and technological domains. The use of nanoparticles is very well known in energy storage and sensing applications[1], [2]. On the other hand, the capability of building over flexible surfaces opens the possibility to a broad field of wearable applications[3], and, at the same time, explores the viability of reducing the size, volume, and cost of the final devices. This work describes two techniques for depositing silica-based nanoporous layers onto various carbon-based materials. These can be scaffolds for low-cost, environmentally friendly energy harvesters [1], [4].

353 nm diameter silica nanoparticles have been deposited onto three different carbon-based substrates. As deposition methods, two different techniques have been explored: Electrospraying and drop casting. Electrospray technique involves a syringe pump connected to a high-voltage power supply, which creates a strong electric field between the capillary needle and a counter-electrode. The electric field induces formation of a Taylor cone at the needle tip due to surface tension. The flow rate and applied voltage were optimized depending on the solution type used for electrospray [4]. Drop casting consists in depositing a small volume of nanoparticle solution onto a tissue using a pipette or a syringe. The solution is carefully spread over the desired area, forming a thin film, which enables gradual evaporation of the solvent. The carbon-based substrate Hydrophilic carbon paper is manufactured from carbon paper via coating with organic materials, the surface of the carbon paper is hydroxylated and hydrophilic, Super hydrophilic carbon cloth fiber is manufactured from carbon cloth coated with organic matter, its surface is hydroxylated and hydrophilic and the Hydrophilic CnT/MnO is made via coating the surface of carbon cloth by a layer of manganese oxide.

Fig 1 shows the different methods used for the deposit of silica nanoparticles, Fig 2 shows Scanning Electron Microscopy (SEM) images of the layers obtained by electrospray. The applied voltage was 5751 V, distance 7 cm, pumping rate 0,4 ml/h, silica solution concentration 5% (by weight?), drying for 24 hours at room temperature. This allows the nanoparticles to achieve good adhesion to the substrate, Fig 3 shows Scanning Electron Microscopy (SEM) images of the layers obtained via drop-casting. The distance is 1 cm, silica solution concentration 5%, rate 0,05 ml/min, drying for 24 hours at room temperature. Electrospray technique allows a greater control and homogeneity of the layer thickness. Besides, the deposited layers formed by electrospray present a more regular arrangement of the nanoparticles. The adhesion is very good in both cases. A greater growth of nanoparticles is observed on hydrophilic substrates with lower porosity of carbon and on hydrophilic CnT/MnO. This is due to the smaller spacing between the carbon fibers, enabling the nanoparticles to better adhere to the surface. The super hydrophilic carbon cloth substrate is more porous, which allows the nanoparticles to penetrate between the fibers.

This work has been supported by the European Union (Project H2020-FETOPEN-2018-696 2019-2020-01-964524 “Energy harvesting via wetting/drying cycles with nanoporous electrodes (EHAWEDRY)), and by the Spanish Government MCIN/AEI (TED2021-131552B-C22).

[1] H. Wang et al., Colloids Surf A Physicochem Eng Asp, vol. 671, p. 131653.
[2] M. C. Mata et al., Sens Actuators A Phys, vol. 357, p. 114398, Aug. 2023.
[3] G. Luo et al., Chemical Engineering Journal, vol. 451, p. 138549, Jan. 2023.
[4] B. Véliz et al., Colloids and Interface Science Communications, vol. 25, pp. 16–21.

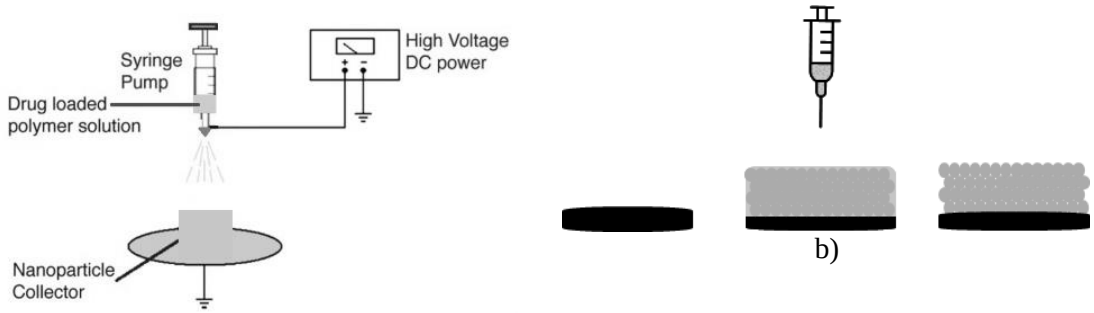

Figure 1. Different methods for the deposit of nanoparticles a) Electrospray b) Drop casting.

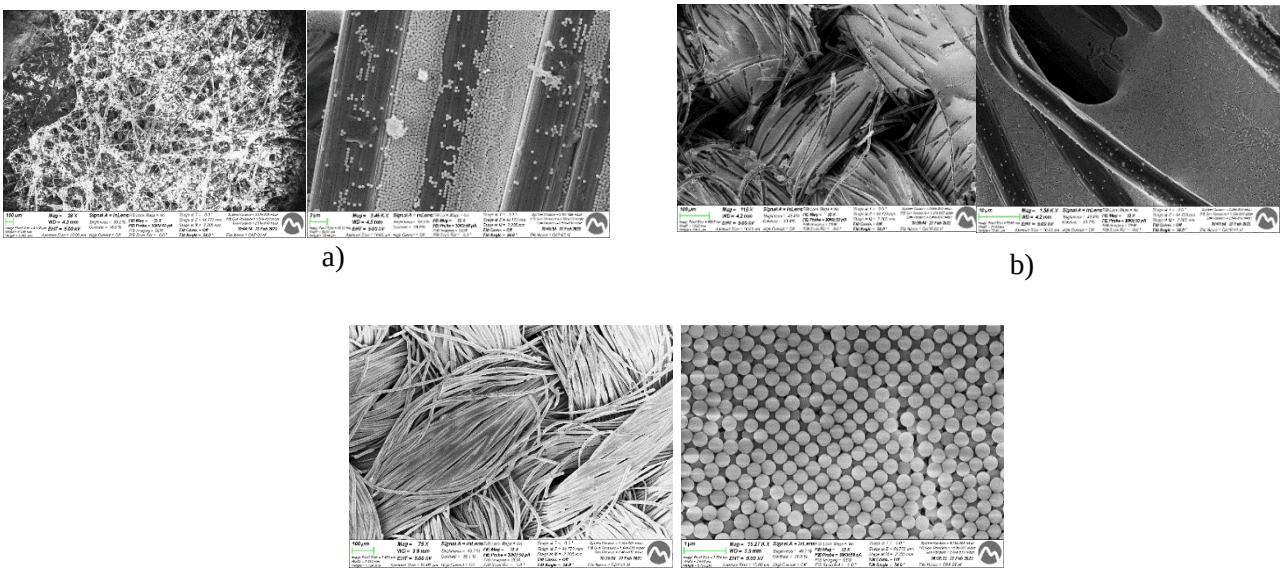

Figure 2. Scanning Electron Microscopy (SEM) images of the layers obtained by electrospray: The 0.353µm silica nanoparticles have been deposited over the a) Hydrophilic porous carbon, b) Super hydrophilic carbon cloth fiber and c) the Hydrophilic CnT/MnO.

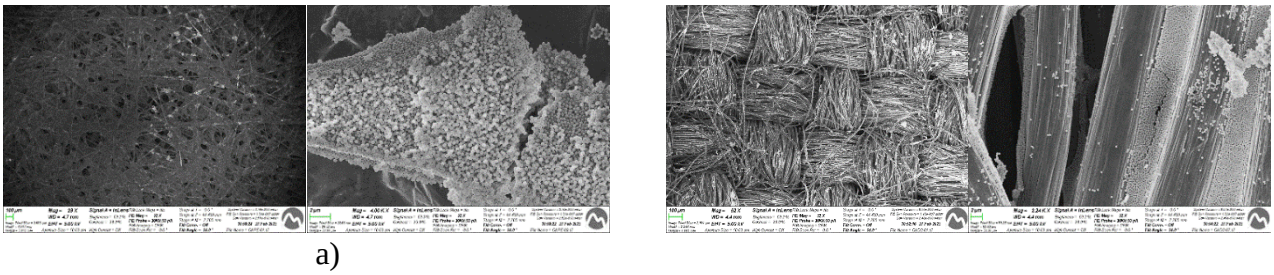

Figure 3. Scanning Electron Microscopy (SEM) images of the deposits obtained using Drop Casting. The 0. 353µm silica nanoparticles have been deposited over a) Hydrophilic porous carbon, b) Super hydrophilic carbon cloth fiber.

Circuit-level Macro Modeling for Behaviors of Hole Accumulated Current during ERS Operation in 3D Charge Trap Flash Memories

Sunghwan Cho [a,b], Byoungdeog Choi [c]

[a] Dep. of Semiconductor and Display Engineering, Sungkyunkwan University Suwon 16419, South Korea
[b] Memory Business, Samsung Electronics Co., Ltd. Hwasung 18448, South Korea
[c] Dep. of Electrical and Computer Engineering, Sungkyunkwan University Suwon 16419, South Korea
e-mail: joboss9999@gmail.com

Abstract - In this paper, we developed circuit-level macro model as a framework for circuit simulation during erase operation in 3D charge trapping flash (CTF) memory device focusing on the behaviors of hole accumulated current at the bottom of the 3D channel. After analyzing the difference of channel electrostatic potential in the string which is attributed by the difference of hole barrier in ground select line (GSL), we derived a formula for the hole accumulated current by transforming the subthreshold current in BSIM-CMG model. To extract model parameters, we fitted our SPICE simulation results for 2 representative GSL conditions with TCAD simulation results and experimental data.

1. Introduction - As growing difficulty in the scaling down for the memory devices, 3D charge trapping flash (CTF) memory continues to be regarded as the most promising alternative to planar memory devices due to higher density restricting increase of cell feature size [1,2]. However, in comparison to the rapid growth of technology in 3D CTF devices [3,4], a suitable framework for analyzing the behaviors by circuit simulation is insufficient. Furthermore, despite characteristics of erase operation owing to structural difference with 3D gate-all-around (GAA) with floated body are studied recently [5], it is still difficult for circuit designer to optimize design achieving better performance in erase operation due to a lack of framework. In this work, we have proposed a circuit-level macro model focusing on the behaviors of hole current in the bottom of the channel string, which is significant mechanisms for erase operation in 3D CTF memory device. Based on conventional BSIM-CMG [6], equivalent circuit for GAA structure is extended. Accurate characteristics with Simulation Program with Integrated Circuit Emphasis (SPICE) simulation is verified by Technology Computer-Aided Design (TCAD) simulation results and experimental data.

2. Macro Model and Simulation Results - Fig. 1 shows the schematics of modeling structure which is investigated in this work. Based on behaviors of accumulated holes from bottom p-well to 3D channel beyond hole barrier during erase operation, corresponding equivalent circuit is proposed describing hole accumulated current by attaching voltage controlled current source (VCCS). Cylindrical MOS transistor for GAA structure in 3D CTF memory is implemented using conventional BSIM-CMG model and previous work [7]. Fig. 2 illustrates band diagram for 2 representative cases according to GSL condition. In the case of V_{GSL1}, which is same as V_{PWELL} attributed by coupling capacitance between floated gate of GSL transistor and p-well, accumulated holes are blocked by intrinsic hole barrier and channel electrostatic potential (V_{CH}) in the CTF cell string is too low to execute erase operation. On the other hand, in the case of V_{GSL2} which is enough lower than V_{PWELL}, accumulated holes can flow over the barrier resulting in same potential as V_{PWELL} in the channel and corresponding effective erase operation. Fig. 3 shows SPICE simulation results comparing with TCAD simulation results and experimental data for 2 representative cases which is exactly same but gate bias in GSL transistor. As shown in Fig. 3(a), V_{CH} for V_{GSL2} in the cell string is same as V_{PWELL} potential due to accumulated hole current sufficiently flowing over the lower barrier, whereas V_{CH} for V_{GSL1} is extremely low since accumulated holes are blocked by higher barrier. Thus, experimental results for erase speed shows quite different erase efficiency even though only gate bias condition in GSL transistor is different between V_{GSL1} and V_{GSL2}, as shown in Fig. 3(b). By using VCCS for accumulated hole current in our work, which is transformed by subthreshold current equation in BSIM 4.5 for derivation of hole barrier and diffusion, behaviors of V_{CH} in cell string and erase speed for 2 representative cases by SPICE simulation are well fitted to TCAD simulation results and measurement data, as shown in Fig. 3(a) and 3(b). Fig. 4 shows detailed information by SPICE simulation during stepwise erase execution for V_{GSL1} and V_{GSL2} conditions. Due to almost 100 times larger amount of accumulated hole current over the barrier at V_{GSL2} condition than V_{GSL1}, as shown in Fig. 4(b), V_{CH} of cell string at V_{GSL2} condition is much higher than V_{GSL1} and almost same as V_{PWELL} potential, as shown in Fig. 4(c). Sufficient convey of hole potential from p-well to channel contributes large electric field between charge trapping layer and channel. Fig. 4(d) shows corresponding difference of FN current (I_{ERS}) between V_{GSL1} and V_{GSL2} conditions, which results in different erase efficiency as shown previously in Fig. 3(b).

3. Conclusion - In this paper, we developed a circuit-level macro model for accurate prediction of erase operation in 3D CTF memory device. By using equivalent circuit and transformed formula for accumulated hole current flowing over the various barrier height, we fitted our model to TCAD simulation results and experimental data for different condition of gate potential in GSL transistor. This work would equip circuit designer to predict precisely the behaviors of erase operation and to optimize efficiency of erase execution in circuit simulation of 3D CTF memory device.

References

[1] R. Micheloni, S. Aritome, L. Crippa, Proceedings of the IEEE, vol. 105, no. 9, pp. 1634-1649, 2017.
[2] A. Goda, IEEE Transactions on Electron Devices, vol. 67, no. 4, pp. 1373-1381, 2020.
[3] K. Parat and C. Dennison, IEEE International Electron Devices Meeting, 2015, pp. 3.3. 1-3.3. 4.
[4] Kim, Jun Hyoung, et al. 2021 Symposium on VLSI Technology. IEEE, 2021.
[5] Kul Lee and Hyungcheol Shin. Japanese Journal of Applied Physics , 60(12), 2021.
[6] [Online] Available: http://bsim.berkeley.edu.
[7] Sunghwan Cho, and Byoungdeog Choi. Solid-State Electronics (2023): 108655.

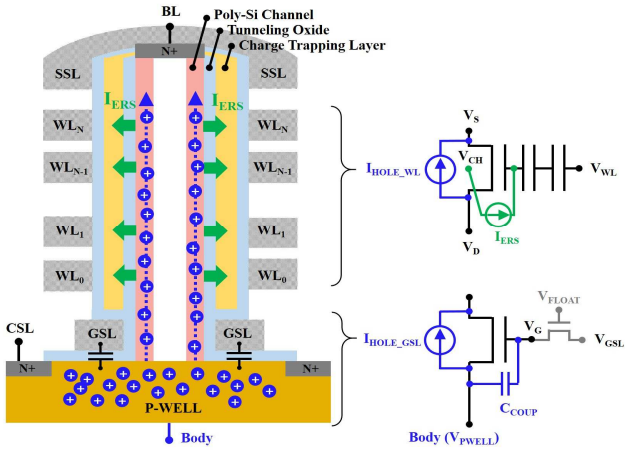

Figure 1. Schematics for modeling structure and proposed equivalent circuit.

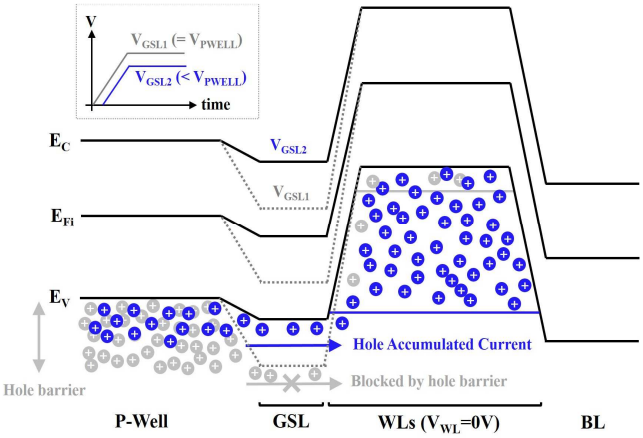

Figure 2. Band diagram and corresponding hole accumulated current according to V_{GSL} conditions.

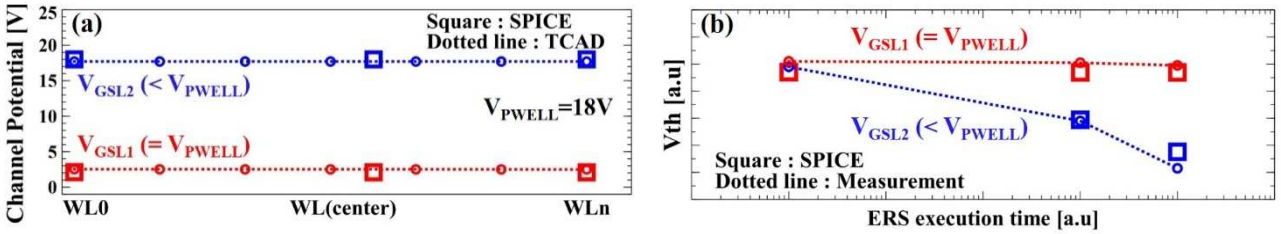

Figure 3. SPICE simulation results comparing with (a) TCAD (b) experimental data for verification.

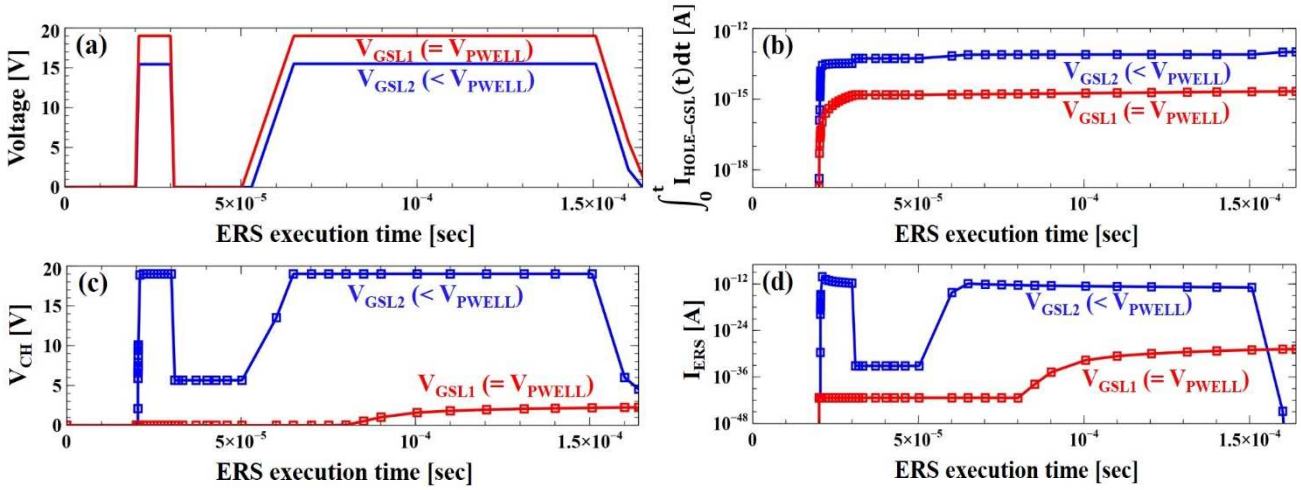

Figure 4. SPICE simulation results according to (a) V_{GSL} Conditions for (b) I_{HOLE}, (c) V_{CH} and (d) I_{ERS}

Damascene Versus Etch-Back Chemical Mechanical Planarization for Resistive Memory Crossbars Back-End-Of-Line Integration

R. Dawant, M. Gaudreau, M.-A. Roy, J. Arias-Zapata, D. Drouin, S. Ecoffey
Institut Interdisciplinaire d'Innovation Technologique (3IT), Université de Sherbrooke, Sherbrooke J1K 0A5, Canada
Laboratoire Nanotechnologies Nanosystèmes (LN2) – CNRS IRL-3463 – 3IT, Sherbrooke J1K 0A5, Canada

Keywords: CMP, crossbar memory array, memristive memory, BEOL integration

Memristive memories have attracted significant interest due to their compatibility with Back-End-of-Line (BEOL) integration, offering potential benefits for in-memory computing applications [1]. To implement memristive memories in crossbar array structure, the Bottom Electrode (BE) is usually planarized to improve the circuit performance [2-3]. Two technics are widely used in BEOL to planarize the interconnections [4] and have been exploited to fabricate resistive memories: Damascene [2] and Etch-back [3]. This study proposes to investigate both technics for BEOL memristive memory array integration.

We fabricated TiO_x-based resistive memory using the Damascene approach where the Chemical Mechanical Planarization (CMP) is performed on the metal as shown in Fig.1 (a) and the etch-back approach where the CMP is done on the dielectric, as shown Fig.1 (b). The two process flows differ only in the BE fabrication. Fig.2 shows (a) Atomic Force Microscopy (AFM) measurements of the BE fabricated by Damascene, showing metal dishing of 10 nm, and (b) Focused Ion Beam (FIB) cross-section of 3 memory points highlighting trenching on the BE edges. Fig.3 presents the results of the BE crossbar array fabricated by Etch-back, with (a) AFM measurements revealing metal lines protrusions of less than 3 nm and (b) FIB cross-section showing no trenching effect.

The material options for connecting the TiO_x-based memory to the metallic electrode are limited, and in this study, we opted for TiN. The etch-back approach can be used with a stacking of different metals. This gives a huge advantage in terms of access resistance as lower resistivity Al can be used below the TiN in the stack. [5]. On the other hand, Damascene is the standard for electroplated Cu interconnections fabrication in CMOS BEOL. In our process, the TiN is deposited by sputtering which exacerbates the trenching defects on the sidewall leading to filling voids in the BE, as shown in Fig.2 (b). This type of defect leads to a lower interface quality between the BE and the memory stack. Devices fabricated using both approaches exhibit similar cycling behavior and performances as shown in Fig.4. Both the SET/RESET voltages and the resistance ratio are similar. We demonstrated the integration of full crossbar in the BEOL of a 130 nm TSMC CMOS circuit with the Damascene approach as shown in the FIB cross section of Fig.5.

This study presents a comprehensive comparative analysis of the Damascene and Etch-back approaches for crossbar memristive memory array fabrication. The results indicate that the Etch-back technique exhibits greater potential due to its effective mitigation of undesirable trench effects observed in the Damascene approach, thereby improving the crucial interface quality for the cycling behavior of the memory. Additionally, the Etch-back technique enables the use of multi-stack metals that decrease the access resistance compared to the Damascene approaches. The discussion will focus on which approach is more suitable for CMOS integration and explores the potential for 3D integration of crossbar arrays.

This work was supported by the Natural Sciences and Engineering Research Council of Canada (NSERC) HIDATA project 506289-2017, Mitacs Accelerate program IT19472 and Fond Recherche Quebec Nature and Technologies – Teams Grant.

[1] Zidan, Strachan, et Lu, Nature Electronics, doi.org/10.1038/s41928-017-0006-8
[2] El Mesoudy et al., Microelectronic Engineering, doi.org/10.1016/j.mee.2021.111706
[3] Kim et al., Nature Communications, doi.org/10.1038/s41467-021-25455-0
[4] Nishi, Y., & Doering, R. (Eds.). (2008), doi.org/10.1201/9781420017663
[5] Amirsoleimani et al., Advanced Intelligent Systems, doi.org/10.1002/aisy.202000115.

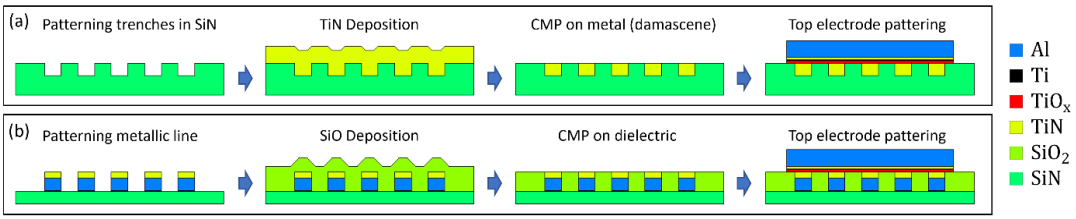

Figure 1: Memristive crossbar memory arrays process flows: (a) Damascene: Si3N4 trench patterning, TiN deposition and CMP planarization. (b) Etch-Back: Metallic electrodes etching, SiO2 deposition and CMP planarization. In both strategies, the top electrode and active layer undergo identical processing steps.

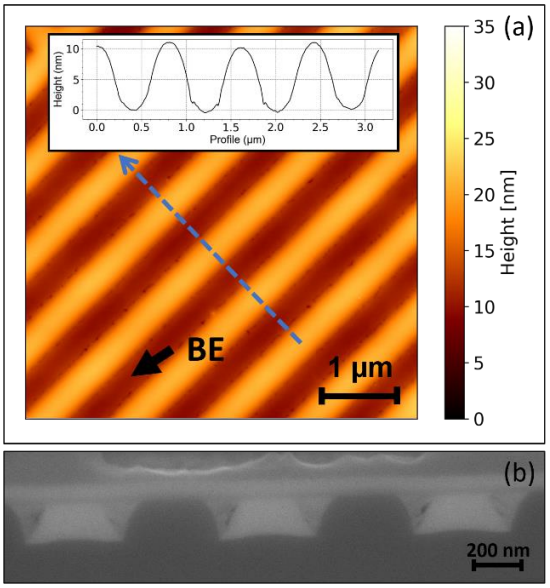

Figure 2: Damascene. (a) AFM measurements of the BE surface. (b) FIB cross-section image. (c) Switching behavior of the resistive memory

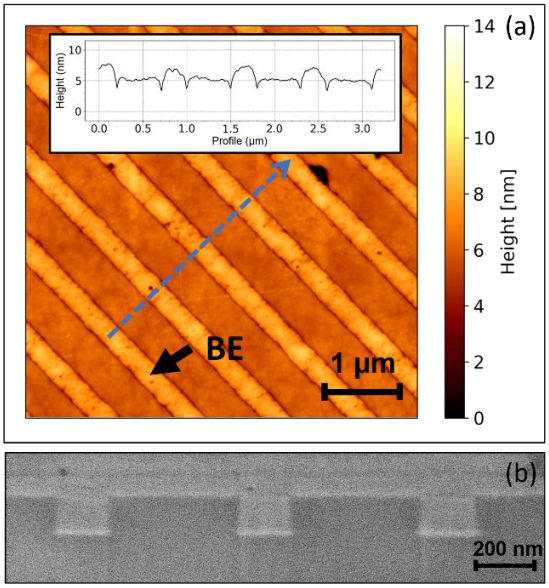

Figure 3: Etch-back. (a) AFM measurements of the BE surface. (b) FIB cross-section image. (c) Switching behavior of the resistive memory

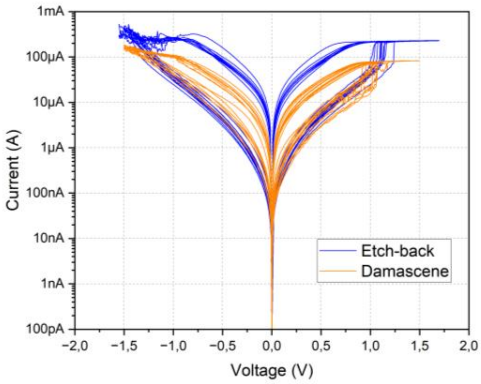

Figure 4: Cycling behavior of memory devices for both approaches. The SET/REST voltage are equal. The Etch-back approaches have slightly better resistance ratio.

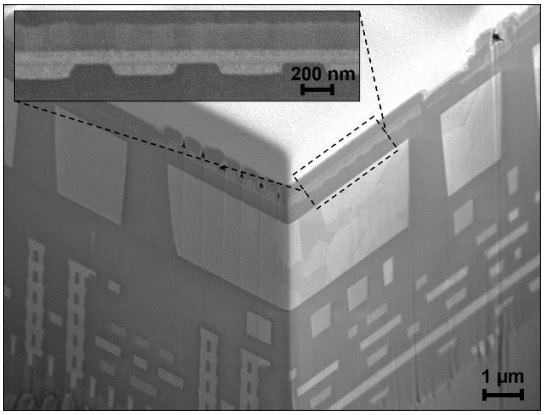

Figure 5: FIB images of crossbar memristive memory arrays fabricated using the Damascene approach, integrated into the BEOL of a TSMC CMOS chip at a 130 nm node.

Resolution enhancement of Scanning Electron/Atomic Force Microscope images using a computational method based on Fourier spectra stitching

E. Stai[a,b], V. Constantoudis[a,c], A. Kaidatzis[a], E. Gogolides[a,c]

[a] Institute of Nanoscience and Nanotechnology, NCSR Demokritos, Aghia Paraskevi 15341, Attiki, Greece
[b] Department of Physics, National and Kapodistrian University of Athens, Greece
[c] Nanometrisis p.c., Agia Paraskevi, Attiki 15310, Greece
e-mail: e.stai@inn.demokritos.gr

Atomic Force Microscopy (AFM) and Scanning Electron Microscopy (SEM) are widely used in nanoscience and nanotechnology to display and quantify surface roughness and nanostructure morphology. However, their measurements suffer from scale and position (locality) limitations since they can display surface fluctuations within scales ranged between pixel size and field of view but also at the same time they are obtained from a specific surface position ignoring the vast surface area outside it. On the other side, the applications of nanorough surfaces usually involve much wider spectra of scales and larger surface areas demonstrating the need to overcome these limitations. The aim of this work is to bridge the gap between what we can measure by Scanning Microscopies and what we should measure to optimize the use of nanofabricated surfaces in applications by proposing a computational method which enables the generation of multiple surface measurements (release from locality limitation) with enhanced scale content and increased resolution (release from scale limitation) successfully mimicking the real ones. The method conforms to the common experimental practice and demands as input just a small number of measurements taken with different magnifications. Its main idea is based on the proper stitching of Fourier spectra of input measurements and is easy in its implementation and fast in performance. The so-called Fourier Spectra Stitching (FSS) has been first validated in synthesized rough surfaces with predetermined roughness parameters and resolution to demonstrate its accuracy. Then it has been applied in real experimental surfaces with very promising results.

Figure 1 displays a graphical representation of the FSS method. Firstly, few measurements of surface morphology (three in the shown example) with different magnifications (pixel size and measurement range) are obtained all having the same number of pixels (256x256 in our example). It follows the computation of the 2D Fourier spectra of all three surfaces and then assuming surface isotropy we obtain the 1D circular average of Fourier amplitudes. The blue Fourier spectrum refers to the small magnification measurement while the green and red to the middle and large magnifications respectively. Then the three Fourier spectra are stitched appropriatelly and we obtain the new full-scale Fourier spectrum (cyan in Fig.1). Finally, we apply the stohastic inverse Fourier transform and we get the scale-enhanced reconstructed image characterized by the small pixel size of the high megnification image and the large measurement range of the small magnification image. In the specific example of Fig.1, the reconstructed image has measurement range 2.304μmx2.304μm and pixel-size 1nm. One should notice that the FSS method does not reconstruct the surface pixel-by-pixel but it can generate statistically similar copies of the initial surface in conformity with the stochastic nature of the initial surface.

The FSS method has been applied in AFM images (Fig.2) of CoFeTa thin film which has been deposited using magnetron sputtering and has a thickness of 50 nm. Oxidized commercial Si substrates were used as growth substrates. The surface morphology images were obtained using a NT-MDT solver atomic force microscope in non-contact mode and commercial AFM probes (Nanosensors PPP-NCH). Fig.2a shows the experimental AFM image of low magnification used as input in FSS (with measurement range $5x5\mu m^2$ and pixel size 9.8nm) while the FSS-based reconstructed surface is displayed in Fig.2b characterized by a similar measurement range but much smaller pixel size (1.96nm). The magnified portions of images shown in Fig.2 reveal the five times resolution enhancement achieved by FSS method. Besides the above-described polar FSS method, other versions of FSS method have also been developed including the fully 2D FSS method or its deterministic counterpart.

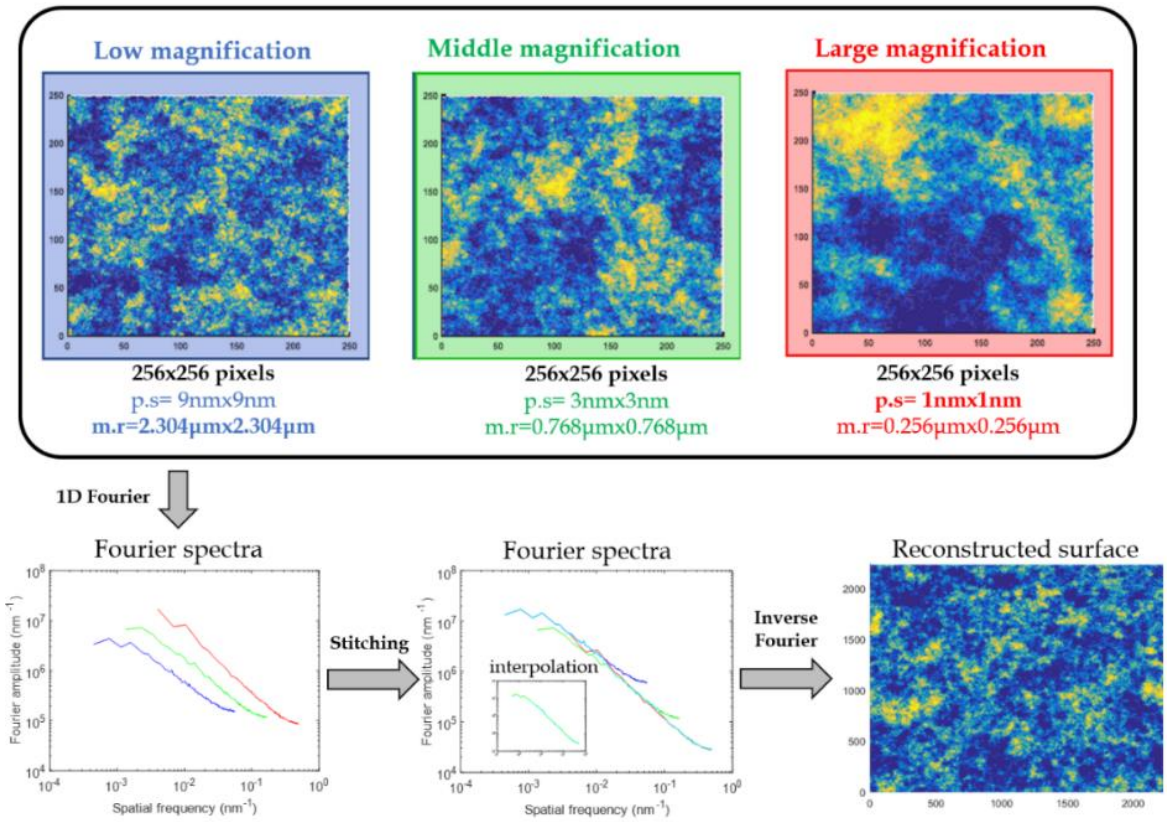

Figure 1. Graphical representation of the FSS method.

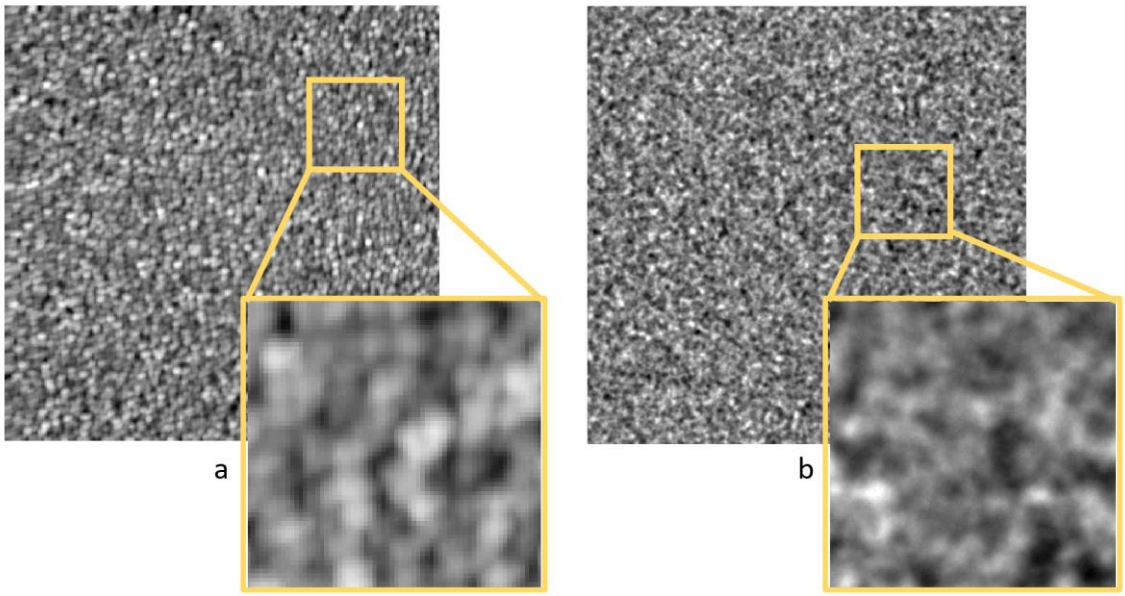

Figure 2. a. Low magnification SEM image of CoFeTa thin film with measurement range 5x5µm^2 and pixel-size 10x10nm^2. b. Generated scale-enhanced image with measurement range 5x5µm^2 and pixel-size 2x2nm^2.

Acknowledgement
This work has been funded by the ERANET Project 'Carbyne Films: Synthesis of a New Class of Carbon Allotrope and Novel Applications in Sensors and Biosensors (CarbyneSense)', MIS 5161208.

Calculation of magnetic force between current-carrying circular and arbitrary shaped filament: segmentation method

Kirill V. Poletkin [a], Pavel Udalov [b], Alexei Lukin [b]

[a] School of Instrument Science and Opto-electronics Engineering, Hefei University of Technology, Hefei, Anhui, 230009, China, e-mail: 2022810003@hfut.edu.cn
[b] High School of Applied Mechanics and Control Processes, Peter the Great St. Polytechnic University (SPbPU), St. Peterburg, 195251, Russia

A new formula for calculation of magnetic force between current-carrying circle and line segment is derived by using Mutual Inductance Method (MIM) [1]. Using the fact that any curve can be interpolated by a set of line segments, a method for calculation of magnetic force between a circular filament and filament having an arbitrary shape in the space is proposed based on the derived analytical formulas (Segmentation Method (SM)) [2]. The proposed SM method was successfully applied to the calculation of the magnetic force between the circular filament and the following special curves such as polygons, and circles.

Analytical and semi-analytical methods in the calculation of parameters of electrical circuits and force interaction between their elements play an important role in developing micro- and nano-system devices and their applications in the different fields of science, including electrical and electronic engineering, medicine, physics, nuclear magnetic resonance, mechatronics, robotics, and *etc*. In particular, in the framework of recently developed quasi-finite element model (quasi-FEM) approach [3], the derived set of formulas helps us further to comprehensively simulate the static and dynamic behaviour of hybrid levitation micro-actuators (HLMAs). HLMAs dramatically increase capabilities of levitated micro-systems through implementing, for instance, multi-stable mechanisms, coherent cooperative actuation and demonstrate a wide range of different operation modes such as the linear and angular positioning, bi-stable linear and angular actuations, and the adjustment of stiffness components as it was reported in Ref. [4].

Fig. 1 shows the filament system consisting of a primary circular filament and a secondary filament represented as a line segment, which is arbitrarily positioned in the space with respect to the primary circle [2]. Assuming that the primary and secondary filaments carry the currents of I_p and I_s, respectively, hence, the magnetic force can be calculated by taking the first derivatives of the function of the magnetic energy stored in such the system with respect to the appropriate coordinates. Hence, magnetic force can be calculated by $F_{\mathrm{q}} = I_p I_s \, \partial M / \partial q$, where $q = x_C, y_C, z_C$ and M is the mutual inductance between these filaments [2]. The derivatives of mutual inductance are shown in Tab. 1 and 2.

The secondary filament having an arbitrary shape is considered as shown in Fig. 2, left. The secondary filament is given, for instance, by a 3D parametric curve $\sigma = \sigma(l)$, where l is the parameter defined within a finite interval $[\varphi_0, \varphi_1]$ and the following inequality $\varphi_1 > \varphi_0 \geq 0$ is valid. It is assumed that the curve is sampled by n points, so that we have $\underline{p}_0(h_0)$, $\underline{p}_1(h_1)$, $\underline{p}_2(h_2)$, ..., $\underline{p}_{n-1}(h_{n-1})$, $\underline{p}_n(h_n)$. The points can be defined in the following way $\underline{p}_i(h_i) = [x_\sigma(h_i)\ y_\sigma(h_i)\ z_\sigma(h_i)]^T$, as (3×1)-column-matrices, where x_σ, y_σ, and z_σ are the coordinates of the σ -curve and $h_i = h_{i-1} + (\varphi_1 - \varphi_0)/n$, so that $h_0 = \varphi_0$. Using the set of points, the σ-curve can be interpolated by line segments as shown in Fig. 2, right. Hence, performing summation of all n terms of F_{qi}, the formula for magnetic force between current-carrying circular and arbitrary shaped filament can be written as follows: $F_{\mathrm{q}\sigma} = \sqrt{R_p} I_p I_s \mu_0 / \pi \int_0^1 \sum_{i=1}^n \sqrt{L_{si}} \cdot \partial\big(U_i \cdot \Phi(k_i)\big)/\partial q \, d\bar{l}$. Fig. 3, 4 and 5 show the three illustrative arrangements of the current-carrying coils. In these arrangements, it is assumed that the currents are units. The results of calculation are tabulated in Tab. 3, 4 and 5, respectively, and agree well with FEM and MIM [5].

[1] K. V. Poletkin and J. G. Korvink., J. Magn. Magn. Mater. 483 (2019) 10–20.
[2] K. V. Poletkin, et al., J. Magn. Magn. Mater. (2023) accepted.
[3] K. V. Poletkin, IEEE ASME Trans Mechatron. 26 (2021) 753–764.
[4] K. V. Poletkin, et al., J. Microelectromech Syst. 24 (2015) 1248–1250.
[5] K. V. Poletkin, Int. Journal of Mechanical Sciences. 220 (2022) 107159.

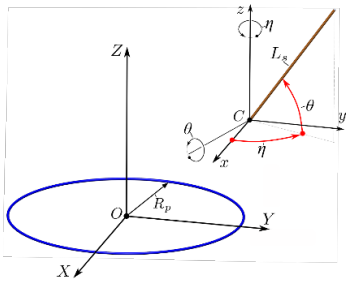

Figure 1. General scheme of arbitrarily positioning the line segment with respect to the circular filament: R_p is the radius of the circle and L_s is the length of the line segment.

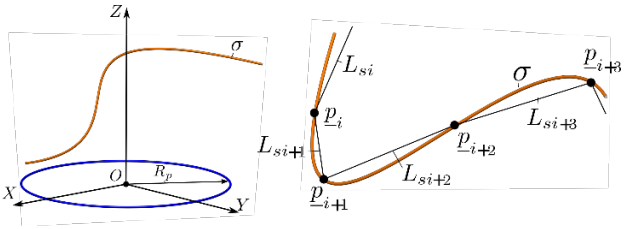

Figure 2. General scheme of arbitrary shaped filament and the circular filament (left); Interpolation of the σ curve by line segments (right).

Table 1. x_C- and y_C- derivatives of M.

$$\frac{\partial M}{\partial q}=\frac{\mu_0}{\pi}\sqrt{\frac{R_p}{L_s}}\int_0^1\frac{\partial U}{\partial g}\Phi(k)+U\frac{d\Phi(k)}{dk}\frac{\partial k}{\partial g}d\bar{l},$$

where $g=x$, and y, $\bar{l}=l/L_s$, $x=x_c/L_s, y=y_c/L_s, z=z_c/L_s$, $U=R/\rho^{1.5}=(t_1-t_2)/\rho^{1.5}cos\,\theta$, $t_1=\sin\eta\cdot\left(x+\bar{l}\cos\theta\cos\eta\right)$, $t_2=\cos\eta\cdot\left(y+\bar{l}\cos\theta\sin\eta\right)$,
$s=\sqrt{x^2+y^2}$, $k^2=4\nu\rho/((\nu\rho+1)^2+\nu^2z_\lambda^2)$, $\nu=R_s/R_p$,
$\rho=\sqrt{s^2+2\bar{l}\cos\theta\cdot(x\cos(\eta)+y\sin(\eta))+\bar{l}^2\cos^2\theta}$,
$\Phi(k)=1/k\,[(1-k^2/2)K(k)-E(k)]$,
$z_\lambda=z+r\tan\theta\sin\theta$,
$\frac{d\Phi(k)}{dk}=\frac{1}{k^2}\left[\frac{2-k^2}{2(1-k^2)}E(k)-K(k)\right]$,
$\frac{\partial U}{\partial g}=\left(\frac{\partial R}{\partial g}\rho-1.5\cdot R\cdot\frac{\partial\rho}{\partial g}\right)/\rho^{2.5}$, $\frac{\partial R}{\partial x}=\sin\eta$,
$\frac{\partial R}{\partial y}=-\cos\eta$, $\frac{\partial k}{\partial g}=\frac{2/k-k(\nu\rho+1)}{(\nu\rho+1)^2+\nu^2z_\lambda^2}\cdot\nu\frac{\partial\rho}{\partial g}$,
$\frac{\partial\rho}{\partial x}=\left(\bar{l}\cos\theta\cdot\sin\eta+y\right)/\rho$,
$\frac{\partial\rho}{\partial y}=\left(\bar{l}\cos\theta\cdot(y\cos\eta-x\sin\eta)\right)/\rho$.

$K(k)$ and $E(k)$ are the complete elliptic functions of the first and second kind, respectively.

Table 2. The z_C - derivative of M.

$$\frac{\partial M}{\partial z_C}=\frac{\mu_0}{\pi}\sqrt{\frac{R_p}{L_s}}\int_0^1 U\cdot\frac{d\Phi(k)}{dk}\cdot\frac{\partial k}{\partial z}d\bar{l},$$

where $z=z_C/L_s$,
$\frac{\partial k}{\partial z}=-\sqrt{4\nu\rho}\cdot\nu^2z_\lambda/((\nu\rho+1)^2+\nu^2z_\lambda^2)^{3/2}$,
the k- derivative of Φ is given in Tab. 1.

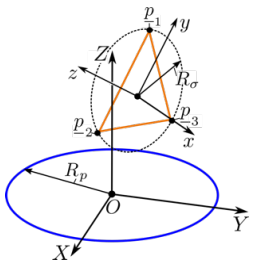

Figure 3. The primary circle has a radius of R_p =0.16m. The triangular filament (n = 3 sides) is inscribed in a circle having a radius of R_σ= 0.1m. The coordinates of centre are x_C = 0.0cm, y_C= 4.3301cm, z_C = 17.5cm. The angular misalignment is defined by Grover's angles, namely, θ= 60.0° and η = 45° [2].

Table 3. Force calculation for the arrangement shown in Fig. 3 (Example 6 in [2]).

Force, nN	SM	FEM
F_x	43.3802	43.2426
F_y	−57.9754	−57.8478
F_z	−54.3679	−54.2297

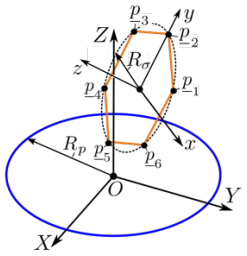

Figure 4. The hexagon (n = 6 sides) is inscribed in the secondary circle of the same arrangement as in Fig. 3.

Table 4. Result of calculation for the arrangement shown in Fig. 4 (Example 8 in [2]).

Force, nN	SM	FEM
F_x	86.8021	86.5084
F_y	−114.0307	−113.8180
F_z	−112.8408	−112.8011

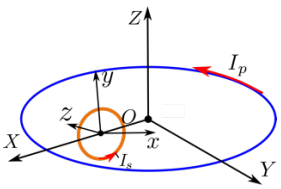

Figure 4. The primary and secondary circles have radii R_p =0.005m and R_s =0.001m, respectively. The centre of the secondary circle is located at x_C = 0.003m, y_C=0.001m, z_C =0.0005m. The angular misalignment is defined by θ= 57.6885° and η = 108.4349°.

Table 5. Result of calculation for the arrangement shown in Fig. 4 (Example 12 in [2]).

Force, nN	SM (n=200)	MIM [5]
F_x	136.9822	137.0009
F_y	45.6607	45.6669
F_z	98.5462	98.5674

Interfacing free-space beams and suspended silicon photonic waveguides with a low back-reflection fully etched grating coupler

Søren Engelberth Hansen [a], Guillermo Arregui [a], Ali Nawaz Babar [a, b], Marcus Albrechtsen [a], Babak Vosoughi Lahijani [a], Rasmus Ellebæk Christiansen [b, c], Søren Stobbe [a, b]

[a] Department of Electrical and Photonics Engineering, DTU Electro, Technical University of Denmark, DK-2800 Kgs. Lyngby, Denmark
[b] NanoPhoton - Center for Nanophotonics, Technical University of Denmark, DK-2800 Kgs. Lyngby, Denmark
[c] Department of Civil and Mechanical Engineering, DTU Construct, Technical University of Denmark, DK-2800 Kgs. Lyngby, Denmark
e-mail: senha@dtu.dk

Silicon-on-insulator (SOI) is a widely used material platform for making photonic integrated circuits that combine multiple components, such as waveguides, resonators, modulators, and splitters, into compact and scalable devices for applications such as sensing, imaging, telecommunication, and quantum networks. The device layer in the SOI wafer must be patterned to define the high index-contrast photonic structures, which can then be covered with glass to form embedded structures or be suspended by removing the oxide beneath. The suspended platform offers exciting possibilities of combining optical functionality with mechanical degrees of freedom [1, 2], either via the direct use of optical forces or by electromechanical actuation. The use of opto-electro-mechanical systems has the potential to replace thermo-optical and electro-optical actuation with a smaller footprint, lower power consumption, and higher speed for devices such as optical switches in programmable networks. An efficient interface to such a suspended platform is required, which calls for the development of efficient couplers to suspended waveguides. We present the recent development of a grating coupler that is suspended and fully etched to facilitate fabrication in a single lithography step in conjunction with the rest of the suspended photonic circuit [3]. We design the coupler for normal-incidence free-space coupling through an optical microscope to a rectangular suspended waveguide, which allows simple alignment and testing of suspended photonic circuit components. However, the vertical scattering angle does not automatically suppress back-reflection like the tilt-angle used in conventional fiber grating couplers [4], and thus it requires an explicit inclusion of back-reflection in the numerical optimization formulation. By treating all lines in the grating as design parameters, we have created a grating coupler optimized for C-band telecommunication wavelengths. The design optimization yields an aperiodic grating with good transmission of 21.8 %, minimal back-reflection of 0.2 %, and a 3 dB bandwidth of 75 nm. We fabricate the grating couplers, shown in Fig 1, on SOI wafers with a 220 nm device layer and 2 μm buried-oxide layer and perform an extensive experimental validation of the transmission and reflection characteristics for multiple photonic circuits. We present the applied characterization method, which uses a Fabry-Pérot resonator model in addition to windowed Fourier transforms, to understand and directly extract the reflections from the fringes in the measured transmitted power of the full photonic circuit.

References:

[1] T. H. Stievater, M. W. Pruessner, W. S. Rabinovich, D. Park, R. Mahon, D. A. Kozak, J. B. Boos, S. A. Holmstrom, and J. B. Khurgin, Appl. Opt. (2015), **54**, F164–F173.
[2] L. Midolo, A. Schliesser, and A. Fiore, Nat. Nanotechnol. (2018), **13**, 11–18, 276.
[3] S. E. Hansen, G. Arregui, A. N. Babar, M. Albrechtsen, B. V. Lahijani, R. E. Christiansen, and S. Stobbe, Opt. Express (2023), **31**, 17424-17436.
[4] D. Taillaert, P. Bienstman, and R. Baets, Opt. Lett. (2004), **29**(23), 2749–2751.

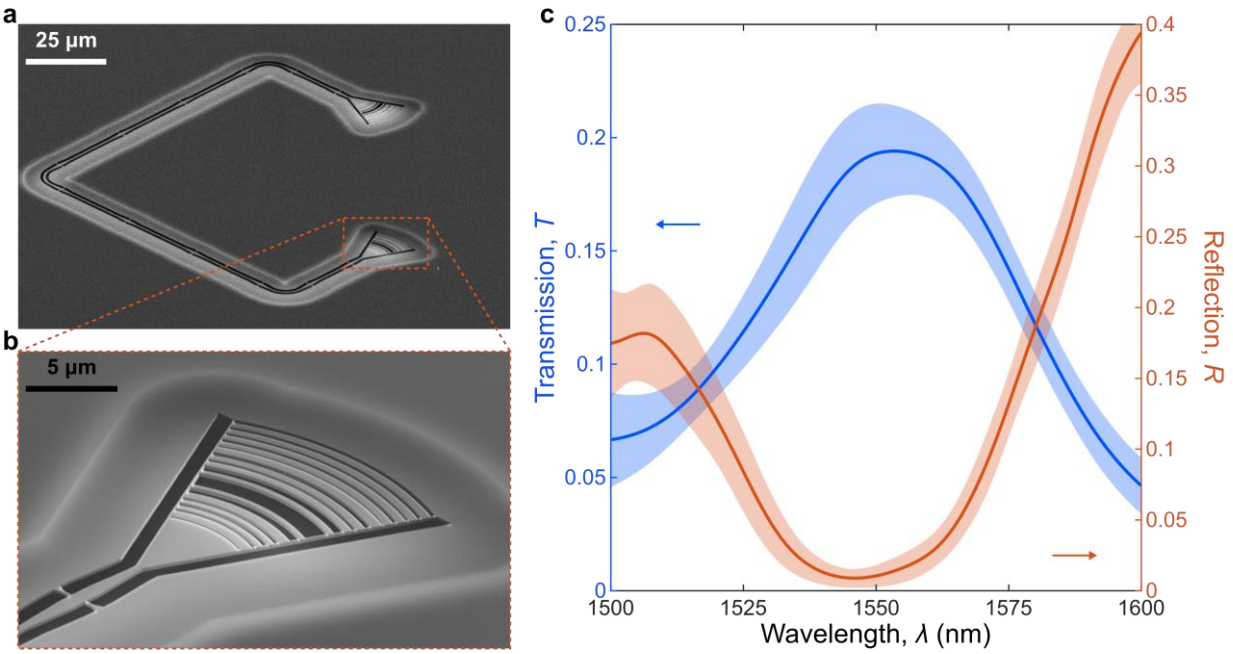

Figure 1. Fabricated grating coupler and measured performance. a, Scanning electron micrograph of suspended photonic circuit. b, Scanning electron micrograph of grating coupler. C, Measured transmission and reflection of grating coupler with the mean (solid line) and error (shaded area region showing the 95 % confidence interval).

Strain Rate Dependency of Mechanical Property in Micro-Compression of Electrodeposited Gold toward Design of MEMS Components

Shota Kanno, Taro Omura, Tomoyuki Kurioka, Chun-Yi Chen, Parthojit Chakraborty, Katsuyuki Machida, Hiroyuki Ito, Yoshihiro Miyake, Masato Sone, Tso-Fu Mark Chang

Tokyo Institute of Technology, Yokohama, 226-8503, Japan
e-mail: kanno@ames.pi.titech.ac.jp

Gold-based micro-electro-mechanical systems (MEMS) accelerometers are promising devices to simultaneously realize high sensitivity and miniaturization by suppressing the thermal-mechanical noise due to the high mass density of gold (19.3 g/cm^3) [1]. Components in MEMS devices often have sizes on micro-scale or smaller, and metallic materials are reported to exhibit the sample size effect [2], which a smaller-is-stronger effect or smaller-is-weaker effect is observed when the sizes are reduced to micro-scale or smaller. Therefore, clarifying the micro-scale mechanical property is a prerequisite for design of MEMS components. On the other hand, mechanical properties of a metallic material obtained from a mechanical testing are dependent on the strain rate used in the measurement, and the strain rate dependency could be quantified by a value called strain rate sensitivity [3].

In this study, strain rate dependency of micro-mechanical properties of electrodeposited gold is evaluated for the design of movable components in MEMS deceives. In particular, the strain rate sensitivity is calculated from the yield stress values obtained from compression tests of micro-pillars with a square cross-section fabricated from electrodeposited gold by focused ion beam (FIB).

A piece of electrodeposited gold film with approximate 30 μm of thickness was prepared on at a constant current density of 1.0 A/dm^2. Three micro-pillars with different dimensions were fabricated from the electrodeposited gold film by FIB: Pillar A (10 × 10 × 20 μm^3), Pillar B (15 × 15 × 30 μm^3), and Pillar C (18 × 18 × 36 μm^3). The compression test was conducted using three different strain rates as follows: 2.5 × 10^{-2} s^{-1}, 2.5 × 10^{-3} s^{-1} and 2.5 × 10^{-4} s^{-1}. Fig. 1 shows an image of the self-developed micro-mechanical testing machine used in this work.

All micro-pillars deformed into a barrel shape after the compression test as illustrated in Fig. 2. This barrel shape deformation behavior was a result of ductile deformation, and which is commonly observed in specimens composed of polycrystals [4]. The 0.2% yield strength was calculated from the engineering stress-engineering strain curve obtained from the compression test and used as the yield strength. Fig. 3 shows a plot of logarithm scale of the yield strength versus logarithm scale of the strain rate. Generally, the yield strength increased as the pillar size decreased due to the sample size effect, and the strengthening was also observed following an increase in the strain rate. When connecting data points of micro-pillars with the same sizes, a linear relationship was observed between the log(strain rate) and the log(yield strength). By the slope of the linear lines, the strain rate dependency could be quantified as the strain rate sensitivity (m). The m's of the three types of the micro-cantilevers were all at around 0.03, which suggest a weak correlation between the sample size and the m. Possible explanations are as follow: (1) face-centered cubic (FCC) metals are known to have weak strain rate dependency and (2) the average grain size also influence the strain rate dependency, which the strain rate dependency is anticipated to be low when there is a large number of grains in the cross-section of the specimen. On the other hand, the m's obtained in this study were all much larger than that of coarse-grained bulk-size samples, which is reported to be at around 0.004 [5].

Acknowledgment:
This study was supported by JST CREST Grant Number JPMJCR21C5, Japan, and JSPS KAKENHI Grant Number JP21H01668.

References:
[1] D. Yamane et al., Appl. Phys. Lett., 104 (2014) 074102.
[2] J.R. Greer et al., Prog. Master. Sci, 56 (2011) 654–724.
[3] T.Y. Tsui, J. Jang et al., Acta Mater., 127 (2017) 332–340.
[4] M. Sone et al., Microelectron. Eng., 213 (2019) 18–23.
[5] Q. Wei et al., Mater. Sci. Eng. A., 381 (2004) 71-79.

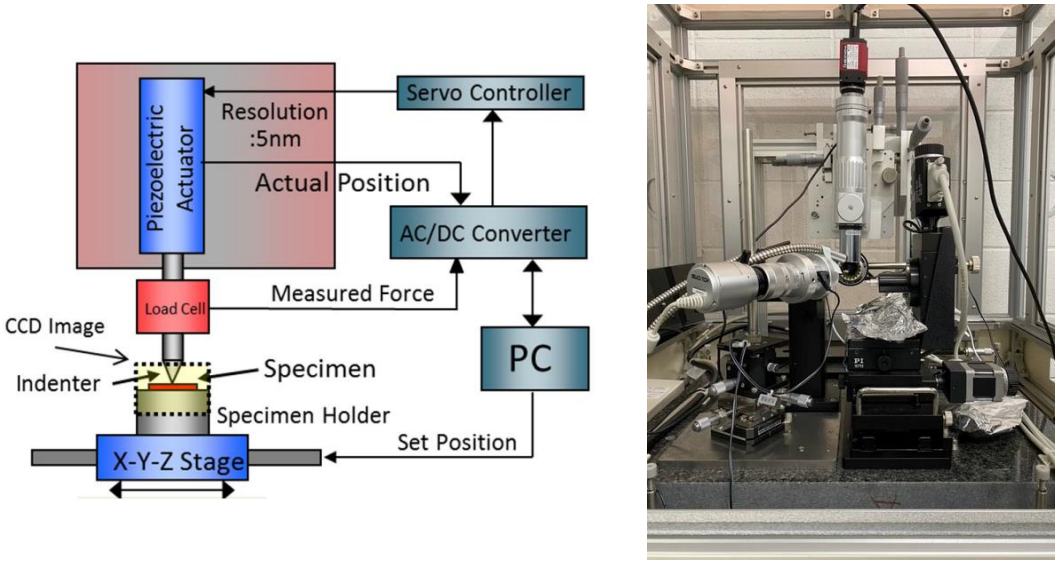

Figure 1. Micro-mechanical testing machine use in this study.

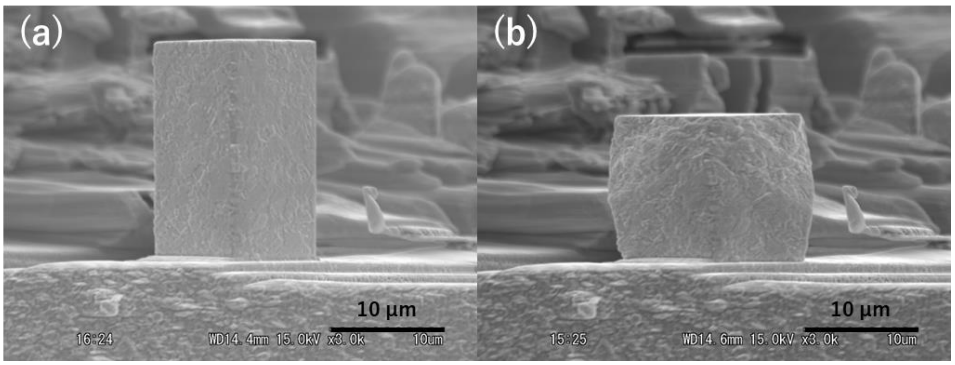

Figure 2. SEM images of Pillar A (a) before and (b) after the compression test at a strain rate of 2.5 × 10^{-3} s^{-1}.

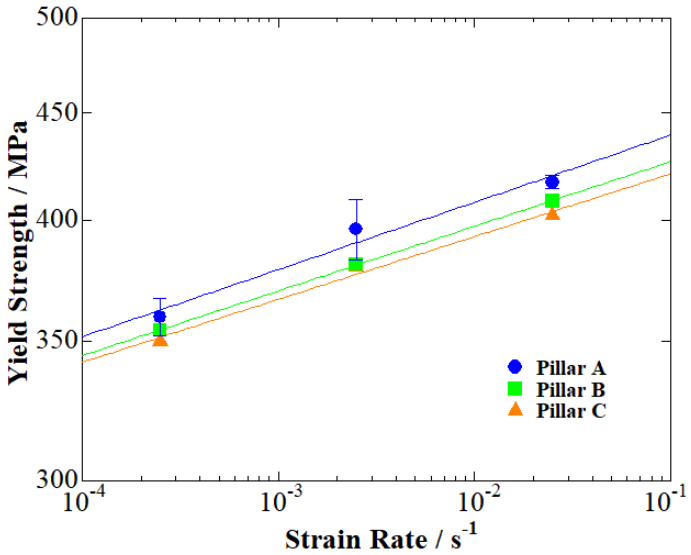

Figure 3. The relationship between the yield stress and strain rate. Slopes of the straight lines are calculated as the strain rate sensitivity.

Comprehensive Evaluation of Geometric Effects on Long-Term Structure Stability of Ti/Au Multi-Layered Micro-Cantilevers toward Gold-MEMS Capacitive Accelerometer

Ryosuke Miyai, Tomoyuki Kurioka, Chun-Yi Chen, Tso-Fu Mark Chang, Akira Onishi, Parthojit Chakraborty, Katsuyuki Machida, Hiroyuki Ito, Yoshihiro Miyake, Masato Sone

Tokyo Institute of Technology, Yokohama, 226-8503, Japan
e-mail: miyai@ames.pi.titech.ac.jp

Gold-based micro-electro-mechanical-system (MEMS) capacitive accelerometers are promising devices to detect extremely weak acceleration of less than micro-G (1 G = 9.8 m/s^2) by suppressing the Brownian noise because of the high mass density of gold (d = 19.3g/cm^3 at 298 K) [1]. On the other hand, mechanical strengths of gold materials are generally weaker than materials commonly used in MEMS devices [2,3], which lead to concerns about the long-term reliability of gold-based MEMS accelerometers [4]. In addition, on the basis of the Euler-Bernoulli beam theory, mechanical strengths of a cantilever are affected by the geometry, and movable components employed in a MEMS device could have various geometries. In this study, effects of the geometrical parameters of gold micro-cantilevers on their long-term structural stability are evaluated by long-term vibration test.

Figure 1 shows schematics of a Ti/Au single-layered (SL) micro-cantilever and Ti/Au multi-layered structures used in this study. The proposed structures were simultaneously fabricated on a test element group (TEG) by the multi-layer metal technology [1]. Six types of Ti/Au layered structures were prepared: three SL structures, two double-layered (DL) structures, and one triple-layered (TL) structure. A total of 240 micro-cantilevers with different width (w [μm] = 8, 9, 10, 11, 12, 13, 15, 20), length (l [μm] = 200, 400, 600, 800, 1000) were fabricated. Long-term vibration tests were performed at a frequency of 10 Hz and an acceleration of 1 G with a cycle number of 10^3–10^7. The height of the micro-cantilever tip from the substrate was measured by a 3D optical microscope (OM). The structural stability was evaluated from the amount of change (Δh_{tip}) in the tip height before and after the vibration test, and Δh_{tip} was defined as the following equation:

$$\Delta h_{tip} = h_{tip} - h_{tip,0}$$

where $h_{tip,0}$ is the tip height before the vibration test, and h_{tip} is the tip height after the vibration test.

Figure 2(a) shows an OM image of the Ti/Au multi-layered micro-cantilevers. No obvious deformation in directions parallel to the substrate surface was observed. After 10^7 cycles of the vibration, the micro-cantilever slight deflected up as revealed in Figure 2(b).

Figure 3 shows the geometric effects (l, t and w) on the Δh_{tip} after 10^7 cycles of the vibration. Generally, the w was found to scarecely affect the structural stability, which corresponded well with the Euler-Bernoulli beam theory. In contrast, the Δh_{tip} was found to be dependent on both the l and t. The micro-cantilevers with a shorter l tended to have a smaller Δh_{tip} after the vibration test, which indicates an improved structural stability. Thickening the t also resulted a smaller Δh_{tip}.

In summary, the width, length, and thickness of the Ti/Au layered micro-cantilevers each contributed differently to the long-term structural stability. Reducing the l and thickening the t both were beneficial to the long-term structural stability. These findings are critical for the design of MEMS movable components having a complex geometry.

Acknowledgement
The authors would like to thank T. Sakai and S. Iida, T. Konishi, NTT-AT Corp., for their technical support. This work was supported by JST, CREST Grant Number JPMJCR21C5, Japan.

Refarences
[1] K. Masu *et al*., ECS Trans. 97 (2020) 91–108.
[2] H. D. Espinosa *et al*., J. Mech. Phys. Solids 52 (2004) 667–689.
[3] J. D. Zahn *et al*., Biomed. Microdevices 24 (2000) 295–303.
[4] K. Nitta *et al*., Microelectron. Eng. 215 (2019) 111001.

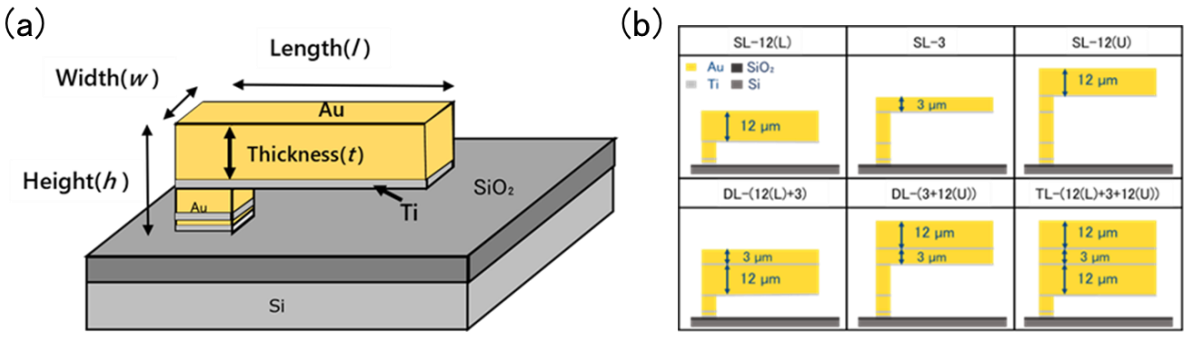

Figure 1. Schematic of a Ti/Au (a) single-layered and (b) multi-layered micro-cantilevers.

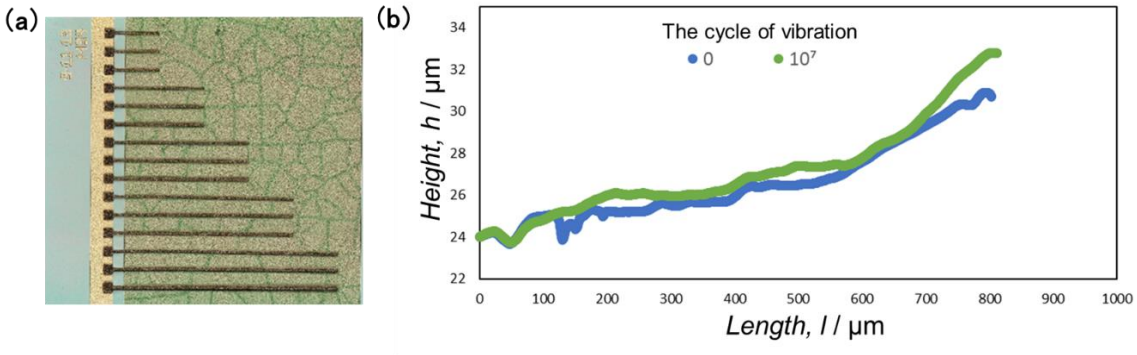

Figure 2. (a) OM images of Ti/Au multi-layered micro-cantilevers before test.
(b) Height profiles of DL-(12(L)+3) before and after 10^7 cycles of the vibrations.

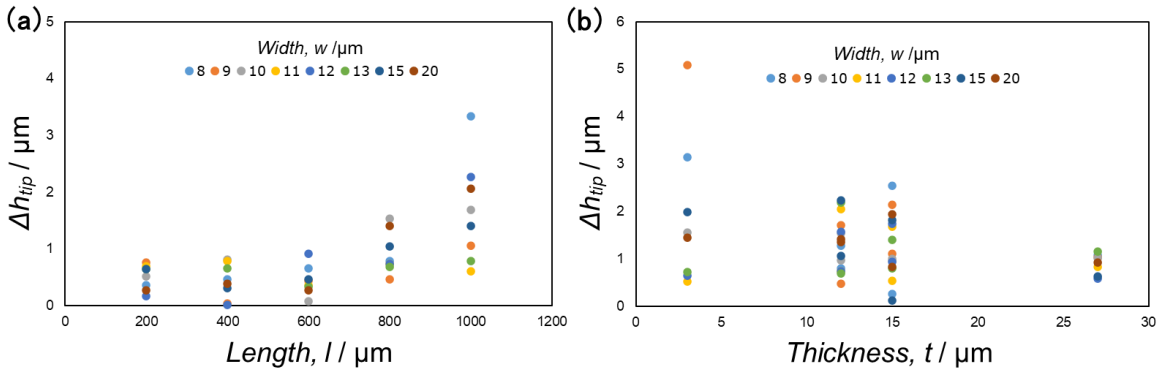

Figure 3. (a) Relationship between l of SL-12(L) micro-cantilevers and their Δh_{tip}.
(b) Relationship between t of micro-cantilevers with the length (l) of 800 μm and their Δh_{tip}.

Enhanced Fe-FET Performance with HZO and MoS_2-Based Dielectric Structures for Non-volatile Memory

Jee Hwan Lee [a,b] , Yoon Do Kyung [a,b] and Woo Jong Yu

[a] Department of Semiconductor and Display Engineering, Sungkyunkwan University, Suwon 16419, Republic of Korea
[b] Memory CVD Technology Team, Hwaseong 18448, Republic of Korea
[c] Department of Electrical and Computer Engineering, Sungkyunkwan University, Suwon 16419, Republic of Korea
e-mail: micco21@skku.edu

Ferroelectric devices have emerged due to lower power consumption, faster switching speeds and improved data retention. [1],[2] Moreover, HZO($Hf_{0.5}Zr_{0.5}O_2$) films have shown high permittivity, which refers to the material's ability to store electrical energy when an electric field is applied, high dielectric constant, making it suitable for applications where high charge storage density is desired, such as in non-volatile memory devices and excellent endurance making them suitable for repeated switching cycles without significant degradation. [3] HZO exhibits ferroelectric properties as structural changes occur due to stress between the electrode and the thin film at a temperature of 400℃. It has ferroelectric properties due to the change of crystal structure from the conventional monoclinic phase to the orthorhombic phase through heat treatment, and at a Zr composition ratio of 50%. [4],[5]
In this Study, We fabricated 10-nm-thick ferroelectric HZO($Hf_{0.5}Zr_{0.5}O_2$) thin films as a Ferroelectric dielectric with MoS_2 TMDS film as a Semiconductor. HZO Film was deposited by Thermal-atomic layer deposition (TE-ALD) at 250°C with H_2O ligand and a post annealing process at 500°C. The transfer characteristic of this Fe-FET was demonstrated with operating voltage that was smaller than 10 V, memory window about 0.5 V, and small subthreshold slope (SS) about 400 mV/dec. This $Hf_{0.5}Zr_{0.5}O_2$ Fe-FET Device can be attractive for various applications in advanced electronic devices.

[1] Z. Wen and D. Wu, Adv Mater, 32, e1904123 (2020).
[2] J. Y. Kim, M. J. Choi, and H. W. Jang, APL Materials, 9, 021102 (2021)
[3] T. S. Böscke, J. Müller, D. Bräuhaus, U. Schröder, and U. Böttger, Applied Physics Letters, 99,102903(2011).
[4] J. Müller, T. S. Böscke, U. Schröder, S. Mueller, D. Bräuhaus, U. Böttger, L. Frey, and T. Mikolajick, Nano Letters, 12, 4318 (2012).
[5] P. S. Chen, and C. W. Liu, Materials Research Express, 6, 095045 (2019).

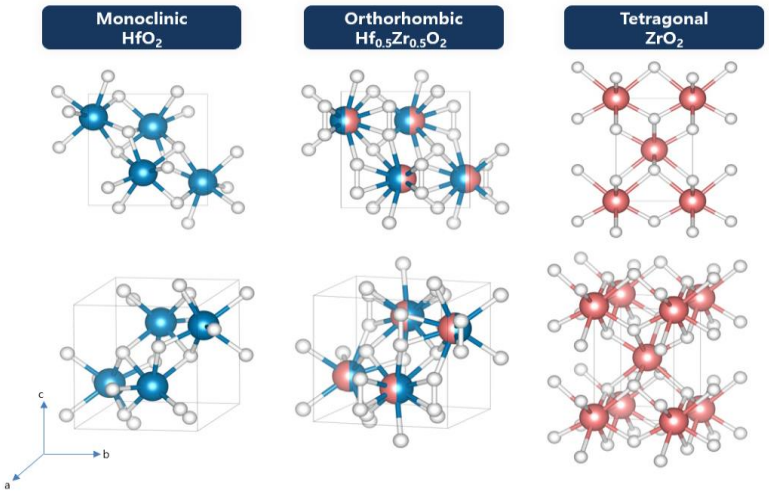

Figure 1. Characteristics of HfO2 phase change according to ZrO2 doping.

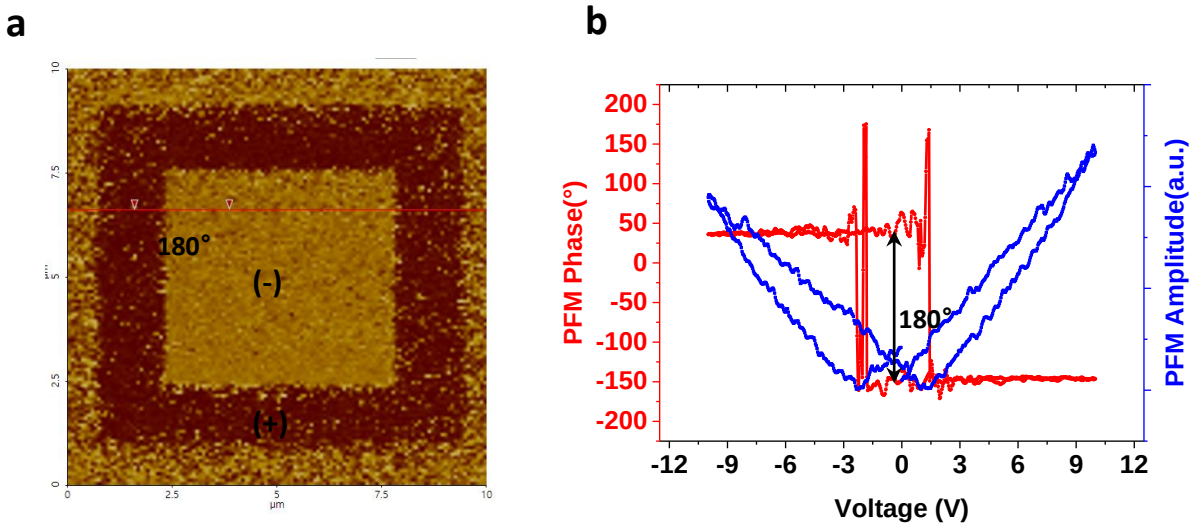

Figure 2. **a,** Phase-contrast PFM images demonstrating remanent polarization states for HZO film **b,** Phase and amplitude switching spectroscopy loops for a HZO film, demonstrating ferroelectric hysteresis.

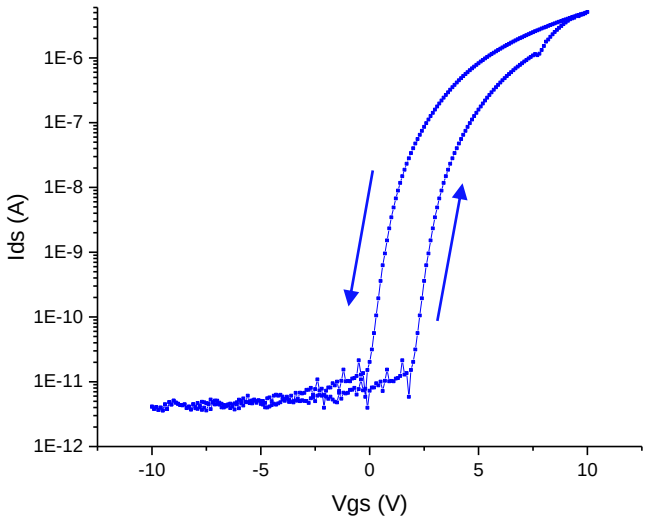

Figure 3. Transfer curves with V_{ds}=1V for $Hf_{0.5}Zr_{0.5}O_2$ Fe-FET

Thermal characterization of IMS substrates with different design parameters for Power Modules Devices

Spano Chiara [a, b], Galfrè Giulio [a], Mattiuzzo Emilio [b], D'Ancona Lorenzo [b], Scaltrito Luciano [a], Ferrero Sergio [a], Bertana Valentina [a]

[a] Politecnico di Torino, Torino, 10129, Italy
[b] VISHAY Semiconductor Italiana S.P.A, Borgaro Torinese, 10071, Italy
e-mail: chiara.spano@polito.it

Power semiconductor modules are responsible for processing and transferring electrical power between a source and a load, according to customer requirements. Due to recent advancements in semiconductors, the demanded efficiency of these systems is getting higher, making the performances of the materials and the reliability of the package, the focus of a new generation of power devices [1].
Power modules are made up mainly by two parts: a substrate, whose purpose is to accommodate the semiconductors, to provide the electrical connections and the insulation between the components, and a package, whose aim is to protect the inner components from the environment and to enhance the mechanical robustness of the system. Direct Bonded Copper (DBC) is a multilayered copper/ceramic substrate that found large application in these devices over the last decades for its high thermal conductivity and electrical insulation. However, the new thermal requirements are leading to an increase in the mismatch between the copper and ceramic, in terms of Coefficient of Thermal Expansion (CTE), causing higher thermal stresses at the interfaces and increasing the brittleness of the ceramic [2].
This study aims to thermally evaluate improved substrates without ceramic as dielectric layer, to overcome potential thermo-mechanical criticalities of the DBC under working conditions. For this reason, Insulated Metal Substrates (IMSs) were chosen as valid alternative substrates for power modules and also because they are compatible with the new requirements [3]. IMS is a multilayered structure made up of aluminum or copper on the bottom layer, an intermediate polymer layer with ceramic fillers as dielectric and a copper foil on the top layer.
The selected power module is a silicon diode-based device with a full bridge configuration. It was used as vehicle to validate six different IMS substrates, obtained by varying the design parameters of thickness, materials, and thermal conductivity of the layers. Every IMS substrate has been previously evaluated through a Finite Element Analysis (FEA) in a steady state condition, replicating the setup in Comsol Multiphysics. **Figure 1** illustrates all the geometries that were included in the simulation. Each silicon die dissipated about 110 W, while the ambient temperature was set at 25°C. Moreover, each module was simulated as mounted on a water-cooled heatsink with an interposed thermal grease layer. The water heatsink was characterized by a flow rate of 2 m^3h^{-1} and an inflow temperature of 16°C. The 3D thermal plot is visible in **Figure 2**.
Then, an experimental characterization of the IMS devices was conducted in this work to make a comparison with an equal DBC module and test how design parameters can affect thermal performances and the values of Thermal Resistance (Rth). The simulation results and the experimental values are almost aligned and show that, the Thermal Resistance junction to heatsink ($Rth_{j\text{-}s}$) of the IMS groups, with the higher thermal conductivity, are almost aligned or slightly better than DBC. The most performing IMS substrate is the one having 1 mm thick copper on the backside and a thermal conductivity of the polymer equal to 5.7 $Wm^{-1}K^{-1}$. Although DBC and some IMS groups have similar Rth values, the materials contributions to the Rth are different from each other, as shown in **Figure 3**. Indeed, DBC better dissipates heat between the die and the substrate (case), while IMS between the substrate (case) and the heatsink.

[1] J. Broughton et al., J. Electron. Packag. 140 (2018) 40801 1-11.
[2] E. Gurpinar et al., J. Electron. Packag. 142 (2020) 041107 1-10.
[3] S. Chowdhury et al., IEEE Energy Conversion Congress and Exposition (ECCE) (2020) 195-202.

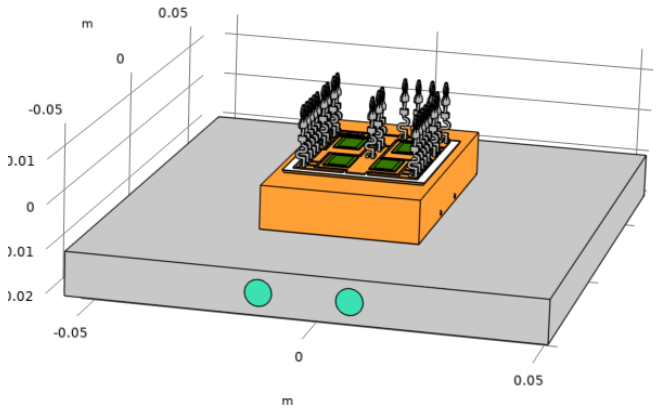

Figure 1: IMS module and water-based heatsink geometry. Each material is associated to a color: orange for copper, green for silicon die, white for polymer insulator, grey for aluminum, light blue for water.

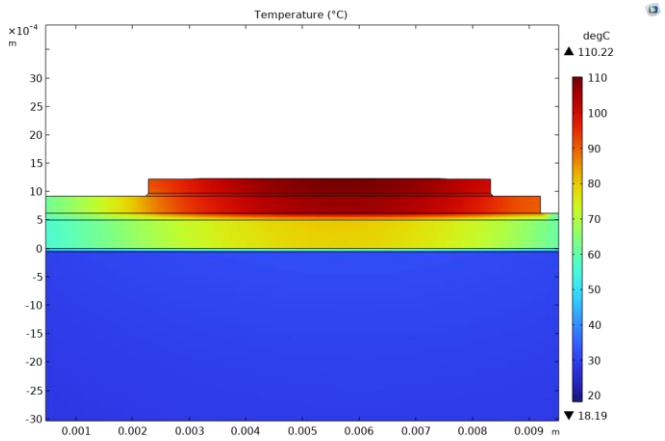

Figure 2: 2D thermal plot across the maximum temperature cross section of an IMS module with a single silicon die turned on.

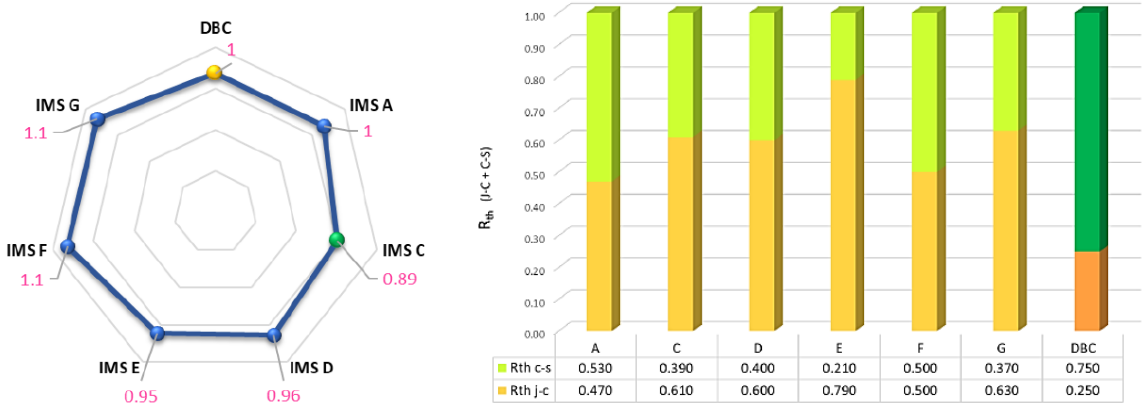

a) b)

Figure 3: (a) Normalized values of Rth j-s for each substrate; (b) Different contributions of Rth j-c and Rth c-s for each substrate: IMS (A, C, D, E, F, G) and DBC.

PZT sensor compatible with the 2D piezo-scanners dedicated to 1550 nm long-range LIDAR

L.Mollard [a], C.Dieppedale [a], T.Verdot [a], A.Hamelin [a], F.Gardien [a], K.Benedetto [a]
[a] University Grenoble Alpes, CEA, Leti, F-38000 Grenoble, France
e-mail: laurent.mollard@cea.fr

This paper presents the development of a PZT (lead zirconium titanate) sensor that can be integrated in-situ into our 2D piezo-scanners previously reported in [1]. These piezo-scanners are dedicated to 1550 nm long range (>100 m) LIDAR (LIght Detection And Ranging). LIDAR is considered as a crucial sensor for autonomous driving as it can provide high-density point clouds with accurate three-dimensional information. In this way, the MEMS-LIDAR based on MEMS-mirrors is the best candidate for long-range application [2,3]. The system specifications requires an average optical power of 2W on the 2×2 mm^2 side mirror. Therefore, eye-safety is a key issue for both 905 nm and 1550 nm lasers. Since the eye transmits 905 nm light to the retina, which is not the case at 1550 nm, the 905 nm laser is limited to 10-time less incident laser power than 1550 nm laser, and so has a lower range detection. However, even a wavelength of 1550 nm can cause eye damage [3] especially in the case of a fixed beam.
The purpose of this PZT sensor is to ensure that the PZT actuators, and thus the mirror, are always in motion. This is because if the actuators break or stop, the mirror, and therefore the reflected beam, is no longer scanned across the scene of interest. In this case, the reflected optical power is focused on a restricted area, or a specific point of the scene, encountering a real risk to eye safety.
This paper presents the fabrication of a PZT sensor integrated with a PZT cantilever. These cantilevers have similar dimensions, thickness and PZT material to the four actuators on our 2D piezo-scanner [1]. These piezo-scanners integrate a Bragg or Gold reflector and achieve an optical angle close to 8° for a drive voltage of 20V, as shown in Figure 1, using the FoM developed in [4].
It will present a series of experimental results to ensure, when the LIDAR system is operating, the PZT-actuators are in motion. The developments present the integration of a sensor/actuator technology with the same PZT material. The main challenge was to achieve a monolithic (no manual step) and collective process, without additional technological steps compare to the manufacturing process of piezo-scanner. For comparison, capacitive and piezo-resistive (PR) sensors are the most common [5]. However, despite their great sensor sensibilities, capacitive sensors require hybrid integration, while PR sensors requires expensive manufacturing. In contrast to them, the PZT sensor requires no extra manufacturing steps and no additional cost.
As shown in Figure 2, to limit electrical crosstalk, the sensor and actuator were designed with separate electrodes and a ground ring was placed between the actuator and sensor. The PZT sensor was placed inside the PZT actuators near the edge of the cantilever. The signal from the PZT sensor is amplified by dedicated electronics based on voltage amplification. Using this test cantilever, a swept frequency was applied to the PZT actuator from 0 to 2000 Hz and the evolution of the detection signal was measured. The experimental measurements show, in Figure 3, that the frequency of the sensor signal follows that of the actuation. To ensure that the sensor probe will be able to detect the breakage of an actuator, and thus the fact that the mirror is stationary, the cantilever was intentionally broken and the measurements were re-started with the same actuation signals. The measurements show a clear change before and after the breakage of the cantilever (10 dB shift). Finally, the natural frequency is clearly evident (@1600 Hz) in the sensor amplitude evolution but also on the phase measurements.

[1] Mollard, L.; Riu, J.; Biaxial Piezoelectric MEMS Mirrors with low absorption Coating for 1550 nm Long-Range LIDAR. Micromachines 2023, in press
[2] Wang, D.; Watkins, C.; Xie, H. MEMS mirrors for LIDAR: A review. *Micromachines* **2020**, *11*, 456. https://doi.org/10.3390/mi11050456.
[3] Kasturi, A.; Milanovic, V.; Lovell, D.; Hu, F.; Ho, D.; Su, Y.; Ristic, L. Comparison of MEMS Mirror LIDAR Architectures. In Proceedings of the MOEMS and Miniaturized Systems XIX Conference, San Francisco, CA, USA, 1–6 February 2020. https://doi.org/10.1117/12.2556248.
[4] Wang, D.; Watkins, C.; Xie, H. MEMS mirrors for LIDAR: A review. *Micromachines* **2020**, *11*, 456. https://doi.org/10.3390/mi11050456.
[5] Vergara, A.; Tsukamoto, T.; Fang, W., Tanaka, S. Feedback Controlled PZT Micromirror with integrated Buried Piezoresistors. In proceedings of the 35th International Conference on Micro Electro Mechanical Systems Conference (MEMS), Tokyo, Japan, 09-13 January 2022. 10.1109/MEMS51670.2022.9699754

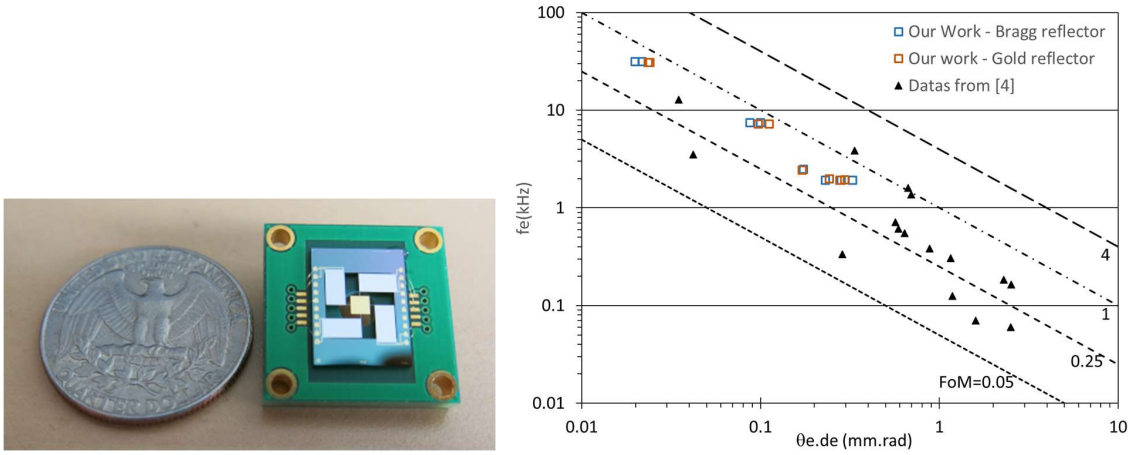

Figure 1. MEMS-scanner top-view and FoM values previously reported in [1]

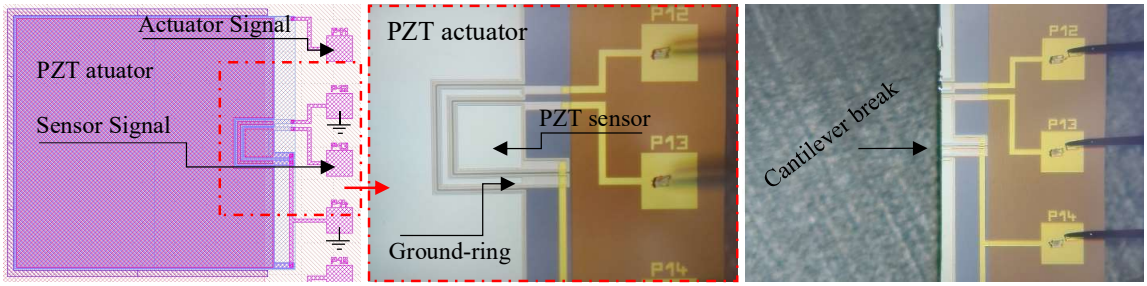

Figure 2. Sensor/actuator design (Left), and before cantilever break (Centre), after cantilever break (Right)

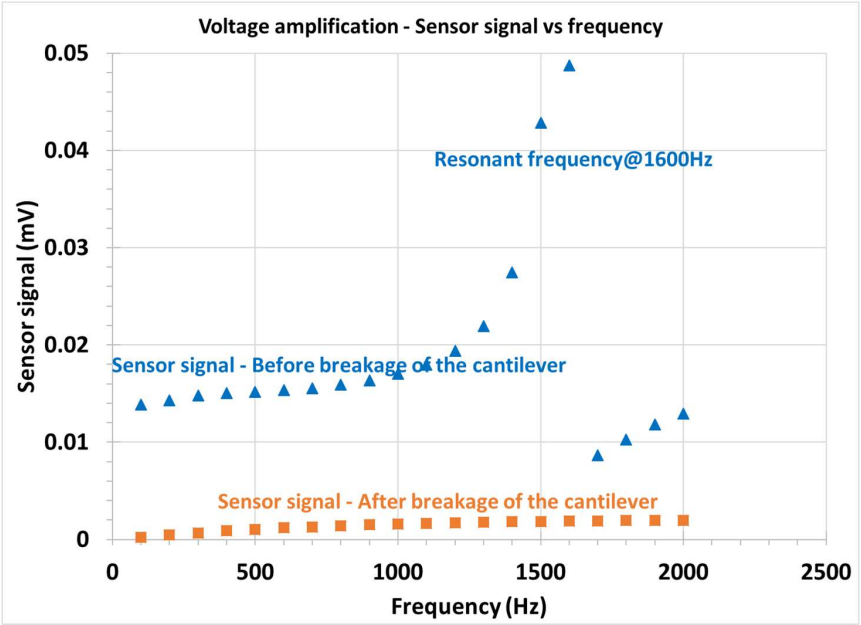

Figure 3. Sensor signal peak-to-peak amplitude vs actuation frequency – ▲/■ before/after cantilever break

Direct ink writing of high-detail resolution cellulose structures

Farnaz Rezaei [a], Jonas Lindh [a], Daniel Carlsson [b], Jimmy Hedin Dahlström [b], Stefan Johansson [a]

[a] Uppsala University 1, Uppsala, SE-751 03, Sweden
[b] Cytiva, Uppsala, 753 23, Sweden
e-mail: Farnaz.rezaei@angstrom.uu.se

3-D printing, also called additive manufacturing (AM), is a method for creating 3D structures. Different 3D models are created with CAD (computer-aided design) and in the next step printed layer by layer [1]. Using AM techniques gives the possibility of building complex structures with a range of printable materials [2]. There are a few AM techniques for printing structures on the micrometer scale, like two-photon polymerization (2PP), and direct ink writing (DIW) [2, 3]. In the TPP technique, the number of printable inks is limited, however, the main advantage of DIW is the diversity of printable materials. In the DIW technique, the desired printable ink is extruded through the nozzle layer by layer on a flat substrate with high detail resolution DIW could be utilized to print structures for different applications, e.g., drug delivery, microfluidics, biosensors, and separation science [1, 4].

This project investigates printing parametersneeded to achieve high detail resolution cellulose structures. DIW has been chosen as the 3D printing technique, and cellulose acetate was selected as a biodegradable ink. We aimed to use inks with various viscosities to check their printability with high detail resolution. For this reason, nozzles with different diameters have been studied.

Figure 1, shows the developed in-house setup. A glass slide is mounted on a stage that can be moved in X, Y, and Z directions using LabView software. The syringe is filled with ink and in this study cellulose acetate (CA) with different amounts (5%, 7.5%, 10%, 12.5%, 15%) and molecular weight (30.000, 50.000, 100.000) is evaluated. A syringe is fixed in a holder and by running the linear motor (100 to 1000 pl/s) ink is dispensed onto the glass substrate. The size of the nozzle is one of the parameters that could control the printing resolution. In this study we attached glass nozzles with a few micrometer diameters to the syringe. Figure 2, shows the nozzle with an internal diameter of 3 µm and an outer diameter of 10 µm. The structure in Figure 3 was printed to study the possibility of printing several hundred layers and, in this test the nozzle in the figure 2 and ink with 10% CA (50 kDa) was used. After printing more than 300 layers the printing was terminated. To evaluate the influence of ink concentration, the same nozzle (internal 3 µm and external 10 µm) was used to print two inks with different viscosities. An SEM image of the printed structure with an ink containing 5% CA (50 kDa) is shown in Figure 4 (a) and the result indicates that the width of the printed strand is 12 µm which is more than the size of the nozzle. However, by increasing the amount of CA to 10% it is possible to reduce the width of the printed strands to almost the internal size of the nozzle, Figure 4 (b). We also increased the ink viscosity by varying the concentration of CA to 12.5 and 15% and, examined different molecular weights. Although it is possible to enhance the printing resolution by increasing the viscosity of the ink, the challenge of nozzle clogging hinders the printing process. The evaluation demonstrates that it is possible to print high detail resolution cellulose structures with AM.

[1] L. Wang and M. Pumera, “Recent advances of 3D printing in analytical chemistry: Focus on microfluidic, separation, and extraction devices,” *TrAC - Trends Anal. Chem.*, vol. 135, p. 116151, 2021, doi: 10.1016/j.trac.2020.116151.

[2] Z. X. Low, Y. T. Chua, B. M. Ray, D. Mattia, I. S. Metcalfe, and D. A. Patterson, “Perspective on 3D printing of separation membranes and comparison to related unconventional fabrication techniques,” *J. Memb. Sci.*, vol. 523, no. May 2016, pp. 596–613, 2017, doi: 10.1016/j.memsci.2016.10.006.

[3] G. M. Gratson and J. A. Lewis, “Phase behavior and rheological properties of polyelectrolyte inks for direct-write assembly,” *Langmuir*, vol. 21, no. 1, pp. 457–464, 2005, doi: 10.1021/la048228d.

[4] U. Simon and S. Dimartino, “Direct 3D printing of monolithic ion exchange adsorbers,” *J. Chromatogr. A*, vol. 1587, pp. 119–128, 2019, doi: 10.1016/j.chroma.2018.12.017.

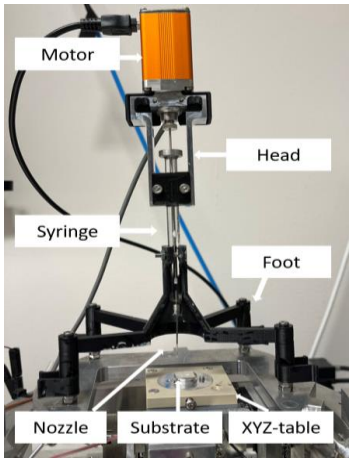

Figure 1. Set-up of the direct ink writing printer.

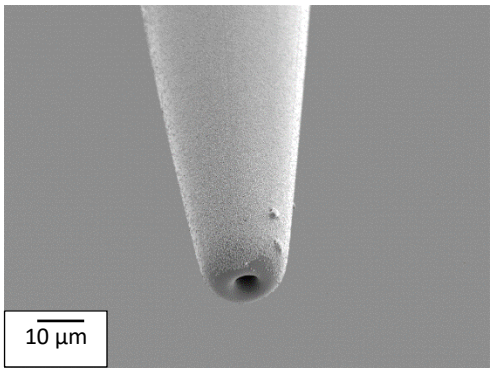

Figure 2 . SEM image of the capillary with an internal diameter of 3 µm and external diameter of 9 µm.

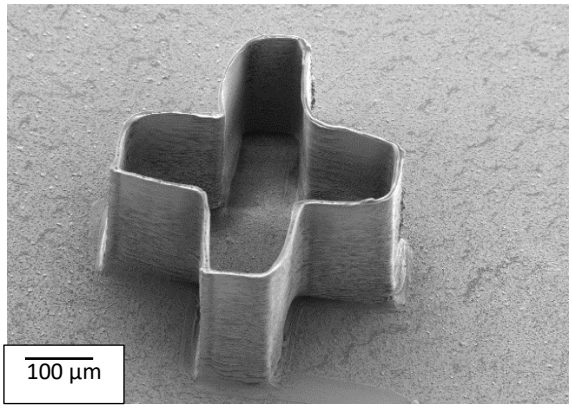

Figure 3. SEM image of 3D printed cross-shaped structure with more than 300 layers.

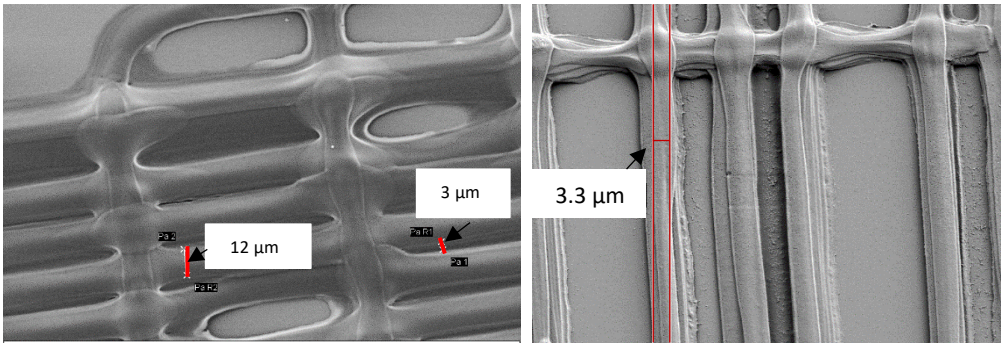

Figure 4. SEM images of inks with a) 5% CA (50 kDa), and b) 10% CA (50 kDa).

A Study about Bump Non-Contact Failure of Flip Chip at sub-20nm DRAM

Dongsik Park [a], Gyo Seon Choi [b], Byoungdeog Choi [a]

[a] Department of Semiconductor and Display Engineering, Sungkyunkwan University, Suwon-Si, Gyeonggi-do, Korea, Republic of (South)
[b] Samsung Electronics Co., Hwaseong-si, Gyeonggi-do, Korea, Republic of (South)
e-mail: bdchoi@skku.edu

(Abstract) In this paper, we proposed “Bump Non-Contact Failure” model that occurs during the bump and the PCB bonding in the DRAM Flip-chip process. Also, how to improve its failure was introduced.
As a result of TEM image analysis and bump fail test checked, the chip warpage is one of the important causes of the defect. Two improvement methods were presented. The defect rate can be reduced by Mount Force up test, because the solder area is easier to touch the PCB due to the strong pressing force. And, change of the solder height increases the possibility of contact because solder is more widespread in the bump compared to pillar area. These experiments were conducted with in sub 20nm technology in Samsung Electronics.

1. INTRODUCTION

DRAM device’s design-rule continues to shrink, thus high-speed and large-capacity data transmission is required. So, DRAM packaging technology is also evolving, rapidly moving from traditional Wire- bonding to Flip-chip packaging processes that can reduce chip size.[1] The Flip-chip process is a method of applying bumps to the pads to transmit data, and Samsung's sub-20nm bump technology is as follows.[2] (Fig.1)

As the DRAM pad size decreases, Bump Non-Contact Failure (BNCF) occurs in the Flip-chip. This is because the solder and PCB pad do not adhere well when joining with the PCB, which cause high resistance. [3][4] There are two types of BNCF defects, as shown in Fig.2. First, the solder ball area is well formed. But, the solder and the PCB pad are not in good contact because the interface failure which caused by oxide-based impurities on the contact surface. (Surface failure) The other is that the solder in the specific bump does not dissolve well or reflow, so the solder and the PCB pad are not in good contact. (Physical failure) These experiments try to focus on the latter. (Fig.2)

2. EXPERIMENT AND RESULTS

2.1 Defect Area Analysis

After packaging the DRAM product, we performed a DC voltage test to ensure that all the solder and the PCB areas in all chips were in good contact. The number of bump failures was checked in all areas of chips. At this time, it was confirmed that the defective region was concentrated in the center area in chip. (Fig.3)

TEM analysis was performed to determine why defects were concentrated in the center of the chips. Three areas in the chip were analyzed. Two are the left and right edge areas where the defect mainly occurred, and one is the center area. As a result of TEM image checked, it was confirmed that the left and right bump were shifted toward the center. This revealed that the warpage of the chip was one of the causes of the defect. (Fig.4) For defective and normal samples, the distance from the pillar end to the PCB pad end was measured. In general, the center region was high, and the defective sample was up to 6um higher than the normal sample. The chip warpage indicates that BNCF are concentrated in the center of the chip and need to be evaluated to overcome the minimum 6um gap between the solder and the PCB pad. (Fig.5)

2.2 Increase of Mount Force

Mount Force test was evaluated to improve defective bumps in all areas, especially the center area. Mount Force refers to the pressure to apply, after placing the wafer on the PCB. The reference condition was “A” and the 50% up condition was “B”. At the case “B”, there is a 0.64% improvement in the chip fail index. The reason for the improvement is that the solder area is easier to touch the PCB pad due to the strong pressing force. Even if there is defective bumps due to warpage, the defect rate can be reduced by pressing hard. [Table.1]

2.3 Bump Height Test

In order to investigate the correlation BNCF according to bump height, we experimented by changing the pillar and solder height, as shown in Table 2. It was found that the defect rate tends to decrease with the height of the solder. In addition, the effect on pillar height was relatively small. [Table.2]
The reason is that by increasing the potion in the solder area, which is relatively well deformed, the possibility of contact increases. As shown in case.6 image, solder is more widespread in the bump compared

to pillar area. Therefore, in order to improve BNCF while matching the height of the entire bump, it was found that the optimal direction is to increase the height of Solder and reduce the height of pillar. [Fig.6]

3. CONCLUSION

In this paper, we examined the causes of “Bump Non-Contact Failure” defect that occurs during bumps and PCB bonding in the DRAM Flip-chip process. In addition, as improvement methods, the Mount Force strengthening method and the bump height re-design were proposed. In addition, further evaluation is needed to improve chip warpage.

REFERENCES

[1] Refai-Ahmed, Gamal, et al. "Lidless and lidded flip chip packages for advanced applications." 2020 IEEE 22nd Electronics Packaging Technology Conference (EPTC). IEEE, 2020.

[2] Koh, Wei, Barry Lin, and Johnson Tai. "Copper pillar bump technology progress overview." 2011 12th International Conference on Electronic Packaging Technology and High Density Packaging. IEEE, 2011.

[3] Yeo, Alfred, Wong Foo Lam, and Charles Lee. "Development of novel joint resistance modeling technique for flip chip interconnection systems." 2006 Thirty-First IEEE/CPMT International Electronics Manufacturing Technology Symposium. IEEE, 2006.

[4] Lee, Teck Kheng, et al. "Fluxless flip chip bonding with joint-in-via architecture." Thin Solid Films 504.1-2 (2006): 436-440.

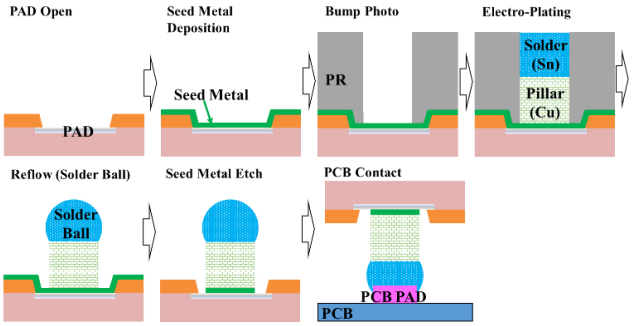

Figure 1. Process flow of Bump and Flip-chip Patterning in Sub 20nm DRAM

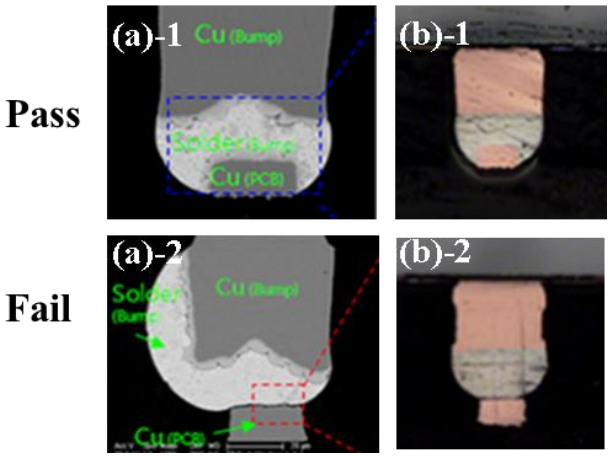

Figure 2. Two-Types BNCF defects (a) Surface failure (b) Physical failure

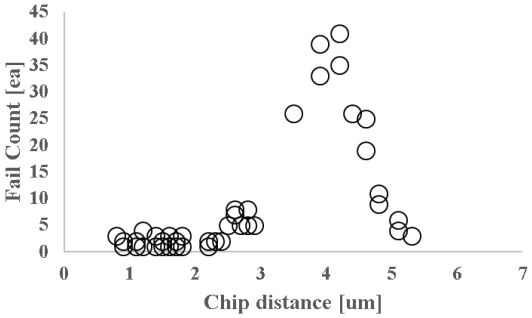

Figure 3. The number of Bump Fail count in chip area

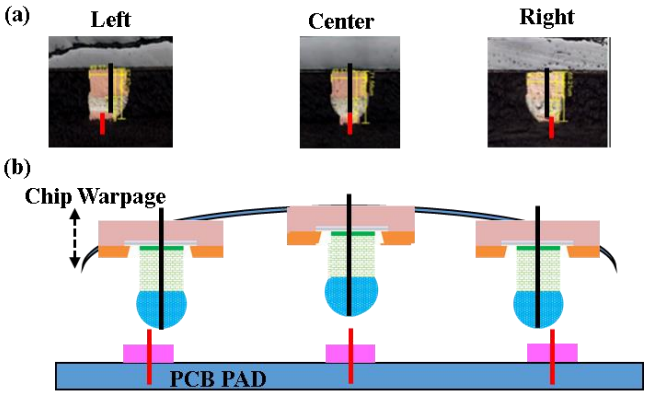

Figure 4. (a) Three area's bump TEM images. (b) Schematic diagram about bump shifted images by chip warpage

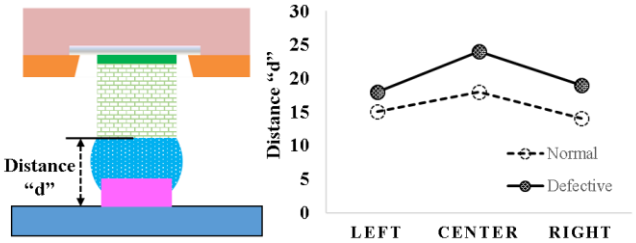

Figure 5. The distance from the pillar end to the PCB pad end

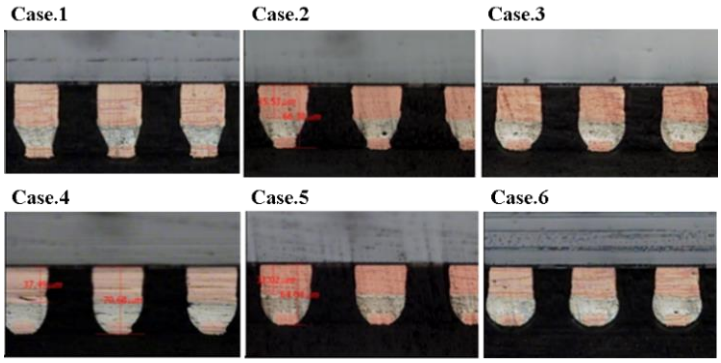

Figure 6. Bump TEM images according to pillar and solder height

Condition	Total Chip [ea]	Open Fail [ea]	Fail Portion [%]
A	18173	129	0.71
B (50% up)	10405	7	0.07

Table 1. Chip fail count and portion according to Mount force condition "A" and "B : 50% up"

Condition	Pillar Height	Solder Height	Total Chip [ea]	Open Fail [ea]	Fail Portion [%]
1	10% Up	10% Down	5708	35	0.61
2	Reference	Reference	14476	3	0.02
3	5% Down	10% Down	5699	0	0.00
4	Reference	10% Up	11929	1	0.01
5	10% Down	10% Up	8444	1	0.01
6	15% Down	15% Up	5693	0	0.00

Table 2. Open fail count and portion according to bump height conditions

A study on the silicon dislocation in DRAM STI structure

Bonhwi Gu [a, b], Injae Bae [b], Byoungdeog Choi [a]

[a] Department of Electrical and Computer Engineering, Sungkyunkwan University, Suwon-Si, Gyeonggi-do 16419, Korea, Republic of (South)
[b] Samsung Electronics Co., Hwaseong-si, Gyeonggi-do 18448, Korea, Republic of (South)
e-mail: bdchoi@skku.edu

Abstract
Silicon dislocation in DRAM is usually caused by thermal stress of insulators (silicon oxide, silazane) in shallow trench isolation (STI), which will result in fatal reliability issues. In fabrication process, many factors such as STI depth, STI width ratio, oxide/silazane film characteristics, etc., are considered to improve such failure. Despite those efforts, dislocation is still occurring intermittently. Here, we find another factor that is tensile stress induced by silicon nitride in STI and present a new design rule related to nitride. To prevent dislocation, we should forbid certain condition, which includes specific size of STI width mainly filled with nitride and ratio of STI width beside active region. This evaluation was performed with Samsung Electronics' 18nm node DRAM technology.

Experiment
Failure samples
As a result of physical failure analysis (p-FA) of dislocation failure samples (reliability claim sample of 18nm DRAM), it was confirmed that all failures occurred in the same area as shown in Fig.1. Despite satisfying all the requirements of current dislocation design rule, newly discovered failures meant the need of design rule revision.
Simulation 1
First, we simulated applied stress caused by the decrease in STI width F3 size. As a result, it was proved that the smaller was the F3 size, the higher was the stress that adjacent active region received as shown in Fig.2.

Discussion
STI is filled with side wall oxide / liner SiN (silicon nitride) / TOSZ (Tonen silazane) as shown in Fig.3. Among them, SiN exhibits high tensile stress compared to oxide and TOSZ. Therefore, in those places of the volume of SiN are relatively larger than oxide and TOSZ, accumulated stress makes the adjacent active region vulnerable to dislocation. In order to avoid dislocation failure, forbidden area design was proposed in relation to STI width size as shown in Fig.4.

Conclusions
Through simulations and TEM GPA analysis, we defined a new boundary condition for the STI width where the stress upon active region becomes intolerable due to the influence of SiN having high tensile stress. This boundary of design rule is newly proposed since the previously known boundary condition was restricted from the volume difference of TOSZ. We named it dislocation forbidden area. This area depends on each process conditions of oxide / SiN / TOSZ. So, we had to define each DRAM product's dislocation forbidden area. Based on this, we revised conventional design rule for dislocation and defined the dislocation forbidden area of each DRAM products according to this rule. As a result, it will have a great effect on preventing reliability failures of DRAM products in advance.

References
[1] Fahey, Paul M., et al., Stress-induced dislocations in silicon integrated circuits., IBM journal of research and development 36.2 (1992) 158-182.
[2] Izumi, S., et al., Application of three-dimensional dislocation dynamics simulation to the STI semiconductor structure., Materials Science and Engineering A 395.1-2 (2005) 62-69.
[3] Stiffler, Scott R., et al., Oxidation-induced defect generation in advanced DRAM structures., IEEE transactions on electron devices 37.5 (1990) 1253-1287.

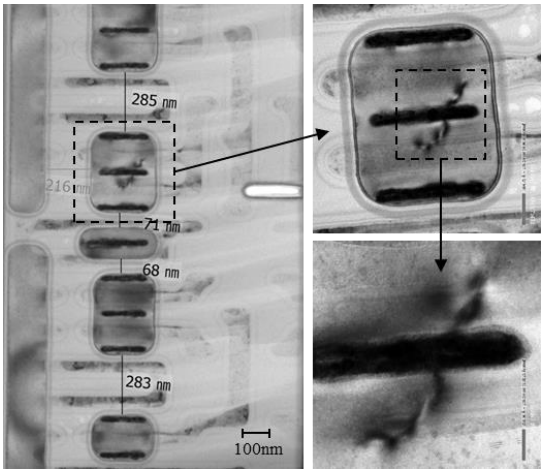

Figure 1. TEM images of dislocation failure samples in DRAM.

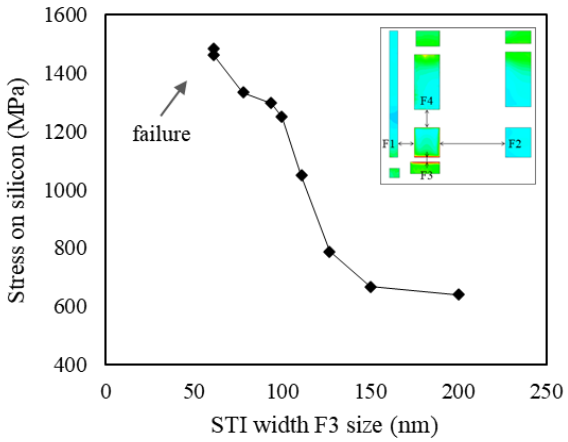

Figure 2. Result of simulation 1. Stress on silicon according to STI width F3 size.

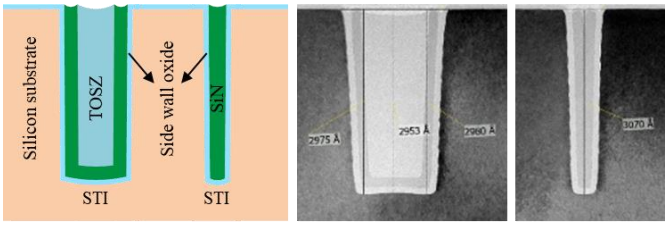

Figure 3. Images of STI structure filled with oxide / liner SiN (silicon nitride) / TOSZ (Tonen silazane).

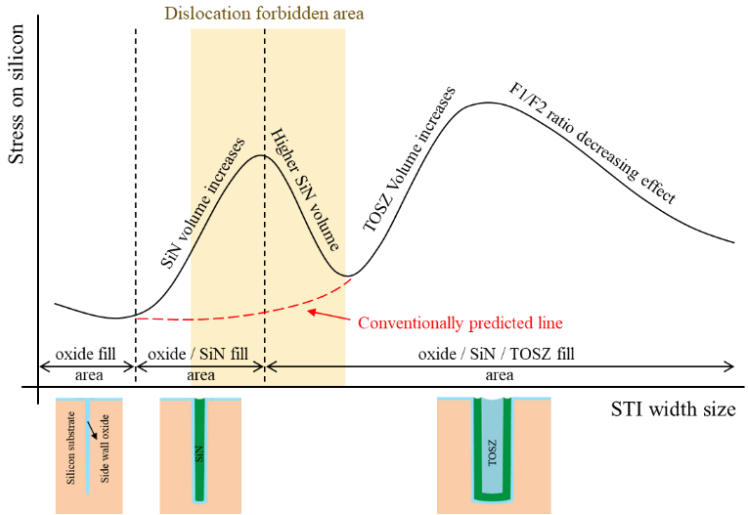

Figure 4. Definition of dislocation forbidden area.

Bioinspired Microfluidic Flow Sensors with Magnetic Artificial Cilia for Organ-on-Chip Applications

Bhavana B. Venkataramanachar [a,b], Max Verhoef [a], Tanveer ul Islam [a,b], and Jaap M.J. den Toonder[a,b]

[a]Department of Mechanical Engineering, Eindhoven University of Technology, The Netherlands
[b]Institute for Complex Molecular Systems, Eindhoven University of Technology, The Netherlands
e-mail: J.M.J.d.Toonder@tue.nl

Abstract

Measuring flow in a microfluidic chip presents an inherent challenge of flow sensing at very small scales. The methods adopted presently either result in altering the fluid properties or require unsuitable additional bulky components. Inspired by the sensing ability of a hairlike microstructure existing in nature, called cilium, we present a novel microfluidic flow sensing concept using magnetic artificial cilia in a microfluidic chip. The cilium undergoes deflection due to an existing flow, which is sensed by a magnetic field sensor integrated in the chip. Here, we show the device fabrication and the basic proof-of-principle of this concept using experiments and simulations.

Introduction

Current microfluidic flow sensors predominantly rely on thermodynamic principles, which involve heating the fluid and measuring the dissipation of heat to determine flow. However, these sensors are not suitable for temperature-sensitive processes existing in organ-on-a-chip systems. Additionally, they pose integration challenges and require bulky peripheral components therefore limiting their applicability in microfluidic devices. To address these limitations, nature-inspired cilia structures that perform various sensing functions, including fluid flow detection by undergoing deflection, have been exploited. [1] Various methods have been used to develop artificial cilia for sensing applications, involving the use of various transducing principles, such as piezoelectricity, [2] capacitance, [3] and magnetism, [4] to convert mechanical stimuli into detectable electrical signals. Among these, magnetic artificial cilia-based flow sensors offer high sensitivity and are capable of resolving flow velocities as low as 15 μm/s. Furthermore, the magnetic sensing is compatible with biological applications in organ-on-a-chip systems. However, existing sensing artificial cilia suffer from large dimensions and rigid mechanical properties, making them unsuitable for microfluidic applications. In this study, we aim to develop a miniaturized and integrated magnetic artificial cilia-based flow sensor for microfluidic chips, suitable for organ-on-chip applications.

Experimental

The working principle is depicted in Figure 1(a), where flexible magnetic artificial cilia are incorporated into a microchannel. These cilia experience deflection in response to fluid flow, leading to a local change in an induced magnetic field. The detection of this variation in the magnetic field is achieved using an integrated magnetic field sensor, such as a Giant Magnetoresistive (GMR) sensor, located on the channel surface. In our initial sensor design, we fabricated cilia measuring 350 μm in length and 50 μm in thickness using a PDMS-magnetic particle composite material [6]. The microfluidic chip itself was fabricated from PDMS using soft lithography techniques. To induce fluid flow, an external syringe pump was employed, while microscopic imaging was used to measure the deflection of the cilia. Furthermore, we performed 2D COMSOL finite element modeling to predict the anticipated change in the magnetic field that would be sensed by the integrated magnetic sensor.

Results

In Figure 1(b), we present our first-generation flow sensing chip featuring four integrated artificial cilia. The deflection of these artificial cilia under applied flow is illustrated in Figure 1(c). To assess the feasibility of utilizing integrated Giant Magnetoresistive (GMR) sensors to detect the corresponding magnetic field changes resulting from these deflections, we conducted finite element simulations as depicted in Figure 2(a). The

simulation outcome in Figure 2(b) reveals that at a flow rate of 250 µl/min, the cilia deflection induces typical magnetic field changes of 0.173 mT at the sensor location 0. These values fall well within the detectable range of standard GMR sensors, which typically can measure magnetic field changes lower than 0.01 mT [7].

Conclusion

Our first-generation magnetic artificial cilia-based flow sensor has demonstrated cilia deflection under applied flow. Finite element models indicate that the resulting magnetic field change can be detected using an integrated GMR sensor. Our next steps involve realizing a fully integrated sensing chip, validating the principle, and exploring the integration of submicron cilia. Figure 2(c) shows submicron cilia we have realized, to be integrated in the flow sensing chip.

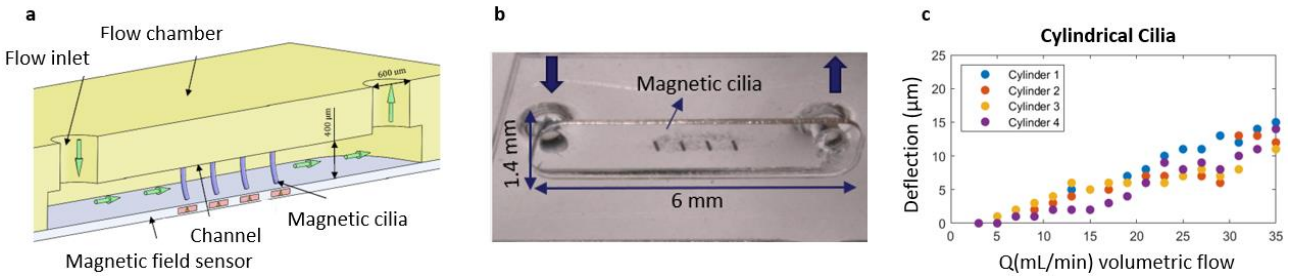

Figure 1: (a) A schematic illustration of our flexible flow sensor utilizing magnetic artificial cilia, incorporating magnetic field sensing elements on the surface. (b) Our initial flow sensing chip, equipped with four integrated magnetic artificial cilia measuring 350 µm in length and 50 µm in diameter. (c) The deflection of the cilia depicted in (b) is measured as a function of the applied flow rate, utilizing microscopic imaging.

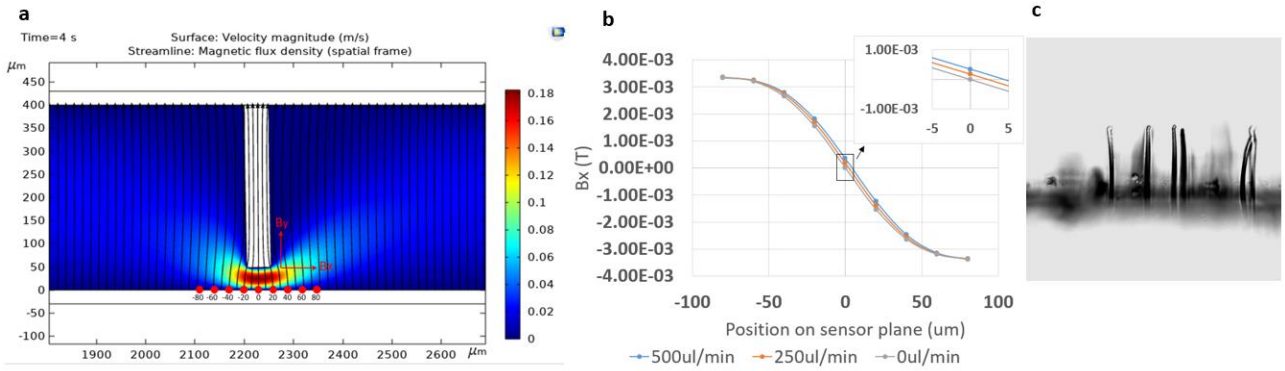

Figure 2: (a) Simulation results of the interaction between fluid and paramagnetic cilia under a uniform applied magnetic field, obtained using 2D finite element analysis. (b) The resulting change in magnetic field at the location of the GMR sensor for cilia with a thickness of 50µm, subjected to fluid flow ranging from 0 to 500µl/min. The insert illustrates the magnetic field variation at position 0 for different flow rates. (c) Microscopic images of cilia structures made from a unique magnetic polymer, featuring a diameter of 3 µm and a length of 47 µm.

References

[1] Mayne, R., and den Toonder, J.M.J. eds. Atlas of cilia bioengineering and biocomputing. River Publishers, 2018.
[2] Fan, Zhifang, et al. Journal of Micromechanics and Microengineering 12.5 (2002): 655.
[3] Krijnen, Gijs JM, et al. Nanotechnology 17.4 (2006): S84.
[4] Alfadhel, Ahmed, et al. Lab on a Chip 14 (2014): 4362-4369.
[5] ul Islam, T., et al. Lab on a Chip, 22 (2022), 1650-1679.
[6] Zhang, S., et al. Sensors & Actuators B 263 (2018), 614-624.
[7] Soares, A. R. et al. IEEE Magn. Lett. 10 (2019), 3–7.
[8] ul Islam, Tanveer, Yves Bellouard, and Jaap MJ den Toonder. Proceedings of the National Academy of Sciences 118.35 (2021).

Ultrathin Si nanostring resonators with widely tunable dynamic behaviour

Amit Banerjee [a], Wei Yu [a], Jun Hirotani [a], Toshiyuki Tsuchiya [a]

[a] Department of Micro Engineering, Kyoto University, Kyoto, 615-8540, Japan
e-mail: banerjee.amit.3v@kyoto-u.ac.jp

Nanomechanical resonators devices are building blocks for a number of emerging technologies[1], such as ultrasensitive sensing, efficient signal and information processing, quantum computing, etc. Moreover, nanoresonators made of atomic-scale materials (CNT, graphene, MoS_2, etc.) provide ultrawide electrostatic tunability of their resonance frequencies and dynamic behavior, offering a new paradigm for developing novel nanoelectronic applications of nanoresonators[2]. In this work, we have developed ultrathin Si nanoresonator devices (~ 20 nm in thickness (t), and ~ 200 μm in length (L)) by conventional top-down microfabrication of single-crystal Si wafers and in the fabricated devices we observed wide electrostatic tuning of the resonance frequency (~ 70%) and the cubic-nonlinearity at room temperature using moderate gate-voltage. Such wide electrostatic tunability has not been achieved before in top-down microfabricated nanoresonator devices to the best of our knowledge. This research is expected to aid in the development of scalable fabrication process of widely tunable ultrathin resonators for commercial applications.

Background

Nanoresonator device made of atomic-scale materials, such as, CNT, graphene, MoS_2, etc. offers ultrawide electrostatic tuning of resonance frequency and nonlinear-behavior, which are useful for enhancing frequency-stability and the linear-dynamic range, developing voltage-controlled-oscillators, frequency and mode-matching, multiband filtering, etc. However, developing a scalable fabrication process for rapid commercialization of these devices is hindered by lack of standardized material and complex fabrication process. Therefore, it is beneficial if comparable tunability can be achieved in conventional Si resonator devices using monolithic microfabrication of single-crystal Si wafers. In this work, we successfully created ultrathin Si nanostring resonators (aspect ratio: $L/t > 10^3$) of ~ 20 nm thickness, which allows tunability of resonance frequency and cubic-nonlinear-stiffness comparable to atomic-scale resonators.

Results and discussion

Our Si nanoresonator devices are made of a double-clamped Si nanostring of 20 – 300 nm thickness, 100 – 300 μm length, ~ 7.5 μm width, and two side-gate electrodes on each side (gap ~ 2 μm) for electrostatic actuation and capacitive detection of motion (Fig. 1). All components are fabricated from Si-on-insulator wafers with 7.5 μm thick single-crystal device layer using UV and electron-beam lithography, deep-reaction-ion-etching, sacrificial ion etching processes. Si nanostring are actuated by dc (V_{dc}) and ac (V_{ac}) voltages and the resulting amplitude-frequency responses, such as the one shown in Fig. 2, are measured by a lock-in amplifier. Resonance frequencies (f_0) of fundamental in-plane flexural mode vibration show stringlike behavior due to axial-tensile-stress (σ) instead of following the predicted frequency (f_{EB}) for a Euler-Bernoulli beam. f_0/f_{EB} values in the range of 2 – 20 are observed depending on the thickness of the string.

Resonance-frequency of the nanostrings can be significantly tuned by V_{dc}. Both downward and upward tuning of f_0 is observed depending on the relative strength of the electrostatic-softening ($df_0/dV_{dc} < 0$) and the geometric-stretching ($df_0/dV_{dc} > 0$) effects[3] at a given V_{dc}. Downward tuning of ~ 10% (Fig. 3(a)) and upward tuning of ~ 70% (Fig. 3(b)) is achieved in nanostrings of 40 nm and 300 nm thicknesses, respectively. At larger amplitude, response of the nanostrings shows the effect of cubic nonlinearity in stiffness (α) via jumps and hysteresis. α in our nanostrings is also widely tunable by V_{dc}. We show this by almost cancelling α and then reversing its sign by V_{dc} in a nanostring of t ~ 100 nm and L ~100 μm (Fig. 4). Electrostatic tunability of f_0 and α achieved in our ultrathin Si nanostrings is comparable to those achieved in atomic scale resonators [2]. Thus, we believe, this research can potentially offer a scalable fabrication route for producing widely tunable nanoresonators for rapid commercialization.

[1] S. Schmid et al., Fundamentals of Nanomechanical Resonators (Springer, 2016).
[2] B. Xu et al., *ACS Nano* **16**, 15545-15585 (2022)
[3] J. Lee et al., Sci. Adv. **4**, eaao6653 (2018)

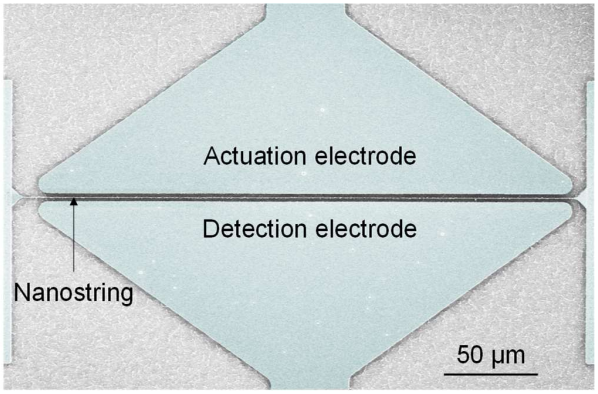

Fig. 1: Scanning electron micrograph of an ultrathin Si nanostring resonator device.

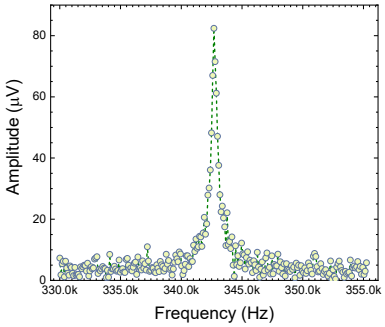

Fig. 2: Resonance peak acquired from a Si nanostring resonator.

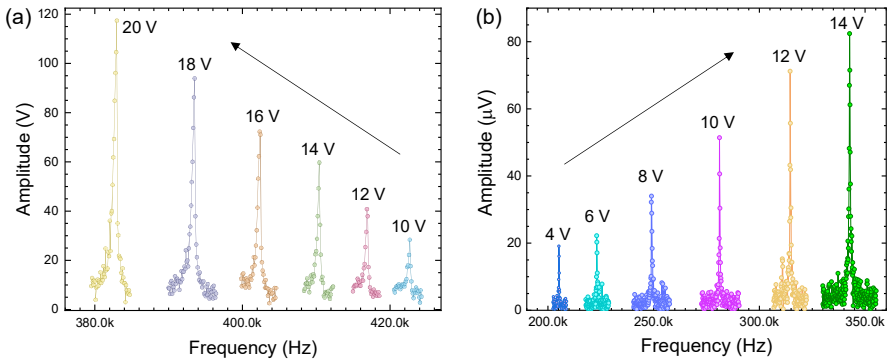

Fig. 3: Resonance frequency tuning by V_{dc}, showing (a) downward tuning, (b) upward tuning.

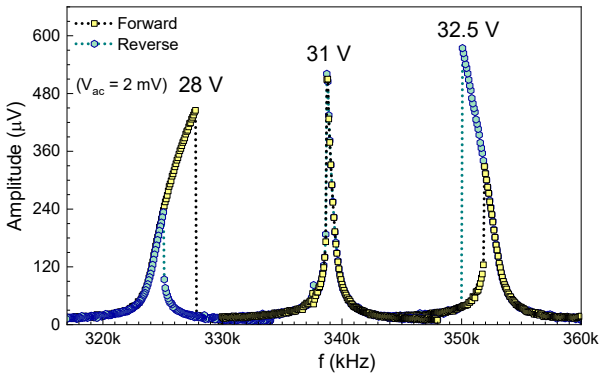

Fig. 4: Tuning cubic nonlinearity coefficient (α) by V_{dc} ($\alpha > 0$ at 28 V, $\alpha \approx 0$ at 31 V, $\alpha < 0$ at 32.5 V).

Fabrication of the atomically-stepped ultrasmooth conducting polymer thin film on the flexible transparent polyimide sheet

Mamoru Yoshimoto[*] [a], Yuto Maeda [a], Akifumi Matsuda [a], Satoru Kaneko [b, a]

[a] Department of Materials Science and Engineering, Tokyo Institute of Technology,
4259 Nagatsuta, Midori-ku, Yokohama, Kanagawa, 226-8502, Japan
[b] Kanagawa Institute of Industrial Science and Technology,
705-1 Shimoimaizumi, Ebina-shi, Kanagawa, 243-0435, Japan
[*]e-mail: yoshimoto.m.aa@m.titech.ac.jp

Conductive polymer materials have become increasingly important as substrates with features, such as flexibility, large area, and lightweight, in the flexible electronics field and are applicable to organic thin-film solar cells and other devices [1]. Poly(3,4-ethylenedioxythiophene): poly(styrenesulfonate) (PEDOT: PSS) conductive polymers (as seen in Fig.1) are attracting much attention as alternative materials for conducting Indium-Tin-Oxide (ITO) because of their excellent transparency, conductivity, and water dispersibility [2]. The morphology of PEDOT: PSS polymer in water is found to be in a colloidal state with hydrophilic PSS molecules surrounding water-insoluble PEDOT molecules [3]. In the construction of electronic devices on these polymer thin film electrodes, surface flatness and atomic- and/or nano-level surface control of conductive polymer thin films are essential for formation of fine and highly integrated devices. Micro- and nanofabrication of PEDOT: PSS conducting polymer thin film surfaces have been performed using either conventional or soft lithography techniques using elastomeric stamps, molds, and conformable photomasks [4]. Thermal or UV nanoimprinting technique has recently attracted significant attention for surface nanopatterning of polymers or glasses, enabling large-area nanofabrication [5,6].

So far, by using the ultra-smooth sapphire (α-Al_2O_3 single crystal) wafers with self-organized approx. 0.3-nm high atomic-step straight nanopatterns as nanoimprinting molds [7], we had reported on the fabrication of ultrasmooth substrates by transferring their nanoscale patterns onto the surfaces of oxide glasses and thermoplastic polymers [8-10]. On the other hand, as for nanopatterning of PEDOT: PSS having no thermoplasticity, there were only a few reports on stripe surface patterning (10nm depth and 700nm period) onto the thin film for increase of the organic photovoltaic device efficiency [11]. In this work, for formation of the atomically smooth surface on the PEDOT: PSS conducting polymer thin film, we investigated transcription of 0.3nm-high atomic-step and atomically flat terrace pattern of the sapphire mold onto the spin-coated PEDOT: PSS thin film surface via thermal nanoimprinting. We also characterized electric properties as well as the thermal durability of the nanoimprinted conducting polymer thin film coated on the flexible transparent polyimide sheet.

In experiment, a flexible transparent polyimide sheet (PI; t~20 μm, ECRIOS® VICT-Bnp, Mitsui Chemicals Co., Japan) was used as a polymer substrate for thin film deposition. PEDOT: PSS thin films were prepared by spin-coating PEDOT: PSS aqueous dispersion and drying at 170°C for 60 min. Thermal nanoimprinting was then performed at 200 - 270°C and 15 MPa for 10 - 60 min in vacuum on the PEDOT: PSS thin film surface using the sapphire mold with 0.34nm-high atomic steps and flat terrace width of about 600 nm, as seen in Fig.2.

As a result, it was confirmed that an atomic step and terrace pattern corresponding to the sapphire mold could be transferred accurately onto the PEDOT: PSS thin film coated on the polyimide sheet in case of nanoimprinting at 260°C and 15MPa for 40 min, as shown in Fig.3. Figure 4 shows the sheet resistances of the as-deposited and PEDOT: PSS thin films nanoimprinted at some temperatures. The sheet resistance at room temperature of the as-deposited thin film was about 390 Ω/sq. (resistivity of about 5.1×10^{-3} Ω・cm). As seen in Fig. 4, the resistance remained almost constant when nanoimprinted at 260°C (or lower) compared to the as-deposited thin film before nanoimprinting. However, the resistance of the thin film imprinted at 270°C increased approximately twice as much as before nanoimprinting.

References

[1] K. Gurunathan et al., Mater. Chem. Phys. 61 (1999) 173-191.
[2] Y. H. Kim et al., Adv. Funct. Mater. 21 (2011) 1076-1087.
[3] A. M. Nardes et al., Phys. Rev. B 76, (2007) 085208-1-7.
[4] N. Tang et al., Nanotechnology 28, (2017) 485301-1-8.

[5] S. Y. Chou et al., Science 272, (1996) 85-87.
[6] H. Oda et al., Langmuir 25, (2009) 6604-6606.
[7] M. Yoshimoto et al., Appl. Phys. Lett. 67, (1995) 2615-2617.
[8] Y. Miyake et al., Jpn. J. Appl. Phys., 50, (2011) 078002-1-3.
[9] G. Tan et al., Appl. Phys. Express., 7, (2014) 055202-1-3.
[10] K. Shimada et al., Jpn. J. Appl. Phys., 55, (2016) 098002-1-3.
[11] J. B. Emah et al., Appl. Phys. Lett. 93, (2008) 103301-103303.

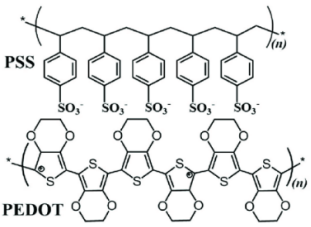

Figure 1. The chemical structure of PEDOT: PSS conducting polymer.

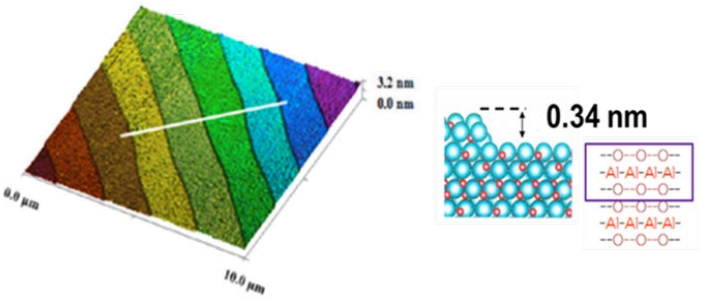

Figure 2. The AFM surface image (10 × 10 μm^2) (left) and the cross-sectional model of the atomic step (right) [7] for the atomically stepped sapphire (10$\bar{1}$2) (r-plane) substrate used as the thermal nanoimprint mold.

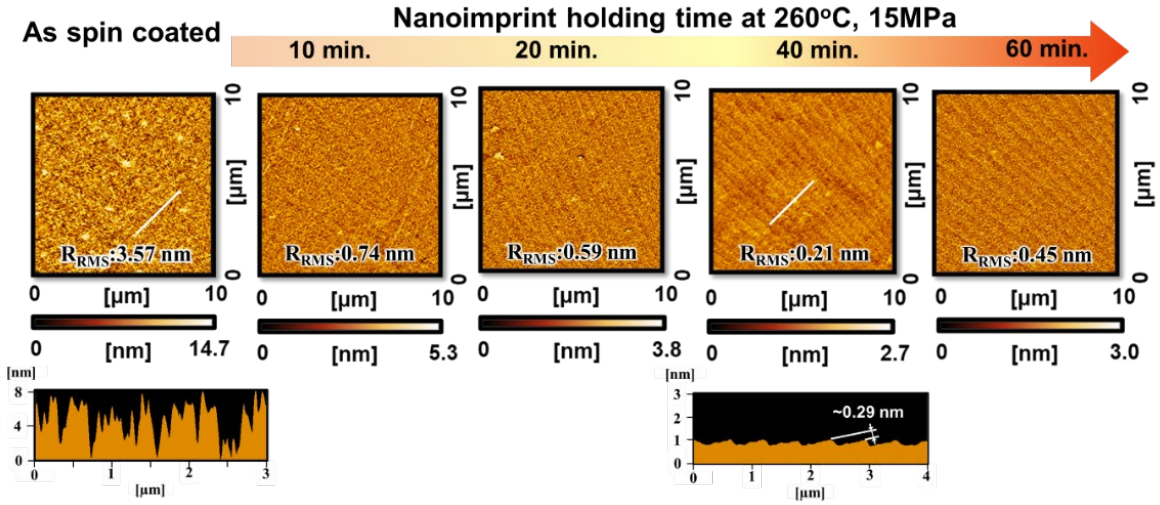

Figure 3. AFM images of the as-spin coated and nanoimprinted PEDOT:PSS thin films with holding time of 10 - 60 min at 260°C and 15MPa. R_{RMS} indicates the root-mean-square (RMS) surface roughness.

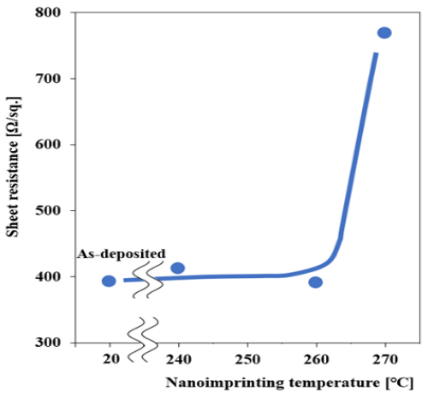

Figure 4. Sheet resistances of the PEDOT: PSS thin films nanoimprinted at some temperatures.

Adjustable arrangement of Polystyrene Micro Spheres by Using 3D Micro Printing and Colloidal Lithography

Li-En Kang [a*], Yu-Sheng Hsieh [a] and Yeeu-Chang Lee [a**]

[a] Department of Mechanical Engineering, Chung Yuan Christian University, Chung Li 32023, TAIWAN

*e-mail: kawasaki3500@gmail.com **e-mail: yclee@cycu.edu.tw

Keywords: 3D micro printing, colloidal lithography, polystyrene spheres

Abstract:

The efficiency of many optoelectronic devices can be enhanced by applying surface microstructures, such as anti-reflective surface features on GaAs solar panels [1, 2] or roughened surfaces on LED light sources to optimize extraction [3, 4]. Micropatterned and textured surface also play an important role in cell and tissue architecture in vitro [5,6]. At present, most of the microstructures are fabricated using methods developed for IC fabrication using expensive equipment. In the current study, we developed a novel approach to the fabrication of 3D microstructures as a template for the arrangement of polystyrene (PS) micro-spheres in conjunction with colloidal lithography.

Our objective in developing this fabrication process was to create microstructures in arbitrary configurations. To this end, we developed a 3D micro printing machine that uses a 405nm wavelength laser for the curing of UV epoxy. As shown in Fig. 1, the laser targeting is controlled by three linear stages respectively driven by single stepper motor, to provide movement along the X, Y and Z direction. To enhance printing resolution, a condenser is used to narrow the laser beam to 3-4 micrometers. The precision of the 3D printer was assessed by creating a grid, as well as concentric circles, and a honeycomb structures (see Figs. 3-5). It is possible to arrange PS micro-spheres in wide range of patterns. However, the typical arrangement is a triangular lattice. In this study, we mix 5um diameter of PS spheres in methanol at a ratio of 1:10. After injecting the sphere mixture on top of the microstructure, the micro-spheres that randomly settled on the structure were subjected to vibration for 5 minutes and heating at 65°C to ensure that the spheres are stably connected with the structure (see Fig. 2).

As shown in Figs. 6-8, the arrangement of PS Spheres in a grid structure resulted in a simple cubic lattice, whereas the concentric circles formed an close-packed lattice, while the honeycomb presented a pattern of displaced hexagons. Polydimethylsiloxane (PDMS) was then applied over the structure and PS micro spheres to form a soft mold for the creation of optical diffusers. As shown in Figs. 10-11, a 655nm laser beam transmitted through the diffusers generated constructive optical interference patterns, the strength of which was further increased when we performed the same experiments with 1um PS spheres surrounding 5um PS spheres(see Fig. 9). The diffusion characteristics of devices based on a grid structure were not as strong as those based on a microstructure of concentric circles or honeycomb. In the future, we will explore other microstructures as templates for colloid lithography.

Reference:

[1] K. S. Cho, P. Mandal, K. Kim, I. H. Baek, S. Lee, H. Lim, D. J. Cho, S. Kim, J. Lee, F. Rotermund, 2011, "Improved efficiency in GaAs solar cells by 1D and 2D nanopatterns fabricated by laser interference lithography", *Optics Communications*, Vol. 284, pp. 2608-2612

[2] Y. Y. Chou, C. C. Chang and Y. C. Lee**,** 2014, **"**Fabrication of sub-wavelength antireflective structure to enhance the efficiency of InGaAs solar cells", *International Journal of Automation and Smart Technology*, Vol. 4, pp. 174-178.

[3] T. Fujii, Y. Gao, R. Sharma, E. L. Hu, S. P. DenBaars, and S. Nakamura, 2004 "Increase in the extraction efficiency of GaN-based light-emitting diodes via surface roughening," *Applied Physics Letters*, Vol. 84, 855–857.

[4]Y. C. Lee, S. C. Yeh, Y. Y. Chou, P. J. Tsai , J. W. Pan, H. M. Chou, C. H. Hou, Y. Y. Chang, M. S. Chu, C. H. Wu, C. H. Ho, 2013 "High-efficiency InGaN-based LEDs grown on patterned sapphire substrates using nanoimprinting technology", *Microelectronic Engineering*, Vol.105, pp. 86–90.

[5] Elisa D'Arcangelo and Alison P McGuigan, 2015 "Micropatterning strategies to engineer controlled cell and tissue architecture in vitro", Biotechniques, Vol. 58, pp. 13-23.

[6] M. Théry, 2010 "Micropatterning as a tool to decipher cell morphogenesis and functions", ***Journal of Cell Science***, Vol.123, pp. 4201–4213.

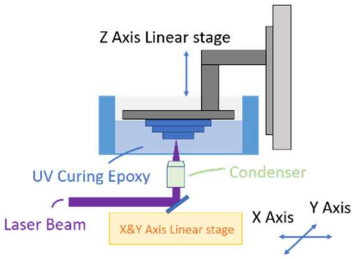

Figure 1. 3D micro- printing system with movement in the X, Y and Z directions to create arbitrary micro structures

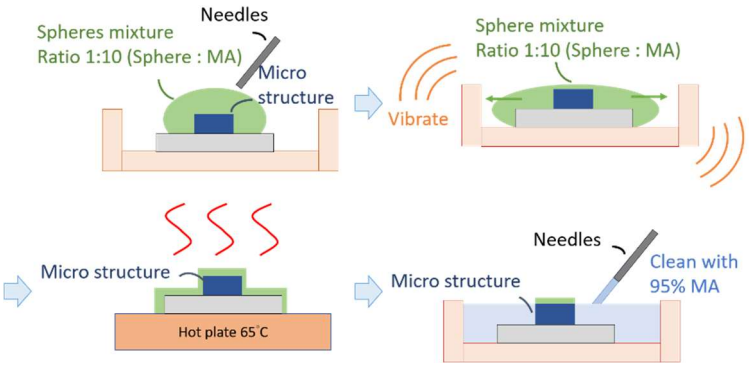

Figure 2. Process used in PS micro sphere arrangement to settle on different micro structures.

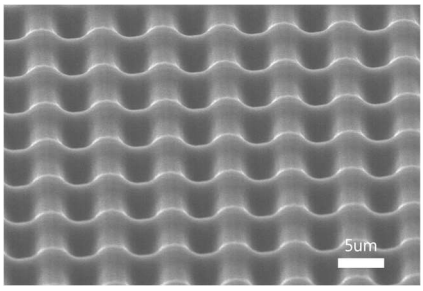

Figure 3. SEM image showing grid structure with 4um line width

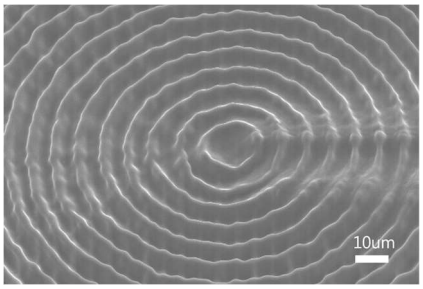

Figure 4. SEM image showing concenter circle structure with 4um line width

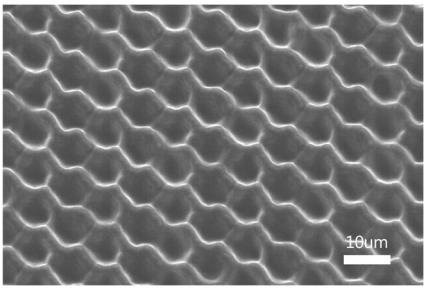

Figure 5. SEM image showing honeycomb structure with 3um line width

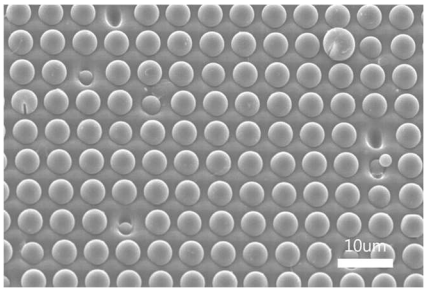

Figure 6. SEM image showing grid structure filled with 5um PS micro-spheres

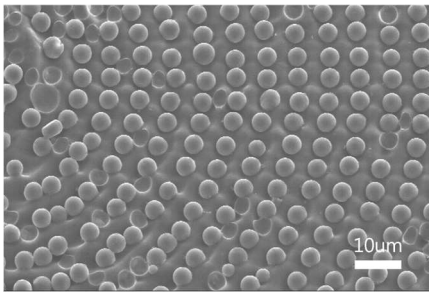

Figure 7. SEM image showing concentric circle structure filled with 5um PS micro-spheres

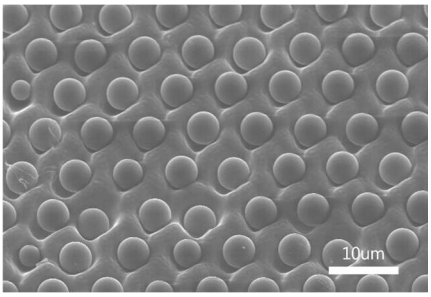

Figure 8. SEM image showing honeycomb structure filled with 5um PS micro-spheres

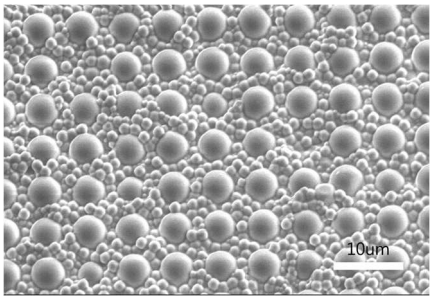

Figure 9. SEM image showing diffuser of grid structure filled with 5um and 1um PS micro-spheres

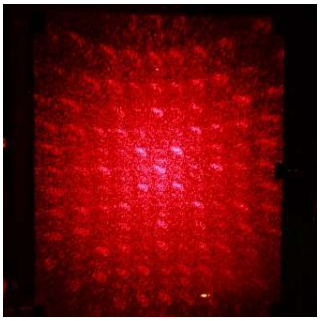

Figure 10. Diffuse pattern of grid structure with 5um and 1um PS micro-spheres

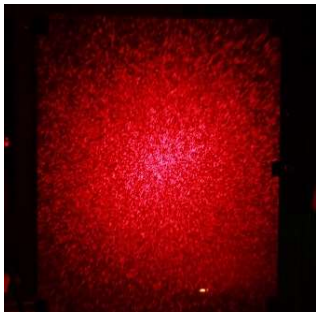

Figure 11. Diffuse pattern of concentric circles structure with 5um and 1um PS micro-spheres

Calculation of magnetic stiffness over torque between two current-carrying circular filaments arbitrary oriented in the space

Kirill V. Poletkin,

School of Instrument Science and Opto-electronics Engineering, Hefei University of Technology, Hefei, Anhui, 230009, China, e-mail: 2022810003@hfut.edu.cn

A new set of formulas for calculation of magnetic stiffness over torque between two circular filaments arbitrarily oriented in space were derived by using Mutual Inductance Method (MIM) (Kalantarov- Zeitlin's method) [1]. Formulas are presented in an analytical form through integral expressions, whose kernel function is expressed in terms of the elliptic integrals of the first and second kinds. The derived new formulas were successfully validated by Grover's method (GM) [2].

Analytical and semi-analytical methods in the calculation of parameters of electrical circuits and force interaction between their elements play an important role in developing micro- and nano-system devices and their applications in the different fields of science, including electrical and electronic engineering, medicine, physics, nuclear magnetic resonance, mechatronics and robotics, to name the most prominent. In particular, in the framework of recently developed quasi-finite element model (quasi-FEM) approach [3], the derived set of formulas helps us further to systematically and comprehensively simulate the static and dynamic behaviour of hybrid levitation micro-actuators (HLMAs). HLMAs dramatically increase capabilities of levitated micro-systems [4] through implementing, for instance, multi-stable mechanisms, coherent cooperative actuation and demonstrate a wide range of different operation modes such as the linear and angular positioning, bi-stable linear and angular actuations, and the adjustment of stiffness components as it was reported in Ref. [5] and presented by the author at Transducers 2017 [6].

Fig. 1 shows the general scheme of arbitrarily positioning of two circular filaments with respect to each other. The primary circular filament (the primary circle) and the secondary circular filament (the secondary circle) have radii of R_p and R_s, respectively. A coordinate frame (CF) denoted as *XYZ* is assigned to the primary circle in such a way that the *Z* axis is coincident with the circle axis and the *XOY* plane of the CF lies on circle's plane, where the origin *O* corresponds to the centre of primary circle. The *xyz* CF is assigned to the secondary circle in a similar way so that its origin *C* is coincident with the centre of the secondary circle. The angular misalignment of the secondary circle is defined by using Grover's angles θ and η as shown in Fig. 2. Assuming that the primary and secondary circular filaments carry the currents of I_p and I_s, respectively, hence, the magnetic stiffness over the torque can be calculated by taking the second derivatives of the function of the magnetic energy stored in such the system with respect to the appropriate angular coordinates. Hence, magnetic stiffness can be calculated by $S_q = -I_p I_s \, \partial^2 M/\partial q^2$, where $q = \theta, \eta$ and M is the mutual inductance between these two filaments [1]: $M = \mu_0 \sqrt{R_s R_p}/\pi \int_0^{2\pi} r \cdot U \cdot \Phi(k) d\varphi$, where $r = \cos\theta/\sqrt{\sin^2(\varphi-\eta) + \cos^2\theta \cos^2(\varphi-\eta)}$, $U = R/\rho^{1.5} = (r + t_1 \cdot \cos\varphi + t_2 \cdot \sin\varphi)/\rho^{1.5}$, $\Phi(k) = 1/k\,[(1-k^2/2)K(k) - E(k)]$, $k^2 = 4\nu\rho/\left((\nu\rho+1)^2 + \nu^2 z_\lambda^2\right)$, $\nu = R_s/R_p$, $z_\lambda = z + r\tan\theta\sin(\varphi-\eta)$, $\rho = \sqrt{r^2 + 2r\cdot(x\cos(\varphi) + y\sin(\varphi)) + s^2}$, $s = \sqrt{x^2+y^2}$, $t_1 = x + 0.5r^2\tan^2\theta\sin\left(2(\varphi-\eta)\right)y$, $t_2 = y - 0.5r^2\tan^2\theta\sin\left(2(\varphi-\eta)\right)x$, and $x = x_c/R_s, y = y_c/R_s, z = z_c/R_s$, $K(k)$ and $E(k)$ are the complete elliptic functions of the first and second kind, respectively. The derivatives of mutual inductance are shown in Tab. 1, 2, and 3. Fig. 3 and 4 show the two illustrative arrangements of the current-carrying coils. In both arrangements, it is assumed that the currents are units. The results of calculation are tabulated in Tab. 4 and 5, respectively, and agree excellently with Grover's results.

[1] K. V. Poletkin and J. G. Korvink., J. Magn. Magn. Mater. 483 (2019) 10–20.
[2] F. W. Grover, Proceedings of the IRE, 32 (1944) 620–629.
[3] K. V. Poletkin, IEEE ASME Trans Mechatron. 26 (2021) 753–764.
[4] K. V. Poletkin, et al., Actuators. 7 (2018).
[5] K. V. Poletkin, et al., J. Microelectromech Syst. 24 (2015) 1248–1250.
[6] K. V. Poletkin, A novel hybrid contactless suspension with adjustable spring constant, in: Digest Tech. Papers Transducers'17 Conference, (Kaohsiung, Taiwan, 2017) 934–937.

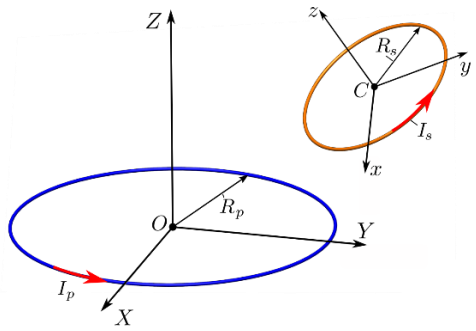

Figure 1. General scheme of arbitrarily positioning two circular filaments with respect to each other: the linear misalignment of the secondary circle with respect to the primary one is defined by the coordinates of the centre C (x_c , y_c , z_c).

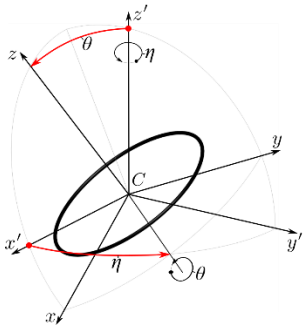

Figure 2. Manner for determining the angular position of the secondary circle with respect to the primary one via Grover's angles.

Table 1. The second θ - and η - derivatives of M.

$$\frac{\partial^2 M}{\partial q^2} = \frac{\mu_0\sqrt{R_s R_p}}{\pi}\int_0^{2\pi}\left[\frac{\partial^2 r}{\partial q^2}U + 2\frac{\partial r}{\partial q}\frac{\partial U}{\partial q} + r\frac{\partial^2 U}{\partial q^2}\right]\Phi(k)$$
$$+2\left[\frac{\partial r}{\partial q}U + r\frac{\partial U}{\partial q}\right]\cdot\frac{d\Phi(k)}{dk}\frac{\partial k}{\partial q} + r$$
$$\cdot U\left(\frac{d^2\Phi(k)}{dk^2}\left(\frac{\partial k}{\partial q}\right)^2 + \frac{d\Phi(k)}{dk}\frac{\partial^2 k}{\partial q^2}\right)d\varphi,$$

where $\partial U/\partial q = (\partial R/\partial q\,\rho - 1.5\cdot R\cdot\partial\rho/\partial q)/\rho^{2.5}$,

$$\partial \mathrm{R}/\partial q = {}^{\partial r}/_{\partial q} + \partial \mathrm{t}_1/\partial q\cdot\cos\varphi + \partial \mathrm{t}_2/\partial q\cdot\sin\varphi,$$

$$\frac{d\Phi(k)}{dk} = \frac{1}{k^2}\left[\frac{2-k^2}{2(1-k^2)}E(k) - K(k)\right],$$

$$\frac{\partial k}{\partial q} = \left(G\cdot\nu\frac{\partial\rho}{\partial q} - F\right)/H,\ G = 2/k - k(\nu\rho+1),$$

$$H = (\nu\rho+1)^2 + \nu^2 z_\lambda^2,\ F = k\nu^2\cdot z_\lambda\,\partial z_\lambda/\partial q,$$

$$\partial\rho/\partial q = D/\rho\cdot\partial r/\partial\rho$$
$$= (r + y\cdot\sin\varphi + x\cdot\cos\varphi)/\rho\cdot\partial r/\partial q\,;$$

$$\frac{\partial^2 \mathrm{k}}{\partial \mathrm{q}^2} = \left[\nu\frac{\partial G}{\partial q}\frac{\partial\rho}{\partial q} + \nu G\frac{\partial^2\rho}{\partial q^2} - \frac{\partial F}{\partial q}\right]/H - \left[G\cdot\nu\frac{\partial\rho}{\partial q} - F\right]\frac{\partial H}{\partial q}/H^2,$$

$$\frac{\partial^2\rho}{\partial q^2} = \frac{1}{\rho}\left\{\left[\frac{\partial r}{\partial q} - \frac{D}{\rho}\frac{\partial\rho}{\partial q}\right]\cdot\frac{\partial r}{\partial q} + D\cdot\frac{\partial^2 r}{\partial q^2}\right\},$$

$$\frac{d^2\Phi(k)}{dk^2} = -\frac{(4-7k^2+k^4)E(k)}{2k^3(k^2-1)^2} - \frac{(-4+9k^2-5k^4)K(k)}{2k^3(k^2-1)^2},$$

$$\partial^2 U/\partial q^2 =$$
$$\frac{\left[\frac{\partial^2 R}{\partial q^2}\rho - 0.5\frac{\partial R}{\partial q}\frac{\partial\rho}{\partial q} - 1.5R\frac{\partial^2\rho}{\partial q^2}\right]\rho - 2.5\left[\frac{\partial R}{\partial q}\rho - 1.5R\frac{\partial\rho}{\partial q}\right]\frac{\partial\rho}{\partial q}}{\rho^{3.5}},$$

Please see also Tab. 2 and 3.

Table 2. The θ -derivatives of the r function

$$\frac{\partial r}{\partial\theta} = \frac{A}{B} = \frac{-\sin\theta\sin^2(\eta-\phi)}{(1-\sin^2\theta\cos^2(\eta-\phi))^{1.5}},$$
$$\frac{\partial^2 r}{\partial\theta^2} = \frac{\frac{\partial A}{\partial\theta}B - A\frac{\partial B}{\partial\theta}}{B^2},\ \frac{\partial A}{\partial\theta} = -\sin^2(\eta-\phi)\cos\theta,$$
$$\partial B/\partial\theta = -3.0(1-\sin^2\theta\cos^2(\eta-\phi))^{0.5}$$
$$\times\sin\theta\cos\theta\cos^2(\eta-\phi).$$

Table 3. The η -derivatives of the r function

$$\frac{\partial r}{\partial\eta} = \frac{C}{B} = \frac{\sin(\varphi-\eta)\cos(\varphi-\eta)}{(1-\sin^2\theta\cos^2(\eta-\phi))^{1.5}},$$
$$\frac{\partial^2 r}{\partial\eta^2} = \left(\frac{\partial C}{\partial\eta}B - C\frac{\partial B}{\partial\eta}\right)/B^2,$$
$$\partial C/\partial\eta = (1-2\cos^2(\varphi-\eta))\cos\theta\,(1-\cos^2\theta),$$
$$\frac{\partial B}{\partial\theta} = \sqrt{1-\sin^2\theta\cos^2(\eta-\phi)}\sin^2\theta\cos(\eta-\varphi)\sin(\eta-\varphi).$$

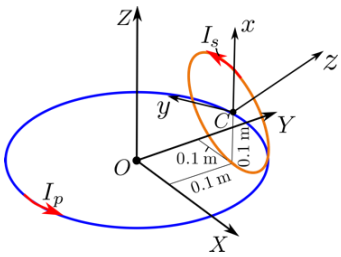

Figure 3. The primary and secondary circles have radii R_p =0.2m and R_s =0.1m. The centre of the secondary circle is located at x_C = 0.1m, y_C=0.1m, z_C =0.1m. The angular misalignment is θ= 54.7356 ° and η = 135°.

Table 4. Result of calculation for the arrangement shown in Fig. 3.

Stiffness,	**MIM,** μNm/rad	**GM,** μNm/rad
$\mathbf{S}_\theta$	0.3047032341	0.3047032341
$\mathbf{S}_\eta$	0.07264347826	0.07264347826

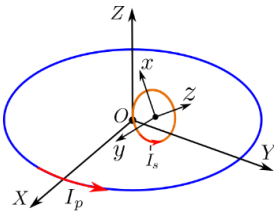

Figure 4. The primary and secondary circles have radii R_p =0.005m and R_s =0.001m. The centre of the secondary circle is located at x_C = 0.0m, y_C=0.001m, z_C =0.0005m. The angular misalignment is θ= 57.6885° and η = 165.0°.

Table 5. Result of calculation for the arrangement shown in Fig. 4.

Stiffness,	**MIM,** nNm/rad	**GM,** nNm/rad
$\mathbf{S}_\theta$	0.1894662588	0.1894662588
$\mathbf{S}_\eta$	0.009513776957	0.009513776957

Synchronous vibration of 1×2 torsional micromirror array

Mikiya Oki [a], Amit Banerjee [a], Jun Hirotani [a], and Toshiyuki Tsuchiya [a]
[a] Kyoto University, Kyoto, 615-8540, Japan
e-mail: m_ohki@nms.me.kyoto-u.ac.jp

We report a synchronized 1×2 torsional micromirror array for high speed, large scan angle, and large aperture optical devices. Despite its merit of being compact, light, and low power consumption, the performance of applications using torsional micromirrors is limited because of the difficulty in achieving large deflection angle, large mirror size, and high resonant frequency at the same time. A micromirror array proposed in our previous report achieved a large deflection angle, high resonant frequency, and large aperture but the variations in the vibration amplitude and phase were the problem. In this study, we propose a synchronizing method to reduce the variations and demonstrate it using a 1×2 torsional micromirror array.

Background

A torsional micromirror is being used in spatial light scanning systems such as laser display, endoscopy, and LIDAR [1]. In these applications, improvements in performance such as resolution, framerate, and scan range are demanded so that large mirror size, high resonant frequency, and large deflection angle should be achieved. However, it is difficult to achieve them at the same time due to mechanical limitations such as dynamic deformation caused by inertial loads [2], a trade-off between the resonant frequency and the deflection angle, and the torsional stress on the supporting beams. Our previous work [3] proposed an array of miniaturized mirrors with thin torsional beams. Miniaturizing the mirror size reduces the deformation and achieves the high resonant frequency while the torsional stress on the beams decreases. The array arrangement compensates for the small aperture of the miniaturized mirrors. On the other hand, vibration synchronization of the mirrors still exists as a problem caused by their different resonant frequencies due to fabrication errors. Therefore, we propose a synchronization method that reduces the difference in amplitude and phase of the mirrors. In this report, the method is demonstrated using a 1×2 micromirror array.

Descriptions of 1×2 micromirror array and synchronizing method

Figure 1 shows a schematic view of the designed micromirror array. A 150-μm-square mirror plate which is suspended by a pair of 2-μm-width torsional beams is fabricated on a 10-μm-thick silicon on insulator (SOI) wafer. Since the torsional stress is proportional to the thickness, the thickness of the beams is designed to be 2 μm while the mirror plate has a larger thickness of 10 μm to reduce the dynamic deformation. As shown in Fig. 2, to fabricate structures of different thicknesses on the SOI device layer, we adopt a multi-step deep reactive ion etching (DRIE) which has better etching controllability than the silicon nanowire (SiNW) fabrication process [4]. In the fabrication, double-layer masks are used to conduct two-step etching. The gaps and openings were defined by the first etching. By removing the photoresist mask before the second etching, the beams were formed while the mirror plate was protected by the SiO_2 hard mask. On synchronization, we utilize electrostatic tuning to reduce the mismatch of the resonant frequencies. The bias dc voltage applied on the left mirror induces electrostatic spring effect which increases the resonant frequency (Fig. 3). After the tuning, synchronization is achieved by adjusting the amplitude and phase of the driving square wave.

Results

A 1×2 micromirror array with torsional beams of 2.2-μm-wide and 2.1-μm-thick was successfully fabricated (Fig. 4). The resonant frequency and the vibration response were measured using a laser doppler vibrometer at atmospheric pressure. The resonant frequencies were measured to be 14.12 kHz for the left mirror and 14.35 kHz for the right. On synchronization, the frequency of the oscillating square wave voltage was fixed to 28.76 kHz which is twice the vibration frequency, and the amplitude of that for the right mirror was fixed to 10 V. The driving amplitude, bias dc voltage, and the driving phase for the left mirror were adjusted. As shown in Fig. 5, we successfully synchronized the vibration of two mirrors by applying the bias dc voltage of 10 V, the driving amplitude of 15.05 V, and the driving phase advance of 8.065 deg to the left mirror. The measured difference in amplitude and phase were 0.37% and 0.0028 deg, respectively.

[1] S. T. S. Holmström, et al., *J. Microelectromech. Syst.* 23 (2014), pp. 259-275
[2] P. J. Brosens, *Applied Optics*, 11.12 (1972), pp. 2987-2989.
[3] T. Nakamura, et al., Proc. IEEE MEMS 2020, pp. 1157-1160

[4] T. Tsuchiya, et al., *Appl. Sci.* 2018, 8(6), 880.

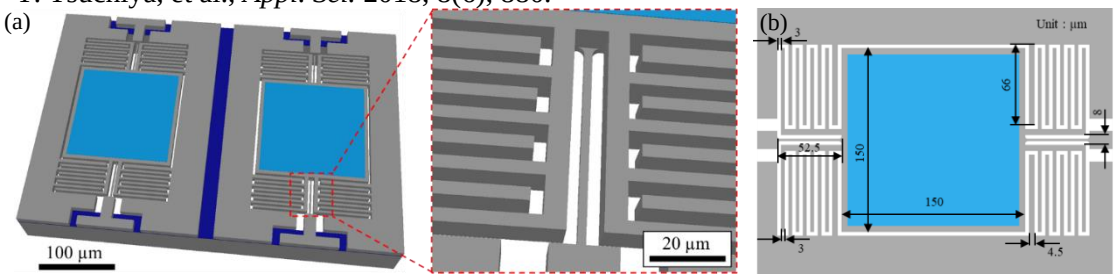

Figure 1. (a) Schematic view of 1×2 micromirror array (b) designed dimensions of single mirror

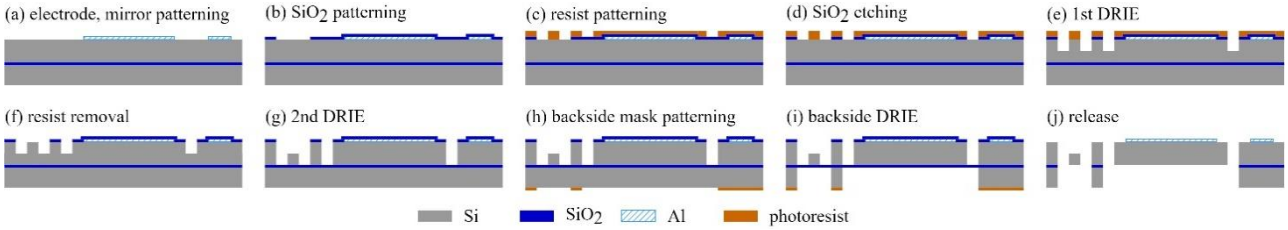

Figure 2. Fabrication process.

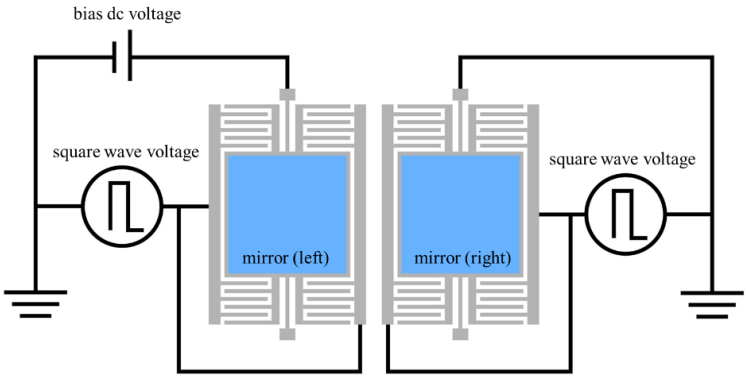

Figure 3. Schematic diagram of 1×2 micromirror array and driving circuit

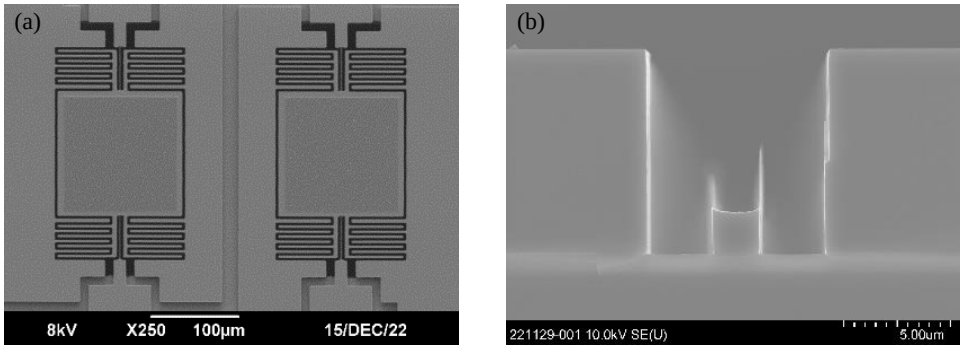

Figure 4. SEM image of (a) 1×2 micromirror array (b) cross-section of beam after second DRIE

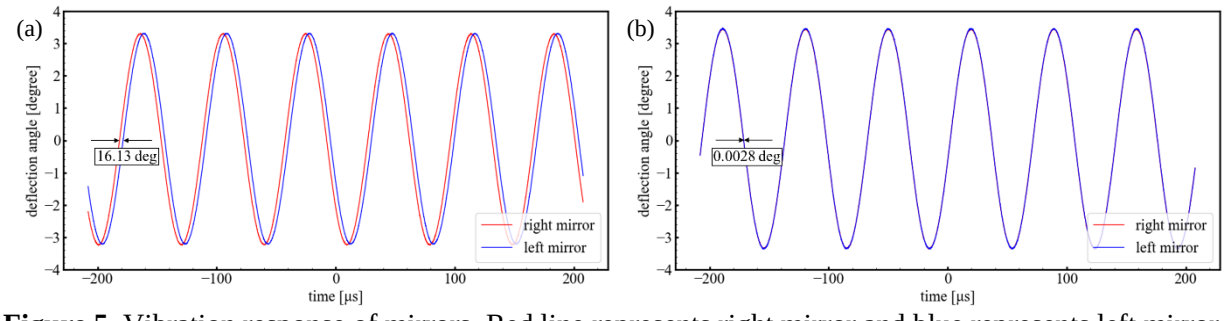

Figure 5. Vibration response of mirrors. Red line represents right mirror and blue represents left mirror. (a) vibration response before adjusting phase (b) vibration response after adjusting phase

Comparison of Pt- and W-based FEBID-grown nano-cones

C. Glessi [a], M.L. Simons [a], A. Mahgoub [a], T. van Marken [a], C.W. Hagen [a]

[a] TU Delft, Delft, 2628CJ, Netherlands
e-mail: m.l.simons@tudelft.nl

Focused Electron Beam Induced Deposition (FEBID) is an additive technology which can be used to create structures on the nanoscale, much like a 3D printer. A focused electron beam is used to decompose a precursor gas adsorbed to a surface, leading to the production of a solid deposit. By depositing this material on top of previously grown layers, free-standing three-dimensional structures can be built. Precursor supply, beam parameters and writing strategy significantly influence the obtained structure. The growth of double cones for the Nano Aperture Ion Source (NAIS) is used as a case study [1].

The target nanostructures are two concentric, radially symmetric nano-cones placed on two substrates separated by a small spacing, a double membrane structure (size and geometrical specifications in Figure 1). The double cones will be exposed to high doses of electrons and ions during the operation of the NAIS chip [1]. In previous work we produced PtC_x based nano-cones using $MeCpPtMe_3$ as a precursor molecule. A sufficient degree of control over the shape of the cones was achieved, but during high current electron exposure tests the PtC_x cones proved to be insufficiently stable to the exposure to electrons and Argon ions. PtC_x may well be consisting of a partially decomposed material, that under further irradiation loses undecomposed ligands and fragments, resulting in a change of shape and composition [2]. Tungsten hexacarbonyl $W(CO)_6$, however, has been identified as a more suitable precursor for the fabrication of highly conductive ion and electron beam induced deposits, with mainly tungsten carbide as the deposited material [3, 4], a much more robust material than PtC_x. The first steps of the explorations consisted of a translation of the deposition conditions between PtC_x and the W-C structures. A growth rate comparison indicated the necessity of an order of magnitude higher currents for the deposition of W-C compared to PtC_x, while the patterning strategy could be kept the same. We were able to produce concentric W-C cones close to the specified dimensions, using currents and energies as previously reported to yield highly conductive nanowires (20 kV, 1.3 nA) [3]. We will present a systematic comparison of the 3D patterning of these two most frequently used FEBID precursors, and discuss the performance of double cones under harsh electron exposure conditions.

[1] L. van Kouwen et al., The Nano-Aperture Ion Source, in: Advances in Imaging and Electron Physics, Vol 212 (Elsevier, Amsterdam, 2019).
[2] I. Utke et al., Chem. Rev. 458 (2022) 213851.
[3] P. Orús et al., [version 1; peer review: 2 approved] Open Res Europe 2:102 (2022).
[4] P. Orús et al., Nanomaterials 12 (2022) 1367.

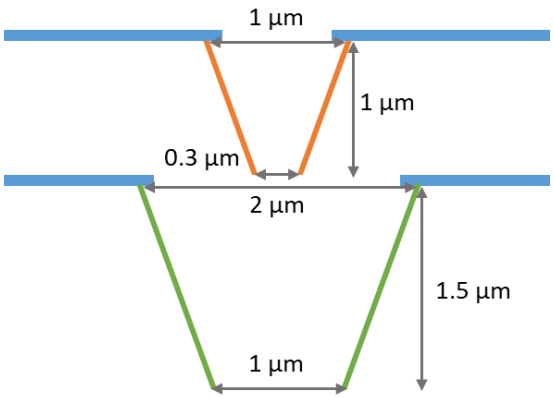

Figure 1. Double membrane of the NAIS chip and target dimensions of the concentric nano-cones.

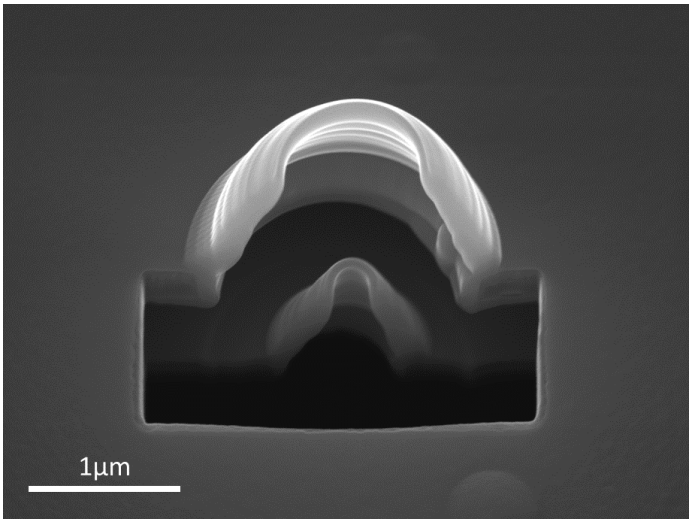

Figure 2. Cross section of a tungsten carbide (W-C) double cone structure.

Transport of Droplets via Magnetically-Responsive Microwall Arrays with Path-Guide

Soyeon Kwon [a], Jihun Kim [a], Yoobin Do [a], Hyun-Taek Lee [a]
[a] Inha University, Incheon, 22212, Republic of Korea
e-mail: htlee@inha.ac.kr

Abstract

Stimulus-responsive micropillars or microwalls have garnered significant attention in current research due to their wide range of potential applications in diverse fields, including micro mixers, micro pumps, droplet transportation, and surface manipulation. [1, 2] This study focuses on the development of activated microwalls and investigates their operation through the utilization of magnetic fields. Specifically, we explore the use of a periodic magnetic field [3, 4] generated by a Halbach array [5] to enable controlled droplet transport, allowing for manipulation of both transport speed and path. In this research, a flexible microwall arrays responsive to magnetic fields was fabricated using soft lithography techniques. The fabrication process involved creating a master mold through maskless lithography and incorporating a magnetic-responsive composite material called carbonyl iron powder (CIP) into polydimethylsiloxane (PDMS). The microwalls achieved adjustable bending angles and significant bending variations, allowing for precise droplet transport. By comparing structures with linear patterned walls to those with droplet path-guide, it was found that the inclusion of path-guide prevented droplet detachment and enabled more accurate control over the droplet transport path. Through the manipulation of microwall patterns and magnetic field application, the trajectory of droplets was governed with precision, presenting a promising development for droplet control systems.

Acknowledgements. This work was supported by the National Research Foundation of Korea(NRF) grant funded by the Korea government(MSIT) (IRS-2023-00240464).

References

[1] Tanveer ul Islam et al., Lab Chip 22 (2022), 1650–1679.
[2] Chen Yang et al., Advances in Colloid and Interface Science 306 (2022), 102724.
[3] Shaojun Jiang et al., Nano Letters 20 (2020), 7519–7529.
[4] D.L. Trumper et al., IEEE Transactions on Industry Applications 32 (1996), 371–379.
[5] Klaus Halbach., Nuclear Instruments and Methods in Physics Research 187 (1981), 109–117.

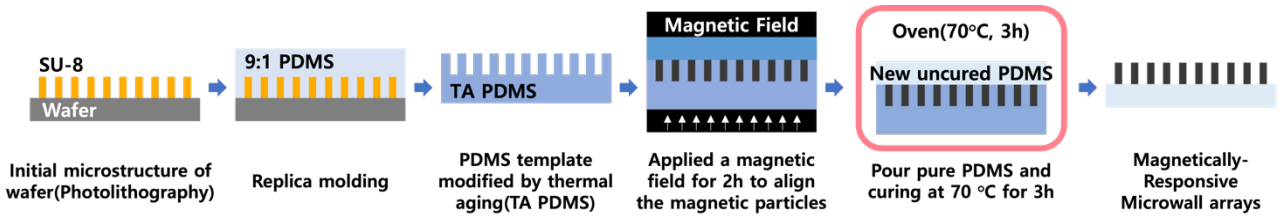

Figure 1. Schematic of the fabrication process.

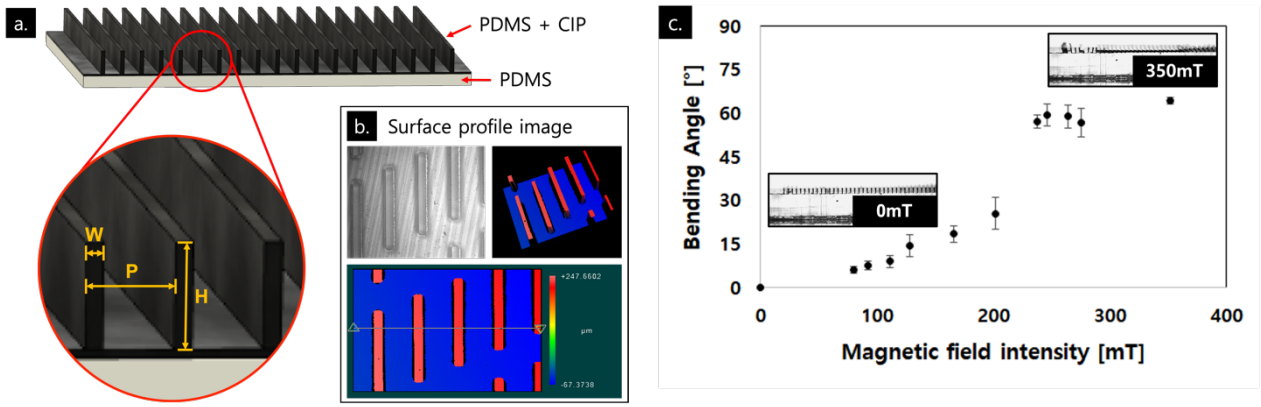

Figure 2. Magnetically-Responsive Microwall arrays. (a) The geometry of the Magnetically-Responsive Microwall arrays include wall width (W), pitch (P), and height (H), which are 65 μm, 300 μm, and 280 μm, respectively. (b) The surface profile image measeured by 3D optical profiler. (c) Bending angle variation based on the magnetic field intensity.

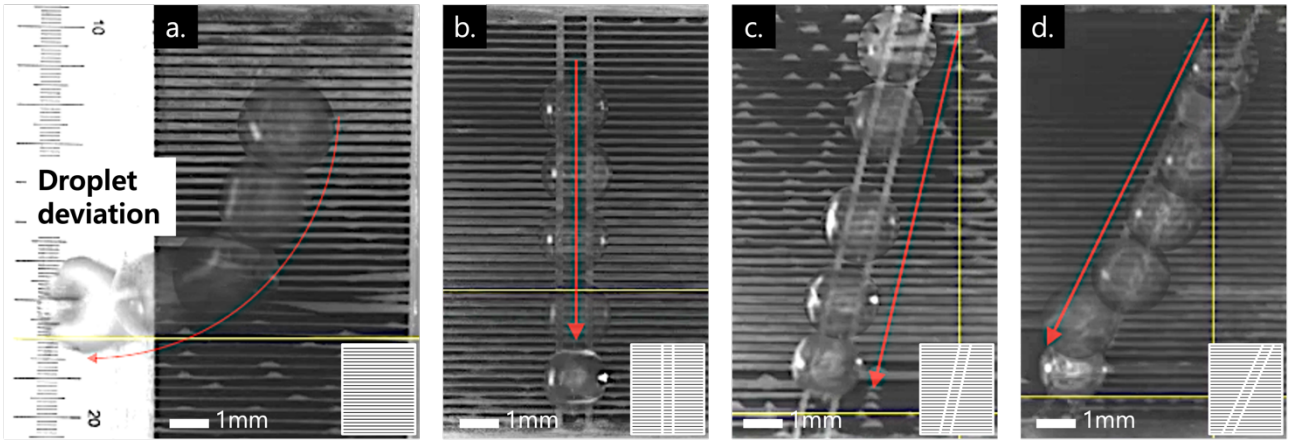

Figure 3. Droplet transport paths according to the pattern design. (a) Without droplet path-guide, (b-d) With droplet path-guide (b. slope: 0°, c. slope: 15°, d. slope: 30°)

Direct Printing Process of High-Refractive-Index Polymer for Practical Fabrication of High-Performance Metasurfaces

Dong Kyo Oh [a], Joohoon Kim [a], Hyunjung Kang [a], Junsuk Rho [a,b,c,d]

[a] Department of Mechanical Engineering, Pohang University of Science and Technology (POSTECH), Pohang 37673, Republic of Korea
[b] Department of Chemical Engineering, Pohang University of Science and Technology (POSTECH), Pohang 37673, Republic of Korea
[c] POSCO-POSTECH-RIST Convergence Research Center for Flat Optics and Metaphotonics, Pohang 37673, Republic of Korea
[d] National Institute of Nanomaterials Technology (NINT), Pohang 37673, Republic of Korea
e-mail: jsrho@postech.ac.kr

Visible metasurfaces, consisting of periodic nanostructures, have been attractive because of their fine control of electromagnetic waves for various purposes such as holograms, lenses, and optical sensors. [1] While these metasurfaces become more delicate and smaller to realize either high-performance or multifunctional devices, high-resolution electron-beam lithography (EBL) commonly used to fabricate them is still expensive and time-consuming, impeding the practical fabrication of metasurfaces.

Recently, high-refractive-index materials in visible wavelength have been researched to achieve highly efficient metasurfaces, but they still exist in a condition of thin films which need additional processes such as etching and a lift-off process. In this study, we present a direct printing process of a polymer with high-refractive-index nanoparticles for the practical fabrication of high-performance metasurfaces.[2-4]

By mixing TiO_2 nanoparticles in the polymer, the effective refractive index of the mixture can be controlled up to 1.9 depending on the concentration of TiO_2 nanoparticles, as shown in **Fig. 1**. Next, a rigorous analysis based on the effective medium theory yields an optimized design of metasurfaces (**Fig. 2**). Finally, the direct printing process of the polymer results in high-performance metasurfaces on flexible substrates, which is verified by comparing the diffraction efficiency of the fabricated metasurface, as shown in **Fig. 3**. By extension, we believe various functional materials in addition to TiO_2 can be granulated for the unprecedented practical fabrication of both highly efficient and multifunctional metasurfaces.[5,6]

[1] C. Jung et al., Chem. Rev. 121 (2021) 13013-13050.
[2] J. Kim et al., Laser Photon. Rev. 16 (2022) 2200098.
[3] G. Yoon et al., Nature Commun. 11 (2020) 2268.
[4] K. Kim et al., ACS Appl. Mater. Interfaces 11 (2019) 26109-26115.
[5] J. Kim et al., Light-Sci. Appl. 12 (2023) 68.
[6] G. Yoon et al., ACS Nano 15 (2021) 698-706.

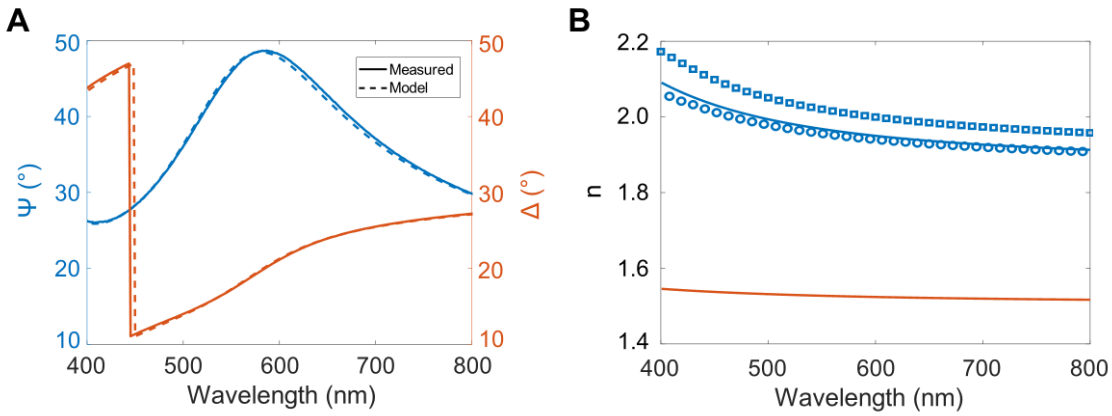

Figure 1. Measured and modeled optical properties of the polymer with TiO_2 nanoparticles and comparison with conventional UV-curable polymer.

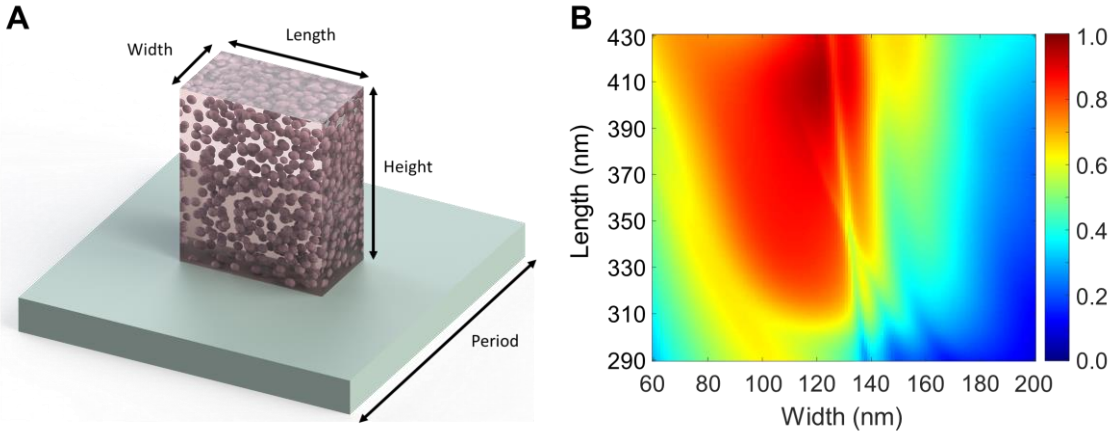

Figure 2. Rigorous analysis of metaatom dimensions depending on the effective polymer. The height of the metaatom is fixed at 910 nm.

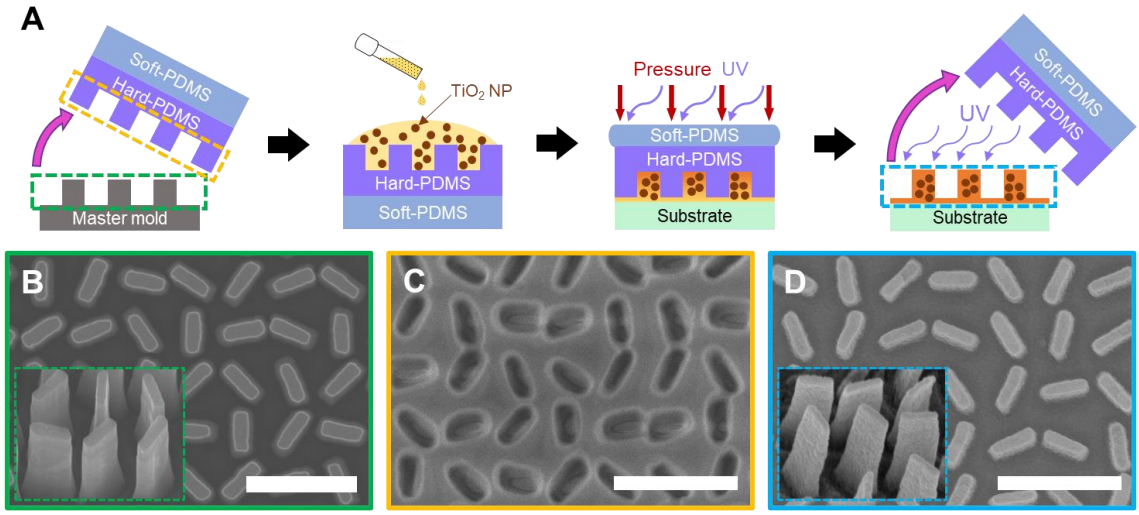

Figure 3. Overview of the direct printing process of high-refractive-index polymer and its SEM images. All scale bars: 1 µm.

Design and Simulation of Miniatured Piezoresistive Diaphragm Pressure Sensor for High Vacuum Applications

Jian Lu, Lan Zhang, Yuichi Kurashima, Hideki Takagi

National Institute of Advanced Industrial Science and Technology (AIST), Tsukuba, 305-8564, Japan
e-mail: jian-lu@aist.go.jp

In situ monitoring of pressure variations by microelectromechanical system (MEMS) in pipes, vacuum chamber, etc. is one of the key technologies for industry 4.0 [1]. MEMS Pirani sensor has been well investigated in recent years with a full range of 0.1~1000 Pa and an extremely high resolution of 0.01 Pa, while it needs complicated calibration due to gas dependency and temperature dependency [2][3]. An absolute MEMS capacitance vacuum sensor with a full range of 1~1000 Pa has been developed with an achievable resolution of 0.5 Pa and a sensitivity of 33.03 fF/Pa [4]. However, it is difficult to be used under strong and high frequency electric fields, since the inductive current may induce noise or even breakdown the device. In this work, a piezoresistive diaphragm pressure sensor was proposed with miniatured size of 2.2 mm × 2.2 mm, which is expected to use in the pressure range of 1~100 Pa with good linearity and a resolution of better than 0.1 Pa. The design and simulation results will be presented herein in detail. The device fabrication process and evaluation results will be discussed as well.

Fig. 1(a) shows schematic view of the device structure. A low-pressure gas, which marked as P_0, was sealed in the cavity to ensure a good sensitivity at high vacuum. A Wheatstone bridge was designed by using piezoresistive gauge on the surface of a membrane to detect deformation of the membrane induced by pressure variations. To investigate the effects of membrane geometry on sensitivity, the membranes with channel etching under piezoresistive gauge and reduced thickness at the center were also designed as shown in fig. 1(b) and fig. 1(c), respectively. Since zero-point calibration near P_0 is needed for the pursuit of good linearity and enough high sensitivity in the pressure range of 1~100 Pa, a variable resistor and a fixed resistor were assembled beside the Wheatstone bridge, as shown in fig. 2(a). Deformation of the membrane, stress of the membrane and the piezoresistive gauge, and output voltage of the Wheatstone bridge were then simulated by using finite element method (COMSOL Multiphysics®, COMSOL Inc. Burlington), as shown in fig. 2(b)-(d).

For better linearity, the maximum deformation of the membrane should less than 1/5 of its thickness under external pressure [5]. One the other hand, cavity pressure P_0 should as near as possible to 1~100 Pa to maintain an elastic deformation under the expected working environments. According to the simulation results in Table 1 and the feasibilities of the fabrication process, the membrane size w1 was therefore designed as 1200 um × 1200 um, the membrane thickness t_1 was set as 5 um, and the cavity pressure P_0 was targeted to 500 Pa. The simulation results in Table 2 clearly indicated that for above devices, the membrane with TYPE-A and TEYP-C geometry have similar sensitivity, which is 2 times higher than that of TYPE-B.

Fig. 3 shows device fabrication process in detail. It started from an SOI wafer. Ion-implantation was used to create piezoresistive gauge on the surface of the membrane. Finally, the cavity was formed by using Au-Au low temperature bonding under a reduced pressure P_0 of 500 Pa. Fig. 4 shows photo of the device under processing. To achieve expected resolution of better than 0.1 Pa, a signal processing module, including a 300 × amplifier and a low-pass filter, was fabricated in this work too for device evaluation. Further device evaluation results and discussion will be presented in the conference.

[1] T.Kalsoom, N.Ramzan, S.Ahmed et al., Sensors 20 (2020) 6783.
[2] L.Zhang, J.Lu, H.Takagi, S.Matsumoto et al., Micromachines 13 (2022) 1686.
[3] S.Xu, N.Zhou, M.Shi et al., Micromachines 13 (2022) 945.
[4] M.Xu, X.Han, C.Zhao et al., Journal of Microelectromechanical Systems 29(6) (2020) 1556-1562.
[5] J.Zhang, J.Chen, M.Li et al., Micromachines 9(3) (2018) 104.

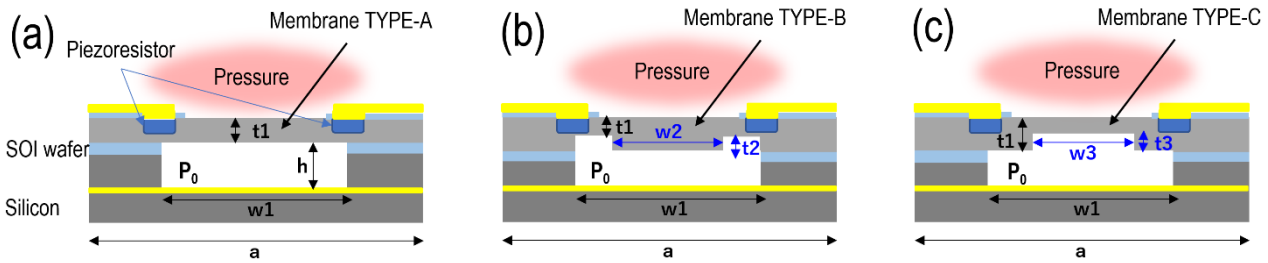

Figure 1. Schematic view of the device structure with various membrane geometries: (a) TYPE-A with uniform membrane thickness; (b) TYPE-B with channel etching under piezoresistive gauge; (c) TYPE-C with reduced membrane thickness at the center.

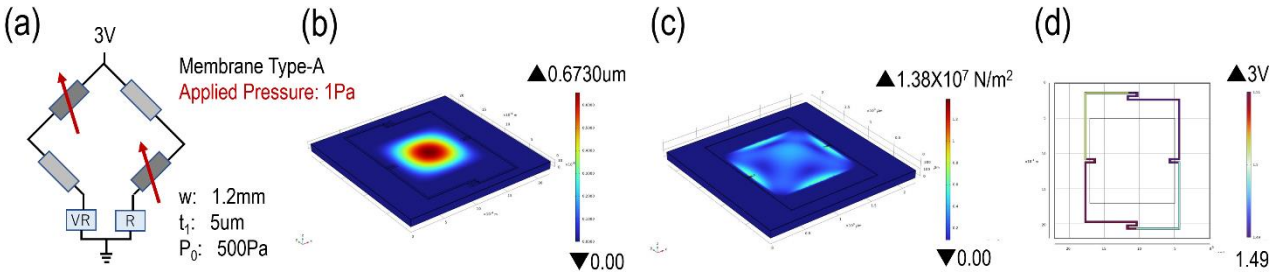

Figure 2. Simulation results by using COMSOL Multiphysics®: (1) Wheatstone bridge layout; (2) deformation of the membrane; (3) stress of the membrane and the piezoresistive gauge; (d) output voltage of the Wheatstone bridge.

w 1 (um)	t1 (um)	P0 (Pa)	Deformation @1Pa (um)	Deformation @100Pa (um)
1000 × 1000	2	10,000	71.8	
		1,000	7.17	
		500	3.6	2.89
		200	1.44	0.72
		100	0.71	0
	5	10,000	6.51	
		1,000	0.65	0.59
		500	0.32	0.26
1200 × 1200	5	10,000	13.5	
		1,000	1.35	1.22
		500	0.67	0.54

Table 1. Simulation results of the max. deformation of the membrane with applied pressure of 1 Pa and 100 Pa at various device geometries.

TYPE	t1	t2	t3	w2	w3	P0 (Pa)	Sensitivity @1-100Pa (mV/Pa)
	(um)						
A	5	--				1000	0.00882
						500	0.00885
B	5	10	--	700	--	1000	0.00496
						500	0.00497
		30	--	700	--	1000	0.00412
						500	0.00413
C	5		2.5	--	700	1000	0.00908
						500	0.00906

Table 2. Simulation results of the device sensitivity between 1 Pa and 100 Pa at various membrane types (w1=1200um×1200um).

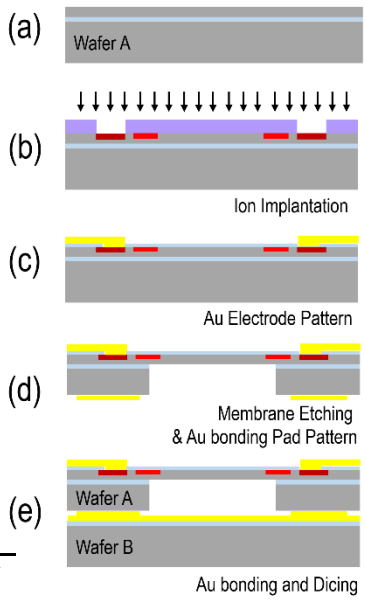

Figure 3. Device fabrication process: (a) starting SOI wafer; (b) ion implantation for piezoresistive gauge; (c) Au electrode patterning for Wheatstone bridge; (d) membrane etching and backside Au bonding Pad patterning; (e) low temperature Au-Au bonding at reduced pressure of 500 Pa.

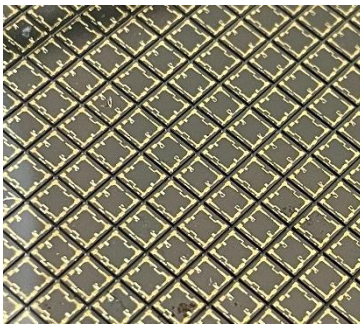

Figure 4. Photo of the devices under processing.

Poster Session2.2: Track 4 - Papers

New optical detection method of home-made explosives based on lab on paper chemical sensors

Viktoriia Lastivka[a], Piotr Kasprzak[b], Izabela Mazur[b], Piotr Baran[b], Warzyniec Pniewski[b], Ilona Grabowska-Jadach[a], Michał Chudy[a], Katarzyna Tokarska[c], Kamil Żukowski[c], Artur Dybko[a]

[a] Faculty of Chemistry, Warsaw University of Technology, 00-661 Warsaw, Poland
[b] Military Institute of Armament Technology, 05-220 Zielonka, Poland
[c] CEZAMAT, 02-822 Warsaw, Poland
e-mail: artur.dybko@pw.edu.pl

Home-made explosives (HME) are gaining the interest of security forces in the whole world since they are intensively utilised by terrorists. These explosive materials belong to the peroxide group and can be easily prepared from the compounds available on the market without any restriction to access. There are no nitro groups nor aromatic rings in the peroxide structure. Thus the methods developed for the determination of nitrogenous groups are not effective. The methods of HME detection usually require the utilisation of additional chemical compounds (for example concentrated acid) to react with the peroxide and then a product of such a reaction can be detected [1,2].

This paper presents a new fast colorimetric method for visual detection of HME, i.e. triacetone triperoxide (TATP), hexamethylene triperoxide diamine (HMTD) based on the application of micro paper-based analytical devices (uPAD) [3,4]. To authors' the best knowledge, this is the first paper describing such a colorimetric test. The chemical sensors were based on Whatman chromatography paper, which was covered with a wax layer. A precise wax pattern was deposited using a Xerox wax printer Colorqube 8700. Afterward, the chromatography paper was heated up to 170 ˚C for 2 min. In this way, the wax layer penetrates the paper and creates a hydrophobic barrier. Fig.1 A) presents the architecture of the uPAD sensor. There are 4 sensing zones of circular shape where a chemical indicator can be immobilised. The sample under the test is dropped on the central point of the sensor and then capillary forces deliver the sample to the sensing zones. Fig. 1 B) presents a close-up of the sensing zone before and after heating. Initially, a diameter of the sensing zone was designed as a 5mm circle. After heating, it was observed that the inner diameter decreased to 3.5 mm (see Fig. 1 C). During the heating, wax penetrates the paper but also it is spreading out on the surface. Intrudingly, careful examination of the bottom of the sensing zone indicates that there are some cellulose fibres not covered by the wax (see Fig. 1D). However, their interactions with the delivered sample are not so big to induce capillary force flow outside the zone. It was experimentally determined that the volume of an indicator placed on the sensing zone is as small as 0.5 ul, whereas the total volume of the sample under test is equal to 10 ul. A precise micropipette (Mettler Toledo) was used to drop the liquids.

We have developed a new sensing principle for HME visual detection. HME can be considered as highly oxidising compounds so it was decided to use the very well-known starch iodide test. Firstly, a solution of starch (0.1g/ml) was dropped on the sensing zone and left to dry in a laboratory. Then a solution of potassium iodide (0.1 M) was deposited. In both cases, 0.5 ul volumes were applied. Solutions of TATP and HMTD in an acetone/water (50:50%) mixture were prepared with a concentration of 1 mg/ml, and they were treated as the initial solutions. Then these solutions were diluted 10 and 100 times. 10 ul of the diluted solutions was dropped on the central point of the sensor. Within one minute the sensing zone changed color into deep red/wine (see Fig. 2) for TATP, and red/orange for HMTD. Hydrogen peroxide was also used giving dark brown/black result. It can be concluded that the designed sensors can be used for the detection of HME up to the concentrations 0.01 mg/ml. The sensors exhibit selective color change for the HME tested. A special application in LabVIEW environment was developed for RGB evaluation during the measurements (see Fig.3).

References:

[1] P. Michel, J.L. Boudenne, F. Robert-Peillard, B. Coulomb, Trends Anal.Chem. 158 (2023) 116884.
[2] Y. Li, X. Liu, G. Zhang, R. Wang, R. Yue, G. Liao, Z. Sun, Y. Liu, J.Chem.Res. July-Aug (2022) 1-11.
[3] A.W. Martinez, S.T. Phillips, M.J. Butte, G.M. Whitesides, Angew Chem Int Ed 46 (2007) 1318–1320.

[4] G. Musile, Y. Agard, L. Wang, E. Franco De Palo, B. McCord, F. Tagliaro, Trends Anal.Chem. 143 (2021) 116406.

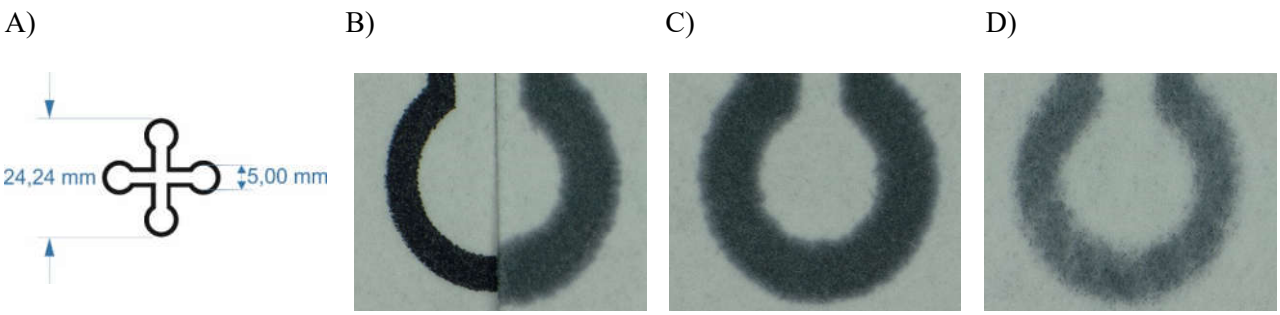

Figure 1. Lab on paper chemical sensor. A) sensor configuration B) sensing zone before (left) and after heating (right), C) top view of sensing zone (inner diameter decreased from 5 mm into 3.5 mm after heating), D) bottom view.

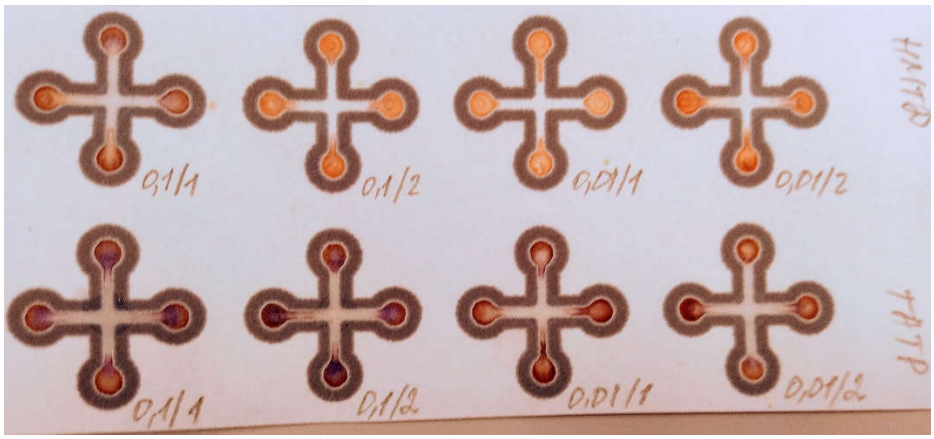

Figure 2. Photographs lab on paper sensors. A) just after indicator immobilization, B) with a solution of TATP, C) with a solution of HMTD.

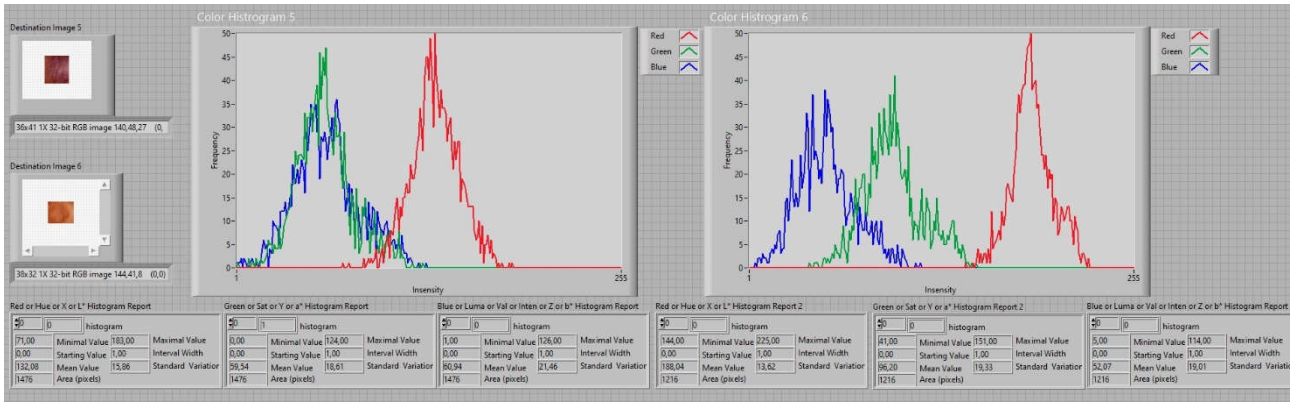

Figure 3. LabVIEW application for RGB measurements.

ACKNOWLEDGMENTS
The authors would like to thank the National Center for Research and Development for support of this project through DOB SZAFIR/12/A/029/01/2020.

Electroplating-based engineering of plasmonic nanorod metamaterials

Mihir Kumar Sahoo [a], Abhay Anand VS [a], & *Anshuman Kumar [a]

[a] Laboratory of Optics of Quantum Materials (LOQM), Department of Physics, IIT Bombay, Mumbai, 400076, Maharashtra, India

*Corresponding Author e-mail: anshuman.kumar@iitb.ac.in

Electron beam lithography (EBL) is an effective technique for fabricating low-dimensional, reproducible nanostructures. Vertical cylindrical AuNR array fabrication is carried out via EBL, followed by metallization. Among various physical vapour deposition (PVD) techniques sputtering and e-beam evaporation techniques are popular due to the smooth and uniform thin film deposition of Au. However, the PVD techniques require a vacuum environment to deposit Au, which is costly, time-consuming, and thickness-limited. On the contrary, chemical deposition, i.e., electroplating deposit [1] with higher thickness in less time and at lower cost, becomes an alternative method for Au deposition. In this work, we present a detailed optimization for the electroplating-based fabrication of these metamaterials. We find that slightly acidic ($6.0 < pH < 7.0$) gold sulfite solution supports immersion deposition, which should be minimized to avoid uncontrolled Au deposition. Immersion deposition leads to plate-like (for smaller radius AuNR) or capped-like, i.e., mushroom (for higher radius AuNR) structure formation. The electroplating time and DC supply are the tuning parameters that decide the geometry of the vertically aligned AuNR array in area-dependent electroplating deposition. This work will have implications for developing plasmonic metamaterial-based sensors.

Figure 1 shows the schematic for experimental procedures involved in fabricating vertical Au NR array via EBL and metallization [2]. One-millimeter-thick quartz substrate (2.5×2.5 cm^2) was cut into 1×1 cm^2 and cleaned using an ultrasonic sonicator in trichloroethylene, acetone, and isopropyl alcohol (IPA) solution (each for five minutes). Piranha cleaning (H_2SO_4 : H_2O_2 :: 7 : 3) was carried out for 30 minutes in an ambient atmosphere to remove sodium and potassium remnants. A five nm thin adhesive Ti-layer was deposited on the cleaned quartz substrate via DC sputtering (2.1 nm/min). To make a transparent and conducting quartz substrate, a 20 nm Au thin film layer was deposited via DC sputtering (17 nm/min) on the adhesive Ti-layer. EBL was carried out to make the vertical AuNR array pattern on the sample. A monolayer PMMA (A2: 950K, 2%) was spin-coated (1000 rpm, 50 s) on the baked (180°C for one minute) marker sample and post-baked for five minutes at 180°C. Then the vertical AuNR array pattern was written on the PMMA layer at 20kV, a dosage of 450 μC/cm^2, beam aperture of 10 μm with a current density of 0.0296 nA. Then the sample was first kept in methyl isobutyl ketone (MIBK) and IPA solution (MIBK : IPA :: 3 : 1) for 35 s to develop the pattern and then put in IPA solution (70 s) to cease further development.

The Au electroplating was carried out on a hot plate at 120°C with a magnetic stirrer speed of 100 rpm (as shown in Figure 2 (left)) to avoid chunk formation [2]. The temperature of the measured gold sulfite solution (TSG-250, one troy ounce of gold per gallon) (kept in the beaker) was 50°C. In the chemical deposition method, platinum (Pt) metal was used as an anode, and Au deposited quartz substrate (sample) was dipped inside the gold sulfite solution as a cathode. The DC power supply was operated in constant current mode at 0.001 A DC for 30 sec. As the gold sulfite solution is slightly acidic/neutral (pH: 6.0-7.0), the sample was immediately removed and dipped in DI water to avoid immersion deposition. At lower EBL dosage (450 μC/cm^2), a perfectly cylindrical AuNR array was formed (as shown in Figure 2 (a) and (c)) whose dimensions were uniform (125 nm diameter with 400 nm periodicity) throughout the whole array. However, the tilted view of the AuNR array formed at higher EBL dosage (500 μC/cm^2) shows a uniform (170 nm diameter with 400 nm periodicity) cap-like or mushroom-like top structure on the top AuNR array (as shown in Figure 2 (b) and (d)).

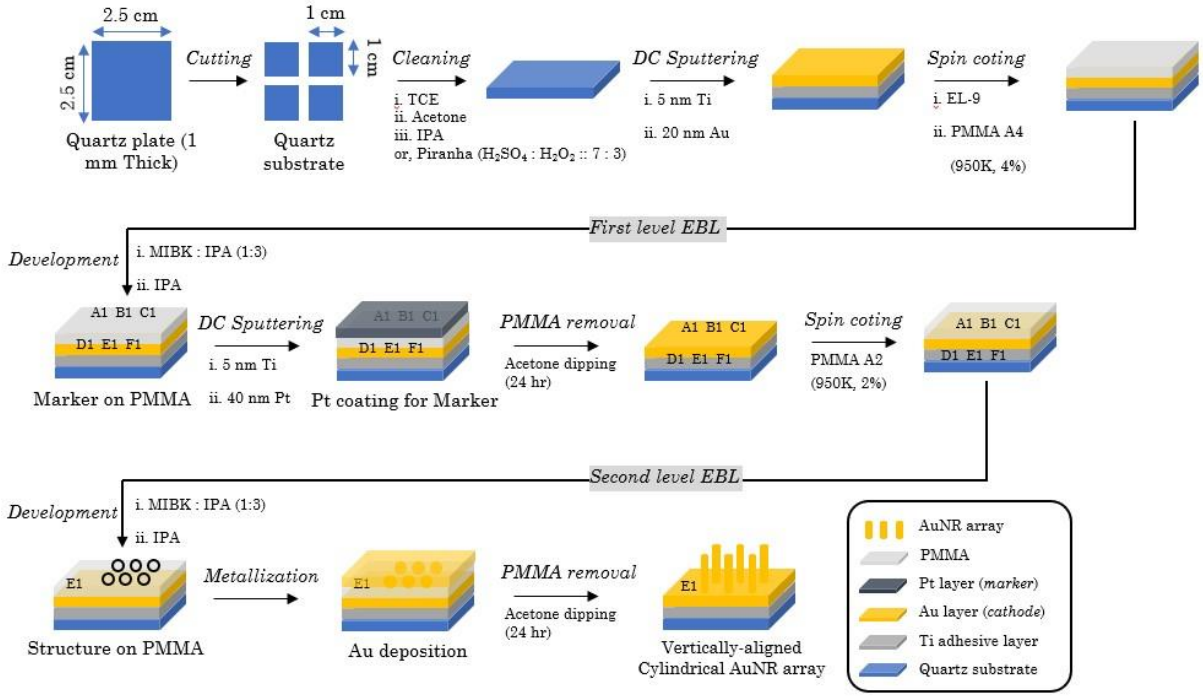

Figure 1. Schematic of an experimental procedure to fabricate a vertical AuNR array via electron beam lithography (EBL) and metallization.

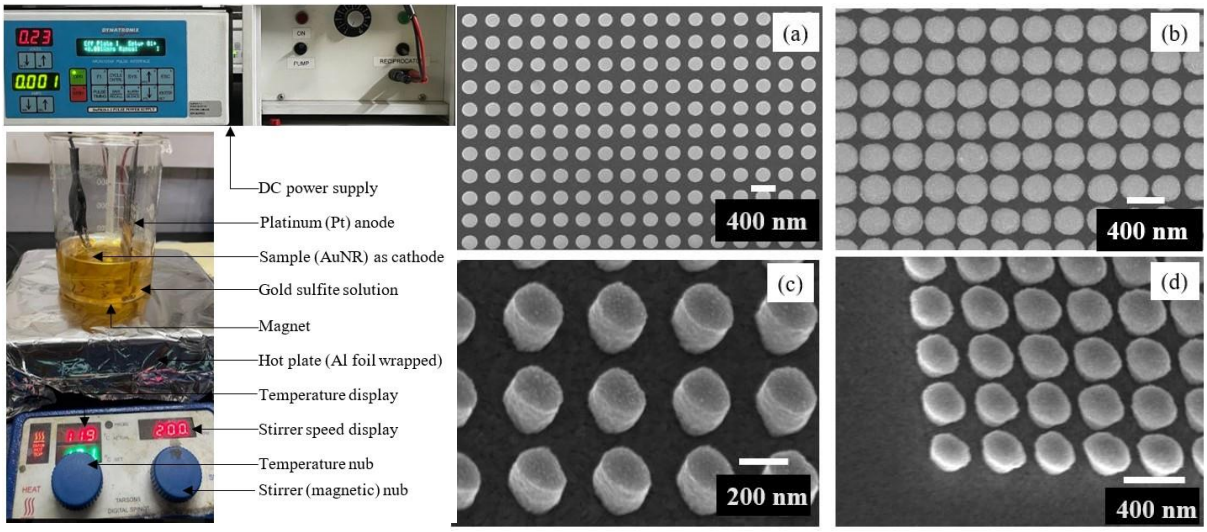

Figure 2. Experimental set-up for Au deposition via electroplating (left). SEM images of vertically aligned AuNR array fabricated via electroplating for EBL dosage at 450 μC/cm^2 (a) surface view, (c) titled-view (27°), and at 500 μC/cm^2 (b) surface view, and (d) titled-view (27°), whose measured height was 180 nm for the cases (right).

References:

[1] R. Yan et al., Photonics Research 10 (2022), 84-95.

[2] MK Sahoo et al., Nanotechnology 34 (2023), 195301-195309.

Color imaging-based Optomechanical system for gas sensing

Ferran Pujol-Vila[a], Mar Alvarez[a,b]

[a]Instituto de Microelectrónica de Barcelona (IMB-CNM, CSIC), Campus UAB, Bellaterra, 08193 Barcelona, Spain
[b]Networking Research Centre on Bioengineering, Biomaterials and Nanomedicine (CIBER-BBN), Spain
e-mail: mar.alvarez@imb-cnm.csic.es

Over the past decades, several gas-sensing mechanisms have been reported [1,2], however, accurate detection of target environmental gases remains challenging in spite the advanced and help provided by the artificial intelligent algorithms (e.j. electronic noses), especially due to the cross-reactivity of the species, the low multisensing capabilities or high-power consumption. To solve these limitations, we have developed a label-free colorimetric mechanical sensing platform for the remote quantification of VOC by image analysis. The platform is based on an array of bimorph optomechanical sensors (e.g. bridges) with structural coloration derived from the periodic nanostructuration of one of its surfaces. With this approach, the light diffraction on the photonic surface generates an associated structural coloration of the sensors that converts the induced mechanical motion into color shifts (mechanochromism). The bimorph optomechanical bridges are made of a layer of solvent resistance off-stoichiometry thiol-ene polymer (OSTE), and a PDMS layer, which have high swelling to solvents. During the detection of gases, the bimorph optomechancial cantilever experiment a bending due to the different swelling ratio of both materials.

For manufacturing the bimorph sensors, a commercial linear (1D) diffraction grating was used as master mould. First, a PDMS replica was obtained and the PDMS and OSTE polymer was spin-coated over the PDMS mould achieving a bilayer (~ 15 μm thickness) after curing the PDMS and the Ostemer layer. The sensors' shape was defined by laser cutting. The structures were released with the help of a piece of pressure-sensitive adhesive, obtaining arrays of suspended bridges with one periodically nanostructured surface (d = 1600 nm) and dimensions L = 4000 μm, h = 15 μm, w = 50 μm (Figure 1a). A transparent polymethyl methacrylate (PMMA) microfluidic system (v = 160 μL) was fabricated by laser cutting, allowing gas flow management and simultaneous color imaging of the sensors. The light diffracted by the sensors surface was measured in Littrow configuration using a home-made black PMMA structure integrating a collimated white light source, a beam-splitter, and an USB-microscope (Dino-Lite) (Figure 1b,1c). Real time color analysis was perfomed using the *colorevo* open source code (https://doi.org/10.5281/zenodo.5646732.), by pre-selecting one region of interest (ROIs) per bridge [3-4].

As a proof of concept, we demonstrate the detection of vapor of ethanol. Figure 2a shows the not treated response of the bridges inside the gas chamber when exposed three times to same concentration of vapor of ethanol at 20% v/v, during two seconds. The color was analyzed close to the clamped region. Due to the initial different pre-stress, each bridge present a different initial color. The bridges experience a fast bend up due to the swelling of the PDMS during the exposure, followed by a slow recovering of the initial position during the de-swelling. The response of the bridges depends on the proximity of each sensor to the gas entrance, presenting the bridge closer to the gas entrance (bridge 1) the highest signal. Figure 2b shows the response of the sensors at different ethanol gas concentrations.

[1] U. Yaqoob & M.I. Younis, Sensors **21** (2021) 2877.
[2] Lang, H. P. Cantilever-Based Gas Sensing. in Solid State Gas Sensing (eds. Comini, E., Faglia, G. & Sberveglieri, G.) 1–24 (Springer US, 2009).
[3] P. Güell-Grau, P. Escudero, F. G. Perdikos, J. F. López-Barbera, C. Pascual-Izarra, R. Villa, J. Nogués, B. Sepúlveda and M. Alvarez, ACS Appl. Mater. Interfaces 13 (2021) 47871–47881.
[4] F. Pujol-Vila, P. Escudero, P. Güell-Grau, C. Pascual-Izarra, R. Villa and M. Alvarez, Small Methods, **n/a**, 2101283.

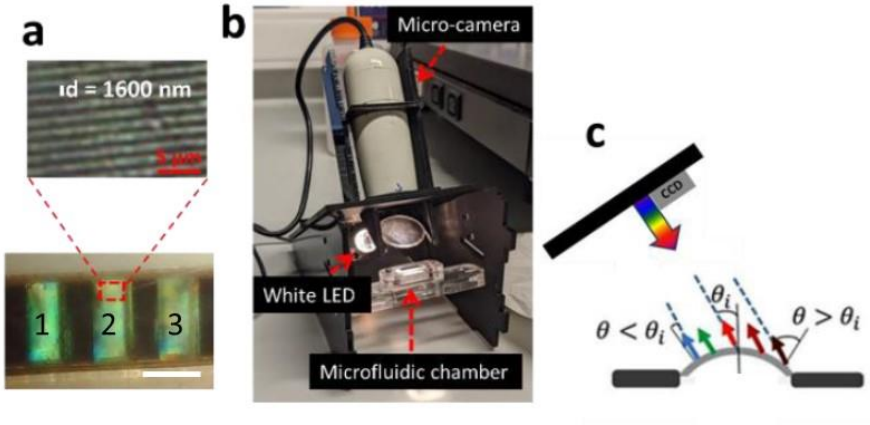

Figure 1. (a) Image of the bimorph optomechanical bridges and a zoom of the periodical surface structure. (b) Color imaging setup. (c) Detection scheme of the sensors color (Litrow configuration).

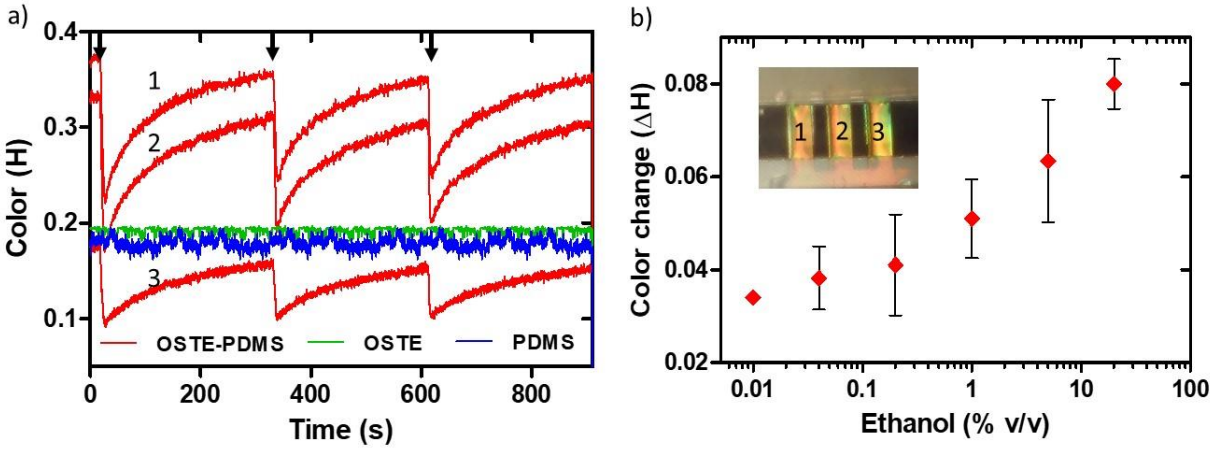

Figure 2. a) Color evolution during the exposure to vapor of ethanol at 20% v/v. Bridges of only OSTE or PDMS do not show any change. b) Color change at different concentrations of ethanol.

Benchmarking of ion-based nanopatterning techniques on stainless steel injection molding inlays for automotive applications

Florian Schlachter [a], Jens Bolten [a], Olatz Adarraga [b], Yordan M. Georgiev [c], Tommy Schönherr [c], Ana Zuzuarregui [d], Evgenii Modin [d], Max Christian Lemme [a,e]

[a] AMO GmbH, Otto-Blumenthal-Str. 25, 52074 Aachen, Germany
[b] TECNALIA, Basque Research and Technology Alliance (BRTA), San Sebastián, Spain
[c] Institute of Ion Beam Physics and Materials Research, Helmholtz-Zentrum Dresden-Rossendorf (HZDR), Dresden, Germany
[d] CICnanoGUNE-External Services Department, Basque Research and Technology Alliance (BRTA), San Sebastián, Spain
[e] Chair of Electronic Devices, RWTH Aachen University, Aachen, Germany

e-mail: schlachter@amo.de

Keywords: Reactive Ion Etching, Reactive Ion Beam Etching, Ion Beam Milling, Nanoimprint Lithography

Nanostructured surfaces have large commercial potential due to their enhanced functionalities for a range of applications, such as controlled reflectivity in photonic devices, antireflective and smudge free surfaces for electronics displays and anti-fingerprint, self-cleaning [1] or anti-icing [2] surfaces in plastic parts for the automotive industry. The current state-of-the-art manufacturing processes for nanostructured surfaces are based on two sequential steps. The desired part with its macro shape is produced based on an injection molding process and the functionality is realized by a coating layer added in a subsequent process that adds production time and costs. There is a strong demand in the industry for single-step processes that provide the macro shape and the desired functionality simultaneously. Direct Laser Interference Patterning (DLIP) [3] or electrochemical approaches [4] are methods that can pattern steel injection molding inlays with nanostructures. However, they are not ready for mass production due to technological challenges like varying pattern morphologies or inhomogeneous film formation.

Here, we report on a novel approach for the nanotexturing of steel inlays for manufacturing automotive interior surfaces based on a combination of nanoimprint lithography (NIL) and an ion-based structuring process. The NIL produces the nanomask, while the latter transfers the nanopattern into a steel substrate. We used UNE 1.2083 steel in our experiments, which is widely used as a mold material in the injection molding of plastic parts.

Pillars with 450 nm period, 225 nm pillar diameter, and 120 nm pillar height were chosen as benchmark nanostructures and a respective master for NIL stamp manufacturing was produced by Interference Lithography on a 6” Si wafer. These pillars were obtained by NIL into AMONIL imprint resist on a 60nm thick Cr hard mask evaporated on the steel substrates (see fig.1). The removal of the imprint resist residual layer and the etching of the Cr hard mask were achieved by Reactive Ion Etching (RIE) using chlorine (Cl2) and fluoroform (CHF3) as etching gases, respectively.

Three different ion-based patterning techniques to transfer the nanopattern into the steel substrate were benchmarked: RIE, Reactive Ion Beam Etching (RIBE) and Ion Milling. RIE was carried out with a gas mixture of boron trichloride (BCl3) and chlorine (Cl2) as chemical etchants together with helium (He) as the physical etchant. This process failed in transferring the initial pillar pattern to the steel substrate. However, it did result in a nanotexture consisting of alloy components selectively revealed by the chemical etchants but without the targeted functionality.

RIBE with argon (Ar) ions led to a roughening of the substrate surface on the nm-scale . This patterning approach etches the steel to a certain degree, the selectivity of the Cr hard mask was not sufficient to transfer the pattern with high fidelity (see fig.2). The Ion Milling approach, also based on Ar ions,

demonstrated the highest potential for patterning the steel substrates. It led to a fully transferred pillar array in the steel with high pattern fidelity. The result is shown in the Transmission Electron Microscopy (TEM) image in Figure 4 and further corroborated by energy dispersive x-ray spectroscopy (EDX).

In conclusion, three different ion-based nanopatterning techniques for the transfer of nanostructures into steel substrates have been benchmarked. The Ion Milling approach has proven as the method of choice for manufacturing nanostructured steel injection molding inlays for automotive applications.

Parts of this work have been performed with financial support by the European Commission under the Horizon 2020 programme in the research project “SUN-Pilot” (Grant No. 760915).

[1] S. Milles et al., Applied Surface Science 525 (2020)
[2] L. Feng et al., Applied Physics A: Materials Science and Processing. 124 (2018)
[3] D. Wyn Müller et al., Sci Rep 10, 3647 (2020)
[4] S. Chen et al., Sci Rep 7, 5326 (2017)

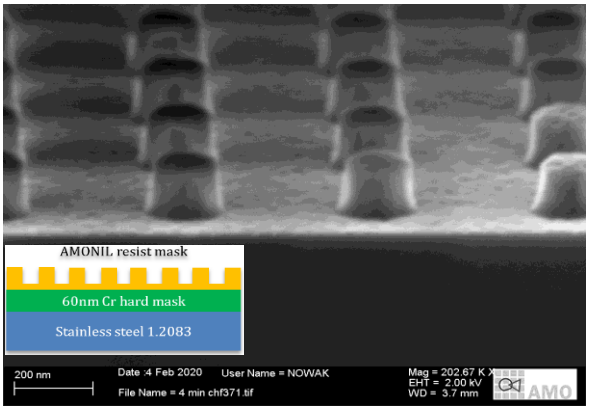

Figure 1. SEM image of the AMONIL pillar mask with the residual layer already being removed and the respective schematic of the mask layer stack.

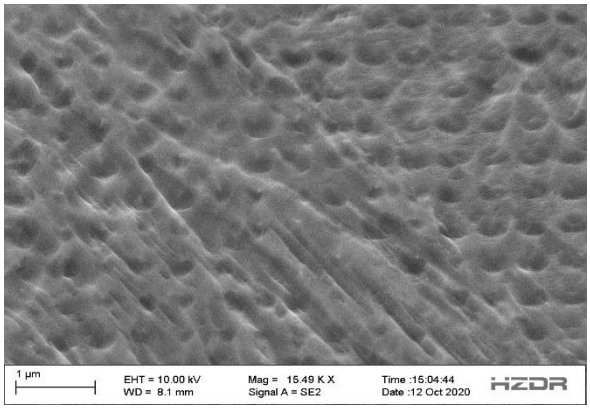

Figure 2. SEM image of the steel surface after the patterning approach by RIBE.

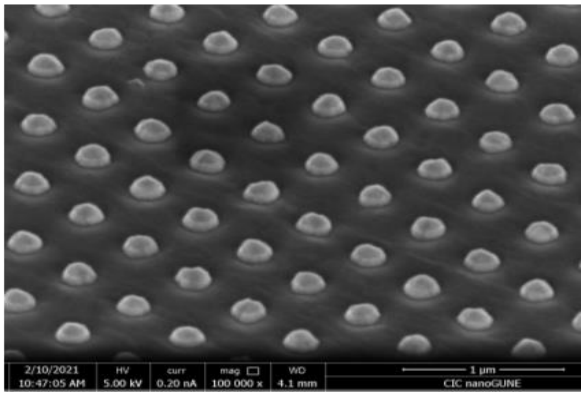

Figure 3. SEM image of the transferred nanopillar pattern in the steel substrate by Ion Milling.

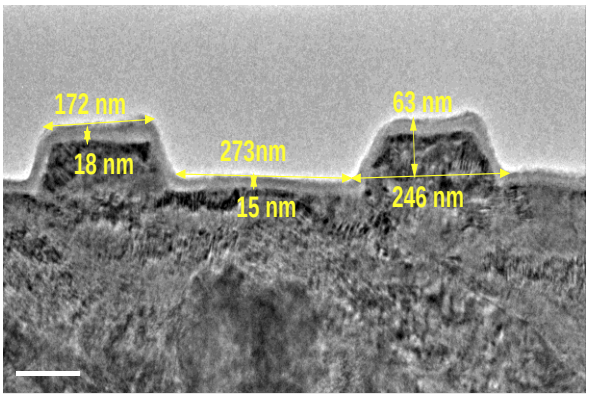

Figure 4. TEM cross section of the nanopillars in steel.

Development of Atomic Gold Decorated Polyaniline Derivative Electrodes toward Electrochemical Alcohol Sensing

Tomoyuki Kurioka, Keisuke Okamoto, Shohei Yoshida, Kengo Watanabe,
Chun-Yi Chen, Parthojit Chakraborty, Takamichi Nakamoto, Masato Sone, Tso-Fu Mark Chang

Tokyo Institute of Technology, Yokohama, 226-8503, Japan
e-mail: kurioka.t.aa@m.titech.ac.jp

Alcohol sensing is widely used in various areas ranging from health care to automobile safety because alcohols are common molecules observed in natural and commercial products. Alcohol sensors based on electrochemical reactions receive significan attention because of their easy operation, fast response, and high sensitivity [1]. The performance of electrochemical alcohol sensors is related to electrode materials. Among electrode materials, hybrid materials composed of atomic size gold clusters (denoted as Au_N, where N indicates the atomic size of the Au cluster) and polyaniline (PANI) are promising due to their good electrocatalytic activities derived from large specific surface area of Au_N [2,3]. PANI is a suitable supporting matrix of Au_N because of its large surface area, high electrical conductivity, and good stability [4]. Generally, the electrocatalytic abilities of the hybrid materials are affected by their morphologies and nanostructures, which are changed by chemical structures of supporting materials [4]. PANI derivatives, such as poly(*o*-methoxy aniline) (POMA) and poly(*o*-toluidine) (POT), are also known to serve as supporting matrices of noble metal nanoparticles because of their similar chemical properties to those of PANI [4]. Therefore, we envisage that Au_N-decorated PANI (denoted as Au_N/PANI) derivatives are also promising electrode materials for electrochemical alcohol sensing. In this presentation, the development of Au_N/PANI derivative electrodes (i.e., Au_N/PANI, Au_N/POMA, and Au_N/POT) and their electrocatalytic abilities for alcohol oxidation are reported.

PANI derivatives were prepared onto a platinum (Pt) disc electrode (ϕ = 3 mm) by electrochemical polymerization of corresponding monomers in HBF_4 aqueous solution. Au_N/PANI derivative electrodes (N = 1 or 2) were fabricated by atom-by-atom gold deposition [2,3]. Figs. 1 show an image of a flow cell used for this deposition process and its schematic procedure. Their electrocatalytic abilities were evaluated by performing cyclic voltammetry (CV) measurements for 1-propanol (1-PrOH) in KOH aqueous solution.

First, the electrochemical redox behavior of PANI derivatives was investigated by performing CV measurements in $HClO_4$ aqueous solution. Fig. 2 shows cyclic voltammograms for PANI derivatives. Although PANI derivatives exhibited different redox behaviors depending on their chemical structures, all of their voltammograms were reversible under the measured potential range, which indicated that PANI derivatives were also expected to serve as a stable supporting material as well as PANI.

Next, CV measurements for 1-PrOH were performed in KOH aqueous solution using Au_N/PANI derivative electrodes (N = 1 or 2). Figs. 3 show the obtained cyclic voltammograms. Their electrocatalytic abilities were compared by the oxidation peak current (I_p) observed around +0.15 V (vs. Ag/Ag^+). Au_1/POMA and Au_1/POT electrodes provided about two times greater I_p than Au_1/PANI, indicating that chemical structures of supporting material affected their electrocatalytic abilities. Decoration of PANI derivatives with Au_2 resulted in different trends depending on supporting materials. I_p of Au_2/POMA was almost the same as that of Au_1/PANI. On the other hand, I_p of Au_2/PANI and Au_2/POT were about two times greater than that of Au_1/PANI and Au_1/POT, presumably because of odd-even effects of Au_N [5].

In conclusion, we successfully proved the electrocatalytic abilities of Au_N/PANI derivatives for 1-PrOH oxidation. Au_2/POT was found to give higher electrocatalytic activity than other Au_N/PANI derivatives.

Acknowledgment
This work was supported by JSPS KAKENHI Grant Numbers JP22K20475 and JP21K04827.

References
[1] L. P. Fonseca et al., *Biosens. Bioelectron.* **2005**, *21*, 235–247.
[2] P. Chakraborty et al., *IEEE Sens. J.* **2020**, *20*, 12479–12487.
[3] T. Nakamoto et al., *Sensors* **2020**, *20*, 3640.
[4] J. Han et al., *Prog. Polym. Sci.* **2017**, *70*, 52–91.
[5] J. Janata et al., *J. Electrochem. Soc.* **2012**, *159*, P40–P43.

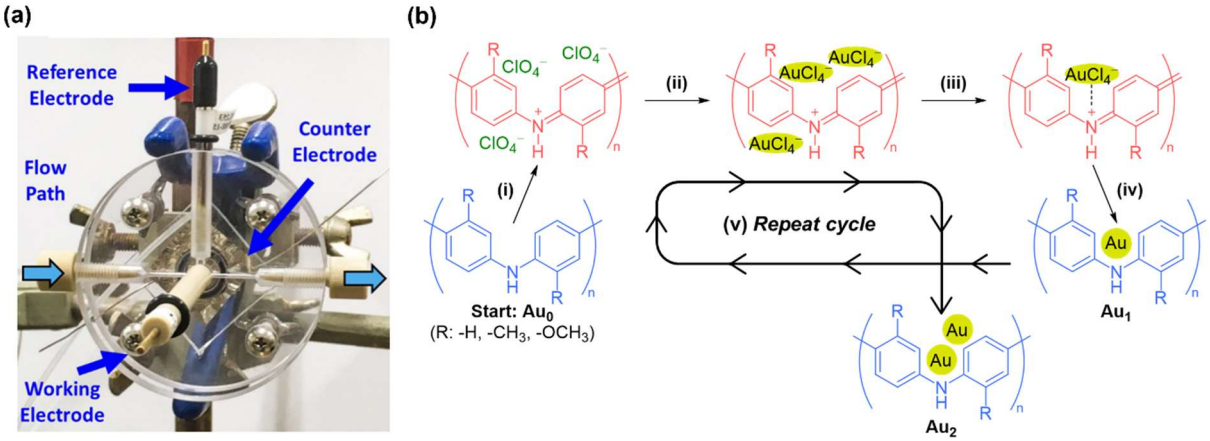

Figure 1. (a) A flow electrolysis cell used for the atom-by-atom gold deposition process. (b) Deposition of single (Au_1) or bi-atomic gold clusters (Au_2) onto polyaniline derivatives: (i) electrochemical doping in 0.1 M $HClO_4$, (ii) replacement of ClO_4^- with $AuCl_4^-$, iii) rinse with 0.1 M $HClO_4$, iv) reduction of $AuCl_4^-$ to Au atom (Au_1), and v) repeating the same process. +0.8 V (vs. Ag/Ag^+) was applied to the working electrode (WE) from process (i) to (iii), and −0.2 V (vs. Ag/Ag^+) was applied to the WE in process (iv).

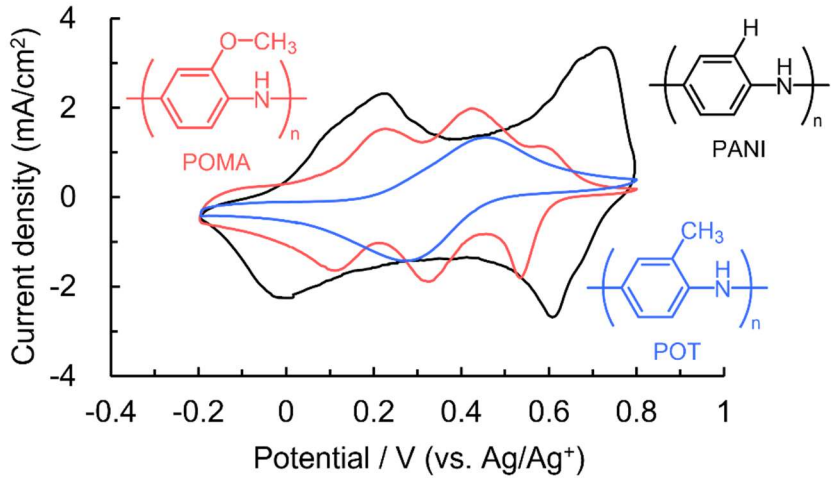

Figure 2. Cyclic voltammograms of PANI derivatives on a Pt disc electrode performed in 0.1 M $HClO_4$ at a scan rate of 50 mV/sec: PANI (black), POMA (red), and POT (blue). Fifth scans of CV measurements for each polymer are shown.

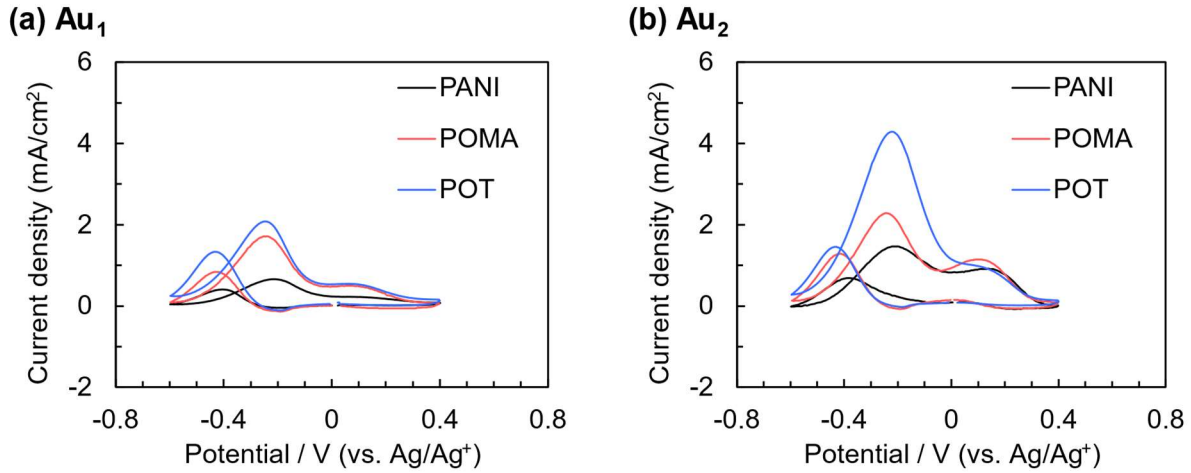

Figure 3. Cyclic voltammograms for 0.5 M 1-PrOH in 1 M KOH aqueous solution using Au_N ($N = 1$ (a), or 2 (b)) decorated PANI derivative electrodes at a scan rate of 50 mV/sec: PANI (black), POMA (red), and POT (blue). Tenth scans of CV measurements for each polymer are shown.

High-Response Ethanol Gas Sensor Based on $LaFeO_3/In_2O_3$ Composite

Ninghao Chu [a], Zhenyu Yuan [a]
[a] Northeastern University College of Information Science and Engineering, Shenyang, 110819, China
e-mail: yuanzhenyu@ise.neu.edu.cn

Ethanol is a common industrial material and also a symbol of alcohol driving, so it is necessary to effectively detect ethanol gas. In_2O_3 is a typical n-type semiconductor material, but its gas sensing performance still needs to be further improved. $LaFeO_3$, as a perovskite structured p-type semiconductor, has special physical and chemical properties and catalytic activity, which can be used to improve the gas sensing performance of gas sensors. Therefore, we prepared $LaFeO_3/In_2O_3$ composite by Hydrothermal method to obtain high-performance ethanol sensor. The innovation of this work is utilizing the catalytic performance of perovskite structured $LaFeO_3$ and forming $LaFeO_3/In_2O_3$ heterojunctions to significantly improve the response of In_2O_3 sensors, achieving high response detection of ethanol gas.

In this work, we firstly prepared pure $LaFeO_3$ using $La(NO_3)_3{\cdot}6H_2O$, $Fe(NO_3)_3{\cdot}9H_2O$, $C_6H_8O_7$ and PVP, prepared In_2O_3 using $In(NO_3)_3{\cdot}5H_2O$, CN_2H_4O and PVP as control groups (Sample1 and Sample2). Then, we add different mass amount $LaFeO_3$(0.02 g, 0.01 g, and 0.005 g) into the In_2O_3 hydrothermal reaction solution to prepare $LaFeO_3/In_2O_3$ composite (Sample3-Sample5).

The $LaFeO_3/In_2O_3$ sensor exhibits selectivity for ethanol gas at the optimal operating temperature of 220℃. The gas sensing performance of the In_2O_3 material composed by 0.01 g $LaFeO_3$ is the best, with a response of 147 to 100 ppm ethanol gas at the optimal operating temperature that is 2.8 times of the response of pure In_2O_3 sensor. The response of the sensor to other gases is all below 40, has positive selectivity. The lower limit of detection is 500 ppb. The response of Sample4 to ethanol gas at various concentrations is higher than that of other sensors. The 5 times response curve of the sensor to 100 ppm ethanol gas at the optimal operating temperature is same, it indicates that $LaFeO_3/In_2O_3$ composite has n-type semiconductor conductivity and continuity. The response of the sensor to 100 ppm ethanol gas at the optimal operating temperature for a month is higher than 120. The sensor has long-term stability. This indicating that $LaFeO_3/In_2O_3$ composite materials have potential application value in the detection of ethanol gas.

When $LaFeO_3/In_2O_3$ composite is exposed to ethanol gas, the ethanol molecule is adsorbed on the material surface and occurs redox reaction with the adsorbed oxygen. $LaFeO_3$ is a new type of catalyst material in the field of catalyst, which can effectively catalyze redox reactions. Furthermore, the heterogeneous junction formed between $LaFeO_3$ and In_2O_3 is another crucial factor affecting the sensing performance. Electrons flow from In_2O_3 to $LaFeO_3$, and holes move from $LaFeO_3$ to In_2O_3 form Fermi energy level, which would cause the formation of depletion layer. This increases the adsorption oxygen content on the surface and adsorption site for the ethanol gas, furtherly improving the response of the sensor.

[1] Wenbo Qin, Renze Zhang, et al., Perovskite-structured $LaCoO_3$ modified ZnO gas sensor and investigation on its gas sensing mechanism by first principle. Sensors and Actuators B: Chemical. 34 (2021) 130015.
[2] Xinhui Jin, Yanwei Li, Zhang B, et al., Temperature-dependent dual selectivity of hierarchical porous In_2O_3 nanospheres for sensing ethanol and TEA. Sensors and Actuators B: Chemical. 330 (2020) 129271.
[3] Kun Zhang, g, Shuaiwei Qin, et al., Ultra-sensitive ethanol gas sensors based on nanosheet-assembled hierarchical ZnO-In_2O_3 heterostructures. Journal of Hazardous Materials. 391 (2020) 122191.
[4] Thi To Nga Phan, Thi Tra My Dinh, et al., Hierarchically Structured $LaFeO_3$ with Hollow Core and Porous Shell as Efficient Sensing Material for Ethanol Detection. Sensors and Actuators B: Chemical. 345 (2022) 131195.

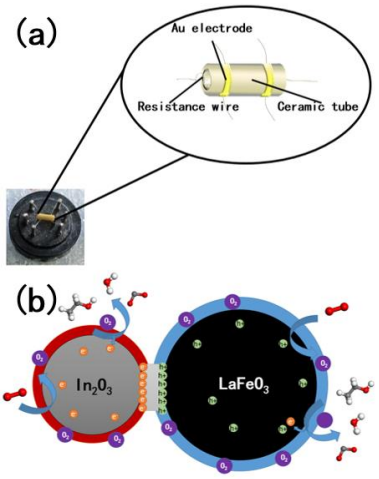

Figure 1. (a)Sensor structures. (b)Process diagram of redox reaction of ethanol molecules on $LaFeO_3/In_2O_3$ surface.

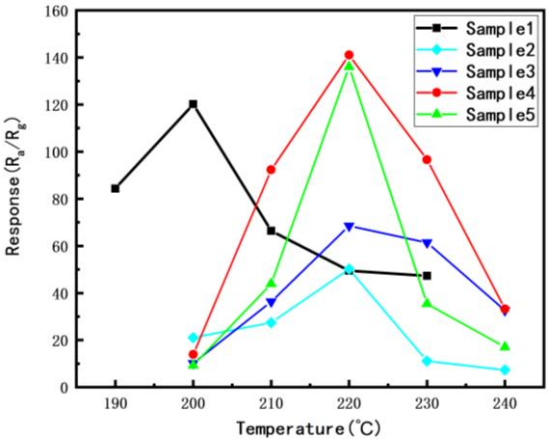

Figure 2. Response curve of the sensor to 100ppm ethanol gas at different operating temperatures

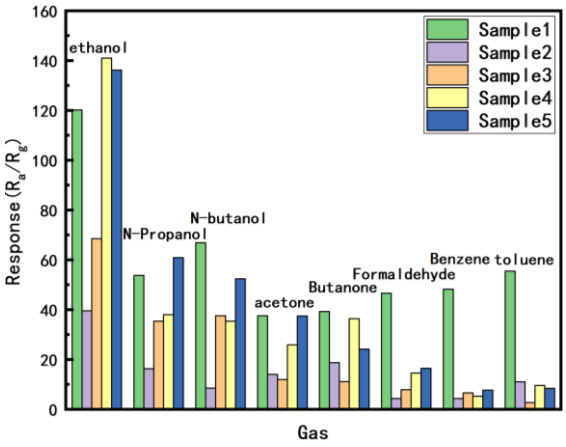

Figure 3. Histogram of sensor response to 100ppm different gases at optimal operating temperature.

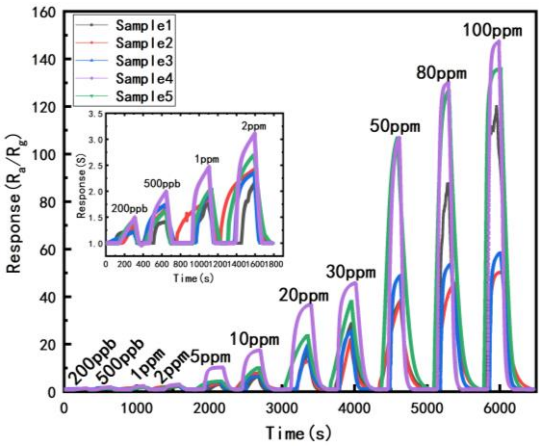

Figure 4. Response and recovery curve of the sensors to different concentrations of ethanol gas at optimal operating temperature.

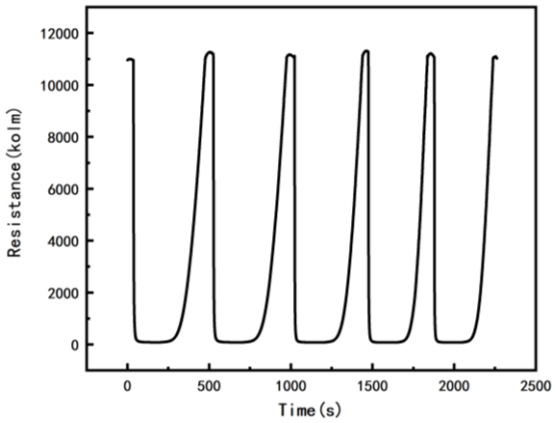

Figure 5. Continuity of Sample 4.

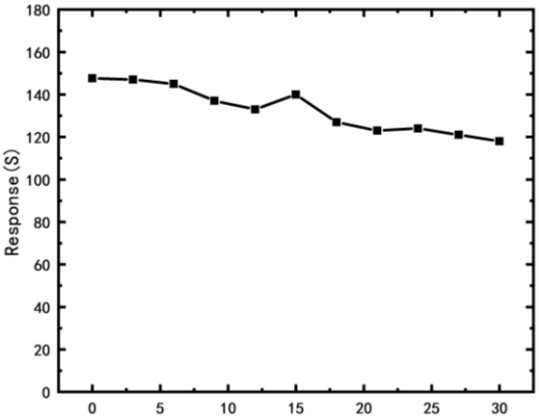

Figure 6. Stability of Sample4.

Spin valve effect in Fe_3GeTe_2/ZnO/Ni heterostructure with low resistance-area product

Whan Kyun Kim [a,b], Namgun Kim [a,b], Yong Ha Shin [c], and Woo Jong Yu [c*]

[a] Department of Semiconductor and Display Engineering, Sungkyunkwan University, Suwon 16419, Republic of Korea
[b] Semiconductor R&D Center, Samsung Electronics, Hwaseong 18448, Republic of Korea
[c] Department of Electrical and Computer Engineering, Sungkyunkwan University, Suwon 16419, Republic of Korea
e-mail: micco21@skku.edu

Two-dimensional (2D) van der Waals (vdW) magnetic materials have drawn extensive investigative interest since 2017 [1]. Various materials like $Cr_2Ge_2Te_6$, CrI_3, and Fe_3GeTe_2 have been examined, but Fe_3GeTe_2 stands out due to its perpendicular magnetic anisotropy and metallic properties [2]. This material exhibits superior compatibility with prevalent traditional magnetic 3d transition metals like Fe, Co, and Ni, making it more valuable for applications, especially spin valves. Yet, despite many studies on 2D materials-based spin valves, experimental research leveraging both typical ferromagnetic metal and 2D magnetic materials simultaneously in metal electrodes for spin valves remains scant. In addition, most studies employing materials such as h-BN, MoS_2, WSe_2, and InSe as tunnel barriers for Fe_3GeTe_2-based spin valves mainly target the enhancement of magnetoresistance (MR) [3-6].

For spin valves or magnetic tunnel junctions (MTJ) to operate efficiently and at high speed, both low resistance-area product (RA) and high MR are crucial. This study incorporates ZnO, a wide band gap semiconductor of the wurtzite structure, recently investigated as a tunneling barrier for low RA-based MTJ, between Fe_3GeTe_2 and Ni to determine the spin valve effect in the low RA. Ni deposited via e-beam evaporation at 10^{-7} Torr pressure was covered with ZnO through atomic layer deposition and placed mechanically exfoliated Fe_3GeTe_2 on the ZnO to fabricate Fe_3GeTe_2/ZnO/Ni heterostructure spin valve device (see Figs 1). We conducted all Fe_3GeTe_2-involved device fabrication steps in an argon-filled glove box to circumvent oxidation. Due to the perpendicular and in-plane magnetic anisotropy of Fe_3GeTe_2 and Ni, respectively, the stray field around the Ni electrode initiates an in-plane spin direction shift in Fe_3GeTe_2 within near zero magnetic field region (see Figs 2). Moreover, when an adequate magnetic field is introduced, it prompts an extra MR change as it fully alters the spin direction of Fe_3GeTe_2. The spin valve demonstrates a MR of 15.6 % at a RA of 37.6 $k\Omega/\mu m^2$ at 2 K (see Figs 3). Our device exhibits an RA three times smaller than the Fe_3GeTe_2/InSe/Fe_3GeTe_2 spin valve reported in a previous study, while achieving a comparable MR [4]. Our results unveil the potential of vdW layered magnetic material as a ferromagnetic electrode in conventional MTJs.

[1] M. Koperski et al., Nat. Nanotechnol. 14 (2019) 408-419.
[2] Y. Deng et al., Nature 563 (2018) 94-99.
[3] L. Zhou et al., Infomat 5 (2022) e12371.
[4] W. Zhu et al., Adv. Mater. (2021) 2104658.
[5] K.-H. Min et al., Nat. Mater. 21 (2022) 1144-1149.
[6] H. Lin et al., ACS Appl. Mater. Interfaces 12 (2020) 43921–43926.

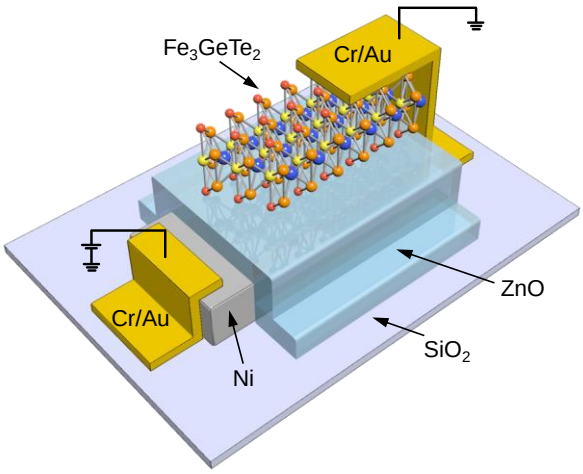

Figure 1. Schematic diagram of vertically stacked Fe_3GeTe_2/ZnO/Ni heterostructure spin valve

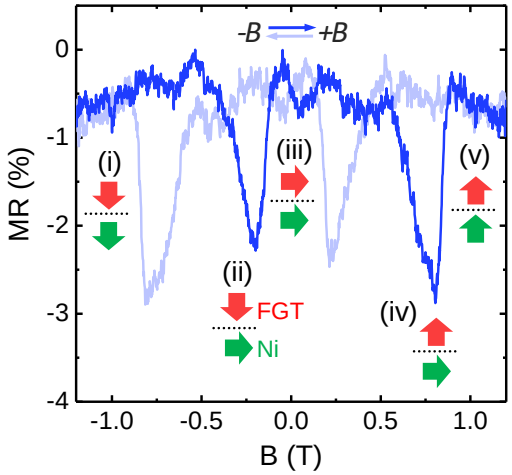

Figure 2. Spin valve effect of Fe_3GeTe_2/ZnO/Ni heterostructure. MR curves of the junction measured at the fixed voltage of 5 mV at 2 K. The blue and light blue horizontal arrows indicate the sweeping directions of the magnetic field. The red and green arrows denote the magnetization alignment directions of the Fe_3GeTe_2 and Ni, respectively.

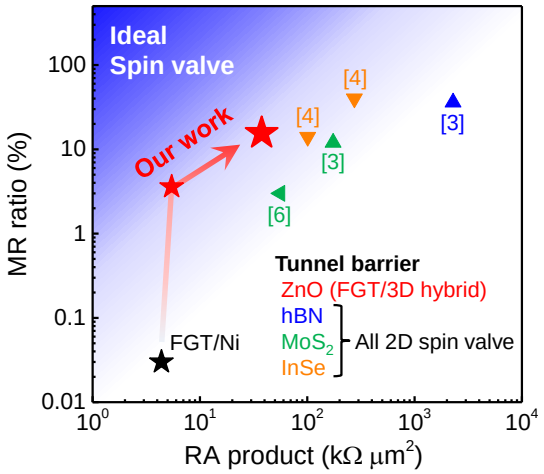

Figure 3. Comparison of RA product and MR ratio of our devices with those of Fe_3GeTe_2-based spin valves from previous studies.

4D printing of soft responsive polymer microstructures

Marcin Piekarczyk[a], Daniel Maher[a], Yekaterina Tskhe[b], Larisa Florea[b], Colm Delaney[b], Ada-Ioana Bunea[a],
[a] DTU Nanolab, Technical University of Denmark, Kongens Lyngby, 2800 Denmark
[b] School of Chemistry & AMBER, Trinity College Dublin, Dublin, 2 Ireland

e-mail: adabu@dtu.dk

Hydrogels have gained tremendous attention in several fields across the biomedical sector due to their excellent biocompatibility, water absorption capacity, stimuli responsive behaviour and good mechanical properties [1]. Those characteristics make them a promising material for various applications. For example, microrobotic devices are innovative tools, capable of executing a handful of different tasks, including chemical sensing [2, 3]. Efficient chemical sensing is required across different applications in research and industry related fields and the ability to respond to different pH levels on the microscale opens many opportunities for successful screening and detection of chemicals and chemical reactions. Another area where hydrogels are promising is the fabrication of biomimetic cell scaffolds, which after surface functionalization can mimic human cell membranes [4]. This lays a solid foundation for future research in biomedical applications [5].

Traditional hydrogel fabrication methods often lack the capability to create complex 3D geometries and functional dynamic behavior required for successful applications. 4D printing, a new generation of additive manufacturing, has emerged as a promising approach to overcome these limitations, creating material systems capable of changing their shape, structure or functions directly off the printing bed. With recent breakthroughs in micro 3D printing technologies, such as two-photon polymerization (2PP), the creation of microstructures has advanced significantly [5]. Combining 4D printing and the 2PP technique, new possibilities emerge not only in what we can print, but also in what we can make those prints do.

Our study demonstrates the potential of 4D printing of hydrogels, using a Nanoscribe Photonic Professional GT+ 3D printer using the 2PP technique. Several complex microstructures were fabricated and characterized in terms of material shape change of the custom hydrogel in aqueous solutions with different pH levels. The acrylate based photoresin for 4D printing was mixed on site, according to a custom recipe. Microrobots with different designs were fabricated with a sweep of printing parameters, to determine under which conditions chosen material is suitable for obtaining stable microrobotic scaffold together with sensing element in one-step procedure. We focused on examing influence of laser power and scan speed, corresponding to varying the exposure dose and hence the material's degree of croslinking (**Fig. 1**). The obtained microrobotic scaffolds are slightly deformed, which calls for further print parameter optimization, or using a hard polymer material for improved structure stability. In addition, a range of biomimetic cell structures was fabricated to determine if the soft hydrogel material could be used for further research in the biomedical field (**Fig. 2**). The pH actuation test of 4D printed structures was performed in a batch system by exposing simple micron scale cylinders and cuboids to a drop of d aqueous solutions with different pH levels in a cycle, starting from dry state, following through pH ~6.5, pH ~2 and pH ~13. The shape change behaviour was investigated using optical microscopy and the swelling degree was determined using ImageJ software by comparing the structure dimensions between dry and wet stage at different pH levels (**Fig. 3**). The 4D printed hydrogel material expresses a reversible shape change behaviour between the dry and wet states. Across different pH levels, the structures exhibit swelling behaviour, expanding up to 40% in pH ~13 and 15% pH~2, which makes a noticeable change that can be visually observed while being exposed to external stimuli.

To conclude, we fabricated hydrogel microstructures by 2PP 4D printing and characterized their response to different pH levels. Such hydrogel elements will further be incorporated into e.g. multimaterial microrobots.

[1] Mantha et al., *Materials* 12. (2019) 12203323
[2] A.-I. Bunea & R. Taboryski, *Micromachines* 11 (2020) 1048.
[3] A.-I. Bunea et al., *Adv. Intell. Syst.* 3 (2021) 2000256
[4] D.-S. Rovira et al., *Mater. Des.*201. (2021) 109486
[5] A.-I. Bunea et al., *Micro* 1 (2021) 164-180

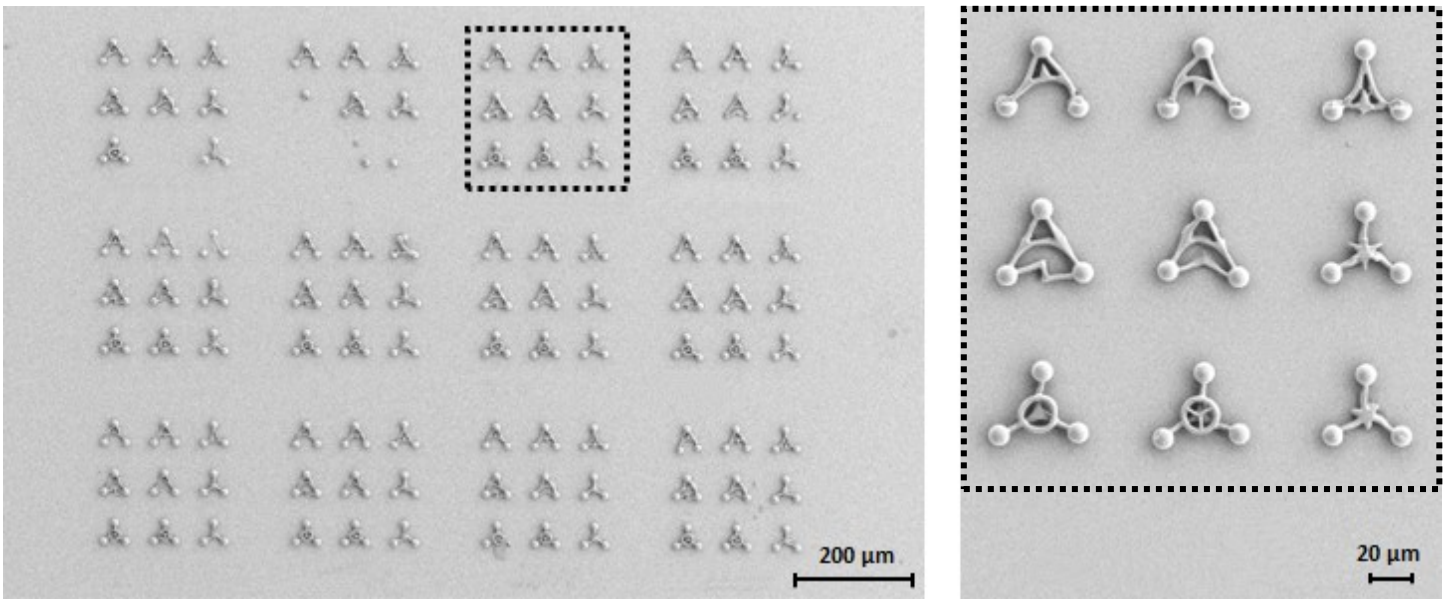

Figure 1. SEM images of microrobots using different printing parameters (laser power and scan speed).

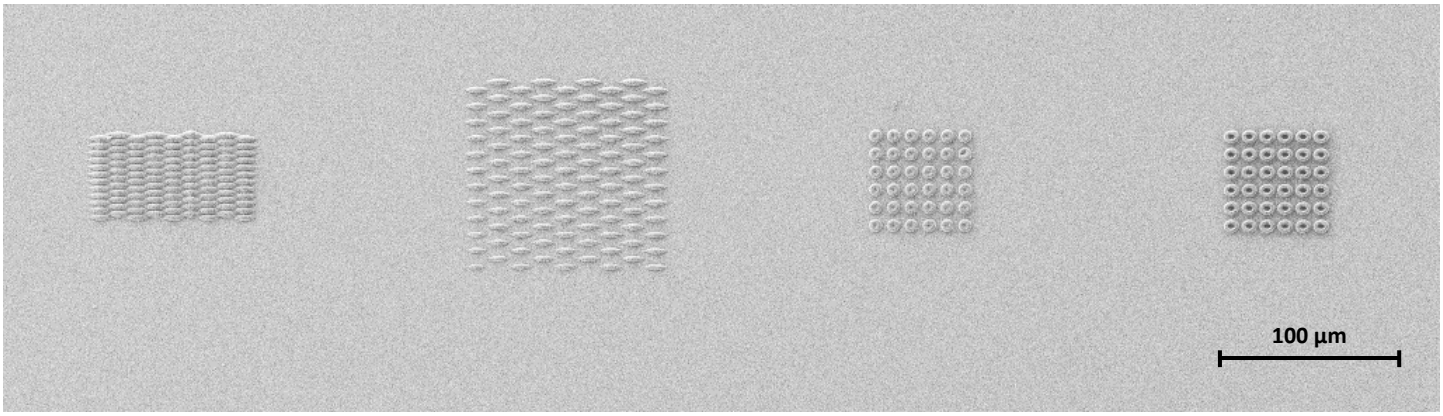

Figure 2. SEM images of fabricated scaffolds of smooth muscle cells (left) and red blood cells (right).

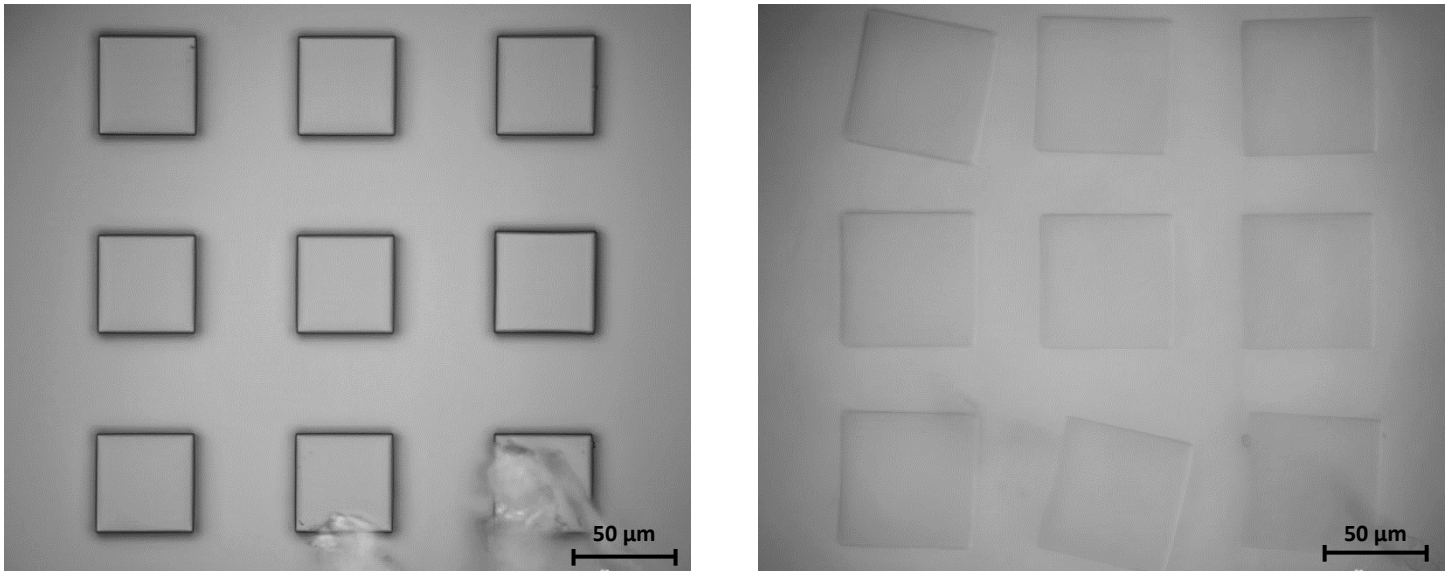

Figure 3. Optical microscopy images showing an example of an actuation swelling test in aqueous solution: left – pH ~6.5, right – pH ~13.

Lowering dissipation in Electro-Optomechanical resonators for quantum transducing RF to optical signals

E. Serra [a,b], M. Bonaldi [c] , A. Borrielli [c], G. di Giuseppe [d,e], N. Malossi [d,e], B. Morana [b], R. Natali[d,e], P. Piergentili[d,e], P.M. Sarro[b], D. Vitali[d,e]

[a] Istituto Nazionale di Fisica Nucleare, TIFPA, 38123 Povo (TN), Italy
[b] Dept. of Microelectronics and Computer Engineering /ECTM/EKL, Delft University of Technology, Feldmanweg 17, 2628 CT Delft, The Netherlands
[c] Institute of Materials for Electronics and Magnetism, Nanoscience-Trento-FBK Division, 38123 Povo, Trento
[d] Physics Division, School of Science and Technology, University of Camerino, I-62032 Camerino (MC), Italy
[e] INFN, Sezione di Perugia, 06123 Perugia (PG), Italy

e-mail: enrico.serra@tifpa.infn.it

Optomechanics with nano/micro silicon/silicon nitride resonating devices [1] is a growing field for the detection of extremely weak signals. The domain of application of these devices ranges from fundamental physics experiments to the search for quantum gravity effects [2] or quantum technology applications. In fact, these devices can be functionalized with metallization and used as a testbed for exploring new ways of implementing quantum communication protocol [3]. For instance, in a quantum computer based on superconductive qubits, quantum information is manipulated within an ultra-cryogenic superconductive cavity and then transmitted through high-efficiency optical fibers to prevent the decoherence of the quantum state. The mechanism involved in the conversion process is based on the capacitive modulation of the microwave field by the displacement field of the nanomembrane that is in turn dispersively coupled to a high-finesse Fabry-Pérot optical cavity. This means that electromagnetic energy can flow in two directions between the LC resonant circuit working at the radio frequency and the optical cavity read out by a homodyne detection scheme.

Our Electro-Optomechanical (EO) resonator (see Fig.1) is a nano/microfabricated device based on a stressed LPCVD silicon nitride nanomembrane with a titanium nitride conductive layer used as the floating armature of a capacitive element. To preserve the ultra-high mechanical quality factor of the resonating part of the device, the membrane is supported by an on-chip mechanical filter stage that shields the recoil losses originating from the vibrations of the membrane [4]. This silicon filtering stage is developed by double-side bulk micromachining based on the Bosch process and is also effective in reducing mechanical loss due to the coupling with the supporting wafer. Intrinsic losses are reduced by selective patterning the metallization over the membrane and taking care of the cleaning at the device edge with proper wet chemicals (see Fig.2).

In this contribution, we describe the design and fabrication of the mechanical resonating part of the Electro-Optomechanical resonator. The characterization of the mechanical Q-factor by a ring-down interferometric measurement (see Fig.3) demonstrates that the oscillator reaches quality factors of more than one million in the MHz range inside a vacuum chamber (Table 1). The device can be effectively assembled with any read-out electrode and potentially used to transduce RF weak classical signals in a Nuclear-Magnetic-Resonace (NMR) apparatus. Currently, the system is optimized to be embedded into the optical cavity for the sympathetic ground state cooling of an LC resonating circuit [5].

[1] E. Serra et al., Journal of Applied Physics 130, 064503 (2021)
[2] M. Bawaj, C. Biancofiore, M. Bonaldi, et al., Nature Commun. 6 (2015), 7503.
[3] Andrews, R., Peterson, R., Purdy, T. et al., Nature Phys. 10 (2014), 321–326
[4] A. Borrielli et al., Phys. Rev. B 94, 121403
[5] N. Malossi et al., Phys. Rev. A 103 (2021), 033516

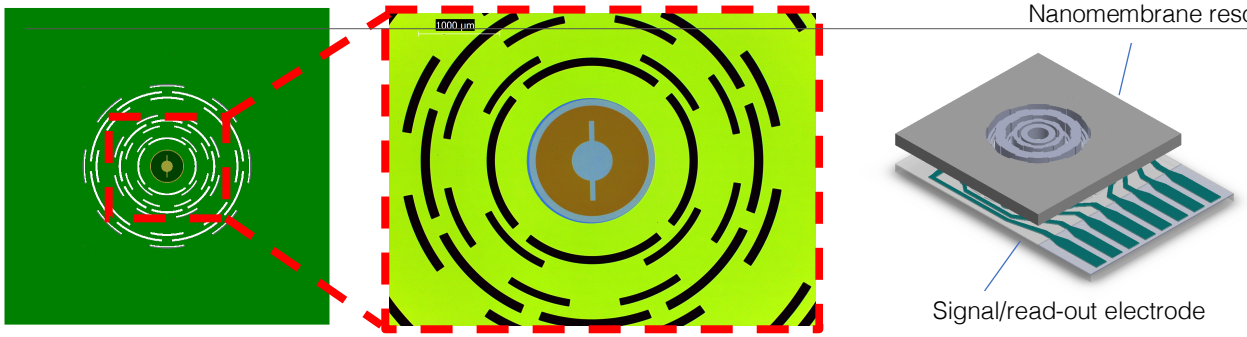

Figure 1. (left) The front side of the nanomembrane resonator chip with a detailed view of the insulation stages, the silicon nitride membrane, and the floating Titanium Nitride electrode (optical image); (right) The components of the EO device: nanomembrane resonator chip and signal/read-out electrode.

.

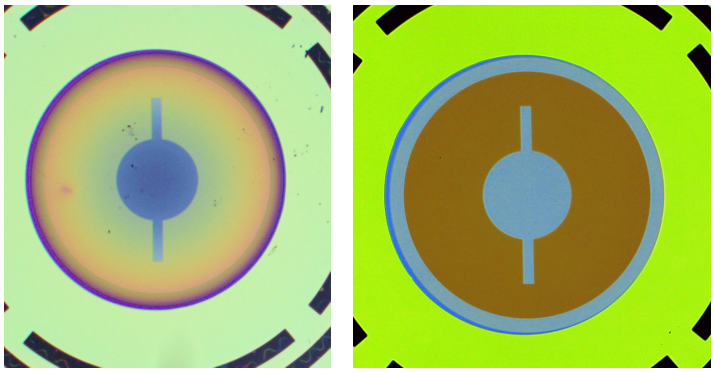

Figure 2. Image of the nanomembrane and the nanomembrane resonator before (left) and after (right) HF release & Isopropyl acid/DI water cleaning.

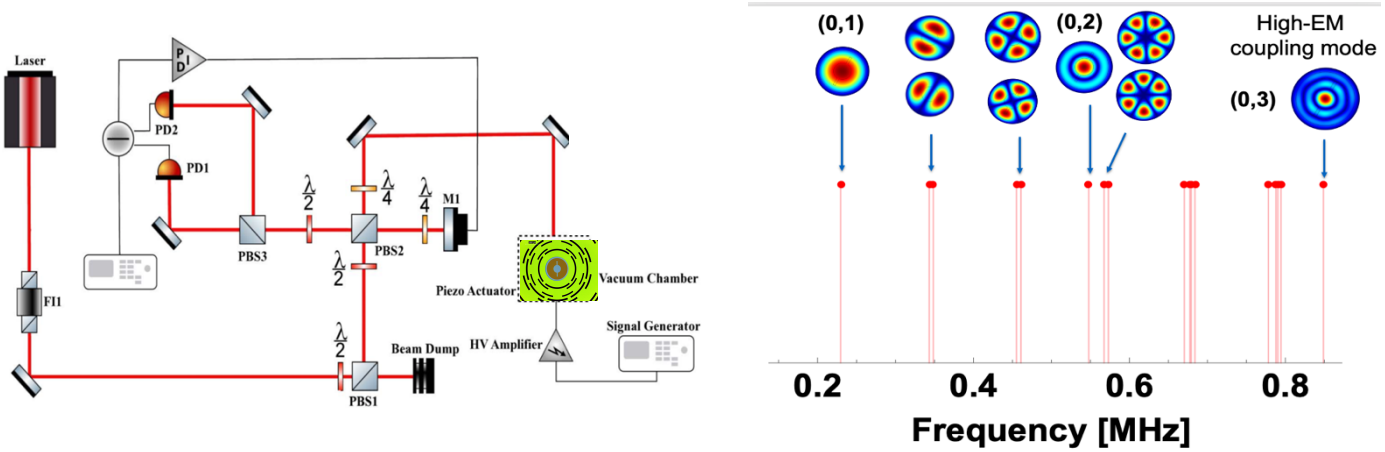

Figure 3. Image of the optical setup for the characterization of the mechanical Q-factor (left) and resonant modes of the membrane in the range [0-900 kHz] (right).

Modal index	Frequency [MHz]	Q-factor (10^6)
(0,1)	0.293	2
(0,2)	0.545	5

Table 1. Measured Q-factor at room temperature by the interferometric setup (shown in Figure 3) for two axisymmetric modes.

2

Atomic Pd_xAu_y Clusters Decorated Polyaniline for Electrochemical Sensing of 1-Propanol

Shohei Yoshida, Keisuke Okamoto, Tomoyuki Kurioka, Chun-Yi Chen, Parthojit Chakraborty, Takamichi Nakamoto, Masato Sone, Tso-Fu Mark Chang
Tokyo Institute of Technology, Kanagawa, 226-0026, Japan
E-mail: yoshida@ames.pi.titech.ac.jp

Electrochemical sensors are capable to fast-detect chemicals with a high sensitivity at a low cost. By these advantages, electrochemical sensors are promising for detections of biomolecules, such as glucose, dopamine, uric acid, etc. The catalytic electrode in an electrochemical sensor is composed of noble metals, such as Au and Pd, and a supporting material. Polyaniline (PANI) [1] is an ideal supporting material for noble metal clusters because of its good electrical conductivity, high stability, large active surface area, and simple preparation process. Recently, PANI decorated with atomic-level noble metal clusters is reported to show distinct catalytic activity for the electrochemical oxidation of alcohols [1]. In addition, the preparation of heterogeneous atomic noble metal clusters is attracting attention as a way to obtain even higher catalytic activity than that of homogeneous atomic metal clusters. In this presentation, the effects of the number of the metal atoms and the sequence of the atomic level deposition step in the atomic level noble metal clusters on the catalytic activity in electrochemical sensing of 1-propanol (1-PrOH) are reported.

Fig.1 shows the outline of the experiment. The PANI was deposited on a Pt disk electrode (ϕ = 3 mm) by electrochemical polymerization in a 2 M HBF_4 aqueous solution containing 0.1 M of aniline. Then, the PANI deposited electrode was decorated with mono-atomic, bi-atomic, tri-atomic, or tetra-atomic noble metal clusters. The atomic noble metal clusters are denoted as Pd_xAu_y, where x represents the number of Pd atoms in a cluster and y is the number of the Au atoms. The catalytic activity for the electrochemical sensing of 1-PrOH was evaluated by cyclic voltammetry (CV) measurements with an aqueous solution containing 0.5 M 1-PrOH and 1 M KOH.

The CVs are shown in Fig. 2. For atomic metal clusters composed of only Pd, the catalytic activity was higher for the Pd_2 and Pd_4 decorated PANI electrodes than those of the Pd_1 and Pd_3 decorated PANI electrodes, which revealed the odd-even pattern effect as reported in a previous study [2]. Next, for bi-atomic metal clusters, the catalytic properties of heterogeneous bi-atomic metal clusters decorated PANI electrodes were lower. On the other hand, for tri-atomic and tetra-atomic metal clusters, the catalytic activity was higher for heterogenous atomic metal clusters.

Acknowledgment:
This work was supported by JSPS KAKENHI Grant Number JP21K04827 and JP21H01668, and the Cooperative Research Project of Research Center for Biomedical Engineering.

References:

[1] A.P. Jonke, J.L. Steeb, M. Josowicz, J. Janata, *Catal Lett* **2013**, *143*, 531–538.
[2] Y. Ito, T.F.M. Chang, Y.A. Chien, C.Y. Chen, P. Chakraborty, T. Nakamoto, M. Sone, *Electrochem* **2020**, 1, 3941–399.

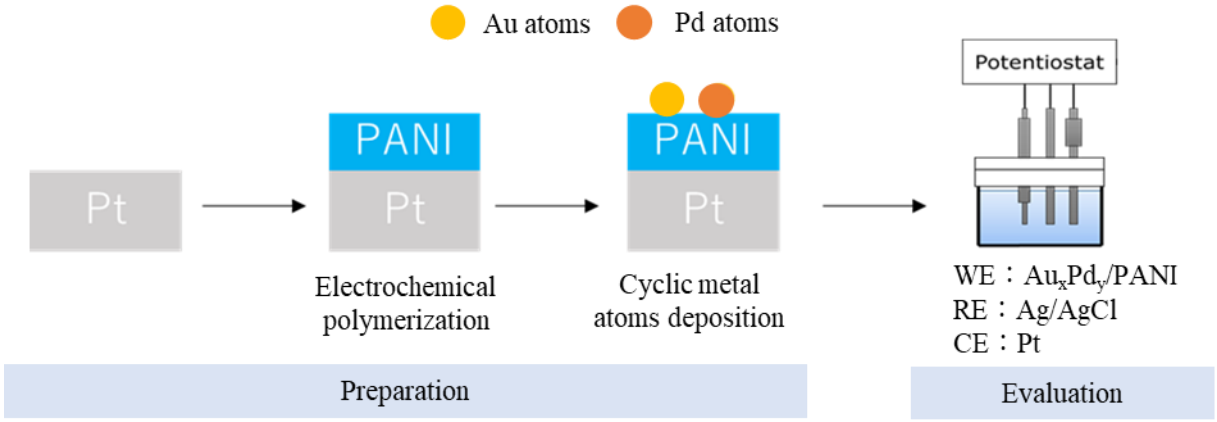

Fig. 1. Outline of the atomic metal cluster decoration process.

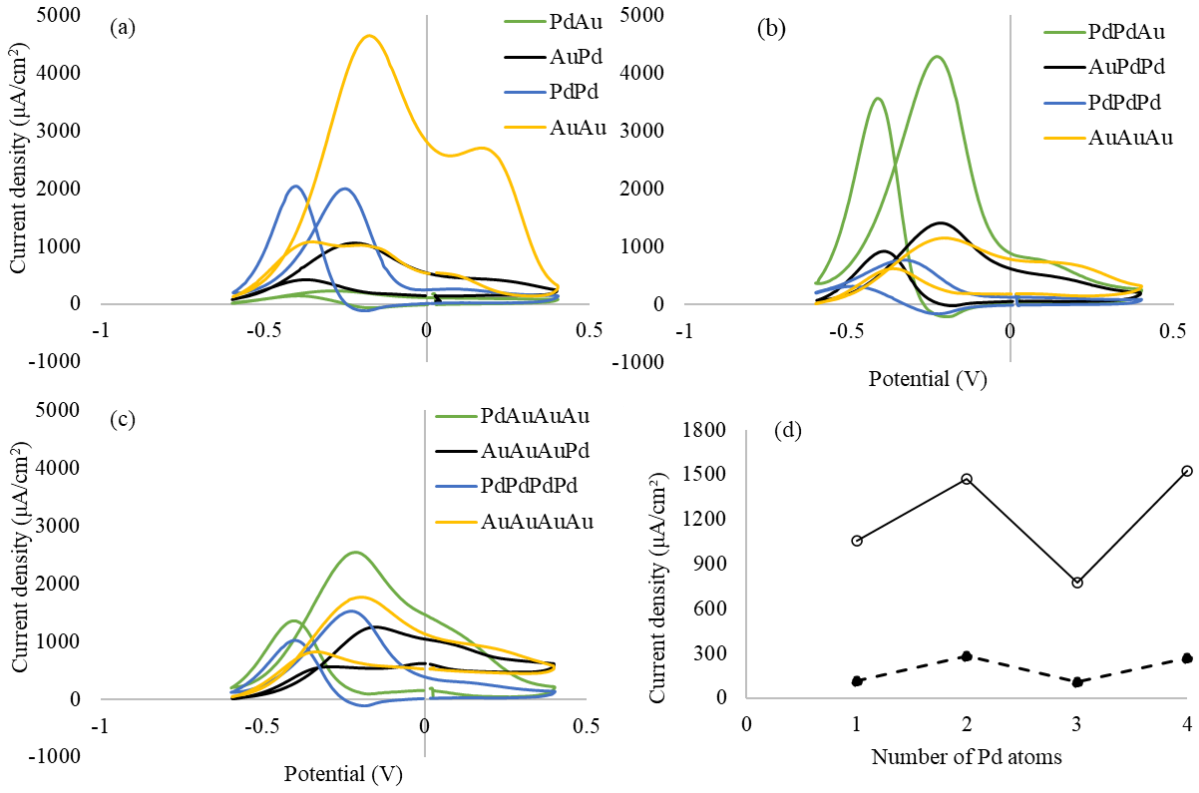

Fig. 2. CVs for (a) bi-atomic, (c) tri-atomic, and (d) tetra-atomic metal clusters. (d) A summary of peak current densities for atomic pure Pd clusters, and the solid line shows the 1st oxidation peak and the dashed line shows the 2nd oxidation peak.

Fabrication and Characterization of Plasmon-Active Infra-Red Enhanced Micromembranes for Gas Diffusion Studies

K. Srivastava [a], J.J.A. Lozeman [a], A. van den Berg [a], W. van der Stam [b], M. Odijk [a]

[a] BIOS Lab on Chip Group, University of Twente, Enschede, 7522 NB, The Netherlands
[b] Inorganic Chemistry and Catalysis, Universiteit Utrecht, Utrecht, 3584 CG, The Netherlands
e-mail: k.srivastava@utwente.nl

Abstract:
Surface Enhanced Infra-Red Absorption Spectroscopy (SEIRAS) is an emerging tool for analytical sensing.[1] It has been applied to applications such as catalysis [2], biosensing [3] and studying molecular transport [4]. A typical configuration used in all these systems is the lithographic fabrication of periodic and resonantly tuned nanostructures (ex. nanoslits) supported on dielectric substrates. In this work however, we report an innovative method to fabricate plasmon-active porous micromembranes with an end use in applying them for monitoring gas diffusion. Here, the porosity of the membrane is generated by completely etching of the fabricated nanoslits. To optimize the fabrication process flow, we use and compare two different lithography techniques; electron beam lithography (EBL) and mask-less laser writing (MLW). The membranes are fabricated by etching a 500 nm thick Si-rich nitride (SiRN) layer and are made plasmon-active by sputtering 50 nm gold (Au). The fabrication is carried out by first etching resonantly tuned nanoslits on a SiRN coated Si substrate. A backside KOH etch is then performed to suspend the membrane by removing the excess silicon. A schematic of the fabrication process flow can be seen in Figure 1.
Compared to MLW, EBL offers the advantage of fabricating nanostructures with nanometer precision, with the smallest feature size in the order of 10-100 nm. However, commonly used EBL photoresists are not suitable for fabrication of thick membranes, due to their inability to resist long etching times. MLW however, utilizes standard ultra-voilet photoresists which are durable during long etching steps. MLW also takes only 20 mins to write a pattern design which takes approximately 3 hours with EBL. The only negotiable drawback with MLW is the ability to fabricate nanostructures with the smallest feature size in the range of 500-600 nm. It is visible from the scanning electron microscopy (SEM) image in Figure 2(b) that MLW has more rounding at the edges of the nanoslits as compared to EBL fabricated nanoslits (Figure 2(a)). Figure 2(c) shows the titled SEM view of the micromembrane fabricated with MLW where the complete etching of the SiRN membrane can be seen. A comparative summary of the differences between the two techniques can be found in Table 1.
Keeping in mind the end application, the SEIRAS plasmonic activity of the SiRN membranes is simulated using a finite-difference time-domain (FDTD) software. Figure 3(a) shows the spectral tuning of the membrane that can be achieved by fabricating different slit lengths. The results obtained are also compared to simulations of standard SEIRAS substrates found in literature.[1] Additionally, the simulated enhancement of the porous Au-SiRN membranes can be found in Figure 3(b). It can be clearly seen that the localized sensitivity arises from the pores at the edges of the Au/SiRN interface. With our work, we show the innovative capability to fabricate plasmonic-active SEIRAS micromembranes with the potential to be applied to gas sensing applications. For this we have optimized the SiRN etching process to fabricate porous membranes using MLW lithography.

References

[1] C. Huck *et al.*, 'Gold nanoantennas on a pedestal for plasmonic enhancement in the infrared', *ACS Photonics* (2015), 2, 4, 497–505.
[2] M. Moradzaman and G. Mul, 'Infrared Analysis of Interfacial Phenomena during Electrochemical Reduction of CO2over Polycrystalline Copper Electrodes', *ACS Catal* (2020), 10, 15, 8049–8057.
[3] X. Hui, H. Zhou, D. Li, D. Hu, C. Yang, H. Pan, M. Chen and X. Mu. 'Surface-Enhanced Infrared Absroption-Based Biosensor and its application to DNA identification'*2020 IEEE 33rd International Conference on Micro Electro Mechanical Systems (MEMS)*. IEEE, (2020).
[4] H. Chen, S. Zhang, K. A. Miller, and P. V. Braun, 'Autonomic Molecular Transport for Ultrasensitive Surface-Enhanced Infrared Absorption Spectroscopy', *ACS Appl Polym Mater* (2020), 2, 9, 3929–3935.

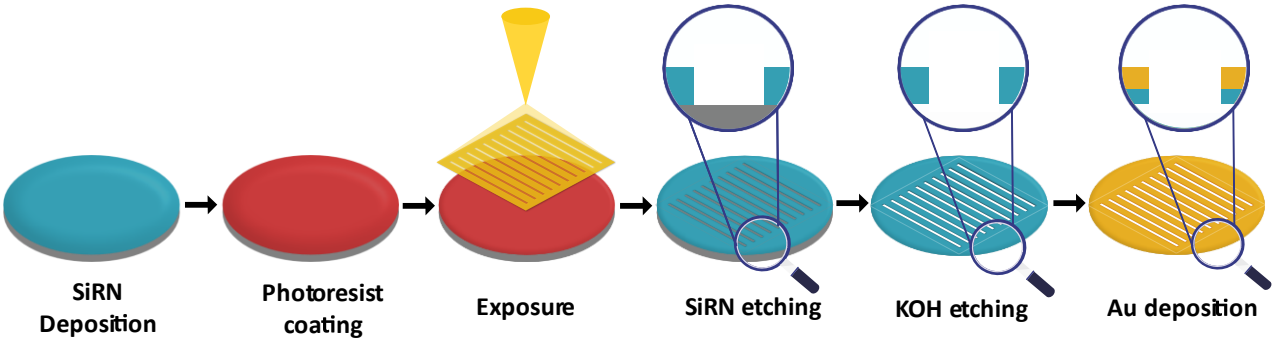

Figure 1: Fabrication process flow for plasmon-active SEIRAS porous micromembranes.

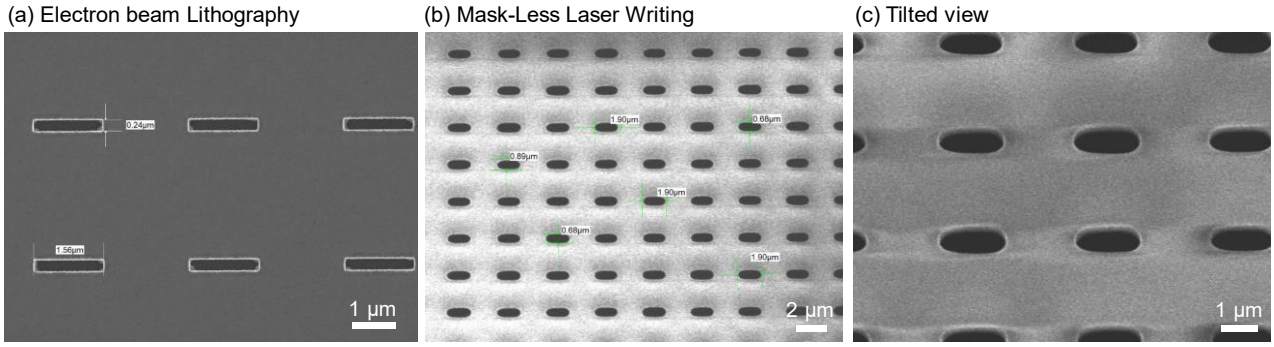

Figure 2: (a) Nanoslits - EBL (l = 1500 nm, w = 230 nm), (b) Micromembrane - MLW (l = 1900 nm, w = 680 nm), (c) Tilted (20˚) and zoomed view of (b), SiRN micromembrane thickness is 500 nm.

Table 1: Comparison of EBL and MLW for SiRN micromembrane fabrication

Characteristic	Electron Beam Lithography	Mask-less Laser Writing
Resist used	Poly(methyl methacrylate)	Olin Oir -17
Resist thickness	255 nm	1.7 µm
Minimum feature size	~ 10 – 100 nm	~ 500 – 600 nm
Writing time	3 hours	20 mins
Suitable for SiRN etching	No	Yes
Sharp features	Yes	No (rounded edges)
Dose	10,000 kV	240 mJ
Exposure	Electron beam	375 nm laser
Developer	MIBK:IPA	OPD 4262

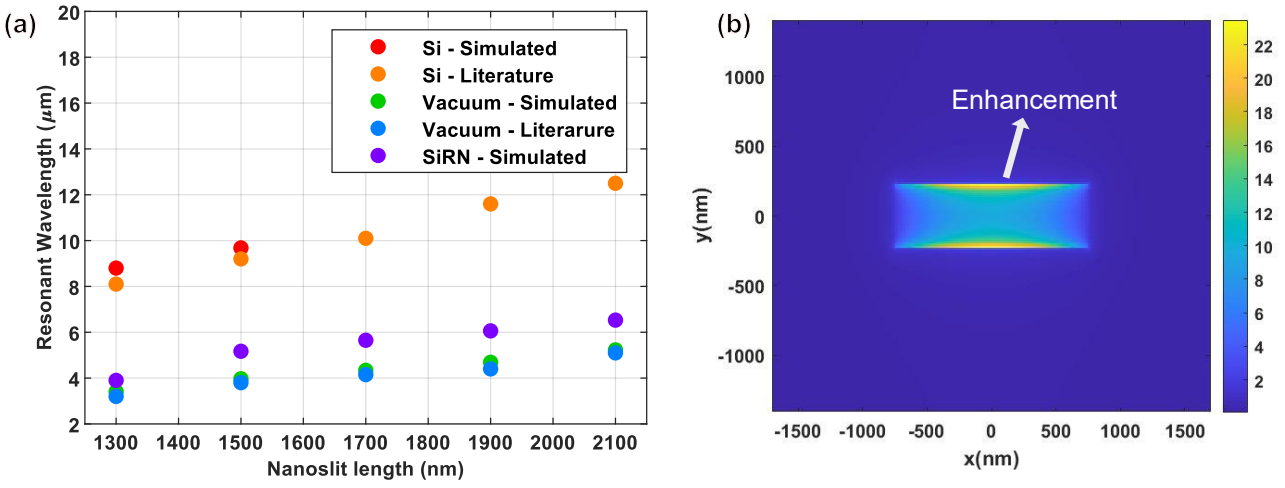

Figure 3: (a) Spectral tuning of nanoslits and comparison to values found in literature, (b) FDTD simulated electric field enhancement ($|E|/|E_o|$) of SIRN micromemebrane (l = 1500 nm, w = 450 nm)

Sensor technology development embedding nanoparticles

Michelle Cedeño Mata [a], Ana Coloma Velez[a], Ramon Bragos [a], Manuel Domínguez-Pumar [a], Sandra Bermejo [a]
[a] Universitat Politècnica de Catalunya, Barcelona, 08034, Spain
e-mail: kristel.michell.cedeno@upc.edu

This study presents the development and analysis of an encapsulated version of the optimized novel capacity proximity sensor (CPS) based on silicon dioxide nanoparticles (SiO_2) and sodium chloride (NaCl) shown in [1]. A comparison of the sensing performance between the encapsulated and non-encapsulated versions of the proposed CPS is reported. This work introduces for the first time an easy, fast and economical approach for developing novel CPSs using SiO_2 nanoparticles and NaCl as the sensing layer and PDMS as the encapsulation layer.

Fig 1 illustrates the fabrication process of the electrosprayed nanoparticles interdigitated capacitive proximity sensor (ENICPS) using SiO_2 nanobeads and NaCl. It involves aluminium interdigitated electrode fabrication, the deposition by electrospray of a solution containing 295nm SiO_2 nanoparticles and NaCl, as described in [1-3], and the PDMS deposition through spin-coating with a curing time of 30 minutes at 70ºC. The sensing performance of the ENICPSs is assessed using electrical impedance spectroscopy (EIS) at room conditions, ranging from 1Hz to 200kHz, with distances between the ENICPSs and the material under test (MUT) ranging from 5-140mm. Fig 2 displays the EIS measurements, highlighting the effect of the PDMS layer on the sensing performance. Fig 3 depicts the calculated impedance, phase, and capacitance sensing responses of the ENICPSs at different operating frequencies. The sensitivities of the impedance, phase, and capacitance responses are determined using equation 1: $S_\gamma = (\Delta\gamma/\gamma_0)/\Delta d$ (1), where $\Delta\gamma$ is the absolute change in the impedance, phase, or capacitance, γ_0 is the value of these parameters when the MUT is absent, and Δd is the distance between the MUT and ENICPSs.

Fig 2 compares the |Z|, phase, and capacitance curves obtained from EIS measurements when the MUT is at different distances. Non-encapsulated and encapsulated ENICPSs exhibit similar trends in their complex impedance data, indicating a consistent sensing mechanism. Nevertheless, the PDMS layer attenuates the sensing response without decreasing the detection range, suggesting a hindrance of the charge distribution stimulated by the MUT presence. Fig 3 displays the impedance, phase, and capacitance responses of the ENICPSs at the selected potential working frequencies. Both ENICPSs demonstrate linear impedance and phase responses. Notably, the non-encapsulated ENICPS reveals impedimetric and phase sensitivities of 4.17%cm^{-1}, 2.52%cm^{-1}, while the encapsulated ENICPS shows sensitivities of 5.78%cm^{-1}, 2.31%cm^{-1}, respectively. The capacitance responses follow an exponential trend. Consequently, capacitance sensitivity is calculated in three different sensing regions: maximum sensitivity (s_1) for distances below 5cm, medium sensitivity (s_2) in the range of 5-9cm, and minimum sensitivity (s_3) for distances larger than 9cm. The non-encapsulated and encapsulated ENICPSs reveal s_1 values of about -4740%cm^{-1} and -40.2%cm^{-1}, respectively.

EIS measurements indicate that the PDMS encapsulation affects the sensing performance without altering the dominant sensing mechanism. In particular, the proposed ENICPSs without and with encapsulation show a detection range of 20-140mm, with s_1 values of -4740%cm^{-1} and -40.2%cm^{-1}, respectively. Their simple and fast fabrication, along with their capability to detect MUT from their impedance, phase, and capacitance responses, enhance their reliability and potential for various fields.

This work has been supported by the Secretariat for Universities and Research of the Ministry of Research and Universities, the European Social Fund, and the project TED2021-131552B-C22.

[1] M. Cedeño Mata et al., Sensors and Actuators A: Physical, vol. 357, pp. 114398, 2023, ISSN: 0924-4247.
[2] A. Coll, S. Bermejo, L. Castañer, Microelectron Eng. 121 (2014) 68–71.
[3] A. Coll et al., Nanoscale Res Lett 8, 26 (2013).

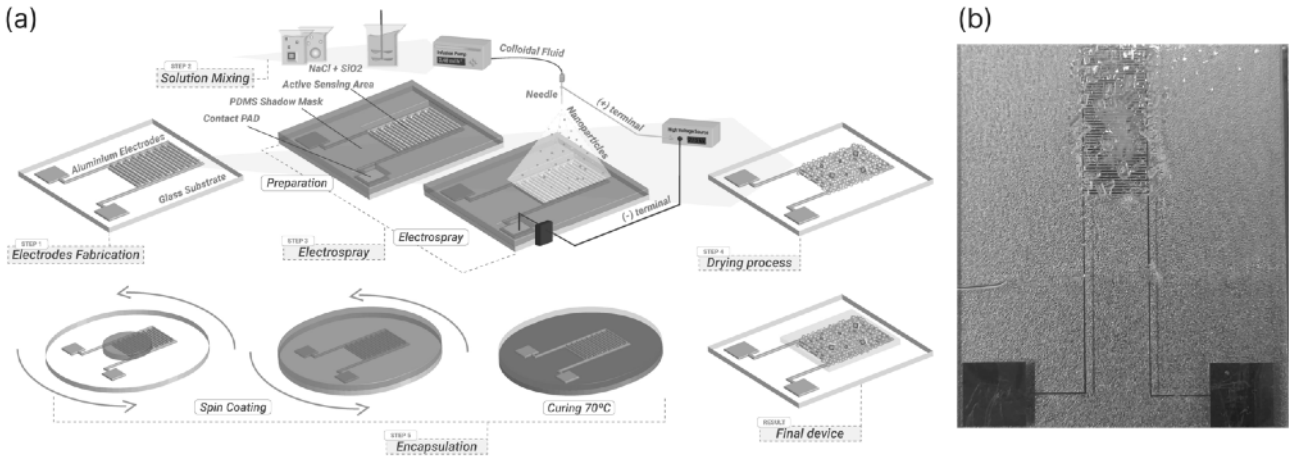

Figure 1. (a) ENICPS fabrication process. Step 1: Fabrication of the electrodes. Step 2: Solution mixing of SiO_2 nanoparticles and NaCl. Step 3: Electrospray of the solution. Step 4: Drying process with high voltage. Step 5: Encapsulation: PDMS spin-coating and curing for 30min at 70ºC. (b) Final device.

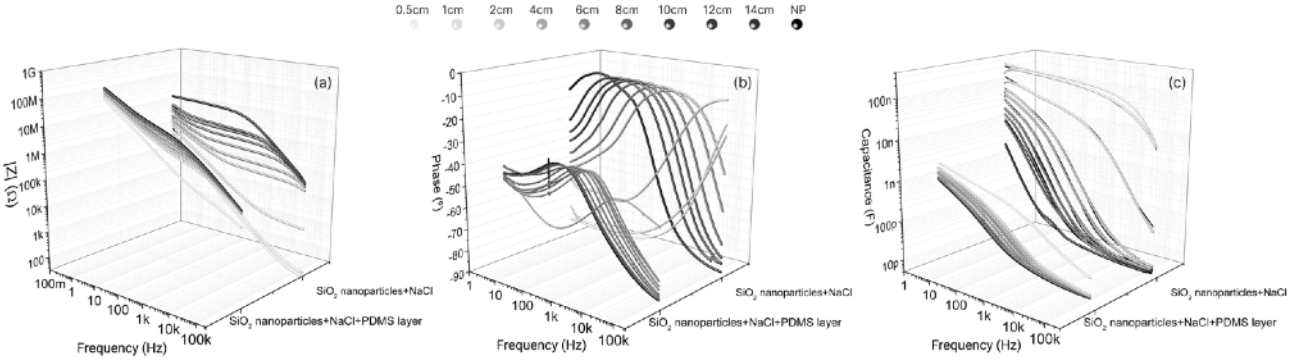

Figure 2. Comparison of: (a) Impedance module vs frequency, (b) Phase curves vs frequency, and (c) Capacitance curves vs frequency. NP (Non-presence).

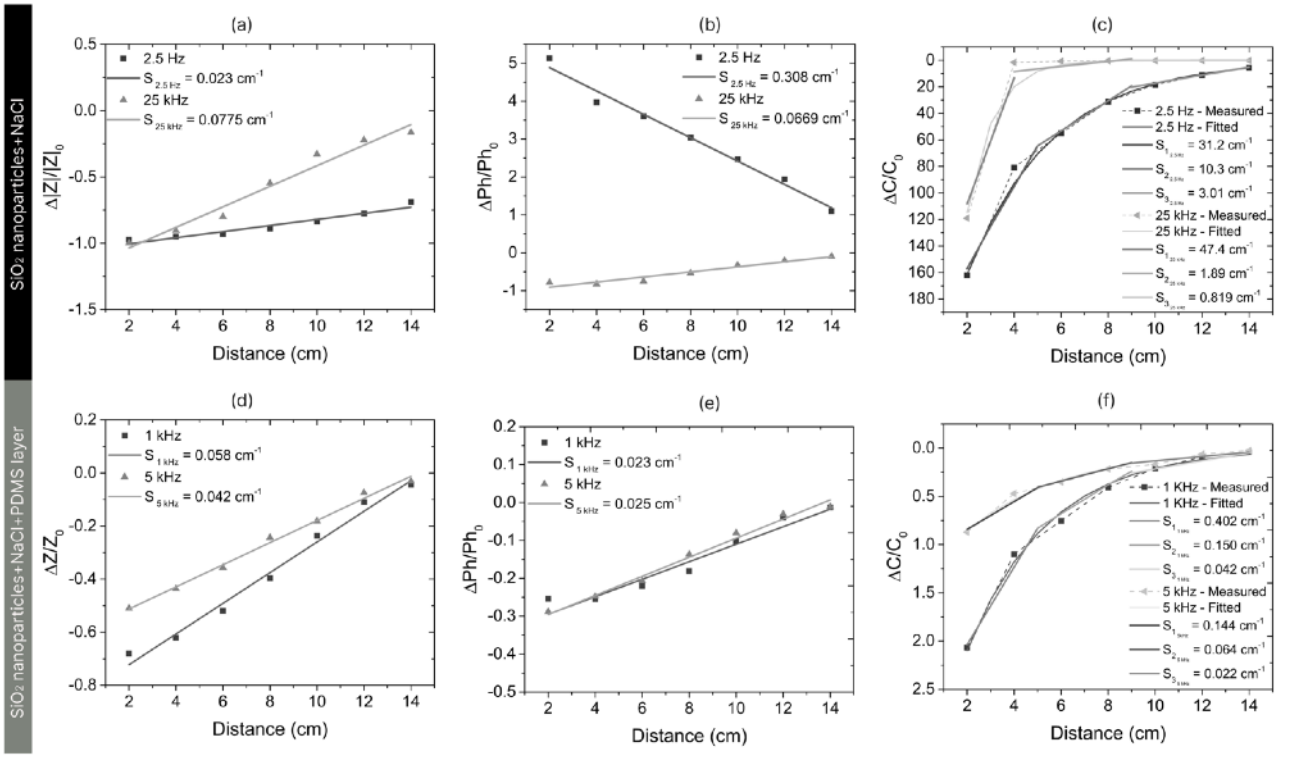

Figure 3. Impedance ((a) and (d)), phase ((b) and (e)) and capacitance ((c) and (f)) responses. The working frequencies for the non-encapsulated and encapsulated ENICSs are 2.5 Hz and 25 kHz, and 1 kHz and 5 kHz

Advances in Micro- and Nanofluidic Devices for Vacuum-Compatible UV Light Experiments

Rukan Nasri [a], Manuel Müller [a], Herbert Atrian Garcia [a], Jeremy Teuber [a], Irene Fernandez-Cuesta [a]

[a] Universität Hamburg, Physics Department, Hamburg, 22761, Germany
e-mail: rnasri@physnet.uni-hamburg.de

UV light is used to analyse a variety of molecular species in solution, being especially useful for spectroscopy of biomolecules. The detection of such biomolecules can be carried out, for example, by absorption or autofluorescence spectroscopy, to obtain intrinsic properties, such as their autofluorescence spectrum or lifetime. In addition, using ultra-short UV laser pulses allows for probing electron dynamics in photoactive processes by performing transient absorption measurements [1].

Extreme UV and short pulses are absorbed, and pulse properties degrade even when propagated in air, so experiments require high vacuum conditions. The state of the art is to use liquid jets to transport and deliver the analytes to the laser beam. Despite their effectiveness, the integration of these jets into vacuum chambers poses significant difficulties and often requires the use of meticulously engineered, costly equipment. Another drawback is that they require relatively large amounts of liquid sample (in the order of mL), which is often expensive and scarce. Micro- and nanofluidic devices would help to overcome these challenges. However, UV light is typically strongly absorbed by most of the materials used to fabricate devices.

To address these challenges, we propose to use micro- and nanofluidic channels in quartz. To confine the liquid, the channels will be sealed with a UV-transparent membrane made from aluminium oxide (Al_2O_3), a few tens of nanometres thick, as an entry point for UV light. Such devices would meet several requirements: (1) the entire material system is UV-transparent; (2) the liquid would be completely contained, preventing leakage into the vacuum chamber; and (3) the UV-transparent membrane would preserve the temporal resolution of short pulses until they interact with the sample. This fluidic chip fabrication concept has the potential to reduce experimental complications and offer an innovative way to perform UV light experiments in vacuum, using only minute amounts of analyte (a few µL).

The device fabrication is based on the combination of imprinting or etching micro- and nanochannels into a substrate, sealing it with a coverslip, and a gas-phase flow-trough process [2] to coat the inner walls of the micro- and nanochannels with a thin layer of Al_2O_3 (Figure 1 (a)). After (selective) coverslip removal, the Al_2O_3 membrane bis released and becomes directly accessible for expereiments. The process has been demonstrated using polymer fluidic chips [2] (Figure 1 (b)), where we have successfully flown micrometric beads (in microchannels), DNA (in nanochannels) and quantum dots (in slits). An additional challenge is that polymers are not compatible with UV light, since they have high autofluorescence and absorption coeficients in that spectral range. Figure 2 (d) shows an example of the autofluorescence that we obtained for typical polymers used for micro- and nanopatterning, like PDMS or Ormostamp. Thus, we are currently extending this technology to quartz substrates (Figure 2).

To test the UV compatibility of the quartz/Al_2O_3 material deposited by our method (Figure 2), we measured the autofluorescence of lambda DNA in TBE 0.5x buffer in a Cary Eclipse fluorescence spectrophotometer using UV light (260 nm) for excitation. We recorded the autofluorescence signal as shown in Figure 3 (a,b), purple lines. We then placed the quartz and quartz/Al_2O_3 samples along the light path and compared the signals obtained (blue and yellow respectively). From the graph we can see that the absorption is negligibly small.

Our results show that the system meets all the requirements, including the feasibility of performing UV light experiments through the proposed material system - aluminium oxide - encapsulated quartz micro- and nanofluidic devices. The next steps include optimising the quartz-based fabrication and testing the vacuum compatibility of the liquid-filled devices.

These devices will allow for simplified experiments with UV light in vacuum chambers, with high control over the liquid sample, while preserving the time resolution of the laser pulses.

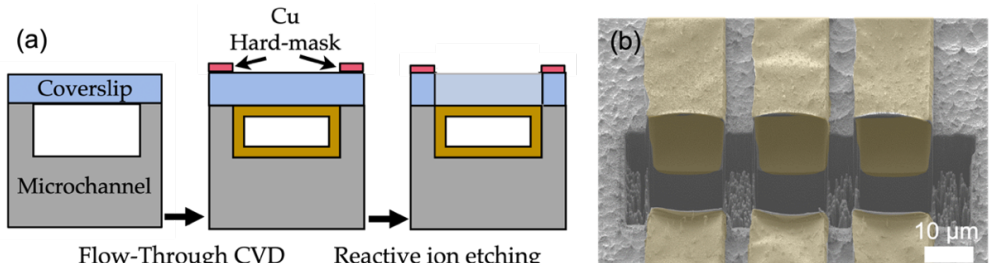

Figure 1: (a) The manufacturing process for the flow cells involves covering a microchannel, etched or imprinted into a substrate, with a coverslip. The channels are then conformally coated with Al_2O_3 using our gas phase deposition process. The coverslip can be etched to reveal the Al_2O_3 layer. (b) Aluminium oxide flow cells in a polymer matrix made of Ormostamp with a fully etched coverslip. The profile can be seen after FIB cross sectioning. Photolithography will be used to define smaller exposed areas for enhanced stability.

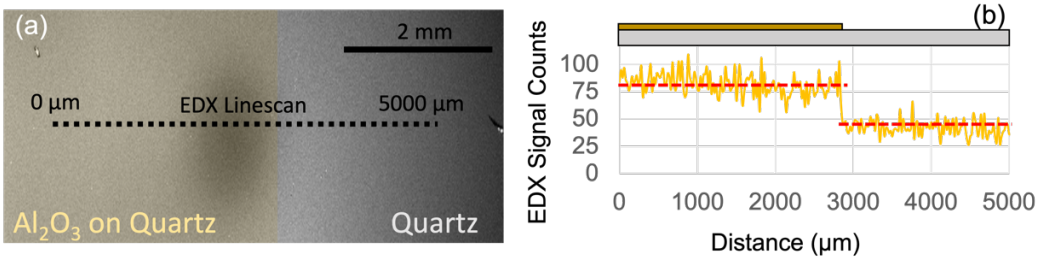

Figure 2: The flat surface of aluminium oxide (30 nm yellow) on a quartz substrate (1mm grey) was inspected via SEM (a) and the elemental composition was verified via EDX (b).

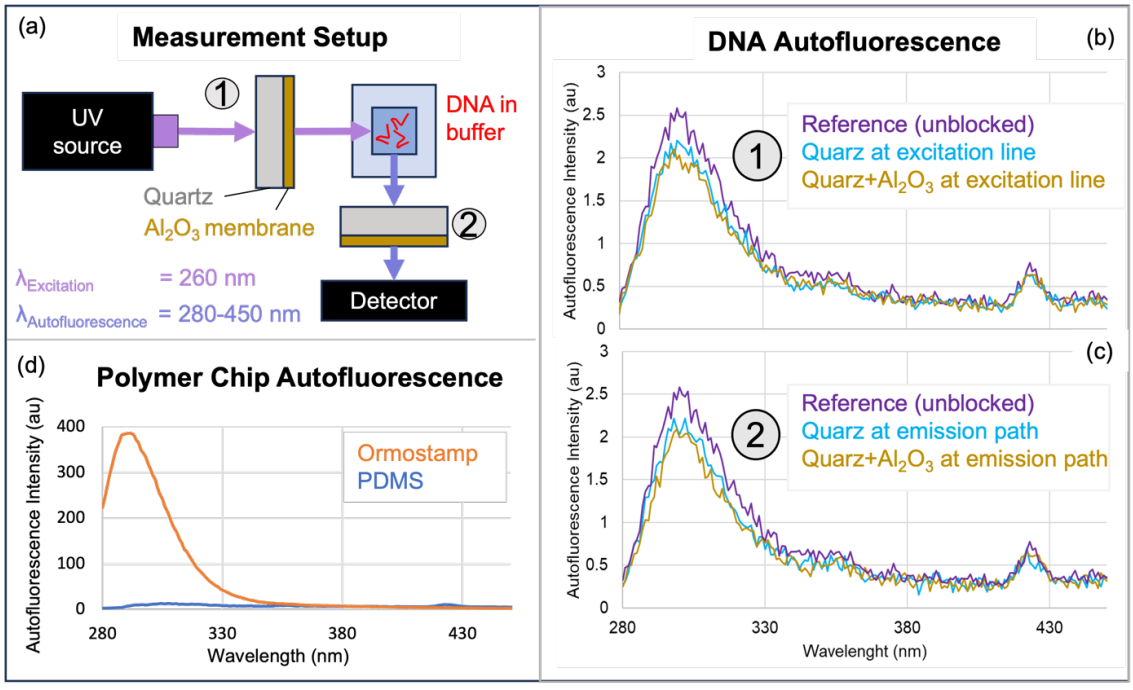

Figure 3: Measurement of autofluorescence of DNA in TBE buffer with 260 nm excitation (a). The autofluorescence signals are shown in (b) and (c), obtained by placing a 1 mm thick quartz substrate (blue lines) or quartz with 30 nm aluminium oxide on top (yellow line) either after excitation (b) or after emission (c). The signal obtained without the samples is shown as a reference (purple line). (d) shows the autofluorescence spectra of two polymers, Ormostamp and PDMS. A comparison of the spectra of DNA and polymers commonly used in microfluidics shows an overlap that makes it impossible to measure the autofluorescence of DNA in these polymer chips.

[1] F. Calegari et al., Science 346 (6207) (2014) 336-339.
[2] M. Müller et al., DE 102020102076A1 (2020) Hamburg, Germany, DPMA.

Enhancing Exciton Emission in Monolayer MoS_2 using Electroplated Plasmonic Gold Nanodiscs

Abhay Anand V S [a], Mihir Kumar Sahoo [a], & *Anshuman Kumar [a]

[a] Laboratory of Optics of Quantum Materials (LOQM), Department of Physics, IIT Bombay, Mumbai, 400076, Maharashtra, India

*Corresponding Author e-mail: anshuman.kumar@iitb.ac.in

The discovery of graphene revamped the field of 2D materials. Transition metal dichalcogenides (TMDCs) are semiconductors in the 2D material family, which gained attention due to their promising optical and electronic properties. MoS_2, $MoSe_2$, WS_2, and WSe_2 are prominent materials in the TMDC family [1,2]. In monolayer form, most TMDCs have a direct bandgap in the visible light spectrum. Atomically thin thickness and low quantum yield are the main challenges which limit TMDC for practical applications. To tackle these challenges of TMDC and achieve effective manipulation of optical properties, integrating subwavelength plasmonic nanostructures with monolayer TMDCs is an effective solution. Plasmonic nanostructures can confine and enhance nearfield intensity during excitation.

In this study, we employed electron beam lithography and electroplating techniques to fabricate an array of gold nanodisc (AuND) capable of significantly enhancing the photoluminescence (PL) of monolayer MoS_2. Quartz is used as a substrate. The cleaned quartz substrate was coated with a five nm-thick adhesive Ti-layer using DC sputtering at a 2.1 nm/min rate. Then, a 20 nm Au film layer was deposited on the Ti-layer using DC sputtering at a 17 nm/min rate, resulting in a transparent and conductive quartz substrate. This conducting layer is essential for electroplating processes. An array of gold nanodisc is created on the sample using electron beam lithography. The nanodisc have a diameter of 300 nm and are spaced 400 nm from centre to centre [3]. Monolayer MoS_2 is grown on the sapphire wafer using the chemical vapour deposition method. The CVD-grown MoS_2 monolayer was transferred onto Gold nanodisc using polystyrene-assisted wet transfer processes.

Monolayer MoS_2 placed on the gold nanodisc array exhibited an impressive photoluminescence enhancement of up to 150 times compared with the non-nanodisc region. To understand the mechanism behind this enhancement, we conducted FDTD simulations. Our findings shed light on the photoluminescence enhancement phenomenon and demonstrate the potential of utilising subwavelength plasmonic nanostructures to overcome the limitations of monolayer MoS_2 and unlock its practical applications in various fields.

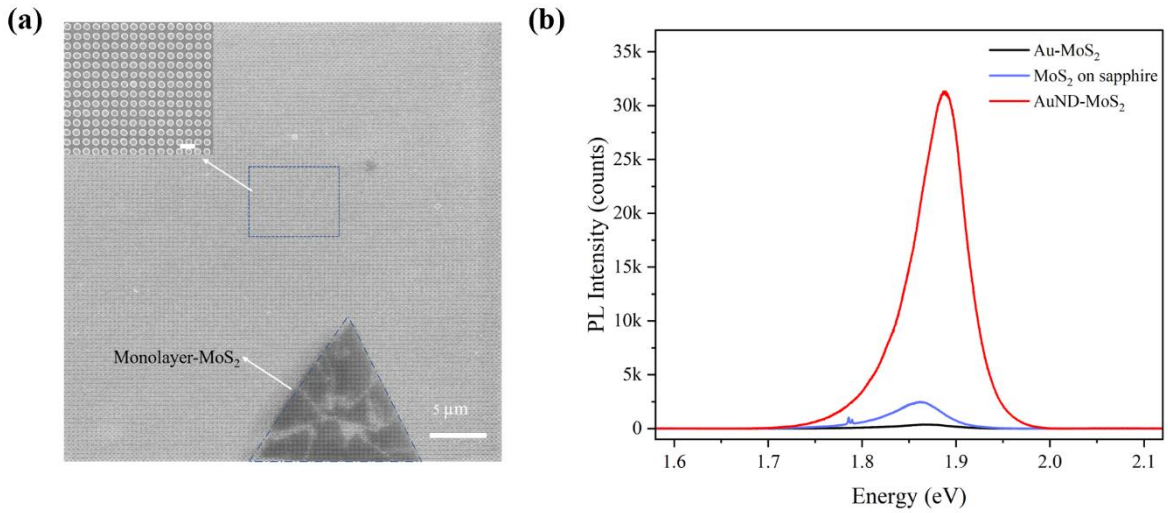

Figure 1. (a) SEM image of AuND-MoS_2 hybrid structure. Inset shows a magnified image of gold nanodisc. The Inset scale bar is 500 nm (b) Emission enhancement results.

References:

[1] KF Mak et al., Physical review letters, 105 (2010), 136805.

[2] Wang et al., Nature Nanotechnology, 7(11), 699-712

[3] MK Sahoo et al., Nanotechnology 34 (2023), 195301-195309.

Novel Developments in Nano/Micro Fabrication Methods and Processes / Track3 - Micro/Nano Engineering for Life Sciences - Papers

Advancements in Fabricating Polymer based Microring Resonators by Nanoimprint Lithography

S. Pandian [a], P. Karvinen [b], H. Rekola [b*], S. Bej [a], P. Muellner[c], M. Eggeling[c], R. Hainberger [c] and T. Niemi [a]

[a] Nanophotonics group, Tampere University, Tampere, Finland
[b] Faculty of Science and Forestry, Department of Physics and Mathematics, University of Eastern Finland, Joensuu, Finland (b* presently with Dispelix)
[c] AIT Austrian Institute of Technology GmbH, Molecular Diagnostics, Vienna, Austria
e-mail: Santhosh.pandian@tuni.fi

Polymeric materials for photonic integrated circuits (PIC) have attracted much interest over the past decades due to their unique properties, including low absorption, wide wavelength range, and simple and low-cost fabrication process [1,2]. When compared to its counterparts (semiconductor materials), the polymer-based materials have the capability to fine tune their refractive index more easily. Polymeric materials also can incorporate active dopants, such as dyes providing optical gain, to realize devices with enhanced functionality. Advanced 3D structures are required to allow a high integration density of the photonic systems. Some of the classic examples of these systems are very large-scale integrated (VLSI) photonics and microring resonators (MRRs) [3]. Polymer based MRRs have been widely used in many applications ranging from optical communication and signal processing to sensing. One important field of application of polymer waveguide MRRs is biosensing, which is highly relevant for medical diagnostics, food analysis, and environmental monitoring due to its high sensitivity and real-time monitoring capabilities [4]. Another interesting area for polymer waveguide MRRs is the realization of miniaturized ultrasonic detectors, which are key elements for photoacoustic imaging [5]. These MRRs have been prepared using the established Nanoimprint Lithography (NIL) technique [1,2,4]. NIL is known for its high resolution, accuracy, and cost-effectiveness in patterning structures on various substrates [1,3].

In this work, we address the fabrication of MRRs that are intended for application as ultrasound detector for photoacoustic imaging in the multimodal bioimaging system. The overarching goal is to reveal drug tolerant persister cells related to breast cancer. While cancer treatment is initially effective in 90% of patients, only 10-25% of breast cancer patients achieve a complete recovery. It is therefore of utmost importance to find the drug tolerant persister cells as early as possible using these imaging platforms and eradicate these therapy resistant breast cancer cells completely [6].

Various substrate materials such as silicon, fused silica, and polymer resists are generally used to fabricate polymer waveguide MRRs via NIL. For our purposes, we chose fused silica substrates due to their high transparency, high thermal stability, and low thermal expansion coefficient. To fabricate the MRRs and other necessary waveguide building blocks such as 1×2 splitters we use the UV-curable hybrid organic-inorganic material ORMOCORE™ as waveguide core material and polydimethyl siloxane as top cladding [2,3,7]. With our NIL process, we achieve a residual layer thickness of <80 nm. In this presentation, we discuss several aspects relevant for achieving improvements compared with previous demonstrations. These include tight confinement of the mode to the waveguide core, low scattering and bending losses, and small ring radii.

Acknowledgements: This work is supported by the REAP project under grant agreement No. 101016964, as a part of the European Union's Horizon 2020 research and innovation programme.

[1] R. Morarescu et al., ICTON IEEE. (2015), 1-4.
[2] R. Landgraf et al., Advanced Sensor Systems and Applications 8561 (2012), 135-146.
[3] R. Kirchner et al., Journal of Lightwave Technology 32 (2014), 1674-1681.
[4] Y. Liang et al., Sensors 19 (2019), 181.
[5] H. Li, et al., Nature Communications 10 (2019), 4277.
[6] M. Liu et al., Journal of Physics: Photonics. 3 (2021), 021001.
[7] https://www.microresist.de/en/produkt/ormocore-and-ormoclad/. Visited 5.6.2023.

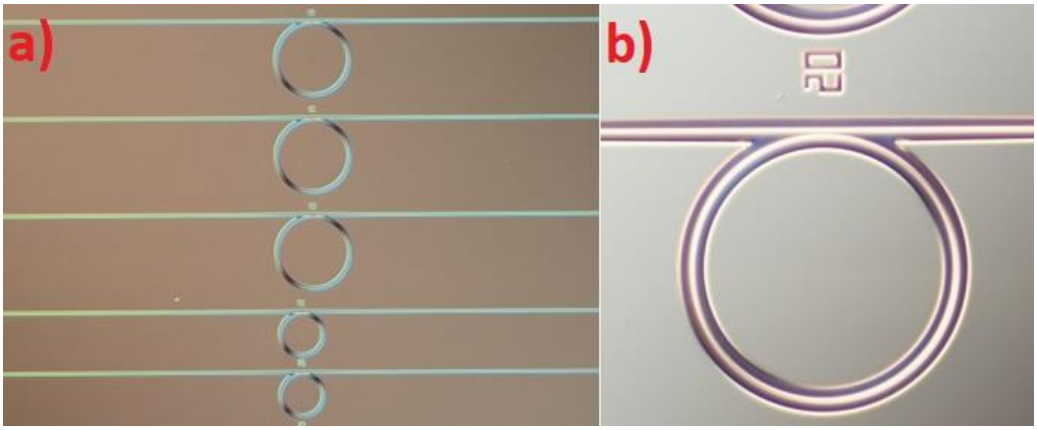

Figure 1. Microscope image of polymer waveguide microring resonators (MRRs) fabricated via UV-cured nanoimprint lithography in ORMOCORE™ on a fused silica substrate: a) MRRs with diameter 70 µm to 120 µm, b) close-up image of a single MRR with 70 µm diameter.

3D Ice Lithography

Bingdong Chang [a], Affan Kaysa Waafi [a], Joachim Lyngholm-Kjærby [a], Rubaiyet I Haque [a], Anpan Han [a]

[a] Department of Civil and Mechanical Engineering, Technical University of Denmark,
Kongens Lyngby, 2800, Denmark
e-mail: anph@dtu.dk

3D lithography has shown its huge potential in micro- and nanofabrication. Based on different interactions mechanisms between materials and energetic particles, various 3D lithography methods have been developed, and the two most popular methods are two-photon lithography (TPL) [1] and focused electron beam induced deposition (FEBID) [2]. TPL requires a delicate photochemical process, which normally happens in liquids and influenced strongly by capillary forces. FEBID can print 3D objects by electron-gas interaction, the resolution limit can be a few nanometers, but the printing speed is limited.

Here we present a 3D lithography strategy with a fundamentally different mechanism compared with TPL and FEBID. By performing a layer-by-layer printing process, focused electron beams interact with condensed vapor films, creating voxels by cross-linking the organic components in each layer. This method is named 3D ice lithography (3DIL), based on the IL technique developed by Han et al. in the last decade [3]. Compared with other 3D lithography methods, 3DIL has some special features: (i) a broad range of materials can be used for fabrication, including organic and organometallic materials, (ii) delicate suspended and hollow structures can be fabricated free from interfacial forces, (iii) hanging structures can be fabricated without using support structures. Besides, 3DIL doesn't require to be operated in expensive cleanroom facilities, and the whole process can be performed with a modified scanning electron microscope (SEM) system, which costs 80.000 euros totally, significantly cheaper than other 3D manufacturing systems like TPL. By using precursors like nonane, the material cost is also much lower compared with photopolymers.

Figure 1 shows the process flow of 3DIL. The printing process starts with design and slicing of 3D models, which will then be transformed into G-code, a standard language for 3D printing. A compact SEM system is then used to read the G-code and scan along coordinates on the sample surface, which is cooled down to cryogenic temperatures and covered by a condensed vapor film. After repeating gas injection and exposure layer by layer, the stage is heated up, leaving a 3D object of cross-linked material. We have designed a printing control program (PCP) to perform the 3DIL process, so the gas injection and e-beam exposure can be executed automatically. The capability of 3DIL is demonstrated by Figure 2. Nonane was used to fabricate an Eiffel tower with up to 500 layers and 28 μm tall (Fig. 2A), the smallest structures are 550 nm wide. A dragon was also fabricated with nonane, where a long hanging "wing" structure is presented (Fig. 2B). An organometallic precursor (dimethyl acetylacetonate gold) was used to fabricate a 3D benchy boat structure (Fig. 2C). With energy-dispersive X-ray spectroscopy (EDS), we can verify the existence of gold element in the 3D structure.

3DIL can be a strong platform for other research fields. We have fabricated 3D woodpile structures with nonane and different designs (Fig. 3A). After an annealing process with argon at 300 °C, the whole structures shrunk by around 30% laterally and 42% vertically (Fig. 3B, Fig. 3C). The reduced lattice size on the structure surface leads to a red shift of reflectance spectrum (Fig. 3D), giving a reddish structural color. Besides, a larger lattice size gives less scattering loss at UV range, making it possible to design nanophotonic devices. Microchannels were also fabricated with an inner diameter between 3.5 – 6.4 μm, and ethanol solution can be observed to move through the channels (Fig. 3E).

We believe 3DIL can complement other existing 3D fabrication methods. It is worth addressing that 3DIL is now supported by Technical University of Denmark to be commercialized for a startup company, we hope this technology to be more accessible for customers from both research institutes and industries in the future.

[1] Q. Ge et al., Sci. Adv. 7.2 (2021) eaba4261
[2] R. Winkler et al., J. Appl. Phys. 125 (2019) 210901.
[3] D. Zhao et al., Sci. Bull. (Beijing) 64 (2019) 865–871

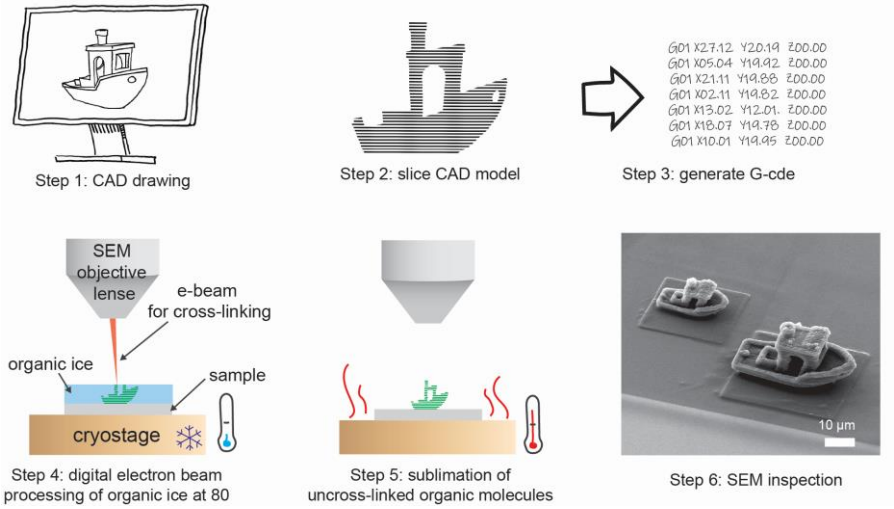

Figure 1. Process flow of 3DIL

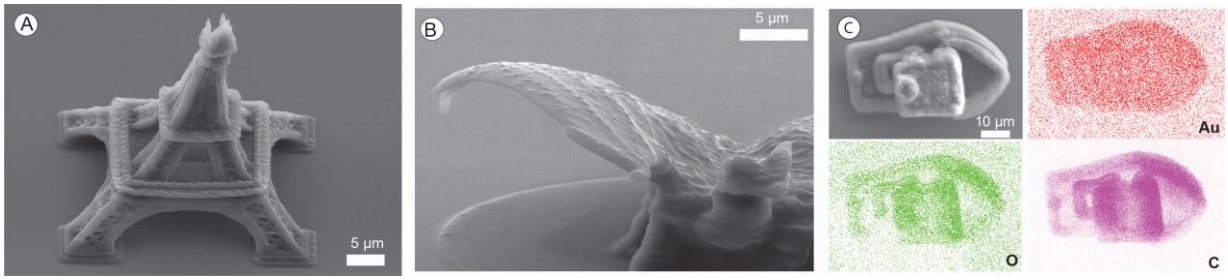

Figure 2. SEM images of 3D fabricated Eiffel tower (A) and dragon (B). SEM image and EDS mapping of 3D benchy boat with organometallic precursor.

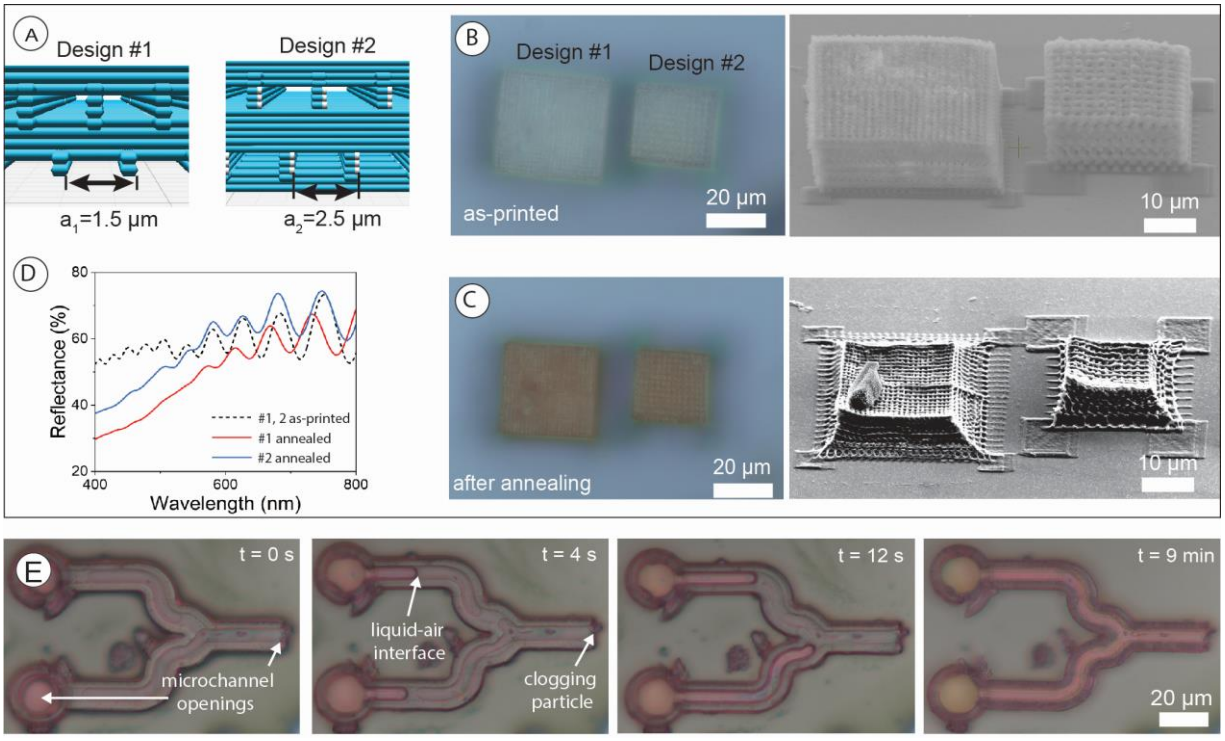

Figure 3. Applications of structures fabricated by 3DIL, including nanophotonic device (A - D) and microfluidic channels (E).

Manipulating droplet motion on superhydrophobic glass by contact electrification

Kuan Ting Chen [a], Jiann Shieh [a],

[a] Department of Materials Science and Engineering, National United University, 36063, Miaoli, Taiwan
e-mail: jshieh@nuu.edu.tw

The manipulation of water droplet movement has garnered significant attention due to its wide range of applications in various fields, such as self-cleaning, heat transfer, and energy harvesting [1]. Various strategies involving both active methods, such as electric and magnetic fields, and passive methods, such as chemical or pressure gradients, have been employed to drive droplet movement. However, a major challenge that remains is overcoming surface resistance to achieve fast movement over long distances. Recently, the generation of static charge through contact electrification has emerged as a promising approach for effective droplet manipulation [2]. While the charging phenomenon has been shown to affect droplet sliding on surfaces and motion in air, the spontaneous repulsion between droplets on surfaces has not been identified, despite being observed in vapor-mediated systems or under external field conditions.

In this study, we present a spontaneous charging method for water droplets to repel each other on surfaces. We grew silica nanowires on a quartz plate to create an insulating superhydrophobic glass [3]. After contact electrification by injecting water, the generated static charge allows pure water droplets to repel each other, preventing them from merging and enabling droplets to become stuck on the surface and even move uphill. Remarkably, these charged droplets can travel at speeds exceeding a few centimeters per second over centimeter-scale distances.

The silica nanowires, grown through active oxidation and vapor-liquid-solid mechanisms, are shown in Fig. 1a. Notably, even after liquid/solid contact electrification, the SEM image reveals that the nanowires remain adhered to the surface, indicating the effectiveness of this process in achieving good adhesion for the nanowires. Following fluoride modification, the glass becomes superhydrophobic, as depicted in the insert in Fig. 1a. The anchoring of fluorine atoms not only reduces the surface energy, but also enhances the ability to capture electrons during water/solid contact. Fig. 1b presents image of water-injection electrification, demonstrating water droplets adhering to the tilt superhydrophobic surface. The charge of a 1×3 cm glass increases from -0.08 nC to -3.308 nC (Fig. 1c) through water-to-glass electron transfer, indicating efficient electrification. The static charge can be almost completely recovered to its initial value after heating at 210°C for 30 minutes (Fig. 1d), supporting that the primary electrification mechanism involves electron transfer [4].

The acquired charge enables droplets to repel each other, as illustrated in Fig. 2a, where a tiny droplet overcomes capillary force and gravity to rebound from a larger droplet. To explore this phenomenon further, we positioned two droplets on an inclined surface (1°) and observed that as they approach each other, they do not coalesce, but instead experience a repulsive force due to their similar charges. This repulsive force can be remarkably strong, propelling the droplets apart, much like being ejected from a slingshot (Fig. 2b). Interestingly, as shown in Fig. 2c, a droplet can even reverse its direction as it encounters another droplet in its

path. For a 9.8-µL water droplet, we measured a transport velocity of 668 mm/s over a distance of 1.27 cm. This nanostructured surface opens up new avenues for investigating the unique properties of regular water droplets, offering exciting prospects for further research.

References:

[1] J. Xu, S. Xiu, Z. Lian, H. Yu, J. Cao, Droplet 1 (2022) 11.

[2] Q. Sun, D. Wang, Y. Li, J. Zhang, S. Ye, J. Cui, L. Chen, Z. Wang, H.-J. Butt, D. Vollmer, X. Deng, Nat. Mater. 18 (2019) 936.

[3] J. Shieh, G.F. Huang, J.Y. Tsai, B.W. Huang, Y.F. Huang, STAR Protocols 3 (2022) 101066.

[4] S. Lin, L. Xu, A. C. Wang, Z.L. Wang, Nat. Commun. 11 (2020) 399.

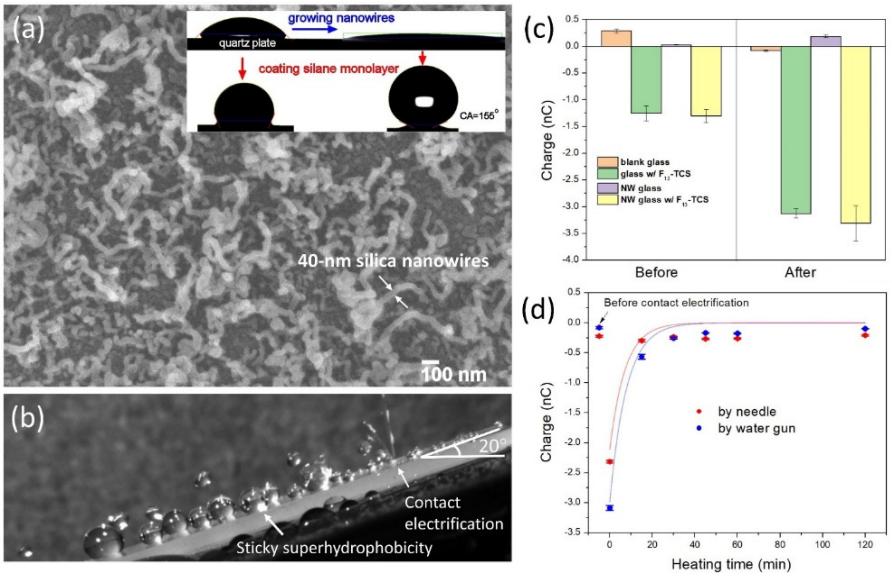

Figure 1. (a) SEM image of silica nanowires. Inset: Contact angle images of silica glass with and without nanowires. (b) Photograph illustrating contact electrification. (c) Charges measured on glass before and after contact electrification. (d) Charge removal by heating.

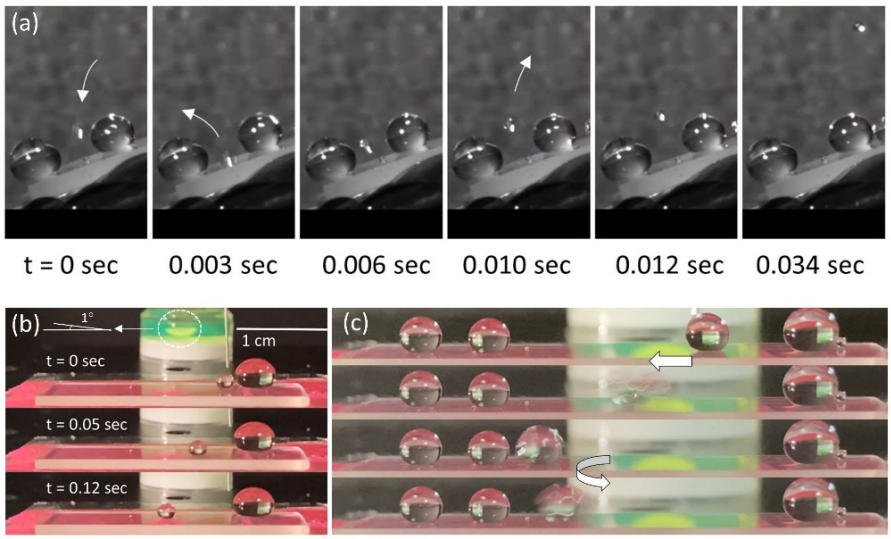

Figure 2. (a) Snapshot of a tiny droplet repelled by a larger one. (b) Picture showing a droplet being ejected by electrostatic forces. (c) Reverse motion of a droplet.

Biodegradable Chitosan / Cellulose Nanocrystals free-standing device as a multifunctional sensor for health applications

Valentina Antonaci [ab], Gaia de Marzo [ab], Laura Blasi [c], Virgilio Brunetti [a], Francesco Rizzi [a], Massimo De Vittorio [ab]

[a] Istituto Italiano di Tecnologia – Center for Biomolecular Nanotechnologies, Lecce, 73010, Italy
[b] Department of Innovation Engineering – Università del Salento, Lecce, 73100, Italy
[c] National Research Council of Italy, Institute for Microelectronics and Microsystems, Campus Ecotekne, Via Monteroni, 73100 Lecce, Italy
email: valentina.antonaci@iit.it

In recent years the use of piezoelectric sensors and biosensors as analytical tools for a quick, accurate, and early diagnosis of human diseases has expanded significantly [1]. For example, their suitability to detect fast pressure-changing stimuli has allowed the development of health monitoring devices, *e.g.* swallowing quality detection in dysphagia-affected people [2]. However, their ability to detect static pressure is much lower, limiting their applications as pressure sensors in artificial electronic skin [3]. A solution is represented by combining piezoelectric materials with nano-materials able to respond to static pressure stimuli by generating visible light signals at different wavelengths, by changing reflection or emitted intensity [4] [5]. In this direction, the use of cellulose nanomaterials (CNM), in particular piezoelectric cellulose nanocrystals (CNC), able to spontaneously self-assemble in colloidal suspension to form a left-handed chiral nematic (or cholesteric) phase, has experienced rapid growth in the fabrication of various type of sensors, such as wearable optical sensor with highly attractive advantages, including inherent electrical safety and immunity to electromagnetic interference [6].

Here we study the morphological characteristics of piezoelectric cellulose nanocrystals in order to enhance the sensing ability of a flexible and biodegradable piezoelectric thin film based on chitosan [7], a biopolymer, derived from crustaceans' exoskeleton and fungi cell walls, which can be significantly recycled from the seafood industry's waste. This approach represents a promising strategy to develop a biodegradable and sustainable material to be employed both in dynamic and static stimuli pressure sensing by combining piezoelectric and optical signal.

We first optimized the synthesis of round-shaped CNCs thus having a large specific surface area with uniform particle size and high thermal stability [8]. We started from pure cellulose powder, as raw material, and we used sulfuric acid hydrolysis to obtain round-shaped CNCs with particle diameter range between 5 and 20 nm. The morphology of CNCs (Fig. 1a) was investigated by Scanning Electron Microscopy (SEM), Atomic Force Microscopy (AFM) and Transmission Electron Microscopy (TEM). The images clearly showed the formation of round-shaped CNCs (Fig.1b and 1c). Then, we realized composite chitosan/CNCs films to investigate how the combination of the two materials can affect the piezoelectric response and we analyzed them by piezoresponse force microscopy (PFM). A wet chitosan film is deposited on a glass substrate prepared by oxygen plasma treatment and coated with an aqueous solution of PEDOT: PSS and Glycerol, working as a bottom electrode, to obtain a flat chitosan surface; then we added CNCs solution onto the chitosan piezoelectric film (Fig. 2a). We investigate the piezoelectric behavior at the nanoscale of both bare chitosan film and composite chitosan/CNCs domains. Indeed, we extrapolated a piezoelectric coefficient (d_{33}) of 8 pC/N for chitosan and 13 pC/N for chitosan/CNCs domains (Fig. 2b). These experimental results demonstrated an improved piezoelectric behavior of the obtained composite material. Finally, in order to fabricate a free-standing, flexible, and biocompatible sensing device we also exploited a layer-by-layer (LbL) technique by depositing CNCs solution directly on electrode surface before chitosan film deposition. The device is then completed with a top electrode and coated with Parylene-C to have both chemical and electrical insulation (Fig. 3a). The piezoelectric response of the so-realized chitosan/CNCs device having an area of about 8 x 8 mm^2, was measured thanks to a customized setup, showing a d_{33} value of 13,7 pC/N (Fig. 3b). Investigation on the optical properties of chitosan/CNCs will be carried out in future work aiming to obtain a sustainable and biodegradable wearable multifunctional sensor.

[1] R. Lay et al., RSC advances 11(2021) 30657-30673.
[2] L. Natta et al., ACS Sens. 6 (2021) 1761–17692021.
[3] L. Yang et al., ACS applied materials & interfaces 11.4 (2019): 4318-4327.
[4] Y. Li et al., Advanced Fiber Materials (2022): 1-9.

[5] D. Lu et al., Advanced Materials 35.7 (2023): 2209117
[6] K. B. Teodoro et al., ACS Applied Materials & Interfaces 12.9 (2019): 10908-1091
[7] G. de Marzo et al., Advanced Electronic Materials (2022), 2200069.
[8] DK. Patel et al., Carbohydrate Polymers 303 (2023): 120464

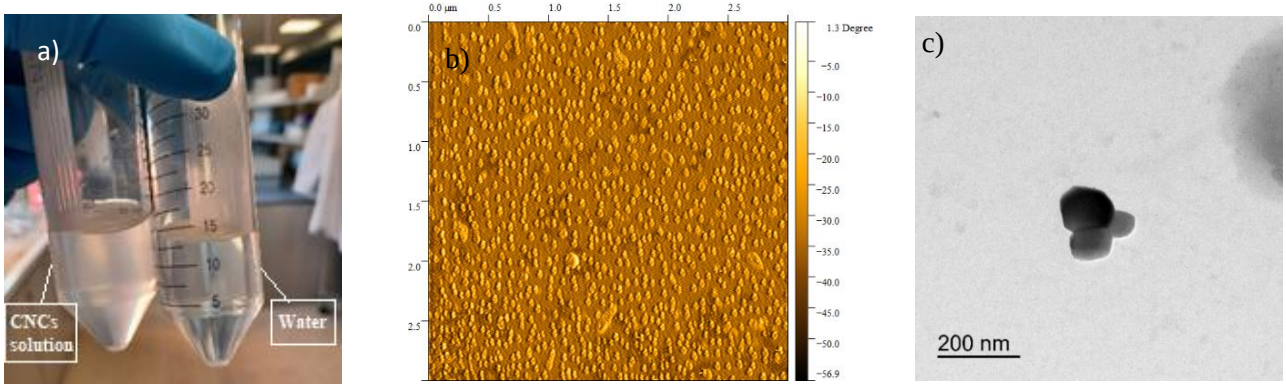

Figure 1. a) Cellulose nanocrystals solution. b) AFM image of the CNCs. c) TEM image of the CNCs

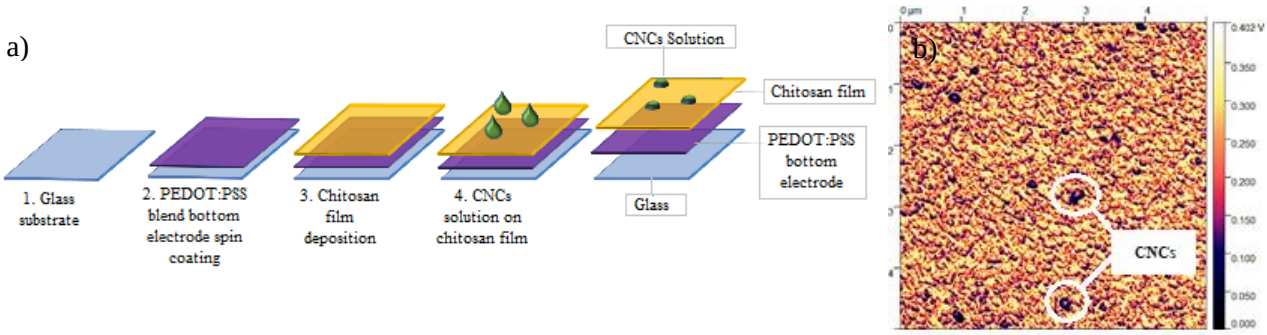

Figure 2. a) Fabrication steps of the Chitosan/CNCs film. b) Piezoelectric force microscopy Chitosan/CNCs film

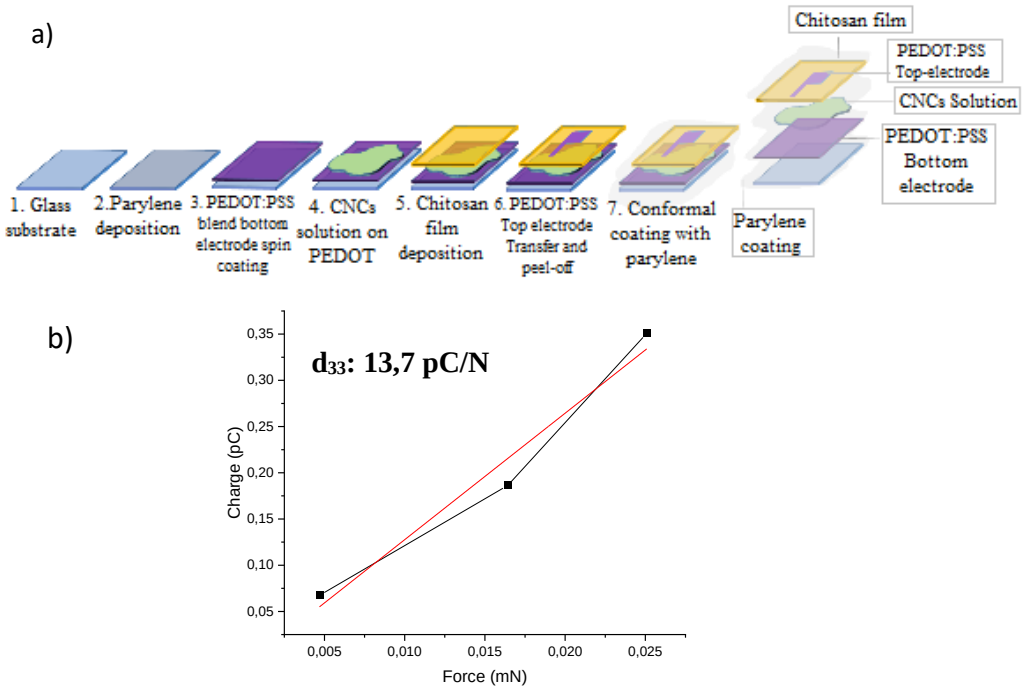

Figure 3. a) Fabrication steps of the Chitosan/CNCs device b) Plot relative of the piezoelectric coefficient obtained by a customized setup

Authors Index


HEIDELBERG
INSTRUMENTS
The power of direct writing

RAITH

ALLRESIST

micro resist technology

AMO

JEOL
Solutions for Innovation

STS ELIONIX

amcoss
systems
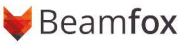
Beamfox

Fraunhofer
ENAS

EVG

FOCUS

GenISys
Advancing the Standard

idonus

nano
scribe
A BICO COMPANY

nanosurf

osiris

OXFORD
INSTRUMENTS

Polytec

SÜSS MicroTec

upnano

vistec
Electron Beam

BMF
BOSTON MICRO FABRICATION

HETEROMERGE
FUNCTIONAL 3D MICRO-PRINTING

ims chips

microlight3D

nano analytik
Fascination of nanoanalytics

PolyPhotonics Berlin e.V.
Great in Optics – Small in Size

PROFACTOR

Quantum Design
EUROPE

SCIL
Nanoimprint solutions

SPS
SEMICONDUCTOR
PRODUCTION
SYSTEMS
Your guide to innovative production

STENSBORG

θmetrisis

Zurich
Instruments

zyvex
LABS

ATTO3D

Copenhagen
Microsystems

ELVEFLOW
MICROFLUIDICS
INNOVATION
CENTER

OpTool

NuFLARE

Quantified Air

SENTECH

TOPPAN
TOPPAN PHOTOMASK

veonis
TECHNOLOGIES